

# Nanocrystals-Related Synthesis, Assembly, and Energy Applications

Guest Editors: Quanqin Dai, Bo Zou, William W. Yu, and Jaetae Seo





---

# **Nanocrystals-Related Synthesis, Assembly, and Energy Applications**

Journal of Nanomaterials

---

**Nanocrystals-Related Synthesis, Assembly,  
and Energy Applications**

Guest Editors: Quanqin Dai, Bo Zou, William W. Yu,  
and Jaetae Seo



---

Copyright © 2011 Hindawi Publishing Corporation. All rights reserved.

This is a special issue published in volume 2011 of “Journal of Nanomaterials.” All articles are open access articles distributed under the Creative Commons Attribution License, which permits unrestricted use, distribution, and reproduction in any medium, provided the original work is properly cited.

## Editor-in-Chief

Michael Z. Hu, Oak Ridge National Laboratory, USA

## Advisory Board

James H. Adair, USA  
C. Jeffrey Brinker, USA  
T. Hyeon, Republic of Korea  
Nathan Lewis, USA

Ed Ma, USA  
Alon V. McCormick, USA  
Gary L. Messing, USA  
Zhonglin Wang, USA

Enge Wang, China  
Ching Ping Wong, USA  
N. Xu, China  
Jackie Y. Ying, Singapore

## Associate Editors

Xuedong Bai, China  
Theodorian Borca-Tasciuc, USA  
Christian Brosseau, France  
Sang-Hee Cho, Republic of Korea  
Cui ChunXiang, China  
Ali Eftekhari, USA  
Claude Estournes, France  
Alan Fuchs, USA  
Lian Gao, China  
Hongchen Chen Gu, China  
Michael Harris, USA  
Justin D. Holmes, Ireland  
David Hui, USA  
Wanqin Jin, China

Rakesh K. Joshi, USA  
Do Kyung Kim, Republic of Korea  
Kin Tak Lau, Australia  
Burtrand Lee, USA  
Jun Li, Singapore  
Shijun Liao, China  
Gong Ru Lin, Taiwan  
J. -Y. Liu, USA  
Jun Liu, USA  
Songwei Lu, USA  
Daniel Lu, China  
Gaurav Mago, USA  
Sanjay R. Mathur, Germany  
Nobuhiro Matsushita, Japan

Sherine Obare, USA  
P. Panine, France  
Edward Andrew Payzant, USA  
Donglu Shi, USA  
Bohua Sun, South Africa  
Maryam Tabrizian, Canada  
Theodore Tsotsis, USA  
Xiaogong Wang, China  
Yong Wang, USA  
Michael S. Wong, USA  
Ping Xiao, UK  
Zhi-Li Xiao, USA  
Doron Yadlovker, Israel  
Kui Yu, Canada

# Contents

**Nanocrystals-Related Synthesis, Assembly, and Energy Applications**, Quanqin Dai, Bo Zou, William W. Yu, Jaetae Seo, and Michael Z. Hu  
Volume 2011, Article ID 237050, 2 pages

**Preparation, Modification, and Application of Starch Nanocrystals in Nanomaterials: A Review**, Ning Lin, Jin Huang, Peter R. Chang, Debbie P. Anderson, and Jiahui Yu  
Volume 2011, Article ID 573687, 13 pages

**Atoms and Nanoparticles of Transition Metals as Catalysts for Hydrogen Desorption from Magnesium Hydride**, N. Bazzanella, R. Checchetto, and A. Miotello  
Volume 2011, Article ID 865969, 11 pages

**Synthesis of Bismuth Ferrite Nanoparticles via a Wet Chemical Route at Low Temperature**, Yongming Hu, Linfeng Fei, Yiling Zhang, Jikang Yuan, Yu Wang, and Haoshuang Gu  
Volume 2011, Article ID 797639, 6 pages

**CdS Nanotubes and Y-Branched Nanochannels in AAM Fabricated by a Double Diffusion Route**, Yong Lv, Weifeng Liu, Jianming Huang, and Lianzeng Yao  
Volume 2011, Article ID 546715, 6 pages

**Synthesis of Vertically Aligned Dense ZnO Nanowires**, Lihong Gong, Xiang Wu, Huibo Chen, Fengyu Qu, and Maozhong An  
Volume 2011, Article ID 428172, 5 pages

**A Rational Self-Sacrificing Template Route to LiMn<sub>2</sub>O<sub>4</sub> Nanotubes and Nanowires**, Baojun Yang, Xinsong Yuan, and Duoli Chai  
Volume 2011, Article ID 197265, 5 pages

**Mechanism and Growth of Flexible ZnO Nanostructure Arrays in a Facile Controlled Way**, Yangping Sheng, Yang Jiang, Xinzheng Lan, Chun Wang, Shanying Li, Xinmei Liu, and Honghai Zhong  
Volume 2011, Article ID 473629, 12 pages

**Synthesis of Ag Nanostructures by Photochemical Reduction Using Citrate-Capped Pt Seeds**, Hyeong-Ho Park, Xin Zhang, Yong-June Choi, Hyung-Ho Park, and Ross H. Hill  
Volume 2011, Article ID 265287, 7 pages

**Core-Shell Nanostructure of  $\alpha$ -Fe<sub>2</sub>O<sub>3</sub>/Fe<sub>3</sub>O<sub>4</sub>: Synthesis and Photocatalysis for Methyl Orange**, Yang Tian, Di Wu, Xiao Jia, Binbin Yu, and Sihui Zhan  
Volume 2011, Article ID 837123, 5 pages

**Hydrothermal Synthesis and Characterization of Single-Crystalline  $\alpha$ -Fe<sub>2</sub>O<sub>3</sub> Nanocubes**, Wenqing Qin, Congren Yang, Ran Yi, and Guanhua Gao  
Volume 2011, Article ID 159259, 5 pages

**Radiolytic Synthesis of Pt-Ru Catalysts Based on Functional Polymer-Grafted MWNT and Their Catalytic Efficiency for CO and MeOH**, Dae-Soo Yang, Kwang-Sik Sim, Hai-Doo Kwen, and Seong-Ho Choi  
Volume 2011, Article ID 134721, 8 pages

**Preparation and Magnetic Properties of ZnFe<sub>2</sub>O<sub>4</sub> Nanotubes**, Yan Xu, Yantian Liang, Lijuan Jiang, Huarui Wu, Hongzhi Zhao, and Desheng Xue  
Volume 2011, Article ID 525967, 5 pages

**Tailored 3D CuO Nanogrid Formation**, Jusang Lee and Pelagia I. Gouma  
Volume 2011, Article ID 863631, 6 pages

**Preparation and Characterization of Nanozeolite NaA from Rice Husk at Room Temperature with Organic Additives**, Zahra Ghasemi and Habibollah Younesi  
Volume 2011, Article ID 858961, 8 pages

**Towards a Reproducible Synthesis of High Aspect Ratio Gold Nanorods**, Susanne Koepl, Christian Solenthaler, Walter Caseri, and Ralph Spolenak  
Volume 2011, Article ID 515049, 13 pages

**Simple Synthesis and Luminescence Characteristics of PVP-Capped GeO<sub>2</sub> Nanoparticles**, Wei Wu, Xu Zou, Quanjun Li, Bingbing Liu, Bo Liu, Ran Liu, Dedi Liu, Zepeng Li, Wen Cui, Zhaodong Liu, Dongmei Li, Tian Cui, and Guangtian Zou  
Volume 2011, Article ID 841701, 5 pages

**Mesoporous Titania Nanocrystals by Hydrothermal Template Growth**, Giuseppe Cappelletti, Silvia Ardizzone, Francesca Spadavecchia, Daniela Meroni, and Iolanda Biraghi  
Volume 2011, Article ID 597954, 9 pages

**Synthesis and Characterization of Nanometer Ce<sub>0.75</sub>Zr<sub>0.25</sub>O<sub>2</sub> Powders by Solid-State Chemical Reaction Method**, Yuying Zheng, Zhengfa Hu, Huimin Huang, Wenjin Ji, Ming Sun, and Changshui Chen  
Volume 2011, Article ID 657516, 7 pages

**A User-Friendly Method for Synthesizing High-Quality NaYF<sub>4</sub>:Yb,Er(Tm) Nanocrystals in Liquid Paraffin**, Sen Liang, Yi Liu, Yue Tang, Yue Xie, Haizhu Sun, Hao Zhang, and Bai Yang  
Volume 2011, Article ID 302364, 7 pages

**Facile Synthesis of Monodisperse ZnO Nanocrystals by Direct Liquid Phase Precipitation**, Lan Chen, Justin D. Holmes, Sonia Ramírez-García, and Michael A. Morris  
Volume 2011, Article ID 853832, 9 pages

**Simple Synthesis of Flower-Like In<sub>2</sub>S<sub>3</sub> Structures and Their Use as Templates to Prepare CuS Particles**, Xia Sheng, Lei Wang, Guanbi Chen, and Deren Yang  
Volume 2011, Article ID 280216, 5 pages

**An Experimental Study on the Shape Changes of TiO<sub>2</sub> Nanocrystals Synthesized by Microemulsion-Solvothermal Method**, Wei Kong, Bo Liu, Bo Ye, Zhongping Yu, Hua Wang, Guodong Qian, and Zhiyu Wang  
Volume 2011, Article ID 467083, 6 pages

**Optical Properties of Linoleic Acid Protected Gold Nanoparticles**, Ratan Das, Siddartha S. Nath, and Ramendu Bhattacharjee  
Volume 2011, Article ID 630834, 4 pages

**Pulsed Current Activated Consolidation of Nanostructured Fe<sub>3</sub>Al and Its Mechanical Property,**

Tae-Wan Kim, In-Yong Ko, Jung-Mann Doh, Jin-Kook Yoon, and In-Jin Shon

Volume 2011, Article ID 798257, 5 pages

**Microstructure and Corrosion Behavior of Ni-Alloy/CrN Nanolayered Coatings,**

Hao-Hsiang Huang, Fan-Bean Wu, Jyh-Wei Lee, and Li-Chun Chang

Volume 2011, Article ID 137498, 6 pages

**Study of the P-Type Doping Properties of ZnS Nanocrystals,**

Xiying Ma

Volume 2011, Article ID 952616, 5 pages

**Structural and Mechanical Properties of CrN<sub>x</sub> Coatings Deposited by Medium-Frequency Magnetron Sputtering with and without Ion Source Assistance,**

Can Xin Tian, Bing Yang, Jun He, Hong Jun Wang, and De Jun Fu

Volume 2011, Article ID 534647, 7 pages

**Structure and Optical Properties of Silicon Nanocrystals Embedded in Amorphous Silicon Thin Films**

**Obtained by PECVD,** B. M. Monroy, A. Remolina, M. F. García-Sánchez, A. Ponce, M. Picquart, and G. Santana

and G. Santana

Volume 2011, Article ID 190632, 9 pages

**Large-Scale Synthesis and Self-Assembly of Monodisperse Spherical TiO<sub>2</sub> Nanocrystals,**

Wei Kong, Chao Chen, Kaiguang Mai, Xinchao Shi, Rong Hu, and Zhiyu Wang

Volume 2011, Article ID 526246, 4 pages

**Controllable Assembly of Hydrophobic Superparamagnetic Iron Oxide Nanoparticle with mPEG-PLA Copolymer and Its Effect on MR Transverse Relaxation Rate,**

Xuan Xie and Chunfu Zhang

Volume 2011, Article ID 152524, 7 pages

**Preparation and Ordered Self-Assembly of Nano-Pd-Ga/PMMA by Ultrasonic,**

Xu Guo Cai, DAI Ming Hu, JI Xiao Li, Zhang Xiao Mei, and Xing Hong Long

Volume 2011, Article ID 368152, 6 pages

**Linear Assemblies of BN Nanosheets, Fabricated in Polymer/BN Nanosheet Composite Film,**

Hong-Baek Cho, Tadachika Nakayama, Tsuneo Suzuki, Satoshi Tanaka, Weihua Jiang, Hisayuki Suematsu, and Koichi Niihara

and Koichi Niihara

Volume 2011, Article ID 693454, 7 pages

**GISAXS View of Induced Morphological Changes in Nanostructured CeVO<sub>4</sub> Thin Films,**

Magdy Lučić Lavčević, Aleksandra Turković, Pavo Dubček, Zorica Crnjak Orel, Bojan Orel, and Sigrid Bernstorff

Bernstorff

Volume 2011, Article ID 303808, 7 pages

**Electronic-Excitation-Induced Processing in GaSb Compound Nanoparticles,**

H. Yasuda and H. Mori

Volume 2011, Article ID 901930, 4 pages

**Constitutive Rheological Modeling of Flow Serration Behaviour in Metallic Glasses Showing Nanocrystallization during Deformation**, M. A. Yousfi, K. Hajlaoui, Z. Tourki, and A. R. Yavari  
Volume 2011, Article ID 910962, 8 pages

**Fluoride Nanoscintillators**, Luiz G. Jacobsohn, Kevin B. Sprinkle, Steven A. Roberts, Courtney J. Kucera, Tiffany L. James, Eduardo G. Yukihara, Timothy A. DeVol, and John Ballato  
Volume 2011, Article ID 523638, 6 pages

**Electrodeposition of Nanometer-Sized Ferric Oxide Materials in Colloidal Templates for Conversion of Light to Chemical Energy**, James M. Gardner, Su Kim, Peter C. Searson, and Gerald J. Meyer  
Volume 2011, Article ID 737812, 8 pages

**CdSe Quantum Dots Sensitized Mesoporous TiO<sub>2</sub> Solar Cells with CuSCN as Solid-State Electrolyte**, Guanbi Chen, Lei Wang, Yu Zou, Xia Sheng, Hongjuan Liu, Xiaodong Pi, and Deren Yang  
Volume 2011, Article ID 269591, 5 pages

**Preparation of Nanoporous TiO<sub>2</sub> Electrodes for Dye-Sensitized Solar Cells**, Hsiue-Hsyan Wang, Chaochin Su, Huei-Siou Chen, Yi-Cheng Liu, Yi-Wen Hsu, Nai-Mu Hsu, and Wen-Ren Li  
Volume 2011, Article ID 547103, 7 pages

**Preparation and Characterization of Pure Rutile TiO<sub>2</sub> Nanoparticles for Photocatalytic Study and Thin Films for Dye-Sensitized Solar Cells**, Huei-Siou Chen, Chaochin Su, Ji-Lian Chen, Tsai-Yin Yang, Nai-Mu Hsu, and Wen-Ren Li  
Volume 2011, Article ID 869618, 8 pages

**Comparative Solid Phase Photocatalytic Degradation of Polythene Films with Doped and Undoped TiO<sub>2</sub> Nanoparticles**, Wasim Asghar, Ishtiaq A. Qazi, Hassan Ilyas, Aftab Ahmad Khan, M. Ali Awan, and M. Rizwan Aslam  
Volume 2011, Article ID 461930, 8 pages

**Photocatalytic Degradation of Nitro and Chlorophenols Using Doped and Undoped Titanium Dioxide Nanoparticles**, Hassan Ilyas, Ishtiaq A. Qazi, Wasim Asgar, M. Ali Awan, and Zahir-ud-din Khan  
Volume 2011, Article ID 589185, 8 pages

**Influence of Lithium on Nanosized Films of Fe<sub>2</sub>O<sub>3</sub>**, A. Turković, M. Ivanda, M. Bitenc, and Z. Crnjak Orel  
Volume 2011, Article ID 967307, 8 pages

**Atomic-Level Investigation of CH<sub>x</sub> and C<sub>2</sub>H<sub>x</sub> Adsorption on  $\beta$ -SiC (111) Surface for CVD Diamond Growth from DFT Calculations**, Naichao Chen and Fanghong Sun  
Volume 2011, Article ID 910372, 6 pages

**Size-Dependent Elastic Modulus and Vibration Frequency of Nanocrystals**, Lihong Liang, Hansong Ma, and Yueguang Wei  
Volume 2011, Article ID 670857, 6 pages

**Initial Stage of Consolidation of Silicon-Carbide Nanocrystals under Pressure: A Tight-Binding Molecular-Dynamics Study**, Kenji Tsuruta  
Volume 2011, Article ID 308495, 6 pages

**Effect of the Dispersibility of Nano-CuO Catalyst on Heat Releasing of AP/HTPB Propellant,**

Yi Yang, Xinjie Yu, Jun Wang, and Yaxue Wang

Volume 2011, Article ID 180896, 5 pages

**In Situ Investigation of the Silicon Carbide Particles Sintering,** Yu Niu, Feng Xu, Xiaofang Hu,

Jianhua Zhao, Hong Miao, Xiaoping Wu, and Zhong Zhang

Volume 2011, Article ID 728617, 6 pages

**$\text{Li}_4\text{Ti}_5\text{O}_{12}$  Heattreated under Nitrogen Ambient with Outstanding Rate Capabilities,** Rui Xu, Junrong Li,

Zilong Tang, and Zhongtai Zhang

Volume 2011, Article ID 635416, 6 pages

## Editorial

# Nanocrystals-Related Synthesis, Assembly, and Energy Applications

Quanqin Dai,<sup>1</sup> Bo Zou,<sup>2</sup> William W. Yu,<sup>3</sup> Jaetae Seo,<sup>4</sup> and Michael Z. Hu<sup>1</sup>

<sup>1</sup>Oak Ridge National Laboratory, Oak Ridge, TN 37831, USA

<sup>2</sup>State Key Laboratory of Superhard Materials, Jilin University, Changchun 130012, China

<sup>3</sup>Center for Biological and Environmental Nanotechnology, Rice University, Houston, TX 77005, USA

<sup>4</sup>Department of Physics, Hampton University, Hampton, VA 23668, USA

Correspondence should be addressed to Quanqin Dai, connectdai@hotmail.com

Received 10 December 2010; Accepted 10 December 2010

Copyright © 2011 Quanqin Dai et al. This is an open access article distributed under the Creative Commons Attribution License, which permits unrestricted use, distribution, and reproduction in any medium, provided the original work is properly cited.

Fundamental material properties have been dramatically altered in the nanoscale regime because of quantum confinement effect. The unique size-tunable functionalities of nanomaterials make them involved in an extensive variety of energy applications, such as light-emitting diodes and solar cells. These applications have been demonstrated to cut energy consumption. In response to the ever-growing energy demands as well as the concerns of global warming, researchers are actively placing their enormous emphasis on the exploration of energy savings. During this exploration, the primary stage requires the design of appropriate strategies for the synthesis of high-quality nanocrystals in terms of size uniformity and superior optical/electronic properties. Especially, there is a need to seek green-chemistry approaches for the synthesis of environmentally benign and user-friendly nanocrystals. Another recent area of focus is the use of individual nanocrystals as building blocks for self-assembly, providing new opportunities to improve the nanocrystal performance.

Therefore, we organize the current special issue for *Journal of Nanomaterials* to provide the authors with a platform and readers with the latest achievements of nanocrystals-related synthesis, assembly, and energy applications. This special issue focuses on the fundamental science and technical applications of nanocrystals, covering the nanocrystals-related research area of synthesis, characterization, properties, assembly, films, processing, modeling, and devices for energy applications.

The articles related to synthesis, characterization and properties in this special issue include studies of the mechanisms and growth of flexible ZnO nanostructure arrays, facile

synthesis of monodisperse ZnO nanocrystals, synthesis of vertically aligned dense ZnO nanowires, CdS nanotubes and Y-branched nanochannels fabricated by a double diffusion route, hydrothermal synthesis and characterization of single-crystalline  $\alpha$ -Fe<sub>2</sub>O<sub>3</sub> nanocubes, a user-friendly method for synthesizing high-quality NaYF<sub>4</sub>:Yb,Er(Tm) nanocrystals, a rational self-sacrificing template route to LiMn<sub>2</sub>O<sub>4</sub> nanotubes and nanowires, synthesis of bismuth ferrite nanoparticles via a wet-chemical route at low temperature, synthesis of Ag nanostructures by photochemical reduction using citrate-capped Pt seeds, study of the P-type doping properties of ZnS nanocrystals, structural and mechanical properties of CrN<sub>x</sub> coatings deposited by medium-frequency magnetron sputtering with and without ion source assistance, optical properties of linoleic acid protected gold nanoparticles, and so on.

Authors also contributed papers to the areas of assembly and films, such as ordered self-assembly of nano-Pd-Ga/PMMA by ultrasonic processing, self-assembly of monodisperse spherical TiO<sub>2</sub> nanocrystals, linear assemblies of BN nanosheets, controllable assembly of hydrophobic superparamagnetic iron oxide nanoparticles with mPEG-PLA copolymers, polythene films with doped and undoped TiO<sub>2</sub> nanoparticles, and the influence of lithium on nano-sized films of Fe<sub>2</sub>O<sub>3</sub>.

The research topic of processing and modeling contains articles on electronic-excitation-induced processing in GaSb compound nanoparticles, and constitutive rheological modeling of flow serration behavior in metallic glasses.

In the applications of nanocrystals, authors report CdSe quantum dot-sensitized mesoporous TiO<sub>2</sub> solar cells with

CuSCN as solid-state electrolyte, fluoride nanoscintillators, and electrodeposition of nanometer-sized ferric oxide materials in colloidal templates for conversion of light to chemical energy.

### **Acknowledgments**

The editors would like to thank the authors for their contributions to this special issue, the reviewers for their time and dedication, and Rasha Magdy (Publishing Editor) and Mostafa Salem (Editorial Staff) for their support and assistance.

*Quanqin Dai*  
*Bo Zou*  
*William W. Yu*  
*Jaetae Seo*  
*Michael Z. Hu*

## Review Article

# Preparation, Modification, and Application of Starch Nanocrystals in Nanomaterials: A Review

Ning Lin,<sup>1</sup> Jin Huang,<sup>1,2,3</sup> Peter R. Chang,<sup>4,5</sup> Debbie P. Anderson,<sup>4</sup> and Jiahui Yu<sup>2</sup>

<sup>1</sup> College of Chemical Engineering, Wuhan University of Technology, 122 Loushi Road, Wuhan 430070, China

<sup>2</sup> Interdisciplinary Science and Technology Institute for Advanced Study, East China Normal University, Shanghai 200062, China

<sup>3</sup> State Key Laboratory of Pulp and Paper Engineering, South China University of Technology, Guangzhou 510640, China

<sup>4</sup> Bioproducts and Bioprocesses National Science Program, Agriculture and Agri-Food Canada, 107 Science Place, Saskatoon, SK, Canada S7N 0X2

<sup>5</sup> Department of Chemical and Biological Engineering, University of Saskatchewan, Saskatoon, SK, Canada S7N 5A9

Correspondence should be addressed to Jin Huang, huangjin@iccas.ac.cn and Peter R. Chang, peter.chang@agr.gc.ca

Received 4 May 2010; Accepted 12 July 2010

Academic Editor: Quanqin Dai

Copyright © 2011 Ning Lin et al. This is an open access article distributed under the Creative Commons Attribution License, which permits unrestricted use, distribution, and reproduction in any medium, provided the original work is properly cited.

During the past decade, much work has been devoted to the preparation of nanomaterials by blending starch nanocrystals from different sources with various polymer matrices. The following paper summarizes the most up-to-date information available relating to starch nanocrystals and their contribution to research, application, and advancement of diversified nanomaterials. This paper provides an overview of aspects related to starch nanocrystals, including methods for extraction and preparation, chemical modification (with particular emphasis on the modification methods and strategies), reinforcing effects and mechanisms, and applications and prospects.

## 1. Introduction

Starch, the major energy reserve of higher plants, is a mixture of two main components: amylose, a linear or slightly branched (1 → 4)- $\alpha$ -D-glucan, and amylopectin, a highly branched macromolecule consisting of (1 → 4)- $\alpha$ -D-glucan short chains linked through  $\alpha$ -(1 → 6) linkages [1]. All starches are biosynthesized as semicrystalline granules containing densely packed polysaccharides and a small amount of water. The conventional model for the inner structure of starch is that it is formed from two regions—crystalline and amorphous lamellae, which together form the crystalline and amorphous growth rings [2]. Figure 1 shows a schematic illustration of the starch granule inner structure and the chemical structure of amylopectin. For the investigation into the intrinsic structure of starch, various measurements were introduced, such as nuclear magnetic resonance (NMR) spectroscopy [1], X-ray microfocus diffraction [3], and small angle X-ray microfocus scattering [4, 5], and it was shown that native starch granules possessed an annular structure of alternant crystalline and semicrystalline layers. The growth

rings, amorphous (single chain) and ordered (double helix) components [6], are arranged alternately and encircle the point of initiation of the granule, called the hilum (shown in Figure 1). The dominant component of the crystalline region in native starch granules is thought to be amylopectin lamellae [7, 8], which pack together to form double helix crystal structure [9, 10]. In crystallites of starch, parallel stranded double helical structure is found in pairs, and all chains are packed in arrays. The pairing of double helices is identical in both polymorphs and corresponds to the interaction between double helices that has the lowest energy [11].

The crystalline regions of starch granules can be isolated by mild acid hydrolysis using hydrochloric or sulfuric acid. It is believed that at temperatures below the gelatinization temperature acid molecules preferentially attack the amorphous regions of the granule [12] resulting in these regions being more rapidly hydrolyzed than the crystalline regions [13]. The residue after acid hydrolysis contains the starch nanocrystals which have high crystallinity and nanoscale platelet morphology. Angellier-Coussy et al. investigated the molecular structure of waxy maize starch nanocrystals and

TABLE 1: Previous studies concerning the effects of different extraction methods and starch sources on starch nanocrystal size.

Starch source	Concentration of acid for hydrolysis	Temperature	Duration	<sup>(a)</sup> Structural parameters	Characterization	Ref.
	2.2 mol/L HCl	36°C	40 days	L = 20–40 nm W = 15–30 nm	TEM	[21]
Waxy corn starch	3.16 mol/L H <sub>2</sub> SO <sub>4</sub>	40°C	5 days	T = 5–7 nm L = 40–60 nm W = 15–30 nm	TEM	[22, 24]
	3.16 mol/L H <sub>2</sub> SO <sub>4</sub>	40°C	5 days	T = 6–8 nm L = 70–100 nm	TEM	[30]
Corn starch	2.87 mol/L H <sub>2</sub> SO <sub>4</sub>	45°C	7 days	L = 50 nm	SEM	[33]
Pea starch	3.16 mol/L H <sub>2</sub> SO <sub>4</sub>	40°C	5 days	L = 60–150 nm W = 15–30 nm	TEM	[19, 25]
	3.16 mol/L H <sub>2</sub> SO <sub>4</sub>	40°C	5 days	L = 30–80 nm	TEM	[34]
Potato starch	3.16 mol/L H <sub>2</sub> SO <sub>4</sub>	40°C	5 days	L = 40–70 nm W = 10–20 nm	TEM	[20]
	2.2 mol/L HCl	35°C	15 days	—	TEM	[32]

<sup>(a)</sup>Data for structural parameters are length ( $L$ ), width ( $W$ ), and thickness ( $T$ ) of starch nanocrystals.

found that there were two major groups of dextrans in the nanocrystals with average degrees of polymerization of 12.2 and 31.7 [14]. The distribution of branched molecules in the two dextrin populations suggests that the starch nanocrystal possesses a regular and largely homogeneous molecular structure. This paper details preparation methods and modification strategies, as well as applications for starch nanocrystals in nanomaterials. The reinforcement mechanism of starch nanocrystals in nanomaterials is recognized and discussed; and the prospects and outlook for chemical modification and application in nanomaterials and biomaterials are presented.

## 2. Preparation of Starch Nanocrystals

In native starch granules, the crystalline and amorphous phases coexist and together form the onion-like structure of the entire starch granule [15]. During the clustering organization process, the amylopectin side chains spiral due to the stacking of nanometric subunits, form the crystalline lamellae and ultimately construct the crystalline region [16]. With acid hydrolysis and/or wet-mashing, regions of low lateral order as well as amorphous phases in the starch granules dissolve, while the highly crystalline water-insoluble lamellae remain. The botanical origin of a starch, namely the type of crystallinity and the relative proportion of amylose and amylopectin, determines the structure and morphology of the starch nanocrystals [17, 18]. The conditions of hydrolysis during the extraction process (such as the type of acid, acid concentration, temperature, and time) affect the size and yield of starch nanocrystals. Table 1 summarizes

the structural characteristics of the crystalline nanolamellae extracted by different acid treatments from various starch sources. Starch nanocrystals derived from various plants have been shown by TEM or SEM to be of various sizes, with the length ranging from 20 to 200 nm, width from 10 to 30 nm, and thickness from 5 to 10 nm. Figures 2(a) and 2(b) show TEM images of starch nanocrystals derived from pea starch [19] and potato starch [20], respectively. Although the starch nanocrystals tend to self-aggregate, the individual and isolated platelets of starch nanocrystals can also be observed.

Through the comparative analysis of data in Table 1, we found that there was little or no variation in the temperature of hydrolysis, which was from 35°C to 45°C. The main reason for low hydrolytic temperature may be to prevent starch gelatinization and destruction of the starch crystalline structure. Of the several factors affecting the hydrolysis process, acid type and duration of hydrolysis are quite distinct, namely, hydrochloric acid (HCl) hydrolysis requires more than 15 days while only 5–7 days are required for sulfuric acid (H<sub>2</sub>SO<sub>4</sub>) hydrolysis.

Putaux et al. investigated the optimization of hydrolysis conditions for the extraction of starch nanocrystals with HCl [21] and H<sub>2</sub>SO<sub>4</sub> [22] and the effects on morphology and yield. The improved process for extraction of starch nanocrystals by acid hydrolysis followed by preservation is illustrated in Figure 3. Although HCl hydrolysis produced individual starch nanoplatelets, the long treatment time and low yield inhibit its application as nanofiller in nanomaterials. H<sub>2</sub>SO<sub>4</sub> hydrolysis was used to prepare starch nanocrystals at a relatively large scale [22]. Response surface methodology was used to optimize the conditions as follows: the initial

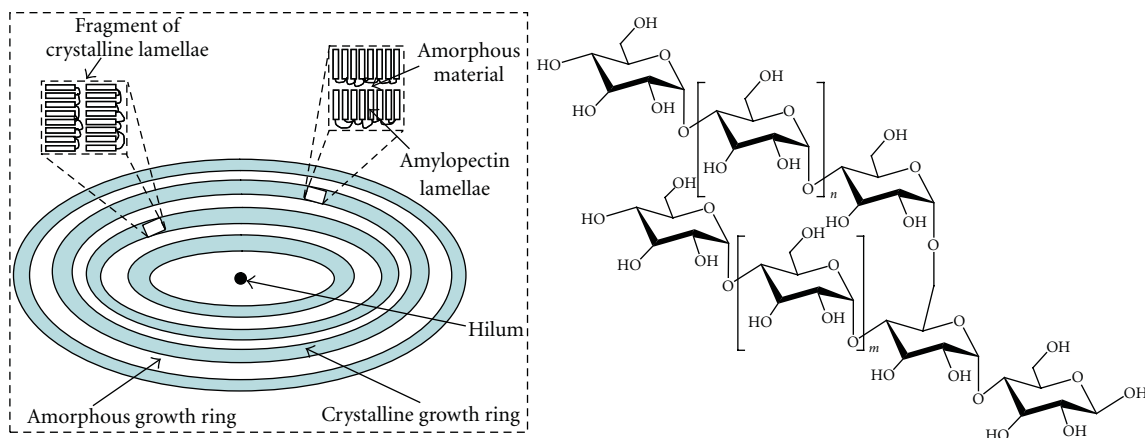


FIGURE 1: Schematic illustration of starch granule structure and chemical structure of amylopectin.

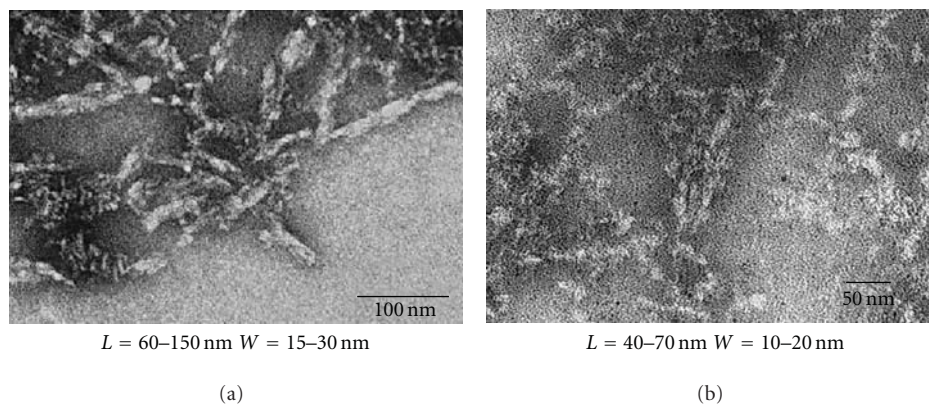


FIGURE 2: TEM images of starch nanocrystals from different sources: pea starch (a) (reproduced from [19] with permission from John Wiley and Sons) and potato starch (b) (reproduced from [20] with permission from Elsevier).

starch with a concentration of 14.69% in 3.16 mol/L  $\text{H}_2\text{SO}_4$  was hydrolyzed at  $40^\circ\text{C}$  with mechanical stirring at 100 rpm for 5 days. The resultant product had the same shape as that from the ca. 6-week HCl hydrolysis, but the yield was significantly enhanced (from 0.5 wt% to 15.7 wt%) while the hydrolysis time was shortened to 5 days. It should be pointed out that with the  $\text{H}_2\text{SO}_4$  hydrolysis method, although the sulfate groups on the surface of the starch nanocrystals contribute to dispersion and stability in aqueous solution, they also decrease the thermal stability of the nanocrystals. To solve this problem, a small amount of ammonia (0.5 wt%) was added to the  $\text{H}_2\text{SO}_4$  starch nanocrystal suspension before successive centrifugation [23]. This enhanced the thermal stability of the freeze-dried starch nanocrystals and made them suitable for chemical modification. The key element in the preparation of starch nanocrystals is to not destroy the starch crystalline structure while completely removing the amorphous region of starch granules. At the same time, isolating the nanocrystalline lamellae and obtaining the individual, low degree of self-aggregated platelet starch nanocrystals should also be desirably created or maintained.

### 3. Chemical Modification of Starch Nanocrystals

Starch nanocrystals possess a reactive surface covered with hydroxyl groups, which provides the possibility of modification via a chemical reaction strategy. The purpose of chemical modification is to contribute to specific functions and to expand the applications of starch nanocrystals. Angellier et al. estimated the surface hydroxyl group content to be ca. 14% of the total amount available, for example, only 0.0025 mol of reactive hydroxyl groups exist in 1.0 g of freeze-dried starch nanocrystals [26]. This percentage was calculated by constructing a simplified model of a single nanocrystal and counting the surface hydroxyl groups accessible to a water molecule using response surface methodology. There are three strategies for chemical modification of starch nanocrystals: modification by chemical reaction with small molecules, grafting onto polymer chains with coupling agents, and grafting from polymer chains with polymerization of a monomer. Evidence for chemical modification can be found by infrared spectroscopy analysis (FTIR), X-ray photoelectron spectrometry (XPS), and elemental

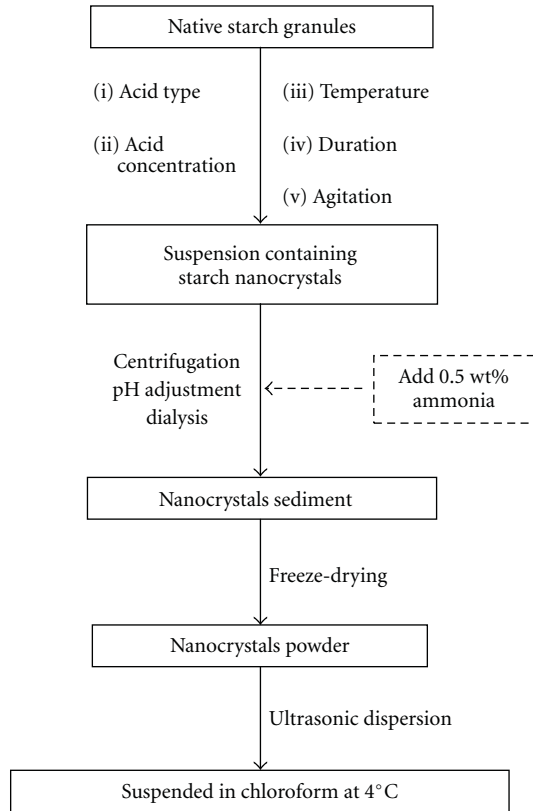


FIGURE 3: Extraction procedure and preservation method for starch nanocrystals.

analysis. Furthermore, the effects of chemical modification of starch nanocrystals, such as changes in morphology and size, solubility or polarity, surface properties, and thermal properties, can be investigated and discussed. It should also be pointed out that any modification strategies must preserve the integrity of the starch nanocrystal's crystalline structure or have a low degree of destruction. The performance of nanomaterials will inevitably be affected because chemical modification transforms the surface characteristics of the starch nanocrystals and hence improves interfacial interactions with the polymer matrix. Strong interfacial adhesion facilitates the transfer of stress and plays a reinforcing role for nanocrystals. In addition, functional modification of the starch nanocrystals, such as grafting to fluorescent molecules, may expand their application in the field of biomedical materials.

**3.1. Modification by “Chemical Reaction”.** The first attempt at modification of starch nanocrystals was a small molecule chemical reaction between hydroxyl groups (–OH) and isocyanate groups (–NCO). Acid hydrolysis of waxy maize starch granules was used to prepare the starch nanocrystals which were then chemically modified on the surface using phenyl isocyanate (PI) in toluene solution [26]. After surface chemical treatment with PI, the platelet-like geometric form of the starch nanocrystals seemed to be preserved, but the size had decreased as compared to unmodified starch fragments. Chemical grafting with PI most probably induced partial

solubilization of starch molecules located at the surface of the nanocrystal. In addition, the solubility and polarity of starch nanocrystals were improved. Unmodified starch nanocrystals are not able to migrate into methylene chloride because it has a much higher affinity for water; the PI-modified starch nanocrystals dispersed well in methylene chloride solution, suggesting a lower polar nature of the nanocrystal surface after chemical modification. Analysis of that the contact angle measurement data showed that the contact angle ( $\theta$ ) values for water changed from  $35.3^\circ$  to  $64.6^\circ$ , the polar component in the starch nanocrystals decreased from  $30.7 \text{ mJ/m}^2$  to  $11 \text{ mJ/m}^2$ , and surface energy ( $\gamma_s$ ) decreased from  $61.9 \text{ mJ/m}^2$  to  $47 \text{ mJ/m}^2$  for the unmodified starch nanocrystals and the PI-modified starch nanocrystals, respectively. These results show that surface chemical modification with isocyanate functions weakened the polarity of the original starch nanocrystals, thereby allowing the use of nonpolar polymers as matrices for composite materials[26].

With the chemical reaction between acetic anhydride and hydroxyl groups, starch nanocrystals can be acetylated and modified by small molecules [27]. The resulting acetylated starch nanocrystals exhibited lower surface energy, increased hydrophobic property, and improved solubility in common organic solvents such as acetone, toluene, *N,N*-dimethylformamide, and carbon tetrachloride. The crystalline structure of acetylated starch nanocrystals was also changed from A-style to style V-style. In addition, the platelet-like starch nanocrystals became sphere-shaped after modification and the size increased from original 20–40 nm to 63–271 nm.

**3.2. Modification Based on the “Graft to” Strategy.** Although modification by chemical reaction between small molecules and starch nanocrystals improved adhesion between the filler and matrix, the three-dimensional networks of the nanomaterials were partially or totally destroyed, leading to a sharp decrease in mechanical performance of the composites when modified starch nanocrystals (after chemical modification) were used as nanofiller in a polymer matrix. Based on the strategy of “grafting to” polymer chains, novel methods have been put forward and grafting of various polymers (such as poly(ethylene glycol) methyl ether (PEGME) [28], poly(propylene glycol) monobutyl ether (PPGME) [29], poly(tetrahydrofuran) (PTHF) [29], poly(caprolactone) (PCL) [29], alkenyl succinic anhydride (ASA) [26], and aliphatic chloride [28, 30]) to the surface of starch nanocrystals using different coupling agents has been attempted. The conditions for all of the “graft to” starch nanocrystal modification reactions, including solvent, catalyst, coupling agent, reaction time, and temperature, are summarized in Table 2.

Grafting reactions using the coupling agent 2,4-toluene diisocyanate (2,4-TDI) can be accomplished via two synthetic routes due to the different number of end groups in the grafted polymers, namely, the polymers possessing one reactive hydroxyl group and those with two reactive hydroxyl groups. It has been shown that the isocyanate at the 4 positions is 7 times more reactive than that at the

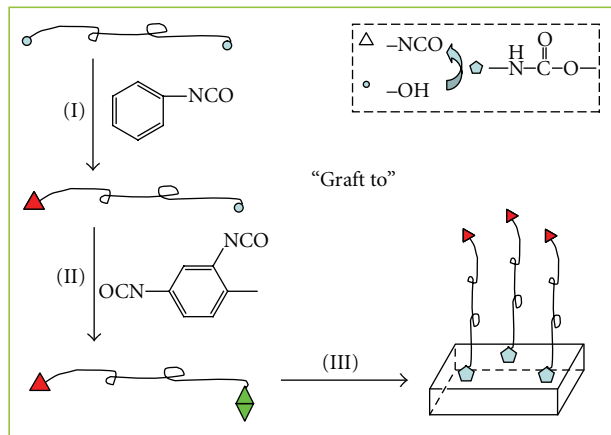


FIGURE 4: Schematic illustration of grafting of polymer chains to the starch nanocrystals based on the “graft to” strategy.

2 positions of 2,4-TDI [31]. Polymers, such as PEGME or PPGBE, with only one end hydroxyl group, are grafted onto the surface of the starch nanocrystals with a two-step process [28]. First, the isocyanate at the 4 position of 2,4-TDI reacts with the polymers, and the end hydroxyl group is modified with the isocyanate group. During the second step, the unreacted second isocyanate at the 2 position is reacted with the surface hydroxyl groups of the starch nanocrystals to graft the polymer chains. When there are two end hydroxyl groups on the polymer chains, such as on PTHF and PCL, a capping reaction for one hydroxyl group using phenyl isocyanate (PI) is necessary [29]. As a result, there are three steps for grafting to polymers with two end hydroxyl groups, that is, (i) end capping of one end group, (ii) functionalizing of the other end group, and (iii) polymer grafting onto the starch nanocrystals. A schematic illustration based on the “graft to” procedure for polymer chains with 2,4-TDI as coupling agent is shown in Figure 4. The morphologies of modified starch nanocrystals vary after grafting onto the polymer, resulting from the different relative molecular weights and lengths of the polymer chains. Modification by grafting polymers blocks the hydrogen bond interactions among starch nanocrystals, which may reduce the polarity and surface energy and result in individualization of the nanoplatelets. The comparative analysis of data from total surface energy ( $\gamma$ ), dispersive surface energy ( $\gamma^D$ ), and polar surface energy ( $\gamma^P$ ) indicated that the grafted PEGME chains were expected to be lying flat on the starch surface rather than assembled in a brush-like structure [28]. Grafting of polymer chains on the surface of starch nanocrystal based on the “graft to” strategy is illustrated in Figure 4.

Reaction between the hydroxyl group and the acid chloride group ( $-\text{COCl}$ ) is another method of modification which grafts polymer chains, such as stearoyl chloride [28], octanoyl, nonanoyl, and decanoyl chloride [30], to the starch nanocrystals. Because of the violent esterification reaction between  $-\text{OH}$  and  $-\text{COCl}$ , the modification conditions, such as temperature and pH, should be mild in order to maintain the crystalline structure of the starch nanocrystals, as shown in Table 2. After grafting onto aliphatic polymers,

the modified nanocrystals were more individualized and slightly larger in size than their unmodified counterparts. It should be pointed out that when stearate polymer was grafted onto the starch nanocrystal surface, the polymer chains were believed to have taken on a crystalline brush-like structure from the starch surface outward and to reinforce the crystallinity of the nanocrystals. This could be attributed mainly to the high level of surface grafting efficiency and to the covalently linked stearates which crystallize at the starch nanocrystal surface [28]. When the octanoyl, nonanoyl, and decanoyl polymers were grafted, the polarity of the starch nanocrystals decreased and dispersion in organic solvent improved. As for the stearate modified starch nanocrystals, it is interesting to note that the polarity of the starch-stearate surface disappeared, which is attributed to efficient surface coverage by the stearate aliphatic chain ends. Grafting to alkyl polymer chains also improved the thermal properties. For example, grafting to stearate chains resulted in an increase of more than  $100^\circ\text{C}$  in the degradation temperature of starch because of the protective crystalline layer formed by the oxygen-poor stearate surface [28]. Similarly, after grafting to octanoyl, nonanoyl, and decanoyl polymers, the low amount of hydroxyl groups remaining after acylation caused the modified starch nanocrystals to have greater thermal stability [30].

In conclusion, the described “graft to” surface modifications clearly change characteristics of the starch nanocrystals, such as morphology, size, polarity, dispersion in aqueous or organic solvents, surface properties, and thermal properties, while keeping the crystalline integrity. The ultimate purpose of chemical modification is to achieve a reinforcing effect in nanomaterials, which would allow the use of nonpolar polymers as matrices for nanocomposite materials, and stimulate the functional application of starch nanocrystals.

### 3.3. Modification Based on the “Graft from” Strategy.

Although various polymers have been used in attempts to modify the surface of starch nanocrystals based on the “graft to” strategy, there are still some shortcomings, such as low controllability and grafting efficiency, as well as difficulty in grafting long-chain polymers. To solve these problems, a novel “graft from” strategy has been proposed in which polymerization of monomers and chain propagation of polymers are induced, and ultimately the polymer chains are coupled with the starch nanocrystals. Using the “graft from” strategy, together with ring-opening polymerization (ROP) for poly( $\epsilon$ -caprolactone) (PCL) [23, 25, 32] and free radical polymerization (FRP) for polystyrene (PS) [33], different polymers have been grafted from the surface of starch nanocrystals. Figure 5 shows a schematic illustration of grafting polymer chains onto a starch nanocrystal based on the “graft from” strategy. With this strategy, a higher grafting density can be realized; and through the selection and control of the grafting polymer chains’ length and type, for example, polar or nonpolar grafting chains, the properties of starch nanocrystals can be regulated. The grafted chains will improve the compatibility between nanocrystals and matrix

TABLE 2: Reaction conditions for the “graft to” strategy for starch nanocrystal modification reactions.

Graft polymers	Coupling agents	Solvent	Catalyst	<sup>(a)</sup> Reaction temperature	<sup>(a)</sup> Reaction time	<sup>(b)</sup> Characterization	Ref.
PEGME <sub>550</sub>	2,4-TDI	Toluene	DTD	70°C	7 days	BET, FTIR, XPS, TEM, CAM	[28]
PPGBE <sub>4000</sub>	2,4-TDI	Toluene	TEA	70–80°C	7 days	FTIR, XPS, EA, TEM, CAM	[29]
PTHF <sub>1400</sub>	2,4-TDI (PI capping first)	Toluene	TEA	70–80°C	7 days	FTIR, XPS, EA, TEM, CAM	[29]
PCL <sub>10000</sub> PCL <sub>42500</sub>	2,4-TDI (PI capping first)	Toluene	TEA	70–80°C	7 days	FTIR, XPS, EA, TEM, CAM	[29]
Stearate polymer	stearic acid chloride	Methyl ethyl ketone	TEA	60°C	4 days	BET, FTIR, XPS, TEM, CAM	[28]
<sup>(c)</sup> Aliphatic polymers	thionyl chloride	Water	—	20°C	20 min	FTIR, EA, TEM	[30]
ASA <sub>350</sub>	—	Toluene	4-DAP	70°C	7 days	FTIR, XPS, TEM, CAM	[26]

TEA: triethylamine, DTD: dibutyltin dilaurate, 2,4-TDI: 2,4-toluene diisocyanate, PI: phenyl isocyanate, ASA: alkenyl succinic anhydride, 4-DAP: dimethyl amino pyridine, BET: Brunauer-Emmett-Teller, FTIR: Fourier transform infrared, EA: elemental analysis, TEM: transmission electron microscopy, XPS: X-ray photoelectron spectrometry, and CAM: contact angle measurement. (a) Reaction temperature and time listed in the table are assigned to the temperature and time of modified polymer chains grafted onto starch nanocrystals. (b) Characterization listed in the table refers to the measurements for proving the success of modification. (c) Aliphatic polymers include octanoic (C8), nonanoic (C9) and decanoic (C10) polymers.

and facilitate the transformation of structures and properties of nanocomposites filled with starch nanocrystals.

Under the different conditions of microwave assisted and thermal ring-opening polymerization, the surfaces of starch nanocrystals were functionalized by grafting with polycaprolactone (PCL) chains. Figure 6 shows a TEM image of PCL-modified starch nanocrystals and the reaction mechanism of ring-opening polymerization based on the “graft from” strategy. As shown in the image, after microwave assisted chemical modification most modified nanocrystals show a platelet-like structure of less than 100 nm, suggesting that the process of grafting PCL chains facilitates the dispersion of nanocrystals [23, 25]. In another work, the method of bulk polymerization was used to graft PCL polymer chains to starch nanocrystals [32]. With the analysis of Differential Scanning Calorimetry (DSC) measurements, it seems that chemical modification caused the decomposition of grafting copolymer in the broader range of temperature but the crystalline structure and morphology of nanocrystals are unaltered.

Another method of chemical modification of starch nanocrystals is free radical polymerization on the starch nanocrystal surface. An amphiphilic starch nanocrystal copolymer was prepared by graft copolymerization of starch nanocrystals with styrene [33]. During the hydrolysis process, the amorphous region of the starch was hydrolyzed and removed, and 50 nm particles were obtained as starch nanocrystals. After grafting the hydrophobic polystyrene chains, the modified starch nanocrystals transformed as the amphiphilic nanoparticles, which exhibited the size of around 80–100 nm spherical morphology. The amphiphilic starch nanocrystals dispersed well in both polar and non-polar solvents. The excellent amphiphilic characteristic was attributed to the different conformation variations of the

hydrophobic polystyrene side chains and to the hydrophilic starch backbone when in polar or nonpolar solvent.

## 4. Application of Starch Nanocrystals

**4.1. Natural Polymers as Matrix.** With natural rubber latex as the matrix and an aqueous suspension of waxy maize starch nanocrystals as the reinforcing phase, starch nanocrystals have been introduced into natural rubber for the preparation of nanocomposites [35]. The basic procedure was as follows: (i) mixing an aqueous suspension of starch nanocrystals and natural rubber latex, (ii) vacuum degassing, (iii) water evaporation, first at 40°C under atmospheric conditions for 6–8 h and then at 60°C under vacuum for 2 h, and (iv) film formation. The starch nanocrystal content in the resultant composites ranged from 2 wt% to 50 wt%. The performance of the nanocomposites and various structural properties (such as morphology, crystallinity, swelling behavior, barrier properties to water vapor and oxygen, thermal properties, and mechanical properties) were investigated. Starch nanocrystal filler was evenly distributed within the natural rubber matrix, which is very important for producing good mechanical properties. Meanwhile, preparation of the nanocomposites did not destroy the crystalline structure of the starch nanocrystals, as verified by wide-angle X-ray diffraction analysis. It is interesting to note that the swelling of nanocomposites in toluene decreased and the swelling in water increased with the introduction of starch nanocrystals to the natural rubber. It was assumed that these phenomena were attributed to the formation of the starch nanocrystal three-dimensional network through hydrogen linkages between starch nanoparticle clusters and also to favorable interactions between the matrix and filler. It should be noted

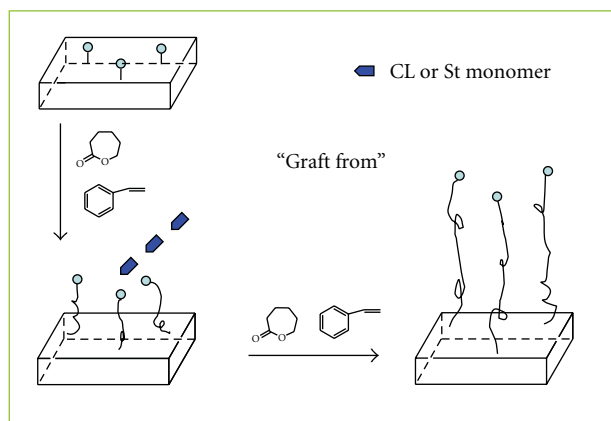


FIGURE 5: Schematic illustration of grafting polymer chains on a starch nanocrystal based on the “graft from” strategy.

that the addition of starch nanocrystals induced a decrease in permeability to both water vapor and oxygen of natural rubber-based nanocomposites. Water Vapor Transmission Rate (WVTR) gradually decreased from 0.078 g/(m·day) for neat natural rubber composite to 0.043 g/(m·day) for nanocomposite with a starch nanocrystal content of 20 wt%. At the same time, the higher the starch content was, the greater the decrease in oxygen permeability, that is, 17.9% for the composite with 10 wt% starch nanocrystals, 20.3% for the composite with 20 wt% starch nanocrystals, and 47% for the composite with 30 wt% starch nanocrystals [35]. It is believed that the platelet-like low permeability structure of starch nanocrystals stands in the way of the water vapor or oxygen molecules, increasing the tortuosity of the diffusion path, and ultimately affecting the barrier properties of the natural rubber based composites. The mechanical properties of composites also improved with the introduction of starch nanocrystals. For example, at room temperature the relaxed modulus of nanocomposites containing 10, 20, and 30 wt% filler was about 10, 75, and 200 times higher, respectively, than the neat natural rubber material. It was shown that with a content of up to 20 wt%, this new filler presented the advantage of effectively reinforcing the natural rubber without significantly decreasing the elongation at break ( $\epsilon_{b,true}$ ) of the material. For example,  $\epsilon_{b,true}$  decreased slightly from 303% to 277% whereas the strength ( $\sigma_{b,true}$ ) increased sharply from 77.1 MPa to 229.5 MPa (the former values are for the neat natural rubber material and the latter values are for the nanocomposite with 20 wt% starch nanocrystal filler) [24, 36]. In view of the positive effects of starch nanoparticles on barrier and mechanical properties of the natural rubber matrix, Novamont (Novara, Italy), working in partnership with Goodyear Tire and Rubber (America), has recently developed tires using nanoparticles derived from corn starch, partially replacing the conventional carbon black and silica used in making tires. This patented innovation, called BioTred, presents environmental advantages but also reduces the rolling resistance of tires [37]. Starch nanocrystals were also proved to have the potential as the substituted nanofiller for natural rubber [35].

Waxy maize starch nanocrystals have also been used as a reinforcing agent in a waxy maize starch matrix with various plasticizers. Contrary to natural rubber, starch is a thermoplastic and polar matrix, and when starch nanocrystals are used as the nanofillers in starch-based materials the chemical structures of the matrix and filler are similar. These particulars promote good miscibility and strong interfacial adhesion between the starch nanocrystal filler and the starch matrix. Angellier et al. and Vigiúe et al. investigated the effects of plasticizer content, starch nanocrystal filler content, and aging on the reinforcing properties of starch-based nanocomposites [38, 39]. When a glycerol content of 25 wt% was selected to plasticize the materials, the mechanical properties of the starch-based nanocomposites reinforced with starch nanocrystals were clearly higher than those of the unfilled matrix, even after aging of the material [38]. This reinforcing effect was attributed to the establishment of strong interactions not only between the starch nanocrystals but also between the filler and the matrix and was probably also due to crystallization that may have occurred at the filler/matrix interface. At the same time, the increase in  $T_g$  for starch-based materials, resulting from hydrogen bonding between the filler and matrix restricting the molecular mobility of the matrix amylopectin segments, slowed retrogradation of the starch matrix considerably. The starch-based nanocomposites plasticized with sorbitol exhibited a similar reinforcing effect on mechanical and thermal properties of starch nanocrystals [39]. In addition, it should be noted that retrogradation of the starch matrix, which occurred in both sorbitol- and amylopectin-rich domains of the unfilled matrix, was restricted to amylopectin-rich domains in the starch nanocrystal reinforced matrix, which may be attributed to the occurrence of the transcrystallization phenomenon.

Alkenyl succinic anhydride (ASA) is a polymer with an acid anhydride group that can be chemically reacted with hydroxyl groups on the starch nanocrystal surface by using 4-dimethyl amino pyridine as the catalyst [26]. Because the modified starch nanocrystals are surrounded by ASA molecules, they exhibit a flocky conglomeration morphology, not the original platelet shape. Surface chemical modification with anhydride functions enhances the nonpolar nature of starch nanocrystals and also preserves the initial crystalline structure.

Glycerol plasticization and compression molding was used to incorporate pea starch nanocrystals into a soy protein isolate (SPI) matrix to produce a class of fully biodegradable nanocomposites [19]. The rigid starch nanocrystals showed a prominent reinforcing function that was dependent upon uniform dispersion and strong interfacial interaction between the filler and matrix. The reinforcing effect was however restricted by size expansion of the starch nanocrystal domains. As a result, in contrast to neat soy protein material, nanocomposite with a low starch nanocrystal loading level (2 wt%) showed the highest strength and Young's modulus, which were enhanced by ca. 50% and 200%, respectively. With an increase in starch nanocrystal content, the number and size of starch nanocrystal domains increased, thus lowering the filler's effective active surface

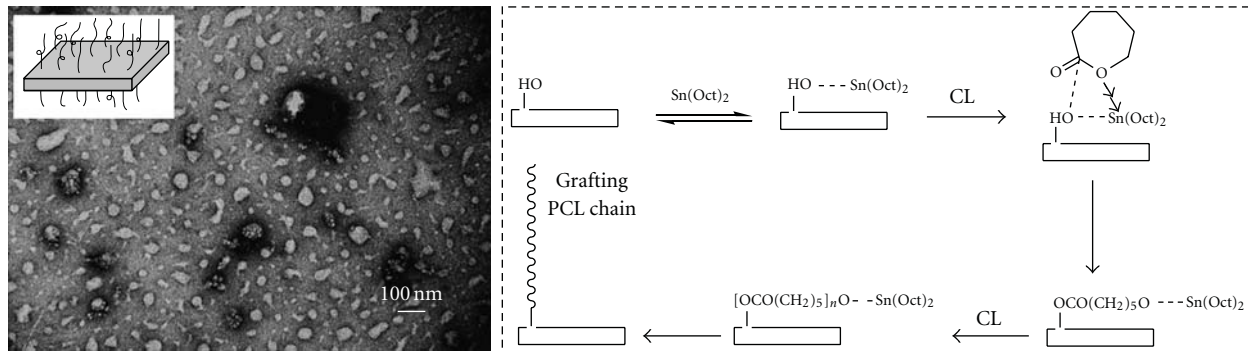


FIGURE 6: TEM image of grafted PCL polymer on starch nanocrystals (reproduced from [25] with permission from Wiley-VCH Verlag GmbH & Co. KGaA); and reaction mechanism of ring-opening polymerization based on the “graft from” strategy (reproduced from [23] with permission from John Wiley and Sons).

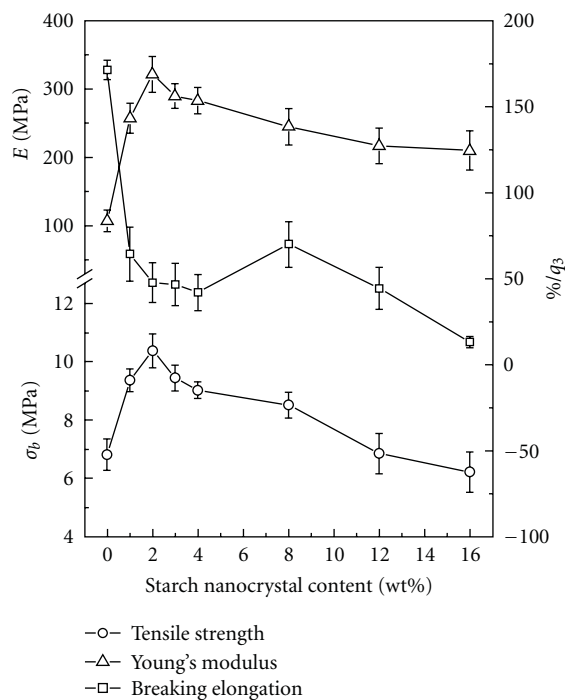


FIGURE 7: Effect of starch nanocrystal content on mechanical performance of soy protein-based nanocomposites (Reproduced from [19] with permission from John Wiley and Sons).

area available for interaction with the soy protein matrix. The increased filler level also destroyed the ordered structure of the soy protein matrix, causing a gradual decrease in strength and Young's modulus. In addition, although the starch nanocrystals introduced were relatively hydrophilic, the water uptake of the nanocomposites showed no obvious change [19]. The effect of starch nanocrystal content on the mechanical performance of soy protein-based nanocomposites is shown in Figure 7. In another case, sorbitol-plasticized pullulan nanocomposites filled with waxy maize starch nanocrystals showed substantial improvement in mechanical and water resistance properties as compared with

the unfilled material [40]. The water barrier properties of the nanocomposites were particularly enhanced with a high filler content (20 wt%), and the thermal stability of pullulan-based material was also improved.

**4.2. Synthetic Polymers as Matrix.** Different from natural polymers, synthetic polymers are versatile materials with many industrial applications because of their excellent physical properties and chemical resistance. The shortcomings of synthetic polymers are also numerous, including the high cost, non-biodegradability, non-biocompatibility, and poor mechanical or thermal performance of some polymers. The introduction of starch nanocrystals into synthetic polymer matrices should ameliorate these problems to some degree. Pea starch nanocrystals were blended with poly(vinyl alcohol) (PVA) to produce nanocomposites [34]. The nanocomposites containing starch nanocrystal at levels of 5 and 10 wt% exhibited improved physical properties, namely, higher light transmittance, tensile strength, elongation at break, and lower moisture uptake, as compared with the neat PVA material. In another work, waxy maize starch nanocrystals were introduced as filler into an acrylic polymer matrix, namely, poly(styrene-co-butyl acrylate) (poly(S-co-BuA)) [41]. Dynamic mechanical analysis (DMA) showed that the mechanical properties of these composites were substantially improved by increasing the amount of filler. With the high loaded level (ranging from 0 to 60 wt%), potato microcrystalline starch was also used to reinforce the thermoplastic poly(S-co-BuA) matrix, which brought a great reinforcing effect, especially at temperatures higher than the  $T_g$  of the synthetic matrix [42].

The introduction of potato starch nanocrystals into waterborne polyurethane (WPU) [20] led to nanocomposites with enhanced tensile strength, Young's modulus, and elongation. With a starch nanocrystal content of only 2 wt%, the strength and elongation of the composite were enhanced by ca. 1.7- and 2.6-fold, respectively, over those of the neat waterborne polyurethane material. The improvements in mechanical performance are mainly attributed to the enduring stress of rigid starch nanocrystals and to the

stress transfer mediated by the strong interfacial interaction between the starch nanocrystal surface and the waterborne polyurethane matrix, as well as to the relatively uniform dispersion of the starch nanocrystals. When the loading level of starch nanocrystals was relatively high (>8 wt%), the size and amount of the starch nanocrystal inevitably expanded due to the strong tendency for self-aggregation of starch nanocrystals. This resulted in a decrease in the effective active surface of the filler phase and weakened the interfacial adhesion, the essential association between filler phase and matrix. At the same time, excess breakage of conventional organization and interaction in the waterborne polyurethane matrix, as well as the formation of a microphase separation in the composites, ultimately inhibits further enhancement of mechanical performance [20]. In another work, waxy maize starch nanocrystals were introduced as the reinforcing phase in the modification of waterborne polyurethane, which exhibited improvements in strength and thermal stability of the materials [43]. Based on a “graft from” strategy, the surface of starch nanocrystals was functionalized by grafting with polycaprolactone (PCL) chains using microwave-assisted ring-opening polymerization [23]. The modified nanocrystals were then loaded into the waterborne polyurethane matrix. The nanocomposite containing the lowest loading level of 5 wt% grafted copolymers showed the maximum tensile strength and elongation, which were also higher than those of neat waterborne polyurethane. The grafted PCL chains used for surface functionality of starch nanocrystals were of the same origin as the soft segment (PCL<sub>2000</sub>) of the waterborne polyurethane matrix, which facilitated the uniform dispersal of the nanoscale fillers and hence improved the miscibility between filler and matrix. As the point of stress concentration, the starch nanocrystals performed the reinforcement function fully, resulting in enhanced strength. At the same time, increasing entanglements mediated with grafted PCL chains facilitated the increase in elongation [23].

Chemically modified starch nanocrystals have also been used as reinforcing filler for synthetic and biodegradable polyester matrices, such as poly(lactic acid) (PLA) and polycaprolactone (PCL). In the case of a “graft from” starch nanocrystal-*graft*-poly( $\epsilon$ -caprolactone) (StN-g-PCL) filled into a poly(lactic acid) matrix, PCL polymer chains were grafted onto the surface of starch nanocrystals via microwave-assisted ring-opening polymerization [25]. The resultant modified nanocrystals were then incorporated into a poly(lactic acid) matrix by solution mixing, and the film was then solidified to produce fully biodegradable nanocomposites. The addition of grafted PCL starch nanocrystals resulted in a pronounced enhancement of elongation together with a decrease in Young's modulus. For example, the  $\sigma_{b,true}$  of nanocomposite with 5 wt% fillers was ca. 10-fold over that of neat PLA material, as shown in Figure 8(a). This was attributed to the introduction of the rubbery PCL component which provided flexibility to the nanocomposite and contributed to the increase in elongation. An increase in modified nanocrystal content, however, led to nanofiller self-aggregation and microphase separation between filler and matrix, resulting in a decrease

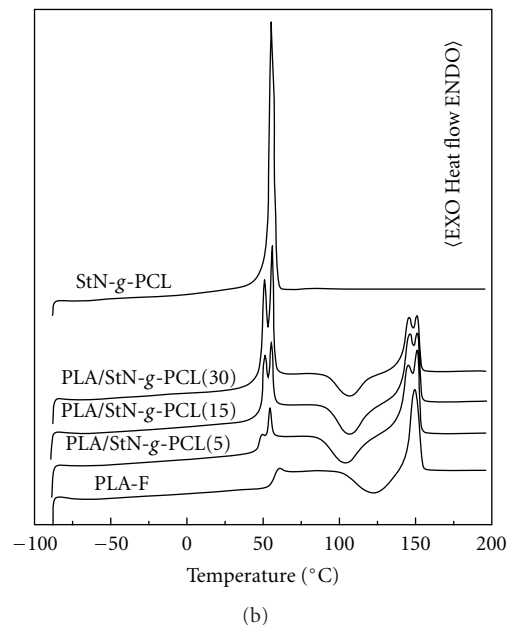
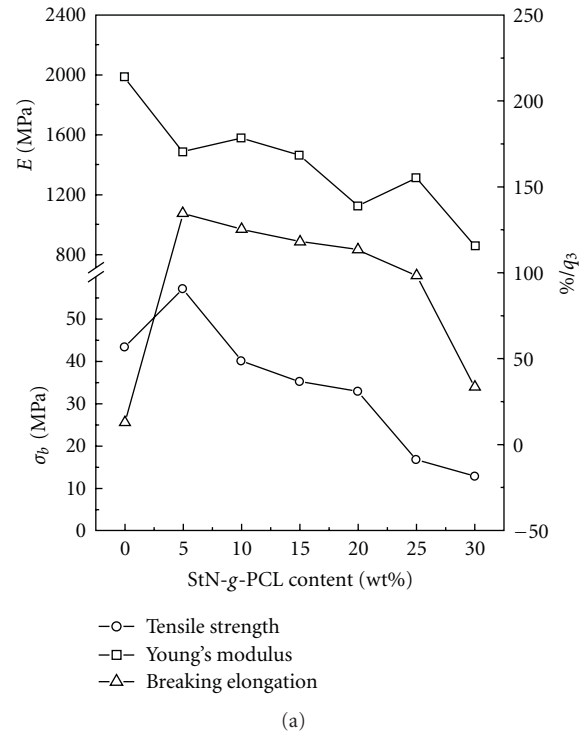


FIGURE 8: Effects of PCL content in copolymer starch nanocrystal grafting on mechanical performance of PLA-based nanocomposites (a) and DSC thermograms of nanocomposites with various grafted copolymer contents (b) (Reproduced from [25] with permission from Wiley-VCH Verlag GmbH & Co. KGaA).

in nanocomposite strength and elongation. The introduction of modified starch nanocrystals into the PLA matrix also affected the thermal properties of the composites. DSC thermograms of nanocomposites with various filler contents are shown in Figure 8(b). The glass transition temperature ( $T_{g,mid}$ ) assigned to PLA shifted from 57.7°C to 47.8°C

for nanocomposite with 5 wt% grafted copolymer filler and was absent in nanocomposites with higher loading levels (>15 wt%). This was attributed to an improvement in freedom of motion of the PLA matrix during melting of the grafted PCL component. In addition, the frozen motion of glassy PLA segments in the interfacial layer (composed of PCL and PLA chains) results in a slight shift to a lower melting temperature ( $T_m$ ) for PCL [25].

The “graft to” method links polycaprolactone (PCL) chains of various molecular weights (PCL<sub>10000</sub> and PCL<sub>42500</sub>) covalently onto the surface of starch nanocrystals by an isocyanate-mediated reaction. Both unmodified and modified nanocrystals were used to prepare highly filled nanocomposites using a casting/evaporation method with a PCL matrix [44]. The addition of PCL-grafted waxy maize starch nanocrystals resulted in a continuous increase in the tensile modulus as verified by DMA experiments. Disappointingly, there was also a gradual decrease in both the strength and elongation at break when PCL-modified starch nanocrystal filler was added, as compared to the neat PCL material. Although grafted chains of the same component as the matrix promote better filler dispersion within the polymeric matrix, low grafting efficiency, resulting from chain entanglements between grafted chains and PCL chains from the matrix, induces a decline in the strength and elongation of composites. For example, the elongation at break decreased from 637% to 83% when 20 wt% of PCL<sub>10000</sub>-grafted starch nanocrystals was added.

#### 4.3. Reinforcement Mechanism of Starch Nanocrystal Filler.

It is well known that the structure and properties of nanocomposites are relevant to the cooperative effects of many factors including the various structures of matrices, the network among nanofillers and polymer matrices, the interfacial interactions, the scale of dispersion, morphology, and the surface functionality of the nanocrystals. A percolation mechanism, determined by three-dimensional networks formed by the interconnection of polysaccharide nanocrystals and stabilized by hydrogen bonding, is the predominant contributor to reinforcement of the resultant nanocomposites as it enhances tensile strength and Young's modulus gives a higher storage modulus, a thermally stable rubbery plateau, and affects the diffusion coefficient [24, 36, 45–48]. The percolation mechanism has been verified by successive tensile experiments, which consist of stretching the material to a given elongation, releasing the force, stretching again to a higher elongation, and repeating. It has been proven that over the percolation threshold ( $\nu_{RC}$ ), the polysaccharide nanocrystals connect and form a tridimensional continuous pathway through the nanocomposite [49]. The formation of this nanocrystal network results from strong interactions between crystals, such as hydrogen bonds [50], and improves the mechanical and thermal properties. This phenomenon is similar to the mechanical properties observed for a sheet of paper, which result from the hydrogen-bonding forces that hold the percolation network of fibers together [49]. The  $\nu_{RC}$  is inversely proportional to the aspect ratio of nanofillers, such as, waxy maize starch nanocrystal-based

nanocomposites—generally displayed improved mechanical properties at the filler content of about 5 wt% [24], which was due primarily to its lower aspect ratio and platelet-like geometry in contrast with rod-like cellulose whiskers. Any factor that affects the formation of the percolation nanocrystal network, or interferes with it, will change the performance of the composite [51]. There are three main parameters affecting the properties of such materials: the morphology and dimensions of the nanocrystals, the processing method, and the microstructure of the matrix and matrix-filler interactions [49]. It should be noted that although chemical reaction modification (ASA modified or PI modified) of starch nanocrystals improves the adhesion between the filler and matrix, it partially or totally destroys the three-dimensional network in the nanocomposites. This leads to a strong decrease in mechanical performance of the composites after chemical modification [24, 35]. Similar results have also been shown in the study of natural rubber nanocomposites reinforced with chemically modified crab shell chitin nanowhiskers [52].

The interfacial interactions among polysaccharide nanocrystals, grafted polymer chains, and the polymer matrix are another crucial factor affecting the structure and properties of composites [23, 25, 53]. Fast freezing during quenching before freeze-drying and high melting viscosity during compounding/molding inhibit the percolation mechanism in many polysaccharide nanocrystal-based nanocomposites. Furthermore, in some systems the percolation threshold is unachieved due to sedimentation of the filler or to low filler/matrix miscibility. In these cases, the interfacial interactions between filler and matrix participate in stress transfer to rigid nanometer sized fillers with higher stress endurance and become dominant in the reinforcement effect and in the simultaneous toughening effects. When starch nanocrystal was grafted from PCL chains and incorporated into PLA or WPU matrices, the entanglement and interaction between grafted polymer chains and polymer matrices facilitated the interfacial adhesion between the nanocrystals and matrices and hence contributed to the rigid nanocrystals endurance of higher stress. At the same time, the rubbery component of the grafted polymer chains, together with the formation of an interfacial layer, improved the elongation of the nanocomposites. The three-phase structure model shown in Figure 9 summarizes the interactions among the nanocrystals, the interfacial layer, and the polymer matrix. In addition, it should be pointed out that, using the same strategy, long and dense “plasticizing” tails of grafted polymer chains on polysaccharide nanocrystals entangle with each other and enable the modified nanocrystals to directly thermoform to make novel nanocomposites [54, 55].

## 5. Conclusions and Outlook

Starch nanocrystals, the nanoscale biofiller derived from native starch granules, have been compounded with many different kinds of polymer matrices. The intrinsic rigidity of starch nanocrystals, special platelet-like morphology, strong interfacial interactions, and the percolation network organized by nanocrystals all contribute to optimized

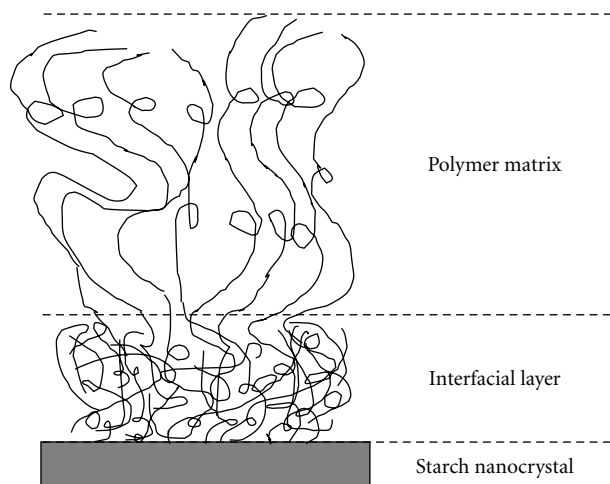


FIGURE 9: Schematic illustration of three-phase structure model.

mechanical performance, thermal properties, solvent absorption, and barrier properties. To improve interfacial adhesion between starch nanocrystals and polymer matrices, a series of chemical modifications based on “chemical reaction”, “graft to”, and “graft from” strategies have been carried out and, in some cases, markedly enhanced the performance of the nanomaterials. Some reinforcing mechanisms were proposed and used to manipulate the performance of starch nanocrystal-filled materials. Novel processing technology should be sought in order to accelerate the application of starch nanocrystals in nanomaterials. Lack of continuous processing technology makes current methods for production of nanomaterials reinforced with starch nanocrystals impractical. Furthermore, environmentally friendly processing and manufacturing must be developed in order to replace the current process which is energy intensive, requires strong/toxic chemicals, and is a burden on our fragile ecosystem and environment. In addition, cellulose nanocrystals have been introduced into the field of biomaterials, noticeably for use in bioimaging applications after fluorescent labeling modifications [56]. Compared to cellulose nanocrystals, the structure of starch nanocrystals is less durable, particularly during functional modification, which impairs the development for use of starch nanocrystals in the biomaterials field. Realization of functional modification of starch nanocrystals under mild reactive conditions would greatly improve its practical utility for the future.

## Acknowledgments

The authors would like to express their gratitude to three anonymous reviewers and the Editor, Dr. Quanqin Dai, for their constructive comments and recommendations. The authors are also grateful to the Program of Energy Research and Development (PERD) of Natural Resources Canada, the Pulse Research Network (PURENet) through Agriculture, Agri-Food Canada’s Agriculture Bioproducts Innovation Program (ABIP), National Natural Science

Foundation of China (50843031), 973 Projects of Chinese Ministry of Science and Technology (2007CB936104), Shanghai Municipality Commission for Special Project of Nanometer Science and Technology (0952nm05300), Shanghai Municipality Commission for International Corporation Project (10410710000) and for Non-Governmental International Corporation Project (09540709000), Fundamental Research Funds for the Central Universities (Self-Determined and Innovative Research Funds of WUT 2010-II-022), Youth Chenguang Program of Science & Technology in Wuhan (200850731383), State Key Laboratory of Pulp and Paper Engineering, South China University of Technology (200906), and Key Laboratory of Cellulose and Lignocellulose Chemistry, Guangzhou Institute of Chemistry, Chinese Academy of Sciences (LCLC-2010-10) for partial funding of this work.

## References

- [1] M. Paris, H. Bizot, J. Emery, J. Y. Buzaré, and A. Buléon, “Crystallinity and structuring role of water in native and recrystallized starches by  $^{13}\text{C}$  CP-MAS NMR spectroscopy. 1: spectral decomposition,” *Carbohydrate Polymers*, vol. 39, no. 4, pp. 327–339, 1999.
- [2] P. J. Jenkins, R. E. Comerson, A. M. Donald et al., “In situ simultaneous small and wide angle X-ray scattering: a new technique to study starch gelatinization,” *Journal of Polymer Science B*, vol. 32, no. 8, pp. 1579–1583, 1994.
- [3] T. A. Waigh, I. Hopkinson, A. M. Donald, M. F. Butler, F. Heidelbach, and C. Riekkel, “Analysis of the native structure of starch granules with X-ray microfocus diffraction,” *Macromolecules*, vol. 30, no. 13, pp. 3813–3820, 1997.
- [4] T. A. Waigh, A. M. Donald, F. Heidelbach, C. Riekkel, and M. J. Gidley, “Analysis of the native structure of starch granules with small angle X-ray microfocus scattering,” *Biopolymers*, vol. 49, no. 1, pp. 91–105, 1999.
- [5] T. Suzuki, A. Chiba, and T. Yano, “Interpretation of small angle X-ray scattering from starch on the basis of fractals,” *Carbohydrate Polymers*, vol. 34, no. 4, pp. 357–363, 1998.
- [6] M. J. Gidley and S. M. Bociek, “Molecular organization in starches: a  $^{13}\text{C}$  CP/MAS NMR study,” *Journal of the American Chemical Society*, vol. 107, no. 24, pp. 7040–7044, 1985.
- [7] S. Perez, P. Baldwin, and D. J. Gallant, “Structural features of starch granules I,” in *Starch: Chemistry and Technology*, R. Whistler and J. BeMiller, Eds., pp. 149–192, Academic Press, New York, NY, USA, 3rd edition, 2009.
- [8] P. J. Jenkins and A. M. Donald, “The influence of amylose on starch granule structure,” *International Journal of Biological Macromolecules*, vol. 17, no. 6, pp. 315–321, 1995.
- [9] J.-L. Putaux, A. Buléon, and H. Chanzy, “Network formation in dilute amylose and amylopectin studied by TEM,” *Macromolecules*, vol. 33, no. 17, pp. 6416–6422, 2000.
- [10] A. C. O’Sullivan and S. Perez, “The relationship between internal chain length of amylopectin and crystallinity in starch,” *Biopolymers*, vol. 50, no. 4, pp. 381–390, 1999.
- [11] A. Imberty, A. Buléon, V. Tran, and S. Péerez, “Recent advances in knowledge of starch structure,” *Starch—Stärke*, vol. 43, no. 10, pp. 375–384, 1991.
- [12] P. J. Jenkins and A. M. Donald, “The effect of acid hydrolysis on native starch granule structure,” *Starch—Stärke*, vol. 49, no. 7–8, pp. 262–267, 1997.

- [13] Y.-J. Wang, V.-D. Truong, and L. Wang, "Structures and rheological properties of corn starch as affected by acid hydrolysis," *Carbohydrate Polymers*, vol. 52, no. 3, pp. 327–333, 2003.
- [14] H. Angellier-Coussy, J.-L. Putaux, S. Molina-Boisseau, A. Dufresne, E. Bertoft, and S. Perez, "The molecular structure of waxy maize starch nanocrystals," *Carbohydrate Research*, vol. 344, no. 12, pp. 1558–1566, 2009.
- [15] M. S. Buttrose, "Submicroscopic development and structure of starch granules in cereal endosperms," *Journal of Ultrastructure Research*, vol. 4, no. 3-4, pp. 231–257, 1960.
- [16] T. A. Waigh, P. Perry, C. Riekel, M. J. Gidley, and A. M. Donald, "Chiral side-chain liquid-crystalline polymeric properties of starch," *Macromolecules*, vol. 31, no. 22, pp. 7980–7984, 1998.
- [17] L. Jayakody and R. Hoover, "The effect of lintnerization on cereal starch granules," *Food Research International*, vol. 35, no. 7, pp. 665–680, 2002.
- [18] C. Gérard, P. Colonna, A. Buléon, and V. Planchot, "Order in maize mutant starches revealed by mild acid hydrolysis," *Carbohydrate Polymers*, vol. 48, no. 2, pp. 131–141, 2002.
- [19] H. Zheng, F. Ai, P. R. Chang, J. Huang, and A. Dufresne, "Structure and properties of starch nanocrystal-reinforced soy protein plastics," *Polymer Composites*, vol. 30, no. 4, pp. 474–480, 2009.
- [20] G. Chen, M. Wei, J. Chen, J. Huang, A. Dufresne, and P. R. Chang, "Simultaneous reinforcing and toughening: new nanocomposites of waterborne polyurethane filled with low loading level of starch nanocrystals," *Polymer*, vol. 49, no. 7, pp. 1860–1870, 2008.
- [21] J.-L. Putaux, S. Molina-Boisseau, T. Momaur, and A. Dufresne, "Platelet nanocrystals resulting from the disruption of waxy maize starch granules by acid hydrolysis," *Biomacromolecules*, vol. 4, no. 5, pp. 1198–1202, 2003.
- [22] H. Angellier, L. Choisnard, S. Molina-Boisseau, P. Ozil, and A. Dufresne, "Optimization of the preparation of aqueous suspensions of waxy maize starch nanocrystals using a response surface methodology," *Biomacromolecules*, vol. 5, no. 4, pp. 1545–1551, 2004.
- [23] P. R. Chang, F. Ai, Y. Chen, A. Dufresne, and J. Huang, "Effects of starch nanocrystal-graft-porycaprolactone on mechanical properties of waterborne polyurethane-based nanocomposites," *Journal of Applied Polymer Science*, vol. 111, no. 2, pp. 619–627, 2009.
- [24] H. Angellier, S. Molina-Boisseau, and A. Dufresne, "Mechanical properties of waxy maize starch nanocrystal reinforced natural rubber," *Macromolecules*, vol. 38, no. 22, pp. 9161–9170, 2005.
- [25] J. Yu, F. Ai, A. Dufresne, S. Gao, J. Huang, and P. R. Chang, "Structure and mechanical properties of poly(lactic acid) filled with (starch nanocrystal)-graft-poly( $\epsilon$ -caprolactone)," *Macromolecular Materials and Engineering*, vol. 293, no. 9, pp. 763–770, 2008.
- [26] H. Angellier, S. Molina-Boisseau, M. N. Belgacem, and A. Dufresne, "Surface chemical modification of waxy maize starch nanocrystals," *Langmuir*, vol. 21, no. 6, pp. 2425–2433, 2005.
- [27] Y. Xu, W. Ding, J. Liu et al., "Preparation and characterization of organic-soluble acetylated starch nanocrystals," *Carbohydrate Polymers*, vol. 80, no. 4, pp. 1078–1084, 2010.
- [28] W. Thielemans, M. N. Belgacem, and A. Dufresne, "Starch nanocrystals with large chain surface modifications," *Langmuir*, vol. 22, no. 10, pp. 4804–4810, 2006.
- [29] M. Labet, W. Thielemans, and A. Dufresne, "Polymer grafting onto starch nanocrystals," *Biomacromolecules*, vol. 8, no. 9, pp. 2916–2927, 2007.
- [30] H. Namazi and A. Dadkhah, "Convenient method for preparation of hydrophobically modified starch nanocrystals with using fatty acids," *Carbohydrate Polymers*, vol. 79, no. 3, pp. 731–737, 2010.
- [31] M. N. Belgacem, J. Quillerou, and A. Gandini, "Urethanes and polyurethanes bearing furan moieties-3. Synthesis, characterization and comparative kinetics of the formation of diurethanes," *European Polymer Journal*, vol. 29, no. 9, pp. 1217–1224, 1993.
- [32] H. Namazi and A. Dadkhah, "Surface modification of starch nanocrystals through ring-opening polymerization of  $\epsilon$ -caprolactone and investigation of their microstructures," *Journal of Applied Polymer Science*, vol. 110, no. 4, pp. 2405–2412, 2008.
- [33] S. Song, C. Wang, Z. Pan, and X. Wang, "Preparation and characterization of amphiphilic starch nanocrystals," *Journal of Applied Polymer Science*, vol. 107, no. 1, pp. 418–422, 2008.
- [34] Y. Chen, X. Cao, P. R. Chang, and M. A. Huneault, "Comparative study on the films of poly(vinyl alcohol)/pea starch nanocrystals and poly(vinyl alcohol)/native pea starch," *Carbohydrate Polymers*, vol. 73, no. 1, pp. 8–17, 2008.
- [35] H. Angellier, S. Molina-Boisseau, L. Lebrun, and A. Dufresne, "Processing and structural properties of waxy maize starch nanocrystals reinforced natural rubber," *Macromolecules*, vol. 38, no. 9, pp. 3783–3792, 2005.
- [36] H. Angellier, S. Molina-Boisseau, and A. Dufresne, "Waxy maize starch nanocrystals as filler in natural rubber," *Macromolecular Symposia*, vol. 233, no. 1, pp. 132–136, 2006.
- [37] T. Materne, F. Corvasce, and P. Leitz, European patent no. EP0995775A1, 2000.
- [38] H. Angellier, S. Molina-Boisseau, P. Dole, and A. Dufresne, "Thermoplastic starch—waxy maize starch nanocrystals nanocomposites," *Biomacromolecules*, vol. 7, no. 2, pp. 531–539, 2006.
- [39] J. Vigié, S. Molina-Boisseau, and A. Dufresne, "Processing and characterization of waxy maize starch films plasticized by sorbitol and reinforced with starch nanocrystals," *Macromolecular Bioscience*, vol. 7, no. 11, pp. 1206–1216, 2007.
- [40] E. Kristo and C. G. Biliaderis, "Physical properties of starch nanocrystal-reinforced pullulan films," *Carbohydrate Polymers*, vol. 68, no. 1, pp. 146–158, 2007.
- [41] H. Angellier, J.-L. Putaux, S. Molina-Boisseau, D. Dupeyre, and A. Dufresne, "Starch nanocrystal fillers in an acrylic polymer matrix," *Macromolecular Symposia*, vol. 221, no. 1, pp. 95–104, 2005.
- [42] A. Dufresne, J. Cavaillé, and W. Helbert, "New nanocomposite materials: microcrystalline starch reinforced thermoplastic," *Macromolecules*, vol. 29, no. 23, pp. 7624–7626, 1996.
- [43] Y. Wang and L. Zhang, "High-strength waterborne polyurethane reinforced with waxy maize starch nanocrystals," *Journal of Nanoscience and Nanotechnology*, vol. 8, no. 11, pp. 5831–5838, 2008.
- [44] Y. Habibi and A. Dufresne, "Highly filled bionanocomposites from functionalized polysaccharide nanocrystals," *Biomacromolecules*, vol. 9, no. 7, pp. 1974–1980, 2008.
- [45] K. G. Nair and A. Dufresne, "Crab shell chitin whisker reinforced natural rubber nanocomposites. 1. Processing and swelling behavior," *Biomacromolecules*, vol. 4, no. 3, pp. 657–665, 2003.

- [46] K. G. Nair and A. Dufresne, "Crab shell chitin whisker reinforced natural rubber nanocomposites. 2. Mechanical behavior," *Biomacromolecules*, vol. 4, no. 3, pp. 666–674, 2003.
- [47] Y. Lu, L. Weng, and L. Zhang, "Morphology and properties of soy protein isolate thermoplastics reinforced with chitin whiskers," *Biomacromolecules*, vol. 5, no. 3, pp. 1046–1051, 2004.
- [48] A. Dufresne and J.-Y. Cavaillé, "Clustering and percolation effects in microcrystalline starch-reinforced thermoplastic," *Journal of Polymer Science B*, vol. 36, no. 12, pp. 2211–2224, 1998.
- [49] A. Dufresne, "Polysaccharide nanocrystal reinforced nanocomposites," *Canadian Journal of Chemistry*, vol. 86, no. 6, pp. 484–494, 2008.
- [50] V. Favier, J. Y. Cavaillé, S. C. Shrivastava, and G. R. Canova, "Mechanical percolation in cellulose whisker nanocomposites," *Polymer Engineering and Science*, vol. 37, no. 10, pp. 1732–1739, 1997.
- [51] A. Dufresne, "Comparing the mechanical properties of high performances polymer nanocomposites from biological sources," *Journal of Nanoscience and Nanotechnology*, vol. 6, no. 2, pp. 322–330, 2006.
- [52] K. G. Nair, A. Dufresne, A. Gandini, and M. N. Belgacem, "Crab shell chitin whiskers reinforced natural rubber nanocomposites. 3. Effect of chemical modification of chitin whiskers," *Biomacromolecules*, vol. 4, no. 6, pp. 1835–1842, 2003.
- [53] N. Lin, G. Chen, J. Huang, A. Dufresne, and P. R. Chang, "Effects of polymer-grafted natural nanocrystals on the structure and mechanical properties of poly(lactic acid): a case of cellulose whisker-graft-polycaprolactone," *Journal of Applied Polymer Science*, vol. 113, no. 5, pp. 3417–3425, 2009.
- [54] G. Chen, A. Dufresne, J. Huang, and P. R. Chang, "A novel thermoformable bionanocomposite based on cellulose nanoerystal-graft-poly( $\epsilon$ -caprolactone)," *Macromolecular Materials and Engineering*, vol. 294, no. 1, pp. 59–67, 2009.
- [55] L. Feng, Z. Zhou, A. Dufresne, J. Huang, M. Wei, and L. An, "Structure and properties of new thermoforming bionanocomposites based on chitin whisker-graft-polycaprolactone," *Journal of Applied Polymer Science*, vol. 112, no. 5, pp. 2830–2837, 2009.
- [56] S. Dong and M. Roman, "Fluorescently labeled cellulose nanocrystals for bioimaging applications," *Journal of the American Chemical Society*, vol. 129, no. 45, pp. 13810–13811, 2007.

## Review Article

# Atoms and Nanoparticles of Transition Metals as Catalysts for Hydrogen Desorption from Magnesium Hydride

**N. Bazzanella, R. Checchetto, and A. Miotello**

*Dipartimento di Fisica Università degli Studi di Trento, 38123 Povo, Italy*

Correspondence should be addressed to A. Miotello, antonio.miotello@unitn.it

Received 9 April 2010; Accepted 18 August 2010

Academic Editor: Bo Zou

Copyright © 2011 N. Bazzanella et al. This is an open access article distributed under the Creative Commons Attribution License, which permits unrestricted use, distribution, and reproduction in any medium, provided the original work is properly cited.

The hydrogen desorption kinetics of composite materials made of magnesium hydride with transition metal additives (TM: Nb, Fe, and Zr) was studied by several experimental techniques showing that (i) a few TM at.% concentrations catalyse the H<sub>2</sub> desorption process, (ii) the H<sub>2</sub> desorption kinetics results stabilized after a few H<sub>2</sub> sorption cycles when TM atoms aggregate by forming nanoclusters; (iii) the catalytic process occurs also at TM concentration as low as 0.06 at.% when TM atoms clustering is negligible, and (iv) mixed Fe and Zr additives produce faster H<sub>2</sub> desorption kinetics than single additive. The improved H<sub>2</sub> desorption kinetics of the composite materials can be explained by assuming that the interfaces between the MgH<sub>2</sub> matrix and the TM nanoclusters act as heterogeneous sites for the nucleation of the Mg phase in the MgH<sub>2</sub> matrix and promote the formation of fast diffusion channels for H migrating atoms.

## 1. Introduction

Because of the high hydrogen storage capacity of MgH<sub>2</sub>, ~7.6 wt.%, low cost, and weight, magnesium is still currently investigated for H<sub>2</sub> storage applications. Most research efforts are dedicated to the improvement of the kinetic H<sub>2</sub> sorption process that is too slow even at temperatures larger than 500 K. The hydrogen desorption process results from many single steps taking place in series: the nucleation of the Mg phase in the MgH<sub>2</sub> parent phase and the diffusion of hydrogen atoms through transformed Mg and/or not transformed MgH<sub>2</sub> layers to the sample surface where the H<sub>2</sub> recombinative desorption occurs. The velocity of these reaction steps could be limited by the surface Mg oxide layer impeding the H<sub>2</sub> surface processes [1, 2] or by the presence of a continuous MgH<sub>2</sub> layer acting as hydrogen diffusion barrier [3]. On the contrary, the hydrogen absorption and desorption kinetic in Mg can be improved by microstructural refinements such as the reduction of the Mg or MgH<sub>2</sub> grain size: grain boundaries are, in fact, active nucleation sites for the formation or dissociation of the hydride phase and act as preferential diffusion paths for H atoms [4].

The major improvements are generally obtained by the use of a proper metal or metal oxide additive. Transition metals or transition metal oxides additives favour the H<sub>2</sub> dissociation [5] and can further improve the H<sub>2</sub> sorption kinetics in different ways. Nanocomposite materials formed by milling MgH<sub>2</sub> and Nb or Nb oxide powders are the most studied systems. Time-resolved X-rays synchrotron analysis suggested the transformation during H<sub>2</sub> desorption at 573 K of the NbH nanocatalyst in the metastable, H vacancy rich NbH<sub>0.6</sub> phases: the catalytic effect was thus explained as an enhanced transfer of H atoms from the MgH<sub>2</sub> matrix to the Mg surface by H diffusion through the catalyst layers [6]. Recent studies on the structural analysis of MgH<sub>2</sub> samples catalysed by Nb [7] or Nb oxides [8] suggest the formation of Mg-Nb perovskite phases by reaction of Nb<sub>2</sub>O<sub>5</sub> and Mg: the perovskite was suggested to act as preferential “pathways” for hydrogen diffusion.

We have recently studied the H<sub>2</sub> desorption process from MgH<sub>2</sub> samples where the metallic additives, single or mixed atomic species, were completely included inside the MgH<sub>2</sub> matrix [9–15]. These samples allow to specifically investigate the role of the additives, in the bulk processes, leading to

the decomposition of  $\text{MgH}_2$  phase and to the  $\text{H}_2$  desorption process. In this paper we present a comprehensive review of our experimental results.

In particular, in Section 2 we review the studies on the hydrogen desorption kinetics from pure and Nb-catalysed  $\text{MgH}_2$ , and then we discuss the role of the Nb additive when it is distributed inside the  $\text{MgH}_2$  matrix at concentration ranging from  $<0.1$  to about 5 at. %.

In Section 3 we will present the results of the experimental analysis dedicated to the structural and chemical-physical characterization of the Nb additive when dispersed in the Mg or  $\text{MgH}_2$  matrix.

In Section 2 we present a study on the comparison between the catalytic effect of different TM additives contained inside the  $\text{MgH}_2$  matrix at concentration  $\sim 5$  at. %.

Finally, in Section 3, we will present results on a novel route to enhance the hydrogen desorption kinetics from  $\text{MgH}_2$  by using mixed TM additive.

## 2. Hydrogen Desorption Properties of Nb-Doped $\text{MgH}_2$ Samples

Samples of pure Mg and Nb-doped Mg with different concentrations of Nb (see Table 1) were deposited by RF magnetron sputtering in form of films with thickness  $\sim 10$ – $20 \mu\text{m}$  on 5 cm diameter polished graphite wafers. The Nb doping was obtained by putting a few numbers of small Nb fragments on the surface of Mg target in such a way that sputtering process involves both Mg and Nb, that is, a co sputtering procedure was utilized to prepare Mg-doped samples [9]. To prevent the surface oxidation and stimulate the  $\text{H}_2$  dissociation at the Mg surface, samples were coated with a 15 nm thick Pd capping layer without interrupting the vacuum conditions in the deposition chamber. Pd is known to split hydrogen, and splitting is an important step in the hydrogen sorption process though it might be not the rate-limiting step. Indeed, at temperatures larger than 250–300 K, Pd is transparent to hydrogen [16].

The Nb concentration was measured, after deposition, by Energy Dispersion Spectroscopy (EDS) while Secondary Ions Mass Spectroscopy (SIMS) was employed with samples having Nb concentration lower than 1 at. % and to verify the uniform distribution of the Nb catalyst into the Mg layers [12]. After deposition, Mg samples peeled off from the substrate and the self-supporting samples were introduced in a Sievert-type apparatus to study the hydrogen absorption and desorption kinetics: details on the sample preparation, activation procedure, and experimental analysis are described elsewhere [9, 17].

In Figure 1 we present the hydrogen desorption kinetics from  $\text{MgH}_2$  at 623 K in samples having different Nb concentrations. The figure shows a strong increase of the reaction velocity for all the Nb-doped Mg: the reaction half-time  $\tau_{1/2}$ , that is the interval time needed to have half of  $\text{MgH}_2$  transformed to h-Mg, decreases from  $3250 \pm 50$  s for pure  $\text{MgH}_2$  to  $110 \pm 10$  s for the 2- to 5 at. % Nb-doped  $\text{MgH}_2$ . Intermediate values of  $\tau_{1/2}$  are observed at lower Nb concentrations:  $290 \pm 10$  s for 1 at. % and  $2390 \pm 30$  s for

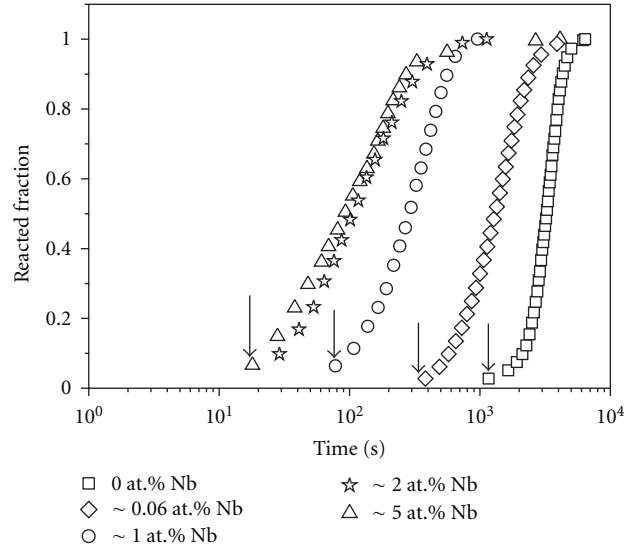


FIGURE 1: Hydrogen desorption kinetics at 623 K from  $\text{MgH}_2$  samples with different Nb concentrations.

0.06 at. %. A corresponding reduction of the incubation time, that is the typical time needed for the nucleation of the Mg phase, can also be observed in Figure 1 (arrows indicate the reacted fraction firstly evidenced that roughly corresponds to the incubation time).

The desorption processes of Figure 1 have been satisfactorily described in the framework of the Johnson-Mehl-Avrami theory for solid-state transformation [18]. The relevant effective parameters of the model, say, the values of the reaction order,  $n$ , and activation energy,  $E_a$ , are reported in Table 1. The obtained different values suggest that different mechanisms control the  $\text{H}_2$  desorption kinetics at different Nb concentrations.

The value  $n = 4$  obtained for pure  $\text{MgH}_2$  indicates that the continuous formation of stable Mg nuclei in the  $\text{MgH}_2$  parent phase is the rate-limiting step in the  $\text{H}_2$  desorption kinetics.  $n = 1$  for  $\text{MgH}_2$  samples with Nb content of 2–5 at. % indicates an instantaneous nucleation of the Mg metallic phase in the  $\text{MgH}_2$  followed by its diffusional growth [9]. The evaluated value of the activation energy,  $51 \pm 5$  kJ/mol H, suggests that the diffusional growth is limited by H atomic diffusion in Mg layers: this value is, in fact, close to that of the activation energy for H diffusion in bulk Mg, 40 kJ/mol H [19]. Structural analysis by X-Ray Diffraction (XRD) and Extended X-ray Absorption Fine Structure (EXAFS) [12] evidenced, as we will report below, the formation of Nb:H nanoclusters. We thus explained the kinetic results by assuming that (a) the interface between the Nb:H nanoclusters and the  $\text{MgH}_2$  matrix offers sites where the instantaneous nucleation of the Mg phase occurs (heterogeneous nucleation) and (b) H atoms dissociated from the Mg hydride migrate to the sample surface (where desorption occurs) through domains of transformed Mg. Kinetic data presented in Figure 1 indicate that the same behaviour is shown by samples with Nb dopant concentration  $\geq 2$  at. %. This result is relevant for application because it shows that

TABLE 1: Evaluated values of the half-reaction time ( $\tau_{1/2}$ ) at  $T = 623$  K, order of reaction ( $n$ ), and activation energy ( $E_a$ ) of  $\text{MgH}_2$  samples with different Nb concentrations.

Sample	$\tau_{1/2}$ (s)	$n$	$E_a$ (kJ mol <sup>-1</sup> H)
Pure Mg	3250 $\pm$ 50	4	141 $\pm$ 5
Mg + 0.06 at.% Nb	2390 $\pm$ 30	2	140 $\pm$ 5
Mg + 1 at.% Nb	290 $\pm$ 10	1.5	78 $\pm$ 5
Mg + 2 $\div$ 5 at.% Nb	110 $\pm$ 10	1	51 $\pm$ 5

the optimum catalyst concentration can be lower than 5 at.%, the concentration usually reported for ball-milled Mg [20]. Note that only a few other catalysts were tested at so low concentration [21].

Relevant differences on hydrogen desorption kinetics are observed in samples with Nb concentration lower than 2–5 at.%.: the kinetic curve for 1 at.% Nb concentration is reproduced with  $n = 1.5$  and  $E_a = 78 \pm 5$  kJ/mol H. The XRD spectrum of such sample (see [12]) shows that Nb atoms form Nb:(H) nanoclusters with size nearly equal to that observed in samples with larger Nb content. Because of the lower Nb concentration, there is thus a larger distance between the Nb:H nanoclusters and a lower specific  $\text{MgH}_2$ -Nb:H interface area as compared to the 2–5 at.% Nb-doped samples. The larger value of the activation energy (78 versus 51 kJ/mol) cannot be simply explained as an effective value describing the  $\text{H}_2$  effusion kinetics of a material that consists of a fraction of Nb-catalysed  $\text{MgH}_2$  and a fraction of pure  $\text{MgH}_2$ : effusion simulation carried out by assuming that the hydride consists of a larger fraction of  $\text{MgH}_2$  with embedded Nb clusters, and a lower fraction of pure  $\text{MgH}_2$  cannot reproduce the observed  $\text{H}_2$  desorption kinetics. On the contrary, by assuming that the observed kinetics still obeys a diffusion-controlled kinetics, the evaluated values of  $n = 1.5$  and  $E_a = 78$  kJ/mol can be explained by observing that:

- the presence of Nb:H clusters still provide a large density of Mg phase nucleation centers with low activation energy barriers (as in the case of 5 at.% Nb); this point is confirmed by the reduced values of the incubation time when compared with the pure Mg hydride;
- the increased distance between the Nb clusters in the  $\text{MgH}_2$  matrix limits the onset of interconnected Mg domains which favour the H atomic diffusion [9].

The evaluated value of the activation energy,  $78 \pm 5$  kJ/mol H, is not much different from the value of the activation energy,  $100 \pm 10$  kJ/mol H, for H diffusion in  $\text{MgH}_2$  as reported by Fernández et al. [22]. This suggests that the rate-limiting step in the H diffusion is given by the energy barrier to be overcome by the migrating species in not transformed  $\text{MgH}_2$  phase.

A final interesting result comes out from the analysis of the sample with the lower Nb concentration, 0.06 at.%. Here the clustering of the Nb atoms is a negligible process because the Nb concentration is close to the solubility limit of Nb in Mg,  $[\text{Nb}/\text{Mg}] \sim 10^{-4}$  [23]. A catalytic effect of Nb on hydrogen desorption can be still observed as

indicated by the reduction of the  $\tau_{1/2}$  parameter with respect to that observed in the undoped  $\text{MgH}_2$ . After repeated  $\text{H}_2$  absorption-desorption cycles, the catalytic properties decrease and the 0.06 at.% Nb- $\text{MgH}_2$  exhibits a value of the  $\tau_{1/2}$  parameter comparable to that of pure  $\text{MgH}_2$  but lower incubation time. This means that the Mg nucleation process still results in acceleration. Because the relevant activation energy value of the desorption process is just the same as in the case of pure Mg (see Table 1), we may conclude that single Nb atoms may constitute seeds for heterogeneous Mg nucleation in the same way as homogeneous seeds operate in pure Mg.

In particular, we suggest that the atomic environment around the Nb impurity atom acts as nucleation seed for the Mg phase given the presence of local elastic strains due to the atomic size difference between solute (Nb) and solvent atoms (Mg, H). The decrease of the phase transition velocity after the first absorption-desorption cycles is explained by impurity segregation at extended defects, such as grain boundaries, that reduce the availability of heterogeneous nucleation seeds.

In conclusion, several different mechanisms influence the hydrogen kinetics in  $\text{MgH}_2$  depending on the Nb atomic concentration: specifically, at concentration larger than 1 at.%, Nb forms nanoclusters that affect both the Mg nucleation process and hydrogen diffusion. At very low concentration, 0.06 at.%, Nb remains atomically dispersed (clustering of the Nb atoms should be negligible because the Nb concentration, as indicated above, is close to the solubility limit in Mg) and the only effect of Nb is on favouring the Mg-phase nucleation.

### 3. EXAFS and TEM Analysis of Nb-Doped $\text{MgH}_2$

In order to further clarify the role of the Nb doping element, we studied the evolution of the chemical-physical state of the Nb atoms dispersed in the Mg matrix upon hydrogen absorption and desorption cycles. The analyses were carried out by EXAFS, XRD, and Transmission Electron Microscopy (TEM) analysis on three representative Nb-doped Mg samples: (i) as-deposited sample, (ii) activated  $\text{MgH}_2$  samples after partial  $\text{MgH}_2$  to Mg phase transition (hereafter, hydrogenated sample), and (iii) activated sample after complete  $\text{MgH}_2$  to Mg phase transition (hereafter, dehydrogenated sample). Details on the measurements and data analysis are reported in [11].

Results show that stable catalytic effects of Nb are connected with the formation of Nb nanoclusters dispersed

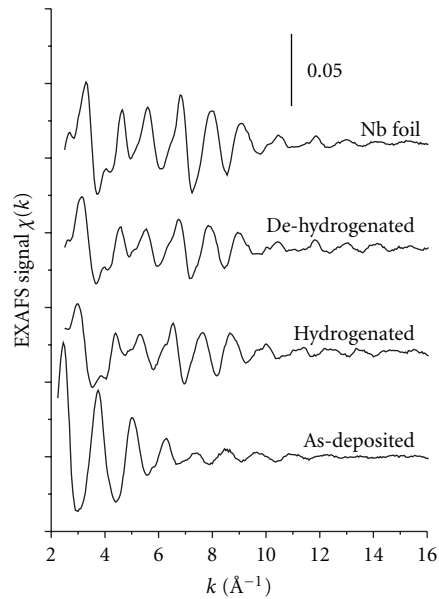


FIGURE 2: Nb  $K$ -edge EXAFS spectra from Nb-doped (5 at.%) Mg samples; the spectra of the hydrogenated and dehydrogenated samples are pertinent to fully activated samples.

in the Mg matrix while no evidence of Nb oxidation could be deduced from previous analysis.

In Figure 2 we present the EXAFS spectra of the samples together with the spectrum of crystalline Nb: we observe that the spectrum of the as-deposited sample is different from the spectra of the hydrogenated and dehydrogenated samples which are similar to that of crystalline Nb.

In Figure 3 we show the moduli of the Fourier transformed spectra compared with the corresponding best-fit curves of the first two interatomic correlation signals: the spectrum of the as-deposited sample differs from that of the metallic Nb; the other two are quite similar, except for the fact that for the hydrogenated sample the peaks located at about 2.7 and 3.1 Å are shifted towards higher  $R$  (the interatomic distance) values with respect to the Nb foil spectrum. The results of the EXAFS analysis are reported in Table 2.

In the as-deposited sample, the average local structure around Nb is composed mainly of Mg atoms, at a distance that is shorter with respect to the corresponding value of the crystalline Mg and appears in agreement with the first Nb-Mg coordination distance obtained by simulating an Nb substitutional impurity in an Mg cluster. Besides this main signal, the analysis evidenced also an Nb-Nb correlation, as shown in Figure 3(b), where in the backtransformed  $k$ -space the filtered data and fit are compared and the different contributions to the fit are reported. The Nb-Nb correlation indicates the presence of Nb aggregates: the fact that the coordination number is low (about 1) and the Nb-Nb distance is shorter than for the bulk Nb strongly suggests that the clusters are composed of few Nb atoms. In the hydrogenated sample, the Nb-Mg signal is below the detectable limit; two Nb-Nb correlations are evident

indicating the presence of Nb-containing nanoclusters: the Nb-Nb distances are  $\sim 4.5\%$  longer than the corresponding values in crystalline Nb. We ascribe this fact to the presence of H atoms into the Nb clusters increasing the interatomic distance: the local structure around Nb is in agreement with both the  $\alpha$ Nb-H phase (with an H/Nb atomic ratio of 0.9) [24] and with the orthorhombic  $\beta$ Nb-H phase (with an H/Nb atomic ratio higher than 0.8) [25]. It is worth noting that the coordination number is lower than the corresponding value in the bulk Nb, due to the fraction of Nb atoms located on the cluster surface and, possibly, to Nb atoms dispersed in the Mg matrix. After the hydrogen desorption process, the Nb is still aggregated in nanoclusters: in this case, the Nb-Nb coordination distances are those of the corresponding bulk phase: this indicates the H desorption from the Nb clusters (see [6] to gain insight on formation, decomposition, and general features on stability of NbH). The fact that the coordination numbers in this case are even lower than those of the hydrogenated sample could likely indicate a smaller size of the nanoclusters and/or a larger fraction of Nb atoms dispersed into the Mg matrix. As in the hydrogenated sample, the Nb-Mg signal is below the detectable limit for the EXAFS spectroscopy.

The XRD spectrum of the as-deposited sample [9] shows a preferential growth of the Mg film with the (0001) planes parallel to the substrate. After hydrogenation, the sample shows a complex pattern formed of many peaks; see Figure 4: the peaks can be attributed to a tetragonal  $\text{MgH}_2$  phase with lattice parameters  $a = 0.4517$  nm and  $c = 0.30205$  nm (ICDD card n. 12-697) and to an orthorhombic  $\beta$ - $\text{NbH}_{0.89}$  phase with lattice parameters  $a = 0.484$  nm,  $b = 0.490$  nm, and  $c = 0.345$  nm (ICDD card n. 7-263). The unindexed peaks are due to Mg layers that have lost the absorbed hydrogen. The mean grains size of the  $\beta$ - $\text{NbH}_{0.89}$  phase, estimated by using the Scherrer equation after deconvolution of the  $\text{Mg}(101)$  and  $\text{NbH}_{0.89}(200)$  peaks, see the inset of Figure 4, is  $\sim 20$  nm. The presence of metallic Nb was never detected in the hydrogenated sample. The dehydrogenated sample shows a very simple XRD pattern where, apart from the unindexed Mg peaks, only the first three peaks of metallic Nb (bcc,  $a = 0.33066$  nm, ICDD card n. 35-789) are present; see Figure 5. The mean grains size of the metallic Nb, calculated from the measurement of the FWHM of the Nb(110) peak, is  $\sim 15$  nm. It is worth to note that in this case the Mg- and Nb-hydrides are completely disappeared.

TEM observations performed on the as-deposited sample evidenced the preferential growth of the film, in agreement with the XRD results, as well as the absence of any nanocluster or precipitate inside the Mg grains. The size of these grains ranges from 0.1 to 1.5  $\mu\text{m}$ . The electron diffraction pattern has a ring structure attributable to Mg. In this case, the few-atom aggregates detected by the EXAFS spectroscopy are most likely too small to give a significant contribution to the whole diffraction pattern. A completely different appearance is shown by the hydrogenated sample: spherical nanoclusters with dimensions ranging from 5 to 25 nm, not uniformly dispersed inside the grains, are clearly visible after few minutes of permanence under the electron

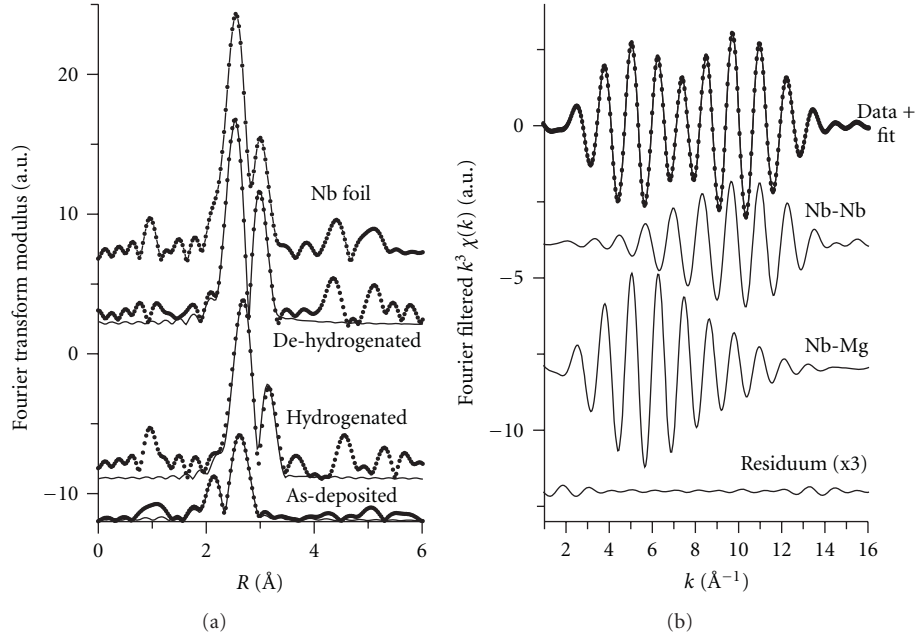


FIGURE 3: EXAFS analysis of the Nb-doped (5 at.%) Mg samples. (a)  $k^3$ -weighted Fourier transform moduli (transformation range  $k = 3$ – $13$  Å<sup>-1</sup> for the as-deposited sample,  $k = 3$ – $16$  Å<sup>-1</sup> for the others) of the EXAFS spectra (markers) and corresponding best-fit curves (solid line) of the first two coordination signals (Nb-Mg and Nb-Nb for the as-deposited sample, two Nb-Nb for the others); no back-scatterer phase-shift correction was applied in the figure. (b) Fourier filtered spectrum (markers) in the fitting range and superimposed fit (solid line) of the as-deposited EXAFS spectrum; the residuum and the two single-scattering signals that contribute to the fit are reported.

TABLE 2: Results of the Nb  $K$ -edge EXAFS analysis on Nb-doped Mg films; for each pair of atoms,  $N$  is the coordination number,  $R$  the interatomic distance, and  $\sigma^2$  the Debye-Waller factor. The uncertainty in the fitting results corresponds to a confidence level of 68%. Crystallographic data for metallic Nb and the simulation of the local structure around an Nb substitutional impurity into the Mg lattice are also reported.

Sample		$N$	$R$ (Å)	$\sigma^2$ ( $10^{-4}$ Å <sup>2</sup> )
As-deposited	Nb-Nb	$1.2 \pm 0.4$	$2.73 \pm 0.01$	$38 \pm 9$
	Nb-Mg	$9.6 \pm 0.9$	$3.08 \pm 0.01$	$99 \pm 8$
Hydrogenated	Nb-Nb	$5.6 \pm 0.3$	$3.00 \pm 0.02$	$57 \pm 6$
	Nb-Nb	$4.2 \pm 0.2$	$3.45 \pm 0.02$	$66 \pm 8$
dehydrogenated	Nb-Nb	$4.0 \pm 0.2$	$2.87 \pm 0.01$	$44 \pm 4$
	Nb-Nb	$3.0 \pm 0.2$	$3.32 \pm 0.01$	$40 \pm 4$
metallic Nb	Nb-Nb	8	2.8638	
	Nb-Nb	6	3.3068	
Nb-doped Mg (simulation)	Nb-Mg	6	3.075	
	Nb-Mg	6	3.195	

beam (a longer permanence induces the decomposition of the Mg- and Nb-hydrides). The electron diffraction pattern of the sample only shows the presence of Mg rings and a very weak ring attributable to metallic Nb. Finally, the dehydrogenated sample is stable under the electron beam, and its structure is formed of spherical nanoclusters with dimensions in the range 10–20 nm. These nanoclusters are not uniformly distributed inside the grains; see Figure 6, where the Nb particles appear as small black dots. The electron diffraction pattern of this sample is formed of spotty rings due to Mg and few well evident extra spots due to metallic Nb.

The present structural analysis thus shows that the accelerated H<sub>2</sub> desorption kinetics is connected to the presence of the Nb nanoclusters [12]. As suggested by the analysis of the desorption curves, the role of the nanoclusters is connected to the accelerated nucleation of the Mg phase in the MgH<sub>2</sub> matrix: the interface between the Nb:H nanoclusters and the MgH<sub>2</sub> matrix favours the instantaneous nucleation of the Mg phase (heterogeneous nucleation). An embryo of the Mg phase can reduce its energetic formation cost at the MgH<sub>2</sub>-Nb:H interface as discussed in general framework; see [26, 27]. In addition, the MgH<sub>2</sub>-Nb:H interface can favour the Mg phase growth. Indeed, in diffusional phase

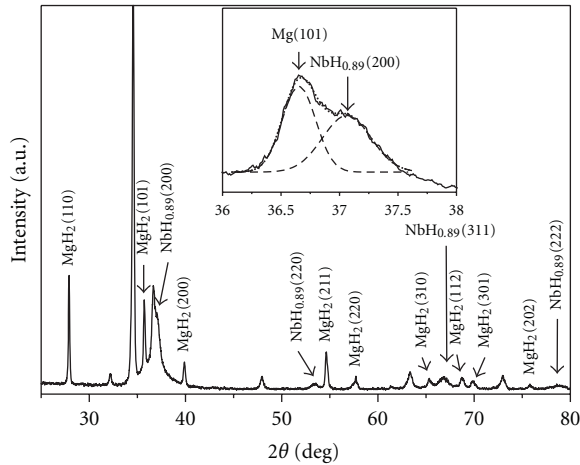


FIGURE 4: XRD spectrum of the 5 at.% Nb-doped  $\text{MgH}_2$  sample, partially dehydrogenated. The inset shows the deconvolution of the Mg (101) and  $\text{NbH}_{0.89}$  (200) peaks: continuous line: experimental data, dashed line: fitting, and dotted line: envelope of the fitted curves.

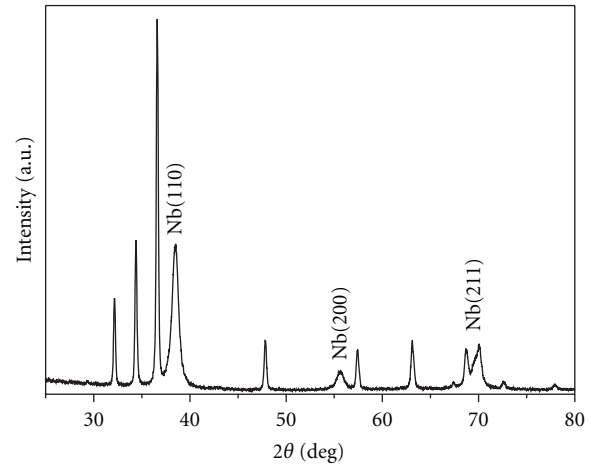


FIGURE 5: XRD spectrum of the dehydrogenated 5 at.% Nb-doped samples.

transitions where transport of the atomic components occurs over paths longer than the interatomic distance, new phases are often observed to nucleate at grain boundaries of the parent phase. These extended defects result in fast diffusion channels for migrating atoms thus giving rise, in the lattice layers around them, to the critical solute concentration for the phase transition [26, 27]. In the present Nb-doped  $\text{MgH}_2$  samples, the  $\text{MgH}_2$ -Nb:H interface can play a similar role allowing an effective removal of the H atoms dissociated from adjacent  $\text{MgH}_2$  layers and thus favouring the formation of Mg nuclei having critical size.

#### 4. Comparison between Desorption Kinetics of Nb-, Zr-, and Fe-Doped $\text{MgH}_2$

In this section we present a comparative study on the  $\text{H}_2$  desorption from the  $\text{MgH}_2$  matrix doped with different metallic elements dispersed in atomic concentration, say, 2–5 at.% [13]. Results on Nb were reported above and now we consider, for comparison, Fe and Zr because (i) they are transition metals (TM) with catalytic properties for the  $\text{H}_2$  sorption kinetics in Mg and (ii) they do not form binary phases with Mg and show negligible solubility [23]. Nb, Zr, and Fe have different “affinity” with hydrogen in the temperature range ( $400 \text{ K} < T < 700 \text{ K}$ ). Nb forms interstitial alloys with hydrogen: the  $\alpha$  phase is a random interstitial alloy of H in bcc Nb with H/Nb ratio  $< 0.31$ . Zr forms stable phase: the  $\delta$  phase having fcc structure with  $1.31 < \text{H/Nb} < 2$ . Fe does not form any binary hydride phase and shows negligible H solubility [28]. In these new composite samples, the atomic % concentration, as detected by EDS, was  $\sim 5$  at.% for Fe (the same as for Nb) and  $\sim 3$  at.% for Zr: these concentrations are larger than the maximum solubility of the TM in Mg, 0.00043 at.% for Fe at the eutectoid temperature of 920 K, close to  $1.3 \times 10^{-4}$  for Nb in liquid Mg at 1500 K, and lower than 0.1 at.% for Zr at temperatures

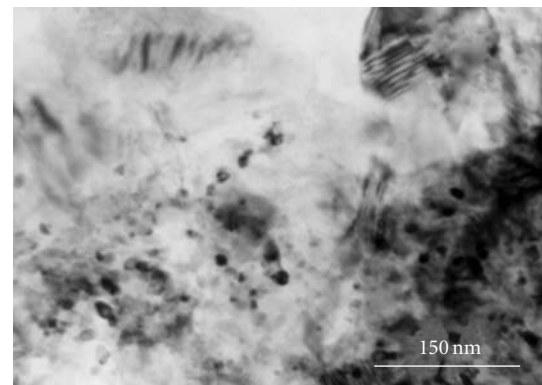


FIGURE 6: TEM micrograph of the dehydrogenated sample showing distribution and size of the metallic Nb nanoclusters.

lower than 700 K [23]. These equilibrium properties indicate that precipitation of the metal additive atoms is expected upon the thermal treatment leading to the sample activation at 623 K and/or during  $\text{H}_2$  cycling.

The room temperature XRD spectra of the TM-doped samples, partially dehydrogenated, confirm cluster formation. While Fe remains in the metallic state, see Figure 7, Nb and Zr form hydride phase as shown by the  $\text{NbH}_{0.89}$  and  $\text{ZrH}_{1.66}$  reflection peaks in Figures 8 and 9, respectively: no evidence of metallic Nb or Zr was found in the partially desorbed samples. The obtained TM-H phases are appropriate to equilibrium phase diagram at room temperature [28]. The Debye-Scherrer analysis of the XRD peak indicates the formation of TM nanoclusters having dimensions in the  $10 \div 20 \text{ nm}$  range while Mg and  $\text{MgH}_2$  maintain the microcrystalline structure [9–11]. The aggregation of TM atoms to form nanoclusters during cycling in hydrogen is confirmed by the evolution of XRD spectra from as-deposited to fully cycled samples [9, 11] and by also comparing with EXAFS analysis [11].

In Figure 10 we present the isothermal  $\text{H}_2$  desorption curves of the pure and metal-doped  $\text{MgH}_2$  samples at the

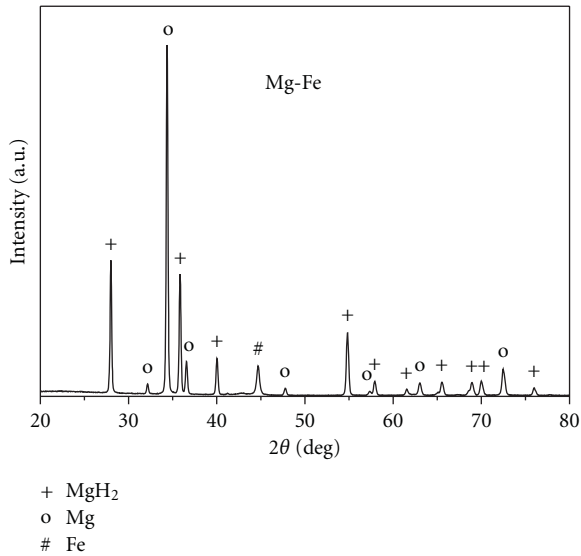


FIGURE 7: Room temperature XRD spectra of the 5 at.% Fe doped MgH<sub>2</sub> samples, partially dehydrogenated after full activation.

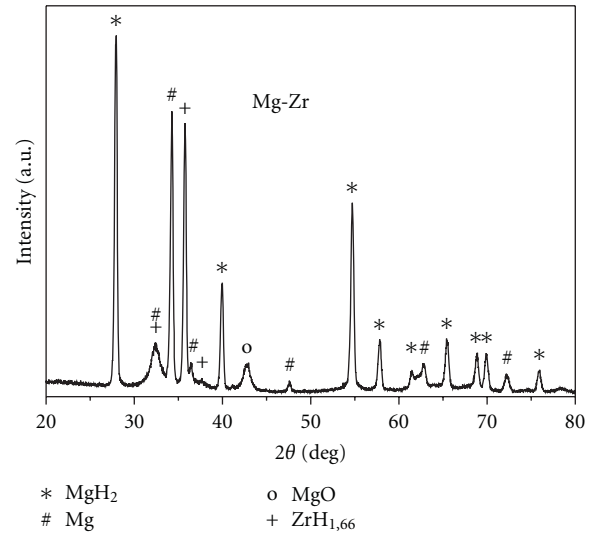


FIGURE 9: Room temperature XRD spectra of the 3 at.% Zr-doped MgH<sub>2</sub> samples, partially dehydrogenated after full activation.

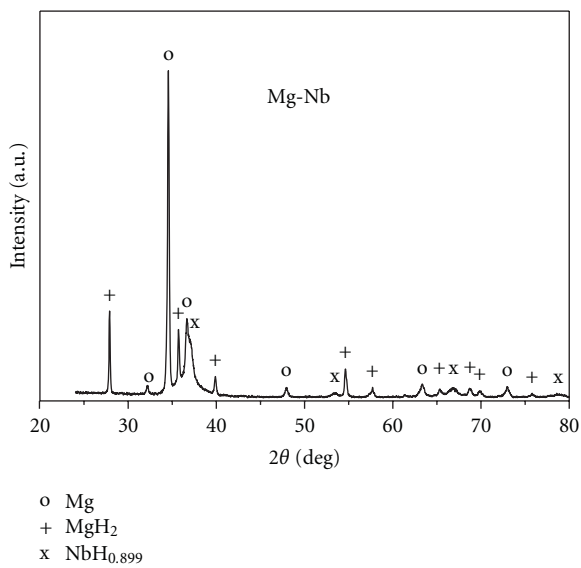


FIGURE 8: Room temperature XRD spectra of the 5 at.% Nb-doped MgH<sub>2</sub> samples, partially dehydrogenated after full activation.

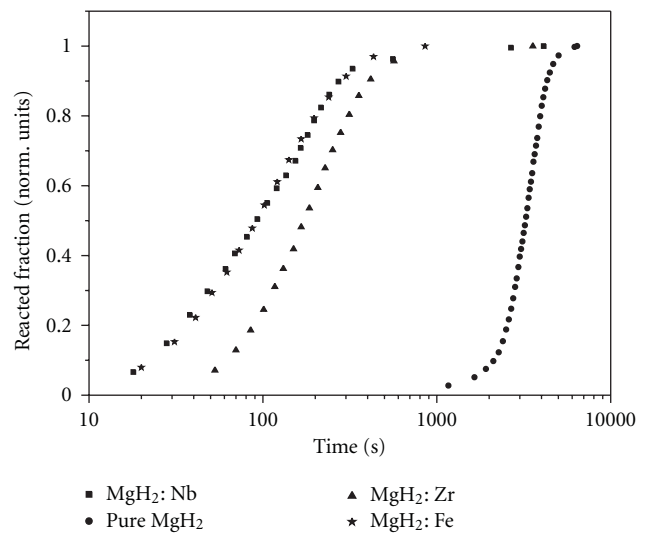


FIGURE 10: Isothermal H<sub>2</sub> desorption curves of the pure and TM-doped MgH<sub>2</sub> samples at 623 K, after their fully activation.

representative temperature of 623 K. The curves show a strong improvement of the H<sub>2</sub> desorption kinetics in the examined TM-doped samples when compared to the pure MgH<sub>2</sub>: at this temperature the interval time required for 50% transformation decreases from ~3000 s for pure MgH<sub>2</sub>, to ~200 s for the Zr-doped sample, and to ~100 s for Nb- and Fe-doped samples.

In Figure 11 we present the TDS spectra of the pure and TM-doped MgD<sub>2</sub> samples after their complete activation. (For the TDS analysis deuterium was chosen rather than hydrogen to improve the signal-to-noise ratio: at 2% of the TDS peak height the signal-to-noise ratio of the  $m/e = 4$  signal was better than 10<sup>2</sup>).

The most important information provided by the spectra is the position of the peak temperature  $T_p$  at which the desorption rate reaches its maximum: this temperature allows a direct comparison of the influence of the TM additive on the thermal stability of the MgD<sub>2</sub> phase. The obtained spectra confirm the trend observed in the isothermal curves evidencing lower thermal stability of the TM-doped samples as compared to pure MgD<sub>2</sub>. The Fe- and Nb-doped samples show TDS peaks at ~470 and ~480 K, respectively while the Zr-doped samples show TDS peaks at ~535 K. Pure MgD<sub>2</sub> shows the TDS peak at a larger temperature, close to 630 K.

The present H<sub>2</sub> (or D<sub>2</sub>) desorption results show that the dispersion of different TM nanoclusters inside the MgH<sub>2</sub> matrix accelerates the H<sub>2</sub> desorption process and that TM

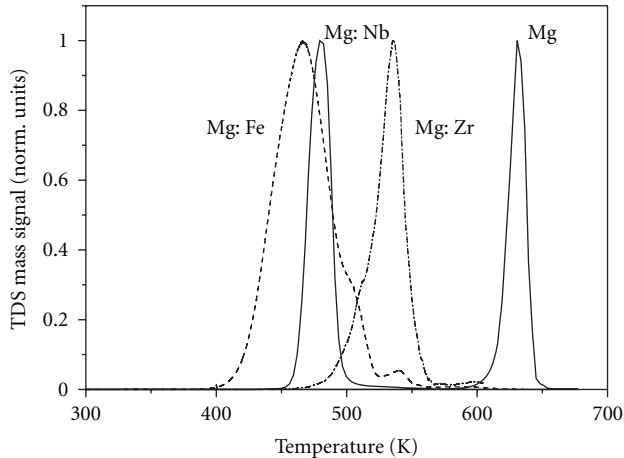


FIGURE 11: TDS spectra of the pure and TM-doped  $\text{MgD}_2$  samples after their fully activation.

nanoclusters distributed in the  $\text{MgH}_2$  matrix catalyse the Mg phase nucleation even if they present different chemical affinity with hydrogen. This point is also confirmed by the strong reduction of the nucleation time (Figure 10) shown by the isothermal desorption curves of the TM doped samples ( $\sim 10$  s for Nb and Fe and  $\sim 50$  s for Zr) as compared to that pertinent to the pure  $\text{MgD}_2$ ,  $\sim 1000$  s.

In conclusion, composite materials consisting on TM-doped Mg (TM: Nb, Fe, and Zr) with TM content of a few at.% concentration show accelerated  $\text{H}_2$  desorption kinetics when compared to the pure  $\text{MgH}_2$  samples (the diffusion of migrating hydrogen atoms has been measured by “in situ” EXFAS for the  $\text{MgH}_2/\text{Nb}_2\text{O}_5$  system [29]); while in the pure  $\text{MgH}_2$  the  $\text{H}_2$  desorption kinetics is controlled by the nucleation and growth of the Mg phase, in TM-doped samples the  $\text{H}_2$  release is controlled by the H diffusion through Mg layers. The improved  $\text{H}_2$  desorption kinetics can be explained by the presence of extended interfaces between  $\text{MgH}_2$  and TM nanoclusters acting as heterogeneous sites for the nucleation of the Mg phase and promoting the formation of fast diffusion channels for H migrating atoms.

## 5. Mixed Zr-Fe Catalysts

In the previous sections we observed that the presence of TM nanoclusters dispersed in the  $\text{MgH}_2$  matrix accelerates the H desorption kinetics. Two additional effects were also evidenced by the experiments [12]. First, in Mg samples with Nb content in the at.% level, the hydrogen desorption kinetics, when Nb does not form precipitates, was faster than that observed in the activated sample where Nb forms nanoclusters. Second, catalytic effects were also observed when the metallic additive was present at levels lower than 0.1 at.% in the Mg matrix, that is, close to the solubility limit of Nb in Mg. The desorption curves presented the same kinetics (nucleation and growth mechanisms) and activation energy as that of the pure  $\text{MgH}_2$  samples but a shorter nucleation time: we thus suggested that also Nb atoms (or few-atom aggregates) dispersed in the Mg matrix act as

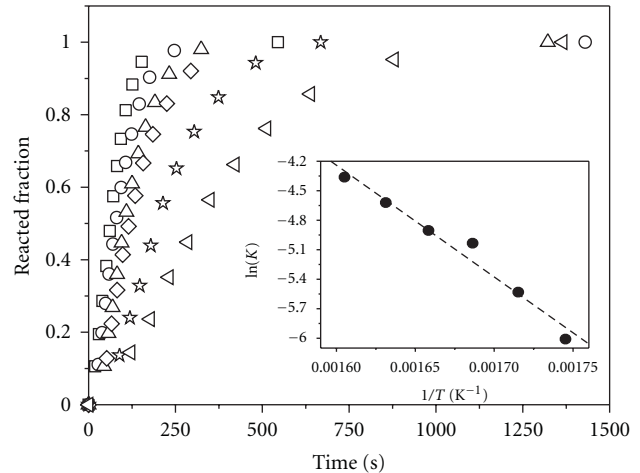


FIGURE 12: Dehydrogenated fraction versus time at various temperatures for the Mg sample with mixed Fe-Zr additives at  $\square$  623 K,  $\circ$  613 K,  $\triangle$  603 K,  $\diamond$  593 K,  $\star$  583 K, and  $\nabla$  573 K. In the insert we present the Arrhenius plot of the desorption rate constant  $k$ : the straight line is the least square fit.

nucleation centres for the Mg phase in the parent  $\text{MgH}_2$  phase [12].

These results suggest that a route to accelerate the  $\text{H}_2$  desorption kinetics is to limit the aggregation of the additives in form of large clusters and to favour a better distribution of the catalyst in form of small clusters or few atoms aggregates into the  $\text{MgH}_2$  matrix. To this purpose we have prepared  $\text{MgH}_2$  samples with mixed TM additives: in this section we report on the hydrogen desorption from magnesium hydride samples containing Fe and Zr, at a few at.% concentration [14].

We have used Zr and Fe because they have catalytic effects when dispersed in form of nanocluster in the  $\text{MgH}_2$  matrix and because they do not form binary phases with Mg matrix. Finally Zr is heavier than Fe and has larger atomic diameter, 4.32 versus 3.44 Å: they thus have different mobility values and we thus expect different clustering processes when sharing the same host matrix (Mg).

The Fe atoms will preferentially form clusters thus limiting the aggregation process of Zr atoms because Fe atoms can faster reach extended defects in the Mg (or  $\text{MgH}_2$ ) matrix which are the typical nucleation centers. To experimentally study this process we prepared Mg samples with (i) Fe single additive (5 at.%), (ii) Zr single additive (3 at.%), and (iii) mixed additive with 7 at.% ( $\sim 5$  and  $\sim 2$  at.% content for Fe and Zr, resp.).

XRD analysis of the as-deposited samples showed no evidence of metallic Fe and Zr: this means that the presence of the additive is in atomic form or in form of a few atoms aggregates as previously observed with Mg samples containing the Nb additive [11]. Based on previous XRD analysis of TM-doped Mg, it is really difficult to suppose the presence of metallic amorphous phase. In Figure 12 we report the  $\text{H}_2$  desorption data pertinent to fully activated  $\text{MgH}_2$  samples with Fe-Zr mixed additive [18]. For comparison in Figure 13 we present the  $\text{H}_2$  desorption data at the representative

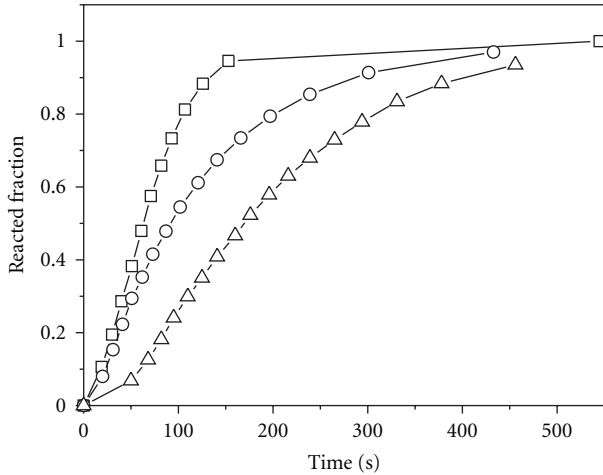


FIGURE 13: Dehydrogenated fraction versus time at 623 K of  $\text{MgH}_2$  sample with Zr ( $\Delta$ ) and Fe ( $\circ$ ) single additive and mixed Fe-Zr additives ( $\square$ ). The lines are only guide for the eyes.

temperature of 623 K pertinent to the  $\text{MgH}_2$  samples with single catalyst: symbols ( $\Delta$ ) for Zr, symbols ( $\circ$ ) for Fe. Symbols ( $\square$ ) are pertinent to the sample with Fe-Zr mixed additives.

In Table 3 we report the kinetic parameters pertinent to samples containing the mixed additives and, as reference, those pertinent to samples with a single additive and to pure  $\text{MgH}_2$ . We note that in presence of mixed additives the hydride to metal phase transition obeys a nucleation-and-growth mechanism while in presence of a single catalyst (5 at.% Fe or 5 at.% Nb) the phase transformation has diffusive character as shown by the different values of the reaction order  $n$  and of activation energy  $E_a$ . The most important result is the fact that the mixed additives induce faster desorption kinetic as compared to pure  $\text{MgH}_2$  and to  $\text{MgH}_2$  with Fe or Nb as single additive as shown by the  $\tau_{1/2}$  parameter. Table 3 also indicates that the hydride decomposition kinetic with mixed additives is very similar to that of the sample with 1 at.% Nb reported in Section 2: the order of reaction is the same, and the activation energy values are very similar. The much better catalytic effect of the mixed additives is related to the impressive increase of pre-exponential factor ( $A$ ) growing from  $\sim 10^4$  to  $\sim 10^8 \text{ sec}^{-1}$ . We remark that the improved kinetics compared to that of the sample with single Fe or Zr additive cannot be attributed to the larger additive content because there is a saturation effect in the desorption catalysis with additive contents of  $\sim 2$  at.% [12].

In Figure 14 we present the XRD spectrum of a fully activated sample after  $\text{H}_2$  desorption that provides information on the physical state of the Fe and Zr additives. In the spectrum we observe reflection peaks pertinent to Mg and the (110), (200), and (211) Bragg reflections of the  $\alpha$ -Fe phase but no XRD peak attributable to Zr nor to any Fe-Zr phase. Because Zr and Fe as single additive cannot produce the fast desorption kinetics shown in Figure 12, we may suppose that the improved catalytic effect of the

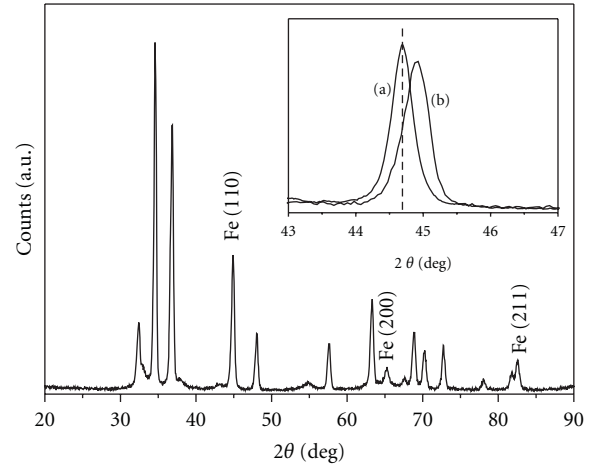


FIGURE 14: XRD spectra pertinent to Mg samples with mixed Fe-Zr additives (completely activated) after  $\text{H}_2$  desorption: in the figure only the Fe reflection peaks are labelled and all others peaks are pertinent to h-Mg reflections. In the inset we present the Fe (110) reflection peak pertinent to a sample with only the Fe additive, line (a), and to a sample with mixed Fe-Zr additives, line (b). The thick line is the reference position of the Fe (110) peak [ICDD 06-0696].

mixed additives has two causes: (i) aggregation of Fe into nanoclusters and (ii) atomic dispersion of Zr (that could also form aggregates but consisting on few atoms). We remark that the second effect has permanent character because, contrarily to the samples with single additive, no evidence of Zr clustering is observed also after repeated  $\text{H}_2$  sorption cycles.

By using the Williamson-Hall method [30] the size of the  $\alpha$ -Fe crystallites was determined to be lower than 20 nm. We can also evaluate a low microstrain value of  $\epsilon \sim 6 \times 10^{-4}$  not observed in the Mg sample with single Fe additive. The intensity ratio of these diffraction peaks indicates that the  $\alpha$ -Fe nanoclusters have a random distribution in the Mg matrix. The  $\alpha$ -Fe clusters size is lower than in Mg samples with single Fe additive,  $\sim 30$  nm, as evaluated by the Bragg-Brentano analysis of the (110) reflection peak presented in the inset of Figure 14, line (a) (this is the only  $\alpha$ -Fe reflection in the XRD spectrum). Both samples have the same Fe content,  $\sim 5$  at.%, and assuming that all Fe atoms form precipitates, we conclude that the sample with mixed additives presents a higher Fe cluster density.

In the Mg sample with Zr as single additive, after segregation upon diffusion, Zr atoms aggregate forming clusters [13]. In the sample with mixed additives these Zr clusters are not observed: the larger Fe mobility suggests that a possible mechanism impeding the Zr aggregation is the Fe clustering in the disposable nucleation centres which anticipates the Zr precipitation. The lower size of the Fe clusters in the Mg sample with mixed additives can be explained by a larger density of available nucleation sites as compared to that in the Mg sample with single Fe additive: reasonably, the Zr few-atom aggregates may constitute precipitation centres for Fe atoms.

TABLE 3: Evaluated values of the half-reaction time ( $\tau_{1/2}$ ) at  $T = 623$  K, order of reaction ( $n$ ), activation energy ( $E_a$ ), and pre-exponential factor ( $A$ ) of pure and TM-doped (TM: Nb, Fe, and Zr + Fe) MgH<sub>2</sub> samples.

Sample	$\tau_{1/2}$ (s)	$n$	$E_a$ (kJ mol <sup>-1</sup> H)	$A$ (s <sup>-1</sup> )
Pure Mg	3250 ± 50	4	141 ± 5	~10 <sup>8</sup>
Mg + 5 at.% Nb	110 ± 10	1	51 ± 5	~10 <sup>2</sup>
Mg + 1 at.% Nb	290 ± 10	1.5	78 ± 5	~10 <sup>4</sup>
Mg + 5 at.% Fe	100 ± 10	1	51 ± 5	~10 <sup>2</sup>
Mg + (Fe-Zr)	70 ± 10	1.5	94 ± 5	~10 <sup>8</sup>

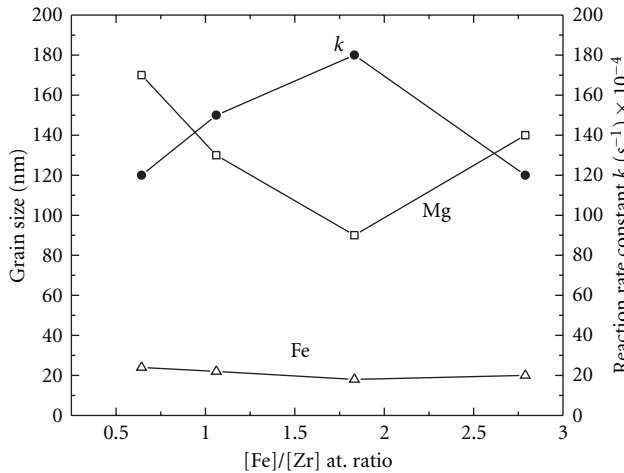


FIGURE 15: Fe cluster size (triangles), Mg grain size (squares) and desorption rate constant (circles) at different  $[\text{Fe}]/[\text{Zr}]$  atomic ratios. The lines are only a guide for the eye.

To gain a deeper understanding on the kinetic processes in presence of mixed additives and to determine which is the optimum Fe and Zr atomic concentrations, we have prepared samples with fixed metal content, about 7 at.%, by changing the  $[\text{Fe}]/[\text{Zr}]$  atomic ratio [31]. In Figure 15 we summarize the results by showing the size of the Fe nanoclusters, the Mg grain size, and the desorption rate constant  $k$  ( $T = 623$  K) as function of the  $[\text{Fe}]/[\text{Zr}]$  ratio. From Figure 15 we observe that (i) the H<sub>2</sub> desorption rate constant attains its maximum value when the  $[\text{Fe}]/[\text{Zr}]$  atomic ratio is ~1, (ii) Fe forms nanoclusters with 20 nm grain size independently on the  $[\text{Fe}]/[\text{Zr}]$  atomic ratio, (iii) at  $[\text{Fe}]/[\text{Zr}] \sim 1.8$  the Mg grain size attains its minimum value of about 100 nm, and (iv) there is not evidence of Zr atoms aggregates.

To explain the previous results, we suggest that the synergetic effect of the mixed Fe and Zr additives consists of (i) Fe aggregation forming nanosized clusters that act as Mg nucleation centers and promote the formation of interconnected Mg domains for fast H diffusion and (ii) Zr atoms playing most probably a role by favoring and stabilizing the aggregation of the Fe additive and as Mg grain refiner by limiting Mg grain growth [32]: grain refinement certainly contributes to increase kinetic favoring diffusion through grain boundaries.

In the future it would be interesting to investigate the possible existence of correlation effects on diffusion

when different dopants are moving and clustering occurs as observed in [33].

## 6. Conclusions

We have studied the hydrogen desorption kinetics of TM-doped MgH<sub>2</sub> samples to analyse the catalytic role of TM atoms and nanoparticles dispersed into the magnesium hydride matrix. We observed that (i) TMs are able to enhance hydrogen desorption also at very low concentration (0.06 at.%) which means that they are atomically dispersed or form a few-atom aggregates, (ii) TM-doped samples show stable desorption properties after a number of H<sub>2</sub> sorption cycles when TM nanoclusters are formed with radius on the order of 10–20 nm, and (iii) mixed TM (in the present case Fe and Zr) can further enhance the desorption kinetics as compared to the single additive.

The improved H<sub>2</sub> desorption properties of the single TM additive are explained by the presence of interfaces between the MgH<sub>2</sub> and the TM nanoclusters acting as heterogeneous nucleation sites and promoting the formation of fast diffusion channels for H migrating atoms. In our case mixed TM (Fe-Zr) additive in the Mg matrix optimizes the distribution and size of TM nanoclusters contained inside the MgH<sub>2</sub> matrix.

## PACS

- 64.70.K-: Solid–solid transitions
- 61.46.+w: Nanoscale materials: clusters, nanoparticles, nanotubes and nanocrystals
- 61.05.C-: X-ray diffraction and scattering
- 68.37.Lp: Transmission electron microscopy (TEM)
- 68.43.Nr: Desorption kinetics
- 68.43.Vx: Thermal desorption
- 81.05.-t: Specific materials: fabrication, treatment, testing, and analysis
- 82.65.+r: Surface and interface chemistry; heterogeneous catalysis at surfaces
- 84.60.Ve: Energy storage systems, including capacitor banks.

## Acknowledgments

The authors thank Cristina Armellini for XRD analysis, Chiara Maurizio for EXAFS analysis, Paolo Mengucci for TEM analysis, Paolo Mazzoldi and Cinzia Sada for SIMS analysis, Romina Belli for EDS analysis, and Ashwin Kale

for support on Mg samples preparation with mixed TM additives. The research activity is financially supported by the Hydrogen-FISR Italian Project.

## References

- [1] R. Gonzalez, Y. Chen, and K. L. Tsang, "Diffusion of deuterium and hydrogen in doped and undoped MgO crystals," *Physical Review B*, vol. 26, no. 8, pp. 4637–4645, 1982.
- [2] O. Friedrichs, J. C. Sánchez-López, C. López-Cartes et al., "Chemical and microstructural study of the oxygen passivation behaviour of nanocrystalline Mg and MgH<sub>2</sub>," *Applied Surface Science*, vol. 252, no. 6, pp. 2334–2345, 2006.
- [3] G. Friedlmeier and M. Groll, "Experimental analysis and modelling of the hydriding kinetics of Ni-doped and pure Mg," *Journal of Alloys and Compounds*, vol. 253–254, pp. 550–555, 1997.
- [4] A. Zaluska, L. Zaluski, and J.O. Ström-Olsen, "Structure, catalysis and atomic reactions on the nano-scale: a systematic approach to metal hydrides for hydrogen storage," *Applied Physics A*, vol. 72, no. 2, pp. 157–165, 2001.
- [5] G. Barkhordarian, T. Klassen, and R. Bormann, "Catalytic mechanism of transition-metal compounds on Mg hydrogen sorption reaction," *Journal of Physical Chemistry B*, vol. 110, no. 22, pp. 11020–11024, 2006.
- [6] J. F. Pelletier, J. Huot, M. Sutton et al., "Hydrogen desorption mechanism in MgH<sub>2</sub>-Nb nanocomposites," *Physical Review B*, vol. 63, no. 5, Article ID 052103, pp. 1–4, 2001.
- [7] H. G. Schimmel, J. Huot, L. C. Chapon, F. D. Tichelaar, and F. M. Mulder, "Hydrogen cycling of niobium and vanadium catalyzed nanostructured magnesium," *Journal of the American Chemical Society*, vol. 127, no. 41, pp. 14348–14354, 2005.
- [8] O. Friedrichs, J. C. Sánchez-López, C. López-Cartes, T. Klassen, R. Bormann, and A. Fernández, "Nb<sub>2</sub>O<sub>5</sub> "pathway effect" on hydrogen sorption in Mg," *Journal of Physical Chemistry B*, vol. 110, no. 15, pp. 7845–7850, 2006.
- [9] N. Bazzanella, R. Checchetto, and A. Miotello, "Catalytic effect on hydrogen desorption in Nb-doped microcrystalline MgH<sub>2</sub>," *Applied Physics Letters*, vol. 85, no. 22, pp. 5212–5214, 2004.
- [10] R. Checchetto, N. Bazzanella, A. Miotello, and P. Mengucci, "Deuterium storage in Mg-Nb films," *Journal of Alloys and Compounds*, vol. 404–406, pp. 461–464, 2005.
- [11] R. Checchetto, N. Bazzanella, A. Miotello et al., "Nb clusters formation in Nb-doped magnesium hydride," *Applied Physics Letters*, vol. 87, no. 6, Article ID 061904, 3 pages, 2005.
- [12] N. Bazzanella, R. Checchetto, A. Miotello, C. Sada, P. Mazzoldi, and P. Mengucci, "Hydrogen kinetics in magnesium hydride: on different catalytic effects of niobium," *Applied Physics Letters*, vol. 89, no. 1, Article ID 014101, 3 pages, 2006.
- [13] R. Checchetto, N. Bazzanella, A. Miotello, and P. Mengucci, "Catalytic properties on the hydrogen desorption process of metallic additives dispersed in the MgH<sub>2</sub> matrix," *Journal of Alloys and Compounds*, vol. 446–447, pp. 58–62, 2007.
- [14] N. Bazzanella, R. Checchetto, and A. Miotello, "Catalytic effect of mixed Zr-Fe additives on the hydrogen desorption kinetics of MgH<sub>2</sub>," *Applied Physics Letters*, vol. 92, no. 5, Article ID 051910, 2008.
- [15] R. Checchetto, N. Bazzanella, A. Miotello, R. S. Brusa, A. Zecca, and A. Mengucci, "Deuterium storage in nanocrystalline magnesium thin films," *Journal of Applied Physics*, vol. 95, no. 4, pp. 1989–1995, 2004.
- [16] M. A. Pick, J. W. Davenport, M. Strongin, and G. J. Dienes, "Enhancement of hydrogen uptake rates for Nb and Ta by thin surface overlayers," *Physical Review Letters*, vol. 43, no. 4, pp. 286–289, 1979.
- [17] R. Checchetto, G. Trettel, and A. Miotello, "Sievert-type apparatus for the study of hydrogen storage in solids," *Measurement Science and Technology*, vol. 15, no. 1, pp. 127–130, 2004.
- [18] J. W. Christian, *The Theory of Transformations in Metals and Alloys. Part I*, Pergamon, Oxford, UK, 2002.
- [19] J. Renner and H. J. Grabke, "Determination of diffusion coefficients in the hydriding of alloys," *Zeitschrift fuer Metallkunde*, vol. 69, no. 10, pp. 639–642, 1978.
- [20] G. Liang, J. Huot, S. Boily, A. Van Neste, and R. Schulz, "Catalytic effect of transition metals on hydrogen sorption in nanocrystalline ball milled MgH<sub>2</sub>-Tm (Tm = Ti, V, Mn, Fe and Ni) systems," *Journal of Alloys and Compounds*, vol. 292, no. 1–2, pp. 247–252, 1999.
- [21] G. Barkhordarian, T. Klassen, and R. Bormann, "Kinetic investigation of the effect of milling time on the hydrogen sorption reaction of magnesium catalyzed with different Nb<sub>2</sub>O<sub>5</sub> contents," *Journal of Alloys and Compounds*, vol. 407, no. 1–2, pp. 249–255, 2006.
- [22] J. F. Fernández and C. R. Sánchez, "Rate determining step in the absorption and desorption of hydrogen by magnesium," *Journal of Alloys and Compounds*, vol. 340, no. 1–2, pp. 189–198, 2002.
- [23] A. A. Nayeb-Hashemy and J. B. Clark, *Phase Diagrams of Binary Magnesium Alloys*, ASM International, Metal Park, Ohio, USA, 1988.
- [24] G. Alefeld and J. Völkl, *Hydrogen in Metals*, Springer, Berlin, Germany, 1978.
- [25] M. A. Pick and R. Bausch, "The determination of the force-dipole tensor of hydrogen in niobium," *Journal of Physics F*, vol. 6, no. 10, article no. 008, pp. 1751–1763, 1976.
- [26] D. A. Porter and K. E. Easterling, *Phase Transformation in Metals and Alloys*, Chapman & Hall, London, UK, 1992.
- [27] D. Turnbull, *Solid State Physics*, vol. 3, Academic Press, New York, NY, USA, 1956.
- [28] F. D. Manchester, *Phase Diagrams of Binary Hydrogen Alloys*, ASM International, Materials Park, Ohio, USA, 2000.
- [29] O. Friedrichs, D. Martínez-Martínez, G. Guílera, J. C. S. López, and A. Fernández, "In situ energy-dispersive XAS and XRD study of the superior hydrogen storage system MgH<sub>2</sub>/Nb<sub>2</sub>O<sub>5</sub>," *Journal of Physical Chemistry C*, vol. 111, no. 28, pp. 10700–10706, 2007.
- [30] G. K. Williamson and W. H. Hall, "X-ray line broadening from filed aluminium and wolfram," *Acta Metallurgica*, vol. 1, no. 1, pp. 22–31, 1953.
- [31] A. Kale, N. Bazzanella, R. Checchetto, and A. Miotello, "Synergy on catalytic effect of Fe-Zr additives mixed in different proportions on the hydrogen desorption from MgH<sub>2</sub>," *Applied Physics Letters*, vol. 94, no. 20, Article ID 204103, 2 pages, 2009.
- [32] E. F. Emley, *Principles of Magnesium Technology*, Pergamon, Oxford, UK, 1966.
- [33] A. Miotello, G. De Marchi, G. Mattei, P. Mazzoldi, and C. Sada, "Clustering of gold atoms in ion-implanted silica after thermal annealing in different atmospheres," *Physical Review B*, vol. 63, no. 7, Article ID 075409, 7 pages, 2001.

## Research Article

# Synthesis of Bismuth Ferrite Nanoparticles via a Wet Chemical Route at Low Temperature

Yongming Hu,<sup>1,2</sup> Linfeng Fei,<sup>1</sup> Yiling Zhang,<sup>1</sup> Jikang Yuan,<sup>1</sup> Yu Wang,<sup>1</sup> and Haoshuang Gu<sup>2</sup>

<sup>1</sup>Department of Applied Physics, Materials Research Center, The Hong Kong Polytechnic University, Kowloon, Hong Kong

<sup>2</sup>Key Laboratory of Ferro- & Piezoelectric Materials and Device of Hubei Province, Faculty of Physics and Electronic Technology, Hubei University, Wuhan 430062, China

Correspondence should be addressed to Yu Wang, apywang@inet.polyu.edu.hk and Haoshuang Gu, guhsh583@yahoo.com.cn

Received 28 March 2010; Accepted 21 July 2010

Academic Editor: Jaetae Seo

Copyright © 2011 Yongming Hu et al. This is an open access article distributed under the Creative Commons Attribution License, which permits unrestricted use, distribution, and reproduction in any medium, provided the original work is properly cited.

Nanoparticles (NPs) of multiferroic bismuth ferrite ( $\text{BiFeO}_3$ ) with narrow size distributions were synthesized via a wet chemical route using bismuth nitrate and iron nitrate as starting materials and excess tartaric acid and citric acid as chelating agent, respectively, followed by thermal treatment. It was found that  $\text{BiFeO}_3$  NPs crystallized at  $\sim 350^\circ\text{C}$  when using citric acid as chelating agent. Such crystallization temperature is much lower than that of conventional chemical process in which other types of chelating agent are used.  $\text{BiFeO}_3$  NPs with different sizes distributions show obvious ferromagnetic properties, and the magnetization is increased with reducing the particle size.

## 1. Introduction

In recent years, much research interest has been drawn to bismuth ferrite ( $\text{BiFeO}_3$ , abbreviated as BFO), which is known to be the only multiferroic compound that exhibits simultaneous ferroelectric and G-type antiferromagnetic orders over a broad range above room temperature (Curie temperature  $>800^\circ\text{C}$ , Neel temperature =  $370^\circ\text{C}$ ) [1–6]. As a partially covalent oxide, BFO has a rhombohedrally distorted perovskite structure belonging to a space group of  $R3c$  [7]. Nevertheless, it exhibits weak magnetism at room temperature due to a spiral magnetic spin cycloid with a periodicity of  $\sim 62$  nm [4]. So far, most studies on BFO have been performed on two-dimensional epitaxial thin films grown on various substrates [8–11], where epitaxial strain is manifested so as to alter some important properties including crystal lattice structure, polarization, and magnetization. However, more recent approaches are focusing on polycrystals as well as substrate-free nanostructures such as low-dimensional nanostructures, especially zero-dimensional materials like nanoparticles (NPs) [12–17]. Meanwhile, studies on finite size effect of BFO have been carried out by different authors and some interesting

properties (e.g., shift of Neel temperature, gas sensing properties, etc.) have been reported [18–22].

Previous studies have demonstrated that synthesis of BFO NPs through a traditional solid-state method produces poor reproducibility and causes formation of coarser powders as well as  $\text{Bi}_2\text{O}_3/\text{Bi}_2\text{Fe}_4\text{O}_9$  impurity phase [4]. Up to date, several chemical routes (e.g. hydrothermal treatment, mechanochemical synthesis method, and sol-gel methodology, etc.) have been successfully employed for fabricating BFO nanoparticles. However, these approaches have certain shortcomings such as impurities in the final products. Ghosh et al. reported a ferrioxalate precursor method to synthesize BFO NPs through solutions of some specific salts at a temperature of  $600^\circ\text{C}$  [23]. Despite the efforts made through enhancing sintering temperature to avoid impurities, a small amount of  $\text{Bi}_2\text{O}_3$  was found in the final product. Han et al. have accomplished the morphologies tunable synthesis of bismuth ferrites using hydrothermal method [24]. The resulting size of BFO NPs was sometimes large (up to several hundred nanometers) although no impurities were found in the final products. Using the same method, Chen et al. prepared pure phase BFO nanocrystallites at  $200^\circ\text{C}$  using KOH concentration of 4 M. In this study, impurity phases

of  $\text{Bi}_2\text{Fe}_4\text{O}_9$  and  $\text{Bi}_{25}\text{FeO}_{40}$  were easily formed with only a slight change in the KOH concentration [25]. Selbach et al. synthesized BFO NPs through a modified Pechini method using nitrates as metal precursors [26]. Although pure phase BFO was obtained in this study, contaminant produced by decomposition of the precursor was present. Ghosh et al. synthesized nanosized bismuth ferrite using a soft chemical route with tartaric acid as a template material and nitric acid as an oxidizing agent [27]. However, the crystallinity of the resulting BFO NPs was unsatisfactory and the existence of an impure  $\text{Bi}_2\text{O}_3$  amorphous phase in the host at low temperature product of  $400^\circ\text{C}$  was evident. To deal with the issues mentioned above, our recent research suggests that excess tartaric acid and/or citric acid to be added in the solution so that the crystallinity of BFO NPs can be improved. Herein, we reported a general wet chemical route for synthesizing uniform BFO NPs at about  $350^\circ\text{C}$ . To our best knowledge, this is the lowest temperature employed in the literature for BFO fabrication with the exception of certain high pressure techniques such as hydrothermal or solvothermal methods. In addition, the magnetic properties were also investigated for BFO NPs with different size distributions.

## 2. Experimental

All of the reagents were of analytical grade and used without further purification. Following a typical procedure, bismuth nitrate [ $\text{Bi}(\text{NO}_3)_3 \cdot 5\text{H}_2\text{O}$ ] and iron nitrate [ $\text{Fe}(\text{NO}_3)_3 \cdot 9\text{H}_2\text{O}$ ] were weighed in stoichiometric proportions and dissolved in deionized water to make a solution with an independent concentration of 0.2 M before adding 20 mL diluted nitric acid (65~68%  $\text{HNO}_3$ ) to the mixture. Then 10 g of citric acid ( $\text{C}_6\text{H}_8\text{O}_7$ ) were added to the solutions as chelating agent. The light-yellow-colored solution was heated under vigorous stirring until no liquid was left in the beaker to form gel deposit. Each beaker with solid deposit was kept in the oven at  $150^\circ\text{C}$  for another 2~3 h. Subsequently, powders were quarterly divided and calcined in the oven for 2 h at 350, 450, and  $550^\circ\text{C}$ , respectively, to obtain well-crystallized BFO NPs with controllable sizes. For comparison, another group of powders were synthesized by modifying a typical soft chemical route by using excess tartaric acid as chelating agents [27].

The gel (intermediate product) was subjected to thermal analysis in order to determine the subsequent sintering temperature with simultaneous Thermogravimetric Analysis & Differential Scanning Calorimetry (TG-DSC) system (NETZSCH STA 449 C Jupiter). After heat treatment, the sample was characterized using X-ray diffraction (XRD) with a Bruker AXS D8 ADVANCE X-ray diffractometer with  $\text{Cu K}\alpha$  radiation ( $\lambda = 0.154178\text{ nm}$ ). Fourier transformation infrared (FT-IR) spectra were obtained on a Perkin-Elmer Spectrum one FT-IR spectrometer at a resolution of  $4\text{ cm}^{-1}$  with an HgCdTe detector. Transmission electron microscopy (TEM) images and high-resolution transmission electron microscopy (HRTEM) images were obtained on a JEOL 2011 transmission electron microscope at an acceleration voltage

of 200 kV. Magnetization measurements were taken on a LakeShore Vibrating Sample Magnetometry (VSM) system.

## 3. Results and Discussion

The TG/DSC curves of the precipitated and dried powders are carried out and shown in Figure 1. Since tartaric acid and citric acid can form different chelate compounds with  $\text{Bi}^{3+}$  and  $\text{Fe}^{3+}$  ions (as schematically shown in Figures 4(a) and 4(b)), different thermal behaviors were observed from the curves. There are four weight-loss segments in both Figures 1(a) and 1(b). It can be seen that the first and last segments are due to the evaporation of crystalline water and the crystallization process of BFO. The major mass loss of the two intermediate segments in tartaric acid precursor are derived from volatilization of excess tartaric acid, decomposition of chelate complex, and a small amount of nitrate. However, in the citric acid precursor, this loss is caused by the decomposition process only. The analysis results provided us a detailed guide to our subsequent heat treatment process, which showed that citric acid precursor has a relatively lower crystallization temperature (indicated by red arrows in Figure 1), that is, nearly  $100^\circ\text{C}$  lower than that of the tartaric acid precursor. More importantly, to our best knowledge, a crystallize temperature of about  $350^\circ\text{C}$  is far lower than those reported in the literature.

XRD measurements were performed to characterize the crystal structure of the calcined powders. As shown in Figure 2, all the XRD patterns can be indexed to pure rhombohedral perovskite structure, which are in good agreement with the powder data of JCPDS Card number 20-169. After heat treatment at  $350^\circ\text{C}$ , the sample from citric acid precursor begins to generate pure phase BFO while another sample from tartaric acid precursor is still of amorphous feature. It is clear that the crystallization of BFO completed at a temperature of  $350^\circ\text{C}$  for citric acid precursor while  $450^\circ\text{C}$  for tartaric acid precursor, which is in good line with the TG-DSC analysis. Meanwhile, the particle size of BFO changed remarkably after further heat treatment. Calcined at temperatures above  $450^\circ\text{C}$ , well-crystallized and pure phase BFO can be obtained for either precursor. As discussed in early literatures, the grain sizes of BFO NPs grow up with increasing the temperature in soft chemical routes [21, 26]. This can be also confirmed by the peak sharpening of XRD curves (data not shown).

The morphology of the calcined BFO nanoparticles was examined on TEM. Typical TEM images are shown in Figure 3. It is clear that the spherical NPs formed from both precursors are sufficiently fine and uniform on copper grid, and the particle sizes are about 12 and 4 nm, respectively. Hardly any aggregation could be found in our samples compared with traditional approaches. The corresponding selected area electron diffraction patterns (as shown in Figures 3(c) and 3(f)) suggest that our NPs are well crystallized, and both can be indexed to pure BFO rhombohedral crystal structure. The HRTEM image of individual BFO NP (Figure 3(b)) clearly shows an interplanar spacing of  $2.778\text{ \AA}$ , corresponding to the (110) crystal planes. Furthermore, we

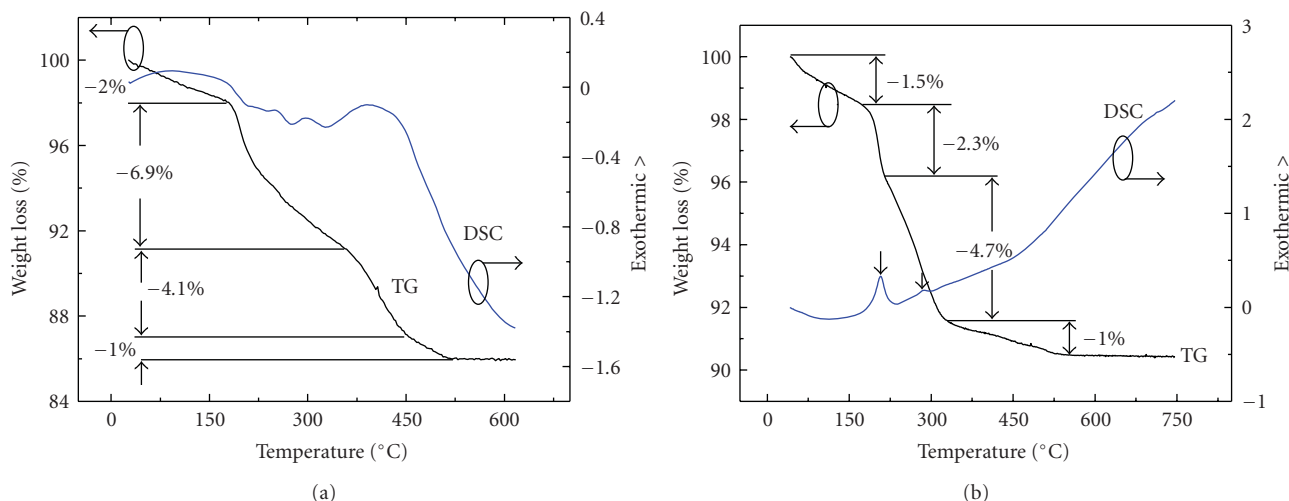


FIGURE 1: TG-DSC curves of the gel reminders acquired by using (a) tartaric acid and (b) citric acid as chelating agent.

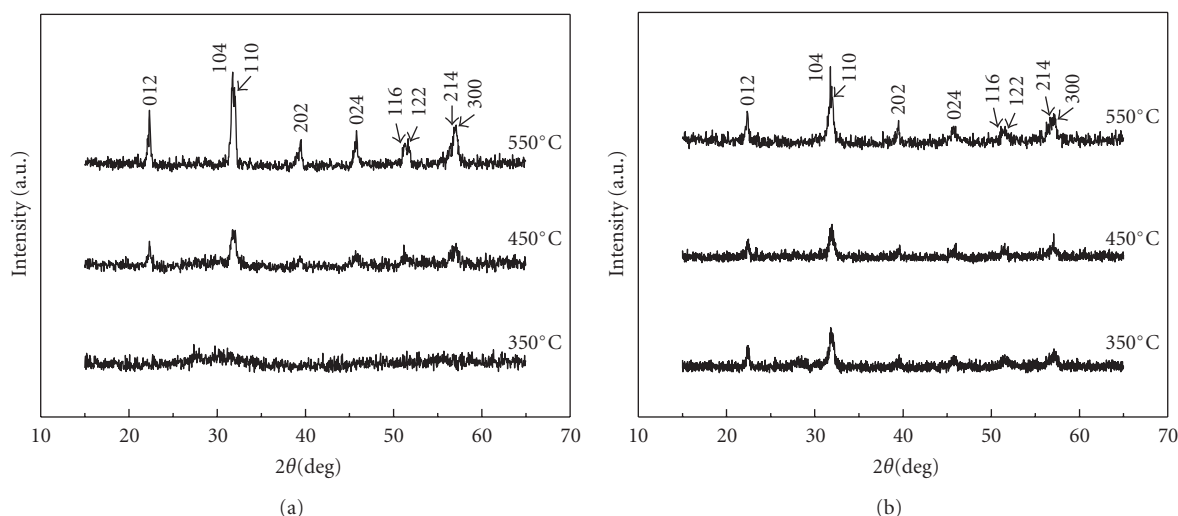


FIGURE 2: XRD patterns of BiFeO<sub>3</sub> samples synthesized by wet chemical route using different chelating agents followed by calcination at 350°C, 450°C and 550°C, respectively. (a) Tartaric acid and (b) citric acid.

can acquire NPs with an average particle size of about 4, 12, 30, and 80 nm through keeping the calcination temperatures at 350, 450, 550, and 650°C, respectively.

Figure 4 shows the FTIR spectra of BiFeO<sub>3</sub> precursors using tartaric acid and citric acid as chelating, respectively. As shown, eight characteristic IR peaks appeared for BFO precursor (tartaric acid), while four characteristic IR peaks together with some weak peaks appeared for BFO precursor using citric acid as chelating. Both samples have two sharp and one wide IR peaks, which correspond to the stretching vibrations of C=O and -OH. The IR wide peaks located at 3466 cm<sup>-1</sup> in (a) and (b) were assigned to the stretching vibrations of structural hydroxyl (OH) groups, and the intense peaks at 1628–1672 cm<sup>-1</sup> were assigned to the stretching vibrations of C=O (corresponding to the groups of tartaric and citric acid). The IR peaks located at 1374 cm<sup>-1</sup>

were attributed to the symmetry bending vibration of C-H. In addition, a sharp IR peak located at 1278 cm<sup>-1</sup> was assigned to the stretching vibration of single bond of C-O for tartaric acid precursor sample, while it cannot be observed for citric acid precursor sample. The IR peaks below 1000 cm<sup>-1</sup> (such as 492, 806, and 902 cm<sup>-1</sup> for tartaric acid precursor, 477, 551, 613, 858, and 910 cm<sup>-1</sup> for citric acid precursor) were corresponding to the vibrations bonds of Bi-O or Fe-O, respectively.

A possible mechanism for the formation of BFO NPs was proposed based on previous analysis (as shown in Figure 5). Firstly, Bi(NO<sub>3</sub>)<sub>3</sub>·5H<sub>2</sub>O and Fe(NO<sub>3</sub>)<sub>3</sub>·9H<sub>2</sub>O along with chelating agents were added to the deionized water and formed the complex of Bi and Fe (Figures 5(a) and 5(b)). Secondly, sol-like precursor and irregular particles come into being followed by aqueous solution were dried

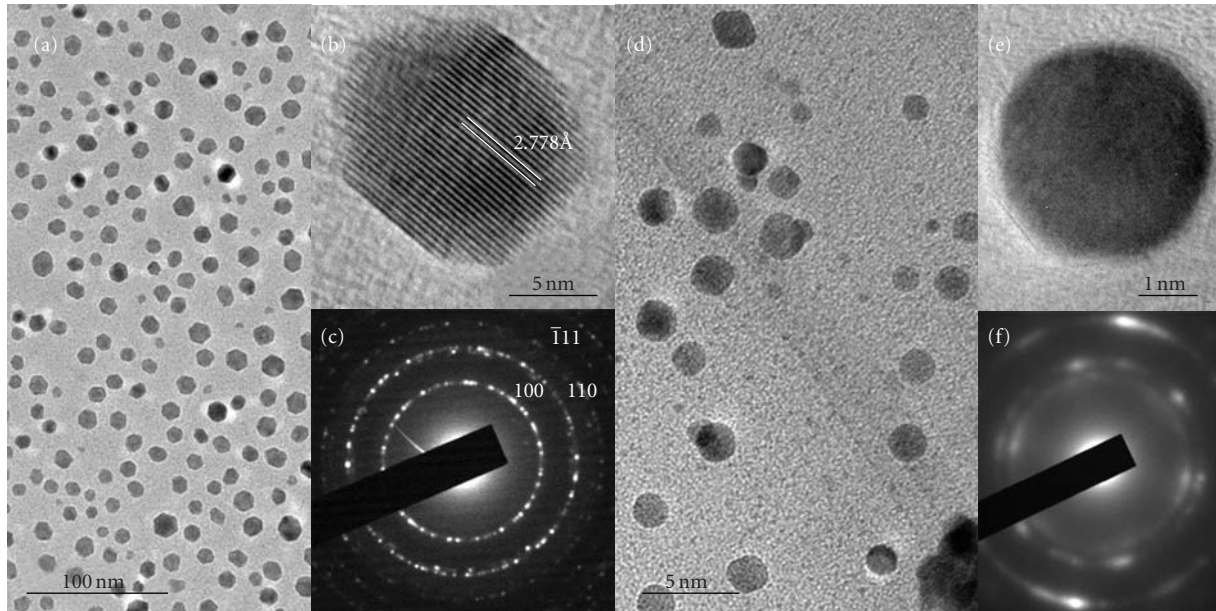


FIGURE 3: TEM images of  $\text{BiFeO}_3$  NPs at low and high magnification, and corresponding SAED patterns: (a), (b), and (c) for nanoparticles from tartaric acid and calcined at  $450^\circ\text{C}$ , while (d), (e), and (f) for NPs from citric acid and calcined at  $350^\circ\text{C}$ .

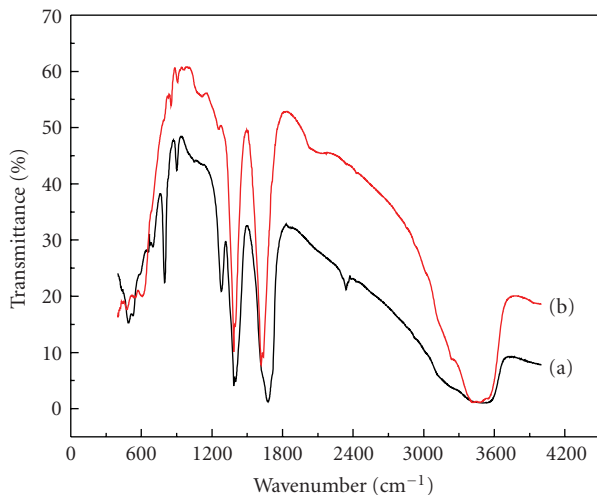


FIGURE 4: FTIR spectra of  $\text{BiFeO}_3$  precursors formed by tartaric acid (a) and citric acid (b), respectively.

(which can be inferred from FTIR spectra of BFO precursors using tartaric and citric acid as chelating, as shown in Figure 4). Finally, the precursor decomposed and BFO NPs started to generate accompanied by the calcination stage under different temperature. It is believed that the chelating compounds plays an important role in controlling shape and size of particles and the decomposition temperatures of the precursor will partially determine the crystallization temperature of BFO NPs in our synthesis. The investigations show that the grain size of the BFO NPs increases with increasing calcination temperature, implying a facile way

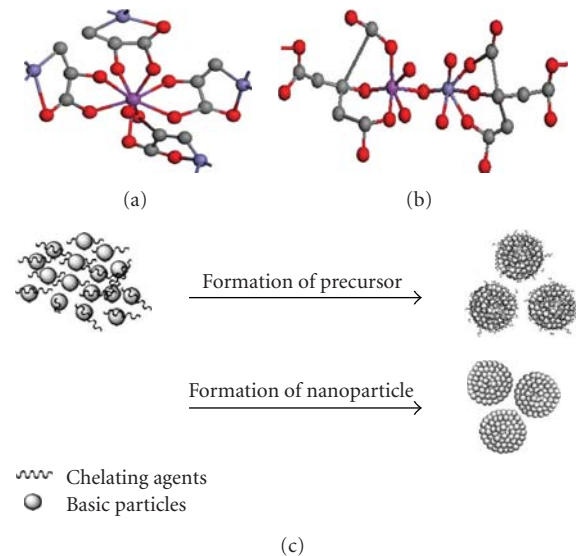


FIGURE 5: Schematic for different chelating complex formed by tartaric acid (a) and citric acid (b), where purple stands for Bi, blue for Fe, red for oxygen, and gray for carbon atoms. (c) Possible formation processes of  $\text{BiFeO}_3$  NPs under wet chemical environment using tartaric acid and citric acid as chelating agents, respectively.

to BFO NPs with controllable sizes. The geometry of the grains becomes more complicated with higher temperature, a result of better crystallization under high temperature. Higher temperatures cause the grains to grow much bigger so that we can obtain sharper monocrystal SAED image as shown in Figure 6.

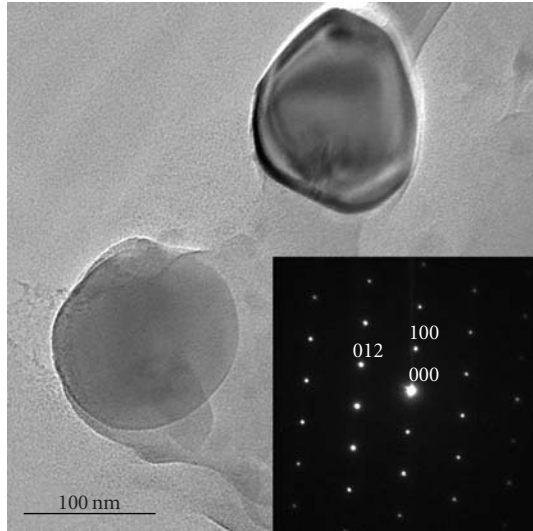


FIGURE 6: TEM image of BiFeO<sub>3</sub> NPs calcined at 650°C and the corresponding SAED pattern (inset), indicated by the black square.

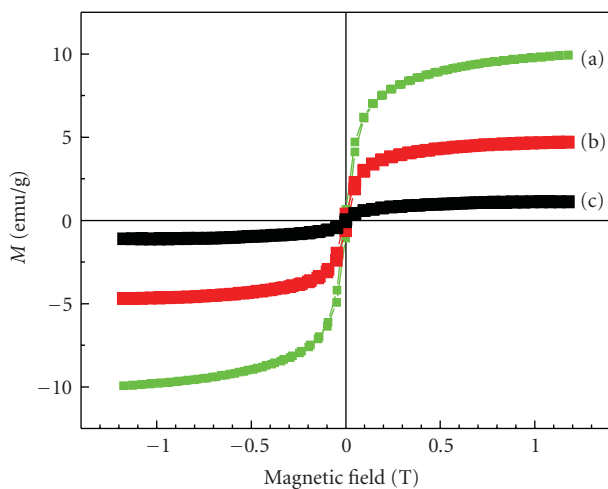


FIGURE 7: Magnetization hysteresis loops of BiFeO<sub>3</sub> NPs with different particle size distributions. (a) 4 nm, (b) 12 nm, and (c) 30 nm.

The magnetization hysteresis loops of BFO NPs samples with three different particle sizes were measured over  $\pm 1$  T at room temperature, as shown in Figure 7. All loops exhibit a finite exchange bias field and vertical asymmetry with visibly greater saturation magnetizations compared to what has been reported previously [21]. This could be a result of uniform particle sizes and the additional lattice strains caused by the large amount of surfaced atoms from small grain size [28]. According to the theory of BFO's ferromagnetism, magnetization drops as its grain size increases [21]. As the calcination temperature raises, the magnetization of BFO NPs with diameters of 12 and 30 nm decreases as expected. One possible explanation may be that some grains may not have spontaneous magnetic moments and therefore fail to contribute to the magnetization. The

possibility of superparamagnetic behaviors in BFO NPs can be ruled out from the finite coercivity and the finite exchange bias field at room temperature (varies within 60 to 90 Oe), which confirms the ferromagnetic order as well as spin pinning at the ferromagnetic—antiferromagnetic interfaces [28]. The magnetization is nearly linear with the external magnetic field for the sample heat treatment at 650°C, which means the NPs has almost lost its ferromagnetic property (the result is not shown here). This finding matches well with what have been found previously, that is, crystallites larger than 62 nm display bulk lattice parameters and hence do not present any ferromagnetic property, namely, the hysteresis loop.

#### 4. Conclusions

In summary, pure phase BFO NPs with an average diameters ranging from 4 to 30 nm were synthesized by a simple soft chemical route using citric acid as chelating agent followed by calcination at a relatively low temperature. TG/DSC, XRD, and TEM were used to confirm the phase and size distribution of the nanoparticles and VSM was utilized to measure the size-dependent magnetic behaviors of the as-prepared nanoparticles. Precursors of the nanoparticles in the experiments as well as the formation mechanism are proposed. This method avoids using traditional high temperature and therefore could be easily extended to other systems.

#### Acknowledgments

This paper was financially supported by the Research Grants Council of Hong Kong (GRF no. PolyU 5309/08E), and the National Science Foundation of China (NSFC) (Grant nos. 50902046, 50872031). Support from the Center for Smart Materials of the Hong Kong Polytechnic University is also acknowledged.

#### References

- [1] W. Eerenstein, N. D. Mathur, and J. F. Scott, "Multiferroic and magnetoelectric materials," *Nature*, vol. 442, no. 7104, pp. 759–765, 2006.
- [2] P. Fischer, M. Polomska, I. Sosnowska, and M. Szymanski, "Temperature dependence of the crystal and magnetic structures of BiFeO<sub>3</sub>," *Journal of Physics C*, vol. 13, no. 10, pp. 1931–1940, 1980.
- [3] C. Tabares-Munoz, J. P. Rivera, A. Monnier, and H. Schmid, "Measurement of the quadratic magnetoelectric effect on single crystalline BiFeO<sub>3</sub>," *Japanese Journal of Applied Physics*, vol. 24, pp. 1051–1053, 1985.
- [4] Y. P. Wang, L. Zhou, M. F. Zhang, X. Y. Chen, J.-M. Liu, and Z. G. Liu, "Room-temperature saturated ferroelectric polarization in BiFeO<sub>3</sub> ceramics synthesized by rapid liquid phase sintering," *Applied Physics Letters*, vol. 84, no. 10, pp. 1731–1733, 2004.
- [5] M. Fiebig, T. H. Lottermoser, D. Fröhlich, A. V. Goltsev, and R. V. Pisarev, "Observation of coupled magnetic and electric domains," *Nature*, vol. 419, no. 6909, pp. 818–820, 2002.

- [6] N. Hur, S. Park, P. A. Sharma, J. S. Ahn, S. Guha, and S.-W. Cheong, "Electric polarization reversal and memory in a multiferroic material induced by magnetic fields," *Nature*, vol. 429, no. 6990, pp. 392–395, 2004.
- [7] J. Wang, J. B. Neaton, H. Zheng et al., "Epitaxial BiFeO<sub>3</sub> multiferroic thin film heterostructures," *Science*, vol. 299, no. 5613, pp. 1719–1722, 2003.
- [8] H. W. Jang, D. Ortiz, S.-H. Baek et al., "Domain engineering for enhanced ferroelectric properties of epitaxial (001) BiFeO<sub>3</sub> thin films," *Advanced Materials*, vol. 21, no. 7, pp. 817–823, 2009.
- [9] S. K. Singh, Y. K. Kim, H. Funakubo, and H. Ishiura, "Epitaxial BiFeO<sub>3</sub> thin films fabricated by chemical solution deposition," *Applied Physics Letters*, vol. 88, no. 16, Article ID 162904, 2006.
- [10] Y. Wang, Q. H. Yang, H. C. He, and C.-W. Nan, "Enhanced ferroelectricity in Ti-doped multiferroic BiFeO<sub>3</sub> thin films," *Applied Physics Letters*, vol. 89, no. 5, Article ID 052903, 2006.
- [11] Y.-H. Lee, J.-M. Wu, Y.-C. Chen, Y.-H. Lu, and H.-N. Lin, "Surface chemistry and nanoscale characterizations of multiferroic BiFeO<sub>3</sub> thin films," *Electrochemical and Solid-State Letters*, vol. 8, no. 10, pp. F43–F46, 2005.
- [12] Z. J. Shen, W. P. Chen, G. L. Yuan, J. M. Liu, Y. Wang, and H. L. W. Chan, "Hydrogen-induced degradation in multiferroic BiFeO<sub>3</sub> ceramics," *Materials Letters*, vol. 61, no. 22, pp. 4354–4357, 2007.
- [13] Z. Yan, K. F. Wang, J. F. Qu, Y. Wang, Z. T. Song, and S. L. Feng, "Processing and properties of Yb-doped BiFeO<sub>3</sub> ceramics," *Applied Physics Letters*, vol. 91, no. 8, Article ID 082906, 2007.
- [14] U. A. Joshi, J. S. Jang, P. H. Borse, and J. S. Lee, "Microwave synthesis of single-crystalline perovskite BiFeO<sub>3</sub> nanocubes for photoelectrode and photocatalytic applications," *Applied Physics Letters*, vol. 92, no. 24, Article ID 242106, 2008.
- [15] J. Chen, X. Xing, A. Watson et al., "Rapid synthesis of multiferroic BiFeO<sub>3</sub> single-crystalline nanostructures," *Chemistry of Materials*, vol. 19, no. 15, pp. 3598–3600, 2007.
- [16] Y. Wang, G. Xu, Z. Ren et al., "Mineralizer-assisted hydrothermal synthesis and characterization of BiFeO<sub>3</sub> nanoparticles," *Journal of the American Ceramic Society*, vol. 90, no. 8, pp. 2615–2617, 2007.
- [17] J. Wei and D. Xue, "Low-temperature synthesis of BiFeO<sub>3</sub> nanoparticles by ethylenediaminetetraacetic acid complexing sol-gel process," *Materials Research Bulletin*, vol. 43, no. 12, pp. 3368–3373, 2008.
- [18] X.-L. Yu, Y. Wang, Y.-M. Hu, C.-B. Cao, and H. L.-W. Chan, "Gas-sensing properties of perovskite BiFeO<sub>3</sub> nanoparticles," *Journal of the American Ceramic Society*, vol. 92, no. 12, pp. 3105–3107, 2009.
- [19] C. M. Cho, J. H. Noh, I.-S. Cho, J.-S. An, K. S. Hong, and J. Y. Kim, "Low-temperature hydrothermal synthesis of pure BiFeO<sub>3</sub> nanopowders using triethanolamine and their applications as visible-light photocatalysts," *Journal of the American Ceramic Society*, vol. 91, no. 11, pp. 3753–3755, 2008.
- [20] S. Li, Y.-H. Lin, B.-P. Zhang, C.-W. Nan, and Y. Wang, "Photocatalytic and magnetic behaviors observed in nanostructured BiFeO<sub>3</sub> particles," *Journal of Applied Physics*, vol. 105, no. 5, Article ID 056105, 2009.
- [21] T.-J. Park, G. C. Papaefthymiou, A. J. Viescas, A. R. Moodenbaugh, and S. S. Wong, "Size-dependent magnetic properties of single-crystalline multiferroic BiFeO<sub>3</sub> nanoparticles," *Nano Letters*, vol. 7, no. 3, pp. 766–772, 2007.
- [22] S. Chattopadhyay, S. D. Kelly, V. R. Palkar, L. Fan, and C. U. Segre, "Investigation of size effects in magnetoelectric BiFeO<sub>3</sub>," *Physica Scripta*, vol. T115, pp. 709–713, 2005.
- [23] S. Ghosh, S. Dasgupta, A. Sen, and H. S. Maiti, "Low temperature synthesis of bismuth ferrite nanoparticles by a ferrioxalate precursor method," *Materials Research Bulletin*, vol. 40, no. 12, pp. 2073–2079, 2005.
- [24] J.-T. Han, Y.-H. Huang, X.-J. Wu et al., "Tunable synthesis of bismuth ferrites with various morphologies," *Advanced Materials*, vol. 18, no. 16, pp. 2145–2148, 2006.
- [25] C. Chen, J. Cheng, S. Yu, L. Che, and Z. Meng, "Hydrothermal synthesis of perovskite bismuth ferrite crystallites," *Journal of Crystal Growth*, vol. 291, no. 1, pp. 135–139, 2006.
- [26] S. M. Selbach, T. Tybell, M.-A. Einarsrud, and T. Grande, "Size-dependent properties of multiferroic BiFeO<sub>3</sub> nanoparticles," *Chemistry of Materials*, vol. 19, no. 26, pp. 6478–6484, 2007.
- [27] S. Ghosh, S. Dasgupta, A. Sen, and H. S. Maiti, "Low-temperature synthesis of nanosized bismuth ferrite by soft chemical route," *Journal of the American Ceramic Society*, vol. 88, no. 5, pp. 1349–1352, 2005.
- [28] R. Mazumder, P. Sujatha Devi, D. Bhattacharya, P. Choudhury, A. Sen, and M. Raja, "Ferromagnetism in nanoscale BiFeO<sub>3</sub>," *Applied Physics Letters*, vol. 91, no. 6, Article ID 062510, 3 pages, 2007.

## Research Article

# CdS Nanotubes and Y-Branched Nanochannels in AAM Fabricated by a Double Diffusion Route

Yong Lv,<sup>1</sup> Weifeng Liu,<sup>1,2</sup> Jianming Huang,<sup>1</sup> and Lianzeng Yao<sup>1,2</sup>

<sup>1</sup>Department of Materials Science and Engineering, University of Science and Technology of China, Hefei, Anhui 230026, China

<sup>2</sup>CAS Key Laboratory of Materials for Energy Conversion, Chinese Academy of Sciences, Hefei, Anhui 230026, China

Correspondence should be addressed to Weifeng Liu, liuwf@ustc.edu.cn

Received 31 March 2010; Revised 25 May 2010; Accepted 6 July 2010

Academic Editor: Bo Zou

Copyright © 2011 Yong Lv et al. This is an open access article distributed under the Creative Commons Attribution License, which permits unrestricted use, distribution, and reproduction in any medium, provided the original work is properly cited.

Polycrystalline CdS nanotubes and a novel partition nanostructure were prepared in an anodic alumina membrane (AAM) template using a double diffusion method at room temperature. Transmission electron microscopy (TEM), selected area electron diffraction (SAED) and energy dispersive X-ray spectroscopy (EDX) investigations indicate that the nanotubes consisting of CdS grains have been synthesized in the AAM nanoholes. The influence of the reagent concentration on the morphology of the nanotubes has been systemically studied using a field emission scanning electron microscope (FE-SEM). It is confirmed that the Y-branched nanochannels can only formed under certain concentrations of the reactants (CdCl<sub>2</sub> and Na<sub>2</sub>S solutions). This novel Y-branched nanostructure may have potential applications for preparation of complicated nanostructure materials.

## 1. Introduction

One-dimensional (1D) semiconductor nanostructures have attracted tremendous attention because of their interesting chemical or physical properties and potential applications in nanodevices [1–3]. In the recent years, many studies have been focused on the CdS nanotubes and nanochannels owing to their large specific interfacial area, and various methods have been reported to synthesize the CdS nanotubes, such as the arc-electrodeposition technique [4], the CVD method [5, 6], the chemical bath deposition [7], the ultrasonic irradiation [8], the template methods [9–13], and so on. Among these methods, the double diffusion-template synthetic method is an effective and simple strategy to form CdS nanotubes.

Porous anodic alumina membranes (AAM) have been widely used as templates to prepare 1D nanostructural materials owing to their uniform and parallel porous structure. However, the morphology of the products crucially depends on the templates, that is, a normal AAM template can only be used to fabricate nanowires or nanotubes. As far as we know, few work focused on the complicated structures in the AAM. Lee et al. [14] reported a Y-branched nanochannel AAM template by adding a pore widening

treatment between the second and the third anodization. Ho et al. [15] also fabricated multitiered branched porous anodic alumina (PAA) substrates consisting of an array of pores branching into smaller pores in succeeding tiers. These three-dimensional nanostructures offer a new way to fabricate complicated nanomaterials in the AAM. In this paper, we report a facile way to obtain Y-branched nanochannels which may have potential applications for conformation of complicated nanomaterials.

## 2. Experiments

High-purity aluminum foil (purity > 99.999%) annealed in a high-vacuum furnace was used in this work. A two-step anodic oxidation technique was applied to prepare the porous alumina template. The anodization was carried out in 0.3 M oxalic acid with 40 V at a temperature around 0°C. It took 10 and 24 h for the first and the second anodization, respectively. After the first-step anodization, the templates were immersed in a mixed solution containing 0.6 M H<sub>3</sub>PO<sub>4</sub> and 0.15 M H<sub>2</sub>CrO<sub>4</sub> at room temperature for 10 h to dissolve alumina. After the second anodization, a mixed solution of 1 M CuCl<sub>2</sub> and 0.1 M HCl was used to remove the remaining aluminum metal. The barrier layer at the bottom

of the membrane was dissolved to make a through-hole template, and the pores were widened in 0.5 M  $\text{H}_3\text{PO}_4$  at room temperature. Then, the templates were immersed in deionized water to eliminate the residual  $\text{AlPO}_4$  and  $\text{H}_3\text{PO}_4$ . Finally, they were dried in an oven at  $60^\circ\text{C}$  for 4 h.

The deposition experiments were carried out in home-made equipment having two equal troughs, and the schematic illustration is showed in Figure 1. In order to avoid air bubble formation in the channels, the membrane was immersed in deionized water and sonicated for a few minutes. Subsequently, the membrane was placed between the two troughs. A  $\text{Na}_2\text{S}$  solution (0.01 M) was poured into one trough slowly. A few minutes later, a  $\text{CdCl}_2$  solution with a concentration varying from 0.003 to 0.01 M was filled into the other one. Furthermore, the two liquid levels should be equal. The experiment was performed at room temperature for 1 h. The templates turned yellow rapidly at the beginning. After completion of the reaction, the templates were thoroughly washed with deionized water and dried in the oven for characterization.

The morphology of the as-synthesized samples was observed using a field-emission scanning electron microscope (FE-SEM, JSM-6700F) and a transmission electron microscope (TEM, H-800). The energy dispersive X-ray spectroscopy (EDX) attached on the TEM was employed to check the chemical composition of the as-prepared nanotubes. For TEM investigations, the samples were completely dissolved in a 2 M  $\text{NaOH}$  aqueous solution, washed with deionized water several times, and finally sonicated in ethanol for a few minutes.

### 3. Results and Discussion

Typical FE-SEM images of the AAM template are shown in Figure 2. It can be seen in Figure 2(a) that the AAM template possesses well-ordered cylindrical pores with a diameter of about 50 nm. Figure 2(b) is the cross-section of the AAM template, which reveals that the channels are straight with smooth inner surface and the thickness of the walls is about 50 nm.

Figure 3 demonstrates the morphology and structure of the as-prepared samples. The top-view of the surface immersed in the  $\text{CdCl}_2$  solution is shown in Figure 3(a). It is planar because the  $\text{CdCl}_2$  solution does not react with the AAM template. Comparing with the original AAM template (shown in Figure 2(a)), the diameter of the nanoholes is smaller and some of them are filled up, which implies that  $\text{CdS}$  has deposited in the pores, and the nanotubes are formed. The Y-branched nanostructures can be seen in Figure 3(b), and the boundary is smooth without any breaches. As the sample was slightly destroyed during preparation for FE-SEM observations, some defects could be found in the micrograph.

Figure 4 presents the TEM images and SAED patterns of the as-prepared  $\text{CdS}$  nanotubes. A single  $\text{CdS}$  nanotube is displayed in Figure 4(a). It can be observed that the nanotube is made of  $\text{CdS}$  grains, and single-crystal  $\text{CdS}$  nanotubes are hardly formed because of the inherent disadvantage of this method. The diameter of the  $\text{CdS}$  nanotube is about

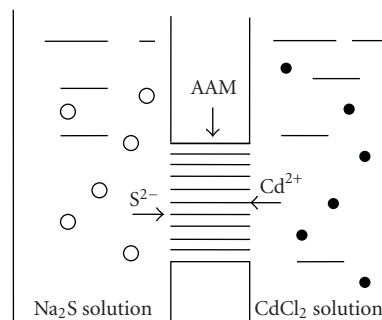
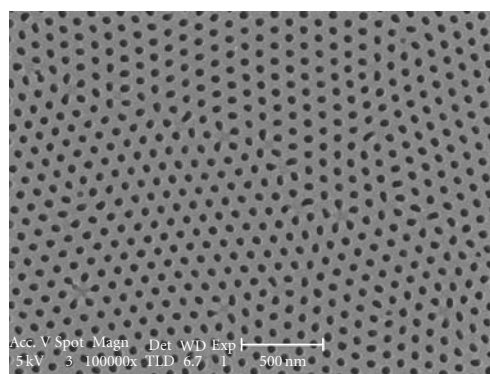
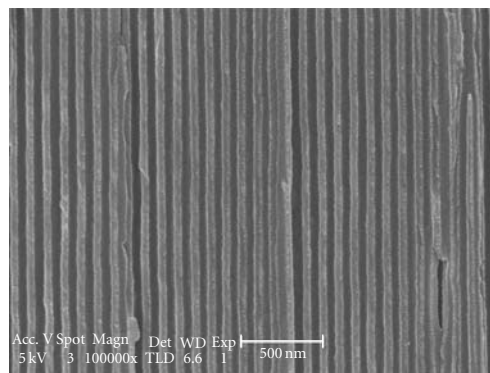


FIGURE 1: The schematic illustration of the double diffusion route experiment.



(a)



(b)

FIGURE 2: Typical FE-SEM images of the as-prepared AAM template. (a) top-view; (b) cross-section.

50 nm consistent with the pore size of the AAM template. After sonication treatment, broken  $\text{CdS}$  nanotubes and  $\text{CdS}$  grains can be found in Figure 4(b). The EDX spectrum investigation of the as-synthesized samples (not showed here) reveals that only S, Cu, and Cd can be detected. The Cu signal in the spectrum originates from the copper grid, and the quantitative analysis indicates that the average atomic ratio of Cd : S is near 1 : 1. Figure 4(c) show the SAED pattern of the nanotubes, which reveals that the samples have a polycrystalline structure with cubic spialuterite, and the

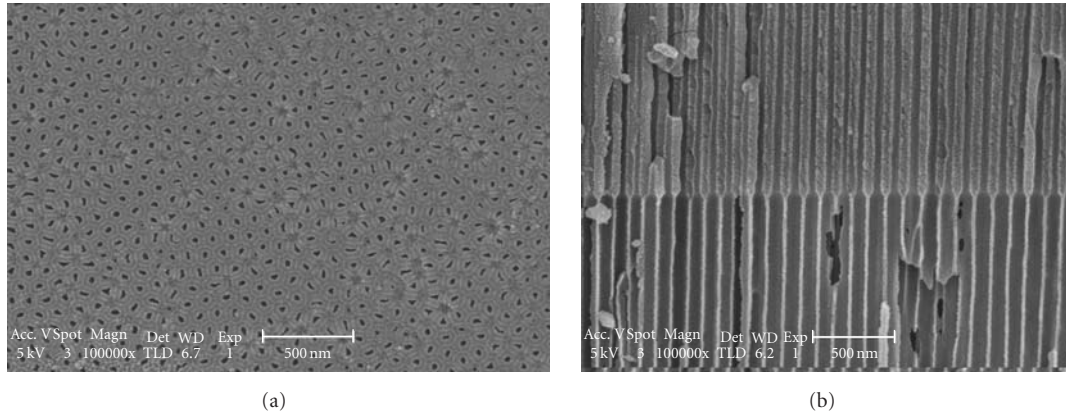


FIGURE 3: FE-SEM images of the as-synthesized sample under concentrations of 0.005 M CdCl<sub>2</sub> and 0.01 M Na<sub>2</sub>S. (a) top-view; (b) cross-section.

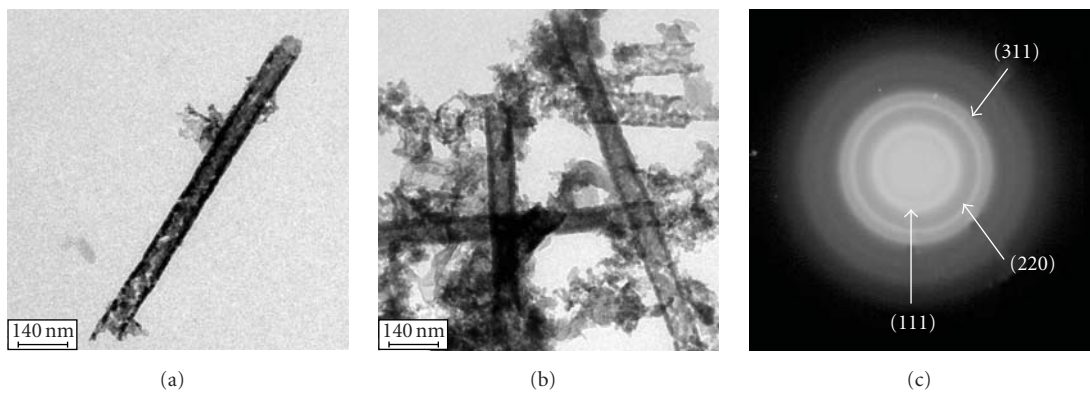
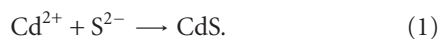


FIGURE 4: TEM images of the CdS nanotubes and their corresponding SAED pattern. (a) a single CdS nanotube; (b) some CdS nanotubes; (c) SAED pattern.

pattern can be indexed to (111), (220) and (311) lattice fringes.

In recent years, various nanomaterials were synthesized using this double diffusion method [16–19]. In fact, the essence of the double diffusion route is a chemical precipitation. Two different solutions are separated by the AAM template which can slow down the diffusion and the rate of crystallization to prevent overly rapidly mixing. The deposition occurs when Cd<sup>2+</sup> and S<sup>2-</sup> meet in the pores at the position where  $C_{\text{Cd}^{2+}} * C_{\text{S}^{2-}} > K_{\text{sp}}_{\text{CdS}}$ , where  $K_{\text{sp}}$  is the solubility of the product at the reaction temperature. The net reaction can be written as:



As the pore walls are positively charged, S<sup>2-</sup> is likely to be adsorbed onto the walls [20]. Then, the nucleation occurs on the walls and the crystallites finally form CdS nanotubes. If the reaction lasts long enough, the nanopores may be filled up and nanowires will be obtained [21].

Y-branched nanochannels would form when the two troughs filled with two different molar solutions (0.01 M Na<sub>2</sub>S and 0.005 M CdCl<sub>2</sub>). In comparison with Figure 2(b), the pore diameter in Figure 3(b) upon the boundary is

smaller, while that below it is much larger. The pore diameter below the boundary is nearly 100 nm, almost two times of the original value. It is evident that the pores below the boundary are eroded by the Na<sub>2</sub>S solution. As we know, S<sup>2-</sup> has a larger ionic radius than Cd<sup>2+</sup>. Therefore, Cd<sup>2+</sup> diffuses faster than S<sup>2-</sup> in an aqueous solution, and S<sup>2-</sup> is likely to aggregate in the pores near the Na<sub>2</sub>S solution. And S<sup>2-</sup>, keeping diffusing into the AAM channels, not only to reacts with Cd<sup>2+</sup> to form the CdS nanotubes but also makes the pores widened because the AAM is easy to be eroded in an alkalescence solution. Consequently, the Y-branched nanochannels form in the AAM.

The concentration of solutions is crucial to the fabrication of special nanostructures. In this work, the influence of the reactant concentrations on the morphology of the products was investigated by varying the CdCl<sub>2</sub> concentration and keeping the other one unchanged (0.01 M Na<sub>2</sub>S). The CdS grains are deposited on the surface of the AAM template and no CdS nanotube is formed in the nanopores when the concentration of the CdCl<sub>2</sub> solution decreases to 0.003 M. Since the CdCl<sub>2</sub> concentration in the solution is so low, that very little Cd<sup>2+</sup> can diffuse into the nanopores and react with S<sup>2-</sup> to form CdS nanotubes. Therefore, S<sup>2-</sup> travels straight

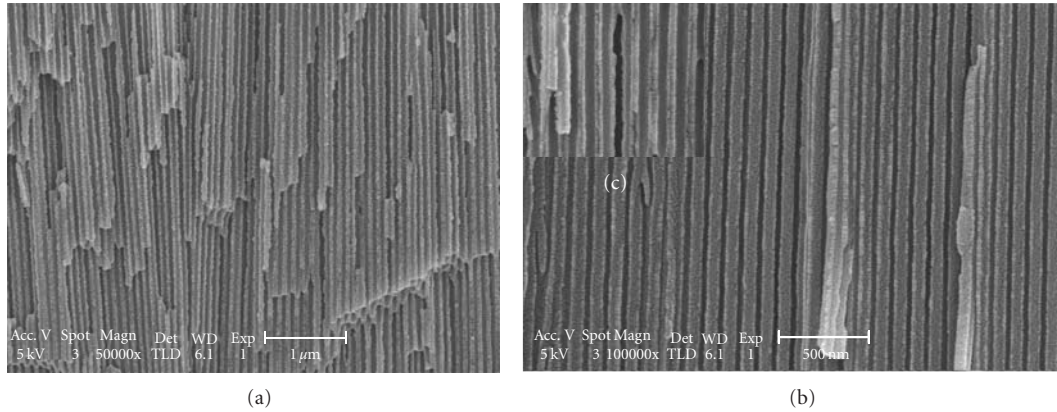


FIGURE 5: FE-SEM images of the prepared samples with different  $\text{CdCl}_2$  concentration. (a) 0.008 M; (b) 0.01 M; (c) magnification of (b).

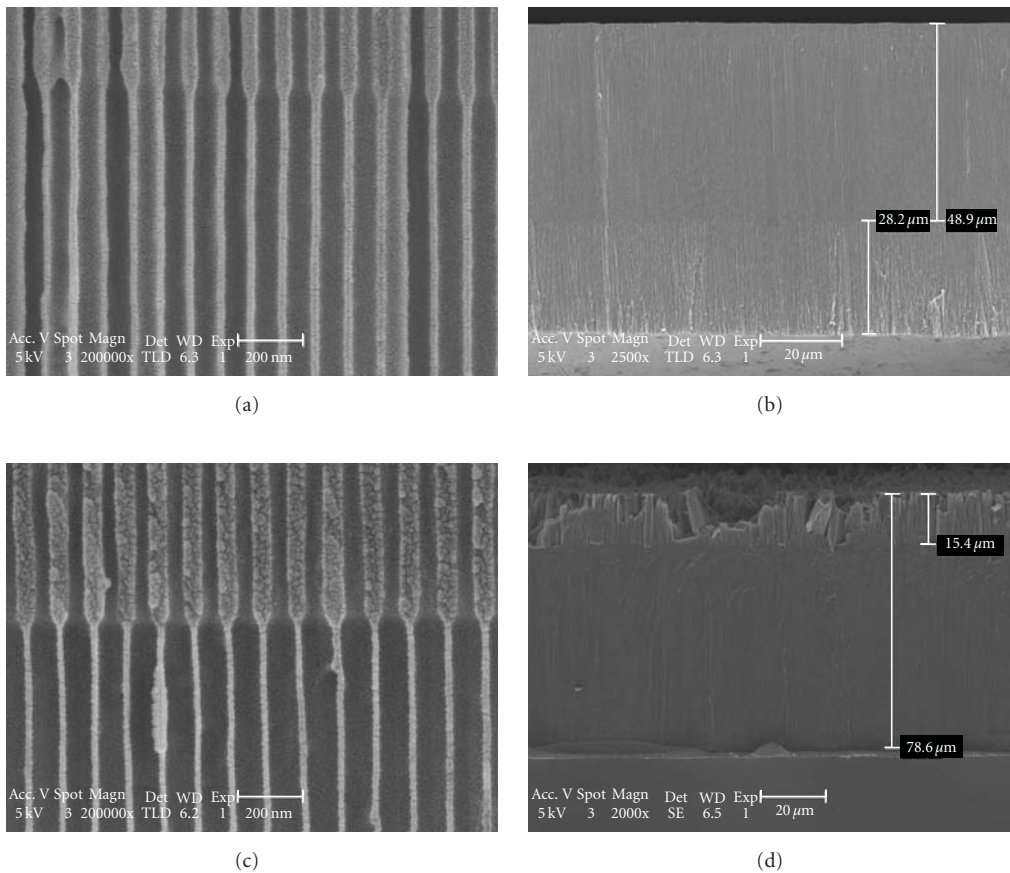


FIGURE 6: FE-SEM images of as-prepared samples under concentrations of 0.005 M  $\text{CdCl}_2$  and 0.01 M  $\text{Na}_2\text{S}$  with different reaction time (a, b) 40 min; (c, d) 60 min.

through the nanopores and reacts with  $\text{Cd}^{2+}$  on the surface near the  $\text{CdCl}_2$  solution to produce  $\text{CdS}$  particles.

Figure 5 gives FE-SEM images of the samples prepared under different  $\text{CdCl}_2$  concentrations. It can be seen from Figure 5 that the nanotube diameter is obviously different at the two ends of the AAM template. The diameter of the

nanotubes near the  $\text{Na}_2\text{S}$  solution is about 100 nm, which is larger than that in the other end. It is found in Figure 5 that the diameter of the nanotubes in the end close to the  $\text{Na}_2\text{S}$  solution becomes small as the  $\text{CdCl}_2$  concentration increases. However, if the concentration of the  $\text{CdCl}_2$  solution is high enough ( $>0.02$  M), the  $\text{CdS}$  nanotubes cannot form

in the pores. In the case of a high  $\text{CdCl}_2$  concentration, the diffusion rate of  $\text{Cd}^{2+}$  is so high that most of  $\text{Cd}^{2+}$  travels through the nanopores directly and reacts with  $\text{S}^{2-}$  to form the CdS particles on the surface of the AAM template immersing in the  $\text{Na}_2\text{S}$  solution.

When the reaction concentration of  $\text{CdCl}_2$  is 0.005 M (the concentration of  $\text{Na}_2\text{S}$  was set at 0.01 M), Y-branched nanochannels with different diameter nanopores can be observed (see Figure 3(b)). The length and diameter of the Y-branched nanochannels can be varied with the reaction time. Figure 6 presents the FE-SEM photographs of the samples prepared with different reaction time. Figures 6(a) and 6(c) reveal that the pore diameter upon the boundary for the sample prepared for 60 min is smaller than that for 40 min. The pore diameter of the sample below the boundary, on the contrary, is getting larger as the reaction time increases. The panorama of the two different samples is shown in Figures 6(b) and 6(d). It can be seen that, with increasing the reaction time, the corrosion proportion turns large and more CdS nanoparticles deposit on the walls of the nanochannels resulting in the small pore diameter. Moreover, the length of the CdS nanotubes in the AAM nanopores increases clearly with the reaction time, and the surface of the AAM membrane are destroyed as shown in Figure 6(d). This new nanostructure may have great potential applications for synthesis of complicated nanomaterials using an electrochemical deposition, a sol-gel template method and so on.

#### 4. Conclusion

In summary, CdS nanotubes and Y-branched nanochannels templates have been prepared at room temperature using a double diffusion method. The as-prepared nanotubes consist of the CdS grains. It is found that the concentration of the reactants contributes to the formation of the special nanostructures. This Y-branched nanostructure may be used as a template to synthesize complicated nanomaterials in the AAM.

#### References

- [1] A. M. Morales and C. M. Lieber, "A laser ablation method for the synthesis of crystalline semiconductor nanowires," *Science*, vol. 279, no. 5348, pp. 208–211, 1998.
- [2] J. Hone, B. Batlogg, Z. Benes, A. T. Johnson, and J. E. Fischer, "Quantized phonon spectrum of single-wall carbon nanotubes," *Science*, vol. 289, no. 5485, pp. 1730–1733, 2000.
- [3] M. S. Gudiksen, L. J. Lauhon, J. Wang, D. C. Smith, and C. M. Lieber, "Growth of nanowire superlattice structures for nanoscale photonics and electronics," *Nature*, vol. 415, no. 6872, pp. 617–620, 2002.
- [4] C. Wang, J. Fang, J. He, and C. J. O'Connor, "Convenient arc-electrodeposition technique to synthesize CdS nanotubes at room temperature," *Journal of Materials Science Letters*, vol. 22, no. 6, pp. 413–415, 2003.
- [5] X.-P. Shen, A.-H. Yuan, F. Wang, J.-M. Hong, and Z. Xu, "Fabrication of well-aligned CdS nanotubes by CVD-template method," *Solid State Communications*, vol. 133, no. 1, pp. 19–22, 2005.
- [6] H. Pan, C. K. Poh, Y. Zhu et al., "Novel CdS nanostructures: synthesis and field emission," *Journal of Physical Chemistry C*, vol. 112, no. 30, pp. 11227–11230, 2008.
- [7] H. Zhang, X. Ma, J. Xu, and D. Yang, "Synthesis of CdS nanotubes by chemical bath deposition," *Journal of Crystal Growth*, vol. 263, no. 1–4, pp. 372–376, 2004.
- [8] M. Shao, Z. Wu, F. Gao, Y. Ye, and X. Wei, "Surfactant-free route to hexagonal CdS nanotubes under ultrasonic irradiation in aqueous solution at room temperature," *Journal of Crystal Growth*, vol. 260, no. 1–2, pp. 63–66, 2004.
- [9] T. Peng, H. Yang, K. Dai, X. Pu, and K. Hirao, "Fabrication and characterization of CdS nanotube arrays in porous anodic aluminum oxide templates," *Chemical Physics Letters*, vol. 379, no. 5–6, pp. 432–436, 2003.
- [10] S.-M. Zhou, S. Feng, and L.-D. Zhang, "A two-step route to self-assembly of CdS nanotubes via electrodeposition and dissolution," *European Journal of Inorganic Chemistry*, no. 9, pp. 1794–1797, 2003.
- [11] X. Li, H. Chu, and Y. Li, "Sacrificial template growth of CdS nanotubes from  $\text{Cd}(\text{OH})_2$  nanowires," *Journal of Solid State Chemistry*, vol. 179, no. 1, pp. 96–102, 2006.
- [12] D. Mo, J. Liu, H. J. Yao et al., "Preparation and characterization of CdS nanotubes and nanowires by electrochemical synthesis in ion-track templates," *Journal of Crystal Growth*, vol. 310, no. 3, pp. 612–616, 2008.
- [13] Y. Piao, H. Lim, J. Y. Chang, W.-Y. Lee, and H. Kim, "Nanostructured materials prepared by use of ordered porous alumina membranes," *Electrochimica Acta*, vol. 50, no. 15, pp. 2997–3013, 2005.
- [14] J. S. Lee, G. H. Gu, H. Kim, K. S. Jeong, J. Bae, and J. S. Suh, "Growth of carbon nanotubes on anodic aluminum oxide templates: fabrication of a tube-in-tube and linearly joined tube," *Chemistry of Materials*, vol. 13, no. 7, pp. 2387–2391, 2001.
- [15] A. Y. Y. Ho, H. Gao, Y. C. Lam, and I. Rodríguez, "Controlled fabrication of multitiered three-dimensional nanostructures in porous alumina," *Advanced Functional Materials*, vol. 18, no. 14, pp. 2057–2063, 2008.
- [16] Y. Mao and S. S. Wong, "General, room-temperature method for the synthesis of isolated as well as arrays of single-crystalline ABO<sub>4</sub>-type nanorods," *Journal of the American Chemical Society*, vol. 126, no. 46, pp. 15245–15252, 2004.
- [17] N. Wada, K. Yamashita, and T. Umegaki, "Effects of divalent cations upon nucleation, growth and transformation of calcium carbonate polymorphs under conditions of double diffusion," *Journal of Crystal Growth*, vol. 148, no. 3, pp. 297–304, 1995.
- [18] R. J. Park and F. C. Meldrum, "Shape-constraint as a route to calcite single crystals with complex morphologies," *Journal of Materials Chemistry*, vol. 14, no. 14, pp. 2291–2296, 2004.
- [19] F. Peters and M. Epple, "Crystallisation of calcium phosphates under constant conditions with a double diffusion set-up," *Journal of the Chemical Society, Dalton Transactions*, no. 24, pp. 3585–3592, 2001.

- [20] O. Ikeda, M. Ohtani, T. Yamaguchi, and A. Komura, "Direct electrochemistry of cytochrome c at a glassy carbon electrode covered with a microporous alumina membrane," *Electrochimica Acta*, vol. 43, no. 8, pp. 833–839, 1997.
- [21] S. P. Mondal, K. Das, A. Dhar, and S. K. Ray, "Characteristics of CdS nanowires grown in a porous alumina template using a two-cell method," *Nanotechnology*, vol. 18, no. 9, Article ID 095606, 2007.

## Research Article

# Synthesis of Vertically Aligned Dense ZnO Nanowires

Lihong Gong,<sup>1,2</sup> Xiang Wu,<sup>2</sup> Huibo Chen,<sup>2</sup> Fengyu Qu,<sup>2</sup> and Maozhong An<sup>1</sup>

<sup>1</sup> College of Chemical Engineering and Technology, Harbin Institute of Technology, Harbin 150001, China

<sup>2</sup> College of Chemistry and Chemical Engineering, Harbin Normal University, Harbin 150025, China

Correspondence should be addressed to Xiang Wu, wuxiang05@gmail.com and Maozhong An, mzan@hit.edu.cn

Received 1 April 2010; Revised 26 May 2010; Accepted 23 June 2010

Academic Editor: Quanqin Dai

Copyright © 2011 Lihong Gong et al. This is an open access article distributed under the Creative Commons Attribution License, which permits unrestricted use, distribution, and reproduction in any medium, provided the original work is properly cited.

We reported the synthesis of vertically aligned dense ZnO nanowires using Zn powder as the source material by a hydrothermal method and a postannealing process at 200°C. The as-synthesized ZnO nanowires are 100–200 nm in diameter and several micrometers in length and each nanowire has a tapered tip. The morphologies of the products remain after post-annealing treatment. Structural analysis indicates the ZnO nanowire is single crystalline and grows along the [0001] direction. The possible growth mechanism for ZnO nanowire bundles is proposed.

## 1. Introduction

Nanostructured materials have been a wide research focus due to their versatile morphologies and excellent physical and chemical properties superior to the corresponding bulk counterparts [1–3]. One-dimensional (1D) nanostructures are investigated not only for their fundamental scientific significance but also for their diverse technological applications in electrical, optical, and sensing fields [4–7]. In general, it is believed that 1D nanomaterials can show quantum size effect when the sizes are less than the exciton Bohr radius. In view of applications, single nanostructure like nanowire and nanorod should be assembled into devices, in succession integrated into a system. Therefore, recent studies have been inverted into constructing hierarchical and well-aligned 1D nanostructures [8–10]. A lot of efforts have been devoted to synthesize ordered nanostructures, for example, vertically or horizontally aligned nanowire arrays [11, 12]. The vertically aligned nanowires arrays are in the spotlight owing their conveniences and attractive properties in using as nanodevices, including the nanogenerator [13–15]. 1D nanostructures can be fabricated in various methods, such as vapor deposition [16], laser ablation [17], AAO template plating [18], solution growth [19–21]. Much progress has been made in the growth of 1D nanostructures, it is still a challenge to assemble well-aligned nanostructures in a rational pathway.

ZnO is a direct bandgap semiconductor with the band gap energy of 3.37 eV at room temperature and large exciton binding energy of 60 meV [2]. Research of 1D ZnO nanostructures can be ascended to the two papers published in the magazine of *Science* in 2001 [22, 23], from then on the synthesis of ZnO nanostructures has been a hot issue, splendid morphologies of ZnO have been synthesized, such as nanonails [24, 25], nanorings [26], nanohelices [27], nanowire arrays [28], superlattice structures [29], even hierarchical [30], and hetero-structures [31]. Herein, we reported the synthesis of highly oriented ZnO nanowire bundles by a two-step process. The growth mechanism of ZnO nanowire bundles is proposed based on the experimental conditions. The aligned ZnO bundled nanostructures presented here can be applicable in micro- and nano-optoelectronic devices.

## 2. Experimental Details

Two grams of zinc powder (Alfa Aesar, 99.99% purity) was put into 10 ml deionized water and stirred at the room temperature ceaselessly, and then transferred to an autoclave together with a preblended solution, which is obtained by mixing 5 ml  $Zn(NO_3)_2$  solution with 0.5 M concentration and 15 ml NaOH solution with 5 M concentration. Silicon substrates were also put into the autoclave to collect products. The zinc powder and mixed solution were heated at

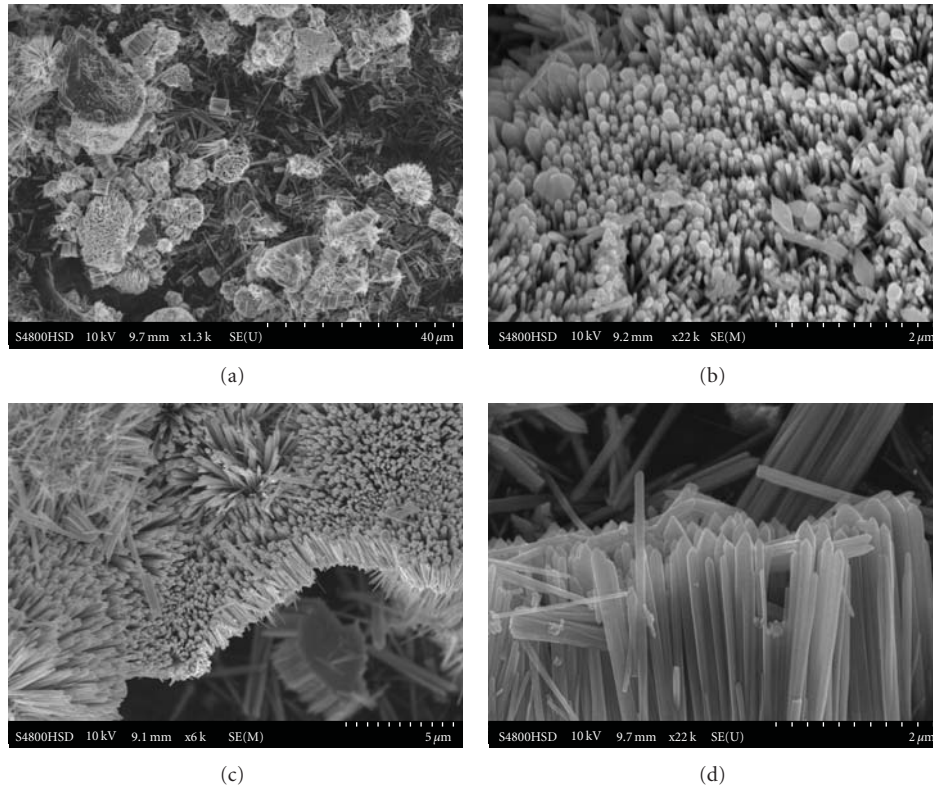


FIGURE 1: SEM images of as-synthesized products before annealing treatment (a) general low-magnification image (b) a top image, (c) a side image and (d) a local image showing a tapered tip.

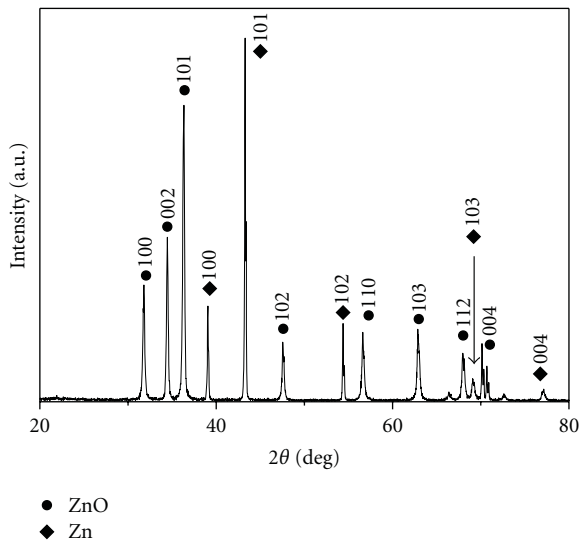


FIGURE 2: XRD pattern of as-grown ZnO nanowires.

120°C for 2 hours and then cooled down. The product was washed using deionized water and ethanol and dried at 200°C. As-synthesized products were characterized by X-ray powder diffraction using Cu K $\alpha$  radiation (XRD, Rigaku Dmax-rB,  $\lambda = 0.1542$  nm), scanning electron microscope (SEM, Hitachi S-4800), and transmission electron micro-

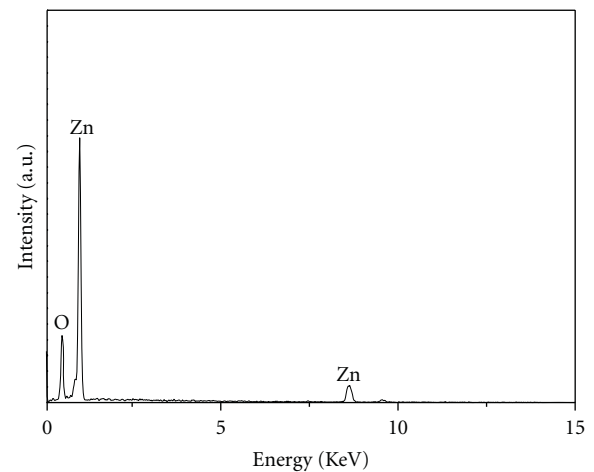


FIGURE 3: EDS spectrum of as-grown ZnO nanowires.

scope (TEM, JEOL 2010EX) affiliated with energy dispersive X-ray spectrometer (EDS).

### 3. Results and Discussion

As-synthesized ZnO nanostructures are shown in Figure 1. The nanowire arrays are found to be vertically aligned in the surfaces of the precursors, similar to the result reported by

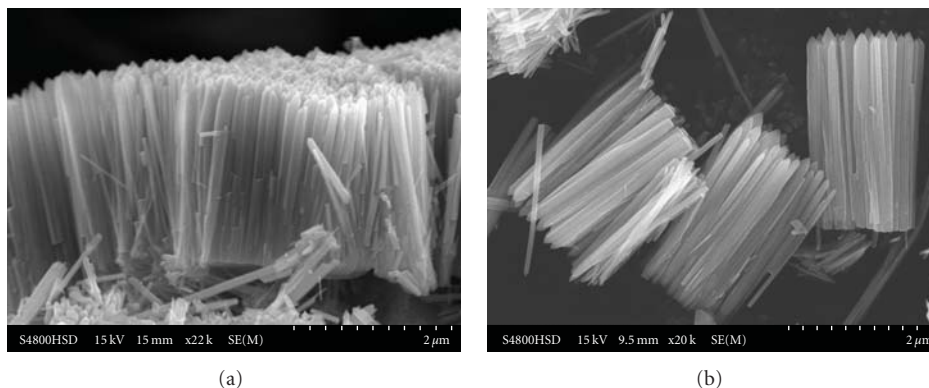


FIGURE 4: SEM images of as-synthesized products after annealing treatment ((a)–(c)) side images of dense wire bundles; (d) a local image showing several dispersed bundles.

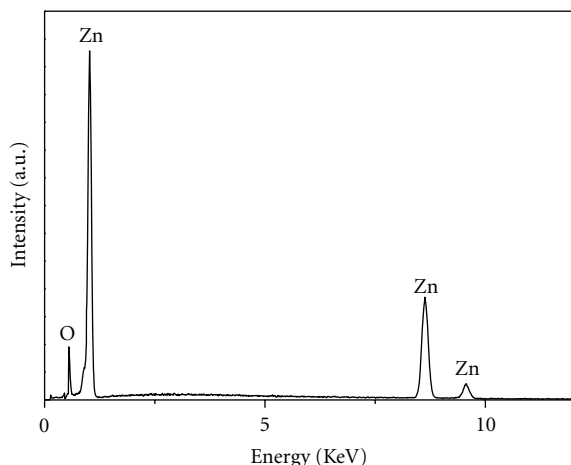


FIGURE 5: EDS spectrum of as-grown ZnO nanowires after annealing.

Gu et al. [32], which is realized by a vapor phase process. Each ZnO nanowires have a tapered tip, a diameter around 200 nm and a length-diameter ratio of over 10. The XRD spectrum (Figure 2) shows that the as-grown sample is made up of ZnO and a trace of Zn, without any other phase. This result is consistent with the EDS spectrum, which shows only Zn and O (Figure 3). In order to remove the residual Zn, the as-grown samples were annealed at 200°C for 2 h. The morphologies still remain (shown in Figure 4) after annealing because ZnO has a very high melting point of 1975°C. EDS spectrum of as-obtained product is also presented in Figure 5. TEM is used to study the microstructure of as-grown product. Figure 6(a) is a bright field TEM image of a single nanowire, and the corresponding selected area electron diffraction (SAED) pattern is shown in the inset in Figure 6(a), which indicates that the nanowire are crystalline and grown along the [0001] crystal direction, a common fast growth direction of ZnO. HRTEM image of the ZnO nanowire showed in Figure 6(b) is consistent with SAED pattern.

Li et al. synthesized hierarchical ZnO nanowire arrays at elevated temperatures, and found that ZnO nanowire arrays were formed by multistep route. Hexagonal disks of ZnO were firstly formed as basic floor, whose surface may be roughened. ZnO nanowires were then assembled into a highly oriented array on the top/bottom surfaces of disks in the presence of dense ammonia [33]. Yang et al. synthesized ZnO nanorod arrays utilizing Zn foil as Zn source and water and aqueous ammonia as the solvent at 100°C, respectively. The as-synthesized nanorods own a smooth tip [34]. Zhang et al. synthesized double tower-tip-like hierarchical Cu<sub>2</sub>O nanostructure. It is thought that the microemulsion system is a prerequisite for the formation of Cu<sub>2</sub>O nanostructures [35]. In this work, ZnO nanowires array is synthesized at 120°C without using ammonia or other organic solution, and the as-synthesized ZnO nanowires present tapered tips. It means that morphology of as-grown product is relative with not only types and concentration of solvent but also the reaction temperature. Concentration and pH value of solvent probably also play an important role. A possible growth mechanism of the nanowire bundles we synthesized can be initially proposed as follows: the formation of nanostructure can be divided into two steps, that is nucleation and growth. ZnO nucleation occurs at first, Zn reacts with OH<sup>-</sup> and forms ZnO<sub>2</sub><sup>2-</sup> in alkali sodium hydroxide solution. Once the concentration of ZnO<sub>2</sub><sup>2-</sup> ions reaches saturation ZnO<sub>2</sub><sup>2-</sup> shall react with H<sub>2</sub>O and induces the nucleation, and subsequent growth of ZnO nanowire bundles. There is a tapered tip at the top of each nanowire, and it is suggested that sudden perturbation of temperature may lead to formation of tapered tip. Actually reduction of the concentration of reactant is also a factor for growth of nanostructure with tapered tip [36].

#### 4. Conclusion

ZnO nanowire bundles have been synthesized on large scale by a two-step process using Zn powder as the source. The experimental results indicate the as-synthesized product owns bundle-like morphology in a well-aligned manner.

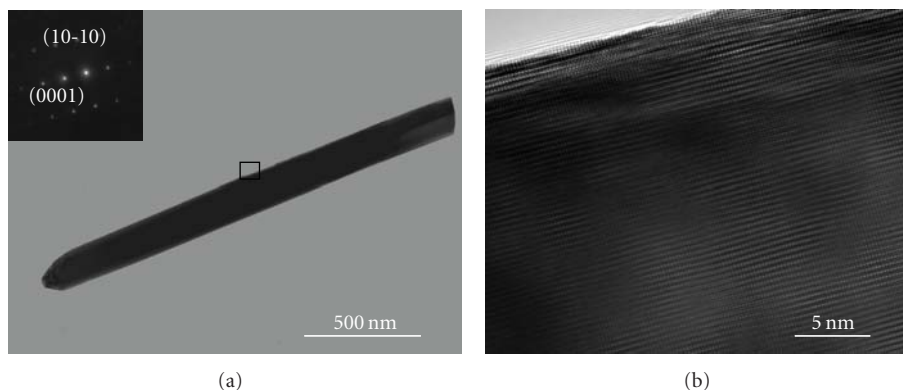


FIGURE 6: (a) TEM image of as-grown ZnO nanowires, the inset is the corresponding SAED pattern. (b) HRTEM image taken from the label in Figure 5(a).

Each nanowire forming bundle is 100–200 nm in diameter and several micrometers in length, and owns a tapered tip. Formation mechanism for nanowire bundles is elucidated based on the reaction conditions. As-grown ZnO nanowire bundles are expected as ideal functional units for micro-/nanodevices. Furthermore, this growth approach can also be used to fabricate nanostructures of other oxide nanostructures.

## Acknowledgment

This paper was supported by the Science Technology and Research Project of Education Bureau, Heilongjiang Province (nos.11551117,11531236)

## References

- [1] F. Cheng, J. Zhao, W. Song et al., "Facile controlled synthesis of MnO<sub>2</sub> nanostructures of novel shapes and their application in batteries," *Inorganic Chemistry*, vol. 45, no. 5, pp. 2038–2044, 2006.
- [2] Q. Wan, Q. H. Li, Y. J. Chen et al., "Fabrication and ethanol sensing characteristics of ZnO nanowire gas sensors," *Applied Physics Letters*, vol. 84, no. 18, pp. 3654–3656, 2004.
- [3] C. Burda, X. Chen, R. Narayanan, and M. A. El-Sayed, "Chemistry and properties of nanocrystals of different shapes," *Chemical Reviews*, vol. 105, no. 4, pp. 1025–1102, 2005.
- [4] H. Chen, X. Wu, L. Gong, C. Ye, F. Qu, and G. Shen, "Hydrothermally grown ZnO micro/nanotube arrays and their properties," *Nanoscale Research Letters*, vol. 5, no. 3, pp. 570–575, 2010.
- [5] Z. L. Wang and J. Song, "Piezoelectric nanogenerators based on zinc oxide nanowire arrays," *Science*, vol. 312, no. 5771, pp. 243–246, 2006.
- [6] X. Wu, P. Jiang, W. Cai, X.-D. Bai, P. Gao, and S.-S. Xie, "Hierarchical ZnO micro-/nano-structure film," *Advanced Engineering Materials*, vol. 10, no. 5, pp. 476–481, 2008.
- [7] J. Zhou, P. Fei, Y. Gao et al., "Mechanical-electrical triggers and sensors using piezoelectric microwires/nanowires," *Nano Letters*, vol. 8, no. 9, pp. 2725–2730, 2008.
- [8] X. Wu, J. Sui, W. Cai, and F. Qu, "Growth of dendritic SnO<sub>2</sub> nanoarchitectures," *Materials Chemistry and Physics*, vol. 112, no. 2, pp. 325–328, 2008.
- [9] P. Jiang, J.-J. Zhou, H.-F. Fang, C.-Y. Wang, Z. L. Wang, and S.-S. Xie, "Hierarchical shelled ZnO structures made of bunched nanowire arrays," *Advanced Functional Materials*, vol. 17, no. 8, pp. 1303–1310, 2007.
- [10] S. Sun, G. Meng, G. Zhang, J.-P. Masse, and L. Zhang, "Controlled growth of SnO<sub>2</sub> hierarchical nanostructures by a multistep thermal vapor deposition process," *Chemistry*, vol. 13, no. 32, pp. 9087–9092, 2007.
- [11] Z.-J. Li, Z. Qin, Z.-H. Zhou, L.-Y. Zhang, and Y.-F. Zhang, "SnO<sub>2</sub> nanowire arrays and electrical properties synthesized by fast heating a mixture of SnO<sub>2</sub> and CNTs waste soot," *Nanoscale Research Letters*, vol. 4, no. 12, pp. 1434–1438, 2009.
- [12] G. Z. Shen, Y. Bando, J. Q. Hu, and D. Golberg, "High-symmetry ZnS hepta- and tetrapods composed of assembled ZnS nanowire arrays," *Applied Physics Letters*, vol. 90, no. 12, Article ID 123101, 2007.
- [13] J. Liu, P. Fei, J. Zhou, R. Tummala, and Z. L. Wang, "Toward high output-power nanogenerator," *Applied Physics Letters*, vol. 92, no. 17, Article ID 173105, 2008.
- [14] Y.-F. Lin, J. Song, Y. Ding, S.-Y. Lu, and Z. L. Wang, "Piezoelectric nanogenerator using CdS nanowires," *Applied Physics Letters*, vol. 92, no. 2, Article ID 022105, 2008.
- [15] Z. L. Wang, "Towards self-powered nanosystems: from nanogenerators to nanopiezotronics," *Advanced Functional Materials*, vol. 18, no. 22, pp. 3553–3567, 2008.
- [16] S. Mathur and S. Barth, "Molecule-based chemical vapor growth of aligned SnO<sub>2</sub> nanowires and branched SnO<sub>2</sub>/V<sub>2</sub>O<sub>5</sub> heterostructures," *Small*, vol. 3, no. 12, pp. 2070–2075, 2007.
- [17] J. X. Ding, J. A. Zapien, W. W. Chen, Y. Lifshitz, S. T. Lee, and X. M. Meng, "Lasing in ZnS nanowires grown on anodic aluminum oxide templates," *Applied Physics Letters*, vol. 85, no. 12, pp. 2361–2363, 2004.
- [18] T. Li, S. Yang, and Y. Du, "Strongly luminescent Cr-doped alumina nanofibres," *Nanotechnology*, vol. 16, no. 4, pp. 365–368, 2005.
- [19] S.-H. Yu, B. Liu, M.-S. Mo, J.-H. Huang, X.-M. Liu, and Y.-T. Qian, "General synthesis of single-crystal tungstate nanorods/nanowires: a facile, low-temperature solution approach," *Advanced Functional Materials*, vol. 13, no. 8, pp. 639–647, 2003.
- [20] X. P. Gao, Z. F. Zheng, H. Y. Zhu et al., "Rotor-like ZnO by epitaxial growth under hydrothermal conditions," *Chemical Communications*, no. 12, pp. 1428–1429, 2004.

- [21] Y. J. Chen, X. Y. Xue, Y. G. Wang, and T. H. Wang, "Synthesis and ethanol sensing characteristics of single crystalline SnO<sub>2</sub> nanorods," *Applied Physics Letters*, vol. 87, no. 23, Article ID 233503, 3 pages, 2005.
- [22] Z. W. Pan, Z. R. Dai, and Z. L. Wang, "Nanobelts of semiconducting oxides," *Science*, vol. 291, no. 5510, pp. 1947–1949, 2001.
- [23] M. H. Huang, S. Mao, H. Feick et al., "Room-temperature ultraviolet nanowire nanolasers," *Science*, vol. 292, no. 5523, pp. 1897–1899, 2001.
- [24] G. Shen, Y. Bando, B. Liu, D. Golberg, and C.-J. Lee, "Characterization and field-emission properties of vertically aligned ZnO nanonails and nanopencils fabricated by a modified thermal-evaporation process," *Advanced Functional Materials*, vol. 16, no. 3, pp. 410–416, 2006.
- [25] X. Wu, J. Sui, and W. Cai, "Preparation and characterization of semiconductor ZnO submicron nails," *Rare Metal Materials and Engineering*, vol. 37, no. 3, pp. 547–550, 2008.
- [26] X. Wu, F. Qu, X. Zhang, W. Cai, and G. Shen, "Fabrication of ZnO ring-like nanostructures at a moderate temperature via a thermal evaporation process," *Journal of Alloys and Compounds*, vol. 486, no. 1-2, pp. L13–L16, 2009.
- [27] X. Wu, W. Cai, and F.-Y. Qu, "Spontaneous formation of single crystal ZnO nanohelices," *Chinese Physics B*, vol. 18, no. 4, pp. 1669–1673, 2009.
- [28] T.-J. Hsueh, S.-J. Chang, Y.-R. Lin, S.-Y. Tsai, I.-C. Chen, and C.-L. Hsu, "A novel method for the formation of ladder-like ZnO nanowires," *Crystal Growth and Design*, vol. 6, no. 6, pp. 1282–1284, 2006.
- [29] P. X. Gao, Y. Ding, W. Mai, W. L. Hughes, C. Lao, and Z. L. Wang, "Materials science: conversion of zinc oxide nanobelts into superlattice-structured nanohelices," *Science*, vol. 309, no. 5741, pp. 1700–1704, 2005.
- [30] F. Xu, K. Yu, Q. Li, Z. Zhu, and T. Yao, "Two-dimensional growth and field emission properties of ZnO microtowers," *Journal of Physical Chemistry C*, vol. 111, no. 11, pp. 4099–4104, 2007.
- [31] X. Wu, P. Jiang, Y. Ding, W. Cai, S.-S. Xie, and Z. L. Wang, "Mismatch strain induced formation of ZnO/ZnS heterostructured rings," *Advanced Materials*, vol. 19, no. 17, pp. 2319–2323, 2007.
- [32] Z. Gu, M. P. Paranthaman, J. Xu, and Z. W. Pan, "Aligned ZnO nanorod arrays grown directly on zinc foils and zinc spheres by a low-temperature oxidation method," *ACS Nano*, vol. 3, no. 2, pp. 273–278, 2009.
- [33] H. Li, M. Xia, G. Dai et al., "Growth of oriented zinc oxide nanowire array into novel hierarchical structures in aqueous solutions," *Journal of Physical Chemistry C*, vol. 112, no. 45, pp. 17546–17553, 2008.
- [34] H. Yang, Y. Song, L. Li et al., "Large-scale growth of highly oriented ZnO nanorod arrays in the Zn-NH<sub>3</sub>-H<sub>2</sub>O hydrothermal system," *Crystal Growth and Design*, vol. 8, no. 3, pp. 1039–1043, 2008.
- [35] H. Zhang, X. Zhang, H. Li, Z. Qu, S. Fan, and M. Ji, "Hierarchical growth of Cu<sub>2</sub>O double tower-tip-like nanostructures in water/oil microemulsion," *Crystal Growth and Design*, vol. 7, no. 4, pp. 820–824, 2007.
- [36] G. Z. Wang, Y. Wang, M. Y. Yau, C. Y. To, C. J. Deng, and D. H. L. Ng, "Synthesis of ZnO hexagonal columnar pins by chemical vapor deposition," *Materials Letters*, vol. 59, no. 29-30, pp. 3870–3875, 2005.

## Research Article

# A Rational Self-Sacrificing Template Route to $\text{LiMn}_2\text{O}_4$ Nanotubes and Nanowires

Baojun Yang,<sup>1</sup> Xinsong Yuan,<sup>2</sup> and Duoli Chai<sup>1</sup>

<sup>1</sup>Anhui Key Laboratory of Controllable Chemistry Reaction & Material Chemical Engineering, School of Chemical Engineering, Hefei University of Technology, Hefei 230009, China

<sup>2</sup>Department of Chemistry and Chemical Engineering, Hefei Normal University, Hefei 230061, China

Correspondence should be addressed to Baojun Yang, lhmybigy@mail.ustc.edu.cn and Xinsong Yuan, yuanxinsong520@163.com

Received 5 April 2010; Accepted 11 July 2010

Academic Editor: William W. Yu

Copyright © 2011 Baojun Yang et al. This is an open access article distributed under the Creative Commons Attribution License, which permits unrestricted use, distribution, and reproduction in any medium, provided the original work is properly cited.

Single-crystalline  $\text{LiMn}_2\text{O}_4$  nanotubes and nanowires have been synthesized via a low-temperature molten salt synthesis method, using the prepared  $\beta\text{-MnO}_2$  nanotubes and  $\alpha\text{-MnO}_2$  nanowires as the precursors and self-sacrificing template. The materials were investigated by a variety of techniques, including X-ray powder diffraction (XRD), transmission electron microscopy (TEM), field emission scanning electron microscopy (FESEM), and high-resolution transmission electron microscopy (HRTEM). The results indicate that the prepared  $\text{LiMn}_2\text{O}_4$  nanotube and nanowire samples are both spinel phase, have lengths up to several micrometers and diameters of hundreds and tens of nanometers, respectively.

## 1. Introduction

One-dimensional (1D) nanomaterials, with their large surface areas and possible quantum confinement effects, exhibit distinct electronic, optical, chemical, and thermal properties [1]. Nanotubes and nanowires are always the focus of study of 1D nanomaterials, so the exploration of simple synthetic methods that can be generalized is a significant challenging field [2].

In recent years, the self-sacrificing template synthesis has been proved to be a facile and efficient route to nanotubes [3–6] and nanowires [7–9]. The idea of converting nanostructures of manganese dioxide to lithium manganese oxide has been described by several groups [10–15]. A sol-gel-AAO or polycarbonate membrane template strategy was used to synthesize  $\text{LiMn}_2\text{O}_4$  nanotubes by Li et al. [16] and Li et al. [17] and  $\text{LiMn}_2\text{O}_4$  nanowires by Zhou et al. [18] and Liu et al. [19]; an electrospinning technique was also utilized to prepare  $\text{LiMn}_2\text{O}_4$  nanowires by Yu et al. [20] and Fu et al. [21]. Hosono et al. [22] reported a high temperature molten salt reaction to prepare  $\text{LiMn}_2\text{O}_4$  nanowires at 450°C, using the prepared  $\text{Na}_{0.44}\text{MnO}_2$  nanowires as a self-sacrificing template and converting  $\text{Na}_{0.44}\text{MnO}_2$  nanowires to  $\text{LiMn}_2\text{O}_4$  nanowires. However, to the best of our knowledge, a

simple route to 1D  $\text{LiMn}_2\text{O}_4$  nanotubes and nanowires at low temperature has still rarely been reported. Herein, we report a low-temperature molten salt route to synthesize  $\text{LiMn}_2\text{O}_4$  nanotubes and nanowires, using the prepared  $\beta\text{-MnO}_2$  nanotubes and  $\alpha\text{-MnO}_2$  nanowires as self-sacrificing templates.

## 2. Experimental Section

**2.1. Synthesis Procedures.** The precursor  $\beta\text{-MnO}_2$  nanotubes were prepared following a procedure found in the literature [23]. In a typical process, 4 mmol of  $\text{MnSO}_4 \cdot \text{H}_2\text{O}$  was dissolved in 10 mL of distilled water, and 4.5 mmol of PVP (K30, polymerization degree 360) was added slowly to it with vigorous stirring. When the solution clarified, 8 mL of aqueous solution containing 8 mmol of  $\text{NaClO}_3$  was added to the above solution under continuous stirring. The resulting transparent solution was then transferred into a Teflon-lined stainless steel autoclave (20 mL) of 70% capacity of the total volume. The autoclave was sealed and maintained at 160°C for 10 h. After the reaction was completed, the autoclave was allowed to cool to room temperature naturally. The solid black precipitate was filtered, washed several times with

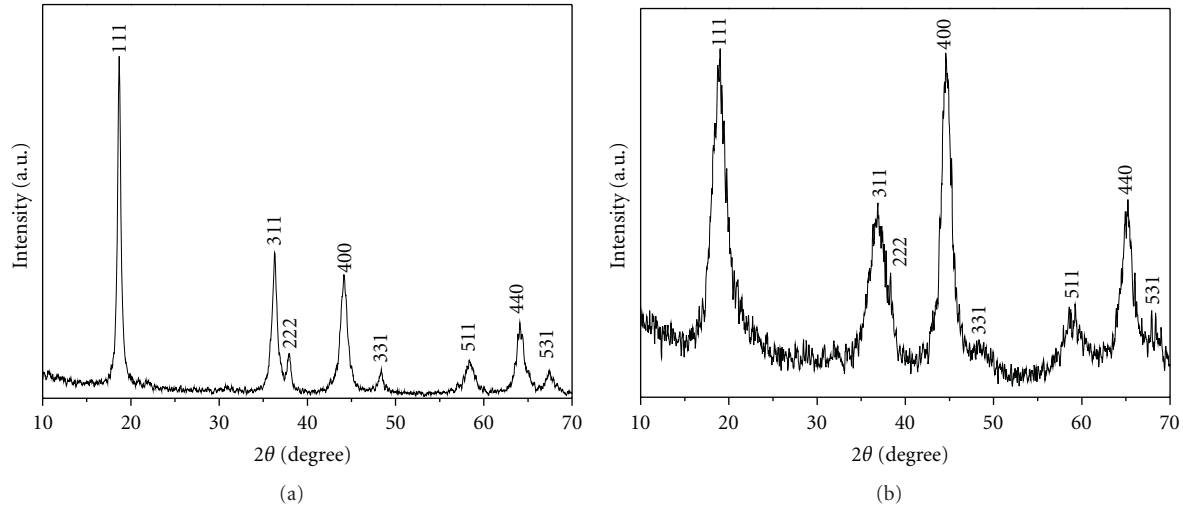


FIGURE 1: Typical XRD patterns of sample 1 (a) and sample 2 (b).

distilled water and absolute ethanol to remove impurities, and then dried at 50 °C for 4 h.

The precursor  $\alpha$ - $\text{MnO}_2$  nanowires were synthesized using the technique reported previously in [24]. In a typical process, 0.008 mol  $\text{MnSO}_4 \cdot \text{H}_2\text{O}$ , 0.02 mol  $(\text{NH}_4)_2\text{SO}_4$ , and 0.008 mol  $(\text{NH}_4)_2\text{S}_2\text{O}_8$  were put into distilled water at room temperature to form a homogeneous solution, which was then transferred into a 40 mL Teflon-lined stainless steel autoclave, sealed, and maintained at 140 °C for 12 h. After the reaction was completed, the resulting solid products were filtered, washed with distilled water to remove the remnant ions, and finally dried at 60 °C for 4 h.

For the synthesis of  $\text{LiMn}_2\text{O}_4$  nanotubes (noted as sample 1) and nanowires (noted as sample 2), 0.59  $\text{LiNO}_3$ –0.41  $\text{LiOH}$  flux (melting point = 183 °C) were used as lithium salts [25]. In a typical experimental procedure, 10 mmol  $\text{MnO}_2$  powders ( $\beta$ - $\text{MnO}_2$  nanotubes or  $\alpha$ - $\text{MnO}_2$  nanowires) and an appropriate amount (for example 100 mmol) of the flux were firstly mixed with a mortar and pestle, heated at  $\sim 230$  °C for  $\sim 10$  h in air, and then air-cooled to room temperature. The resulting products were collected, washed repeatedly with distilled water, filtered, and finally dried in an oven at 60 °C for 4 h.

**2.2. Characterization.** The samples were characterized by X-ray powder diffraction (XRD), which was recorded on a Japan Rigaku Dmax- $\gamma$ A X-ray powder diffractometer with graphite-monochromatized  $\text{Cu-K}\alpha$  radiation ( $\lambda = 0.154056$  nm). The transmission electron microscopy (TEM) images and selected-area electron diffraction (SAED) pattern were captured on a Hitachi Model H-800 instrument at an acceleration voltage of 200 kV. High-resolution transmission electron microscopy (HRTEM) images and Energy-dispersive X-ray spectrum (EDS) were obtained with a JEOL-2010 transmission electron microscope, employing an accelerating voltage of 200 kV. Field-emission scanning electron microscope (FESEM) images were taken on a field-emission microscope (JEOL JSM-6700F, 5 kV).

### 3. Results and Discussions

Figures 1(a) and 1(b) show the typical XRD patterns of sample 1 and sample 2. All of the intensive and sharp peaks can be readily indexed to the pure spinel structure of crystalline  $\text{LiMn}_2\text{O}_4$  [space group:  $Fd\bar{3}m$ ] (JCPDS 35-782).

TEM and FESEM images of the precursor  $\text{MnO}_2$  nanotubes (Figures 2(a) and 2(e)) and nanowires (Figures 2(c) and 2(g)) indicate that the morphology and size of the prepared precursors are in good agreement with those in the studies in [23, 24]. Figures 2(b) and 2(f) show TEM and FESEM images of sample 1, from which, one can see that these  $\text{LiMn}_2\text{O}_4$  nanotubes have diameters of hundreds of nanometers and lengths up to several micrometers, basically retain the morphology of the precursor  $\text{MnO}_2$  nanotubes. Figures 2(d) and 2(h) show TEM and FESEM images of sample 2, which reveal that the  $\text{LiMn}_2\text{O}_4$  nanowires have diameters of tens of nanometers and lengths up to several micrometers, and the morphology of the precursor  $\text{MnO}_2$  nanowires is also mainly maintained. The above phenomenon suggests that the precursor  $\text{MnO}_2$  nanotubes and nanowires may serve as self-sacrificing template for the formation of  $\text{LiMn}_2\text{O}_4$  nanotubes and nanowires.

We have also characterized the as-synthesized  $\text{LiMn}_2\text{O}_4$  nanotubes and nanowires using HRTEM, SAED, and EDS. A representative HRTEM image of a section of a single nanotube is shown in Figure 3(a). The discriminable lattice fringes illustrate that the prepared  $\text{LiMn}_2\text{O}_4$  nanotubes are single crystals in the area shown. The lattice fringes, parallel to the axial direction of the nanotube, have spacing of 0.475 nm, which match well with the separations between the neighboring lattices of the (111) planes of cubic  $\text{LiMn}_2\text{O}_4$ . This result indicates that the  $\text{LiMn}_2\text{O}_4$  nanotube has preferential growth direction perpendicular to [111] direction. The clear and symmetrical spots in the corresponding SAED pattern also indicate that the single nanotube is single-crystalline in nature. The composition of the sample as calculated from the EDS analysis (Figure 3(b))

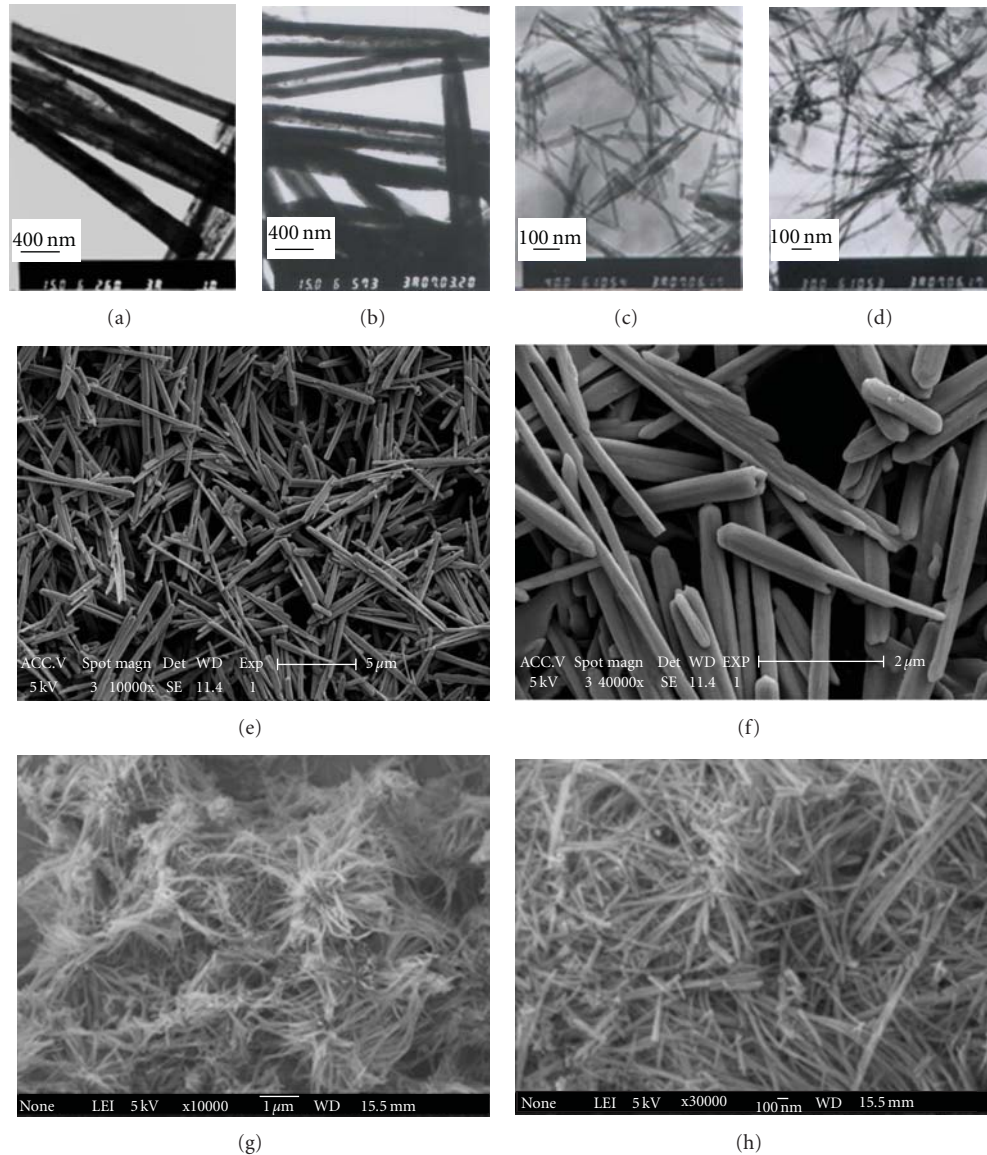


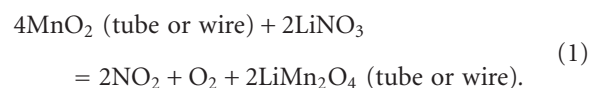
FIGURE 2: Typical TEM images of precursor  $\text{MnO}_2$  nanotubes and nanowires (a and c) and sample 1 and 2 (b and d), FESEM images of precursor  $\text{MnO}_2$  nanotubes and nanowires (e and g) and sample 1 and 2 (f and h).

gives an Mn : O atomic ratio of 1 : 2.08, which is close to the stoichiometry of  $\text{LiMn}_2\text{O}_4$ . The HRTEM image (Figure 3(c)) taken from a single wire shows two sets of distinct fringe spacings of ca. 0.477 and 0.291 nm that match well with the separation between the  $(1\bar{1}1)$  and  $(220)$  lattice planes of cubic  $\text{LiMn}_2\text{O}_4$ , respectively, which indicate that the growth direction of the wire is along  $[110]$  direction. The inset SAED pattern of the nanowire was recorded with the electron beam along the  $[\bar{1}12]$  zone axis. It also demonstrates that this nanowire is single crystal and may have a growth direction of  $[110]$ . The composition of the nanowires as calculated from the EDS spectrum (Figure 3(d)) gives an Mn : O atomic ratio of 1 : 2.07, which is close to the stoichiometry of  $\text{LiMn}_2\text{O}_4$ .

The specific formation mechanism of the  $\text{LiMn}_2\text{O}_4$  nanotubes and nanowires is not yet clear and warrants further investigation. Concerning the formation mechanisms

for nanotubes and nanowires, we think that converting nanostructures of manganese dioxide to lithium manganese oxide is based on a lithiation reaction [10–12], and the 1D tubes and wires can be mainly retained in the present synthetic conditions.

The net lithiation reaction might be simply formulated by:



Xia et al. believe that the formation of  $\text{Ag}_2\text{Se}$  nanowires from Se nanowires is based on an in situ reaction and a straightforward transformation of Se nanowire template [7]. In our previous report of the synthesis of  $\text{Bi}_2\text{O}_3$  nanotubes from Bi nanotubes [3] and  $\text{Bi}_2\text{S}_3$  nanorods

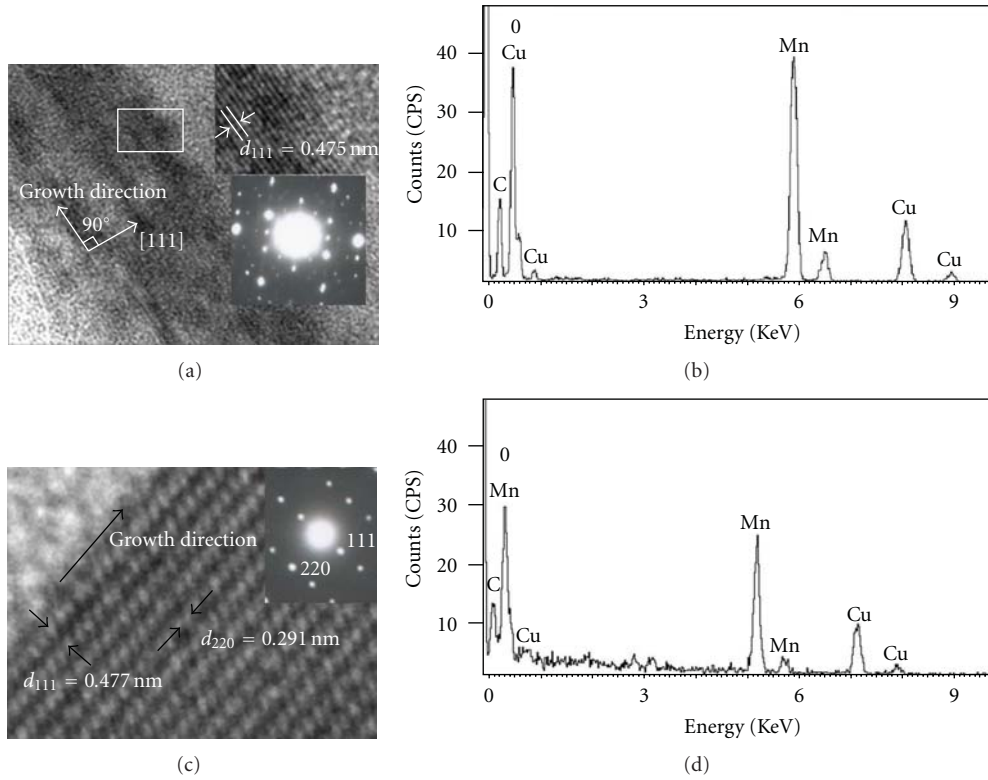


FIGURE 3: HRTEM (a) and the associated EDS (b) image of a typical  $\text{LiMn}_2\text{O}_4$  nanotube. The lower inset in (a) is the corresponding SAED pattern and the upper gives an enlarged view of the HRTEM image taken from the zone marked by the rectangle; HRTEM (c) and the associated EDS (d) image of a typical  $\text{LiMn}_2\text{O}_4$  nanowire. The inset in (c) is the corresponding SAED pattern.

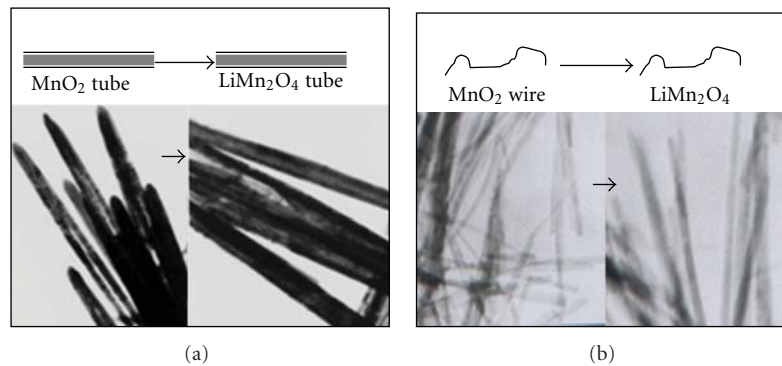


FIGURE 4: Schematic pictures of the net transition of  $\beta\text{-MnO}_2$  nanotubes and  $\alpha\text{-MnO}_2$  nanowires to  $\text{LiMn}_2\text{O}_4$  nanotubes (a) and nanowires (b).

from Bi nanotubes [26], we have provided a rational self-sacrificing template mechanism. For the transformation of  $\text{MnOOH}$  nanorods to  $\text{LiMn}_2\text{O}_3$  nanorods, Yang et al. [12] and Zhang et al. [13] have also given the similar explanations. Herein, we hypothesize that the conversion of the manganese dioxide nanotubes and nanowires to lithium manganese oxide nanotubes and nanowires might be simply described by the schematic pictures in Figures 4(a) and 4(b). However, the intermediate process and the specific mechanism of the formation of the  $\text{LiMn}_2\text{O}_4$  nanotubes and nanowires are not yet clear and warrant further investigation.

#### 4. Conclusions

In conclusion, we have synthesized spinel phase  $\text{LiMn}_2\text{O}_4$  nanotubes and nanowires via a low-temperature lithiation reaction, using  $\beta\text{-MnO}_2$  nanotubes and  $\alpha\text{-MnO}_2$  nanowires as the precursors. Besides, we hypothesize that the formation process of the as-prepared  $\text{LiMn}_2\text{O}_4$  nanotubes and nanowires is based on a self-sacrificing template converting mechanism. This method requires no complex apparatus or technique, and the conditions are mild, and the present

study may supply a general strategy to design and synthesize nanostructured oxide materials.

## Acknowledgments

This paper was supported by Anhui Colleges and Universities Provincial Natural Science key research Projects (KJ2008A066) and Anhui Colleges and Universities Provincial Natural Science Research Project (KJ2010B174).

## References

- [1] Y. Xia, P. Yang, Y. Sun et al., "One-dimensional nanostructures: synthesis, characterization, and applications," *Advanced Materials*, vol. 15, no. 5, pp. 353–389, 2003.
- [2] L. Li, Y.-W. Yang, G.-H. Li, and L.-D. Zhang, "Conversion of a Bi nanowire array to an array of Bi-Bi<sub>2</sub>O<sub>3</sub> core-shell nanowires and Bi<sub>2</sub>O<sub>3</sub> nanotubes," *Small*, vol. 2, no. 4, pp. 548–553, 2006.
- [3] B. Yang, M. Mo, H. Hu et al., "A rational self-sacrificing template route  $\beta$ -Bi<sub>2</sub>O<sub>3</sub> nanotube arrays," *European Journal of Inorganic Chemistry*, no. 9, pp. 1785–1787, 2004.
- [4] J. Zhao, X. Wang, T. Sun, and L. Li, "In situ templated synthesis of anatase single-crystal nanotube arrays," *Nanotechnology*, vol. 16, no. 10, pp. 2450–2454, 2005.
- [5] C. Wu, S.-H. Yu, S. Chen, G. Liu, and B. Liu, "Large scale synthesis of uniform CuS nanotubes in ethylene glycol by a sacrificial templating method under mild conditions," *Journal of Materials Chemistry*, vol. 16, no. 32, pp. 3326–3331, 2006.
- [6] L. Pan, L. Pu, Y. Shi et al., "Synthesis of polyaniline nanotubes with a reactive template of manganese oxide," *Advanced Materials*, vol. 19, no. 3, pp. 461–464, 2007.
- [7] B. Gates, Y. Wu, Y. Yin, P. Yang, and Y. Xia, "Single-crystalline nanowires of Ag<sub>2</sub>Se can be synthesized by templating against nanowires of trigonal Se," *Journal of the American Chemical Society*, vol. 123, no. 46, pp. 11500–11501, 2001.
- [8] G. H. Du and G. Van Tendeloo, "Cu(OH)<sub>2</sub> nanowires, CuO nanowires and CuO nanobelts," *Chemical Physics Letters*, vol. 393, no. 1–3, pp. 64–69, 2004.
- [9] G. H. Du, Z. Y. Yuan, and G. Van Tendeloo, "Transmission electron microscopy and electron energy-loss spectroscopy analysis of manganese oxide nanowires," *Applied Physics Letters*, vol. 86, no. 6, Article ID 063113, 3 pages, 2005.
- [10] M. Rossouw, A. de Kock, L. de Picciotto, M. Thackeray, W. David, and R. Ibberson, "Structural aspects of lithium-manganese-oxide electrodes for rechargeable lithium batteries," *Materials Research Bulletin*, vol. 25, no. 2, pp. 173–182, 1990.
- [11] T. Ohzuku, M. Kitagawa, and T. Hirai, "Electrochemistry of manganese dioxide in lithium nonaqueous cell. III. X-ray diffractational study on the reduction of spinel-related manganese dioxide," *Journal of the Electrochemical Society*, vol. 137, no. 3, pp. 769–775, 1990.
- [12] X. Yang, W. Tang, H. Kanoh, and K. Ooi, "Synthesis of lithium manganese oxide in different lithium-containing fluxes," *Journal of Materials Chemistry*, vol. 9, no. 10, pp. 2683–2690, 1999.
- [13] W. Zhang, Y. Liu, Z. Yang, S. Tang, and M. Chen, "Synthesis and characterization of nanostructured Li<sub>2</sub>MnO<sub>3</sub> from nanostructured MnOOH precursors," *Solid State Communications*, vol. 131, no. 7, pp. 441–445, 2004.
- [14] J. Luo, L. Cheng, and Y. Xia, "LiMn<sub>2</sub>O<sub>4</sub> hollow nanosphere electrode material with excellent cycling reversibility and rate capability," *Electrochemistry Communications*, vol. 9, no. 6, pp. 1404–1409, 2007.
- [15] F. Zhou, X. Zhao, Y. Liu, L. Li, and C. Yuan, "Size-controlled hydrothermal synthesis and electrochemical behavior of orthorhombic LiMnO<sub>2</sub> nanorods," *Journal of Physics and Chemistry of Solids*, vol. 69, no. 8, pp. 2061–2065, 2008.
- [16] X. Li, F. Cheng, B. Guo, and J. Chen, "Template-synthesized LiCoO<sub>2</sub>, LiMn<sub>2</sub>O<sub>4</sub>, and LiNi<sub>0.8</sub>Co<sub>0.2</sub>O<sub>2</sub> nanotubes as the cathode materials of lithium ion batteries," *The Journal of Physical Chemistry B*, vol. 109, no. 29, pp. 14017–14024, 2005.
- [17] N. Li, C. J. Patrissi, G. Che, and C. R. Martin, "Rate capabilities of nanostructured LiMn<sub>2</sub>O<sub>4</sub> electrodes in aqueous electrolyte," *Journal of the Electrochemical Society*, vol. 147, no. 6, pp. 2044–2049, 2000.
- [18] Y.-K. Zhou, C.-M. Shen, J. Huang, and H.-L. Li, "Synthesis of high-ordered LiMn<sub>2</sub>O<sub>4</sub> nanowire arrays by AAO template and its structural properties," *Materials Science and Engineering B*, vol. 95, no. 1, pp. 77–82, 2002.
- [19] X. Liu, J. Wang, J. Zhang, and S. Yang, "Fabrication and characterization of Zr and Co co-doped LiMn<sub>2</sub>O<sub>4</sub> nanowires using sol-gel-AAO template process," *Journal of Materials Science: Materials in Electronics*, vol. 17, no. 11, pp. 865–870, 2006.
- [20] N. Yu, C. Shao, Y. Liu, H. Guan, and X. Yang, "Nanofibers of LiMn<sub>2</sub>O<sub>4</sub> by electrospinning," *Journal of Colloid and Interface Science*, vol. 285, no. 1, pp. 163–166, 2005.
- [21] Z.-W. Fu, J. Ma, and Q.-Z. Qin, "Nanostructured LiCoO<sub>2</sub> and LiMn<sub>2</sub>O<sub>4</sub> fibers fabricated by a high frequency electrospinning," *Solid State Ionics*, vol. 176, no. 17–18, pp. 1635–1640, 2005.
- [22] E. Hosono, T. Kudo, I. Honma, H. Matsuda, and H. Zhou, "Synthesis of single crystalline spinel LiMn<sub>2</sub>O<sub>4</sub> nanowires for a lithium ion battery with high power density," *Nano Letters*, vol. 9, no. 3, pp. 1045–1051, 2009.
- [23] D. Zheng, S. Sun, W. Fan et al., "One-step preparation of single-crystalline  $\beta$ -MnO<sub>2</sub> nanotubes," *The Journal of Physical Chemistry B*, vol. 109, no. 34, pp. 16439–16443, 2005.
- [24] X. Wang and Y. Li, "Synthesis and formation mechanism of manganese dioxide nanowires/nanorods," *Chemistry: A European Journal*, vol. 9, no. 1, pp. 300–306, 2003.
- [25] C.-H. Han, Y.-S. Hong, and K. Kim, "Cyclic performances of HT-LiCo<sub>0.8</sub>Mn<sub>0.2</sub>O<sub>2</sub> (M = Al, Ni) powders prepared by the molten salt synthesis method," *Solid State Ionics*, vol. 159, no. 3–4, pp. 241–247, 2003.
- [26] D. Chai, X. Yuan, B. Yang, and Y. Qian, "A rational route to synthesize Bi<sub>2</sub>S<sub>3</sub> nanorods in large scale," *Solid State Communications*, vol. 148, no. 9–10, pp. 444–447, 2008.

## Research Article

# Mechanism and Growth of Flexible ZnO Nanostructure Arrays in a Facile Controlled Way

**Yangping Sheng, Yang Jiang, Xinzheng Lan, Chun Wang, Shanying Li, Xinmei Liu, and Honghai Zhong**

*School of Materials Science and Engineering, Hefei University of Technology, Hefei, Anhui 230009, China*

Correspondence should be addressed to Yang Jiang, apjiang2002@yahoo.com

Received 8 April 2010; Accepted 26 May 2010

Academic Editor: Quanqin Dai

Copyright © 2011 Yangping Sheng et al. This is an open access article distributed under the Creative Commons Attribution License, which permits unrestricted use, distribution, and reproduction in any medium, provided the original work is properly cited.

Nanostructure arrays-based flexible devices have revolutionary impacts on the application of traditional semiconductor devices. Here, a one-step method to synthesize flexible ZnO nanostructure arrays on Zn-plated flexible substrate in  $\text{Zn}(\text{NO}_3)_2/\text{NH}_3 \cdot \text{H}_2\text{O}$  solution system at 70–90°C was developed. We found out that the decomposition of  $\text{Zn}(\text{OH})_2$  precipitations, formed in lower  $\text{NH}_3 \cdot \text{H}_2\text{O}$  concentration, in the bulk solution facilitates the formation of flower-like structure. In higher temperature, 90°C, ZnO nanoplate arrays were synthesized by the hydrolysis of zinc hydroxide. Highly dense ZnO nanoparticle layer formed by the reaction of  $\text{NH}_3 \cdot \text{H}_2\text{O}$  with Zn plating layer in the initial self-seed process could improve the vertical alignment of the nanowire arrays. The diameter of ZnO nanowire arrays, from 200 nm to 60 nm, could be effectively controlled by changing the stability of  $\text{Zn}(\text{NH}_3)_4^{2+}$  complex ions by varying the ratio of  $\text{Zn}(\text{NO}_3)_2$  to  $\text{NH}_3 \cdot \text{H}_2\text{O}$  which further influence the release rate of  $\text{Zn}^{2+}$  ions. This is also conformed by different amounts of the Zn vacancy as determined by different UV emissions of the PL spectra in the range of 380–403 nm.

## 1. Introduction

Flexible devices based on inorganic materials are beginning to show great promises for technical or commercial interests [1–3]. And in situ fabricating of inorganic materials from flexible substrate will promote the development of flexible devices [4]. Among the inorganic materials, ZnO is one of the most important wide-band-gap semiconducting materials due to optoelectronic, catalytic, lasing, electrical, and piezoelectric properties [5–7]. ZnO nanowire arrays have been broadly investigated because of their applications in solar cells [8–10], sensors [11–13], lasers [14], light-emitting diodes [15, 16], and so on [17–19]. Various physical [20–22], chemical [23–32], and electrochemical methods [33–36] have been developed to synthesize ZnO nanowire arrays. Among these methods, physical methods like thermal evaporation involve complex procedures, sophisticated equipment, and relative high temperature. In contrast, chemical methods, also called solution methods, have advantages in their

easy procedures, simple equipment, and low temperature. Meanwhile, solution methods for preparing ZnO nanowire arrays have appealing potential for scale-up to meet the needs of industrial applications.

The generally employed solution methods reported are seeded growth on ZnO nanoparticles or film-coated substrates [37, 38]. Aligned ZnO nanowire arrays can be synthesized via a two-step process. The first step is formation of a ZnO-seeded layer by pretreated methods [24, 31, 32, 37, 38] or self-seeded technology [39]. Textured ZnO nanocrystal and ZnO thin film have been successfully demonstrated to produce large-scale ZnO nanowire arrays [24, 37, 38]. The next step is solution growth by controlling the supersaturation of the solution, through the formation of  $\text{Zn}^{2+}$  complex, to retard the homogeneous nucleation in bulk solution and promote the heterogeneous nucleation onto the seeded layer [40, 41]. However, the coatings of seed layer are complex and are difficult to reproduce [42]. For self-seeded technology, seeded layers are formed onto

the substrates from the solution in the initial growth stage which do not need any pretreatment of the substrates. And the ZnO nanowire arrays can be directly fabricated onto the substrate without pretreatment. The choices of substrates, however, are also limited by the phase match between the substrates and the ZnO nanowire arrays. Only some substrates with good phase match properties can be used [39, 43, 44]. The development of flexible devices needs novel synthesis methods of direct growth of ZnO nanoarrays onto the flexible substrates with broad choices. Therefore, ZnO nanowire or other nanostructure arrays grown on various substrates in large-scale low-cost way with high reproducibility is still challenging.

Plating technologies can be applied to various substrates, that is, polymer substrates by metalizing process, flexible metal substrates [45, 46]. And the plating layer generally has good contact with the substrate, which can guarantee the stability of device performance. There have been already some reports on fabricating ZnO nanostructures from Zn foil [43, 47–50]. If Zn foil can be replaced with Zn plating layer, the growth of ZnO nanowire arrays could be extended to various substrates, not Zn foil only. Meanwhile, the electric conductive property of the Zn plating layer can meet the needs of the electrical contact with the substrates in the applications of devices. In this work, by combining the Zn plating technology and solution methods, ZnO nanowire arrays were successfully fabricated from the Zn plating layer on the flexible copper foils, which are highly conductive and have not been used as substrate for ZnO nanowire arrays. The prepared ZnO nanostructures have good contact with the substrates. The morphology of the Zn plating layer was found to have little effect on the growth of ZnO nanowire arrays. By controlling the growth parameters like concentrations of  $\text{NH}_3 \cdot \text{H}_2\text{O}$  and  $\text{Zn}^{2+}$  ions and growth temperature, well-aligned ZnO nanowire arrays, nanoplate arrays, and flower-like structure can be achieved, and the aspect ratio, density, and alignment of ZnO nanowires arrays can also be turned. Photoluminescence measurements were conducted to investigate the optical properties of the synthesized ZnO nanostructures, and they were determined by solution growth conditions. Zn plating technology has been maturely employed in industry and can be applied to various substrates. Thus this method is easy to scale up and applicable to various other substrates.

## 2. Experimental Sections

All chemicals were purchased from Shanghai Chemical Reagent Co, Ltd, and used as received without further purification.

**2.1. Zn Plating.** Zinc plating was performed according to [51] with some modification. Nickel, stainless, and copper foils were used for demonstration as flexible substrates. The plating bath was composed of  $\text{ZnCl}_2$  (65 g/L), KCl (190 g/L), and  $\text{H}_3\text{BO}_3$  (25 g/L), and pH was adjusted to 5 by 1 M hydrochloric acid. A piece of copper foil (2 cm × 4 cm × 1 mm) was used as cathode substrate and Zn foil as anode. The

plating was performed under a constant current density of 20 mA/cm<sup>2</sup>, temperature 25 °C for 0.5–1 h. A white layer of Zn was covering the flexible substrates. Here, copper foils were used for experiment convenience.

**2.2. ZnO Nanostructures Growth Procedures.** The syntheses were performed in a 50 ml pyrex glass bottle with a screw cap.  $\text{Zn}(\text{NO}_3)_2$  was prepared to 0.03 M aqueous solution, and a certain amount of ammonia (0.1 g, 1 g) (85 wt%) was slowly added. With several minutes stirring, Zn-plated copper foil was suspended upside down in the solution. Then the bottle was sealed and heated at 80 °C for 12 h. After growth, the substrate was removed from the solution, rinsed with deionized water, and then dried at 60 °C for 6 hours. The white Zn plating layer was changed into a gray layer of ZnO.

The crystal structure analysis was carried out by powder X-ray diffraction (XRD) using  $\text{Cu K}\alpha$  radiation at room temperature. The morphologies of the ZnO nanostructure were researched by field emission scanning electron microscopy (FESEM) with accelerating voltage of 5 KV in Sirion200 (FEI, 10KV) and energy dispersive X-ray spectroscopy (EDX). Room temperature photoluminescence (PL) spectra were recorded on a JY-Labram spectrometer with a continuous wave He-Cd laser focused at  $\sim 2 \mu\text{m}$  as the exciting source at 325 nm.

## 3. Results and Discussion

The surface morphology of the Zn layer electroplated on the copper foil is shown in Figure 1. In Figure 1(a), we can see that the Zn plating layer is a continuous film and is composed of hexagonal platelets. In higher magnification, scale bar 500 nm, as shown in the inset picture of Figure 1(a), the Zn grain is highly crystalline and has smooth grain surface. This can be conformed by XRD pattern, as shown in Figure 1(b). All the peaks can be indexed to Hexagonal Zn (JCPDS Card NO. 04-0831, space group P63/mmc) and the substrate cubic Cu (JCPDS Card NO. 04-0836, space group Fm3m). The (101) peak of Zn and (111) peak of Cu are very close, thus it is hard to distinguish those two peaks. The influences of Zn plating layer will be discussed later in mechanism section.

Figure 2(a) illustrates the low magnification SEM image of ZnO nanowire arrays grown on the Zn-plated Cu foil with using 1 g  $\text{NH}_3 \cdot \text{H}_2\text{O}$  at 80 °C for 10 hours. It can be seen that ZnO nanowire arrays grow normal to the Cu substrate with fine alignment. The optical image of the arrays on the flexible Cu foil is illustrated on the inset of Figure 2(c). It shows that as-prepared ZnO nanowires arrays are grey and cover well the flexible Cu foil. The pattern of nanowire arrays is also affected by the surface morphology of the Zn plating layer. As shown in Figure 1(a), the surface of Zn plating layer is not smooth, with some hill-like protrusion morphology. Thus, the ZnO nanowire arrays are not uniformly covered on the Cu foil but duplicate the topography of Zn plating layer. However, the nanowire arrays vertically rise from the Zn layer as shown in higher magnification in Figures 2(b) and 2(c). Note that, with this method to produce nanowire arrays, the quality of the arrays is not affected by the roughness of the

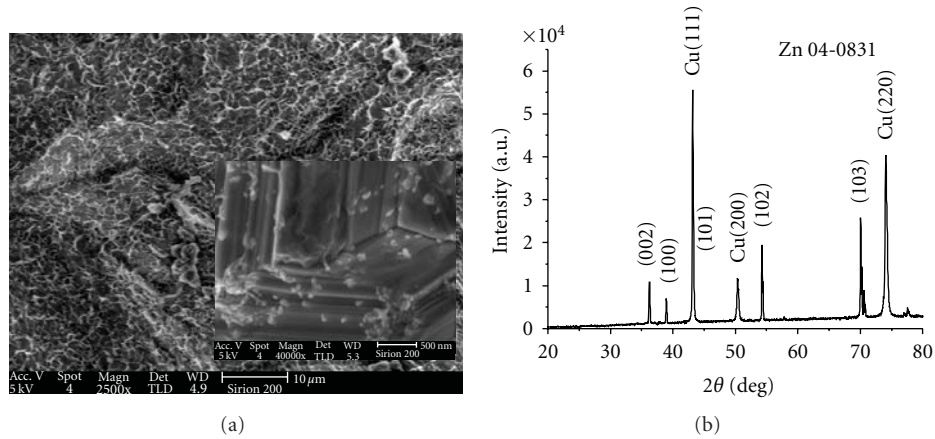


FIGURE 1: (a) SEM image of Zn plating layer; the scale bar is 10 μm. The inset is a higher magnification image with scale bar 500 nm. (b) XRD pattern of Zn-plated copper foil.

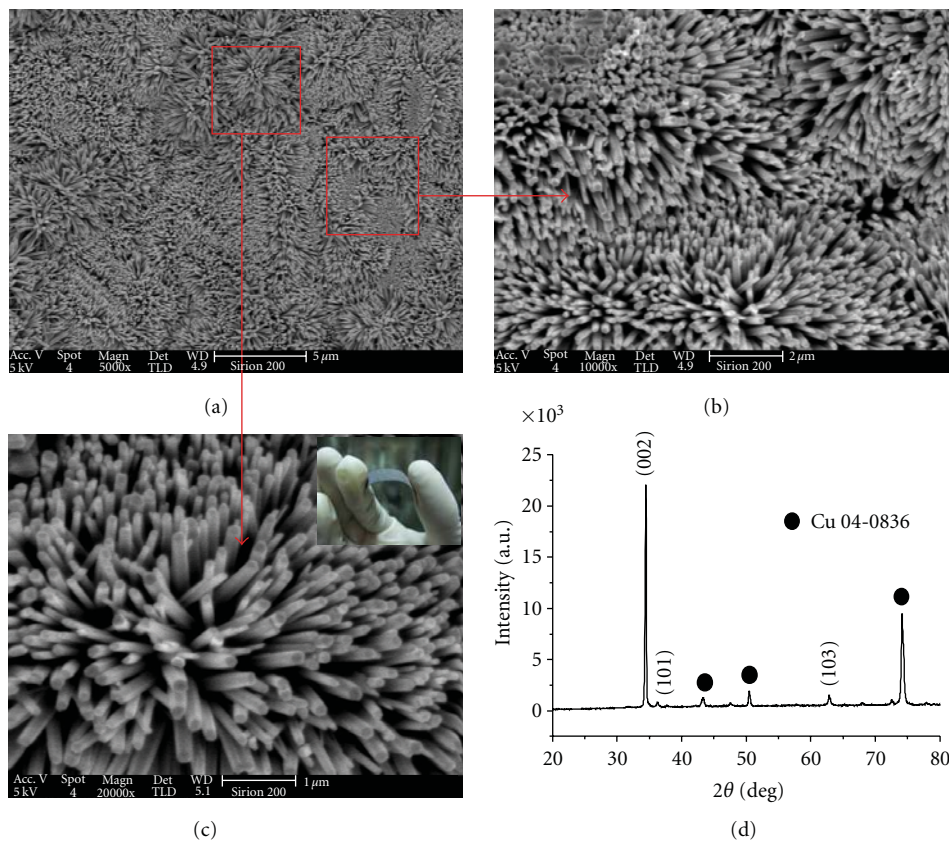


FIGURE 2: SEM images of ZnO nanowire arrays. Scale bar of (a) is 5 μm, (b) 2 μm, and (c) 1 μm. (d) XRD pattern of the ZnO nanowire arrays on the copper foil. The inset of (c) is the photograph of the ZnO nanowire arrays on the flexible copper foil.

plating layer. Meanwhile, designing the topography of the plating layer rationally may open a new economic way to pattern the nanowire arrays which may have 3-dimensional distribution [45, 46]. From Figures 2(b) and 2(c), we can clearly see the good orientation of the arrays and that single ZnO nanowires have smooth surface and average diameters of 130 nm. In addition, to investigate the contact between the ZnO nanowire arrays and substrate, ultrasonic treatment

was performed. After two minutes of treatment, the ZnO nanowire arrays were still adhered to the substrate tightly; no peel off was observed. This means good contact properties to the substrate, which would have obvious advantages in device fabrication.

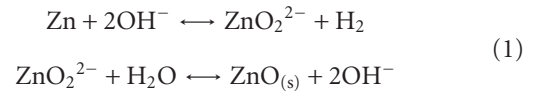
The crystallinity of the ZnO nanowire arrays is also investigated by the XRD methods. In Figure 2(d), the XRD patterns of the ZnO nanowire arrays grown on the Zn-plated

Cu foil were show. The peaks marked with solid circles are assigned to the cubic copper (JCPDS Card NO. 04-0836, space group Fm3m). These peaks are from the copper substrate. The rest of the peaks are in agreement with the typical wurtzite structure of ZnO diffraction pattern (JCPDS Card NO. 36-1451, space group P6<sub>3</sub>mc). The sharp (002) peak of the ZnO nanowire indicates good crystallinity, and favorable growth direction of ZnO crystals is (002). As reported in other literatures [52], the extrastrong (002) reflections of the ZnO nanowire also indicate good alignment of the nanoarrays. The disappearing of the reflections of Zn layer indicated that the Zn layer reacted with solution completely.

The growth of ZnO nanowire arrays is a complex way and mostly considered to be a process including the formation of a ZnO seed layer and subsequent growth of crystal. Many researches have suggested that the quality of seed layer influences the alignment and density of the ZnO nanowire arrays [53, 54]. In the first seed layer step, preseed texture layer was generally employed by most synthesis routes [23–32, 37, 38]. The self-seed method in which a seed layer is formed preceding the crystal growth during the solution reaction is a more competitive way. The preparation of ZnO nanowire arrays based on Zn metal powder or layer has been reported to be similar to self-seed methods. The seed layer in this system is formed by a reaction of converting Zn metal into ZnO. Thus the seed layer is also affected by the quality of Zn metal excluding the effects of the growth solution. This makes understanding the growth character complicated. A series of experiments were designed to understand the growth mechanism of ZnO nanowire arrays in our system. It was found that the growth of ZnO crystal depended on the amount of NH<sub>3</sub>·H<sub>2</sub>O, reaction temperature, zinc ion concentration, and the zinc plating layer.

In order to show the influence of NH<sub>3</sub>·H<sub>2</sub>O, different amounts (0.1 g, 1 g, and 2 g) were used, while keeping other parameters unchanged. In 0.1 g NH<sub>3</sub>·H<sub>2</sub>O, the solution was turbid with some Zn(OH)<sub>2</sub> precipitation. When the amount of NH<sub>3</sub>·H<sub>2</sub>O was further increased to 1 g, 2 g the solution became clear. The morphologies of the synthesized ZnO nanowire arrays were shown in Figures 3(a) and 3(b), (0.1 g) and Figures 3(c) and 3(d), (2 g). The diameter of ZnO nanowire increased with the increase of NH<sub>3</sub>·H<sub>2</sub>O from 100 nm to 220 nm. This may be caused by the fast growth speed of ZnO crystal in higher pH value which resulted from the increase amount of NH<sub>3</sub>·H<sub>2</sub>O. Moreover, the alignment of ZnO nanowire arrays was also improved with the increase of ammonia addition. This is different with the result reported by Tak and Yong [49]. In their report, the alignment of the nanowire arrays degraded with much more NH<sub>3</sub>·H<sub>2</sub>O addition due to the initial overetching and degradation of zinc seed layer in the high pH solution. However, we replaced the thermal-deposited Zn metal layer with electroplating Zn layer in our works. Commonly, the thickness of the electroplating Zn layer, several micrometers, is thicker than the thermal-deposited layer which is only in the scale of nanometer. Thus overetching can be avoided in our system. In addition, their chemical reaction activities are totally different. Compared with the thermal-deposited

Zn layer, the electroplated Zn layer is easier to react with the solution due to the intrinsic crystal defects like screw dislocation. The conversion of Zn metal into ZnO reacts as follows [49, 55]:



Zinc metal reacts with hydroxide ions produced by NH<sub>3</sub>·H<sub>2</sub>O to produce soluble zincate ions ZnO<sub>2</sub><sup>2-</sup>. Then the zincate ions react with water and deposit back to the surface of Zn layer to form solid-phase ZnO. With the improvement of the concentration of OH<sup>-</sup>, caused by the increase of NH<sub>3</sub>·H<sub>2</sub>O addition, reaction will turn to right more fast and produce much more ZnO<sub>2</sub><sup>2-</sup>, which results in the deposition of much more solid-phase ZnO. Furthermore, a dense layer of ZnO nanoparticles with smaller diameters is formed in higher NH<sub>3</sub>·H<sub>2</sub>O concentration. The alignments of the nanowire arrays could be improved by increasing the density of the seed layer [53, 54].

To verify the deduction above, we conducted the experiment etching the Zn plating layer with different amounts of NH<sub>3</sub>·H<sub>2</sub>O (0.1 g, 1 g) only at 80°C for 1 h. The obtained surface morphologies of Zn layer were shown in Figure 4(a) (0.1 g) and Figure 4(b) (1 g). The surface in the condition of 0.1 g NH<sub>3</sub>·H<sub>2</sub>O was covered by a layer of ZnO particle with much larger diameter than that in 1 g NH<sub>3</sub>·H<sub>2</sub>O addition. Meanwhile, the densities were also reduced by decreasing the amount of NH<sub>3</sub>·H<sub>2</sub>O. Thus, increasing NH<sub>3</sub>·H<sub>2</sub>O will result in reducing the diameter of the initial ZnO nanoparticle. By investigating the early stage of the reaction, 30 min, the effects were much more obvious. Figures 4(c) and 4(d) illustrate well-oriented ZnO nanoparticle formed in 30 min when 1 g NH<sub>3</sub>·H<sub>2</sub>O was added into the solution. In condition of 0.1 g NH<sub>3</sub>·H<sub>2</sub>O, as shown in Figures 4(e) and 4(f), a layer of the ZnO nanoparticle was also formed but the orientation is not as good as that in 1 g NH<sub>3</sub>·H<sub>2</sub>O. As reported by many researchers [56, 57], the orientation of the initial ZnO layer has a strong effect on the alignment of the ZnO nanowire arrays. In our work, the increased amount of NH<sub>3</sub>·H<sub>2</sub>O improved the orientation of the initial ZnO layer and then improved the alignments of ZnO nanowire arrays.

The growth of ZnO nanowire arrays was also conducted at different reaction temperatures. We found that the aspect ratio increased (smaller diameters) with the increase of the reaction temperature, but the density decreased. The tips of the nanowire grown at higher temperature also become sharper. In lower temperature, 70°C, shown in Figures 3(e) and 3(f), the nanowire arrays showed average diameter of 160 nm. When heated to 90°C the average diameter becomes smaller, ca. 90 nm. And as clearly shown in Figure 3(f), the tips are sharper and begin to fuse together. As some other researchers have reported [58, 59], the small but highly uniform diameter nanowires tend to bundle and align in the same growth direction and can be described by the phenomena of multiplication growth and the oriented attachment process.

The concentration of the Zinc ions was lowered to further investigate the growth of the ZnO nanowire arrays. When

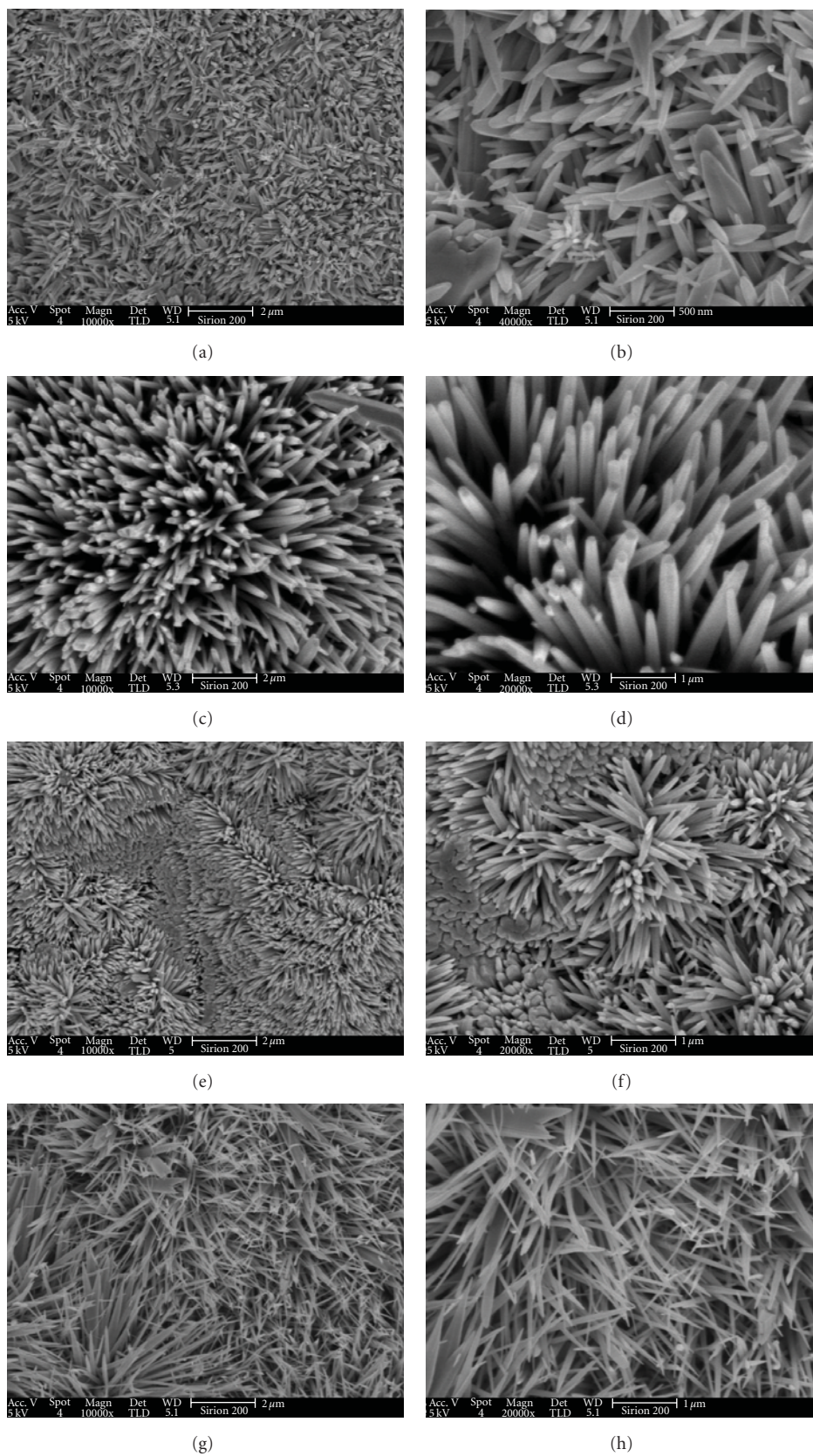


FIGURE 3: Effect of the amount of the ammonia and temperature, (a, b) 0.1 g, (c, d) 2 g. Effect of temperature (e, f) 70°C (g, h) 90°C.

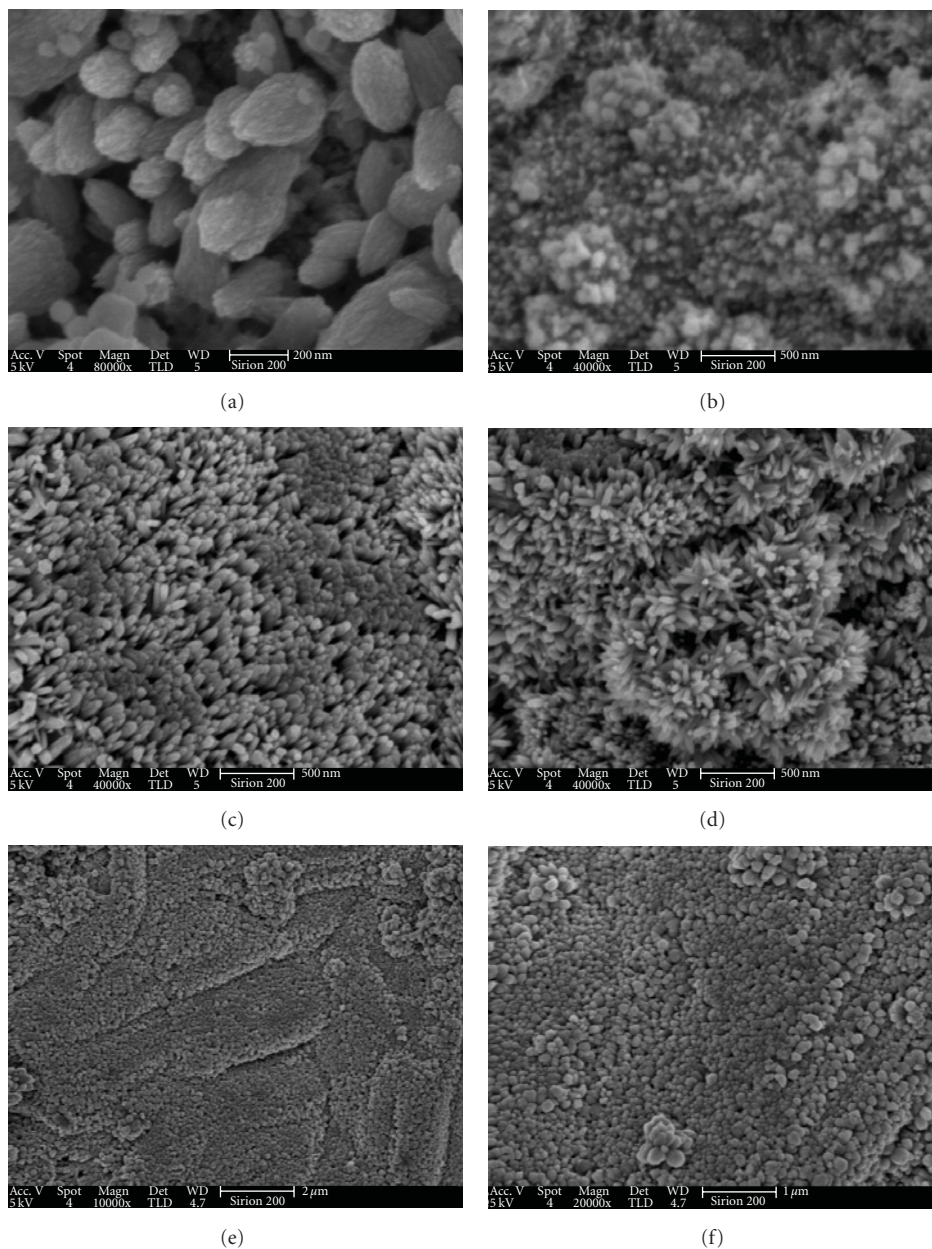


FIGURE 4: Zn transformed into ZnO in 30 mins, (a, b) only  $\text{NH}_3 \cdot \text{H}_2\text{O}$ , (a) 0.1 g, (b) 1 g, (c, d) 1 g  $\text{NH}_3 \cdot \text{H}_2\text{O}$ , 30 min, (e, f) 0.1 g  $\text{NH}_3 \cdot \text{H}_2\text{O}$ , 30 min.

the zinc ions were decreased to 0.003 M, while keeping  $\text{NH}_3 \cdot \text{H}_2\text{O}$  1 g unchanged, long ZnO nanowire arrays were achieved for 12-hour reaction. The SEM picture of the long ZnO nanowire arrays was shown in Figure 5(a), the inset was enlarged image. The average diameter of the long nanowire arrays was 80 nm and the nanowires fuse together, which was similar to the nanowires synthesized at  $90^\circ\text{C}$ . The XRD pattern in Figure 5(b) can be indexed to wurtzite ZnO diffraction pattern (JCPDS Card NO. 36-1451, space group  $P6_3mc$ ). The intensified (101) reflection is caused by the fusion of nanowire arrays. In addition to the ZnO reflection peaks, there also are some peaks indexed to Zn metal retained. We examined the evolution of the long nanowire arrays by different reaction times,

30 min, 1 h, and 6 h. The morphologies of these results were illustrated in Figures 5(c)–5(h). After 30 min of reaction, a dense layer of ZnO nanoparticle, functioned as seed layer, was formed. Figures 5(c) and 5(d) illustrated two typical morphologies of the ZnO nanoparticle. No matter how the different topographies of Zn plating layer presented, the seed layer duplicated the morphologies. When the reaction continued to 1 h, as shown in Figures 5(e) and 5(f), nanowire arrays formed with average diameter of 50 nm. When it was further prolonged to 6 h, the average diameter increased to 60 nm (Figures 5(g) and 5(h)). The diameter increased with the continuing of the reaction and decreased with the lowering of the concentration of  $\text{Zn}^{2+}$  ions.

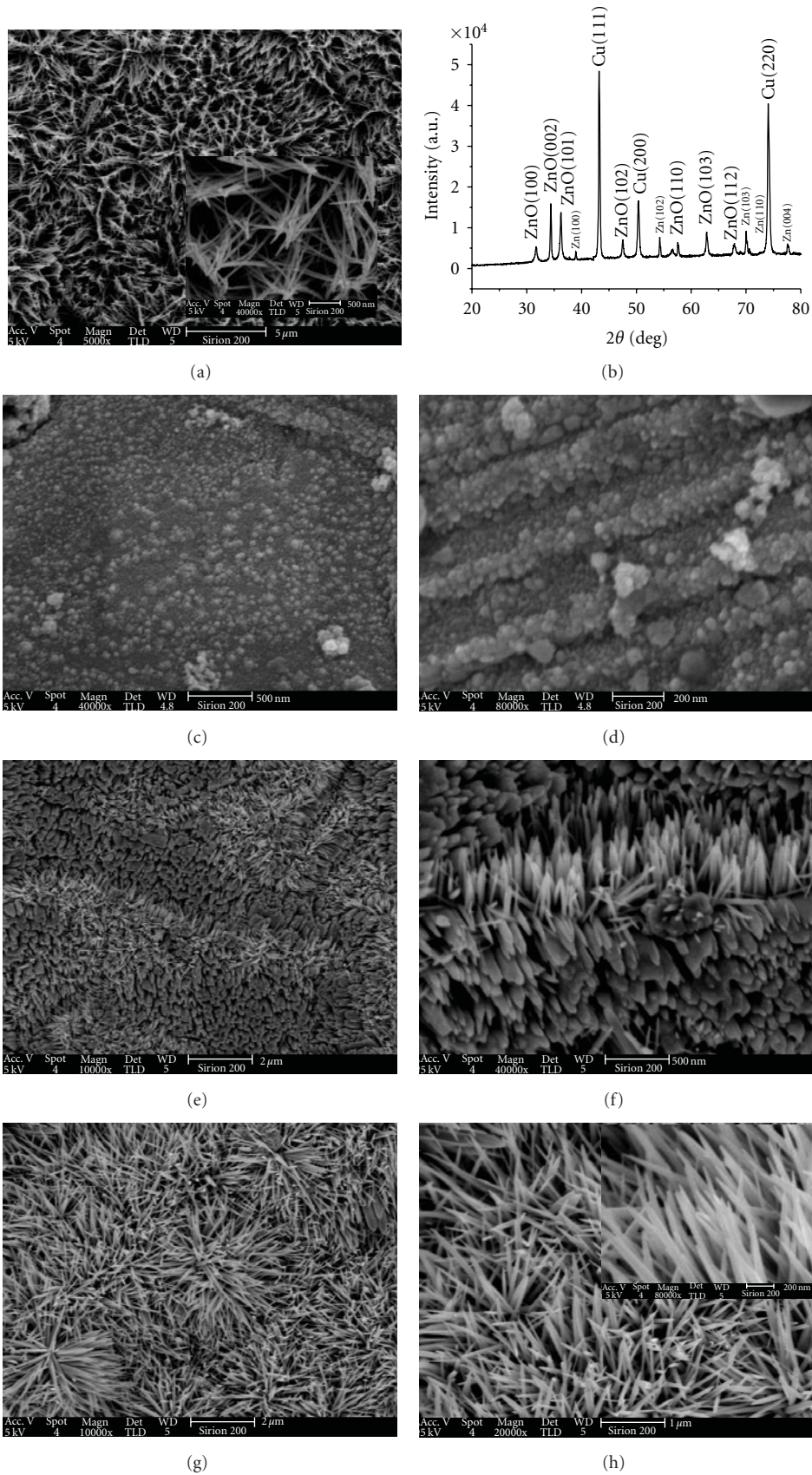


FIGURE 5: SEM image of long ZnO nanowire arrays (a) 12 h, (c, d) 30 min, (e, f) 1 h, (g, h) 6 h, (b) XRD pattern of long nanowire arrays. The inset of (a) shows enlarged picture with scale bar 500 nm.

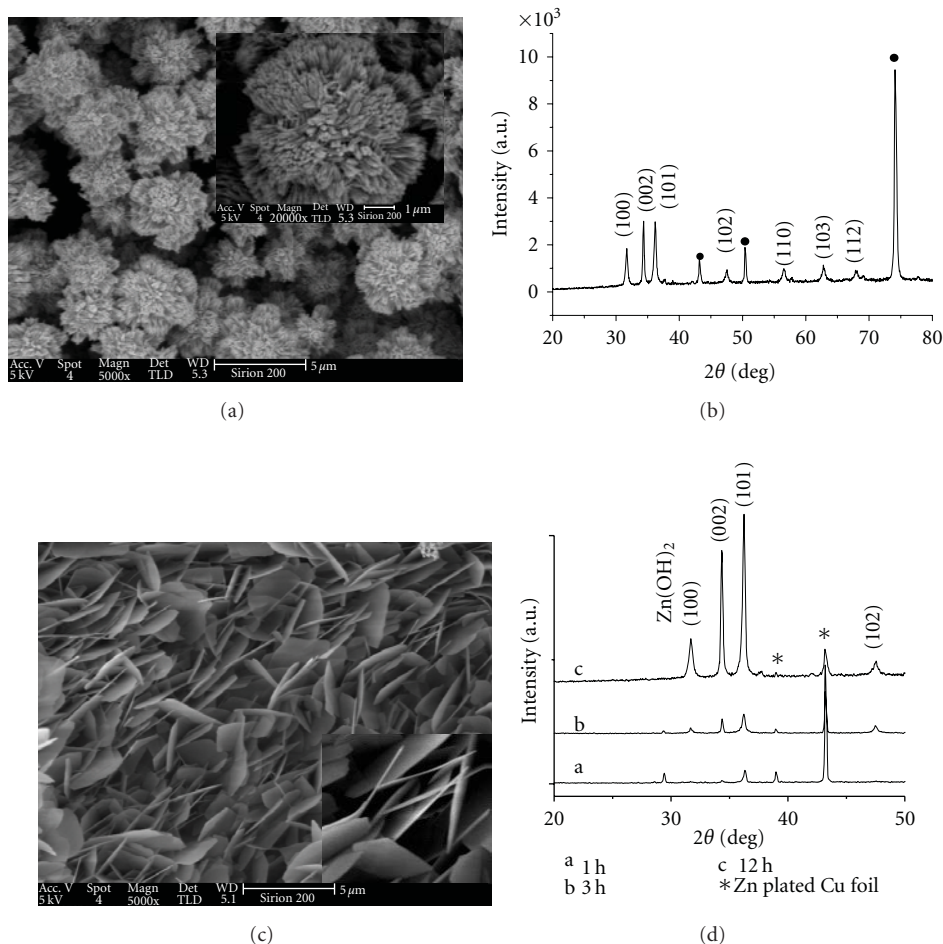


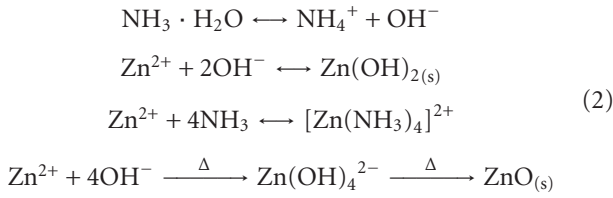
FIGURE 6: (a) SEM image of flower structure, inset is the image of single flower structure with scale bar 1 μm. (b) XRD pattern of flower structure. (c) SEM image of nanoplate arrays. (d) XRD pattern of nanoplate arrays with time 1 h, 3 h, and 12 h.

Interestingly, two other different morphologies, flower-like structure and nanoplate arrays were achieved in our experiments. We found a white layer deposited on the nonzinc plating side of Cu foil in the solution of 0.1 g  $\text{NH}_3 \cdot \text{H}_2\text{O}$  and 0.03 M  $\text{Zn}(\text{NO}_3)_2$  at 80°C. The morphology of this white layer is illustrated in Figure 6(a). A uniform ZnO layer with flower-like structure was observed. As shown in the inset of Figure 6(a), the surface of the flower-like particle was composed of ZnO nanorod arrays. This is a useful structure with high surface area. The corresponding XRD pattern is shown in Figure 6(b). All peaks can be indexed to wurtzite ZnO (JCPDS Card NO. 36-1451, space group  $\text{P6}_3\text{mc}$ ) except the peaks from the Cu substrates. The (100), (101) reflection are intensified compared with the XRD pattern of ZnO nanowire arrays. Moreover the intensities of (002) and (101) are almost the same, which is like the XRD pattern of other reported ZnO flower-like structures. Generally, homogeneous reaction in the solution and heterogeneous on the substrate happened in the same time. When the amount of  $\text{NH}_3 \cdot \text{H}_2\text{O}$  was 0.1 g, the solution was turbid, indicating the formation of  $\text{Zn}(\text{OH})_2$  precipitations. With the heating of the solution,  $\text{Zn}(\text{OH})_2$  decomposed to ZnO nuclei in the bulk solution. This

process facilitated the growth of ZnO crystal in the solution. As reported by others [60, 61], the growth of ZnO in solution makes it easy to bundle together to form flower-like structure.

In 0.1 g  $\text{NH}_3 \cdot \text{H}_2\text{O}$ , 0.03 M  $\text{Zn}(\text{NO}_3)_2$  condition, when the temperature increased to 90°C, nanoplate arrays were prepared (Figure 6(c)). The inset is the enlarged image. The thickness of the plate is 50–60 nm, and the average diameters of a single plate are several micrometers. Liu and Zeng [55] also get a hollow ZnO dandelions structure with plate-like building units using Zn metal powder as substrates in higher temperature. However, they did not discuss the formation mechanism of the plate like structure. ZnO nanoplate arrays have been reported to be due to the hydrolysis of zinc hydroxide which is usually plate-like. According to the XRD pattern of different growth times (Figure 6(d)1–3), 30 min, 3 h, and 12 h, a reflection at 29.4 degree was observed in the first 30 min stage which is indexed to  $\text{Zn}(\text{OH})_2$ . When the reaction continued, this reflection diminished and reflection peaks of ZnO appeared. Figure 6(d)-3 is the XRD pattern of well-developed ZnO nanoplate arrays. And it can be indexed to the hexagonal wurtzite phase ZnO (JCPDS Card NO.36-1451, space group  $\text{P6}_3\text{mc}$ ).

The chemical reaction, in our experiments is shown in the following:



When the  $\text{NH}_3 \cdot \text{H}_2\text{O}$  was added, it hydrolyzed to  $\text{NH}_4^+$  ion and  $\text{OH}^-$  ion, as shown in (2). The produced  $\text{OH}^-$  ion reacts with  $\text{Zn}^{2+}$  ion quickly to form  $\text{Zn}(\text{OH})_2$  white precipitation (4), and the solution turned turbid. With continued addition of  $\text{NH}_3 \cdot \text{H}_2\text{O}$ , the solution became clear by the formation of  $[\text{Zn}(\text{NH}_3)_4]^{2+}$  (5). When the temperature elevated, the (5) turned to left, and the  $[\text{Zn}(\text{NH}_3)_4]^{2+}$  complex decomposed to produce  $\text{Zn}^{2+}$ . Then  $\text{Zn}(\text{OH})_4^{2-}$  formed, which served as the basic growth units of ZnO nanoforms, hydrolyzed to  $\text{ZnO}_{(s)}$  (6). For the growth of ZnO nanowire arrays, the heterogeneous nucleation took place preferentially on the ZnO seed surface due to the reduced nucleation barrier by decreasing the interface energy. In addition, we can get much more understanding of the growth of ZnO nanowire arrays if the crystal habits are considered. Wurtzite ZnO crystal is a polar crystal, exhibiting a positive polar plane that is rich in Zn (0001) and a negative polar plane that is rich in O (000-1). The growth rates of different planes are reported to be  $V(0001) > V(10-11) > V(1010) > V(000-1)$ . In addition, the negative charged  $\text{Zn}(\text{OH})_4^{2-}$  complex ions are preferentially adsorbed onto the positive charged (0001) Zn face and subsequently dehydrate and enter into the crystal lattice. The growth rate of the (0001) face is greatly favored, and the more rapid the growth rate, the quicker the disappearance of the basal plane. Thus, nanowire structure with elongated c-axis surrounded by six {10-10} facets is formed. While the growth rates of some {10-11} facets are relatively smaller than those of (0001), and they remained to form needle like tips.

When the amount of  $\text{NH}_3 \cdot \text{H}_2\text{O}$  was increased, the stability of  $[\text{Zn}(\text{NH}_3)_4]^{2+}$  complex ions was also enhanced. As a result, the supersaturation of the solution was lowered. Homogeneous nucleation in the bulk solution was prohibited in low supersaturation, and the heterogeneous nucleation and growth onto the seed layer dominated. As discussed before, the  $\text{Zn}(\text{OH})_4^{2-}$  growth unit was preferentially attracted onto the (0001) positive charged plane. Monodentate ligand  $\text{NH}_3$  can not be efficiently adsorbed onto the neutral {10-10} side faces [62]; thus the increased amount of  $\text{NH}_3$  could not reduce the diameter. Therefore, the growth rate of the ZnO nanowire was improved in higher amount of  $\text{NH}_3 \cdot \text{H}_2\text{O}$ , and the diameter of the nanowire was also increased. At higher temperature, the decomposition rate of  $[\text{Zn}(\text{NH}_3)_4]^{2+}$  complex ions was improved, which further increased the formation of the  $\text{Zn}(\text{OH})_4^{2-}$  complex ions. Thus the growth along the (0001) direction was improved and the diameter of the nanowire was decreased. When we decreased the concentration of  $\text{Zn}^{2+}$  ions and kept the amount of  $\text{NH}_3 \cdot \text{H}_2\text{O}$  and temperature unchanged,

the ratio of  $\text{Zn}^{2+}$  ions to  $\text{NH}_3$  was decreased. This resulted in further decrease in supersaturation of the solution. The homogeneous nucleation was retarded, and the heterogeneous nucleation onto the seeded ZnO crystal was promoted in addition. Also, the critical diffusion of monomers and the subsequent limited growth in the solution of lowered  $\text{Zn}^{2+}$  ions concentration helped to decrease the diameter of the nanowire. Thus, in the same temperature, when the concentration of  $\text{Zn}^{2+}$  ions was decreased, the diameter of as-prepared ZnO nanowire was also decreased, and much longer nanowire arrays were achieved, which is similar to the results of Lionel Vayssieres [26].

The room temperature photoluminescence (PL) spectra of the ZnO nanowire arrays, flower-like structure, nanoplate arrays, and long nanowire arrays were measured by using a He-Cd 325 nm wavelength laser as the excitation source, as shown in Figure 7. For the nanowire arrays, Figure 7(a), room temperature PL spectra showed a strong UV emission around 392 nm (3.16 eV) and a broad green emission at ~550 nm (2.25 eV). The PL spectra of flower-like structure exhibited a strong emission around 403 nm (3.07 eV) and a broad green emission at ~550 nm (Figure 7(b)). For the nanoplate arrays, Figure 7(c), a strong UV emission around 383 nm (3.23 eV) and a broad green emission at ~550 nm were observed. The long nanowire arrays, in Figure 7(d), showed an intensive emission around 400 nm (3.09 eV), and the green emission at ~550 nm was relatively weak. Generally, the strong UV emission ranging from 380 to 400 nm is the band-edge emission resulting from the recombination of free excitons, while the green emission centered at about 550 nm is attributed to the singly ionized oxygen vacancy, and the emission results from the radiative recombination of a photogenerated hole with an electron occupying the oxygen vacancy. The shift of the strong UV emission is contributed to an increase in crystal intrinsic defects. Lin et al. [63] have calculated the energy levels of various intrinsic defect centres, such as vacancies of oxygen and zinc, interstitial oxygen and zinc, and antisite oxygen in ZnO. The energy gap between the conduction band ( $E_c$ ) and the valence band ( $E_v$ ) is considered to be 3.36 eV. The emission energy of electronic transition from the bottom of the conduction band to the vacancy of zinc ( $V_{\text{Zn}}$ ) level is 3.06 eV, and the emission energy of electronic transition from the bottom of the conduction band to the antisite oxygen ( $O_{\text{Zn}}$ ) level is 2.38 eV. Thus, the shift of UV emission from 383 nm to 403 nm of different ZnO nanostructures indicated different contents of the vacancy of zinc in each nanostructure which was achieved in different growth conditions. In our solution synthesis, the growth units are  $[\text{Zn}(\text{OH})_4]^{2-}$  produced by the reaction between  $\text{Zn}^{2+}$  and  $\text{OH}^-$ , and  $\text{Zn}^{2+}$  is released from the stabilized  $[\text{Zn}(\text{NH}_3)_4]^{2+}$  complex ions;  $\text{OH}^-$  is released from reagent  $\text{NH}_3 \cdot \text{H}_2\text{O}$ . ZnO is crystallized by continuously adding the O-contained growth units to the as-formed nuclei. The deficiency of  $\text{Zn}^{2+}$  ion in long ZnO nanowire condition accounts for the vacancy of the zinc. With increasing growth temperature, the release of  $\text{Zn}^{2+}$  is improved by the decrease of thermostabilization of the  $[\text{Zn}(\text{NH}_3)_4]^{2+}$  complex ions. Thus, in higher temperature, ZnO nanoplate arrays have less  $V_{\text{Zn}}$  than that of the flower-like structure which synthesized

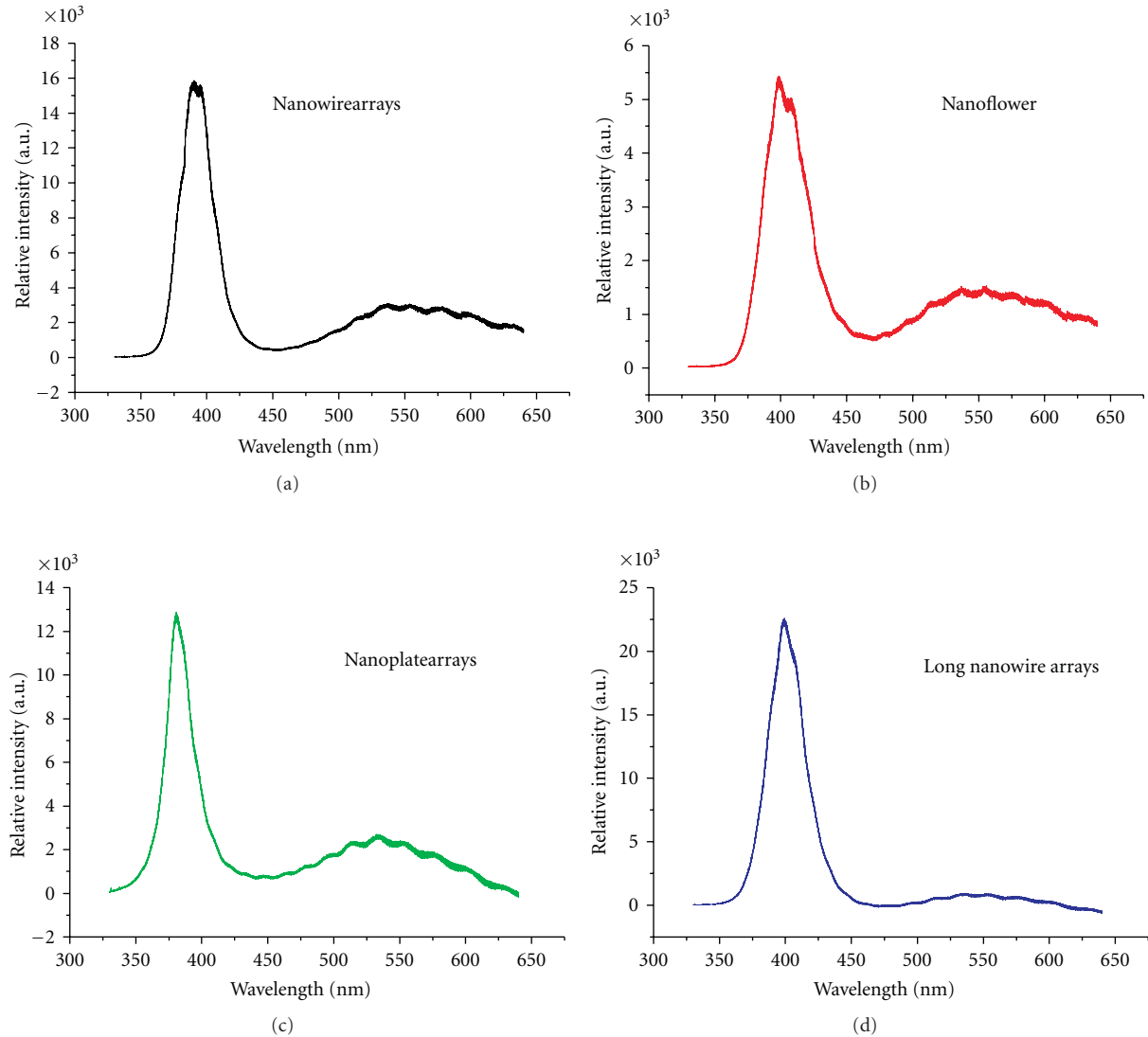


FIGURE 7: PL spectra of various ZnO nanostructures.

at lower temperature. Therefore, the optical properties can be turned by the growth condition in the solution methods.

#### 4. Conclusion

In conclusion, Zn plating layer on the flexible substrates (copper foil for demonstration here) was successfully applied to prepare ZnO nanostructure arrays via mild solution methods ( $\text{Zn}(\text{NO}_3)_2/\text{NH}_3\cdot\text{H}_2\text{O}$  solution system) in  $70\text{--}90^\circ\text{C}$ . Various synthetic conditions were demonstrated to influence the nanostructure arrays. It was found that, by varying the ratio of  $\text{NH}_3\cdot\text{H}_2\text{O}$  to  $\text{Zn}(\text{NO}_3)_2$ , the achieved ZnO nanostructure controllably changed from flower-like to nanowire arrays in which the seed layer formation process and diffusion rates of  $\text{Zn}^{2+}$  ions played important roles. By increasing the growth temperature, or reducing the  $\text{Zn}^{2+}$  ion concentration, the diameter of ZnO nanowire arrays can also be reduced greatly from 200 nm to 60 nm. It is

noted that the amounts of  $\text{NH}_3\cdot\text{H}_2\text{O}$  have great effects on the formation of ZnO seed layer in the initial stage. Dense and orientated seed layers formed in 1 g  $\text{NH}_3\cdot\text{H}_2\text{O}$  are effective for achieving aligned ZnO nanowire arrays. ZnO nanoplate arrays were achieved in 0.03 M  $\text{Zn}(\text{NO}_3)_2$  and 0.1 g  $\text{Zn}(\text{NO}_3)_2$  in  $70^\circ\text{C}$ . Moreover, we found that the pattern of ZnO nanowire arrays duplicated the surface morphology of the Zn plating layer which can be changed by controlling the electroplating parameters like electric density. Thus, a new patterning method for ZnO nanowire arrays can be developed by designing the pattern of the Zn plating layer. PL measurement has demonstrated intensive UV exciton luminescence of these ZnO structures which is in the range of 380–403 nm. Therefore, our methods provide an easier and more economic way to produce ZnO nanowire arrays on the flexible conductive substrates and will be applicable to flexible devices like solar cell and gas sensors.

## Acknowledgments

The authors thank the financial supports from the National High Technology Research and Development Program of China (no. 2007AA03Z301), the Natural Science Foundations of China (no. 20771032, no. 60806028) and Anhui Province (070414200), and the National Basic Research Program of China (no. 2007CB9-36001).

## References

- [1] R. F. Service, "Inorganic electronic begin to flex their muscle," *The Science*, vol. 312, no. 5780, pp. 1593–1594, 2006.
- [2] R. H. Reuss, B. R. Chalamala, A. Mousessian et al., "Macro-electronics: perspectives on technology and applications," *Proceedings of the IEEE*, vol. 93, no. 7, pp. 1239–1256, 2005.
- [3] Z.-Y. Fan, H. Razavi, J.-W. Do et al., "Three-dimensional nanopillar-array photovoltaics on low-cost and flexible substrates," *Nature Materials*, vol. 8, no. 8, pp. 648–653, 2009.
- [4] W.-X. Zhang and S.-H. Yang, "In situ fabrication of inorganic nanowire arrays grown from and aligned on metal substrates," *Accounts of Chemical Research*, vol. 42, no. 10, pp. 1617–1627, 2009.
- [5] Z. L. Wang, "ZnO nanowire and nanobelt platform for nanotechnology," *Materials Science and Engineering R*, vol. 64, no. 3-4, pp. 33–71, 2009.
- [6] Z. L. Wang, "Theme issue: inorganic nanotubes and nanowires," *Journal of Materials Chemistry*, vol. 19, no. 7, pp. 826–827, 2009.
- [7] L. Xu, Y.-S. Ding, C.-H. Chen et al., "3D flowerlike  $\alpha$ -nickel hydroxide with enhanced electrochemical activity synthesized by microwave-assisted hydrothermal method," *Chemistry of Materials*, vol. 20, no. 1, pp. 308–316, 2008.
- [8] M. T. Lloyd, R. P. Prasankumar, M. B. Sinclair, A. C. Mayer, D. C. Olson, and J. W. P. Hsu, "Impact of interfacial polymer morphology on photoexcitation dynamics and device performance in P3HT/ZnO heterojunctions," *Journal of Materials Chemistry*, vol. 19, no. 26, pp. 4609–4614, 2009.
- [9] M. Law, L. E. Greene, J. C. Johnson, R. Saykally, and P. Yang, "Nanowire dye-sensitized solar cells," *Nature Materials*, vol. 4, no. 6, pp. 455–459, 2005.
- [10] Y. Tak, S. J. Hong, J. S. Lee, and K. Yong, "Fabrication of ZnO/CdS core/shell nanowire arrays for efficient solar energy conversion," *Journal of Materials Chemistry*, vol. 19, no. 33, pp. 5945–5951, 2009.
- [11] L. C. Tien, P. W. Sadik, D. P. Norton et al., "Hydrogen sensing at room temperature with Pt-coated ZnO thin films and nanorods," *Applied Physics Letters*, vol. 87, no. 22, Article ID 222106, 3 pages, 2005.
- [12] G. Shen, P.-C. Chen, K. Ryu, and C. Zhou, "Devices and chemical sensing applications of metal oxide nanowires," *Journal of Materials Chemistry*, vol. 19, no. 7, pp. 828–839, 2009.
- [13] S.-K. Kim and S. B. Lee, "Highly encoded one-dimensional nanostructures for rapid sensing," *Journal of Materials Chemistry*, vol. 19, no. 10, pp. 1381–1389, 2009.
- [14] M. H. Huang, S. Mao, H. Feick et al., "Room-temperature ultraviolet nanowire nanolasers," *The Science*, vol. 292, no. 5523, pp. 1897–1899, 2001.
- [15] W. I. Park and G.-C. Yi, "Electroluminescence in n-ZnO nanorod arrays vertically grown on p-GaN," *Advanced Materials*, vol. 16, no. 1, pp. 87–90, 2004.
- [16] J. W. Stouwdam and R. A. J. Janssen, "Red, green, and blue quantum dot LEDs with solution processable ZnO nanocrystal electron injection layers," *Journal of Materials Chemistry*, vol. 18, no. 16, pp. 1889–1894, 2008.
- [17] X. Wang, J. Song, J. Liu, and L. W. Zhong, "Direct-current nanogenerator driven by ultrasonic waves," *The Science*, vol. 316, no. 5821, pp. 102–105, 2007.
- [18] X. D. Wang, J. Zhou, C. S. Lao, J. H. Song, N. S. Xu, and Z. L. Wang, "In situ field emission of density-controlled ZnO nanowire arrays," *Advanced Materials*, vol. 19, no. 12, pp. 1627–1631, 2007.
- [19] C. Badre, T. Pauporté, M. Turmine, and D. Lincot, "A ZnO nanowire array film with stable highly water-repellent properties," *Nanotechnology*, vol. 18, no. 36, Article ID 365705, 2007.
- [20] Z. W. Pan, Z. R. Dai, and Z. L. W. Wang, "Nanobelts of semiconducting oxides," *The Science*, vol. 291, no. 5510, pp. 1947–1949, 2001.
- [21] H.-J. Kim, K. Sung, K.-S. An et al., "ZnO nanowhiskers on ZnO nanoparticle-deposited Si(111) by MOCVD," *Journal of Materials Chemistry*, vol. 14, no. 23, pp. 3396–3397, 2004.
- [22] M. H. Huang, Y. Wu, H. Feick, N. Tran, E. Weber, and P. Yang, "Catalytic growth of zinc oxide nanowires by vapor transport," *Advanced Materials*, vol. 13, no. 2, pp. 113–116, 2001.
- [23] Z. R. Tian, J. A. Voigt, J. Liu et al., "Complex and oriented ZnO nanostructures," *Nature Materials*, vol. 2, no. 12, pp. 821–826, 2003.
- [24] L. E. Greene, M. Law, J. Goldberger et al., "Low-temperature wafer-scale production of ZnO nanowire arrays," *Angewandte Chemie International Edition*, vol. 42, no. 26, pp. 3031–3034, 2003.
- [25] D. B. Mitzi, "Solution-processed inorganic semiconductors," *Journal of Materials Chemistry*, vol. 14, no. 15, pp. 2355–2365, 2004.
- [26] L. Vayssieres, "Growth of arrayed nanorods and nanowires of ZnO from aqueous solutions," *Advanced Materials*, vol. 15, no. 5, pp. 464–466, 2003.
- [27] J. Wang and L. Gao, "Wet chemical synthesis of ultralong and straight single-crystalline ZnO nanowires and their excellent UV emission properties," *Journal of Materials Chemistry*, vol. 13, no. 10, pp. 2551–2554, 2003.
- [28] Y. Sun, G. M. Fuge, N. A. Fox, D. J. Riley, and M. N. R. Ashfold, "Synthesis of aligned arrays of ultrathin ZnO nanotubes on a Si wafer coated with a thin ZnO film," *Advanced Materials*, vol. 17, no. 20, pp. 2477–2481, 2005.
- [29] J. S. Bendall, G. Visimberga, M. Szachowicz et al., "An investigation into the growth conditions and defect states of laminar ZnO nanostructures," *Journal of Materials Chemistry*, vol. 18, no. 43, pp. 5259–5266, 2008.
- [30] H. E. Unalan, P. Hiralal, D. Kuo, B. Parekh, G. Amaratunga, and M. Chhowalla, "Flexible organic photovoltaics from zinc oxide nanowires grown on transparent and conducting single walled carbon nanotube thin films," *Journal of Materials Chemistry*, vol. 18, no. 48, pp. 5909–5912, 2008.
- [31] Y. H. Tong, Y. C. Liu, L. Dong et al., "Growth of ZnO nanostructures with different morphologies by using hydrothermal technique," *Journal of Physical Chemistry B*, vol. 110, no. 41, pp. 20263–20267, 2006.
- [32] L. E. Greene, M. Law, D. H. Tan et al., "General route to vertical ZnO nanowire arrays using textured ZnO seeds," *Nano Letters*, vol. 5, no. 7, pp. 1231–1236, 2005.

- [33] D. Pradhan and K. T. Leung, "Controlled growth of two-dimensional and one-dimensional ZnO nanostructures on indium tin oxide coated glass by direct electrodeposition," *Langmuir*, vol. 24, no. 17, pp. 9707–9716, 2008.
- [34] C. Lévy-Clément, R. Tena-Zaera, M. A. Ryan, A. Katty, and G. Hodes, "CdSe-sensitized p-CuSCN/nanowire n-ZnO heterojunctions," *Advanced Materials*, vol. 17, no. 12, pp. 1512–1515, 2005.
- [35] R. Tena-Zaera, J. Elias, G. Wang, and C. Lévy-Clément, "Role of chloride ions on electrochemical deposition of ZnO nanowire arrays from O<sub>2</sub> reduction," *Journal of Physical Chemistry C*, vol. 111, no. 45, pp. 16706–16711, 2007.
- [36] B. Cao, Y. Li, G. Duan, and W. Cai, "Growth of ZnO nanoneedle arrays with strong ultraviolet emissions by an electrochemical deposition method," *Crystal Growth and Design*, vol. 6, no. 5, pp. 1091–1095, 2006.
- [37] Y. Sun, D. J. Riley, and M. N. R. Ashford, "Mechanism of ZnO nanotube growth by hydrothermal methods on ZnO film-coated Si substrates," *Journal of Physical Chemistry B*, vol. 110, no. 31, pp. 15186–15192, 2006.
- [38] X. D. Yan, Z. W. Li, R. Q. Chen, and W. Gao, "Template growth of ZnO nanorods and microrods with controllable densities," *Crystal Growth and Design*, vol. 8, no. 7, pp. 2406–2410, 2008.
- [39] J. P. Liu, X. T. Huang, Y. Y. Li et al., "Vertically aligned 1D ZnO nanostructures on bulk alloy substrates: direct solution synthesis, photoluminescence, and field emission," *Journal of Physical Chemistry C*, vol. 111, no. 13, pp. 4990–4997, 2007.
- [40] L. Vayssieres, K. Keis, S.-E. Lindquist, and A. Hagfeldt, "Purpose-built anisotropic metal oxide material: 3D highly oriented microrod array of ZnO," *Journal of Physical Chemistry B*, vol. 105, no. 17, pp. 3350–3352, 2001.
- [41] L. Vayssieres, "On the design of advanced metal oxide nanomaterials," *International Journal of Nanotechnology*, vol. 1, no. 1-2, pp. 1–41, 2004.
- [42] H. Yu, Z. Zhang, M. Han, X. Hao, and F. Zhu, "A general low-temperature route for large-scale fabrication of highly oriented ZnO nanorod/nanotube arrays," *Journal of the American Chemical Society*, vol. 127, no. 8, pp. 2378–2379, 2005.
- [43] F. Xu, Z.-Y. Yuan, G.-H. Du et al., "Simple approach to highly oriented ZnO nanowire arrays: large-scale growth, photoluminescence and photocatalytic properties," *Nanotechnology*, vol. 17, no. 2, pp. 588–594, 2006.
- [44] J. W. P. Hsu, Z. R. R. Tian, N. C. Simmons, C. M. Matzke, J. A. Voigt, and J. Liu, "Directed spatial organization of zinc oxide nanorods," *Nano Letters*, vol. 5, no. 1, pp. 83–86, 2005.
- [45] W. Schwarzacher, "Electrodeposition: a technology for the future," *Electrochemical Society Interface*, vol. 15, no. 1, pp. 32–33, 2006.
- [46] M. Wery, J. C. Catonné, and J. Y. Hihn, "Barrel zinc electrodeposition from alkaline solution," *Journal of Applied Electrochemistry*, vol. 30, no. 2, pp. 165–172, 2000.
- [47] S.-H. Jung, E. Oh, K.-H. Lee, W. J. Park, and S.-H. Jeong, "A sonochemical method for fabricating aligned ZnO nanorods," *Advanced Materials*, vol. 19, no. 5, pp. 749–753, 2007.
- [48] C. H. Lu, L. M. Qi, J. H. Yang, L. Tang, D. Y. Zhang, and J. M. Ma, "Hydrothermal growth of large-scale micropatterned arrays of ultralong ZnO nanowires and nanobelts on zinc substrate," *Chemical Communications*, no. 33, pp. 3551–3553, 2006.
- [49] Y. Tak and K. Yong, "Controlled growth of well-aligned ZnO nanorod array using a novel solution method," *Journal of Physical Chemistry B*, vol. 109, no. 41, pp. 19263–19269, 2005.
- [50] B. Liu and C. H. Zeng, "Fabrication of ZnO "Dandelions" via a modified Kirkendall process," *Journal of the American Chemical Society*, vol. 126, no. 51, pp. 16744–16746, 2004.
- [51] Biddulph, C.; Marzano, M.; Zinc Plating, Pavco Inc, Cleveland, P 323.
- [52] J. B. Baxter, A. M. Walker, K. V. Ommering, and E. S. Aydil, "Synthesis and characterization of ZnO nanowires and their integration into dye-sensitized solar cells," *Nanotechnology*, vol. 17, no. 11, pp. S304–S312, 2006.
- [53] J. C. Liu, J. She, S. Z. Deng, J. Chen, and N. S. Xu, "Ultrathin seed-layer for tuning density of ZnO nanowire arrays and their field emission characteristics," *Journal of Physical Chemistry C*, vol. 112, no. 31, pp. 11685–11690, 2008.
- [54] J.-I. Hong, J. Bae, Z. L. Wang, and R. L. Snyder, "Room-temperature, texture-controlled growth of ZnO thin films and their application for growing aligned ZnO nanowire arrays," *Nanotechnology*, vol. 20, no. 8, Article ID 085609, 2009.
- [55] B. Liu and H. C. Zeng, "Fabrication of ZnO "Dandelions" via a modified Kirkendall process," *Journal of the American Chemical Society*, vol. 126, no. 51, pp. 16744–16746, 2004.
- [56] J. Song and S. Lim, "Effect of seed layer on the growth of ZnO nanorods," *Journal of Physical Chemistry C*, vol. 111, no. 2, pp. 596–600, 2007.
- [57] R. Ghosh, M. Dutta, and D. Basak, "Self-seeded growth and ultraviolet photoresponse properties of ZnO nanowire arrays," *Applied Physics Letters*, vol. 91, no. 7, Article ID 073108, 3 pages, 2007.
- [58] K. Govender, D. S. Boyle, P. B. Kenway, and P. O'Brien, "Understanding the factors that govern the deposition and morphology of thin films of ZnO from aqueous solution?" *Journal of Materials Chemistry*, vol. 14, no. 16, pp. 2575–2591, 2004.
- [59] H. Zhang, D. R. Yang, Y. J. Ji, X. Y. Ma, J. Xu, and D. L. Que, "Low temperature synthesis of flowerlike ZnO nanostructures by cetyltrimethylammonium bromide-assisted hydrothermal process," *Journal of Physical Chemistry B*, vol. 108, no. 13, pp. 3955–3958, 2004.
- [60] J. Bico, B. Roman, L. Moulin, and A. Boudaoud, "Elastocapillary coalescence in wet hair," *Nature*, vol. 432, no. 7018, p. 690, 2004.
- [61] C. Lu, L. M. Qi, J. Yang, L. Tang, D. Zhang, and J. M. Ma, "Hydrothermal growth of large-scale micropatterned arrays of ultralong ZnO nanowires and nanobelts on zinc substrate," *Chemical Communications*, no. 33, pp. 3551–3553, 2006.
- [62] M.-S. Mo, D. B. Wang, X. S. Du et al., "Engineering of nanotips in ZnO submicrorods and patterned arrays," *Crystal Growth and Design*, vol. 9, no. 2, pp. 797–802, 2009.
- [63] B. X. Lin, Z. X. Fu, and Y. B. Jia, "Green luminescent center in undoped zinc oxide films deposited on silicon substrates," *Applied Physics Letters*, vol. 79, no. 7, pp. 943–945, 2001.

## Research Article

# Synthesis of Ag Nanostructures by Photochemical Reduction Using Citrate-Capped Pt Seeds

Hyeong-Ho Park,<sup>1,2</sup> Xin Zhang,<sup>3</sup> Yong-June Choi,<sup>1</sup> Hyung-Ho Park,<sup>1</sup> and Ross H. Hill<sup>3</sup>

<sup>1</sup>Department of Materials Science and Engineering, Yonsei University, 134 Shinchon-dong, Seodaemun-gu, Seoul 120-749, Republic of Korea

<sup>2</sup>Nano Process Division, Patterning Process Department, Korea Advanced Nano Fab Center, Suwon 443-270, Republic of Korea

<sup>3</sup>4D Labs and Department of Chemistry, Simon Fraser University, Burnaby, BC, Canada V5A 1S6

Correspondence should be addressed to Hyung-Ho Park, hhpark@yonsei.ac.kr

Received 9 April 2010; Revised 26 May 2010; Accepted 26 July 2010

Academic Editor: Bo Zou

Copyright © 2011 Hyeong-Ho Park et al. This is an open access article distributed under the Creative Commons Attribution License, which permits unrestricted use, distribution, and reproduction in any medium, provided the original work is properly cited.

A simple synthesis of Ag nanostructures such as nanorods and nanowires has been demonstrated with citrate-capped Pt seeds. UV-visible spectra and photographs of the synthesized solutions at different UV exposure times showed that the citrate-capped Pt seed played a crucial role in the growth of Ag nanostructures. After UV exposure of the colloidal solution for 60 min, the average diameter, length, and aspect ratio of the Ag nanostructures were about 95 nm, 2.1  $\mu\text{m}$ , and 22, respectively. The photochemical reduction is hypothesized to result from photoelectron transfer from adsorbed citrate to Pt nanoparticle seed allowing Ag ions to form Ag nanostructures. Based on X-ray diffraction spectra and transmission electron microscope images, the synthesized Ag nanostructures were a face-centered cubic single crystal with good purity. These results suggest that the photochemical reduction method can provide Ag nanostructures in the presence of citrate-capped Pt seeds at room temperature for anisotropic Ag products.

## 1. Introduction

The field of one-dimensional (1D) nanomaterials research constitutes one of the most important frontiers in materials science. The unusual physicochemical and optoelectronic properties of nanomaterials hold tremendous potential in the synthesis and design of various advanced materials [1]. Among all metals, Ag has attracted a great deal of attention due to the high electrical and thermal conductivities of bulk Ag, which is an important material in many fields [2]. In addition, Ag nanorods and nanowires have recently attracted extensive attention due to their interesting applications, which include photonic crystals [3], infrared polarizers [4], and catalysts [5].

A number of chemical approaches have been extensively explored to process Ag into 1D materials [2, 3]. For instance, a polyol process has been investigated for the preparation of

Ag nanorods and nanowires, in which the Ag nanostructures were produced by reducing  $\text{AgNO}_3$  in ethylene glycol (EG) with the addition of poly(vinyl pyrrolidone) (PVP) [6]. Recently, Sun et al. reported that Pt nanoparticles could serve as seeds for the heterogeneous nucleation and growth of Ag nanorods and nanowires that were produced in solution via the reduction of  $\text{AgNO}_3$  with EG by refluxing at  $\sim 160^\circ\text{C}$  [2]. In addition, Tsuji et al. reported Ag nanostructures such as nanorods and nanowires by a microwave-polyol method under microwave heating in the presence of Pt seeds [7]. Despite these advances, it is desirable to be able to produce Ag nanostructures at room temperature. Recently, the photochemical reduction method of producing nanomaterials has become an important technique in nanotechnology [8]. It is more convenient and environmental friendly than either electrodeposition using anodic alumina membranes [9] or catalytic CVD growth [10]. Here, we explore a new

photochemical synthesis of 1-dimensional Ag nanostructures using UV irradiation with citrate-capped Pt nanoparticles, which can be accomplished at room temperature.

## 2. Experimental

Chloroplatinic acid hydrate ( $\text{H}_2\text{PtCl}_6 \cdot x\text{H}_2\text{O}$ , 99.9%), sodium borohydride ( $\text{NaBH}_4$ , 98.5%), and sodium citrate tribasic dihydrate ( $\text{C}_6\text{H}_5\text{Na}_3\text{O}_7 \cdot 2\text{H}_2\text{O}$ , 99%) were used for synthesis of citrate-capped Pt nanoparticle seeds as a catalyst, while silver nitrate ( $\text{AgNO}_3$ , 99%) and PVP ( $(\text{C}_6\text{H}_9\text{NO})_x$ ,  $M_w \sim 55,000$ , 99%) were used for Ag nanorods and nanowires. All chemicals were purchased from Sigma-Aldrich, Inc. Ultrapure deionized water was used to prepare all aqueous solutions for citrate-capped Pt nanoparticle seeds, Ag nanorods, and nanowires. Pt nanoparticle seeds, 4 nm in size, capped with citrate, were produced as follows. 1 mL of 10 mM  $\text{NaBH}_4$  was added all at once to a 20 mL solution for a final concentration of 0.47 mM  $\text{H}_2\text{PtCl}_6 \cdot x\text{H}_2\text{O}$  and 0.47 mM  $\text{C}_6\text{H}_5\text{Na}_3\text{O}_7 \cdot 2\text{H}_2\text{O}$  with vigorous stirring. Stirring was stopped after 30 s and the resultant solution was aged for 2 h before use. For synthesis of Ag nanorods and nanowires, 0.5 mL of the citrate-capped Pt nanoparticle seed solution was transferred to a 10 mL vial containing 3 mL of an aqueous solution of 0.75 mM  $\text{AgNO}_3$  and 0.50 mM PVP. The solution was irradiated with a 1000 W mercury arc lamp ( $\lambda_{\text{max}} = 365 \text{ nm}$ ) at room temperature. UV-visible spectra of the colloidal solutions with different UV exposure times were recorded on a Jasco V-570 UV/vis/NIR spectrophotometer. The samples were prepared by mounting a few drops of the colloidal solutions on a p-Si(100) wafer to observe the morphological features of the Ag structures using a scanning electron microscope (SEM). X-ray diffractometer (XRD) samples were prepared on a corning 1737 glass to measure the crystallinity of Ag nanostructures; the XRD used  $\text{Cu } k_\alpha$  radiation. Particle size distributions of the citrate-capped Pt seed solutions with different UV exposure times were measured by a particle size analyzer (PSA) (Malvern Instruments Ltd., Zetasizer Nano Series). Transmission electron microscope (TEM) and electron diffraction studies were performed with a JEOL JEM-4010 microscope operated at 400 kV. Samples for TEM were prepared by dispersing a few drops of the colloid solution on a carbon film supported by molybdenum grids.

## 3. Results and Discussion

UV/vis/NIR spectroscopy is a reliable method for detecting the presence of one-dimensional metallic nanostructures [2, 11]. Specific signature peaks can be used to extract information on the aspect ratio of the nanostructures. UV-visible spectra of the synthesized solutions were measured at different UV exposure times with and without citrate-capped Pt seeds in the range of 250–900 nm, and the results are given in Figure 1. In the case where citrate-capped Pt seeds were used, UV-visible spectra of the colloidal solutions were different for different UV exposure times, while there was no change in the solution synthesized without citrate-capped Pt seeds.

The introduction of foreign nuclei significantly reduces the nucleation energy and enhances catalysis for the formation of metal nanostructures [12]. In our case, we can infer that citrate-capped Pt nanoparticle seeds serve as a catalyst for the nucleation and growth of Ag nanostructures. As shown in Figure 1(b), after 15 min of exposure to UV, the appearance of a plasmon peak at  $\sim 410 \text{ nm}$  indicated the formation of Ag nanostructures [13, 14]. It is well known that the UV-visible absorption spectrum of Ag nanostructures depends on the size of the nanostructures, that is, the wavelength at maximum absorption ( $\lambda_{\text{max}}$ ) increases as the aspect ratio of the nanostructure increases [14]. Increases in aspect ratio are apparent with increasing exposure time, since, for UV exposure of the colloidal solutions for 15, 45, and 60 min, the values of  $\lambda_{\text{max}}$  were 407, 420, and 450 nm, respectively. In the spectrum corresponding to UV exposure for 60 min, a shoulder peak around 350 nm becomes more apparent, as a result of increasing aspect ratio of Ag nanostructures. The absorption peak at 350 nm can be attributed to the plasmon response peak from the longitudinal vibration in Ag nanowires [15]. In the case of polyol processes, Ag nanowires were obtained only under heat treatment at  $\sim 160^\circ\text{C}$  for 40 min [2, 16]. However, here, UV exposure of the colloidal solutions for 60 min at room temperature is sufficient for the growth of Ag nanowires. In addition, the role of UV light was checked to follow the advance of the silver salt reduction in the presence of citrate-capped Pt nanoparticle seeds at room temperature without UV irradiation according to storage in various times as shown in Figure 1(c). There was no change in the UV-visible spectra of solutions synthesized without UV irradiation. So, we can deduce that during UV irradiation the citrate-capped Pt nanoparticle seeds played a crucial role for the formation of Ag nanostructures.

The morphologies and sizes of synthesized products irradiated by UV exposure for 45 and 60 min were observed using an SEM. In our case, after UV exposure of the colloidal solution for 45 min, we observed the formation of Ag nanoparticles and nanorods as shown in Figure 2(a). After UV exposure for 60 min, Figure 2(b), Ag nanoparticles, nanorods, and nanowires were formed. Nanorods and nanowires can be distinguished from their aspect ratio, 2–20 and  $>20$ , respectively [7, 14]. In polyol processes, the evolution of Ag nanostructures went from Ag nanoparticles and nanorods to Ag nanorods and nanowires with various heating times [2, 16]. Similarly, the evolution of Ag nanostructures formed by photochemical reduction went from a 0 dimension to a 1 dimension morphology according to the UV exposure time. Analysis of SEM micrographs indicates that the product UV irradiated for 45 min contains mainly spherically shaped Ag nanoparticles that have diameters of about 86 nm. In the case of the product UV irradiated for 60 min, the average diameter, length, and aspect ratios of the Ag nanostructures are about 95 nm,  $2.1 \mu\text{m}$ , and 22, respectively. From the results of UV-Visible spectra (Figure 1), the symmetric absorption peak implies that the size distribution of the Ag nanoparticles is narrow and the asymmetric absorption peak implies that wire-shaped Ag nanostructures, that is, long Ag nanowires grow due to an

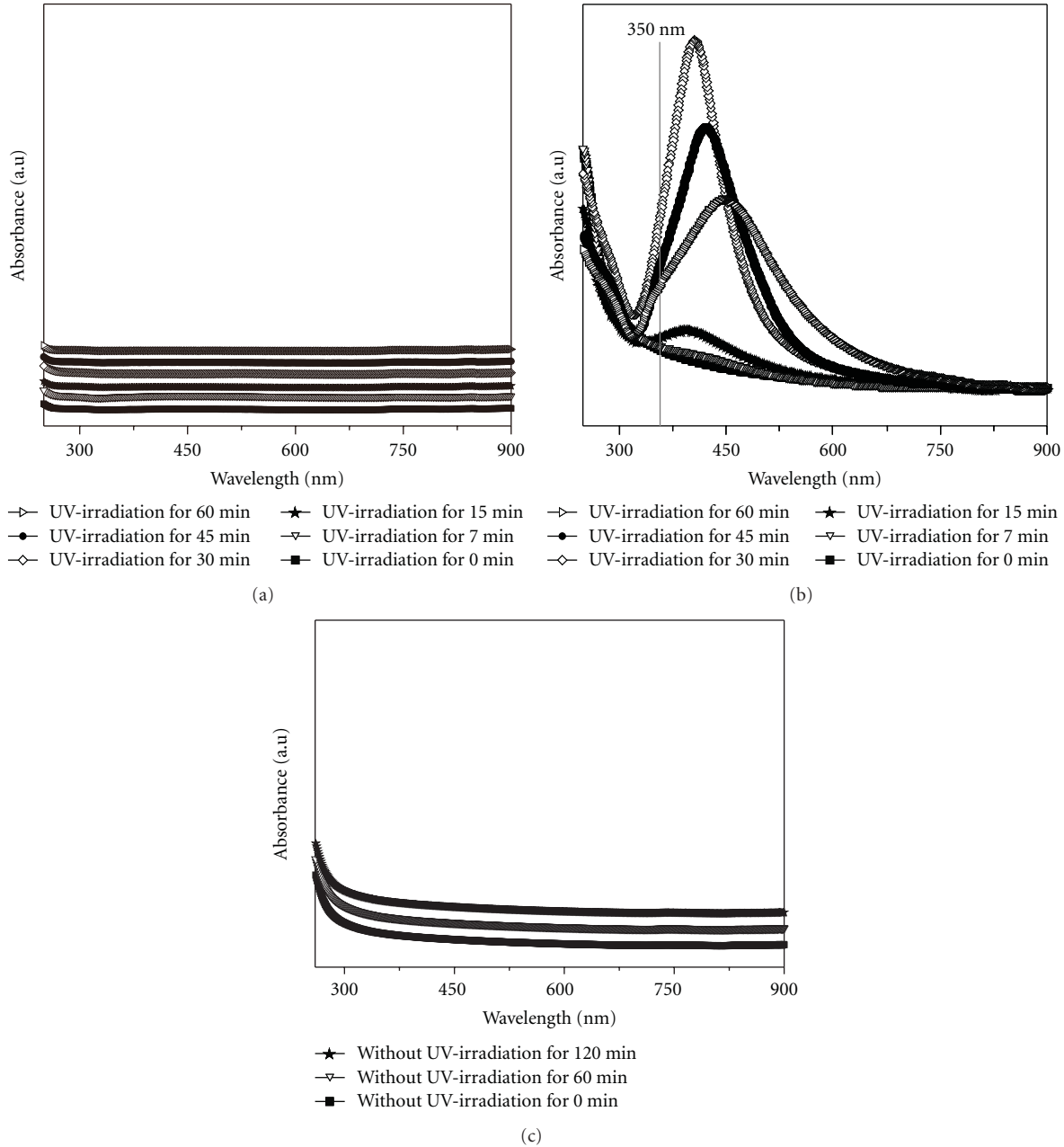


FIGURE 1: UV-visible absorption spectra of the synthesized solutions: (a) without Pt seeds, (b) with Pt seeds, and (c) with Pt seeds and without UV irradiation.

extra absorption peak around 350 nm. In this experiment, the main photoproduct is a mixture of Ag nanoparticles until for 45 min of UV irradiation, however, after 60 min, additional photoproduct is achieved in an anisotropic growth for the Ag nanorods/nanowires as shown in Figure 2(b).

XRD spectra of the product UV irradiated for 60 min and the standard powder pattern of Ag (Joint Committee on Powder Diffraction Standards (JCPDS) File 04-0783) are shown in Figure 3. All the peaks are indexed with a face-centered cubic (fcc) single crystal, which indicates that the products were Ag, with good purity. The average crystallite size of the product UV irradiated for 60 min was calculated

from the XRD line broadening using the Scherrer equation [17]:

$$B = \frac{0.93\lambda}{(L \cos \theta)}, \quad (1)$$

where  $\lambda$  is the wavelength of the incident X-rays ( $\lambda = 1.54178 \text{ \AA}$ ),  $L$  is the full width at half maximum of the (111) diffraction, and  $\theta$  is the angle of diffraction. The average crystallite size of the product UV irradiated for 60 min was 78.9 nm, which is relatively close to the average diameter (95 nm) of the Ag nanostructures as shown in the SEM image.

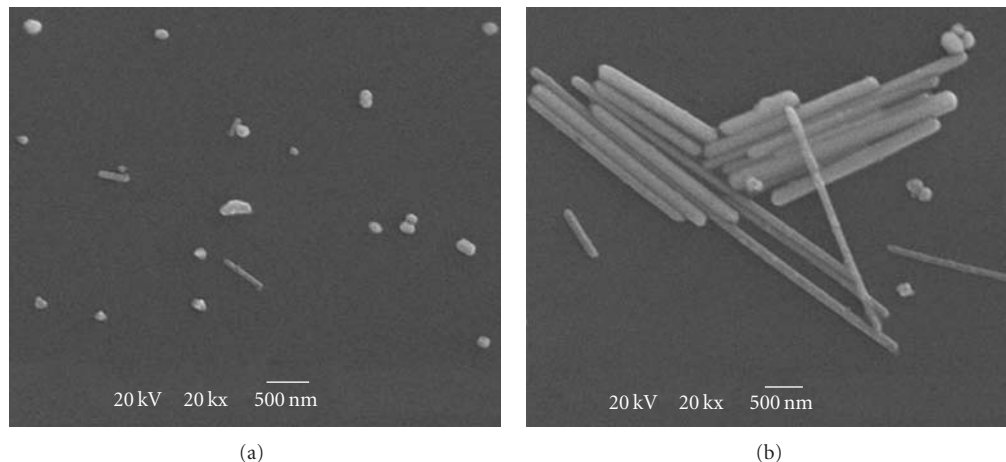


FIGURE 2: SEM micrographs of as-synthesized samples of Ag nanostructures after UV exposure for (a) 45 and (b) 60 min.

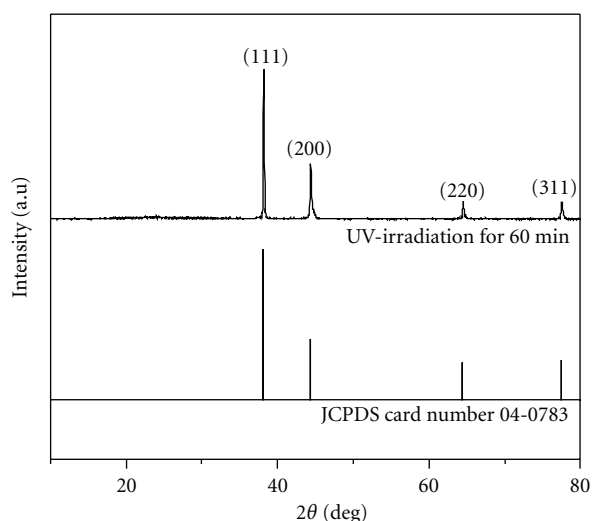
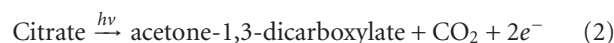


FIGURE 3: XRD spectra of Ag nanostructures irradiated by UV for 60 min and simulated results of Ag powder from JCPDS 04-0783.

Figure 4(a) exhibits a low-magnification TEM image of a Ag nanorod with a diameter of about 100 nm. Furthermore, selected area electron diffraction (SAED) was used to confirm the high crystallinity of the synthesized Ag nanorods. Figure 4(b) shows the typical SAED pattern of a Ag nanorod, which was obtained by focusing the electronic beam along the [011] zone axis of an individual nanorod. Judging from the results of Figures 4(b) and 4(c), the synthesized Ag nanorods have predominantly grown along the [100] direction. From the high-resolution TEM (HRTEM) image shown in Figure 4(d), the values of the interplanar spacing of {200} and {111} planes were 0.205 and 0.231 nm, respectively, in good agreement with the lattice spacing of fcc Ag. This result revealed that the Ag nanostructures formed by photochemical reduction at room temperature were single-crystalline with a well-resolved interference fringe spacing. It can be recalled from the results of UV-Visible spectra, a

red-shift of the wavelength at maximum absorption can be inferred due to either the increment of aspect ratio of Ag nanostructures or uniform growth of Ag particles. Analysis of SEM and TEM micrographs indicates that the product UV irradiated for 45 min contains mainly spherically shaped Ag nanoparticles/nanorods, and the product UV irradiated for 60 min consists of Ag nanoparticle, nanorods and nanowires. A red shift of the wavelength at  $\lambda_{\max}$  would be mainly due to the increment of aspect ratio of Ag nanostructures. Also, as indicated in the UV-visible spectra in Figure 1(a), Ag nanostructures were not formed in the solution without citrate-capped Pt nanoparticle seeds. Therefore, the citrate-capped Pt nanoparticle seed played a crucial role as a catalyst for the formation of Ag nanostructures.

The mechanism for the formation of Ag nanostructures by a photochemical reduction in the presence of Pt seeds has not yet been reported; based on our experimental data, we propose a mechanism here. Munro et al. [18] reported a mechanism for the reduction of  $\text{Ag}^+$  by citrate through a thermal approach. In their paper, a model was proposed for the interaction and orientation of citrate ions on the surface of Ag nanoparticles. Redmond et al. [19] reported a mechanism for the reduction of  $\text{Ag}^+$  by citrate through a photochemical approach. In both of above-mentioned mechanisms, heating [18], or photon excitation [19], results in the donation of electrons from citrate ions to Ag nanoparticle seeds, leading to both the formation of Ag nanoparticles with extra electrons and the decomposition of citrate ions. The Ag nanoparticles with extra electrons then become the reducing source for  $\text{Ag}^+$ . The decomposition of citrate ions in the photochemical approach has been described through the following reaction [19, 20].



In order to confirm the decomposition of citrate on Pt nanoparticle seeds, solutions containing only citrate-capped

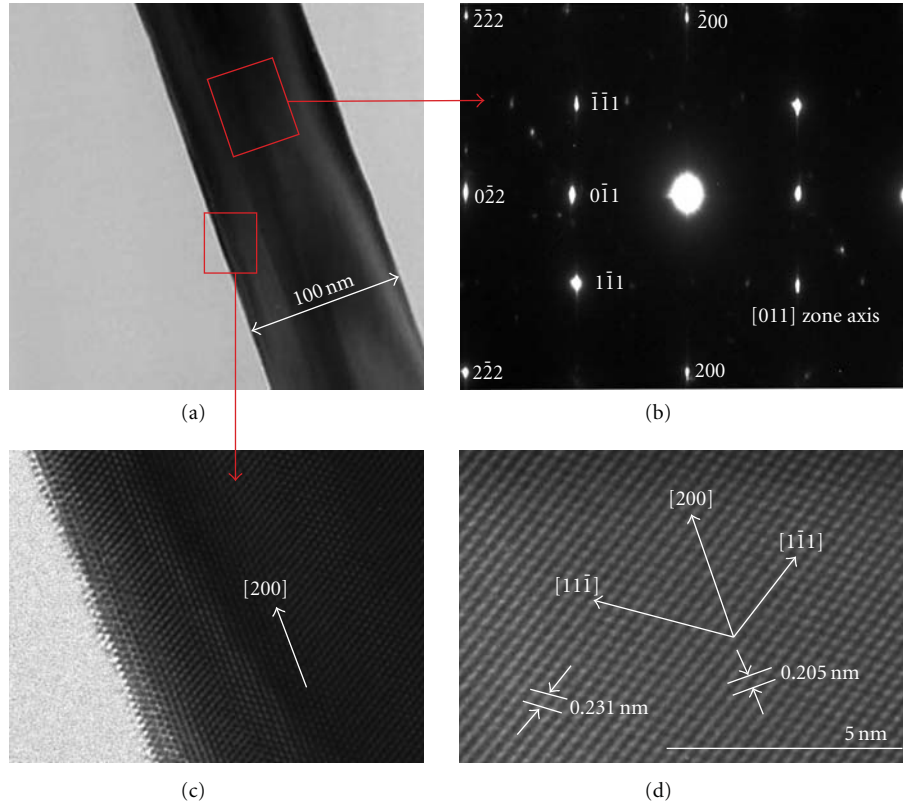
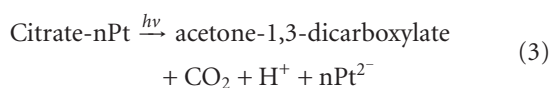


FIGURE 4: (a) Low magnification, (b) electron diffraction pattern, and (c, d) high-magnification TEM micrographs of a Ag nanorod synthesized by UV exposure for 60 min.

Pt nanoparticles were irradiated by UV light at various exposure times. At UV exposure times of 0, 15, 30, 45, and 60 min, the average particle sizes were obtained by using PSA as 4.23, 21.13, 21.67, 36.43, and 76.83 nm, respectively. This result means that the citrate on Pt nanoparticle seeds decomposed during photochemical reduction. As a result, the average particle size of Pt nanoparticle seeds increased with increasing UV exposure time.

As shown in (2), acetone-1,3-dicarboxylate, carbon dioxide, and electrons are formed due to the photochemical excitation of citrate. Nucleophilic adsorption of the carboxylic anions causes the citrate to bind onto the surface of Ag nanoparticles. Upon absorption of a photon, the carboxylic groups directly attached to Ag nanoparticles presumably undergo ligand to metal charge transfer, where the electrons directly transfer to the Ag nanoparticles [19, 20]. These Ag nanoparticles, acting as a reactive electron storage and transfer medium, make it more likely to reduce  $\text{Ag}^+$  on their surface [20].

In our case, the Pt nanoparticle seeds are believed to play a role similar to that of the Ag nanoparticle seeds used in the above reports. Therefore, we propose the following equation to describe the photochemical reaction of citrate in the presence of Pt nanoparticle seeds as shown in Figure 5.

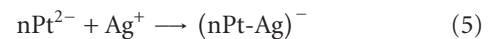


Upon the absorption of a photon, the adsorbed citrate undergoes a ligand to metal charge transfer, resulting in a citrate radical and a Pt seed with an extra electron. The unstable citrate radical undergoes further photochemical and thermal decomposition, leading to the formation of an acetone-1,3-dicarboxylate, a  $\text{CO}_2$ , and a  $\text{H}^\bullet$  radical. The  $\text{H}^\bullet$  radical is in close proximity to the Pt seed and will very likely encounter the Pt seed, resulting in the release of an electron to the Pt seed and the formation of an  $\text{H}^+$ . The resultant Pt seed with extra electrons,  $\text{nPt}^{2-}$ , can now reduce the  $\text{Ag}^+$  it encounters. It has been proposed [21, 22] that  $\text{H}_2\text{O}$  could also be decomposed by UV irradiation as shown below.



The reactive  $\text{H}^\bullet$  and  $\text{OH}^\bullet$  radicals can be the reducing source for  $\text{Ag}^+$  as well. However, we believe (4) is not dominant in our case.

For a  $\text{Ag}^+$  ion, electron capture happens when the ion encounters a seed with extra electrons.  $\text{Ag}^+$  ions can encounter the Pt nanoparticle seeds as shown below.



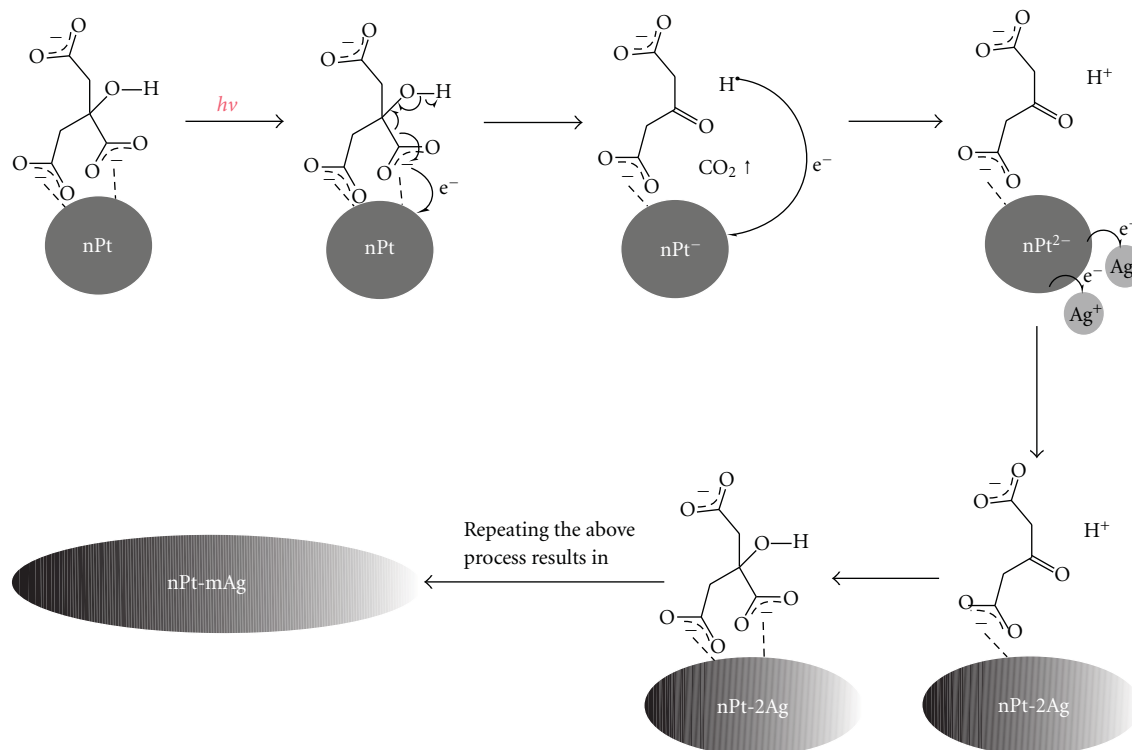


FIGURE 5: A plausible mechanism for the synthesis of Ag nanostructures formed by a photochemical reduction.

The process described by (3), (5), and (6) repeats continuously during UV irradiation, resulting in the growth of Ag on the Pt seeds, nPt-mAg in Figure 5. Although further evidence needs to be obtained, we suggest the following process for the formation of Ag nanowires. During the growth of Ag nanostructures, once the reduced Ag atoms bind to the surface of a Pt seed, the Pt seed becomes a particle partially coated with Ag. Due to the fact that Pt has a much higher work function than Ag, the coated Ag on Pt seed is more reducing than the Pt seed [23]. This means that  $Ag^+$  ions are more likely to be reduced at the coated Ag on the polar particle. Also, due to the assistance of rod-like PVP micelles [24], Ag nanostructure growth in one direction becomes possible.

#### 4. Conclusion

A simple approach to the synthesis of Ag nanostructures such as nanorods and nanowires by a photochemical reduction at room temperature was demonstrated. Citrate-capped Pt nanoparticle seeds played a crucial role as a catalyst for the growth of Ag nanostructures. From the results of UV-visible spectra, photographs of the synthesized solution, SEM and TEM images, we can deduce the synthesis of single-crystalline Ag nanorods and nanowires by a photochemical reduction at room temperature. These experiments helped to outline the mechanism of Ag nanostructure formation using citrate-capped Pt nanoparticle seeds prepared by photochemical reduction. Our Ag nanostructures are anticipated to have important applications in electronics such as the

miniaturization of electronic devices and the improvement of ultralarge-scale integrated circuits.

#### Acknowledgments

This paper was supported by Nano R&D program through the National Research Foundation of Korea funded by the Ministry of Education, Science and Technology (2009-0082604). The experiments at the PLS were supported in part by the MOST and the POSTECH.

#### References

- [1] A. P. Alivisatos, "Semiconductor clusters, nanocrystals, and quantum dots," *Science*, vol. 271, no. 5251, pp. 933–937, 1996.
- [2] Y. Sun, B. Gates, B. Mayers, and Y. Xia, "Crystalline silver nanowires by soft solution processing," *Nano Letters*, vol. 2, no. 2, pp. 165–168, 2002.
- [3] X. Hu and C. T. Chan, "Photonic crystals with silver nanowires as a near-infrared superlens," *Applied Physics Letters*, vol. 85, no. 9, pp. 1520–1522, 2004.
- [4] Y. T. Pang, G. W. Meng, Q. Fang, and L. D. Zhang, "Silver nanowire array infrared polarizers," *Nanotechnology*, vol. 14, no. 1, pp. 20–24, 2003.
- [5] R. J. Chimentão, I. Kirm, F. Medina et al., "Different morphologies of silver nanoparticles as catalysts for the selective oxidation of styrene in the gas phase," *Chemical Communications*, vol. 10, no. 7, pp. 846–847, 2004.
- [6] Y. Gao, P. Jiang, D. F. Liu et al., "Synthesis, characterization and self-assembly of silver nanowires," *Chemical Physics Letters*, vol. 380, no. 1-2, pp. 146–149, 2003.

- [7] M. Tsuji, Y. Nishizawa, M. Hashimoto, and T. Tsuji, "Syntheses of silver nanofilms, nanorods, and nanowires by a microwave-polyol method in the presence of Pt seeds and polyvinylpyrrolidone," *Chemistry Letters*, vol. 33, no. 4, pp. 370–371, 2004.
- [8] K. Esumi, T. Matsumoto, Y. Seto, and T. Yoshimura, "Preparation of gold-, gold/silver-dendrimer nanocomposites in the presence of benzoin in ethanol by UV irradiation," *Journal of Colloid and Interface Science*, vol. 284, no. 1, pp. 199–203, 2005.
- [9] R.-L. Zong, J. Zhou, Q. Li et al., "Synthesis and optical properties of silver nanowire arrays embedded in anodic alumina membrane," *Journal of Physical Chemistry B*, vol. 108, no. 43, pp. 16713–16716, 2004.
- [10] Z. Yu, Z. Yang, S. Wang et al., "Growth of GaN nanorods via Au catalyst-assisted CVD," *Chemical Vapor Deposition*, vol. 11, no. 10, pp. 433–436, 2005.
- [11] Y. Gao, P. Jiang, L. Song et al., "Growth mechanism of silver nanowires synthesized by polyvinylpyrrolidone-assisted polyol reduction," *Journal of Physics D*, vol. 38, no. 7, pp. 1061–1067, 2005.
- [12] D. Poondi and J. Singh, "Synthesis of metastable silver-nickel alloys by a novel laser-liquid-solid interaction technique," *Journal of Materials Science*, vol. 35, no. 10, pp. 2467–2476, 2000.
- [13] C.-S. Hong, H.-H. Park, S.-J. Wang, J. Moon, H.-H. Park, and R. H. Hill, "Formation of photoresist-free patterned ZnO film containing nano-sized Ag by photochemical solution deposition," *Applied Surface Science*, vol. 252, no. 21, pp. 7739–7742, 2006.
- [14] C. J. Murphy and N. R. Jana, "Controlling the aspect ratio of inorganic nanorods and nanowires," *Advanced Materials*, vol. 14, no. 1, pp. 80–82, 2002.
- [15] D. Zhang, L. Qi, J. Yang, J. Ma, H. Cheng, and L. Huang, "Wet chemical synthesis of silver nanowire thin films at ambient temperature," *Chemistry of Materials*, vol. 16, no. 5, pp. 872–876, 2004.
- [16] Y. Sun, Y. Yin, B. T. Mayers, T. Herricks, and Y. Xia, "Uniform silver nanowires synthesis by reducing  $\text{AgNO}_3$  with ethylene glycol in the presence of seeds and poly(vinyl pyrrolidone)," *Chemistry of Materials*, vol. 14, no. 11, pp. 4736–4745, 2002.
- [17] A. L. Patterson, "The scherrer formula for X-ray particle size determination," *Physical Review*, vol. 56, no. 10, pp. 978–982, 1939.
- [18] C. H. Munro, W. E. Smith, M. Garner, J. Clarkson, and P. C. White, "Characterization of the surface of a citrate-reduced colloid optimized for use as a substrate for surface-enhanced resonance raman scattering," *Langmuir*, vol. 11, no. 10, pp. 3712–3720, 1995.
- [19] P. L. Redmond, X. Wu, and L. Brus, "Photovoltage and photocatalyzed growth in citrate-stabilized colloidal silver nanocrystals," *Journal of Physical Chemistry C*, vol. 111, no. 25, pp. 8942–8947, 2007.
- [20] M. Maillard, P. Huang, and L. Brus, "Silver nanodisk growth by surface plasmon enhanced photoreduction of adsorbed  $[\text{Ag}^+]$ ," *Nano Letters*, vol. 3, no. 11, pp. 1611–1615, 2003.
- [21] K. Mallick, M. J. Witcomb, and M. S. Scurrall, "Polymer stabilized silver nanoparticles: a photochemical synthesis route," *Journal of Materials Science*, vol. 39, no. 14, pp. 4459–4463, 2004.
- [22] Y. Zhou, L. Hao, Y. Hu, Y. Zhu, and Z. Chen, "Synthesis of nanowires and coral-shaped nanostructures of Ag by an ultraviolet photo-reduction technique at room temperature," *Chemistry Letters*, no. 11, pp. 1192–1193, 2001.
- [23] B. Pellegrini, "Properties of silicon-metal contacts versus metal work-function, silicon impurity concentration and bias voltage," *Journal of Physics D*, vol. 9, no. 1, pp. 55–68, 1976.
- [24] D. Chen and L. Gao, "Large-scale growth and end-to-end assembly of silver nanorods by PVP-directed polyol process," *Journal of Crystal Growth*, vol. 264, no. 1–3, pp. 216–222, 2004.

## Research Article

# Core-Shell Nanostructure of $\alpha$ -Fe<sub>2</sub>O<sub>3</sub>/Fe<sub>3</sub>O<sub>4</sub>: Synthesis and Photocatalysis for Methyl Orange

Yang Tian,<sup>1</sup> Di Wu,<sup>1</sup> Xiao Jia,<sup>2</sup> Binbin Yu,<sup>1</sup> and Sihui Zhan<sup>3</sup>

<sup>1</sup>Department of Chemistry, Capital Normal University, Beijing 100048, China

<sup>2</sup>Institute of Functional Materials, College of Chemistry and Chemical Engineering, Fuzhou University, Fujian 350002, China

<sup>3</sup>College of Environmental Science and Engineering, Nankai University, Tianjin 300071, China

Correspondence should be addressed to Yang Tian, tianyang@mail.sdu.edu.cn

Received 9 April 2010; Accepted 1 June 2010

Academic Editor: William W. Yu

Copyright © 2011 Yang Tian et al. This is an open access article distributed under the Creative Commons Attribution License, which permits unrestricted use, distribution, and reproduction in any medium, provided the original work is properly cited.

Fe<sub>3</sub>O<sub>4</sub> nanoparticle was synthesized in the solution involving water and ethanol. Then,  $\alpha$ -Fe<sub>2</sub>O<sub>3</sub> shell was produced in situ on the surface of the Fe<sub>3</sub>O<sub>4</sub> nanoparticle by surface oxidation in molten salts, forming  $\alpha$ -Fe<sub>2</sub>O<sub>3</sub>/Fe<sub>3</sub>O<sub>4</sub> core-shell nanostructure. It was showed that the magnetic properties transformed from ferromagnetism to superparamagnetism after the primary Fe<sub>3</sub>O<sub>4</sub> nanoparticles were oxidized. Furthermore, the obtained  $\alpha$ -Fe<sub>2</sub>O<sub>3</sub>/Fe<sub>3</sub>O<sub>4</sub> core-shell nanoparticles were used to photocatalyse solution of methyl orange, and the results revealed that  $\alpha$ -Fe<sub>2</sub>O<sub>3</sub>/Fe<sub>3</sub>O<sub>4</sub> nanoparticles were more efficient than the self-prepared  $\alpha$ -Fe<sub>2</sub>O<sub>3</sub> nanoparticles. At the same time, the photocatalyzer was recyclable by applying an appropriate magnetic field.

## 1. Introduction

Owing to their tunable properties and large surface-to-volume ratios, nanocrystals (NCs) are being considered for a wide range of applications including photovoltaics, biomedical imaging, photocatalysts, and optoelectronics [1–4]. Nanocrystal heterostructures (NCHs) are an emerging subclass of NCs where two or more chemically distinct components are brought together epitaxially [5]. The best known example is the core/shell structure where the outer shell enhances the properties of the core (e.g., increasing photoluminescence quantum yields of CdSe NCs with ZnS or CdS shell [6, 7]). These core-shell nanostructures expand single-component nanoparticles to hybrid nanostructures with discrete domains of different materials arranged in a controlled fashion. Thus, different functionalities can be integrated, with the dimension and material parameters of the individual components optimized independently even providing entirely novel properties via the coupling between different components. In view of the scientific importance of these materials, it is not surprising that a wide variety of approaches for their synthesis have been reported [8–13]. Specifically, the surface oxidation method has attracted much

attention because it could be utilized as a simplistic route to obtain core/shell nanostructures [11, 12].

Magnetic separation provides a convenient method for removing and recycling magnetized species by applying an appropriate magnetic field. So, magnetic nanoparticles combining with catalysts could not only increase the durability of the catalysts but also help to separate and recycle the catalyst particles. For example, magnetic nanoparticles have been immobilized in a mesoporous silica shell with molybdenum oxide forming a magnetically recyclable epoxidation catalyst [14]. A core-shell structure of TiO<sub>2</sub>/BaFe<sub>12</sub>O<sub>19</sub> composite nanoparticle that can photodegrade organic pollutants in the dispersion system effectively and can be recycled easily by a magnetic field was also reported [15]. Another magnetically separable photocatalyst TiO<sub>2</sub>/SiO<sub>2</sub>/NiFe<sub>2</sub>O<sub>4</sub> (TSN) nanosphere with egg-like structure was prepared by Xu et al. [16]. However, there are few reports on the magnetic nanoparticles integrating with lower cost photocatalysis,  $\alpha$ -Fe<sub>2</sub>O<sub>3</sub> for the photodegradation [17–19]. Here, we fabricated  $\alpha$ -Fe<sub>2</sub>O<sub>3</sub>/Fe<sub>3</sub>O<sub>4</sub> core-shell nanostructures by a surface oxidation method on the surface of primary Fe<sub>3</sub>O<sub>4</sub> nanoparticles in molten salts, which showed high efficiency and good recycling for photocatalysis of methyl orange (MO).

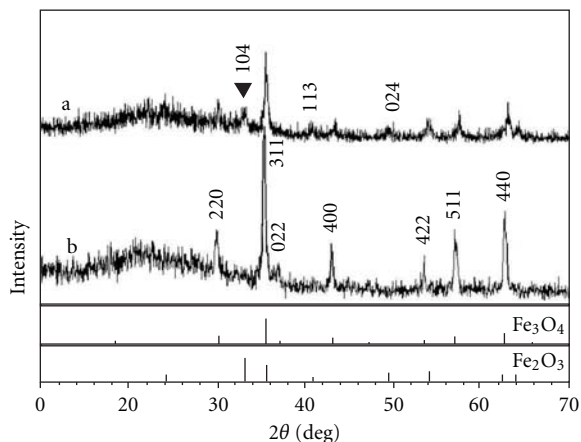


FIGURE 1: XRD patterns of the obtained  $\alpha\text{-Fe}_2\text{O}_3/\text{Fe}_3\text{O}_4$  (a) and  $\text{Fe}_3\text{O}_4$  (b).

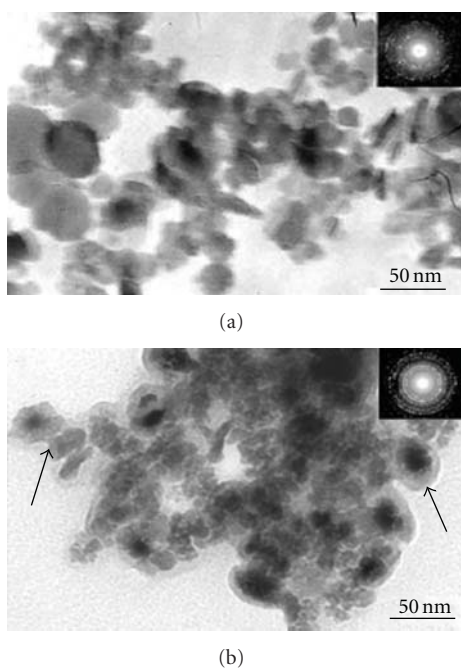


FIGURE 2: TEM image of the obtained primary  $\text{Fe}_3\text{O}_4$  nanoparticles (a) and  $\alpha\text{-Fe}_2\text{O}_3/\text{Fe}_3\text{O}_4$  nanoparticles (b), the insets are SAED patterns of them, respectively.

## 2. Experiments

**2.1. Synthesis of Primary  $\text{Fe}_3\text{O}_4$  Nanoparticles.** All the chemicals were analytically pure and used without purifying further. In a 250 mL three-neck flask, sodium nitrate (0.5 g, Shanghai Chemical Reagent) and ferrous (II) sulfate (1.6 g, Shanghai Chemical Reagent) were dissolved in a mixture solution of distilled water (30 mL) and absolute ethanol (30 mL, Shanghai Chemical Reagent) under a vacuum surround. On the other hand, sodium hydroxide (1 g, Tianjin Chemical Reagent) was dissolved in 10 mL distilled water and then was injected into the three-neck flask by an injector under magnetic stirring. The reaction lasted for about 10

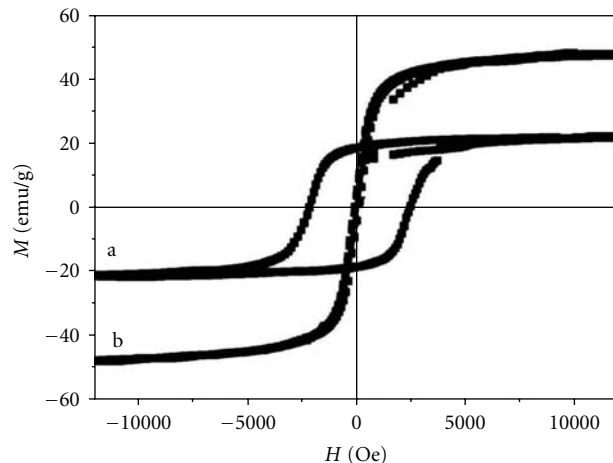


FIGURE 3: Magnetic hysteresis loops for the  $\text{Fe}_3\text{O}_4$  nanoparticles (a) and  $\alpha\text{-Fe}_2\text{O}_3/\text{Fe}_3\text{O}_4$  (b)

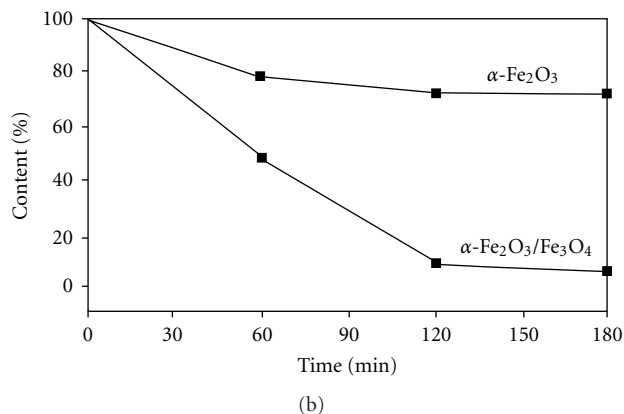
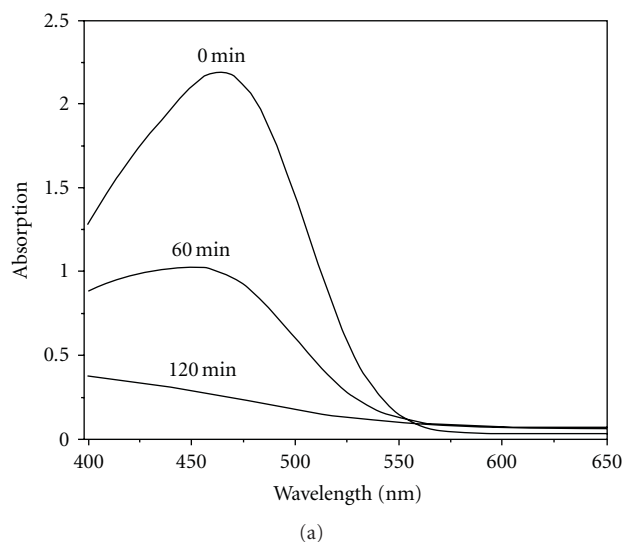


FIGURE 4: Absorption spectra (a) of the MO solution for 0 min, 60 min and 120 min, and photocatalysis performance (b) of the core-shell sample and  $\alpha\text{-Fe}_2\text{O}_3$  sample.

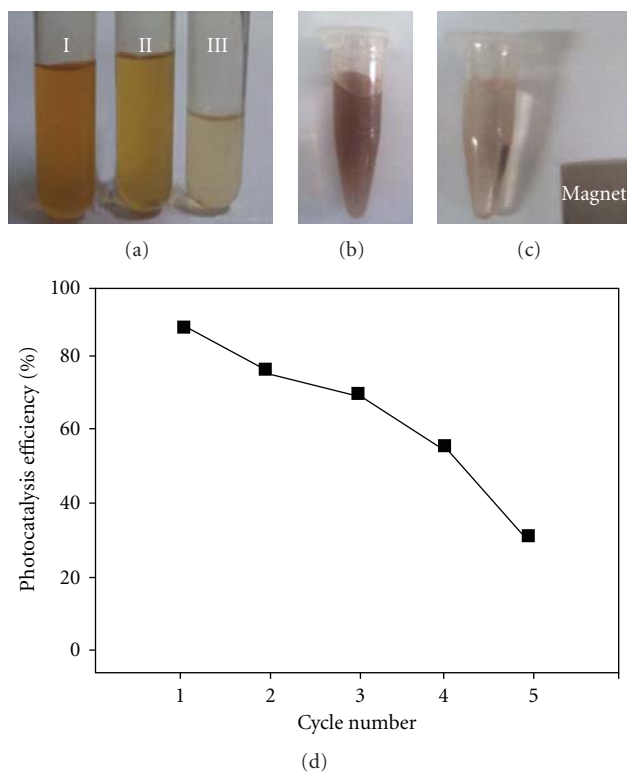


FIGURE 5: Optical image (a) of the MO solution after photocatalysis lasted 0 min, 60 min, and 120 min (b) and (c) are the optical images of the catalyst being separated by a magnet; (d) is efficiency curve for multiple cycles of photocatalysis.

minutes in a vacuum surround under strong stirring until the white precipitate became black. The obtained black precipitate was collected by centrifugation separating and then was washed with distilled water for 4 times. Finally the precipitate was dried at 80°C for 12 hours to obtain the Fe<sub>3</sub>O<sub>4</sub> nanoparticles.

**2.2. Synthesis of  $\alpha$ -Fe<sub>2</sub>O<sub>3</sub>/Fe<sub>3</sub>O<sub>4</sub>.** Sodium nitrate (4.2 g) and potassium nitrate (2.5 g) were mixed in a crucible (30 mL) and heated up to 310°C to melt. The obtained Fe<sub>3</sub>O<sub>4</sub> nanoparticles were put into the crucible to react for 30 minutes, and then the molten salt was cooled to room temperature. The product was obtained by washing the fusion with deionized water to remove the nitrates and filtration for three times. Finally, the precipitate was dried at 80°C for 12 hours to obtain the  $\alpha$ -Fe<sub>2</sub>O<sub>3</sub>/Fe<sub>3</sub>O<sub>4</sub> nanoparticles.

**2.3. Measurement of Photocatalytic Activity.** The evaluation of photocatalytic activity for the prepared samples decolorizing MO aqueous solution was performed at ambient temperature. The obtained  $\alpha$ -Fe<sub>2</sub>O<sub>3</sub>/Fe<sub>3</sub>O<sub>4</sub> core-shell catalyst (0.02 g) was placed into a tubular quartz reactor of 100 mL 20 mg/L MO aqueous solution. The reactor was surrounded with a UV lamp (125 W) with stirring. After the reaction began, the mixture was sampled at different times and separated by a magnet to discard any sediment. Then,

absorption spectra were obtained through a wavelength scan on a UV-Vis spectrophotometer.

**2.4. Characterization.** The X-ray diffraction (XRD) patterns of the samples were collected using a diffractometer (Rigaku D/Max 2200PC) with CuK $\alpha$  radiation ( $\lambda = 1.5418 \text{ \AA}$ ) and graphite monochromator from 10 to 80° at a scanning rate 5.0°/min. Unit cell dimensions were determined in the JADE 5 program for X-ray diffraction pattern processing, identification, and quantification. The size and morphology of the products were characterized by transmission electron microscopy (TEM, JEM100-CXII) with the potential of performing selected-area electron diffraction (SAED). Magnetometry measurements were taken with a Quantum Design PPMS SQUID magnetometer. The absorption spectra of MO solution were obtained by a UV-vis spectrophotometer (Shimadzu UV-vis 2550).

### 3. Results and Discussion

To form  $\alpha$ -Fe<sub>2</sub>O<sub>3</sub>/Fe<sub>3</sub>O<sub>4</sub> core-shell nanostructure, the appropriate reaction conditions were explored in our work as shown in Table 1. It reveals that when the primary Fe<sub>3</sub>O<sub>4</sub> nanoparticles were obtained in water without ethanol, they were difficultly oxidized into  $\alpha$ -Fe<sub>2</sub>O<sub>3</sub> even in molten salts of 380°C for 30 min; however, when the primary Fe<sub>3</sub>O<sub>4</sub> nanoparticles were obtained in 20 mL H<sub>2</sub>O and 40 mL ethanol (the content of ethanol was 2/3), they were oxidized into  $\alpha$ -Fe<sub>2</sub>O<sub>3</sub> completely without Fe<sub>3</sub>O<sub>4</sub> leaving even in 310°C for only 10 min (Figure S1(a) in Supplementary Material available online at doi: 10.1155/2011/837123). When the primary Fe<sub>3</sub>O<sub>4</sub> nanoparticles were obtained in 30 mL H<sub>2</sub>O and 30 mL ethanol (the content of ethanol was 1/2), they could be oxidized partially forming  $\alpha$ -Fe<sub>2</sub>O<sub>3</sub>/Fe<sub>3</sub>O<sub>4</sub> core-shell nanostructure in 310°C for 30 min (Figure 1(a)) but oxidized completely in 380°C for only 10 min (Figure S1(b) in Supplementary Material available online at doi: 10.1155/2011/837123). So, increasing the content of ethanol in the solution for preparing Fe<sub>3</sub>O<sub>4</sub> nanoparticles is beneficial to subsequent oxidation reaction of Fe<sub>3</sub>O<sub>4</sub> to form  $\alpha$ -Fe<sub>2</sub>O<sub>3</sub>/Fe<sub>3</sub>O<sub>4</sub> core-shell nanostructure. However, excess ethanol over 1/2 content would result in complete and rapid oxidization of Fe<sub>3</sub>O<sub>4</sub> nanoparticles in our molten salts, which went against forming core-shell structure. This phenomenon could be explained from XRD patterns of the prepared Fe<sub>3</sub>O<sub>4</sub> (Figure S2 and Figure 1(b)) which show that the crystallization grew lower as the content of ethanol was enhanced. It is obvious that the crystallized Fe<sub>3</sub>O<sub>4</sub> well is more stable and difficult to oxidize into  $\alpha$ -Fe<sub>2</sub>O<sub>3</sub>.

To characterize phase and crystallization of the products, powder X-ray diffraction (XRD) was performed from the obtained  $\alpha$ -Fe<sub>2</sub>O<sub>3</sub>/Fe<sub>3</sub>O<sub>4</sub> and Fe<sub>3</sub>O<sub>4</sub> samples. The XRD pattern for Fe<sub>3</sub>O<sub>4</sub> nanoparticles (Figure 1(b)) shows that all the peaks are in good agreement with the cubic structure [space group: *Fd-3m*] known from Fe<sub>3</sub>O<sub>4</sub> crystal (JCPDS Card 65-3107), meaning its high crystallization and few impurities. The crystal cell dimension of the sample is calculated to be  $a = 0.8396 \text{ nm}$  by Jade 5, which is accorded with the

TABLE 1: Different samples obtained from adjusting reaction conditions: different molar ratios of H<sub>2</sub>O and EtOH, oxidation temperature, and oxidation time.

Sample	H <sub>2</sub> O/mL	EtOH/mL	Primary product	Oxidation Temp./°C	Oxidation Time/min	Oxidation product
S1	60	0	Fe <sub>3</sub> O <sub>4</sub>	380	30	Fe <sub>3</sub> O <sub>4</sub>
S2	30	30	Fe <sub>3</sub> O <sub>4</sub>	380	10	$\alpha$ -Fe <sub>2</sub> O <sub>3</sub>
S3	30	30	Fe <sub>3</sub> O <sub>4</sub>	310	30	$\alpha$ -Fe <sub>2</sub> O <sub>3</sub> /Fe <sub>3</sub> O <sub>4</sub>
S4	20	40	Fe <sub>3</sub> O <sub>4</sub>	310	10	$\alpha$ -Fe <sub>2</sub> O <sub>3</sub>

value given in the JCPDS Card 65-3107 file for Fe<sub>3</sub>O<sub>4</sub> ( $a = 0.8391$  nm). Furthermore, according to the full width at half maximum (FWHM) of (121) reflections, the average size of the crystalline particles for the primary Fe<sub>3</sub>O<sub>4</sub> is calculated to be 30.7 nm based on the Debye-Scherrer formula. Figure 1(a) is the XRD pattern for the  $\alpha$ -Fe<sub>2</sub>O<sub>3</sub>/Fe<sub>3</sub>O<sub>4</sub> obtained from surface oxidation of Fe<sub>3</sub>O<sub>4</sub> in molten salt. It reveals that these nanoparticles were composed of cubic-structured Fe<sub>3</sub>O<sub>4</sub> and  $\alpha$ -Fe<sub>2</sub>O<sub>3</sub> (JCPDS No. 04-0784).

Figure 2(a) shows the representative TEM image of the obtained Fe<sub>3</sub>O<sub>4</sub> nanoparticles. It shows that the sizes of nanocrystals are about 20–50 nm but not uniform, which is roughly closed to the average size resulted from the Debye-Scherrer formula. The inset of Figure 2(a) is corresponding SAED pattern, exhibiting the high crystalline nature of cubic-phase Fe<sub>3</sub>O<sub>4</sub>. Figure 2(b) is TEM image of the  $\alpha$ -Fe<sub>2</sub>O<sub>3</sub>/Fe<sub>3</sub>O<sub>4</sub>, which shows clear core-shell nanostructure for the sample. Furthermore, it shows the size of Fe<sub>3</sub>O<sub>4</sub> core decrease to be about 15–30 nm.

The magnetic properties of the as-prepared  $\alpha$ -Fe<sub>2</sub>O<sub>3</sub>/Fe<sub>3</sub>O<sub>4</sub> and Fe<sub>3</sub>O<sub>4</sub> nanoparticles were investigated with a Quantum magnetometer at room temperature. The magnetic hysteresis loop (curve a in Figure 3) for the Fe<sub>3</sub>O<sub>4</sub> nanoparticles indicates their ferromagnetism at room temperature. The coercivity (H<sub>c</sub>) is shown to be about 2330 Oe, the saturation magnetization (M<sub>s</sub>) is 22.6 emu/g, and the remnant magnetization (M<sub>r</sub>) is 18.9 emu/g. However, the hysteresis loop of the obtained  $\alpha$ -Fe<sub>2</sub>O<sub>3</sub>/Fe<sub>3</sub>O<sub>4</sub> nanostructure shows near superparamagnetism at room temperature, which is different from the primary Fe<sub>3</sub>O<sub>4</sub> nanoparticles distinctly. It is well known that the surface spin disorder enhancing caused by the decreasing of particles size [20] and the coercivity would approach zero under a short thermal fluctuation (so-called super paramagnetism) if the crystal size is small enough. Thus, the transformation from ferromagnetism to superparamagnetism indicates the average size decrease when the primary Fe<sub>3</sub>O<sub>4</sub> nanoparticles became into the Fe<sub>3</sub>O<sub>4</sub> cores of  $\alpha$ -Fe<sub>2</sub>O<sub>3</sub>/Fe<sub>3</sub>O<sub>4</sub>, which is accorded with the result of TEM. At the same time, it reveals that the saturation magnetization (M<sub>s</sub>) for Fe<sub>3</sub>O<sub>4</sub> cores of  $\alpha$ -Fe<sub>2</sub>O<sub>3</sub>/Fe<sub>3</sub>O<sub>4</sub> nanoparticles is about 48.7 emu/g, and the remnant magnetization (M<sub>r</sub>) is about 8.6 emu/g.

To evaluate the potential application in water treatment of the obtained  $\alpha$ -Fe<sub>2</sub>O<sub>3</sub>/Fe<sub>3</sub>O<sub>4</sub> complex nanostructure, the photocatalysis capacities for the organic pollutant were investigated. Here, MO was chosen as the model organic pollutant. The initial concentration of the MO solution was set to be 20 mg/L. Figure 4(a) shows the visible absorption

spectra of for MO solution by the degradation of complex nanostructured  $\alpha$ -Fe<sub>2</sub>O<sub>3</sub>/Fe<sub>3</sub>O<sub>4</sub> with different time. The spectra show that the concentration of MO decreased to 54.4% after reacted for 60 min comparing the original concentration, and the maximum removal capacity of the photocatalysis reached about 90.1% in a time period of 120 min. At the same time, additional experiments were made to compare the photocatalysis performance between the core-shell sample (S3 of Table 1) and  $\alpha$ -Fe<sub>2</sub>O<sub>3</sub> sample (S2 of Table 1) at the entirely same photocatalysis conditions. As shown in Figure 4(b), the  $\alpha$ -Fe<sub>2</sub>O<sub>3</sub>/Fe<sub>3</sub>O<sub>4</sub> core-shell nanostructure behaved higher photocatalysis efficiency for MO. The rapid removal of MO may be associated with the electrostatic attraction between the  $\alpha$ -Fe<sub>2</sub>O<sub>3</sub> shell and Fe<sub>3</sub>O<sub>4</sub> core of the complex nanostructure. Under the ultraviolet radiation, electrons in the valence band (VB) of  $\alpha$ -Fe<sub>2</sub>O<sub>3</sub> were excited to its conduction band (CB), with same amount of holes left in VB. Driven by the decreased potential energy band gap of  $\alpha$ -Fe<sub>2</sub>O<sub>3</sub> is  $\sim 2.20$  eV and band gap of Fe<sub>3</sub>O<sub>4</sub> is  $\sim 0.10$  eV), the photogenerated electrons in CB of  $\alpha$ -Fe<sub>2</sub>O<sub>3</sub> tended to transfer to that of Fe<sub>3</sub>O<sub>4</sub>. So, the photogenerated electrons and holes were separated at the  $\alpha$ -Fe<sub>2</sub>O<sub>3</sub>/Fe<sub>3</sub>O<sub>4</sub> interfaces, which reduced their recombination probability, and enhanced the efficiency of generating hydroxyl radicals.

Figure 5(a) is the optical image for the MO solution with different photocatalysis time, which shows the solution became clear gradually from I to III by photocatalysis. Furthermore, the used catalyst of  $\alpha$ -Fe<sub>2</sub>O<sub>3</sub>/Fe<sub>3</sub>O<sub>4</sub> nanostructure could be recycled by a magnet. Figure 5(b) and 5(c) shows the optical image of the catalyst being separated by a magnet. So, the photocatalyst could be recycled by a magnetic field, which would be assistance to the recycle of the photocatalyst. Furthermore, to study the recyclability of the photocatalyzer, experiments in multiple cycles of photocatalysis plus magnetic separation were performed, and it revealed that the photocatalyzer owned good recyclability as shown in Figure 5(d).

## 4. Conclusion

In summary, we fabricated Fe<sub>3</sub>O<sub>4</sub> nanoparticles in a mixture solution of water and ethanol, and then  $\alpha$ -Fe<sub>2</sub>O<sub>3</sub> shell was produced in situ on the surface of the Fe<sub>3</sub>O<sub>4</sub> nanoparticle by surface oxidation to form  $\alpha$ -Fe<sub>2</sub>O<sub>3</sub>/Fe<sub>3</sub>O<sub>4</sub> core-shell nanostructure in molten salts. To remove MO in the water by our  $\alpha$ -Fe<sub>2</sub>O<sub>3</sub>/Fe<sub>3</sub>O<sub>4</sub> core-shell nanostructure showed better photocatalysis property. At the same time, the photocatalyst could be recycled by the magnetic field, which would be

assistance to the recycle of the photocatalyst. These studies not only enrich the contents of core-shell nanostructure chemistry but also are beneficial to investigate their potential application in photocatalysis.

## Acknowledgments

This work is supported by the Beijing Natural Science Foundation (Grant no. 2103048), Natural Science Foundation of China (Grant no. 20907022), and Funding Project for Academic human Resources Development in Institutions of Higher Learning Under the Jurisdiction of Beijing Municipality (PHR20100718).

## References

- [1] P. V. Kamat, "Meeting the clean energy demand: nanostructure architectures for solar energy conversion," *Journal of Physical Chemistry C*, vol. 111, no. 7, pp. 2834–2860, 2007.
- [2] X. Michalet, F. F. Pinaud, L. A. Bentolila et al., "Quantum dots for live cells, in vivo imaging, and diagnostics," *Science*, vol. 307, no. 5709, pp. 538–544, 2005.
- [3] X. Chen and S. S. Mao, "Titanium dioxide nanomaterials: synthesis, properties, modifications and applications," *Chemical Reviews*, vol. 107, no. 7, pp. 2891–2959, 2007.
- [4] J. Zhao, J. A. Bardecker, A. M. Munro et al., "Efficient CdSe/CdS quantum dot light-emitting diodes using a thermally polymerized hole transport layer," *Nano Letters*, vol. 6, no. 3, pp. 463–467, 2006.
- [5] P. D. Cozzoli, T. Pellegrino, and L. Manna, "Synthesis, properties and perspectives of hybrid nanocrystal structures," *Chemical Society Reviews*, vol. 35, no. 11, pp. 1195–1208, 2006.
- [6] B. O. Dabbousi, J. Rodriguez-Viejo, F. V. Mikulec et al., "(CdSe)ZnS core-shell quantum dots: synthesis and characterization of a size series of highly luminescent nanocrystallites," *Journal of Physical Chemistry B*, vol. 101, no. 46, pp. 9463–9475, 1997.
- [7] X. Peng, M. C. Schlamp, A. V. Kadavanich, and A. P. Alivisatos, "Epitaxial growth of highly luminescent CdSe/CdS core/shell nanocrystals with photostability and electronic accessibility," *Journal of the American Chemical Society*, vol. 119, no. 30, pp. 7019–7029, 1997.
- [8] L. Wang, H.-Y. Park, S. I.-I. Lim et al., "Core@shell nanomaterials: gold-coated magnetic oxide nanoparticles," *Journal of Materials Chemistry*, vol. 18, no. 23, pp. 2629–2635, 2008.
- [9] Z. Sun, Z. Yang, J. Zhou et al., "A general approach to the synthesis of gold-metal sulfide core-shell and heterostructures," *Angewandte Chemie*, vol. 48, no. 16, pp. 2881–2885, 2009.
- [10] T. Zhou, M. Lu, Z. Zhang, H. Gong, W. S. Chin, and B. Liu, "Synthesis and characterization of multifunctional FePt/ZnO core/shell nanoparticles," *Advanced Materials*, vol. 21, no. 3, pp. 403–406, 2009.
- [11] A. C. Johnston-Peck, J. Wang, and J. B. Tracy, "Synthesis and structural and magnetic characterization of Ni(Core)/NiO(Shell) nanoparticles," *ACS Nano*, vol. 3, no. 5, pp. 1077–1084, 2009.
- [12] C. Wang, D. R. Baer, J. E. Amonette, M. H. Engelhard, J. Antony, and Y. Qiang, "Morphology and electronic structure of the oxide shell on the surface of iron nanoparticles," *Journal of the American Chemical Society*, vol. 131, no. 25, pp. 8824–8832, 2009.
- [13] S. Sacanna and A. P. Philipse, "A generic single-step synthesis of monodisperse core/shell colloids based on spontaneous pickering emulsification," *Advanced Materials*, vol. 19, no. 22, pp. 3824–3826, 2007.
- [14] M. Shokouhimehr, Y. Piao, J. Kim, Y. Jang, and T. Hyeon, "A magnetically recyclable nanocomposite catalyst for olefin epoxidation," *Angewandte Chemie*, vol. 46, no. 37, pp. 7039–7043, 2007.
- [15] W. Fu, H. Yang, M. Li et al., "Preparation and photocatalytic characteristics of core-shell structure TiO<sub>2</sub>/BaFe<sub>12</sub>O<sub>19</sub> nanoparticles," *Materials Letters*, vol. 60, no. 21–22, pp. 2723–2727, 2006.
- [16] S. Xu, W. Shangguan, J. Yuan, M. Chen, J. Shi, and Z. Jiang, "Synthesis and performance of novel magnetically separable nanospheres of titanium dioxide photocatalyst with egg-like structure," *Nanotechnology*, vol. 19, no. 9, Article ID 095606, 2008.
- [17] S.-W. Cao and Y.-J. Zhu, "Hierarchically nanostructured  $\alpha$ -Fe<sub>2</sub>O<sub>3</sub> hollow spheres: preparation, growth mechanism, photocatalytic property, and application in water treatment," *Journal of Physical Chemistry C*, vol. 112, no. 16, pp. 6253–6257, 2008.
- [18] X.-L. Fang, C. Chen, M.-S. Jin et al., "Single-crystal-like hematite colloidal nanocrystal clusters: synthesis and applications in gas sensors, photocatalysis and water treatment," *Journal of Materials Chemistry*, vol. 19, no. 34, pp. 6154–6160, 2009.
- [19] E. Montiel-Palacios, A. K. Medina-Mendoza, A. Sampieri, C. Angeles-Chávez, I. Hernández-Pérez, and R. Suarez-Parra, "Photo-catalysis of phenol derivatives with Fe<sub>2</sub>O<sub>3</sub> nanoparticles dispersed on SBA-15," *Journal of Ceramic Processing Research*, vol. 10, no. 4, pp. 548–552, 2009.
- [20] Y. Tian, D. Chen, and X. Jiao, "La<sub>1-x</sub>Sr<sub>x</sub>MnO<sub>3</sub> (x = 0, 0.3, 0.5, 0.7) nanoparticles nearly freestanding in water: preparation and magnetic properties," *Chemistry of Materials*, vol. 18, no. 26, pp. 6088–6090, 2006.

## Research Article

# Hydrothermal Synthesis and Characterization of Single-Crystalline $\alpha$ -Fe<sub>2</sub>O<sub>3</sub> Nanocubes

Wenqing Qin,<sup>1,2</sup> Congren Yang,<sup>1,2</sup> Ran Yi,<sup>1,2</sup> and Guanhua Gao<sup>1,2</sup>

<sup>1</sup> School of Minerals Processing and Bioengineering, Central South University, Changsha, Hunan 410083, China

<sup>2</sup> Key Laboratory of Biometallurgy of Ministry of Education, Central South University, Changsha, Hunan 410083, China

Correspondence should be addressed to Wenqing Qin, qinwenqing369@126.com

Received 11 April 2010; Accepted 15 June 2010

Academic Editor: Quanqin Dai

Copyright © 2011 Wenqing Qin et al. This is an open access article distributed under the Creative Commons Attribution License, which permits unrestricted use, distribution, and reproduction in any medium, provided the original work is properly cited.

Single-crystalline  $\alpha$ -Fe<sub>2</sub>O<sub>3</sub> nanocubes were successfully obtained in large quantities through a facile one-step hydrothermal synthetic route under mild conditions. In this synthetic system, aqueous iron (III) nitrate (Fe(NO<sub>3</sub>)<sub>3</sub> · 9H<sub>2</sub>O) served as iron source and triethylamine served as precipitant and alkaline agent. By prolonging reaction time from 1 h to 24 h, the evolution process of  $\alpha$ -Fe<sub>2</sub>O<sub>3</sub>, from nanorhombhedra to nanohexahedron, and finally nanocube, was observed. The products were characterized by Powder X-ray Diffraction (XRD), Scanning Electron Microscopy (SEM), Transmission Electron Microscopy (TEM), High-resolution Transmission Electron Microscopy (HRTEM), Selected-Area Electron Diffraction (SAED), and Fourier Transform Infrared Spectrometry (FTIR). The possible formation mechanism was discussed on basis of the experimental results.

## 1. Introduction

Iron oxides are conventional semiconductor materials, mainly in forms of  $\alpha$ - and  $\gamma$ -Fe<sub>2</sub>O<sub>3</sub>. The unit cell of  $\alpha$ -Fe<sub>2</sub>O<sub>3</sub> (hematite) is hexagonal, containing only octahedral coordinated Fe<sup>3+</sup> atoms (corundum structure), while  $\gamma$ -Fe<sub>2</sub>O<sub>3</sub> (magnetite) particles have cubic unit cells with both octahedral and tetrahedral coordinated Fe<sup>3+</sup> sites (defect spinel structure) [1]. They are both technologically important because of their special magnetic and electrical properties, and potential applications in sorbents [2], ion exchangers [3], information storage [4], and magnetic refrigeration [5]. Controlling the morphologies of these materials during synthetic process is of great importance because of their shape-dependent properties. Various synthetic methods are continually being improved. To date, a variety of novel shapes of iron oxides nanocrystals have been successfully synthesized via various approaches. Magnetite nanorods with high aspect ratio have been synthesized by one-step wet chemistry process that a surfactant, polyethylene glycol, served as the template, and a ferrous ammonia sulphate served as iron source [6]. Uniform  $\alpha$ -Fe<sub>2</sub>O<sub>3</sub> particles within the nanometer range (100–300 nm) have been obtained by precipitation of iron (III) perchlorate in the presence of urea.

Different morphology, from spheres to ellipsoidal particles with axial ratio up to 10, was obtained by adding to the initial solution increasing amounts of phosphate anions up to 7 mM [7]. Plate-shaped  $\gamma$ -Fe<sub>2</sub>O<sub>3</sub> nanocrystals have been successfully prepared in a water system by a simple reduction-oxidation method at room temperature and under ambient pressure. The reactions contain two steps: first, Fe(II) is reduced into Fe atoms by  $\gamma$ -ray irradiation in nitrogen atmosphere; then, Fe atoms are oxidized into  $\gamma$ -Fe<sub>2</sub>O<sub>3</sub> in air [8]. Continuous iron oxide gel fibers were prepared by the sol-gel method using ferric alkoxide and acetic acid as starting materials and alcohol as solvent, and continuous hollow  $\alpha$ -Fe<sub>2</sub>O<sub>3</sub> fibers produced after the gel fibers were heat treated at 400 degrees C for 1 hour [9]. Vertically aligned iron oxide nanobelt and nanowire arrays have been synthesized on a large-area surface by direct thermal oxidation of iron substrates under the flow of O<sub>2</sub>. It was found that nanobelts (width, tens of nanometers; thickness, a few nanometers) were produced in the low-temperature region (similar to 700°C) whereas cylindrical nanowires which are tens of nanometers thick are formed at relatively higher temperatures (similar to 800°C) [10]. Sphere-like maghemite ( $\gamma$ -Fe<sub>2</sub>O<sub>3</sub>) nanocrystals are formed by utilizing a solution-based one-step thermolysis method; modulating

the growth parameters, such as the type and amount of capping ligands as well as the growth time, is shown to have a significant effect on the overall shape and size of the obtained nanocrystals and on the ripening process itself [11]. Hou et al. report a facile organic-phase synthesis of monodisperse FeO nanoparticles through high-temperature reductive decomposition of iron (III) acetylacetonate ( $[\text{Fe}(\text{acac})_3]$ ) with oleic acid (OA) and oleylamine (OAm) both as surfactants and solvents; the sizes of the particles are tuned from 14 to 100 nm by controlling the heating conditions and the shapes of the particles are controlled to be either spherical or truncated octahedral depending on the volume ratio of OA and OAm used in the reaction. Thermal annealing under an argon atmosphere converted these FeO nanoparticles into composite Fe-Fe<sub>3</sub>O<sub>4</sub> nanoparticles, while controlled oxidation of the FeO nanoparticles resulted in the formation of Fe<sub>3</sub>O<sub>4</sub>,  $\gamma$ -Fe<sub>2</sub>O<sub>3</sub>, or  $\alpha$ -Fe<sub>2</sub>O<sub>3</sub> nanoparticles [12]. The highly crystalline and monodisperse  $\gamma$ -Fe<sub>2</sub>O<sub>3</sub> nanocrystallites are fabricated from the controlled oxidation of uniform iron nanoparticles which are generated from the thermal decomposition of iron complex. Particle size can be varied from 4 to 16 nm by controlling the experimental parameters [13]. Nevertheless, the production of Fe<sub>2</sub>O<sub>3</sub> nanocubes has not been realized ever. Nanocubes exposed a specific surface, which provided an ideal model for the study of surface related properties [14, 15].

In this paper, we demonstrated that single-crystalline  $\alpha$ -Fe<sub>2</sub>O<sub>3</sub> nanocubes could be successfully synthesized via a facile hydrothermal synthetic method under mild conditions. The morphologies of  $\alpha$ -Fe<sub>2</sub>O<sub>3</sub> samples could be easily controlled via simply varying the reaction time, and the probable formation mechanism was proposed to explain their growth processes. Moreover, this synthetic approach provided a simple and economical route to synthesize nanocrystals, some of which have a variety of potential applications.

## 2. Experimental Procedures

The aqueous iron (III) nitrate ( $\text{Fe}(\text{NO}_3)_3 \cdot 9\text{H}_2\text{O}$ ) was purchased from Sinopharm Chemical Reagent Co., Ltd. The triethylamine was purchased from Beijing Chemical Factory, China. Both  $\text{Fe}(\text{NO}_3)_3 \cdot 9\text{H}_2\text{O}$  and triethylamine were of analytical grade and no further purification was conducted. Deionized water was used throughout the experiment.

**2.1. Synthesis.** In a typical procedure, 0.404 g  $\text{Fe}(\text{NO}_3)_3 \cdot 9\text{H}_2\text{O}$  and 3 mL triethylamine were dissolved in deionized water (10 mL) to form a homogeneous solution and then the solution was stirred vigorously for 5 minutes. After that, the solution was sealed in a 50 mL teflon-lined autoclave filled with deionized water till up to 80% of the total volume, and the container was maintained at 160°C for 1–24 hours without shaking or stirring. The resulting products were filtered and then washed successively with deionized water and anhydrous ethanol for several times, and finally, the product was dried for 5 h under vacuum at a temperature of 50°C.

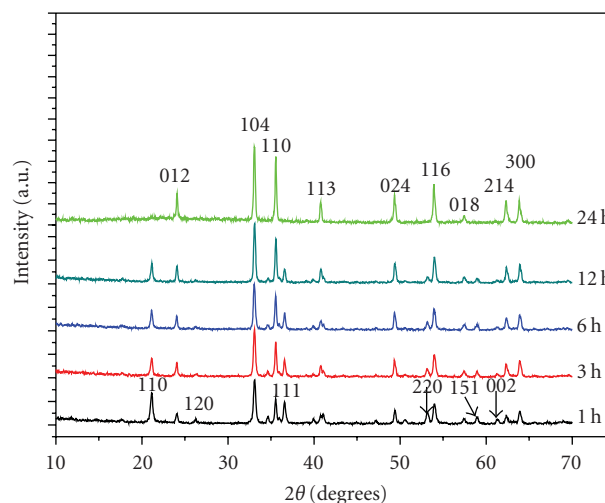


FIGURE 1: X-ray powder diffraction pattern of various as-prepared sample.

**2.2. Characterization.** The obtained samples were characterized by powder X-ray diffraction (XRD) with a D/max2550 VB+, and Cu K $\alpha$  ( $\lambda = 1.54178 \text{ \AA}$ ) was used as the radiation source, while the operation voltage and current were kept at 40 kV and 40 mA, respectively. Particle size and morphology of the as-synthesized products were observed using field emission scanning electron microscopy (FESEM) with Philips XL30 S-FEG at an accelerating voltage of 20 kV and transmission electron microscopy (TEM) with JEM-200CX at an accelerating voltage of 160 kV and high-resolution transmission electron microscopy (HRTEM) with JEOL JEM-2010F at an accelerating voltage of 200 kV. Meanwhile, selected area electron diffraction (SAED) was performed to identify the crystallinity. The Fourier transform infrared (FTIR) spectra was recorded on a Nicolet Impact 410 infrared spectrophotometer, and, as for sample preparation, the synthesized powder was added into KBr to press a KBr pellet for FTIR analysis.

## 3. Results and Discussion

**3.1. Crystal Structure.** XRD pattern of the sample obtained at 160°C for 24 hours was shown in Figure 1. It could be concluded that all the diffraction peaks could be readily indexed as the pure rhombohedral  $\alpha$ -Fe<sub>2</sub>O<sub>3</sub> ( $a = 5.038 \text{ \AA}$ ,  $c = 13.772 \text{ \AA}$ ) (JCPDS file Card, no. 33-0664). The XRD diffraction patterns peaks of  $\alpha$ -Fe<sub>2</sub>O<sub>3</sub> became narrower with prolonging the reaction time, and the narrower peaks suggested that the  $\alpha$ -Fe<sub>2</sub>O<sub>3</sub> samples were higher crystalline, and it testified that iron oxide nanocrystallines could be synthesized through this method. No other peaks were observed, indicating high purity of the as-prepared samples.

The characteristic peaks of orthorhombic  $\alpha$ -FeOOH ( $a = 4.6048 \text{ \AA}$ ,  $b = 9.9595 \text{ \AA}$ ,  $c = 3.023 \text{ \AA}$ ) (JCPDS file Card, no. 81-0464) were observed in Figure 1 when the reaction time was 1 hour, 3 hours, 6 hours, and 12 hours, but the characteristic peaks of  $\alpha$ -FeOOH decreased with prolonging

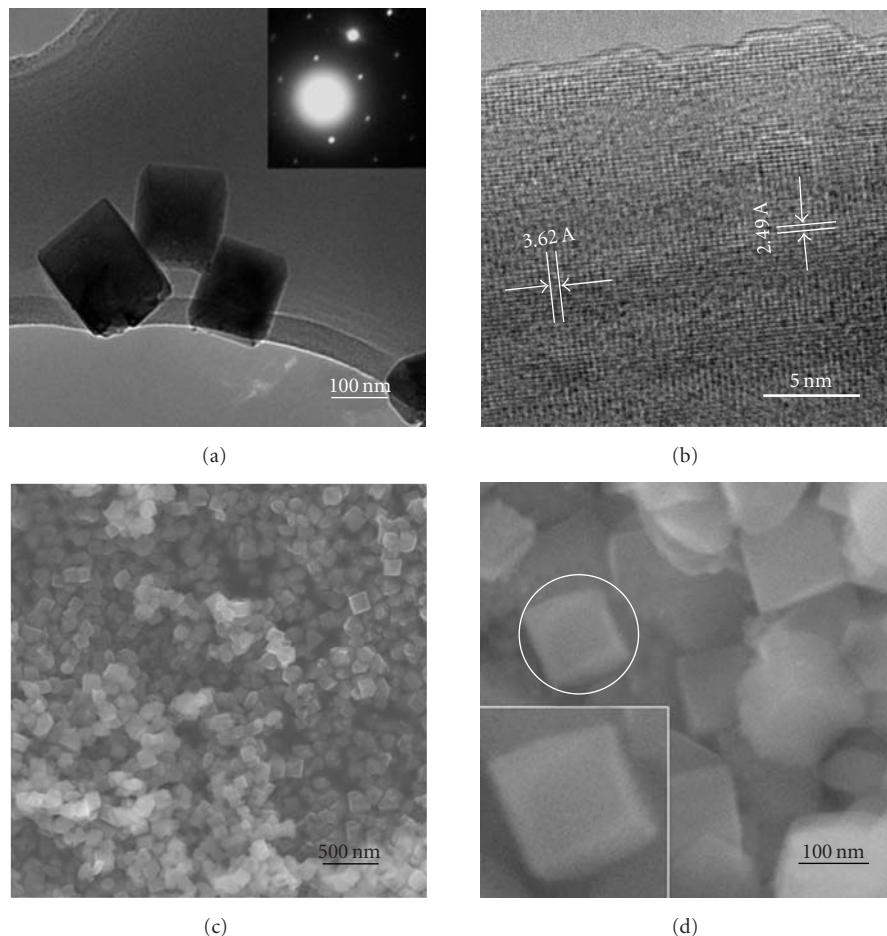


FIGURE 2: (a) TEM image of  $\text{Fe}_2\text{O}_3$  nanocubes prepared at  $160^\circ\text{C}$  for 24 hours with 3 mL triethylamine, and the Inset is the SAED image. (b) HRTEM image of the  $\text{Fe}_2\text{O}_3$  nanocubes. (c), (d) SEM images of the  $\text{Fe}_2\text{O}_3$  nanocubes. The Inset in (d) is the high magnification image taken from the highlighted section marked by the circle, which indicates that these particles are nanocubes.

the reaction time, and there were only the characteristic peaks of  $\alpha\text{-Fe}_2\text{O}_3$  when the reaction time was 24 hours. The narrow sharp peaks suggested that the  $\alpha\text{-Fe}_2\text{O}_3$  samples were highly crystalline.

**3.2. Morphology.** TEM data and analyses of the iron oxide particles prepared at  $160^\circ\text{C}$  for 24 hours using 3 mL triethylamine were illustrated in Figure 2(a). These cubes had a regular cubic structure and a uniform width of about 100 to 200 nm. The surfaces of the cubes were equal and the boundaries of them are evident. The SAED pattern in Figure 2(a), which was parallel to upright axis of cube surface, indicates that the cubes were single crystallines. The fringe spacing measured 3.62 Å and 2.49 Å (Figure 2(b)), which concurred well with the interplanar spacing of (012) and (110).

Figure 2(c) was a typical SEM image of the  $\text{Fe}_2\text{O}_3$  nanocubes obtained at  $160^\circ\text{C}$  for 24 hours using 3 mL triethylamine and Figure 2(d) is the magnified image of Figure 2(c). Both images showed that the regular  $\text{Fe}_2\text{O}_3$  nanocubes could be prepared by this approach. The nanocubes were 100 to 200 nm in width and the nanocube

morphology was more evident in Figure 2(d). The inset in Figure 2(d) was the high-magnification image of a typical particle in the highlighted section marked with a white colored circle, which indicates that these particles possess regular cubic morphology and had smooth facies.

The influence of reaction time on the morphology of the products was also investigated and TEM images of iron oxides nanocubes obtained at  $160^\circ\text{C}$  using 3 mL triethylamine for 1, 3, 6, and 12 hours were displayed in Figures 3(a), 3(b), 3(c), and 3(d), respectively. For a short reaction time of 1 hour, as shown in Figure 3(a), most of the synthesized particles were in irregular shape and the particle size varied a lot. Yet, by prolonging the reaction time, a tendency was deduced that the particles became more and more regular in size and morphology, and, gradually, these particles formed into cubic patterns, as shown in Figures 3(b), 3(c), and 3(d). Compared with these TEM data, prolonging the reaction time was helpful to the formation of iron oxides nanocubes.

**3.3. FTIR Spectrum.** Figure 4 represented the FTIR spectrum between  $4000$  to  $400\text{ cm}^{-1}$  of  $\alpha\text{-Fe}_2\text{O}_3$  nanocubes. The peaks

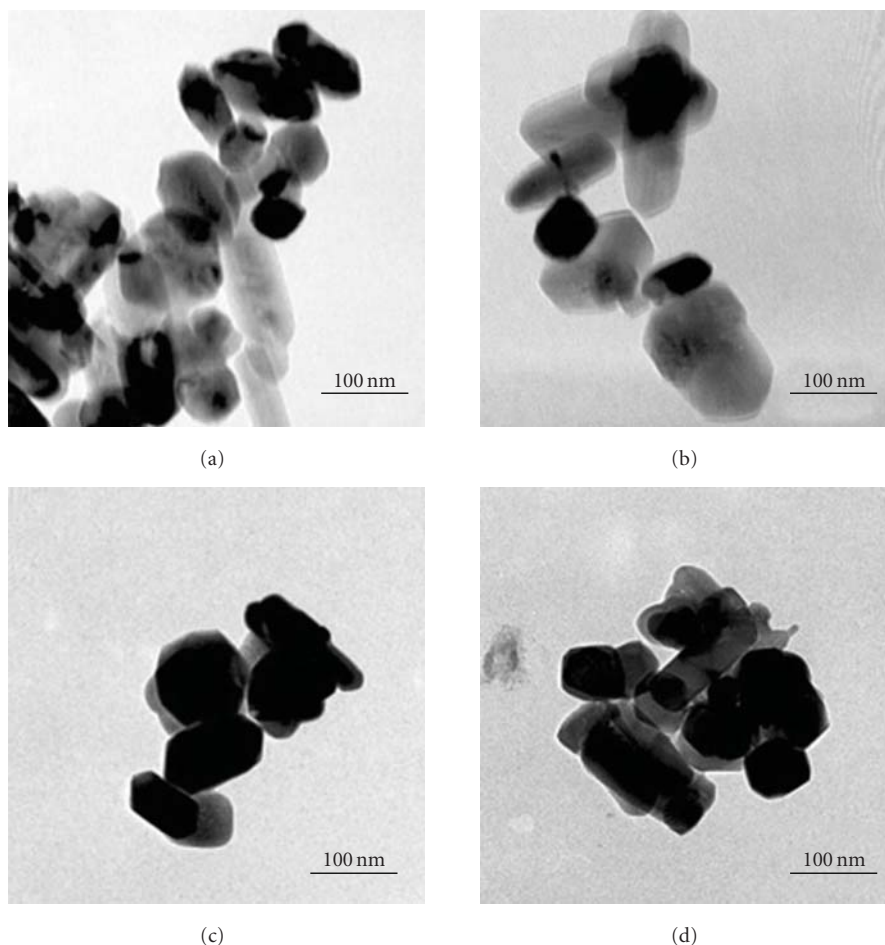


FIGURE 3: TEM images of  $\text{Fe}_2\text{O}_3$  nanocubes were prepared at  $160^\circ\text{C}$  using 3 mL triethylamine for 1 hour (a), 3 hours (b), 6 hours (c) and 12 hours (d).

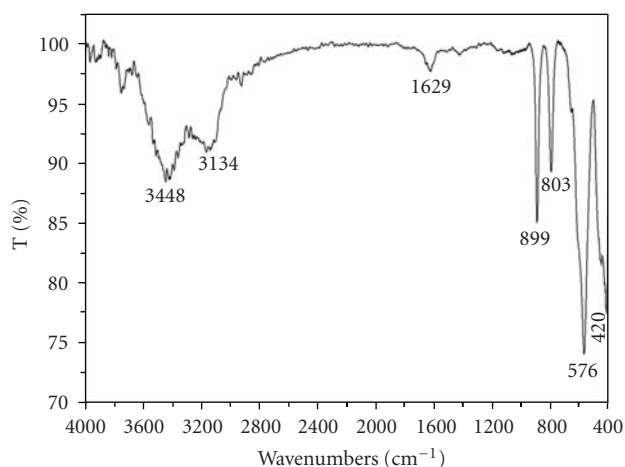


FIGURE 4: FT-IR image of  $\text{Fe}_2\text{O}_3$  sample at  $160^\circ\text{C}$  using 3 mL triethylamine for 24 hours.

at  $420$  and  $576\text{ cm}^{-1}$  attributed to the Fe-O bond vibration of the  $\text{Fe}_2\text{O}_3$ . The spectrum showed the bands at  $899$  and  $803\text{ cm}^{-1}$  corresponds to the out-of-plane C-H vibration

caused by the remnant of triethylamine on the surface of particles and the peaks at around  $1629\text{ cm}^{-1}$  were tentatively assigned to the vibration of C-N bond [16]. The peaks at  $3134\text{ cm}^{-1}$  were assigned to the  $\nu(\text{N}^+-\text{H})$  vibrations [17], and peaks at  $3448\text{ cm}^{-1}$  were assigned to the O-H stretching vibration of absorbed water.

#### 4. Discussion and Conclusion

Iron oxide nanocubes were prepared by a hydrolysis reaction of  $\text{Fe}^{3+}$  in triethylamine at the temperature of  $160^\circ\text{C}$  and the triethylamine provides  $\text{OH}^-$  to form the  $\text{Fe}(\text{OH})_3$  deposition. After reacting in hydrothermal environment, the  $\text{Fe}(\text{OH})_3$  translated into  $\alpha\text{-FeOOH}$  through heat decomposition at first, and then the  $\alpha\text{-FeOOH}$  translated into  $\alpha\text{-Fe}_2\text{O}_3$  through heat decomposition (Figure 1). With the  $\text{Fe}_2\text{O}_3$  crystal particles growing, the cubes were formed because triethylamine influenced the growth rate of some crystal faces. Furthermore, the iron oxide cubes' formation was influenced by reaction time. The formation mechanism and influenced factors of iron oxide cubes will be discussed thoroughly in our further investigation.

In summary, iron oxide nanocubes were successfully synthesized via hydrothermal synthetic route under mild conditions. It is expected that the iron oxide of uniform nanocrystallines may be promoted to some important applications in fields, for example, sensors, magnetic media, and catalytic, and so forth. This synthetic approach provided a simple and economical route to synthesize Nanocrystals. We have also discovered that many of our synthesis techniques could be utilized in the preparation of other nanostructured metal oxides, which will be reported later.

## Acknowledgment

This paper was supported by the National Natural Science Foundation of China (Project no. 50774094).

## References

- [1] P. Praserttham, O. Mekasuwandumrong, J. Phungphadung, A. Kanyanucharat, and W. Tanakulrungsank, "New correlation for the effects of the crystallite size and calcination temperature on the single iron oxide nanocrystallites," *Crystal Growth and Design*, vol. 3, no. 2, pp. 215–219, 2003.
- [2] D. S. Toledano and V. E. Henrich, "Kinetics of  $\text{SO}_2$  adsorption on photoexcited  $\alpha\text{-Fe}_2\text{O}_3$ ," *Journal of Physical Chemistry B*, vol. 105, no. 18, pp. 3872–3877, 2001.
- [3] A. W. Apblett, S. I. Kuriyavar, and B. P. Kiran, "Preparation of micron-sized spherical porous iron oxide particles," *Journal of Materials Chemistry*, vol. 13, no. 5, pp. 983–985, 2003.
- [4] S. Sun, C. B. Murray, D. Weller, L. Folks, and A. Moser, "Monodisperse FePt nanoparticles and ferromagnetic FePt nanocrystal superlattices," *Science*, vol. 287, no. 5460, pp. 1989–1992, 2000.
- [5] R. D. McMichael, R. D. Shull, L. J. Swartzendruber, L. H. Bennett, and R. E. Watson, "Magnetocaloric effect in superparamagnets," *Journal of Magnetism and Magnetic Materials*, vol. 111, no. 1-2, pp. 29–33, 1992.
- [6] S. Chen, J. Feng, X. Guo, J. Hong, and W. Ding, "One-step wet chemistry for preparation of magnetite nanorods," *Materials Letters*, vol. 59, no. 8-9, pp. 985–988, 2005.
- [7] M. Ocaña, M. P. Morales, and C. J. Serna, "Homogeneous precipitation of uniform  $\alpha\text{-Fe}_2\text{O}_3$  particles from iron salts solutions in the presence of urea," *Journal of Colloid and Interface Science*, vol. 212, no. 2, pp. 317–323, 1999.
- [8] Y. Ni, X. Ge, Z. Zhang, and Q. Ye, "Fabrication and characterization of the plate-shaped  $\gamma\text{-Fe}_2\text{O}_3$  nanocrystals," *Chemistry of Materials*, vol. 14, no. 3, pp. 1048–1052, 2002.
- [9] C. Gong, D. Chen, X. Jiao, and Q. Wang, "Continuous hollow  $\alpha\text{-Fe}_2\text{O}_3$  and  $\alpha\text{-Fe}$  fibers prepared by the sol-gel method," *Journal of Materials Chemistry*, vol. 12, no. 6, pp. 1844–1847, 2002.
- [10] X. Wen, S. Wang, Y. Ding, Z. L. Wang, and S. Yang, "Controlled growth of large-area, uniform, vertically aligned arrays of  $\alpha\text{-Fe}_2\text{O}_3$  nanobelts and nanowires," *Journal of Physical Chemistry B*, vol. 109, no. 1, pp. 215–220, 2005.
- [11] J. Cheon, N.-J. Kang, S.-M. Lee, J.-H. Lee, J.-H. Yoon, and S. J. Oh, "Shape evolution of single-crystalline iron oxide nanocrystals," *Journal of the American Chemical Society*, vol. 126, no. 7, pp. 1950–1951, 2004.
- [12] Y. Hou, Z. Xu, and S. Sun, "Controlled synthesis and chemical conversions of FeO nanoparticles," *Angewandte Chemie. International Edition*, vol. 46, no. 33, pp. 6329–6332, 2007.
- [13] T. Hyeon, S. S. Lee, J. Park, Y. Chung, and H. B. Na, "Synthesis of highly crystalline and monodisperse maghemite nanocrystallites without a size-selection process," *Journal of the American Chemical Society*, vol. 123, no. 51, pp. 12798–12801, 2001.
- [14] X. Liu, G. Qiu, Z. Wang, and X. Li, "Rationally synthetic strategy: from nickel hydroxide nanosheets to nickel oxide nanorolls," *Nanotechnology*, vol. 16, no. 8, pp. 1400–1405, 2005.
- [15] C. J. Murphy, "Materials science: Nanocubes and nanoboxes," *Science*, vol. 298, no. 5601, pp. 2139–2141, 2002.
- [16] G. Wojciechowski and B. Brzezinski, "Formation of hydrogen-bonded chains through inter- and intra-molecular hydrogen bonds by 5,5'-dinitro-2,2'-biphenol with a strong base of guanidine-like character and triethylamine," *Journal of Molecular Structure*, vol. 607, no. 2-3, pp. 149–154, 2002.
- [17] G. Wojciechowski and B. Brzezinski, "Formation of hydrogen-bonded complexes of 3,3',5,5'-tetrabromo-2,2'-biphenol with MTBD and triethylamine," *Journal of Molecular Structure*, vol. 616, no. 1–3, pp. 67–71, 2002.

## Research Article

# Radiolytic Synthesis of Pt-Ru Catalysts Based on Functional Polymer- Grafted MWNT and Their Catalytic Efficiency for CO and MeOH

Dae-Soo Yang, Kwang-Sik Sim, Hai-Doo Kwen, and Seong-Ho Choi

Department of Chemistry, Hannam University, Daejeon 305-811, Republic of Korea

Correspondence should be addressed to Seong-Ho Choi, shchoi@hnu.kr

Received 12 April 2010; Revised 4 June 2010; Accepted 23 June 2010

Academic Editor: William W. Yu

Copyright © 2011 Dae-Soo Yang et al. This is an open access article distributed under the Creative Commons Attribution License, which permits unrestricted use, distribution, and reproduction in any medium, provided the original work is properly cited.

Pt-Ru catalysts based on functional polymer-grafted MWNT (Pt-Ru@FP-MWNT) were prepared by radiolytic deposition of Pt-Ru nanoparticles on functional polymer-grafted multiwalled carbon nanotube (FP-MWNT). Three different types of functional polymers, poly(acrylic acid) (PAAc), poly(methacrylic acid) (PMAc), and poly(vinylphenyl boronic acid) (PVPBac), were grafted on the MWNT surface by radiation-induced graft polymerization (RIGP). Then, Pt-Ru nanoparticles were deposited onto the FP-MWNT supports by the reduction of metal ions using  $\gamma$ -irradiation to obtain Pt-Ru@FP-MWNT catalysts. The Pt-Ru@FP-MWNT catalysts were then characterized by XRD, XPS, TEM, and elemental analysis. The catalytic efficiency of Pt-Ru@FP-MWNT catalyst was examined for CO stripping and MeOH oxidation for use in a direct methanol fuel cell (DMFC). The Pt-Ru@PVPBac-MWNT catalyst shows enhanced activity for electro-oxidation of CO and MeOH oxidation over that of the commercial E-TEK catalyst.

## 1. Introduction

Although carbon-supported Pt-Ru nanoparticles (Pt-Ru/C) are known to be the best anode catalysts for direct methanol fuel cell (DMFC), they are still insufficient for the commercial application. Many researcher efforts have been devoted to improving the catalytic performance of Pt-Ru/C by catalyst dispersion [1–3]. In previous paper, we deposited Pt-Ru nanoparticles on the surface of the various carbon supports, including Vulcan XC-71, Ketjen-300, Ketjen-600, SWNTs, and MWNTs for use as fuel cell catalysts [4]. However, the metallic alloy nanoparticles were aggregated on the surface of the carbon supports due to their hydrophobic nature. The metal (Ag or Pd) and alloy (Pt-Ru) nanoparticles were also deposited on the surface of single-walled carbon nanotubes (SWNTs) [5], and porous carbon supports using  $\gamma$ -irradiation without protecting agents [6]. Silva et al. [7] reported the preparation of Pt-Ru/C electrocatalysts using  $\gamma$ -irradiation in water/ethylene glycol. This paper showed the patterns of Pt-Ru nanoparticles on carbon supports; however, it did not indicate the catalytic efficiency of MeOH oxidation based on the aggregation degree. It is proposed that

the catalytic efficiency is affected by the metallic nanoparticle aggregation degree on carbon supports.

To overcome the aggregation of the metallic nanoparticles, the carbon support surface was modified with hydrophobic properties to obtain hydrophilic properties by *in-situ* polymerization of  $\beta$ -caprolactone, methacrylate, and pyrrole using oxidizing agents as the initiator [8]. Pt-Ru nanoparticles were then deposited on the polymer-wrapped MWNT supports to produce a direct methanol fuel cell (DMFC) catalyst. Pt-Ru at poly(pyrrole)-MWNT catalysts obtained high catalytic efficiency for CO stripping and methanol oxidation. The surface of MWNTs was then coated using conductive polymers such as aniline, pyrrole, and thiophene to go from hydrophobic properties to hydrophilic properties [9]. Finally, the metallic nanoparticles were deposited on conducting polymer-wrapped MWNTs. However, the prepared Pt-Ru catalysts provided lower catalytic efficiency compared to that of commercial E-TEK catalyst.

Radiation-induced graft polymerization (RIGP) is a useful method for the introduction of functional groups onto different polymer materials using specially selected monomers. There have been several reports about RIGP

of polar monomers onto polymer substrates to obtain hydrophilic properties for versatile applications [10–14]. The RIGP method can easily functionalize the surface of MWNTs to the desired properties. In a previous paper, we described the functionalization of MWNTs by RIGP of derivatives vinyl monomers and their application in enzyme-free biosensors [15]. However, little has been reported about the deposition of Pt-Ru nanoparticles on the functionalized MWNT supports by  $\gamma$ -irradiation for DMFC catalysts.

In this study, Pt-Ru nanoparticles were deposited on the functional polymer (FP)-grafted MWNT obtained from RIGP using  $\gamma$ -irradiation to produce an anode catalyst for DMFCs. The obtained Pt-RuatFP-MWNT catalysts were characterized by XRD, XPS, TEM, and elemental analysis. Furthermore, the catalytic efficiency of the Pt-RuatFP-MWNT catalyst was evaluated for CO stripping and MeOH oxidation for use in a DMFC and compared to the catalytic efficiency of the commercial E-TEK catalyst.

## 2. Experimental

**2.1. Chemicals.**  $\text{H}_2\text{PtCl}_6 \times \text{H}_2\text{O}$  (37.5% Pt),  $\text{RuCl}_3 \times \text{H}_2\text{O}$  (41.0% Ru), acrylic acid (AAc), methacrylic acid (MAc), and 4-vinylphenylboronic acid (VPBAc) were of analytical reagent grade (Sigma-Aldrich, USA) and used without further purification. MWNTs (CM-95) were supplied by Hanwha Nanotech Co., Ltd (Korea). The commercial E-TEK catalyst (metallic content, 30 wt-%) was purchased from E-TEK (BASF Fuel Cell Inc., NJ, USA). Nafion (perfluorinated ion-exchange resin, 5% (w/v) solution in a solution of 90% aliphatic alcohol/10% water mixture) was also purchased from Sigma-Aldrich (USA). Solutions for the experiments were prepared with water purified in a Milli-Q puls water purification system (Millipore Co. Ltd. USA), the final resistance of water was  $18.2 \text{ M}\Omega\text{cm}^{-1}$  and degassed prior to each measurement. Other chemicals were of reagent grade.

**2.2. RIGP of Functional Monomers on the Surface of MWNTs.** MWNTs were purified to remove the catalyst and noncrystallized carbon impurities with phosphoric acid solution. The purified MWNTs were used as the supporting materials for grafting of various vinyl monomers. The MWNTs (2.0 g) and AAc (2.0 g) were then mixed in aqueous solution (20 mL). Nitrogen gas was bubbled through the solution for 30 minutes to remove oxygen gas, and the solution was irradiated from a Co-60 source under atmospheric pressure and ambient temperature. A total irradiation dose of 30 kGy (dose rate =  $6.48 \times 10^5/\text{h}$ ) was used. The other functional polymer-grafted MWNTs were prepared using a similar procedure.

**2.3. Preparation of Pt-RuatFP-MWNT Catalysts by  $\gamma$ -Irradiation.** The Pt-RuatPVPBAc-MWNT catalysts were prepared as follows:  $\text{H}_2\text{PtCl}_6 \times \text{H}_2\text{O}$  (0.43 g) and  $\text{RuCl}_3 \times \text{H}_2\text{O}$  (0.41 g) were dissolved in deionized water (188 mL) in 2-propanol (12.0 mL) as the radical scavenger. 1.00 g of PVPBAc-MWNT support was added to the above solution. Nitrogen was bubbled for 30 min through the solution to remove oxygen and then irradiated under atmospheric

pressure and ambient temperature. A total irradiation dose of 30 kGy (a dose rate =  $6.48 \times 10^5/\text{h}$ ) was applied. Pt-Ru nanoparticle-deposited PVPBAc-MWNT catalysts were precipitated after  $\gamma$ -irradiation. The Pt-RuatPAAc-MWNT and Pt-RuatPMAc-MWNT catalysts were prepared as described above.

**2.4. Characteristics of Pt-RuatFP-MWNT Catalysts.** Particle size and morphology of the Pt-RuatFP-MWNT catalysts were analyzed by HR-TEM (JEOL, JEM-2010, USA). The content of Pt and Ru in samples was analyzed by inductively coupled plasma-atomic emission spectrometer (ICP-AES) (Jobin-Yvon, Ultima-C, USA). X-ray diffraction (XRD) patterns for samples were obtained using a Japanese Rigaku D/max  $\gamma\text{A}$  X-ray diffractometer equipped with graphite monochromatized Cu K $\alpha$  radiation ( $\lambda = 0.15414 \text{ nm}$ ). The scanning range was  $5\text{--}80^\circ$  with a scanning rate of  $5^\circ/\text{min}$ .

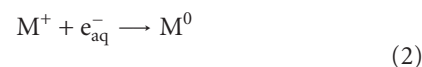
To evaluate the catalytic efficiency of Pt-RuatFP-MWNT catalysts for the electro-oxidation of CO and MeOH, the Pt-RuatFP-MWNT-coated electrode was prepared as follows. Firstly, the catalytic inks were prepared by mixing of Pt-RuatFP-MWNT catalysts (5.0 mg) and 5% Nafion solution (0.05 mL) and stirred for 24 hrs. Secondly, the catalytic inks were applied on a glass carbon ( $0.02 \text{ cm}^2$ ) by wet coating and dried in a vacuum oven at  $50^\circ\text{C}$  under nitrogen gas. The electro-oxidation of CO and MeOH (1.0 M) was examined using the Pt-RuatFP-MWNT catalyst electrode, submerged in 0.5 M  $\text{H}_2\text{SO}_4$  electrolyte by cyclic voltammetry (EG&G Instruments, Potentiostat/Galvanostat model 283, USA) at scan rate of 100 mV/s. All the measurements were carried out at room temperature.

## 3. Results and Discussion

**3.1. Radiolytic Preparation of Pt-RuatFP-MWNT Catalysts and Its Characterization.** Pt-RuatFP-MWNT catalysts were prepared by radiolytic reduction of metallic ions in water/2-propanol solution in the presence of FP-MWNT supports at room temperature. When  $\gamma$ -ray irradiated in aqueous solutions, various species were generated, as shown in the following equation [16]:



Among them, the solvated electrons,  $e_{\text{aq}}^-$  and  $\text{H}^\cdot$  radicals can be used as strong reducing agents. The metal ions were reduced to the zero-valent state as shown in the following:



Similarly, multivalent ions, such as  $\text{Pt}^{4+}$  and  $\text{Ru}^{3+}$ , are reduced by a multistep reaction. On the other hand, the hydroxyl radical ( $\text{OH}^\cdot$ ) can be oxidized for the ions or zero-valence metal atom. In order to protect the oxidizing agent ( $\text{OH}^\cdot$ ), 2-propanol was added to the reaction solution. The  $\text{OH}^\cdot$  radical was reacted with 2-propanol as shown in (3). As

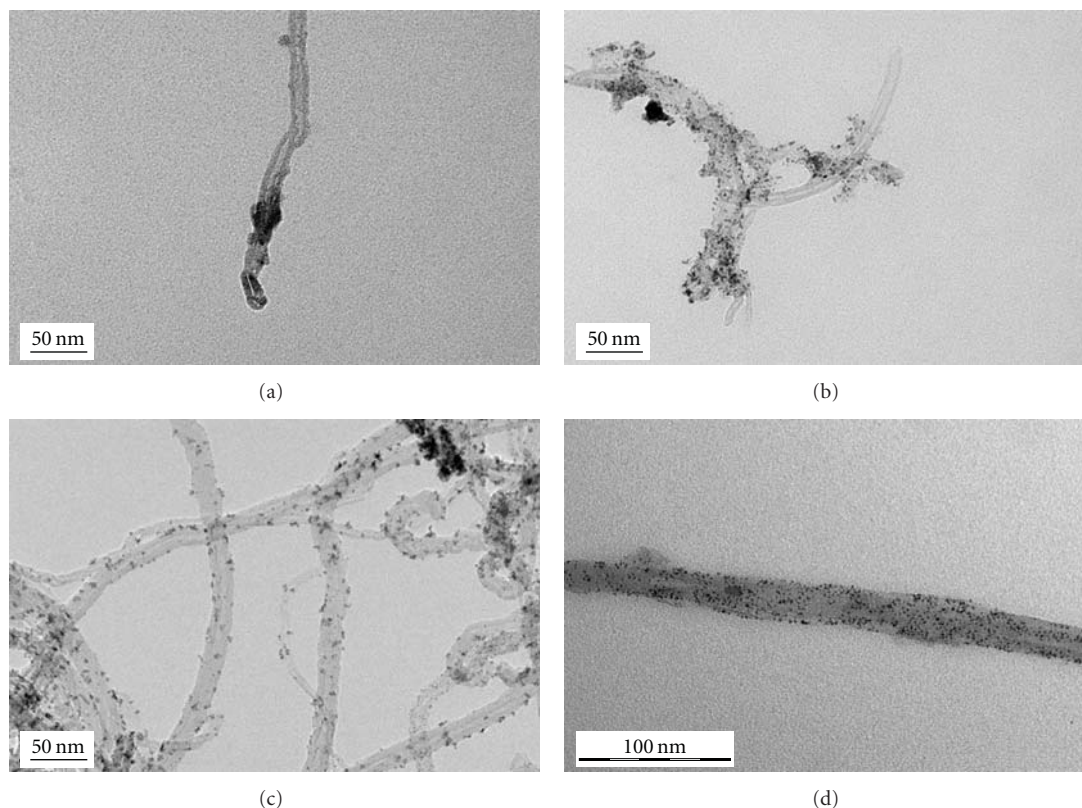


FIGURE 1: TEM images of the Pt-Ru/MWNT (a), Pt-Ru/PAAc-MWNT (b), Pt-Ru/PMAC-MWNT (c) and Pt-Ru/PVPBAC-MWNT (d) catalyst prepared by  $\gamma$ -irradiation.

results, the metal ion was then reduced to zero-valence metal atom by 2-propanol radical as shown in the following.

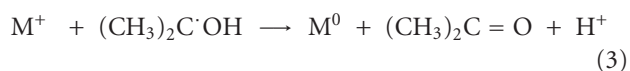


Figure 1 shows the TEM images of the Pt-Ru/MWNT (a), Pt-Ru/PAAc-MWNT (b), Pt-Ru/PMAC-MWNT (c), and Pt-Ru/PVPBAC-MWNT (d) catalysts prepared by  $\gamma$ -irradiation. As shown in Figure 1(a), there are no Pt-Ru nanoparticles on the surface of MWNT, whereas large amounts of Pt-Ru nanoparticles are shown on the surface of FP-MWNT supports, Figures 1(b), 1(c), and 1(d). Large amounts of Pt-Ru nanoparticles were successfully loaded on the surface of FP-MWNT. The mean particle sizes of the Pt-Ru nanoparticle on the surface of PAAc-MWNT, PMAC-MWNT, and PVPBAC-MWNT supports were in the range of 2.5–4.0 nm, 5.0–7.5 nm, and 2.0–2.5 nm, respectively. On the other hand, the commercial E-TEK catalyst showed a mean particle size of  $2.5 \pm 0.7$  nm [17]. As shown in the TEM image, the Pt-Ru nanoparticles were well dispersed on the surface of FP-MWNT supports because the surface of carbon is changed from hydrophobic property to hydrophilic property. The property of metallic nanoparticles was also possessed as hydrophilic property. Thus, these catalysts are expected to have good efficiency for methanol oxidation.

To clarify the chemical state of Pt-Ru nanoparticles deposited on FP-MWNTs, X-Ray photoelectron spectroscopy (XPS) measurements were taken. Figure 2 shows the regional  $\text{Pt}_{4f}$  and  $\text{Ru}_{3p}$  XPS spectra of Pt-Ru/PAAc-MWNT (a), Pt-Ru/PMAC-MWNT (b), and Pt-Ru/PVPBAC-MWNT catalyst (c) prepared by  $\gamma$ -irradiation. The  $\text{Pt}_{4f}$  peaks of the catalysts appeared about 72 eV and 75 eV due to metallic Pt and  $\text{Pt(IV)O}_2$ , respectively. Li and Hsing [18] reported that the  $\text{Pt}_{4f}$  XPS signal was appeared into three components with respective binding energies of 71.8, 72.9, and 74.6 eV. It was concluded that these signals were attributed to the metallic Pt,  $\text{Pt(II)O}$ , and  $\text{Pt(IV)O}_2$  species. On the other hand, the  $\text{Ru}_{3p_{1/2}}$  and  $\text{Ru}_{3p_{3/2}}$  peaks for the Pt-Ru/PAAc-MWNT and Pt-Ru/PMAC-MWNT were shown at 486 eV and 463 eV, respectively. The 463 eV signals are due to metallic Ru(0). Li and Hsing [18] interpreted 463 eV signal due to Ru(0) and  $\text{RuO}_2$ . In Figure 2(c), the  $\text{Ru}_{3p}$  signals of Pt-Ru/PVPBAC-MWNT catalysts were shifted onto the large binding energy compared to that of Pt-Ru/PAAc-MWNT and Pt-Ru/PMAC-MWNT. It may be considered that the hydrous ruthenium oxide,  $\text{RuO}_x\text{H}_y$ , was produced from the reaction of boronic acid group of the grafted PVBAC onto MWNT during  $\gamma$ -irradiation. However, a further investigation is needed to clarify these signals.

Figure 3 shows the X-ray diffraction patterns of the Pt-Ru/FP-MWNT catalysts prepared by  $\gamma$ -irradiation. All samples showed the peak at about  $20^\circ$ , which was associated

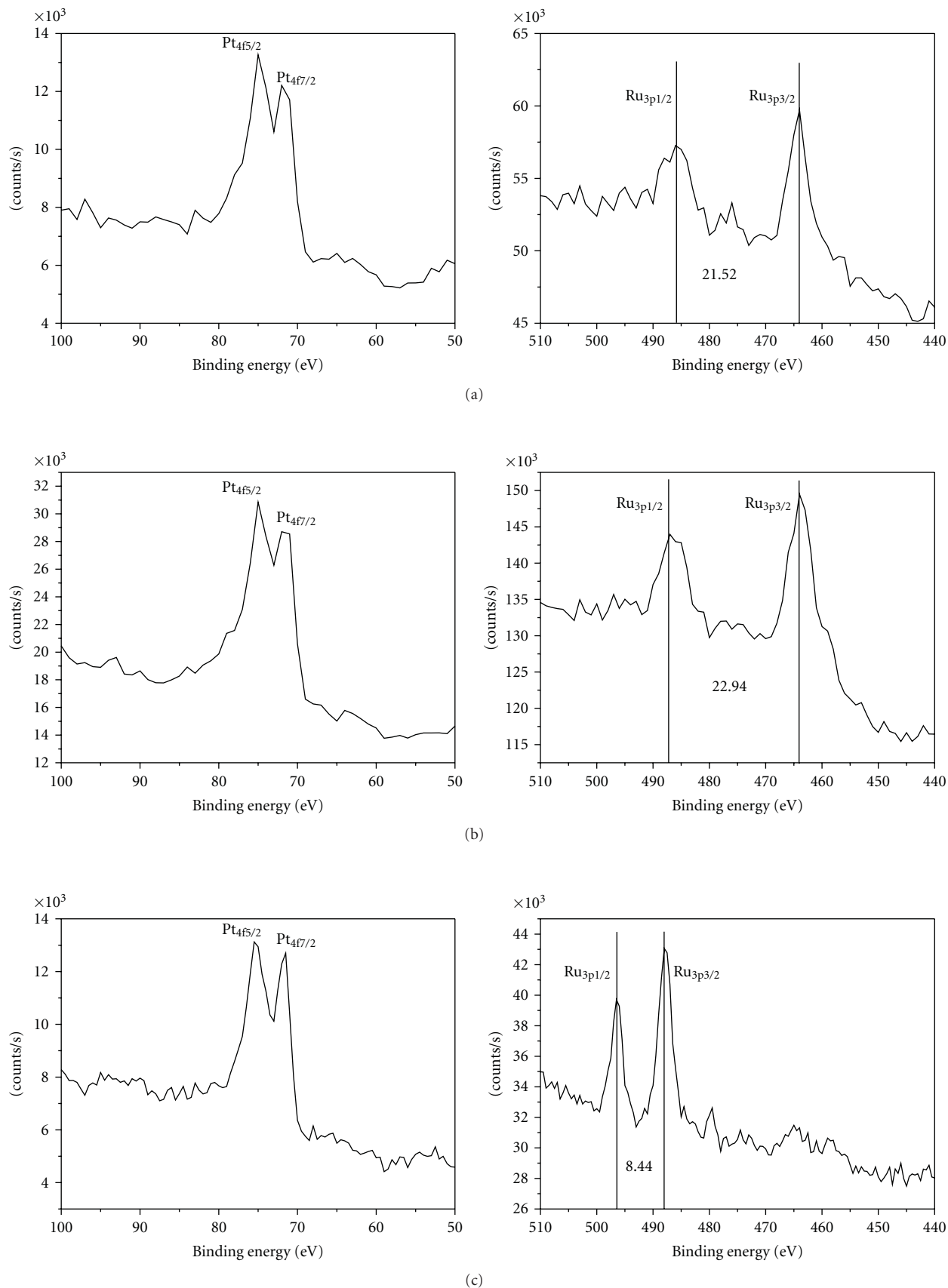


FIGURE 2: X-ray photoelectron spectroscopy (XPS) spectra of Pt and Ru on Pt-RuatPAAc-MWNT (a), Pt-RuatPMAc-MWNT (b) and Pt-RuatPVBAc-MWNT catalyst (c) prepared by  $\gamma$ -irradiation.

TABLE 1: Contents of Pt-Ru on the prepared catalyst<sup>(a)</sup>.

Catalysts	Pt content(wt-%)	Ru content (wt-%)
Pt-Ru at MWNT	ND	ND
Pt-Ru at PAAc-MWNT	8.77	10.8
Pt-Ru at PMAc-MWNT	8.20	9.98
Pt-Ru at PVPBac-MWNT	<b>11.2</b>	<b>6.01</b>
E.TEK catalyst(30 wt-%)	21.6	10.5

<sup>(a)</sup> Metal content (wt-%) was determined by ICP-AES.

to the MWNT supporting material. The crystallinity of Pt-Ru catalysts was confirmed by the presence of peaks around  $39.9^\circ$ ,  $46.2^\circ$ , and  $67.4^\circ$ . These peaks are assigned as Pt(111), (200) planes, and (220), respectively, of the face-centered cubic (fcc) structure of platinum and platinum alloy particles [19]. The XRD peaks corresponding to metallic ruthenium with hexagonal structure were not detected for these samples. The average particle size of the Pt-Ru catalysts can be calculated via XRD patterns according to Scherrer's formula [20, 21].

$$d_{\text{XRD}} = \frac{0.9\lambda}{\beta_{1/2} \cos \theta}, \quad (4)$$

where  $d_{\text{XRD}}$  is the average particle size (nm)  $\lambda$  is the wavelength of the  $x$ -ray (0.15406 nm)  $\theta$  is the angle at the peak maximum  $\beta_{1/2}$  is the width (radians) of the peak at half height. The calculated mean sizes from the diffraction peak of Pt(111) are as follows: 3.2 nm in Figure 3(a), 3.1 nm in Figure 3(b), and 2.9 nm in Figure 3(c). There are no size changes of Pt-Ru catalyst on various functionalized polymer-grafted MWNT. This behavior may show that the growth of nanoparticles is prevented via dimethylketone during  $\gamma$ -irradiation, as shown in (5).

Table 1 shows the content (wt-%) of Pt and Ru elements in the Pt-Ru at FP-MWNT catalysts. In ICP-AES results of the Pt-Ru at FP-MWNT catalyst, the Pt element content (wt-%) in the Pt-Ru at PAAc-MWNT, Pt-Ru at PMAc-MWNT, and Pt-Ru at PVPBac-MWNT catalysts was determined as 8.77%, 8.20%, and 11.20% for all that addition of 16.125% in reaction mixture, respectively. While Ru element content in the Pt-Ru at PAAc-MWNT, Pt-Ru at PMAc-MWNT, and Pt-Ru at PVPBac-MWNT catalysts was obtained as 10.8%, 9.98%, and 6.01%, for all that addition of 16.81% in reaction mixture, respectively. In the case of Pt-Ru at PVPBac-MWNT catalyst, the Pt content is higher than that of the other catalysts. In commercial E-TEK catalyst, the Pt content is higher than Ru content, as shown in Table 1.

**3.2. Catalytic Efficiency of Pt-Ru at FP-MWNT Catalyst for CO and MeOH.** To find the catalytic efficiency of Pt-Ru at FP-MWNT catalysts, they were tested for the electrochemical oxidation of carbon monoxide (CO). Figure 4 shows the cyclic voltammograms (CVs) of electro-oxidation of CO for Pt-Ru at FP-MWNT catalyst prepared by  $\gamma$ -irradiation

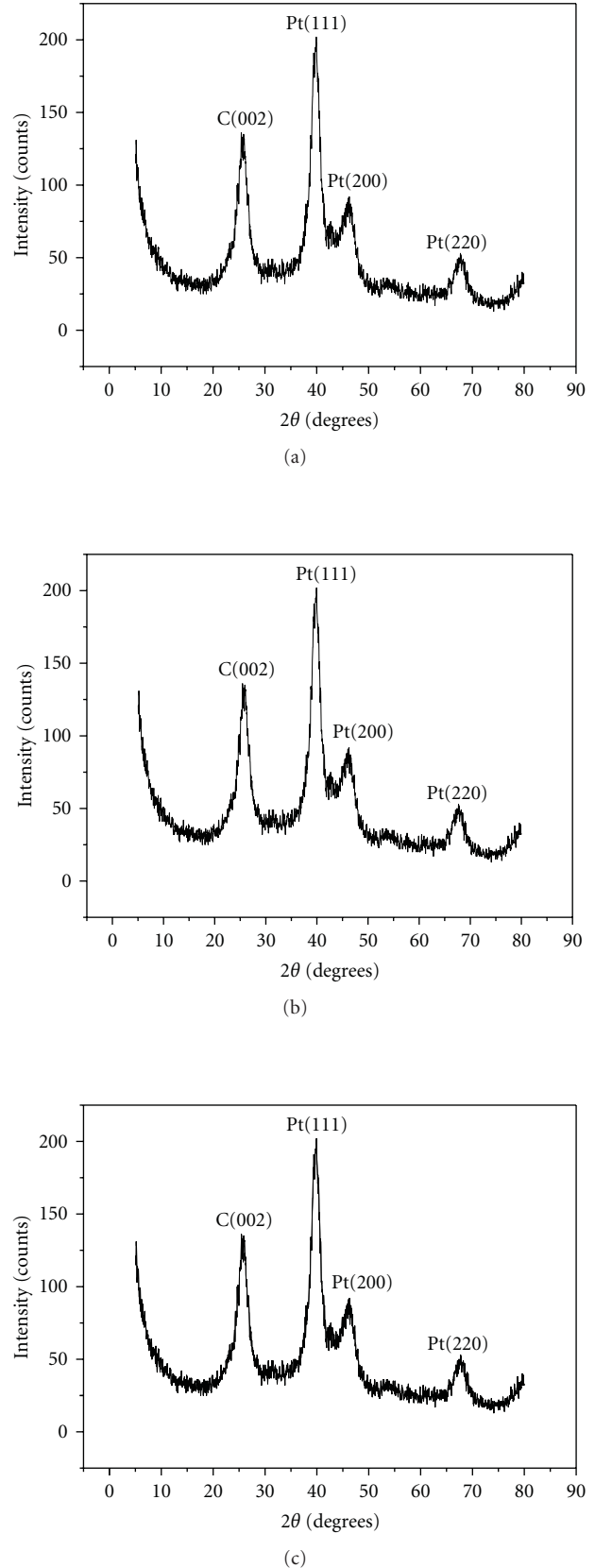


FIGURE 3: XRD spectra of Pt-Ru at PAAc-MWNT (a), Pt-Ru at PMAc-MWNT (b), and Pt-Ru at PVPBac-MWNT (c) catalyst for DMFC.

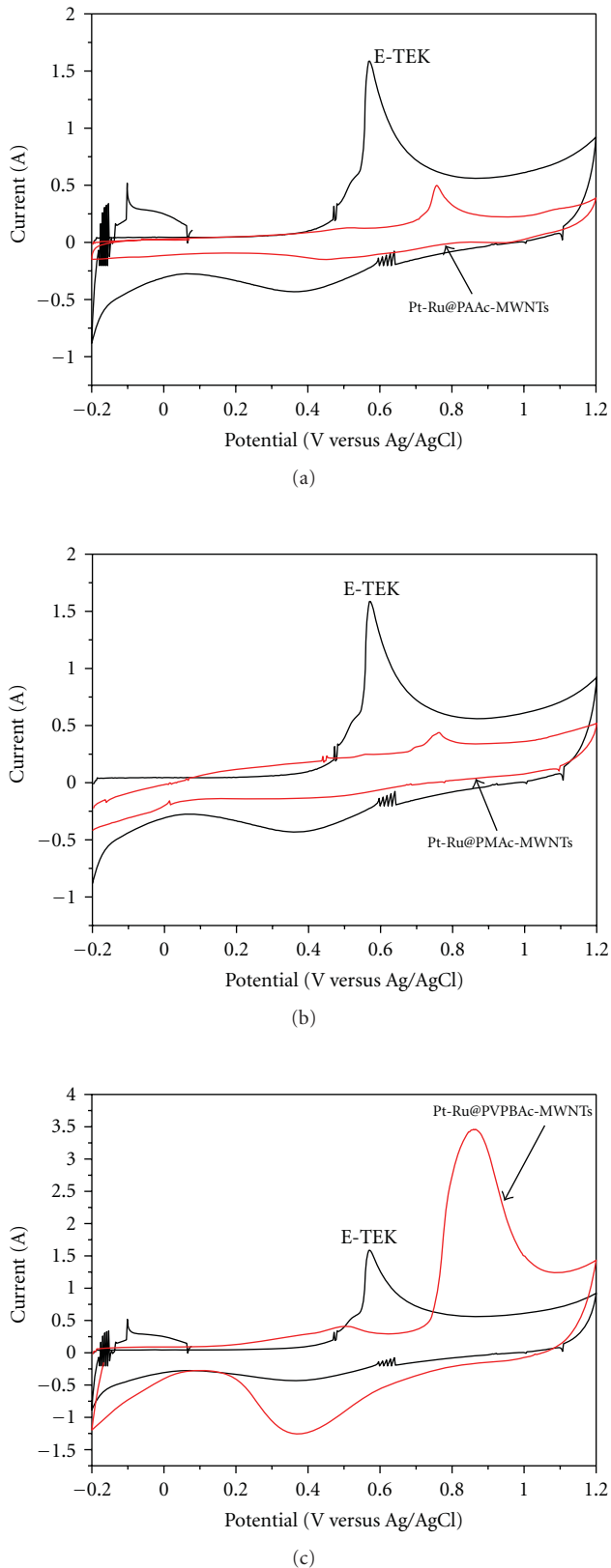


FIGURE 4: Comparison of CO adsorption efficiency in 0.5 M  $\text{H}_2\text{SO}_4$  between E-TEK the catalyst and the prepared catalyst. (a) E-TEK catalyst versus Pt-RuatPAAc-MWNT catalyst, (b) E-TEK catalyst versus Pt-RuatPMAc-MWNT, (c) E-TEK versus Pt-RuatPVPBac-MWNT.

in 0.5 M  $\text{H}_2\text{SO}_4$ : (a) RuatPAAc-MWNT, (b) Pt-RuatPMAc-MWNT, and (c) Pt-RuatPVPBac-MWNT catalyst. To compare CO adsorption efficiency, it was measured and compared to the commercial E-TEK catalyst containing 30 wt% Pt on carbon. The higher CO stripping peak at the commercial E-TEK catalyst electrode is more apparent than that of the Pt-RuatPAAc-MWNT and Pt-RuatPMAc-MWNT catalyst electrodes, as shown in Figures 4(a) and 4(b). However, the measured CO stripping peak at Pt-RuatPVPBac-MWNT catalyst electrode is significantly higher than that of the commercial E-TEK electrode in spite of the metal catalyst in high amount as shown in Figure 4(c). A significant current density is noticed at the Pt-RuatPVPBac-MWNT catalyst electrodes for the CO oxidation starting from 0.72 V. The electrochemically active specific area (SEAS) of the catalysts was calculated using the charges deduced from the CV of CO adsorption and desorption electro-oxidation process and using (5) [22].

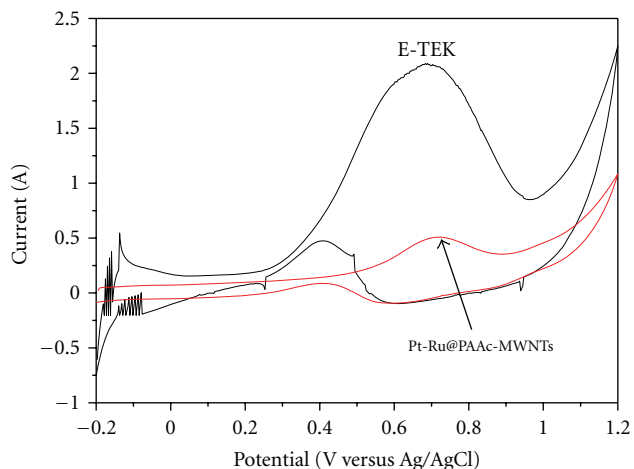
$$\text{SEAS} = \frac{Q_{\text{CO}}}{G} \times 420, \quad (5)$$

where  $Q_{\text{CO}}$  is the charge for CO desorption electro-oxidation in microcoulomb ( $\mu\text{C}$ );  $G$  represents the summation of Pt + Ru metals loading ( $\mu\text{g}$ ) in the electrode, and 420 is the charge required to oxidize a monolayer of CO on the catalysts in  $\mu\text{C cm}^{-2}$ . The electrochemical SEASs are  $60 \text{ m}^2 \text{ g}^{-1}$  for the commercial E-TEK catalysts. In the case of the prepared catalysts, the electrochemical SEASs are 34, 30, and  $126 \text{ m}^2 \text{ g}^{-1}$  for the Pt-RuatPAAc-MWNT, Pt-RuatPMAc-MWNT, and Pt-RuatPVPBac-MWNT catalysts, respectively. The SEAS of Pt-RuatPVPBac-MWNT catalysts prepared by  $\gamma$ -irradiation are higher than that of commercial E-TEK catalysts due to hydrous ruthenium oxide. It might be based on the promotion of CO oxidation on Pt atoms by the second metal (Ru) which provides OH-type species, the more oxidizable second metal, thus promotes catalytic activities.

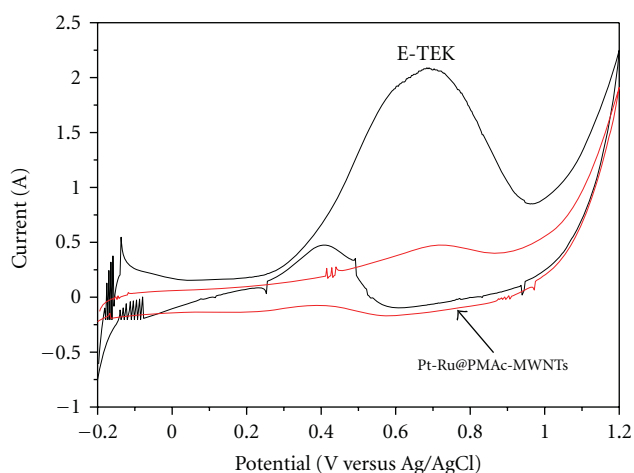
Figure 5 shows the cyclic voltammograms of E-TEK catalyst and the prepared catalysts for 1.0 M MeOH oxidation in 0.5 M  $\text{H}_2\text{SO}_4$  at room temperature. The higher current peak at about 0.6 V versus Ag/AgCl electrode appeared due to methanol oxidation on the commercial E-TEK catalyst, as shown in Figures 5(a), 5(b), and 5(c). However, the methanol oxidation peak for Pt-RuatPAAc-MWNT catalyst and Pt-RuatPMAc-MWNT catalyst were lower than that of the E-TEK catalyst, as shown in Figures 5(a) and 5(b). In the case of Pt-RuatPVPBac-MWNT catalyst, the large catalytic efficiency at 0.8 V was observed. As a result, the prepared Pt-RuatPVPBac-MWNT catalyst can be used on a direct methanol fuel cell electrode.

#### 4. Conclusion

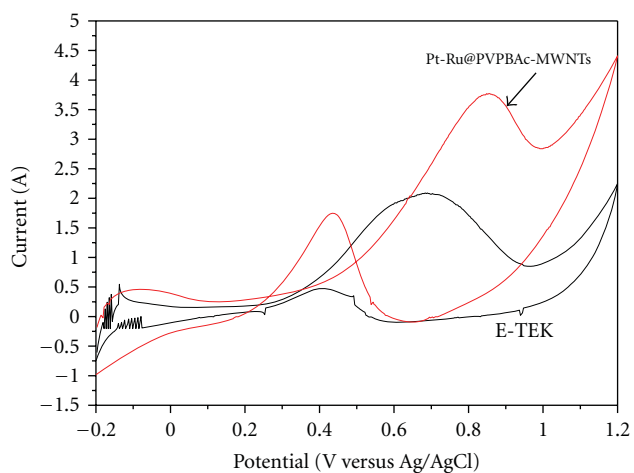
The functionalized MWNTs were prepared by radiation-induced graft polymerization of vinyl monomers with the desired functional group. Subsequently, Pt-Ru nanoparticles were deposited on the surface of the functionalized MWNT for using as a fuel cell-electrode catalyst. The efficiency



(a)



(b)



(c)

FIGURE 5: Comparison of catalytic efficiency among E-TEK catalyst and the prepared catalysts for MeOH oxidation in 0.5 M  $\text{H}_2\text{SO}_4$ . E-TEK catalyst versus Pt-Ru@PAAc-MWNT catalyst, (b) E-TEK catalyst versus Pt-Ru@PMAc-MWNT catalyst, and (c) E-TEK catalyst versus Pt-Ru@PVPBAC-MWNT.

of the prepared catalysts was investigated. The following conclusions are based on the results.

- (1) The catalytic efficiency of Pt-Ru@PVPBAC-MWNT catalyst for CO stripping was higher than that of the commercial E-TECK catalyst in spite of the low metallic content.
- (2) The stripping voltammograms for the adsorbed CO at Pt-Ru@PVPBAC-MWNT catalyst prepared by  $\gamma$ -irradiation reveal that the CO oxidation is energetically favorable at these electrodes.
- (3) The MeOH oxidation peak appeared at 0.8 V on Pt-Ru@PVPBAC-MWNT catalyst prepared by  $\gamma$ -irradiation which appears to be suitable for the electrode assembly in direct methanol fuel cells.

## Acknowledgments

This paper was supported by Nano R&D program and National Nuclear Technology program through the Korea Science and Engineering Foundation funded by the Ministry of Science & Technology. The authors particularly thank the Korea Basic Science Institute (KBSI) for FETEM measurements.

## References

- [1] B. Yang, Q. Lu, Y. Wang et al., "Simple and low-cost preparation method for highly dispersed PtRu/C catalysts," *Chemistry of Materials*, vol. 15, no. 18, pp. 3552–3557, 2003.
- [2] Z. Liu, X. Y. Ling, X. Su, and J. Y. Lee, "Carbon-supported Pt and PtRu nanoparticles as catalysts for a direct methanol fuel cell," *Journal of Physical Chemistry B*, vol. 108, no. 24, pp. 8234–8240, 2004.
- [3] G. Girishkumar, K. Vinodgopal, and P. V. Kamat, "Carbon nanostructures in portable fuel cells: single-walled carbon nanotube electrodes for methanol oxidation and oxygen reduction," *Journal of Physical Chemistry B*, vol. 108, no. 52, pp. 19960–19966, 2004.
- [4] S.-D. Oh, K. R. Yoon, S.-H. Choi et al., "Dispersion of Pt-Ru alloys onto various carbons using  $\gamma$ -irradiation," *Journal of Non-Crystalline Solids*, vol. 352, no. 4, pp. 355–360, 2006.
- [5] S.-D. Oh, B.-K. So, S.-H. Choi et al., "Dispersing of Ag, Pd, and Pt-Ru alloy nanoparticles on single-walled carbon nanotubes by  $\gamma$ -irradiation," *Materials Letters*, vol. 59, no. 10, pp. 1121–1124, 2005.
- [6] K.-D. Seo, S.-D. Oh, S.-H. Choi, S.-H. Kim, H. G. Park, and Y. P. Zhang, "Radiolytic loading of the Pt-Ru nanoparticles onto the porous carbons," *Colloids and Surfaces A*, vol. 313–314, pp. 393–397, 2008.
- [7] D. F. Silva, A. O. Neto, E. S. Pino, M. Linardi, and E. V. Spinacé, "PtRu/C electrocatalysts prepared using  $\gamma$ -irradiation," *Journal of Power Sources*, vol. 170, no. 2, pp. 303–307, 2007.
- [8] H.-B. Bae, J.-H. Ryu, B.-S. Byun, S.-H. Choi, S.-H. Kim, and C.-G. Hwang, "Radiolytic deposition of Pt-Ru catalysts on the conductive polymer coated MWNT and their catalytic efficiency for CO and MeOH," *Advanced Materials Research*, vol. 47–50, part 2, pp. 1478–1481, 2008.
- [9] H.-B. Bae, S.-H. Oh, J.-C. Woo, and S.-H. Choi, "Preparation of Pt-Ru@PPy-MWNT catalysts by  $\gamma$ -irradiation and chemical

- reduction and their adsorption capacity for CO," *Journal Nanoscience and Nanotechnology*, vol. 10, pp. 6901–6906, 2010.
- [10] S.-H. Choi, Y. C. Nho, and G.-T. Kim, "Adsorption of  $Pb^{2+}$  and  $Pd^{2+}$  on polyethylene membrane with amino group modified by radiation-induced graft copolymerization," *Journal of Applied Polymer Science*, vol. 71, no. 4, pp. 643–650, 1999.
- [11] S.-H. Choi and Y. C. Nho, "Adsorption of  $Co^{2+}$  by styrene-g-polyethylene membrane bearing sulfonic acid groups modified by radiation-induced graft copolymerization," *Journal of Applied Polymer Science*, vol. 71, no. 13, pp. 2227–2235, 1999.
- [12] S.-H. Choi and Y. C. Nho, "Adsorption of  $UO_2^{2+}$  by polyethylene adsorbents with amidoxime, carboxyl, and amidoxime/carboxyl group," *Radiation Physics and Chemistry*, vol. 57, no. 2, pp. 187–193, 2000.
- [13] S.-H. Choi and Y. C. Nho, "Radiation-induced graft copolymerization of binary monomer mixture containing acrylonitrile onto polyethylene films," *Radiation Physics and Chemistry*, vol. 58, no. 2, pp. 157–168, 2000.
- [14] S.-H. Choi, K.-P. Lee, and J.-G. Lee, "Adsorption behavior of urokinase by polypropylene film modified with amino acids as affinity groups," *Microchemical Journal*, vol. 68, no. 2-3, pp. 205–213, 2001.
- [15] D.-S. Yang, D.-J. Jung, and S.-H. Choi, "One-step functionalization of multi-walled carbon nanotubes by radiation-induced graft polymerization and their application as enzyme-free biosensors," *Radiation Physics and Chemistry*, vol. 79, no. 4, pp. 434–440, 2010.
- [16] J. Belloni, M. Mostafavi, H. Remita, J.-L. Marignier, and M.-O. Delcourt, "Radiation-induced synthesis of mono- and multi-metallic clusters and nanocolloids," *New Journal of Chemistry*, vol. 22, no. 11, pp. 1239–1255, 1998.
- [17] A. O. Neto, T. R. R. Vasconcelos, R. W. R. V. da Silva, M. Linardi, and E. V. Spinacé, "Electro-oxidation of ethylene glycol on PtRu/C and PtSn/C electrocatalysts prepared by alcohol-reduction process," *Journal of Applied Electrochemistry*, vol. 35, no. 2, pp. 193–198, 2005.
- [18] X. Li and I.-M. Hsing, "Surfactant-stabilized PtRu colloidal catalysts with good control of composition and size for methanol oxidation," *Electrochimica Acta*, vol. 52, no. 3, pp. 1358–1365, 2006.
- [19] M. Tsuji, M. Kubokawa, R. Yano et al., "Fast preparation of PtRu catalysts supported on carbon nanofibers by the microwave-polyol method and their application to fuel cells," *Langmuir*, vol. 23, no. 2, pp. 387–390, 2007.
- [20] Y. Shao, G. Yin, Y. Gao, and P. Shi, "Durability study of PtC and PtCNTs catalysts under simulated PEM fuel cell conditions," *Journal of the Electrochemical Society*, vol. 153, no. 6, pp. A1093–A1097, 2006.
- [21] S. Kim and S.-J. Park, "Effects of chemical treatment of carbon supports on electrochemical behaviors for platinum catalysts of fuel cells," *Journal of Power Sources*, vol. 159, no. 1, pp. 42–45, 2006.
- [22] A. Pozio, M. de Francesco, A. Cemmi, F. Cardellini, and L. Giorgi, "Comparison of high surface Pt/C catalysts by cyclic voltammetry," *Journal of Power Sources*, vol. 105, no. 1, pp. 13–19, 2002.

## Research Article

# Preparation and Magnetic Properties of ZnFe<sub>2</sub>O<sub>4</sub> Nanotubes

Yan Xu,<sup>1</sup> Yantian Liang,<sup>1</sup> Lijuan Jiang,<sup>1</sup> Huarui Wu,<sup>1</sup> Hongzhi Zhao,<sup>1</sup> and Desheng Xue<sup>2</sup>

<sup>1</sup>Physics Department, Xinxiang University, Xinxiang 453003, China

<sup>2</sup>Key Laboratory for Magnetism and Magnetic Materials of the Ministry of Education, Lanzhou University, Lanzhou 730000, China

Correspondence should be addressed to Yan Xu, xuyan04@lzu.cn

Received 19 April 2010; Revised 3 June 2010; Accepted 14 June 2010

Academic Editor: William W. Yu

Copyright © 2011 Yan Xu et al. This is an open access article distributed under the Creative Commons Attribution License, which permits unrestricted use, distribution, and reproduction in any medium, provided the original work is properly cited.

Ordered ZnFe<sub>2</sub>O<sub>4</sub> nanotube arrays with the average outer diameter of 100 nm were prepared in porous anodic aluminum oxide template using an improved sol-gel approach. The morphology was studied by transmission electron and field emission scanning electron microscope. X-ray diffraction result shows that the nanotubes were polycrystalline in structure. The magnetic properties of the prepared ZnFe<sub>2</sub>O<sub>4</sub> nanotubes were also studied. The results show that the sample shows typical superparamagnetism at room temperature and obvious ferromagnetism below blocking temperature.

## 1. Introduction

Spinel ferrites belong to a kind of magnetic materials that can be used in many areas, such as magnetic devices and switching devices [1–3]. Zinc ferrite (ZnFe<sub>2</sub>O<sub>4</sub>) is of interest not only to basic research in magnetism, but also has great potential in technological application, such as magnetic materials [4–10], gas sensors [11], catalysts [12], photocatalysts [13], and absorbent materials [14–18], described by the formula (A)[B]<sub>2</sub>O<sub>4</sub>. Spinel ferrites, which possess the cubic structure, are the (A) and [B] that indicate tetrahedral and octahedral cation sites in a face-centered cubic anion (oxygen) sublattice, respectively. Bulk ZnFe<sub>2</sub>O<sub>4</sub> has a normal spinel structure with Zn<sup>2+</sup> ions in the A-site and Fe<sup>3+</sup> ions in the B-sites. For bulk Zn-ferrite prepared by the conventional ceramic method, the inversion parameter  $\delta$  equals zero (normal spinel). However, in contrast to bulk compound, the nanocrystalline ZnFe<sub>2</sub>O<sub>4</sub> system always shows up as a mixed spinel in which Zn<sup>2+</sup> and Fe<sup>3+</sup> ions are distributed over the A and B-sites. This cationic rearrangement leads to the formation of two magnetic sublattices, which is responsible for the enhanced magnetization displayed when compared with normal ZnFe<sub>2</sub>O<sub>4</sub> [19–21]. It is known that the bulk ZnFe<sub>2</sub>O<sub>4</sub> is a paramagnet at room temperature, however, magnetic order has been observed in its nanoparticles at room temperature [22–28], and similar reports of magnetic properties in ZnFe<sub>2</sub>O<sub>4</sub> ferrite thin films [29–33].

Up to now, only a few groups reported the preparation of ZnFe<sub>2</sub>O<sub>4</sub> nanotubes [34, 35]. There are a few reports of magnetic properties for ZnFe<sub>2</sub>O<sub>4</sub> nanotubes. Thus, the synthesis and magnetic study of ZnFe<sub>2</sub>O<sub>4</sub> nanotubes should be of substantial interest from both fundamental and applied perspective. Herein, we synthesized ZnFe<sub>2</sub>O<sub>4</sub> nanotube arrays by an improved sol-gel template method. The structure and morphology of the ZnFe<sub>2</sub>O<sub>4</sub> nanotubes were characterized and its magnetic properties were studied. Our results show that the sample has superparamagnetism at room temperature, and ferromagnetic below  $T_B$ .

## 2. Experimental

Anodic aluminum oxide (AAO) templates with a pore diameter of about 100 nm were prepared by anodic oxidation of 99.99% pure Al foil in oxalic acid (1.2 M) under two-step anodizing process [36]. The precursor solution was prepared as follows. Fe(NO<sub>3</sub>)<sub>3</sub> and Zn(NO<sub>3</sub>)<sub>2</sub> with a molar ratio of 2 : 1 were dissolved in distilled water to form 0.045 M aqueous solution of nitrate. An amount of citric acid equal to NO<sub>3</sub><sup>-</sup> was dissolved in the mixture solution as a surfactant. The pH value of the solution was adjusted to near 7 by adding ammonia, and then an amount of urea as complexing agent was added into the solution, the molar ratio of NO<sub>3</sub><sup>-</sup> and urea was 1 : 10. All chemicals were of analytical grade and used without further purification. The AAO templates

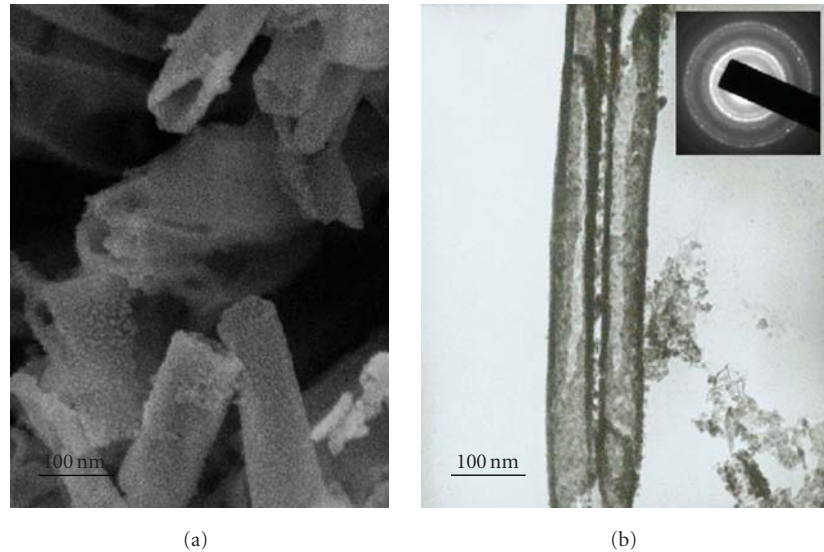


FIGURE 1: (a) SEM (b) TEM and SAED pattern images of the  $\text{ZnFe}_2\text{O}_4$  nanotubes.

were immersed in the precursor solution for the desired time at  $80^\circ\text{C}$ . When the solution was heated, the pH value of the solution increased because of urea undergoing hydrolysis above  $60^\circ\text{C}$ , the  $\text{OH}^-$  combined with  $\text{Fe}^{3+}$ , and  $\text{Zn}^{2+}$  formed negatively charged  $\text{Fe}_2\text{Zn}[(\text{OH})_x](\text{H}_2\text{O})_y$  sol, which is similar to the previous report [37]. Meanwhile, the pore walls of the AAO were positively charged [38]. As coexistence of the charge interaction and the capillary action, it is reasonable that the nanotubes firstly formed near wall areas of the pores and then extended to the center area gradually. Subsequently, the AAO templates were taken out and placed into saturated  $\text{HgCl}_2$  solution to separate templates from the Al substrate. After rinsing with distilled water, the precursor in templates was heat treated in a tube furnace at  $600^\circ\text{C}$  for 10 h in air, and the arrays of  $\text{ZnFe}_2\text{O}_4$  nanotubes inside the AAO templates were obtained.

Field Emission Scanning Electron Microscope (FE-SEM) was performed by using a Hitachi S-4800 $\times$  microscope operated at 10 kV. Structural and morphology data were collected by X-ray diffraction (XRD) using an X'Pertpro Philips diffractometer with  $\text{Cu K}\alpha$  radiation and transmission electron microscope (TEM, Hitachi H-600), respectively. The magnetic properties were measured by a vibrating sample magnetometer (VSM, Lakeshore 7300) and Quantum Design MPMS magnetometer based on superconducting quantum interference device (SQUID).

### 3. Result and Discussion

Figure 1 shows the SEM, TEM images of  $\text{ZnFe}_2\text{O}_4$  nanotubes with diameters of 100 nm. It is apparent that the  $\text{ZnFe}_2\text{O}_4$  nanotubes have a uniform diameter. The mean outer diameter of these nanotubes is about 100 nm, corresponding to the diameter of channels in the AAO template. The thickness of tube wall is about 18 nm. The inset of Figure 1(b) shows the selective area electron diffraction (SAED) pattern of the  $\text{ZnFe}_2\text{O}_4$  nanotubes. The SAED pattern indicates that

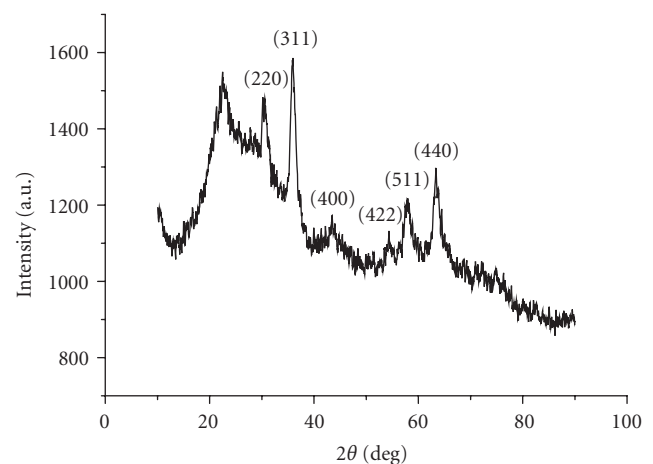


FIGURE 2: X-ray diffraction pattern of the  $\text{ZnFe}_2\text{O}_4$  nanotubes annealed at  $600^\circ\text{C}$ .

the  $\text{ZnFe}_2\text{O}_4$  nanotube is polycrystalline in structure. The pattern for the sample is well resolved in XRD patterns.

Figure 2 shows the X-ray diffraction pattern of the  $\text{ZnFe}_2\text{O}_4$  nanotubes. The reflection peaks are clearly distinguishable. The main peaks correspond to a spinel-type lattice (Fd3m) with lattice parameter  $a = 8.35 \text{ \AA}$ . The lattice parameter  $a$  is smaller than that of bulk ( $a = 8.443 \text{ \AA}$ ) because of crystallite size reduction plus lattice disorder. No other obvious reflections were detected indicating inexistence of a second crystal phase.

The results of zero-field-cooled (ZFC) and field-cooled (FC) measurements of magnetization as function of temperature for the  $\text{ZnFe}_2\text{O}_4$  nanotubes are presented in Figure 3. In order to avoid the nonlinearity effect [6], these measurements were performed at a low field of 50 Oe. For antiferromagnetic materials, typical ZFC/FC curves show a sharp cusp at the Neel temperature. There is no such a cusp

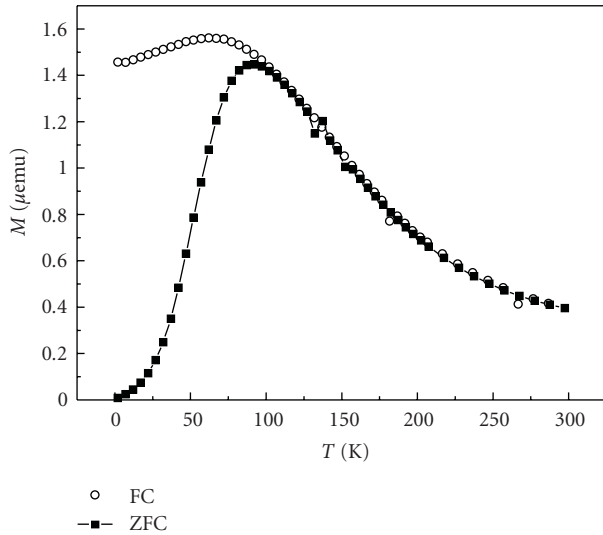


FIGURE 3: Field cooling (FC) and zero-field cooling (ZFC) magnetization curves for  $\text{ZnFe}_2\text{O}_4$  nanotubes measured under a 50 Oe field.

in the present case. However, the ZFC curve shows a peak appearing at about 90 K. This behaviour of ZFC is typical of a superparamagnetic system. The blocking temperature ( $T_B$ ) of 90 K is higher than the Néel temperature of 10 K for the bulk. This may indicate that the samples are indeed the mixed spinels with the Curie temperature at least higher than the observed blocking temperature. Below the blocking temperature, the ZFC and FC curves significantly diverge and the  $\text{ZnFe}_2\text{O}_4$  nanotubes are in the ferrimagnetic state. Above  $T_B$ , the ZFC and FC curves coincide due to the fact that the nanotubes are at the superparamagnetic state.

Figure 4 shows the hysteresis loops measured at 10 K and 150 K. The temperatures are so chosen that one is well below and the other is above the blocking temperature (90 K) for the sample. The inset in Figure 4 is the magnified view of the  $M-H$  curves. The loops at 10 K and 150 K are quite different. At 150 K, the coercivity is near to zero, which shows that the sample is completely superparamagnetic. This is well expected, as for a superparamagnetic system the coercivity is zero. But at 10 K the coercivity is as high as 1420 Oe, and the remanence is obvious. This clearly shows ferrimagnetic coupling due to the A–O–B superexchange interaction and hence existence of a significant amount of cation inversion. Cation distribution has changed from normal to mixed spinel type, that is, some  $\text{Fe}^{3+}$  ions occupy the tetrahedral A-sites and switch on the A–B superexchange interaction. Up to 30 kOe, the magnetization is far from being saturated and still increases with increasing magnetic field, due to the presence of a linear and reversible contribution. Such behaviour indicates the presence of a paramagnetic phase, as it has already pointed out by other authors [39].

#### 4. Conclusion

In summary, we have prepared  $\text{ZnFe}_2\text{O}_4$  nanotube arrays with a diameter of 100 nm by an improved sol-gel template

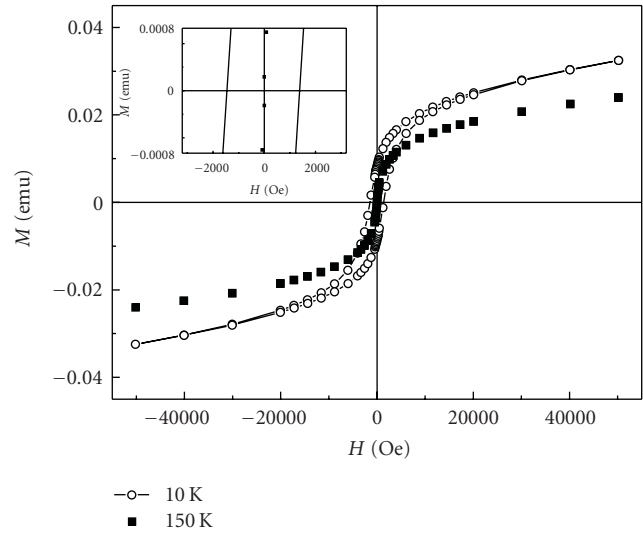


FIGURE 4: Magnetic hysteresis loops of the  $\text{ZnFe}_2\text{O}_4$  nanotubes measured at different temperature.

method. The  $\text{ZnFe}_2\text{O}_4$  nanotube has a uniform diameter with tube wall of about 18 nm. The sample shows typical  $T_B$  temperature of 90 K. When the measured temperature below  $T_B$  at 10 K, the coercivity is as high as 1420 Oe, and the remanence is obvious. These indicate that the nanocrystalline  $\text{ZnFe}_2\text{O}_4$  system shows up as a mixed spinel.

#### Acknowledgments

This work is supported by NSFC (Grant no. 50671046) and J0630313, Program for basic and advanced technology research of Henan Province.

#### References

- [1] R. W. Chantrell and K. O'Grady, "The magnetic properties of fine particles," in *Applied Magnetism*, p. 113, Kluwer Academic Publishers, Dordrecht, The Netherlands, 1994.
- [2] T. Nakamura, T. Tsutaoka, and K. Hatakeyama, "Frequency dispersion of permeability in ferrite composite materials," *Journal of Magnetism and Magnetic Materials*, vol. 138, no. 3, pp. 319–328, 1994.
- [3] T. Tsutaoka, M. Ueshima, T. Tokunaga, T. Nakamura, and K. Hatakeyama, "Frequency dispersion and temperature variation of complex permeability of Ni-Zn ferrite composite materials," *Journal of Applied Physics*, vol. 78, no. 6, pp. 3983–3991, 1995.
- [4] H. Ehrhardt, S. J. Campbell, and M. Hofmann, "Magnetism of the nanostructured spinel zinc ferrite," *Scripta Materialia*, vol. 48, no. 8, pp. 1141–1146, 2003.
- [5] S. Bid and S. K. Pradhan, "Preparation of zinc ferrite by high-energy ball-milling and microstructure characterization by Rietveld's analysis," *Materials Chemistry and Physics*, vol. 82, no. 1, pp. 27–37, 2003.
- [6] A. Kundu, C. Upadhyay, and H. C. Verma, "Magnetic properties of a partially inverted zinc ferrite synthesized by a new coprecipitation technique using urea," *Physics Letters A*, vol. 311, no. 4–5, pp. 410–415, 2003.

- [7] K. Tanaka, M. Makita, Y. Shimizugawa, K. Hirao, and N. Soga, "Structure and high magnetization of rapidly quenched zinc ferrite," *Journal of Physics and Chemistry of Solids*, vol. 59, no. 9, pp. 1611–1618, 1998.
- [8] F. Grasset, N. Labhsetwar, D. Li et al., "Synthesis and magnetic characterization of zinc ferrite nanoparticles with different environments: powder, colloidal solution, and zinc ferrite-silica core-shell nanoparticles," *Langmuir*, vol. 18, no. 21, pp. 8209–8216, 2002.
- [9] H. Deng, X. Li, Q. Peng, X. Wang, J. Chen, and Y. Li, "Monodisperse magnetic single-crystal ferrite microspheres," *Angewandte Chemie. International Edition*, vol. 44, no. 18, pp. 2782–2785, 2005.
- [10] M. H. Sousa, F. A. Tourinho, J. Depeyrot, G. J. Da Silva, and M. C. F. L. Lara, "New electric double-layered magnetic fluids based on copper, nickel, and zinc ferrite nanostructures," *Journal of Physical Chemistry B*, vol. 105, no. 6, pp. 1168–1175, 2001.
- [11] X. Niu, W. Du, and W. Du, "Preparation and gas sensing properties of  $ZnM_2O_4$  ( $M = Fe, Co, Cr$ )," *Sensors and Actuators B*, vol. 99, no. 2-3, pp. 405–409, 2004.
- [12] J. A. Toledo-Antonio, N. Nava, M. Martínez, and X. Bokhimi, "Correlation between the magnetism of non-stoichiometric zinc ferrites and their catalytic activity for oxidative dehydrogenation of 1-butene," *Applied Catalysis A*, vol. 234, no. 1-2, pp. 137–144, 2002.
- [13] J. Qiu, C. Wang, and M. Gu, "Photocatalytic properties and optical absorption of zinc ferrite nanometer films," *Materials Science and Engineering B*, vol. 112, no. 1, pp. 1–4, 2004.
- [14] M. Kobayashi, H. Shirai, and M. Nunokawa, "Measurements of sulfur capacity proportional to zinc sulfidation on sorbent containing zinc ferrite-silica composite powder in pressurized coal gas," *Industrial and Engineering Chemistry Research*, vol. 41, no. 12, pp. 2903–2909, 2002.
- [15] M. Kobayashi, H. Shirai, and M. Nunokawa, "Estimation of multiple-cycle desulfurization performance for extremely low-concentration sulfur removal with sorbent containing zinc ferrite-silicon dioxide composite powder," *Energy and Fuels*, vol. 16, no. 6, pp. 1378–1386, 2002.
- [16] M. Pineda, J. M. Palacios, E. García, C. Cilleruelo, and J. V. Ibarra, "Modelling of performance of zinc ferrites as high-temperature desulfurizing sorbents in a fixed-bed reactor," *Fuel*, vol. 76, no. 7, pp. 567–573, 1997.
- [17] N.-O. Ikenaga, Y. Ohgaito, H. Matsushima, and T. Suzuki, "Preparation of zinc ferrite in the presence of carbon material and its application to hot-gas cleaning," *Fuel*, vol. 83, no. 6, pp. 661–669, 2004.
- [18] F. Tomás-Alonso and J. M. P. Latasa, "Synthesis and surface properties of zinc ferrite species in supported sorbents for coal gas desulphurisation," *Fuel Processing Technology*, vol. 86, no. 2, pp. 191–203, 2004.
- [19] V. Sepelak, M. Zatroch, K. Tkacova, P. Petrovic, S. Wibmann, and K. D. Becker, "Structure and properties of the ball-milled spinel ferrites," *Materials Science and Engineering A*, vol. 22, pp. 226–228, 1997.
- [20] S. A. Oliver, V. G. Harris, H. H. Hamdeh, and J. C. Ho, "Large zinc cation occupancy of octahedral sites in mechanically activated zinc ferrite powders," *Applied Physics Letters*, vol. 76, no. 19, pp. 2761–2763, 2000.
- [21] B. Jeyadevan, K. Tohji, and K. Nakatsuka, "Structure analysis of coprecipitated  $ZnFe_2O_4$  by extended x-ray-absorption fine structure," *Journal of Applied Physics*, vol. 76, no. 10, pp. 6325–6327, 1994.
- [22] C. N. Chinnasamy, A. Narayanasamy, N. Ponpandian, K. Chattopadhyay, H. Guérault, and J.-M. Greneche, "Magnetic properties of nanostructured ferrimagnetic zinc ferrite," *Journal of Physics Condensed Matter*, vol. 12, no. 35, pp. 7795–7805, 2000.
- [23] F. S. Li, L. Wang, J. B. Wang et al., "Site preference of Fe in nanoparticles of  $ZnFe_2O_4$ ," *Journal of Magnetism and Magnetic Materials*, vol. 268, no. 3, pp. 332–339, 2004.
- [24] L. D. Tung, V. Kolesnichenko, G. Caruntu et al., "Annealing effects on the magnetic properties of nanocrystalline zinc ferrite," *Journal of Magnetism and Magnetic Materials*, vol. 319, no. 1–4, pp. 116–121, 2002.
- [25] C. Upadhyay, H. C. Verma, V. Sathe, and A. V. Pimpale, "Effect of size and synthesis route on the magnetic properties of chemically prepared nanosize  $ZnFe_2O_4$ ," *Journal of Magnetism and Magnetic Materials*, vol. 312, no. 2, pp. 271–279, 2007.
- [26] H. Xue, Z. Li, X. Wang, and X. Fu, "Facile synthesis of nanocrystalline zinc ferrite via a self-propagating combustion method," *Materials Letters*, vol. 61, no. 2, pp. 347–350, 2007.
- [27] M. Atif, S. K. Hasanain, and M. Nadeem, "Magnetization of sol-gel prepared zinc ferrite nanoparticles: Effects of inversion and particle size," *Solid State Communications*, vol. 138, no. 8, pp. 416–421, 2006.
- [28] C. Yao, Q. Zeng, G. F. Goya et al., " $ZnFe_2O_4$  nanocrystals: synthesis and magnetic properties," *Journal of Physical Chemistry C*, vol. 111, no. 33, pp. 12274–12278, 2007.
- [29] S. Nakashima, K. Fujita, K. Tanaka, and K. Hirao, "High magnetization and the high-temperature superparamagnetic transition with intercluster interaction in disordered zinc ferrite thin film," *Journal of Physics Condensed Matter*, vol. 17, no. 1, pp. 137–149, 2005.
- [30] J. Chen, G. Srinivasan, S. Hunter, V. Suresh Babu, and M. S. Seehra, "Observation of superparamagnetism in rf-sputtered films of zinc ferrite," *Journal of Magnetism and Magnetic Materials*, vol. 146, no. 3, pp. 291–297, 1995.
- [31] R. Nawathey, R. D. Vispute, S. M. Chaudhari et al., "Pulsed laser-induced vaporization from the surface of a binary oxide (zinc ferrite) and its implications for synthesis of thin films," *Journal of Applied Physics*, vol. 65, no. 8, pp. 3197–3204, 1989.
- [32] M. Taheri, E. E. Carpenter, V. Cestone et al., "Magnetism and structure of  $Zn_xFe_{3-x}O_4$  films processed via spin-spray deposition," *Journal of Applied Physics*, vol. 91, no. 10, Article ID 7595, 3 pages, 2002.
- [33] M. Bohra, S. Prasad, N. Kumar et al., "Large room temperature magnetization in nanocrystalline zinc ferrite thin films," *Applied Physics Letters*, vol. 88, no. 26, Article ID 262506, 2006.
- [34] G. Zhang, C. Li, F. Cheng, and J. Chen, " $ZnFe_2O_4$  tubes: synthesis and application to gas sensors with high sensitivity and low-energy consumption," *Sensors and Actuators B*, vol. 120, no. 2, pp. 403–410, 2007.
- [35] J. Fu, D. Gao, Y. Xu, Z. Yan, and D. Xue, "One-step process to fabricate Fe core/Fe-dimethylsulfoxide shell coaxial nanocables," *Chemistry of Materials*, vol. 20, no. 5, pp. 2016–2019, 2008.
- [36] G. Wu, L. Zhang, B. Cheng, T. Xie, and X. Yuan, "Synthesis of  $Eu_2O_4$  nanotube arrays through a facile sol-gel template approach," *Journal of the American Chemical Society*, vol. 126, no. 19, pp. 5976–5977, 2004.
- [37] J. W. Diggle, T. C. Downie, and C. W. Goulding, "Anodic oxide films on aluminum," *Chemical Reviews*, vol. 69, no. 3, pp. 365–405, 1969.

- [38] L. D. Tung, V. Kolesnichenko, G. Caruntu et al., "Annealing effects on the magnetic properties of nanocrystalline zinc ferrite," *Physica B*, vol. 319, no. 1–4, pp. 116–121, 2002.

## Research Article

# Tailored 3D CuO Nanogrid Formation

Jusang Lee and Pelagia I. Gouma

*Department of Material Science and Engineering, Center for Nanomaterials and Sensor Development,  
State University of New York, Stony Brook, NY 11794, USA*

Correspondence should be addressed to Pelagia I. Gouma, pgouma@notes.cc.sunysb.edu

Received 20 April 2010; Accepted 6 July 2010

Academic Editor: Quanqin Dai

Copyright © 2011 J. Lee and P. I. Gouma. This is an open access article distributed under the Creative Commons Attribution License, which permits unrestricted use, distribution, and reproduction in any medium, provided the original work is properly cited.

This paper reports on the controlled synthesis of 3D CuO nanogrids by the combined use of electrospinning and thermal oxidation of a composite metal mesh/polymer mat architecture. The obtained nanogrids result from three steps encompassing: (i) Cu atom clusters diffusing into the nanofibers producing polymer-metal “core-shell”-type fibers (ii) decomposition of the polymeric shell; (iii) oxidation of the metallic core of the nanofibers to form self-supported, open nanogrids consisting of continuous nanofibers of CuO nanoparticles with an average diameter of 20 nm. The calculated band gap energy of the cupric oxide nanogrids was determined from the UV-Vis spectrum to be 1.32 eV. The unique 3D CuO nanogrids may be used as key components of 3D nanobatteries, photocatalysts, and p-type chemosensors.

## 1. Introduction

Cupric oxide (CuO) is a p-type semiconducting oxide with a monoclinic crystal structure and an indirect band gap of 1.2 eV, with interesting electrochemical, photovoltaic, and catalytic properties [1–3]. CuO have been applied to various applications including heterogeneous catalysis, [1] solar cells, [3] gas sensors, [4] magnetic storage media, [5] and in lithium ion electrodes [6]. Nanostructured CuO offers highly reactive surfaces, and improved optical, electrical, and catalytic properties compared to bulk crystals [7]. The reported variation of the bandgap energy, reducibility, and catalytic reactivity of CuO nanocrystals as a function of crystal shape and size has stimulated interest in exploring novel synthesis methods for this oxide [8–10]. A variety of CuO nanostructures, from nanoneedles and nanoribbons to nanowires, nanorods, and nanosheet configurations, have been fabricated by pulsed laser deposition, sol-gel routes, hydrothermal processing and thermal oxidation [11–20].

Recently, there has been success in producing 3D nanoarchitectures. Liu and Zeng synthesized “dandelion-like” 3D CuO microspheres by a hydrothermal synthesis method, mixing copper nitrate  $\text{Cu}(\text{NO}_3)_2 \cdot 3\text{H}_2\text{O}$  in ethanol solvent, followed by the addition of NaOH,  $\text{NaNO}_3$ , and ammonia

in Teflon-lined stainless steel autoclave at 100°C for 24–36 h [11]. Zhang et al. [12] also fabricated 3D hierarchical CuO “butterfly-like” structures in a solution of cupric chloride ( $\text{CuCl}_2 \cdot 2\text{H}_2\text{O}$ ) and NaOH at 100°C for 15 h by using sodium dodecylbenzene sulfonate (SDBS) as surfactant. However, to the best of our knowledge, there have been no prior reports on the synthesis of 3D CuO nanogrids by the combined use of electrospinning and thermal oxidation.

It was previously shown by other workers that copper clusters can nucleate the growth of copper nanostructures within carbon nanotubes by diffusing through them [21]. In our approach, electrospinning was used to form a nanofibrous template on Cu grids in order to produce interconnected and self-supported 3D nanogrids of pure CuO for the first time by the diffusion and oxidation of Cu inside the polymeric fibers, as discussed below. Transmission electron microscopy studies of metal nanocrystals have shown that the heating effect of a focused electron beam triggers the diffusion of the metal atoms of the material under study within the organic layer of the support grid. This observation led to the hypothesis that tailoring the shape of an organic template to control the diffusion path of Cu atoms under thermal activation along with the synergistic oxidation of the metal may produce controlled 3D nanogrid

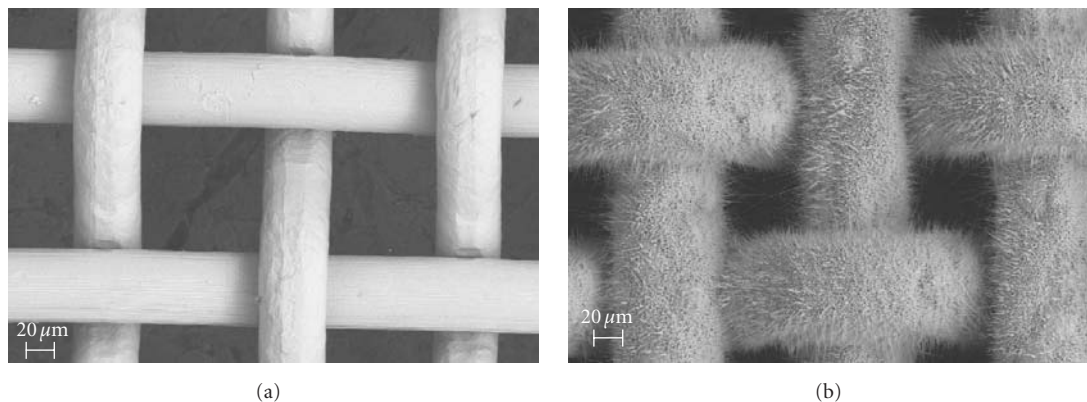


FIGURE 1: (a) SEM image of Cu mesh at room temperature. (b) Cu mesh after thermal oxidation at 600°C for 5 h.

structures. Organic (polyvinylpyrrolidone (PVP) or cellulose acetate (CA)) nanofibers were thus deposited onto the surface of a copper grid (whether an uncoated TEM grid or a plain copper mesh). The obtained 3D CuO nanostructures (continuous and self-supported material, with high porosity and surface area) seem ideal for 3D nanobattery electrodes, catalysts, and p-type chemosensors.

## 2. Experimental Procedure

The synthesis of 3D CuO nanogrids was carried out by thermal oxidation of copper mesh substrates (TWP Inc., 200 mesh, wire dia. 51  $\mu\text{m}$ ) on which PVP (*Sigma-Aldrich*,  $M_w = 1,300,000$ , melting point  $>300^\circ\text{C}$ ) mats were deposited by means of electrospinning (The Cu mesh was first cleaned with ethyl alcohol, then rinsed with deionized water followed by an ultrasonic bath in acetone). PVP precursor solutions were prepared by mixing the powder with ethanol solvent by ultrasonication. The resulting solution was filled into a syringe with a stainless steel needle. The needle was connected to a high-voltage supply and positioned vertically 7 cm above a piece of aluminum foil which acts as a ground electrode. The syringe pump was programmed to dispense 5 mL of 8% (wt/vol) PVP solution at a flow rate of 30  $\mu\text{L}/\text{min}$ . Upon application of a high voltage (18 kV), a solution jet was formed at the needle tip. The solvent evaporated during flight and a nonwoven mat of fibers was deposited on the Cu mesh secured on aluminum foil.

Thermal oxidation of the pure Cu mesh as well as of the composite material (PVP-Cu) was carried out in a resistively heated furnace at a constant rate of 11°C/min in the temperature range from 200°C to 600°C; heating times varied from 2 to 5 hours; and all samples were cooled to ambient temperature. The temperature of the specimen was monitored by placing a thermocouple in the vicinity.

In order to reveal the crystallographic characteristics and to confirm the origin of the CuO nanogrids, to assess the phase evolution involved and the mechanism of formation of the 3D architecture, detailed structural and chemical analyses were performed using high resolution (HRTEM), scanning

transmission (STEM), and analytical electron microscopy (AEM). The morphology and microstructure of the samples were studied using scanning electron microscopy (SEM, LEO 1550) and high-resolution transmission electron microscopy (HRTEM, JEOL JEM-2100F). Scanning transmission electron microscopy (STEM, JEOL JEM-2100F) and energy dispersive spectroscopy (EDS, JEOL JEM-2100F) were used for the chemical characterization of the samples. The CuO nanogrid samples were deposited on holey carbon copper grids for the microscopy and microanalysis studies. The optical absorption spectra of the nanogrids were recorded using UV-Visible spectrometer (ThermoScientific Evolution 300) in the wavelength range of 250–1000 nm at room temperature.

## 3. Results/Discussion

Figure 1(a) shows a scanning electron micrograph of the as-received, pure Cu mesh. It is well-established in the literature [17], that thermal oxidation of the pure Cu mesh produces nanorod structures of copper oxides. Figure 1(b) shows a scanning electron micrograph of the Cu mesh of Figure 1(a) following a heat treatment at 600°C for 5 hours. The Cu meshes treated in air at elevated temperature forms rod shaped nanostructures all over the surface. The diameter and length of these structures could be controlled by varying the temperature and annealing time [17].

This is not the case when a nonwoven polymer mat is deposited on the Cu mesh. Figure 2(a) is a SEM viewgraph of the as-spun PVP nanofibers deposited onto the Cu mesh at ambient conditions. Smooth nanofibers form a non-woven mat on the Cu substrate; the PVP fiber diameters are 500 nm in average and some grew up to 0.8  $\mu\text{m}$  upon branching and at junctions. The structural evolution of the as-synthesized composite nanofiber network is given in Figures 2(b) and 2(c) as a function of processing conditions used. Figure 2(b) is an SEM image illustrating the characteristic morphology of the Cu-PVP structures oxidized in air at 200°C for 2 h, while Figure 2(c) shows the same material following oxidation at 400°C for 2 h. To get an understanding of the growth mechanism of 3D nanogrids, the thermal reaction

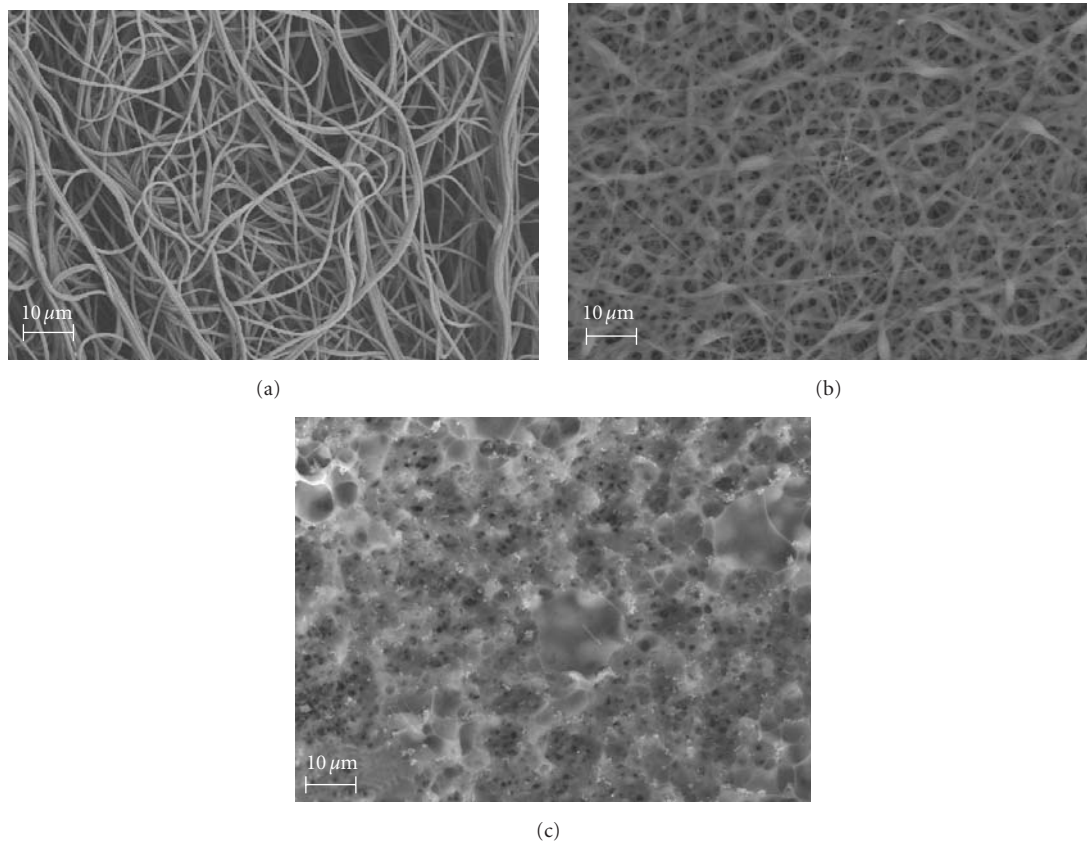


FIGURE 2: (a) SEM image of PVP nanofibers deposited on the Cu mesh substrate by electrospinning at ambient condition. (b) PVP nanofibers deposited on the Cu mesh substrate by electrospinning after thermal oxidation at 200°C for 2 hrs. (c) PVP nanofibers deposited on the Cu mesh substrate by electrospinning after thermal oxidation at 400°C for 2 hrs.

products were captured and analyzed at different stages during their formation.

At the earliest formation stage of the reaction product while the PVP has not yet fully decomposed, that is after a thermal treatment at 200°C for 2 h, the PVP fibers are already filled with Cu (see STEM image in Figure 3). AEM results in STEM mode confirmed the presence of Cu in the core of the “core-shell” configured composite nanofibers (see inset in Figure 3). Thus, copper has diffused and migrated within the fibers that the Cu mesh was in contact with, upon thermal activation. It was not that the Cu deposited onto the electrospun nanofibers by evaporation.

Nanogrids prepared by heat-treating the PVP covered Cu mesh in air at 400°C for 2 hrs were shown to consist of numerous nanocrystals, ranging in size between 16 and 60 nm, connected to each other to form a 3D nanofiber network with open porosity. Figure 4(a) is a montage of five HRTEM micrographs acquired in a sequence illustrating the inner details of the structure of a single nanofiber in the grid (The cropped SEM image is the detailed morphology of the polycrystalline nanofiber originated from Figure 2(c)). Figure 4(b) is an enlarged view of the first micrograph in the sequence of Figure 4(a) and clearly shows that the crystals are interconnected and that pores exist along each individual polycrystalline nanofiber. During these processed the PVP

selectively burned so only oxide 3D nanogrids remained. Figure 4(c) is a further enlarged view of the particle arrangements within the fiber. Measurements of the spacing of their respective lattice planes shown here reveal that they are indeed CuO nanocrystals (the measured lattice spacings are 0.275 and 0.253 nm corresponding to the CuO (110) and CuO (-110) planes, resp.). The corresponding FFT patterns (insert in Figure 4(c)) are consistent with the HRTEM observation. The nanogrids consist of 3D, self-supporting, porous networks of continuous polycrystalline nanowires of CuO equiaxed nanoparticles. Thus, a novel “templating” method has been devised for the synthesis of CuO nanogrids.

In summary, on the basis of combined SEM, HRTEM, STEM, and AEM analyses, the growth mechanism of CuO nanogrids involves the migration and diffusion of Cu atoms/clusters from the metallic substrate through the original polymer nanofibers which act as templates for the development of 3D networks of core-shell type Cu-PVP nanowires; the polymer shell decomposes and the metallic core oxidizes producing porous CuO arrangements upon further thermal treatment. Figure 5 provides a schematic illustration of the suggested process.

The formation of Cu clusters inside the PVP fibers implies that the total free energy of polymer is lowered by the presence of metal atoms, according to the fundamental

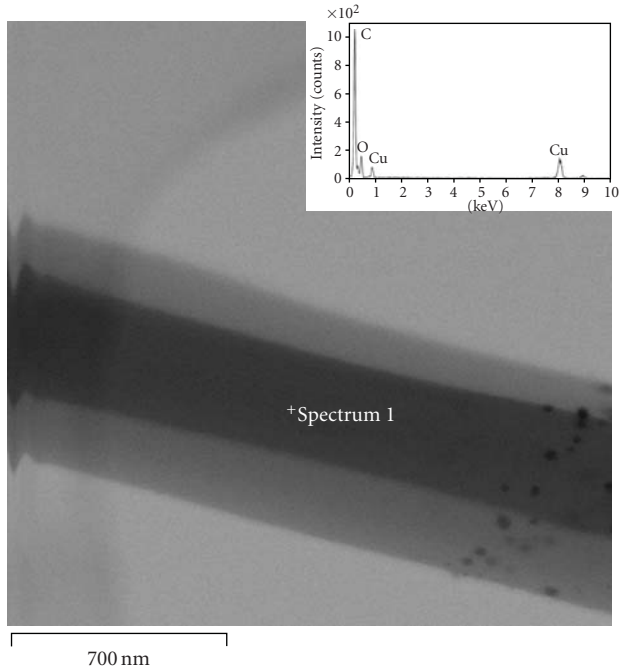
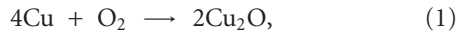


FIGURE 3: STEM image and EDS spectra of the as-prepared copper filled PVP nanofiber heated at 200°C for 2 h. The “+” on the image shows the location of the spectra collected.

nucleation theory [22]. This is the case when PVP undergoes the phase transformation, such the transition to glass. The glass transition temperature of PVP is 180°C. The presence of Cu clusters inside the polymer fibers after a heat-treatment at 200°C (Figure 3) supports the argument made above.

After the calcinations of polymer fiber, the Cu clusters go through these possible oxidation steps:



The oxidation of aggregated Cu cluster and the shrinkage of the fiber structure upon transition from Cu to CuO [20], may explain the formation of the porous nanostructure.

This synthesis method may be applied to other functional metal/metal oxide systems. The high surface area of the nanogrids and the self-supported nature of these nanostructures make them suitable to gas-sensing applications, used as catalysts and potentially as electrodes in 3D miniaturized batteries. With respect to their electronic properties, the band gap energy of the CuO nanogrids has been calculated. The UV-Visible spectrum of CuO 3D nanogrids is presented in Figure 6(a), which shows the optical absorption edge near 940 nm. The optical bandgap energy is estimated using the Kubelka-Munk function

$$F(R) = \frac{(1-R)^2}{2R} = k/s, \quad (3)$$

where  $R$  is the reflectance,  $k$  absorption coefficient, and  $s$  scattering coefficient, respectively, [23]. Figure 6(b) shows a plot of  $(k/s)$  spectrum versus photon energy derived from

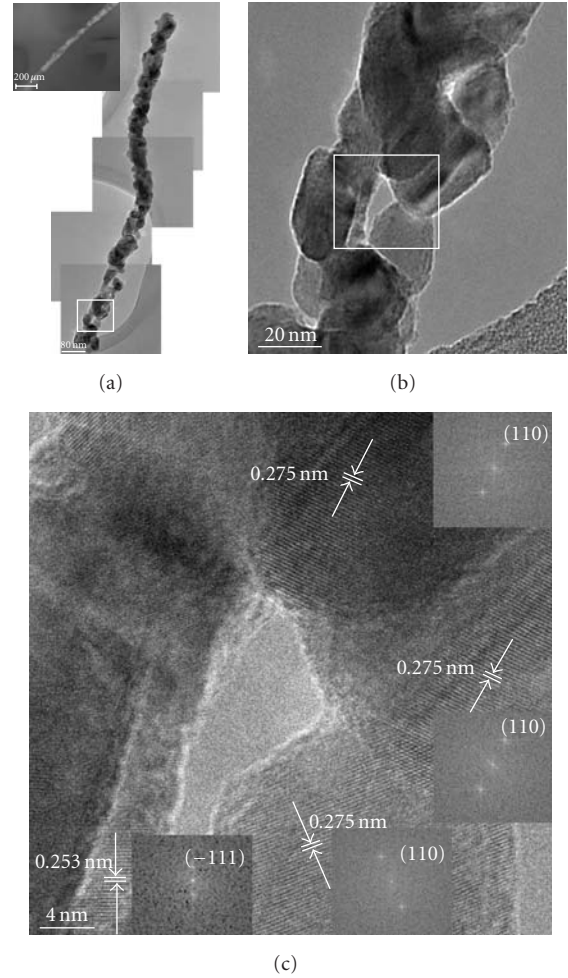


FIGURE 4: (a) Montage of five HRTEM image of the structure of a single nanofiber in the grid oxidized at 400°C for 2 h in air (the cropped SEM image originated from Figure 2(c)). (b) and (c) enlarged view of the particle arrangements within the fiber, corresponding FFT patterns are consistent with the HRTEM observation.

Kubelka-Munk function. The extrapolated value of photon energy at  $k/s = 0$  indicates a bandgap energy ( $E_g$ ) = 1.32 eV. The calculated band gap is slightly larger than the previous reported value for bulk CuO ( $E_g = 1.2$  eV) [1]. According to other workers, these such narrow bandgap materials have many applications in the infrared [24]; therefore, these nanogrids might also be important to photothermal and photoconductive applications [25].

## 4. Conclusion

3D CuO nanogrids were synthesized by direct thermal oxidation of composite substrates consisting of a Cu mesh and electrospun PVP nanofibers deposited on it. The templating action of electrospun nanomats of polymers forms 3D self-organized structures. The average diameter of the CuO grains is 20 nm, while the diameter of the primary 3D nanogrids is 0.5 μm. The estimated band gap energy is ~1.32 eV, which is

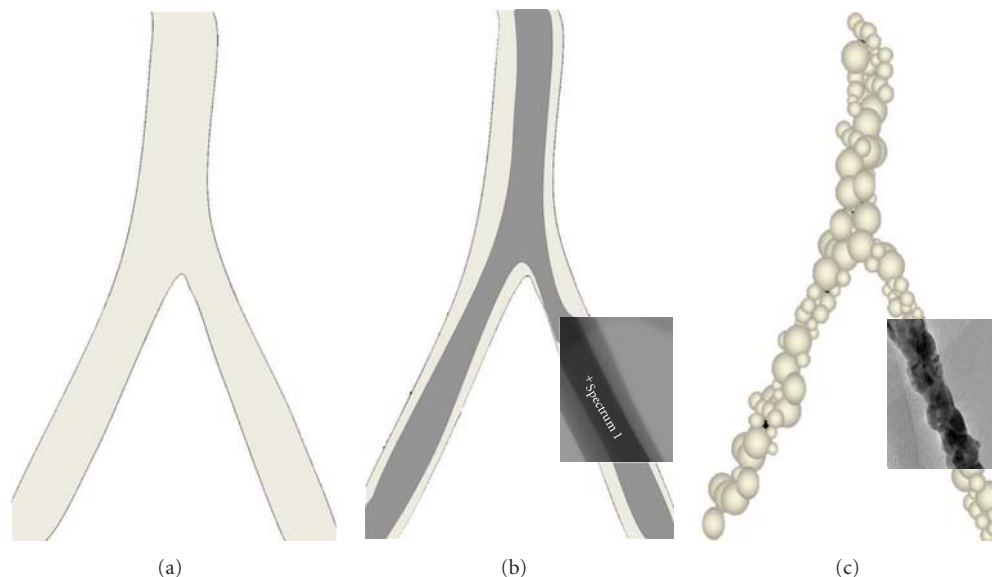


FIGURE 5: A schematic illustration and overlapped TEM images of the formation of CuO 3D nanogrids. (a) PVP nanofibers on the mat deposit on Cu mesh by electrospinning at room temperature; (b) “core-shell” type Cu-PVP nanofiber formation by Cu diffusion and migration through PVP nanofibers (after thermal treatment at 200°C for 2 h (Figure 3)); and (c) Polycrystalline CuO nanowire formed by removal of PVP and oxidation of Cu core (after thermal treatment at 400°C for 2 hrs (Figure 4)).

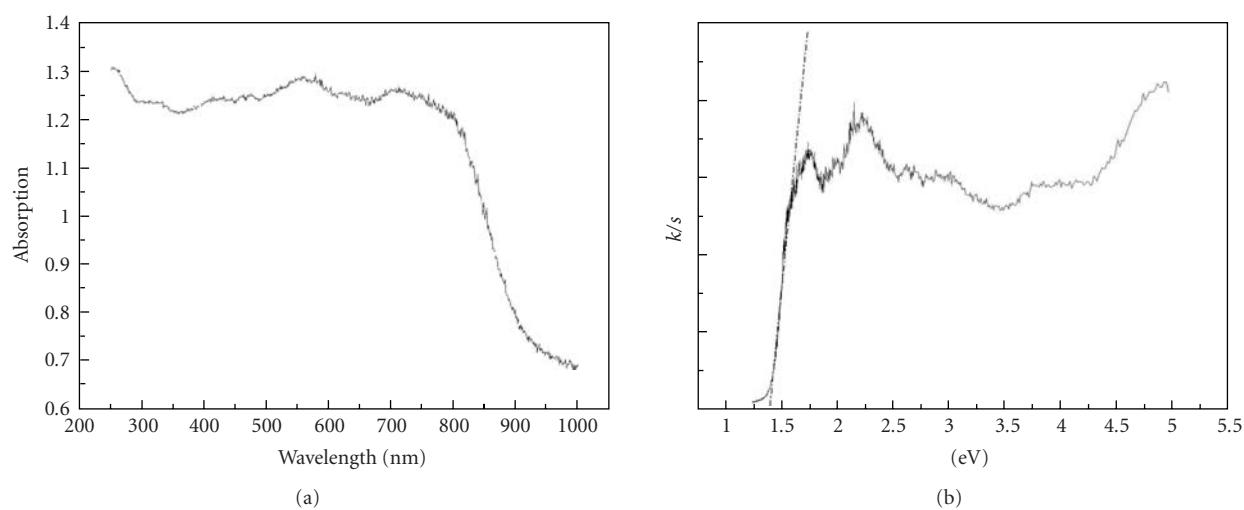


FIGURE 6: (a) UV-vis absorption spectrum of the 3D CuO nanogrids. (b) The corresponding  $k/s$  versus  $E_{\text{phot}}$  curve, indicating that the band gap is 1.32 eV.

larger than the reported value for bulk CuO ( $E_g = 1.2$  eV). Considering the simplicity of the synthesis method of such open 3D nanoarchitectures, the high surface areas of the nanogrids applications are envisioned as 3D nanobattery electrode, photocatalysts and advanced chemo sensors.

## Acknowledgments

The authors wish to thank the Center for Functional Nanomaterials at the Brookhaven National laboratory (Dr. E. Sutter in particular) for access to transmission electron microscopy and microanalysis facilities, and the Lab of Consortium for Inter-Disciplinary Environmental Research

(CIDER) (Dr. A. Orlov) for access to UV-Visible spectrometer. Part of this work was funded by the National Science Foundation.

## References

- [1] J. A. Switzer, H. M. Kothari, P. Poizot, S. Nakanishi, and E. W. Bohannan, “Enantiospecific electrodeposition of a chiral catalyst,” *Nature*, vol. 425, no. 6957, pp. 490–493, 2003.
- [2] K. Nagase, Y. Zheng, Y. Kodama, and J. Kakuta, “Dynamic study of the oxidation state of copper in the course of carbon monoxide oxidation over powdered CuO and Cu<sub>2</sub>O,” *Journal of Catalysis*, vol. 187, no. 1, pp. 123–130, 1999.

- [3] E. Barrera-Calva, J. Méndez-Vivar, M. Ortega-López, L. Huerta-Arcos, J. Morales-Corona, and R. Olayo-González, "Silica-copper oxide composite thin films as solar selective coatings prepared by dipping sol gel," *Research Letters in Materials Science*, vol. 2008, Article ID 190920, 5 pages, 2008.
- [4] J. Zhang, J. Liu, Q. Peng, X. Wang, and Y. Li, "Nearly monodisperse Cu<sub>2</sub>O and CuO nanospheres: preparation and applications for sensitive gas sensors," *Chemistry of Materials*, vol. 18, no. 4, pp. 867–871, 2006.
- [5] R. V. Kumar, Y. Diamant, and A. Gedanken, "Sonochemical synthesis and characterization of nanometer-size transition metal oxides from metal acetates," *Chemistry of Materials*, vol. 12, no. 8, pp. 2301–2305, 2000.
- [6] H. Wu, D. Lin, and W. Pan, "Fabrication, assembly, and electrical characterization of CuO nanofibers," *Applied Physics Letters*, vol. 89, no. 13, Article ID 133125, 3 pages, 2006.
- [7] Z.-S. Hong, Y. Cao, and J.-F. Deng, "A convenient alcohol-thermal approach for low temperature synthesis of CuO nanoparticles," *Materials Letters*, vol. 52, no. 1-2, pp. 34–38, 2002.
- [8] H.-M. Xiao, S.-Y. Fu, L.-P. Zhu, Y.-Q. Li, and G. Yang, "Controlled synthesis and characterization of CuO nanostructures through a facile hydrothermal route in the presence of sodium citrate," *European Journal of Inorganic Chemistry*, no. 14, pp. 1966–1971, 2007.
- [9] S. Anandan and S. Yang, "Emergent methods to synthesize and characterize semiconductor CuO nanoparticles with various morphologies—an overview," *Journal of Experimental Nanoscience*, vol. 2, no. 1-2, pp. 23–56, 2007.
- [10] K. Zhou, R. Wang, B. Xu, and Y. Li, "Synthesis, characterization and catalytic properties of CuO nanocrystals with various shapes," *Nanotechnology*, vol. 17, no. 15, pp. 3939–3943, 2006.
- [11] S. Q. Wang, J. Y. Zhang, and C. H. Chen, "Dandelion-like hollow microspheres of CuO as anode material for lithium-ion batteries," *Scripta Materialia*, vol. 57, no. 4, pp. 337–340, 2007.
- [12] Y. Zhang, W. O. Siu, X. Wang et al., "Hydrothermal synthesis of three-dimensional hierarchical CuO butterfly-like architectures," *European Journal of Inorganic Chemistry*, no. 1, pp. 168–173, 2009.
- [13] H. Guan, C. Shao, B. Chen, J. Gong, and X. Yang, "A novel method for making CuO superfine fibres via an electrospinning technique," *Inorganic Chemistry Communications*, vol. 6, no. 11, pp. 1409–1411, 2003.
- [14] W. Qian, F. Wei, T. Liu, and Z. W. Wang, "The formation mechanism of the coaxial carbon-metal nanowires in a chemical vapor deposition process," *Solid State Communications*, vol. 126, no. 7, pp. 365–367, 2003.
- [15] A. Chen, H. Long, X. Li, Y. Li, G. Yang, and P. Lu, "Controlled growth and characteristics of single-phase Cu<sub>2</sub>O and CuO films by pulsed laser deposition," *Vacuum*, vol. 83, no. 6, pp. 927–930, 2009.
- [16] Y. Liu, L. Liao, J. Li, and C. Pan, "From copper nanocrystalline to CuO nanoneedle array: synthesis, growth mechanism, and properties," *Journal of Physical Chemistry C*, vol. 111, no. 13, pp. 5050–5056, 2007.
- [17] X. Jiang, T. Herricks, and Y. Xia, "CuO nanowires can be synthesized by heating copper substrates in air," *Nano Letters*, vol. 2, no. 12, pp. 1333–1338, 2002.
- [18] A. Kumar, A. K. Srivastava, P. Tiwari, and R. V. Nandedkar, "The effect of growth parameters on the aspect ratio and number density of CuO nanorods," *Journal of Physics: Condensed Matter*, vol. 16, no. 47, pp. 8531–8543, 2004.
- [19] J. F. Xu, W. Ji, Z. X. Shen et al., "Preparation and characterization of CuO nanocrystals," *Journal of Solid State Chemistry*, vol. 147, no. 2, pp. 516–519, 1999.
- [20] S. Han, H.-Y. Chen, Y.-B. Chu, and H. C. Shih, "Phase transformations in copper oxide nanowires," *Journal of Vacuum Science & Technology B*, vol. 23, no. 6, pp. 2557–2560, 2005.
- [21] H. J. Hwang, O.-K. Kwon, and J. W. Kang, "Copper nanocluster diffusion in carbon nanotube," *Solid State Communications*, vol. 129, no. 11, pp. 687–690, 2004.
- [22] J. H. Das and J. E. Morris, "Diffusion and self-gettering of ion-implanted copper in polyimide," *Journal of Applied Physics*, vol. 66, no. 12, pp. 5816–5820, 1989.
- [23] J. B. Gillespie, J. D. Lindberg, and L. S. Laude, "Kubelka-Munk optical coefficients for a barium sulfate white reflectance standard," *Applied Optics*, vol. 14, no. 4, pp. 807–809, 1975.
- [24] T. C. McGill and D. A. Collins, "Prospects for the future of narrow bandgap materials," *Semiconductor Science and Technology*, vol. 8, no. 1S, pp. S1–S5, 1993.
- [25] A. E. Rakhshani, "Preparation, characteristics and photovoltaic properties of cuprous oxide—a review," *Solid State Electronics*, vol. 29, no. 1, pp. 7–17, 1986.

## Research Article

# Preparation and Characterization of Nanozeolite NaA from Rice Husk at Room Temperature with Organic Additives

**Zahra Ghasemi and Habibollah Younesi**

*Department of Environmental Science, Faculty of Natural Resources and Marine Sciences, Tarbiat Modares University, P.O. Box 46414-356, Noor, Iran*

Correspondence should be addressed to Habibollah Younesi, [hunesi@modares.ac.ir](mailto:hunesi@modares.ac.ir)

Received 21 April 2010; Revised 23 August 2010; Accepted 21 November 2010

Academic Editor: Quanqin Dai

Copyright © 2011 Z. Ghasemi and H. Younesi. This is an open access article distributed under the Creative Commons Attribution License, which permits unrestricted use, distribution, and reproduction in any medium, provided the original work is properly cited.

Nanozeolite NaA was synthesized by the hydrothermal method with silica extracted from rice husk as silica source. Amorphous silica with 87.988 wt% SiO<sub>2</sub> was extracted from rice husk ash by a suitable alkali solution. The effect of the crystallization time and the ratio of Na<sub>2</sub>O/SiO<sub>2</sub> on the properties of the final product was investigated. The synthesized nanozeolite was characterized by X-ray diffraction (XRD), scanning electron microscope (SEM), transmission electron microscopy (TEM), energy-dispersive X-ray (EDX) techniques, and Brunauer-Emmett-Teller (BET) method. Results revealed that the crystallization time and alkalinity have significant effects on the structural properties of nanozeolite. Nanocrystals NaA with crystal sizes ranging from 50 to 120 nm were synthesized at room temperature with 3 days aging, without adding any organic additives.

## 1. Introduction

Zeolites are a series of microporous crystals with intricate pores and channels. They have widely been used as catalysts, adsorbents, and ion exchangers [1, 2]. During the past decade, decreasing of the crystallization time at moderate temperature in the preparation of zeolite-type materials has successfully been achieved [3, 4]. Indeed, natural zeolites are often formed at low temperature in closed alkaline and saline lake systems [5]. The crystallization at a moderate temperature has a pronounced effect on the ultimate zeolite crystal size. In addition, the preparation of mesoporous materials at moderate temperature has economic and environmental benefits and can be used for fundamental studies of chemical reactions during the crystallization period [6].

Various types of nanometer-sized zeolites, including NaA, faujasite-X and -Y, ZSM-5, and silicalite-1, have been synthesized by hydrothermal procedures using clear aluminosilicate solutions in the presence of organic templates [7–12]. Recently, Pan et al. reported the synthesis of zeolite A nanocrystals in a two-phase liquid segmented microfluidic reactor using a manipulated organic-template-free system

[13]. However, the application of the organic-templates has several disadvantages. They are nonrecyclable, costly, and require calcinations which results in the production pollution problems [12, 14].

Rice husk has been used as an active silica source for the synthesis of A [15], beta [16], and ZSM-5 zeolites [17]. As an alternative to the pure chemical sources used previously, rice husk is a practical silica source, because it is cheap, less selective, and highly active [18].

Initially, rice husk is burned completely to produce ash, converting the organic siliceous material of the husk into white ash, silica, which is considered an unreactive and useless mineral [19], but by a suitable alkali solution, amorphous silica, which is highly reactive for some zeolites synthesis, can be extracted from the rice husk ash, thus showing rice husk to be an excellent source of high-grade silica [20–22].

The aims of this paper were to extract active amorphous silica from rice husk and to synthesize crystalline zeolite NaA in nanometer size using extracted silica from rice husk at room temperature without adding any organic additives. In order to decrease the cost of the synthesis and reduce

the crystallization time, special attention was paid to the alkalinity and the  $\text{Na}_2\text{O}/\text{SiO}_2$  ratio of initial system which control the kinetics of the zeolite growth.

## 2. Experimental Methods

**2.1. Silica Extraction from Rice Husk.** Rice husks were sieved to eliminate clay particles. They were washed with distilled water, filtered, and then soaked in HCl (Merck, 37%) solution (1 M) for 8 h. After leaching with HCl, they were washed well with distilled water, dried in air, and calcined at  $700^\circ\text{C}$  for 6 h with a constant heating rate  $10^\circ\text{C}/\text{min}$ . The obtained rice husk ash was dissolved in NaOH (2 M, Merck, 98%, 2 M) solution followed by refluxing for 12 h. For complete precipitation, concentrated HCl was added to the dissolved rice husk ash. Above-mentioned precipitated solution was filtered, washed with distilled water till free from chloride ions, and finally dried in an oven at  $110^\circ\text{C}$  overnight.

**2.2. Nanozeolite NaA Preparation.** The nanometer-sized NaA zeolite was synthesized by hydrothermal crystallization [23]. Colloidal crystals of zeolite A were formed in a clear homogenized solution with the following molar composition:  $\text{Na}_2\text{O} : 0.55\text{Al}_2\text{O}_3 : 1\text{SiO}_2 : 150\text{H}_2\text{O}$  in which  $x = 0.9, 6,$  and  $9$  to determine the optimal  $\text{Na}_2\text{O}/\text{SiO}_2$  ratio for synthesis of nanozeolite NaA. The gel composition of NaA nanozeolite was calculated based on the results of the XRF analysis of extracted silica source. Typically, 7.79 g of NaOH was dissolved in 2.77 mol of  $\text{H}_2\text{O}$  and then divided into two equal portions. For the synthesis of NaA zeolite, 1.26 g of silica source, extracted from rice husk ash, was completely dissolved in one portion of the NaOH solution. An aluminate solution was prepared by mixing 2.04 g of  $\text{NaAlO}_2$  (Merck) with another portion of the NaOH solution. After achieving clearness of the solutions, the silicate solution was slowly poured into the aluminate solution with vigorous stirring, which resulted in a clear homogenous solution. The resultant mixture was stored in an oil bath at room temperature ( $T = 25 \pm 2^\circ\text{C}$ ), in a sealed polypropylene bottle under stirrer (250 rpm) conditions for different crystallization periods (1, 2, and 3 days). The solid product obtained in the synthesis was separated by centrifugation (17000 rpm, 30 min) then washed several times with distilled water until the pH value dropped to 8.5. The products were dried in an oven at  $110^\circ\text{C}$  overnight.

**2.3. Characterization.** Proximate analysis of rice husk was measured by ASTM method [24]. The chemical composition of extracted silica powder from rice husk was determined by X-ray fluorescence (XRF, Philips PW2404 Spectrometer). The powder X-ray diffraction (XRD) patterns of NaA zeolite and extracted silica were measured by a Philips diffractometer (X'Pert, PW1800). The patterns were run with Ni-filtered copper radiation ( $K\alpha = 1.5404 \text{ \AA}$ ) at 30 kV voltage and 10 mA current with scanning speed of  $2\theta = 2.5^\circ/\text{min}$ .

The morphology and size of the prepared materials were determined using a scanning electron microscope (SEM,

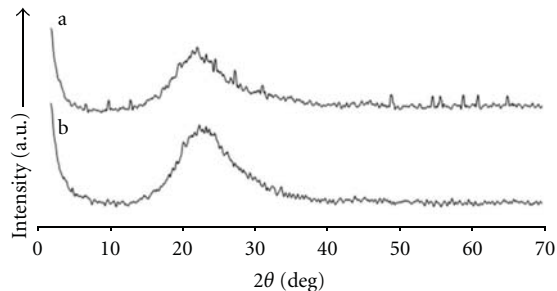


FIGURE 1: The XRD analysis of (a) rice husk ash and (b) extracted silica powder.

Philips XL30, operated at 30 KV). Prior to placing into the microscope, the prepared materials of the NaA zeolite were sprinkled uniformly over an adhesive tape and sputter coated with a thin layer of gold, and an electron acceleration voltage of 20 kV was applied.

Scanning transmission electron microscopy (STEM, Philips CM200 at 200 kV) coupled with selected area electron diffraction (SAED) was used to characterize synthesized zeolite crystals.

The Si/Al ratio of the final nanosized NaA was determined by energy-dispersive X-ray (EDX) spectrophotometer of above-mentioned SEM and XRF techniques.

Nitrogen adsorption/desorption isotherms were measured at  $77^\circ\text{K}$  using a conventional volumetric apparatus. The specific surface area was obtained using the BET (Brunauer-Emmett-Teller) method. The micropore volume and the external surface area were obtained from the  $t$ -plot method.

The loss of ignition (LOI) test was carried out following the SIRIM procedure (ISO 3262-1975). About 1 g of dried sample of the extracted silica was placed in a platinum crucible and ignited in the muffled furnace at  $1000^\circ\text{C}$  for 30 minutes to achieve a constant mass, followed by cooling in a desiccator. The loss of ignition, as a percentage by mass, is given by the formula:

$$\text{LOI, \%} = \frac{M_0 - M_1}{M_0} \times 100, \quad (1)$$

where  $M_0$  is the mass of the sample and  $M_1$  is the mass of the sample after ignition.

## 3. Results and Discussion

**3.1. Characterization of Rice Husk Ash and Extracted Silica.** Proximate analysis showed the presence of 9.26% moisture, 71.62% volatile matter, 18.63% ash, and 0.49% fixed carbon in RHA. The XRD spectra of the ash and extracted silica are shown in Figure 1.

Rice husk was burned completely to produce carbon-free white ash. The silica content of calcined rice husk showed a weight loss of more than 70%. The organic matter of rice husk was removed by heating treatments at high temperatures, but this led to the crystallization of the ash [25]. The XRD analysis of ash (Figure 1(a)), which was heat treated at  $700^\circ\text{C}$  for 6 h, showed the crystalline phase

TABLE 1: The XRF analysis results of ash and extracted silica powder.

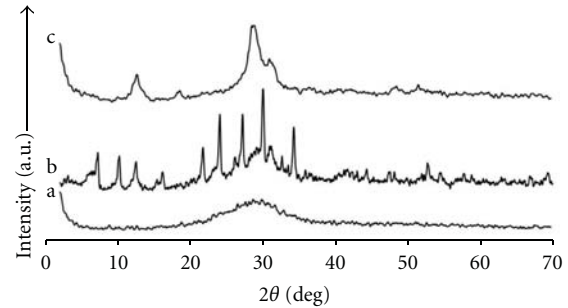
Composition	Ash (wt %)	Extracted silica powder (wt %)
Fe <sub>2</sub> O <sub>3</sub>	0.104	0.047
CaO	0.539	0.085
K <sub>2</sub> O	0.103	0.121
SiO <sub>2</sub>	95.913	87.988
Al <sub>2</sub> O <sub>3</sub>	0.192	0.477
MgO	0.24	0.077
Na <sub>2</sub> O	—	0.566
P <sub>2</sub> O <sub>5</sub>	0.302	—
SO <sub>3</sub>	0.044	—
LOI	2.562	10.64

of the supplied rice husk ash in the form of cristobalite, tridymite, and quartz. The existence of peaks at  $2\theta = 21.9^\circ$ ,  $28.5^\circ$ ,  $31.5^\circ$ , and  $36.3^\circ$  corresponds to the cristobalite [26]. The main characteristic signals at  $20.6^\circ$ ,  $23.3^\circ$ ,  $27.5^\circ$ ,  $30.2^\circ$ , and  $36.1^\circ$  [16] and at  $20.88^\circ$ ,  $26.66^\circ$ ,  $50.18^\circ$ , and  $60^\circ$  [27] were assigned to tridymite and quartz, respectively. The crystallization of the contained silica of the rice husk ash occurs when the husk burning conditions are uncontrolled [28]. The crystalline form of ash in this study is attributed to heating at high temperature rather than to uncontrolled burning conditions, because the burning was controlled at the rate of  $10^\circ\text{C}/\text{min}$ .

The silica powder was extracted from obtained ash by a NaOH solution. According to the XRD analysis (Figure 1(b)), the extracted silica powder was amorphous. The broad peak at  $2\theta$  angle of  $22^\circ$  confirmed the amorphous nature of the silica in this study [29]. Similar properties of rice husk have been reported by Kalapathy et al. [29]. This amorphous form is an advantage towards the preparation of silicon-based materials like zeolites, because the silica is rendered active in its amorphous form [30].

The results of the XRF analysis of rice husk ash and extracted silica powder are listed in Table 1. As the table shows, the weight percent of impurities including Fe<sub>2</sub>O<sub>3</sub>, CaO, MgO, P<sub>2</sub>O<sub>5</sub>, and SO<sub>3</sub> was reduced in extracted silica powder in comparison with rice husk ash, but the weight percent of K<sub>2</sub>O, Al<sub>2</sub>O<sub>3</sub>, and Na<sub>2</sub>O was increased and their amount was calculated and applied for synthesis of the nanozeolite.

The LOI was determined by heating certain quantities of rice husk ash and extracted silica samples in the muffled furnace at  $1000^\circ\text{C}$  for 30 minutes according to the SIRIM procedure (ISO 3262-1975). The LOI amount of rice husk ash was 2.562 which corresponds to the removal of moisture and the coexisting unburned carbon from samples [26]. The LOI amount of extracted silica powder was 10.64%. Considering the LOI amount of ash which showed the little amount of unburned carbon, most of LOI amounts of the extracted silica powder just corresponded to the removal of moisture from sample.

FIGURE 2: The XRD patterns of the final products synthesized using the Na<sub>2</sub>O/SiO<sub>2</sub> ratio equal (a) 0.9, (b) 6, and (c) 9.

The composition of the nanozeolite NaA initial system was calculated based on the XRF analysis results of extracted silica.

**3.2. Effect of Alkalinity and Na<sub>2</sub>O/SiO<sub>2</sub> Ratio.** The effects of Na<sub>2</sub>O/SiO<sub>2</sub> ratio on the NaA nanozeolite was investigated with the compositions of Na<sub>2</sub>O : 0.55Al<sub>2</sub>O<sub>3</sub> : SiO<sub>2</sub> : 150H<sub>2</sub>O, where  $x = 0.9, 6, \text{ and } 9$ . The initial composition of ashes and resulted silica are summarized in Table 2.

The reaction temperature and time are fixed at  $25 \pm 2^\circ\text{C}$  and 3 days, respectively. The crystallization kinetics of any particular zeolite is affected by the alkalinity and composition of the reaction mixture. The Na<sub>2</sub>O/SiO<sub>2</sub> ratio had the most pronounced effect on the kinetics of zeolite formation [6]. The Na cation was added in the form of NaOH, resulting in the concentration of OH<sup>-</sup> being controlled simultaneously by the concentration of cation [31].

The hydroxide ion affects dissolution and polymerization-depolymerization reactions of silicates and aluminosilicates [32].

The increase of this ratio from 0.9 to 6 leads to the growth of the zeolite crystals on the 3rd day. The Na<sub>2</sub>O/SiO<sub>2</sub> = 9 in the system did not form the zeolite A. Figure 2 shows the XRD patterns of A1, A2, and A3. The Na<sub>2</sub>O/SiO<sub>2</sub> = 0.9 is the minimum ratio to dissolve this kind of silica source and to achieve a clear solution with the silica source. The Na<sub>2</sub>O/SiO<sub>2</sub> = 0.9 has resulted in the amorphous phase of the final products (Figure 2(a)).

Peaks at  $2\theta = 7.10, 10.19, \text{ and } 12.49$  [33] show that the pure phase of NaA zeolite was produced with the Na<sub>2</sub>O/SiO<sub>2</sub> = 6 (Figure 2(b)). Al-rich zeolites such as LTA are commonly prepared under basic conditions by using alkali-metal hydroxides as the alkali source. The nature of the inorganic cation is important for the crystallization and the formation of the framework structures of zeolites. Zeolite NaA could be formed from the aluminosilicate gel system in the presence of sodium-containing species [32].

Alkali-metal cations as the source of hydroxide ions are needed to solubilize silicate and aluminate species and a limited structure-directing role to form cage-like structures [34].

The XRD pattern in Figure 2(c) shows that a zeolite phase other than the NaA type is present in the sample A3 with

TABLE 2: Effects of  $\text{Na}_2\text{O}/\text{SiO}_2$  ratio on the final products.

Run	Molar composition of initial solution	$\text{Na}_2\text{O}/\text{SiO}_2$ ratio	Product
A1	$0.9\text{Na}_2\text{O} : 0.55\text{Al}_2\text{O}_3 : 1\text{SiO}_2 : 150\text{H}_2\text{O}$	0.9	Amorphous
A2	$6\text{Na}_2\text{O} : 0.55\text{Al}_2\text{O}_3 : 1\text{SiO}_2 : 150\text{H}_2\text{O}$	6	NaA
A3	$9\text{Na}_2\text{O} : 0.55\text{Al}_2\text{O}_3 : 1\text{SiO}_2 : 150\text{H}_2\text{O}$	9	Na-P1

$\text{Na}_2\text{O}/\text{SiO}_2 = 9$ . The existence of peaks at  $2\theta = 12.46^\circ$ ,  $21.67^\circ$ , and  $28.10^\circ$  [35], which correspond to the zeolite Na-P1, indicates the presence of zeolite Na-P1 instead of zeolite NaA in A3.

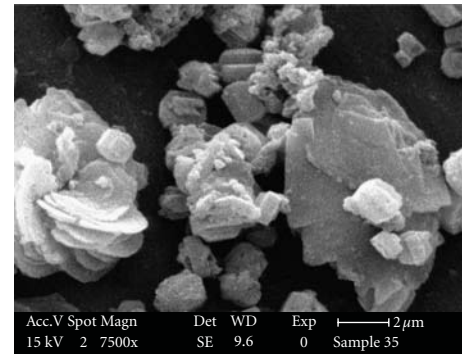
The formation of zeolite P might be due to the silica extracted from the rice husk, which is not reactive towards the formation of zeolite NaA. The silicate source is an additional parameter that can influence the particle size of the product [36]. It was found that the zeolite formation is very sensitive to the nature of the reactants, in particular that of the silica source [6]. This factor is important in the nucleation kinetics [36]. The silica source can influence different aspects of the zeolite crystallization, including the kinetics of crystal growth and the properties of the final product [37, 38]. The use of different silica sources significantly influences the outcome of the synthesis experiments [38]. It has been reported that zeolites synthesized from less reactive rice husk ash silica consist of a mixture of zeolite Y and P [39].

To obtain zeolite A in a reasonable period of time at room temperature, a highly alkaline condition was applied by mixing freshly prepared aluminate and silicate solutions as shown above. A higher alkalinity increases the solubility of the Si and Al sources, decreases the polymerization degree of the silicate anions, and accelerates the polymerization of the polysilicate and aluminate anions. Consequently, the increase of alkalinity will shorten the induction and nucleation periods and speed up the crystallization of zeolites [32].

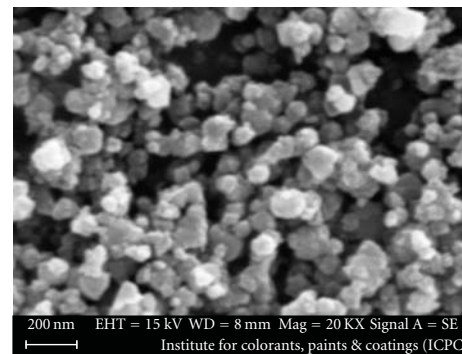
Scanning electron microscopy images were recorded for the extracted silica-synthesized zeolitic samples, some of which are shown in Figure 3. Figure 3(a) shows products in sample A3 of which P type of zeolite was synthesized. Figure 3(b) shows the SEM images of prepared nanozeolite NaA. Figure 3(b) indicates that the particle size of synthesized nanozeolite NaA is fine and within a range of 50–120 nm.

**3.3. Effect of Crystallization Time.** The crystallization time is one of the significant parameters in the synthesis of zeolites. To examine the effect of time, a series of experiments were conducted by changing the crystallization period (1, 2, and 3 days) with the initial system composition constant. The times of crystallization as well as the resulted products with initial composition:  $6\text{Na}_2\text{O} : 0.55\text{Al}_2\text{O}_3 : 1\text{SiO}_2 : 150\text{H}_2\text{O}$  are summarized in Table 3.

The powder X-ray diffraction patterns taken after different hydrothermal crystallization periods, while using the extracted silica as source, maintaining the same (room) temperature and stirrer conditions, are presented in Figure 4. Furthermore, by increasing the reaction time from 1 to 3



(a)



(b)

FIGURE 3: SEM images of the final products synthesized using the  $\text{Na}_2\text{O}/\text{SiO}_2$  ratio equal (a) 9 and (b) 6.TABLE 3: Effects of heating time on the synthesis of NaA zeolite with initial composition:  $6\text{Na}_2\text{O} : 0.55\text{Al}_2\text{O}_3 : 1\text{SiO}_2 : 150\text{H}_2\text{O}$ .

Run	Heating time (d)	Product
A4	1	Amorphous
A5	2	Amorphous
A2	3	NaA

days, the crystallinity of samples increased significantly. It was found that NaA nanocrystals are formed after heating for 3 days at room temperature (Figure 4(c)).

In general, the crystallinity and crystal size increase with increasing time [3]. In present study, we synthesize zeolite NaA at room temperature with nanometer size without using any organic template during 3 days. The crystallization at a moderate temperature has a pronounced effect on the ultimate zeolite crystal size [6].

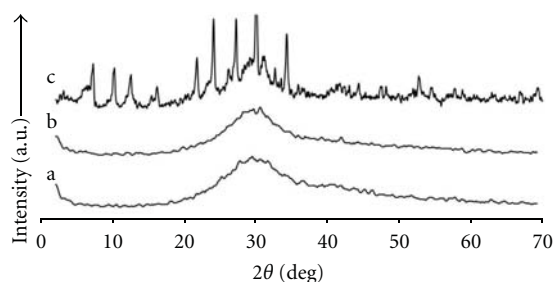


FIGURE 4: The X-ray diffraction patterns of final products after (a) 1, (b) 2, and (c) 3 day.

The increase in temperature will increase both the nucleation rate and the crystal growth rate, in particular the crystal growth rate over the nucleation rate. Thus, higher growth rates and larger crystals have been obtained at higher temperature [32]. As a rule, lower temperatures lead to smaller particle sizes, however, at the expense of a substantial decrease in the rate of crystallization [6]. Sand et al. [40] obtained LTA-type zeolite after 30 days at room temperature. Valtchev and Bozhilov [41] synthesized FAU type of zeolite containing 100–300 nm spherical aggregates under room temperature in a template-free system after 3 weeks of synthesis.

As mentioned above, to obtain nanozeolite NaA in a reasonable period of time at room temperature, a highly alkaline condition was employed. The increase of alkalinity will speed up the crystallization of zeolites. The change of alkalinity also has an effect on the particle size of zeolites. The increase in alkalinity resulted in a decrease of particle size [32].

There are some studies dealing with zeolite synthesis using rice husk ash as an alternative silica source [15–17, 26, 42, 43]. Although rice husk has been used for zeolite synthesis instead of pure chemical sources in all the above-mentioned studies, in the present study, the result of XRD and SEM analysis confirmed synthesis of zeolite NaA with extracted silica from rice husk as source without adding any organic-template and in nanometer size in 3 days, which has not yet been reported.

The synthesis of nanozeolite NaA at room temperature favored the nucleation process, since the activation energy of crystal growth is generally higher than that of nucleation. This is one key route to synthesize nanozeolites without using any organic additives [3, 6, 44].

We have used extracted silica from rice husk as an alternative silica source which reduces the costs of synthesis effectively through utilization of cheap raw materials considering low cost of rice husk. Therefore, utilization of this agricultural byproduct for nanozeolite NaA synthesis would result in the conversion of a low-cost raw material into a high-value added product.

Also, the zeolite NaA synthesized in nanometer size from rice husk without the use of organic template has the advantage of low-cost and other advantages. Most studies on zeolite synthesis have used an organic template [26, 42, 43] which increases the cost of nanozeolite synthesis. Organic

templates, for example, tetramethylammonium hydroxide (TMAOH), make 50% of the production cost and require calcinations which result in the production of  $\text{CO}_2$  and  $\text{NO}_x$  pollution problems [45]. In our environmentally friendly process, no expensive organic template was used, and so, the cost of synthesis can be decreased. Moreover, specialized instruments for burning excess TMA after synthesis were avoided which resulted in lower disposal costs.

Approximately one fifth of the ash is obtained on burning rice husk in air [46]. About 95.913 g of silica was extracted per 100 g of rice husk ash (Table 1). In our study, 1.26 g of extracted silica yielded 0.39 g nanozeolite NaA approximately. Totally, about 74.22 kg of nanozeolite NaA was produced per ton of rice husk, considering low cost of rice husk. Therefore, utilization of this agricultural byproduct for nanozeolite NaA synthesis would result in the conversion of a low-cost raw material into a high-value added product.

**3.4. STEM and SAED Analysis of Synthesized Nanozeolite NaA.** The scanning transmission electron microscopy (STEM) images and selected area electron diffraction (SAED) pattern of the synthesized nanozeolite (sample A2) are shown in Figure 5. The STEM image indicates that the products are crystalline aggregates with a diameter of about 150 nm of NaA nanocrystals (Figure 5(a)). The STEM images confirm that synthesized NaA zeolite has nanometer particle size ranging from 20 to 120 nm (Figure 5(b)).

The SAED pattern (Figure 5(c)) from the synthesized nanozeolite showed that the axes of all whiskers are parallel to the [111] direction, indicating the LTA-type structure [47] and is in well agreement with the XRD study. The diffraction rings also demonstrated that the LTA types were crystalline.

**3.5. EDX and XRF Analysis of Synthesized Nanozeolite NaA.** Typically, zeolite LTA is synthesized with framework Si/Al ratio of 1 [33]. By using tetramethylammonium cation ( $\text{TMA}^+$ ) as the SDA, the Si/Al ratio of LTA framework could be increased up to about 3 [32]. The Si/Al and  $\text{Na}_2\text{O}/\text{SiO}_2$  ratios resulting in nanozeolite NaA after 3 days with  $\text{Na}_2\text{O}/\text{SiO}_2 = 6$  were determined by EDX technique as 1.49 and 0.18, respectively. Figure 6 shows the EDX analysis of obtained nanozeolite NaA. The XRF analysis results of synthesized nanozeolite NaA were LOI : 19.29,  $\text{SiO}_2$  : 35.778,  $\text{Al}_2\text{O}_3$  : 29.444, and  $\text{Na}_2\text{O}$  : 15.295 (wt%). According to the XRF results, the Si/Al and  $\text{Na}_2\text{O}/\text{SiO}_2$  ratios were 1.071 and 0.427, respectively. Thus, the zeolite NaA was confirmed by the EDX and XRF techniques.

**3.6. Surface Texture of Synthesized Nanozeolite NaA.** Figure 7 shows the  $\text{N}_2$  adsorption/desorption isotherm of the prepared NaA nanozeolite. The NaA nanocrystals were characterized by using  $\text{N}_2$  adsorption/desorption measurements to determine their pore volume and surface area. As is known, zeolite A in its sodium form does not adsorb the  $\text{N}_2$  molecule. Indeed, the adsorption/desorption isotherm of the product was of type III, typical of nonporous materials. The increase in the volume adsorbed at very low relative

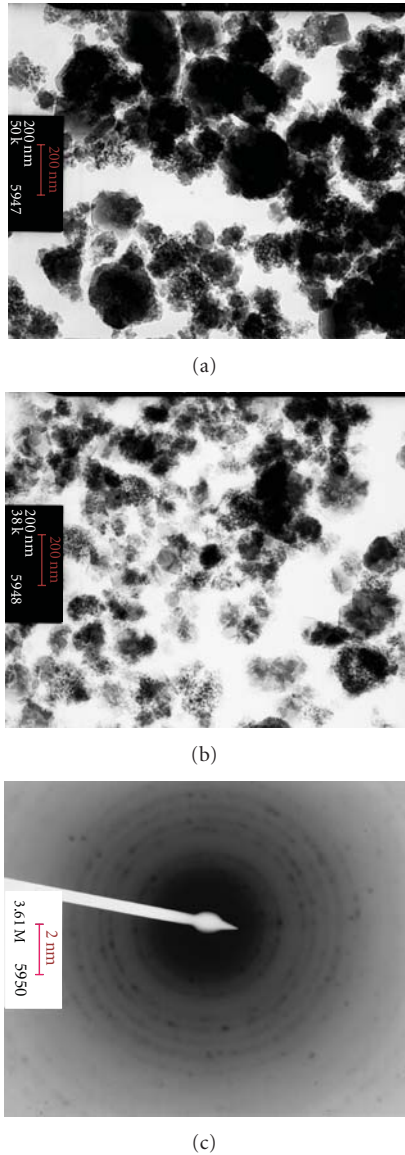


FIGURE 5: (a and b) STEM images of nanosized NaA crystals and (b) SAED pattern obtained from the synthesized nanozeolite.

pressures was due to the presence of a small amount of micropores, most probably related to the adsorption of  $N_2$  molecules at the pore openings [6]. The specific surface area of this sample was  $64.203 \text{ m}^2 \text{ g}^{-1}$ , which suggests nanometer-sized particles. The large external surface of the resulting NaA zeolite was  $62.520 \text{ m}^2 \text{ g}^{-1}$ , which further supports that NaA nanocrystals have small crystallite sizes.

In contrast to pure microporous materials, the steep uptake at low relative pressure is not followed by a flat curve. Instead, an inclination of the curve with an increase of the relative pressure and a second uptake at a high relative pressure, indicative of some textural mesoporosity, can be observed. Due to this secondary porosity, the material synthesized at room temperature showed a higher total pore volume compared to that of the reference zeolite A sample [6].

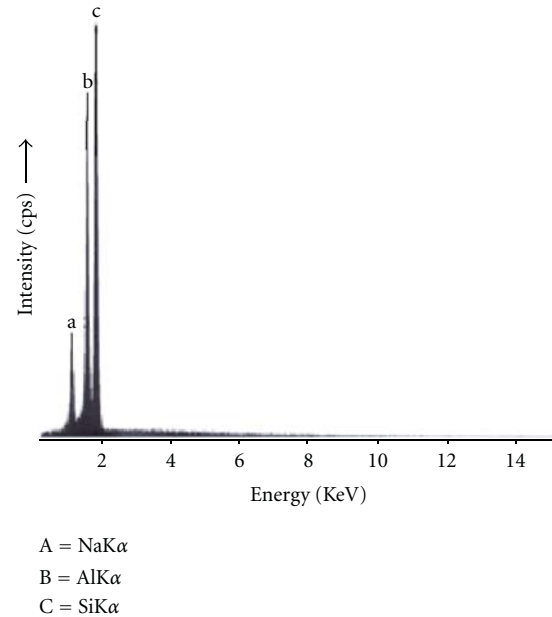


FIGURE 6: The EDX analysis pattern of obtained nanozeolite NaA.

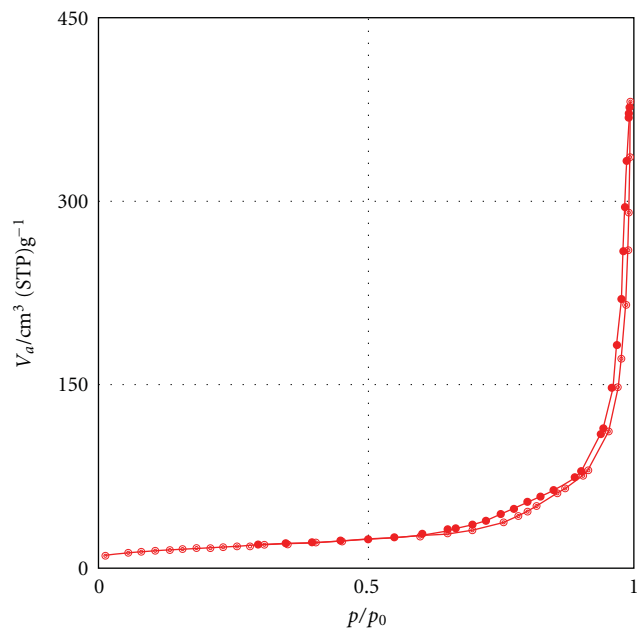


FIGURE 7: The  $N_2$  adsorption/desorption isotherm of the prepared nanozeolite NaA.

#### 4. Conclusion

In this paper, instead of pure chemicals, rice husk which is an agricultural waste was used as silica source for the synthesis of nanozeolite NaA, because silica extracted from rice husk is cheap, less selective, and highly active. Amorphous extracted silica powder was composed of 87.988 wt%  $SiO_2$ . We have successfully synthesized nanometer-sized NaA nanozeolite with extracted silica at room temperature

without using any organic additives. Also, the effect of alkalinity and  $\text{Na}_2\text{O}/\text{SiO}_2$  ratio of initial system, as well as time of crystallization, on the properties of the final product was investigated. Zeolite NaA nanocrystals with crystallite size ranging from 50–120 nm were obtained from a sodium aluminosilicate solution at room temperature in 3 days under  $\text{Na}_2\text{O}/\text{SiO}_2 = 6$  conditions. Thus the aims to lower costs and to shorten crystallization time were both found possible through the study.

To the best of our knowledge, this is the first report on the hydrothermal synthesis of zeolite NaA nanocrystals with rice husk as source of extracted silica, without using any organic additives during the whole crystallization process. Our environmentally friendly process reduces the costs of synthesis effectively through the utilization of cheap raw materials and also by avoiding consumption of expensive chemical sources as template.

## Acknowledgments

This study was supported by a research grant from Tarbiat Modares University (TMU), Iran Nanotechnology Initiative Council, and SPAG Zeolite R & D Group. The authors wish to thank Mr. F. Farhadi, Mr. M. Sardari, and Mr. I. Sourinejad for their technical assistance during the experiments and Ellen Vuosalo Tavakoli for the final editing of the English text.

## References

- [1] D. W. Breck, *Zeolite Molecular Sieves*, John Wiley & Sons, London, UK, 1974.
- [2] R. M. Barrer, *Hydrothermal Chemistry of Zeolites*, Academic Press, London, UK, 1982.
- [3] B. Z. Zhan, M. A. White, M. Lumsden et al., "Control of particle size and surface properties of crystals of NaX zeolite," *Chemistry of Materials*, vol. 14, no. 9, pp. 3636–3642, 2002.
- [4] S. Mintova, N. H. Olson, V. Valtchev, and T. Bein, "Mechanism of zeolite a nanocrystal growth from colloids at room temperature," *Science*, vol. 283, no. 5404, pp. 958–960, 1999.
- [5] R. W. Tschernich, *Zeolites of the World*, Geoscience Press Inc., Phoenix, Ariz, USA, 1992.
- [6] V. P. Valtchev, L. Tosheva, and K. N. Bozhilov, "Synthesis of zeolite nanocrystals at room temperature," *Langmuir*, vol. 21, no. 23, pp. 10724–10729, 2005.
- [7] G. Zhu, S. Qiu, J. Yu et al., "Synthesis and characterization of high-quality zeolite LTA and FAU single nanocrystals," *Chemistry of Materials*, vol. 10, pp. 1483–1486, 1998.
- [8] R. Ravishankar, C. Kirschhock, B. J. Schoeman et al., "Physicochemical characterization of silicalite-1 nanophase material," *Journal of Physical Chemistry B*, vol. 102, no. 15, pp. 2633–2639, 1998.
- [9] S. Mintova, V. Valtchev, I. Kiricsi, G. Pál-Borbély, J. B. Nagy, and H. G. Karge, *Synthesis of Nanosized FAU-Type Zeolite Studies in Surface Science and Catalysis*, Elsevier, Cambridge, Mass, USA, 1999.
- [10] C. Madsen and C. J. H. Jacobsen, "Nanosized zeolite crystals - Convenient control of crystal size distribution by confined space synthesis," *Chemical Communications*, no. 8, pp. 673–674, 1999.
- [11] M. Xu, M. Cheng, and X. Bao, "Growth of ultrafine zeolite Y crystals on metakaolin microspheres," *Chemical Communications*, no. 19, pp. 1873–1874, 2000.
- [12] H. Wang, Z. Wang, and Y. Yan, "Colloidal suspensions of template-removed zeolite nanocrystals," *Chemical Communications*, no. 23, pp. 2333–2334, 2000.
- [13] Y. Pan, M. Ju, J. Yao, L. Zhang, and N. Xu, "Preparation of uniform nano-sized zeolite A crystals in microstructured reactors using manipulated organic template-free synthesis solutions," *Chemical Communications*, no. 46, pp. 7233–7235, 2009.
- [14] E. Roland, H. G. Karge, and J. Weitkamp, "Hindustrial production of zeolites," *Studies in Surface Science and Catalysis*, vol. 46, pp. 645–659, 1989.
- [15] H. Nur, "Direct synthesis of NaA zeolite from rice husk and carbonaceous rice husk ash," *Indonesian Journal of Agricultural Sciences*, vol. 1, pp. 40–45, 2001.
- [16] D. Prasetyoko, Z. Ramli, S. Endud, H. Hamdan, and B. Sulikowski, "Conversion of rice husk ash to zeolite beta," *Waste Management*, vol. 26, no. 10, pp. 1173–1179, 2006.
- [17] A. V. Rawtani, M. S. Rao, and K. V. G. K. Gokhale, "Synthesis of ZSM-5 zeolite using silica from rice husk ash," *Industrial and Engineering Chemistry Research*, vol. 28, no. 9, pp. 1411–1414, 1989.
- [18] Z. Ramli, *Rhenium-impregnated zeolites: synthesis, characterization and modification as catalysts in the metathesis of alkanes*, Ph.D. thesis, Universiti Teknologi Malaysia, 1995.
- [19] M. Y. A. Fuad, Z. Ismail, Z. A. M. Ishak, and A. K. M. Omar, "Application of rice husk ash as fillers in polypropylene: effect of titanate, zirconate and silane coupling agents," *European Polymer Journal*, vol. 31, no. 9, pp. 885–893, 1995.
- [20] M. Bhagiyalakshmi, R. Anuradha, M. Palanichamy, and H. T. Jang, "Dextero template-free synthesis of ferrisilicate with MFI morphology using rice husk ash," *Journal of Non-Crystalline Solids*, vol. 356, no. 23-24, pp. 1204–1209, 2010.
- [21] A. K. Dalai, M. S. Rao, and K. V. G. K. Gokhale, "Synthesis of NaX zeolite using silica from rice husk ash," *Industrial and Engineering Chemistry Product Research and Development*, vol. 24, no. 3, pp. 465–468, 1985.
- [22] U. Kalapathy, A. Proctor, and J. Shultz, "An improved method for production of silica from rice hull ash," *Bioresource Technology*, vol. 85, no. 3, pp. 285–289, 2002.
- [23] W. Fan, K. Morozumi, R. Kimura, T. Yokoi, and T. Okubo, "Synthesis of nanometer-sized sodalite without adding organic additives," *Langmuir*, vol. 24, no. 13, pp. 6952–6958, 2008.
- [24] X. Shuangning, L. Zhihe, L. Baoming, Y. Weiming, and B. Xueyuan, "Devolatilization characteristics of biomass at flash heating rate," *Fuel*, vol. 85, no. 5-6, pp. 664–670, 2006.
- [25] R. V. Krishnarao, J. Subrahmanyam, and T. Jagadish Kumar, "Studies on the formation of black particles in rice husk silica ash," *Journal of the European Ceramic Society*, vol. 21, no. 1, pp. 99–104, 2001.
- [26] K. Kordatos, S. Gavela, A. Ntziouni, K. N. Pistiolas, A. Kyritsi, and V. Kasselouri-Rigopoulou, "Synthesis of highly siliceous ZSM-5 zeolite using silica from rice husk ash," *Microporous and Mesoporous Materials*, vol. 115, no. 1-2, pp. 189–196, 2008.
- [27] J. Chisholm, "Comparison of quartz standards for X-ray diffraction analysis: HSE A9950 (Sikron F600) and NIST SRM 1878," *Annals of Occupational Hygiene*, vol. 49, no. 4, pp. 351–358, 2005.
- [28] H. Hamdan, M. N. M. Muhid, S. Endud, E. Listiorini, and Z. Ramli, "Si MAS NMR, XRD and FESEM studies of rice husk

- silica for the synthesis of zeolites,” *Journal of Non-Crystalline Solids*, vol. 211, no. 1-2, pp. 126–131, 1997.
- [29] U. Kalapathy, A. Proctor, and J. Shultz, “A simple method for production of pure silica from rice hull ash,” *Bioresource Technology*, vol. 73, no. 3, pp. 257–262, 2000.
- [30] J. Payá, J. Monzó, M. V. Borrachero, A. Mellado, and L. M. Ordoñez, “Determination of amorphous silica in rice husk ash by a rapid analytical method,” *Cement and Concrete Research*, vol. 31, no. 2, pp. 227–231, 2001.
- [31] E. M. Flanigen, B. M. Lok, R. L. Patton et al., “Aluminophosphate molecular sieves and the periodic table,” *Studies in Surface Science and Catalysis*, vol. 28, pp. 103–112, 1986.
- [32] J. Yu, C. Jiri, S. Ferdi et al., “Chapter 3 Synthesis of zeolites,” *Studies in Surface Science and Catalysis*, vol. 168, pp. 39–103, 2007.
- [33] M. M. J. Treacy and J. B. Higgins, *Linde Type A, Hydrated Collection of Simulated XRD Powder Patterns for Zeolites*, Elsevier Science B.V., Amsterdam, The Netherlands, 5th edition, 2007.
- [34] E. J. P. Feijen, J. A. Martens, P. A. Jacobs et al., “Zeolites and their mechanism of synthesis,” *Studies in Surface Science and Catalysis*, vol. 84, pp. 3–21, 1994.
- [35] M. M. J. Treacy and J. B. Higgins, *Collection of Simulated XRD Powder Patterns for Zeolites*, Structure Commission of the International Zeolite Association, 2001.
- [36] F. Kleitz, F. Marlow, G. D. Stucky, and F. Schüth, “Mesoporous silica fibers: synthesis, internal structure, and growth kinetics,” *Chemistry of Materials*, vol. 13, no. 10, pp. 3587–3595, 2001.
- [37] K. E. Hamilton, E. N. Coker, A. Sacco, A. G. Dixon, and R. W. Thompson, “The effects of the silica source on the crystallization of zeolite NaX,” *Zeolites*, vol. 13, no. 8, pp. 645–653, 1993.
- [38] J. C. Jansen, H. V. Bekkum, E. M. Flanigen, P. A. Jacobs, and J. C. Jansen, “Chapter 5A The preparation of oxide molecular sieves A. Synthesis of zeolites,” *Studies in Surface Science and Catalysis*, vol. 137, pp. 175–227, 2001.
- [39] Z. Ramli, E. Listiorini, and H. Hamdan, “Optimization and reactivity study of silica in the synthesis of zeolites from rice husk,” *Journal Teknologi*, vol. 25, pp. 27–35, 1996.
- [40] L. B. Sand, A. Sacco, R. W. Thompson, and A. G. Dixon, “Large zeolite crystals: their potential growth in space,” *Zeolites*, vol. 7, no. 5, pp. 387–392, 1987.
- [41] V. P. Valtchev and K. N. Bozhilov, “Transmission electron microscopy study of the formation of FAU-type zeolite at room temperature,” *Journal of Physical Chemistry B*, vol. 108, no. 40, pp. 15587–15598, 2004.
- [42] S. Loiha, S. Prayoonpokarach, P. Songsiriritthigun, and J. Wittayakun, “Synthesis of zeolite beta with pretreated rice husk silica and its transformation to ZSM-12,” *Materials Chemistry and Physics*, vol. 115, no. 2-3, pp. 637–640, 2009.
- [43] M. M. Mohamed, F. I. Zidan, and M. Thabet, “Synthesis of ZSM-5 zeolite from rice husk ash: characterization and implications for photocatalytic degradation catalysts,” *Microporous and Mesoporous Materials*, vol. 108, no. 1–3, pp. 193–203, 2008.
- [44] M. Smaïhi, O. Barida, and V. Valtchev, “Investigation of the crystallization stages of LTA-type zeolite by complementary characterization techniques,” *European Journal of Inorganic Chemistry*, no. 24, pp. 4370–4377, 2003.
- [45] R. K. Vempati, R. Borade, R. S. Hegde, and S. Komarneni, “Template free ZSM-5 from siliceous rice hull ash with varying C contents,” *Microporous and Mesoporous Materials*, vol. 93, no. 1–3, pp. 134–140, 2006.
- [46] T. H. Liou, “Preparation and characterization of nano-structured silica from rice husk,” *Materials Science and Engineering A*, vol. 364, no. 1-2, pp. 313–323, 2004.
- [47] V. P. Valtchev and K. N. Bozhilov, “Evidences for zeolite nucleation at the solid-liquid interface of gel cavities,” *Journal of the American Chemical Society*, vol. 127, no. 46, pp. 16171–16177, 2005.

## Research Article

# Towards a Reproducible Synthesis of High Aspect Ratio Gold Nanorods

Susanne Koeppel,<sup>1</sup> Christian Solenthaler,<sup>1</sup> Walter Caseri,<sup>2</sup> and Ralph Spolenak<sup>1</sup>

<sup>1</sup>Laboratory for Nanometallurgy, Department of Materials, ETH Zürich, 8093 Zürich, Switzerland

<sup>2</sup>Polymer Technology, Department of Materials, ETH Zürich, 8093 Zürich, Switzerland

Correspondence should be addressed to Walter Caseri, walter.caseri@mat.ethz.ch

Received 29 April 2010; Accepted 18 July 2010

Academic Editor: Quanqin Dai

Copyright © 2011 Susanne Koeppel et al. This is an open access article distributed under the Creative Commons Attribution License, which permits unrestricted use, distribution, and reproduction in any medium, provided the original work is properly cited.

The seed-mediated method in presence of high concentrations of CTAB is frequently implemented in the preparation of high aspect ratio gold nanorods (i.e., nanorods with aspect ratios of 5 or more); however, the reproducibility has still been limited. We rendered the synthesis procedure simpler, decreased the susceptibility to impurities, and improved the reproducibility of the product distribution. As a result of the high aspect ratios, longitudinal plasmon absorptions were shifted up to very high absorption maxima of 1955 nm in UV-vis-NIR spectra (since this band is completely covered in aqueous solution by the strong absorption of water, the gold species were embedded in poly(vinyl alcohol) films for UV-vis-NIR measurements). Finally, the directed particle growth in (110) direction leads to the conclusion that the adsorption of CTAB molecules at specific crystal faces accounts for nanorod growth and not cylindrical CTAB micelles, in agreement with other observations.

## 1. Introduction

The preparation of gold nanorods has found wide attention during the last decade since many characteristics of nanoscale materials are size- and shape-dependent including their optical, electronic, and catalytic properties. Spherical particles form readily in common synthesis methods for gold nanoparticles, but if the generation of spherical particles is suppressed by application of special conditions, besides rods [1, 2] also cubes [3–5], triangles [4, 6], and prisms [6] can arise. The synthesis of low aspect ratio nanorods, that is, nanorods with aspect ratios of 3 or less, has been reported in high yields [3, 4, 7–9] and can readily be reproduced (Figure 1). Yet the controlled and reproducible fabrication of high aspect ratio gold nanorods, that is, nanorods with an aspect ratio of 5 or more, by the most common method is still crucial. Therefore, fundamental aspects such as vis-NIR absorption spectra of high aspect ratio nanorods or their principal growth mechanism are still not connectedly investigated.

A number of synthesis methods for high aspect ratio rod-like nanocrystals have been described [1, 6, 10–14], such

as the template method [15, 16], electrochemical methods [2, 17], microwave rapid heating [18], and the seed-mediated growth method [10, 19, 20]. The last synthesis procedure, which was favorably introduced by Murphy and coworkers in 2001 [1], has found most attention so far. Indeed, this way is accessible with ubiquitous laboratory equipment and offers the possibility to prepare higher quantities of nanoparticles than with other methods [21]. However, it has been pointed out that the reproducibility of the results thus obtained is limited [3, 7], in line with our own experiences: the yield of the nanorods varies considerably—in some attempts high aspect ratio nanorods are almost completely absent, and those samples containing high aspect ratio nanorods contain areas with large fractions of spherical particles or low aspect ratio nanorods, and even large areas without high aspect ratio nanorods are present (Figure 2).

Many approaches have been undertaken to improve the original seed-mediated method, in particular by varying different parameters such as seed aging time [19], seed concentration or metal to seed ratio [4, 10, 19, 20], time intervals between the synthesis steps [10], pH value [10], additives [4, 5, 10, 11, 20], temperature [12], growth time

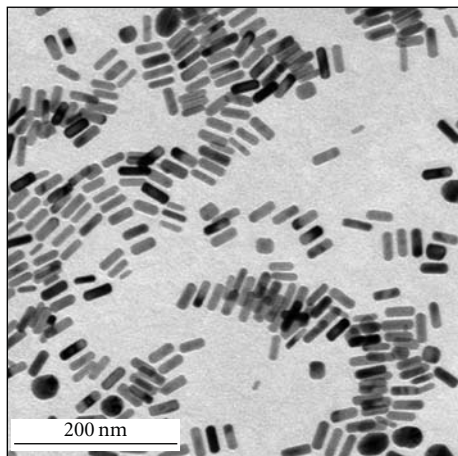


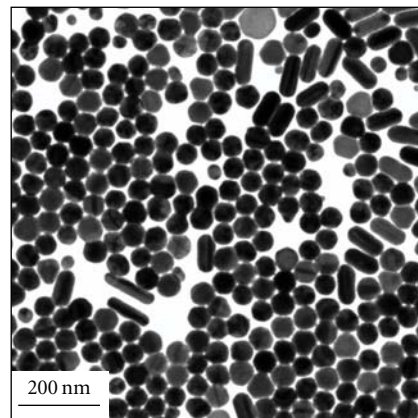
FIGURE 1: TEM image of an area with representative product distribution in samples containing low aspect ratio gold nanorods, prepared according to the seed-mediated method (in presence of small quantities of silver ions [3, 4, 7–9]). This image strongly resembles those reported elsewhere and shows that the synthesis of low aspect ratio gold nanorods is well reproducible (in contrast to high aspect ratio nanorods described so far).

[5], nature of the surfactant required for nanorod generation [6, 8], and the use of cosurfactants [5, 19]. In spite of this, the above addressed problems with respect to the creation of samples with high aspect ratio gold nanorods still persist.

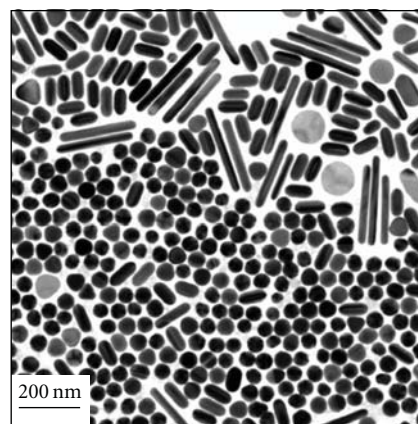
The limited reproducibility associated with the seed-methods described so far could be due to the relatively high number of the involved steps. In fact, we describe in the following that the reproducibility can be improved by the reduction of steps, which also renders the product formation less susceptible to impurities. Also, a simple method for the removal of excess surfactant required for the seed-mediated method was developed. The samples thus obtained were suited for the experimental determination of the position of the longitudinal plasmon absorption band of the gold rods in vis-NIR absorption spectra, which has been explored mainly with low aspect ratio nanorods so far [22–25], although also samples with high aspect ratio have been addressed [26, 27]. Further, the evaluation of electron diffraction patterns and other aspects provided information on the principal growth mechanism of the high aspect ratio nanorods.

## 2. Experimental

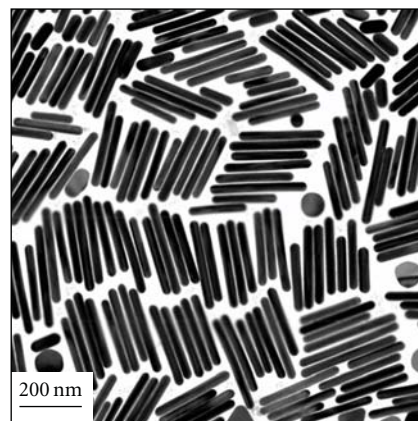
Hexadecyltrimethylammonium bromide (CTAB, designation H6269: 99%, or H5882:  $\geq 98\%$ , resp.) was purchased from Sigma or Fluka (CTAB, 96%), respectively. Hydrogen tetrachloroaurate trihydrate ( $\text{H}[\text{AuCl}_4] \cdot 3\text{H}_2\text{O}$ , 99.99%), hydrogen tetrachloroaurate hydrate ( $\text{H}[\text{AuCl}_4] \cdot x\text{H}_2\text{O}$ , 99.999%,  $x$  is not specified), hydrogen tetrachloroaurate ( $\text{H}[\text{AuCl}_4]$ , 100%), sodium tetrachloroaurate dihydrate ( $\text{Na}[\text{AuCl}_4] \cdot 2\text{H}_2\text{O}$ , 99.99%), and hydrogen tetrabromoaurate hydrate ( $\text{H}[\text{AuBr}_4] \cdot x\text{H}_2\text{O}$ , 99.99%,  $x \approx 5$ ) were purchased from Alfa Aesar. Sodium citrate dihydrate (99%) was purchased from Sigma and sodium borohydride ( $\text{NaBH}_4$ )



(a)



(b)



(c)

FIGURE 2: TEM images of different spots of a sample containing high aspect ratio gold nanorods, prepared according to the seed-mediated method [1, 6, 10–14]. It is obvious that the nanorods are not evenly distributed over the TEM grids.

from Fisher Scientific (general purpose grade), Fluka (96%), or TCI ( $>93\%$ ). L-ascorbic acid was obtained from Hanseler AG (Herisau, Switzerland). Titrisol ampoules were used for sodium hydroxide 0.1 M. All chemicals were used without further purification. For the preparation of all samples, freshly deionized water was used if not otherwise mentioned.

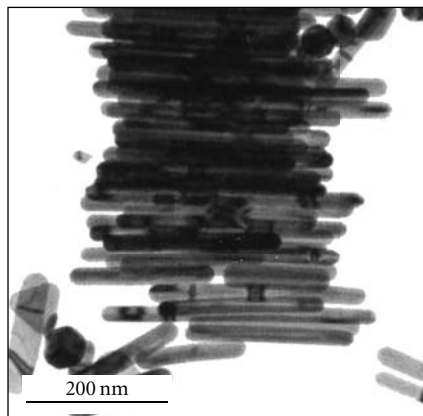


FIGURE 3: TEM image of a spot which is dominated by gold nanorods, prepared according to the “ordinary” synthetic conditions described in the Experimental section. As in the seed-mediated method, areas which do not contain essential fractions of particles other than nanorods can be found.

Poly(vinyl alcohol) (MW  $\approx$  72000, Biochemica, where the type of MW has not been specified by the supplier) was purchased from Axon Lab (Applichem GmbH, Darmstadt, Germany).

**2.1. Synthesis of Gold Nanorods.** In a typical experiment, 2.5 mL of a 0.01 M  $\text{H}[\text{AuCl}_4] \cdot 3\text{H}_2\text{O}$  solution and 3.6445 g hexadecyltrimethylammonium bromide (CTAB) were replenished to 100 mL in a volumetric glass flask. For completely dissolving the CTAB powder, it was necessary to keep this solution at elevated temperature ( $33^\circ\text{C}$ ) for at least 2 hours. This solution, which contained 0.1 M CTAB and  $2.5 \cdot 10^{-4}$  M  $\text{H}[\text{AuCl}_4] \cdot 3\text{H}_2\text{O}$ , was used as *growth solution*.

During the dissolution of the CTAB in the above growth solution, a *seed solution* containing small gold particles was prepared as follows: a volume of 0.5 mL of 0.01 M  $\text{H}[\text{AuCl}_4] \cdot 3\text{H}_2\text{O}$  solution ( $5 \cdot 10^{-6}$  mol  $\text{H}[\text{AuCl}_4] \cdot 3\text{H}_2\text{O}$ , volumetric glass flask, not cooled) was added to 18.4 mL of ice-cooled deionized water in a wide-necked PE-flask (PE = polyethylene). Thereafter, 0.5 mL of freshly prepared 0.01 M sodium citrate solution ( $5 \cdot 10^{-6}$  mol sodium citrate, solution in a volumetric glass flask, not cooled) was added. Thereafter, immediately 0.6 mL of freshly prepared 0.1 M  $\text{NaBH}_4$  solution (in a glass vessel) cooled in an ice-bath was added, and the resulting solution was stirred for 30 s (there was no significant difference in the results whether the used pipettes were previously ice-cooled or not). The solution turned red (after 24 h, particles of a size of approximately 8 nm formed, as evident from transmission electron microscopy). Changing the sequence in the addition of substances in the seed preparation did not lead to significantly different results with respect to nanorod generation.

For the following final reaction steps, cooling was not required. 80  $\mu\text{L}$  of a freshly prepared 0.1 M ascorbic acid solution ( $8.0 \cdot 10^{-6}$  mol ascorbic acid) was added without stirring to 14.4 mL of the growth solution (age between 2 h and 24 h, containing  $3.6 \cdot 10^{-6}$  mol gold). The solution was

mixed by shaking, whereupon the solution became colorless indicating the reduction of Au(III) to Au(I). In the next step, 80  $\mu\text{L}$  of 0.1 M sodium hydroxide solution ( $8.0 \cdot 10^{-6}$  mol NaOH) was added to the solution to modify the pH value. After addition of 16  $\mu\text{L}$  of seed solution (age between 2 h and 24 h, containing  $4.0 \cdot 10^{-9}$  mol gold), the solution was mixed by shaking and became reddish during this period. Then the test tubes were placed in a water bath at  $33^\circ\text{C}$  for 3 h–168 h and finally stored in a refrigerator (temperature  $\approx$   $6^\circ\text{C}$ ) to precipitate a major fraction of CTAB which could be removed by rapid filtration through a sintered glass funnel (pore size G4). The filtered samples were stable for at least 6 months in aqueous solution in the refrigerator or at room temperature. Probably, the dispersion was stabilized by residual surfactant.

**2.2. Transmission Electron Microscopy.** For investigations by transmission electron microscopy (TEM), either a Philips CM200 (160 kV accelerating voltage) or a Philips CM30 (300 kV accelerating voltage) was used. The average length, width, and aspect ratio of the nanorods were determined by counting several hundred particles with an aspect ratio bigger than 2 (manual evaluation of several TEM images). In order to obtain reliable images, a considerable part of the excess of CTAB had to be removed by filtration of the cold solution resulting from the synthesis (see above). Finally, one droplet ( $\approx 0.5 \mu\text{L}$ ) of the filtered solution was put on a commercially available carbon-coated copper TEM grid (Plano GmbH, Wetzlar, Germany).

**2.3. Scanning Electron Microscopy.** For investigation with scanning electron microscopy (SEM), a Zeiss NVision 40 was used. For sample preparation, cold solutions were filtered to remove CTAB, then centrifuged at 5600 rpm for 10 min followed by decantation to remove another part of the excess of CTAB, and finally the remaining solids were dissolved in water. One droplet ( $\approx 0.5 \mu\text{L}$ ) of this solution was put on a pyrolytic graphite (spi supplies, West Chester, PA, USA).

**2.4. UV-vis-NIR Spectra.** UV-vis-NIR absorption spectra were performed with a Lambda 900, Perkin Elmer, Überlingen, Germany.

In order to detect the longitudinal absorption band of the gold nanoparticles, 53.5 mg poly(vinyl alcohol) (PVAL) were dissolved in 5 mL deionized water by heating to  $90^\circ\text{C}$  under stirring. After dissolution of the polymer, the solution was allowed to cool down to room temperature. Under vigorous stirring, 10 mL of a filtered gold particle solution was added to the PVAL solution at room temperature. The homogeneous mixture was poured in a flat aluminum dish, and the solvent was evaporated overnight at ambient conditions.

### 3. Results and Discussion

**3.1. General Procedure of Nanorod Generation.** The seed-mediated method is based on anisotropic particle growth

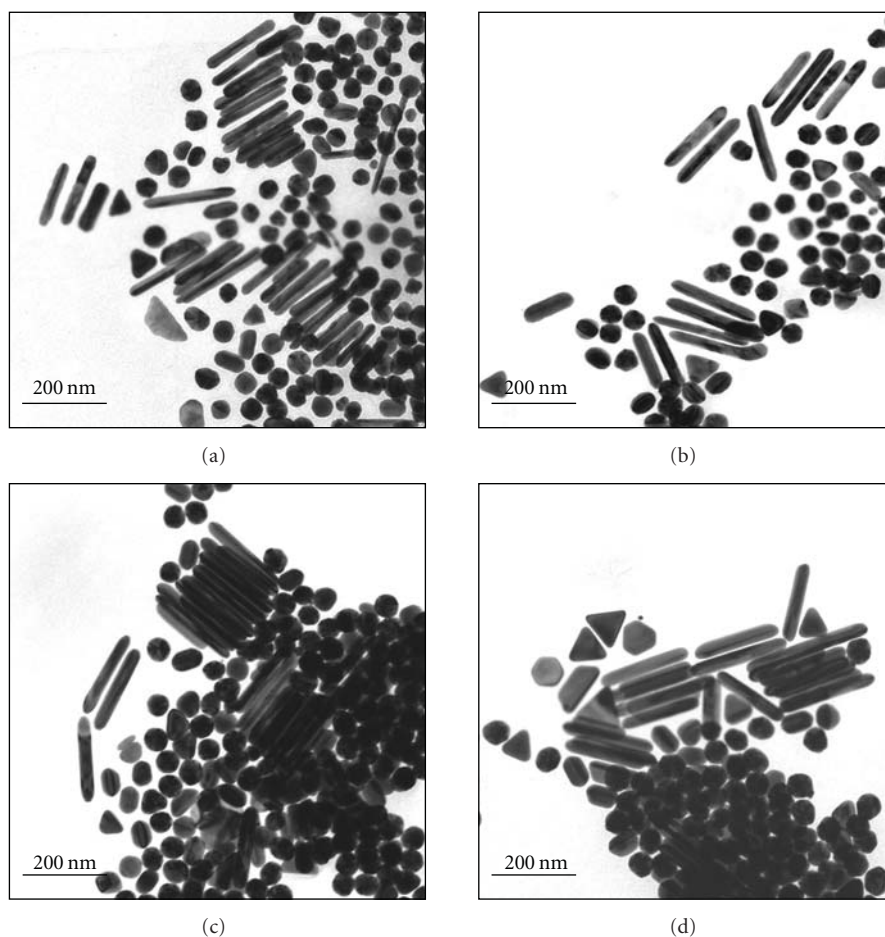


FIGURE 4: TEM images of different samples ((a)–(d)) of gold nanorods. The images illustrate representative ratios between rods and other particles.

by combining a so-called seed solution comprising spherical gold nanoparticles with a growth solution containing tetrachloroaurate(III) and a surfactant. Commonly CTAB (cetyltrimethylammonium bromide, hexadecyltrimethylammonium bromide) is used for this purpose, in presence of a reducing agent, and the resulting solution is subsequently further processed. A main difference between the synthesis procedure described here and the methods reported previously (see Introduction) is keeping additives and processing steps at a minimum. In particular, additives such as silver ions or surfactants in the seed solution, repeated steps of dilution and addition of growth solution, or extended centrifugation procedures of the final solutions are not required anymore. Essential particularities of the seed-mediated method created here are rapid addition of a small volume of seed solution (on the order of  $10\ \mu\text{L}$ ) in the final step of the synthesis procedure and modification of the pH value by a defined quantity of sodium hydroxide. In numerous preliminary experiments, parameters such as growth time, age of the seed and growth solution, and growth temperature were varied which finally resulted in the propitious conditions described in the Experimental section.

The recipe in the Experimental section provided nanorods of aspect ratios around 6 in the average and 10

or more at maximum. When investigating the samples with transmission electron microscopy (TEM), it was possible to find places which showed almost exclusively nanorods (Figure 3); however, significant quantities of spherical and, to a lesser extent, triangular particles also arose, in line with other publications on seed-mediated growth of high aspect ratio gold nanorods [1, 6, 10, 12, 14, 28] and own experiments performed according to previously reported syntheses (Figure 2). It has been reported that spheres and platelets can be substantially removed by sedimentation followed by chemical treatments [27]; however, it was clearly evident from TEM micrographs of products of our experiments that the aspect ratios markedly decreased by this procedure. Representative TEM images of four batches prepared at different days with different starting solutions and by two different persons (samples (a)–(d)) are shown in Figure 4. These samples contain nanorods of similar lengths (Figure 5), widths (Figure 6), and aspect ratios (Figure 7). Further, numerous spherical particles of typically 30 nm–60 nm and particles of other shapes (roughly 1/4 of the number of spherical particles) emerged. The samples' features were similar at reaction times (starting at the combination of growth and seed solution) of 3 h, 24 h, and 168 h, that is, nanorod formation was essentially established within 3 h.

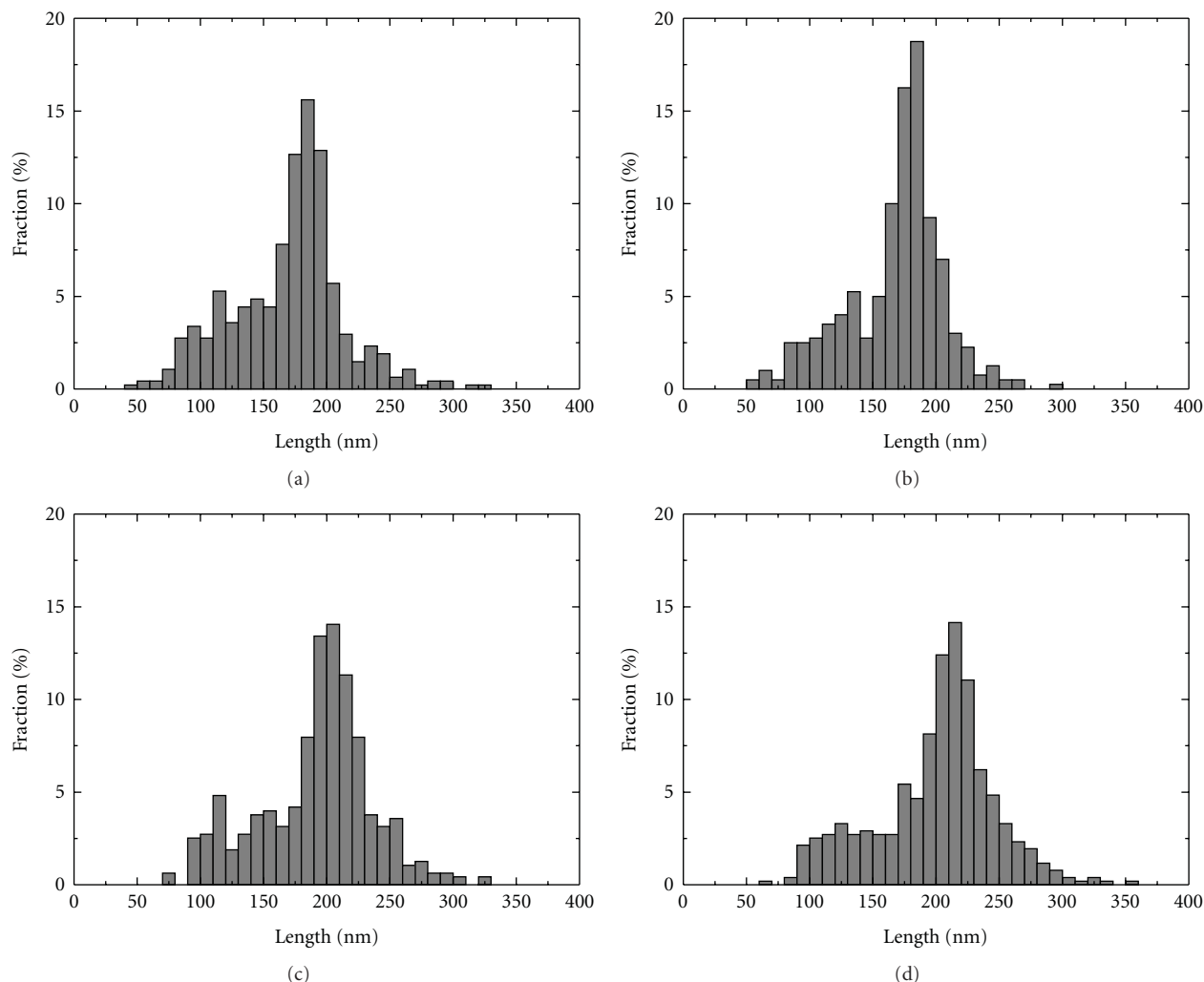


FIGURE 5: Length distributions of the rods corresponding to samples (a)–(d) of Figure 4.

Scanning electron microscopy (SEM) disclosed that the nanorods were not cylindrical but exhibited crystallographic facets (Figure 8).

For some applications, as for instance for investigations of the gold species by TEM, the large excess of CTAB needs to be removed. Thus, a major fraction of CTAB was simply precipitated by storage of the samples at ca. 6°C during 24 h and subsequent filtration. The gold nanorods in such filtrates were stable for at least a few months at room temperature or in the refrigerator. Separation of the CTAB by centrifugation/decantation cycles [1, 3, 4, 6, 7, 9–14, 19, 20, 28, 29] was more laborious and frequently led to the formation of gold particle agglomerates which did not redisperse readily in water.

An additional advantage of the presented synthesis method is the tolerance towards impurities which have otherwise reported to influence the yield, shape, and size of the gold particles. For instance, it was emphasized that ultra-pure water should be employed for nanorod formation by seed-mediated methods [3–10, 12, 19, 24, 28]. We found a minor influence of the water quality; however, surprisingly

the use of common freshly deionized water leads to better reproducibility than ultra-pure water. Maybe the ultra-pure water contained less but more critical impurities than the deionized water. As a consequence, all results reported here refer to experiments with deionized water. Further, impurities (in particular iodide) in the CTAB which depend on the suppliers [9] and the growth temperature [13, 28] have been reported to influence the rod formation. In particular, the commercial products H5882 and H6269 from Sigma and the CTAB from Fluka were reported to lead to strikingly different results in other seed-mediated methods [9]. However, the nanorod formation did not depend considerably on those CTAB qualities in the method presented here. Also, the nature of the gold salt ( $\text{H}[\text{AuCl}_4]$ ,  $\text{H}[\text{AuCl}_4] \cdot x\text{H}_2\text{O}$  where  $x$  is not specified,  $\text{H}[\text{AuCl}_4] \cdot 3\text{H}_2\text{O}$ ,  $\text{H}[\text{AuBr}_4] \cdot x\text{H}_2\text{O}$  with  $x \approx 5$ , and  $\text{Na}[\text{AuCl}_4] \cdot 2\text{H}_2\text{O}$ ) had a minor influence on product formation.

Variation of reaction parameters did not improve the creation of high aspect ratio nanorods over all. When the pH value was varied between 3.4 and 10.1 (compared to 3.9 at “ordinary” conditions) with NaOH, the nanorod generation

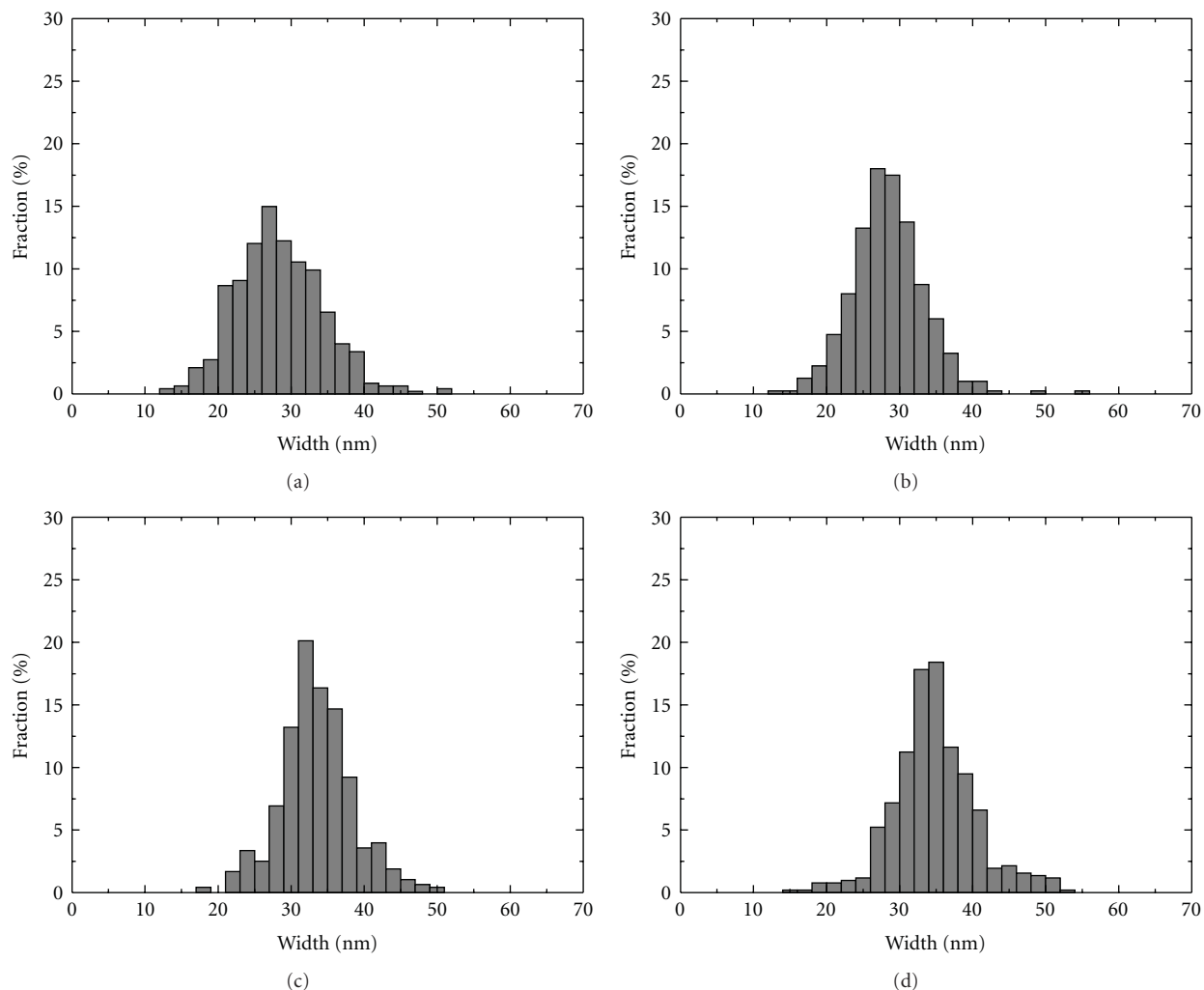


FIGURE 6: Width distributions of the rods corresponding to samples (a)–(d) of Figure 4.

was pronouncedly influenced (Figure 9), as also observed for other seed-mediated methods [10]. A low pH value (3.4) induced the formation of long nanorods, as also found in other seed-mediated procedures [26, 30], with a length on the order of 400 nm and a width between 15 and 20 nm, but the yield of these rods was very low and the aspect ratio distribution was relatively broad. Above a pH value of 6.6 or more, no rods arose anymore.

In the literature, an increase in seed particle concentration resulted in a decrease of the aspect ratio [19, 20]; however, the concentrations of the seeds were typically higher than in our experiments and we could not find a noteworthy improvement in aspect ratio when the concentration of the seed particles (age 24 hours, average diameter  $\approx 8$  nm) was varied between 0 and  $3.77 \cdot 10^{-7}$  M (the concentrations refer to gold atoms in the final solutions). Yet the experiments showed clearly that the addition of seeds is necessary to grow rod-shaped particles as otherwise only spherical or irregularly shaped particles emerged.

When the concentration of the tetrachloroauric acid in the growth solution was varied, the molar ratio ascorbic

acid/sodium hydroxide/tetrachloroaurate(III) was kept constant. An increase in the tetrachloroaurate(III) concentration by a factor of 2 or 3 lead to an increase in aspect ratio of the nanorods (typically to 8 and 12, resp.), which was, however, accompanied by an increase in polydispersity (Figure 10). Yet when the tetrachloroaurate(III) concentration was increased by a factor of 6, the nanorods became thicker and shorter, that is, the aspect ratio decreased to typical values of 4–5, and larger particles, such as triangles and spheres, also emerged in higher quantities.

Finally, we attempted to separate the gold nanorods from other particles according to the depletion-induced shape and size selection method [31]; however, we could not significantly enhance the fraction of nanorods in the samples.

**3.2. Influence of the CTAB Concentration and Growth Mechanism.** As far as we are aware of, it has not been pointed out in the context of seed-mediated nanorod formation that the phase diagram of CTAB [32] exhibits a triple point around a concentration of 0.1 M and a temperature around  $25^\circ\text{C}$  where crystals, individually dissolved molecules, and

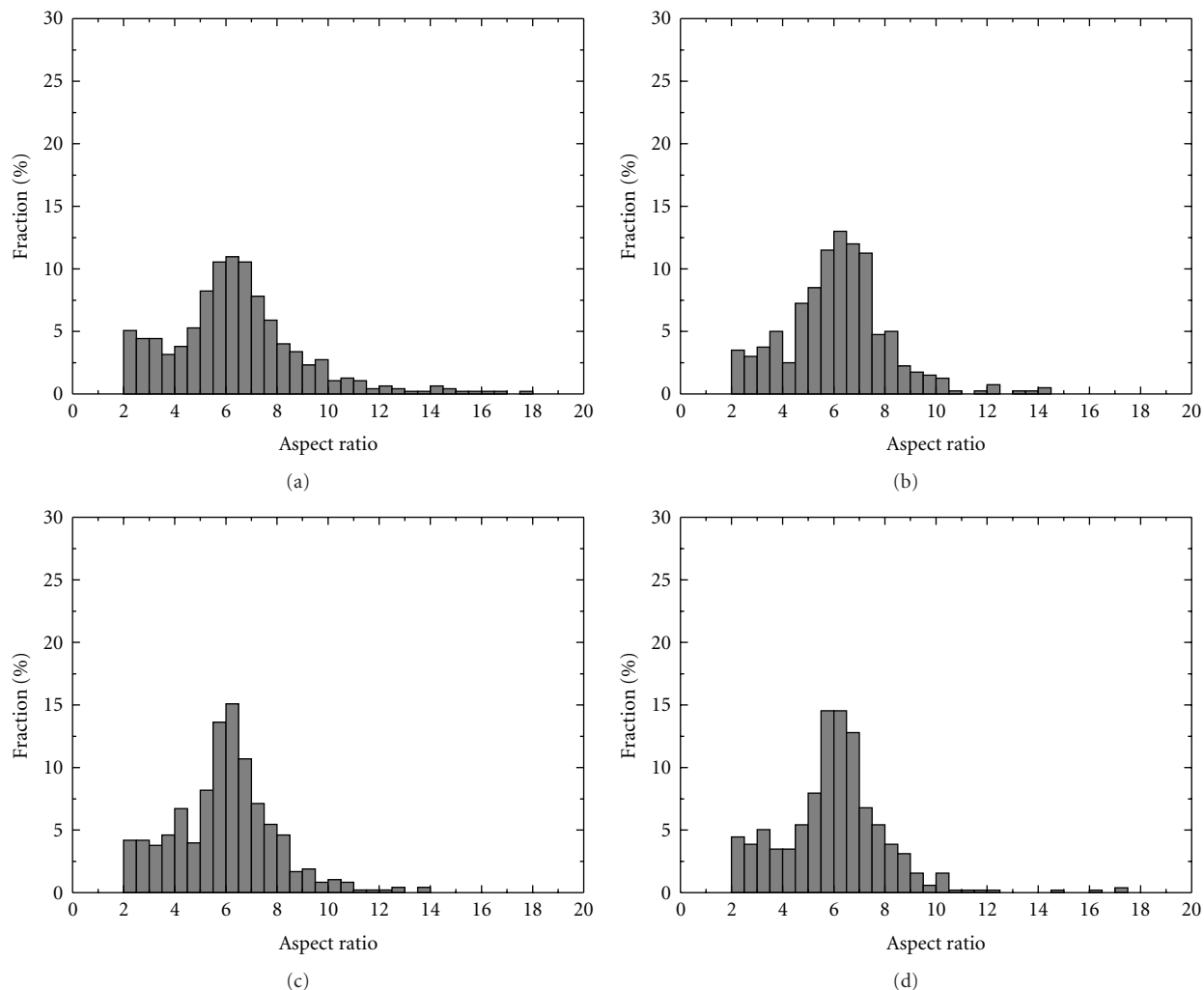


FIGURE 7: Aspect ratio distributions of the rods corresponding to samples (a)–(d) of Figure 4.

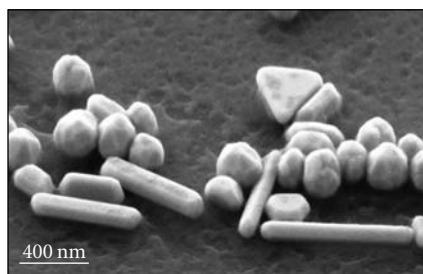


FIGURE 8: SEM image of gold nanorods and other species, taken at a tilt angle of  $54^\circ$ .

spherical micelles coexist. Accordingly, we kept the solutions containing 0.1 M CTAB at  $33^\circ\text{C}$  (enhancement of the temperature to  $50^\circ\text{C}$  did not alter the nanorod formation noteworthy, in contrast to other seed-mediated procedures [13, 28]) in order to avoid precipitation of CTAB which indeed slowly occurred in 0.1 M solutions close to  $25^\circ\text{C}$ .

Since CTAB is essential for nanorod formation, the CTAB concentration in the growth solution, which is 0.1 M if not otherwise mentioned as common in other seed-mediated methods, was also decreased to 0.01 M or increased to 0.25 and 0.5 M, respectively. It was reported in other seed-mediated methods that at a CTAB concentration of 0.01 M higher aspect ratios result when the synthesis is performed at  $0^\circ\text{C}$  [13]; we note, however, that CTAB precipitates under these conditions by our experience, in agreement with the above-mentioned phase diagram. At a concentration of 0.01 M of CTAB at  $33^\circ\text{C}$ , only spherical particles and egg-like shaped particles arose (Figure 11), while an increase in the CTAB concentration from 0.1 M to 0.25 M did not lead to a significant change of aspect ratio and yield of gold nanorods. However, at a CTAB concentration of 0.5 M, only a few very big spherical particles and triangles emerged (Figure 11). These findings are different from those of other seed-mediated methods where the yield of high aspect ratio nanorods increased with decreasing CTAB concentration [13], while, in contrast, other authors report that the aspect ratio increases with higher CTAB concentrations [26].

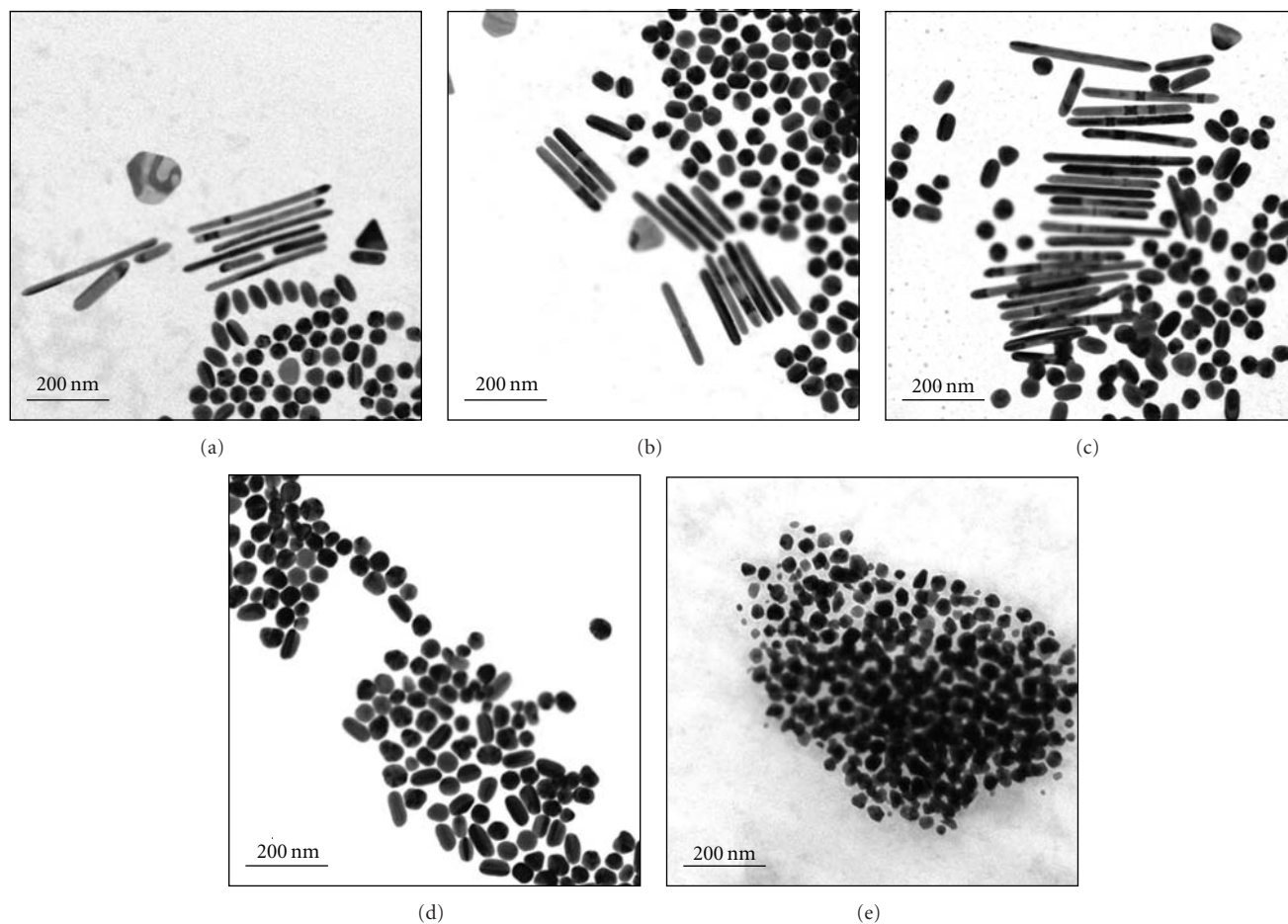


FIGURE 9: TEM images of gold nanorods prepared at pH values of 3.4 (a), 3.9 (b), 5.9 (c), 6.6 (d) and, 10.1 (e).

Of course, the CTAB concentration is associated with the growth mechanism of the nanorods. A growth mechanism which has been discussed in the literature is based on the ability of CTAB to form micelles [1]. Accordingly it was proposed that the gold particles grow inside these micelles and their shape is therefore determined by the shape of the micelles which depends on the concentration of the surfactant. However, with regard to the above mentioned phase diagram of CTAB, spherical and not cylindrical micelles are expected at the conditions commonly applied in seed-mediated methods (0.1 M CTAB), and only at higher concentration (above around 0.3 M), cylindrical micelles arise [32]; yet our experiments with 0.5 M CTAB did not yield nanorods. Therefore, we consider the formation of nanorods within CTAB micelles not to be likely. In this context, it is also worth to note that the nanorods' shapes are not cylindrical (see Figure 8).

As an alternative explanation for nanorod formation, the CTAB molecules could adsorb preferentially to certain crystal faces and therewith inhibit isotropic crystal growth, thus producing the shape of a rod [13]. This mechanism would explain at least that rod formation did not occur at low CTAB concentrations (0.01 M) assuming that the equilibrium constant is in these cases too low for an effective

adsorption of CTAB at the crystal faces. On the other hand, at the highest concentration applied here (0.5 M), for instance, the formation of cylindrical micelles might compete with CTAB adsorption at the gold crystal faces, that is, less CTAB molecules might be available for adsorption at gold particles which then could lead to isotropic particle growth, that is, formation of spherical particles. Importantly, electron diffraction patterns (Figure 12) identified the (110) direction as the growth direction. This indeed implies that the nanorod growth is associated with adsorption of CTAB molecules at specific crystal faces as otherwise a random growth direction of the rods is expected.

**3.3. UV-vis-NIR Absorption Spectra.** Extensive UV-vis-NIR studies have been performed previously with low aspect ratio gold nanorods [22–25, 29], and corresponding measurements were only performed for wavelengths ranging from 300 nm to 1300 nm. Basically, gold nanorods give rise to two absorption bands. One of them is caused by transverse oscillations of the electrons (transverse absorption band), which is typically located in the visible wavelength region, and one due to the longitudinal oscillations of the electrons (longitudinal absorption band) [33]. The longitudinal

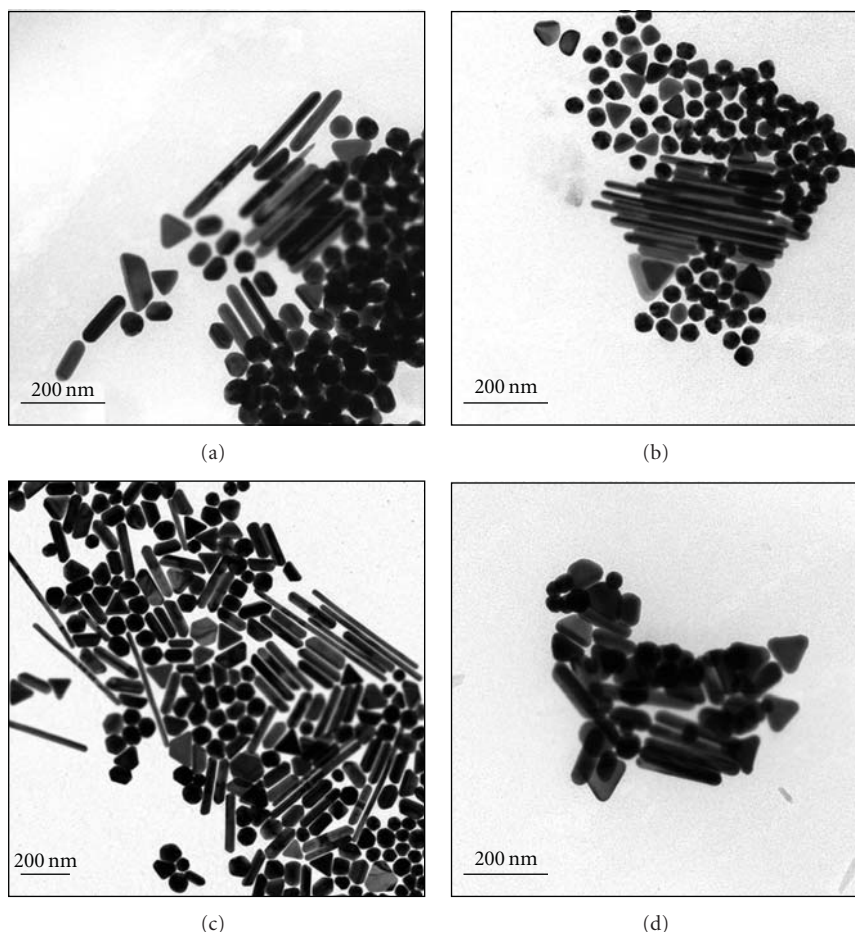


FIGURE 10: TEM images of gold nanorods prepared with different concentrations of tetrachloroauric acid in the growth solution:  $2.5 \cdot 10^{-4}$  M (a),  $5 \cdot 10^{-4}$  M (b),  $7.5 \cdot 10^{-4}$  M (c), and  $1.5 \cdot 10^{-3}$  M (d).

absorption band is shifted from the visible towards the near-infrared region with increasing aspect ratio, whereas the transverse band can interfere with the absorption of spherical gold particles.

Remarkably, reliable experimental information on the longitudinal band for high aspect ratio gold nanorods is rarely available so far. Indeed, the longitudinal absorption band of such particles in UV-vis-NIR spectra falls in the absorption region of water (ca. 1300 nm–above 2500 nm) and is therefore not accessible in the aqueous solutions finally resulting from the nanorod synthesis (subtraction of the water absorption band does not lead to reliable results due to the very high (“infinite”) absorbance at common experimental setups). Therefore, we used a technique which bases on embedding the particles in poly(vinyl alcohol) (PVAL), which is water-soluble, does not absorb pronouncedly in the UV-vis-NIR region, and readily forms transparent free-standing composite films with gold by solution casting (see Experimental part). In order to investigate if the residual water content in PVAL influences the UV-vis-NIR spectra of the gold particles, a PVAL film with and without gold, respectively, was measured after drying the film at ambient conditions for 3 days at room temperature, subsequently

a second spectrum after drying under vacuum (ca. 1 mbar) for one day, and finally a third spectrum after storing the dried PVAL film in an atmosphere with humidity of ca. 99% for 18 days was recorded. The three spectra are shown in Figure 13, after subtraction of the spectrum of analogously treated blank PVAL films (the absorbance of which, however, was only marginal). It is obvious that the two absorption maxima at 520 nm and around 1955 nm (broad) are independent of the water content (minor differences may occur because the exact position of the sample in the spectrometer is not identical in the three spectra). A less pronounced absorption maximum or shoulder around 675 nm varies to a certain extent in relative intensity, which might be due to swelling effects [34]. The peaks in the region of 500–700 nm are attributed to the more or less spherical particles, triangles and the transversal plasmon absorption of the nanorods and that around 1955 nm to the longitudinal absorption of the nanorods. This band is shifted markedly to higher wavelengths compared to that of particles reported with lower aspect ratio (520 nm–1000 nm [23, 25]). Therefore, the UV-vis-NIR spectra confirm that a significant fraction of gold nanorods with relatively high aspect ratio is present in the sample.

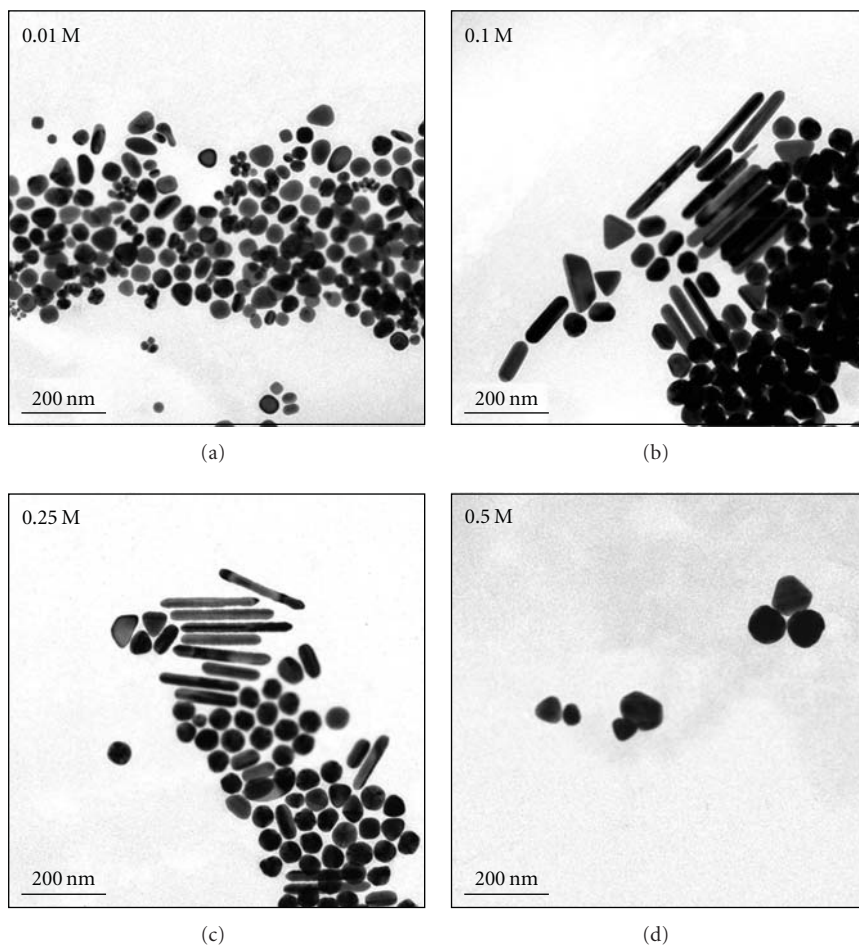


FIGURE 11: TEM images of gold nanorods prepared with different concentrations of CTAB; that is, 0.01 M, 0.1 M, 0.25 M, and 0.5 M.

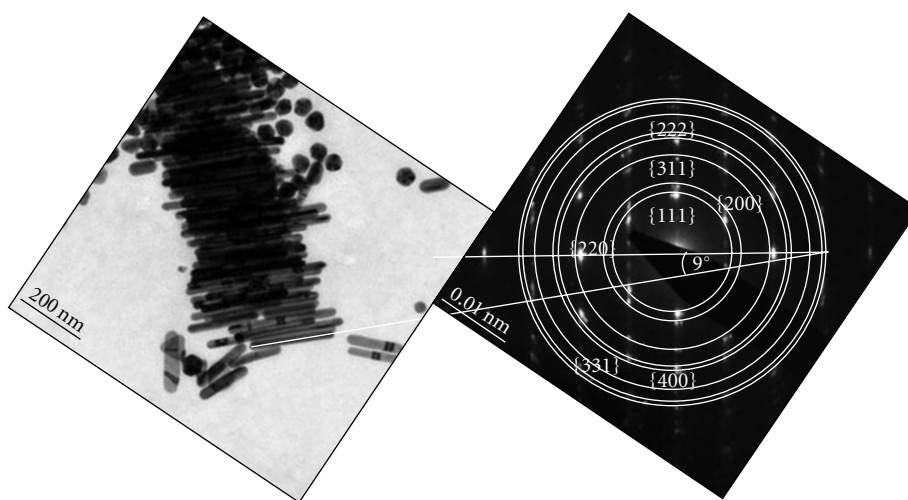


FIGURE 12: TEM image and related electron diffraction pattern used for the evaluation of the growth direction of the nanorods. The angle of  $9^\circ$  corresponds to the instrumental rotation of the diffraction pattern towards the bright field image at the employed magnification and camera length.

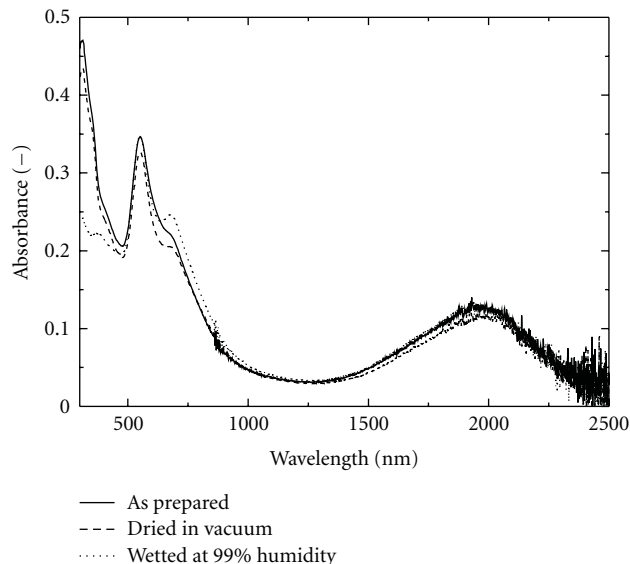


FIGURE 13: UV-vis-NIR spectra of gold particles (prepared according to the “ordinary” synthetic conditions described in the Experimental section) embedded in poly(vinyl alcohol) at different drying states after background subtraction.

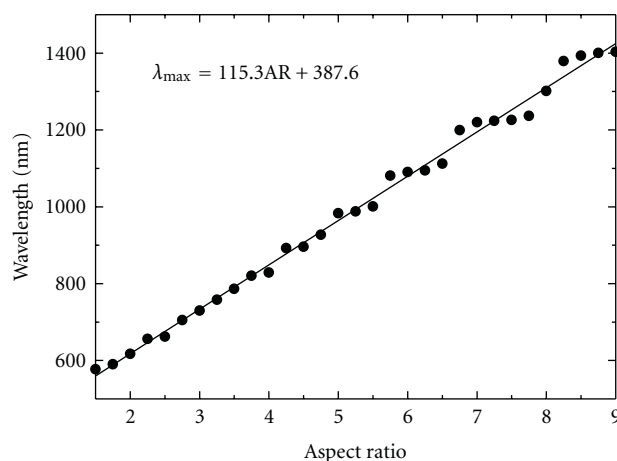


FIGURE 14: Calculated correlation between aspect ratio of gold nanoparticles embedded in poly(vinyl alcohol) and the absorption maximum of the longitudinal absorption band.

A linear correlation between the absorption maximum of the aspect ratio and the longitudinal absorption band was reported on the basis of Gans’ extension of Mie’s theory [33, 35]. However, the calculations referred to aqueous solutions which exhibit dielectric constants that clearly differ from those of poly(vinyl alcohol). Hence, we used the Gans formula for the recalculation of the aspect ratio-absorption maximum correlation with a dielectric constant for poly(vinyl alcohol) of 2.28 (average of indicated values for this polymer [2.2201–2.3409], calculated from the refractive index [36]), which resulted in the formula

$$\lambda_{\max} = 115.3AR + 387.6 \quad (1)$$

as derived from Figure 14 obtained by fitting of the wavelength of the longitudinal absorption maximum as a function of the aspect ratio (AR). Accordingly, the experimentally found absorption maximum of 1955 nm corresponds to an aspect ratio of 13.6 which is somewhat higher but still reasonably close to the average aspect ratios of the considered sample which may contribute to the respective absorption (obtained from TEM images, Figure 15). Deviations between theoretical and experimental values could be a consequence of, for example, the limited precision of the dielectric constant of poly(vinyl alcohol) (a range of dielectric constants is reported), the limited precision in the determination of the absorption maximum due to the broadness of the peak, the limited number of nanorods that can be evaluated by TEM compared to the total number of nanorods in the system, the presence of cylindrical instead of ellipsoidal shapes (the latter being the basis of Gans’ theory), or limits in the availability of the applied formula. The high value of 1955 nm is in the range of that of gold nanorod samples prepared by Wei et al. (1635 nm in D<sub>2</sub>O) [26] and Khanal et al. (1567 in D<sub>2</sub>O) [27].

#### 4. Summary

An improvement in reproducibility of the gold species with high aspect ratio was achieved by reducing the steps in the seed-mediated growth method in presence of high concentrations of CTAB, which is based on the rapid addition of a small volume of seed particles (on the order of 10  $\mu$ L). A major part of the CTAB could be removed after synthesis simply by precipitation at 6°C followed by filtration. Further, the synthesis route is less susceptible to impurities in the water or in the CTAB than indicated in other reports on the seed-mediated growth of gold nanorods. Nanorods with lengths on the order of 200 nm and aspect ratios around 6 in the average and 10 or more at maximum formed in significant amounts (the higher values, however, were accompanied by an increase in polydispersity), which was confirmed by UV-vis-NIR measurements, where the longitudinal plasmon absorption could readily be detected when the gold particles were embedded in poly(vinyl alcohol). Thus, maximum absorptions of nanoparticles with high aspect ratios were found at the extraordinarily high wavelength of 1955 nm. As evident from SEM, the rods were not cylindrical but exhibited crystallographic facets. Considering this fact, the phase diagram of CTAB and in particular electron diffraction patterns of the nanorods, nanorod formation appears to be induced rather by preferential CTAB adsorption at specific faces of the growing crystals than by particle growth in the interior of cylindrical CTAB micelles.

#### Acknowledgments

The authors thank Pascal Wolfer for synthesizing a badge of gold nanoparticles, Michael Roth, Barbara Grant, Anita Bardill, and Daniel Schmid for experimental help in our initial attempts, Stephan Frank for providing the MatLab routine for size evaluation, and Giancarlo Pigozzi for acquiring the diffraction patterns, support by the electron

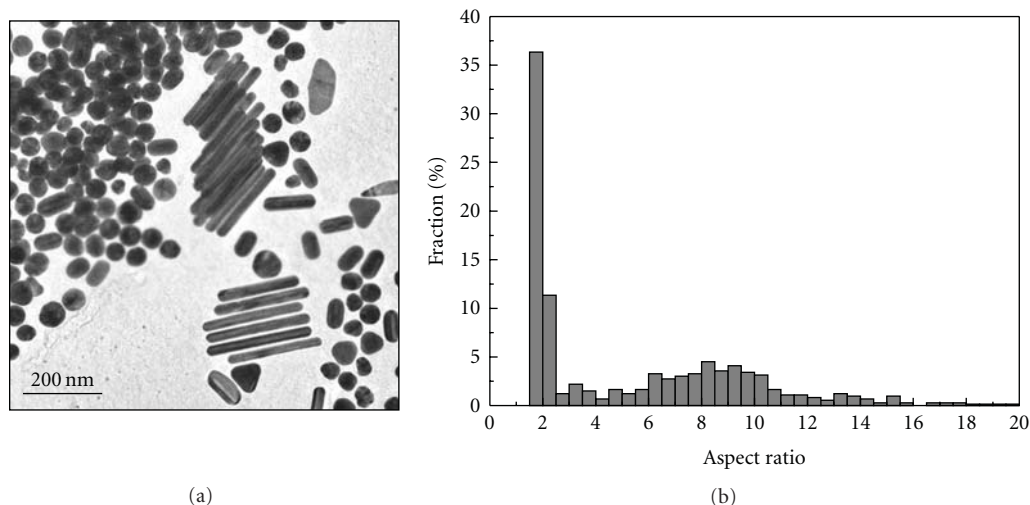


FIGURE 15: TEM image and aspect ratio distribution of the gold nanorods of the sample shown in Figure 13, which substantiate that indeed the absorption in the NIR region is associated with a high aspect ratio of gold nanorods.

microscopy center (EMEZ) of ETH Zurich and the Swiss National Science Foundation (SNF) for financial support under Project no. 200021-113463.

## References

- [1] N. R. Jana, L. Gearheart, and C. J. Murphy, "Wet chemical synthesis of high aspect ratio cylindrical gold nanorods," *Journal of Physical Chemistry B*, vol. 105, no. 19, pp. 4065–4067, 2001.
- [2] Y. Yu, S. Chang, C. Lee, and C. R. C. Wang, "Gold nanorods: electrochemical synthesis and optical properties," *Journal of Physical Chemistry B*, vol. 101, no. 34, pp. 6661–6664, 1997.
- [3] X. C. Jiang and M. P. Pileni, "Gold nanorods: influence of various parameters as seeds, solvent, surfactant on shape control," *Colloids and Surfaces A*, vol. 295, no. 1–3, pp. 228–232, 2007.
- [4] T. K. Sau and C. J. Murphy, "Seeded high yield synthesis of short Au nanorods in aqueous solution," *Langmuir*, vol. 20, no. 15, pp. 6414–6420, 2004.
- [5] B. Nikoobakht and M. A. El-Sayed, "Preparation and growth mechanism of gold nanorods (NRs) using seed-mediated growth method," *Chemistry of Materials*, vol. 15, no. 10, pp. 1957–1962, 2003.
- [6] J. Gao, C. M. Bender, and C. J. Murphy, "Dependence of the gold nanorod aspect ratio on the nature of the directing surfactant in aqueous solution," *Langmuir*, vol. 19, no. 21, pp. 9065–9070, 2003.
- [7] X. C. Jiang, A. Brioude, and M. P. Pileni, "Gold nanorods: limitations on their synthesis and optical properties," *Colloids and Surfaces A*, vol. 277, no. 1–3, pp. 201–206, 2006.
- [8] D. K. Smith and B. A. Korgel, "The importance of the CTAB surfactant on the colloidal seed-mediated synthesis of gold nanorods," *Langmuir*, vol. 24, no. 3, pp. 644–649, 2008.
- [9] D. K. Smith, N. R. Miller, and B. A. Korgel, "Iodide in CTAB prevents gold nanorod formation," *Langmuir*, vol. 25, no. 16, pp. 9518–9524, 2009.
- [10] B. D. Busbee, S. O. Obare, and C. J. Murphy, "An improved synthesis of high-aspect-ratio gold nanorods," *Advanced Materials*, vol. 15, no. 5, pp. 414–416, 2003.
- [11] H.-Y. Wu, W.-L. Huang, and M. H. Huang, "Direct high-yield synthesis of high aspect ratio gold nanorods," *Crystal Growth and Design*, vol. 7, no. 4, pp. 831–835, 2007.
- [12] H. J. Park, C. S. Ah, W.-J. Kim, I. S. Choi, K.-P. Lee, and W. S. Yun, "Temperature-induced control of aspect ratio of gold nanorods," *Journal of Vacuum Science and Technology A*, vol. 24, no. 4, pp. 1323–1326, 2006.
- [13] S. K. Kang, S. Chah, C. Y. Yun, and J. Yi, "Aspect ratio controlled synthesis of gold nanorods," *Korean Journal of Chemical Engineering*, vol. 20, no. 6, pp. 1145–1148, 2003.
- [14] A. Gole and C. J. Murphy, "Seed-mediated synthesis of gold nanorods: role of the size and nature of the seed," *Chemistry of Materials*, vol. 16, no. 19, pp. 3633–3640, 2004.
- [15] M. Wirtz, S. Yu, and C. R. Martin, "Template synthesized gold nanotube membranes for chemical separations and sensing," *Analyst*, vol. 127, no. 7, pp. 871–879, 2002.
- [16] C. R. Martin, "Membrane-based synthesis of nanomaterials," *Chemistry of Materials*, vol. 8, no. 8, pp. 1739–1746, 1996.
- [17] S.-S. Chang, C.-W. Shih, C.-D. Chen, W.-C. Lai, and C. R. C. Wang, "The shape transition of gold nanorods," *Langmuir*, vol. 15, no. 3, pp. 701–709, 1999.
- [18] F.-K. Liu, Y.-C. Chang, F.-H. Ko, and T.-C. Chu, "Microwave rapid heating for the synthesis of gold nanorods," *Materials Letters*, vol. 58, no. 3–4, pp. 373–377, 2004.
- [19] J. Pérez-Juste, L. M. Liz-Marzán, S. Carnie, D. Y. C. Chan, and P. Mulvaney, "Electric-field-directed growth of gold nanorods in aqueous surfactant solutions," *Advanced Functional Materials*, vol. 14, no. 6, pp. 571–579, 2004.
- [20] N. R. Jana, L. Gearheart, and C. J. Murphy, "Evidence for seed-mediated nucleation in the chemical reduction of gold salts to gold nanoparticles," *Chemistry of Materials*, vol. 13, no. 7, pp. 2313–2322, 2001.
- [21] J. Pérez-Juste, I. Pastoriza-Santos, L. M. Liz-Marzán, and P. Mulvaney, "Gold nanorods: synthesis, characterization and applications," *Coordination Chemistry Reviews*, vol. 249, no. 17–18, pp. 1870–1901, 2005.
- [22] B. M. I. Van Der Zande, L. Pagès, R. A. M. Hikmet, and A. Van Blaaderen, "Optical properties of aligned rod-shaped gold particles dispersed in poly(vinyl alcohol) films," *Journal of Physical Chemistry B*, vol. 103, no. 28, pp. 5761–5767, 1999.

- [23] S. Eustis and M. El-Sayed, "Aspect ratio dependence of the enhanced fluorescence intensity of gold nanorods: experimental and simulation study," *Journal of Physical Chemistry B*, vol. 109, no. 34, pp. 16350–16356, 2005.
- [24] J. Pérez-Juste, B. Rodríguez-González, P. Mulvaney, and L. M. Liz-Marzán, "Optical control and patterning of gold-nanorod-poly(vinyl alcohol) nanocomposite films," *Advanced Functional Materials*, vol. 15, no. 7, pp. 1065–1071, 2005.
- [25] S. Eustis and M. A. El-Sayed, "Determination of the aspect ratio statistical distribution of gold nanorods in solution from a theoretical fit of the observed inhomogeneously broadened longitudinal plasmon resonance absorption spectrum," *Journal of Applied Physics*, vol. 100, no. 4, Article ID 044324, 2006.
- [26] Q. Wei, A. Ji, and J. Shen, "PH controlled synthesis of high aspect-ratio gold nanorods," *Journal of Nanoscience and Nanotechnology*, vol. 8, no. 11, pp. 5708–5714, 2008.
- [27] B. P. Khanal and E. R. Zubarev, "Purification of high aspect ratio gold nanorods: complete removal of platelets," *Journal of the American Chemical Society*, vol. 130, no. 38, pp. 12634–12635, 2008.
- [28] S. K. Kang, Y. Kim, M. S. Hahn, I. Choi, J. Lee, and J. Yi, "Aspect ratio control of Au nanorods via temperature and hydroxylamine concentration of reaction medium," *Current Applied Physics*, vol. 6, no. 1, pp. e114–e120, 2006.
- [29] C. J. Murphy and C. J. Orendorff, "Alignment of gold nanorods in polymer composites and on polymer surfaces," *Advanced Materials*, vol. 17, no. 18, pp. 2173–2177, 2005.
- [30] F. Kim, K. Sohn, J. Wu, and J. Huang, "Chemical synthesis of gold nanowires in acidic solutions," *Journal of the American Chemical Society*, vol. 130, no. 44, pp. 14442–14443, 2008.
- [31] K. Park, H. Koerner, and R. A. Vaia, "Depletion-induced shape and size selection of gold nanoparticles," *Nano Letters*, vol. 10, no. 4, pp. 1433–1439, 2010.
- [32] N. K. Raman, M. T. Anderson, and C. J. Brinker, "Template-based approaches to the preparation of amorphous, nanoporous silicas," *Chemistry of Materials*, vol. 8, no. 8, pp. 1682–1701, 1996.
- [33] R. Gans, "Über die Form ultramikroskopischer Goldteilchen," *Annalen der Physik*, vol. 342, pp. 881–900, 1912, *Drude's Ann.* Vol. 37, pp. 881–900, 1912.
- [34] D. I. Uhlenhaut, P. Smith, and W. Caseri, "Color switching in gold—polysiloxane elastomeric nanocomposites," *Advanced Materials*, vol. 18, no. 13, pp. 1653–1656, 2006.
- [35] G. Mie, "Beiträge zur Optik rüber Medien, speziell kolloidaler Metallösungen," *Annalen der Physik*, vol. 330, pp. 377–445, 1908, *Drude's Ann.*, Vol. 25, pp. 377–445, 1908.
- [36] J. C. Seferis, "Refractive indices of Polymers," in *Polymer Handbook*, J. Brandrup and E. H. Immergut, Eds., pp. VI/451–VI/461, Wiley, New York, NY, USA, 1989.

## Research Article

# Simple Synthesis and Luminescence Characteristics of PVP-Capped GeO<sub>2</sub> Nanoparticles

Wei Wu, Xu Zou, Qianjun Li, Bingbing Liu, Bo Liu, Ran Liu, Dedi Liu, Zepeng Li, Wen Cui, Zhaodong Liu, Dongmei Li, Tian Cui, and Guangtian Zou

State Key Laboratory of Superhard Materials, Jilin University, Changchun 130012, China

Correspondence should be addressed to Bingbing Liu, liubb@jlu.edu.cn

Received 30 April 2010; Accepted 28 July 2010

Academic Editor: Quanqin Dai

Copyright © 2011 Wei Wu et al. This is an open access article distributed under the Creative Commons Attribution License, which permits unrestricted use, distribution, and reproduction in any medium, provided the original work is properly cited.

Polyvinylpyrrolidone (PVP)-capped rutile GeO<sub>2</sub> nanoparticles were synthesized through a facile hydrothermal process. The obtained nanoparticles were characterized by X-ray diffraction (XRD), transmission electron microscopy (TEM), Fourier transform infrared spectroscopy (FTIR), thermo gravimetric analysis (TGA), and photoluminescence spectroscopy (PL). The capped GeO<sub>2</sub> nanoparticles showed significantly enhanced luminescence properties compared with those of the uncapped ones. We attributed this result to the effect of reducing surface defects and enhancing the possibility of electron-hole recombination of the GeO<sub>2</sub> nanoparticles by the PVP molecules. PVP-capped GeO<sub>2</sub> nanoparticles have potential application in optical and electronic fields.

## 1. Introduction

Germanium oxide (GeO<sub>2</sub>) is an important semiconductor material that has attracted much interest owing to its unique optical property and silica analogue [1, 2]. Moreover, nanostructured GeO<sub>2</sub> possesses the superior physical and chemical properties compared with its bulk counterparts. Nowadays, it is being widely used in optoelectronic devices, vacuum technology, and catalysis. For example, GeO<sub>2</sub> nanowires were used in one-dimensional luminescence nanodevices by Sahnoun et al. [3]. And GeO<sub>2</sub> nanotubes and nanorods as an important optical fibre material have been used in thermal vacuum test successfully by Jiang et al. [4].

It is well known that GeO<sub>2</sub> forms in two stable crystalline structures at ambient temperature, the  $\alpha$ -quartz trigonal structure and the rutile tetragonal structure [5]. Over the past decades several properties of  $\alpha$ -quartz-type GeO<sub>2</sub> have been investigated, for instance blue luminescence and dielectric properties. Compared with  $\alpha$ -quartz-type GeO<sub>2</sub>, rutile GeO<sub>2</sub> has some unique properties, such as excellent transmissivity and green luminescence [6–8]. For these properties, rutile GeO<sub>2</sub> has been considered as a potential material for luminescent device [9]. However, rutile GeO<sub>2</sub>

nanoparticles, like other semiconductor nanoparticles, have high surface energy, and they agglomerate or coalesce extremely quickly [10]. For this reason, many methods have been used to improve the stability of nanoparticles, such as changing of annealing temperature and doping of semiconductor and surfaces capped by various organic or inorganic layers, [11–13]. Among these methods, polymer capping as a newly chemical method has been developed to synthesize nanoparticles with high surface stability and also has significant influence on the morphology and optical properties of nanoparticles [14]. Moreover, compared with the aforementioned methods, it also has several other advantages, such as facile process and gentle reaction conditions. However, the rutile GeO<sub>2</sub> modified by PVP had never been synthesized successfully before. So this is a problem that should be solved quickly.

In this present work, we report, for the first time, the synthesis of PVP-capped rutile GeO<sub>2</sub> nanocrystals through a simple hydrothermal process. PVP, which is a water soluble polymer, was used as capping polymer molecule to stabilize the GeO<sub>2</sub> nanoparticles. Through the surface modification by PVP, highly monodisperse GeO<sub>2</sub> nanoparticles were prepared, which exhibited highly chemical stability and

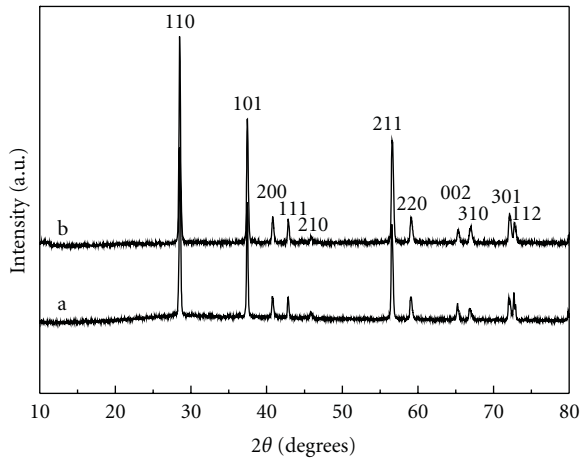


FIGURE 1: XRD pattern of the uncapped (a) and PVP-capped (b)  $\text{GeO}_2$  nanoparticles.

significantly enhanced luminescence. Our study provides a new hybrid material which has potential application in the field of nanoscale device.

## 2. Experimental Section

**2.1. Material and Methods.** We synthesize the samples through hydrothermal synthesis method. In a typical preparation process, 0.1 g  $\text{GeO}_2$  was added in 15 mL HCl aqueous solution (PH = 1) in a Teflon-lined autoclave of 20 mL capacity. The autoclave was maintained at 180°C for 12 hours and then naturally cooled to room temperature. The obtained solution was discarded. The powder samples were then redispersed in distilled water in an ultrasonic bath. The centrifugation was repeated twice so as to remove the HCl residue. After that, the powder samples were dried in an oven at 60°C for 24 hours in air. Then the powder samples were added in a Teflon-lined autoclave of 20 ml capacity again with 15 mL distilled water and 0.2 g PVP. The autoclave was maintained at 140°C for 6 hours and then cooled to room temperature naturally. The centrifugation was repeated twice so as to remove the aqueous solution PVP again. The powder samples were dried in an oven at 60°C for 24 hours in air. Then PVP-capped  $\text{GeO}_2$  was obtained. These powder samples were collected for further characterization. All the chemical reactants were analytical grade.

**2.2. Characterizations Used.** The as-prepared products were characterized using X-ray powder diffractometer (XRD, Rigaku, D/max-RA), transmission electron microscopy (TEM, HITACHI H-8100), Fourier transform infrared spectrometer (FTIR, NA-360), thermogravimetric analyzer (TGA, Perkin-Elmer), and Raman spectrometer (Renishaw 1000) using excitation wavelengths of 325 nm (He-Cd laser). Besides, the particle size and distribution were determined by measuring the maximum diameter of more than 100 particles on the TEM images.

## 3. Results and Discussion

**3.1. XRD.** Figure 1 shows a typical powder XRD pattern of uncapped (a) and PVP-capped (b)  $\text{GeO}_2$  nanocrystals prepared by the hydrothermal experiments. All the diffraction peaks could be indexed to rutile structure  $\text{GeO}_2$  with cell constants  $a_0 = 4.831 \text{ \AA}$  and  $c_0 = 5.568 \text{ \AA}$ . These XRD peaks are in good agreement with those of the JCPDS card (no. 88-0285). It indicates that the obtained products are all of pure rutile phase  $\text{GeO}_2$ . No obvious differences can be observed in the XRD patterns of the uncapped (Figure 1(a)) and PVP-capped (Figure 1(b))  $\text{GeO}_2$  nanoparticles. This shows that PVP modification does not influence the structure of  $\text{GeO}_2$ .

**3.2. TEM.** Figure 2 shows typical TEM images of the non-capped (Figure 2(a)) and PVP-capped (Figure 2(b))  $\text{GeO}_2$  nanoparticles. We also provide the particle size and distribution histograms of the noncapped (Figure 3(a)) and PVP-capped (Figure 3(a))  $\text{GeO}_2$  nanoparticles. Average sizes of the uncapped  $\text{GeO}_2$  are in the range of 700–800 nm estimated from TEM images (Figure 2(a)). The obvious aggregation of the uncapped  $\text{GeO}_2$  nanocrystals may be due to the high surface energy of the nanocrystals. From Figure 2(b), the PVP-capped  $\text{GeO}_2$  nanoparticles had the same size (about 500 nm) compared with those without PVP modification. Moreover, we found that there were some smaller particles appeared in the TEM images. We thought that these small particles are also done when the  $\text{GeO}_2$  samples were uncapped with PVP. Because of the aggregation are much bigger than single particle, especially for the small size particle. When the small size is particle adsorbed on the aggregation, it is difficult to find it in the TEM images. Above all, from the TEM images, we could find that PVP plays an important role in monodispersion property of the  $\text{GeO}_2$  nanoparticles. In this process PVP lowered the surface energy of the nanocrystals, so capped  $\text{GeO}_2$  nanoparticles with monodispersion property were obtained as observed [15].

**3.3. FTIR.** The polymer capping of germanium oxide is confirmed through FTIR spectroscopy. Figure 4 shows typical FTIR spectra of  $\text{GeO}_2$  nanoparticles (Figure 4(a)) and the  $\text{GeO}_2$  nanoparticles modified with PVP (Figure 4(b)). The absorption bands around  $3400 \text{ cm}^{-1}$  observed in both spectra are attributed to O-H stretching mode of water and hydroxyl. The band (Figure 4(a)) at  $\sim 550 \text{ cm}^{-1}$  corresponds to Ge-OH stretching motion, and the band at  $\sim 899 \text{ cm}^{-1}$  corresponds to Ge-O-Ge stretching motion. The two stretching vibration bands located at  $\sim 550$  and  $\sim 889 \text{ cm}^{-1}$  are the characteristic peaks of  $\text{GeO}_2$  crystal [16]. The FTIR spectrum of PVP-capped  $\text{GeO}_2$  shows some remarkable spectral changes. The most prominent and informative bands in the spectrum of compounds occur in the high frequency range between  $400$  and  $1900 \text{ cm}^{-1}$ . For example the band at  $750 \text{ cm}^{-1}$  replaces the dominant peak of  $\text{GeO}_2$ , which corresponds to the Ge-O-C bending [17]. The most convincing evidence from FTIR spectra of the PVP-modified  $\text{GeO}_2$  is the absorption peaks at  $1265$  and  $1628 \text{ cm}^{-1}$  which

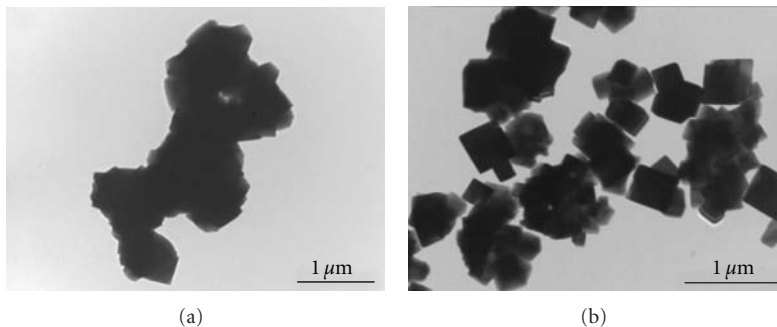


FIGURE 2: TEM images of the noncapped (a) and PVP-capped (b)  $\text{GeO}_2$  nanoparticles.

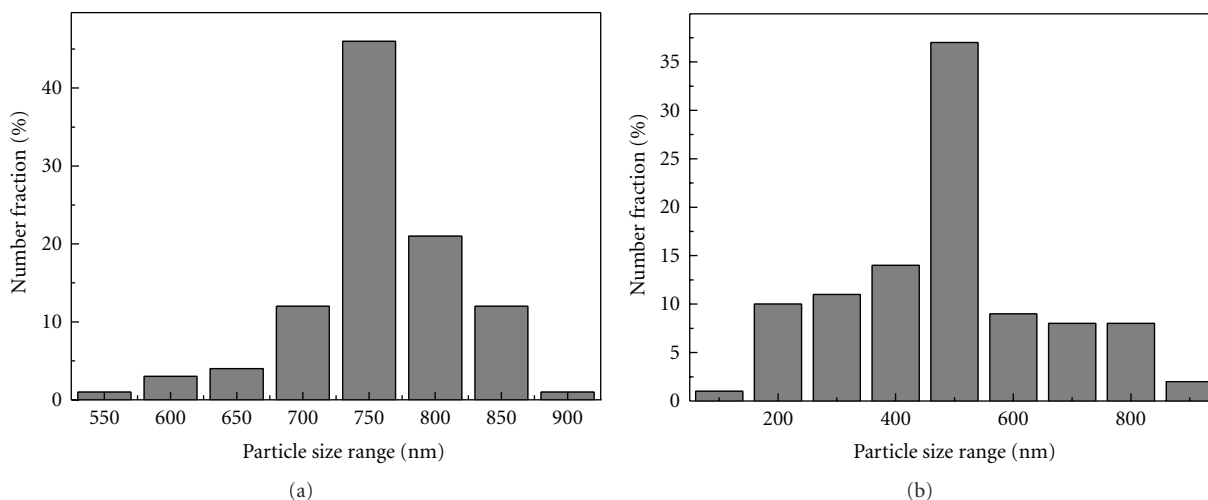


FIGURE 3: Particle size distribution histograms of the noncapped (a) and PVP-capped (b)  $\text{GeO}_2$  nanoparticles.

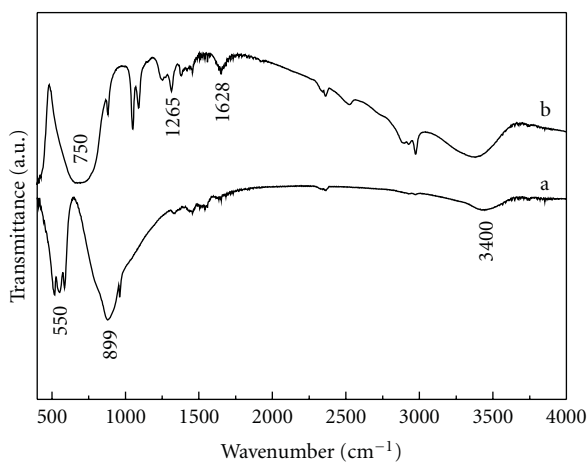


FIGURE 4: FTIR spectra of noncapped (a) and PVP-capped (b)  $\text{GeO}_2$  nanoparticles.

correspond to C-N stretching motion and C=O stretching motion of monomer for PVP, respectively [18–20]. The band at  $\sim 680 \text{ cm}^{-1}$  of Ge-O-C indicates that stable bonding exists between the  $\text{GeO}_2$  and some organic. Moreover

the absorption peaks at  $1265$  and  $1628 \text{ cm}^{-1}$  occurred in Figure 4(b), this is due to the presence of PVP [21]. These previous discussions of the FTIR spectroscopy confirm that the surface of obtained  $\text{GeO}_2$  particles is modified with PVP successfully.

**3.4. TGA.** The TGA of PVP-capped  $\text{GeO}_2$  samples was carried out in an inert nitrogen atmosphere in the temperature range of  $50\sim 900^\circ\text{C}$ . The heating rate employed was  $20^\circ\text{C}/\text{min}$ . The obtained TGA curve is shown in Figure 5. A continuous weight loss in TGA from  $500$  to  $700^\circ\text{C}$  indicates PVP decomposition. This suggests that the PVP decomposition in  $\text{GeO}_2$  modified by PVP starts at a temperature much higher than its synthesized temperature ( $\sim 150^\circ\text{C}$ ). These results indicate that the  $\text{GeO}_2$  nanoparticles were also successfully modified with PVP.

**3.5. PL Spectra.** The PL spectra were recorded with the excitation wavelength of  $325 \text{ nm}$ . The PL spectra of the noncapped (Figure 6(a)) and PVP-capped (Figure 6(b))  $\text{GeO}_2$  nanoparticles were shown in Figure 6. Both samples exhibited an emission band from  $570$  to  $690 \text{ nm}$ , but the relative intensity varied. Contrasting the PL spectra of PVP-capped and uncapped  $\text{GeO}_2$  nanoparticles, it is obvious that

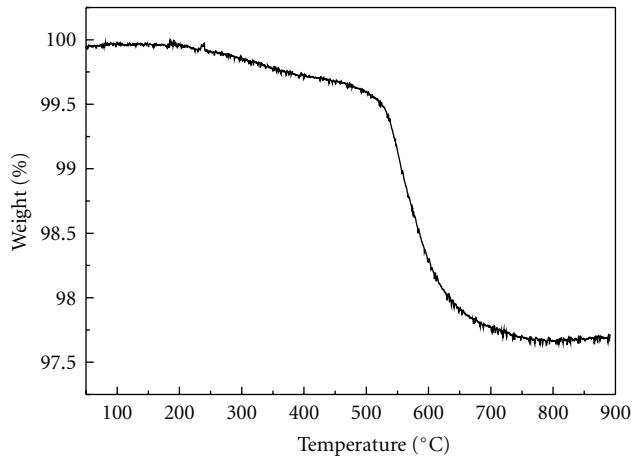


FIGURE 5: TGA curve for PVP-capped  $\text{GeO}_2$  taken in nitrogen atmosphere.

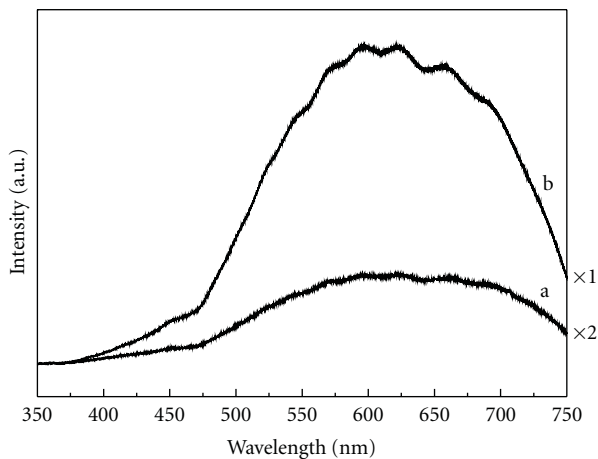


FIGURE 6: PL spectra of the noncapped (a) and PVP-capped (b)  $\text{GeO}_2$  nanoparticles.

the emission band of the uncapped particle is quite broad, and the PL intensity of capped nanoparticles is enhanced about one order of magnitude stronger than that of the noncapped ones. This result clearly justifies that the PVP as the capping agent can significantly enhance the PL intensity for  $\text{GeO}_2$  nanoparticles.

As it is known, the emission band was assigned to the surface trap-induced fluorescence, which involved the recombination of electrons trapped inside a germanium vacancy with a hole in the valence band of the  $\text{GeO}_2$  nanoparticles [22]. In our case, the enhanced luminescence properties of the capped  $\text{GeO}_2$  nanoparticles may be due to the PVP surface modification which may have the effect of minimizing surface defects and enhance the possibility of electron-hole recombination [23]. Besides PVP, other polymers, such as poly(ethylene glycol) (PEG), cetyltrimethylammonium bromide (CTAB), and oleic acid were also used. However, PVP was the effective polymer that could improve the luminescence properties of  $\text{GeO}_2$  nanoparticles obviously.

## 4. Conclusion

In summary, we have successfully synthesized monodisperse PVP-capped rutile  $\text{GeO}_2$  nanoparticles, via a facile hydrothermal process. This result indicates that PVP could control the morphology of rutile  $\text{GeO}_2$  effectively. In addition, the PL intensity of capped nanoparticles is enhanced about one order of magnitude stronger than that of the noncapped ones. We suggested that this performance improvement is due to the PVP surface modification which has the effect of minimizing surface defects and enhance the possibility of electron-hole recombination.

## Acknowledgments

This paper was supported financially by the NSFC (10979001 and 20773043), the National Basic Research Program of China (2005CB724400), the Program for the Changjiang Scholar and Innovative Research Team in University (IRT0625), the Cheung Kong Scholars Programme of China, and the National Fund for Fostering Talents of Basic Science (J0730311).

## References

- [1] S. Grandi, P. Mustarelli, S. Agnello, M. Cannas, and A. Cannizzo, "Sol-gel  $\text{GeO}_2$ -doped  $\text{SiO}_2$  glasses for optical applications," *Journal of Sol-Gel Science and Technology*, vol. 26, no. 1–3, pp. 915–918, 2003.
- [2] T. M. Davis, M. A. Snyder, and M. Tsapatsis, "Germania nanoparticles and nanocrystals at room temperature in water and aqueous lysine sols," *Langmuir*, vol. 23, no. 25, pp. 12469–12472, 2007.
- [3] M. Sahnoun, C. Daul, R. Khenata, and H. Baltache, "Optical properties of germanium dioxide in the rutile structure," *European Physical Journal B*, vol. 45, no. 4, pp. 455–458, 2005.
- [4] Z. Jiang, T. Xie, G. Z. Wang et al., " $\text{GeO}_2$  nanotubes and nanorods synthesized by vapor phase reactions," *Materials Letters*, vol. 59, no. 4, pp. 416–419, 2005.
- [5] L. Pajasová, "Optical properties of  $\text{GeO}_2$  in the ultraviolet region," *Czechoslovak Journal of Physics*, vol. 19, no. 10, pp. 1265–1270, 1969.
- [6] A. Trukhin, M. Kink, Y. Maksimov, J. Jansons, and R. Kink, "Luminescence of  $\text{GeO}_2$  glass, rutile-like and  $\alpha$ -quartz-like crystals," *Journal of Non-Crystalline Solids*, vol. 352, no. 2, pp. 160–166, 2006.
- [7] E. Ghobadi and J. A. Capobianco, "Crystal properties of  $\alpha$ -quartz type  $\text{GeO}_2$ ," *Physical Chemistry Chemical Physics*, vol. 2, no. 24, pp. 5761–5763, 2000.
- [8] M. Micoulaut, L. Cormier, and G. S. Henderson, "The structure of amorphous, crystalline and liquid  $\text{GeO}_2$ ," *Journal of Physics Condensed Matter*, vol. 18, no. 45, pp. R753–R784, 2006.
- [9] M. R. Khanlary, P. D. Townsend, and N. Gustavsson, "Luminescence of rutile-like  $\text{GeO}_2$  crystals," *Radiation Effects and Defects in Solids*, vol. 127, no. 1, pp. 61–74, 1993.
- [10] H. P. Wu, J. F. Liu, M. Y. Ge et al., "Preparation of monodisperse  $\text{GeO}_2$  nanocubes in a reverse micelle system," *Chemistry of Materials*, vol. 18, no. 7, pp. 1817–1820, 2006.
- [11] M. Zheng, M. Gu, Y. Jin, and G. Jin, "Preparation, structure and properties of  $\text{TiO}_2$ -PVP hybrid films," *Materials Science and Engineering B*, vol. 77, no. 1, pp. 55–59, 2000.

- [12] A. A. Bol and A. Meijerink, "Doped semiconductor nanoparticles—a new class of luminescent materials?" *Journal of Luminescence*, vol. 87, pp. 315–318, 2000.
- [13] S. J. Xu, X. C. Wang, S. J. Chua et al., "Effects of rapid thermal annealing on structure and luminescence of self-assembled InAs/GaAs quantum dots," *Applied Physics Letters*, vol. 72, no. 25, pp. 3335–3337, 1998.
- [14] S. V. Manorama, K. Madhusudan Reddy, C. V. Gopal Reddy, S. Narayanan, P. Rajesh Raja, and P. R. Chatterji, "Photostabilization of dye on anatase titania nanoparticles by polymer capping," *Journal of Physics and Chemistry of Solids*, vol. 63, no. 1, pp. 135–143, 2002.
- [15] N. Varghese, K. Biswas, and C. N. R. Rao, "Investigations of the growth kinetics of capped CdSe and CdS nanocrystals by a combined use of small angle X-ray scattering and other techniques," *Chemistry*, vol. 3, no. 8-9, pp. 1435–1442, 2008.
- [16] Y.-W. Chiu and M. H. Huang, "Formation of Hexabranched GeO<sub>2</sub> Nanoparticles via a Reverse Micelle System," *Journal of Physical Chemistry C*, vol. 113, no. 15, pp. 6056–6060, 2009.
- [17] R. Fajgar, M. Jakoubková, Z. Bastl, and J. Pola, "Germanium-containing coatings by IR laser-induced decomposition of ethoxy(trimethyl) germane and tetramethylgermane," *Applied Surface Science*, vol. 86, no. 1–4, pp. 530–532, 1995.
- [18] X. Feng, Y. Liu, C. Lu, W. Hou, and J.-J. Zhu, "One-step synthesis of AgCl/polyaniline core-shell composites with enhanced electroactivity," *Nanotechnology*, vol. 17, no. 14, pp. 3578–3583, 2006.
- [19] X. Lu, L. Li, W. Zhang, and C. Wang, "Preparation and characterization of Ag<sub>2</sub>S nanoparticles embedded in polymer fibre matrices by electrospinning," *Nanotechnology*, vol. 16, no. 10, pp. 2233–2237, 2005.
- [20] E. Hao and T. Lian, "Buildup of polymer/Au nanoparticle multilayer thin films based on hydrogen bonding," *Chemistry of Materials*, vol. 12, no. 11, pp. 3392–3396, 2000.
- [21] M. Zawadzki and J. Okal, "Synthesis and structure characterization of Ru nanoparticles stabilized by PVP or  $\gamma$ -Al<sub>2</sub>O<sub>3</sub>," *Materials Research Bulletin*, vol. 43, no. 11, pp. 3111–3121, 2008.
- [22] M. Sahnoun, C. Daul, R. Khenata, and H. Baltache, "Optical properties of germanium dioxide in the rutile structure," *European Physical Journal B*, vol. 45, no. 4, pp. 455–458, 2005.
- [23] S. H. Liu, X. F. Qian, J. Yin, X. D. Ma, J. Y. Yuan, and Z. K. Zhu, "Preparation and characterization of polymer-capped CdS nanocrystals," *Journal of Physics and Chemistry of Solids*, vol. 64, no. 3, pp. 455–458, 2003.

## Research Article

# Mesoporous Titania Nanocrystals by Hydrothermal Template Growth

**Giuseppe Cappelletti, Silvia Ardizzone, Francesca Spadavecchia, Daniela Meroni, and Iolanda Biraghi**

*Dipartimento di Chimica Fisica ed Elettrochimica, Università degli Studi di Milano, Via Golgi 19, 20133 Milano, Italy*

Correspondence should be addressed to Giuseppe Cappelletti, giuseppe.cappelletti@unimi.it

Received 6 May 2010; Revised 30 June 2010; Accepted 22 July 2010

Academic Editor: William W. Yu

Copyright © 2011 Giuseppe Cappelletti et al. This is an open access article distributed under the Creative Commons Attribution License, which permits unrestricted use, distribution, and reproduction in any medium, provided the original work is properly cited.

Mesoporous TiO<sub>2</sub> nanocrystals have been synthesized by a classical sol-gel route integrated by an hydrothermal growth step using monomeric (dodecylpyridinium chloride, DPC) or dimeric gemini-like (GS3) surfactants as template directing agents. Adsorption isotherms at the solid/liquid interface of the two surfactants have been obtained on aqueous dispersion of titania; the nature of the oxide/adsorbate interactions and the molecules orientation/coarea are discussed. The effects produced by the presence of the two surfactants on the different morphological (surface area, porosity, and shape) and structural (phase composition and aggregate size) features of the final TiO<sub>2</sub> samples, calcined at 600°C, are discussed.

## 1. Introduction

In recent years, the achievement of mesoporous titania nanomaterials, characterized by desired grain size, specific shape, high surface area, and tailored pore network, has become fundamental for photocatalytic and photovoltaic applications [1–4].

Several liquid-crystal templating (LCT) techniques, exploiting three-dimensional structures of ionic/nonionic surfactants [5–10] and block copolymers [11–13] have been proposed to synthesize mesoporous titanium oxides. The presence of mesoscopic pores in TiO<sub>2</sub> for dye-sensitized solar cells is of great importance; in fact when the pores are filled with a conducting medium, charge carriers can easily percolate across the mesoscopic particle network making the whole internal surface area electronically accessible [14]. However, the fine control of the, often divergent, features of the material is very complex and the presence of the organic templating surfactant with the inherent high decomposition temperature may imply undesired effects. Just for these reasons, the extension of LCT techniques to pure titanium oxide has still remained elusive; the fast grain growth of the oxide, which occurs upon calcination of the surfactant-rich

precursor, provokes, in fact, pore collapse with degradation of the mesostructure.

Besides the possible promotion of a controlled pore network, the presence of an amphiphilic molecule can intervene in different ways by tuning the sample final morphology. Very interesting is, for instance, the recent work by Chen et al. [16], where three-dimensionally ordered arrays of mesoporous titania spheres have successfully been synthesized through opal (ordered closed-packed face-centered cubic lattice of silica or latex spheres) template and triblock copolymer (Pluronic P123) as a mesopore-directing agent. The mean diameter of the titania spheres has been observed to be *ca.* 165 nm with a narrow distribution of the mesopore size in the range of 2–6 nm.

Together with the surface area/porosity, also the grain size and relative enrichment in the different oxide polymorphs should be controlled through template routes to promote the best efficiency of the TiO<sub>2</sub>-based semiconductors [9, 10]. Crystallite sizes in the range of 10–80 nm are considered optimal for both optical absorption and electron transport in the conversion of solar light to electric current, by dye-sensitized solar cells [14, 17, 18]. Anatase exhibits the highest activity for photovoltaic applications, while a

controlled mixture of anatase and rutile or brookite is reported to produce the best activity in photodegradation experiments [19, 20]. Mohamed et al. [5] reported that an hydrothermal treatment in the presence of cationic surfactants (cetyltrimethylammonium bromide, CTAB and cetylpyridinium bromide, CPB) as templates may control not only the surface properties (surface area of 240–418 m<sup>2</sup> g<sup>-1</sup>, pore size in the range of 23.2–43.7 Å) and morphology (from nano-sized spheres to cotton fibrils) but also the bulk features (crystallites size in the range of 10.1–18.2 nm) and phase composition (rutile phase at 350°C).

Here we report on the synthesis, of TiO<sub>2</sub> nanocrystals, through a simple process implying a sol-gel starting reaction, followed by a growth step in solution, performed, also, in the presence of monomeric or dimeric “gemini-like” alkylpyridinium surfactants. The latter ones are composed by two conventional single-tail amphiphilic moieties chemically connected by spacer groups, usually polymethylene or short poly(oxyethylene) chains [10, 21]. Recently, many studies concerning the practical use of gemini molecules appeared in the literature [22–25], showing that the first speculative interests were followed by practical applications, due to their unusual properties, such as the lower critical micellar concentration (CMC) values, the better adsorption behavior at both the air/water and the solid/water interfaces with respect to their single monomers, and the tendency to form micelles of different shapes and dimensions (i.e., spherical, rodlike, threadlike, vesicles), even at low concentration, when compared with similar nongemini surfactants. In this work, the concentration of surfactants in the ageing solution is varied in order to produce different conditions of self-aggregation between the surfactant molecules themselves. The surfactant/oxide interactions at the solid/liquid interface are evaluated by adsorption isotherms on aqueous suspension of titanium dioxide. The features of the calcined (600°C) powders are investigated with respect to the phase composition/crystallinity, the surface area/porosity, and morphological aspects to evidence the effects provoked by the conditions of the particle template growth.

## 2. Experimental Section

All the chemicals were of reagent grade purity and were used without further purification; bi-distilled water passed through a Milli-Q apparatus was used to prepare solutions and suspensions.

**2.1. Sample Preparation.** TiO<sub>2</sub> particles were obtained by following a room-temperature sol-gel reaction starting from Ti(C<sub>4</sub>H<sub>9</sub>O)<sub>4</sub> and adopting a water/alkoxide molar ratio of 81.7 and a water/propanol molar ratio of 8.5. The xerogel powders were purified by centrifugation-resuspension cycles and then powder fractions were aged at 80°C, at pH 8 (i.e., condition of attractive electrostatic interactions between the oxide and the cationic surfactants), for fixed timelength (5 h) with different surfactants concentrations: 1–100 mM and 0.1–50 mM for dodecylpyridinium chloride, DPC (compound 1) and 1, 1'-didodecil-2, 2'-trimetilendipiridinio-dicloruro, “gemini spacer 3” GS3 (compound 2), respectively.

After the ageing, the suspensions were dried again at 80°C. Finally the powders were thermally treated at 600°C for 6 hours under an oxygen stream.

**2.2. Sample Characterization.** Room-temperature X-ray powder diffraction (XRPD) patterns were collected between 10 and 80° with a Siemens D500 diffractometer, using Cu K<sub>α</sub> radiation. Rietveld refinement has been performed using the GSAS software suite and its graphical interface EXPGUI [26, 27]. The average diameter of the crystallites, <D>, was estimated from the most intense reflection of the anatase (101) and rutile (110) TiO<sub>2</sub> phases using the Scherrer equation [28].

Specific surface areas were determined by the classical BET procedure using a Coulter SA 3100 apparatus. Desorption isotherms were used to determine the pore size distribution using the Barret-Joyner-Halander (BJH) method.

Scanning electron microscopy (SEM) photographs are acquired with a LEO 1430.

The values of the critical micelle concentration (CMC) of DPC and gemini surfactants were obtained by conductometric determinations as a function of the temperature. Therefore, using as a guideline an average increasing slope with the temperature of the CMC of DPC and GS3, obtained from the present results and literature data [15, 21, 29–32], a concentration range roughly corresponding to a possible CMC at 80°C was estimated for both surfactants (18–22 mM, for DPC and 2–4 mM in the case of GS3).

The adsorption isotherm of GS3 at the TiO<sub>2</sub> interface was obtained under the following conditions:  $T = 25 \pm 0.3^\circ\text{C}$ ;  $\text{pH} = 8.0 \pm 0.2$ ; equilibration time = 4 h; ionic strength  $I = 2 \times 10^{-3}$  M KCl. At the end of the adsorption time, the supernatant solution was sampled for the residual surfactant concentration by spectrophotometric characterization at 265 nm for the gemini salt. Data on DPC adsorption on TiO<sub>2</sub>, obtained by Koopal et al. [15] are elaborated and reported for comparison ( $T = 21 \pm 1^\circ\text{C}$ ;  $\text{pH} = 8.0 \pm 0.2$ ; equilibration time = 12 h; ionic strength  $I = 1 \times 10^{-3}$  M NaCl). Adsorption isotherms of the two surfactant molecules are reported by plotting the surface excess ( $\Gamma$ ) as a function of the final concentration at equilibrium.

## 3. Results and Discussion

**3.1. Adsorption at TiO<sub>2</sub>-Solution Interface.** Figure 1 reports the experimental adsorption isotherms, at the TiO<sub>2</sub> solution interface, of both monomeric DPC (Figure 1(a), elaborated from data in [15]) and dimeric “gemini-like” GS3 (Figure 1(b)) surfactants. The shape of the two curves is markedly different. The monomer isotherm (Figure 1(a)) is S-shaped showing a low adsorbent-adsorbate affinity due to weak interactions between the surfactant and the oxide [15]; moreover, it can be proposed that the adsorption leads to the formation of surface ion pairs, Ti–O<sup>-</sup>Py<sup>+</sup> (the surface charge of TiO<sub>2</sub> at pH 8 is negative), provoking a partial compensation of the surfactant aromatic charge, in accordance with our previous XPS results [10]. The curve pertaining to the gemini (Figure 1(b)), instead, follows the trend classified in the literature as L-type, which is generally

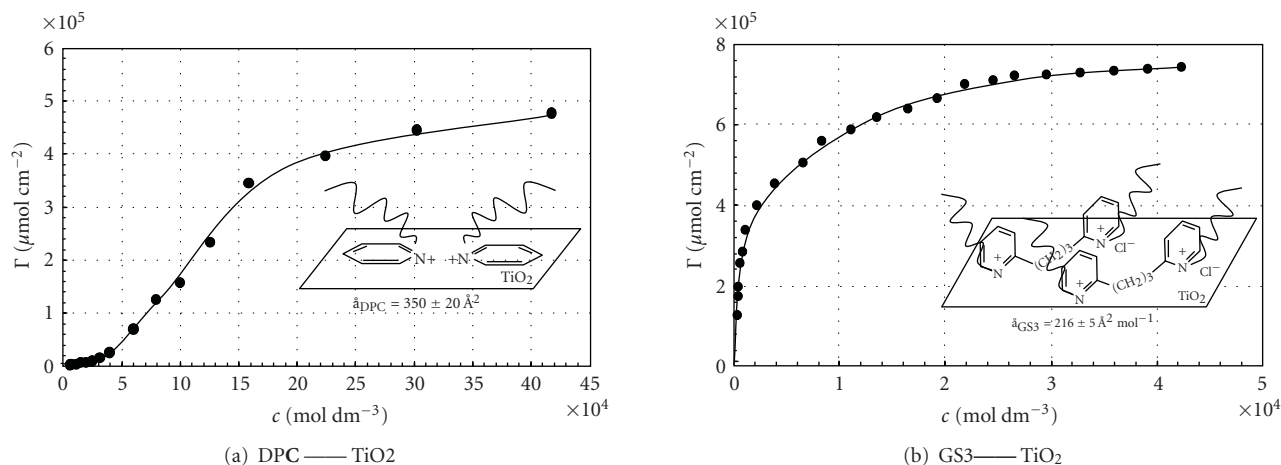
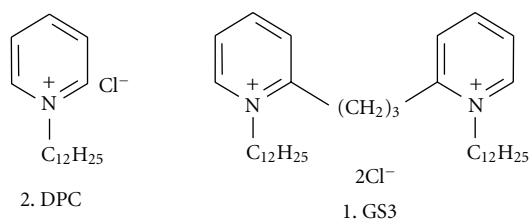


FIGURE 1: Adsorption isotherms (surface excess versus equilibrium concentrations) at the  $\text{TiO}_2$ /solution interface of (a) monomeric DPC and (b) dimeric GS3 surfactants. Inset: sketches of possible disposition/orientations of the adsorbed surfactant at the titania surface;  $\hat{a}$  is the adsorbate coarea value, calculated from the maximum coverage ( $\Gamma_{\max}$ ). Data of DPC are reelaborated from [15].



SCHEME 1

associated with coverage of the solid surface by a monolayer of adsorbate molecules and is characterized by a strong adsorbent-adsorbate interaction. The higher affinity of the gemini GS3 for the solid appears also from the larger adsorbed amounts ( $\Gamma_{\max} = 7.7 \times 10^{-5} \mu\text{mol cm}^{-2}$ ) in the quasiplateau regions with respect to the maximum surface excess ( $\Gamma_{\max} = 4.8 \times 10^{-5} \mu\text{mol cm}^{-2}$ ) of the monomeric DPC surfactant. For these reasons, the data relative to the DPC and GS3 isotherms were elaborated on the basis of the Langmuir (strong adsorbent-adsorbate interaction, no lateral interactions between adsorbate molecules) and the Frumkin-Fowler-Guggenheim (FFG, weak adsorbent-adsorbate interaction, electrostatic and nonelectrostatic lateral interactions [33–35]) model equations, respectively. The parameters obtained from the treatment of the data are reported in Table 1. The linear correlation ( $R^2$ ) is good in both cases, justifying the choice of the two different model approaches. The adsorption equilibrium constants ( $\beta$ ) and the relative standard adsorption Gibbs energy ( $\Delta G^0$ ) values support the dramatic increase in adsorption at the  $\text{TiO}_2$  surface passing from the monomer to the dimer [36]. In the case of the DPC isotherm, the lateral interaction parameter ( $a$ ) is positive, that is, it represents electrostatic repulsion interactions between the positive charges of the surfactant headgroups, in agreement with what reported by Mehrian et al. [37] in the case of DPC adsorption on clays. They studied the influence of the electrolyte concentration on

TABLE 1: Data ( $\beta$ , adsorption equilibrium constant;  $\Delta G_0$ , standard adsorption Gibbs energy;  $a$ , lateral interaction parameter) from the elaboration of GS3 and DPC isotherms.

isotherm	model	$R^2$	$\beta$	$\Delta G^0 \text{ kJ mol}^{-1}$	$a$
DPC	FFG	0.97	$160 \pm 20$	$-5.6 \pm 0.2$	$3.2 \pm 0.2$
GS3	Langmuir	0.997	$48000 \pm 6000$	$-27.1 \pm 0.3$	—

the adsorption of DPC on Na-kaolinite; an attractive lateral term was obtained only in the case of high ionic strength (100 mM), while repulsion prevailed at lower electrolyte concentrations (5 and 20 mM).

The limiting areas ( $\hat{a}$ , co-area) for DPC and GS3 (350 and  $216 \text{ \AA}^2$ , resp.) at maximum packing ( $\Gamma_{\max}$ ) calculated from the surface excess at maximum coverage are higher than those present in the literature. Ottewill et al. [38] reported two different values of coarea for DPC molecule, obtained by surface tension at the air-water interface, in the case of flat-lying ( $110 \text{ \AA}^2$ ) and vertical ( $35 \text{ \AA}^2$ ) orientations. Thus, on the basis of these considerations, the present size of adsorbed DPC molecule could be interpreted as being due to a flat orientation (sketch inset Figure 1), with the formation of a diluted film, characterized by electrostatic repulsion between the charged pyridinium heads. On the contrary, the lower value of  $\hat{a}$  for the GS3 surfactant could be ascribable to a vertical orientation (see sketch inset Figure 1) in which, in agreement with our previous results of adsorption of gemini zero-spacer on  $\text{TiO}_2$  [36], only one pyridinic group is directly involved in the electrostatic interactions with the oxide, whereas the second one is compensated by its counterion ( $\text{Cl}^-$ ).

Further information concerning the surfactant adsorption isotherms can be appreciated from the log-log coordinates (Figure 2). The primary advantage of using a log-log plot is that it amplifies the features of the isotherm at low surface excess values. The general form of isotherms plotted in this manner and the morphology of adsorbed

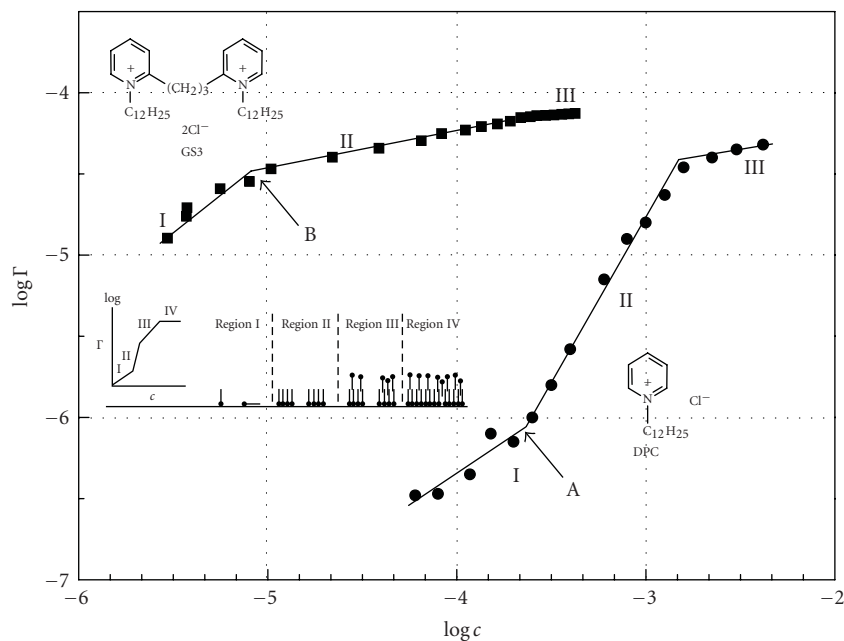


FIGURE 2: Log-log plot of the surface excess ( $\Gamma$ ) as a function of the equilibrium concentration for DPC and GS3 surfactants. Inset: the general shape of surfactants adsorption isotherms at solid substrates and the proposed four-region model of adsorption.

structures associated with each region are depicted schematically in the inset of Figure 2. Somasundaran et al. [39, 40] proposed the four-region model attributed, respectively, to the adsorption of (I) monomers by electrostatic interactions, (II) surface aggregates (hemimicelles) up to the substratum charge compensation, (III) headout molecules by chain-chain interactions, and (IV) fully formed bilayer. Further increases in the solution surfactant concentration do not lead to any further increases in the surface excess. From the plot (Figure 2), only three regions are appreciable since the isotherms are limited to monolayer coverage (for both surfactants,  $c_{\text{SURF}} < \text{CMC}$ ) without the complete formation of bilayers. The surfactant concentration relative to the beginning of hemimicelle formation is about  $1.8 \times 10^{-4}$  M and  $8.0 \times 10^{-6}$  M, respectively for DPC (A point) and GS3 (B point); these values could be compared with the bulk CMC values (DPC:  $1.6 \times 10^{-2}$  M, GS3:  $1.5 \times 10^{-3}$  M at  $25^\circ\text{C}$ ) obtained from conductimetric/tensiometric determinations [15, 21, 29–32], following the criterion reported by Fuerstenaue and Jang [41] that hemimicelles may occur in about 1/100th of the CMC.

The trend between the two isotherms (the shift along the  $x$ -axis, the variation of the slope in the different regions and the distribution of surface excesses) is the expected one due to the presence of a second homologous pyridinic ring in the case of GS3 species. For both surfactants, the slope of the plot in the Region I (the Henry region) is unity in the ideal situation ( $\Delta G^0$  is constant) [15]. The initial slope of the experimental isotherms cannot be determined accurately, but they are, within experimental error, almost equal to unity. The slope of the DPC curve increases passing from Region I to Region II, where hemimicelles form, indicating that the adsorption is enhanced by the formation of surface

aggregates. This trend is typical for S-shaped isotherms [15]. In the case of the gemini molecules the slope is, instead, depressed in the region of hemimicelles, possibly due to the steric hindrance.

### 3.2. Self-Aggregation Features of DPC and GS3 Surfactants.

It is well known that many physicochemical properties of a solution show sudden changes when a characteristic concentration of a surfactant is exceeded. This change is attributed to the formation of colloidal aggregates and occurs over a relatively small concentration range characteristic for the surfactant. The formation of direct micelles of DPC in water and in aqueous salt solutions has been the object of numerous studies performed in time by different experimental approaches. By scattering techniques, DPC is reported to form in water, globular micelles with aggregation number of about 20, with a corresponding micellar radius of about 1.9 nm, comparable with the extended length of a  $C_{12}$  chain (1.67 nm) [30–32, 42, 43]. Spherical DPC micelles are not reported to aggregate in tridimensional structures [31]. The corresponding gemini surfactant (GS3) having short spacer ( $n = 3$ ) has a particular behavior since it binds its counterions more strongly than the “single” does, as the  $n$ - $s$ - $n$  ammonium gemini amphiphiles [44–47]. The lack of conformational freedom could be the result of the sharing of one counterion between the two pyridinium head groups [21]. As a consequence, the short spacer surfactant (GS3) is probably aggregating in nonspherical micelles, but in elongated forms, like rods, as reported in the literature for ammonium gemini surfactants [48–50]. In particular, Manne et al. [48] found that symmetric gemini  $C_{12}$ - $s$ - $C_{12}$  ( $s \leq 6$ ) surfactants composed by linear hydrocarbon tail with quaternary ammonium headgroups may assemble

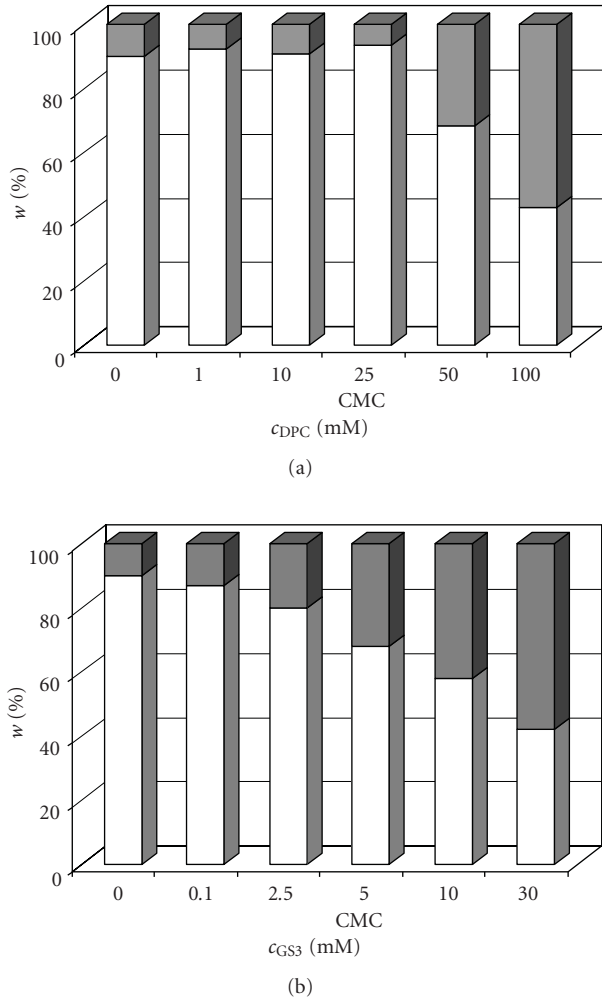


FIGURE 3: Relative phase enrichment in anatase (□) and rutile (■)  $\text{TiO}_2$  polymorphs of samples grown in surfactant solutions and subsequently calcined at  $600^\circ\text{C}$ . (a) DPC, (b) GS3.

in hexagonal cylinders in silicate mesophase and parallel cylinders at the mica surface with average spacings of  $4.2 \pm 0.4$  nm. Thus, possibly cylinders in hexagonal arrangement for gemini spacer 3 could also occur at high surfactant concentrations.

**3.3. Structural and Morphological Results of Surfactant-Assisted Titania Samples.** Recently a great interest was devoted to the growth of titania particles with controlled morphology and porosity through template and template-free procedures [51–53]. Yu et al. obtained by a template-free preparation of  $\text{TiO}_2$  a fine control of macro and mesoporosity up to about  $500^\circ\text{C}$ . For higher calcination temperatures, a total collapse of both surface area and porosity took place.

In the present work, the effects provoked by the concentration of both monomeric (DPC) and gemini (GS3) alkylpyridinium salts in the growth solution, on the features of the  $\text{TiO}_2$  particles are considered. Figure 3 reports the

TABLE 2: Anatase (A), rutile (R) domain sizes and BET surface area for all samples.

Sample	$\langle D_A \rangle$ (nm)	$\langle D_R \rangle$ (nm)	$S_{\text{BET}}$ ( $\text{m}^2 \text{g}^{-1}$ )
no SURF	28	—	18
1 mM	20	—	19
10 mM	22	—	19
DPC 25 mM (~CMC)	24	—	16
50 mM	32	86	8
100 mM	41	>100	5
0.1 mM	23	—	20
2.5 mM	30	54	16
GS3 5 mM (~CMC)	37	63	13
10 mM	44	73	14
30 mM	43	76	11

relative phase enrichment (histograms) at different surfactant concentrations of samples submitted to a hydrothermal growth step in the presence of the DPC and GS3, subsequently calcined at  $600^\circ\text{C}$ . The anatase and rutile amount in the samples appears to depend on the concentration of the surfactant in the solution adopted for the ageing. When the concentration corresponds to the existence of nonaggregated surfactant units (1, 10 mM for DPC and 1, 2.5 mM for GS3), the anatase polymorph is prevalent; the crystallite sizes (Table 2) appear to be smaller than those in the absence of surfactant. The specific surface areas of the calcined oxide remain quite the same (Table 2). By increasing the surfactant concentration at values larger than the CMC (>25 mM for DPC and >5 mM for GS3), the amount of anatase decreases and the anatase and rutile structures are almost equally promoted. The formation of rutile is paralleled by larger crystallite sizes and lower surface areas (Table 2). Moreover, the presence of GS3 at higher concentrations seems to preserve the surface area ( $11$ – $14 \text{ m}^2 \text{g}^{-1}$ ) and to limit the increase in rutile crystallite sizes ( $\sim 75$  nm) with respect to the DPC surfactant ( $5$ – $8 \text{ m}^2 \text{g}^{-1}$  and  $>85$  nm, resp.).

These results are considered to be significant since after a calcination at  $600^\circ\text{C}$  both the surface area and the total pore volume are still appreciable at variance with samples prepared by template-free procedures [51–53]. The trend in Figure 3 is in agreement with the generally reported lower surface energy of anatase with respect to rutile [54, 55] and with the consistent finding that the phase transformation to rutile occurs after the anatase grains have grown to a certain threshold size, of about 30–40 nm [56]. Actually, during the hydrothermal step particle growth through Ostwald ripening can be expected to occur [57]. When the growth occurs in the presence of a non-aggregated surfactant, the surface of the precursor particles is shielded from the deposition of soluble Ti species by the presence of the surfactant film. The growth is slightly depressed, the particles remain smaller and stable supporting the formation of anatase. At higher

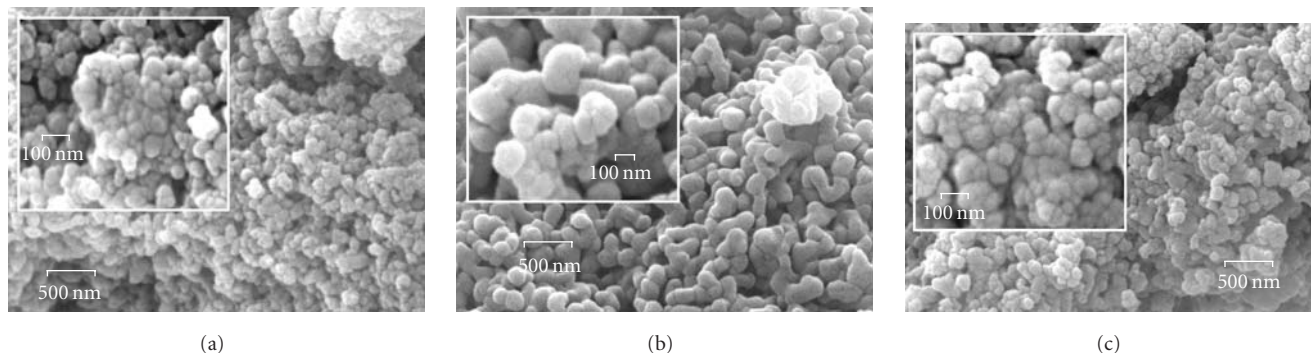


FIGURE 4: SEM micrographs of titania particles hydrothermally grown in absence of surfactant (a) and in presence of high concentration of (b) DPC (100 mM) and (c) GS3 (30 mM), subsequently calcined at 600°C.

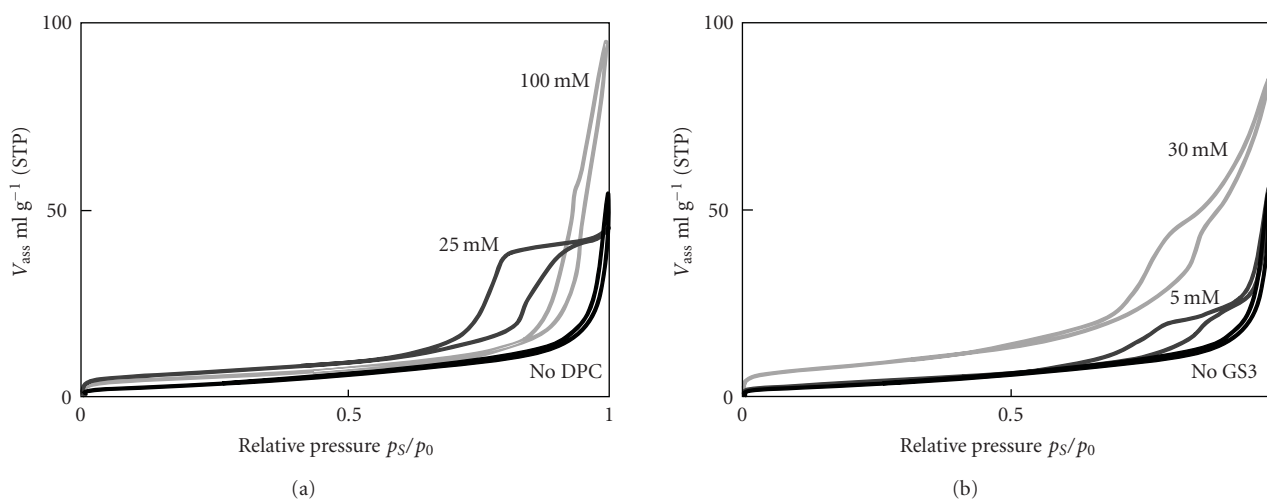


FIGURE 5:  $N_2$  adsorption—desorption isotherms of  $TiO_2$  samples aged in different surfactant solutions and calcined at 600°C. (a) DPC, (b) GS3

concentrations, the micelles may act as carriers for the soluble Ti containing species promoting the growth. Further, the micelles may be, also, adsorbed at the surface of different particles and may therefore promote bridging phenomena leading to larger particles.

These considerations are closely mirrored by the particle morphology as apparent in SEM micrographs (Figure 4). In the case of the sample prepared in the absence of the surfactant (Figure 4(a)), small spheroidal particles with an average size of about 30 nm grouped in raspberry-like aggregates can be appreciated; in the case instead of the sample grown at high DPC concentration (Figure 4b) the particles are much larger, with sizes ranging from about 100 nm (single crystals) and to about 200–300 nm as the result of sintering between crystallites. The large particles in Figure 4(b), show a particularly smooth surface. This effect is presumably the result of a surface annealing provoked by the heat released during the surfactant combustion. In the case of titania particles grown at high GS3 concentration, the shape of the aggregates remains spheroidal, characterized by a diameter of  $\sim 60$ –70 nm.

The mesoporosity induced by micelles and further three-dimensional organization of both surfactants can be appreciated by the hysteresis loop of the nitrogen adsorption—desorption isotherm (Figure 5), with respect to the reference material prepared without surfactant. The hydrothermal treatment in the presence of DPC micelles ( $c_{DPC} = 25$  mM, Figure 5 (a)) leads to titania particles with bottle-neck shaped pores mainly in the range of  $6 < d < 10$  nm (Figure 6 (a)), comparable with the average diameter of the globular DPC micelles ( $\sim 4$  nm) [48]. When the particles are grown at  $c_{DPC} > CMC$ , the shape of hysteresis loops is similar to the reference sample; the total pore volume increases, but the fraction of desired mesopores is not relevant. On the other hand, the presence of GS3 cylindrical micelles and three-dimensional hexagonal arrangements (sketches in Figure 6 (b)) produces an increase of total pore volume at increasing surfactant concentration (Figure 6 (b)), especially the fraction of mesopores with diameters in the range  $6 < d < 20$  nm. The shape of the hysteresis loop is typical of open-ended slit-shaped pores (Figure 5 (a)). A typical pore size distribution curve for the hydrothermally treated

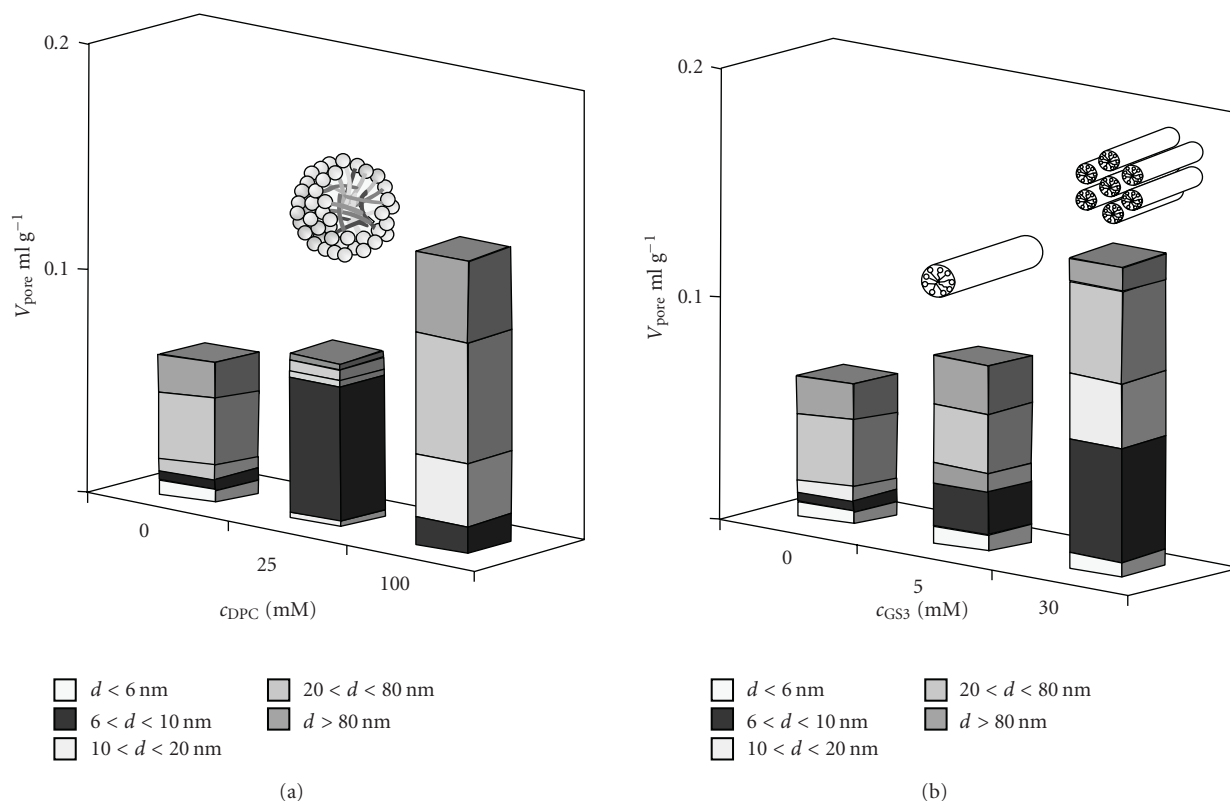


FIGURE 6: Pore volume distribution of  $\text{TiO}_2$  samples after (a) DPC and (b) GS3 ageing as a function of surfactant concentration and calcined at  $600^\circ\text{C}$ . Insets: possible surfactant three-dimensional aggregations.

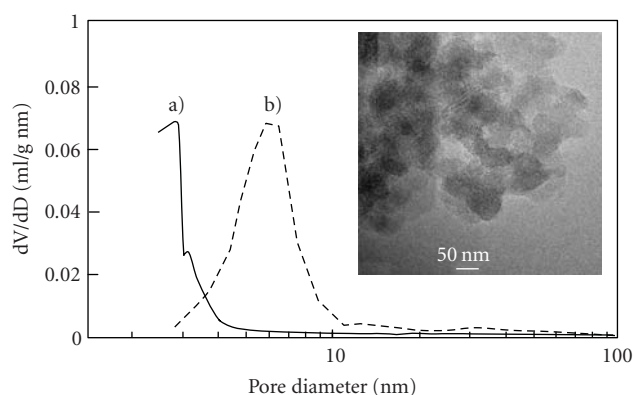


FIGURE 7: Pore size distribution curve of (a)  $\text{TiO}_2$  bare particles and (b) after GS3 ageing (30 mM) calcined at  $600^\circ\text{C}$ . Inset: HRTEM image of GS3 hydrothermally treated and calcined sample.

$\text{TiO}_2$  in the presence of three-dimensional GS3 hexagonal arrangements is shown in Figure 7. A fairly narrow size distribution, 6–20 nm, is achieved for the present sample at variance with the untreated one (calcined at  $600^\circ\text{C}$ ), which shows almost no porosity. This result indicates that the hydrothermal template treatment of the  $\text{TiO}_2$  particles leads to their aggregation with evolution of a mesoporosity probably arising from the template structure, which is successively thermally decomposed. Part of the mesoporous

structure can be appreciated in the HRTEM image of inset of Figure 7.

These results, together with the surface and morphological aspects, could be explained by invoking the different local heat of combustion (during the calcination step) for DPC and GS3, especially for higher surfactant concentrations. Possible ordered hexagonal GS3 arrangements with respect to unstructured spherical DPC micelles with random size distribution may lead to lower surfactant/oxide ratio in the template growth, even if the GS3 surfactant is formed by double aromatic ring.

#### 4. Conclusion

The features of the adsorption isotherms of monomeric (DPC) and gemini (GS3) alkylpyridinium surfactants at the  $\text{TiO}_2$  solution interface are markedly different. DPC gives rise to a very diluted surface film, characterized by weak adsorbate/adsorbent interactions and repulsive lateral interactions. This behaviour is paralleled by a weak self-aggregation tendency, apparent in the sole formation of very small, globular micelles and no long range ordered mesostructures. The behaviour of the gemini, instead, is typical of strong (chemi- and physi-) interactions with  $\text{TiO}_2$  occurring in the absence of lateral interactions. The vertical orientation of the molecule, suggested on the grounds of the

present adsorption data, is fully consistent with the formation of elongated rods and further hexagonal arrangements proposed for gemini surfactant mesostructures.

The above-mentioned specific features of the two surfactants are actually the reason why they produce different effects on the final oxide characteristics, especially on its mesoporosity.

For growths performed at concentrations larger than the CMC, very numerous small DPC micelles are randomly embedded into the oxide, giving rise, during the ensuing calcinations step, to large heats of combustion, particle sintering, and an almost uncontrolled mesoporosity.

In the case of gemini, instead, the relevant surfactant/oxide interactions allow the templating function of the surfactant to significantly occur. The much lower surfactant/oxide ratio than in the case of DPC, inherent in the rods versus globule structure, leads to a lower heat of combustion and to controlled particle shape, size, and mesoporosity.

## Acknowledgments

The authors wish to thank Professor G. Viscardi and Professor P. Quagliotto of Università di Torino for the synthesis of the gemini spacer 3 (GS3) surfactant. This research has been supported by the University of Milan Research Funds (FIRST, PUR).

## References

- [1] A. S. Attar, M. S. Ghamsari, F. Hajiesmaeilbaigi, SH. Mir-damadi, K. Katagiri, and K. Koumoto, "Sol-gel template synthesis and characterization of aligned anatase-TiO<sub>2</sub> nanorod arrays with different diameter," *Materials Chemistry and Physics*, vol. 113, no. 2-3, pp. 856–860, 2009.
- [2] H. Chen, J. Yan, Z. Ye et al., "One pot synthesis of mesostructured non-silica oxides nanocrystallites," *Journal of Materials Science*, vol. 44, no. 24, pp. 6531–6537, 2009.
- [3] D. P. Wang and H. C. Zeng, "Nanocomposites of anatase-polyaniline prepared via self-assembly," *Journal of Physical Chemistry C*, vol. 113, no. 19, pp. 8097–8106, 2009.
- [4] F. Spadavecchia, G. Cappelletti, S. Ardizzone et al., "Solar photoactivity of nano-N-TiO<sub>2</sub> from tertiary amine: role of defects and paramagnetic species," *Applied Catalysis B*, vol. 96, no. 3-4, pp. 314–322, 2010.
- [5] M. M. Mohamed, W. A. Bayoumy, M. Khairy, and M. A. Mousa, "Synthesis of micro-mesoporous TiO<sub>2</sub> materials assembled via cationic surfactants: morphology, thermal stability and surface acidity characteristics," *Microporous and Mesoporous Materials*, vol. 103, no. 1-3, pp. 174–183, 2007.
- [6] A. Mitra, A. Bhaumik, and B. K. Paul, "Synthesis and characterization of mesoporous titanium dioxide using self-assembly of sodium dodecyl sulfate and benzyl alcohol systems as templates," *Microporous and Mesoporous Materials*, vol. 109, no. 1-3, pp. 66–72, 2008.
- [7] A.-C. Lee, R.-H. Lin, C.-Y. Yang, M.-H. Lin, and W.-Y. Wang, "Preparations and characterization of novel photocatalysts with mesoporous titanium dioxide (TiO<sub>2</sub>) via a sol-gel method," *Materials Chemistry and Physics*, vol. 109, no. 2-3, pp. 275–280, 2008.
- [8] D. Chandra and A. Bhaumik, "Super-microporous TiO<sub>2</sub> synthesized by using new designed chelating structure directing agents," *Microporous and Mesoporous Materials*, vol. 112, no. 1-3, pp. 533–541, 2008.
- [9] G. Cappelletti, C. L. Bianchi, and S. Ardizzone, "XPS study of the surfactant film adsorbed onto growing titania nanoparticles," *Applied Surface Science*, vol. 253, no. 2, pp. 519–524, 2006.
- [10] S. Ardizzone, C. L. Bianchi, and G. Cappelletti, "Growth of TiO<sub>2</sub> nanocrystals in the presence of alkylpyridinium salts: the interplay between hydrophobic and hydrophilic interactions," *Surface and Interface Analysis*, vol. 38, no. 4, pp. 452–457, 2006.
- [11] D. S. Kim, S. J. Han, and S.-Y. Kwak, "Synthesis and photocatalytic activity of mesoporous TiO<sub>2</sub> with the surface area, crystallite size, and pore size," *Journal of Colloid and Interface Science*, vol. 316, no. 1, pp. 85–91, 2007.
- [12] C. Tian, Z. Zhang, J. Hou, and N. Luo, "Surfactant/copolymer template hydrothermal synthesis of thermally stable, mesoporous TiO<sub>2</sub> from TiOSO<sub>4</sub>," *Materials Letters*, vol. 62, no. 1, pp. 77–80, 2008.
- [13] J. Procházka, L. Kavan, V. Shklover et al., "Multilayer films from templated TiO<sub>2</sub> and structural changes during their thermal treatment," *Chemistry of Materials*, vol. 20, no. 9, pp. 2985–2993, 2008.
- [14] M. Grätzel, "Photoelectrochemical cells," *Nature*, vol. 414, no. 6861, pp. 338–344, 2001.
- [15] L. K. Koopal, E. M. Lee, and M. R. Böhmer, "Adsorption of cationic and anionic surfactants on charged metal oxide surfaces," *Journal of Colloid and Interface Science*, vol. 170, no. 1, pp. 85–97, 1995.
- [16] J. Chen, Z. Hua, Y. Yan, A. A. Zakhidov, R. H. Baughman, and L. Xu, "Template synthesis of ordered arrays of mesoporous titania spheres," *Chemical Communications*, vol. 46, no. 11, pp. 1872–1874, 2010.
- [17] M. Grätzel, "Mesoscopic solar cells for electricity and hydrogen production from sunlight," *Chemistry Letters*, vol. 34, no. 1, pp. 8–13, 2005.
- [18] Q. Shen and T. Toyoda, "Studies of optical absorption and electron transport in nanocrystalline TiO<sub>2</sub> electrodes," *Thin Solid Films*, vol. 438-439, pp. 167–170, 2003.
- [19] D. C. Hurum, A. G. Agrios, K. A. Gray, T. Rajh, and M. C. Thurnauer, "Explaining the enhanced photocatalytic activity of Degussa P25 mixed-phase TiO<sub>2</sub> using EPR," *Journal of Physical Chemistry B*, vol. 107, no. 19, pp. 4545–4549, 2003.
- [20] R. Andreozzi, V. Caprio, A. Insola, and R. Marotta, "Advanced oxidation processes (AOP) for water purification and recovery," *Catalysis Today*, vol. 53, no. 1, pp. 51–59, 1999.
- [21] P. Quagliotto, G. Viscardi, C. Barolo et al., "Gemini pyridinium surfactants: synthesis and conductometric study of a novel class of amphiphiles," *Journal of Organic Chemistry*, vol. 68, no. 20, pp. 7651–7660, 2003.
- [22] S. K. Hait and S. P. Moulik, "Gemini surfactants: a distinct class of self-assembling molecules," *Current Science*, vol. 82, no. 9, pp. 1101–1111, 2002.
- [23] R. Zana, "Gemini (dimeric) surfactants," *Current Opinion in Colloid and Interface Science*, vol. 1, no. 5, pp. 566–571, 1996.
- [24] M. J. Rosen and D. J. Tracy, "Gemini surfactants," *Journal of Surfactants and Detergents*, vol. 1, no. 4, pp. 547–554, 1998.
- [25] F. M. Menger and J. S. Keiper, "Gemini surfactants," *Angewandte Chemie*, vol. 39, no. 11, pp. 1906–1920, 2000.
- [26] A. C. Larson and R. B. Von Dreele, "GSAS: General Structural Analysis System," Laboratory Report LAUR 86-748, Los Alamos National Laboratory, Los Alamos, NM, USA, 1994.
- [27] B. H. Toby, "EXPGUI, a graphical user interface for GSAS," *Journal of Applied Crystallography*, vol. 34, no. 2, pp. 210–213, 2001.

- [28] T. Boiadjeva, G. Cappelletti, S. Ardizzone, S. Rondinini, and A. Vertova, "The role of surface electrification on the growth and structural features of titania nanoparticles," *Physical Chemistry Chemical Physics*, vol. 6, no. 13, pp. 3535–3539, 2004.
- [29] M. A. Bhat, A. A. Dar, A. Amin, P. I. Rashid, and G. M. Rather, "Temperature dependence of transport and equilibrium properties of alkylpyridinium surfactants in aqueous solutions," *Journal of Chemical Thermodynamics*, vol. 39, no. 11, pp. 1500–1507, 2007.
- [30] B. Simončič and J. Špan, "Thermodynamics of micellization of n-alkylpyridinium chlorides: a potentiometric study," *Acta Chimica Slovenica*, vol. 45, no. 2, pp. 143–152, 1998.
- [31] K. Fujo and S. Ikeda, "Size of Micelles of 1-Dodecylpyridinium Chloride in Aqueous NaCl Solutions," *Bulletin of the Chemical Society of Japan*, vol. 65, pp. 1406–1410, 1992.
- [32] J. J. Galán, A. González-Pérez, J. L. Del Castillo, and J. R. Rodríguez, "Thermal parameters associated to micellization of dodecylpyridinium bromide and chloride in aqueous solution," *Journal of Thermal Analysis and Calorimetry*, vol. 70, no. 1, pp. 229–234, 2002.
- [33] A. N. Frumkin, "Die kapillarkurve der höheren fettsäuren und die zustandsgleichung der oberflächenschicht," *Zeitschrift für Physikalische Chemie*, vol. 166, pp. 466–484, 1925.
- [34] R. H. Fowler and E. A. Guggenheim, *Statistical Thermodynamics*, Cambridge University Press, London, UK, 1965.
- [35] A. de Keizer and L. G. J. Fokkink, "Specific adsorption of organic cations at the silver iodide-electrolyte interface," *Colloids and Surfaces*, vol. 51, pp. 323–337, 1990.
- [36] S. Ardizzone, C. L. Bianchi, P. Quagliotto, and G. Viscardi, "Adsorption of cationic 'gemini' surfactants at the TiO<sub>2</sub>/solution interface," *Surface and Interface Analysis*, vol. 34, no. 1, pp. 652–656, 2002.
- [37] T. Mehrian, A. de Keizer, A. J. Korteweg, and J. Lyklema, "Thermodynamics of adsorption of dodecylpyridinium chloride on Na-kaolinite," *Colloids and Surfaces A*, vol. 73, pp. 133–143, 1993.
- [38] R. H. Ottewill and M. C. Rastogi, "The stability of hydrophobic sols in the presence of surface-active agents—part 3. An examination by microelectrophoresis of the behaviour of silver iodide sols in the presence of cationic surface-active agents," *Transactions of the Faraday Society*, vol. 56, pp. 880–892, 1960.
- [39] P. Somasundaran and D. W. Fuerstenau, "Mechanisms of alkyl sulfonate adsorption at the alumina-water interface," *Journal of Physical Chemistry*, vol. 70, no. 1, pp. 90–96, 1966.
- [40] A. Fan, P. Somasundaran, and N. J. Turro, "Adsorption of alkyltrimethylammonium bromides on negatively charged alumina," *Langmuir*, vol. 13, no. 3, pp. 506–510, 1997.
- [41] D. W. Fuerstenau and H. M. Jang, "On the nature of alkylsulfonate adsorption at the rutile/water interface," *Langmuir*, vol. 7, no. 12, pp. 3138–3143, 1991.
- [42] M. J. Rosen, M. Dahanayake, and A. W. Cohen, "Relationship of structure to properties in surfactants. 11. surface and thermodynamic properties of N-dodecyl-pyridinium bromide and chloride," *Colloids and Surfaces*, vol. 5, no. 2, pp. 159–172, 1982.
- [43] W. P. J. Ford, R. H. Ottewill, and H. C. Parreira, "Light-scattering studies on dodecylpyridinium halides," *Journal of Colloid and Interface Science*, vol. 21, no. 5, pp. 522–533, 1966.
- [44] R. Zana, M. Benrraou, and R. Rueff, "Alkanediyl- $\alpha,\omega$ -bis(dimethylalkylammonium bromide) surfactants. 1. Effect of the spacer chain length on the critical micelle concentration and micelle ionization degree," *Langmuir*, vol. 7, no. 6, pp. 1072–1075, 1991.
- [45] R. Zana, H. Levy, D. Papoutsis, and G. Beinertdagger, "Micellization of two triquatery ammonium surfactants in aqueous solution," *Langmuir*, vol. 11, no. 10, pp. 3694–3698, 1995.
- [46] R. Zana, "Critical micellization concentration of surfactants in aqueous solution and free energy of micellization," *Langmuir*, vol. 12, no. 5, pp. 1208–1211, 1996.
- [47] E. Alami, G. Beinert, P. Marie, and R. Zana, "Alkanediyl- $\alpha,\omega$ -bis(dimethylalkylammonium bromide) surfactants. 3. Behavior at the air-water interface," *Langmuir*, vol. 9, no. 6, pp. 1465–1467, 1993.
- [48] S. Manne, T. E. Schäffet, Q. Huo et al., "Gemini surfactants at solid-liquid interfaces: control of interfacial aggregate geometry," *Langmuir*, vol. 13, no. 24, pp. 6382–6387, 1997.
- [49] M. Cao, X. Song, J. Wang, and Y. Wang, "Adsorption of hexyl- $\alpha,\omega$ -bis(dodecyltrimethylammonium bromide) gemini surfactant on silica and its effect on wettability," *Journal of Colloid and Interface Science*, vol. 300, no. 2, pp. 519–525, 2006.
- [50] R. Atkin, V. S. J. Craig, E. J. Wanless, and S. Biggs, "Adsorption of 12-s-12 gemini surfactants at the silica-aqueous solution interface," *Journal of Physical Chemistry B*, vol. 107, no. 13, pp. 2978–2985, 2003.
- [51] J. Yu, Y. Su, and B. Cheng, "Template-free fabrication and enhanced photocatalytic activity of hierarchical macro-/mesoporous titania," *Advanced Functional Materials*, vol. 17, no. 12, pp. 1984–1990, 2007.
- [52] J. Yu, L. Zhang, B. Cheng, and Y. Su, "Hydrothermal preparation and photocatalytic activity of hierarchically sponge-like macro-/mesoporous Titania," *Journal of Physical Chemistry C*, vol. 111, no. 28, pp. 10582–10589, 2007.
- [53] J. Yu, W. Wang, B. Cheng, B. Huang, and X. Zhang, "Preparation and photocatalytic activity of multi-modally macro-/mesoporous titania," *Research on Chemical Intermediates*, vol. 35, no. 6-7, pp. 653–665, 2009.
- [54] H. Zhang and J. F. Banfield, "Thermodynamic analysis of phase stability of nanocrystalline titania," *Journal of Materials Chemistry*, vol. 8, pp. 2073–2076, 1998.
- [55] M. Lazzari, A. Vittadini, and A. Selloni, "Structure and energetics of stoichiometric TiO<sub>2</sub> anatase surfaces," *Physical Review B*, vol. 63, no. 15, Article ID 155409, pp. 1–9, 2001.
- [56] C.-C. Wang and J. Y. Ying, "Sol-gel synthesis and hydrothermal processing of anatase and rutile titania nanocrystals," *Chemistry of Materials*, vol. 11, no. 11, pp. 3113–3120, 1999.
- [57] G. Cappelletti, C. Ricci, S. Ardizzone, C. Parola, and A. Anedda, "Aged titania nanoparticles: the simultaneous control of local and long-range properties," *Journal of Physical Chemistry B*, vol. 109, no. 10, pp. 4448–4454, 2005.

## Research Article

# Synthesis and Characterization of Nanometer $\text{Ce}_{0.75}\text{Zr}_{0.25}\text{O}_2$ Powders by Solid-State Chemical Reaction Method

Yuying Zheng,<sup>1</sup> Zhengfa Hu,<sup>2</sup> Huimin Huang,<sup>1</sup> Wenjin Ji,<sup>1</sup> Ming Sun,<sup>1</sup> and Changshui Chen<sup>3</sup>

<sup>1</sup> College of Light and Chemical Engineering, Guangdong University of Technology, Guangzhou, 510006, China

<sup>2</sup> College of Physics and Optoelectronics Engineering, Guangdong University of Technology, Guangzhou, 510006, China

<sup>3</sup> School of Information and Optoelectronic Science and Engineering, South China Normal University, Guangzhou, 510631, China

Correspondence should be addressed to Yuying Zheng, zyyzhengyuying@163.com and Zhengfa Hu, zhfh@gdut.edu.cn

Received 8 May 2010; Revised 8 July 2010; Accepted 24 August 2010

Academic Editor: Bo Zou

Copyright © 2011 Yuying Zheng et al. This is an open access article distributed under the Creative Commons Attribution License, which permits unrestricted use, distribution, and reproduction in any medium, provided the original work is properly cited.

The nanostructure  $\text{Ce}_{0.75}\text{Zr}_{0.25}\text{O}_2$  powders have been successfully synthesized by using the mechanically activated solid-state chemical reaction method for the first time, with  $\text{Ce}_2(\text{CO})_3$ ,  $\text{ZrOCl}_2 \cdot 8\text{H}_2\text{O}$ , and  $\text{H}_2\text{C}_2\text{O}_4 \cdot 2\text{H}_2\text{O}$  as raw materials. The structure and morphology of  $\text{Ce}_{0.75}\text{Zr}_{0.25}\text{O}_2$  powders were characterized to be in the single cubic phase and spherical shape via X-ray powder diffraction, transmission electron microscopy, X-ray Photoelectron Spectrometer, and BET surface area testing technique. The average size of particles was measured to be less than 20 nm, and the specific surface area was 85.4  $\text{m}^2/\text{g}$ . The TG-DTA investigation was used to reveal the possibly chemical reaction mechanism during the synthesis process. The activity of  $\text{Ce}_{0.75}\text{Zr}_{0.25}\text{O}_2$  oxide solution in three-way catalysts was also valued in this work.

## 1. Introduction

The nanostructure,  $\text{Ce}_{1-x}\text{Zr}_x\text{O}_2$  materials have drawn extraordinary research interests in recent years due not only to its good mechanical and electrical properties [1–4], but also to the potentials of applications in various fields, such as the catalysts [5–7], solid oxide electrolyte materials [8–10], and advanced ceramics [11–13]. There have been many methods to prepare nano- $\text{Ce}_{1-x}\text{Zr}_x\text{O}_2$  solid solution, such as coprecipitation [14, 15], sol-gel [16, 17], high-temperature calcinations [18], high-energy mechanical milling, and hydrothermal method [19]. However, the procedure of the above approaches is so complicated that they are inevitably limited to apply to industrial and commercial situations.

Although substantial efforts have been exerted to the development of new synthetic methodologies for both efficiently making nano- $\text{Ce}_{1-x}\text{Zr}_x\text{O}_2$  and greatly lowering the synthesis costs, big difficulties still exist in the industrialization and productivity of each method. So far, the mechanically activated solid state chemical reaction method has gradually become a novel synthesis way that it exhibited

high efficiency and lower cost of water and energy [20]. By comparing with other methods, the mechanically activated solid state chemical reaction method was considered to be a more simple industrial art without needing of plenty of solvents. In this work, the nanostructured  $\text{Ce}_{0.75}\text{Zr}_{0.25}\text{O}_2$  was prepared by the mechanically activated solid state chemical reaction method for the first time. The characterization and properties of nano- $\text{Ce}_{0.75}\text{Zr}_{0.25}\text{O}_2$  were investigated and determined. Their catalysis efficiency was also checked at the aspect of potential applications.

## 2. Experimental

### 2.1. Preparation

**2.1.1. Synthesis of Nano- $\text{Ce}_{1-x}\text{Zr}_x\text{O}_2$  Powders.** The particles of nano- $\text{Ce}_{0.75}\text{Zr}_{0.25}\text{O}_2$  were prepared by mechanically activated solid-state chemical reaction method for the first time. At first, precursors were prepared by mixing of  $\text{ZrOCl}_2 \cdot 8\text{H}_2\text{O}$ ,  $\text{Ce}_2(\text{CO}_3)_3$  and  $\text{H}_2\text{C}_2\text{O}_4 \cdot 2\text{H}_2\text{O}$  at the molar

ratio of  $n(\text{ZrOCl}_2 \cdot 8\text{H}_2\text{O}) : n(\text{Ce}_2(\text{CO}_3)_3) : n(\text{C}_2\text{H}_2\text{O}_4 \cdot 2\text{H}_2\text{O}) = 0.25 : 0.375 : 0.375$ , then, the precursors were placed into the ball mill (model No. XQM-4L), operating at the initial angular speed 150 r/min for 2 hour. The amount of grinding media was kept a ratio of 10 : 1 to precursors. After one and a half hours grinding, the surfactant (5% total weight) was doped into the ball milling pot. At last the white resultant composition was calcined for 3 hours at the temperature of 600°C, and the yellow nanoparticles of  $\text{Ce}_{0.75}\text{Zr}_{0.25}\text{O}_2$  were obtained.

**2.1.2. Preparation of Catalysts.** Catalyst A was mainly composed of the two noble metals totally taking a fraction 0.40% of weight in the three-way catalyst (TWC) [21, 22]. Pd and Rh took 0.25% and 0.15%, respectively. Here the preparation was briefly outlined Firstly,  $\text{Ce}_{0.75}\text{Zr}_{0.25}\text{O}_2$  were blended with  $\gamma\text{-Al}_2\text{O}_3$  under mechanical mixing, which only takes 30% of total weight. Secondly, the mixture of water solutions of  $\text{PdCl}_2$  and  $\text{RhCl}_3$  was prepared at the mass ratio of  $m(\text{Pd}^{2+})$  and  $m(\text{Rh}^{3+}) = 5 : 3$ ; then the mixture of water solutions of Pd- and Rh-contained salts was loaded into the mixture of  $\text{Ce}_{0.75}\text{Zr}_{0.25}\text{O}_2$  and  $\gamma\text{-Al}_2\text{O}_3$  for necessary reactions by incipient wetness method. Finally, the composite was calcined at 500°C for 2 hours and subsequently reduced at 500°C under atmosphere of  $\text{H}_2$  for 2 hours.

**Preparation of catalyst B.** The preparation process was almost the same as catalyst A. The difference was that nano- $\text{Ce}_{0.75}\text{Zr}_{0.25}\text{O}_2$  powders were prepared by coprecipitation method, within which,  $\text{Ce}(\text{NO}_3)_3 \cdot 8\text{H}_2\text{O}$  and  $\text{ZrOCl}_2 \cdot 8\text{H}_2\text{O}$  were firstly dissolved in water, respectively, to form water solutions both in 0.2 mol/L, and then they were mixed together. Subsequently, aqueous ammonia in 1 mol/L was poured into the solutions mixtures until the pH = 9.8 under continuously stirring. Finally, precipitate was washed and dried, then calcined at 600°C for 3 hours.

**2.2. Characterization.** TG-DTA analysis was performed based on SPA409PC analytic apparatus operated at the 30 mL/min airflow rate and the 5°C/min temperature rise rate. X-ray powder diffraction (XRD) measurements were made with a Rigaku D/Max-3B diffractometer employing Cu-K $\alpha$  radiation. Transmission electron microscopy (TEM) (JEM-100CXII) was used to study the crystallization property and the size of the particles. Particle size distribution histograms were obtained on the basis of measurements from about 300 particles. X-ray photoelectron spectra (XPS) were recorded on an Scanning ESCA Microprobe (Quantum-2000, PHI) photoelectron spectrometer using Al-K $\alpha$  radiation under a vacuum environment of  $1 \times 10^{-6}$  Pa. The binding energy of C<sub>1s</sub> (284.6 eV) was used for the calibration of all binding energies. The specific surface area ( $S_{\text{BET}}$ ) of the products was checked by measuring the adsorptive capacity of N<sub>2</sub> at -196°C by using full-automatic adsorption instrument ASAP2010M.

**2.3. Catalysis.** As for the activity of catalysts, it was evaluated by monitoring the contents of five components such as NO,

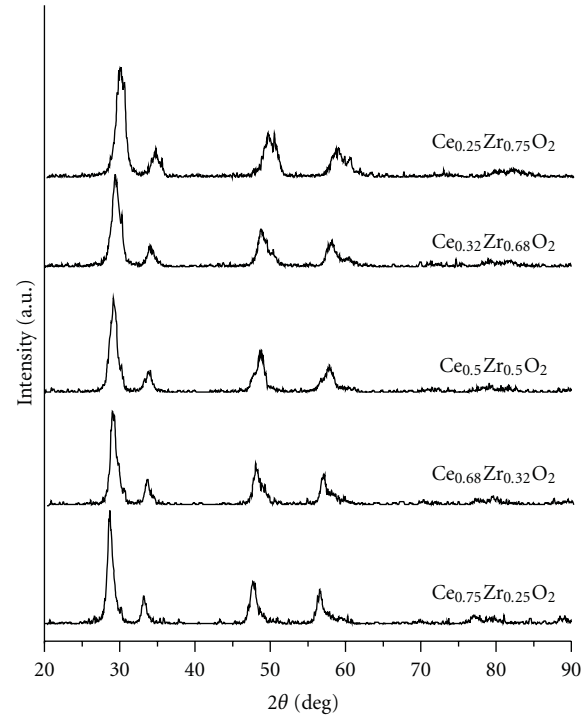


FIGURE 1: XRD spectra of  $\text{Ce}_x\text{Zr}_{1-x}\text{O}_2$  solid solutions.

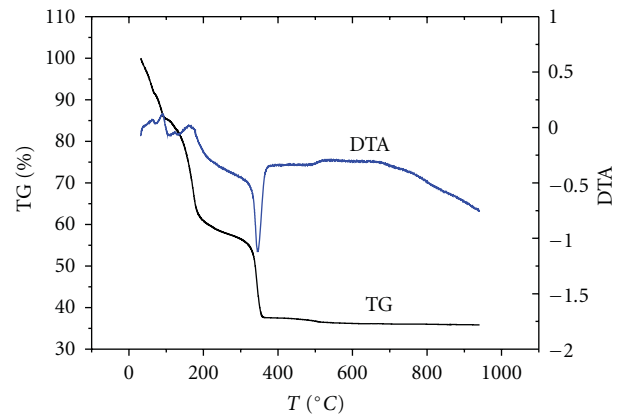


FIGURE 2: TG-DTA curves of the precursors.

CH, CO, O<sub>2</sub>, and CO<sub>2</sub> in automobile exhaust gas by using gas chromatograph (GC 9790) and the automobile exhaust analytic system (FGA-4100), with the reference exhaust composed of  $\varphi(\text{NO}) = 0.1\%$ ,  $\varphi\{\text{CH}[\text{V}(\text{C}_3\text{H}_8) : \text{V}(\text{C}_3\text{H}_6) = 1 : 1]\} = 0.1\%$ ,  $\varphi(\text{CO}) = 1.5\%$ , and  $\varphi(\text{O}_2) = 1.37\%$  in volume fraction. The instruments were run with He as buffer gas at S.V. = 40000 h<sup>-1</sup> and air/fuel (A/F) ratio of 14.6. The temperature rise rate was set at 10°C per minute. The rate of conversion could be calculated as following:

$$X = \frac{\sigma_0 - \sigma_1}{\sigma_0} \times 100\%, \quad (1)$$

where  $X$  denotes the rate of conversion,  $\sigma_0$  and  $\sigma_1$  stand by the starting volume fraction and final volume fraction of gases, respectively.

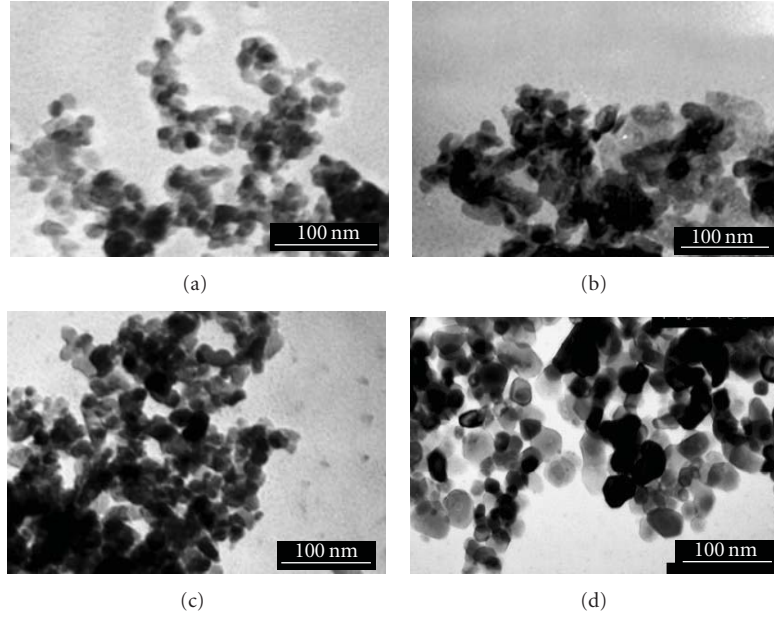


FIGURE 3: TEM images of  $\text{Ce}_{0.75}\text{Zr}_{0.25}\text{O}_2$  produced under surfactants (a) Tween-60, (b) neopelex, (c) PEG-400, and (d) CTAB.

TABLE 1: Different molar ratios of raw materials correspond to different products and particle size.

Sample No.	Molar ratio of raw materials $\text{ZrOCl}\cdot 8\text{H}_2\text{O}:\text{Ce}_2(\text{CO}_3)_3:\text{C}_2\text{H}_2\text{O}_4\cdot 2\text{H}_2\text{O}$	Product	Crystal volume ( $\text{nm}^3$ )
1	0.25 : 0.375 : 0.375	$\text{Ce}_{0.75}\text{Zr}_{0.25}\text{O}_2$	0.15141
2	0.32 : 0.34 : 0.48	$\text{Ce}_{0.68}\text{Zr}_{0.32}\text{O}_2$	0.14595
3	0.5 : 0.25 : 0.75	$\text{Ce}_{0.5}\text{Zr}_{0.5}\text{O}_2$	0.14310
4	0.68 : 0.16 : 1.02	$\text{Ce}_{0.32}\text{Zr}_{0.68}\text{O}_2$	0.14198
5	0.75 : 0.125 : 1.125	$\text{Ce}_{0.25}\text{Zr}_{0.75}\text{O}_2$	0.14012

### 3. Results and Discussion

**3.1. Determination of Solid Solution Manner.** Figure 1 and Table 1 displayed that XRD patterns of the final products prepared from the different ratio of raw materials, and the corresponding crystal volumes, respectively. As can be seen, the crystal volume decreases gradually with the increment of the concentration of  $\text{Zr}^{4+}$  ions. In general, there are two ways that  $\text{Zr}^{4+}$  ions could be doped into the crystal lattice of  $\text{CeO}_2$ , one is that  $\text{Zr}^{4+}$  is filled into the crystal lattice in the form of gap ions, the existence of  $\text{Zr}^{4+}$  ion thus causes a vacancy of  $\text{Ce}^{4+}$ , leading to enlargement of the volume of  $\text{Ce}_{1-x}\text{Zr}_x\text{O}_2$  crystal cell. The other is that  $\text{Zr}^{4+}$  fully substituted for  $\text{Ce}^{4+}$  leading to the compactness of the crystal lattice as the ionic radius of  $\text{Zr}^{4+}$  (0.079 nm) is less than that of  $\text{Ce}^{4+}$  (0.092 nm). The experimental results obviously showed that the lattice constant ( $d_{\text{XRD}}$ ) declined with the increasing amount of  $\text{Zr}^{4+}$ , in accordance with the second doping manner of Zr ions, namely,  $\text{Ce}^{4+}$  ions in  $\text{CeO}_2$  were partially replaced by  $\text{Zr}^{4+}$  in the  $\text{Ce}_{1-x}\text{Zr}_x\text{O}_2$  solid solution, resulting in the reduction of the crystal volume.

XRD patterns of  $\text{Ce}_{0.75}\text{Zr}_{0.25}\text{O}_2$  solid solution in Figure 1 indicated that  $\text{Ce}_{0.75}\text{Zr}_{0.25}\text{O}_2$  solid solution has a crystal

structure in a cubic phase. From the analysis of XRD pattern, we could calculate the  $d_{\text{XRD}}$  and the degree of crystallization ( $X_c$ ). The  $X_c$  was calculated according to

$$X_c = \frac{I_c}{I_c + I_a} \times 100\%, \quad (2)$$

where  $I_c$  denotes the area of crystallinity phase, and  $I_a$  stands for the area of amorphous phase. As a result, the  $d_{\text{XRD}}$  and the degree of crystallization ( $X_c$ ) were obtained to be 14.46 nm and 95.3%, respectively. No peak of impurity was found in the XRD patterns referenced by the standard card 28-271 in Powder Diffraction File (PDF).

**3.2. TG-DTA Analysis.** The TG-DTA data were plotted in Figure 2. The TG curve displayed three main stages through the whole process. Loss of free water from precursors surface firstly took place at about 116°C. A further loss of weight followed, as seen from the exothermic peak on the DTA curve at 170°C. Continuous loss of water from oxalate and heat decomposition of excessive oxalic acid resulted in the reduction of weight. The loss of weight was up to about 22% after this step. Then the heat decomposition of oxalate began

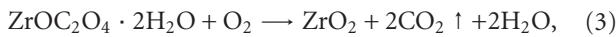
TABLE 2: Referenced binding energy of Zr 3d, Ce 3d, and O 1s in oxides [23].

Element	Core level	Oxide	Binding energy/eV
Zr	3d <sub>5/2</sub>	ZrO <sub>2</sub>	183.1
Zr	3d <sub>3/2</sub>	ZrO <sub>2</sub>	185.5
Zr	3d <sub>3/2</sub>	ZrO <sub>2</sub> /(CeO <sub>x</sub> +Y <sub>2</sub> O <sub>3</sub> +ZrO <sub>2</sub> )	182.6
Ce	3d <sub>5/2</sub>	Ce <sub>2</sub> O <sub>3</sub> /(CeO <sub>x</sub> +Y <sub>2</sub> O <sub>3</sub> +ZrO <sub>2</sub> )	885.6
Ce	3d <sub>3/2</sub>	Ce <sub>2</sub> O <sub>3</sub> /(CeO <sub>x</sub> +Y <sub>2</sub> O <sub>3</sub> +ZrO <sub>2</sub> )	903.7
Ce	3d <sub>5/2</sub>	CeO <sub>2</sub> /(CeO <sub>x</sub> +Y <sub>2</sub> O <sub>3</sub> +ZrO <sub>2</sub> )	882.4
Ce	3d <sub>3/2</sub>	CeO <sub>2</sub> /(CeO <sub>x</sub> +Y <sub>2</sub> O <sub>3</sub> +ZrO <sub>2</sub> )	900.9
Ce	3d <sub>5/2</sub>	CeO <sub>2</sub>	881.8
Ce	3d <sub>3/2</sub>	CeO <sub>2</sub>	916.7
Ce	3d <sub>5/2</sub>	Ce <sub>2</sub> O <sub>3</sub>	880.7
O	1s	CeO <sub>2</sub> /(CeO <sub>x</sub> +Y <sub>2</sub> O <sub>3</sub> +ZrO <sub>2</sub> )	530.0
O	1s	Ce <sub>2</sub> O <sub>3</sub> /(CeO <sub>x</sub> +Y <sub>2</sub> O <sub>3</sub> +ZrO <sub>2</sub> )	532.0

TABLE 3: Light-off temperature of catalysts A and B.

Catalyst	T <sub>50</sub> (CH)/°C	T <sub>50</sub> (CO)/°C	T <sub>50</sub> (NO)/°C
A	295.7	239.1	230.6
B	293.2	239.2	231.8

and lasted from 240°C to 600°C, resulting in the reduction of the precursors weight by 26.5%, which was basically consistent with the theoretical the loss of weight of 27.7%. According to the TG-DTA analysis, the following chemical reactions occurred within the process of heat decomposition:



Equations (3) and (4) indicated the heat decomposition reactions, whilst (5) showed the stoichiometric reaction without the loss of weight. As shown in Figure 1, Ce<sub>2</sub>(CO<sub>3</sub>)<sub>3</sub> was not involved in the reaction with H<sub>2</sub>C<sub>2</sub>O<sub>4</sub>·2H<sub>2</sub>O, only ZrOCl<sub>2</sub>·8H<sub>2</sub>O reacted with H<sub>2</sub>C<sub>2</sub>O<sub>4</sub>·2H<sub>2</sub>O during the process of ball milling.

**3.3. Influence of Surfactant.** In order to avoid the aggregation, the influence of surface active agents onto the product was also investigated. TEM images of the nanosized samples, prepared under the introduction of different surface active agents to the precursors, were shown in Figure 3, indicating the effect of different surfactants onto the crystallization property and the size of the particles. The cationic surfactant of hexadecyl trimethyl ammonium bromide (CTAB) showed no distinct effect. The anionic surfactant of neopelex made the particles size rise up to 37.4 nm. On the contrary, the neutral surfactants PEG-400 and Tween-60 enabled the particles to maintain relatively small sizes of less than 25 nm

and more homogeneous distributions. With tween-60 as surfactant, the property of the particles was superior to those prepared under other surface active agents. The experimental results demonstrated that the particles were in more uniformly spherical shape with homogeneous dispersion. The average size of particles was obtained to be less than 20 nm, and the S<sub>BET</sub> was 85.4 m<sup>2</sup>/g, obviously larger than the S<sub>BET</sub> of 60.2 m<sup>2</sup>/g, 76.9 m<sup>2</sup>/g, and 69.7 m<sup>2</sup>/g, corresponding to surfactants (b), (c), and (d) in Figure 3.

The experimental results also indicated that the neutral surfactant could effectively prevent the aggregation of particles such that the particle size could be well controlled. The nonionic surfactant was hardly affected by the inorganic ions during the grind and could facilitate the formation of hydrogen bond, thus a protectively hydrophilic film was easily formed on the surface of the powder. The hydrophilic film enabled the powders to have spatially steric hindrance and electrostatic effects, preventing product particles from aggregation into large size. However, the cationic surfactant could easily react with the H<sub>2</sub>C<sub>2</sub>O<sub>4</sub>·2H<sub>2</sub>O due to the alkalinity, so that no obvious effect was brought onto the particles. The anionic surfactant could cause the rising of the particles sizes.

**3.4. XPS Analysis.** The XPS spectra of Zr 3d, Ce 3d, and O 1s in Ce<sub>0.75</sub>Zr<sub>0.25</sub>O<sub>2</sub> oxides were displayed in Figure 4. The binding energies of Zr 3d, Ce 3d, and O 1s in oxides were listed in Table 2 for reference and comparison [23]. Based on the fitting of XPS spectra with a Gaussian shape, we obtained the binding energies (*E<sub>b</sub>*) of Ce 3d<sub>5/2</sub> and Ce 3d<sub>3/2</sub> to be 882.42 eV and 900.85 eV, respectively, comparatively close to the reference *E<sub>b</sub>*(Ce 3d<sub>5/2</sub>) = 884.98 eV and *E<sub>b</sub>*(Ce 3d<sub>3/2</sub>) = 903.68 eV measured in solid solution of oxides CeO<sub>2</sub>/(CeO<sub>x</sub>+Y<sub>2</sub>O<sub>3</sub>+ZrO<sub>2</sub>) and Ce<sub>2</sub>O<sub>3</sub>/(CeO<sub>x</sub>+Y<sub>2</sub>O<sub>3</sub>+ZrO<sub>2</sub>), respectively. So it was reasonable to believe that both Ce<sup>3+</sup> and Ce<sup>4+</sup> exist in the products. *E<sub>b</sub>* (Zr 3d) was measured to be 182.6 eV, equal to the binding energy of Zr 3d in ZrO<sub>2</sub>/(CeO<sub>x</sub>+Y<sub>2</sub>O<sub>3</sub>+ZrO<sub>2</sub>). As for the *E<sub>b</sub>* (O 1s), two binding energies, 529.98 eV and 532.03 eV, were obtained, corresponding to 530.0 and

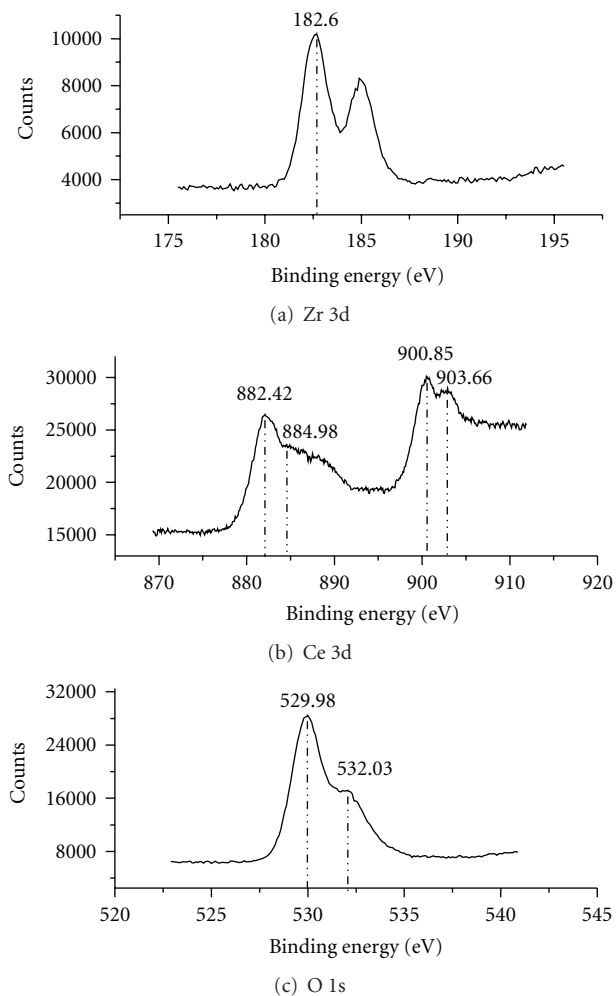


FIGURE 4: XPS spectra of Zr 3d, Ce 3d and O 1s in  $\text{Ce}_{0.75}\text{Zr}_{0.25}\text{O}_2$ .

532.0 eV in solid solution of  $\text{CeO}_2/(\text{CeO}_x+\text{Y}_2\text{O}_3+\text{ZrO}_2)$  and  $\text{Ce}_2\text{O}_3/(\text{CeO}_x+\text{Y}_2\text{O}_3+\text{ZrO}_2)$ , respectively. These facts proved that the products prepared by mechanically activated solid state chemical reaction to be in the state of solid solution of oxides, which was favored by the XRD results.

**3.5. Evaluation of Catalyst.** Catalyst A and B were used to decontaminate the automotive exhaust. The catalysis efficiency was determined by monitoring the contents of greenhouse gas, such as NO, CH, and CO, through the conversion rate. The conversion rates in percentage of NO, CH and CO have been calculated according to (1) and shown in Figure 5. The light-off temperatures ( $T_{50}$ ) of the above gases were listed in Table 3. As seen from Figure 5 and Table 3, no obvious difference could be found between the two catalysts, except for the fluctuation of  $1 \sim 2^\circ\text{C}$  at the light-off temperature. Although the two catalysts, prepared by different methods, they almost had the same catalysis function. The mechanically activated solid state chemical reaction method still possessed obvious advantages of easily manufacturing, energy saving, and less solvent, indicating its promisingly commercial and industrial potentials.

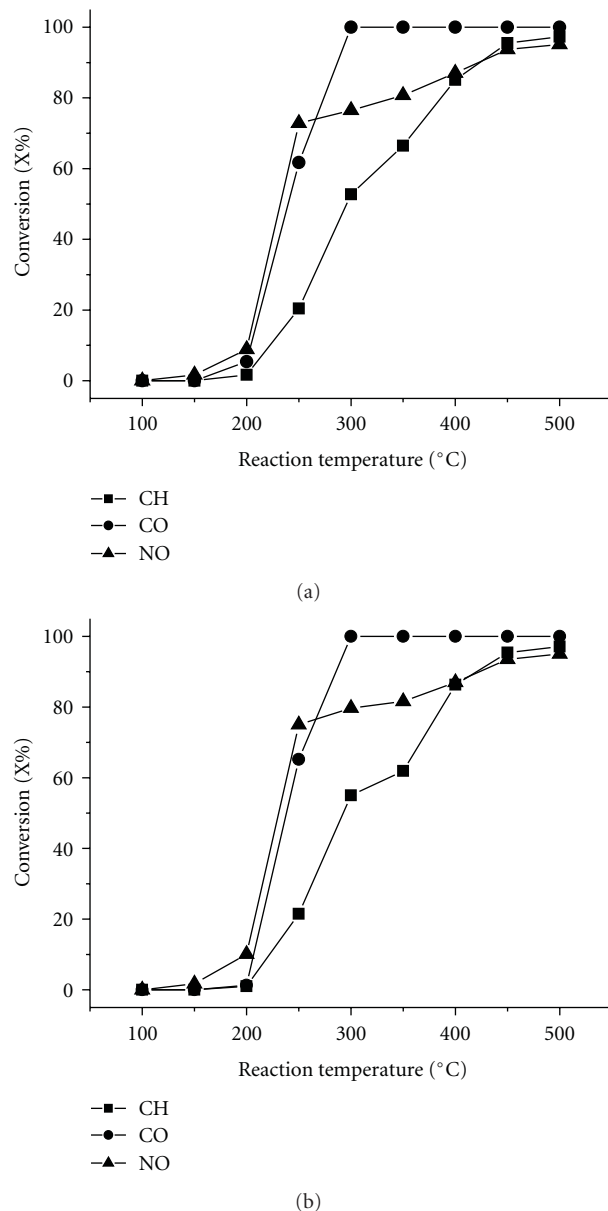


FIGURE 5: The catalysis activity of catalyst (a) and (b).

## 4. Conclusion

In summary, Nano- $\text{Ce}_{0.75}\text{Zr}_{0.25}\text{O}_2$  powders were prepared by using the solid-solid chemical reaction method under the action of mechanical power. The products were determined to be in the single-cubic-phase. The particles were found to be in more spherical shape with the average size less than 20 nm, the better specific surface area of  $85.4 \text{ m}^2/\text{g}$ , and more uniform dispersion.

The effects of surfactants employed in the synthesis process of the products have also been investigated. The facts proved that Tween-60 and PEG-400 had better effects on the control of particle sizes.

The mechanically activated solid state chemical reaction method possessed obvious advantages in manufacturing, energy-saving, and less solvent.

## Acknowledgments

This work was supported financially by Government of Guangdong Province for 211 Subject Construction. The authors are also grateful to the financial support from National Natural Science Foundation of China (NSFC) under Grant no. 60977029, 10774031, and 60878063, and from High Technology Research Program 2007AA021806. Y. Zhang and Z. Hu equally contributed to this work.

## References

- [1] W. J. Stark, M. Maciejewski, L. Mädler, S. E. Pratsinis, and A. Baiker, "Flame-made nanocrystalline ceria/zirconia: structural properties and dynamic oxygen exchange capacity," *Journal of Catalysis*, vol. 220, no. 1, pp. 35–43, 2003.
- [2] S. K. Tadokoro and E. N. S. Muccillo, "Physical characteristics and sintering behavior of ultrafine zirconia-ceria powders," *Journal of the European Ceramic Society*, vol. 22, no. 9–10, pp. 1723–1728, 2002.
- [3] S. Bernal, G. Blanco, J. J. Calvino et al., "Some recent results on the correlation of nano-structural and redox properties in ceria-zirconia mixed oxides," *Journal of Alloys and Compounds*, vol. 451, no. 1–2, pp. 521–525, 2008.
- [4] E. N. S. Muccillo and D. M. Ávila, "Impedance spectroscopy of tetragonal zirconia polycrystals doped with ceria," *Materials Letters*, vol. 56, no. 4, pp. 454–459, 2002.
- [5] A. Martorana, G. Deganello, A. Longo et al., "Structural evolution of Pt/ceria-zirconia TWC catalysts during the oxidation of carbon monoxide," *Journal of Solid State Chemistry*, vol. 177, no. 4–5, pp. 1268–1275, 2004.
- [6] M. LI, Z. LIU, Y. HU, M. WANG, and H. LI, "Effect of doping elements on catalytic performance of CeO<sub>2</sub>-ZrO<sub>2</sub> solid solutions," *Journal of Rare Earths*, vol. 26, no. 3, pp. 357–361, 2008.
- [7] J. A. Wang, T. López, X. Bokhimi, and O. Novaro, "Phase composition, reducibility and catalytic activity of Rh/zirconia and Rh/zirconia-ceria catalysts," *Journal of Molecular Catalysis A*, vol. 239, no. 1–2, pp. 249–256, 2005.
- [8] N. M. Sammes and C. Zhihong, "Ionic conductivity of ceria/yttria stabilized zirconia electrolyte materials," *Solid State Ionics*, vol. 100, no. 1–2, pp. 39–44, 1997.
- [9] C. H. Lee and G. M. Choi, "Electrical conductivity of CeO<sub>2</sub>-doped YSZ," *Solid State Ionics*, vol. 135, no. 1–4, pp. 653–661, 2000.
- [10] Q. X. Fu, W. Zhang, R. R. Peng, D. K. Peng, G. Y. Meng, and B. Zhu, "Doped ceria-chloride composite electrolyte for intermediate temperature ceramic membrane fuel cells," *Materials Letters*, vol. 53, no. 3, pp. 186–192, 2002.
- [11] E. N. S. Muccillo and D. M. Ávila, "Synthesis and characterization of submicron zirconia-12 mol% ceria ceramics," *Ceramics International*, vol. 25, no. 4, pp. 345–351, 1999.
- [12] W. Pyda, K. Haberko, and Z. Zurek, "Zirconia stabilized with a mixture of the rare earth oxides," *Journal of the European Ceramic Society*, vol. 10, no. 6, pp. 453–459, 1992.
- [13] Y. L. Zhang, X. J. Jin, and T. Y. Hsu, "Thermodynamic calculation of Ms in ZrO<sub>2</sub>-CeO<sub>2</sub>-Y<sub>2</sub>O<sub>3</sub> system," *Journal of the European Ceramic Society*, vol. 23, no. 5, pp. 685–690, 2003.
- [14] S. Rossignol, Y. Madier, and D. Duprez, "Preparation of zirconia-ceria materials by soft chemistry," *Catalysis Today*, vol. 50, no. 2, pp. 261–270, 1999.
- [15] C. LI, X. GU, Y. WANG et al., "Synthesis and characterization of mesostructured ceria-zirconia solid solution," *Journal of Rare Earths*, vol. 27, no. 2, pp. 211–215, 2009.
- [16] K. S. Kumar and T. Mathews, "Sol-gel synthesis and microwave assisted sintering of zirconia-ceria solid solution," *Journal of Alloys and Compounds*, vol. 391, no. 1–2, pp. 177–180, 2005.
- [17] X. Wu, J. Fan, R. Ran, and D. Weng, "Effect of preparation methods on the structure and redox behavior of platinum-ceria-zirconia catalysts," *Chemical Engineering Journal*, vol. 109, no. 1, pp. 133–139, 2005.
- [18] C. E. Hori, H. Permana, K. Y. S. Ng et al., "Thermal stability of oxygen storage properties in a mixed CeO<sub>2</sub>-ZrO<sub>2</sub> system," *Applied Catalysis B: Environmental*, vol. 16, no. 2, pp. 105–117, 1998.
- [19] S. Enzo, R. Frattini, F. Delogu, A. Primavera, and A. Trovarelli, "Neutron diffraction studies of ceria-zirconia catalysts prepared by high-energy mechanical milling," *Nanostructured Materials*, vol. 12, no. 5, pp. 673–676, 1999.
- [20] Q. Q. Tan, Z. L. Tang, and Z. T. Zhang, "Preparation and microstructure of nanometer tetragonal polycrystal zirconia powder at low temperature condition," *Journal of Materials Engineering*, vol. 11, p. 57, 2004.
- [21] S. S. Deshmukh, M. Zhang, V. I. Kovalchuk, and J. L. D'Itri, "Effect of SO<sub>2</sub> on CO and C<sub>3</sub>H<sub>6</sub> oxidation over CeO<sub>2</sub> and Ce<sub>0.75</sub>Zr<sub>0.25</sub>O<sub>2</sub>," *Applied Catalysis B*, vol. 45, no. 2, pp. 135–145, 2003.
- [22] H. S. Gandhi, G. W. Graham, and R. W. McCabe, "Automotive exhaust catalysis," *Journal of Catalysis*, vol. 216, no. 1–2, pp. 433–442, 2003.
- [23] NIST X-ray Photoelectron Spectroscopy Database, <http://srdata.nist.gov/xps/>.

## Research Article

# A User-Friendly Method for Synthesizing High-Quality NaYF<sub>4</sub>:Yb,Er(Tm) Nanocrystals in Liquid Paraffin

Sen Liang,<sup>1</sup> Yi Liu,<sup>1</sup> Yue Tang,<sup>1</sup> Yue Xie,<sup>1</sup> Haizhu Sun,<sup>1,2</sup> Hao Zhang,<sup>1</sup> and Bai Yang<sup>1</sup>

<sup>1</sup> State Key Laboratory of Supramolecular Structure and Materials, College of Chemistry, Jilin University, Changchun 130012, China

<sup>2</sup> College of Chemistry, Northeast Normal University, Changchun 130024, China

Correspondence should be addressed to Hao Zhang, hao\_zhang@jlu.edu.cn

Received 17 May 2010; Accepted 1 July 2010

Academic Editor: Quanqin Dai

Copyright © 2011 Sen Liang et al. This is an open access article distributed under the Creative Commons Attribution License, which permits unrestricted use, distribution, and reproduction in any medium, provided the original work is properly cited.

Application of “green chemistry” concept to synthesize nanomaterials is the current goal in developing new techniques for producing materials in commercial scale. In this study, we reported a low-cost and convenient method for synthesizing high-quality NaYF<sub>4</sub>:Yb,Er(Tm) nanocrystals (NCs) in liquid paraffin. Experimental results indicated that the as-prepared NCs possessed pure  $\beta$ -phase structure, narrow size distribution, as well as strong up-conversion fluorescence. By varying the doped lanthanides, Er or Tm, the emission color of up-conversion fluorescence was tunable. In comparison to other high-boiling-point organic solvents, liquid paraffin is cheaper and prolific in oil industry. Besides, 280°C was the optimal temperature for NaYF<sub>4</sub>:Yb,Er(Tm) synthesis, which was lower than that in the previous reports using other high-boiling-point organic solvents. Accordingly, this user-friendly method will facilitate the synthesis of high-quality lanthanide-doped NaYF<sub>4</sub> NCs in commercial scale.

## 1. Introduction

During the past decade, significant attentions have been paid on up-conversion luminescent nanocrystals (NCs) owing to their unique property, which absorbs two or more lower energy exciting photons but emits one higher energy photon [1–4]. In contrast, conventional down-conversion organic dyes and quantum dots emit only through adsorbing higher energy exciting photon [5, 6]. Consequently, it is capable for up-conversion NCs to generate visible emission by near-IR (NIR) excitation. This property makes them applicable both in academic studies and technical applications, such as solid lasers, light emitting devices, bio-labeling, biological assays, high throughput screening, and low intensity IR imaging [1–5, 7]. In addition, due to the atomic like emissions, up-conversion NCs usually possess sharp luminescence bands and immunize to photo-bleaching [8–11]. Furthermore, NIR exciting sources are cheaper and easier to obtain in comparison to UV-visible ones [12]. These advantages make up-conversion NCs become alternatives to organic dyes and quantum dots, especially in biological applications [1, 13–17].

Among various up-conversion NCs, lanthanide-doped NaYF<sub>4</sub>, such as Yb/Er or Yb/Tm codoped NaYF<sub>4</sub>, is becoming the focus, because NaYF<sub>4</sub> host materials have low vibrational energy, low nonradiative decay rate, and high radiative emission rate, which are the prerequisites to achieve high luminescence [18–20]. To date, lanthanide-doped NaYF<sub>4</sub> NCs are prepared mainly via colloidal chemistry routes, including coprecipitation, thermal decomposition, hydrothermal, or solvothermal synthesis, and sol-gel processing [4, 5, 21–24]. The thermal decomposition strategy is the most successful method for synthesizing high-quality NCs, represented by the highly crystalline phase and narrow size distribution of the products [3, 25]. Since a separated nucleation and growth of NCs is achievable just through manipulating the reaction temperature, it further allows for controlling NC size, shape, as well as crystal structure [26–28]. However, the raw materials used in thermal decomposition method are expensive and air-sensitive, and the synthesis is operated at high temperature, such as at 320°C and generates toxic by-product [25, 29, 30]. For the synthesis of NCs in commercial scale, it requires to develop synthetic techniques close to “green chemistry” concept, such as using environment- and

user-friendly solvents, saving energy, and avoiding waste [31].

In this study, we demonstrated a nearly “green chemistry” and mild method for synthesizing high-quality NaYF<sub>4</sub>:Yb,Er(Tm) NCs with pure  $\beta$ -phase crystal structure. A cheap and user-friendly solvent of liquid paraffin was chosen as the reaction medium. The as-prepared NCs exhibited strong NIR-to-visible up-conversion luminescence, which was tunable by varying the codoped lanthanides. Besides, experimental result indicated that 280°C was the optimal temperature for NaYF<sub>4</sub>:Yb,Er(Tm) synthesis, lower than that in the previous reports using other high-boiling-point organic solvents.

## 2. Materials and Methods

**2.1. Materials.** Sodium hydroxide (NaOH), ammonium fluoride (NH<sub>4</sub>F), ethanol, methanol, oleic acid (OA, technical grade, 90%), liquid paraffin, yttrium chloride hexahydrate (YCl<sub>3</sub>·6H<sub>2</sub>O, 99.9%), ytterbium chloride hexahydrate (YbCl<sub>3</sub>·6H<sub>2</sub>O, 99.99%), erbium chloride hexahydrate (ErCl<sub>3</sub>·6H<sub>2</sub>O, 99.9%), and thulium chloride hexahydrate (TmCl<sub>3</sub>·6H<sub>2</sub>O, 99.9%) were all commercial products and used as received.

**2.2. Synthesis of NaYF<sub>4</sub>:Yb,Er(Tm) NCs.** NaYF<sub>4</sub>:18%Yb, 2%Er NCs were synthesized following this project: YCl<sub>3</sub>·6H<sub>2</sub>O (0.2420 g), YbCl<sub>3</sub>·6H<sub>2</sub>O (0.0700 g), and ErCl<sub>3</sub>·6H<sub>2</sub>O (0.0076 g) were mixed with 6 ml OA and 15 ml liquid paraffin in a 100 mL three-necked flask and degassed at 100°C for 1 h under vacuum. After cooled down to room temperature, a solution of NaOH (0.1 g) and NH<sub>4</sub>F (0.148 g) in 10 ml methanol was added and the mixture was degassed at 100°C for 30 min again under vacuum. With the protection of N<sub>2</sub>, the mixture was gradually heated to 280°C and kept at this temperature for 1 h under vigorous magnetic stirring. Then the products were precipitated through the addition of ethanol and washed with ethanol/water (1 : 1 v/v) for three times at room temperature. Finally, the resultant mixture was separated by centrifugation, and the precipitates were collected without any size-selection process. The resultant NCs were redispersible in various nonpolar solvents, such as hexane and toluene. Following a similar procedure, except using TmCl<sub>3</sub>·6H<sub>2</sub>O instead of ErCl<sub>3</sub>·6H<sub>2</sub>O, NaYF<sub>4</sub>:Yb,Tm NCs were synthesized.

**2.3. Characterization.** Transmission electron microscopy (TEM) was conducted using a Hitachi H-800 electron microscope at an acceleration voltage of 200 kV with a CCD camera. High-resolution TEM (HRTEM) imaging was implemented by a JEM-2100F electron microscope at 300 kV. X-ray powder diffraction (XRD) investigation was carried out by using Siemens D5005 diffractometer. Up-conversion fluorescence spectra were performed with a Hitachi F-4500 fluorescence spectrophotometer with a 980 nm laser at room temperature.

## 3. Results and Discussion

In our method, liquid paraffin was used as the reaction medium for synthesizing NaYF<sub>4</sub>:Yb,Er NCs. Figures 1(a) and 1(b) showed the TEM images of the as-prepared NaYF<sub>4</sub>:Yb,Er NCs. Under TEM, isolated NCs with spherical morphology were observed, which suggested that the adsorption of the capping ligand of oleic acid on the crystal surface prevented the further aggregation of NaYF<sub>4</sub> toward macroscopic crystals, leading to the formation of NCs. NCs also possessed very narrow size distribution with an average diameter of 30 nm and the deviation less than 5%. HRTEM image indicated that the NCs were single crystal, with an interplanar distance of 0.52 nm (Figure 1(c)), which was consistent with the (100) plane of  $\beta$ -phase NaYF<sub>4</sub> bulk crystals (viz. 0.516 nm) [32]. The selected area electron diffraction pattern exhibited a series of diffraction rings, which was consistent with the (100), (110), (111), (201), (311), and (321) planes of  $\beta$ -phase NaYF<sub>4</sub> (Figure 1(d)) [2, 32, 33]. Furthermore, as shown in Figure 1(e), the XRD peak positions and relative intensities of the as-prepared NCs were well agreed with the corresponding values of  $\beta$ -phase NaYF<sub>4</sub> (JCPDS standard card no.028-1192) [30, 32–35].

The as-prepared NCs could be facily separated from liquid paraffin by centrifugation and redispersible in non-polar solvents, such as hexane and toluene, making it possible for spectral characterization. Figure 2 showed the up-conversion fluorescence spectrum of a hexane solution with 1 wt% NaYF<sub>4</sub>:Yb,Er NCs, which was excited by 980 nm NIR laser. Four emission peaks, respectively at 408, 520, 539, and 651 nm, were observed. These emissions were generated by the transitions between the energy levels <sup>4</sup>H<sub>9/2</sub>, <sup>4</sup>H<sub>11/2</sub>, <sup>4</sup>S<sub>3/2</sub>, and <sup>4</sup>F<sub>9/2</sub> to <sup>4</sup>I<sub>15/2</sub> of Er<sup>3+</sup> (Figure 3) [1, 20, 36]. In this context, the transition between <sup>4</sup>S<sub>3/2</sub> and <sup>4</sup>I<sub>15/2</sub> was the strongest, corresponding to the 539 nm emission. As a result, the solution of NaYF<sub>4</sub>:Yb,Er NCs presented a green emission under 980 nm excitation (Figure 2 inset). Note that the generation of the emission related to an up-conversion mechanism, namely, absorbing two 980 nm photons but emitting one higher energy photon. The efficiency of up-conversion fluorescence strongly depended on the crystal phase of the NCs. As reported previously, NaYF<sub>4</sub>:Yb,Er NCs had two different crystal phases,  $\alpha$ -phase and  $\beta$ -phase. The up-conversion efficiency of  $\beta$ -phase is greatly stronger than that of  $\alpha$ -phase. In the current synthesis, moreover, the as-prepared NCs possessed a pure  $\beta$ -phase (Figure 1(e)), leading to the strong up-conversion fluorescence [37]. Overall, the highly crystalline structure, narrow size distribution, and strong up-conversion fluorescence of the products indicated that the NaYF<sub>4</sub>:Yb,Er NCs synthesized in liquid paraffin possessed a high quality, which was comparable to the corresponding NCs synthesized in the conventional solvent of octadecene (ODE) [2, 3, 38].

The growth temperature greatly influenced the size monodispersity and the crystal phases of the as-prepared NaYF<sub>4</sub>:Yb,Er NCs. As shown in Figure 1(b), NCs synthesized at 280°C possessed the best size monodispersity, whereas the increase of reaction temperature from 280

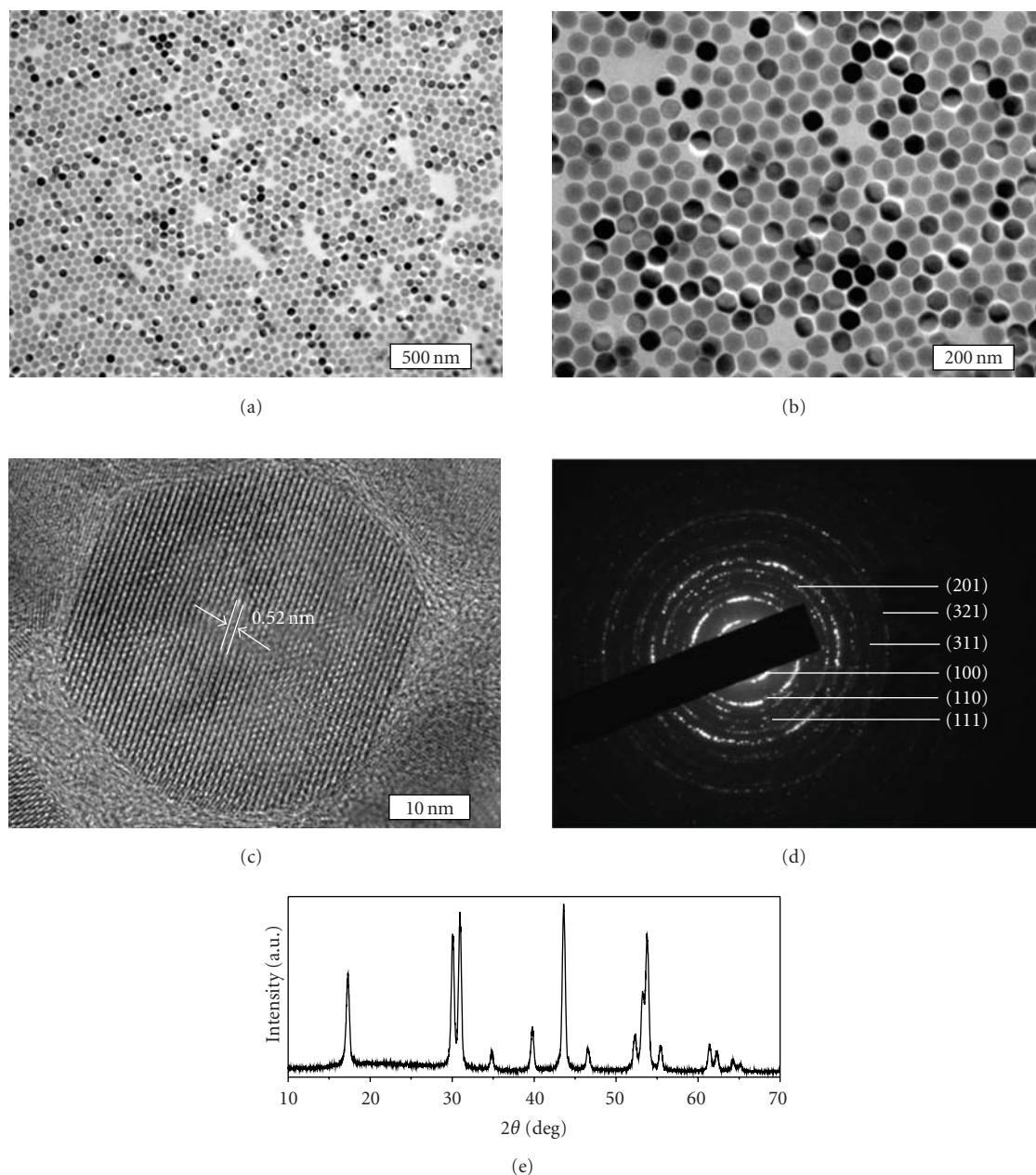


FIGURE 1: (a) Low- and (b) high-magnification TEM images, (c) HRTEM image, (d) selected area electron diffraction, and (e) XRD pattern of  $\text{NaYF}_4:\text{Yb,Er}$  NCs synthesized at  $280^\circ\text{C}$ .

to  $320^\circ\text{C}$  obviously decreased the size monodispersity (Figure 4). Besides spherical particles, anisotropic nanorods were also observed (Figure 4(b)). It should be mentioned that the optimal temperature for synthesizing monodisperse  $\text{NaYF}_4:\text{Yb,Er}$  NCs in ODE was  $320^\circ\text{C}$ ,  $40^\circ\text{C}$  higher than in liquid paraffin. This difference was attributed to the different viscosity of them. The viscosity of liquid paraffin was lower than that of ODE due to the shorter alkyl chains of liquid paraffin, thus facilitating the diffusion of various atoms and molecules at a given temperature. According to the classical model of NC growth in high-boiling-point organic solvents, the growth rate, size distribution, and morphology were

mainly dominated by a diffusion-limited process [1, 4, 39]. In brief, NC growth was the equilibrium of kinetics and thermodynamics. If atoms and molecules had lower diffusion rate, the deposition of them on NC surface would follow thermodynamics-favored process, namely, growth with less face selectivity. It led to quasispherical particles. In contrast, higher diffusion rate made the atom stacking have face selectivity via kinetics-favored process. The growth along high energy faces resulted in anisotropic NCs as well as poor size distribution [1, 34, 39]. Since the diffusion rate of atoms and molecules in liquid paraffin was higher than those in ODE at a given temperature, it was comprehensible that the

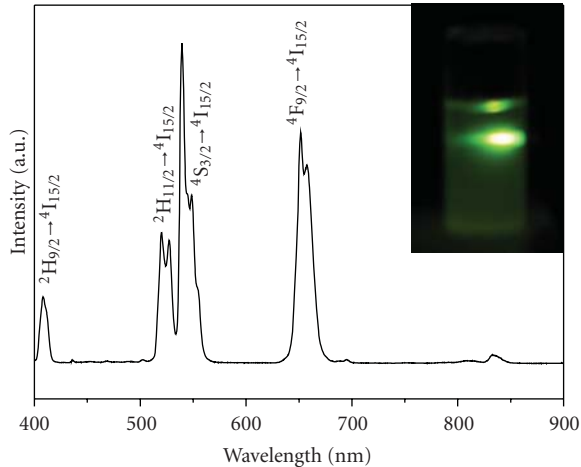


FIGURE 2: Up-conversion fluorescence spectrum of NaYF<sub>4</sub>:Yb,Er NCs synthesized at 280°C. Inset: the corresponding fluorescent image.

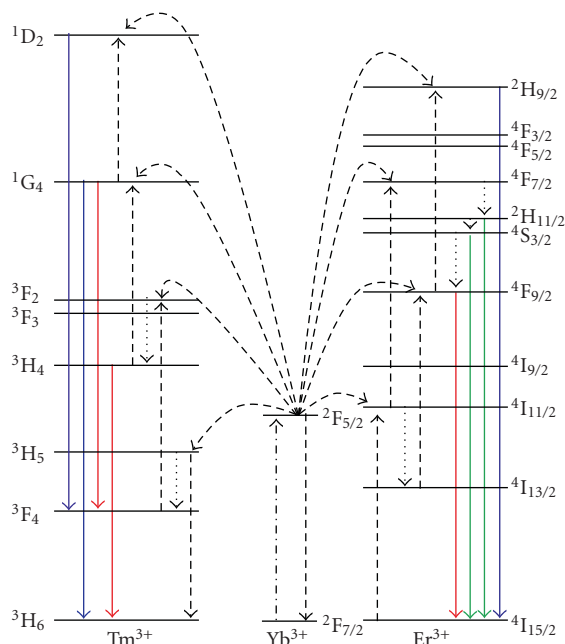
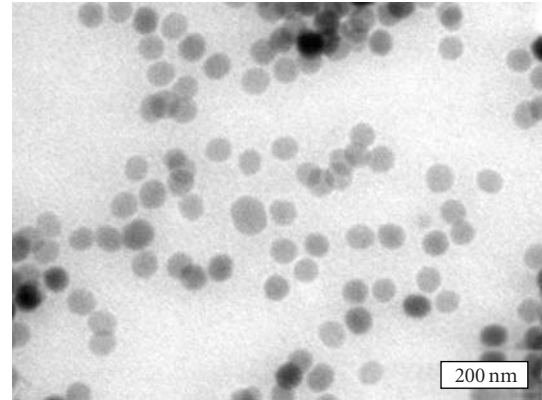


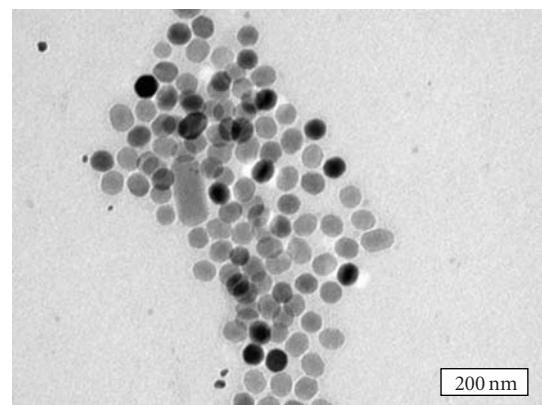
FIGURE 3: Schematic illustration of the transition energy levels of NaYF<sub>4</sub>:Yb,Er and NaYF<sub>4</sub>:Yb,Tm NCs.

optimal temperature for synthesizing NaYF<sub>4</sub>:Yb,Er NCs in liquid paraffin should be lower than in ODE.

As indicated in the previous reports, high growth temperature facilitated the formation of  $\beta$ -phase NaYF<sub>4</sub>:Yb,Er NCs. So, the conventional synthesis was operated at 320°C. However, in our method, the as-prepared NaYF<sub>4</sub>:Yb,Er NCs synthesized at 280°C already had pure  $\beta$ -phase. Control experiment showed that below 280°C, the as-prepared NCs were the mixtures of  $\alpha$ -phase and  $\beta$ -phase, indicating 280°C was the lower limit of temperature to obtain pure  $\beta$ -phase NCs. This result revealed an advantage using liquid paraffin



(a)



(b)

FIGURE 4: TEM images of NaYF<sub>4</sub>:Yb,Er NCs synthesized at 300 (a) and 320°C (b).

as solvent, namely, the capability to synthesize high-quality NCs at relative low reaction temperature.

Current method was also extendable for synthesizing up-conversion NCs doped with other lanthanides, such as NaYF<sub>4</sub>:Yb,Tm. As shown in Figure 5(a), NaYF<sub>4</sub>:Yb,Tm NCs also possessed very narrow size distribution with an average diameter about 30 nm, which was similar to NaYF<sub>4</sub>:Yb,Er NCs. HRTEM image indicated that the as-prepared NCs had highly crystalline structure, and corresponding to  $\beta$ -phase NaYF<sub>4</sub> crystals (Figure 5(b)) [32]. Figure 5(c) showed the up-conversion fluorescence spectrum and fluorescent image of NaYF<sub>4</sub>:Yb,Tm NCs. Four emission peaks centered at 451, 475, 644, and 799 nm were observed, which were, respectively, attributed to the transition from the energy levels  $^1D_2$  to  $^3F_4$ ,  $^1G_4$  to  $^3H_6$ ,  $^1G_4$  to  $^3F_4$ , and  $^3H_4$  to  $^3H_6$  of Tm<sup>3+</sup> (Figure 3) [32, 33, 40]. Besides, the apparent emission color of NaYF<sub>4</sub>:Yb,Tm NCs was blue, consistent with the  $^1D_2$  to  $^3F_4$  and  $^1G_4$  to  $^3H_6$  transitions (Figure 5(c) inset).

#### 4. Conclusions

In summary, we demonstrated a low-cost and convenient method for synthesizing high-quality lanthanide-codoped

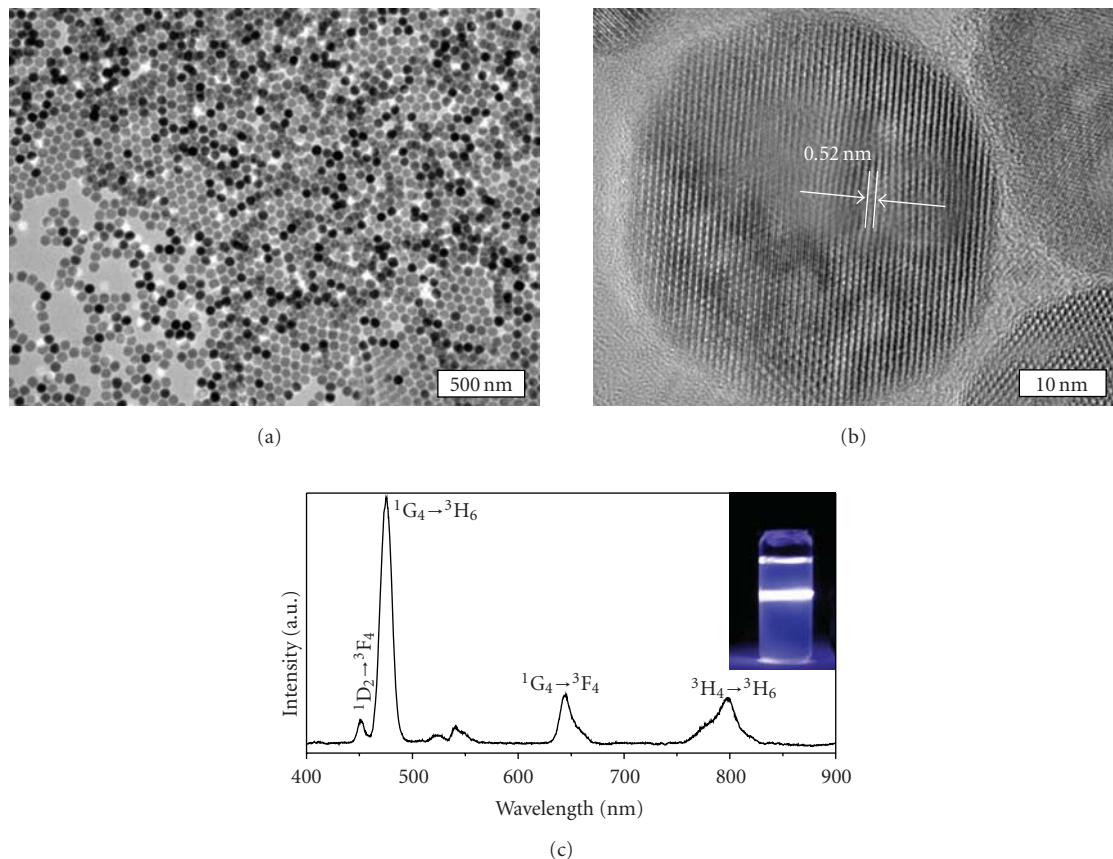


FIGURE 5: (a) TEM and (b) HRTEM images of  $\text{NaYF}_4:\text{Yb,Tm}$  NCs. (c) Up-conversion fluorescence spectrum of  $\text{NaYF}_4:\text{Yb,Tm}$  NCs. Inset: the corresponding fluorescent image.

$\text{NaYF}_4$  NCs in liquid paraffin. The as-prepared NCs possessed good crystalline structure, narrow size distribution, and strong up-conversion fluorescence. The color of up-conversion fluorescence was tunable by codoping different lanthanide, such as Yb/Er and Yb/Tm. In comparison to other high-boiling-point organic solvents, liquid paraffin is cheaper and prolific in oil industry. Besides,  $280^\circ\text{C}$  was the optimal temperature for the current synthesis, which was lower than that in the previous reports using other high-boiling-point organic solvents. Consequently, this user-friendly method will facilitate the synthesis of high-quality lanthanide-codoped  $\text{NaYF}_4$  NCs in commercial scale. Further investigations are underway to synthesize various rare-earth fluoride NCs as well as control their morphologies in liquid paraffin.

## Acknowledgment

This work was supported by NSFC (20804008, 20974038, 50973039), the 973 Program of China (2007CB936402, 2009CB939701), the FANEDD of China (200734), the Special Project from MOST of China, the Basic Scientific Research Fund of Ministry of Education (200905008), and the Program for New Century Excellent Talents in University.

## References

- [1] F. Wang and X. Liu, "Recent advances in the chemistry of lanthanide-doped upconversion nanocrystals," *Chemical Society Reviews*, vol. 38, no. 4, pp. 976–989, 2009.
- [2] J.-C. Boyer, L. A. Cuccia, and J. A. Capobianco, "Synthesis of colloidal upconverting  $\text{NaYF}_4:\text{Er}^{3+}/\text{Yb}^{3+}$  and  $\text{Tm}^{3+}/\text{Yb}^{3+}$  monodisperse nanocrystals," *Nano Letters*, vol. 7, no. 3, pp. 847–852, 2007.
- [3] S.-Z. Zhang, L.-D. Sun, H. Tian, Y. Liu, J.-F. Wang, and C.-H. Yan, "Reversible luminescence switching of  $\text{NaYF}_4:\text{Yb,Er}$  nanoparticles with controlled assembly of gold nanoparticles," *Chemical Communications*, no. 18, pp. 2547–2549, 2009.
- [4] L. Wang and Y. Li, "Controlled synthesis and luminescence of lanthanide doped  $\text{NaYF}_4$  nanocrystals," *Chemistry of Materials*, vol. 19, no. 4, pp. 727–734, 2007.
- [5] Z. Li and Y. Zhang, "Monodisperse silica-coated polyvinylpyrrolidone/ $\text{NaYF}_4$  nanocrystals with multicolor upconversion fluorescence emission," *Angewandte Chemie International Edition*, vol. 45, no. 46, pp. 7732–7735, 2006.
- [6] M. Wang, C.-C. Mi, W.-X. Wang et al., "Immunolabeling and NIR-excited fluorescent imaging of HeLa cells by using  $\text{NaYF}_4:\text{Yb,Er}$  upconversion nanoparticles," *ACS Nano*, vol. 3, no. 6, pp. 1580–1586, 2009.
- [7] J. Shan, X. Qin, N. Yao, and Y. Ju, "Synthesis of monodisperse hexagonal  $\text{NaYF}_4:\text{Yb, Ln}$  (Ln = Er, Ho and Tm) upconversion nanocrystals in TOPO," *Nanotechnology*, vol. 18, no. 44, Article ID 445607, 2007.

- [8] P. Li, Q. Peng, and Y. D. Li, "Synthesis of NaYF<sub>4</sub> nanocrystals with predictable phase and shape," *Advanced Materials*, vol. 21, pp. 1945–1948, 2009.
- [9] J. Shan and Y. Ju, "A single-step synthesis and the kinetic mechanism for monodisperse and hexagonal-phase NaYF<sub>4</sub>:Yb, Er upconversion nanophosphors," *Nanotechnology*, vol. 20, no. 27, Article ID 275603, 2009.
- [10] M. Yu, F. Li, Z. Chen et al., "Laser scanning up-conversion luminescence microscopy for imaging cells labeled with rare-earth nanophosphors," *Analytical Chemistry*, vol. 81, no. 3, pp. 930–935, 2009.
- [11] G. Chen, H. Liu, G. Somesfalean, H. Liang, and Z. Zhang, "Upconversion emission tuning from green to red in Yb<sup>3+</sup>/Ho<sup>3+</sup>-codoped NaYF<sub>4</sub> nanocrystals by tridoping with Ce<sup>3+</sup> ions," *Nanotechnology*, vol. 20, no. 38, Article ID 385704, 2009.
- [12] M. Zhang, S. Shi, J. Meng et al., "Preparation and characterization of near-infrared luminescent bifunctional core/shell nanocomposites," *Journal of Physical Chemistry C*, vol. 112, no. 8, pp. 2825–2830, 2008.
- [13] D. K. Chatterjee, L. S. Fong, and Y. Zhang, "Nanoparticles in photodynamic therapy: an emerging paradigm," *Advanced Drug Delivery Reviews*, vol. 60, no. 15, pp. 1627–1637, 2008.
- [14] M. Nyk, R. Kumar, T. Y. Ohulchanskyy, E. J. Bergey, and P. N. Prasad, "High contrast in vitro and in vivo photoluminescence bioimaging using near infrared to near infrared up-conversion in Tm<sup>3+</sup> and Yb<sup>3+</sup> doped fluoride nanophosphors," *Nano Letters*, vol. 8, no. 11, pp. 3834–3838, 2008.
- [15] N. M. Idris, Z. Li, L. Ye et al., "Tracking transplanted cells in live animal using upconversion fluorescent nanoparticles," *Biomaterials*, vol. 30, no. 28, pp. 5104–5113, 2009.
- [16] M. Kumar, Y. Guo, and P. Zhang, "Highly sensitive and selective oligonucleotide sensor for sickle cell disease gene using photon upconverting nanoparticles," *Biosensors and Bioelectronics*, vol. 24, no. 5, pp. 1522–1526, 2009.
- [17] F. Wang and X. Liu, "Upconversion multicolor fine-tuning: visible to near-infrared emission from lanthanide-doped NaYF<sub>4</sub> nanoparticles," *Journal of the American Chemical Society*, vol. 130, no. 17, pp. 5642–5643, 2008.
- [18] S. Schietinger, T. Aichele, H.-Q. Wang, T. Nann, and O. Benson, "Plasmon-enhanced upconversion in single NaYF<sub>4</sub>:Yb<sup>3+</sup>/Er<sup>3+</sup> codoped nanocrystals," *Nano Letters*, vol. 10, no. 1, pp. 134–138, 2010.
- [19] X. Yu, M. Li, M. Xie, L. Chen, Y. Li, and Q. Wang, "Dopant-controlled synthesis of water-soluble hexagonal NaYF<sub>4</sub> nanorods with efficient upconversion fluorescence for multicolor bioimaging," *Nano Research*, vol. 3, no. 1, pp. 51–60, 2010.
- [20] C.-J. Carling, J.-C. Boyer, and N. R. Branda, "Remote-control photoswitching using NIR light," *Journal of the American Chemical Society*, vol. 131, no. 31, pp. 10838–10839, 2009.
- [21] F. Wang, Y. Han, C. S. Lim et al., "Simultaneous phase and size control of upconversion nanocrystals through lanthanide doping," *Nature*, vol. 463, no. 7284, pp. 1061–1065, 2010.
- [22] L. W. Qian, J. T. Zai, Z. Chen, J. Zhu, Y. P. Yuan, and X. F. Qian, "Control of the morphology and composition of yttrium fluoride via a salt-assisted hydrothermal method," *CrystEngComm*, vol. 12, pp. 199–206, 2010.
- [23] Y. Y. Zhang, L. W. Yang, C. F. Xu, J. X. Zhong, and C. Q. Sun, "Sensitized deep-ultraviolet up-conversion emissions of Gd<sup>3+</sup> via Tm<sup>3+</sup> and Yb<sup>3+</sup> in hexagonal NaYF<sub>4</sub> nanorods," *Applied Physics B*, vol. 98, no. 2-3, pp. 243–247, 2010.
- [24] L. Gao, X. Ge, Z. Chai, G. Xu, X. Wang, and C. Wang, "Shape-controlled synthesis of octahedral  $\alpha$ -NaYF<sub>4</sub> and its rare earth doped submicrometer particles in acetic acid," *Nano Research*, vol. 2, no. 7, pp. 565–574, 2009.
- [25] C. Lin, M. T. Berry, R. Anderson, S. Smith, and P. S. May, "Highly luminescent NIR-to-visible upconversion thin films and monoliths requiring no high-temperature treatment," *Chemistry of Materials*, vol. 21, no. 14, pp. 3406–3413, 2009.
- [26] Z. Li and Y. Zhang, "An efficient and user-friendly method for the synthesis of hexagonal-phase NaYF<sub>4</sub>:Yb, Er/Tm nanocrystals with controllable shape and upconversion fluorescence," *Nanotechnology*, vol. 19, no. 34, Article ID 345606, 2008.
- [27] H.-X. Mai, Y.-W. Zhang, R. Si et al., "High-quality sodium rare-earth fluoride nanocrystals: controlled synthesis and optical properties," *Journal of the American Chemical Society*, vol. 128, no. 19, pp. 6426–6436, 2006.
- [28] H.-X. Mai, Y.-W. Zhang, L.-D. Sun, and C.-H. Yan, "Size- and phase-controlled synthesis of monodisperse NaYF<sub>4</sub>:Yb,Er nanocrystals from a unique delayed nucleation pathway monitored with upconversion spectroscopy," *Journal of Physical Chemistry C*, vol. 111, no. 37, pp. 13730–13739, 2007.
- [29] K. W. Krämer, D. Biner, G. Frei, H. U. Güdel, M. P. Hehlen, and S. R. Lüthi, "Hexagonal sodium yttrium fluoride based green and blue emitting upconversion phosphors," *Chemistry of Materials*, vol. 16, no. 7, pp. 1244–1251, 2004.
- [30] S. J. Budijono, J. Shan, N. Yao et al., "Synthesis of stable block-copolymer-protected NaYF<sub>4</sub>:Yb<sup>3+</sup>, Er<sup>3+</sup> up-converting phosphor nanoparticles," *Chemistry of Materials*, vol. 22, no. 2, pp. 311–318, 2010.
- [31] J. Han, H. Zhang, H. Sun, D. Zhou, and B. Yang, "Manipulating the growth of aqueous semiconductor nanocrystals through amine-promoted kinetic process," *Physical Chemistry Chemical Physics*, vol. 12, no. 2, pp. 332–336, 2010.
- [32] C. Liu, H. Wang, X. Li, and D. Chen, "Monodisperse, size-tunable and highly efficient  $\beta$ -NaYF<sub>4</sub>:Yb,Er(Tm) up-conversion luminescent nanospheres: controllable synthesis and their surface modifications," *Journal of Materials Chemistry*, vol. 19, no. 21, pp. 3546–3553, 2009.
- [33] G. S. Yi and G. M. Chow, "Synthesis of hexagonal-phase NaYF<sub>4</sub>:Yb,Er and NaYF<sub>4</sub>:Yb,Tm nanocrystals with efficient up-conversion fluorescence," *Advanced Functional Materials*, vol. 16, no. 18, pp. 2324–2329, 2006.
- [34] C. Li, J. Yang, Z. Quan, P. Yang, D. Kong, and J. Lin, "Different microstructures of  $\beta$ -NaYF<sub>4</sub> fabricated by hydrothermal process: effects of pH values and fluoride sources," *Chemistry of Materials*, vol. 19, no. 20, pp. 4933–4942, 2007.
- [35] J. Zhang, C. M. Shade, D. A. Chengelis, and S. Petoud, "A strategy to protect and sensitize near-infrared luminescent Nd<sup>3+</sup> and Yb<sup>3+</sup>: organic tropolonate ligands for the sensitization of Ln<sup>3+</sup>-doped NaYF<sub>4</sub> nanocrystals," *Journal of the American Chemical Society*, vol. 129, no. 48, pp. 14834–14835, 2007.
- [36] S. Heer, K. Kömpe, H.-U. Güdel, and M. Haase, "Highly efficient multicolour upconversion emission in transparent colloids of lanthanide-doped NaYF<sub>4</sub> nanocrystals," *Advanced Materials*, vol. 16, no. 23-24, pp. 2102–2105, 2004.
- [37] D.-K. Ma, S.-M. Huang, Y.-Y. Yu, Y.-F. Xu, and Y.-Q. Dong, "Rare-earth-ion-doped hexagonal-phase NaYF<sub>4</sub> nanowires: controlled synthesis and luminescent properties," *Journal of Physical Chemistry C*, vol. 113, no. 19, pp. 8136–8142, 2009.
- [38] H. P. Zhou, C. H. Xu, W. Sun, and C. H. Yan, "Clean and flexible modification strategy for carboxyl/aldehyde-functionalized upconversion nanoparticles and their optical applications," *Advanced Functional Materials*, vol. 19, pp. 3892–3900, 2009.

- [39] X. Liang, X. Wang, J. Zhuang, Q. Peng, and Y. Li, "Synthesis of NaYF<sub>4</sub> nanocrystals with predictable phase and shape," *Advanced Functional Materials*, vol. 17, no. 15, pp. 2757–2765, 2007.
- [40] X. Liu, J. Zhao, Y. Sun et al., "Ionothermal synthesis of hexagonal-phase NaYF<sub>4</sub>:Yb<sup>3+</sup>,Er<sup>3+</sup>/Tm<sup>3+</sup> upconversion nanophosphors," *Chemical Communications*, no. 43, pp. 6628–6630, 2009.

## Research Article

# Facile Synthesis of Monodisperse ZnO Nanocrystals by Direct Liquid Phase Precipitation

Lan Chen, Justin D. Holmes, Sonia Ramírez-García, and Michael A. Morris

Department of Chemistry, University College Cork, Cork, Ireland

Correspondence should be addressed to Michael A. Morris, m.morris@ucc.ie

Received 21 May 2010; Accepted 6 July 2010

Academic Editor: Quanqin Dai

Copyright © 2011 Lan Chen et al. This is an open access article distributed under the Creative Commons Attribution License, which permits unrestricted use, distribution, and reproduction in any medium, provided the original work is properly cited.

ZnO nanocrystals can be synthesized by a variety of methods. Among them, only a few nonhydrolytic methods have been successful at low synthesis temperatures in terms of size, crystallinity, morphology and surface-defect control. These methods require very careful control of conditions and carefully engineered precursors. A new methodology—*direct liquid phase precipitation*—is reported here that can produce nanocrystals (NCs) which are a little difficult to obtain for these complex synthesis techniques in a more facile and efficient way (i.e., at room temperature). This technique results in high quality ZnO nanocrystals of diameter 5–12 nm and different morphologies. Characterisation of ZnO products shows that both synthesis and ageing conditions have significant effects on the formation of the nanocrystals. Capping agents and ageing temperature/time can be used to control both size and crystallinity of the products. The use of *in situ* or *ex situ* ageing conditions can result in different particle morphologies. Both *in situ* and *ex situ* ageing shows that mild ageing conditions (e.g., 60–80°C and 24–48 hours) are required to produce the highest quality nanomaterials.

## 1. Introduction

ZnO semiconductor nanocrystals (NCs) are receiving much attention due to their novel optical [1–3] and electronic properties [4] and applications in solar cells [5, 6], light emitting diodes [7, 8] and catalysis [9]. Recent advances in charge transfer doping to make band gap variable nanocrystals [10–14] further enhance their potential as components of future nanotechnology. One of the key features in this system is the use of surface organic capping moieties which facilitate control of the unique properties which arise in the nanometre size scale regime.

A key ingredient for the study and applications of ZnO NCs is a reliable synthetic route to high-quality materials. While ZnO nanocrystals can be synthesized by a variety of methods, the most successful in terms of controlled size, size-dispersion and crystallinity has been the high-temperature decomposition of organometallic precursors in a coordinating solvent [15–17]. However, these methods usually require complex laboratory equipment and use expensive precursors. Experiments are strictly engineered by choice of ligands and solvents so that the zinc precursor complex is stable at low temperatures but unstable at higher

leading to particle development. The solvents used must have relatively high boiling point and be inert to either the precursors or the products. Recently, there have been several reports of solution-phase synthesis of ZnO colloids at low temperature, mainly based on the hydrolysis of zinc salts [18–20] or zinc alkoxides [21, 22] (in organic solvents) and on electrochemical routes [23, 24]. The use of advanced engineered polymer templates [25–27] and reverse micelles [22, 28] have also been exploited in order to control both particle morphologies and sizes. However, unless extreme thermal treatments are applied after the synthesis, such preparative routes provide nanocrystalline ZnO with hydroxylated surfaces and/or organic molecules that can significantly affect material properties. This is important as surface-related defects account for both radiative and nonradiative decay channels competing with the ZnO band-edge emission [29], while surface-bound molecules [30, 31] or acid-basic sites can influence emission properties as well as redox potentials and interfacial electron-transfer rates [32].

Because of the limitations of the methodologies used thus far, there is a clear requirement to develop simple synthetic nonhydrolytic approaches coupled to the use of so-called capping ligands that coordinate to the surface and limit

growth whilst controlling surface chemistry (e.g., passivation of surface traps, particle dispersion in solvents, etc.). The goal of many studies is to provide a facile methodology, using common chemicals and laboratory apparatus to achieve size, shape, crystallinity and surface defect control by *in situ* synthesis and functionalization in a simple, cost-effective, and convenient way. The direct liquid phase precipitation (DLPP) strategy [33, 34] developed recently by us provides a facile, nonhydrolytic way to synthesise most binary or even ternary metal oxides at room temperature (RT). In this paper modification of this strategy is demonstrated for the synthesis of size monodispersed ZnO NCs at room temperature (RT). Compared with other low temperature solution phase approaches, DLPP can produce the ZnO NCs with higher quality in terms of shape-, size, crystallinity, and surface defect control whilst being a chemically convenient, efficient and energy saving (no calcination or heat input required) method to synthesise ZnO NCs in a readily scalable way.

## 2. Experimental

**2.1. Materials.** All chemicals are reagent grade and used as received. Na<sub>2</sub>O (97%), ZnCl<sub>2</sub> (99%), oleic acid (OLA), methanol, and anhydrous ethanol were purchased from Aldrich. Hexadecylamine (HDA) was purchased from Fluka.

**2.2. Synthesis of ZnO NCs.** A typical synthesis consists of mixing of two prepared solutions. In solution 1, Na<sub>2</sub>O and 2 mmol of hexadecylamine (the role of HDA is complex and discussed in detail below) was dissolved into 20 mL anhydrous ethanol to form a 0.1 M Na<sub>2</sub>O solution. In solution 2, ZnCl<sub>2</sub> together with oleic acid (OLA) at fixed molar ratios indicated in the text was mixed in ethanol to yield a 0.1 M zinc cation solution. Solution 1 and 2 are combined under vigorously magnetic stirring at room temperature (RT) or as specified for 2 hours. On mixing, the solution becomes immediately turbid followed by the formation of white precipitate (nanocrystal aggregates). It is proposed that the DLPP method involves the direct reaction of O<sup>2-</sup> anions with metal cations to yield the metal oxide [33, 34]. Under continued stirring the solution gradually becomes clearer (a little cloudy at RT but clearer at the elevated temperature, e.g., 60°C) as the as-formed “sticky” precipitate settles. The resulting white precipitate was aged *in situ* in the solution at 60–105°C for 24–188 h and the precipitate was collected by filtration (0.2 μm filter paper) and washed with ethanol and then acetone twice. For *ex situ* ageing, the filtrate was dispersed into 10 mL of toluene which results in rapid redispersion of the precipitate which was then reformed by the addition of 70 mL of methanol and the mixture was aged at 60°C for 10–120 hours. The precipitate was harvested and washed as described above. The typical ageing temperature, time, and oleic acid/Zn<sup>2+</sup> ratio, unless otherwise stated, refer to 60°C, 24 hours, and 1 : 2, respectively, in this paper.

**2.3. Analyses.** The powder samples were analyzed by: a JEOL 2000FX transmission electron microscope (TEM) operating at 200 kV, a Phillips Xpert MPD X-ray diffractometer (XRD) using Cu Kα radiation at an anode voltage of 40 kV (with a high sensitivity X'Celerator detector) and a high performance AXIS 165 X-ray photoelectron spectrometer (XPS) using a pass energy of 20 eV. In addition, UV-vis (ultra-violet-visible) and photoluminescence spectra were recorded using a Cary 50 UV-visible spectrophotometer and a Perkin Elmer LS50B fluorescence spectrometer, respectively.

## 3. Results and Discussion

ZnO NCs are immediately formed upon the mixing of two portions of reactant solutions in the one-step synthesis. It should be noted that the products formed are weak aggregates of the nanocrystals but these can be rapidly dispersed in nonpolar solvents. Figure 1(a) shows the *in situ* ageing temperature has significant influence on the nanocrystal (NC) size (note the OLA/Zn<sup>2+</sup> molar ratio = 1 : 2). ZnO NCs of 5 nm (using Scherrer formulism) are produced by synthesis at 60°C for 24 hours whilst the NC size increases to about 10 nm are produced when the ageing temperature is increased to 80°C. However, the increase of NC size with ageing temperature is complex (see Figure 1(d)) and crystal size is seen to decrease if the ageing temperature exceeds 100°C. Ageing time also affects the NC size and structure. The NCs grow from 7.5 nm to 10 nm, after the ageing time changes from 24 to 67 hours at 60°C as seen in Figure 1(b). However, this is a maximum size as the NC size decreases to about 6 nm on extended times (67 h). This is surprising as the maximum size of bare ZnO NCs formed in the absence of ligands is expected to be only determined by the metal cation concentration. It is suggested that this limited NC size results from competitive solution equilibria resulting from both the precipitation, and dissolution of ZnO species in ethanol. These solution equilibria arise from the presence of the strongly coordinating ligands. Carboxyl-containing long chain molecules have strong affinity to the ZnO matter due to the strong interaction between Zn<sup>2+</sup> and carboxyl as they are coordinated in the form of zinc oleate and stearate salts [35, 36] and form a ligand passivation shell on the surface of ZnO NCs. The presence of OLA and HDA can be expected to lead to partially dissolution (etching) of the nanoparticles. Reactions to consider are the formation of soluble zinc oleate and the possibility of HDA-OLA reactions leading to stripping of a protective OLA layer. As might be expected, the NC size decreases with the increase of OLA/Zn<sup>2+</sup> ratio as shown in Figure 1(c) and it can be verified that these ligands significantly inhibit the growth of the ZnO NCs.

The XRD data of the samples prepared with different OLA/Zn<sup>2+</sup> ratio are apparently contradicted by TEM analysis. The micrographs shown in Figure 2 appear to indicate that the “nanocrystals” decrease in size with a decrease in the OLA/Zn<sup>2+</sup> ratio. The average particle sizes measured by TEM are 11.31 (6.1), 4.85 (6.3), 4.88 (6.9) and 4.82 (7.9) nm (standard deviations given in brackets and all data

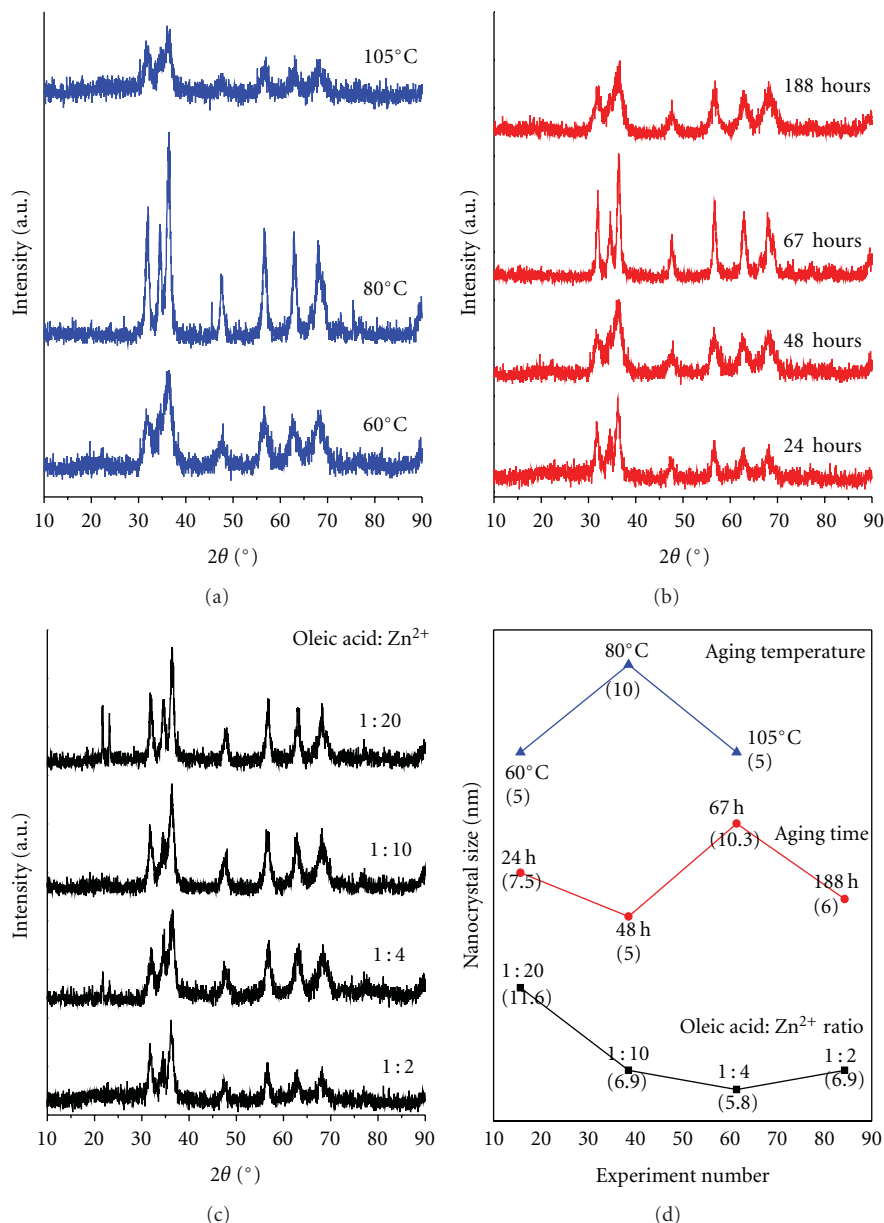


FIGURE 1: X-ray diffraction (XRD) patterns of the OLA-ZnO nanocrystals (NCs). (a) Aged in situ at different temperature for 48 hours with oleic acid/Zn<sup>2+</sup> ratio of 1:2, (b) aged in situ at 60°C for different time oleic acid/Zn<sup>2+</sup> ratio of 1:2, (c) aged in situ at 60°C for 24 hours with different oleic acid/Zn<sup>2+</sup> ratio and (d) the nanocrystal size (shown in the parenthesis) under different ageing conditions calculated by Scherrer's equation.

are estimated from particle size distributions (PSDs) which are provided in the supporting information for all TEM data reported here) as the OLA/Zn<sup>2+</sup> molar ratio decreases from 1:2, 1:4, 1:10, to 1:20, respectively. This contradiction between the characterisation methods can be attributed to the fact that synthesis results in the formation of individual particles consisting of a few aggregated nanocrystals or polycrystal grain structures which are observed by HRTEM (Figure 5(b)). XRD indicates the component nanocrystal size whilst TEM indicates the total particle size. It can be seen in the data that increasing OLA/Zn<sup>2+</sup> ratio not only reduces the NC size but also improves the size dispersivity.

This is probably related to the OLA preventing NC growth which improves size monodispersivity by limiting the growth process.

The complexity of effects resulting from changes in *in situ* ageing time and temperature revealed by XRD are also observed in the TEM data, as shown in Figures 3(a)–3(d). It was generally observed that particle size decreases on extended ageing at similar temperatures (but monodispersivity is improved as explained above). An example is shown in Figure 3(e) for 60°C ageing where the particle size changes from 6.1 to 4.7 nm after ageing at 48 and 188 h, respectively. The ageing temperature has a profound

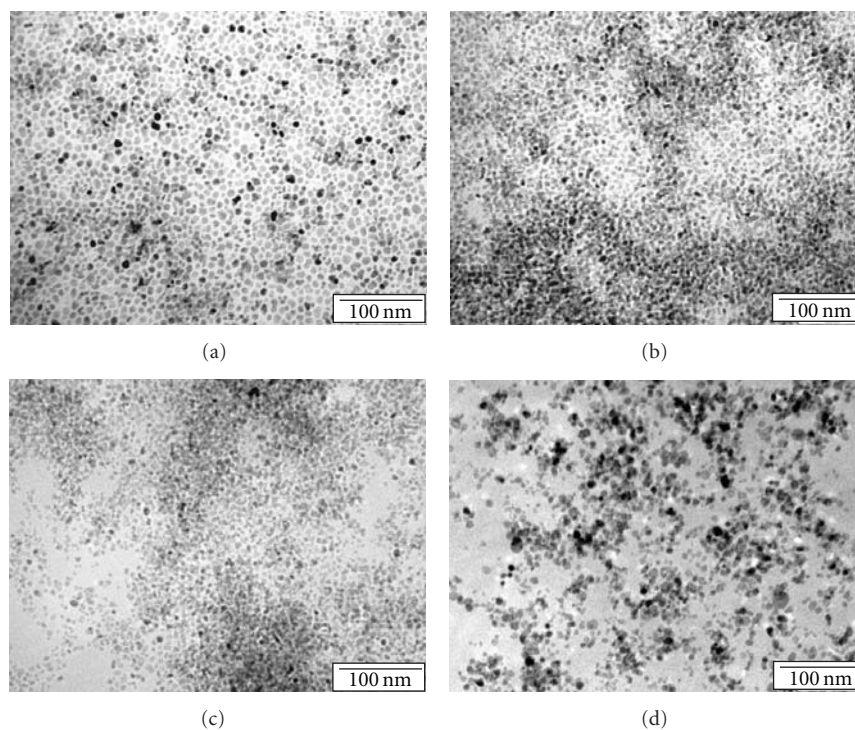


FIGURE 2: Transmission electron microscopy (TEM) images of the OLA-ZnO NCs synthesized by different molar ratio of oleic acid to  $Zn^{2+}$ : (a) 1 : 2; (b) 1 : 4; (c) 1 : 10 and (d) 1 : 20. All scale bars are 100 nm.

effect on the shape of the ZnO nanocrystals as revealed in Figures 3(a), 3(c), and 3(d). At 60°C ageing temperatures, the products are generally uniform in shape but at 80°C (Figure 3(c)) the crystals become elongated to rod-like structures. However, at higher age temperatures of 105°C more uniform particles are formed presumably because of ZnO solubility as described above. As seen by XRD, high ageing temperatures (105°C, NC size = 5.4 nm) result in a decrease in the size of the particles compared to lower temperatures (80°C, NC size = 8.6 nm). This decrease in the NC size can also be ascribed to the partial dissolution of the NCs as described above, since particle dissolution might be expected to become more important at high ageing temperature/time. The growth of particles at lower temperatures appears to result from an Ostwald ripening mechanism. If the reaction is carried out as usual (60°C) and stirred for two hours, subsequent addition of solid  $ZnCl_2$  and  $Na_2O$  (stoichiometric amounts equivalent to those already present in solution) results in well-sized dispersed particles (Figure 3(f)) suggesting that the previously formed nanocrystals “consume” the newly formed smaller size materials efficiently and all ZnO NCs reach the same size provided that the ageing time is long enough. Understanding the high temperature behavior is probably related to the presence of HDA. Although it is commonly used in ZnO synthesis, its role of HDA is probably not as a simple surfactant (particle spacer) or surface complexing agent. Zhong and Knoll [37] have suggested that it controls particle morphology by determining the OLA interaction with the ZnO component. It was found here that HDA molecules

cannot form stable HDA-ZnO complexes and almost all HDA molecules are removed from the product ZnO during precipitate washing with only trace nitrogen being observed by elemental analysis. On the basis of this work, we suggest that at reaction between HDA and OLA occurs at the highest age temperatures resulting in removal of the capping OLA ligands and so promoting ZnO dissolution as postulated earlier. Evidence for this assertion can be seen in Figures 4(a), 4(b), 4(c), and 4(d). Here, the *ex situ* ageing which results in HDA removal prior to ageing shows a simple variation of nanocrystal size with time. The NC size increases progressively from 6.8 to 12.1, 13.2, and 13.7 nm after ageing at 10, 24, 72, and 120 h. Extended ageing only results in a slow crystal growth, and this is related to decreasing solution concentration. As might be expected the polydispersity increases with age time (from a value of around 10 to 15 nm—see supporting information) and is consistent with the statistical nature of Ostwald ripening.

It should be noted that the OLA-ZnO NCs are highly dispersible and readily “soluble” in nonpolar solvents, for example, toluene, hexane, and chloroform, and the nanocrystal aggregates are reformed rapidly from the dispersed NCs in ethanolic and methanolic solutions. The term “soluble” is used as these solutions are clear because the dispersed particle size is well below that required for light scattering although evidence for small aggregates is present in UV-vis analysis (as detailed below). During growth the presence of these nonpolar solvents have dramatic effects of particle morphology. Figure 5(a) shows typical data from an *ex situ* ageing experiment carried out without addition of methanol

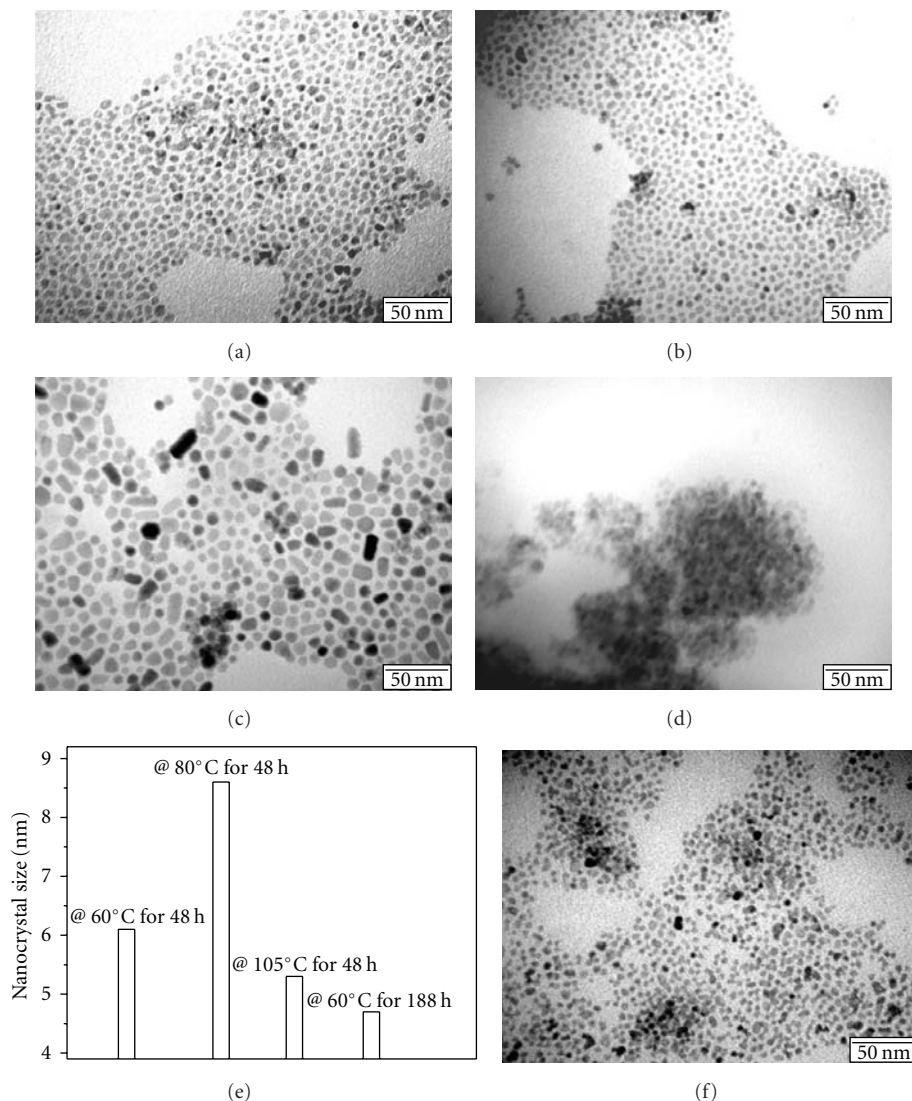


FIGURE 3: TEM images of the OLA-ZnO NCs obtained under different in situ ageing conditions: (a) 60°C for 48 hours; (b) 60°C for 188 hours; (c) 80°C for 48 hours; (d) 105°C for 48 hours and (e) the maximum mode of the nanocrystal size distribution from image (a)–(d); and (f) a sequential addition of metal cations where the reaction is initiated and run for two hours and additional stoichiometric amounts of  $\text{Na}_2\text{O}$  and  $\text{ZnCl}_2$  solids are added during the extended ageing treatment (60°C for 188 hours). All scale bars are 50 nm.

(i.e., toluene only aged). Well-defined ZnO NCs where the crystals have flake-like polygonal shape; for example, rectangle, pentagon, and hexagon are formed. Lattice images can be observed by high resolution TEM as shown in Figure 5(b). The interspace distance between two adjacent white lines is 2.45 Å, and this is in agreement with the known spacing (1 0 1) planes of the zinc oxide (JCPDF no: 36-1451) structure (2.48 Å).

As well as the TEM and XRD analysis, spectroscopic evidence for the formation of ZnO nanocrystals is provided. UV-vis spectra (Figure 6(a)) of ZnO NCs (60°C for 188 h synthesis as described in Figure 3(b)) dispersed in hexane (following simple treatment in an ultrasonic bath) show a sharp peak at 230 nm (5.40 eV) and a steep slope centered at 361 nm (3.43 eV) and both these absorption energies are significantly higher than that of the bulk ZnO (3.3 eV). The

sharp peak may be ascribed to the monodispersed ZnO NCs while the slope line corresponds to a UV absorbance caused by larger NC aggregates [38] that persist in solution. Figure 6(b) shows three obvious PL emission bands at 380 (3.26 eV), 421 (2.94 eV), and 520 nm (2.38 eV) and can be observed at two different photon excitation wavelengths (250 and 300 nm). The peak at 380 nm is attributed to the recombination though free exciton while the small peak at 421 nm is probably related to a deep-level carrier recombination [39]. However, the large broad feature centered at 520 nm corresponds to the defect-related emission [40].

An XPS survey spectrum of ZnO NCs (60°C for 188 h synthesis as described in Figure 3(b)) as shown in Figure 7(a) provides elemental analysis and is typical of the materials prepared here. All X-ray photoelectron peaks are identified

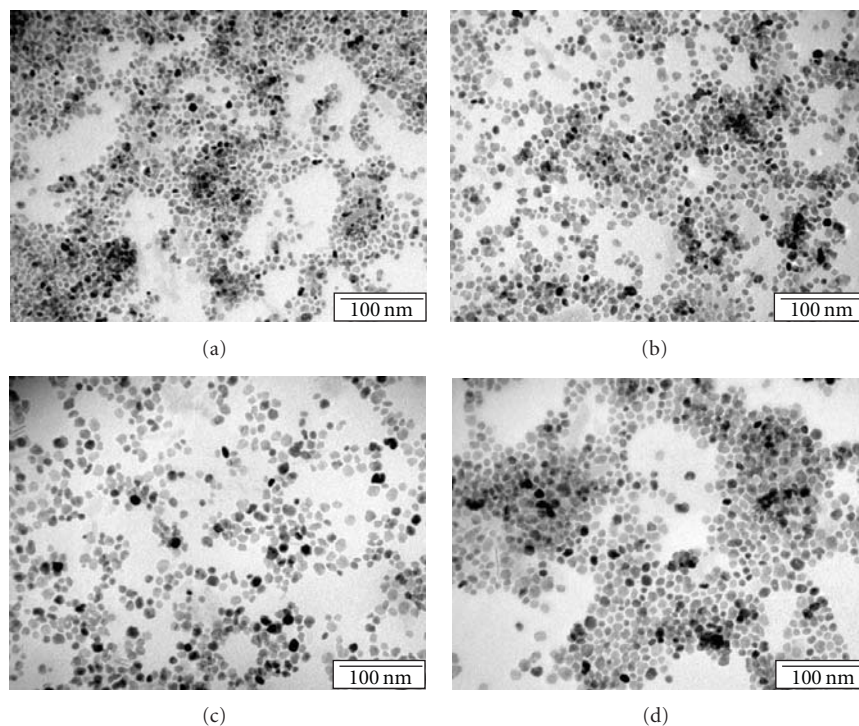


FIGURE 4: TEM images of the as-synthesized OLA-ZnO NCs aged *ex situ* at 60°C for different time: (a) 10, (b) 24, (c) 72, and (d) 120 hours. All scale bars are 100 nm.

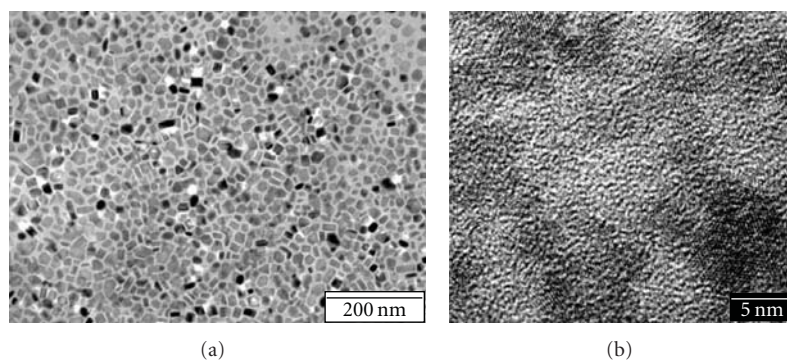


FIGURE 5: TEM images of the OLA-ZnO NCs synthesized at 60°C for 67 hours (a) and the corresponding high resolution TEM image (b).

in the figure and are consistent with the synthesis of carbon containing ZnO nanocrystals. Any unmarked peaks are from the complex set of Zn Auger features. There is a very weak contribution at 1070 eV due to Na (Na1s). The carbon (C1s peak position centered at 285.0 eV and typical of aliphatic carbon) is around 85% of the total photoelectron yield and is as expected for ZnO particles with dense outer ligand shells of oleic at the surface. Only trace nitrogen (N1s peak at 405 eV) is detected in the XPS spectra and this also conforms to the results obtained by the element analysis. The Zn2p and O1s signals are shown in high resolution form in Figure 7(b). The peak area ratio is consistent with the formation of ZnO and the binding energy positions (Zn2p<sub>3/2</sub> = 1022 eV and O1s = 530 eV) are also typical of ZnO.

#### 4. Conclusions

ZnO nanocrystals with a diameter of 5–12 nm have been successfully synthesized in a facile, quick, laboratory-friendly manner via one-step precipitation reaction of Zn<sup>2+</sup> and O<sup>2-</sup> species in nonaqueous solvents. The presence of both long-chain amine and oleic acid makes the synthesis controllable in terms of size, morphology, and crystallinity and highly solvent dispersible products are, therefore, synthesized. The results show that both the reaction conditions, for example, the OLA/Zn<sup>2+</sup> ratio and the ageing conditions have profound effect on the nanocrystal size and dispersivity. The use of *in situ* or *ex situ* ageing conditions can also result in different particle morphologies. Both *in situ* and *ex situ* ageing showing that mild ageing conditions (e.g., 60–80°C

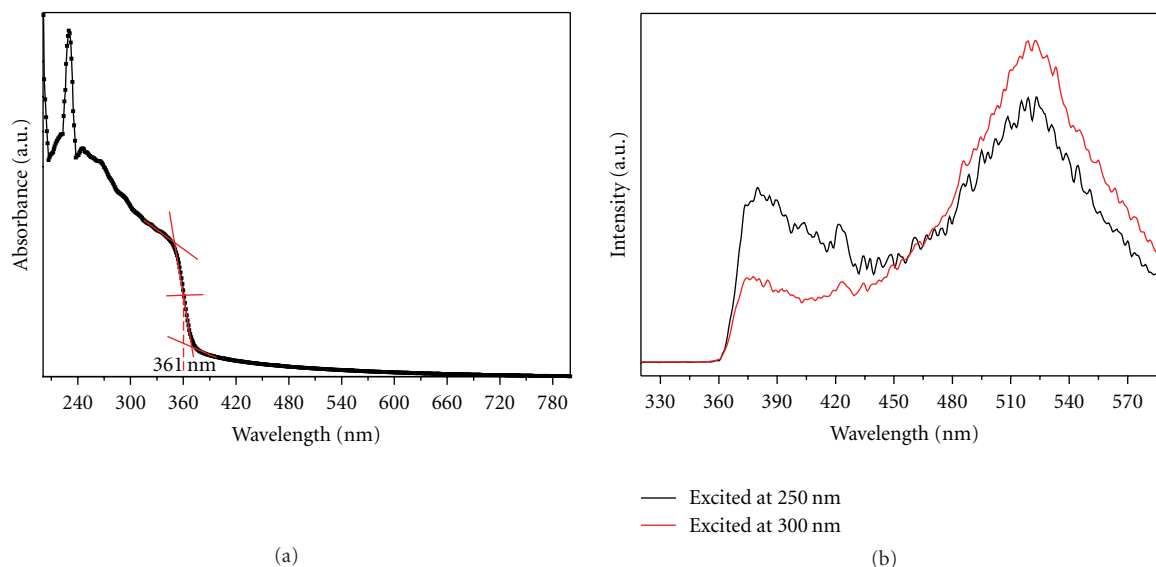


FIGURE 6: UV-vis absorbance spectrum (a) and photoluminescence (PL) emission spectra (b) of OLA-ZnO NCs (60°C for 188 h synthesis described in Figure 3(b) and text) dispersed in hexane.

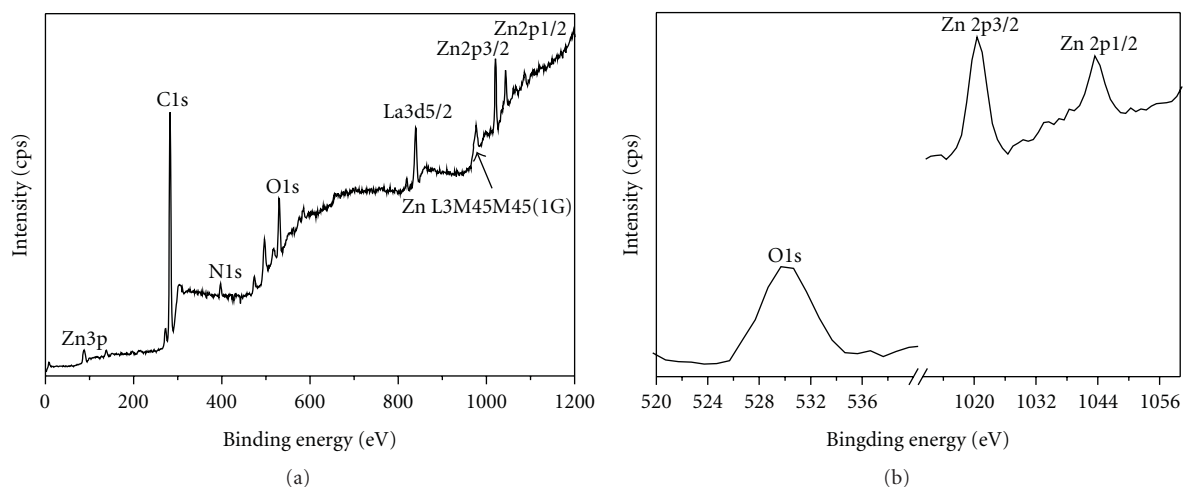


FIGURE 7: X-ray photoelectron (XPS) survey spectrum (a) of OLA-ZnO NCs (60°C for 188 h synthesis described in Figure 3(b) and text) and its detailed Zn and O element XPS spectrum (b).

and 24–48 hours) are required to produce the highest quality nanomaterials. Under the mild ageing conditions, a longer time, and higher temperature favour the formation of higher quality NCs while the effect is more complex when the precipitated nanomaterials is treated under harsher conditions. The OLA capped ZnO nanocrystals are stable and highly dispersible in most nonpolar solvents, where UV-vis absorbance features show a significant quantum size effect on the monodispersed ZnO NCs whilst PL emissions demonstrate both size- and defect-related energy processes.

### Supporting Information Available

Particle size distributions (PSDs) data is available free of charge via the internet at <http://www.hindawi.com/journals/jnm/>.

### Acknowledgment

The authors thank SFI (Science Foundation of Ireland) for the funding supports through the BIONANOINTERACT Strategic Research Cluster Grant 07/SRC/B1155.

## References

- [1] U. Banin and O. Millo, "Tunneling and optical spectroscopy of semiconductor nanocrystals," *Annual Review of Physical Chemistry*, vol. 54, pp. 465–492, 2003.
- [2] J. Geng, B. Liu, L. Xu, F.-N. Hu, and J.-J. Zhu, "Facile route to Zn-based II-VI semiconductor spheres, hollow spheres, and core/shell nanocrystals and their optical properties," *Langmuir*, vol. 23, no. 20, pp. 10286–10293, 2007.
- [3] P. E. Lippens and M. Lannoo, "Optical properties of II-VI semiconductor nanocrystals," *Semiconductor Science and Technology*, vol. 6, no. 9A, pp. A157–A160, 1991.
- [4] R. Viswanatha, P. K. Santra, and D. D. Sarma, "Self assembly and electronic structure of ZnO nanocrystals," *Journal of Cluster Science*, vol. 20, no. 2, pp. 389–398, 2009.
- [5] Q. Zhang, T. P. Chou, B. Russo, S. A. Jenekhe, and G. Cao, "Aggregation of ZnO nanocrystallites for high conversion efficiency in dye-sensitized solar cells," *Angewandte Chemie International Edition*, vol. 47, no. 13, pp. 2402–2406, 2008.
- [6] J. Bouclé, H. J. Snaith, and N. C. Greenham, "Simple approach to hybrid polymer/porous metal oxide solar cells from solution-processed ZnO nanocrystals," *Journal of Physical Chemistry C*, vol. 114, no. 8, pp. 3664–3674, 2010.
- [7] M. C. Newton, S. Firth, and P. A. Warburton, "Photoresponse of ZnO tetrapod nanocrystal Schottky diodes," *IEEE Transactions on Nanotechnology*, vol. 7, no. 1, pp. 20–23, 2008.
- [8] E. Sun, F.-H. Su, Y.-T. Shih et al., "An efficient Si light-emitting diode based on an n-ZnO/SiO<sub>2</sub>-Si nanocrystals-SiO<sub>2</sub>/p-Si heterostructure," *Nanotechnology*, vol. 20, no. 44, Article ID 445202, 2009.
- [9] M. L. Kantam, K. B. S. Kumar, and Ch. Sridhar, "Nanocrystalline ZnO as an efficient heterogeneous catalyst for the synthesis of 5-substituted 1H-tetrazoles," *Advanced Synthesis and Catalysis*, vol. 347, no. 9, pp. 1212–1214, 2005.
- [10] A. S. Pereira, M. Peres, M. J. Soares et al., "Synthesis, surface modification and optical properties of Tb<sup>3+</sup>-doped ZnO nanocrystals," *Nanotechnology*, vol. 17, no. 3, pp. 834–839, 2006.
- [11] Y. S. Wang, P. J. Thomas, and P. O'Brien, "Optical properties of ZnO nanocrystals doped with Cd, Mg, Mn, and Fe ions," *Journal of Physical Chemistry B*, vol. 110, no. 43, pp. 21412–21415, 2006.
- [12] M. Peres, A. Cruz, S. Pereira et al., "Optical studies of ZnO nanocrystals doped with Eu<sup>3+</sup> ions," *Applied Physics A*, vol. 88, no. 1, pp. 129–133, 2007.
- [13] Y. Liu, W. Luo, R. Li, H. Zhu, and X. Chen, "Near-infrared luminescence of Nd<sup>3+</sup> and Tm<sup>3+</sup> ions doped ZnO nanocrystals," *Optics Express*, vol. 17, no. 12, pp. 9748–9753, 2009.
- [14] Y. S. Liu, W. Q. Luo, R. F. Li, and X. Y. Chen, "Optical properties of Nd<sup>3+</sup> ion-doped ZnO nanocrystals," *Journal of Nanoscience and Nanotechnology*, vol. 10, no. 3, pp. 1871–1876, 2010.
- [15] M. Epifani, J. Arbiol, R. Díaz, M. J. Perálvarez, P. Siciliano, and J. R. Morante, "Synthesis of SnO<sub>2</sub> and ZnO colloidal nanocrystals from the decomposition of Tin(II) 2-ethylhexanoate and Zinc(II) 2-ethylhexanoate," *Chemistry of Materials*, vol. 17, no. 25, pp. 6468–6472, 2005.
- [16] Y. C. Zhang, X. Wu, X. Y. Hu, and R. Guo, "Low-temperature synthesis of nanocrystalline ZnO by thermal decomposition of a "green" single-source inorganic precursor in air," *Journal of Crystal Growth*, vol. 280, no. 1-2, pp. 250–254, 2005.
- [17] S. Labuayai, V. Promarak, and S. Maensiri, "Synthesis and optical properties of nanocrystalline ZnO powders prepared by a direct thermal decomposition route," *Applied Physics A*, vol. 94, no. 4, pp. 755–761, 2009.
- [18] L. Spanhel and M. A. Anderson, "Semiconductor clusters in the sol-gel process: quantized aggregation, gelation, and crystal growth in concentrated ZnO colloids," *Journal of the American Chemical Society*, vol. 113, no. 8, pp. 2826–2833, 1991.
- [19] E. A. Meulenkaamp, "Synthesis and growth of ZnO nanoparticles," *Journal of Physical Chemistry B*, vol. 102, no. 29, pp. 5566–5572, 1998.
- [20] E. M. Wong, J. E. Bonevich, and P. C. Searson, "Growth kinetics of nanocrystalline ZnO particles from colloidal suspensions," *Journal of Physical Chemistry B*, vol. 102, no. 40, pp. 7770–7775, 1998.
- [21] C. L. Carnes and K. J. Klabunde, "Synthesis, isolation, and chemical reactivity studies of nanocrystalline zinc oxide," *Langmuir*, vol. 16, no. 8, pp. 3764–3772, 2000.
- [22] D. Kaneko, H. Shouji, T. Kawai, and K. Kon-No, "Synthesis of ZnO particles by ammonia-catalyzed hydrolysis of zinc dibutoxide in nonionic reversed micelles," *Langmuir*, vol. 16, no. 9, pp. 4086–4089, 2000.
- [23] R. M. Nyffenegger, B. Craft, M. Shaaban, S. Gorer, G. Erley, and R. M. Penner, "A hybrid electrochemical/chemical synthesis of zinc oxide nanoparticles and optically intrinsic thin films," *Chemistry of Materials*, vol. 10, no. 4, pp. 1120–1129, 1998.
- [24] S. Mahamuni, K. Borgohain, B. S. Bendre, V. J. Leppert, and S. H. Risbud, "Spectroscopic and structural characterization of electrochemically grown ZnO quantum dots," *Journal of Applied Physics*, vol. 85, no. 5, pp. 2861–2865, 1999.
- [25] L. Guo, S. Yang, C. Yang et al., "Synthesis and characterization of poly(vinylpyrrolidone)-modified zinc oxide nanoparticles," *Chemistry of Materials*, vol. 12, no. 8, pp. 2268–2274, 2000.
- [26] A. Taubert, G. Glasser, and D. Palms, "Kinetics and particle formation mechanism of zinc oxide particles in polymer-controlled precipitation from aqueous solution," *Langmuir*, vol. 18, no. 11, pp. 4488–4494, 2002.
- [27] A. Taubert, D. Palms, Ö. Weiss, M.-T. Piccini, and D. N. Batchelder, "Polymer-assisted control of particle morphology and particle size of zinc oxide precipitated from aqueous solution," *Chemistry of Materials*, vol. 14, no. 6, pp. 2594–2601, 2002.
- [28] B. S. Zou, V. V. Volkov, and Z. L. Wang, "Optical properties of amorphous ZnO, CdO, and PbO nanoclusters in solution," *Chemistry of Materials*, vol. 11, no. 11, pp. 3037–3043, 1999.
- [29] A. van Dijken, E. A. Meulenkaamp, D. Vanmaekelbergh, and A. Meijerink, "The kinetics of the radiative and nonradiative processes in nanocrystalline ZnO particles upon photoexcitation," *Journal of Physical Chemistry B*, vol. 104, no. 8, pp. 1715–1723, 2000.
- [30] S. Monticone, R. Tufeu, and A. V. Kanaev, "Complex nature of the UV and visible fluorescence of colloidal ZnO nanoparticles," *Journal of Physical Chemistry B*, vol. 102, no. 16, pp. 2854–2862, 1998.
- [31] S. Sakohara, M. Ishida, and M. A. Anderson, "Visible luminescence and surface properties of nanosized ZnO colloids prepared by hydrolyzing zinc acetate," *Journal of Physical Chemistry B*, vol. 102, no. 50, pp. 10169–10175, 1998.
- [32] M. Che, C. Naccache, and B. Imelik, "Electron spin resonance studies on titanium dioxide and magnesium oxide-Electron donor properties," *Journal of Catalysis*, vol. 24, no. 2, pp. 328–335, 1972.
- [33] L. Chen, J. Xu, D. A. Tanner et al., "One-step synthesis of stoichiometrically defined metal oxide nanoparticles at room

- temperature,” *Chemistry: A European Journal*, vol. 15, no. 2, pp. 440–448, 2009.
- [34] L. Chen, J. Xu, J. D. Holmes, and M. A. Morris, “A facile route to ZnO nanoparticle superlattices: synthesis, functionalization, and self-assembly,” *Journal of Physical Chemistry C*, vol. 114, no. 5, pp. 2003–2011, 2010.
- [35] W. S. Chiu, P. S. Khiew, D. Isa et al., “Synthesis of two-dimensional ZnO nanopellets by pyrolysis of zinc oleate,” *Chemical Engineering Journal*, vol. 142, no. 3, pp. 337–343, 2008.
- [36] C. Li, Y. Li, Y. Wu, B. S. Ong, and R. O. Loutfy, “Synthesis of zinc oxide nanocrystals by thermal decomposition of Zn-oleate in organic medium,” *Science in China Series E*, vol. 51, no. 12, pp. 2075–2079, 2008.
- [37] X. Zhong and W. Knoll, “Morphology-controlled large-scale synthesis of ZnO nanocrystals from bulk ZnO,” *Chemical Communications*, no. 9, pp. 1158–1160, 2005.
- [38] C. V. Santilli, S. H. Pulcinelli, M. S. Tokumoto, and V. Briois, “In situ UV-vis and EXAFS studies of ZnO quantum-sized nanocrystals and Zn-HDS formations from sol-gel route,” *Journal of the European Ceramic Society*, vol. 27, no. 13–15, pp. 3691–3695, 2007.
- [39] C. P. Chen, M. Y. Ke, C. C. Liu, Y. J. Chang, F. H. Yang, and J. J. Huang, “Observation of 394 nm electroluminescence from low-temperature sputtered n-ZnO/SiO<sub>2</sub> thin films on top of the p-GaN heterostructure,” *Applied Physics Letters*, vol. 91, no. 9, Article ID 091107, 2007.
- [40] S. Chakrabarti, D. Ganguli, and S. Chaudhuri, “Photoluminescence of ZnO nanocrystallines confined in sol-gel silica matrix,” *Journal of Physics D*, vol. 36, no. 2, pp. 146–151, 2003.

## Research Article

# Simple Synthesis of Flower-Like $\text{In}_2\text{S}_3$ Structures and Their Use as Templates to Prepare CuS Particles

Xia Sheng, Lei Wang, Guanbi Chen, and Deren Yang

State Key Laboratory of Silicon Materials, Department of Materials Science and Engineering, Zhejiang University, Hangzhou 310027, China

Correspondence should be addressed to Deren Yang, mseyang@zju.edu.cn

Received 31 May 2010; Revised 2 August 2010; Accepted 6 September 2010

Academic Editor: Quanqin Dai

Copyright © 2011 Xia Sheng et al. This is an open access article distributed under the Creative Commons Attribution License, which permits unrestricted use, distribution, and reproduction in any medium, provided the original work is properly cited.

Flower-like structure  $\text{In}_2\text{S}_3$  particles are prepared by a simple and rapid method. The reaction proceeds in a polyalcohol system without using any complex precursors. The phase and morphology of the  $\text{In}_2\text{S}_3$  are investigated. Furthermore, flower-like structure CuS particles are synthesized via the reaction of  $\text{Cu}^{2+}$  ions with the obtained  $\text{In}_2\text{S}_3$  as templates. Both the  $\text{In}_2\text{S}_3$  and CuS particles can be used in preparing compound solar cell material  $\text{CuInS}_2$ .

## 1. Introduction

Indium sulfide ( $\text{In}_2\text{S}_3$ ) is an important III-VI semiconductor and exists in mainly three phases:  $\alpha$ - $\text{In}_2\text{S}_3$  which is a defective cubic structure and stable up to 693 K;  $\beta$ - $\text{In}_2\text{S}_3$  which is a defective spinel structure and stable up to 1027 K;  $\gamma$ - $\text{In}_2\text{S}_3$  which is a higher temperature structure and stable above 1027 K [1, 2]. Among these phases, n-type  $\beta$ - $\text{In}_2\text{S}_3$  with a band gap of 2.0–2.8 eV has the most wide applications. In particular, the nanostructure  $\text{In}_2\text{S}_3$ , owing to its unique catalytic, optical, electronic, and gas-sensing properties, can be used in many fields, such as catalysts, solar cells, optoelectronic devices, luminophores, and acoustic devices [3–12]. In particular,  $\text{In}_2\text{S}_3$  nanostructures could be used as precursors to fabricate  $\text{CuInS}_2$  thin film which is one of the most important thin film solar cells, and has been widely investigated in last two decades. So far, various shapes of nanostructure  $\text{In}_2\text{S}_3$  have been reported, such as nanofibers, half shells, nanobelts, nanorods, flower-like structures, and hollow microsphere [13–17]. Among these structures, flower-like structure is a kind of 3D porous structure and has large surface area which will benefit for the application in catalysts and optoelectronic devices such as solar cells. Therefore, in recent years, flower-like structures have been prepared by different techniques, such as templates, surfactants, complex precursors,

solvents, thermal decomposition, or hydrothermal synthesis [18–22]. However, those processes were complicated, and most fabricated flower-like  $\text{In}_2\text{S}_3$  were larger than  $1\ \mu\text{m}$  in size.

Furthermore,  $\text{In}_2\text{S}_3$  nanostructures exist as incompletely coordinated sulfur atoms and can serve as a host for other metal ions [8]. It was reported that  $\text{Cu}^{2+}$  and  $\text{Zn}^{2+}$  could displace  $\text{In}^{3+}$  in  $\text{In}_2\text{S}_3$  nanostructures [23]. But, there are few reports about the synthesis of CuS nanostructures by using  $\text{In}_2\text{S}_3$  as templates.

In this paper, we use a simple and rapid chemical method to synthesize  $\text{In}_2\text{S}_3$  flower-like structures with a diameter about 300–600 nm. The synthesis proceeds in polyalcohol system below  $150^\circ\text{C}$  and does not use any complex agents. Furthermore, the obtained  $\text{In}_2\text{S}_3$  are used as templates to synthesize flower-like CuS structures under room temperature. Both the  $\text{In}_2\text{S}_3$  and CuS can be used in preparing compound solar cell material  $\text{CuInS}_2$ .

## 2. Experimental Details

**2.1. Chemicals.** All the used chemicals are analytical grade: indium(III) trichloride,  $\text{InCl}_3 \cdot 4\text{H}_2\text{O}$ ; copper(II) dichloride,  $\text{CuCl}_2 \cdot 2\text{H}_2\text{O}$ ; thiourea (TA); thioacetamide (TAA); hexadecyl trimethyl ammonium bromide (CTAB); diethylene glycol (DEG).

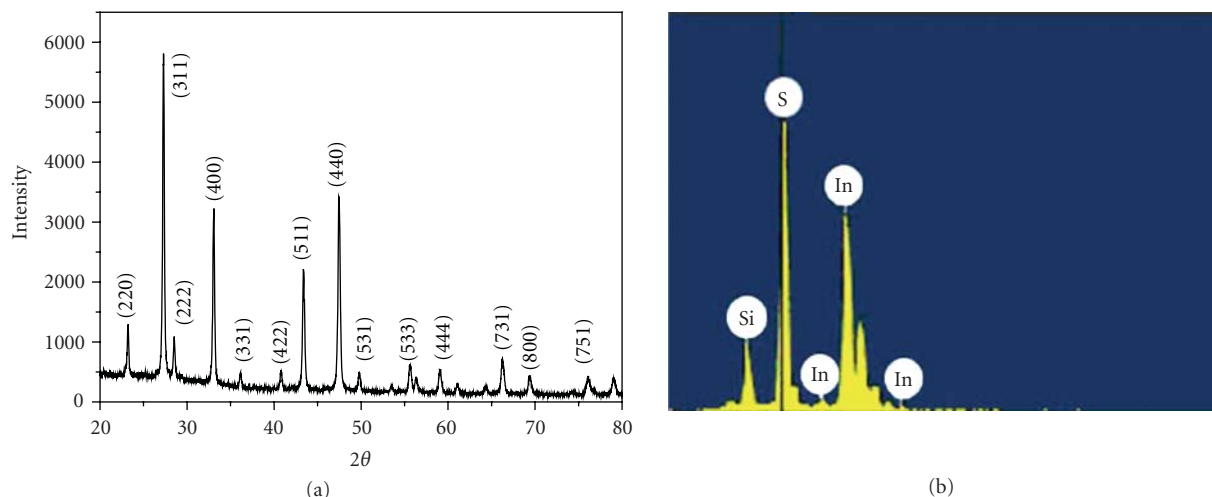


FIGURE 1: XRD pattern (a) and EDS spectrum (b) of the  $\text{In}_2\text{S}_3$  particles reacting by  $\text{InCl}_3$  and TA at  $140^\circ\text{C}$  for 60 minutes.

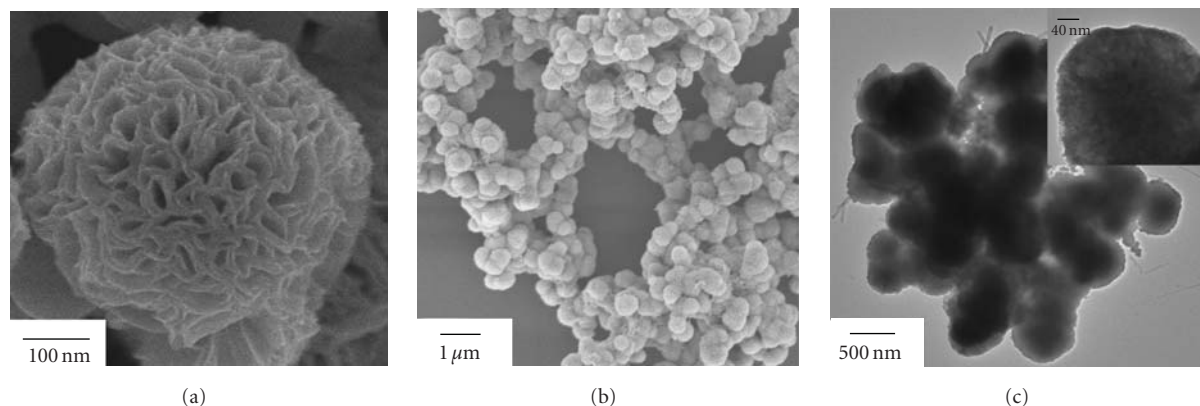


FIGURE 2: SEM ((a) and (b)) and TEM (c) images of the  $\text{In}_2\text{S}_3$  particles reacting by  $\text{InCl}_3$  and TA at  $140^\circ\text{C}$  for 60 minutes.

**2.2. The Synthesis of  $\text{In}_2\text{S}_3$  Particles.** The  $\text{In}_2\text{S}_3$  particles are synthesized through the following process. 1 mmol  $\text{InCl}_3 \cdot 4\text{H}_2\text{O}$  is dissolved in 35 mL DEG in a three-neck flask. The solution is stirred under the protection of  $\text{N}_2$  atmosphere at  $140^\circ\text{C}$ . Then 4 mmol TA or TAA dissolved in 5 mL DEG is slowly added into the solution. After 30–60 minutes reaction, the flask is removed from the heater and cooled to the room temperature. Then the particles are separated by centrifugation at 6500 rpm for 5 minutes and washed in ethanol for several times. At last, the particles are baked under  $80^\circ\text{C}$  for several hours.

**2.3. The Synthesis of  $\text{CuS}$  Particles Using Obtained  $\text{In}_2\text{S}_3$  as Template.** The obtained  $\text{In}_2\text{S}_3$  particles are dispersed in ethanol by an ultrasonic vibration equipment. Then 1 mmol  $\text{CuCl}_2 \cdot 2\text{H}_2\text{O}$  power is added into the solution, reacting by ultrasonic vibration at room temperature for 30 minutes. The obtained particles are also washed and dried following a same procedure as that of  $\text{In}_2\text{S}_3$  particles.

**2.4. Materials Characterization.** The particles are characterized by X-ray diffraction (XRD), scanning electron

microscopy (SEM), and transmission electron microscopy (TEM).

XRD is carried out to study the crystal structures of all the samples, by using a X'Pert PRO (PANalytical) diffractometer equipped with a  $\text{CuK}\alpha$  radiation source. Data is collected by step scanning of  $2\theta$  from  $20^\circ$  to  $80^\circ$  with a step of  $0.02^\circ$  and counting time of 1 s per step.

Morphology of the particles is investigated by SEM and TEM. The SEM images are taken by using a SEM Hitachi S4800. The compositions of samples are determined by energy-dispersive X-ray spectroscopy (EDS) attached with SEM. The operating parameters for EDS are as follows: acceleration voltage 20 kV, measuring time 80 s, working distance 15 mm, and counting rate 2.3 kcps. TEM Philips CM200UT is employed for TEM characterizations.

### 3. Results and Discussion

Size, shape, and dimensionality strongly affect the properties of nanomaterials [8]. In this paper, TA and TAA are used as two kinds of different S sources to synthesize  $\text{In}_2\text{S}_3$ . Due to their different release rates of  $\text{S}^{2-}$  ions, the obtained particles

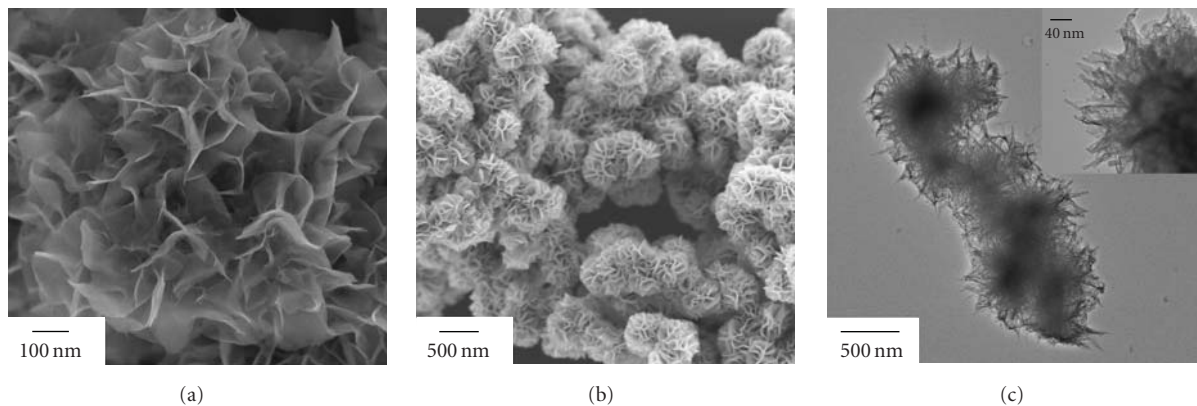


FIGURE 3: SEM ((a) and (b)) and TEM (c) images of  $\text{In}_2\text{S}_3$  particles reacting by  $\text{InCl}_3$  and TAA at  $140^\circ\text{C}$  for 30 minutes.

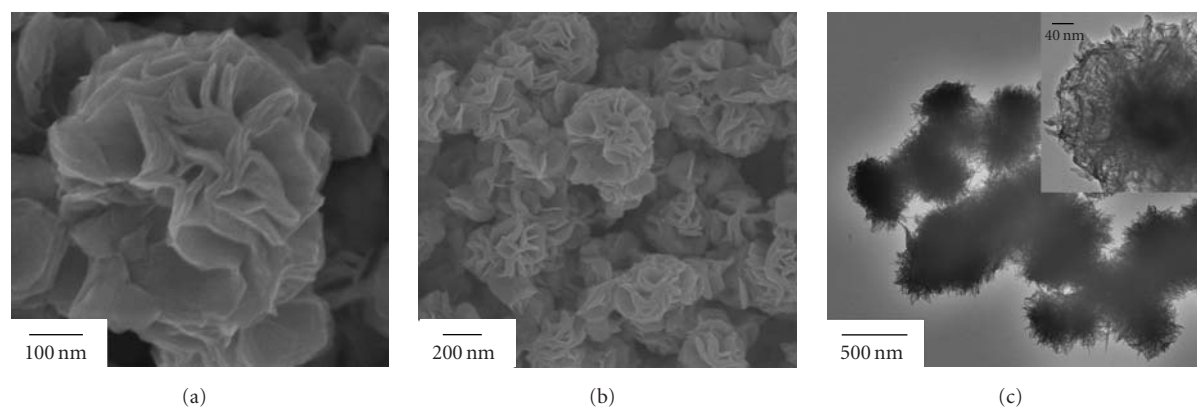


FIGURE 4: SEM ((a) and (b)) and TEM (c) images of the  $\text{In}_2\text{S}_3$  particles using CTAB as surfactant reacting at  $140^\circ\text{C}$  for 60 minutes.

may be different in surface morphologies. Besides, we use CTAB as a kind of surfactant to adjust the shape of the particles.

The XRD pattern and EDS spectrum of  $\text{In}_2\text{S}_3$  particles via  $\text{InCl}_3$  and TA reacting at  $140^\circ\text{C}$  for 60 minutes are shown in Figures 1(a) and 1(b). The similar XRD pattern by using  $\text{InCl}_3$  and TAA as reactants has been obtained, which is not shown in this paper. All the peaks shown in Figure 1(a) can be readily indexed as a cubic phase of  $\beta\text{-In}_2\text{S}_3$  without any other phase. The peaks are considerably narrow and strong, which indicates that the obtained particles are well crystallized. EDS spectrum of the  $\text{In}_2\text{S}_3$  particles in Figure 1(b) shows that the samples are composed by In, S atoms (Si is from the substrate of the sample).

Figures 2(a) and 2(b) show the different magnification SEM images of the  $\text{In}_2\text{S}_3$  particles reacting by  $\text{InCl}_3$  and TA at  $140^\circ\text{C}$  for 60 minutes; and Figure 2(c) is their TEM image which further confirms the structure. It can be seen that the  $\text{In}_2\text{S}_3$  particles are all flower-like porous structures with a diameter in range of 300–600 nm, while most of them are about 500 nm. The “petals” of the flowers are about 10–30 nm through careful examination.

Figures 3(a) and 3(b) show the different magnification SEM images of  $\text{In}_2\text{S}_3$  particles reacting by  $\text{InCl}_3$  and TAA at  $140^\circ\text{C}$  for 30 minutes. Similarly the images show that the

$\text{In}_2\text{S}_3$  particles are also flower-like structures. But compared with Figure 2, it is found that the flake “petals” are much thinner, with a thickness of about 5–10 nm. Meanwhile, due to the thinner petals, leading to much more surface areas, the particles are conjugated to each other. Furthermore, the products using TA as S source are more spherical, whereas the products using TAA as S source are slightly fluffy. The TEM images which are shown in Figure 3(c) also prove this result.

For cubic  $\beta\text{-In}_2\text{S}_3$ , the crystallites are self-organized into spherical assemblies with protruding petals with a puffy flower-like manifestation [17]. TAA has faster release rates of  $\text{S}^{2-}$  ions than TA, leading to faster reaction speed with  $\text{In}^{3+}$ . This can be seen by the reaction phenomenon (the solution turns yellow quicker by using TAA). Thus, using TAA has a very fast growth rate along the petals. Therefore, the petals seem thinner and the whole flower-like structures are fluffier.

Furthermore, the CTAB is added to adjust and control the shape of the particles. Figures 4(a) and 4(b) show the SEM images of the  $\text{In}_2\text{S}_3$  particles using  $\text{InCl}_3$  and TA as reactants and using CTAB as surfactant. The TEM image is shown in Figure 4(c). It can be seen that the samples are still flower-like porous structures with a diameter around 300–600 nm and with a petal thickness about 10–30 nm. However, compared with Figure 2, the products get less flake petals,

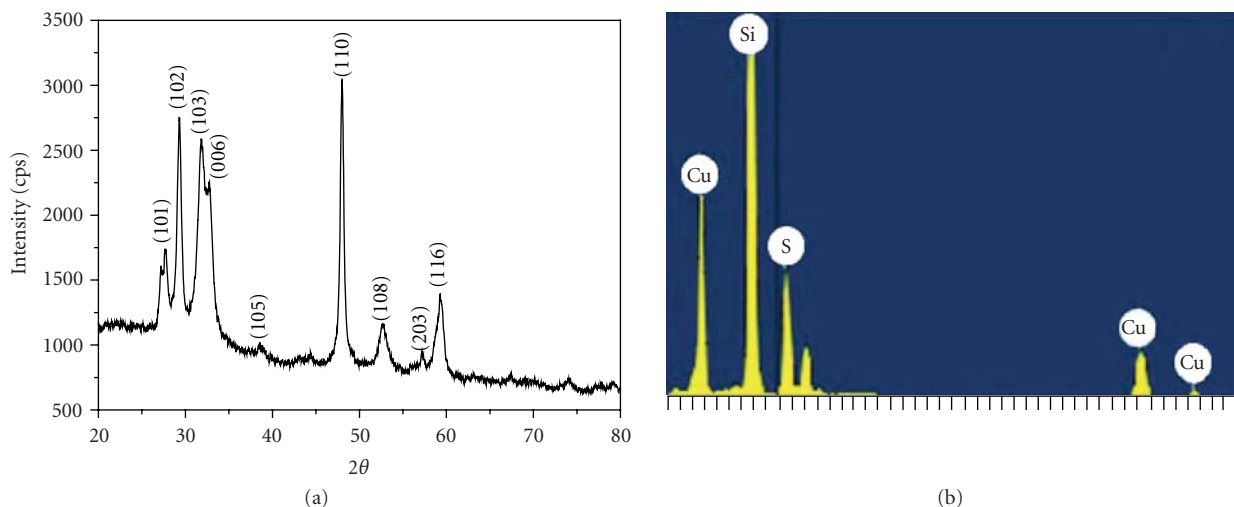


FIGURE 5: XRD pattern (a) and EDS spectrum (b) of the CuS synthesized by the reaction of  $\text{In}_2\text{S}_3$  particles and  $\text{CuCl}_2$ .

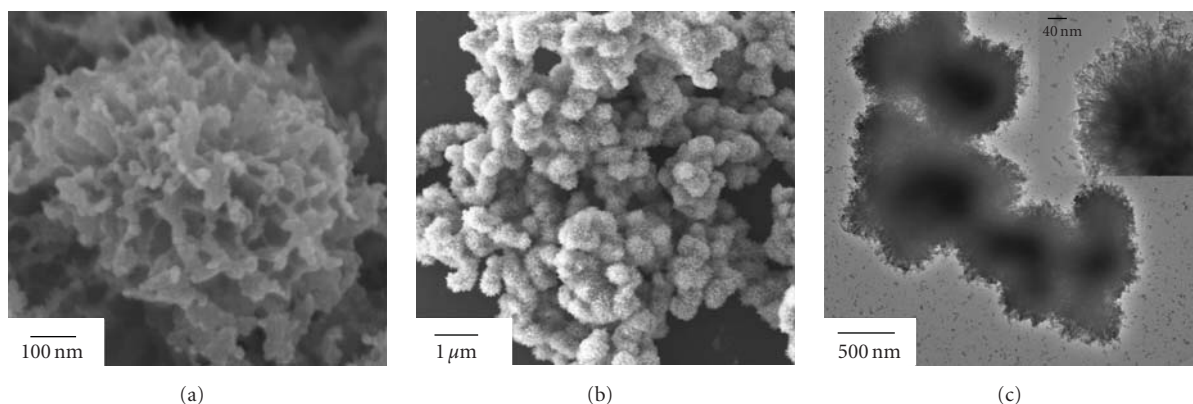


FIGURE 6: SEM ((a) and (b)) and TEM (c) images of the CuS synthesized by the reaction of  $\text{In}_2\text{S}_3$  particles and  $\text{CuCl}_2$ .

as well as the bigger pores between the petals. Since CTAB is a kind of amphoteric surfactant and more tend to act as cationic surfactant, it is generally used to prepare hollow structures [24]. In this reaction, the CTAB and  $\text{In}^{3+}$  are together dissolved in the DEG first. CTAB may scatter around  $\text{In}^{3+}$ . Then when S sources are added,  $\text{S}^{2-}$  is easily attracted with one side of CATB. In the nucleation process, the other side of CTAB molecules may cause repulsion between flake petals and then make the flowers expand bigger.

Moreover, CuS particles are obtained by using the flower-like structure  $\text{In}_2\text{S}_3$  as templates. In fact, CuS with flower-like structure has been fabricated by some methods such as polyol route or hydrothermal route [25, 26], and their structures are normally larger than  $1\ \mu\text{m}$ . In our experiments, the CuS flower-like structures with the diameter about 300–600 nm are synthesized at room temperature via  $\text{CuCl}_2$  reacting with  $\text{In}_2\text{S}_3$  particles as shown in Figure 2. Figures 5(a) and 5(b) show the XRD pattern and EDS spectrum of the CuS nanostructures synthesized by the reaction of  $\text{In}_2\text{S}_3$  particles and  $\text{CuCl}_2$ . The XRD pattern shows that the

obtained products are well-crystallized hexagonal phase CuS and no any  $\text{In}_2\text{S}_3$  peaks are found, indicating that  $\text{In}_2\text{S}_3$  is turned to CuS after reaction. EDS spectrum also verifies this since no hints of In are found.

Figures 6(a)–6(c) show the SEM and TEM images of the CuS synthesized by  $\text{In}_2\text{S}_3$  particles and  $\text{CuCl}_2$ . It can be seen that the obtained CuS particles are also flower-like structures with a diameter around 300–600 nm, indicating the CuS particles are synthesized by  $\text{In}_2\text{S}_3$  flower-like structures as templates.

The possible mechanism of this reaction is discussed as follows.  $\text{In}_2\text{S}_3$  nanostructures exist incompletely coordinated sulfur atoms [8], and the flower-like structures appear a kind of porous surface and have large surface areas. Therefore there are numerous  $\text{S}^{2-}$  ions with high reactivity existing on the surface of flower-like  $\text{In}_2\text{S}_3$  particles. And after  $\text{Cu}^{2+}$  ions are added,  $\text{Cu}^{2+}$  react with  $\text{S}^{2-}$  to form CuS. In addition, since the solubility degree of  $\text{In}_2\text{S}_3$  is much bigger than that of ZnS and CuS, ions like  $\text{Cu}^{2+}$  and  $\text{Zn}^{2+}$  can displace  $\text{In}^{3+}$  in  $\text{In}_2\text{S}_3$  nanostructure [23], whereas  $\text{In}^{3+}$  ions in the solution

are washed away during the centrifugation process and that is the reason why we have not detected any hints of In. So at last, the flower-like CuS particles of pure phase are obtained.

#### 4. Conclusion

In conclusion,  $\text{In}_2\text{S}_3$  particles are prepared by a simple and rapid method. The obtained flower-like  $\text{In}_2\text{S}_3$  structures have a diameter around 300–600 nm. By changing the S sources and, or adding surfactant, the  $\text{In}_2\text{S}_3$  particles appear different in surface morphologies. Moreover,  $\text{Cu}^{2+}$  ions are added to react with  $\text{In}_2\text{S}_3$  particles, and CuS with the similar structures and size are obtained. The mechanism of this reaction is probably due to the  $\text{Cu}^{2+}$  ions reacting with the high reactivity  $\text{S}^{2-}$  ions on the surface of flower-like  $\text{In}_2\text{S}_3$  structures and in the same time displacing  $\text{In}^{3+}$  ions.

#### Acknowledgment

The authors would like to appreciate the financial supports from 973 project (no. 2007CB613403).

#### References

- [1] A. Datta, G. Sinha, S. K. Panda, and A. Patra, "Growth, optical, and electrical properties of  $\text{In}_2\text{S}_3$  zigzag nanowires," *Crystal Growth and Design*, vol. 9, no. 1, pp. 427–431, 2009.
- [2] L. J. Liu, W. D. Xiang, and J. S. Zhong, "Flowerlike cubic  $\beta$ - $\text{In}_2\text{S}_3$  microspheres: synthesis and characterization," *Journal of Alloys and Compounds*, vol. 493, pp. 309–313, 2010.
- [3] H. X. Bai, L. X. Zhang, and Y. C. Zhang, "Simple synthesis of urchin-like  $\text{In}_2\text{S}_3$  and  $\text{In}_2\text{O}_3$  nanostructures," *Materials Letters*, vol. 63, no. 9–10, pp. 823–825, 2009.
- [4] S. Gorai and S. Chaudhuri, "Sonochemical synthesis and characterization of cage-like  $\beta$ -indium sulphide powder," *Materials Chemistry and Physics*, vol. 89, no. 2–3, pp. 332–335, 2005.
- [5] A. Datta, S. Gorai, D. Ganguli, and S. Chaudhuri, "Surfactant assisted synthesis of  $\text{In}_2\text{S}_3$  dendrites and their characterization," *Materials Chemistry and Physics*, vol. 102, no. 2–3, pp. 195–200, 2007.
- [6] X. Chen, Z. Zhang, X. Zhang, J. Liu, and Y. Qian, "Single-source approach to the synthesis of  $\text{In}_2\text{S}_3$  and  $\text{In}_2\text{O}_3$  crystallites and their optical properties," *Chemical Physics Letters*, vol. 407, no. 4–6, pp. 482–486, 2005.
- [7] L.-Y. Chen, Z.-D. Zhang, and W.-Z. Wang, "Self-assembled porous 3d flowerlike  $\beta$ - $\text{In}_2\text{S}_3$  structures: synthesis, characterization, and optical properties," *Journal of Physical Chemistry C*, vol. 112, no. 11, pp. 4117–4123, 2008.
- [8] L. Liu, H. Liu, H.-Z. Kou et al., "Morphology control of  $\beta$ - $\text{In}_2\text{S}_3$  from chrysanthemum-like microspheres to hollow microspheres: synthesis and electrochemical properties," *Crystal Growth and Design*, vol. 9, no. 1, pp. 113–117, 2009.
- [9] S. Abelló, F. Medina, D. Tichit et al., "Nanoplatelet-based reconstructed hydrotalcites: towards more efficient solid base catalysts in aldol condensations," *Chemical Communications*, no. 11, pp. 1453–1455, 2005.
- [10] Y. Liu, H. Xu, and Y. Qian, "Double-source approach to  $\text{In}_2\text{S}_3$  single crystallites and their electrochemical properties," *Crystal Growth and Design*, vol. 6, no. 6, pp. 1304–1307, 2006.
- [11] R. Yoosuf and M. K. Jayaraj, "Optical and photoelectrical properties of  $\beta$ - $\text{In}_2\text{S}_3$  thin films prepared by two-stage process," *Solar Energy Materials and Solar Cells*, vol. 89, no. 1, pp. 85–94, 2005.
- [12] W. Lee, S.-K. Min, G. Cai et al., "Polymer-sensitized photoelectrochemical solar cells based on water-soluble polyacetylene and  $\beta$ - $\text{In}_2\text{S}_3$  nanorods," *Electrochimica Acta*, vol. 54, no. 2, pp. 714–719, 2008.
- [13] X. Zhu, J. Ma, Y. Wang et al., "Fabrication of indium sulfide nanofibers via a hydrothermal method assisted by AAO template," *Materials Research Bulletin*, vol. 41, no. 8, pp. 1584–1588, 2006.
- [14] P. Gao, Y. Xie, S. Chen, and M. Zhou, "Micrometre-sized  $\text{In}_2\text{S}_3$  half-shells by a new dynamic soft template route: properties and applications," *Nanotechnology*, vol. 17, no. 1, pp. 320–324, 2006.
- [15] W. Du, J. Zhu, S. Li, and X. Qian, "Ultrathin  $\beta$ - $\text{In}_2\text{S}_3$  nanobelts: shape-controlled synthesis and optical and photocatalytic properties," *Crystal Growth and Design*, vol. 8, no. 7, pp. 2130–2136, 2008.
- [16] W. Lee, S. Baek, R. S. Mane et al., "Liquid phase deposition of amorphous  $\text{In}_2\text{S}_3$  nanorods: effect of annealing on phase change," *Current Applied Physics*, vol. 9, no. 1, pp. S62–S64, 2009.
- [17] S. D. Naik, T. C. Jagadale, S. K. Apte et al., "Rapid phase-controlled microwave synthesis of nanostructured hierarchical tetragonal and cubic  $\beta$ - $\text{In}_2\text{S}_3$  dandelion flowers," *Chemical Physics Letters*, vol. 452, no. 4–6, pp. 301–305, 2008.
- [18] X. Huang, Y. Yang, X. Dou, Y. Zhu, and G. Li, "In situ synthesis of  $\text{Bi}/\text{Bi}_2\text{S}_3$  heteronanowires with nonlinear electrical transport," *Journal of Alloys and Compounds*, vol. 461, no. 1–2, pp. 427–431, 2008.
- [19] D. Keyson, D. P. Volanti, L. S. Cavalcante, A. Z. Simões, J. A. Varela, and E. Longo, "CuO urchin-nanostructures synthesized from a domestic hydrothermal microwave method," *Materials Research Bulletin*, vol. 43, no. 3, pp. 771–775, 2008.
- [20] F. Cao, W. Shi, R. Deng et al., "Uniform  $\text{In}_2\text{S}_3$  octahedron-built microspheres: bioinspired synthesis and optical properties," *Solid State Sciences*, vol. 12, no. 1, pp. 39–44, 2010.
- [21] Y. Xiong, Y. Xie, G. Du, X. Tian, and Y. Qian, "A novel in situ oxidization-sulfidation growth route via self-purification process to  $\beta$ - $\text{In}_2\text{S}_3$  dendrites," *Journal of Solid State Chemistry*, vol. 166, no. 2, pp. 336–340, 2002.
- [22] Z. Li, X. Tao, Z. Wu, P. Zhang, and Z. Zhang, "Preparation of  $\text{In}_2\text{S}_3$  nanoparticle by ultrasonic dispersion and its tribology property," *Ultrasonics Sonochemistry*, vol. 16, no. 2, pp. 221–224, 2009.
- [23] P. Yang, M. K. Lü, C. Feng Song et al., "Luminescence of  $\text{Cu}^{2+}$  and  $\text{In}^{3+}$  co-activated ZnS nanoparticles," *Optical Materials*, vol. 20, no. 2, pp. 141–145, 2002.
- [24] T.-Y. Ding, M.-S. Wang, S.-P. Guo, G.-C. Guo, and J.-S. Huang, "CuS nanoflowers prepared by a polyol route and their photocatalytic property," *Materials Letters*, vol. 62, no. 30, pp. 4529–4531, 2008.
- [25] L. Chen, W. Yu, and Y. Li, "Synthesis and characterization of tubular CuS with flower-like wall from a low temperature hydrothermal route," *Powder Technology*, vol. 191, no. 1–2, pp. 52–54, 2009.
- [26] A. Zhang, Q. Ma, M. Lu, G. Yu, Y. Zhou, and Z. Qiu, "Copper-indium sulfide hollow nanospheres synthesized by a facile solution-chemical method," *Crystal Growth and Design*, vol. 8, no. 7, pp. 2402–2405, 2008.

## Research Article

# An Experimental Study on the Shape Changes of TiO<sub>2</sub> Nanocrystals Synthesized by Microemulsion-Solvothermal Method

Wei Kong,<sup>1</sup> Bo Liu,<sup>1</sup> Bo Ye,<sup>1</sup> Zhongping Yu,<sup>1</sup> Hua Wang,<sup>2</sup> Guodong Qian,<sup>1</sup> and Zhiyu Wang<sup>1</sup>

<sup>1</sup> State Key Laboratory of Silicon Materials, Department of Materials Science and Engineering, Zhejiang University, Hangzhou 310027, China

<sup>2</sup> Center of Analysis and Measurement, Zhejiang University, Hangzhou 310029, China

Correspondence should be addressed to Zhiyu Wang, wangzhiyu@zju.edu.cn

Received 19 March 2010; Revised 22 April 2010; Accepted 14 June 2010

Academic Editor: William W. Yu

Copyright © 2011 Wei Kong et al. This is an open access article distributed under the Creative Commons Attribution License, which permits unrestricted use, distribution, and reproduction in any medium, provided the original work is properly cited.

Titanium dioxide (TiO<sub>2</sub>) nanocrystals of different shape were successfully synthesized in a new microemulsion system through a solvothermal process. The TiO<sub>2</sub> nanocrystals were prepared from the reaction of tetrabutyl titanate (TBT), H<sub>2</sub>O, and oleic acid (OA), which were used as solvent and surfactant at 300°C and 240°C in a stainless steel autoclave. The sphere, polygon, and rhombus-shaped nanocrystals have been prepared at 300°C and the dot- and- rod shaped nanocrystals have been synthesized at 240°C. The effect of the reaction time on the shape and size of TiO<sub>2</sub> nanocrystals in this method was studied in the present paper. The size distribution of TiO<sub>2</sub> nanocrystals prepared at 300°C for different hours is also studied. In addition, an attempt to describe the mechanism of shape change of TiO<sub>2</sub> nanocrystals was presented in this paper.

## 1. Introduction

Nanosized metal oxide particles have attracted great attention because of their unusual size-dependent optical and electronic properties over the last two decades. Among all the metal oxide, TiO<sub>2</sub>, an important semiconductor, has been widely used in pigment, paints, additive, photovoltaic cell, gas sensors and photocatalysis. It is reported that nano-scale TiO<sub>2</sub> has peculiar properties which is not expected in bulk materials. TiO<sub>2</sub> is an anisotropic material with different phases, its properties are usually dependent on the size, shape, morphology, crystal structure, surface area and porosity [1]. It is essential to study the shape changes in the TiO<sub>2</sub> nano-crystalline growth process. There are a lot of reports focusing on the synthesis of various shapes of TiO<sub>2</sub> nanoparticles, such as sphere [2], rod [3], needle [4], wire [5], cube [6], bullet [7], diamond [7]. Several studies [3, 7] have synthesized two shapes in just one kind of chemical process, while few of them have studied the shape change process of the nano-crystalline in the chemical reactions.

Although numerous techniques were successfully used to synthesize nano-crystalline TiO<sub>2</sub>, there were still several problems which were difficult to be solved. The TiO<sub>2</sub> nanomaterials prepared by the micelle method normally have amorphous structure, and calcination is usually necessary in order to induce high crystallinity, this process usually leads to the growth and agglomeration of TiO<sub>2</sub> nanoparticles [8]. Poor stability of the microemulsion systems, large size of TiO<sub>2</sub> nanocrystals and poor dispersion stability also exist under solvothermal conditions. In recently years, a series of new ways for nanoparticle synthesis have been designed. Microemulsion-hydrothermal/solvothermal method is a kind of way of them. This new method combines microemulsion techniques with a hydrothermal/solvothermal process, and it has been explored for the preparation of lots of nanocrystals such as SrCO<sub>3</sub> nanostructures [9], Ca<sub>10</sub>(PO<sub>4</sub>)<sub>6</sub>(OH)<sub>2</sub> nanofibers [10], BaF<sub>2</sub> whiskers [11], wollastonite nanowires [12], cobalt nanorods [13], aluminium orthophosphate nanocrystals [14], PbS nanocrystals [15] and CdS nanorods [16].

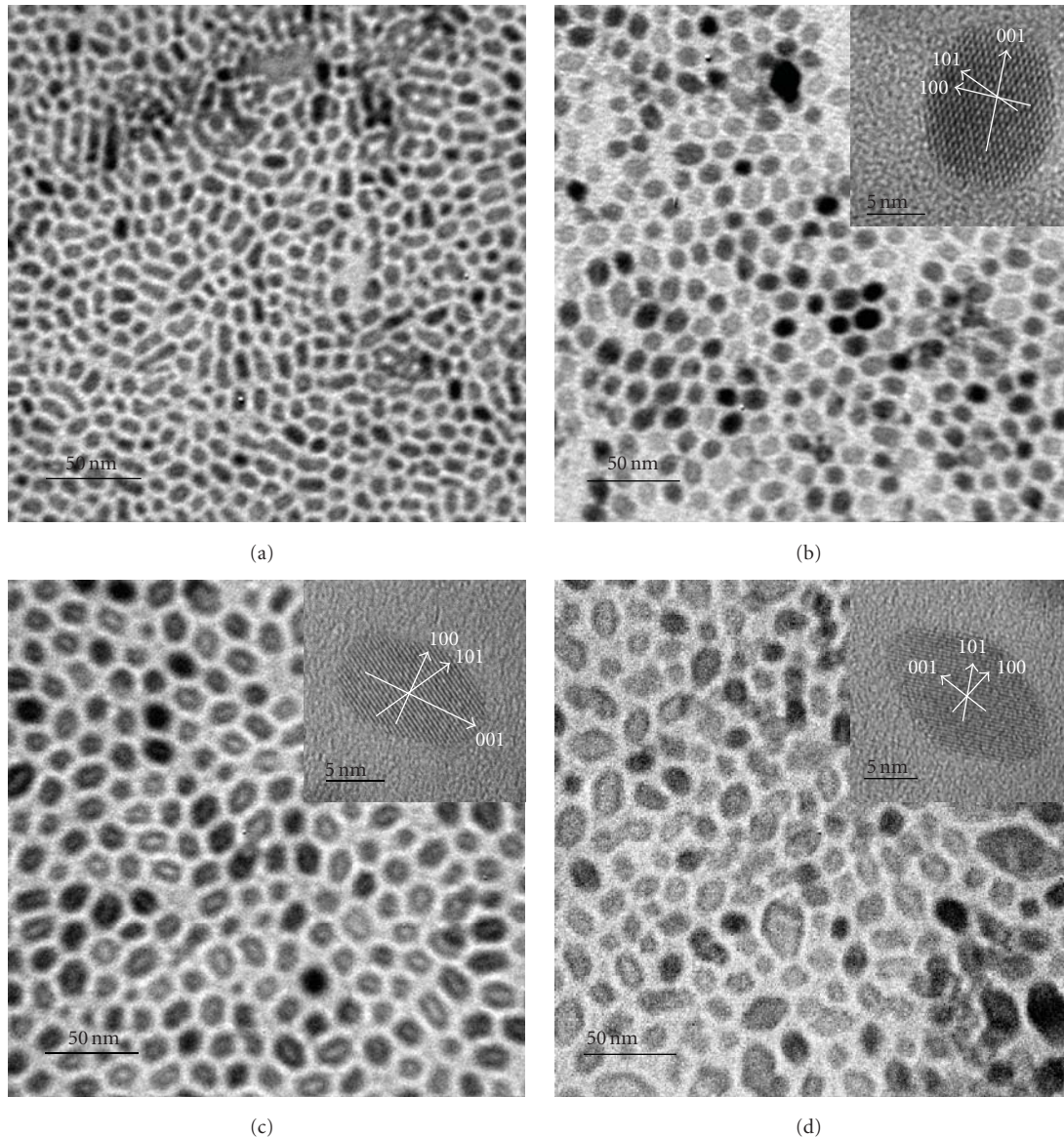


FIGURE 1: TEM images and HRTEM images of TiO<sub>2</sub> nanocrystals synthesized at 300°C for different times: (a) 0.5 hours; (b) 2 hours; (c) 4 hours; (d) 17 hours.

Here we introduced a new microemulsion-solvothermal method. A kind of new microemulsion system was prepared and a higher solvothermal temperature was chosen to obtain a better crystalline state. It was found that four kinds of shape of TiO<sub>2</sub> nanocrystals including sphere, polygon, rhombus and rod were successfully synthesized. The shape change process of TiO<sub>2</sub> nanocrystals were studied based on the experimental analysis.

## 2. Experimental

**2.1. Synthesis.** The TiO<sub>2</sub> nanocrystals were prepared by a microemulsion-solvothermal method. TBT and OA were of analytical grade and purchased from Shanghai Chemical Reagent Co. without further purification. The formation of

monodisperse TiO<sub>2</sub> nanocrystals could be divided into two steps. Step 1: the synthesis of the microemulsion precursor. Step 2: the manufacture of TiO<sub>2</sub> nanocrystals in solvothermal process.

*Step 1.* 1.7 mL of TBT was dissolved in 18 ml of OA under vigorous stirring at room temperature. After an hour, 2.7 mL of deionized water was added into this solution dropwise. All the mixture solution was kept stirring for another 1 hour at room temperature in a separate flask to obtain a microemulsion precursor.

*Step 2.* The microemulsion precursor was put into a stainless steel autoclave. The autoclave was kept at 300°C for different reaction time (0.5 hours, 2 hours, 4 hours and 17 hours) in an electric oven. For comparison, the temperature at 240°C

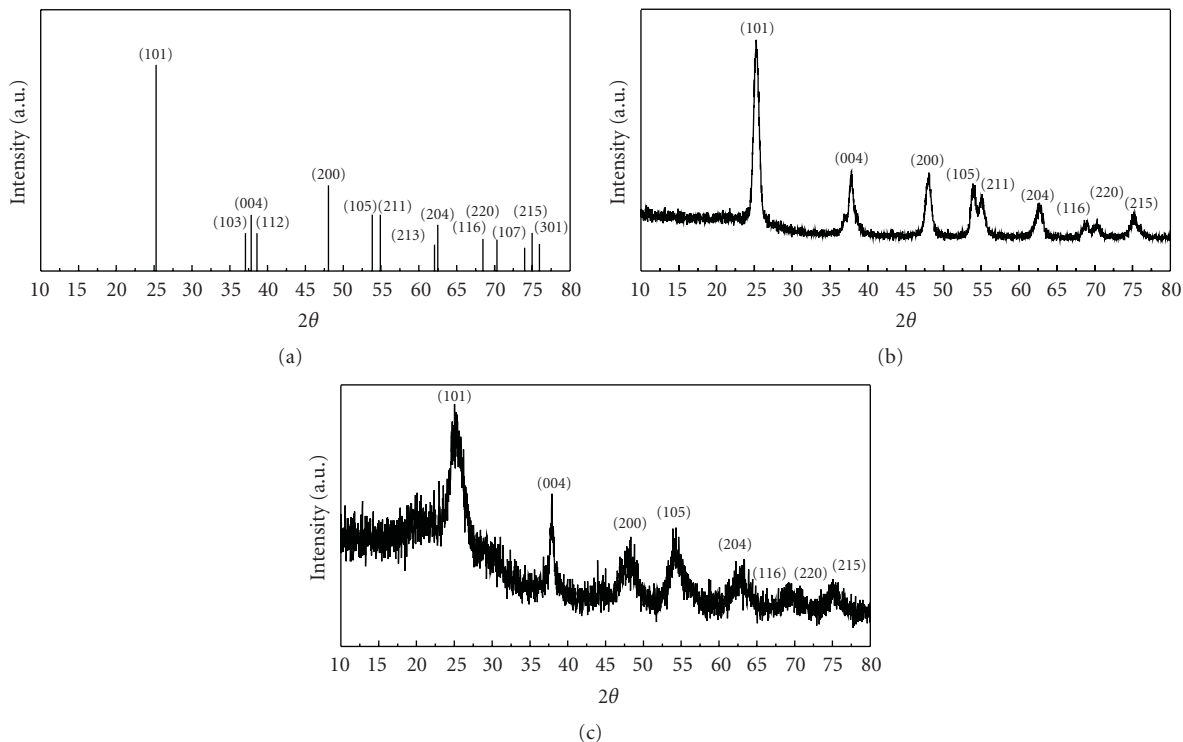


FIGURE 2: X-ray diffraction pattern of TiO<sub>2</sub> nanocrystals synthesized for 2 hours at 300°C and 240°C: (a) The standard spectrum of anatase titanium dioxide, (b) 300°C, (c) 240°C.

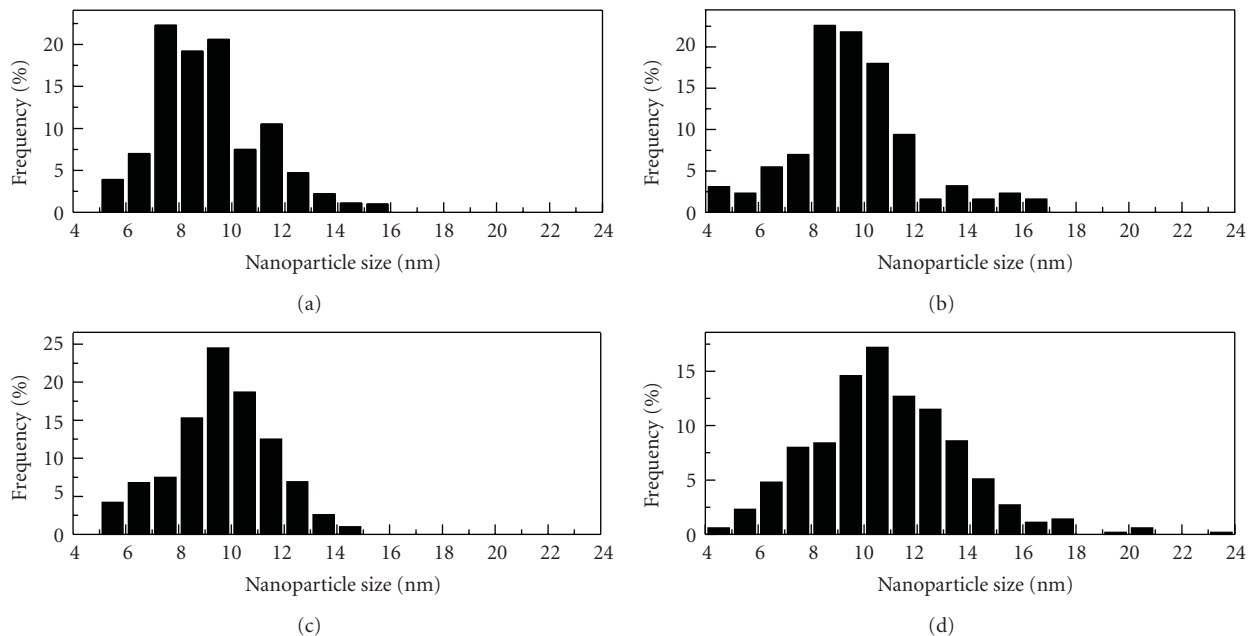


FIGURE 3: TiO<sub>2</sub> nanoparticle size distribution histogram (a) 300°C, 0.5 hours; (b) 300°C, 2 hours; (c) 300°C, 4 hours; (d) 300°C, 17 hours.

was also studied. After reaction, the TiO<sub>2</sub> nanocrystals were harvested by centrifugation and washed with ethanol once.

2.2. *Characterization.* Powder X-ray diffraction (XRD) data of the samples were collected on a philips PW1050 powder

diffractometer with Cu K $\alpha$  radiation source at 40 kV in the  $2\theta$  range of 10–80°. Transmission electron microscopy (TEM) measurement was carried out with a JEM-1230 microscope operating at 80 kV. High-resolution transmission electron microscopy (HRTEM) measurement was carried out with

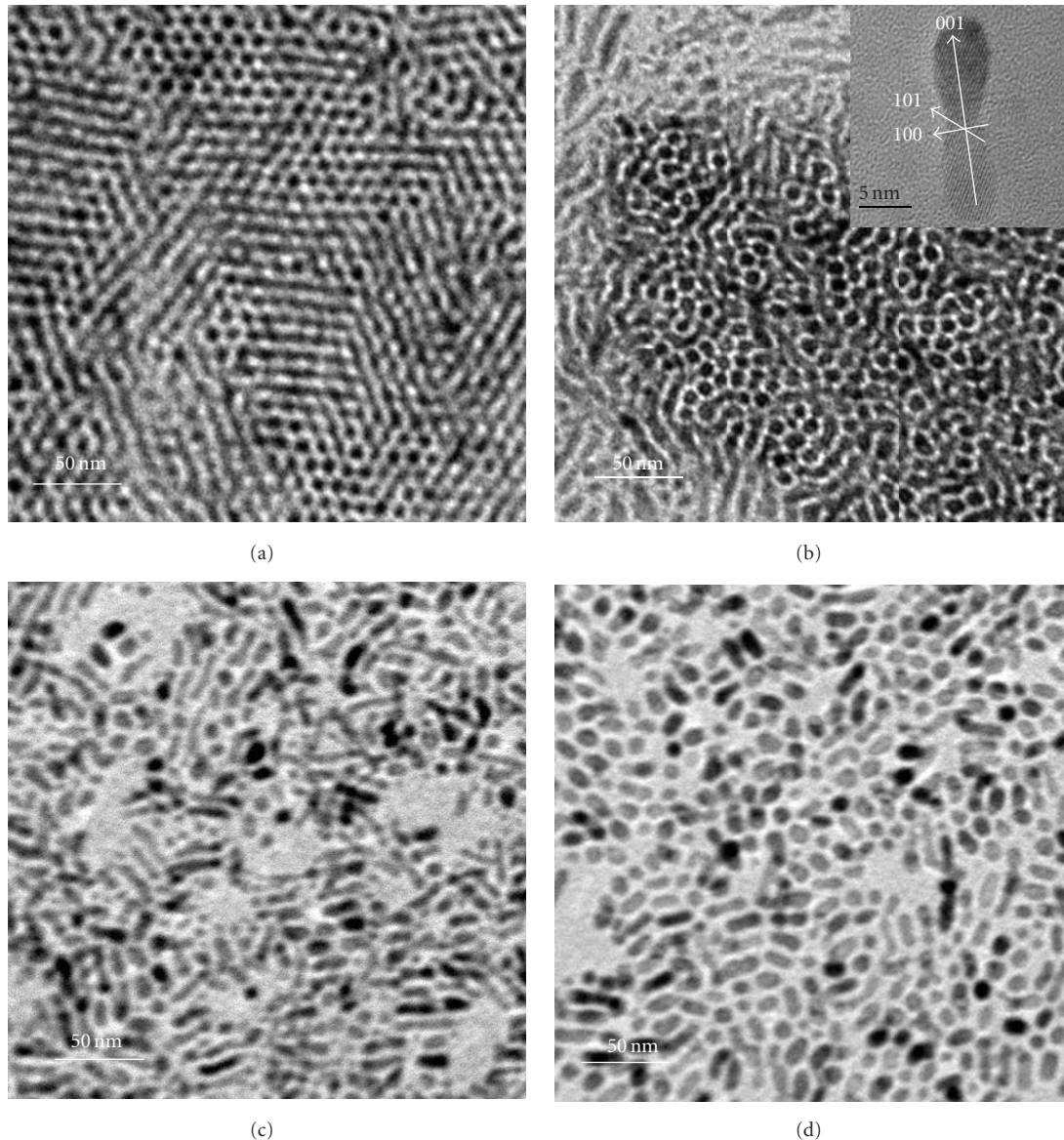


FIGURE 4: TEM images and HRTEM images of  $\text{TiO}_2$  nanocrystals synthesized at  $240^\circ\text{C}$  for different time: (a) 0.5 hours; (b) 2 hours; (c) 4 hours; (d) 17 hours.

a JEM-200CX operating at 160 kV. The size distribution is obtained from TEM which contain thousands of nanocrystals using Scnimage, Photoshop and Origin software. For TEM and HRTEM specimen preparation, the products were redispersed in hexane and dried on the carbon-coated copper grid at room temperature before performance.

### 3. Result and Discussion

**3.1.  $\text{TiO}_2$  Nanocrystals Synthesis at  $300^\circ\text{C}$ .** Figure 1 represents the TEM image of the  $\text{TiO}_2$  nanocrystals prepared by microemulsion-solvothermal method for different time at  $300^\circ\text{C}$ . Several special shapes of  $\text{TiO}_2$  nanocrystals including sphere, polygon and rhombus were obtained at this temperature. Figure 1(a) shows the TEM images of  $\text{TiO}_2$

nanocrystals with sphere and smaller nanorods prepared at  $300^\circ\text{C}$  for 0.5 hours. Figure 1(b) shows the TEM and HRTEM images for nanocrystals with sphere shape prepared at  $300^\circ\text{C}$  for 2 hours. The  $\text{TiO}_2$  nanocrystals are nearly close-packed and atomic lattice structure are clearly observed in HRTEM. Figures 1(c) and 1(d) shows the TEM and HRTEM images of  $\text{TiO}_2$  nanocrystals with polygon and rhombus prepared at  $300^\circ\text{C}$  for 4 hours and 17 hours, respectively. Anisotropic crystal growth for  $\text{TiO}_2$  nanocrystals could be observed from the HRTEM image of Figure 1(d). The growth rate in the (001) direction is much faster than those in other directions. Figure 2(b) shows the XRD pattern of this kind of  $\text{TiO}_2$  nanocrystals. Compared with the standard spectrum of anatase titanium dioxide shown in Figure 2(a), the main peaks corresponding to anatase  $\text{TiO}_2$  including (101), (004),

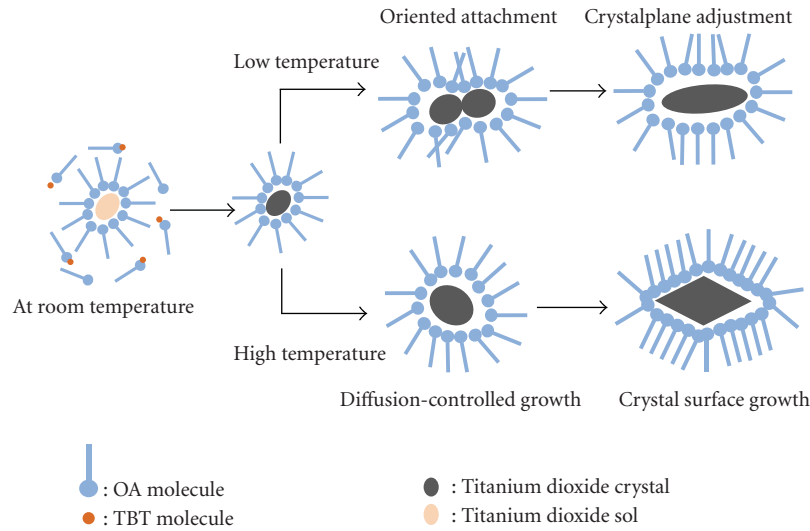


FIGURE 5: Schematic process on the nucleation and growth of the  $\text{TiO}_2$  nanocrystals.

(200), (105), (211) and (204) are observed. The result is consistent with the XRD pattern of  $\text{TiO}_2$  samples with 13 nm diameters reported by Niederberger [17]. In order to study the homogeneity of the nanocrystalline, we assume that these nanocrystals are spherical. The software can be used to calculate area of each nanocrystals, and then the distribution of nanocrystals can be geted by the corresponding diameter. The size distribution of  $\text{TiO}_2$  nanocrystals prepared at  $300^\circ\text{C}$  for different hours are also present in Figure 3. As the time increased, the average diameter of  $\text{TiO}_2$  nanocrystals become larger and the particle size distribution become less uniform.

**3.2.  $\text{TiO}_2$  Nanocrystals Synthesis at  $240^\circ\text{C}$ .** Figure 4 represents the TEM image of the  $\text{TiO}_2$  nanocrystals by microemulsion-solvothermal method for different time at  $240^\circ\text{C}$ . Sphere and rod shapes of  $\text{TiO}_2$  nanocrystals were obtained. Figure 4(a) shows a number of spherical nanocrystals prepared at  $240^\circ\text{C}$  for 0.5 hours. The spherical nanocrystals were combined together. A similar phenomenon could be seen more clearly in Figure 4(b) which shows TEM images of  $\text{TiO}_2$  nanocrystals prepared at  $240^\circ\text{C}$  for 2 hours. Lots of nanorods rather than nanodots are also found in Figure 4(b) and a nanorod is chosen for HRTEM analysis. The nanorod is around 25 nm long and 6 nm wide and it can be seen as a combination of two smaller nanorods along (001) direction. Figures 4(c) and 4(d) shows the TEM images of  $\text{TiO}_2$  nanorods at  $240^\circ\text{C}$  for 4 hours and 17 hours, respectively. More nanorods could be observed as the time increased, sphere nanocrystals disappeared for 17 hours. Figure 2(c) presents the XRD pattern of the  $\text{TiO}_2$  nanorods at  $240^\circ\text{C}$ . The main peaks indicate the highly anatase1 crystalline structure of the  $\text{TiO}_2$ . Compared with Figure 2(b), the main peaks is quite broad, That represents the value of degree of crystallization synthesized at  $240^\circ\text{C}$  is much lower than that synthesized at  $300^\circ\text{C}$ .

**3.3. The Shape Change Process of  $\text{TiO}_2$  Nanocrystals.** Figure 5 shows schematic process on the shape changes of the  $\text{TiO}_2$  nanocrystals. It could be described as follows. In the presence of OA, reverse micelles are easily formed in nonaqueous media after a water drop. Moreover, TBT reacts with water in reverse micelles vigorously. As a result, spherical titanium dioxide sol micelles are formed at room temperature after water added. This process takes a long time along with the hydrolysis reaction. As the temperature is increased, the sol evolves will quickly transform into nanocrystalline, leading to the formation of small  $\text{TiO}_2$  nanodots. When the reaction temperature is set at  $300^\circ\text{C}$ , due to the rapid nucleation of reactive intermediates, the  $\text{TiO}_2$  nanodots will grow in a diffusion-control pattern, leading to the formation of spherical  $\text{TiO}_2$  nanocrystals. With the extension of reaction time, the crystal surface energy will play a more important role for the shape of  $\text{TiO}_2$  nanocrystals. Due to high surface energy of the {001} face [18], the spherical  $\text{TiO}_2$  nanocrystals generated at the initial reaction stage grow along (001) direction. As a result, the spherical nanocrystals are easily transformed into polygon prismatic nanocrystals. As the nanocrystals grow along (001) direction, the specific surface area of  $\text{TiO}_2$  nanocrystals along (001) direction is gradually lower, leading to two-dimensional growth of  $\text{TiO}_2$  nanocrystals. Because the surface energy of the {100} face is higher than that of the {101} face, the shape of  $\text{TiO}_2$  nanocrystals finally transform into rhombus with a further extension of time. When the reaction temperature is set at  $240^\circ\text{C}$ , the reaction rate of reactive intermediates decreases. As a result, the  $\text{TiO}_2$  nanodots are easy to assemble together to form nano-rods by a kind of oriented attachment mechanism. The oriented attachment mechanism has been reported for a variety of metal oxide system [19, 20]. It is said that the oriented attachment between several sphere shaped nanocrystals makes the reduction of surface energy (it is usually observed in (001) direction because of high surface energy along (001) direction). Therefore

more stable rod shaped nanocrystals are formed at low temperature. These are our correlation analysis on the basis of experimental result, some detailed formation process of the TiO<sub>2</sub> nanocrystals still needs to be investigated further.

#### 4. Conclusion

The anatase TiO<sub>2</sub> nanocrystals of different shapes have been successfully synthesized by microemulsion-solvothermal method using a new microemulsion system prepared by OA, TBT and H<sub>2</sub>O. The sphere, polygon and rhombus shaped nanocrystals have been prepared at 300°C for 2 hours, 4 hours and 17 hours, respectively. and the dot and rod shaped nanocrystals has been synthesized at 240°C for 0.5 hours and 17 hours. The result indicates that the shape of TiO<sub>2</sub> nanocrystals could change from dot to sphere, polygon, rhombus at 300°C, and it could also change from dot to rod at 240°C with the increase of reaction time. This microemulsion-solvothermal method could provide another new way for the synthesis and control of other nanocrystals with some special morphology.

#### Acknowledgment

Funded by the Zhejiang Provincial Natural Science Foundation of China (Grant no. Z4080021).

#### References

- [1] H. Jia, Z. Zheng, H. Zhao, L. Zhang, and Z. Zou, "Nonaqueous sol-gel synthesis and growth mechanism of single crystalline TiO<sub>2</sub> nanorods with high photocatalytic activity," *Materials Research Bulletin*, vol. 44, no. 6, pp. 1312–1316, 2009.
- [2] J. Tang, F. Redl, Y. Zhu, T. Siegrist, L. E. Brus, and M. L. Steigerwald, "An organometallic synthesis of TiO<sub>2</sub> nanoparticles," *Nano Letters*, vol. 5, no. 3, pp. 543–548, 2005.
- [3] Z. Zhang, X. Zhong, S. Liu, D. Li, and M. Han, "Aminolysis route to monodisperse titania nanorods with tunable aspect ratio," *Angewandte Chemie. International Edition*, vol. 44, no. 22, pp. 3466–3470, 2005.
- [4] C.-C. Weng, C.-P. Chen, C.-H. Ting, and K.-H. Wei, "Using a solution crystal growth method to grow arrays of aligned, individually distinct, single-crystalline TiO<sub>2</sub> nanoneedles within nanocavities," *Chemistry of Materials*, vol. 17, no. 13, pp. 3328–3330, 2005.
- [5] D. K. Yi, S. J. Yoo, and D.-Y. Kim, "Spin-on-based fabrication of titania nanowires using a sol-gel process," *Nano Letters*, vol. 2, no. 10, pp. 1101–1104, 2002.
- [6] Y. Zhou, E.-Y. Ding, and W.-D. Li, "Synthesis of TiO<sub>2</sub> nanocubes induced by cellulose nanocrystal (CNC) at low temperature," *Materials Letters*, vol. 61, no. 28, pp. 5050–5052, 2007.
- [7] Y.-W. Jun, M. F. Casula, J.-H. Sim, S. Y. Kim, J. Cheon, and A. P. Alivisatos, "Surfactant-assisted elimination of a high energy facet as a means of controlling the shapes of TiO<sub>2</sub> nanocrystals," *Journal of the American Chemical Society*, vol. 125, no. 51, pp. 15981–15985, 2003.
- [8] X. Chen and S. S. Mao, "Titanium dioxide nanomaterials: synthesis, properties, modifications and applications," *Chemical Reviews*, vol. 107, no. 7, pp. 2891–2959, 2007.
- [9] M. Cao, X. Wu, X. He, and C. Hu, "Microemulsion-mediated solvothermal synthesis of SrCO<sub>3</sub> nanostructures," *Langmuir*, vol. 21, no. 13, pp. 6093–6096, 2005.
- [10] M. Cao, Y. Wang, C. Guo, Y. Qi, and C. Hu, "Preparation of ultrahigh-aspect-ratio hydroxyapatite nanofibers in reverse micelles under hydrothermal conditions," *Langmuir*, vol. 20, no. 11, pp. 4784–4786, 2004.
- [11] M. Cao, C. Hu, and E. Wang, "The first fluoride one-dimensional nanostructures: microemulsion-mediated hydrothermal synthesis of BaF<sub>2</sub> whiskers," *Journal of the American Chemical Society*, vol. 125, no. 37, pp. 11196–11197, 2003.
- [12] K. Lin, J. Chang, and J. Lu, "Synthesis of wollastonite nanowires via hydrothermal microemulsion methods," *Materials Letters*, vol. 60, no. 24, pp. 3007–3010, 2006.
- [13] W. Liu, W. Zhong, X. Wu, N. Tang, and Y. Du, "Hydrothermal microemulsion synthesis of cobalt nanorods and self-assembly into square-shaped nanostructures," *Journal of Crystal Growth*, vol. 284, no. 3–4, pp. 446–452, 2005.
- [14] M. Cao, X. He, X. Wu, and C. Hu, "Microemulsion-based solvothermal synthesis of aluminium orthophosphate nanocrystals," *Nanotechnology*, vol. 16, no. 10, pp. 2129–2133, 2005.
- [15] J. Xiang, S.-H. Yu, B. Liu, Y. Xu, X. Gen, and L. Ren, "Shape controlled synthesis of PbS nanocrystals by a solvothermal-microemulsion approach," *Inorganic Chemistry Communications*, vol. 7, no. 4, pp. 572–575, 2004.
- [16] P. Zhang and L. Gao, "Synthesis and characterization of CdS nanorods via hydrothermal microemulsion," *Langmuir*, vol. 19, no. 1, pp. 208–210, 2003.
- [17] M. Niederberger, M. H. Bartl, and G. D. Stucky, "Benzyl alcohol and titanium tetrachloride—a versatile reaction system for the nonaqueous and low-temperature preparation of crystalline and luminescent titania nanoparticles," *Chemistry of Materials*, vol. 14, no. 10, pp. 4364–4370, 2002.
- [18] M. Adachi, Y. Murata, J. Takao, J. Jiu, M. Sakamoto, and F. Wang, "Highly efficient dye-sensitized solar cells with a titania thin-film electrode composed of a network structure of single-crystal-like TiO<sub>2</sub> nanowires made by the oriented attachment mechanism," *Journal of the American Chemical Society*, vol. 126, no. 45, pp. 14943–14949, 2004.
- [19] D.-F. Zhang, L.-D. Sun, J.-L. Yin, and C.-H. Yan, "Low-temperature fabrication of highly crystalline SnO<sub>2</sub> nanorods," *Advanced Materials*, vol. 15, no. 12, pp. 1022–1025, 2003.
- [20] C. Pacholski, A. Kornowski, and H. Weller, "Self-assembly of ZnO: from nanodots to nanorods," *Angewandte Chemie. International Edition*, vol. 41, no. 7, pp. 1188–1191, 2002.

## Research Article

# Optical Properties of Linoleic Acid Protected Gold Nanoparticles

**Ratan Das, Siddartha S. Nath, and Ramendu Bhattacharjee**

*Department of Physics, Assam University, Silchar, Assam 788011, India*

Correspondence should be addressed to Siddartha S. Nath, nathssrd@gmail.com

Received 16 April 2010; Revised 3 July 2010; Accepted 22 July 2010

Academic Editor: Quanqin Dai

Copyright © 2011 Ratan Das et al. This is an open access article distributed under the Creative Commons Attribution License, which permits unrestricted use, distribution, and reproduction in any medium, provided the original work is properly cited.

Linoleic acid-protected gold nanoparticles have been synthesized through the chemical reduction of tetrachloroaurate ions by ethanol in presence of sodium linoleate. The structure of these nanoparticles is investigated using transmission electron microscopy, which shows that the Au nanoparticles are spherical in shape with a narrow size distribution which ranges from 8 to 15 nm. Colloidal dispersion of gold nanoparticles in cyclohexane exhibits absorption bands in the ultraviolet-visible range due to surface plasmon resonance, with absorption maximum at 530 nm. Fluorescence spectra of gold nanoparticles also show an emission peak at 610 nm when illuminated at 450 nm. UV-Vis spectroscopy reveals that these nanoparticles remain stable for 10 days.

## 1. Introduction

Nanoparticles (1–100 nm) have been a source of intense interest due to their novel electrical, optical, physical, chemical, and magnetic properties. They have significant potential for a wide range of applications such as catalysis, magnetic recording media, optoelectronic materials, magnetic fluids, composite materials, fuel cells, pigments, and sensors. Their uniqueness arises from their high ratio of surface area to volume [1–6]. The synthesis of noble metal nanoparticles with desired size/shape has enormous importance, especially in the emerging field of nanotechnology. There is presently great interest in the optical properties of gold nanoparticles due to the various applications they have in different fields. These gold colloids show bright colour due to surface plasmon resonance (SPR). This surface plasmon resonance is the transverse oscillations of the surface electrons of the particle on interaction with light of suitable wavelength. Gold colloids show an absorption band in the visible range. Here gold nanoparticles have been prepared by a simple and convenient reduction method [7], which is a promising approach for highly efficient synthesis of gold nanoparticles with a more uniform particle size. The prepared gold nanoparticles have been dispersed in cyclohexane and then examined using X-ray diffraction (XRD), Transmission Electron Microscope (TEM), UV/Vis absorption spectroscopy,

and fluorescence spectroscopy (PL). The most important factor is that the gold nanoparticles prepared by this process remain stable for 10 days.

## 2. Materials and Method

Uniform gold nanoparticles can be obtained through the reduction of tetrachloroaurate ions by ethanol at temperatures between 30°C to 60°C under atmospheric conditions [7]. In this synthesis process, 25 mL of aqueous solution containing tetrachloroauric acid (1 g of  $\text{HAuCl}_4$ ), 3 g sodium linoleate ( $\text{C}_{18}\text{H}_{32}\text{ONa}$ ), 20 mL ethanol ( $\text{C}_2\text{H}_5\text{OH}$ ), and 5 mL linoleic acid ( $\text{C}_{18}\text{H}_{32}\text{O}_2$ ) are added in a capped tube under agitation. The system is well capped and treated at the temperature range 30°C to 60°C for 2 hours. In the aqueous solution of tetrachloroauric acid, sodium linoleate and the mixture of linoleic acid and ethanol are combined in order: a solid phase of sodium linoleate, a liquid phase of ethanol and linoleic acid, and water ethanol solution phase containing tetrachloroaurate ions forms in the system. Ethanol in the liquid and solution phases reduces the tetrachloroaurate ions into gold nanoparticles. Along with the reduction process, among all the reactant, only the linoleic acid gets absorbed on the surface of the gold nanoparticles with the alkyl chains on the outside through which the produced nanoparticles gain hydrophobic surfaces. In this simple reduction process,



FIGURE 1: Pale reddish colour of the gold nanoparticles dispersed in cyclohexane.

the role of linoleic acid is to protect the gold nanoparticle from agglomeration, making a layer over it with its alkyl chains on the outside giving a hydrophilic surroundings to the nanoparticles. On changing the concentration of the electrolyte, it is found that the colour becomes reddish on adding linoleic acid at the same proportion. This reddish colour of prepared nanoparticles indicates the conversion of tetrachloroaurate ions into gold nanoparticles.

The produced nanoparticles having reddish brown in colour actually, collected at the bottom of vessel after cooling to room temperature, are then dispersed in cyclohexane to form a homogenous colloidal solution of gold nanoparticles. The colour of the colloidal solution of gold nanoparticles becomes pale reddish due to dispersion in cyclohexane as shown in Figure 1.

The structure of prepared gold nanoparticles has been investigated by Bruker AXS model X-ray diffractometer. Size and shape of the gold nanoparticles has been obtained from TEM photographs which was performed on a JEM 1000C X II model instrument. The absorption spectra of the gold nanoparticles was taken on a Perkin Elmer Lambda 351.24 model whereas fluorescence spectra was performed on Hitachi; F-2500 model.

### 3. Results and Discussion

**3.1. XRD Analysis.** The XRD patterns of the sample prepared by the present reduction method are shown in Figure 2. The crystalline nature of the as-synthesized product is demonstrated in the XRD measurements. The diffraction peaks at 45.3 degrees and 64.5 degrees match with those of a face-centred cubic (fcc) Au as in JCPDS correspond to the planes of (200) and (220), respectively. From this study, average particle size is estimated by using Debye-Scherrer formula [8, 9]. Here the instrumental broadening at 45.3 degrees and 64.5 degrees are 0.00632 and 0.00912. Considering

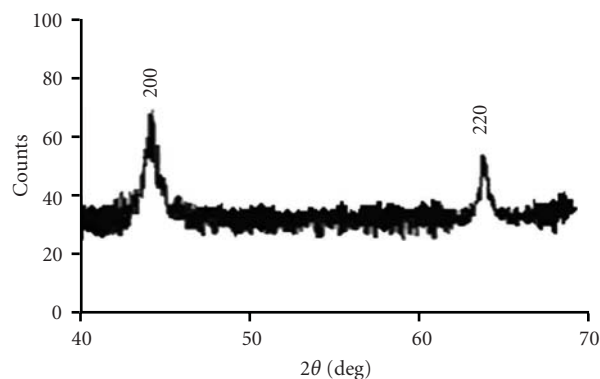


FIGURE 2: XRD pattern of gold nanoparticles.

the instrumental broadening, the average particle size is calculated to be around  $(11 \pm 2)$  nm with 14% experimental error.

**3.2. TEM Analysis.** Samples for TEM studies are prepared by placing a drop of the gold colloidal solution on TEM carbon-coated copper grid. The films on the TEM grids are allowed to dry for a few hours after removing the extra solution using blotting paper. TEM micrograph of the prepared colloidal solution of gold nanoparticles is shown in Figure 3(a) with a graphic of statistical size distribution of particles in Figure 3(b). The Au nanoparticles (black portion) are spherical in shape with smooth surface morphology. Though the size range of the nanoparticle lie between 8 and 15 nm, about 80% of the nanoparticles were found to have size approximately 12 nm. After 10 days, it is found that the reddish colour of the colloidal solution starts to deteriorate slowly and the particles starts to agglomerate with time. So, after 10 days particles remain no longer stable.

**3.3. UV/Vis Spectroscopy Analysis.** Noble metal nanoparticles (Au, Ag, P, etc.) show a strong absorption band in the visible range due to surface plasmon resonance. Surface plasmon resonance is the coherent motion of free electrons in the conduction band caused by interaction with an electromagnetic field. The electric field of an incoming light wave induces a polarization of electrons with respect to the heavier ionic core of the nanoparticles. This induces a dipolar oscillation of all the free electrons with the same phase. When the frequency of the light wave become resonant with the electron motion, a strong absorption occurs which is the origin of observed colour of colloids. Width of the absorption band and wavelength corresponding to the surface plasmon resonance peak strongly depend on size, shape, dielectric constant of nanoparticle, as well as on the surrounding medium. For small metal particles (diameter < 20 nm), absorption spectra significantly depend only on the dipole oscillation [5, 6, 10–13]. This reduction method by ethanol produces spherical gold nanoparticles around 12 nm. The UV/Vis absorption spectra of the gold nanoparticles dispersed in cyclohexane is shown in Figure 4. The absorption (SPR) peak is obtained in the visible range at 530 nm which matches well with others result. Moreover,

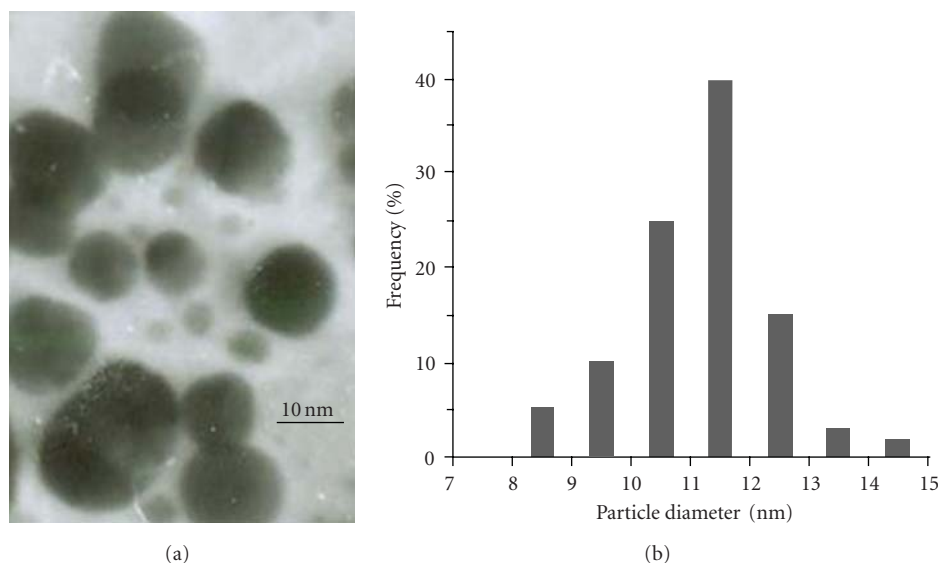


FIGURE 3: (a) TEM image of gold nanoparticles. (b) Graphic for particle size distribution.

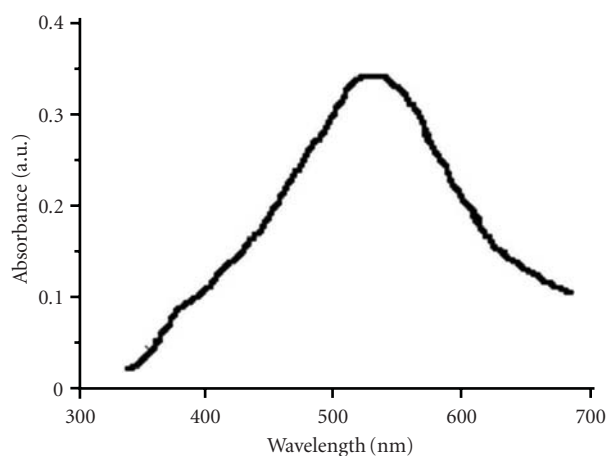


FIGURE 4: UV-Vis spectra of gold nanoparticles.

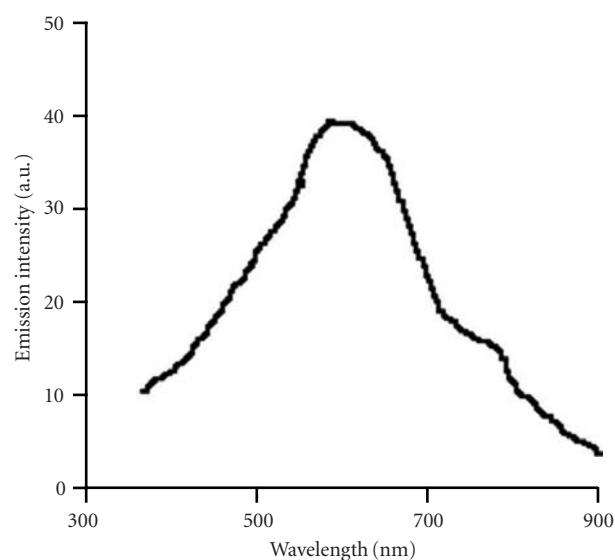


FIGURE 5: Fluorescence spectra of gold nanoparticles.

as absorption peak and width remains the same for 10 days, so it indicates that nanoparticles remain stable for 10 days without any agglomeration.

**3.4. Fluorescence Spectroscopy.** In gold nanoparticles, 5d valence and 6sp-conduction electrons play the role for fluorescence spectra [12–18]. It has been reported by Liao et al. [14] and Varnavski et al. [18] that 15 nm particles produce fluorescence. Eichelbaum et al. [16] reported that 10 nm gold nanoparticles show photoluminescence. The reason for photoluminescence is attributed to the interband transition from sp-conduction band above the Fermi level to the d-band below. The radiative recombination of electron hole pairs between this d-band and sp-conduction band produces emission [12–18], which occurs at 610 nm for linoleic acid protected gold nanoparticles (8–15 nm), when excited with 450 nm of optical source (Xenon lamp-150 watt). Moreover, the absorbed linoleic acid on gold nanoparticles

surface further enhances the intensity of emission [14–17]. Fluorescence spectra for gold nanoparticle are shown in Figure 5.

#### 4. Summary

We have prepared gold nanoparticles through the reduction of tetrachloroaurate ions by ethanol, which is dispersed in cyclohexane. Here, linoleic acid acts as a stabilizer. XRD analysis, UV/Vis spectra, and TEM micrograph reveal that the prepared nanoparticles are spherical in shape with an average size of 12 nm which remain stable for 10 days. SPR peak is observed at 530 nm whereas fluorescence peak is obtained at 610 nm.

## Acknowledgments

The authors thank to Dr D. K. Avasthi (Scientist H) Material Science, IUAC, New Delhi, India, Dr B. DKHR (S.O.) NEHU, Shillong, India, Dr. S. Sharma (S.O.), IIT, Guwahati, Assam, India and Dr. Sudip Choudhury, lecturer, G. C. College, Silchar, Assam, India for their suggestions and assistance during the work.

## References

- [1] G. Cao, *Nanostructures and Nanomaterials*, Imperial College Press, London, UK, 2004.
- [2] M. A. Reed and T. Lee, *Molecular Nanoelectronics*, American Scientific, Stevenson Ranch, Calif, USA, 2003.
- [3] C. P. Poole and F. J. Owens, *Introduction to Nanotechnology*, Wiley Interscience, New York, NY, USA, 2003.
- [4] A. Taleb, C. Petit, and M. P. Pileni, "Optical properties of self-assembled 2D and 3D superlattices of silver nanoparticles," *Journal of Physical Chemistry B*, vol. 102, no. 12, pp. 2214–2220, 1998.
- [5] M. A. Noginov, G. Zhu, M. Bahoura et al., "The effect of gain and absorption on surface plasmons in metal nanoparticles," *Applied Physics B*, vol. 86, no. 3, pp. 455–460, 2006.
- [6] C. Sönnichsen, T. Franzl, T. Wilk, G. Von Plessen, and J. Feldmann, "Plasmon resonances in large noble-metal clusters," *New Journal of Physics*, vol. 4, pp. 93.1–93.8, 2002.
- [7] X. Wang, J. Zhuang, Q. Peng, and Y. Li, "A general strategy for nanocrystal synthesis," *Nature*, vol. 437, no. 7055, pp. 121–124, 2005.
- [8] D. Mohanta, S. S. Nath, N. C. Mishra, and A. Choudhury, "Irradiation induced grain growth and surface emission enhancement of chemically tailored ZnS:Mn/PVOH nanoparticles by  $\text{Cl}^{+9}$  ion impact," *Bulletin of Materials Science*, vol. 26, no. 3, pp. 289–294, 2003.
- [9] S. S. Nath, D. Chakdar, G. Gope et al., "Green luminescence of ZnS and ZnS:Cu quantum dots embedded in zeolite matrix," *Journal of Applied Physics*, vol. 105, no. 9, Article ID 094305, 2009.
- [10] R. Das, S. S. Nath, D. Chakdar, G. Gope, and R. Bhattacharjee, "Preparation of silver nanoparticles and their characterization," *Journal of Nanotechnology*, vol. 5, pp. 1–6, 2009.
- [11] R. Das, S. S. Nath, D. Chakdar, G. Gope, and R. Bhattacharjee, "Synthesis of silver nanoparticles and their optical properties," *Journal of Experimental Nanoscience*, vol. 5, no. 4, pp. 357–362, 2010.
- [12] M. P. Pileni, "Optical properties of nanosized particles dispersed in colloidal solutions or arranged in 2D or 3D superlattices," *New Journal of Chemistry*, vol. 22, no. 7, pp. 693–702, 1998.
- [13] S. Link and M. A. El-Sayed, "Shape and size dependence of radiative, non-radiative and photothermal properties of gold nanocrystals," *International Reviews in Physical Chemistry*, vol. 19, no. 3, pp. 409–453, 2000.
- [14] H. Liao, W. Wen, and G. K.L. Wong, "Photoluminescence from Au nanoparticles embedded in Au:oxide composite films," *Journal of the Optical Society of America B*, vol. 23, no. 12, pp. 2518–2521, 2006.
- [15] J. Zhang, J. Malicka, I. Gryczynski, and J. R. Lakowicz, "Oligonucleotide-displaced organic monolayer-protected silver nanoparticles and enhanced luminescence of their salted aggregates," *Analytical Biochemistry*, vol. 330, no. 1, pp. 81–86, 2004.
- [16] M. Eichelbaum, B. E. Schmidt, H. Ibrahim, and K. Rademann, "Three-photon-induced luminescence of gold nanoparticles embedded in and located on the surface of glassy nanolayers," *Nanotechnology*, vol. 18, no. 35, Article ID 355702, 8 pages, 2007.
- [17] J. Xu, X. Han, H. Liu, and Y. Hu, "Synthesis and optical properties of silver nanoparticles stabilized by gemini surfactant," *Colloids and Surfaces A*, vol. 273, no. 1–3, pp. 179–183, 2006.
- [18] O. Varnavski, R. G. Ispasoiu, L. Balogh, D. Tomalia, and T. Goodson III, "Ultrafast time-resolved photoluminescence from novel metal-dendrimer nanocomposites," *Journal of Chemical Physics*, vol. 114, no. 5, pp. 1962–1965, 2001.

## Research Article

# Pulsed Current Activated Consolidation of Nanostructured Fe<sub>3</sub>Al and Its Mechanical Property

Tae-Wan Kim,<sup>1</sup> In-Yong Ko,<sup>1</sup> Jung-Mann Doh,<sup>2</sup> Jin-Kook Yoon,<sup>2</sup> and In-Jin Shon<sup>1,3</sup>

<sup>1</sup>Division of Advanced Materials Engineering, Research Center for Advanced Materials Development, Engineering College, Chonbuk National University, 664-14 Deokjin-dong 1-ga, Deokjin-gu, Jeonju, Jeonbuk 561-756, Republic of Korea

<sup>2</sup>Advanced Functional Materials Research Center, Korea Institute of Science and Technology, PO Box 131, Cheongryang, Seoul 130-650, Republic of Korea

<sup>3</sup>Department of Hydrogen and Fuel Cells Engineering, Specialized Graduate School, Chonbuk National University, Chonbuk, 561-756, Republic of Korea

Correspondence should be addressed to In-Jin Shon, [ijshon@chonbuk.ac.kr](mailto:ijshon@chonbuk.ac.kr)

Received 18 April 2010; Revised 30 May 2010; Accepted 14 June 2010

Academic Editor: William W. Yu

Copyright © 2011 Tae-Wan Kim et al. This is an open access article distributed under the Creative Commons Attribution License, which permits unrestricted use, distribution, and reproduction in any medium, provided the original work is properly cited.

A nanopowder of Fe<sub>3</sub>Al was synthesized from 3Fe and Al by high-energy ball milling. A dense nanostructured Fe<sub>3</sub>Al was consolidated by pulsed current activated sintering method within 2 minutes from mechanically synthesized powders of Fe<sub>3</sub>Al and horizontally milled powders of 3Fe+Al. The grain size, sintering behavior, and hardness of Fe<sub>3</sub>Al sintered from horizontally milled 3Fe+Al powders and high-energy ball milled Fe<sub>3</sub>Al powder were compared.

## 1. Introduction

Iron aluminide (Fe<sub>3</sub>Al) is of interest for structural applications at elevated temperature in hostile environments. This is because it generally possess excellent oxidation and corrosion resistance, relatively lower density and lower material cost than Ni-based alloy [1, 2]. However, its use has been limited by its brittleness at room temperature. This drawback can be improved by grain size reduction. Nanocrystalline materials have received much attention as advanced engineering materials with improved physical and mechanical properties [3, 4]. As nanomaterials possess high strength, high hardness, excellent ductility, and toughness, undoubtedly, more attention has been paid for the application of nanomaterials [5, 6].

Conventional methods of processing iron aluminides, including melting and casting have been investigated till now [7, 8]. However, none of these methods yield nanostructures. In recent years, some efficient methods were reported to fabricate the fine grain size materials, such as mechanical alloying, pulsed current activated sintering [9, 10]. The mechanical alloying process, which involves a repeated cold-working, fracture, and welding, makes microstructure refinement and

alloy formation. The pulsed current-activated sintering is a rapid consolidation processing method where uniform, dense, and fine grain materials can be obtained by applying pressures and passing pulsed current the compact. And the process, due to spark plasma formed between the powder particles, enhances the distorted energy of the particles and increases the rate of the diffusion between the particles [11–14].

The purpose of this study is to produce nanopowder of Fe<sub>3</sub>Al and densify nanocrystalline Fe<sub>3</sub>Al compound within two minutes from mixtures of 3Fe+Al powders and mechanically synthesized Fe<sub>3</sub>Al, respectively, using this pulsed current activated sintering method and to evaluate its mechanical properties and grain size.

## 2. Experimental Procedures

Powders of 99.5% Fe (<10 μm, Alfa, Inc) and 99% pure Al (–200 mesh, Samchun Chemical, Inc) were used as a starting materials. 3Fe and Al powders ratio were mixed by two-type methods. Firstly, the powders were milled in a high-energy ball mill, Pulverisette-5 planetary mill with 250 rpm

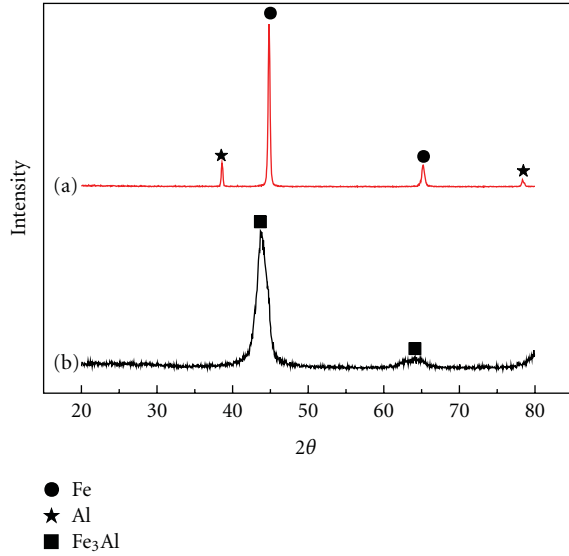


FIGURE 1: XRD patterns of milled powder: (a) horizontal milled 3Fe and Al powder, (b) high-energy ball milled Fe<sub>3</sub>Al powder.

and for 10 hrs. Tungsten carbide balls (8.5 mm in diameter) were used in a sealed cylindrical stainless steel vial under argon atmosphere. The weight ratio of ball-to-powder was 30:1. Secondly, the powders were mixed in polyethylene bottles using zirconia balls with ethanol and the process was performed at a horizontal rotation velocity of 250 rpm for 10 h. The grain sizes of Fe<sub>3</sub>Al were calculated using Suryanarayana and Grant Norton's formula [15]

$$B_r (B_{\text{crystalline}} + B_{\text{strain}}) \cos \theta = k \frac{\lambda}{L} + \eta \sin \theta, \quad (1)$$

where  $B_r$  is the full width at half-maximum (FWHM) of the diffraction peak after instrument correction;  $B_{\text{crystalline}}$  and  $B_{\text{strain}}$  are FWHM caused by small grain size and internal stress, respectively;  $k$  is constant (with a value of 0.9);  $\lambda$  is wavelength of the X-ray radiation;  $L$  and  $\eta$  are grain size and internal strain, respectively;  $\theta$  is the Bragg angle. The parameters  $B$  and  $B_r$  follow Cauchy's form with the relationship:  $B = B_r + B_s$ , where  $B$  and  $B_s$  are FWHM of the broadened Bragg peaks and the standard sample's Bragg peaks, respectively.

After milling, the mixed powders were placed in a graphite die (outside diameter, 45 mm; inside diameter, 20 mm; height, 40 mm) and then introduced into the pulsed current activated sintering system made by Eltek in South Korea [9]. The four major stages in the synthesis are as follows. The system was evacuated (stage 1). And a uniaxial pressure of 80 MPa was applied (stage 2). A pulsed current (on time: 20  $\mu$ s; off time: 10  $\mu$ s) was then activated and maintained until densification was attained as indicated by a linear gauge measuring the shrinkage of the sample (stage 3). Temperature was measured by a pyrometer focused on the surface of the graphite die. At the end of the process, the sample was cooled to room temperature (stage 4).

The relative densities of the synthesized sample were measured using the Archimedes method. Microstructural

information was obtained from product samples which were polished and etched using a solution of H<sub>2</sub>SO<sub>4</sub> (20 vol.%) and H<sub>2</sub>O (80 vol.%) for 35 s at room temperature. Compositional and microstructural analyses of the products were made through X-ray diffraction (XRD) and scanning electron microscopy (SEM) with energy dispersive X-ray analysis (EDAX). Vickers hardness was measured by performing indentations at load of 20 kg and a dwell time of 15 s on the sintered samples.

### 3. Results and Discussion

XRD patterns of milled powder is shown in Figure 1. Fe<sub>3</sub>Al was not synthesized during the horizontal rotation ball milling in ethanol, but synthesized during high-energy ball milling. The average grain size of Fe<sub>3</sub>Al measured by Suryanarayana and Norton's formula [15] was 5 nm. Figure 2 shows FE-SEM image of Fe<sub>3</sub>Al powder synthesized by high-energy ball milling and X-ray mapping of Fe and Al. From the X-ray mapping, Fe and Al were uniformly distributed and the particles of milled Fe<sub>3</sub>Al shown in Figure 2 are bigger. I think the reason in milling processing, iron and aluminum powders were wrapped with each other by server plastic deformation, resulting in grain refinement and mechanical alloying.

The changes in shrinkage displacement and temperature of the surface of the graphite die with heating time during the processing of Fe-Al system are shown in Figure 3. As the pulsed current was applied, the shrinkage displacement of Fe<sub>3</sub>Al continuously increased with temperature up to about 1000°C, but the shrinkage of 3Fe+Al gradually increased with temperature up to (A) point and then abruptly increased. When the reactant mixture of 3Fe and Al was heated under 80 MPa pressure to (A) point, no reaction took place as judged by subsequent XRD analysis. X-ray diffraction result, shown in Figure 4(a), exhibits only peaks pertaining to the Fe and Al. However, when the temperature was raised to 1150°C, the starting powders (3Fe+Al) reacted producing highly dense products (Fe<sub>3</sub>Al), shown in Figure 4(b). The abrupt increase in the shrinkage displacement at the ignition temperature is due to the increase in density as a result of molar volume change associated with the formation of Fe<sub>3</sub>Al from 3Fe and Al reactant and the consolidation of the product.

Figure 5 shows FE-SEM images of Fe<sub>3</sub>Al sintered from (a) horizontally milled Fe+Al powders and (b) high-energy ball milled Fe<sub>3</sub>Al powder. The grain size of Fe<sub>3</sub>Al sintered from high-energy ball milled Fe<sub>3</sub>Al is smaller than that of Fe<sub>3</sub>Al sintered from horizontally milled 3Fe+Al powders. The grain size of Fe<sub>3</sub>Al sintered from high-energy ball milled Fe<sub>3</sub>Al and from horizontally milled 3Fe+Al powders are about 40 nm and 300 nm, respectively. And the corresponding relative density of Fe<sub>3</sub>Al are 97% and 96%, respectively. The grain size of Fe<sub>3</sub>Al sintered from horizontally milled 3Fe+Al powders is higher than that of Fe<sub>3</sub>Al sintered from high-energy ball milled Fe<sub>3</sub>Al because Fe<sub>3</sub>Al can have grain growth due to exothermic energy when Fe<sub>3</sub>Al synthesized from 3Fe and Al during the sintering.

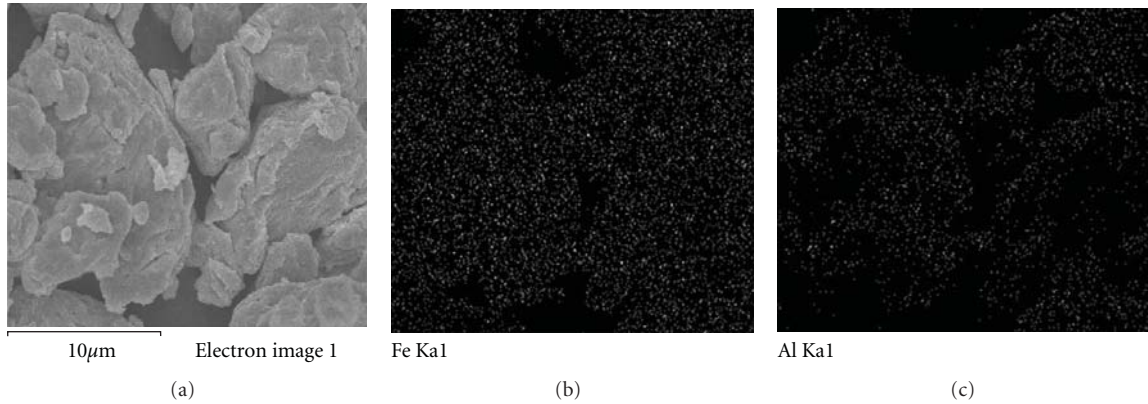


FIGURE 2: FE-SEM image of  $\text{Fe}_3\text{Al}$  and X-ray mapping of Fe and Al in high-energy ball milled powder.

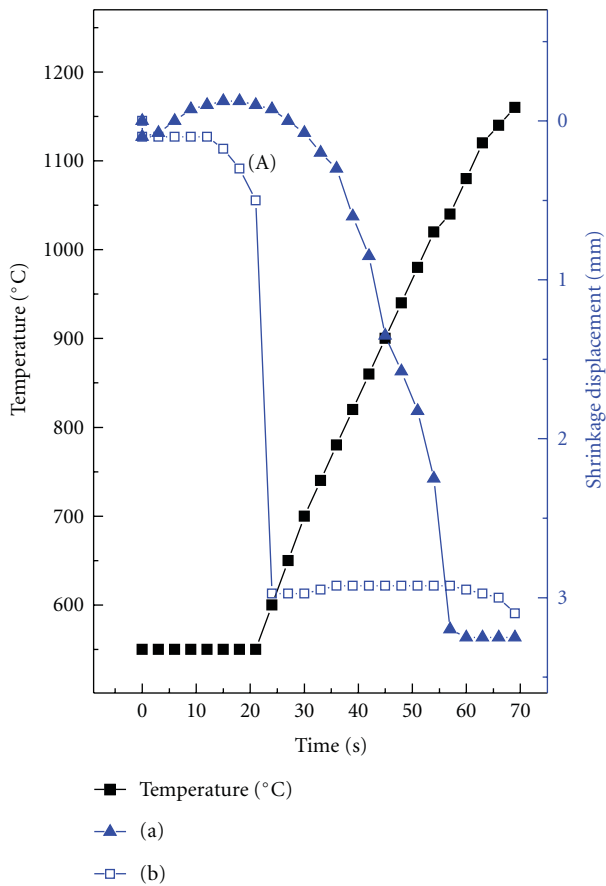


FIGURE 3: Variations of temperature and shrinkage displacement with heating time during pulsed current activated sintering of Fe-Al system: (a) high-energy ball milled  $\text{Fe}_3\text{Al}$  powder, (b) horizontal milled 3Fe and Al powder.

The average grain size of the sintered  $\text{Fe}_3\text{Al}$  is not greatly larger than that of the initial powder, indicating the absence of great grain growth during sintering. This retention of the grain size is attributed to the high-heating rate and the relatively short-term exposure of the powders to the high temperature. The role of the current (resistive or inductive)

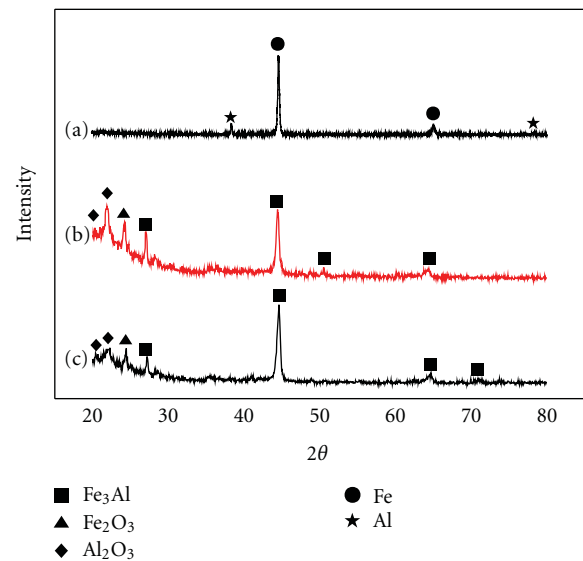


FIGURE 4: XRD patterns of the Fe-Al system: (a) sample heated to (A) point (b) heated to  $1150^\circ\text{C}$  from horizontal milled 3Fe and Al powder, (c) heated to  $1150^\circ\text{C}$  high-energy ball milled  $\text{Fe}_3\text{Al}$  powder.

in sintering and or synthesis has been focus of several attempts aimed at providing an explanation to the observed enhancement of sintering and the improved characteristics of the products. The role played by the current has been variously interpreted, the effect being explained in terms of fast heating rate due to Joule heating, the presence of plasma in pores separating powder particles [16], and the intrinsic contribution of the current to mass transport [17–19].

Vickers hardness measurements were made on polished sections of the  $\text{Fe}_3\text{Al}$  using a  $20\text{ kg}_f$  load and 15 s dwell time. The calculated hardness values of  $\text{Fe}_3\text{Al}$  sintered from (a) horizontally milled 3Fe+Al powders and (b) high energy ball milled  $\text{Fe}_3\text{Al}$  powder were  $317\text{ kg/mm}^2$  and  $458\text{ kg/mm}^2$ , respectively. This value represents an average of five measurements. Cracks were not observed to propagate from the indentation corner. So, fracture toughness cannot be calculated from crack length. The hardness of  $\text{Fe}_3\text{Al}$  sintered

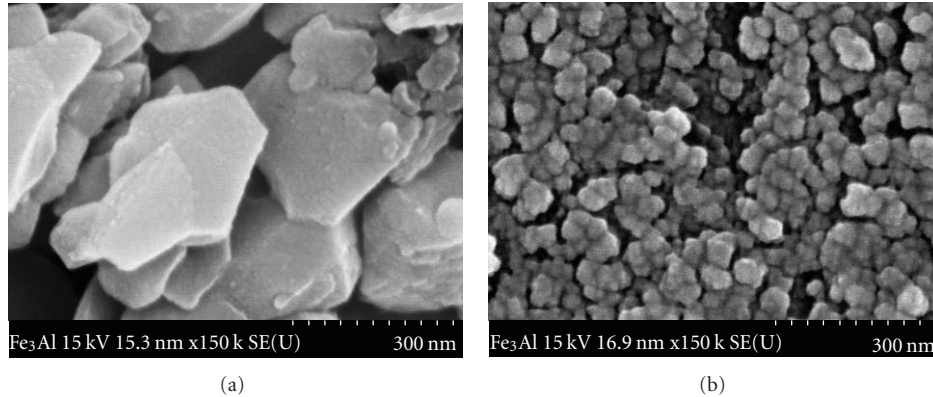


FIGURE 5: FE-SEM images of  $\text{Fe}_3\text{Al}$  sintered at  $1150^\circ\text{C}$ : (a) horizontal milled 3Fe and Al powder, (b) high-energy ball milled  $\text{Fe}_3\text{Al}$  powder.

from high-energy ball milled  $\text{Fe}_3\text{Al}$  is higher than that of  $\text{Fe}_3\text{Al}$  sintered from horizontally milled 3Fe+Al powders due to refinement of grain and high density. Zhang and Liu investigated  $\text{Fe}_3\text{Al}$  prepared by vacuum induction melting followed by hot spinning forging. The hardness of  $\text{Fe}_3\text{Al}$  was about  $270 \text{ Kg/mm}^2$  [20]. The hardness of this study is higher than that of Zhang's work due to refinement of grain size.

#### 4. Conclusions

Using the pulsed current activated sintering method, the densification of nanostructured  $\text{Fe}_3\text{Al}$  was accomplished from mechanically synthesized powder of  $\text{Fe}_3\text{Al}$  and milled 3Fe+Al powders. Nearly full density of  $\text{Fe}_3\text{Al}$  can be achieved within duration of 2 minutes for the applied pressure of 80 MPa and the pulsed current. The average grain sizes of  $\text{Fe}_3\text{Al}$  prepared by pulsed current activated sintering method from horizontally milled 3Fe+Al powders and high-energy ball milled  $\text{Fe}_3\text{Al}$  powder were about 300 nm and 40 nm, respectively. The calculated hardness values of  $\text{Fe}_3\text{Al}$  sintered from horizontally milled 3Fe+Al powders and high-energy ball milled  $\text{Fe}_3\text{Al}$  powder were  $317 \text{ kg/mm}^2$  and  $458 \text{ kg/mm}^2$ , respectively.

#### Acknowledgments

This work was supported by New & Renewable Energy R&D program (2009T00100316) under the Ministry of Knowledge Economy, Republic of Korea.

#### References

- [1] C. T. Liu, E. P. George, P. J. Maziasz, and J. H. Schneibel, "Recent advances in B2 iron aluminide alloys: deformation, fracture and alloy design," *Materials Science and Engineering A*, vol. 258, no. 1-2, pp. 84–98, 1998.
- [2] S. C. Deevi and V. K. Sikka, "Nickel and iron aluminides: an overview on properties, processing, and applications," *Intermetallics*, vol. 4, no. 5, pp. 357–375, 1996.
- [3] M. S. El-Eskandarany, "Structure and properties of nanocrystalline TiC full-density bulk alloy consolidated from mechanically reacted powders," *Journal of Alloys and Compounds*, vol. 305, no. 1-2, pp. 225–238, 2000.
- [4] L. Fu, L. H. Cao, and Y. S. Fan, "Two-step synthesis of nanostructured tungsten carbide-cobalt powders," *Scripta Materialia*, vol. 44, no. 7, pp. 1061–1068, 2001.
- [5] K. Kondoh, T. Threrujirapapong, H. Imai, J. Umeda, and B. Fugetsu, "CNTs/TiC reinforced titanium matrix nanocomposites via powder metallurgy and its microstructural and mechanical properties," *Journal of Nanomaterials*, vol. 2008, no. 1, Article ID 127538, 4 pages, 2008.
- [6] S. Berger, R. Porat, and R. Rosen, "Nanocrystalline materials: a study of WC-based hard metals," *Progress in Materials Science*, vol. 42, no. 1–4, pp. 311–320, 1997.
- [7] V. K. Sikka, in *Proceedings of the 5th Annual Conference on Fossil Energy Materials*, p. 197, Oak Ridge, Tenn, USA, 1991.
- [8] J. R. Knibloe, R. N. Wright, and V. K. Sikka, in *Advanced in Powder Metallurgy*, E. R. Andreotti and P. J. McGreehan, Eds., p. 219, Metal Powder Industries Federation, Princeton, NJ, USA, 1990.
- [9] S.-K. Bae, I.-J. Shon, J.-M. Doh, J.-K. Yoon, and I.-Y. Ko, "Properties and consolidation of nanocrystalline  $\text{NbSi}_2$ -SiC- $\text{Si}_3\text{N}_4$  composite by pulsed current activated combustion," *Scripta Materialia*, vol. 58, no. 6, pp. 425–428, 2008.
- [10] I.-J. Shon, D.-K. Kim, K.-T. Lee, and K.-S. Nam, "Properties and consolidation of nanostructured  $\text{Ce}_{0.8}\text{Gd}_{0.2}\text{O}_{1.9}$  by pulsed-current-activated sintering," *Metals and Materials International*, vol. 14, no. 5, pp. 593–598, 2008.
- [11] Z. Shen, M. Johnsson, Z. Zhao, and M. Nygren, "Spark plasma sintering of alumina," *Journal of the American Ceramic Society*, vol. 85, no. 8, pp. 1921–1927, 2002.
- [12] J. E. Garay, S. C. Glade, U. Anselmi-Tamburini, P. Asoka-Kumar, and Z. A. Munir, "Electric current enhanced defect mobility in  $\text{Ni}_3\text{Ti}$  intermetallics," *Applied Physics Letters*, vol. 85, no. 4, pp. 573–575, 2004.
- [13] J. R. Friedman, J. E. Garay, U. Anselmi-Tamburini, and Z. A. Munir, "Modified interfacial reactions in Ag-Zn multilayers under the influence of high DC currents," *Intermetallics*, vol. 12, no. 6, pp. 589–597, 2004.
- [14] J. E. Garay, U. Anselmi-Tamburini, and Z. A. Munir, "Enhanced growth of intermetallic phases in the Ni-Ti system by current effects," *Acta Materialia*, vol. 51, no. 15, pp. 4487–4495, 2003.
- [15] C. Suryanarayana and M. Grant Norton, *X-Ray Diffraction: A Practical Approach*, Plenum Press, New York, NY, USA, 1998.

- [16] Z. Shen, M. Johnsson, Z. Zhao, and M. Nygren, "Spark plasma sintering of alumina," *Journal of the American Ceramic Society*, vol. 85, no. 8, pp. 1921–1927, 2002.
- [17] J. E. Garay, S. C. Glade, U. Anselmi-Tamburini, P. Asoka-Kumar, and Z. A. Munir, "Electric current enhanced defect mobility in Ni<sub>3</sub>Ti intermetallics," *Applied Physics Letters*, vol. 85, no. 4, pp. 573–575, 2004.
- [18] J. R. Friedman, J. E. Garay, U. Anselmi-Tamburini, and Z. A. Munir, "Modified interfacial reactions in Ag-Zn multilayers under the influence of high DC currents," *Intermetallics*, vol. 12, no. 6, pp. 589–597, 2004.
- [19] J. E. Garay, U. Anselmi-Tamburini, and Z. A. Munir, "Enhanced growth of intermetallic phases in the Ni-Ti system by current effects," *Acta Materialia*, vol. 51, no. 15, pp. 4487–4495, 2003.
- [20] Z.-R. Zhang and W.-X. Liu, "Mechanical properties of Fe<sub>3</sub>Al-based alloys with addition of carbon, niobium and titanium," *Materials Science and Engineering A*, vol. 423, no. 1-2, pp. 343–349, 2006.

## Research Article

# Microstructure and Corrosion Behavior of Ni-Alloy/CrN Nanolayered Coatings

Hao-Hsiang Huang,<sup>1</sup> Fan-Bean Wu,<sup>1</sup> Jyh-Wei Lee,<sup>2</sup> and Li-Chun Chang<sup>2</sup>

<sup>1</sup>Department of Materials Science and Engineering, National United University, Miaoli 36003, Taiwan

<sup>2</sup>Department of Materials Science and Engineering, Ming Chi University of Technology, Taipei 24301, Taiwan

Correspondence should be addressed to Fan-Bean Wu, fbwu@nuu.edu.tw

Received 23 April 2010; Accepted 19 August 2010

Academic Editor: Bo Zou

Copyright © 2011 Hao-Hsiang Huang et al. This is an open access article distributed under the Creative Commons Attribution License, which permits unrestricted use, distribution, and reproduction in any medium, provided the original work is properly cited.

The Ni-alloy/CrN nanolayered coatings, Ni-Al/CrN and Ni-P/CrN, were deposited on (100) silicon wafer and AISI 420 stainless steel substrates by dual-gun sputtering technique. The influences of the layer microstructure on corrosion behavior of the nanolayered thin films were investigated. The bilayer thickness was controlled approximately 10 nm with a total coating thickness of 1  $\mu\text{m}$ . The single-layer Ni-alloy and CrN coatings deposited at 350°C were also evaluated for comparison. Through phase identification, phases of Ni-P and Ni-Al compounds were observed in the single Ni-alloy layers. On the other hand, the nanolayered Ni-P/CrN and Ni-Al/CrN coatings showed an amorphous/nanocrystalline microstructure. The precipitation of Ni-Al and Ni-P intermetallic compounds was suppressed by the nanolayered configuration of Ni-alloy/CrN coatings. Through Tafel analysis, the  $E_{\text{corr}}$  and  $I_{\text{corr}}$  values ranged from  $-0.64$  to  $-0.33$  V and  $1.42 \times 10^{-5}$  to  $1.14 \times 10^{-6}$  A/cm<sup>2</sup>, respectively, were deduced for various coating assemblies. The corrosion mechanisms and related behaviors of the coatings were compared. The coatings with a nanolayered Ni-alloy/CrN configuration exhibited a superior corrosion resistance to single-layer alloy or nitride coatings.

## 1. Introduction

Nanolayered thin film was recognized as a coating with alternating layers of two different materials with dissimilar physical, chemical, and related characteristics. With proper control of layer composition and microstructure, multilayered coatings could yield superior mechanical properties than monolayer ones [1–5]. Chromium nitride thin films have been investigated and demonstrated to exhibit good mechanical performance, thermal properties, and antioxidation behavior [6, 7]. Also, Ni-based alloy coatings were frequently adopted as protective alloy coatings due to their various merits, including corrosion resistance, toughness, and wear resistance [8–10]. The combination of these two materials systems to form a dual layer composite coating was a possible way to further the coating properties [11–13]. Several materials systems with nanolayer configuration, such as CrN/AlN, TiN/CrN, Ag/Pd, and Au/Ag, had been developed [1, 14–16]. However, limited literature on nitride/alloy coating systems were published. The integration

of CrN and Ni-alloy in a nanolayered feature was thus of great interest. Moreover, the control of the nanolayered configuration, layer microstructure, and related properties was not fully understood. In this study, Ni-P/CrN and Ni-Al/CrN nanolayered coatings were fabricated by dual-gun sputtering technique. The microstructure and phases of the multilayer coatings were controlled by process temperature during sputtering. The corrosion behavior of the multilayer coatings was investigated through electrochemical potentiodynamic analysis. The relationship between microstructure, phases, and corrosion behavior of the nanolayered Ni-P/CrN and Ni-Al/CrN coatings was discussed.

## 2. Experimental Details

The Ni-alloy/CrN nanolayered coatings were deposited on the silicon (100) and 420 stainless substrates by dual-gun sputtering technique. The Ni<sub>70</sub>Al<sub>30</sub> and Ni<sub>75</sub>P<sub>25</sub> (in at.%) sputtering targets of 50.8 mm in diameter were employed for alloy layer fabrication. The CrN coating was deposited

using a Cr target with 99.9% in purity and  $N_2$  gas as reactive source. Before deposition, the chamber was evacuated down to  $4.0 \times 10^{-4}$  Pa. The high purity Ar flow was introduced to a working pressure of  $2.7 \times 10^{-1}$  Pa. Presputtering was performed for 10 minutes to clean the target surface followed by the fabrication process. The target powers were D.C. 100 W for Ni-alloy and R.F. 200 W for Cr. The working pressure was  $2.7 \times 10^{-1}$  Pa for Ni-alloy fabrication, while a working pressure of  $6.7 \times 10^{-1}$  Pa was adopted for CrN due to the coinlet of  $N_2$  gas. The process temperature was fixed at  $350^\circ\text{C}$  for all coating assemblies. Nanolayered Ni-alloy/CrN coatings were prepared with fixed bilayer period of 10 nm. The deposition time of individual layer of multilayer Ni-alloy/CrN coatings during sequential sputtering were modified from 30 to 120 seconds. The total thickness of the multilayer coating systems was controlled around  $1.0 \mu\text{m}$ . The thickness ratio of Ni-alloy and CrN was fixed at 1.0. An X-ray diffractometer (Shimadzu, XRD-6000, Japan) with continuous  $\theta$ - $2\theta$  scan was used to identify the phases in the coatings. The  $2\theta$  scan ranged from  $30^\circ$  to  $65^\circ$  with a step width of  $0.02^\circ$  at a scanning speed of  $6^\circ/\text{min}$ . The microstructure and surface morphology of the coatings were evaluated by FE-SEM (JSM-6500, JEOL, Japan). The compositions of selected areas of corroded coatings were inspected by an energy dispersion spectra inspected analyzer (INCA Energy 350, Oxford, UK). The depth profile was measured by Auger electron nanoscope (PHI 700, ULVAC-PHI, Japan). The corrosion behavior was measured by an electrochemical workstation (Jiehan-5000, Jiehan, Taiwan). The corrosion test was operated in 3.5 M NaCl aqueous solution at room temperature with the saturated calomel electrode (SCE) as the reference electrode. The scanning range was from  $-0.25$  to  $+0.25$  V according to the open circuit potential of each sample. The potentiodynamic curves were fitted using CorrView software. For convenience, coatings deposited on Si substrates were applied in cross-sectional SEM observation, nano-Auger analysis, and XRD phase identification. Corrosion test and related analyses were conducted on coatings deposited on stainless steel substrates.

### 3. Results and Discussion

The cross-sectional view of the Ni-P/CrN and Ni-Al/CrN nanolayered coatings was presented in Figure 1. Smooth and dense coating configurations were recognized by sputtering fabrication process. The total thickness of all coatings estimated from FE-SEM images were about  $1 \mu\text{m}$ . In the magnified regions, as indicated in Figure 1, the smooth configuration of the Ni-P and CrN stacking was observed. A bilayer thickness of approximately 10 nm could be measured. To confirm the multilayer feature, the depth analysis of Ni-P/CrN nanolayered coating was conducted by nano-Auger technique. The sputter time was set to be 3 nm/min. The depth profile of Ni, P, Cr, and N showed a sequentially alternating distribution with a bilayer thickness around 10 nm, as shown in Figure 2. A nanolayered structure of the coating was again demonstrated. The X-ray patterns of single and nanolayer coatings were shown in Figure 3. The diffraction peaks of CrN (111), (200), and (220) were found

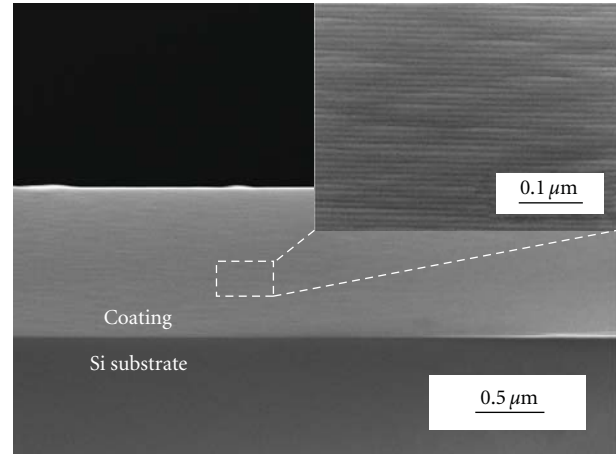


FIGURE 1: The cross-sectional FE-SEM images of NiP/CrN nanolayered coatings.

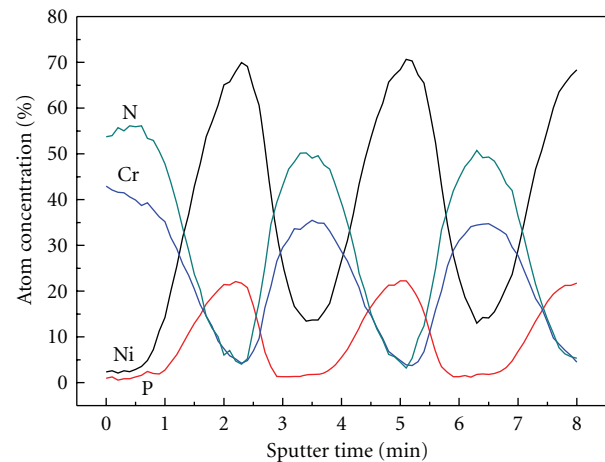


FIGURE 2: Nano-Auger depth analysis of NiP/CrN nanolayered coating.

for CrN coating. The  $Ni_3Al$  precipitation was identified in the single-layer Ni-Al coating, while the Ni crystalline phase and  $Ni_3P$  precipitation was discovered in the Ni-P coating. This indicated that sputtering process and substrate heating enhanced the precipitation of the Ni-P and Ni-Al coatings. It should be noted that the peaks of Ni-P and Ni-Al intermetallic compounds were not fully resolved according to their broadened peak widths. In the Ni-Al/CrN and Ni-P/CrN coatings, the diffraction peaks were further broadened that a nanocrystalline/amorphous microstructure was expected. Since the thickness of each layer was 5 nm, the precipitation of Ni-Al, Ni-P intermetallics, and CrN phases was restricted by nanolayer feature. In the Ni-Al/CrN coating, three major peaks of CrN were recognized. However, a few peaks of Ni crystallites found in single Ni-Al coating layer vanished. Similar situation was found for single Ni-P and nanolayered Ni-P/CrN coatings. It was believed that the precipitation of intermetallic compounds was suppressed by

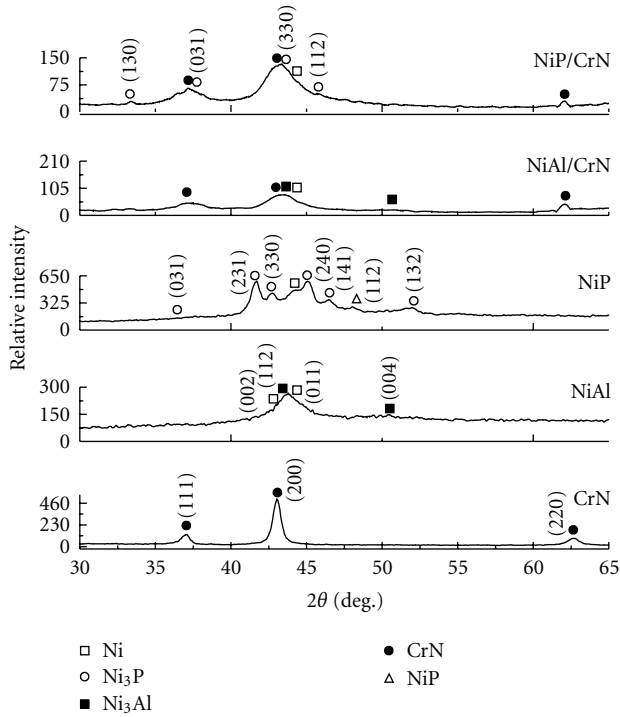


FIGURE 3: The XRD patterns of various coating systems.

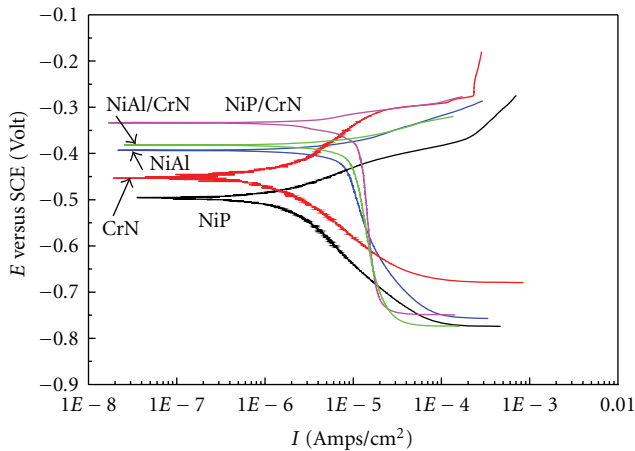


FIGURE 4: The electrochemical polarization curves of various coating systems.

nanolayered sequential deposition. To summarize, the Ni-Al and Ni-P single coatings exhibited precipitated structure, while nanolayered coatings showed CrN phases with Ni-alloy nanocrystalline layers.

The results of potentiodynamic analysis for various coating systems were indicated in Figure 4. The trend of corrosion resistance in different coatings systems could be discovered. The numerical results of  $I_{\text{corr}}$  and  $E_{\text{corr}}$  were listed in Table 1. The  $E_{\text{corr}}$  values were from  $-0.64$  to  $-0.33$  V. The  $I_{\text{corr}}$  values ranged from  $1.42 \times 10^{-5}$  to  $1.14 \times 10^{-6}$  A/cm<sup>2</sup>. All the coatings showed better corrosion potentials than that of AISI 420 substrate. Firstly, for the

TABLE 1: The  $E_{\text{corr}}$  and  $I_{\text{corr}}$  values of various coating systems.

Materials	$E_{\text{corr}}$ (V versus SCE)	$I_{\text{corr}}$ (A/cm <sup>2</sup> )
420 SS	$-0.64$	$1.42 \times 10^{-5}$
NiAl	$-0.39$	$1.20 \times 10^{-5}$
NiP	$-0.50$	$1.34 \times 10^{-6}$
CrN	$-0.45$	$1.14 \times 10^{-6}$
NiAl/CrN	$-0.38$	$1.18 \times 10^{-5}$
NiP/CrN	$-0.33$	$7.50 \times 10^{-6}$

\*The test was conducted in a 3.5 M NaCl solution at room temperature.

single-layer coatings, the Ni-Al coating showed the most nonnegative  $E_{\text{corr}}$  value of  $-0.39$  Volts. The Ni-P and Cr-N coatings exhibited the less  $I_{\text{corr}}$  values of  $1.14 \times 10^{-6}$  and  $1.34 \times 10^{-6}$ , respectively. This could be due to different corrosion behavior for the Ni-Al, Ni-P, and CrN coatings. For the Ni-Al coating, the corrosion occurred homogeneously and isotropically on coating surface [10]. On the other hand, the Ni-P and CrN showed in-depth pitting corrosion on localized areas [12, 17]. This could be referred to the corroded surface morphology of Ni-Al, Ni-P, and CrN, as shown in Figures 5(a), 5(b), and 5(c). Large but homogeneously distributed corroded areas were observed for the Ni-Al coating. On the contrary, localized small etching pits were found for Ni-P and CrN coatings, as indicated in Figures 5(b) and 5(c). Secondly, take Ni-Al, CrN, and Ni-Al/CrN coatings for comparison, the  $E_{\text{corr}}$  and  $I_{\text{corr}}$  values of these two coatings were similar. Figure 5(d) showed the surface morphology of Ni-Al/CrN coating. The pits were less than other single-layer coatings. However, the large  $I_{\text{corr}}$  of Ni-Al was not significantly decreased by nanolayered feature. Through EDX analysis, a few Fe concentration were detected in the single Ni-Al coating, indicating some of the Ni-Al was coating etched away. Nevertheless, in the Ni-Al/CrN coating, the substrate was well protected by the coating. The corrosion behavior of Ni-P, CrN, and Ni-P/CrN was also compared. The Ni-P/CrN exhibited a superior corrosion resistance than those of other thin films. It should be noted that the Ni-P coating exhibited a lowest  $E_{\text{corr}}$  value between all materials systems. The enhancement of nanolayered Ni-P/CrN as compared to CrN coating was evident. The surface morphology of Ni-P/CrN after corrosion test was shown in Figure 5(e). The etching pits were significantly reduced. The corrosion resistance was thus improved effectively for the combination of Ni-P and CrN coatings.

The corrosion behaviors of the nanolayered Ni-P/CrN and Ni-Al/CrN coatings were taken into comparison. Even the  $E_{\text{corr}}$  of Ni-P was lower than that of Ni-Al coating, as the Ni-P and Ni-Al were deposited with CrN to form nanolayered coatings, the corrosion resistance of Ni-P/CrN was better than that of Ni-Al/CrN nanolayered coating. This was because Ni-Al layer exhibited a severer layer area corrosion mechanism, while similar localized pitting corrosion was found for both Ni-P and CrN layers. Nevertheless, nanolayered coatings exhibited good protection from corrosion attacks. The corroded surface morphologies of two nanolayered coatings were shown in Figure 6. Though

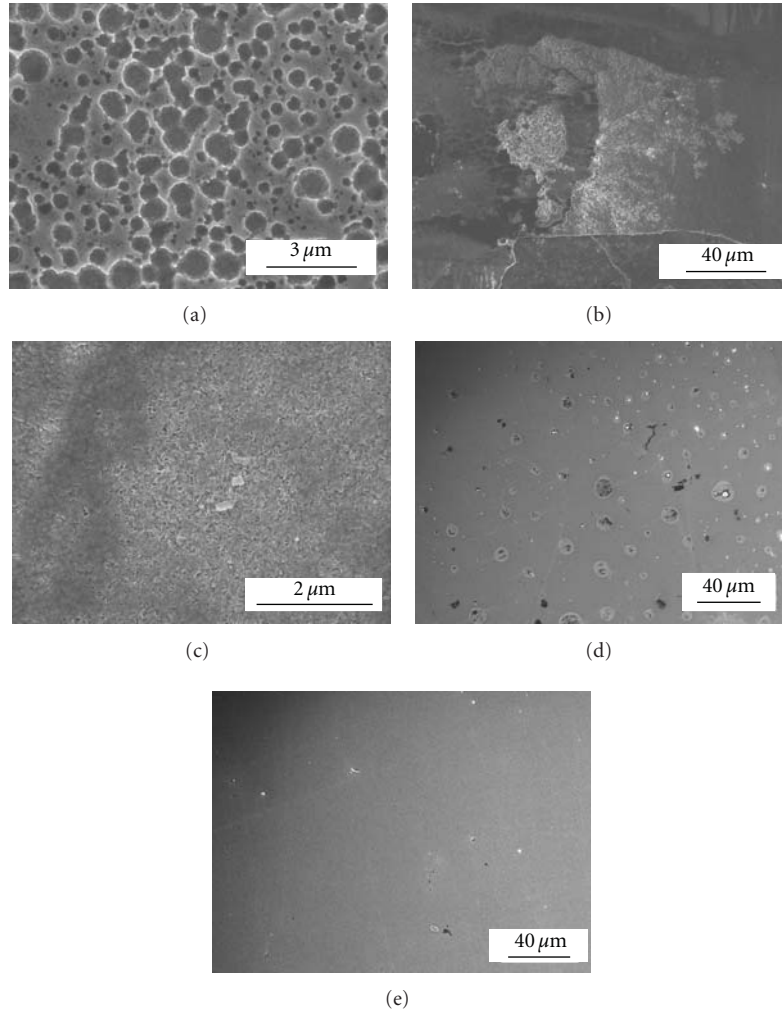


FIGURE 5: The SEM surface images of (a) NiAl, (b) NiP, (c) CrN, (d) NiAl/CrN nanolayered, and (e) NiP/CrN nanolayered coatings on stainless steel substrates after corrosion test.

etching pits were observed at localized area, the substrate was still well covered with coating. This phenomenon was consistent to the fitted results of potentiodynamic curves. Corrosion resistance was improved through Ni-P/CrN and Ni-Al/CrN nanolayered feature.

The corrosion mechanisms of the nanolayered coatings were shown in Figure 7. First, the corrosion resistance of Ni-Al/CrN nanolayered could be slightly improved by the nanolayer feature. Localized etching pits in CrN layers with homogenous corrosion behavior in the Ni-Al layer were expected for the Ni-Al/CrN coatings. In the Ni-P/CrN nanolayered coating, due to the pitting behavior of both Ni-P and CrN layers, the corrosion attack detoured in the interface and elongated the corrosion path. The corrosion resistance was thus improved by such configuration. To sum up, the combination of Ni-alloy and CrN to form a nanolayered coating was beneficial to corrosion protection in surface coatings. The introduction of inter-phase interface elongated the corrosion path and retarded the corrosion attack in the Ni-alloy/CrN nanolayered coatings.

#### 4. Conclusions

Nanolayered Ni-alloy/CrN coatings systems were successfully fabricated by dual-gun sputtering technique. The coatings showed smooth and dense structure, as revealed in FE-SEM cross-sectional images. The Ni-P/CrN and Ni-Al/CrN nanolayered layer coatings exhibited a nanocrystalline/amorphous microstructure because of the restricted precipitation by nanolayer feature. For the single-layer coatings, Ni-Al exhibited a homogeneously large area corrosion phenomenon, while localized pitting within limited regions was found for NiP and CrN coatings. Through Tafel analysis, the Ni-alloy/CrN nanolayered coating exhibited a superior corrosion resistance than monolayer coatings. Moreover, the Ni-P/CrN coating showed an even greater corrosion resistance due to its localized pitting corrosion behavior for both Ni-P and CrN layers. Through morphology observation, the nanolayered Ni-Al/CrN and Ni-P/CrN coatings maintained a solid integrity after corrosion test. The combination of Ni-P and CrN in a nanolayered coating structure to promote the corrosion resistance was demonstrated.

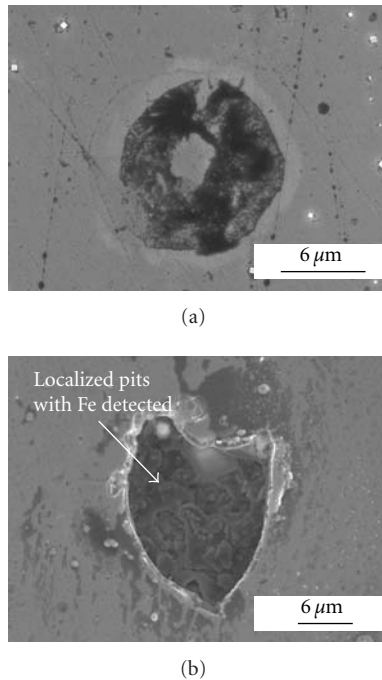


FIGURE 6: The SEM surface images of corroded regions of (a) NiP/CrN, (b) NiAl/CrN nanolayered coatings on stainless steel substrates.

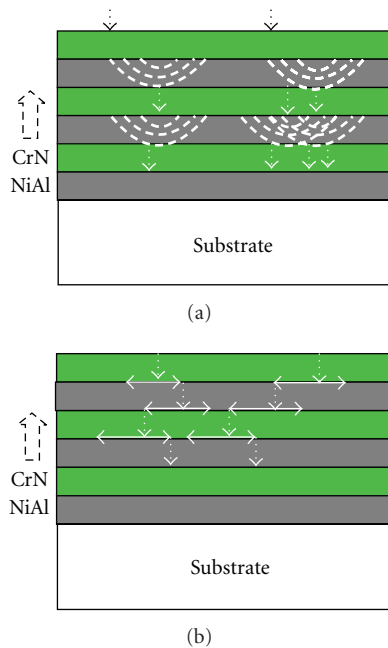


FIGURE 7: The schematic diagram of corrosion mechanism with (a) NiAl/CrN and (b) NiP/CrN nanolayered coatings.

## Acknowledgment

This work is supported by the National Science Council, Taiwan, under Contracts nos. NSC-97-2221-E-239-008 and NSC 98-2221-E- 239-009-MY3.

## References

- [1] S.-K. Tien, J.-G. Duh, and J.-W. Lee, "Oxidation behavior of sputtered CrN/AlN multilayer coatings during heat treatment," *Surface and Coatings Technology*, vol. 201, no. 9–11, pp. 5138–5142, 2007.
- [2] Y.-Z. Tsai and J.-G. Duh, "Thermal stability and microstructure characterization of CrN/WN multilayer coatings fabricated by ion-beam assisted deposition," *Surface and Coatings Technology*, vol. 200, no. 5-6, pp. 1683–1689, 2005.
- [3] P. C. Yashar and W. D. Sproul, "Nanometer scale multilayered hard coatings," *Vacuum*, vol. 55, no. 3, pp. 179–190, 1999.
- [4] M.-S. Wong, G.-Y. Hsiao, and S.-Y. Yang, "Preparation and characterization of AlN/ZrN and AlN/TiN nanolaminate coatings," *Surface and Coatings Technology*, vol. 133-134, pp. 160–165, 2000.
- [5] D. C. Cameron, R. Aimo, Z. H. Wang, and K. A. Pischow, "Structural variations in CrN/NbN superlattices," *Surface and Coatings Technology*, vol. 142-144, pp. 567–572, 2001.
- [6] I. Milošev, H.-H. Strehblow, and B. Navinšek, "XPS in the study of high-temperature oxidation of CrN and TiN hard coatings," *Surface and Coatings Technology*, vol. 74-75, no. 2, pp. 897–902, 1995.
- [7] J.-N. Tu, J.-G. Duh, and S.-Y. Tsai, "Morphology, mechanical properties, and oxidation behavior of reactively sputtered Cr-N films," *Surface and Coatings Technology*, vol. 133-134, pp. 181–185, 2000.
- [8] A. Kawashima, H. Habazaki, and K. Hashimoto, "Highly corrosion-resistant Ni-based bulk amorphous alloys," *Materials Science and Engineering A*, vol. 304-306, no. 1-2, pp. 753–757, 2001.
- [9] G. Lu and G. Zangari, "Corrosion resistance of ternary Ni-P based alloys in sulfuric acid solutions," *Electrochimica Acta*, vol. 47, no. 18, pp. 2969–2979, 2002.
- [10] J. G. González-Rodríguez, J. C. Colín, S. Serna, B. Campillo, and J. L. Albarran, "Effect of macroalloying with Cu on the corrosion resistance of rapidly solidified NiAl intermetallic in 0.5 M H<sub>2</sub>SO<sub>4</sub>," *Materials Science and Engineering A*, vol. 448, no. 1-2, pp. 158–164, 2007.
- [11] F.-B. Wu, J.-J. Li, and J.-G. Duh, "Evaluation of the mechanical properties and tribological behavior of the CrN coating deposited on mild steel modified with electroless Ni interlayer," *Thin Solid Films*, vol. 377-378, pp. 354–359, 2000.
- [12] J.-S. Chen, J.-G. Duh, and F.-B. Wu, "Microhardness and corrosion behavior in CrN/electroless Ni/mild steel complex coating," *Surface and Coatings Technology*, vol. 150, no. 2-3, pp. 239–245, 2002.
- [13] F.-B. Wu and J.-G. Duh, "Scratch behavior and in situ acoustic emission analysis of PVD chromium nitride coatings on mild steel with electroless nickel interlayers," *Surface and Coatings Technology*, vol. 162, no. 1, pp. 106–112, 2003.
- [14] Q. Yang and L. R. Zhao, "Thermal stability of polycrystalline TiN/CrN superlattice coatings," *Journal of Vacuum Science and Technology A*, vol. 21, no. 3, pp. 558–562, 2003.
- [15] A. Bukaluk, "Auger electron spectroscopy investigations of the effect of degradation of depth resolution and its influence on the interdiffusion data in thin film Au/Ag, Cu/Ag, Pd/Au and Pd/Cu multilayer structures," *Applied Surface Science*, vol. 175-176, pp. 790–796, 2001.
- [16] A. Bukaluk, "Influence of depth resolution on the interdiffusion data in thin film bilayer and multilayer Ag/Pd structures," *Vacuum*, vol. 63, no. 1-2, pp. 119–126, 2001.

- [17] M. Ürgen and A. F. Çakir, "The effect of heating on corrosion behavior of TiN- and CrN-coated steels," *Surface and Coatings Technology*, vol. 96, no. 2-3, pp. 236–244, 1997.

## Research Article

# Study of the P-Type Doping Properties of ZnS Nanocrystals

**Xiying Ma**

*School of Mathematics and Physics, Suzhou University of Science and Technology, 1701 Binhe Road, Suzhou, Jiangsu 215011, China*

Correspondence should be addressed to Xiying Ma, [maxy@usx.edu.cn](mailto:maxy@usx.edu.cn)

Received 24 April 2010; Accepted 11 July 2010

Academic Editor: Quanqin Dai

Copyright © 2011 Xiying Ma. This is an open access article distributed under the Creative Commons Attribution License, which permits unrestricted use, distribution, and reproduction in any medium, provided the original work is properly cited.

The paper presents the study of p-type doping properties of ZnS nanocrystals (Ncs) using the local density approximation theory (LDA). Doping with single species of N, P, or As, ZnS nanocrystals are found to have a low-doping concentration and efficiency, which may be limited by the large expelling effect between Zn and impurity atoms and the compensation action from interstitial  $Zn_{int}$  atoms that can offer donor states to compensate the acceptors. To decrease the expelling and the compensation effect, composite dopants, such as N jointed with Ga, In, or Al, are applied to codope ZnS nanocrystals. As a result, ZnS nanocrystals in p-type with high doping density and efficient are completed.

## 1. Introduction

ZnS nanocrystals, with unique optical properties and a direct band gap of 3.68 eV at room temperature, have great potential applications in fabrication of short-wavelength light-emitting devices (LED) and blue injection-laser diodes (LD) [1–3]. To fabricate nanoscaled devices, semiconductor nanocrystals need to be doped in p-, n-types firstly. And the performance of devices depends on the doping types and doping concentration [4]. Doping with other special impurities, semiconductors will not only enhance their conductivity significantly but also exhibit many novel photoelectric properties [5–7]. For semiconductor nanocrystals, however, the doping concentration and steady are much low than that of the bulk materials. The volume of nanocrystals is so small that it limits the doping concentration and allows the doped impurities to easily escape from it.

Also, doping with other metallic ions, the photoelectric properties of ZnS nanocrystals will be widely adjusted and improved [8]. However, it is found that they are easily doped for n-type but hard for p-type [9]. This occurs because a Zn atom in ZnS very easily departs from its lattice site to become an interstitial  $Zn_{int}$  atom, which makes ZnS displaying an intrinsic property of n-type. On the other hand, from the point of system energy, n-type doping will low the system energy while p-type doping will raise

it based on the calculation of the first-principle. At the same time,  $Zn_{int}$  atoms will lift the lattice energy as well. Therefore, ZnS nanocrystals have more difficult in p-type doping [10, 11]. Now, this problem has become a large barrier for their practical use and delayed the development of new nanodevices. Many theoretical and experimental works have been done on the doping problems for ZnS nanocrystals, especially for p-type doping [12–14]. Although some succeeded, the doping concentration and steady still do not meet the requirement of devices. In the present study, we investigate the p-type doping properties of ZnS nanocrystals doped with single dopants of N, P, or As and composite dopants of N:Ga, N:In, or N:Al. Using the local density approximation (LDA) method, we study the activity and doping efficiency of all dopants, and discuss the doping mechanisms and the compensation properties based on the calculated density of states of ZnS. Finally, p-type ZnS nanocrystals with enhanced doping concentration and efficiency are realized.

## 2. Theoretical Model

*2.1. Local Density Approximation Theory (LDA).* According to Schrodinger equation in quantum mechanics,

$$H\Psi = E\Psi, \quad (1)$$

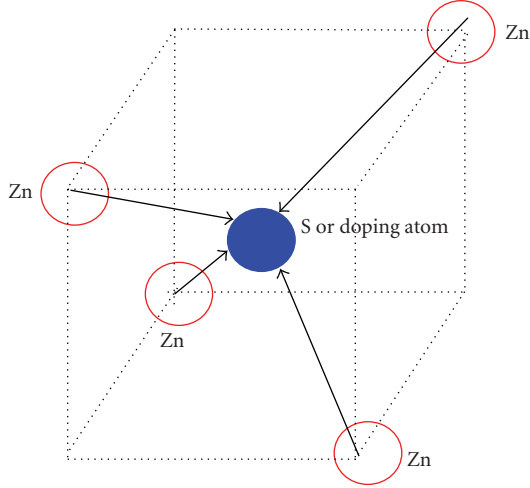


FIGURE 1: (a) A schema of ZnS structure. The red circles and blue spheres stand for Zn and S atom, respectively.

where,  $H$  is Hamiltonian operator,  $E$  is the system energy, and  $\Psi$  describes the state of the system with  $N$  electrons.

$$H = -\frac{1}{2}\nabla^2 - \sum_q \frac{Z_q}{|\vec{r} - \vec{R}_q|} + \frac{\rho(\vec{r})}{|\vec{r} - \vec{r}'|} dr' + V_{xc}(\vec{r}). \quad (2)$$

The density of state (DOS)  $\rho(r)$  of electrons can be written as [1, 11]

$$\Psi_i^k(\vec{r}) = e^{ik \cdot \vec{r}} \sum_g c_i^k(g) e^{ik \cdot \vec{r}}, \quad (3)$$

$$\rho(\vec{r}) = \sum_i n_i \Psi_i^*(\vec{r}) \Psi(\vec{r}). \quad (4)$$

Equation (4) is a local-density approximation (LDA) of  $\rho(r)$ , by which the DOS of a doped ZnS cluster can be calculated.

**2.2. Structure of ZnS and the Simulation Method.** ZnS is characteristic of a zincblende structure with a lattice constant of 0.5046 nm, as shown in Figure 1. Four Zn atoms are located at the corners of a cube forming a tetrahedron; an S atom is positioned at the zenith of the tetrahedron. For p-type doping, S atom is substituted with either N, P, or As single dopants from Column V to offer more vacancy. To decrease the compensation effect from  $Zn_{\text{int}}$  atoms, the composite dopants of N:Ga, N:In, or N:Al are used to codope ZnS nanocrystals as well. For a comparison, the density of state (DOS) and the electronic structures of ZnS nanocrystals with and without doping were investigated using LDA method. In the simulation, we adopt a Von Barth-Hedin exchange correlation potential with the parameters used by Von Barth and Hedin [15]. Brillouin zone integration was carried out for 84-k points in an irreducible wedge and for 24-k points for doped crystals. For valence electrons, we employed  $p$  and  $d$  orbitals for Zn atoms and the outer most  $s$  and  $p$  orbitals for other atoms. From the calculated DOSs, we determined the valence bands, the impurity level and the doping concentration.

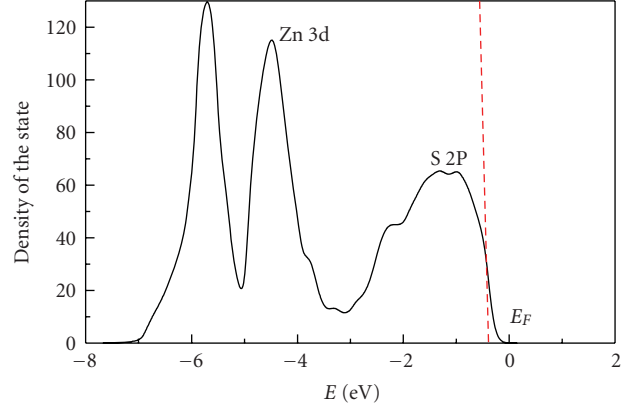


FIGURE 2: The density of state of ZnS nanocrystal without doping.

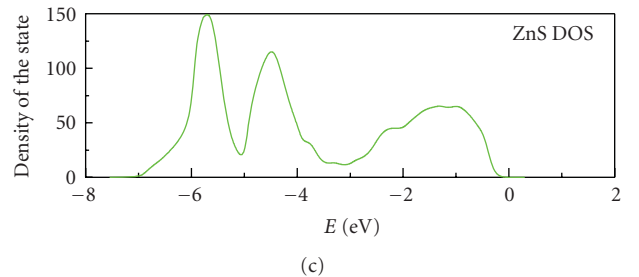
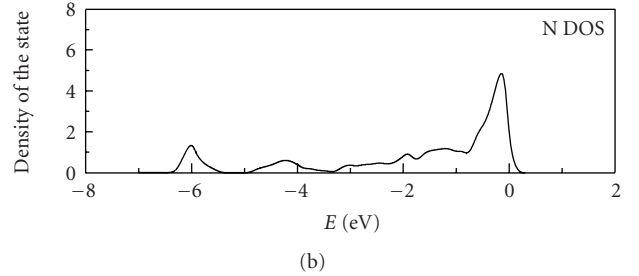
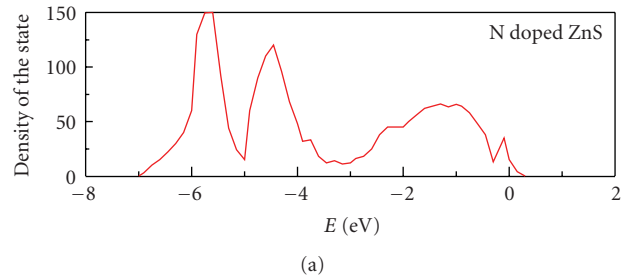


FIGURE 3: (a) DOS of ZnS nanocrystals doped with N atom; (b) DOS of N atom; (c) DOS of the undoped ZnS nanocrystals.

### 3. Results and Discussion

**3.1. Single Doping.** For undoped ZnS nanocrystals, the calculated DOS is shown in Figure 2, where energy is measured from Fermi level ( $E_F$ ), thus the energy zero point is located on top of the valence band. As can be seen, there are three strong bands in the spectrum: the first one is from  $-6.5$  eV to  $-5.0$  eV with a strong character of  $d$ , mostly originating from the  $d$  state of Zn atoms; the second one is a sharp

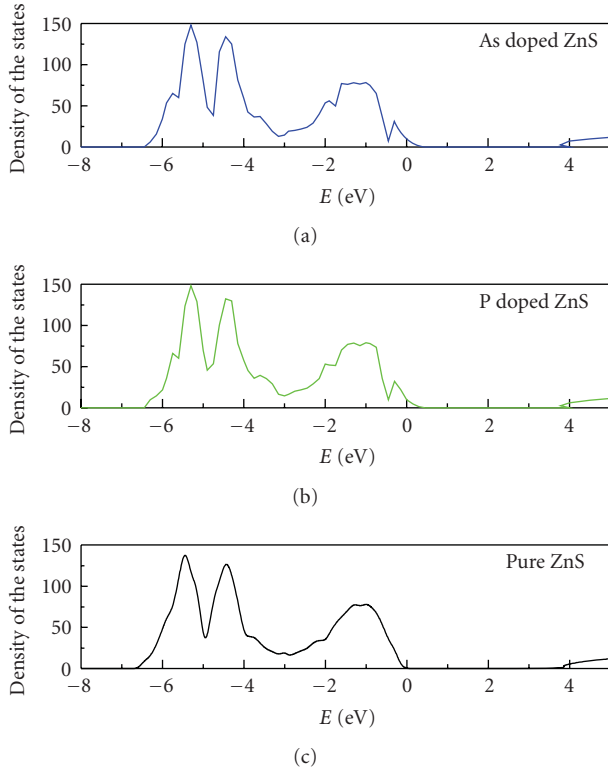


FIGURE 4: DOS spectra of ZnS nanocrystals doped with P, and As atoms.

band located at  $-5.1$  eV to  $-4.0$  eV, mainly contributed by the  $3p$  state S atoms; the third one in the range of  $-3$  eV to  $0$  eV is just nearby the valence band, resulting from a strong hybrid interaction between S  $2p$  and Zn  $2s$  states. The hybrid interaction occurs because the  $3s$ ,  $3p$  states of S atoms overlap with  $4s$  state of Zn atoms, leading to the  $s$  and  $p$  states of Zn atoms shifting to S sites, along with charges are transferred from Zn atoms to S atoms.

For N doped ZnS nanocrystals, the DOS spectrum is shown in Figure 3(a). For comparison, the DOSs of single N atom and the undoped ZnS are shown in Figures 3(b) and 3(c), respectively. Clearly, in addition to the three bands of the undoped ZnS, after doping a small narrow band at  $-0.1$  eV appears on top of the valence band. The narrow band is introduced by N impurities, termed as an acceptor level. From the small band, we can estimate the relative doping density of N to be  $10^{13}$   $\text{cm}^{-3}$ . It shows that ZnS nanocrystals doped with single N have low doping concentration and efficiency. This may be caused by the expelling effect of holes between the valence band and N impurities. The expelling force will localize the state of N on top of the valence band, leading to N atoms hard to ionize. In addition, the doping efficiency is affected by the compensation action of  $\text{Zn}_{\text{int}}$  atoms, which gives rise to multi ionizations: the first and the second ionizing energies of  $\text{Zn}_{\text{int}}$  are  $0.05$  eV and  $0.2$  eV. They offer two donor states that can compensate the acceptors. Thus, the doping efficiency is not high.

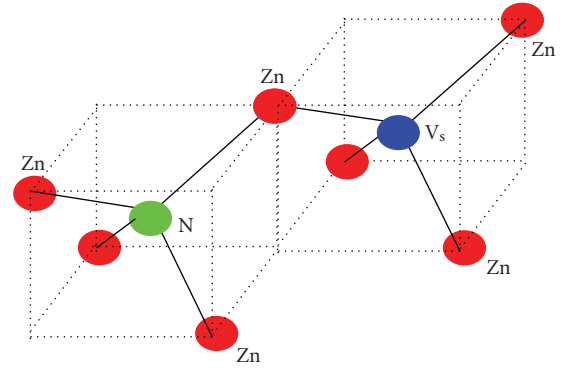


FIGURE 5: A schematic of complex defects in ZnS structure, it involves two unit cells.

For P and As dopants, similarly, a narrow acceptor level is introduced on top of the valence band of ZnS, as shown in Figures 4(a) and 4(b), respectively. Also, because of the strong expelling interaction between  $2p$  states of P or As and Zn atoms, the acceptor levels are localized nearby  $E_F$  level. Thus, the activity of the dopants is depressed, and the doping efficiency decreases as well.

For the doped structures of the three dopants, here referred to as  $\text{N}_S$ ,  $\text{P}_S$ , and  $\text{As}_S$ , we found that  $\text{N}_S$  is quite different from those of  $\text{P}_S$  and  $\text{As}_S$ . An  $\text{N}_S$  atom is positioned at the center of the tetrahedron, and the structure remains symmetrical but its volume shrinks by  $0.48$ .  $\text{P}_S$  and  $\text{As}_S$  atoms shift to the bottom of the relaxed structures by  $0.11$  Å and  $0.13$  Å, respectively. The volume for  $\text{P}_S$  shrinks by  $0.13$  but for  $\text{As}_S$  is almost unchanged. The shifts for  $\text{P}_S$  and  $\text{As}_S$  cause some distortion in the relaxed structures, which low the symmetry of the doped structures. Thus, the structure of  $\text{N}_S$  doped ZnS nanocrystals is the most stable one.

For further increasing the doping concentration of single species, we found that the doping efficiency changes little, that is, the doping efficiency is not limited by the doping concentration but the expelling effect and the compensation action. The latter will become dominative as the doping concentration increases.

Zn atoms very easily deviate from the lattice sites to become interstitial  $\text{Zn}_{\text{int}}$  atoms, which may combine with dopants to form complex defects. For N-doped ZnS, the complex defect is denoted as  $\text{N}_S\text{-Zn}_{\text{int}}$ , where  $\text{N}_S$  means an N atom replacing an S atom in the structure. On the other hand, for heavily p-type doped ZnS nanocrystal, to achieve a stable structure some adjacent point defects may combine together to form complex defects as well, such as  $\text{N}_S\text{-Zn-V}_S$ , where  $\text{N}_S$  and  $\text{V}_S$  atoms are bonded through a Zn atom. We therefore have two complex defect models:  $\text{N}_S\text{-Zn}_{\text{int}}$  and  $\text{N}_S\text{-Zn-V}_S$ . The latter is associated with two neighboring ZnS unit cells, as shown in Figure 5. These complex defects are different from the point defects.  $\text{N}_S\text{-Zn-N}_S$  produces a deep acceptor level while  $\text{N}_S\text{-Zn}_{\text{int}}$  forms a donor level in the band gap of ZnS, both play an important compensation action for p-type doping of ZnS, which makes the p-type doping of ZnS more complex [16, 17].

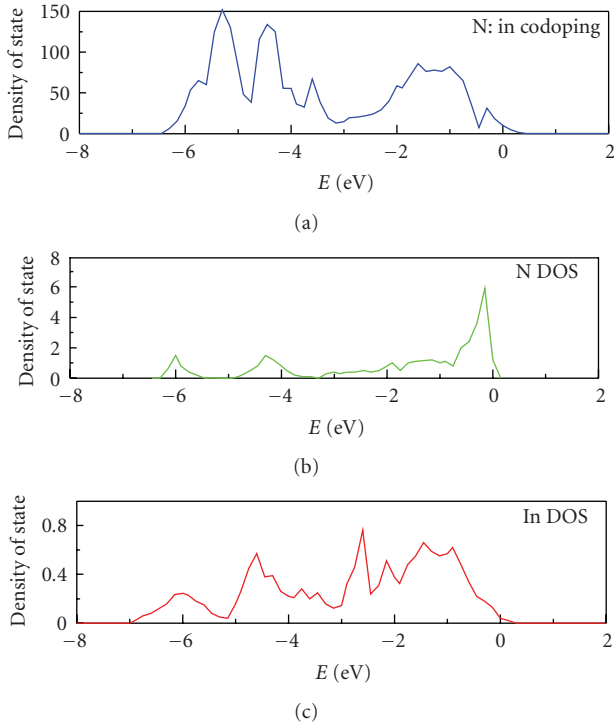


FIGURE 6: (a) DOS of ZnS nanocrystals codoped with N:In elements; (b) DOS of N atom; (c) DOS of In atom.

Above all, due to the expelling and compensation effects, single dopants in Column V cannot achieve the p-type doping for ZnS. The compensation effect is an inherent behavior of ZnS, which can be depressed at low doping concentration. From the point of energy view, the system energy falls with the expelling potential decreasing, and then the compensation is depressed as well. To achieve the p-type doping, therefore, it is necessary to enhance the activity of the acceptors and decrease the expelling effect.

**3.2. Codoping.** Yamamoto et al. [11] studied the p-type doping properties for ZnO with various dopants using LDA, and found that it could be achieved with ally dopants from Column III-V. ZnS will have a similar doping behavior to ZnO for both of them belonging to II-VI semiconductors. Hence, we apply the composite dopants, N:Ga, Al, or In, to codope ZnS Ncs. Figure 6(a) gives the DOS spectrum for ZnS Ncs doped with N:In. As references the DOSs for single N and In elements are shown in Figures 6(b) and 6(c), respectively. Apparently, the DOS of the codoped ZnS is different from that of the single species. Besides the three bands originated from ZnS, a new band at  $-3.67$  eV, closely to In site appeared. Moreover, the acceptor level on top of the valence band becomes much wider than that of the single species. The new band results from the strong interaction between N  $2p$  and In  $3s$  states, meaning a strong coupling action between N and In atoms. This coupling action just cancels the expelling effect between N  $2p$  and Zn  $3p$  states, and increases their orbitals hybridizing. The decreased expelling

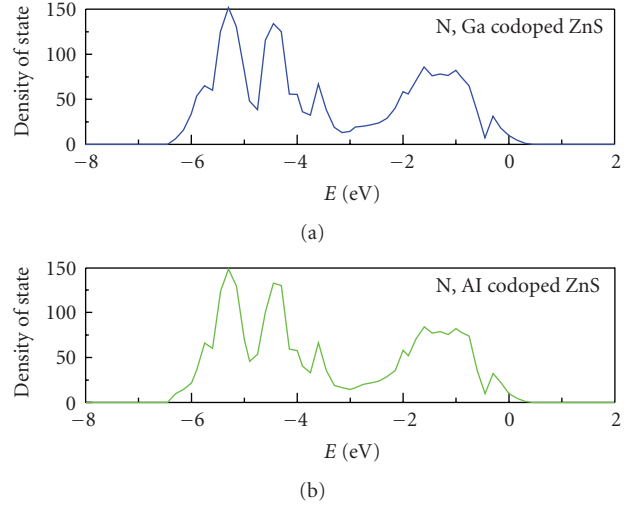


FIGURE 7: (a) DOS of ZnS nanocrystals codoped with N:Ga elements. (b) DOS of ZnS nanocrystals codoped with N:Al elements.

lowers the system energy and the compensation effect; the relative doping concentration of N:Ga can be enhanced to  $10^{16} \text{ cm}^{-3}$ . As a result, the doping efficiency of N is improved.

For N:Ga and N:Al codopants, the DOSs are shown in Figures 7(a) and 7(b), respectively. Similarly, a small new band is located at  $-3.70$  eV resulting from the interaction between N  $2p$  and Ga or Al  $3s$  states. And the acceptor levels on top of valence bands become wider as well. Apparently, the dopants of Ga, Al, or In play a role for activating single species than recombination centers. Among the three dopants, Ga shows the best doping efficiency. Finally, using the composite dopants of N with Column III elements, p-type ZnS with high doping efficiency is completed.

## 4. Conclusions

Using the LDA method, we investigate the p-type doping properties of ZnS nanocrystals doped with both single dopants N, P, or As and the composite dopants N:Ga, In, or Al. For single dopants, the doping efficient is not very high because of the strong compensation of interstitial  $\text{Zn}_{\text{int}}$  and the expelling potential between Zn atom and N impurity, which low the solid concentration in ZnS nanocrystals and restrain the active of the acceptors. For the composite dopants N:Ga, In, or Al, the expelling effect between N and Zn atoms decreases, and the concentration of N impurity is enhanced. Finally, p-type ZnS nanocrystal with high doping efficiency is achieved.

## Acknowledgments

The research work was supported in part by the National Natural Science Foundation (nos. 60776004, 60976071) and the Scientific Project of Shaoxing City (no. 2009A21054).

## References

- [1] T. Yamamoto, S. Kishimoto, and S. Iida, "Materials design for p-type ZnS with blue Ag emission by triple-codoping method," *Physica Status Solidi B*, vol. 229, no. 1, pp. 371–375, 2002.
- [2] H.-J. Jeon and Y. S. Kang, "Synthesis of ZnS:Mn<sup>2+</sup> nanocrystals and luminescence properties of ldpe film containing ZnS:Mn<sup>2+</sup>," *International Journal of Nanoscience*, vol. 1, no. 5-6, pp. 495–499, 2002.
- [3] Y. Y. Chen, J. G. Duh, B. S. Chiou, and C. G. Peng, "Luminescent mechanisms of ZnS:Cu:Cl and ZnS:Cu:Al phosphors," *Thin Solid Films*, vol. 392, no. 1, pp. 50–55, 2001.
- [4] J. R. Heath, "The chemistry of size and order on the nanometer scale," *Science*, vol. 270, no. 5240, pp. 1315–1316, 1995.
- [5] G. D. Yuan, W. J. Zhang, J. S. Jie et al., "p-type ZnO nanowire arrays," *Nano Letters*, vol. 8, no. 8, pp. 2591–2597, 2008.
- [6] H. S. Kang, B. D. Ahn, J. H. Kim et al., "Structural, electrical, and optical properties of p-type ZnO thin films with Ag dopant," *Applied Physics Letters*, vol. 88, no. 20, Article ID 202108, 2006.
- [7] G. D. Yuan, Z. Z. Ye, L. P. Zhu et al., "Control of conduction type in Al- and N-codoped ZnO thin films," *Applied Physics Letters*, vol. 86, no. 20, Article ID 202106, pp. 1–3, 2005.
- [8] T. Kezuka, M. Konishi, T. Isobe, and M. Senna, "Preparation and properties of nanocrystalline ZnS:Mn-polymer composite films," *Journal of Luminescence*, vol. 87, pp. 418–420, 2000.
- [9] L. Svob, C. Thiandoume, A. Lussion, M. Bouanani, Y. Marfaing, and O. Gorochov, "p-type doping with N and Li acceptors of ZnS grown by metalorganic vapor phase epitaxy," *Applied Physics Letters*, vol. 76, no. 13, pp. 1695–1697, 2000.
- [10] S. Kishimoto, A. Kato, A. Naito, Y. Sakamoto, and S. Iida, "Attempts of homo p-n junction formation in ZnS by impurity Co-doping with vapor phase epitaxy," *Physica Status Solidi B*, vol. 229, no. 1, pp. 391–393, 2002.
- [11] T. Yamamoto, S. Kishimoto, and S. Iida, "Control of valence states for ZnS by triple-codoping method," *Physica B*, vol. 308–310, pp. 916–919, 2001.
- [12] S. Kishimoto, T. Hasegawa, H. Kinto, O. Matsumoto, and S. Iida, "Effect and comparison of co-doping of Ag, Ag + In, and Ag + Cl in ZnS:N/GaAs layers prepared by vapor-phase epitaxy," *Journal of Crystal Growth*, vol. 214, pp. 556–561, 2000.
- [13] G. D. Yuan, W. J. Zhang, W. F. Zhang, et al., "p-type conduction in nitrogen-doped ZnS nanoribbons," *Applied Physics Letters*, vol. 93, no. 21, p. 3, 2008.
- [14] L. Svob, C. Thiandoume, A. Lussion, M. Bouanani, Y. Marfaing, and O. Gorochov, "p-type doping with N and Li acceptors of ZnS grown by metalorganic vapor phase epitaxy," *Applied Physics Letters*, vol. 76, no. 13, pp. 1695–1697, 2000.
- [15] U. Von Barth and L. Hedin, "A local exchange-correlation potential for the spin polarized case. I," *Journal of Physics C*, vol. 5, no. 13, article no. 012, pp. 1629–1642, 1972.
- [16] P. Schröer, P. Krüger, and J. Pollmann, "First-principles calculation of the electronic structure of the wurtzite semiconductors ZnO and ZnS," *Physical Review B*, vol. 47, no. 12, pp. 6971–6980, 1993.
- [17] A. V. Singh, R. M. Mehra, A. Wakahara, and A. Yoshida, "p-type conduction in codoped ZnO thin films," *Journal of Applied Physics*, vol. 93, no. 1, pp. 396–399, 2003.

## Research Article

# Structural and Mechanical Properties of CrN<sub>x</sub> Coatings Deposited by Medium-Frequency Magnetron Sputtering with and without Ion Source Assistance

Can Xin Tian,<sup>1</sup> Bing Yang,<sup>2</sup> Jun He,<sup>1</sup> Hong Jun Wang,<sup>1</sup> and De Jun Fu<sup>1</sup>

<sup>1</sup> Department of Physics and Key Laboratory of Artificial Micro- and Nano-Materials of Ministry of Education, Wuhan University, 430072 Wuhan, China

<sup>2</sup> School of Power and Mechanical Engineering, Wuhan University, 430072 Wuhan, China

Correspondence should be addressed to De Jun Fu, djfu@whu.edu.cn

Received 4 May 2010; Revised 27 June 2010; Accepted 2 August 2010

Academic Editor: Bo Zou

Copyright © 2011 Can Xin Tian et al. This is an open access article distributed under the Creative Commons Attribution License, which permits unrestricted use, distribution, and reproduction in any medium, provided the original work is properly cited.

CrN<sub>x</sub> coatings were deposited on Si (100) and WC-Co substrates by a home-made medium-frequency magnetron sputtering system with and without thermal filament ion source assistance. The structure and composition of the coatings were characterized by X-ray diffraction, atomic force microscopy, scanning electron microscopy, and transmission electron microscopy. The mechanical and tribological properties were assessed by microhardness and pin-on-disc testing. The ion source-assisted system showed a deposition rate of 3.88 μm/h, much higher than the value 2.2 μm/h without ion source assistance. The CrN<sub>x</sub> coatings prepared with ion source assistance exhibited an increase in microhardness (up to 16.3 GPa) and a decrease in friction coefficient (down to 0.48) at the optimized cathode source-to-substrate distance.

## 1. Introduction

Transition metal nitrides, especially chromium nitride (CrN), have been studied extensively due to their unique properties, including high hardness, good wear resistance, as well as excellent corrosion and high-temperature oxidation resistance [1–4]. They are widely applied in industry as protective coatings [5–7]. Recent studies also revealed magnetic properties in CrN, and it might find applications in the electronic industries [8, 9]. Many methods have been used for the deposition of CrN films, among which unbalanced magnetron sputtering produces good quality samples at high-deposition rates [2]. The pulsed DC reactive magnetron sputtering technique was characterized by improved ionization and a high ion-to-neutral particle ratio during deposition to enhance the quality of coatings [10], but more importantly it increased the kinetic energy of the ions in the plasma, which can enhance the ion bombardment of the substrate and film [11–14]. Therefore, high-quality CrN coatings have been prepared by pulsed dc magnetron sputtering [15, 16], and the high-power pulsed

magnetron sputtering has also been developed for deposition of CrN coatings [17, 18]. It is known that low ionization efficiency in the plasma is a hurdle of magnetron sputtering; therefore, plasma or ion sources have been developed to improve ionization efficiency [19, 20]. In particular, Wei et al. reported dense and thick films of transition metal nitrides, including ZrN and TiN, by means of plasma-enhanced magnetron sputtering, where an electron source of thermal filament type is a key technology [21, 22]. In order to prepare thick protective coatings with high deposition rate, high microhardness, and ideal surface chemistry, it is necessary to introduce high-density plasma in pulsed dc magnetron sputtering systems.

In this paper, we have prepared CrN<sub>x</sub> coatings at various magnetron cathode source-substrate distances by medium-frequency (40 kHz) magnetron sputtering with a thermal filament ion source and conducted characterization in comparison with samples prepared without the use of the ion source. We intended to find out the influence of cathode source-to-substrate distances and ion source on the deposition rate, microstructural, mechanical, and

tribological properties. Then, we have optimized the source-substrate distance at which the ion source best assists the deposition process, producing  $\text{CrN}_x$  coatings with superior properties.

## 2. Experiment Details

The  $\text{CrN}_x$  coatings were deposited by using a modified closed field twin unbalanced magnetron sputtering system. The vacuum chamber is  $\phi 400 \times 500$  mm in dimension. The ion source was powered by a supply of 20 A and 24 V and was mounted in the middle-upper area of the chamber. Cr sheets with a purity of 99.99% and an area of  $10 \times 40$  cm<sup>2</sup> were used as a cathode source material. Prior to deposition, a base pressure was less than  $5 \times 10^{-3}$  Pa. For substrates, p-type Si (100) and mirror-polished WC-Co plates were ultrasonically cleaned in acetone and methanol, rinsed in de-ionized water, and dried in  $\text{N}_2$  before being loaded into the deposition chamber. Then, they were ion etched for 30 min in Ar atmosphere at a pressure of 2.0 Pa and a negative bias voltage of 800 V applied to the substrate holder.  $\text{N}_2$  (99.99%) and Ar (99.99%) were used as working gases. First, a layer of pure Cr (about 230 nm) was deposited onto the substrate for 5 min in Ar ambient at 0.25 Pa and  $-100$  V to improve the adhesion. Then,  $\text{N}_2$  was let in, and Ar flow rate was tuned to keep an Ar: $\text{N}_2$  ratio of 1:1. The total pressure was kept at 0.25 Pa, and the substrate bias was fixed at  $-100$  V. The medium-frequency power used was 7.0 kW, and cathode source-substrate distance was varied between 50 and 140 mm. The substrates temperature was kept at  $150^\circ\text{C}$ . The ion source was a tungsten filament which emitted electrons when heated by a high current and could produce ions of argon gas fed to the outlet of the filament source. The ion source was installed at the upper part of the chamber, similar to the configuration described in the literature [23].

The crystal structure of the deposited  $\text{CrN}_x$  coatings was characterized by X-ray diffraction (XRD, Bruker-Axs D8 advanced which was operated at voltage and current of 40 kV and 40 mA, resp.) with a Cu  $\text{K}\alpha$  radiation and JEOL JEM 2010 transmission electron microscopy (TEM). The deposition rate was evaluated from the thickness of the films measured with a FTSS2-S4L-3D step profiler. The cross-section micrographs were measured using Sirion FEG scanning electron microscopy (SEM), and the composition of  $\text{CrN}_x$  coatings was determined by using an EDAX genesis 7000 energy dispersive spectroscopy (EDS) system operated at 12 kV. The surface topography was analyzed using an atomic force microscope (AFM) (Shimadzu SPM-9500J3) operated in the tapping mode. The hardness was measured using an HX-1000 microhardness tester with a load of 25 g (the indentation depth was about 250 nm) and taking the average of 5 values. The friction and wear measurements of the  $\text{CrN}_x$  coatings were carried out by using an MS-T3000 ball-on-disk tester which slides in ambient air at  $30^\circ\text{C}$ , at relative humidity of 70%, with a  $\text{Si}_3\text{N}_4$  ball of 3 mm in diameter being used as the mating material, on which a 4 N load was applied. The average sliding speed was 0.02 m/s for a fixed sliding time of 30 min, and the friction coefficients were recorded during the test.

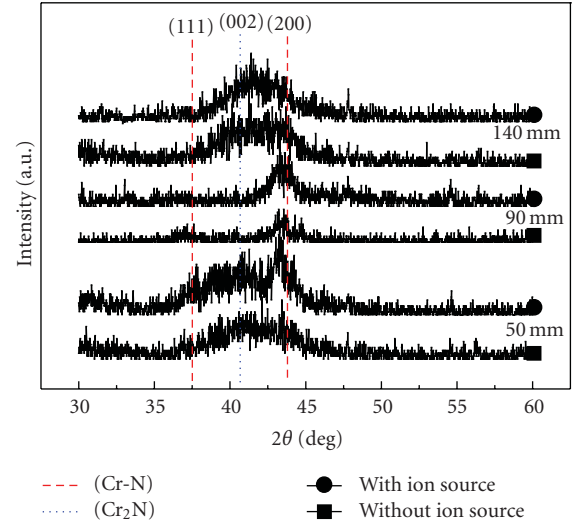


FIGURE 1: XRD patterns of  $\text{CrN}_x$  coatings deposited at various  $d_{ss}$ .

## 3. Results and Discussion

Figure 1 shows the XRD spectra of  $\text{CrN}_x$  coatings deposited under various source-substrate distances,  $d_{ss}$ . The  $\text{CrN}_x$  coatings contain two phases of fcc CrN and hexagonal  $\text{Cr}_2\text{N}$ , their corresponding PDF numbers being 65-2899 and 79-2159, respectively. Only the CrN (200) peak is observed for the coating deposited at  $d_{ss} = 90$  mm. With increasing  $d_{ss}$ , the XRD data show the structure of the  $\text{CrN}_x$  coatings to be changed from CrN to a mixture of  $\text{Cr}_2\text{N} + \text{CrN}$ . At the lower extreme,  $d_{ss} = 50$  mm, the planes of  $\text{Cr}_2\text{N}$  (002), together with CrN (200) and (111), can be seen whereas at larger distance of 140 mm, the films deposited exhibit inconspicuous overlap of  $\text{Cr}_2\text{N}$  (002) and CrN (200) orientations.

The energies of the depositing particles were different at different  $d_{ss}$  because of the collision of ions (N, Ar, and Cr). The particles bombarded the substrate and heat the substrate. The ratio of ion to neutral particles (Ar, N, and Cr) arriving at the growing film would be different at different  $d_{ss}$ . These factors influence the film growth kinetics, which finally determine the orientation and phase structure of the  $\text{CrN}_x$  coatings. The broadening of the diffraction peaks of  $\text{CrN}_x$  coatings is related to the changes in the grain size, thickness, and residual stress in the coating. The different ratio of N/Ar has an influence on the composition of CrN or  $\text{Cr}_2\text{N}$  [24]. Therefore, the formation of CrN or  $\text{Cr}_2\text{N}$  at different  $d_{ss}$  is attributed to the different N/Ar ratio influenced by  $d_{ss}$ .

Also shown in Figure 1 is the influence of the hot filament ion source;  $\text{CrN}_x$  coatings deposited with ion source assistance have different diffraction peaks at all values of  $d_{ss}$ . In particular, at  $d_{ss}$  of 90 mm, the intensity of (200) peak is enhanced. The slightly higher intensity of the XRD peaks in the CrN coatings deposited with the ion source assistance can be related to the enhanced ion bombardment from the plasma, which may lead to a higher substrate temperature as well as a higher ion-to-neutral particle ratio.

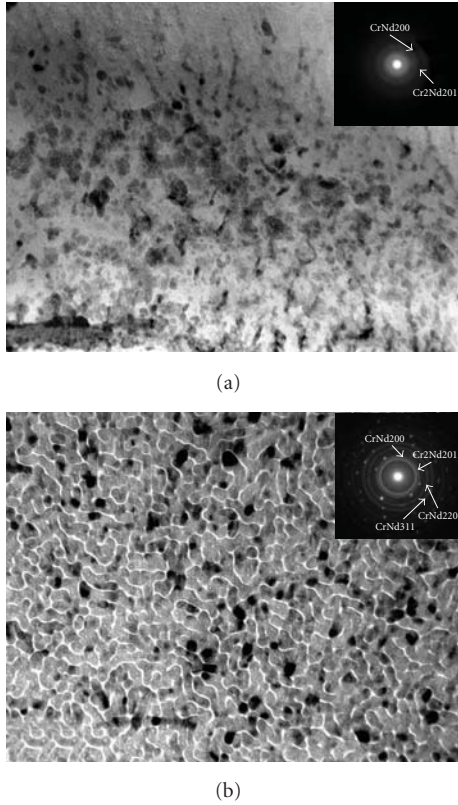


FIGURE 2: Bright-field TEM images and selected area diffraction of  $\text{CrN}_x$  coatings deposited at  $d_{ss} = 90$  mm. The view directions are normal to the coating surface. (a) Samples prepared without ion source assistance, (b) with ion source assistance.

Figure 2(a) shows bright-field TEM images of  $\text{CrN}_x$  coatings deposited without ion source assistance, which reveals nonuniform  $\text{CrN}_x$  grains. The corresponding selected area diffraction pattern reveals obvious CrN and blurry  $\text{Cr}_2\text{N}$  phases. On the contrary, with the use of ion source Figure 2(b), uniform  $\text{CrN}_x$  grains are observed and selected area diffraction shows obvious diffraction rings of CrN and  $\text{Cr}_2\text{N}$ , revealing the polycrystalline nature of the film, with diffraction points attributed to the Si (100) substrate. The uniform  $\text{CrN}_x$  grains with distinct grain boundaries suggest higher microhardness of the corresponding coatings.

Figure 3 shows the deposition rate of the  $\text{CrN}_x$  coatings as a function of  $d_{ss}$ . As a general tendency, the deposition rate of the coatings decreases with increasing  $d_{ss}$ . The deposition rate is further increased at  $d_{ss}$  values of 90 mm and 140 mm with the assistance of the ion source. At  $d_{ss} = 50$  mm, however, the ion source assistance tends to decrease the deposition rate.

At larger source-substrate spacing, the sputter-produced particles arriving at the substrate decrease in number due to the collision of Cr and N atoms with the plasma of  $\text{N}_2$ , Ar,  $\text{N}^+$ ,  $\text{Ar}^+$ , and secondary electrons. However, with the use of thermal filament ion source, more ions, especially Ar ions, were generated, which bombarded the Cr target and produced more Cr particles [3, 25]. As a

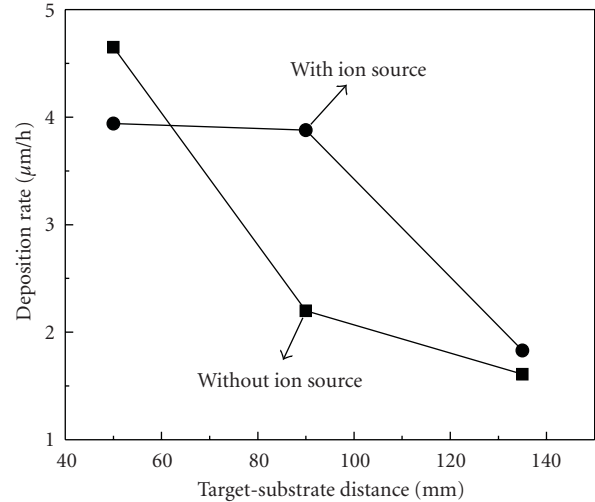


FIGURE 3: Deposition rate as a function of the  $d_{ss}$  of the  $\text{CrN}_x$  coatings.

result, the deposition rate is higher than that without ion source assistance. At close source-substrate spacing ( $d_{ss} = 50$  mm), with thermal filament ion source assistance, the increased amount of Ar and other ions causes severe re sputtering of the film surface. Therefore, the deposition rate becomes lower than that without ion source assistance. With the increase of  $d_{ss}$ , the energies of deposition particles decreased because of the collision in the plasma, especially at  $d_{ss}$  much larger than molecular mean-free-path. Hence, the deposition rate at larger  $d_{ss}$  with the ion source assistance becomes larger than without ion source assistance.

Figure 4 shows typical three-dimensional AFM morphologies taken from the  $\text{CrN}_x$  coatings deposited at  $d_{ss}$  of 50, 90, and 140 mm without and with thermal filament ion source assistance. The topographies shown in Figure 4(a) suggest that the  $\text{CrN}_x$  coatings deposited at 50 mm are composed of columns with irregular tops. When the source-substrate spacing increases to 90 mm, the size of the extrusive tops was significantly reduced (Figure 4(b)). At even larger  $d_{ss}$ , the extrusive tops become more regular and an even smoother surface is observed (Figure 4(c)). Figure 5 shows the root-mean-square (RMS) roughness calculated from the AFM images of the  $\text{CrN}_x$  coatings deposited at various  $d_{ss}$  without and with thermal filament ion source assistance. Corresponding to the AFM observations in Figure 4, the RMS roughness of the  $\text{CrN}_x$  coatings deposited at 50 mm was relatively large at shorter source-substrate distance. The use of thermal filament ion source gives rise to the reduction of RMS roughness from 10.3 to 8.6 nm at  $d_{ss} = 50$  mm. At larger source-substrate distance, the difference becomes negligible.

When the source-substrate spacing is small, the deposition rate is high (Figure 3) and the growth is columnar, which gives a large roughness. More energetic ions bombard the substrate, which affected the nucleation kinetics [26], resulting in rapid growth of the grain, thereby exhibiting larger

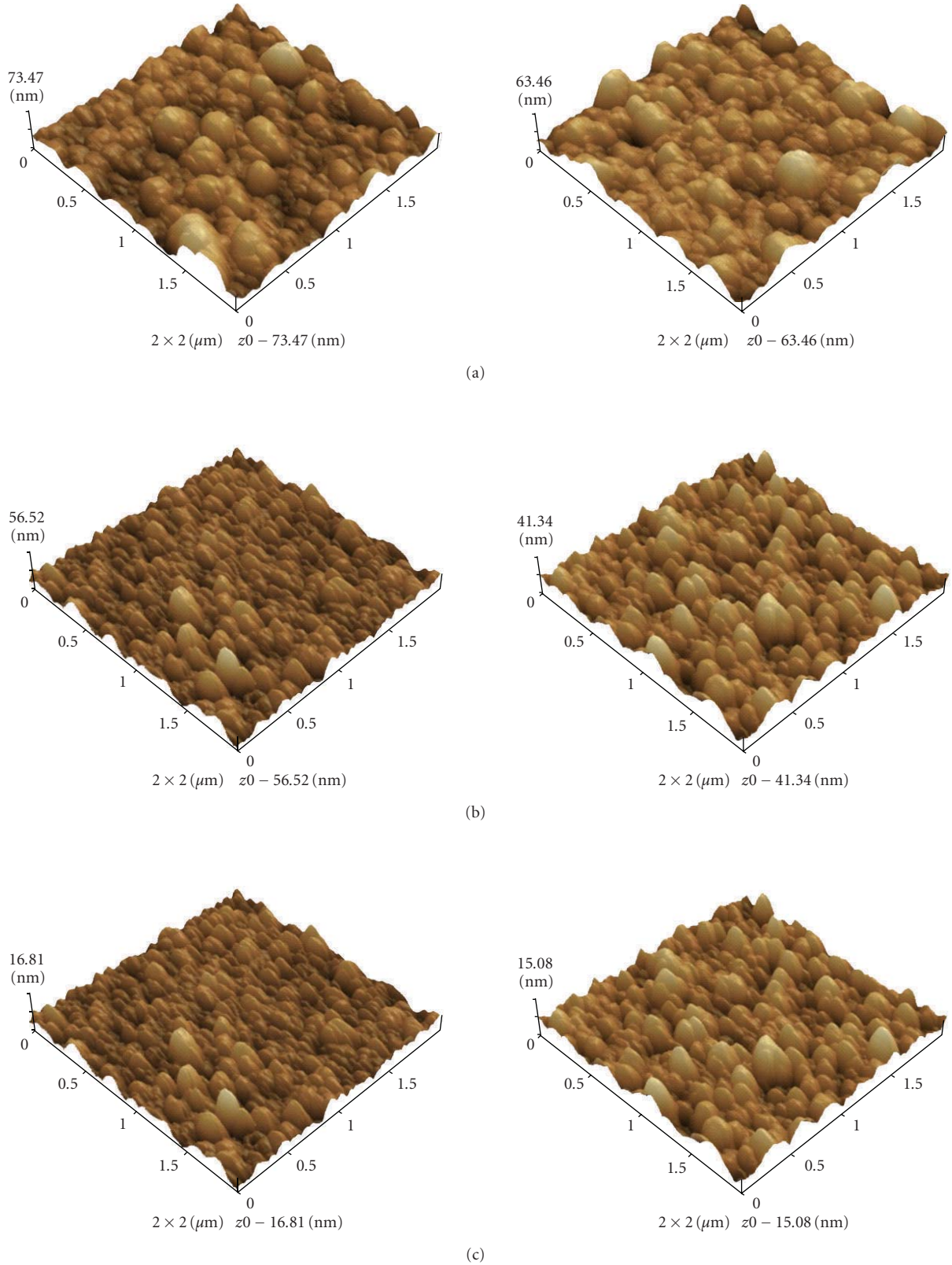


FIGURE 4: AFM morphologies of  $\text{CrN}_x$  coatings deposited at  $d_{ss}$  of 50 mm (a), 90 mm (b), and 140 mm (c). The images on the left-hand side are of samples prepared without ion source, and those on the right-hand side are of samples prepared with ion source assistance.

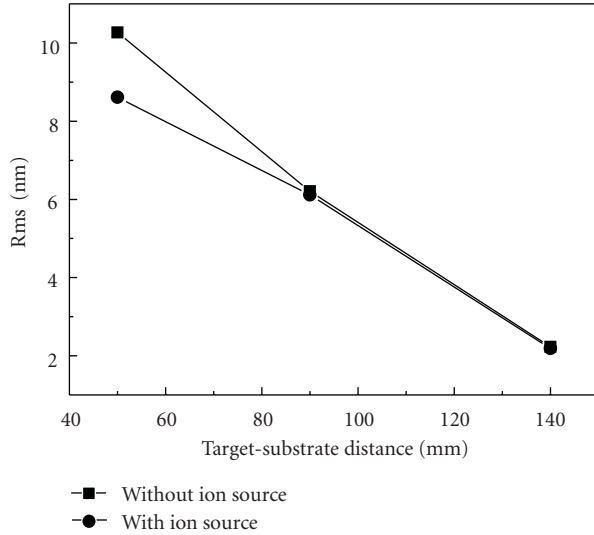
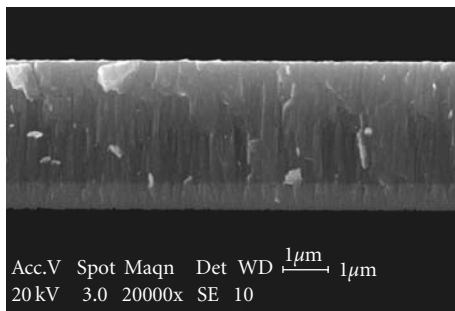
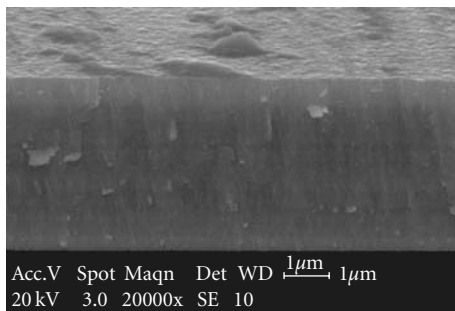


FIGURE 5: Variation in rms roughness measured from AFM images of the  $\text{CrN}_x$  coatings as a function of  $d_{ss}$ .



(a)



(b)

FIGURE 6: Cross-sectional SEM image of  $\text{CrN}_x$  coatings deposited at  $d_{ss} = 90$  mm (a) without and (b) with ion source assistance.

particle sizes. With increasing  $d_{ss}$ , frequent collision reduces the kinetic energies of particles reaching the surface, and the deposition is slowed down, leading to uniform surfaces with extrusions of smaller particle size and higher density.

Figure 6 shows cross-section SEM images of the  $\text{CrN}_x$  coatings deposited without and with ion source assistance at

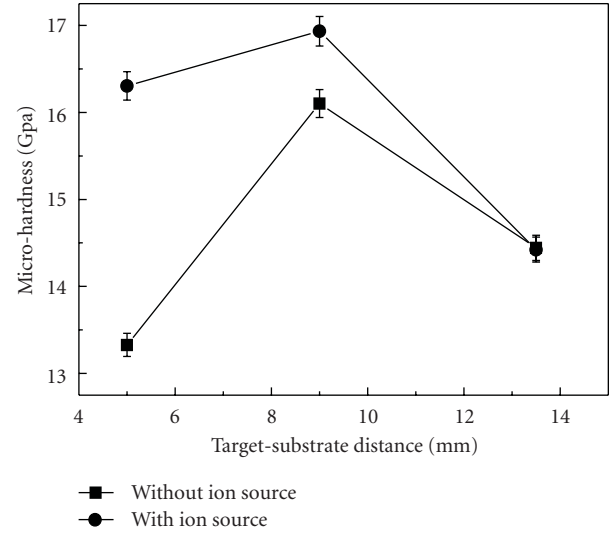


FIGURE 7: Variation of microhardness of  $\text{CrN}_x$  coatings as a function of  $d_{ss}$ .

$d_{ss}$  of 90 mm. One sees a columnar growth throughout the whole film thickness without the ion source assistance. In the process of using ion source, columnar growth is not obvious and the coating becomes denser, apparently resulting from the energetic bombardment by ions produced with the ion source assistance.

Figure 7 shows the microhardness of the  $\text{CrN}_x$  coatings as a function of source-substrate distance, which exhibits the same trend, but the values are higher when ion source assistance is applied during deposition. At  $d_{ss} = 90$  mm, the highest hardness is observed. This is accounted for by better crystallization and higher N concentration (measured by EDS) measured from the samples. The  $\text{CrN}_x$  coating deposited with the thermal filament ion source had higher N concentration (as shown in Figure 8), and the films were denser, with much finer grains (as shown Figure 2). It is believed that the grain size rather than the existence of  $\text{Cr}_2\text{N}$  phase influences the hardness values [27], which explains the further improvement of the microhardness at  $d_{ss} = 90$  mm.

Figure 9 shows the friction coefficients of  $\text{CrN}_x$  coatings. The average friction coefficient of the  $\text{CrN}_x$  films prepared without ion source is 0.53 and is decreased to 0.48 with ion source assistance. This is consistent with the enhanced microhardness and the reduction in the surface roughness of the  $\text{CrN}_x$  coatings.

#### 4. Conclusion

We have prepared  $\text{CrN}_x$  coatings by medium-frequency magnetron sputtering and demonstrated the improvement of the structural and mechanical properties of coatings by introducing thermal filament ion source during deposition. The  $\text{CrN}_x$  coatings deposited with ion source assistance exhibited an increase in microhardness from 13.25–16.3 GPa at a source-substrate distance of 50 mm and from

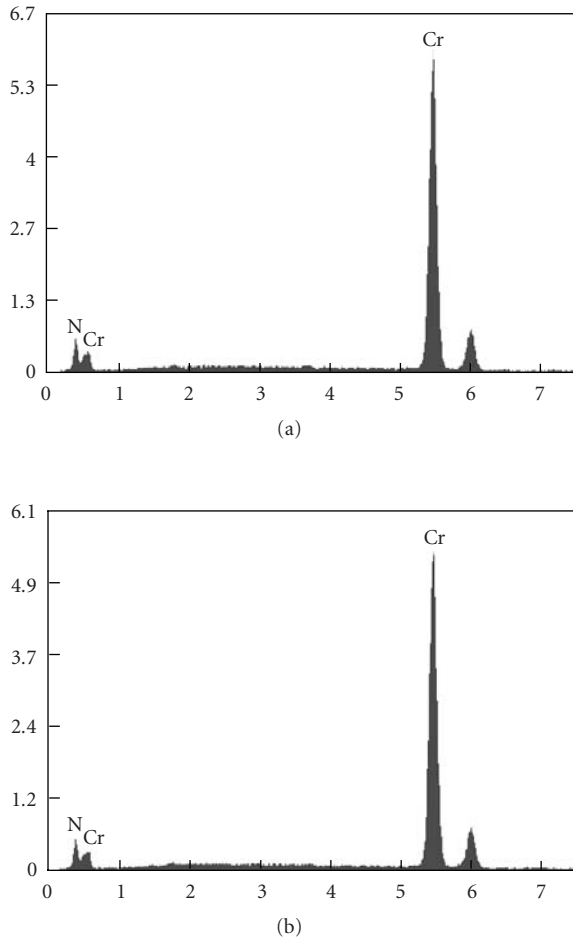


FIGURE 8: The EDS images of CrN<sub>x</sub> coatings deposited at  $D_{ts} = 90$  mm. (a) Samples without ion source assistance, N/Cr = 0.9075; (b) with ion source assistance, N/Cr = 0.9242.

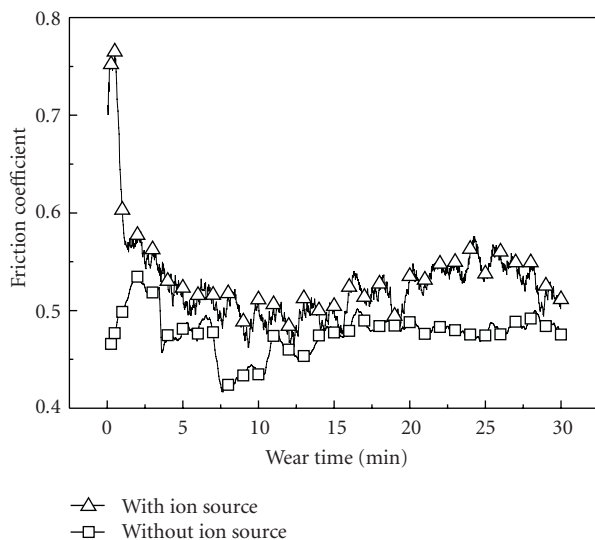


FIGURE 9: Variation of friction coefficient with sliding time of CrN<sub>x</sub> coatings at  $d_{ss} = 90$  mm.

16.0–17.0 GPa at the optimized  $d_{ss}$  of 90 mm. The friction coefficient was decreased typically from 0.53–0.48. A deposition rate of  $3.88 \mu\text{m/h}$  was achieved, and the roughness was 6.0 nm for the coatings deposited at  $d_{ss}$  of 90 mm. The results show that the use of simple ion source assistance may be promising for high-rate deposition of CrN<sub>x</sub> coatings.

## Acknowledgment

This paper was supported by the NSFC under Contract 50905130, China Ministry of Industry and Information Technology under 2009ZX04012-032, Doctoral Fund of Ministry of Education of China for the New Teacher (20090141120067), and the Fundamental Research Funds for the Central Universities.

## References

- [1] X. M. He, N. Baker, B. A. Kehler, K. C. Walter, M. Nastasi, and Y. Nakamura, "Structure, hardness, and tribological properties of reactive magnetron sputtered chromium nitride films," *Journal Vacuum Science Technology A*, vol. 18, no. 1, pp. 30–36, 2000.
- [2] J. J. Olaya, S. E. Rodil, S. Muhl, and E. Sánchez, "Comparative study of chromium nitride coatings deposited by unbalanced and balanced magnetron sputtering," *Thin Solid Films*, vol. 474, no. 1-2, pp. 119–126, 2005.
- [3] G. A. Zhang, P. X. Yan, P. Wang, Y. M. Chen, and J. Y. Zhang, "Influence of nitrogen content on the structural, electrical and mechanical properties of CrN<sub>x</sub> thin films," *Materials Science and Engineering A*, vol. 460-461, pp. 301–305, 2007.
- [4] P. H. Mayrhofer, H. Willmann, and C. Mitterer, "Oxidation kinetics of sputtered Cr-N hard coatings," *Surface and Coatings Technology*, vol. 146-147, pp. 222–228, 2001.
- [5] B. Warcholiński, A. Gilewicz, Z. Kukliński, and P. Myśliński, "Arc-evaporated CrN, CrN and CrCN coatings," *Vacuum*, vol. 83, no. 4, pp. 715–718, 2008.
- [6] C. Öner, H. Hazar, and M. Nursoy, "Surface properties of CrN coated engine cylinders," *Materials and Design*, vol. 30, no. 3, pp. 914–920, 2009.
- [7] S. H. Shin, M. W. Kim, M. C. Kang, K. H. Kim, D. H. Kwon, and J. S. Kim, "Cutting performance of CrN and Cr-Si-N coated end-mill deposited by hybrid coating system for ultra-high speed micro machining," *Surface and Coatings Technology*, vol. 202, no. 22-23, pp. 5613–5616, 2008.
- [8] A. Ney, R. Rajaram, S. S. P. Parkin, T. Kammermeier, and S. Dhar, "Magnetic properties of epitaxial CrN films," *Applied Physics Letters*, vol. 89, no. 11, Article ID 112504, 3 pages, 2006.
- [9] W. J. Feng, D. Li, W. F. Li et al., "Structure and magnetic properties of Cr(N)- $\beta$ -Cr<sub>2</sub>N nanoparticles prepared by arc-discharge," *Journal of Alloys and Compounds*, vol. 425, no. 1-2, pp. 4–9, 2006.
- [10] J.-W. Lee, S.-K. Tien, Y.-C. Kuo, and C.-M. Chen, "The mechanical properties evaluation of the CrN coatings deposited by the pulsed DC reactive magnetron sputtering," *Surface and Coatings Technology*, vol. 200, no. 10, pp. 3330–3335, 2006.
- [11] J. Lin, Z. L. Wu, X. H. Zhang, B. Mishra, J. J. Moore, and W. D. Sproul, "A comparative study of CrN<sub>x</sub> coatings Synthesized by DC and pulsed DC magnetron sputtering," *Thin Solid Films*, vol. 517, no. 6, pp. 1887–1894, 2009.

- [12] J. Lin, J. J. Moore, B. Mishra, M. Pinkas, W. D. Sproul, and J. A. Rees, "Effect of asynchronous pulsing parameters on the structure and properties of CrAlN films deposited by pulsed closed field unbalanced magnetron sputtering (P-CFUBMS)," *Surface and Coatings Technology*, vol. 202, no. 8, pp. 1418–1436, 2008.
- [13] C. Muratore, J. J. Moore, and J. A. Rees, "Electrostatic quadrupole plasma mass spectrometer and Langmuir probe measurements of mid-frequency pulsed DC magnetron discharges," *Surface and Coatings Technology*, vol. 163–164, pp. 12–18, 2003.
- [14] J. W. Bradley, H. Bäcker, Y. Aranda-Gonzalvo, P. J. Kelly, and R. D. Arnell, "The distribution of ion energies at the substrate in an asymmetric bi-polar pulsed DC magnetron discharge," *Plasma Sources Science and Technology*, vol. 11, no. 2, pp. 165–174, 2002.
- [15] T. Elangovan, P. Kuppasami, R. Thirumurugesan, V. Ganesan, E. Mohandas, and D. Mangalaraj, "Nanostructured CrN thin films prepared by reactive pulsed DC magnetron Sputtering," *Materials Science and Engineering B*, vol. 167, no. 1, article 17, 2010.
- [16] J.-W. Lee, Y.-C. Kuo, C.-J. Wang, L.-C. Chang, and K.-T. Liu, "Effects of substrate bias frequencies on the characteristics of chromium nitride coatings deposited by pulsed DC reactive magnetron sputtering," *Surface and Coatings Technology*, vol. 203, no. 5–7, pp. 721–725, 2008.
- [17] J. Lin, J. J. Moore, W. D. Sproul, B. Mishra, Z. Wu, and J. Wang, "The structure and properties of chromium nitride coatings deposited using DC, pulsed DC and modulated pulse power magnetron sputtering," *Surface and Coatings Technology*, vol. 204, no. 14, pp. 2230–2239, 2010.
- [18] A. P. Eghasarian, W.-D. Münz, L. Hultman, U. Helmersson, and I. Petrov, "High power pulsed magnetron sputtered CrN<sub>x</sub> films," *Surface and Coatings Technology*, vol. 163–164, pp. 267–272, 2003.
- [19] X. Yu, C. Wang, Y. Liu, D. Yu, and T. Xing, "Recent developments in magnetron sputtering," *Plasma Science and Technology*, vol. 8, no. 3, pp. 337–343, 2006.
- [20] G. Li, C. Liu, J. Li, C. Zhang, Z. Mu, and Z. Long, "Plasma-ion beam source enhanced deposition system," *Surface and Coatings Technology*, vol. 193, no. 1–3, pp. 112–116, 2005.
- [21] R. Wei, J. J. Vajo, J. N. Matossian, and M. N. Gardos, "Aspects of plasma-enhanced magnetron-sputtered deposition of hard coatings on cutting tools," *Surface and Coatings Technology*, vol. 158–159, pp. 465–472, 2002.
- [22] R. Wei, "Plasma enhanced magnetron sputter deposition of Ti-Si-C-N based nanocomposite coatings," *Surface and Coatings Technology*, vol. 203, no. 5–7, pp. 538–544, 2008.
- [23] R. Wei, E. Lang, C. Rincon, and J. H. Arps, "Deposition of thick nitrides and carbonitrides for sand erosion protection," *Surface and Coatings Technology*, vol. 201, no. 7, pp. 4453–4459, 2006.
- [24] M. L. Kuruppu, G. Negrea, I. P. Ivanov, and S. L. Rohde, "Monolithic and multilayer Cr/CrN, Cr/Cr<sub>2</sub>N, and Cr<sub>2</sub>N/CrN coatings on hard and soft substrates," *Journal of Vacuum Science and Technology A*, vol. 16, no. 3, pp. 1949–1955, 1998.
- [25] Y. M. Lu, W. S. Hwang, W. Y. Liu, and J. S. Yang, "Effect of RF power on optical and electrical properties of ZnO thin film by magnetron sputtering," *Materials Chemistry and Physics*, vol. 72, no. 2, pp. 269–272, 2001.
- [26] C.-L. Huang and Y.-B. Chen, "The effect of deposition temperature and RF power on the electrical and physical properties of the MgTiO<sub>3</sub> thin films," *Journal of Crystal Growth*, vol. 285, no. 4, pp. 586–594, 2005.
- [27] P. H. Mayrhofer, G. Tischler, and C. Mitterer, "Microstructure and mechanical/thermal properties of Cr-N coatings deposited by reactive unbalanced magnetron sputtering," *Surface and Coatings Technology*, vol. 142–144, pp. 78–84, 2001.

## Research Article

# Structure and Optical Properties of Silicon Nanocrystals Embedded in Amorphous Silicon Thin Films Obtained by PECVD

**B. M. Monroy,<sup>1</sup> A. Remolina,<sup>1</sup> M. F. García-Sánchez,<sup>1</sup> A. Ponce,<sup>2</sup>  
M. Picquart,<sup>3</sup> and G. Santana<sup>1</sup>**

<sup>1</sup>*Instituto de Investigaciones en Materiales, Universidad Nacional Autónoma de México,  
A.P. 70-360, 04510 Coyoacán, DF, Mexico*

<sup>2</sup>*Centro de Investigación en Química Aplicada, Boulevard Enrique Reyna Hermosillo no.140, Saltillo, 25290, Coahuila, Mexico*

<sup>3</sup>*Departamento de Física, Universidad Autónoma Metropolitana Iztapalapa, A.P. 55-534, 09340 Iztapalapa, DF, Mexico*

Correspondence should be addressed to B. M. Monroy, marel@iim.unam.mx

Received 28 May 2010; Accepted 10 November 2010

Academic Editor: Jaetae Seo

Copyright © 2011 B. M. Monroy et al. This is an open access article distributed under the Creative Commons Attribution License, which permits unrestricted use, distribution, and reproduction in any medium, provided the original work is properly cited.

Silicon nanocrystals embedded in amorphous silicon matrix were obtained by plasma enhanced chemical vapor deposition using dichlorosilane as silicon precursor. The RF power and dichlorosilane to hydrogen flow rate ratio were varied to obtain different crystalline fractions and average sizes of silicon nanocrystals. High-resolution transmission electron microscopy images and RAMAN measurements confirmed the existence of nanocrystals embedded in the amorphous matrix with average sizes between 2 and 6 nm. Different crystalline fractions (from 12% to 54%) can be achieved in these films by regulating the selected growth parameters. The global optical constants of the films were obtained by UV-visible transmittance measurements. Effective band gap variations from 1.78 to 2.3 eV were confirmed by Tauc plot method. Absorption coefficients higher than standard amorphous silicon were obtained in these thin films for specific growth parameters. The relationship between the optical properties is discussed in terms of the different internal nanostructures of the samples.

## 1. Introduction

For several decades, hydrogenated amorphous silicon (a-Si:H) has been investigated as a possible candidate for the production of inexpensive solar cells [1, 2]. However, the expected efficiency and stability of a-Si:H solar cells has not yet been achieved. The technological utility of this material is hampered by the creation of metastable electronic defects when excess free carriers are generated by light absorption (Staebler-Wronski effect) [3]. This light-induced degradation of a-Si:H depends mainly on changes in the hydrogen bonding configuration and the presence of defects in the films.

In the last decade, Roca i Cabarrocas et al. introduced polymorphous silicon (pm-Si) using silane ( $\text{SiH}_4$ ) as silicon precursor and they obtained a new material characterized by the presence of dispersed nanocrystallines embedded in an amorphous network that is more relaxed than that found in standard a-Si:H [4]. It has already been shown

that this material has better transport properties (enhanced hole mobility and a smaller density of metastable electronic defects) and improved photo stability with respect to a-Si:H [5, 6], thus making it a likely candidate for high efficiency solar cells. There has been considerable research on the structural characteristics and optoelectronic properties of this material [5–9].

The expectation is that replacing the a-Si:H by different forms of pm-Si thin films could reduce the cost of “solar electric power” by increasing the efficiency and stability of silicon-based thin film photovoltaic devices [7]. However, there are some critical issues that remain to be addressed to achieve the best performance of pm-Si in a photovoltaic device: (i) control of the nanocrystallite size distribution and density in the amorphous matrix which determines the optoelectronic properties of pm-Si, (ii) control of the hydrogen incorporation in the films and Medium Range Order (MRO) of the amorphous matrix to minimize the Staebler-Wronski effect, and (iii) optimization of the processing of pm-Si thin

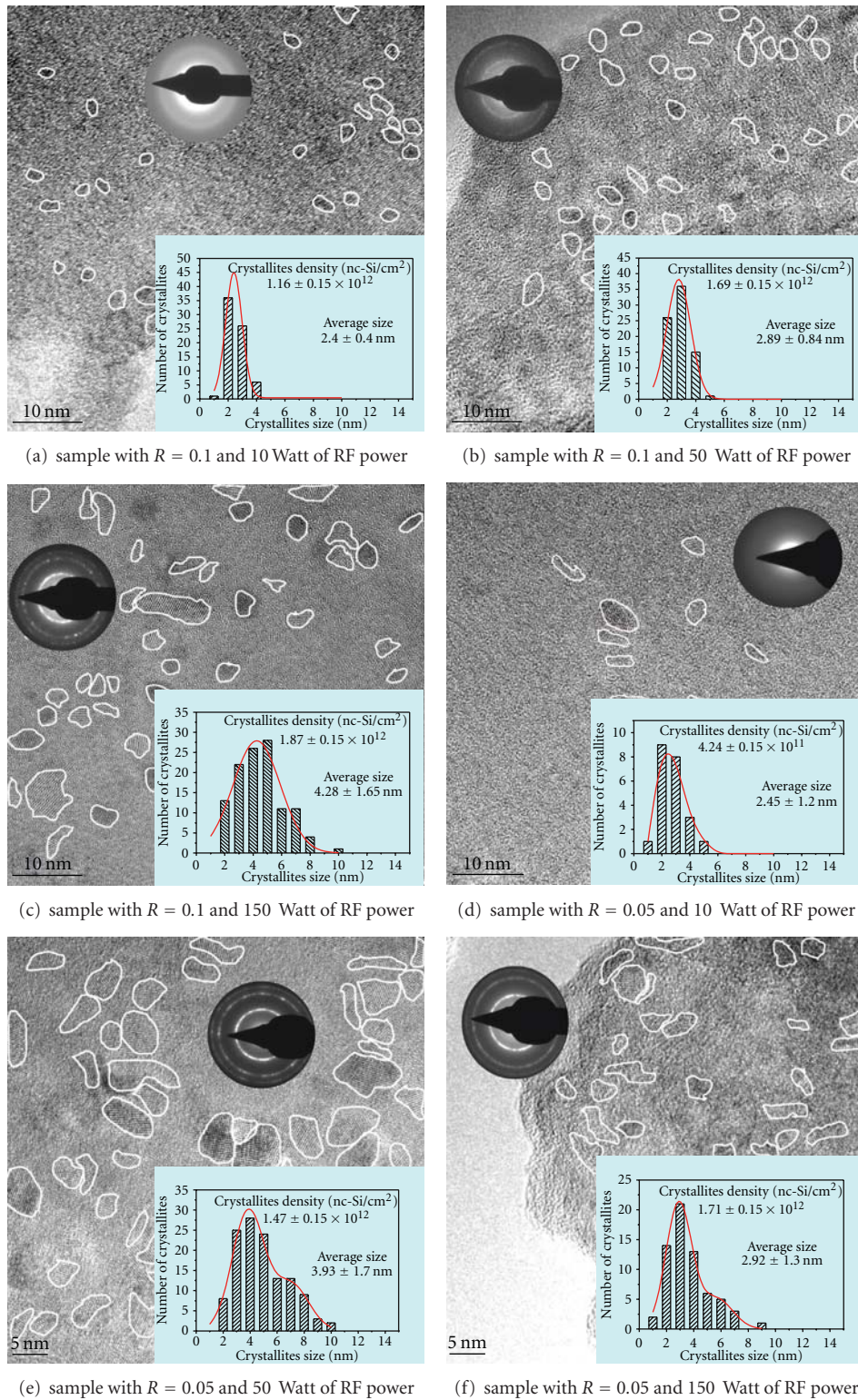


FIGURE 1: Representative HRTEM images for six samples grown with different dichlorosilane to hydrogen flow rate ratios ( $R$ ) and RF powers. The circular inserts show the Small Area Diffraction Patterns of the samples, and the square inserts show the size distributions and number densities of the silicon nanocrystalline inclusions.

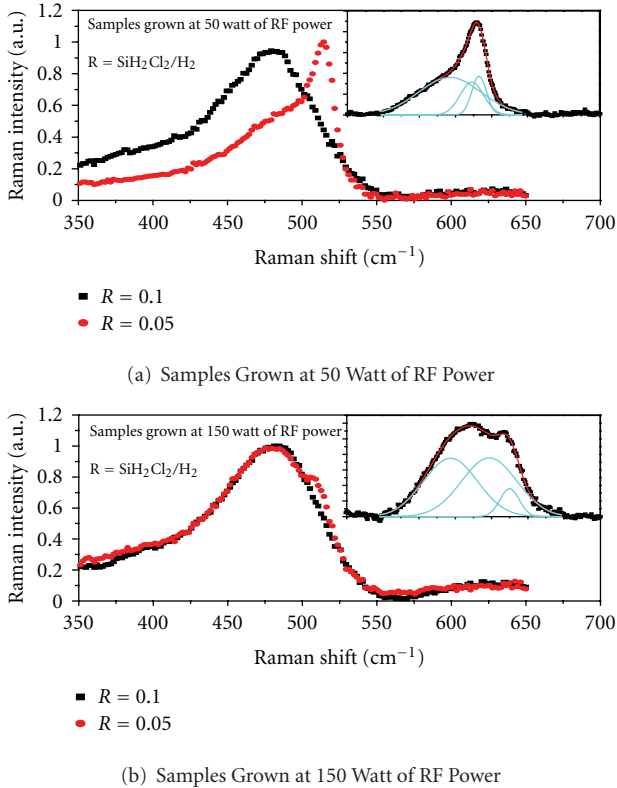


FIGURE 2: Comparison of Raman spectra of polymorphous silicon thin films grown with different  $R = \text{Fr}[\text{SiH}_2\text{Cl}_2]/\text{Fr}[\text{H}_2]$  and RF powers of (a) 50 Watts and (b) 150 Watts. The insert shows an example of the Raman spectra deconvolution in three peaks.

films to comply with the requirements of the photovoltaic industry.

Previously, we have reported the growth of different silicon alloys by plasma enhanced chemical vapor deposition (PECVD) using dichlorosilane ( $\text{SiH}_2\text{Cl}_2$ ) as silicon precursor [10–12]. Due to the chlorine chemistry introduced in the deposition process, it is possible to obtain nanocrystalline silicon inclusions at low deposition temperatures and regulate the hydrogen content of the films, leading to an increased chemical stability of the material. Since the optoelectronic properties of this particular type of silicon thin films, which we also name polymorphous silicon (pm-Si), depend on the size and density of the silicon nanocrystallites (nc-Si) embedded in the amorphous matrix, a study for the determination of the average crystallite sizes and density as a function of growth parameter becomes essential.

The aim of this paper is to show the variations of the optoelectronic properties in pm-Si as a function of the nanocrystalline fraction, which can be regulated by means of specific growth parameters, as the RF power of the PECVD process and through the dichlorosilane to hydrogen flow rate ratio ( $R = \text{Fr}[\text{SiH}_2\text{Cl}_2]/\text{Fr}[\text{H}_2]$ ). Depending on their absorption properties and effective band gap, these materials can be suitable to apply in different parts of amorphous silicon thin film solar cell devices.

## 2. Experimental Procedure

The samples were prepared using a conventional PECVD system with parallel plates of  $150 \text{ cm}^2$  in area and  $1.5 \text{ cm}$  apart, activated by a  $13.56 \text{ MHz}$  RF signal. The system is described in more detail elsewhere [13]. The thin films were deposited simultaneously on high resistivity (100) single-crystalline silicon, fuses silica (quartz), and NaCl substrates to facilitate the different characterizations. Prior to deposit, the substrates were subjected to a standard cleaning procedure, immediately before loading into the deposition chamber. Ultrahigh purity  $\text{SiH}_2\text{Cl}_2$  and  $\text{H}_2$  were used as precursor gases. In all cases, the substrate temperature was kept constant at  $200^\circ\text{C}$  and an argon flow rate of  $50 \text{ sccm}$  was used as diluent gas. The deposition time and pressure were fixed at  $30 \text{ min}$  and  $500 \text{ mTorr}$ , respectively. Plasma powers of  $10 \text{ W}$ ,  $25 \text{ W}$ ,  $50 \text{ W}$ ,  $100 \text{ W}$  and  $150 \text{ W}$  were tested. Two different dichlorosilane to hydrogen flow rate ratios ( $R = \text{Fr}[\text{SiH}_2\text{Cl}_2]/\text{Fr}[\text{H}_2]$ ) were used,  $0.05$  and  $0.1$ , while the hydrogen flow was fixed at  $50 \text{ sccm}$  in all cases. The thickness of the films over all substrates was determined by a Sloan Dektak IIA surface profile measuring system. The deposition conditions, film thickness, and growth rate of the studied samples are summarized in Table 1. The effect of varying the hydrogen dilution and RF power was to change the plasma chemistry and investigate its effect on the optoelectronic properties of the pm-Si films.

High-resolution transmission electron microscopy (HRTEM) studies have been carried out in a TITAN-300 kV field emission gun microscope, which has a symmetrical condenser-objective lens type S-TWIN ( $C_s = 1.3 \text{ mm}$ ). The HRTEM images have been registered in a CCD camera near the Scherzer focus and subsequently analyzed using Digital Micrograph software package. It is important to notice that the samples deposited over NaCl substrates were used for HRTEM analysis. In each case, the substrate was dissolved in distilled water and the film was collected on a Cu grid. In this way, we ensured that no modification of the film structure is produced, as could be the case in conventional ion milling techniques used to prepare samples for HRTEM. For Raman and UV-visible measurements, the samples deposited over quartz were used. The Raman spectra were recorded using a T64000 Jobin-Yvon Horiba triple monochromator using the  $\times 100$  microscope objective. The excitation source was the  $514.5 \text{ nm}$  line from an  $\text{Ar}^+$  Lexel laser. All the measurements were performed at room temperature in open air. The sample was irradiated at a power of  $20 \text{ mW}$  at the laser head. Ten accumulations with an integration time of  $1 \text{ min}$  were performed on each sample in the range  $10\text{--}1200 \text{ cm}^{-1}$ . The Raman signal was detected by a cooled CCD. Transmittance measurements were recorded in a UV-Vis spectrometer Jasco V-630 in a two-beam configuration.

## 3. Results and Discussion

**3.1. HRTEM.** All samples were studied by HRTEM with the aim of determining the sizes, shape, and density of crystallites embedded in the amorphous matrix. Six representative HRTEM images of samples with different nanostructures

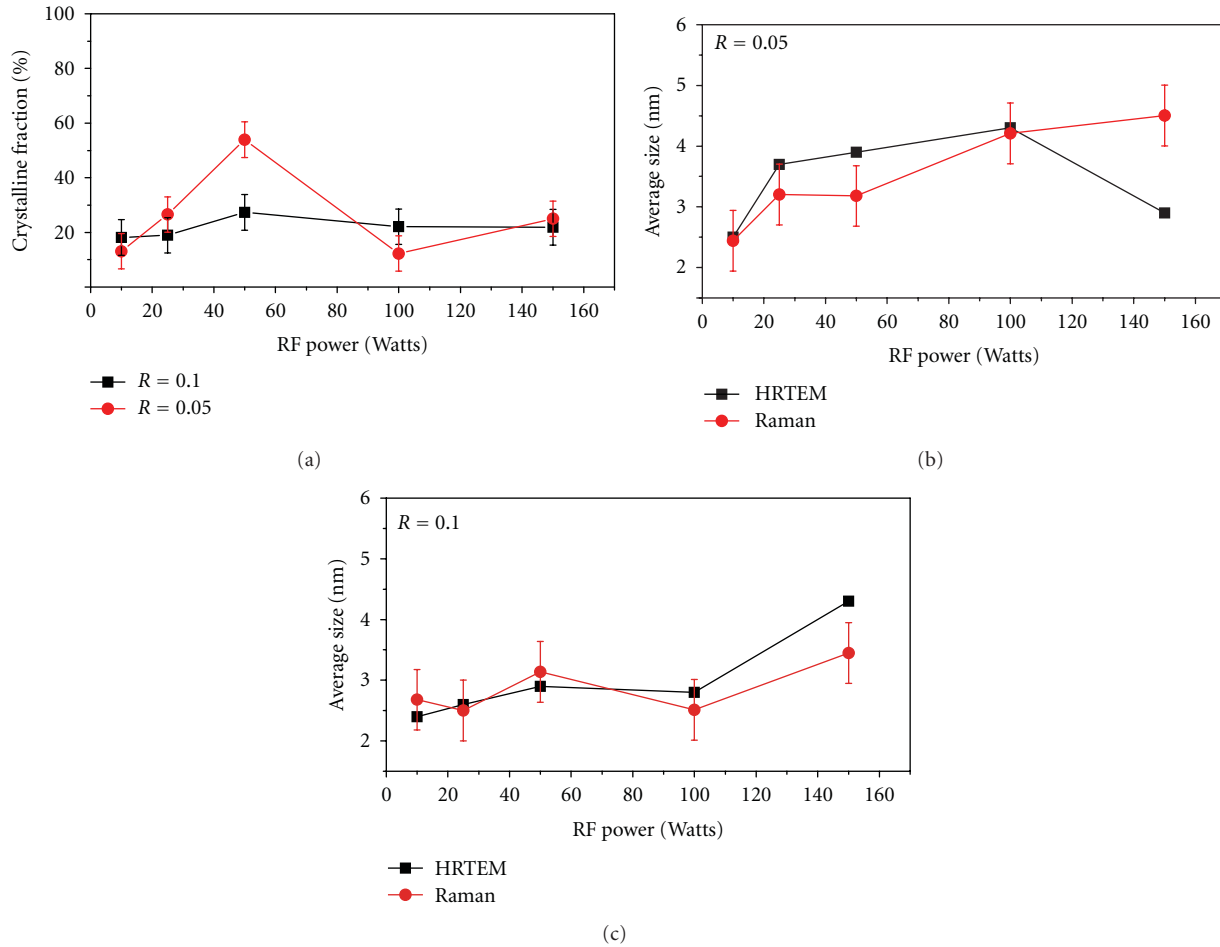


FIGURE 3: (a) Crystalline fraction and average sizes of silicon nanocrystallites obtained by Raman and HRTEM for samples grown with dichlorosilane to hydrogen flow rate ratios of (b)  $R = 0.05$  and (c)  $R = 0.1$ , as a function of the RF power.

deposited with 10, 50, and 150 Watts of RF power, and flow rates  $R$  of 0.05 and 0.1 are shown in Figure 1. As can be observed in the figure, the investigated samples contain randomly oriented crystallites of different sizes and shapes. Such nanometric ordered domains are indicated by a surrounding white line in the figure. Selected Area Electron Diffraction (SAED) patterns from the regions analyzed by HRTEM are included as circular inserts in Figure 1. As the dimensions and density of crystallites increase (Figures 1(c), 1(e) and 1(f)), sharp diffraction rings become more evident. These patterns are representative of nanocrystalline materials [7, 14]. On the other hand, when the size and density of crystallites is small, only diffuse rings characteristic of the amorphous matrix can be distinguished (Figures 1(a), 1(b), and 1(d)). For these samples, the ordered domains were limited to only 5 to 10 planes, showing that the crystallite dimension in one of its axis is between 2 to 6 nm. These small nc-Si tend to be predominantly spherical as shown in Figure 1(a), while the larger crystallites (Figures 1(c), 1(e) and 1(f)) exhibited various shapes and their dimensions can be in the order of 10 nm. The density of nanocrystallites increases slightly with the increase of both  $R$  and the

RF power. A more drastic effect is observed in the size distribution as shown in the inserts of Figure 1. For high RF powers, the size distribution is considerably broadened and it has no longer a Gaussian shape.

The different nanostructures observed by HRTEM can be explained in terms of the chlorine chemistry introduced in the deposition process. As was described in detail in previous works [10–12], metastable  $\text{SiCl}_x\text{H}_y$  precursors that incorporate to the surface are highly reactive with impinging atomic hydrogen ( $\text{H}_{\text{at}}$ ). The Si–Si bond breaking by atomic hydrogen enhances the chemical reactivity of  $\text{SiCl}_d$  ( $d$ : dangling bond) and/or  $\text{SiHCl}$ -related complexes that promotes the creation of nucleation sites for nc-Si [15].

The relative amount of chlorine related species and atomic hydrogen depends importantly on the dichlorosilane to hydrogen flow rate ratio ( $R$ ) and the RF power. We can explain the irregular shapes of the samples with bigger nanocrystallites (Figures 1(c), 1(e), and 1(f)) in terms of the local heating induced by HCl formation. From the HRTEM images, it seems as if they were crystallized areas and not crystallites embedded in amorphous matrix. This is an important difference from previous reports where the silicon

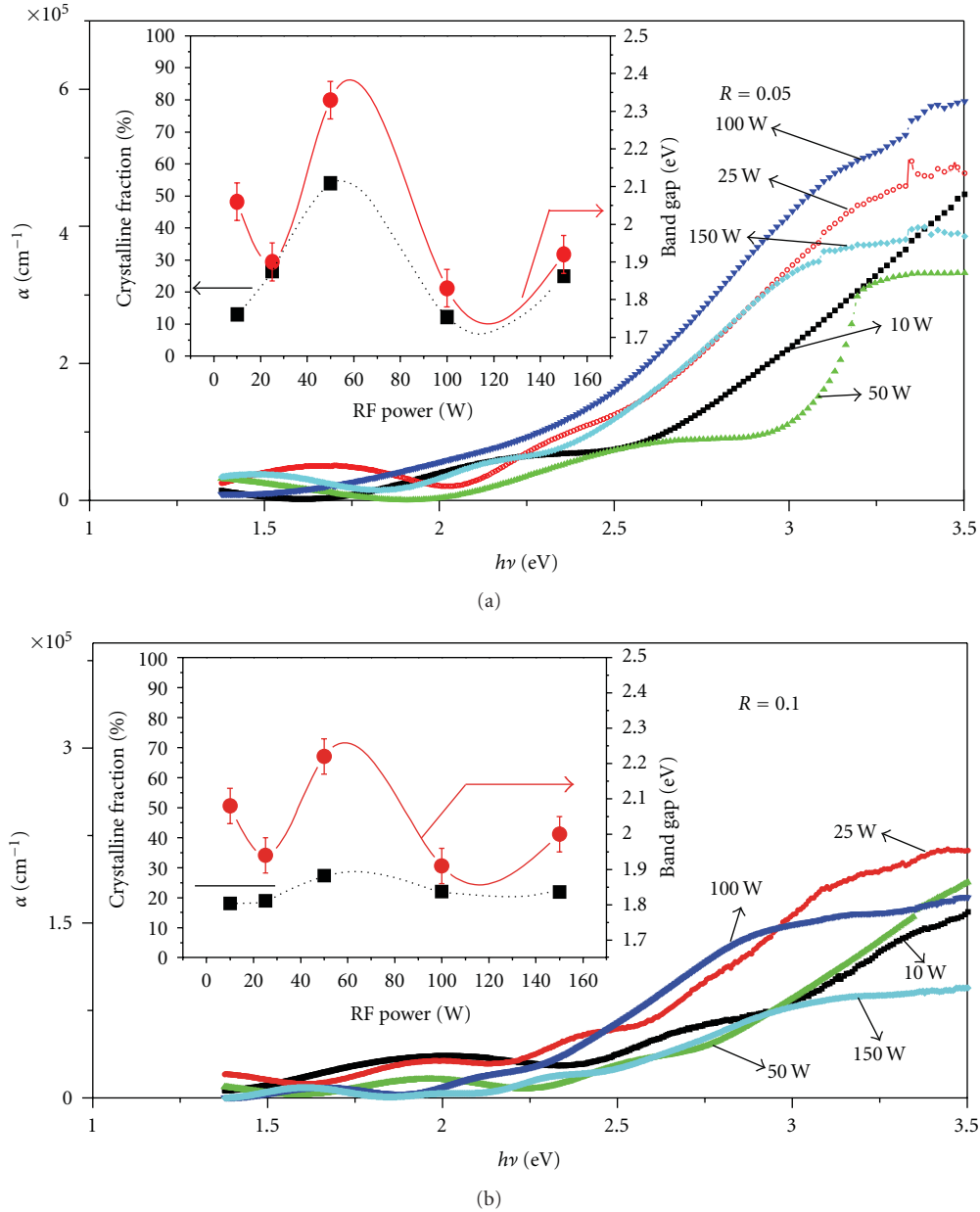


FIGURE 4: Absorption coefficient spectra for samples grown with different  $R = \text{Fr}[\text{SiH}_2\text{Cl}_2]/\text{Fr}[\text{H}_2]$  and RF power. The inserts show de Tauc optical band gap and crystalline fraction for the different samples as a function of the RF power.

nanocrystals in pm-Si thin films are primarily formed in the plasma region, and they incorporate to the a-Si matrix [4–6, 16]. The increment of nc-Si nucleation sites, HCl extraction reactions, and local heating with RF power is expected to cause a broader nc-Si size distribution during the deposition process, as is observed in Figure 1.

**3.2. Raman Spectroscopy.** We performed Raman Spectroscopy (RS) in order to describe quantitatively the variations of the crystalline volume fraction ( $X_C$ ) of the films. It is important to note that the Raman collection depth is less than 100 nm (because the excitation was done at

514 nm). Since all the samples are thicker than this limit, the analyzed volume (or integrated cross-section absorption) is similar in all cases. We also obtained the average crystallite size to compare with the HRTEM results. In general, it is assumed that for amorphous/crystalline mixed phase silicon thin films, such as pm-Si, the Raman spectrum consists of two contributions to the transverse optical (TO) mode peak: a sharp peak around  $520\text{ cm}^{-1}$  and a broad peak around  $480\text{ cm}^{-1}$  which correspond to the microcrystalline and amorphous phases, respectively. In addition, considering the strong phonon confinement due to the nanosize of the crystals, the phonon peak of c-Si is shifted from its

TABLE 1: Films thickness and growth rate of polymorphous silicon thin films deposited by PECVD with different  $R = \text{Fr}[\text{SiH}_2\text{Cl}_2]/\text{Fr}[\text{H}_2]$  and RF powers.

Plasma power (W)	$R = 0.05$		$R = 0.1$	
	Films thickness (nm) $\pm 5$ nm	Growth rate ( $\text{\AA}/\text{s}$ )	Films thickness (nm) $\pm 5$ nm	Growth rate ( $\text{\AA}/\text{s}$ )
10	137	0.7	369	2.0
25	155	0.8	326	1.8
50	171	0.9	247	1.4
100	108	0.6	306	1.7
150	181	1.0	553	3.0

position at  $520\text{ cm}^{-1}$  by an amount  $\Delta\omega$ , which is related to the crystallite size ( $\delta$ ) through the following equation:  $\delta = 2\pi(2.24/\Delta\omega)^{1/2}$  [17]. This confinement model is valid only for small nc-Si with average sizes around 2–10 nm which correspond to frequency shifts between 500 and  $519\text{ cm}^{-1}$ . In our case, the frequency shift was calculated as the difference between the adjusted crystalline TO peak frequency and the TO peak frequency for microcrystalline silicon ( $520\text{ cm}^{-1}$ ). A common form of derivation of the crystalline fraction  $X_C$  was proposed by Bustarret et al. [18],  $X_C = I_C/(I_C + \gamma I_a)$ , where  $I_C$  is the sum of the areas corresponding to the nanocrystalline and microcrystalline fractions and  $\gamma$  is a function of the crystallites size ( $L$ ) expressed in angstroms  $\gamma(L) = 0.1 + \exp(-L/250)$ . In our case, to calculate the crystalline fraction, we used the Brunel model with  $\gamma \cong 0.9$ , because the HRTEM results show that the crystallites average sizes are smaller than 10 nm. The Raman spectra of the samples were analyzed by deconvolution into 3 Gaussian peaks corresponding to the microcrystalline ( $520\text{ cm}^{-1}$ ), nanocrystalline (adjusted between  $500\text{--}518\text{ cm}^{-1}$ ), and amorphous phase ( $480\text{ cm}^{-1}$ ), and the areas of each peak were used to calculate  $I_C$  and  $I_a$ . An example of the deconvolution of Raman spectra is shown in the insert of Figure 2.

Figure 2 shows representative Raman spectra of films deposited with different flow rate ratios  $R$  and different RF power. The change in the crystalline fraction of the samples as a function of the growth parameters is clear from an inspection of the spectra. It can be seen from Figures 2(a) and 2(b) that the films grown with  $R = 0.05$  tend to be more nanocrystalline than the films grown with  $R = 0.1$ . The highest nanocrystallinity is achieved when  $R$  is 0.05 and the RF power is 50 watt. Increasing  $R$  to 0.1 causes the crystalline peak to diminish considerably, while the amorphous peak becomes prominent. Figure 3(a) shows the volumetric crystalline fractions calculated from the Raman spectra deconvolution for the different samples as a function of the RF power. The crystalline fraction for the samples deposited with  $R = 0.1$  does not present a significant variation with RF power. On the other hand,  $X_C$  increases, reaches a maximum, and then decreases for the samples deposited with  $R = 0.05$ .

From Figure 3(a), we can observe that the hydrogen dilution plays an important role in the crystalline fraction of the pm-Si films. The samples deposited with  $R = 0.05$  have a higher hydrogen dilution and the changes in  $X_C$  are

more pronounced with RF power. It is well established that a higher  $H_{\text{at}}$  dilution enhances crystallization in  $\text{SiH}_4/\text{H}_2$  systems as has been reported previously for other deposition conditions of polymorphous and microcrystalline silicon ( $\mu\text{c-Si}$ ) thin films by PECVD [16, 19]. However, in the case of chlorine-related silicon precursors, there is a competition between this process and higher chlorine incorporation in the growing surface, which depends on the relative amount of chlorine related species and atomic hydrogen.  $\text{SiCl}_4$  and  $\text{SiHCl}_3$  complexes incorporated in several monolayers near the growing surface include high amounts of bond angle distortion and bond length fluctuation, which can induce a higher degree of disorder and stress in the amorphous silicon network [20]. This can explain why  $X_C$  decreases with increasing RF power for  $R = 0.05$  and why  $X_C$  is smaller in the samples prepared with a higher amount of chlorine-related precursors ( $R = 0.1$ ).

Figures 3(b) and 3(c) show a comparison of the average crystallite sizes calculated from the shift  $\Delta\omega$  of the Raman c-Si peak and the average crystallite size measured from HRTEM images. The values of  $\Delta\omega$  are reported in Table 2 for all the samples. It is very important to note the great similitude between the HRTEM and Raman results. For high powers, there is a small difference in the average crystallite size obtained from both techniques. This can be attributed to the broad size distribution that was observed in the samples grown at high RF powers. Since Raman is a macroscopic analysis and HRTEM is nanoscopic, such differences in the average sizes are expected.

Additionally, the Raman spectra allow us to estimate a parameter that provides information about the distortion grade of the amorphous silicon network. This parameter is the Root Mean Square (RMS) bond angle deviation ( $\Delta\theta_b$ ) of the amorphous matrix (crystalline silicon in the diamond cubic structure has  $\Delta\theta_b = 0^\circ$ ). Beeman et al. [21] proposed a model that relates the Full Width at Half Maximum (FWHM) of the amorphous silicon Raman peak with the RMS bond angle deviation:  $\text{FWHM} = 15 + 6\Delta\theta_b$ . Based on different models of relaxed amorphous silicon networks, this parameter is in the range  $7.7^\circ \leq \Delta\theta_b \leq 10.5^\circ$ . This relaxed amorphous silicon networks can be obtained only after annealing of the deposited amorphous silicon films at temperatures between  $170^\circ\text{C}\text{--}200^\circ\text{C}$ . On the other hand, according to Beeman et al. the range between  $0^\circ < \Delta\theta_b \leq 6.6^\circ$  cannot be modeled by a homogeneous network so it is related to the amorphous/crystalline transition [21].

TABLE 2: Results of the analysis of Raman spectra: crystalline fraction, bond angle deviation, nanocrystalline Si peak shift, and calculated crystallites average size for samples deposited with different  $R = \text{Fr}[\text{SiH}_2\text{Cl}_2]/\text{Fr}[\text{H}_2]$  and RF powers. The crystallites average size measured by HRTEM is included for comparison.

	RF power (W)	Crystalline fraction (%)	Bond angle deviation $\Delta\theta_b$ ( $^\circ$ )	c-Si shift $\Delta\omega(\text{cm}^{-1})$	Calculated size by model (nm)	HRTEM size (nm)
$R = 0.1$	10	18.1	10.0	12.3	$2.7 \pm 0.5$	$2.4 \pm 0.4$
	25	19.0	8.5	14.2	$2.5 \pm 0.5$	$2.6 \pm 0.5$
	50	27.4	8.1	9.0	$3.1 \pm 0.5$	$2.8 \pm 0.8$
	100	22.1	8.6	14.0	$2.5 \pm 0.5$	$2.8 \pm 1.0$
	150	21.9	8.5	7.4	$3.4 \pm 0.5$	$4.2 \pm 1.6$
$R = 0.05$	10	13.1	7.8	14.8	$2.4 \pm 0.5$	$2.5 \pm 1.2$
	25	26.6	8.7	8.6	$3.2 \pm 0.5$	$3.7 \pm 1.6$
	50	53.9	7.3	8.8	$3.2 \pm 0.5$	$3.9 \pm 1.7$
	100	12.3	7.6	5.0	$4.2 \pm 0.5$	$4.3 \pm 2.0$
	150	25.0	8.2	4.4	$4.5 \pm 0.5$	$2.9 \pm 1.3$

The FWHM values of the deconvoluted Raman peak at  $480 \text{ cm}^{-1}$  are between  $59$  and  $75 \text{ cm}^{-1}$  for our polymorphous silicon thin films, which give values of  $\Delta\theta_b$  between  $7.3$  and  $10$  degrees (see values in Table 2). This indicates that our films have a bond distortion level comparable to relaxed amorphous silicon networks or in some samples (deposited with  $R = 0.05$ ) minor to that obtained in standard silicon amorphous thin films [21]. We believe that this low level of disorder in the amorphous matrix is caused by the existence of crystalline zones, which tend to create a short-range order around nanocrystals boundaries. Besides, the local heating associated to the chlorine chemistry of the deposition process can contribute to stress release and local relaxation of the growing film. Having a relaxed amorphous silicon matrix is important because it can give a greater stability to pm-Si thin films under the action of external agents (solar radiation and sudden temperature changes), which is a critical issue for applications in solar cells.

**3.3. UV-Vis Absorption.** In order to link the crystalline fraction or the internal structure of polymorphous silicon thin films with their optical properties, transmittance measurements of the films grown on the quartz substrates were performed. The effective absorption coefficient ( $\alpha_{\text{eff}}$ ) (not absolute) of the films was derived from a simple model starting from the transmittance measurements (% $T$ ):  $\alpha_{\text{eff}} = (1/d) \ln(100/\%T)$ , where  $d$  is the sample thickness in cm. The purpose of calculating this effective absorption coefficient is to compare between the different samples in this work and mainly in the regions of high absorption where the interference phenomena are not as pronounced.

Figures 4(a) and 4(b) show the effective absorption coefficient of the different samples plotted as a function of the photon energy ( $h\nu$ ) grown with different  $R$  and RF powers. This allows us to compare the different absorption properties between the pm-Si samples in the spectral regions that are of interest in photovoltaic materials. One can observe from the figure that the samples deposited at  $R = 0.05$  present a higher absorption in the UV-visible region (photon

energies from  $2.0$  to  $3.5 \text{ eV}$ ) than the samples deposited with  $R = 0.1$ . Also, the absorption coefficient changes significantly with the variation of RF power for a given  $R$ , but this change is not monotonic. On the other hand, the optical gap  $E_g$  was calculated using the Tauc model [18], which can be applied because in our samples more than  $50\%$ – $80\%$  corresponds to the amorphous matrix. In this method,  $(\alpha h\nu)^{1/2}$  is plotted versus  $h\nu$  and a linear regression is performed in the region around the absorption edge where  $(\alpha h\nu)^{1/2}$  is proportional to  $h\nu$ . The energy-axis intercept of this line is associated with the optical band gap  $E_g$ . With this approximation, an effective optical gap is obtained that is representative of the whole material. The optical band gap  $E_g$  was obtained in the region of high absorption where the interference phenomenon due to thickness is not significant.  $E_g$  is plotted versus RF power in the inserts of Figure 4, along with the crystalline fraction in order to relate them. The Tauc band gap of our pm-Si films varies between  $1.78$  and  $2.37 \text{ eV}$ . This band gap is higher than that of conventional a-Si:H ( $1.5$ – $1.8 \text{ eV}$ ).

The different absorption properties of the samples can be explained by a combination of the heterogeneous microstructure of the films (amorphous matrix and nanocrystallites) characterized by  $X_C$  and quantum confinement effects in the nanocrystallites which depend on the average size and size distribution of the samples. It is important to note that neither the optical band gap ( $E_g$ ) nor the nanocrystalline fraction percent ( $X_C$ ) varies monotonically with the variation of  $R$  and RF power. This is explained again in terms of the chlorine chemistry introduced in the deposition process. The competition between  $\text{H}_{\text{at}}$  generation and chlorine related species can give rise to a growth regime and/or an etching regime that generates different microstructures as has been explained in this work and in previous works [10, 13, 14, 20]. For the sample grown with higher hydrogen dilution,  $E_g$  and  $X_C$  have a similar behavior as a function of the RF power. However, this trend is not so explicit for the samples grown with  $R = 0.1$  that have, in comparison, a smaller nanocrystalline fraction. On the other hand, both for  $R = 0.05$  and  $R = 0.1$ , the optical

band gap decreases at high RF powers. This red-shift can be associated to quantum size effects, since the average size and size distribution of the samples get larger with increasing RF power.

The differences in the absorption properties of these films can be advantageous for silicon solar cells applications. For a given photon energy, the effective absorption coefficient can be as different as one order of magnitude for films grown with different conditions. For example, at 2.3 eV or 540 nm corresponding to the peak of the solar spectrum, the sample grown with  $R = 0.1$  and 50 W has  $\alpha_{\text{eff}} = 0.97 \times 10^4 \text{ cm}^{-1}$  while the sample grown with  $R = 0.05$  and 100 W has  $\alpha_{\text{eff}} = 1.05 \times 10^5 \text{ cm}^{-1}$ . Such a possibility of changing the absorption could be exploited in a PIN type solar cell structure where one could use different pm-Si thin films, one as emitter and the other as intrinsic (absorbent) materials, respectively. This has the additional advantages of material compatibility during device processing and increased stability of polymorphous silicon with respect to conventional amorphous silicon.

#### 4. Conclusions

Different crystalline fractions and average sizes of silicon nanocrystals embedded in amorphous silicon thin films matrix can be obtained by changing the RF power and the dichlorosilane to hydrogen flow rate ratio during the PECVD process. The HRTEM images showed that the biggest nanocrystalline inclusions have irregular shapes supporting the hypothesis that they are, in fact, crystallized areas and not crystallites generated in the plasma region and then embedded in the amorphous matrix. Also, the crystallites size distribution broadens with increasing RF power. The average size obtained from the analysis of Raman spectra are in good agreement with the HRTEM measurements, evidencing that this information can be obtained in a simple way by Raman spectroscopy which is a trustworthy, macroscopic and nondestructive technique. Raman measurements also indicate that the films grown starting from dichlorosilane have a lower bond distortion level comparable to relaxed amorphous silicon networks with annealing, which is important for the stability of the films. The absorption properties and the optical band gap depend on the different internal structures obtained as a function of the growth parameters. For the specific growth conditions corresponding to  $R = 0.05$  (higher hydrogen dilutions), the crystalline fraction and the optical band gap have the same variation trend as a function of the RF power.

#### Acknowledgments

The authors acknowledge partial financial support for this work from the DGAPA-UNAM PAPIIT Projects no. IN116409-2 and IN115909-2, the CONACyT México under project no. 48970, and the ICyTDF project no. PIFUTP08-143. A. Remolina thanks the scholarship grant by CLAF-Brasil and ICyTDF-México DF. M. F. García-Sánchez

acknowledges the postdoctoral fellowship from ICyTDF-México DF. The authors are grateful to Dr. J.C. Alonso and Dr. A. Ortiz<sup>†</sup> for the use of laboratory facilities for sample preparation, M. T. Vázquez Mejía, O. Jimenez, J. Camacho, and C. Gonzalez for technical and information services.

#### References

- [1] M. A. Green, *Third Generation Photovoltaics*, vol. 12 of *Springer Series in Photonics*, Springer, Amsterdam, The Netherlands, 2003.
- [2] J. Poortmans and V. Arkhipov, *Thin Film Solar Cells Fabrication, Characterization and Applications*, John Wiley & Sons, Sussex, UK, 2006.
- [3] D. L. Staebler and C. R. Wronski, "Optically induced conductivity changes in discharge-produced hydrogenated amorphous silicon," *Journal of Applied Physics*, vol. 51, no. 6, pp. 3262–3268, 1980.
- [4] P. Roca i Cabarrocas, A. Fontcuberta I Morral, and Y. Poissant, "Growth and optoelectronic properties of polymorphous silicon thin films," *Thin Solid Films*, vol. 403–404, pp. 39–46, 2002.
- [5] T. Nguyen-Tran, V. Suendo, P. Roca I Cabarrocas, L. N. Nittala, S. N. Bogle, and J. R. Abelson, "Fluctuation microscopy evidence for enhanced nanoscale structural order in polymorphous silicon thin films," *Journal of Applied Physics*, vol. 100, no. 9, Article ID 094319, 2006.
- [6] K. Morigaki, K. Takeda, H. Hikita, and P. Roca I Cabarrocas, "Light-induced defect creation in hydrogenated polymorphous silicon," *Materials Science and Engineering B*, vol. 121, no. 1–2, pp. 34–41, 2005.
- [7] A. Gajović, D. Gracin, K. Juraić, J. Sancho-Parramon, and M. Čeh, "Correlating Raman-spectroscopy and high-resolution transmission-electron-microscopy studies of amorphous/nanocrystalline multilayered silicon thin films," *Thin Solid Films*, vol. 517, no. 18, pp. 5453–5458, 2009.
- [8] D. Han, K. Wang, J. M. Owens et al., "Hydrogen structures and the optoelectronic properties in transition films from amorphous to microcrystalline silicon prepared by hot-wire chemical vapor deposition," *Journal of Applied Physics*, vol. 93, no. 7, pp. 3776–3783, 2003.
- [9] M. Ledinský, A. Vetushka, J. Stuchlík et al., "Crystallinity of the mixed phase silicon thin films by Raman spectroscopy," *Journal of Non-Crystalline Solids*, vol. 354, no. 19–25, pp. 2253–2257, 2008.
- [10] A. Remolina, B. M. Monroy, M. F. García-Sánchez et al., "Polymorphous silicon thin films obtained by plasma-enhanced chemical vapor deposition using dichlorosilane as silicon precursor," *Nanotechnology*, vol. 20, no. 24, Article ID 245604, 2009.
- [11] B. M. Monroy, G. Santana, J. Fandiño, A. Ortiz, and J. C. Alonso, "Growth of silicon nanoclusters on different substrates by plasma enhanced chemical vapor deposition," *Journal of Nanoscience and Nanotechnology*, vol. 6, no. 12, pp. 3752–3755, 2006.
- [12] B. M. Monroy, G. Santana, A. Benami et al., "Photoluminescence of as-grown silicon nanocrystals embedded in silicon nitride: influence of atomic hydrogen abundance," *Journal of Nanoscience and Nanotechnology*, vol. 9, no. 5, pp. 2902–2909, 2009.
- [13] J. C. Alonso, A. Ortiz, and C. Falcony, "Low temperature SiO films deposited by plasma enhanced techniques," *Vacuum*, vol. 43, no. 8, pp. 843–847, 1992.

- [14] G. Viera, S. Huet, M. Mikikian, and L. Boufendi, "Electron diffraction and high-resolution transmission microscopy studies of nanostructured Si thin films deposited by radiofrequency dusty plasmas," *Thin Solid Films*, vol. 403-404, pp. 467-470, 2002.
- [15] H. Shirai, "Role of chlorine in the nanocrystalline silicon film formation by rf plasma-enhanced chemical vapor deposition of chlorinated materials," *Thin Solid Films*, vol. 457, no. 1, pp. 90-96, 2004.
- [16] E. A. G. Hamers, A. Fontcuberta i Morral, C. Niikura, R. Brenot, and P. Roca i Cabarrocas, "Contribution of ions to the growth of amorphous, polymorphous, and microcrystalline silicon thin films," *Journal of Applied Physics*, vol. 88, no. 6, pp. 3674-3688, 2000.
- [17] H. Richter, Z. P. Wang, and L. Ley, "The one phonon Raman spectrum in microcrystalline silicon," *Solid State Communications*, vol. 39, no. 5, pp. 625-629, 1981.
- [18] E. Bustarret, M. A. Hachicha, and M. Brunel, "Experimental determination of the nanocrystalline volume fraction in silicon thin films from Raman spectroscopy," *Applied Physics Letters*, vol. 52, no. 20, pp. 1675-1677, 1988.
- [19] A. Matsuda, "Growth mechanism of microcrystalline silicon obtained from reactive plasmas," *Thin Solid Films*, vol. 337, no. 1-2, pp. 1-6, 1999.
- [20] G. Santana, J. Fandiño, A. Ortiz, and J. C. Alonso, "Low temperature-low hydrogen content silicon nitrides thin films deposited by PECVD using dichlorosilane and ammonia mixtures," *Journal of Non-Crystalline Solids*, vol. 351, no. 10-11, pp. 922-928, 2005.
- [21] D. Beeman, R. Tsu, and M. F. Thorpe, "Structural information from the Raman spectrum of amorphous silicon," *Physical Review B*, vol. 32, no. 2, pp. 874-878, 1985.

## Research Article

# Large-Scale Synthesis and Self-Assembly of Monodisperse Spherical TiO<sub>2</sub> Nanocrystals

Wei Kong, Chao Chen, Kaiguang Mai, Xinchao Shi, Rong Hu, and Zhiyu Wang

State Key Laboratory of Silicon Materials, Department of Materials Science and Engineering of Zhejiang University, Hangzhou 310027, China

Correspondence should be addressed to Zhiyu Wang, wangzhiyu@zju.edu.cn

Received 31 May 2010; Accepted 6 July 2010

Academic Editor: William W. Yu

Copyright © 2011 Wei Kong et al. This is an open access article distributed under the Creative Commons Attribution License, which permits unrestricted use, distribution, and reproduction in any medium, provided the original work is properly cited.

The spherical titanium dioxide nanocrystals were successfully synthesized in a new system through a solvothermal method. Prolonged reaction time can contribute to the improvement of the morphology and self-assembly behavior of TiO<sub>2</sub> nanocrystals. The central features of our approach are the use of rapid heating process and the use of both oleic acid and dodecylamine as two different capping surfactants to synthesize monodisperse TiO<sub>2</sub> nanocrystals. The morphologies and self-assembly behavior of TiO<sub>2</sub> nanocrystals are studied by transmission electron microscopy (TEM) analyses.

## 1. Introduction

The use of nanocrystals as “building blocks” for the self-assembly of new materials has attracted more and more attention these days because it provides a unique opportunity to bring together the inherent functionality and the collective properties of nanocrystals [1–4]. The morphology and interaction between the nanocrystals play an important role in the formation of self-assembled structures [5]. Nevertheless, the synthesis of monodisperse nanocrystals (size variation <5%) without a laborious size-sorting process only succeeds in some specific materials, which accounts for why rational planning of nanocrystals assemblies during synthesis is very difficult and most self-assembly processes are achieved with specific size and shape of nanocrystals [6]. Titanium dioxide (TiO<sub>2</sub>) is one of the most essential semiconductors, playing an important role in many applications such as paints, pigment, additive, gas sensors, photovoltaic cell, and photocatalysis. There are many research groups who succeed in the synthesis of various shapes of TiO<sub>2</sub> nanoparticles, such as sphere [7], sheet [8], rod [9], wire [10], cube [11], needle [12], bullet, [13] and diamond [13]. However, the self-assembly of anatase TiO<sub>2</sub> nanocrystals is not very successful. Our research group has obtained five different packing types (ribbon, smectic, domino, honeycomb, lamellar) of

TiO<sub>2</sub> nanorod and until now still rare studies addressed the nanodot self-assembly of TiO<sub>2</sub> [14]. This is because the monodisperse TiO<sub>2</sub> nanodots are not easy to prepare. The morphology of nanocrystals can be tuned by varying reaction conditions. The surfactant has the ability to control the size and shape of the nanocrystals, especially for the synthesis of metal oxides. The selective bindings of different surfactant molecules to different facets of TiO<sub>2</sub> lead to the crystal growth along different directions [15]. In addition, it is much easier to prepare the monodisperse nanocrystals if we separate the nucleation and growth processes [16].

Here, we report the successful preparation of well-ordered arrays of TiO<sub>2</sub> nanocrystals whose predominant shape is sphere. The solvothermal method is an economical mass-production route for the synthesis of TiO<sub>2</sub> nanodots. Moreover, this provides an opportunity to rational planning of TiO<sub>2</sub> nanodots assemblies during synthesis. The central features of our approach are the use of rapid heating process and the use of both oleic acid and dodecylamine as two different capping surfactants to synthesize monodisperse TiO<sub>2</sub> nanodots. It was found that the morphology and self-assembly behavior of TiO<sub>2</sub> nanodots become perfect with increase of reaction time. The formation of well-ordered arrays of TiO<sub>2</sub> nanocrystals has also been discussed in this paper.

## 2. Experimental

The TiO<sub>2</sub> nanodots were prepared by a solvothermal method. Tetrabutyl titanate (C<sub>16</sub>H<sub>36</sub>O<sub>4</sub>Ti or TBT), oleic acid (C<sub>18</sub>H<sub>34</sub>O<sub>2</sub> or OA), and dodecylamine (C<sub>12</sub>H<sub>27</sub>N or DDA) were of analytical grade and purchased from Sinopharm Chemical Reagent Co., Ltd without further purification. In a typical synthesis, TBT (9 ml) was added dropwise to OA (72 ml) with magnetic stirring at room temperature for 1 h. DDA (18 ml) was then added and the resulting mixture was under stirring kept for 24 h. The solution would gradually tune from pale yellow to orange, indicative of the formation of titanium oleate complex. The high-pressure reactor (High-Pressure Laboratory Reactor BR-100: 100 ml, BERGHOF) was heated to 290°C before the obtained complex was transferred into it to ensure rapid heating. Then, the high-pressure reactor was kept at 300°C for 10 h. After the reaction had proceeded for 1 h, 3 h, 6 h and 10 h, the resulting solution containing the nanocrystals was extracted and then cooled to room temperature. The nanocrystals were finally dispersed into toluene, providing stable optically clear colloidal solution, and then placing a droplet of the colloidal solution onto a carbon-coated Cu grid to allow the solvent to evaporate under ambient condition.

The transmission electron microscopy (TEM) experiments were performed at 80 kV using a JEM-1230 TEM. The powder X-ray diffraction (XRD) data of the sample was collected on a philips PW1050 powder diffractometer with Cu K $\alpha$  radiation source at 40 kV in the  $2\theta$  range of 20–80°.

## 3. Results and Discussion

Figure 1 shows TEM images of TiO<sub>2</sub> nanocrystals synthesized by solvothermal method for different time at 300°C. Average diameter of particles is (a) 5.6, (b) 7.0, (c) 8.0, and (d) 8.9 nm. As we have seen that the TiO<sub>2</sub> nanocrystals continue to grow with reaction times. However, the growth rate decreases due to decrease of titanium oleate complex concentration. The TEM images of Figures 1(a) and 1(b) contain a number of irregularly shaped nanocrystals and a part of the ordered regions. We only obtain a short-range arrangement of the TiO<sub>2</sub> nanocrystals rather than a long-range ordering which is mainly affected by the inhomogeneity of the nanocrystal shape and size. While, the TEM images of Figures 1(c) and 1(d) demonstrating the high size and shape uniformity of the nanocrystals make it possible to manipulate nanocrystals into a long-range ordered structure.

During the direct synthesis of monodisperse TiO<sub>2</sub> nanocrystals, we were able to ascertain that the use of rapid heating process and the use of both oleic acid and dodecylamine as two different capping surfactants can contribute to the preparation of the spherical TiO<sub>2</sub> nanocrystals. On one hand, the separation of nucleation and growth processes of the crystallization, which tend to take place at different temperatures, can help us to synthesize highly uniform nanocrystals [16]. The mixture was under stirring kept for 24 h because the nucleation was occurring at room temperature in the present system. After this, the reaction

mixture was quickly heated to 300°C (Our monitoring data show that the temperature can rise to 213°C in five minutes) to ensure the growth of TiO<sub>2</sub> nanocrystals without additional nucleation. On the other hand, because the growth process is time-dependent, we could obtain different TiO<sub>2</sub> nanocrystals while the reaction mixture was aged at 300°C for different hours. The improvement of TiO<sub>2</sub> nanocrystals can be attributed to the thermodynamic driving force at higher temperature for a relatively long time. On the other hand, it is possible to get nanocrystals of different shapes by varying the surfactants. When only OA was used, it tends to adhere on almost all of the surfaces of TiO<sub>2</sub>. The crystals grow mainly on high surface energy faces and favor the formation of nanorods. DDA have different functional groups with distinct binding strengths, which can be adsorbed on the different surfaces of TiO<sub>2</sub>. It is therefore expected that the shape of TiO<sub>2</sub> nanocrystals can be prepared by modulating the OA/DDA volume ratio. When the TBT/OA/DDA volume ratio is 1 : 8 : 2, the spherical nanocrystals with uniform size are obtained. These results ascertain that the cooperative effect of a specific amount of OA and DDA can contribute to the formation of the spherical TiO<sub>2</sub> nanocrystals.

Figures 1(c) and 1(d) show a TEM of a monolayer TiO<sub>2</sub> nanocrystal, where most of the particles can be identified to have a spherical shape and a long-range ordered structure could be observed. The evaporation dynamics is one of the most parameters affecting the assembly behavior of nanocrystals, which is that the self-assembly of nanocrystals occurring during the solvent evaporation of a nanocrystal-containing solution. Slow solvent evaporation is considered essential to this process, in which the concentration of the nanocrystal-containing droplet increases gradually and the free volume available for each nanocrystal decreases as the solvent has evaporated [17]. A large cluster will be formed inside droplet to play a role as the nucleation site, and a long-range ordered structure will be formed after the new incoming nanocrystals find their preferred location on the growing cluster face. The nanocrystals in order to get together to form a nucleation site are in need for sufficient time and the mobility provided by enough solvent. This explains why there will be no self-assembled pattern observed if the solvent evaporates very soon to dryness. In this experiment, despite using toluene that evaporated rapidly, the formation of the long-range ordered structure was still done. We believe that the self-assembly process may have occurred during the synthesis stage to some extent. This method may provide a reasonable plan to large-scale synthesis and self-assembly of monodisperse spherical TiO<sub>2</sub> nanocrystals.

The typical XRD patterns of powders synthesized by the solvothermal method are shown in Figure 2. The main peaks corresponding to standard anatase TiO<sub>2</sub> including (101), (004), (200), (105), (211), (204), (116), (220), and (215) are observed, which indicated that all samples are pure anatase phase without other TiO<sub>2</sub> polymorphs. It is apparent that no changes in crystal structure of the TiO<sub>2</sub> had occurred with the increase of reaction time. However, all the diffraction peaks of the samples become much sharper and stronger indicating improved degree of crystallinity. In addition, the intensity ratio of the (101) peak relative to the (200) peak is

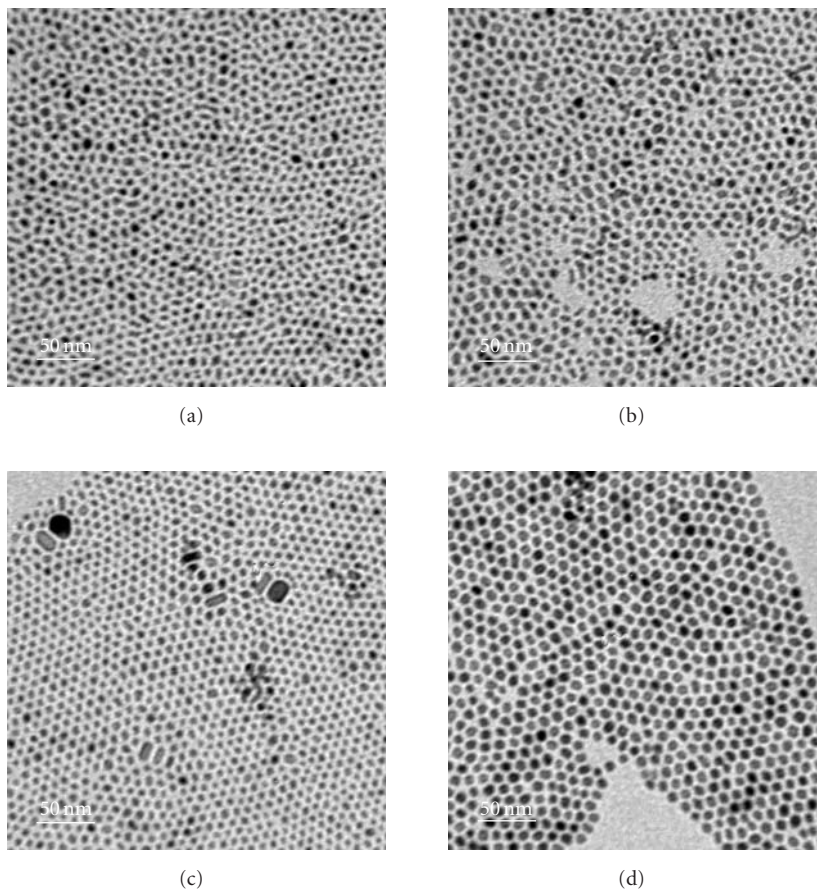


FIGURE 1: TEM images of  $\text{TiO}_2$  nanocrystals grown at  $300^\circ\text{C}$  for different reaction times: (a) 1 h, (b) 3 h, (c) 6 h, and (d) 10 h. Average diameters of particles are (a) 5.6, (b) 7.0, (c) 8.0, and (d) 8.9 nm. All scale bars are 50 nm.

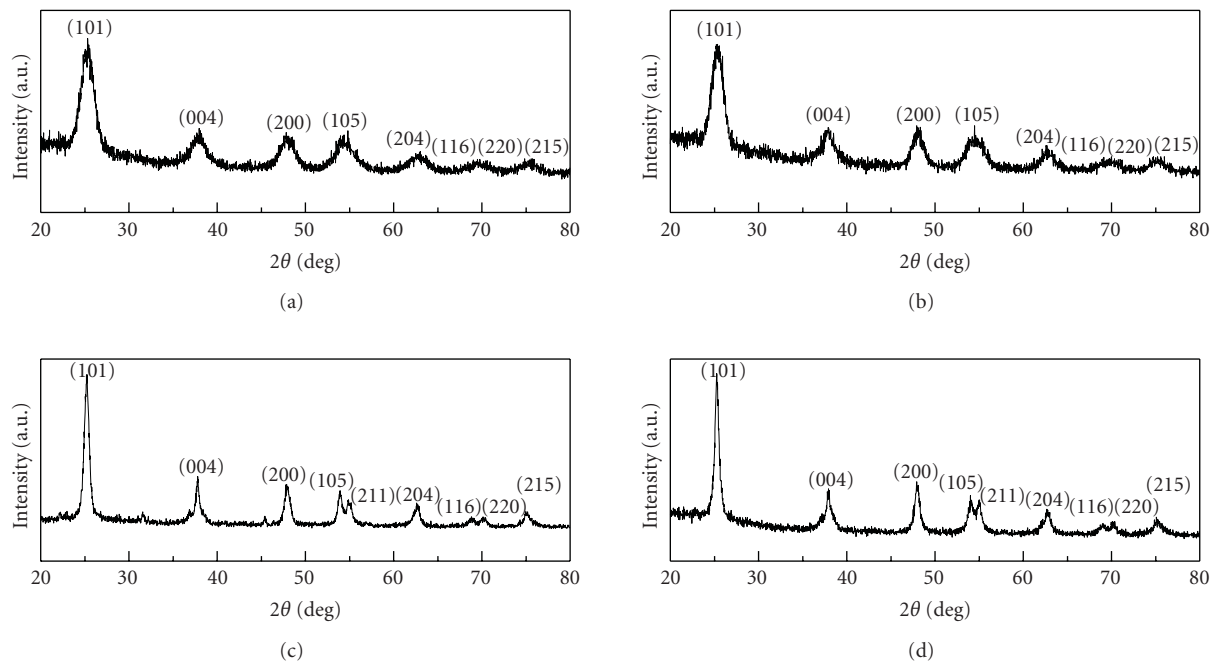


FIGURE 2: X-ray diffraction pattern of  $\text{TiO}_2$  nanocrystals synthesised for different hours at  $300^\circ\text{C}$ : (a) 1 h, (b) 3 h, (c) 6 h, (d) 10 h.

2.75, which is almost consistent with the spherical or bulk TiO<sub>2</sub>. Apart from TEM images of TiO<sub>2</sub> nanocrystals, this provides more evidence that the TiO<sub>2</sub> nanocrystals prepared by this new system are spherical in shape. All these XRD results can be ascribed to the inhibition of anisotropic growth of anatase TiO<sub>2</sub> nanocrystals.

#### 4. Conclusion

In conclusion, we demonstrate the controlled growth of spherical titanium dioxide in a new system through a simple solvothermal method. The use of rapid heating process and the use of both oleic acid and dodecylamine as two different capping surfactants can contribute to the preparation of the monodisperse spherical TiO<sub>2</sub> nanocrystals. When the TBT/OA/DDA volume ratio is 1:8:2, the spherical nanocrystals with different diameters are obtained. With the improvement of the high degree of uniformity of TiO<sub>2</sub> nanocrystals, the self-assembled pattern could be observed. This novel approach could be extended to large-scale synthesis and self-assembly of some other metal oxides.

#### Acknowledgment

This work has been funded by the Zhejiang Provincial Natural Science Foundation of China (Grant no. Z4080021).

#### References

- [1] C. J. Kiely, J. Fink, M. Brust, D. Bethell, and D. J. Schiffrin, "Spontaneous ordering of bimodal ensembles of nanoscopic gold clusters," *Nature*, vol. 396, no. 6710, pp. 444–446, 1998.
- [2] Z. L. Wang, S. A. Harfenist, I. Vezmar et al., "Superlattices of self-assembled tetrahedral Ag nanocrystals," *Advanced Materials*, vol. 10, no. 10, pp. 808–812, 1998.
- [3] D. V. Talapin, E. V. Shevchenko, C. B. Murray, A. Kornowski, S. Förster, and H. Weller, "CdSe and CdSe/CdS nanorod solids," *Journal of the American Chemical Society*, vol. 126, no. 40, pp. 12984–12988, 2004.
- [4] T. S. Sreeprasad, A. K. Samal, and T. Pradeep, "One-, two-, and three-dimensional superstructures of gold nanorods induced by dimercaptosuccinic acid," *Langmuir*, vol. 24, no. 9, pp. 4589–4599, 2008.
- [5] E. V. Shevchenko, D. V. Talapin, N. A. Kotov, S. O'Brien, and C. B. Murray, "Structural diversity in binary nanoparticle superlattices," *Nature*, vol. 439, no. 7072, pp. 55–59, 2006.
- [6] M. Niederberger and N. Pinna, *Metal Oxide Nanoparticles in Organic Solvents: Synthesis, Formation, Assembly and Application*, Springer, New York, NY, USA, 2009.
- [7] J. Tang, F. Redl, Y. Zhu, T. Siegrist, L. E. Brus, and M. L. Steigerwald, "An organometallic synthesis of TiO<sub>2</sub> nanoparticles," *Nano Letters*, vol. 5, no. 3, pp. 543–548, 2005.
- [8] H. G. Yang, G. Liu, S. Z. Qiao et al., "Solvothermal synthesis and photoreactivity of anatase TiO<sub>2</sub> nanosheets with dominant 001 facets," *Journal of the American Chemical Society*, vol. 131, no. 11, pp. 4078–4083, 2009.
- [9] Z. Zhang, X. Zhong, S. Liu, D. Li, and M. Han, "Aminolysis route to monodisperse titania nanorods with tunable aspect ratio," *Angewandte Chemie—International Edition*, vol. 44, no. 22, pp. 3466–3470, 2005.
- [10] D. K. Yi, S. J. Yoo, and D.-Y. Kim, "Spin-on-based fabrication of titania nanowires using a sol-gel process," *Nano Letters*, vol. 2, no. 10, pp. 1101–1104, 2002.
- [11] Y. Zhou, E.-Y. Ding, and W.-D. Li, "Synthesis of TiO<sub>2</sub> nanocubes induced by cellulose nanocrystal (CNC) at low temperature," *Materials Letters*, vol. 61, no. 28, pp. 5050–5052, 2007.
- [12] C.-C. Weng, C.-P. Chen, C.-H. Ting, and K.-H. Wei, "Using a solution crystal growth method to grow arrays of aligned, individually distinct, single-crystalline TiO<sub>2</sub> nanoneedles within nanocavities," *Chemistry of Materials*, vol. 17, no. 13, pp. 3328–3330, 2005.
- [13] Y.-W. Jun, M. F. Casula, J.-H. Sim, S. Y. Kim, J. Cheon, and A. P. Alivisatos, "Surfactant-assisted elimination of a high energy facet as a means of controlling the shapes of TiO<sub>2</sub> nanocrystals," *Journal of the American Chemical Society*, vol. 125, no. 51, pp. 15981–15985, 2003.
- [14] B. Ye, G. Qian, X. Fan, and Z. Wang, "Self-assembled superlattices from colloidal TiO<sub>2</sub> nanorods," *Current Nanoscience*, vol. 6, no. 3, pp. 262–268, 2010.
- [15] C.-T. Dinh, T.-D. Nguyen, F. Kleitz, and T.-O. Do, "Shape-controlled synthesis of highly crystalline titania nanocrystals," *ACS Nano*, vol. 3, no. 11, pp. 3737–3743, 2009.
- [16] J. Park, K. An, Y. Hwang et al., "Ultra-large-scale syntheses of monodisperse nanocrystals," *Nature Materials*, vol. 3, no. 12, pp. 891–895, 2004.
- [17] C. B. Murray, C. R. Kagan, and M. G. Bawendi, "Synthesis and characterization of monodisperse nanocrystals and close-packed nanocrystal assemblies," *Annual Review of Materials Science*, vol. 30, pp. 545–610, 2000.

## Research Article

# Controllable Assembly of Hydrophobic Superparamagnetic Iron Oxide Nanoparticle with mPEG-PLA Copolymer and Its Effect on MR Transverse Relaxation Rate

Xuan Xie and Chunfu Zhang

Med-X Research Institute, Shanghai Jiao Tong University, Shanghai 200030, China

Correspondence should be addressed to Chunfu Zhang, cfzhang@sjtu.edu.cn

Received 2 May 2010; Revised 14 July 2010; Accepted 15 August 2010

Academic Editor: William W. Yu

Copyright © 2011 X. Xie and C. Zhang. This is an open access article distributed under the Creative Commons Attribution License, which permits unrestricted use, distribution, and reproduction in any medium, provided the original work is properly cited.

Assembly of individual superparamagnetic iron oxide nanoparticles (SPION) into cluster is an effective way to prepare MRI contrast agent with high relaxivity. In this study, we fabricated SPION clusters with different sizes and configurations by assembly of amphiphilic mPEG-PLA copolymer with hydrophobic SPION in aqueous solution. The evolution of cluster size and configuration with the amount of copolymer and the effect of cluster size on the transverse relaxivity was studied.  $T_2$  relaxation rates of clusters with different sizes at iron concentration of 0.1 mM were compared with the theoretical predictions. We found that the relative amount of copolymer/SPION was crucial for the formation of SPION cluster. The transverse relaxivity of the condense SPION clusters (CSC) was size-dependent. The experimentally measured  $T_2$  relaxation rates of the clusters were lower than the theoretical predictions. In motional average regime (MAR) region,  $T_2$  relaxation rates were more consistent with the theoretical values when transmission electron microscope (TEM) evaluated size was used. Therefore, for fabrication of SPION clusters with assembly of mPEG-PLA and hydrophobic SPION, delicate balance between the amount of copolymer and SPION should be pursued, and for comparison of experimental  $T_2$  relaxation rate with theoretical predictions, TEM evaluated size was more suitable.

## 1. Introduction

Magnetic resonance imaging (MRI) is among the best noninvasive methodologies today in clinical medicine for assessing anatomy and function of tissues. The MRI technique offers several advantages such as excellent temporal and spatial resolution, the lack of exposure to radiation, rapid in vivo acquisition of images, and long effective imaging window [1]. These strengths make it a highly desirable modality for MR molecular imaging. However, due to its relatively lower sensitivity towards traditional small molecule contrast agents, such as Gd-DTPA, its success in this research field suffers.

Superparamagnetic iron oxide nanoparticle (SPION), because of its biocompatibility and much higher sensitivity than gadolinium contrast agent, is preferable for MR contrast enhancement. Currently, SPION coated with dextran and its derivatives have been used in clinical routine and also

extensively explored for MR molecular imaging [2, 3]. However, for detecting targets with lower expression level, contrast agents with much higher sensitivity are superior. Ultrahigh sensitive MnMEIO probe had been demonstrated not only to detect the expression but also to differentiate the expression level of HER2/Neu on tumor cells [4].

Increasing SPION size can increase its transverse relaxivity [5]. However, the large particles (at a size approximately larger than 15 nm) are not superparamagnetic [6] and easily aggregate in solution. Another way to increase  $T_2$  relaxivity, while keeping the superparamagnetic characteristics, is clustering individual SPION into clusters. Using polyelectrolyte-neutral block copolymers and by electrostatic adsorption and charge compensation between oppositely charged species, Berret et al. [7] fabricated maghemite nanocluster and tuned the size of aggregates in the range of 70–150 nm with aggregation numbers (number of nanoparticles per aggregate) from tens to hundreds. It was found that the transverse

relaxivity,  $r_2$ , was noticeably increased with the size of the magnetic clusters. Ai et al. had also obtained similar result for magnetic nanoparticles encapsulated into the hydrophobic cores of 20–100 nm polymeric micelles [8]. These studies indicated that clustering magnetic nanoparticles resulted in enhanced transverse relaxivity. In recent years, different strategies for fabrication of superparamagnetic magnetic nanoclusters had been put forward [9–11].

mPEG-PLA is an amphiphilic copolymer and ideal for fabrication of SPION cluster for MR molecular imaging *in vivo*. First, both PEG and PLA are FDA allowed. Second, the properties of PLA, such as crystallinity, tensile strength and hydrophobicity, can be easily modulated, thus the loading capacity for hydrophobic SPION can be tuned [12]. In addition, PEG is nonimmunogenic and highly hydrophilic. Surface coating with PEG has been demonstrated to extend nanoparticle circulation time *in vivo*, leading to better targeting behavior [13]. mPEG-PLA micelles have been shown to be able to load hydrophobic SPION and doxorubicin simultaneously and hold great promise for MR molecular imaging [10].

So, in this study, we fabricated SPION cluster with high MR sensitivity by assembly of hydrophobic SPION with amphiphilic mPEG-PLA copolymer. The relaxation rates of the clusters with different sizes and configuration were studied and compared with theoretical predictions. The condense SPION cluster (CSC) contrast agent may find its uses in MR molecular imaging of targets on tumor angiogenic vessels, such as,  $\alpha_v\beta_3$ , VEGFR, and vascular cell adhesion molecule (VCAM).

## 2. Experimental

**2.1. Chemicals.** Poly(ethylene glycol) methyl ether (mPEG, Mw 5000), D,L-lactide, Sn(II) octoate, Fe(acac)<sub>3</sub>, benzyl ether, oleylamine(70%), and 1,2-hexadecanediol(90%) were purchased from Sigma (St. Louis, MO). Other chemical reagents were obtained from Sinopharm Chemical Reagent Co. (China). Toluene was dried by refluxing over sodium under dry argon. All aqueous solutions were prepared with water from a Milli-Q water purification system.

**2.2. Synthesis of mPEG-PLA Copolymer.** mPEG-PLA was synthesized by ring opening polymerization of D,L-lactide at 110°C [10]. In detail, 1 g poly(ethylene glycol) methyl ether (mPEG, Mw 5000) was added into two-necked round flask, heated at 80°C under vacuum for 1 h, and subsequently cooled down to the ambient temperature. D, L-Lactide (1 g) was then added into the flask, and vacuumed overnight. Subsequently, freshly distilled toluene (10 mL) was injected into the flask and the polymerization was initiated by adding tin(II) 2-ethylhexanoate (60  $\mu$ L) as catalyst at 110°C with nitrogen flushing. After the reaction was performed for 4 h, the mixture was allowed to cool down to the ambient temperature, and toluene was removed by rotary evaporator. The final product was purified with THF three times.

**2.3. Synthesis of Hydrophobic SPION.** The hydrophobic SPIONs were synthesized following the published procedure

[11] with little modification. Briefly, Fe(acac)<sub>3</sub> (1 mmol), 1,2-hexadecanediol (5 mmol), oleic acid (3 mmol), oleylamine (3 mmol), and benzyl ether (10 mL) were mixed into a three-necked flask and magnetically stirred under a flow of nitrogen. The mixture was heated to 200°C for 2 h under a blanket of nitrogen and refluxed at 300°C for 1 h. After cooling to the ambient temperature, the solution was treated with ethanol and centrifuged to yield a dark-brown precipitate. The precipitate was washed with ethanol three times and finally dispersed in toluene.

**2.4. Assembly of mPEG-PLA with Hydrophobic SPION.** For assembly of mPEG-PLA with hydrophobic SPION, the hydrophobic SPION in toluene was first dried with nitrogen flow and mixed with mPEG-PLA (in 1 mL THF solution). Then, the mixture was quickly injected into water (5 mL) with vigorous stirring. THF was removed by evaporation at room temperature overnight. By varying the amount of SPION (0.67, 1.33 mg) or mPEG-PLA (0.1–0.5 mg) used, different size and configuration of magnetite clusters were able to be prepared.

### 2.5. Characterizations

**2.5.1. <sup>1</sup>H Nuclear Magnetic Resonance.** The polymerization of mPEG with D, L-Lactide monomers was characterized with nuclear magnetic resonance (Bruker Avance 500 MHz NMR, USA). The degree of polymerization was calculated by comparing integral intensity of characteristic resonance of PLA at 5.2 ppm (-C(=O)-CH(-CH<sub>3</sub>-)) and mPEG resonance at 3.64 ppm(-OCH<sub>2</sub>CH<sub>2</sub>-) in the <sup>1</sup>H spectra.

**2.5.2. Transmission Electron Microscope (TEM).** The morphology, size, and size distribution of the hydrophobic SPION and SPION clusters were characterized by TEM (JEOL 2100F, Japan). The particle suspension was directly deposited onto a carbon-coated copper grid and air-dried at room temperature. The particle size and size distribution were calculated using an image analysis program by measuring the diameter of at least 300 particles.

**2.5.3. Hydrodynamic Size.** The hydrodynamic size of the clusters was measured by dynamic light scattering (DLS) using a Malvern Autosizer 4700/PCS100 spectrometer equipped with an Ar ion laser operating at 488 nm. Triple measurements were performed, and the number- and volume-weighted mean size were taken.

**2.5.4. T<sub>2</sub> Relaxometry.** The relaxometry was performed using a 1.4 T minispec mq60 NMR Analyzer (Bruker, Germany) following the reported method [14]. The micelles were suspended at the iron concentrations between 0.001 and 10 mM. For MR measurements, 0.3 mL micelle dilutions were filled into the test tubes, and T<sub>2</sub> relaxation times were measured at 310 K using a standard Carr-Purcell-Meiboom-Gill pulse sequence with echo time  $\tau_{CP} = 0.5$  ms. The T<sub>2</sub> relaxivities were determined by a linear fit of the inverse relaxation times as a function of the iron concentrations.

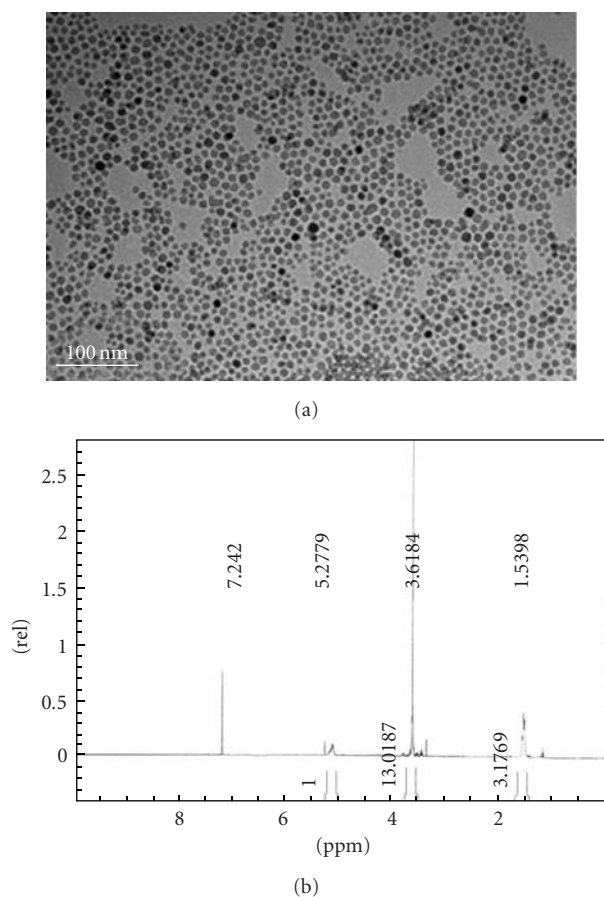


FIGURE 1: (a) TEM image of hydrophobic superparamagnetic iron oxide nanoparticles. The size of the particles is about 6 nm. (b) <sup>1</sup>H NMR spectrum of PEG (5 K)-PLA(2.5 K).

**2.5.5. Vibrating Sample Magnetometer (VSM).** Magnetic properties of hydrophobic SPION and SPION clusters were characterized in a vibrating sample magnetometer (LakeShore7300, USA). The tested samples were lyophilized and dried at 80°C under vacuum prior to analysis. The magnetization ( $M$ , emu g<sup>-1</sup>) of the samples was measured as a function of the magnetic field ( $H$ , Oe) at 298 K.

**2.5.6. Thermogravimetric Analysis (TGA).** TGA analysis for hydrophobic SPION and SPION clusters was performed with a NETZSCH TG 209 F1 iris instrument (NETZSCH, Germany) from room temperature to 1000°C with a heating rate of 10°C min<sup>-1</sup> in a nitrogen flow (20 mL min<sup>-1</sup>). The initial weight of sample was 10 mg. The weight fraction (wt%) of organic component (mPEG-PLA) and SPION in the clusters were deduced from the TGA curve.

### 3. Results and Discussion

**3.1. Synthesis and Characterizations of SPION and SPION Clusters.** By thermal decomposition of iron precursors in the organic solvent in the presence of surfactants, hydrophobic SPION with tunable sizes can be synthesized [11]. In this

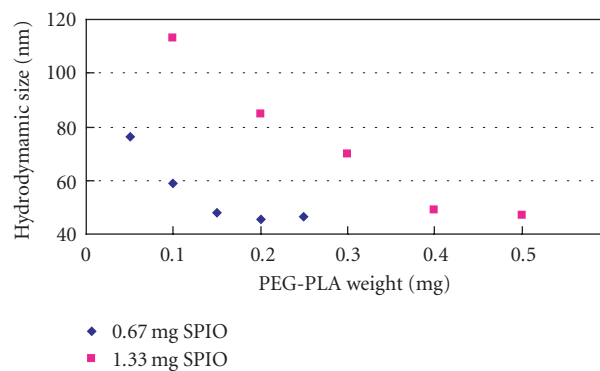


FIGURE 2: Evolution of hydrodynamic size (number weighted) of SPION clusters fabricated with different amounts of hydrophobic SPION or amphiphilic copolymer.

study, the size of SPION synthesized was about 6 nm, and it was coated with oleic acid and dispersed in toluene very well (Figure 1(a)) [15].

The polymerization of D,L-lactide monomers with mPEG induced by hydroxyl group was manifested by <sup>1</sup>H NMR spectrum. The characteristic peaks occurring at 5.2 ppm and 3.64 ppm in the <sup>1</sup>H NMR spectrum were the resonance of methine protons in PLA (-C(=O)-CH(-CH<sub>3</sub>-)) and methylene protons in PEG (-OCH<sub>2</sub>CH<sub>2</sub>-), respectively. By varying the amount of catalyst, mPEG-PLA copolymers with different molecular weights (Mw: 7100, 7500, 8400, and 9340) were synthesized. The representative <sup>1</sup>H NMR spectrum of mPEG-PLA with molecular weight of 7500 was shown in Figure 1(b).

For fabrication of SPION clusters, 0.67 mg hydrophobic SPION was first used to assemble with different amounts of mPEG-PLA. Increasing the amount of copolymer (Mw 7500) from 0.05 mg to 0.2 mg led to the decrease in the assembly size (number-weighted size, Figure 2). When the copolymer mass was more than 0.2 mg, the size of the cluster would not change significantly and maintained at about 45 nm. Morphologically, condense SPION cluster (CSC, Figure 3(a)) or blank mPEG-PLA micelle with SPION adhesion on the surface (referred to “loosen SPION cluster,” LSC) (Figure 3(b)) was observed during the change of cluster sizes. The evolution of cluster size and configuration with polymer amount were similar when double amount of SPION (1.33 mg) was utilized. However, a rise in SPION amount resulted in dramatical size increase (Figure 2).

The assembly of mPEG-PLA with hydrophobic SPION in aqueous solution is the result of strong absorption of SPION with the hydrophobic segment (PLA) of the amphiphilic polymer. Upon mPEG-PLA, SPION, and THF mixture is added into aqueous solution, the hydrophobic PLA chain is preferred to be inserted into the space between the oleic acids on SPION surface with hydrophilic PEG chain extending outside. With increase in mPEG-PLA amount in the aqueous solution, more polymer will be available for individual SPION and less SPION would be included in one cluster, which may decrease the cluster size. However, single SPION coated with mPEG-PLA was not found.

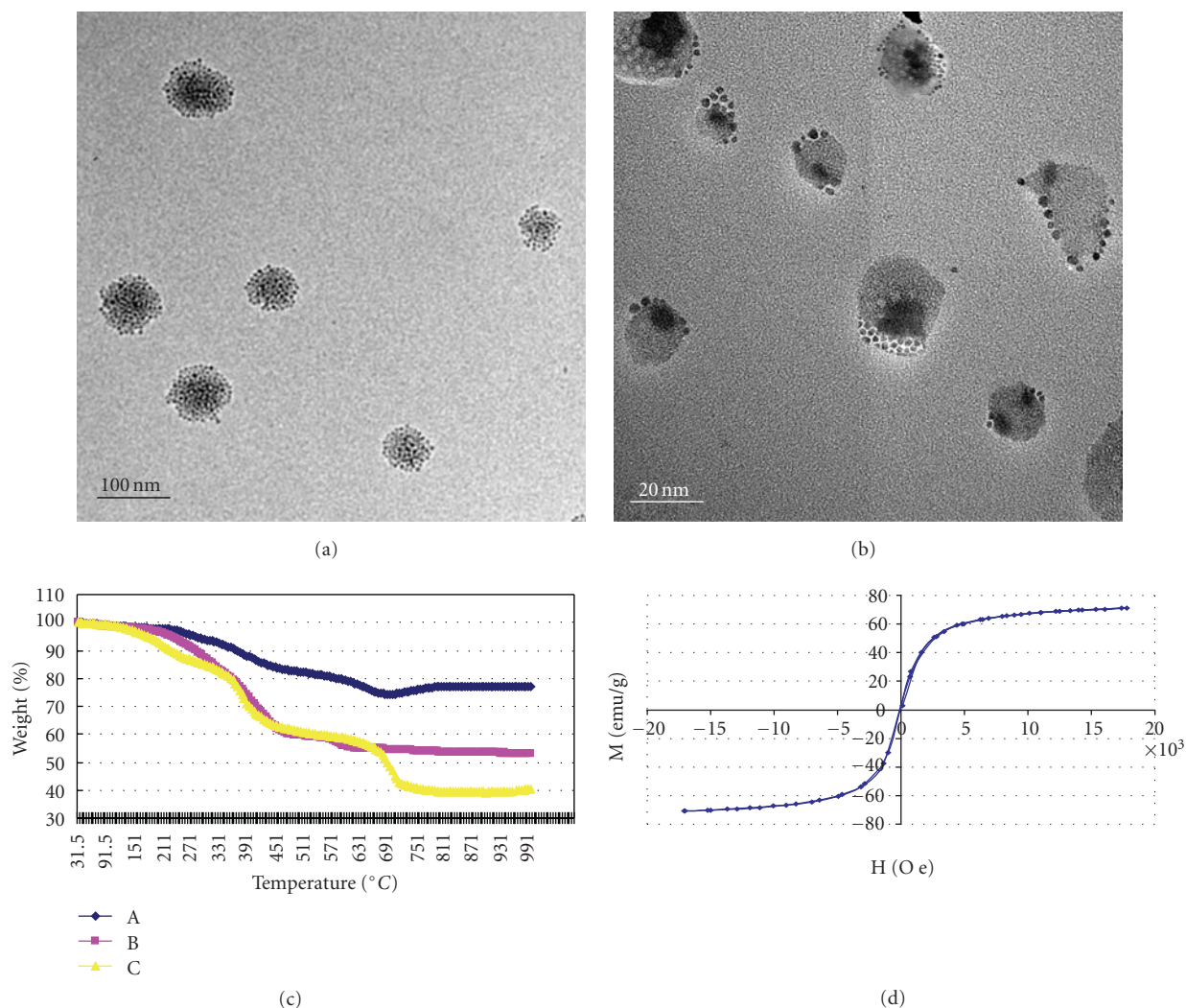


FIGURE 3: Characterizations of SPION clusters. (a) and (b) Representative TEM images of condense SPION clusters (CSC) and loosen SPION cluster (LSC), respectively. (c) TGA curve of hydrophobic SPION (A), condense SPION clusters (B) and loosen SPION cluster (C). (d) Magnetization plot of SPION as a function of the applied field at 298 K.

For fabrication of condense SPION cluster (CSC), Mw of mPEG-PLA did not affect the size of cluster significantly. As shown in Figure 2, in the case of assembly of 0.1 mg copolymer with 0.67 mg SPION with copolymer Mw of 7500, the size of cluster was 58.3 nm. When copolymers of different Mw (7100, 8400, and 9340) were used for assembly with identical mass of copolymer (0.1 mg) and SPION (0.67 mg), the sizes of the clusters were 60.6 nm, 58.1 nm, and 63.2 nm, respectively.

TGA curves of hydrophobic SPION, CSC, or LSC showed that the first step of thermal decomposition was around 100°C and the major decomposition occurred in the temperature range at 200–800°C. Less weight loss occurred at temperatures above 800°C (Figure 3(c)). The initial weight loss was due to removal of surface adsorbed water (hydrophobic SPION: 2.12%, CSC: 3.33%, and LSC: 6.87%). The weight loss between 200–800°C was attributed to the thermal degradation of organic components on the SPION surface or in the clusters (23.56% for hydrophobic SPION,

42.92% for CSC, and 55.55% for LSC). The contents for residues (SPION) were 74.32% for hydrophobic SPION, 53.74% for CSC, and 37.58% for LSC, respectively.

Magnetic properties of hydrophobic SPION, CSC and LSC were studied by using a vibration sample magnetometer (VSM). According to the SPION content deduced from TGA data, the saturation magnetization ( $M_s$ ) value of SPION was found to be 66.73  $\text{emu g}^{-1}$  (Figure 3(d)). The shape of the hysteresis curve was normal and tight with no hysteresis losses, which was expected as the behavior of superparamagnet [16].

$T_2$  relaxation rate ( $1/T_2$ ) of SPION cluster was fitted as a function of iron concentrations (Figure 4(a)). For condense SPION cluster (CSC),  $T_2$  relaxivities were 234, 363, and 413  $\text{s}^{-1}\text{mM}^{-1}$  at the sizes (number-weighted) of 49, 59, and 76 nm, respectively. When the size of the cluster reached 113 nm, the  $T_2$  relaxivity was as high as 512  $\text{s}^{-1}\text{mM}^{-1}$ . These findings were consistent with previous reports that clustering magnetic nanoparticles resulted in

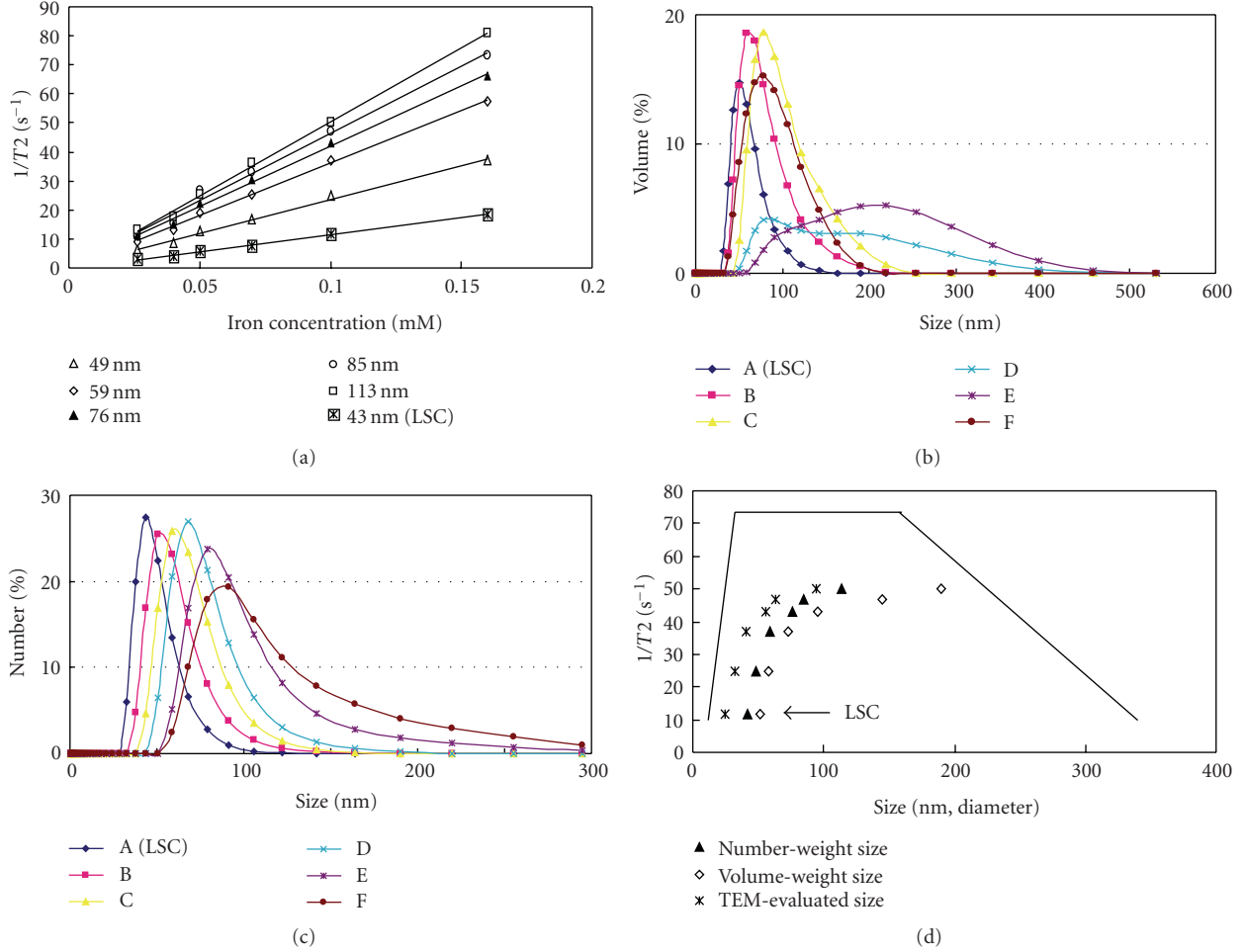


FIGURE 4: MR relaxation property of SPION clusters, these size distributions and comparison of the relaxation rates with theoretical predictions (d). (a) Relaxation rates of SPION clusters as functions of iron concentrations. (b) Size distribution of SPION clusters evaluated with volume-weighted method. (A) loosen SPION clusters (LSC): 58 nm. (B)–(F), condense SPION clusters (CSC): 73 nm, 95 nm, 97 nm, 144 nm and 199 nm, respectively. (c) Size distribution of SPION clusters evaluated with number-weighted method. (A) loosen SPION clusters (LSC): 43 nm. (B)–(F), condense SPION clusters (CSC): 48 nm, 59 nm, 76 nm, 85 nm and 113 nm, respectively. (d) Comparison of relaxation rates of SPION clusters with theoretical predictions with sizes evaluated with TEM or DLS (number-weighted and volume-weighted). The straight lines are fair approximations of the theoretical predictions (MAR, SD and ELR). Loosen SPION clusters (LSC) demonstrate the smallest sizes and relaxation rate.

enhanced transverse relaxivity [7, 8]. Whereas, for loosen SPION cluster (LSC), the  $T_2$  relaxivity was comparatively low (43 nm,  $r_2 = 116.94 \text{ s}^{-1} \text{ mM}^{-1}$ ).

**3.2. Comparison of the Experimental  $T_2$  Relaxation Rates with Theoretical Predictions.** In order to compare the experimental  $T_2$  relaxation rates with theoretical predictions, the  $T_2$  relaxation rates versus volume-weighted (Figure 4(b)) and number-weighted (Figure 4(c)) hydrodynamic sizes of SPION clusters were plotted at 0.1 mM iron concentration. The  $T_2$  relaxation rate of water in magnetic particle suspension is predicted by different regimes according to the size of the particle [17]. When particles are small, the  $T_2$  relaxation rate will be dominated by water molecular motions (motional average regime, MAR).  $1/T_2$  is proportional to  $\tau_D$

$$\frac{1}{T_2} = \frac{16f_v\Delta\omega^2\tau_D}{45}, \quad (1)$$

where  $f_v$  is the volume fraction of magnetic particles,  $\Delta\omega$  is the difference in angular frequency between the local field experienced by a proton at the equatorial line of the cluster surface and in the bulk, and  $\tau_D$  is the translational diffusion time around the cluster, in which

$$\Delta\omega = \frac{\gamma\mu_0 M}{3}, \quad (2)$$

$$\tau_D = \frac{R^2}{D}. \quad (3)$$

$\gamma$  is the proton gyromagnetic ratio (42.58 MHz/T);  $\mu_0$  the vacuum magnetic permeability ( $4\pi \times 10^{-7} \text{ Tm/A}$ );  $M$  the particle magnetization;  $R$  the particle radius;  $D_w$  the self-diffusion coefficient of pure water at 310 K ( $3 \times 10^9 \text{ m}^2 \text{ s}^{-1}$ ) [18].

When particle size increases to a certain size, the  $T_2$  relaxation rate reaches its maximum and is governed by static dephasing regime (SDR):

$$\frac{1}{T_2} = \frac{2\pi\sqrt{3}f_v\Delta\omega}{9}. \quad (4)$$

Above this size, it plateaus. Further size increase would result in decrease of  $T_2$  relaxation rate, which can be predicted by echo-limited regime (ELR). In this regime,  $T_2$  relaxation rate is proportional to  $1/\tau_D$  and is related to  $\tau_{CP}$ , with

$$\frac{1}{T_2} = \frac{1.8f_v(\Delta\omega\tau_{CP})^{1/3}(1.52 + f_v\Delta\omega\tau_{CP})^{5/3}}{\tau_D}. \quad (5)$$

The intersections of SDR with MAR (left edge of SDR,  $\tau_{D1}$ ) and ELR (right edge of SDR,  $\tau_{D2}$ ) are, respectively, at

$$\tau_{D1} = \frac{5\pi\sqrt{3}}{8\Delta\omega}, \quad (6)$$

$$\tau_{D2} = \left(\frac{1.49}{\Delta\omega}\right)(\Delta\omega\tau_{CP})^{1/3}(1.52 + f_v\Delta\omega\tau_{CP})^{5/3}; \quad (7)$$

[18].

Using the measured magnetization of SPION (66.73 emu/g), the theoretical  $1/T_2$  versus size of the particle (diameter) can be calculated by (1), (2), (4), and (5) with  $\tau_{CP} = 0.5$  ms and  $[\text{Fe}] = 0.1$  mM ( $f_v = 1.52 \times 10^{-5} [\text{Fe}]$  [17]). The result was plotted in Figure 4(d) as a line consisting of three straight segments. The experimental  $1/T_2$  data points were also shown in the figure *versus* number-weighted or volume-weighted hydrodynamic size.

According to (6) and (7), the calculated left edge and right edge of SDR are about 30 nm and 160 nm, respectively, which means that SDR is satisfied in this size range and  $T_2$  relaxation rate reaches its maximum ( $73.48 \text{ s}^{-1}$ ) and keeps unchanged. In our case, the sizes of SPION cluster (number-weighted or volume-weighted) all fall in this size range. However, for CSC,  $T_2$  relaxation rates increase (from  $25 \text{ s}^{-1}$  to  $43 \text{ s}^{-1}$ ) with cluster size increase, expressing MAR behavior and reach its maximum at size about 85 nm for number-weighted size and 144 nm for volume-weighted size. Moreover, compared with theoretical prediction, the measured  $T_2$  relaxation rate is much lower (for both MAR and SDR). This phenomena has also been observed for a styrene-acrylic acid copolymer-coated or dextran-coated iron oxide particles [18]. For LSC, the relaxation rate was also lower than that of theoretical prediction.

The possible explanation of the lower experimental value in MAR region may be that size evaluated by DLS with number-weighted or volume-weighted method was overestimated. When TEM-evaluated cluster size, which measures the size in “dry” state and may reflect the size more close to the “real” one, was applied, the measured relaxation rates were more closer to the theoretical line, which was consistent with the observation of micogel iron oxide particles [19]. However, in the SDR region, replacement with TEM size does not narrow the discrepancy between the experimental values and the theoretical prediction. Comparison of the experimental  $T_2$  relaxation rate of a particular SPION

formulation with that of theoretical prediction is complicated, which may involve the methods used for particle size evaluation [20, 21], magnetic property, surface coating, and even different formulation of the particles [18, 20]. The low  $T_2$  relaxation rate of the studied suspensions of iron-oxide particle clusters may be a general phenomena for all water suspensions of iron-oxide particles, and further experimental and theoretical studies are needed to confirm and understand it [18].

## 4. Conclusion

In this study, we fabricated magnetite nanoclusters with hydrophobic SPION (about 6 nm) and mPEG-PLA amphiphilic copolymer and compared the  $T_2$  relaxation rates with theoretical predictions. We found that the relative amount of mPEG-PLA and SPION for assembly played a crucial role in determining the size and configuration of the clusters. Condense SPION cluster or polymer sphere with surface SPION adhesion could be formed with different amounts of copolymer/SPION. For condense SPION clusters,  $T_2$  relaxivity of the cluster was size dependent.  $T_2$  relaxation rates of the clusters were lower than those of theoretical predictions. Compared with DLS method, TEM-evaluated size was more suitable for the comparison of experimental  $T_2$  relaxation rate with the theoretical prediction. In this regard, further experimental and theoretical studies are needed in the future to understand it.

## Acknowledgments

This work was supported by research Grants from National Nature Science Foundation of China (30870682), Science and Technology Commission of Shanghai Municipality (08ZR1411100, 0852nm04600), Major State Basic Research Development Program of China (973 Program) (no. 2010CB834303), SRF for ROCS, SEM, and Research Fund for the Doctoral Program of Higher Education of China (20090073120004).

## References

- [1] P. Debbage and W. Jaschke, “Molecular imaging with nanoparticles: giant roles for dwarf actors,” *Histochemistry and Cell Biology*, vol. 130, no. 5, pp. 845–875, 2008.
- [2] S. Laurent, D. Forge, M. Port et al., “Magnetic iron oxide nanoparticles: synthesis, stabilization, vectorization, physicochemical characterizations and biological applications,” *Chemical Reviews*, vol. 108, no. 6, pp. 2064–2110, 2008.
- [3] C. Corot, P. Robert, J.-M. Idée, and M. Port, “Recent advances in iron oxide nanocrystal technology for medical imaging,” *Advanced Drug Delivery Reviews*, vol. 58, no. 14, pp. 1471–1504, 2006.
- [4] J.-H. Lee, Y.-M. Huh, Y.-W. Jun et al., “Artificially engineered magnetic nanoparticles for ultra-sensitive molecular imaging,” *Nature Medicine*, vol. 13, no. 1, pp. 95–99, 2007.
- [5] M. R. J. Carroll, R. C. Woodward, M. J. House et al., “Experimental validation of proton transverse relaxivity models for superparamagnetic nanoparticle MRI contrast agents,” *Nanotechnology*, vol. 21, no. 3, Article ID 035103, 2010.

- [6] C.P. Bean and J. D. Livingston, "Superparamagnetism," *Journal of Applied Physics*, vol. 30, p. S120, 1959.
- [7] J.-F. Berret, N. Schonbeck, F. Gazeau et al., "Controlled clustering of superparamagnetic nanoparticles using block copolymers: design of new contrast agents for magnetic resonance imaging," *Journal of the American Chemical Society*, vol. 128, no. 5, pp. 1755–1761, 2006.
- [8] H. Ai, C. Flask, B. Weinberg et al., "Magnetite-loaded polymeric micelles as ultrasensitive magnetic-resonance probes," *Advanced Materials*, vol. 17, no. 16, pp. 1949–1952, 2005.
- [9] G. Riess, "Micellization of block copolymers," *Progress in Polymer Science*, vol. 28, no. 7, pp. 1107–1170, 2003.
- [10] N. Nasongkla, E. Bey, J. Ren et al., "Multifunctional polymeric micelles as cancer-targeted, MRI-ultrasensitive drug delivery systems," *Nano Letters*, vol. 6, no. 11, pp. 2427–2430, 2006.
- [11] S. Sun, H. Zeng, D. B. Robinson et al., "Monodisperse  $MFe_2O_4$  ( $M = Fe, Co, Mn$ ) Nanoparticles," *Journal of the American Chemical Society*, vol. 126, no. 1, pp. 273–279, 2004.
- [12] Y. Li, X. R. Qi, Y. Maitani, and T. Nagai, "PEG-PLA diblock copolymer micelle-like nanoparticles as all-trans-retinoic acid carrier: in vitro and in vivo characterizations," *Nanotechnology*, vol. 20, no. 5, Article ID 055106, 2009.
- [13] E. Blanco, C. W. Kessinger, B. D. Sumer, and J. Gao, "Multifunctional micellar nanomedicine for cancer therapy," *Experimental Biology and Medicine*, vol. 234, no. 2, pp. 123–131, 2009.
- [14] N. Sun, D.-X. Chen, H.-C. Gu, and X.-L. Wang, "Experimental study on T2 relaxation time of protons in water suspensions of iron-oxide nanoparticles: waiting time dependence," *Journal of Magnetism and Magnetic Materials*, vol. 321, no. 18, pp. 2971–2975, 2009.
- [15] F. Xu, D. Lei, and X. Du, "Modification of MR molecular imaging probes with cysteine-terminated peptides and their potential for in vivo tumour detection," *Contrast Media and Molecular Imaging*. In press.
- [16] A. Bumb, M. W. Brechbiel, P. L. Choyke et al., "Synthesis and characterization of ultra-small superparamagnetic iron oxide nanoparticles thinly coated with silica," *Nanotechnology*, vol. 19, no. 33, Article ID 335601, 6 pages, 2008.
- [17] A. Roch, Y. Gossuin, R. N. Muller, and P. Gillis, "Superparamagnetic colloid suspensions: water magnetic relaxation and clustering," *Journal of Magnetism and Magnetic Materials*, vol. 293, no. 1, pp. 532–539, 2005.
- [18] D.-X. Chen, N. Sun, Z.-J. Huang, C.-M. Cheng, H. Xu, and H.-C. Gu, "Experimental study on T2 relaxation time of protons in water suspensions of iron-oxide nanoparticles: effects of polymer coating thickness and over-low  $1/T_2$ ," *Journal of Magnetism and Magnetic Materials*, vol. 322, no. 5, pp. 548–556, 2010.
- [19] E. S. M. Lee, B. Shuter, J. Chan et al., "The use of microgel iron oxide nanoparticles in studies of magnetic resonance relaxation and endothelial progenitor cell labelling," *Biomaterials*, vol. 31, no. 12, pp. 3296–3306, 2010.
- [20] D.-X. Chen, N. Sun, and H.-C. Gu, "Size analysis of carboxy-dextran coated superparamagnetic iron oxide particles used as contrast agents of magnetic resonance imaging," *Journal of Applied Physics*, vol. 106, no. 6, Article ID 063906, 2009.
- [21] D.-X. Chen, A. Sanchez, E. Taboada, A. Roig, N. Sun, and H.-C. Gu, "Size determination of superparamagnetic nanoparticles from magnetization curve," *Journal of Applied Physics*, vol. 105, no. 8, Article ID 083924, 2009.

## Research Article

# Preparation and Ordered Self-Assembly of Nano-Pd-Ga/PMMA by Ultrasonic

**Xu Guo Cai, DAI Ming Hu, JI Xiao Li, Zhang Xiao Mei, and Xing Hong Long**

*School of Chemical Engineering, Anhui University of Science and Technology, Huainan 232001, China*

Correspondence should be addressed to Xu Guo Cai, gcxu@aust.edu.cn

Received 12 May 2010; Accepted 20 June 2010

Academic Editor: Quanqin Dai

Copyright © 2011 Xu Guo Cai et al. This is an open access article distributed under the Creative Commons Attribution License, which permits unrestricted use, distribution, and reproduction in any medium, provided the original work is properly cited.

Nano-Ga-Pd/poly methyl methacrylate (PMMA) composite materials were prepared with the palladium chloride solution containing metal gallium, MMA as monomer, and sodium dodecyl sulfate (SDS) as emulsifier without initiator or reducer. Pd, Ga, and Ga<sub>5</sub>Pd phase in PMMA matrix were identified by XRD. The characteristic absorption peak at 200 nm for nano-Ga/PMMA polymer solution, at 209 nm for nano-Pd/PMMA polymer solution were proved by UV-Vis; the binding energy changes of O1s, Ga2p<sub>3</sub>, Ga2d, and Pd3d were characterized by means of X-ray photoelectron spectroscopy. It is concluded that nano-Ga<sub>5</sub>Pd was produced based on segment electronics shifting from Gallium to Palladium, and coordination was formed on segment electronics from Gallium to oxygen of PMMA ester group. The anisotropism ordered assembly of PMMA around nano-Ga-Pd particles were illuminated by transmission electron microscopy; it is further interpreted that nano Ga-Pd particles had ordered-assembly induced effect.

## 1. Introduction

Nanocomposite materials have increasingly become a major part of new synthetic materials all over the world owing to their applications in mechanics, tribology, optics, magnetism, and electronics [1, 2]. Nanoalloy materials, which are different from the general alloy in both size and structure, have been one of the most promising and emerging research areas in advanced materials because of the unique properties [3, 4]. Lee and Shingu [5] in Tokyo University firstly prepared nanoalloy materials by ball milling. Subsequently, lots of new methods were used to prepare nanoalloy materials [6, 7], such as chemical reduction. However, there existed limitations in those methods: the reaction system was more complicated and the properties of the as-synthesized nanoalloy became bad because of initiator or metal reductant used in the preparation process. And in those methods, the as-synthesized nanosized alloy materials conglomerated easily, and so the nano-effect of nanomaterials weakened. To resolve these problems, the idea of the organic-based nanometal came into being and new nanocomposite alloys were reported to possess interesting properties [8, 9].

Ultrasonic radiation method was used widely to prepare nanomaterials because of its convenience, emulsification, dispersion, and cavitation. Works on nanometal particles synthesis in emulsion polymerization without initiator by means of ultrasonic radiation were reported [10], but literature on preparing Pd-Ga alloy nanocomposite particles by ultrasonic radiation cannot be found as far as our knowledge goes, let alone the ordered self-assembly of PMMA-based Pd-Ga nanocomposite. So-called self-assembly is the autonomous organization of components in system into patterns or structures without human intervention [11]. For polymer-based nanocomposites, the polymer chain would possess the ordered self-assembly phenomena due to nano-effect of nanometal particles. South Korean scholars [12] had reported that on nano-Fe<sub>2</sub>O<sub>3</sub> particles into composite would induce polystyrene-block-polypropylene (PS-b-PI) as composite matrix to self-assembly; the results showed that size and content of nano-Fe<sub>2</sub>O<sub>3</sub> into the nanocomposites had great impact on ordered self-assembly structure of PS-b-PI. Chinese scholars had studied that polyethylene (PE) crystallization would be induced by carbon nanotubes, of which the nanocomposites were composited [13]. XU group

[14] preliminarily reported that ordered self-assembly of PMMA was induced by nano-Ag-Ga alloy. The ordered self-assembly with long-range orientation selectivity of PMMA induced by Pd-Ga alloy is studied in the paper. As for ordered self-assembly of polymer into nanocomposites with nanometal particles, no paper was found as far as our knowledge goes.

In the paper, the PMMA-based nano Pd-Ga nanocomposites were prepared by ultrasonic radiation the gallium that has low-melting point (29.78°C) is easily comminuted into nano-granules by ultrasonic radiation, and the nanoalloy composed of both gallium and Palladium is mutually formed by the nano-granules of gallium from the bulk liquid gallium and palladium clusters reduced from palladium salt solution without metal reductant. Meanwhile poly (methyl methacrylate) synthesized by ultrasonication without any initiator in the emulsion system was used to wrap the nanoalloy to prevent the nanoparticles from coagulating, so the Pd-Ga/PMMA nanoalloy composite particles with core-shell structure are prepared.

## 2. Experimental

Preparation of Pd-Ga/PMMA nanoalloy composite particles was carried out as follow. A block of gallium (purity: 99.99%); high-purity palladium (II) chloride (PdCl<sub>2</sub>) (Chen-zhou Xiangchen Hi-tech Industry Co.Ltd, China), and a little of sodium dodecyl sulfate (abbreviated as SDS, purity: 90.0%) were added into a beaker containing a proportional distilled water, then a proportional methyl methacrylate, which was supplied by Shanghai Chemical Reagent Company and washed with 5% aqueous sodium hydroxide and subsequently washed by distilled water to neutrality, was poured into the beaker. Then, N<sub>2</sub> was piped into the mixture in the beaker to get rid of dissolved oxygen in the mixture for 15 min. The output power of the ultrasonic was adjusted to work efficiently before the ultrasonic generator (JY98-III ultrasonic generator, Ningbo Scientz Biotechnology Co., Ltd., China, frequency: 20 KHz, output power: 200~1200 W) was on. The reaction temperature was controlled between 40~45°C by circulating water. The system became emulsion and the color of the system became dusk after the ultrasonication for several minutes. The ultrasonic generator was terminated when the emulsion polymerization of methyl methacrylate and reduction of the palladium ion (II) were finished. The emulsion was refrigerated to demulsificate, then the precipitate was treated by filtering, washing, and drying in vacuum, and finally PMMA-based nano Pd-Ga composite particles were obtained.

The morphology of the nanoparticles was observed by means of high-resolution transmission electron microscope (TEM) (JEOL-2010, Japan Electronics Co., Ltd.) when a little of the powder samples was dispersed in acetone to form dispersion system, and the suspension was dropped to a copper grid. The crystalline phase of the powder was determined by using an X-ray diffractometer (XD-3, Beijing Pur-kinje General Instrument Co. Ltd. China) with DX-2000 ( $\lambda_{\text{CuK}\alpha} = 0.15418 \text{ nm}$ ), using graphite-monochromatic

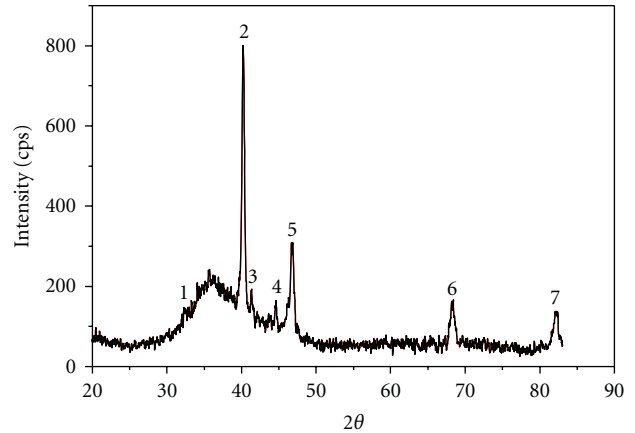


FIGURE 1: XRD pattern of the Pd-Ga/PMMA nanocomposite.

TABLE 1: Values of  $2\theta$  and  $d$  at XRD peaks of Pd-Ga/PMMA nanocomposite.

Peak	1	2	3	4	5	6	7
$2\theta$ (°)	32.30	40.31	41.37	44.48	46.77	68.31	82.23
$d$ (nm)	2.7691	2.2354	2.1809	2.0355	1.9402	1.3717	1.1712
Standard $d$ (nm)	2.7740	2.2407	2.1830	2.0410	1.9405	1.3721	1.1701

Cu-K $\alpha$  radiation ( $r = 0.154 \text{ nm}$ ) with an accelerating voltage of 40 KV, at scanning rate of  $0.02^\circ\text{S}^{-1}$  in  $2\theta$  ranging from  $10^\circ$  to  $85^\circ$ . The UV spectrum of the samples were tested by TU-1901 dual-beam UV spectrophotometer (Beijing PUXI Co. Ltd in China). The chemical composition of Pd-Ga/PMMA nanocomposites was tested by Thermo ESCA-LAB 250 X-ray photoelectron spectroscopy (Thermo Corporation, American).

## 3. Results and Discussion

The infrared spectrum of the nanocomposites was collected after purification and pellet pressed together with potassium bromide, characteristic peak of C=C ( $1638 \text{ cm}^{-1}$ ) nearly disappeared in Pd-Ga/PMMA spectrum, which indicated the polymerization of MMA monomer occurred completely by ultrasonic radiation. Characteristic peak of C=O and C-H in the spectrum of PMMA was shifted to short wave region in that of the nanocomposites, which hinted that there existed interaction between nanoalloy particles with PMMA matrix to some degree.

The X-ray diffraction patterns of Pd-Ga/PMMA composite particles by ultrasonic irradiation were shown in Figure 1; the four strong characteristic peaks, shown as peaks 2, 5, 6, and 7 in Figure 1, of Pd-Ga/PMMA composite lied in  $2\theta = 40.31, 46.77, 68.31,$  and  $82.23$ , which were corresponding to crystal face of [111], [200], [220], and [311] of Pd (PCPDFWIN#870639). The peaks at  $2\theta = 32.30, 41.37,$  and  $44.48$ , respectively, belonged to [211], [213] and [310] of Ga<sub>5</sub>Pd (PCPDFWIN#15-0577). But the peak of [114]

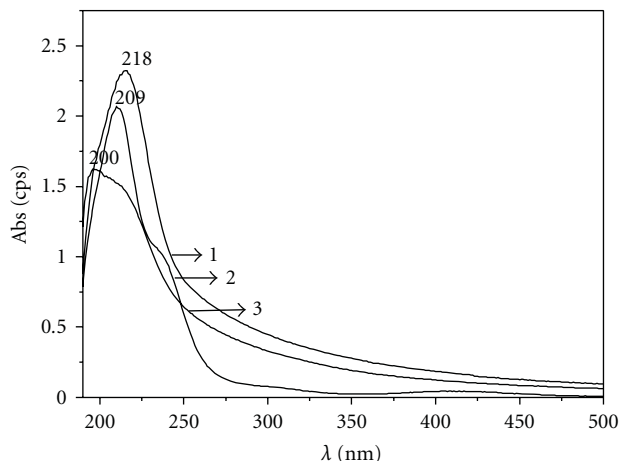


FIGURE 2: UV-Vis spectra of Pd-Ga/PMMA), nano-Pd/PMMA, and Ga/PMMA composites. (1) Pd-Ga/PMMA; (2) Pd/PMMA; (3) Ga/PMMA.

(standard  $d$  values are 2.1960 nm) of  $Ga_5Pd$  was not found, it is possibly explained that the peak of [114] was overlapped by that of [111] of Pd. The peak appeared at  $2\theta = 35^\circ$  was of amorphous peak of Ga with the low-melting point.

UV-visible absorption spectra of the samples are diagrammed in Figure 2. The peak that appeared at 207 nm was from Ga/PMMA composite, the peak at 209 nm from nano-Pd/PMMA composite, and the peak at 218 nm from nano Pd-Ga/PMMA composite. It was obvious that curve 3 at 218 nm for nano Pd-Ga/PMMA composite was different from curve 1 at 207 nm and curve 2 at 209 nm in absorption position and strength; it was indicated that this was contributed from palladium gallium alloy  $Ga_5Pd$  as dispersing nano-phase into nanocomposites.

To further investigate the microstructure information of the nano Pd-Ga/PMMA composites, XPS of the nano Pd-Ga/PMMA composite was performed and shown as in Figure 3(a), the results suggested that there were binding energy peaks of elements of carbon, oxygen, palladium, and gallium. The peaks of Ga2p region of the gallium was shown as Figure 3(b), the peak positioned at 1118.81 eV was correspondant to Ga2p3. In comparison with pure gallium with standard energy spectrum peaks at 1116.6 eV of Ga2p3 electron, the binding energy peaks were shifted to high region, increasing 2.2 eV. The peaks of Ga3d region of the gallium were shown as in Figure 3(c); the peaks positioned at 20.64 eV and 18.02 eV, respectively, were correspondant to Ga3d3/2 and Ga3d5/2, in comparison with pure gallium with standard energy spectrum peaks at 1116.6 eV of Ga2p3 electron. At 2138 eV of Ga3d3/2 and 18.52 eV of Ga3d5/2, respectively, the binding energy peaks were shifted to high region, increasing 2.2 eV, 0.74 eV and 0.5 eV, respectively; this phenomenon indicated that the chemical environment around Ga atoms was changed; the binding energy within the electronic shell was increased because of the decrease of valence electron density and the shielding effects of domestic electronic shell. In Figure 3(c), the energy spectrum peaks of Pd3d electrons positioned at 335.43 eV, which were

dropped down 2.07 eV than the standard energy spectrum peaks of Pd3d electrons that were positioned at 337.5 eV, that is, the energy spectrum peaks of Pd3d electrons within nanocomposites, moved to the low-binding energy region. This illustrated that chemical environment of palladium was changed due to getting some electronics from other atoms. For binding energy change of the gallium atom, on the one hand, in terms of interaction between gallium and palladium, the segment electron in 4d orbital of gallium flowed directly to 5s orbital of palladium in order to form a new alloy, namely,  $Ga_5Pd$  generated from Pd with Ga; on the other hand, coordination energy was based on segment electronics shifting from gallium to oxygen attached to ester group of PMMA into nanoalloy/PMMA composite. The curve of XPS spectrum of O1s pertain to the nano Pd-Ga/PMMA composite was fitted by means of Origin 6.1 shown in Figure 3(e); curve 1 peaked at 531.62 eV, in Figure 3(e) was originated from carboxyl (C=O), curve 2 peaked at 533.39 eV from ester group (C–O–C), and curve 3 from integration fitting peak of O1s in the two chemicals environment. Based on the standard dates of (532.62 eV) carboxyl (C=O) and (533.39 eV) ester group (C–O–C), the O1s binding energy peaks shift to lower region, which were reduced to 0.68 eV and 0.51 eV, respectively; it was probably due to carbonyl oxygen atom accepting electronics cloud to from gallium atom form nanoalloy of Pd-Ga into the nanocomposite. The XPS results proved that there existed interaction between carboxyl (C=O) oxygen and the nanoalloy.

The morphology of the nano Pd-Ga/PMMA composites was shown in Figure 4; it demonstrated that the nanocomposite was small in size about  $\sim 25$  nm with nanometal particles as core and PMMA as shell. The interesting TEM images of the nanocomposites were formed when observed in high-resolution TEM; it hinted that there were ordered self-assembly of PMMA in addition to possessing in ordered distribution state around the nanoalloy in Figure 4; the ordered self-assembly of PMMA possibly had something to do with not only content of nanometal, but also distance and direction apart from surface of nanometal in distribution. The more the content of the nanometal is, the more the obvious is phenomenon of ordered self-assembly of PMMA, comparing Figure 4(a) based on metal content 0.15% with Figure 4(b) based on metal content 0.3%. For selectively of distance and direction apart from surface of nanometal in distribution, on the one hand, ordered direction of PMMA self-assembly was vertical near to the surface of nanometal particles; on the other hand, ordered direction of PMMA self-assembly was changed from vertical to slope even to horizontal direction apart from the surface of the nanometal particles, shown as the inset in Figure 4(b). The mechanism of the ordered self-assembly of PMMA was probably imagined as induced effect of nanometal Pd-Ga particles into nanocomposites due to interaction of nano Pd-Ga with PMMA illustrated above. Based on the interaction of palladium gallium nanocrystals as discontinuous phase with PMMA as continuous phase, why did nanometal contained gallium as one of components into polymer-based nanocomposites would occur the ordered self-assembly, the

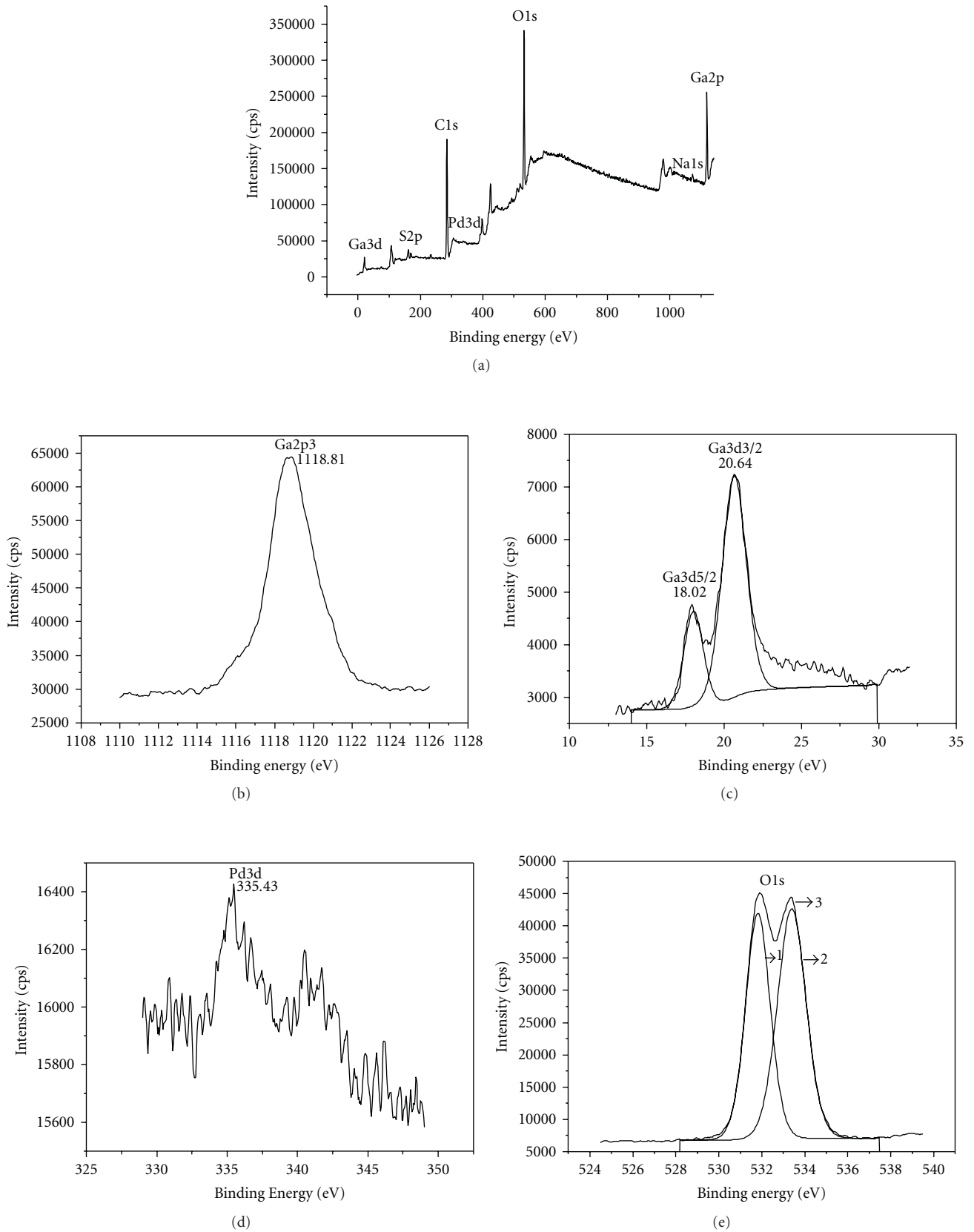


FIGURE 3: XPS of nano-Ga-Pd/PMMA composites powder. (a) XPS survey spectrum of nanocomposites; (b) Ga2p; (c) Ga3d; (d) Pd3d; (e) fitting curve of O1s. (1) C=O; (2) C-O-C; (3) integrate fitting peak of O1s in the two chemicals environment.

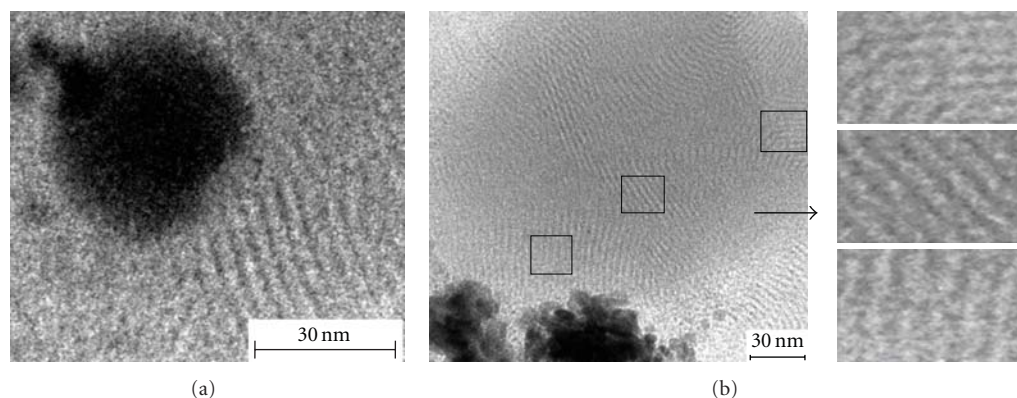


FIGURE 4: TEM images of the Pd-Ga/PMMA nanocomposite. (a) Metal Contention 0.15% (b) Metal Contention 0.3%.

possibly reason was suggested to come from stable atom-chain structure of gallium. Gallium itself possessed property to form stable atom-chain structure [15], and exhibit the most stable “Z” configuration. Gallium was mainly a component in the  $Ga_5Pd$  nanoalloy and was distributed possibly on the surface of the nanoalloy. On coordination of gallium atoms with oxygen of ester group attached to PMMA, oxygen atoms attached to PMMA were arranged along the direction of gallium atom-chain structure as a template; so, there were ordered oxygen atoms array and then ordered self-assembly of PMMA as polymer continuous phase into nanocomposites. The ordered self-assembly of PMMA as continuous phase into nano-Ag-Ga/PMMA composites possessed isotropic phenomenon in reported paper by XU group [14], which was closed ringlike around Ag-Ga particles as dispersing phase into nanocomposites; it was completely different to that of PMMA from the Pd-Ga nanocomposites. The possible reason was suggested that the nanosilver gallium alloy into polymer-based nanocomposites was presented to be isotropic based on hexagonal crystal, whereas the nano-palladium gallium alloy into polymer-based nanocomposites did not, it was found to be antitropic based on tetrahedron crystal.

#### 4. Conclusions

Nano-Ga-Pd /poly methyl methacrylate (PMMA) composite materials were prepared with the palladium chloride solution containing metal gallium without initiator reducer, MMA as monomer, and sodium dodecyl sulfate (SDS) as emulsifier under ultrasonic generator, in which  $Pd^{2+}$  ion was reduced to nano-palladium particles, meanwhile produced  $Ga_5Pd$  with microdrop of liquid gallium, and the monomers were polymerized simultaneously by ultrasonic radiation. The structure of nanocomposite with nano metal was characterized by means of IR, XRD, UV-Vis, TEM, and XPS. Pd, and  $Ga_5Pd$  as dispersing phase in PMMA matrix was identified by XRD. The results of UV-Vis spectrum showed that there was a characteristic absorption peak at 200 nm for nano-Ga/PMMA polymer solution, at 209 nm for nano-Pd/PMMA polymer solution, and at 218 nm for nano Pd-Ga/PMMA;

XPS proved that the O1s binding energy of C=O and C–O–C into nanocomposite was decreased compared to that of the standards, respectively, the meanwhile binding energy of  $Ga_{2p3}$ ,  $Ga_{2d3/2}$ , and  $Ga_{2d5/2}$  into Pd-Ga nanoalloy of the nanocomposite were increased; however, Pd3d binding energy was decreased; it is concluded that nano  $Ga_5Pd$  was formed on shifting of segment electronics of Gallium to Palladium, and coordination of gallium attached to nano Pd-Ga alloy and oxygen of ester group attached to PMMA was found on shifting of segment electronics of gallium to oxygen. So, there was interaction of nano metal particles with the polymer as matrix. Based on the interaction, TEM illuminated that ordered self-assembly of PMMA as continuous phase around nano-Ga-Pd particles into nanocomposites was presented and was found to be of anisotropism; it was further deduced that nano-Ga-Pd particles possessed induced effect on ordered self-assembly of polymer.

#### Acknowledgments

The authors are grateful for the support of the Natural Science Foundation of Anhui Province (Grant 090414183) and Science Foundation of Education, Department of Anhui Province, China (Grant KJ2009A46).

#### References

- [1] R. Ferrando, J. Jellinek, and R. L. Johnston, “Nanoalloys: from theory to applications of alloy clusters and nanoparticles,” *Chemical Reviews*, vol. 108, no. 3, pp. 845–910, 2008.
- [2] H.-J. Chen, Z.-W. Li, B.-B. Hu et al., “Preparation of Bi-Pb-Sn-Cd nanoalloy particles and its tribological properties as an additive in liquid paraffin,” *Mocaxue Xuebao/Tribology*, vol. 25, no. 2, pp. 169–172, 2005.
- [3] H. P. Wang, C.-Y. Liao, F.-L. Chen, C.-H. Huang, and Y. Fukushima, “Applications of Cu@C Nanoparticles in new dye-sensitized solar cells,” *Journal of Nanomaterials*, vol. 2009, Article ID 698501, 4 pages, 2009.
- [4] A. Das, R. Jurk, K. W. Stöckelhuber et al., “Nanoalloy based on clays: intercalated-exfoliated layered silicate in high performance elastomer,” *Journal of Macromolecular Science, Part A*, vol. 45, no. 2, pp. 144–150, 2008.

- [5] K.-M. Lee and P. H. Shingu, "Solid state reaction between powders and foils by low-energy ball milling," *Journal of Alloys and Compounds*, vol. 241, no. 1-2, pp. 153–159, 1996.
- [6] H. Kim and J. Cho, "Synthesis and electrochemical properties of Sn<sub>87</sub>Co<sub>13</sub> alloys by NaBH<sub>4</sub> and sodium naphthalenide reduction methods," *Electrochimica Acta*, vol. 52, no. 12, pp. 4197–4201, 2007.
- [7] H. Chen, Z. Li, Z. Wu, and Z. Zhang, "A novel route to prepare and characterize Sn-Bi nanoparticles," *Journal of Alloys and Compounds*, vol. 394, no. 1-2, pp. 282–285, 2005.
- [8] G. C. Xu, L. X. Xing, L. J. Ji, J. S. Shi, and M. Z. Zhang, "Synthesis and assembly of nano-copper/PMMA-b-PSt by ATRP," *Journal of Thermoplastic Composite Materials*, vol. 22, no. 5, pp. 475–484, 2009.
- [9] W. A. Lopes and H. M. Jaeger, "Hierarchical self-assembly of metal nanostructures on diblock copolymer scaffolds," *Letters to Nature*, vol. 414, no. 6865, pp. 735–738, 2001.
- [10] G. C. Xu, J. Y. Xiong, X. L. Ji, and Y. L. Wang, "Synthesis of nanosilver/PMMA composites via ultrasonically Bi-in situ emulsion polymerization," *Journal of Thermoplastic Composite Materials*, vol. 20, no. 6, pp. 523–533, 2007.
- [11] J. Ming, A. Eisenberg, L. Guojun, and Z. Xi, *Macromolecules Self-Assembly*, Science press, Beijing, China, 2006.
- [12] M. J. Park, J. Park, T. Hyeon, and K. Char, "Effect of interacting nanoparticles on the ordered morphology of block copolymer/nanoparticle mixtures," *Journal of Polymer Science, Part B*, vol. 44, no. 24, pp. 3571–3579, 2006.
- [13] L. Li, C. Y. Li, and C. Ni, "Polymer crystallization-driven, periodic patterning on carbon nanotubes," *Journal of the American Chemical Society*, vol. 128, no. 5, pp. 1692–1699, 2006.
- [14] J. Zhang, G. Xu, Y. Wang, and W. Chen, "Characterization of the structure of Ag-Ga/PMMA nanoparticles," *Acta Materiae Compositae Sinica*, vol. 24, no. 4, pp. 67–70, 2007.
- [15] S.-Q. Wu, G.-Z. Chen, and Z.-Z. Zhu, "Structural stabilities and electronic structures of Ga atomic chains," *Chinese Journal of Chemical Physics*, vol. 19, no. 3, pp. 219–222, 2006.

## Research Article

# Linear Assemblies of BN Nanosheets, Fabricated in Polymer/BN Nanosheet Composite Film

**Hong-Baek Cho, Tadachika Nakayama, Tsuneo Suzuki, Satoshi Tanaka, Weihua Jiang, Hisayuki Suematsu, and Koichi Niihara**

*Extreme Energy-Density Research Institute, Nagaoka University of Technology, 1603-1 Kamitomioka, Nagaoka, Niigata 940-2188, Japan*

Correspondence should be addressed to Hong-Baek Cho, hong-baekcho@etigo.nagaokaut.ac.jp and Tadachika Nakayama, nky15@vos.nagaokaut.ac.jp

Received 2 June 2010; Accepted 25 June 2010

Academic Editor: Bo Zou

Copyright © 2011 Hong-Baek Cho et al. This is an open access article distributed under the Creative Commons Attribution License, which permits unrestricted use, distribution, and reproduction in any medium, provided the original work is properly cited.

Linear assemblies of BN nanosheets (LABNs) were fabricated in polysiloxane/BN nanosheet composite film under a high DC electric field. The hexagonal BN nanosheets were dispersed by sonication in a prepolymer mixture of polysiloxane followed by a high-speed mixing. The homogeneous suspension was cast on a spacer of microscale thickness and applied to a high DC electric field before it became cross-linked. X-ray diffraction, scanning electron microscopy, and digital microscopy revealed that LABNs formed in the polysiloxane matrix and that the BN nanosheets in the LABNs were aligned perpendicular to the film plane with high anisotropy. This is the first time that linear assemblies of nanosheets have been fabricated in an organic-inorganic hybrid film by applying a DC electric field. The enhanced thermal conductivity of the composite film is attributed to the LABNs. The LABN formation and heat conduction mechanisms are discussed. The polysiloxane/BN nanosheet composite film has the potential to be used semiconductor applications that require both a high thermal conductivity and a high electric insulation.

## 1. Introduction

Methods for aligning nanosheets in polymer/nanosheet composites have received considerable interest because the physical properties of such composites can be enhanced when the nanosheets are suitably aligned in the polymer matrix [1–6]. In particular, the deformation, failure, heat resistance, and thermal properties of the polymer can be controlled by adding small quantities of hard inorganic particles. Well-aligned nanosheets with a one-dimensional orientation in a polymer matrix exhibit conductivity percolation at a much lower volume fraction than other powders [7–9]. Composites of anisotropically aligned graphite nanosheets in polymers have been attracting considerable interest since such composites exhibit high thermal and electrical conductivities [1, 6–8]. However, these composites have limited application as electrical insulators because graphite exhibits electrical properties that range from metallic to semiconducting [2–4]. Boron nitride (BN) is a promising

material for replacing graphite for applications that require insulators. It has one of the highest thermal conductivities of all electric insulators [10] and exhibits exceptional semiconducting properties with high band gap energies that vary in range 5.5 to 6.4 eV depending on the polymorph and superior chemical inertness. The thermal conductivity of hexagonal BN increases with increasing anisotropy: when BN nanosheets are aligned perpendicular to the *c*-axis, their thermal conductivity is almost 20 times greater than that when they are aligned parallel to the *c*-axis [10, 11]. Aligning nanosheets by reorientation in a polymer is an important technique; shear forces [12], magnetic forces [1, 2, 13], and electric fields [3, 4, 14] have been widely used to reorient nanosheets in a polymer matrix. Shear-induced assembly can align nanosheets in a polymer matrix without surface modification, but it cannot be used to orient nanosheets perpendicular to the composite film surface [12]. Orientating nanosheets using electric fields and magnetic forces normally requires modifying the nanosheet surface

by adding metal nanoparticles (e.g., iron nanoparticles) to achieve better orientation of the nanosheets [2, 3]. High torques, generated using nanosecond electrical pulses with potentials up to 40 kV, have been applied to avoid surface modification [15]. Orientating objects such as nanoparticles [16], nanotubes [17], and nanosheets [14, 17–19] in a polymer matrix by applying an electric field has been investigated to determine the orientation mechanisms in terms of the structure variation. Linear bundles of carbon nanotubes have been fabricated in organic solvents by applying a DC electric field [17]. Such elongated bundle structures are interesting because, unlike one-dimensional nanotube structures, two-dimensional structures enable nanosheets to be used as conducting fillers. However, no studies have investigated fabricating linear bundles of nanosheets in a solvent or a viscous polymer. Furthermore, there have been very few studies on fabricating ordered BN nanosheet-polymer composite films [15, 20] and there have been no detailed investigations on the dependence of the physical properties of composites on the arrangement of BN nanosheets.

The three objectives of the present study were to fabricate linear assemblies of BN nanosheets (LABNs) in a polymer/nanosheet composite film by applying a high electric field without modifying the surface, to determine the physical properties of the composite, and to clarify the dependence of the physical properties on the arrangement of the BN nanosheets in the polymer matrix. BN nanosheets homogeneously dispersed in a prepolymer mixture of polysiloxane were subjected to a high DC electric field during cross-linking of the system. X-ray diffraction (XRD), scanning electron microscopy (SEM), digital microscopy, and thermal conductivity measurements were used to characterize the composites.

## 2. Experimental

**2.1. Materials.** Polysiloxane/BN nanosheet composite films were prepared by introducing BN nanosheets into a polysiloxane prepolymer mixture. Hexagonal BN nanosheets ( $D_{90} = 10.6 \mu\text{m}$ , density:  $2.26 \text{ g/cm}^3$ , thickness: 2–10 nm) of commercial origin (Denka Co., Ltd.) were used. Two polysiloxane prepolymers with different viscosities were used: YE5822(A) (viscosity:  $1.2 \text{ Pa}\cdot\text{s}$ ), and YE5822(B) (viscosity:  $0.2 \text{ Pa}\cdot\text{s}$ ) (Momentive Performance Materials Inc.).

**2.2. Fabrication of Ordered Polysiloxane/BN Composite Films by Applying a High DC Electric Field.** Polysiloxane/BN nanosheet composites were prepared by the following method. 3 g of silicone YE5820(A) was sonicated for 5 min. 0.3 g of silicone YE5822(B) and 0.416 g of BN (5 vol%) were mixed, introduced into the sonicated silicone YE5820(A) and further sonicated for 10 min. The mixture was stirred using a high-speed mixer at 1500 rpm for 5 min to produce a homogeneous dispersion. It was then cast on a glass spacer ( $1.2 \text{ mm} \times 1.2 \text{ mm} \times 120 \mu\text{m}$ ) and subjected to a DC electric field (2.5 kV) for 16 h to enhance the orientation of the BN nanosheets in the polysiloxane prepolymer mixtures perpendicular to the electrodes. Finally, the prepared composites were dried for 0.5 h at  $80^\circ\text{C}$  to ensure complete curing.

**2.3. Characterization and Measurements.** The anisotropic alignment of BN nanosheets in the polymer films were analyzed by XRD (RINT 2500, Rigaku Co.). Reflections from the BN nanosheets were observed at  $2\theta = 26.76^\circ$  for the (002) plane and at  $2\theta = 41.60^\circ$  for the (100) plane. The linear distribution of BN nanosheets in a polysiloxane matrix was observed by digital microscope (VHX-9000, Keyence Co.). Cross-sections of the polymer/BN composite films were then cut and the surface morphologies of the composites were observed by SEM (JSM-6700F, JEOL Ltd.). The thermal conductivities of prepared composites were analyzed using a thermal diffusivity measurement system that is based on temperature wave analysis (ai-Phase Co., ai-Phase Mobile 1).

## 3. Results and Discussion

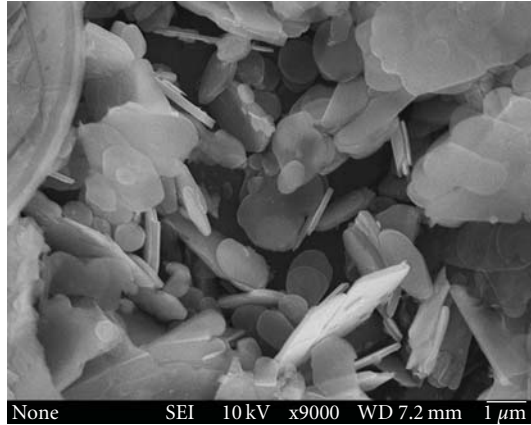
**3.1. Orientation and Linear Assembly of BN Nanosheets.** The relocation of nanoparticles in a suspension by an external torque force is very sensitive to particle size and bulkiness [21, 22]. In particular, when controlling the anisotropy of nanosheets in a viscous polymer by electrophoresis, nanosheets experience a high reversing force due to forces such as viscoelastic forces and a higher shear force than that exerted on nanorods or nanotubes [20]. Therefore, it is important to select BN nanosheets that are small and have high aspect ratios. Figure 1 shows SEM images of hexagonal BN nanosheets with diameters in the range 10–20  $\mu\text{m}$  and thicknesses in the range 2–10 nm; these nanosheets exhibited the highest electrophoretic response in water of all the nanosheets fabricated in a previous study by us [15]. The SEM images reveal that the BN nanosheets have graphite-like planar structures and that some of them have agglomerated, whereas others exist as single sheets. The BN nanosheets have smooth surfaces and curved edges.

As a modified graphite nanosheets and the prepolymer mixture are subject to a magnetic field, the graphite nanosheets orientate themselves to minimize the magnetostatic energy and to overcome the free energy (i.e., Brownian motion) of the system until they form a stable configuration [1]. Nanosheets become polarized in an electrical field, which results in a field-induced torque  $T$  acting on the sheet, which is given by

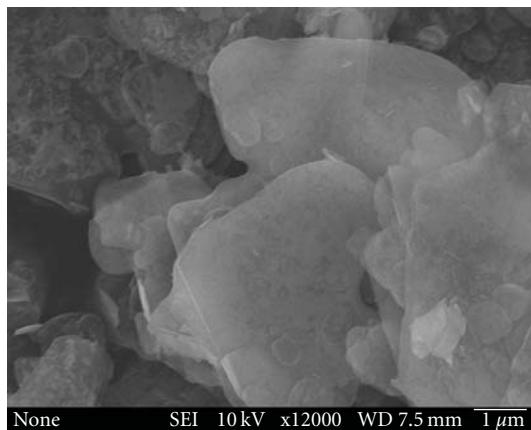
$$T = \mu \times E, \quad (1)$$

where  $\mu$  is the polarization moment and  $E$  is the electric field strength. The polarization can be divided into two contributing components: one parallel to the flake ( $\mu_{\parallel}$ ) and one perpendicular to the flake ( $\mu_{\perp}$ ). The torque orients the graphite parallel to the electric field and it opposes the viscous drag of the resin matrix [20, 23]. The total torque acting on the graphite flake can be expressed as a superposition of the torques due to the electric field which are parallel and perpendicular to its flake,  $T = \mu_{\parallel} \times E_{\perp} + \mu_{\perp} \times E_{\parallel}$  (where  $E_{\parallel} = E \cdot \cos \theta$  and  $E_{\perp} = E \cdot \sin \theta$ ). This can be written as

$$T = \frac{V}{2} \epsilon_0 \epsilon_2 \left( \frac{(\sigma_1 - \sigma_2)^2}{\sigma_1 \sigma_2} \right) \times E^2 \sin 2\theta, \quad (2)$$



(a)



(b)

FIGURE 1: Scanning electron micrographs of BN nanosheets; (a) low magnification (x9000) and (b) high magnification (x12,000).

where  $V$  is the volume of a single graphite flake,  $\theta$  is the angle between the electric field and the flake axis,  $\epsilon_0$  is the permittivity of free space,  $\epsilon_2$  is the relative dielectric constant of the resin matrix, and  $\delta_1$  and  $\delta_2$  are, respectively, the conductivities of the graphite flakes and the resin matrix [20, 23]. BN nanosheets require higher electric fields than GNs to control the anisotropy since BN is semiconducting. In particular, when nanosheets are oriented in a polymer and form a composite film with a thickness of the order of micrometers, the maximum electric field that can be applied is limited by the breakdown voltage of the polymer, which is lower than that of BN. The polysiloxane/BN composites produced in this study, which had thicknesses in the range 240–255  $\mu\text{m}$ , were electrically insulating up to a voltage of 2.5 kV. The effect of DC electric fields on the anisotropic alignment of BN nanosheets in polysiloxane was compared using XRD analysis (Figure 2). The degree of anisotropy of the BN nanosheets perpendicular to the film plane was estimated by comparing the intensity ratios between  $c$ -axis ( $I_{c\text{-axis}}$ ), ( $2\theta = 26.76^\circ$ ) and  $a$ -axis ( $I_{a\text{-axis}}$ ), ( $2\theta = 41.60^\circ$ )

$$\frac{I_{a\text{-axis}}}{I_{a\text{-axis}} + I_{c\text{-axis}}} \times 100(\%). \quad (3)$$

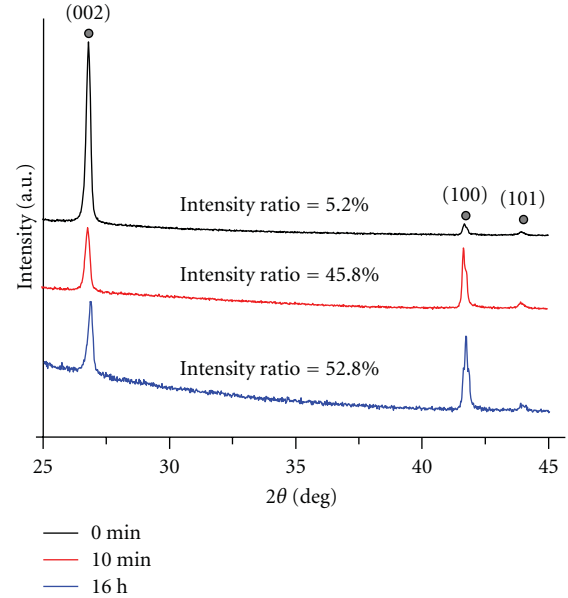


FIGURE 2: XRD patterns of polysiloxane/BN nanosheet composites produced by applying a DC electric field; (a) DC application (0 min), (b) DC application (10 min), (c) DC application (16 h).

The peaks at  $2\theta = 26.76^\circ$  and  $41.60^\circ$  are due to diffraction from the (002) and (100) planes in BN, respectively. If all of the hexagonal BN nanosheets were oriented perpendicular to the normal to the film plane, the (002) BN intensity peak would be low and the (100) peak intensity would be high. When BN nanosheets were introduced into the polymer without applying an electric field, the peak intensity of the (002) plane of BN overwhelmed that of the (100) plane, as observed for the composite that was fabricated without applying an electric field (0 min). The (100) peak intensity increased greatly relative to the (002) peak intensity on application of a DC electric field. Applying an electric field for 10 min increased the intensity ratio of BN to 45.8%; the ratio increased to 52.8% on applying an electric field for 16 h. This indicates that the randomly distributed BN nanosheets were aligned perpendicular to the composite film plane on application of a DC electric field and this effect increases with the duration of the electric field.

Cross-sections of prepared polysiloxane/BN composites were cut and analyzed to investigate the distribution of BN nanosheets in the polymer matrix as function of the application of time of the electric field (Figure 3). The bright regions in the images indicate areas having high densities of BN nanosheets, whereas the darker regions indicate areas with very low densities of BN nanosheets. When agglomerations of BN nanosheets lie beneath the surface being observed, bright, clear images of individual nanosheets will be observed (see Figure 3(a)). When the microscope is focused on one agglomeration of nanosheets in the composite, nanosheets located at different depths will appear bright, but blurred. The BN nanosheets in the composite prepared without applying an electric field have a homogeneous distribution. However, when an electric field

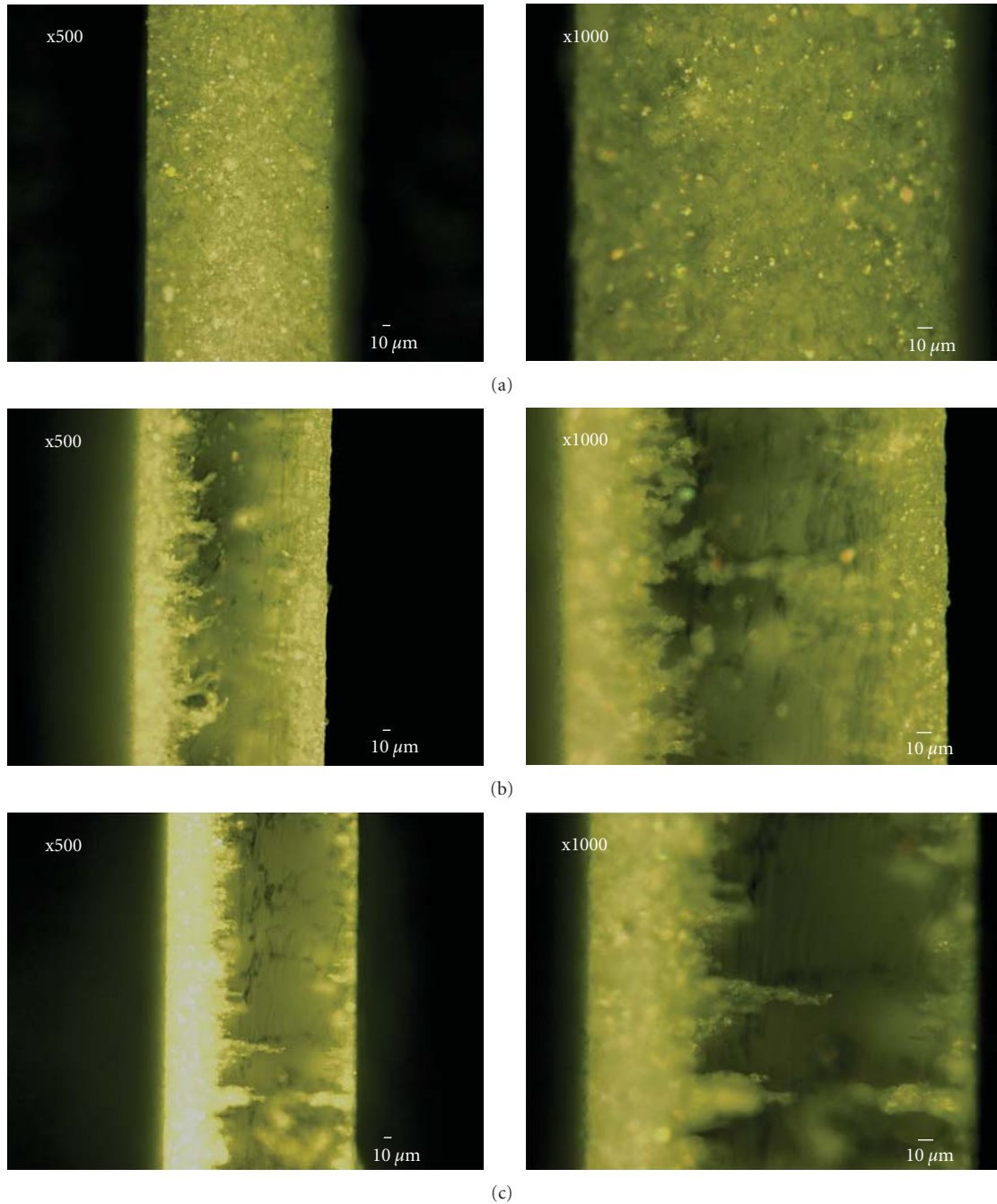


FIGURE 3: Cross-section view of polysiloxane/BN nanosheet composite film by digital microscope; (a) DC application (0 min), (b) DC application (10 min), (c) DC application (16 h).

is applied, the nanosheets moved to the side of the surface where the positive electrode was located. Both Figures 3(b) and 3(c) show higher BN nanosheet densities on the left-hand side, where the positive electrode was located. The BN nanosheet density on the left-hand side increased with longer application of the electric field (Figure 3(c)). In addition, the LABNs form filament-like structures inside the polymer; these structures are also aligned perpendicular to the film plane. Figure 3(b), which shows the sample prepared by applying an electric field for 10 min, reveals that the LABN

tips are bent and that the BN density on the left-hand side (i.e., near the negative electrode), is considerably higher than that for the composite prepared by applying an electric field for 16 h. This indicates that the BN nanosheets move from left to the right by electrophoresis and that this movement had not finished after 10 min. This means that the filament structures of LABNs were formed during application of an electric field for 10 min and were partially destroyed when the electric field was removed because of insufficient cross-linking of the prepolymer. Estimating from the high

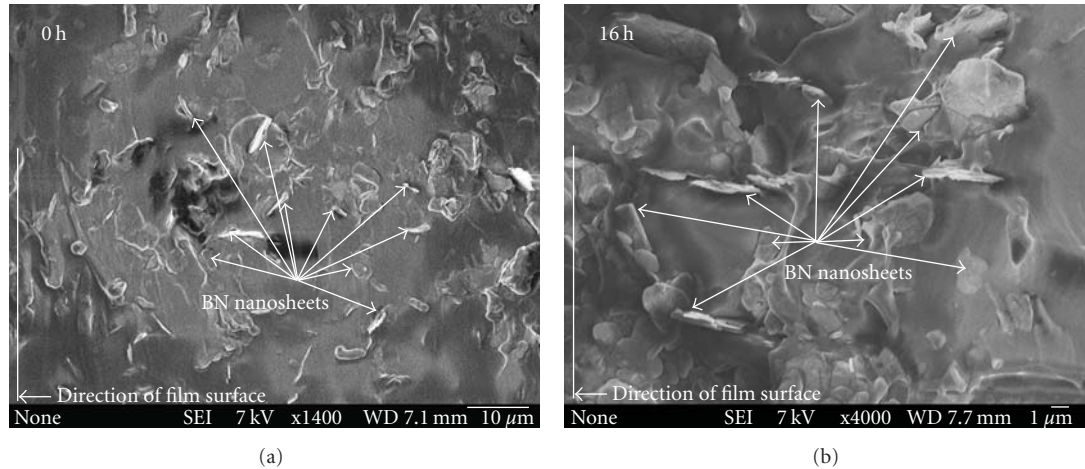


FIGURE 4: Cross-sectional SEM views of polysiloxane/BN composite film; (a) without and (b) with the application of DC electric field.

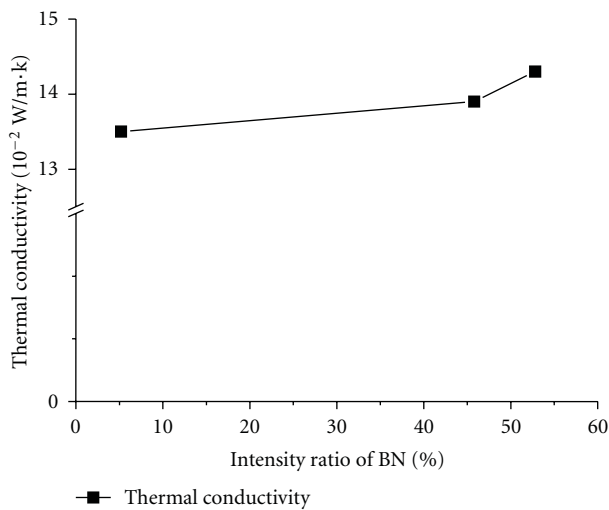


FIGURE 5: Comparison of thermo conductivities of polysiloxane/BN composite film.

intensity ratio of BN nanosheets in the polymer (Figure 2), the BN nanosheets within the filament structures of LABNs are aligned perpendicular to the film plane with a high anisotropy.

The alignment and distribution of the BN nanosheets in the LABNs are shown in cross-sectional SEM images (Figure 4). In the composite prepared without applying an electric field (Figure 4(a)), the BN nanosheets are randomly distributed with a low density. In contrast, the composite prepared by applying a DC electric field for 16 h have a comparatively high BN density and the majority of nanosheets are longitudinally aligned perpendicular to the film plane. Even though the BN nanosheets are tilted in different directions, their longitudinal surfaces are aligned perpendicular with the film plane. It is probable that the BN nanosheets become charged due to the polarization induced by the high DC electric field (2.5 kV). Carbon nanotubes have a high dipole moment along their longitudinal axis,

which is aligned in the direction of electric field [21]. The charge density has been predicted to increase at the edges of single-walled carbon nanotubes (SWCNTs) [13]. Under a high DC electric field, the surfaces of BN nanosheets are polarized stronger at their edges of their longitudinal surfaces and consequently they align parallel to electric flux. Coulombic attraction is another force that acts between the oppositely charged ends of nanotubes [24], and it causes the formation of linear structures at both ends of each nanotube; the nanotubes form very dense groups in solution due to electrophoresis. Linear bundles of SWCNTs have been fabricated in an electric field, but the SWCNT surfaces were modified by tetraoctylammonium ions and the experiment was performed in tetrahydrofuran [17]. The fabrication of LABNs in a polymer in the present study is significant because elongated structures with linearly aligned nanosheets were formed in a polymer resin by applying a high electric field without modifying the BN nanosheet surface.

The thermal conductivities of the prepared composites were measured to investigate the effect of anisotropy and the formation of LABNs on the thermal conductivity. Figure 5 shows a plot of the thermal conductivity as a function of the diffraction intensity ratio of BN nanosheets (5 vol% in the polymer) in the composites. The polysiloxane prepared by cross-linking the prepolymer mixture without adding BN nanosheets had a thermal conductivity of  $9.3 \times 10^{-2}$  W/m·K; this was remarkably increased by adding 5 vol% BN nanosheets. Furthermore, the thermal conductivity increased with increasing BN intensity ratio, which confirms that the thermal conductivity of polysiloxane/BN nanosheet composites increased as the anisotropic alignment of BN nanosheets in the polymer matrix increases.

**3.2. Fabrication Mechanism of LABNs.** The formation of filaments of LABNs contributed to the enhanced thermal conductivity, as shown in Figure 6. As mentioned above, nanosheets can be polarized by a strong DC electric field and the charge density increases toward the longitudinal

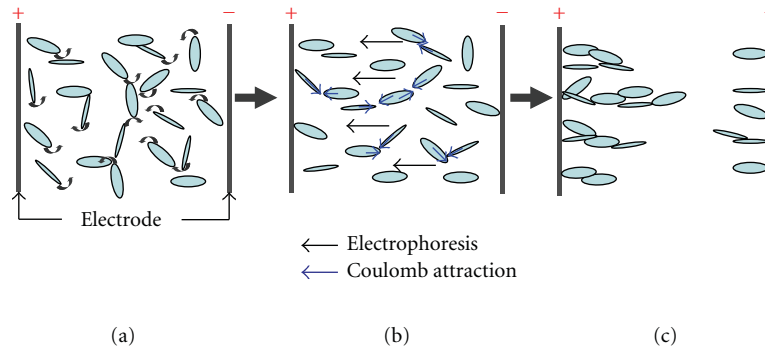


FIGURE 6: Schematic illustration of formation of LABNs under a DC electric field (2.5 kV); (a) rotation, (b) electrophoresis, (c) LABNs bundles.

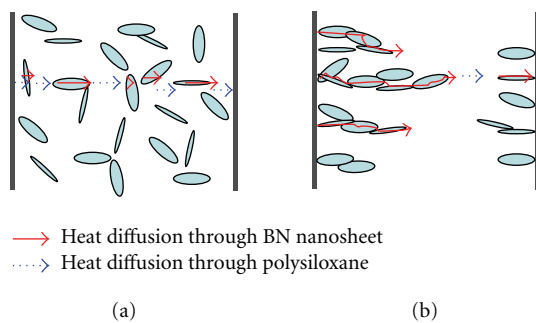


FIGURE 7: Schematic illustration of heat diffusion route in polysiloxane/BN nanosheets composite film; (a) random distribution, (b) ordered distribution with LABNs.

edges [13, 24]. The nanosheets align themselves parallel to the electric field to minimize the electrostatic energy and to overcome the free energy of the system, forming a stable configuration [1, 15]. The edges of BN two nanosheets in close proximity will become attached to each other by Coulomb attraction during electrophoretic movement in the prepolymer mixture before it is completely cured. Based on Figures 3 and 4, the filaments of LABNs are considered to be composed of groups of linearly aligned nanosheets. Some groups are connected while others are separate; they form a linear assembly as one component of the filament structure shown in Figure 6. These LABN structures enhance the thermal conductivity since heat diffuses along the path formed by linearly aligned BN nanosheets and by condensing the heat diffusion through the polymer (Figure 7). This result may be explained by the different thermal conductivities of polysiloxane and BN, and of the  $c$ - ( $\perp$ ) and  $a$ -axis ( $\parallel$ ) of BN nanosheets. The thermal conductivity increases remarkably on the addition of BN nanosheets to the polymer (see Figure 5) and the thermal conductivity of BN nanosheets parallel to the  $a$ -axis ( $\parallel$ ) is 20 times higher than that parallel to the  $c$ -axis ( $\perp$ ) [10, 11]. Consequently, the fabricated LABNs bundles in the polysiloxane/BN nanosheet composite films have the potential to be used in semiconductor applications that require electric insulators with high thermal conductivities.

## 4. Conclusions

Linear assemblies of BN nanosheets (LABNs) were successfully fabricated within polysiloxane/BN nanosheet composite film under a high DC electric field (2.5 kV). The filament structures of LABNs were composed of groups of linearly aligned BN nanosheets, which were fabricated by the mixed effects of polarization, dipole-dipole moment, electrophoresis, and coulombic attraction. The BN nanosheets which make up the LABNs showed high anisotropy, and their linear attachment was regarded to be critical for the higher thermal conductivity of the polysiloxane/BN composite film. The fabricated LABNs were considered to motivate efficient thermal conduction by transferring heat through a series of BN nanosheets which were aligned perpendicular to the composite film plane and by avoiding conduction through the polymer. This paper introduces filament structured linear assemblies of nanosheets fabricated within organic/inorganic nanocomposite material. Further works will focus on the fabrication of linear bundle bridges of BN nanosheets by alternating the DC electric field direction to enhance thermal conductivity.

## Acknowledgments

The authors are grateful for support from the New Energy and Industrial Technology Development Organization (NEDO), Ministry of Economy, Trade and Industry (METI), and the Ultra Hybrid Material Technology Development Project; “Ultra Hybrid”.

## References

- [1] W. Zhao, H. Wang, H. Tang, and G. Chen, “Facile preparation of epoxy-based composite with oriented graphite nanosheets,” *Polymer*, vol. 47, no. 26, pp. 8401–8405, 2006.
- [2] T. Takahashi, K. Suzuki, H. Awano, and K. Yonetake, “Alignment of vapor-grown carbon fibers in polymer under magnetic field,” *Chemical Physics Letters*, vol. 436, no. 4-6, pp. 378–382, 2007.
- [3] H. Wang, H. Zhang, W. Zhao, W. Zhang, and G. Chen, “Electrical conductivity and dielectric properties of PMMA/expanded graphite composites,” *Composites Science and Technology*, vol. 63, no. 2, pp. 225–235, 2003.

- [4] T. Takahashi, T. Murayama, A. Higuchi, H. Awano, and K. Yonetake, "Aligning vapor-grown carbon fibers in polydimethylsiloxane using dc electric or magnetic field," *Carbon*, vol. 44, no. 7, pp. 1180–1188, 2006.
- [5] F. D. C. Fim, J. M. Guterres, N. R. S. Basso, and G. B. Galland, "Polyethylene/graphite nanocomposites obtained by in situ polymerization," *Journal of Polymer Science, Part A*, vol. 48, no. 3, pp. 692–698, 2010.
- [6] M. Xiao, Y. Lu, S. J. Wang, Y. F. Zhao, and Y. Z. Meng, "Poly(arylene disulfide)/graphite nanosheets composites as bipolar plates for polymer electrolyte membrane fuel cells," *Journal of Power Sources*, vol. 160, no. 1, pp. 165–174, 2006.
- [7] X. S. Du, M. Xiao, Y. Z. Meng, and A. S. Hay, "Synthesis and properties of poly(4,4'-oxybis(benzene)disulfide)/graphite nanocomposites via in situ ring-opening polymerization of macrocyclic oligomers," *Polymer*, vol. 45, no. 19, pp. 6713–6718, 2004.
- [8] D. W. Liu, X. S. Du, and Y. Z. Meng, "Preparation of NBR/expanded graphite nanocomposites by simple mixing," *Polymers and Polymer Composites*, vol. 13, no. 8, pp. 815–821, 2005.
- [9] Z. Mo, Y. Sun, H. Chen et al., "Preparation and characterization of a PMMA/Ce(OH)<sub>3</sub>, Pr<sub>2</sub>O<sub>3</sub>/graphite nanosheet composite," *Polymer*, vol. 46, no. 26, pp. 12670–12676, 2005.
- [10] S. L. Rumyantsev, M. E. Levinshstein, A. D. Jackson, et al., "Boron nitride (BN)," in *Properties of Advanced Semiconductor Materials: GaN, AlN, InN, BN, SiC, SiGe*, M. E. Levinshstein, S. L. Rumyantsev, and M. S. Shur, Eds., pp. 67–92, John Wiley & Sons, New York, NY, USA, 2001.
- [11] T. Kawai and T. Kimura, "Magnetic orientation of isotactic polypropylene," *Polymer*, vol. 41, no. 1, pp. 155–159, 2000.
- [12] J. Lu, W. Weng, X. Chen, D. Wu, C. Wu, and G. Chen, "Piezoresistive materials from directed shear-induced assembly of graphite nanosheets in polyethylene," *Advanced Functional Materials*, vol. 15, no. 8, pp. 1358–1363, 2005.
- [13] R. Pascoe and J. P. Foley, "Effect of class I and II organic modifiers on retention and selectivity in vesicle electrokinetic chromatography," *Electrophoresis*, vol. 23, no. 11, pp. 1618–1627, 2002.
- [14] H. Wang, H. Zhang, W. Zhao, W. Zhang, and G. Chen, "Preparation of polymer/oriented graphite nanosheet composite by electric field-inducement," *Composites Science and Technology*, vol. 68, no. 1, pp. 238–243, 2008.
- [15] H.-B. Cho, M. Shoji, T. Fujiwara et al., "Anisotropic alignment of non-modified BN nanosheets in polysiloxane matrix under nano pulse width electricity," *Journal of the Ceramic Society of Japan*, vol. 118, no. 1373, pp. 66–69, 2010.
- [16] H. Watarai, M. Suwa, and Y. Iiguni, "Magnetophoresis and electromagnetophoresis of microparticles in liquids," *Analytical and Bioanalytical Chemistry*, vol. 378, no. 7, pp. 1693–1699, 2004.
- [17] P. V. Kamat, K. G. Thomas, S. Barazzouk, G. Girishkumar, K. Vinodgopal, and D. Meisel, "Self-assembled linear bundles of single wall carbon nanotubes and their alignment and deposition as a film in a dc field," *Journal of the American Chemical Society*, vol. 126, no. 34, pp. 10757–10762, 2004.
- [18] G. H. Kim and Y. M. Shkel, "Polymeric composites tailored by electric field," *Journal of Materials Research*, vol. 19, no. 4, pp. 1164–1174, 2004.
- [19] G. Chen, H. Wang, and W. Zhao, "Fabrication of highly ordered polymer/graphite flake composite with eminent anisotropic electrical property," *Polymers for Advanced Technologies*, vol. 19, no. 8, pp. 1113–1117, 2008.
- [20] H.-B. Cho, Y. Tokoi, T. Nakayama, et al., "Facile preparation of a polysiloxane-based composite with highly-oriented boron nitride nanosheets and an unmodified surface," *Composite Science and Technology*. In press.
- [21] V. Lobaskin, B. Dünweg, M. Medebach, T. Palberg, and C. Holm, "Electrophoresis of colloidal dispersions in the low-salt regime," *Physical Review Letters*, vol. 98, no. 17, Article ID 176105, 4 pages, 2007.
- [22] R. Pascoe and J. P. Foley, "Effect of class I and II organic modifiers on retention and selectivity in vesicle electrokinetic chromatography," *Electrophoresis*, vol. 23, no. 11, pp. 1618–1627, 2002.
- [23] H. Wang, H. Zhang, and G. Chen, "Preparation of unsaturated polyester/graphite nanosheet conducting composite under electric field," *Composites Part A*, vol. 38, no. 10, pp. 2116–2120, 2007.
- [24] C. A. Martin, J. K. W. Sandler, A. H. Windle et al., "Electric field-induced aligned multi-wall carbon nanotube networks in epoxy composites," *Polymer*, vol. 46, no. 3, pp. 877–886, 2005.

## Research Article

# GISAXS View of Induced Morphological Changes in Nanostructured CeVO<sub>4</sub> Thin Films

Magdy Lučić Lavčević,<sup>1</sup> Aleksandra Turković,<sup>2</sup> Pavo Dubček,<sup>2</sup> Zorica Crnjak Orel,<sup>3</sup> Bojan Orel,<sup>4</sup> and Sigrid Bernstorff<sup>5</sup>

<sup>1</sup> Faculty of Chemistry and Technology, University of Split, Teslina 10, 21000 Split, Croatia

<sup>2</sup> Rudjer Boskovic Institute, Bijenička 54, 10000 Zagreb, Croatia

<sup>3</sup> National Institute of Chemistry, Hajdrihova 19, 1000 Ljubljana, Slovenia

<sup>4</sup> Faculty of Computer and Information Science, University of Ljubljana, Trzaska cesta 1001 Ljubljana, Slovenia

<sup>5</sup> Sincrotrone Trieste, Strada Statale 14, km 163,5, in AREA Science Park, 34149 Basovizza, Trieste, Italy

Correspondence should be addressed to Magdy Lučić Lavčević, malula@ktf-split.hr

Received 31 May 2010; Revised 11 September 2010; Accepted 30 October 2010

Academic Editor: Quanqin Dai

Copyright © 2011 Magdy Lučić Lavčević et al. This is an open access article distributed under the Creative Commons Attribution License, which permits unrestricted use, distribution, and reproduction in any medium, provided the original work is properly cited.

Nanostructured CeVO<sub>4</sub> films, designed for applications in electrochemical cells and electrochromic devices, were obtained on glass substrates by the sol-gel process. An analysis of morphological modifications in these films, induced by ultrasonication, annealing, and introduction of lithium ions, was performed, using the grazing-incidence small-angle X-ray scattering technique (GISAXS). The GISAXS results are discussed and related with complementary examinations of the same films in real space, performed by scanning electron microscopy on a different length scale.

## 1. Introduction

The performance and integrity of electrodes in advanced electrochemical cells and electrochromic devices are closely related to their morphological characteristics [1]. It was shown in numerous investigations that sol-gel-derived films of titanium, cerium, and vanadium oxides [2–5] exhibit properties, which are desirable for such electrodes. One of the objectives in the research of advanced cells is intercalation of lithium into metal oxide electrodes [6]. The demands on such electrodes are very stringent: they should have significant capacity for lithium ions and maintain their integrity and electrochemical stability over many cycles. Not all demands can be satisfied by a single material. Composing of materials and, additionally, introducing disorder on different length scales (down to nanometric) into the electrode structure can significantly enhance its performance. This approach to improve the design of electrode systems highlights the potential of nanostructured materials that possess large surface areas and short diffusion paths [7, 8].

The characterization of sol-gel-derived films of various metal oxides suggests that they are porous nanostructures with a large inner surface area [2–5]. In this paper we focus on sol-gel-derived CeVO<sub>4</sub> films, which were prepared with equal molar ratios of vanadium pentoxide (V<sub>2</sub>O<sub>5</sub>) and cerium dioxide (CeO<sub>2</sub>), that is, at 55 atomic percent (55 atom %) of V. As single-material electrodes, transparent CeO<sub>2</sub> films show a good capacity for lithium ions and a passive optical behavior under intercalation [9]. V<sub>2</sub>O<sub>5</sub> films have a layered structure suitable for the intercalation of small ions [1]. As electrodes, they show long-term durability [3]. Previous examinations of film samples, prepared by the sol-gel procedure at different concentrations of V in V<sub>2</sub>O<sub>5</sub>/CeO<sub>2</sub> films (at 32 atom %, 38 atom %, 55 atom %, and 78 atom % of V) showed that they exhibit enhanced electrochemical properties and stability in comparison to standard oxide films [10]. These improvements indicated that nanostructured, mixed V<sub>2</sub>O<sub>5</sub>/CeO<sub>2</sub> films, especially those prepared at 55 atom % of V (i.e., CeVO<sub>4</sub> films) were structurally well designed for lithium intercalation.

Generally, nanostructured sol-gel-derived films can be considered as two-phased systems containing nanosized particles and pores. This model, originally suggested by small-angle X-ray scattering (SAXS) analysis, was also confirmed by complementary investigations performed on films with electron microscopy and X-ray diffraction. Particularly, in case of  $\text{TiO}_2$ , the estimation of the average crystallite sizes with the Debye-Scherrer' method in X-ray diffraction analysis was in accordance with the estimation of the average particle sizes using Guinier's method in SAXS analysis [2]. Our previous SAXS-based morphological analysis of  $\text{CeVO}_4$  films, derived by a standard sol-gel procedure, showed that they could also be considered as systems built of nanosized particles which are distributed throughout the films and which are growing during annealing [5].

As a continuation of the search for the best division of metal oxides in order to improve their electrochemical performance, the present analysis reports on the morphological modifications which can eventually be induced in  $\text{CeVO}_4$  oxide films by ultrasonication, annealing, and introduction of lithium ions. The analysis is based on the use of the two-dimensional grazing-incidence X-ray scattering (2D GISAXS) technique. In this technique, the penetration of X-rays in the film can be controlled by choosing an appropriate grazing angle of incidence. Our measurements were performed with a grazing angle of incidence close to the critical angle of total reflection for  $\text{CeVO}_4$  films. The SAXS analysis is generally suitable for the estimation of the size of scattering objects; the 2D detection of the scattering patterns enables an additional insight into the films' morphology, including eventual anisotropy and correlations effects. However, the interpretation of GISAXS features can be very ambiguous, especially in systems like ours, and the complete morphology description cannot be reached solely by 2D GISAXS analysis. Therefore the nanostructures were investigated also in real space with scanning electron microscopy.

## 2. Experimental

$\text{CeVO}_4$  films were obtained via the inorganic sol-gel process at 55 atom % of V [10]. The preparation of an aqueous dispersion of hydrated oxide (sol)  $\text{V}_2\text{O}_5$ ,  $\text{CeO}_2$ , and mixed  $\text{V}_2\text{O}_5/\text{CeO}_2$  started from a solution of the corresponding metal oxide or metal salt,  $\text{V}_2\text{O}_5$ , and  $\text{Ce}(\text{NH}_4)_2(\text{NO}_3)_6$ , respectively. Crystalline  $\text{V}_2\text{O}_5$  was dissolved in 6% nitric acid to obtain 0.044 M aqueous solution. By the evaporation of water, the desired concentration of  $\text{V}_2\text{O}_5$  was obtained. From the aqueous solution of  $\text{Ce}(\text{NH}_4)_2(\text{NO}_3)_6$  precipitates were obtained by addition of  $\text{NH}_4\text{OH}$  until pH = 9 was reached. The peptization was performed by the addition of equimolar quantity of  $\text{HNO}_3$ , aged up to 363 K. By diluting in water, the  $\text{CeO}_2$  sol of the desired concentration was obtained. Mixed sol was obtained by adding 55 atom % of  $\text{CeO}_2$  sol into the  $\text{V}_2\text{O}_5$  sol. As a new step in the preparation procedure, high energy and high frequency sound (125 W, 20.1 kHz) were applied to the sol for 10 minutes. The films were deposited on  $\text{SnO}_2:\text{F}$  glass substrates ( $2 \times 3 \times 0.1 \text{ cm}^3$ ) by the dip-coating technique, as one-dip layers, with pulling speed of 10 cm/min, and heated at 673 K.

Four samples were prepared: sample A1, prepared as described and annealed for 5 minutes; sample A2, prepared as described and annealed for 15 minutes; sample B1, prepared as A1 and intercalated with lithium ions; sample B2, prepared as A2 and intercalated with lithium ions.

Scattering experiments were performed at the SAXS beamline [11], at the ELETTRA synchrotron radiation source in Trieste (Italy). A photon energy of 8 keV ( $\lambda = 0.155 \text{ nm}$ ) was used, and the beam size was  $4 \text{ mm} \times 0.150 \text{ mm}$  (horizontal  $\times$  vertical). The film samples on glass substrates were examined, using grazing-incidence geometry [12]. For X-rays, the index of refraction,  $n$ , of solids is less than one, that is,  $n = 1 - \eta' - i\eta''$ , where  $\eta'$  and  $\eta''$  are the real (dispersion) and imaginary (absorption) parts of the correction term, respectively. For small incident angles of X-rays, measured with respect to the film surface, it is convenient to introduce the so-called critical angle,  $\alpha_c = \sqrt{2\eta'}$ . Namely, at angles smaller than  $\alpha_c$ , total reflection of X-rays takes place. In grazing-incidence geometry, the grazing-incident angle,  $\alpha_i$ , is close to  $\alpha_c$ . For grazing-incident angles larger than the critical, the reflectivity decreases steeper than the value given by the Fresnel theory because of deviations of the sample surface from ideal flatness. In the case of our samples, the measurements were performed at grazing-incident angles slightly larger than the critical angle, providing a penetration depth up to 100 nm [13]. The critical angle (around  $0,37^\circ$ ) was determined experimentally for each film.

In the used setup for GISAXS measurements, samples were mounted on a stepping-motor-controlled tilting stage with a step resolution of  $0.001^\circ$ . At first, the stage (and the sample surface) was aligned horizontally and parallel to the incoming beam within  $\pm 0.1^\circ$ . The scattering geometry is shown in Figure 1. The sample orientation with respect to the incident beam, specified by the wave vector  $\mathbf{k}_i$ , was chosen in order to keep the grazing-incident angle in the range  $0.4^\circ < \alpha_i < 1.4^\circ$ , for which the effective area of the beam foot print is smaller than the sample surface area ( $20 \text{ mm} \times 20 \text{ mm}$ ). The outgoing beam (with the exit angle  $\alpha_f$ ) is presented by the wave vector  $\mathbf{k}_f$ . The maximum of the scattered intensity is in the direction of the specular reflection,  $\mathbf{k}_{\text{SR}}$ . For the specularly reflected beam, the exit angle equals the incident angle. Together with the reflected beam, a diffuse scattering is present, although of much lower intensity. This diffuse scattering from a surface, measured under nonspecular condition, that is, when the exit angle is different from the incident angle, yields information about structural features along the surface. This diffuse surface scattering contribution is concentrated near the specular plane. When well-defined particles are randomly distributed within the film, they cause additional diffuse scattering. This type of scattering can be easily separated from the surface scattering, since it does not depend on the incident angle. Also, it is easily recognized, since its contribution is a function of the total scattering angle ( $2\theta$ ) only and is constant for  $|\mathbf{q}|^2 \approx q_y^2 + q_z^2 = \text{constant}$ , where  $\mathbf{q} = \mathbf{k}_f - \mathbf{k}_i$  is the total scattering wave vector (Figure 1). The absolute value of the scattering wave vector equals  $q = 2\pi \sin \theta / \lambda$ .

The scattering intensity spectra were recorded by a 2D X-ray CCD detector, containing  $1024 \times 1024$  pixels and

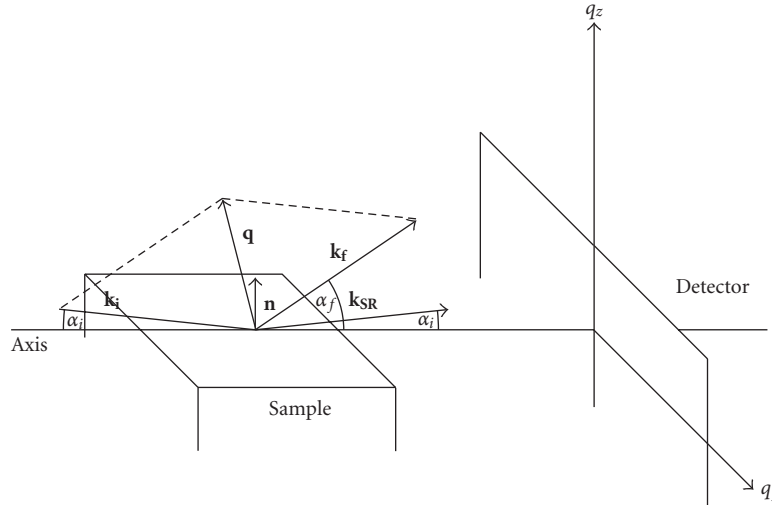


FIGURE 1: The geometry of GISAXS measurements.  $\mathbf{k}_i$  is the wave vector of the incident X-ray beam,  $\mathbf{k}_f$  is the wave vector of the outgoing X-ray beam, and  $\mathbf{q}$  is the scattering wave vector, with the components,  $q_y$  and  $q_z$ . The unit vector  $\mathbf{n}$  is normal to the sample surface. The wave vector  $\mathbf{k}_{SR}$  is in the direction of the specular reflection.

positioned perpendicular to the incident beam. A thin Al strip was placed in front of the detector to avoid its overflow in the specular plane direction, where the usually much stronger surface (specular and diffuse) scattering is present and in order to have better resolution of the diffuse part of the scattering off the specular plane (particle contribution). The recorded spectra were corrected for readout noise and detector response.

Samples were finally analyzed by field emission scanning electron microscopy (FSEM).

### 3. Results and Discussion

2D GISAXS intensity maps, recorded for samples A1, A2, B1 and B2 are shown in Figures 2(a), 2(b), 2(c), and 2(d). The maximum of the scattered intensity is in the direction of the specular plane ( $q_y = 0$ ), which is normal to the surface of the sample. This scattered intensity is partly reduced by a thin Al absorber (vertical strips in the patterns are depleted intensities). The lower part of the scattering is missing because of the absorption in the sample. For exit angles equal to incident critical angle ( $\alpha_f = \alpha_c$ ), there is an enhancement in the scattering intensity due to the refraction effects, which is also known as Yoneda peak.

By comparing the patterns of samples A1 and A2, we see that a change in morphology is induced by prolonged annealing. Furthermore, the differences in the patterns of A1 and B1 indicate that the change in morphology of the initial sample A1 also takes place as a consequence of the intercalation of lithium. There is no qualitative essential difference between patterns of samples A2 and B2, so it seems that intercalation in a prolongedly heated sample does not strongly affect its morphology on the nanoscale.

Besides the analysis of features of the 2D GISAXS maps, the method of interpreting scattering data is based on the analysis of scattering curves, which show the dependence

of the intensity,  $I$ , on the scattering vector,  $\mathbf{q}$ . We extracted 1D scattering curves from the 2D GISAXS intensity maps as vertical (parallel to the specular plane) and horizontal (parallel to the sample surface) scans (or cuts) of scattering intensity versus  $q_z$  and  $q_y$ , respectively. The unique feature exhibited by sample A1, a maximum at a higher  $q$ -value in the specular (vertical) direction, is also seen in Figure 3. In this figure the scattering curves of sample A1 are displayed, extracted as vertical cuts from 2D patterns at a fixed horizontal angle, for three different grazing-incident angles of the X-rays. The position of the peak does not change with the increment of the incident angle, but its intensity grows with the penetration depth. A peak with such characteristics is usually exhibited by systems of very concentrated or strongly correlated particles. In cases of homogenous particles it corresponds to the average distance between particles. Assuming that the position of the peak corresponds to the most prominent length in the vertical direction, we can estimate the value of this length,  $L(q_z) = 2\pi/q_z^{\text{peak}} = 3.5 \text{ nm}$ , where  $q_z^{\text{peak}}$  is the position of the maximum of the scattered intensity in  $q$ -space. (This estimation is not exact—it serves as a rough estimate in characterizing the trends of changes in the morphology.) A possible explanation is that this peak represents a contribution of scattering objects with a rather low dispersion of sizes. With increasing polydispersity, such contribution should rapidly drop. Consequently, from the absence of such a peak in the scattering patterns of samples A2 and B1, it can be concluded that the scattering objects under prolonged annealing as well as under intercalation become polydispersed, disordered systems. However, while the absence of the interference peak is the essential qualitative difference between the patterns of samples A1 and A2/B2, the GISAXS map and the information extracted from the scattering curves of sample B1 indicate that the intercalation process brings up a more drastic change. The intensity scans, taken from Figure 2 at fixed horizontal and vertical angle

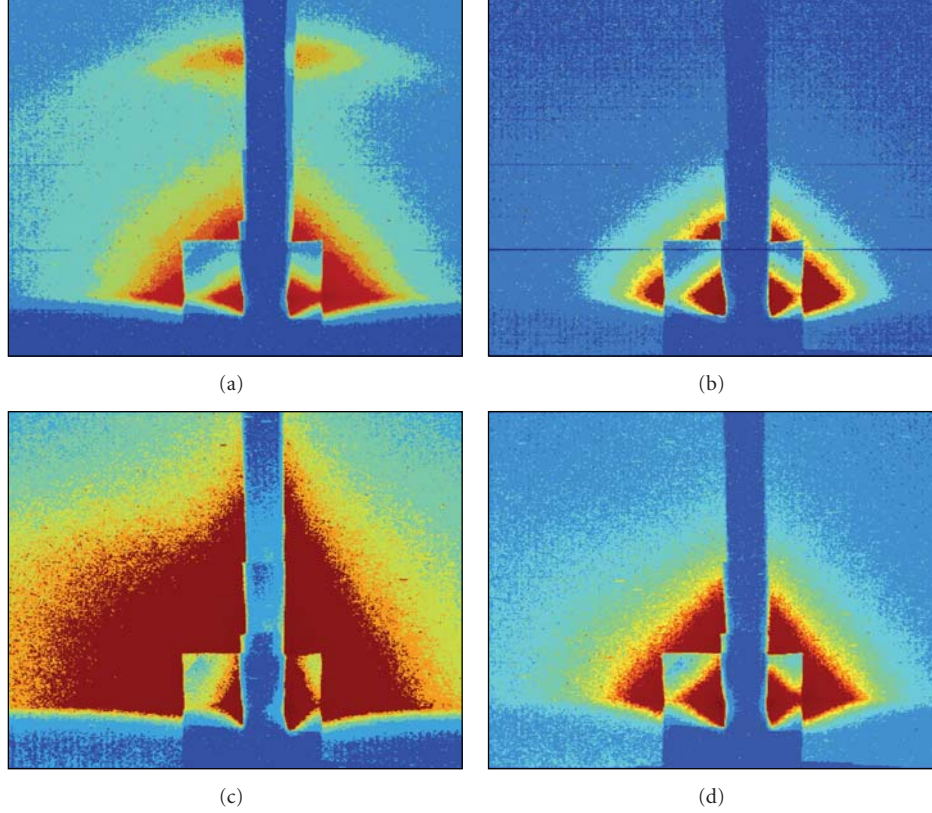


FIGURE 2: 2D GISAXS patterns of (a) sample A1, (b) sample A2, (c) sample B1, and (d) sample B2.

(relatively close to the specular plane and close to the Yoneda peak, resp.), were used to calculate another morphological parameter, the Guinier radius,  $R_G$ , which can be used for the estimation of the average particle size.

In the Guinier approximation, scattering in the small  $q$ -region depends only on the overall size of the particle and not on its shape, so the scattered intensity  $I(q)$  can be expressed as

$$I(q) = C_G \exp\left(-\frac{R_G^2 q^2}{3}\right). \quad (1)$$

The Guinier radius is the average radius of gyration of a dilute set of randomly oriented scattering centers. When this condition is not fulfilled, it still can be calculated as a rough approximation. We determined the radii of gyration from the scattering curves, extracted from the GISAXS patterns of Figure 2 as vertical and horizontal intensity cuts, by plotting the curves in the  $\ln I$  versus  $q^2$  presentation and fitting each of them by a line for very small wave vectors. The fitting of the scattering curves, that is, of a vertical and a horizontal cut, is represented in Figure 4 for the sample A2.

For a slope  $\beta$  of the line, the corresponding Guinier gyration radius is calculated as

$$R_G = (-3\beta)^{1/2}. \quad (2)$$

The determined slopes and gyration radii for the samples A1, A2, B1, and B2 are shown in Table 1.

TABLE 1: The slopes of the fitting lines ( $\beta$ ) and Guinier radii ( $R_G$ ) for samples A1, A2, B1, and B2, calculated from vertical and horizontal intensity cuts.  $L(q_z)$  is the prominent length, estimated for sample A1.

Sample		A1	A2	B1	B2
Vertical cut	$\beta$	-1.1	-3.2	-1.1	-2.4
	$R_G/\text{nm}$	(1.8)	3.1	1.8	2.7
Horizontal cut	$\beta$	-3.2	-8.3	-1.46/ -96	-6.2
	$R_G/\text{nm}$	(3.1)	5.0	2.1/17	4.3
Vertical cut	$L(q_z)/\text{nm}$	3.5	/	/	/

The values of  $R_G$  for sample A1 (in parentheses in Table 1), should be taken with caution in further consideration, because the Guinier approximation is generally not valid for the description of particles systems revealing an interference effect. In such case, the most prominent length,  $L$ , is the most relevant value.

We believe that in sample A1, as a consequence of ultrasonication, a formation of small particles takes place, which are stacked vertically on each other. The value of  $R_G$  in vertical direction roughly corresponds to the estimated prominent length in that direction,  $L(q_z)$ . Any possible correlation in the horizontal direction is not seen by GISAXS with the used setup. If particles were horizontally correlated (with  $L(q_y)$  similar to  $L(q_z)$ ), the correlation peak would be

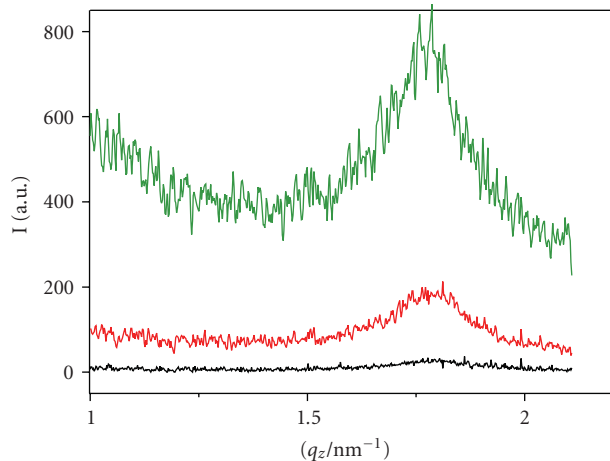


FIGURE 3: Scattering curves of sample A1, extracted as vertical cuts at a constant horizontal angle, showing a peak at  $q_z = 1.8 \text{ nm}^{-1}$  for three incident grazing angles of X-rays: below the critical angle (black) and above the critical angle (red and green).

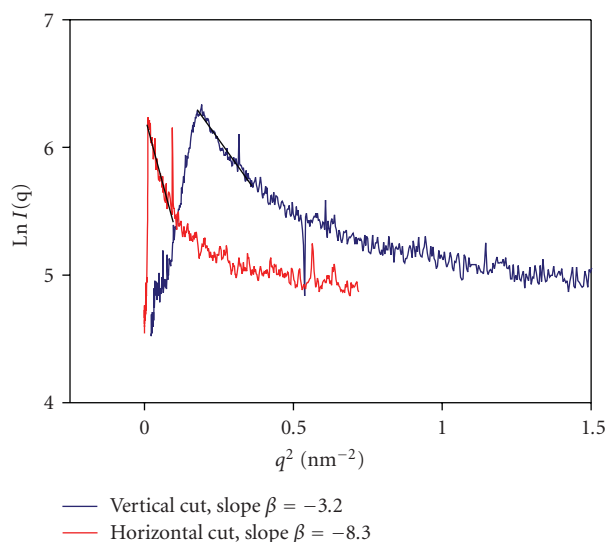


FIGURE 4: Scattering curves of sample A2, extracted as a vertical cut at a constant horizontal angle (blue) and a horizontal cut at a constant vertical angle (red), shown in the presentation suitable for determination of the average gyration radius.  $\beta$  is the slope of the fitting lines (black).

positioned beyond the experimental  $q_y$  range. However, the value of  $R_G$  in horizontal direction (3.1 nm) suggests either aggregation or elongation of particles in the horizontal plane. The FSEM picture of the sample A1 (Figure 5(a)) shows a uniformly structured surface with small grains, and thus supports the existence of the presumed morphology on the nano scale.

The analysis of horizontal scans of sample B1 showed the existence of at least two size distributions of particles, with a significant difference in their average radii. The smaller particles are almost spherical (with an average diameter of around 4 nm), because the values of  $R_G$  are

similar in both directions. Again, the FSEM picture of this sample (Figure 5(c)) can be correlated to the GISAXS view. Obviously, it shows a morphology transformation induced by intercalation of lithium, which causes the lack of its overall homogeneity. It seems that intercalation acts as a trigger for formation of particles with a very broad size distribution which extends over a decade. In such case, vertical cuts are not appropriate for the gyration radius analysis (only small particles are detected). The limited possibilities in the GISAXS detection can also affect the results—the contribution of large particles can be hidden by the beamstop. This, complex morphology of sample B1 explains the development of a diffuse, featureless signal of the GISAXS pattern of this sample (Figure 2(c)).

The gyration radii obtained from a horizontal and a vertical intensity scan, for samples A2 and B2, have different sizes (Table 1), which indicate the anisotropy of the particles. Anisotropy in SAXS results from more or less oriented anisotropic particles. Although Guinier approximation gives only the radius as a measure of particle size, it is also partly sensitive to oriented flat or elongated particles. The radius is obtained from integrating the contribution to scattering over the particle volume and possible orientations. A more complex model, with assumed particle shape, as well as variations of the particle extension in different directions would reproduce the measured scattering more precisely. However, further experimental investigation would be necessary in order to determine some of these variations, or the result of the fitting would be merely a numerical one. The applied, simplest model gives information about the sample anisotropy without unnecessarily relying on numerical calculus.

In conclusion, the above GISAXS results, together with the FSEM scans, are understood as follows: a starting configuration of sample A1, which includes vertically correlated particles, gets changed by postpreparation treatments. Under prolonged annealing (sample A2), particles grow bigger and the order is lost. Lithium intercalation drastically changes the starting configuration of sample A1. The sample B1 consists of a mix of particles, with distribution of sizes (and shapes), which escape any simple description. Obviously, the ordered configuration of sample A1 is not stable enough to be suitable for lithiation. On the other hand, lithiation of the prolongedly heated sample does not abruptly affect the morphology on the nanoscale—samples A2 and B2 exhibit similar parameters. In comparison with sample A2, sample B2 shows a slight reduction of the average gyration radii in both directions (a redistribution of particle sizes takes place in the A2 to B2 transition). So, although the morphology is affected by lithiation, the similarity of the 2D GISAXS patterns and particle sizes suggests that the type of morphology in samples A2 and B2 is the same. A slight smoothing of the surface can be detected by comparing the corresponding FSEM pictures of samples A2 and B2 (Figures 5(b), and 5(d)), which reflect the reduction in the average particle size.

Further investigation of the electrochemical and optical properties and of the stability of films should clarify the correlation between the determined morphological variations and the performance of films as electrodes.

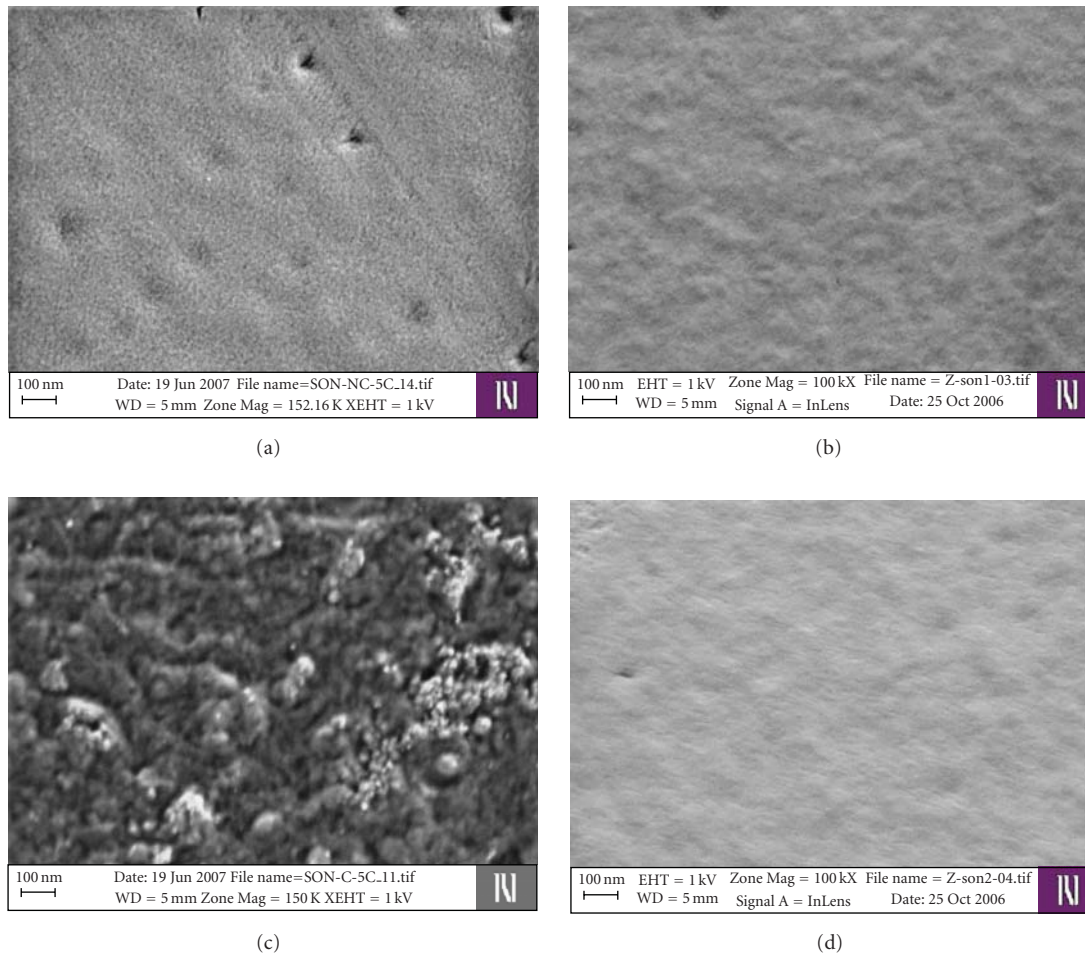


FIGURE 5: FSEM pictures of (a) sample A1, (b) sample A2, (c) sample B1, and (d) sample B2.

## Acknowledgment

The results shown in this work are obtained in the frame of the scientific project “Nanostructures of metal oxides and metals: morphology and properties,” supported by the Ministry of Science, Education and Sport of the Republic of Croatia.

## References

- [1] A. Talledo, A. M. Andersson, and C. G. Granqvist, “Structure and optical absorption of  $\text{LiVO}$  thin films,” *Journal of Applied Physics*, vol. 69, no. 5, pp. 3261–3265, 1991.
- [2] M. L. Lavčević, A. Turković, “Small-angle X-ray scattering and wide-angle X-ray diffraction on thermally annealed nanostructured  $\text{TiO}$  films,” *Thin Solid Films*, vol. 419, no. 1-2, pp. 105–113, 2002.
- [3] F. Zhang, S. Passerini, B. B. Owens, and W. H. Smyrl, “Nanocomposites of  $\text{VO}$  aerogel and  $\text{RuO}$  as cathode materials for lithium intercalation,” *Electrochemical and Solid-State Letters*, vol. 4, no. 12, pp. A221–A223, 2001.
- [4] M. L. Lavčević, A. Turković, P. Dubček, and S. Bernstorff, “Nanostructured  $\text{CeO}$  thin films: a SAXS study of the interface between grains and pores,” *Thin Solid Films*, vol. 515, no. 14, pp. 5624–5626, 2007.
- [5] M. L. Lavčević, P. Dubček, A. Turković, Z. Crnjak-Orel, and S. Bernstorff, “Nanostructural depth profile of vanadium/cerium oxide film as a host for lithium ions,” *Solar Energy Materials and Solar Cells*, vol. 91, no. 7, pp. 616–620, 2007.
- [6] M. Winter, J. O. Besenhard, M. E. Spahr, and P. Novák, “Insertion electrode materials for rechargeable lithium batteries,” *Advanced Materials*, vol. 10, no. 10, pp. 725–763, 1998.
- [7] C. R. Sides, N. Li, C. J. Patrissi, B. Scrosati, and C. R. Martin, “Nanoscale materials for lithium-ion batteries,” *MRS Bulletin*, vol. 27, no. 8, pp. 604–596, 2002.
- [8] A. S. Aricò, P. Bruce, B. Scrosati, J. M. Tarascon, and W. Van Schalkwijk, “Nanostructured materials for advanced energy conversion and storage devices,” *Nature Materials*, vol. 4, no. 5, pp. 366–377, 2005.
- [9] M. Veszelei, L. Kullman, A. Azens, C. G. Granqvist, and B. Hjörvarsson, “Transparent ion intercalation films of  $\text{Zr-Ce}$  oxide,” *Journal of Applied Physics*, vol. 81, no. 4, pp. 2024–2026, 1997.
- [10] Z. C. Orel, “New counter electrode prepared as vanadium oxide and  $\text{V/Ce}$  oxide films: preparation and characterization,” *Solid State Ionics*, vol. 116, no. 1-2, pp. 105–116, 1999.
- [11] H. Amenitsch, S. Bernstorff, and P. Laggner, “High-flux beam-line for small-angle x-ray scattering at ELETTRA,” *Review of Scientific Instruments*, vol. 66, no. 2, pp. 1624–1626, 1995.

- [12] J. R. Levine, J. B. Cohen, Y. W. Chung, and P. Georgopoulos, "Grazing-incidence small-angle X-ray scattering: new tool for studying thin film growth," *Journal of Applied Crystallography*, vol. 22, no. 6, pp. 528–532, 1989.
- [13] P. Dubček, "Nanostructure as seen by the SAXS," *Vacuum*, vol. 80, pp. 92–97, 2005.

## Research Article

# Electronic-Excitation-Induced Processing in GaSb Compound Nanoparticles

**H. Yasuda and H. Mori**

*Research Center for Ultra-High Voltage Electron Microscopy, Osaka University, Osaka 567-0047, Japan*

Correspondence should be addressed to H. Yasuda, yasuda@uhvem.osaka-u.ac.jp

Received 8 April 2010; Revised 2 June 2010; Accepted 25 June 2010

Academic Editor: Bo Zou

Copyright © 2011 H. Yasuda and H. Mori. This is an open access article distributed under the Creative Commons Attribution License, which permits unrestricted use, distribution, and reproduction in any medium, provided the original work is properly cited.

Temperature dependence of electronic-excitation-induced structural changes in nanoparticles has been studied by in situ transmission electron microscopy. When GaSb nanoparticles kept at 340 K were excited by 25 keV electrons, the compound transforms to the porous compound or the two-phase structure consisting of an antimony core and a gallium shell with increasing the total electron dose. On the other hand, in GaSb nanoparticles kept at 293 K the structure remains the original compound phase. It is suggested that such temperature dependence of the structural changes may arise from synergetic behaviors of point defects introduced athermally by the excitation and thermal mobility.

## 1. Introduction

Structural stability in materials under electronic excitation is different from that at the ground state. It is expected that electronic excitation effects on the structural stability will be enhanced in nanoparticles which have high surface-to-volume ratio and high-atomic mobility. Recently, it was found that when GaSb particles were excited by low-energy electrons, the compound transforms to a two-phase consisting of an antimony core and a gallium shell with a nanometer-sized void [1–4]. In the present paper, we studied the temperature dependence of such structural changes induced by low-energy electronic excitation in GaSb particles by in situ transmission electron microscopy.

## 2. Experimental Procedures

Preparation of size-controlled GaSb particles was carried out with the use of a double-source evaporator installed in the specimen chamber of an electron microscope. An amorphous carbon film was used as a supporting film and was mounted on a molybdenum grid. Using the evaporator, gallium was first evaporated from one filament to produce gallium particles on the supporting film, and then antimony

was evaporated from the other filament onto the same film. The supporting film was kept at ambient temperature during the deposition. Vapour-deposited antimony atoms quickly dissolved into gallium particles to form GaSb (Ga-50at%Sb) compound particles [5–7]. The particles were then annealed in the microscope at 573 K for 3.6 ks and were slowly cooled to room temperature in 2.7 ks, in an attempt to homogenize the solute concentration in the particles. Electronic excitation experiments and observations were carried out using the same microscope Hitachi H-7000 TEM operating at an accelerating voltage of 25 kV. The electron flux used for excitations was  $1.0 \times 10^{20} \text{ e m}^{-2} \text{ s}^{-1}$ . The temperature of particles on the supporting films was kept at 293 and 430 K during the experiments. Structural changes associated with electronic excitations were observed in situ by bright-field images (BFIs) and selected-area electron diffraction patterns (SAEDs).

## 3. Results and Discussion

An example of structural changes in GaSb particles by 25 keV electronic excitation at 430 K is shown in Figure 1. Figures 1(a) and 1(a') show a BFI of particles with the mean diameter of approximately 20 nm before excitation

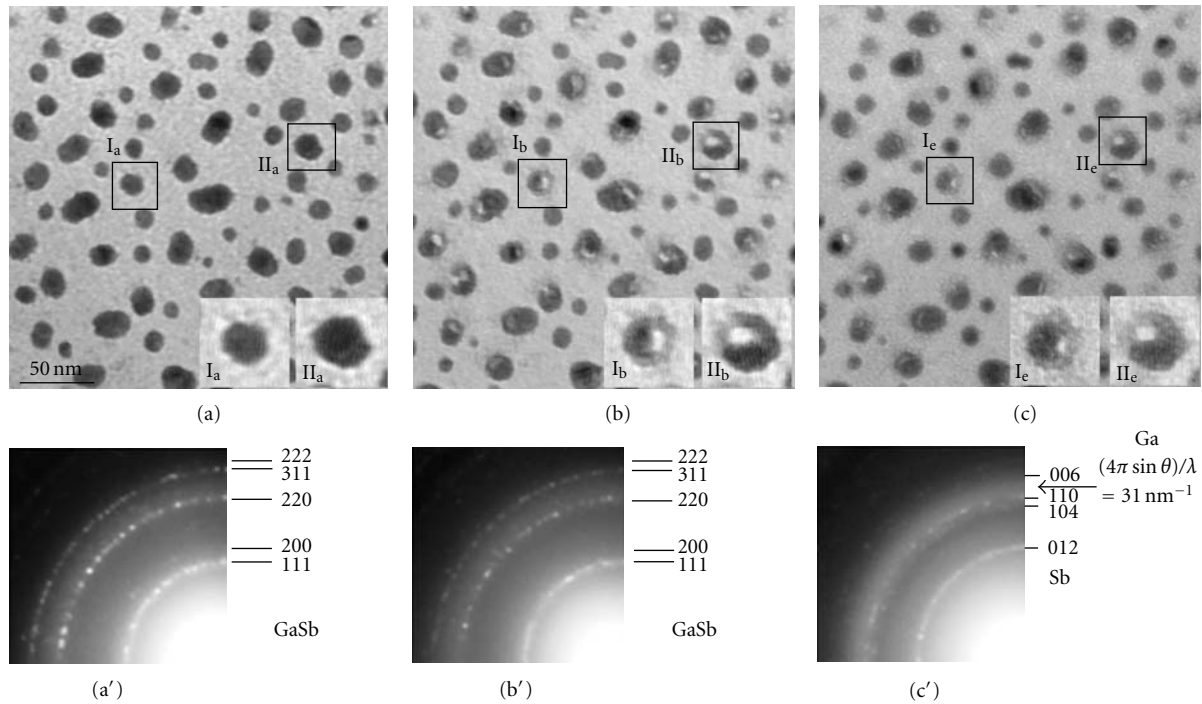


FIGURE 1: An example of the structural changes in GaSb particles kept at 430 K by electronic excitation. (a) A BFI and (a') the corresponding SAED before excitation. (b) The same area after excitation for 60 s and (b') the corresponding SAED. (c) The same area after excitation for 480 s and (c') the corresponding SAED. The parts framed squarely are enlarged in the figures.

and the corresponding SAED, respectively. As indexed in Figure 1(a'), the Debye-Scherrer rings can be consistently indexed as those of GaSb which has the zincblende structure. The same area after excitation for 60 s is shown in Figure 1(b). In the interior of the particles after the excitation, there appear voids with bright contrast. As seen from a comparison of the magnified images I<sub>a</sub> and II<sub>a</sub> in Figure 1(a) with I<sub>b</sub> and II<sub>b</sub> in Figure 1(b), the diameter of nanoparticles after the excitation increased up to 15% compared with those before excitation. In the SAED taken after the excitation as shown in Figure 1(b'), Debye-Scherrer rings of the zincblende structure are recognized again.

Changes in the lattice constant in GaSb particles are shown as a function of total electron dose in Figure 2. After excitation of the dose of  $6.0 \times 10^{21} \text{ e m}^{-2}$ , the lattice constant increased up to 1.8% compared with that before excitation. The lattice constant of GaSb particles under the same excitation condition increased up to about 2.6% with increasing dose. From the above results, it is suggested that the swelling by void formation in the interior of the individual nanoparticles and the increase of the lattice constant of GaSb are caused by vacancies and interstitials introduced by electronic excitation, respectively.

The same area after excitation for 480 s is shown in Figure 1(c). The voids in the individual particles change in the shape and size, as seen from a comparison of the magnified images I<sub>b</sub> and II<sub>b</sub> in Figure 1(b) with I<sub>c</sub> and II<sub>c</sub> in Figure 1(c). In the SAED taken after the excitation as shown in Figure 1(c'), Debye-Scherrer rings of crystalline antimony are recognized, superimposed on a weak halo ring

with the value of the scattering vector ( $K = (4\pi \sin \theta) / \lambda$ ) of approximately  $31.0 \text{ nm}^{-1}$  which is corresponding to the first halo of liquid gallium. This result indicates that a two-phase mixture consisting of a crystalline antimony core and a liquid gallium shell was formed in the particles. From these results, it has been evident that when GaSb particles kept at 430 K were excited by 25 keV electrons, two-phase separation takes place via void formation.

In order to see the temperature dependence of the structural changes, experiments in the particles kept at 293 K were carried out. An example of the behaviors of particles by the same electronic excitation condition as that in Figure 1 is shown in Figure 3. As seen from the comparisons of 3(a) with 3(b) and 3(a') with 3(b'), the particle remains unchanged in both the microstructure and SAED after excitation for 60 s. It has been noted here that such a void formation as observed after excitation at 340 K is absent in the particles kept at 293 K. After excitation for 480 s as shown in Figures 3(c) and 3(c'), no changes are recognized in the microstructure of the particles and Debye-Scherrer rings in the SAED.

As shown in Figure 2, the lattice constant in GaSb particles kept at 293 K is not changed also with increasing dose. From the result, it was evident that when approximately 20 nm-sized GaSb particles kept at 293 K are excited by 25 keV electrons, no structural changes are recognized.

A mechanism of the void formation and phase separation in GaSb nanoparticles will be discussed as follows. In the present case, the final two-hole states in the gallium valence band are formed by the predominant primary K-shell Auger transitions after the excitation. The bonding states under the

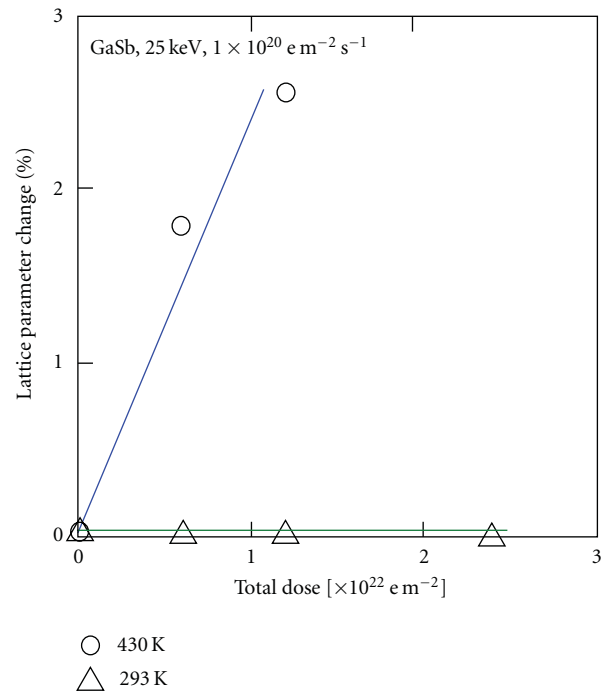


FIGURE 2: Changes in lattice constants of GaSb induced by electronic excitation in nanoparticles as a function of total electron dose.

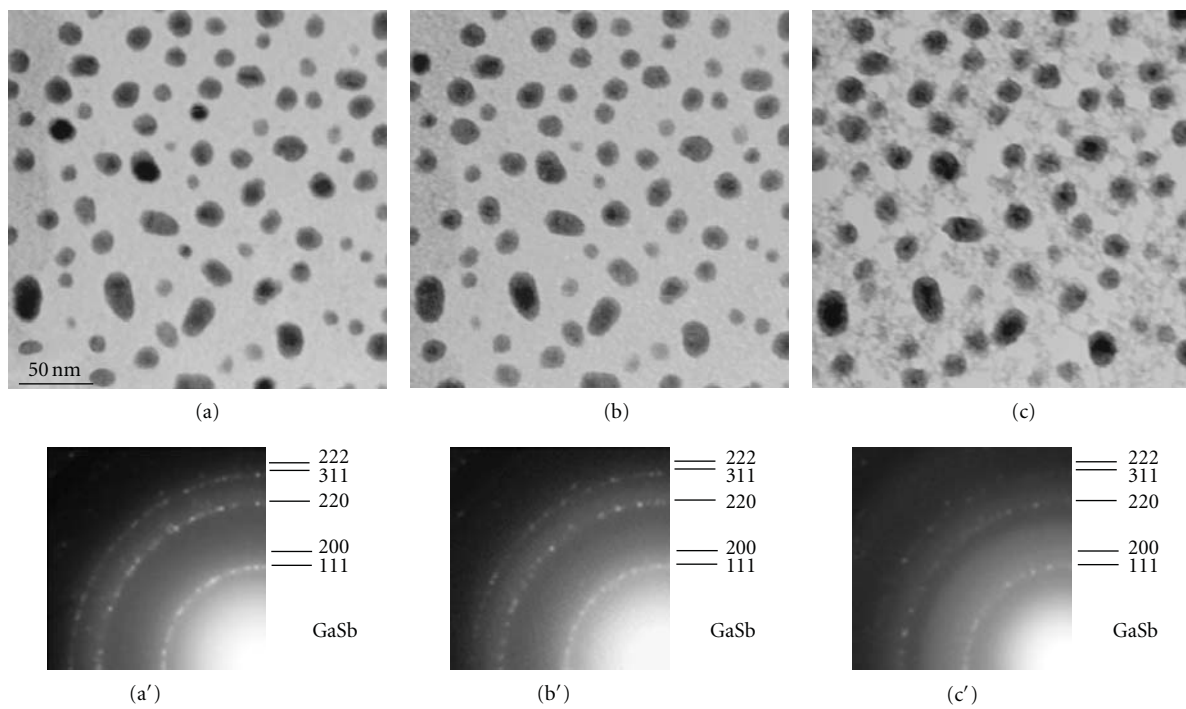


FIGURE 3: An example of the structural changes in GaSb particles kept at 293 K by electronic excitation. (a) A BFI and (a') the corresponding SAED before excitation. (b) The same area after excitation for 60 s and (b') the corresponding SAED. (c) The same area after excitation for 480 s and (c') the corresponding SAED.

presence of the two-hole states in gallium atoms become an antibonding. In this first athermal process the bond breaking takes place, and the excess energy accumulated by the relaxation converts directly into the atomic kinetic energy. When the sum of the kinetic energy and thermal energy is larger than the energy barrier for the atomic displacements, the thermally displaced gallium atom can form a vacancy and interstitial in the crystal. In nanoparticles, such an electronic excitation effect becomes remarkably efficient [8].

At elevated temperatures, vacancies and gallium interstitials become mobile and apart from annihilation by recombination, they contribute to the growth of defect clusters. The interstitials and their clusters have a strong compressive strain field; the lattice constant of GaSb becomes large with increasing of the concentration of interstitials and their clusters. This compressive strain field interacts more strongly with a tensile strain field of the surface layer of the particle. The surface layer of the particle will act as a preferential sink for interstitials and their clusters over the whole particles. On the other hand, the capture cross-section of the surface layer for vacancies and their clusters is smaller than that for interstitials and their clusters. The vacancies and their clusters interact weakly with that of the surface layer. In nanoparticles, only the vacancies in the surface layer which is finite in thickness can disappear toward the top of the surface. Consequently, the vacancy concentration in the particle core is higher than that in the surface layer, but interstitial concentration increases toward the surface. Under the condition of vacancy supersaturation in the particle core the vacancy clusters will grow to form a void, and the subsequent surface segregation of interstitial clusters will bring about the separation to the two-phase structure.

In the GaSb particles kept at room temperature, as the energy barrier is too high to jump to the neighbor site, the gallium atoms return to those original positions. Consequently, no lattice constant and structure change after excitation. This mechanism also gives an explanation for temperature dependence of the electronic excitation effect.

#### 4. Conclusions

Temperature dependence of electronic-excitation-induced structural changes in nanoparticles has been studied by in situ transmission electron microscopy. When GaSb nanoparticles were excited by 25 keV electrons, the compound transforms to the two-phase structure consisting of an antimony core and a gallium shell with void formations, or remains the original compound phase depending on the temperature. It is suggested that such the temperature dependence of the structural changes may arise from synergetic behaviors of point defects introduced athermally by the excitation and thermal mobility.

#### Acknowledgments

This paper was, in part, supported by Priority Assistance for the Formation of Worldwide Renowned Centers of Research-The Global COE Program (Project: Center of Excellence for

Advanced Structural and Functional Materials Design) and "Grant-in-Aid for Scientific Research" from the Ministry of Education, Culture, Sports, Science and Technology (MEXT), Japan.

#### References

- [1] H. Yasuda, H. Mori, and J. G. Lee, "Nonlinear responses of electronic-excitation-induced phase transformations in GaSb nanoparticles," *Physical Review Letters*, vol. 92, no. 13, Article ID 135501, 4 pages, 2004.
- [2] H. Yasuda, H. Mori, and J. G. Lee, "Electron-irradiation-induced phase separation in GaSb nanoparticles," *Physical Review B*, vol. 70, no. 21, Article ID 214105, 6 pages, 2004.
- [3] H. Yasuda, A. Tanaka, H. Usui, H. Mori, and J. G. Lee, "Effect of electron flux on electronic-excitation-induced phase separation in GaSb nanoparticles," *European Physical Journal D*, vol. 37, no. 2, pp. 231–235, 2006.
- [4] H. Yasuda, A. Tanaka, K. Matsumoto, N. Nitta, and H. Mori, "Formation of porous GaSb compound nanoparticles by electronic-excitation-induced vacancy clustering," *Physical Review Letters*, vol. 100, no. 10, Article ID 105506, 4 pages, 2008.
- [5] H. Yasuda and H. Mori, "Spontaneous alloying of zinc atoms into gold clusters and formation of compound clusters," *Physical Review Letters*, vol. 69, no. 26, pp. 3747–3750, 1992.
- [6] H. Yasuda and H. Mori, "Cluster-size dependence of alloying behavior in gold clusters," *Zeitschrift für Physik D*, vol. 31, no. 1, pp. 131–134, 1994.
- [7] H. Yasuda and K. Furuya, "Spontaneous alloying of tin atoms into nanometer-sized gold clusters and phase stability in the resultant alloy clusters," *European Physical Journal D*, vol. 10, no. 2, pp. 279–283, 2000.
- [8] H. Sumi, "Theory on laser sputtering by high-density valence-electron excitation of semiconductor surfaces," *Surface Science*, vol. 248, no. 3, pp. 382–410, 1991.

## Research Article

# Constitutive Rheological Modeling of Flow Serration Behaviour in Metallic Glasses Showing Nanocrystallization during Deformation

M. A. Yousfi,<sup>1</sup> K. Hajlaoui,<sup>2,3</sup> Z. Tourki,<sup>1</sup> and A. R. Yavari<sup>3</sup>

<sup>1</sup>LMMP LAB-STI03, Université de Tunis, ESSTT, Tunis 1008, Tunisia

<sup>2</sup>LGM-MA05, ENIM, Av. Ibn El Jazzar, Monastir 5019, Tunisia

<sup>3</sup>SIMaP-LTPCM, Institut National Polytechnique de Grenoble, 38402 Saint Martin d'Heres, France

Correspondence should be addressed to K. Hajlaoui, k.hajlaoui@yahoo.fr

Received 25 April 2010; Revised 26 June 2010; Accepted 16 July 2010

Academic Editor: Quanqin Dai

Copyright © 2011 M. A. Yousfi et al. This is an open access article distributed under the Creative Commons Attribution License, which permits unrestricted use, distribution, and reproduction in any medium, provided the original work is properly cited.

A simple micromechanism-inspired rheological model is developed that incorporates the serrated flow nature of metallic glasses subjected to compressive deformation at room temperatures. The process of propagation and the arrest of shear bands were addressed in this model. Shear-induced nanocrystallisation was believed to be responsible for strain hardening of material within the shear bands. The model is based on the assumption that the behaviour can be decomposed into two resistances acting in parallel: one captures the initial stiffness and shear softening and the second gives the time-shear-temperature hardening of material.

## 1. Introduction

Metallic Glasses (MGs) (amorphous metals) are a new class of engineering materials which have attracted large technological interests [1–5] and are finding increased use as functional materials in the sporting goods, MEMS (Micro-Electro-Mechanical Systems) and NEMS (Nano-Electro-Mechanical Systems). The first metallic glass system was developed by Klement et al. [6] which consisted of a binary Au–Si alloy. At present, some of the most commonly researched metallic glasses include the Zr-based, Pd-based, Cu-based, and many other alloy systems. These amorphous alloys are produced by the rapid quenching of liquid metals from a molten state to prevent crystallization. Hence, metallic glasses can be considered as nanocrystalline material with ultimate reduction in grain size (in the order of a few nanometers). It has an amorphous structure (structure less), and it is void of dislocations and defects which weaken conventional crystalline alloys. Consequently, MGs possess excellent mechanical properties [7–9], practical physical properties, and unique chemical properties (good corrosion resistance) [10], as well as great potential for

structural and functional applications. While many MGs have demonstrated the highest specific strengths and showed considerable fracture toughness, their deformation mechanisms are basically different from those of crystalline solids due to their lack of long-range atomic order. Usually it is understood that under room temperature and uniaxial stress states, MGs deform through a procedure of highly localized shearing in narrow bands that are thin layers of material being initially only 10 nm thick [11] and fail along one dominant shear band catastrophically [12]. The macroscopic fragility severely limits further exploitation of this class of advanced materials. However, in some cases, values of more than 50% of plastic deformation have been achieved [13] in some monolithic metallic glasses. During deformation, structural changes possibly occur within the shear bands. Several experimental evidences for deformation-induced nanocrystallization in shear bands have been reported in our previous work [14–16] based on transmission electron microscopy (TEM) study. A high plastic strain has been also reported, for example, in Pd-based MG [17] where the authors attribute this result to a nanoscale phase separation which blocks the propagation of shear bands facilitating

their initiation and branching. All MG systems exhibiting large plasticity deform via formation of numerous shear bands all over the compressed specimen, and the degree of the plasticity is predominantly dependent on the total number of shear bands generated during deformation. These “ductile” MGs have generally the characteristic deformation features that are serrated flow, that is, elastically loading and plastically unloading with sharp stress drop, in stress-strain curves. Furthermore, currently, it is accepted that the macroscopic serrated plastic flow behaviour is associated with the shear-banding process on a nanoscale within MGs, and extensive efforts have been made to bare the relationship between them.

As metallic glasses lack crystalline order, and therefore structural features such as dislocations and grain boundaries, the application of conventional metallurgical theory is generally not allowed. As such, significant efforts to develop suitable mechanistic models for the description of mechanical behaviour continue in order to best capture the principal feature of MGs. A constitutive equation accounting for the presence of serrated flow as kinetic phenomenon of plastic deformation in MGs is presented in the present work in light of the recent microscopic findings. Deformation-induced nanocrystal formation in the shear band regions will be highlighted, and the effect of this phenomenon on the arrest of shear bands will be analysed and modeled.

## 2. Aspect of Experimentally Observed Stress-Strain Behaviour

The typical stress-strain behaviour of Metallic Glass at room temperatures is shown in Figure 1. The tested Bulk Metallic Glass (BMG) of compositions  $Zr_{55}Al_{10}Cu_{20}Ni_{10}Pd_5$  was prepared by arc melting the pure elements under Ti-gettered Ar atmosphere followed by casting into a water-cooled copper mould. The resulted ingots were bars with dimensions  $2\text{ mm} \times 4\text{ mm} \times 75\text{ mm}$ . Compression test specimens with dimensions of  $2\text{ mm} \times 2\text{ mm} \times 4\text{ mm}$  (aspect ratio 2:1) were cut from the BMGs. The outer surfaces of the specimens, especially the ends in contact with the cross-head, were mechanically polished to ensure flat and parallel surfaces. Compression tests were conducted at constant strain rate of  $8 \times 10^{-4}\text{ s}^{-1}$  using a Schenck hydraulic testing machine at room temperature. The yield stress is measured to be 1800 MPa, and the maximum plastic strain is 4.7%. The overall plastic deformation is accomplished by serrated flow process. As highlighted by the insert in Figure 1, the “unit” of the plastic flow serrations consists of elastic loading portion followed by a sudden load drop and displacement burst. The amplitude of the stress drops gradually increases with strain, and the slopes of both loading and unloading of the serrations are nearly constant from the yield point to the ultimate failure. The slope of the unloading sections is linked with the inelastic displacements produced by local shear deformation with rapid stress drops.

Recent experiments show that the load serrations are related to the intermittent propagation of individual shear bands [18, 19] which results from the interaction between the

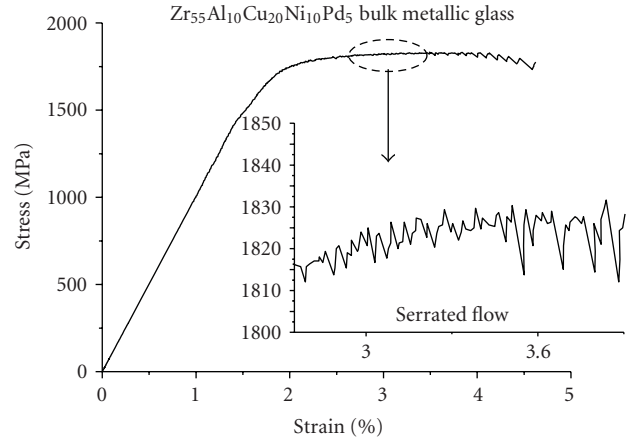


FIGURE 1: A representative compression stress-strain curve of the  $Zr_{55}Al_{10}Cu_{20}Ni_{10}Pd_5$  Bulk Metallic Glass deformed at room temperature and for strain rate of  $8 \cdot 10^{-4}\text{ s}^{-1}$ . The inset shows the magnified view in the serrated flow region.

processes of shear-induced materials softening and structural relaxation [19, 20]. More recently, Chen et al. [21], using in-situ TEM deformation experiments, showed that even for very small size samples, the load-displacement curve indicates occurrence of multiple shear bands, and none of these shear bands run over a long distance upon initiation. They are arrested after a small distance of propagation (20 nm).

The repeated arrest and reactivation of shear bands have not been explained convincingly, and none of the proposed constitutive equations for inhomogeneous plastic flow deal with the serrated flow adequately. It seems that the arrest mechanism that effectively stops the runaway slip along a single shear band plays a significant role in the plasticity of the monolithic BMGs. Thus, the suitable model must include details on micromechanisms of the serrated flow, in particular the arrest of shear bands.

For this reason, the deformed sample was carefully cut along a plane perpendicular to the shear bands and characterized by TEM. Foils preparation and experimental details were well developed in our previous work [14–16]. The dark field image and the broad halo SAED (selected area electron diffraction) obtained from the deformed Zr-based Bulk MG are presented in Figure 2. This figure shows typical white contrast of shear bands surrounded by amorphous regions. Nanocrystals with a size of around 10 nm are distributed within the shear band and cannot be found in the regions out of the band, suggesting that their formation is associated with the localized shear deformation. The nanocrystallization within shear bands can be further confirmed by the fine diffraction rings (see arrow in Figure 2) observed by nanobeam electron diffraction.

Remarkably, as evidenced by TEM imaging, the nanocrystallization from the amorphous phases investigated in this work already occurs during the first stage of deformation due to convinced mechanical activation energy. This phenomenon is well known as the deformation-induced nanocrystallization in metallic glasses and has

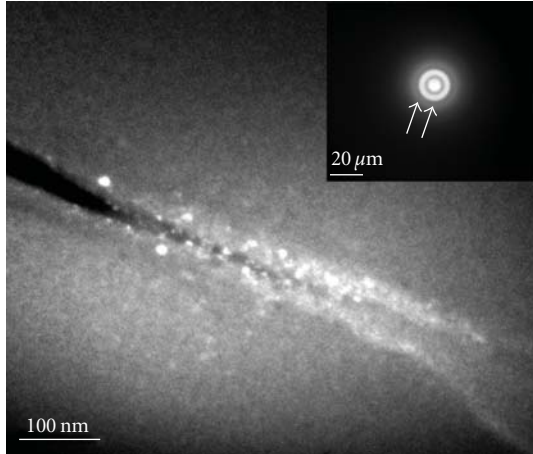


FIGURE 2: TEM dark field micrograph of shear band (followed by cracks propagation) in the uniaxially deformed  $Zr_{55}Al_{10}Cu_{20}Ni_{10}Pd_5$  Bulk Metallic Glass showing the presence of nanocrystallites with an average size of 10 nm embedded in the amorphous matrix. Inset is the corresponding selected area electron diffraction (SAED) pattern recorded from the regions within the shear band.

been observed in a number of MGs with large plastic deformation [22–24]. These studies have demonstrated that nanocrystallites play an important role in increasing the plasticity of amorphous metallic alloys by retarding sudden shear bands propagation. Likewise, the nanocrystallization during shear flow can offer a “self-locking effect” to avoid further propagation of shear bands. Therefore, the influence of the insitu nanocrystallization on the mechanical behaviour of MGs remains to be comprehensively clarified and parameters involving the mechanism of deformation-induced nanocrystallization must be included somewhat in constitutive model for plastic deformation of metallic glasses.

### 3. Constitutive Model: Background and Development

The experimental data presented in the previous section clearly show the complicated behaviour that is exhibited by MGs, particularly the correlation between the yields drops in the load-displacement curve and the nature of dynamic emission and propagation of shear bands. There are obviously two possibilities; the first is that each yield drop step corresponds to the formation of a new shear band the second is that the yield drops are due to intermittent slip on existing shear bands. In Fact, when the propagation of shear band is suddenly suppressed by the disappearance of the confined viscous flow, which results in the nanocrystals formation, then, the other shear band will start to move in the amorphous glassy structure close to the region where the previous shear band was arrested. Repeating the process during deformation, a large plasticity can be obtained by potential shear band branching.

To address these observations, a simple micromechanism inspired model is developed that incorporates the serrated flow nature of deformed material. We will limit this work to highlighting the individual shear striation behaviour under the assumption that each serration is associated with individual shear events. In this section, we describe the details of the microscopic mechanism steps, which we believe is occurring in a very narrow shear zone during deformation in MGs (see Figure 3). Each step will be modelled separately. The development of a physically based constitutive model for the stress-strain behaviour of MGs can now begin with an interpretation of the data discussed previously and schematically presented in Figure 3. The model is interpreted below in terms of a series of two conceptual steps.

*Step 1* (initial dilatation and shear softening). The initial portion of the stress-strain curve displays a stiff response followed by stress drop (see Figure 3(a)). Initial deformation in this step is accompanied by significant shear-induced dilatation of the structure. The strain can be promptly accommodated at the atomic level through variations in neighbourhood, atomic bonds. The exact nature of local atomic motion in straining MGs is not fully determined, although there is general agreement that the basic unit process underlying deformation should be local atoms rearrangement that can accommodate shear strain as schematically shown in Figure 3(b). An equivalent of this local rearrangement is illustrated in the two-dimensional schematic originally proposed by Argon [25] and usually known as “shear transformation zone” (STZ) [25–28] which is basically a local cluster of atoms that endures an inelastic shear distortion.

An alternative, complementary viewpoint on this mechanism is given by the classical “free-volume” model, firstly developed by Turnbull and Cohen [29–31] and applied by Spaepen [32] to the case of MGs deformation. This model considers deformation as sequences of discrete atomic jumps in the metallic glass, as implicitly depicted in Figure 3(b). These mechanisms (whether one subscribes to an STZ-type or diffusive-like jump mechanism) may occur homogeneously over a glass body (for example at high temperatures) [33, 34], or in a localized mode as throughout the formation of a shear band (at room temperature) as the case of the present work where the constitutive model will correspond to what most likely happen in individual shear bands. These microscopic models have been widely used to review the basic features of metallic glass deformation [35–38] as well as the kinetics of structural relaxation of these materials [39, 40]. The equations derived from these models well capture the transition from linear elastic dilatation to stress drop due to shear softening.

We shall then recall these dilatation models for the first step of stress-strain curve. According to Spaepen [32], microscopic flow is occurring as a result of a number of individual atom jumps, each participating to a slight local shear strain. This process occurs at sites where large enough holes or flow defects, with a size larger than a critical value making an atomic diffusive jump possible. The plastic strain rate is given as follows [32]:

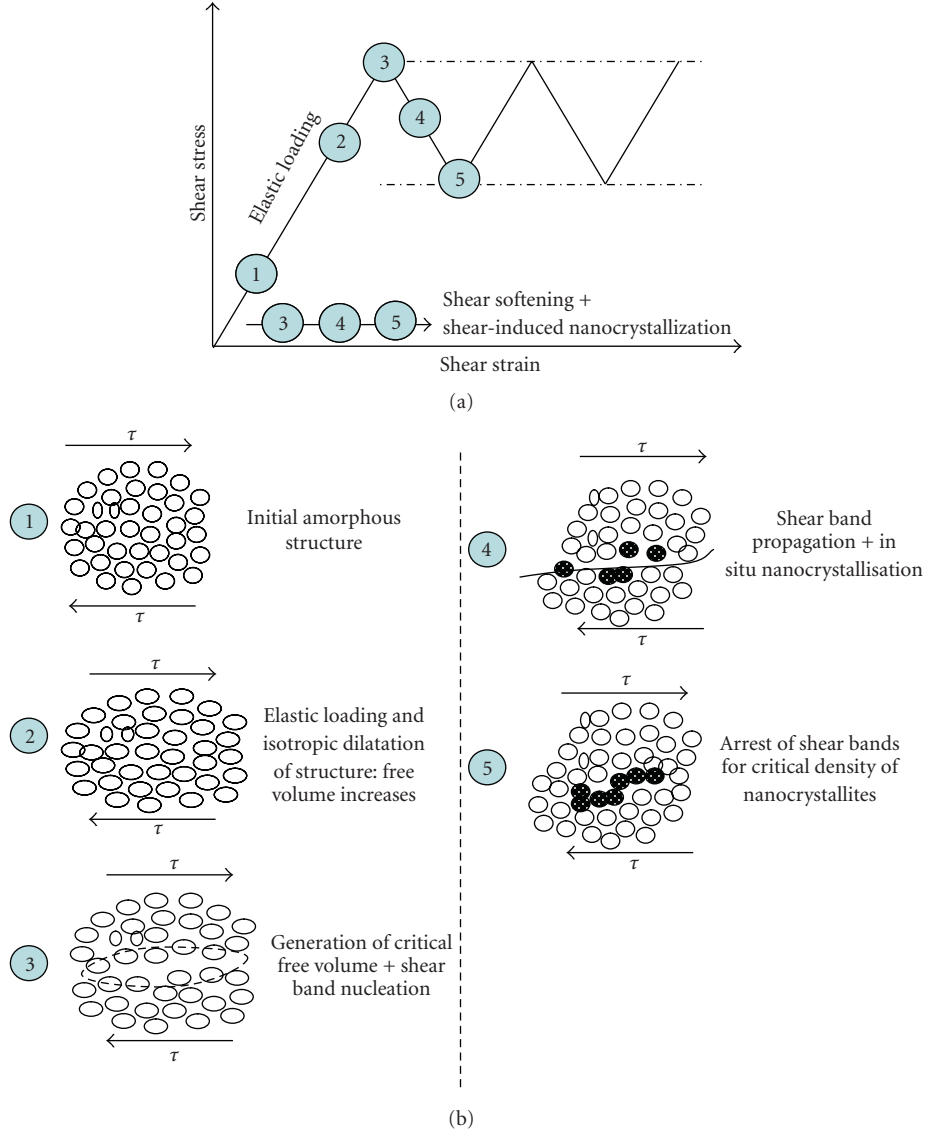


FIGURE 3: (a) Schematic illustration showing the details of the proposed model for serrated flow in metallic glasses. (b) The corresponding atomic illustrations of propagation of individual shear band in nanoscale range: (1)-(2) elastic deformation through conventional structural dilatation mechanism, (3)-(4) free volume creation and shear band propagation at initial stage going with structural segregation and nanocrystallization by concentration of shear stress, (5) suppression of propagation and arrest of shear band by precipitation and growth of nanocrystalline particles within the shear zone.

$(\partial\gamma/\partial t) = (\text{strain produced at each site}) \times (\text{fraction of potential jump sites}) \times (\text{net number of forward jumps at each site per second})$ .

Within the free-volume formalism,  $\partial\gamma/\partial t$  can be written as [32]

$$\frac{\partial\gamma}{\partial t} = 2 \cdot f \cdot C_f \cdot \exp\left[-\frac{\Delta G^m}{k_B \cdot T}\right] \sinh\left(\frac{\tau \cdot \Omega}{2 \cdot k_B \cdot T}\right), \quad (1)$$

where  $\Delta G^m$  is the activation energy for an atomic jump;  $f$  is the jump frequency;  $T$  is the temperature,  $k_B$  is the Boltzmann's constant;  $\Omega$  is the atomic volume;  $C_f = \exp(-\gamma v^*/v_f)$  is the concentration of the flow defects. It

relates to the so-called reduced free volume  $v_f/\gamma v^*$  according to [29] and where  $\gamma v^*$  is approximated as  $0.5 \Omega$  [41], and  $v_f$  is the mean free volume per atom.

The softening observed in stress-strain curves of Figure 3(a) can be justified by several potential causes involving the local creation of flow defects due to flow dilatation [42–45], the local evolution of structural order [46, 47] and the local heat generation [48–50]. Due to these causes, viscosity can decrease dramatically according to the so-called “hybrid” equation [51]:

$$\eta_s(T, C_f) = \eta_0 \cdot \exp\left(\frac{Q_n}{R \cdot T}\right) \left(\frac{1}{C_f}\right), \quad (2)$$

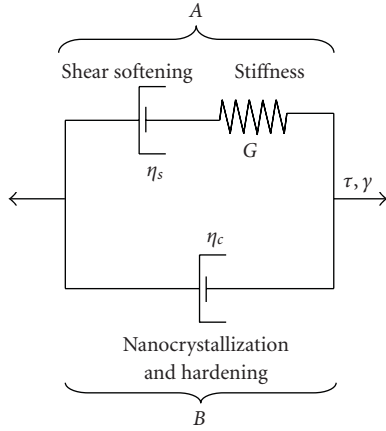


FIGURE 4: Schematic representation of rheological model for mechanical behaviour of individual shear band in light of experimental results (Figure 1) and the proposed micromechanism of deformation in metallic glasses (Figure 3). Interatomic resistance (stiffness) is followed by shear softening ( $\eta_s$ ), acting in parallel with hardening induced by in situ nanocrystallization ( $\eta_c$ ).

where  $\eta_0$  is a pre-exponential factor  $Q_n$  is the activation energy for viscous flow.

The change in the defect concentration  $C_f$  can be estimated as a balance between structural relaxation and strain-induced nucleation. This leads to the general equation [52]

$$\frac{dC_f}{dt} = -k \cdot C_f \cdot (C_f - C_{f,eq}) + a \cdot \dot{\epsilon} \cdot C_f \cdot (\ln C_f)^2. \quad (3)$$

$k$  is a temperature-dependent rate factor for structural relaxation, which has the form of  $k = k_0 \exp(-E_r/RT)$  with  $k_0$  being the attempt frequency and  $E_r$  being the activation energy for relaxation  $a$  is a proportionality factor.  $C_{f,eq}$  denotes the defect concentration in the metastable equilibrium state [51]

Now, we go back to the proposed rheological model of Figure 4, and according to the described microscopic mechanism of deformation, the initial linear dilatation is modeled with a three-dimensional linear elastic spring acting in series with a viscous element denoting the softening part ( $\eta_s(C_f, T)$ ). The spring represents the initially stiff elastic response due to interatomic bonds in material, and the viscosity is taken to be initial as for metallic glasses ( $\eta_0$ ) and is temperature-strain independent according to (2). Once the stress reaches a critical level, critical concentration of defect is overcome, viscosity decreases, and shear flow softening follows. The deformation can therefore be decomposed into elastic and plastic flows with stress softening.

*Step 2 (Strain Hardening and Arrest of Shear Band Propagation).* The Arrest of the shear bands has not been well understood and is still the matter of debate. Chen et al. [53] showed that a propagating shear band initially accelerates and then reaches a steady state, and finally the propagating shear band decelerates and is arrested. This indicates that a mechanism of the blocking in a shear band is operating,

which is a significantly important issue, and it is worthy of progressive study.

Several factors have been suggested to cause the arrest of the shear bands. Recently, Dalla Torre et al. [19] suggested that structural relaxation can occur after a shear event going with the annihilation of strain-created free volume, and therefore it causes a time-dependent hardening in the vicinity of the shear band. Alternatively, deformation-induced nanocrystallization observed in our previous work [14–16] and confirmed in a number of MGs showing large plastic deformation provides a potential reason for the strain-hardening mechanism. The presence of nanocrystallites in shear bands has a direct effect on viscosity, increasing its value with increasing the content of particles. As suggested in our previous work, shear bands can act as semisolid MG slurries since, as discussed in step 1, shear in metallic glasses generates free volume and heat, reduces viscosity, and leads to liquid-like behaviour in the shear bands with a possible rise in temperature. Under these conditions, the increase of the amount of nanocrystals in the shear zone can dramatically increase viscosity according to the correlation between viscosity and the fraction of nanocrystal solids (for semisolid behaviour) [54–56]

$$\eta_c(\gamma, \dot{\gamma}, T) = \eta_l \left( 1 - \frac{\phi_s(\gamma, \dot{\gamma}, T)}{\phi_{cr}} \right)^{-\alpha}, \quad (4)$$

where  $\eta_c$  is the increased viscosity of the flowing system of liquid and solids (nanoparticles)  $\eta_l$  is the viscosity of the liquid  $\phi_s$  is the solid fraction of the suspension  $\alpha$  is a constant,  $\phi_{cr}$  is a critical value of particle fraction beyond which the relationship no longer holds since the system becomes jammed ( $0,5 < \phi_{cr} < 0,6$ ).

The nanocrystallization is a rate-dependent function of shear deformation along shear bands, and the fraction of the crystalline phase increases with shear strains. Therefore, the arrest of shear strain corresponds to a critical value of volume fraction of the crystalline particles (or nanocrystalline) at which the increased viscosity by the nanocrystallization (and subsequent growth) is high enough to prevent the further shearing along the band. This strengthening caused by in situ nanocrystallization can compensate the strain softening ((3)-(4)-(5) steps in Figure 3) and thus prevent the runaway failure along the shear band. Consequently, shear process stops, and system (sample and stiff machine) turns into the elastic form until the creation of a new shear band with further loading (serration behaviour as shown in Figure 1)

The new strain-hardening mechanism acting in parallel with the strain-softening one is modeled with a viscous element where the viscosity  $\eta_c$  is given by (4).

In the end of this phenomenological description of stress-strain behaviour of MGs, it is necessary to address the modeling of flow-induced crystallization. While numerous works showed deformation-induced nanocrystallization during deformation, as of yet, no consensus concerning the microscopic mechanism of mechanically-induced nanocrystallization has been achieved. Recent investigations [57–60], based on TEM observations, have proposed a model for nanocrystallization mechanism in the BMGs. Since

amorphous alloys are not in thermodynamic equilibrium, a phase transformation from an amorphous liquid-like phase to a crystalline phase can take place with the supply of sufficient external energy. Thermal energy [57, 61] and mechanical energy [58, 59] are two major driving forces controlling this transformation as well as the assistance of the local atomic rearrangements in the shear band [60].

Actually, since the amorphous crystal transformation in shear bands is a new phenomenon and not fundamentally addressed, we shall use it for the first assumption of the classical theory of crystallization applied for metallic glasses. Crystallization of an amorphous liquid can be regarded as process taking place by crystal nucleation and subsequent growth. During the nucleation process, a crystalline embryo is formed in the amorphous liquid, and meantime, the interface is formed simultaneously. The overall rate of transformation will reflect the time, temperature, shear, shear rate, and so forth dependence of both nucleation and growth process. This is usually described by the Johnson-Mehl-Avrami equation [58]

$$\phi_s(\gamma, \dot{\gamma}, T) = 1 - \exp(-b(T) \cdot t^n) \approx 1 - \exp\left(-b(T) \cdot \left(\frac{\gamma}{\dot{\gamma}}\right)^n\right), \quad (5)$$

where  $b(T) \approx b_0 \exp(\Delta G^*/RT)$  is a rate constant, and  $n$  is an exponent between 1.5 and 4.  $\Delta G^*$  is the activation energy for overall crystallization process which can be obtained from the thermodynamic point of view of amorphous-to-crystalline phase transformation [24, 59, 60] or from continuous heating experiments using Kissinger's [59, 62] or Ozawa's [63] method

$$\Delta G^*(T, P) = \frac{16\pi \cdot \gamma^3}{3} \left( \frac{V_m^c}{\Delta G_m + E_e + P\Delta V_m} \right)^2, \quad (6)$$

where  $\Delta G_m$  is the molar free energy change for an amorphous-to-crystalline phase transformation;  $E_e$  is the elastic energy induced by the volume change upon phase transformation;  $\gamma$  is the interfacial free energy of the crystalline/amorphous interface;  $V_m^c$  is the molar volume of the crystalline phase;  $\Delta V_m$  is the volume change for forming a crystalline nucleus from an amorphous matrix  $P$  is the applied hydrostatic pressure. Based on (6), Lee et al. [24] demonstrated that a decrease in activation energy for crystallization can occur within the shear bands due to the increased interface thermal-strain energy and contact pressure-promoted nucleation. Hence, the rapid nucleation of crystals in the shear zone can occur under the high strain rate deformation and adiabatic heating.

#### 4. Mathematical Model Formulation

The mathematical representation of the proposed rheological model is based on the representation of the breakdown of the overall deformation resistance into a resistance A acting in parallel with a resistance B as illustrated in Figure 4. As stated earlier, resistance A come up from interatomic interactions and shear softening where the interatomic interactions

are the source of the material's initial stiffness and result in a finite stress at which metallic glasses will plastically soft. In resistance B, hardening by insitu nanocrystallization is a secondary contributor to the shear strain of the material. The two processes (shear softening and material hardening) occur concurrently immediately after the initial stiffness and are therefore modeled as being in parallel after initial elastic strain. The proposed rheological model recognizes that the shear deformation acting on each resistance is equal to the imposed (total) shear deformation  $\gamma$

$$\gamma = \gamma_A = \gamma_B. \quad (7)$$

The total shear stress  $\tau$  is the sum of the shear stress acting on each resistance:

$$\tau = \tau_A + \tau_B. \quad (8)$$

We assume that the viscous flow in shear bands is Newtonian, then:

$$\tau_B = \eta_c \cdot \dot{\gamma}_B = \eta_c \cdot \dot{\gamma}, \quad \dot{\gamma} = \frac{\dot{\tau}_A}{G} + \frac{\tau_A}{\eta_s}. \quad (9)$$

For constant shear strain ( $\partial\gamma/\partial t = \text{constant}$ ), (7), (8), and (9) lead to the general relationship between stress and strain resulting in the proposed rheological model for shear-banding behaviour

$$\dot{\tau} = \frac{G}{\eta_s} [(\eta_s + \eta_c)\dot{\gamma} - \tau]. \quad (10)$$

#### 5. Summary

We conclude our study by a very brief recapitulation of the rheological model that we have proposed. In this paper a new micromechanism-inspired constitutive model has been presented that allows for predictions of single-shear striation behaviour of "ductile" MGs. The model is based on the assumption that the general behaviour can be decomposed into two resistances acting in parallel: one captures the initial stiffness and shear softening, and the second gives the time-shear-temperature hardening of material. The resultant stress-strain curve should be obtained by the resolution of the coupled (1), (3), (4), (5), and (10). Resolution involves a large number of model parameters that must be defined; many of these parameters are fundamental properties of the metallic glasses that can be found in the literature. However, the remaining parameters must be obtained by fitting the above equations to our experimental data and to others recently published data [53, 64]. This is not the aim of this paper, but this study is in progress.

#### References

- [1] A. Peker and W. L. Johnson, "A highly processable metallic glass:  $Zr_{41.25}Ti_{13.75}Cu_{12.5}Ni_{10.0}Be_{22.5}$ ," *Applied Physics Letters*, vol. 63, no. 17, pp. 2342–2344, 1993.
- [2] A. Inoue, "Stabilization of metallic supercooled liquid and bulk amorphous alloys," *Acta Materialia*, vol. 48, no. 1, pp. 279–306, 2000.

- [3] W. H. Wang, C. Dong, and C. H. Shek, "Bulk metallic glasses," *Materials Science and Engineering R*, vol. 44, no. 2-3, pp. 45–89, 2004.
- [4] A. L. Greer, "Metallic glasses," *Science*, vol. 267, no. 5206, pp. 1947–1953, 1995.
- [5] W. F. Wu, Y. Li, and C. A. Schuh, "Strength, plasticity and brittleness of bulk metallic glasses under compression: statistical and geometric effects," *Philosophical Magazine*, vol. 88, no. 1, pp. 71–89, 2008.
- [6] W. Klement, R. H. Willens, and P. Duwez, "Non-crystalline structure in solidified Gold-Silicon alloys," *Nature*, vol. 187, no. 4740, pp. 869–870, 1960.
- [7] A. Inoue, B. Shen, H. Koshiba, H. Kato, and A. R. Yavari, "Cobalt-based bulk glassy alloy with ultrahigh strength and soft magnetic properties," *Nature Materials*, vol. 2, no. 10, pp. 661–663, 2003.
- [8] C. J. Gilbert, R. O. Ritchie, and W. L. Johnson, "Fracture toughness and fatigue-crack propagation in a Zr–Ti–Ni–Cu–Be bulk metallic glass," *Applied Physics Letters*, vol. 71, no. 4, pp. 476–478, 1997.
- [9] A. R. Yavari, J. J. Lewandowski, and J. Eckert, "Mechanical properties of bulk metallic glasses," *MRS Bulletin*, vol. 32, no. 8, pp. 635–638, 2007.
- [10] D. Zander, B. Heisterkamp, and I. Gallino, "Corrosion resistance of Cu–Zr–Al–Y and Zr–Cu–Ni–Al–Nb bulk metallic glasses," *Journal of Alloys and Compounds*, vol. 434–435, pp. 234–236, 2007.
- [11] Y. Zhang and A. L. Greer, "Thickness of shear bands in metallic glasses," *Applied Physics Letters*, vol. 89, no. 7, Article ID 071907, 3 pages, 2006.
- [12] H. J. Leamy, T. T. Wang, and H. S. Chen, "Plastic flow and fracture of metallic glass," *Metallurgical Transactions*, vol. 3, no. 3, pp. 699–708, 1972.
- [13] A. Inoue, W. Zhang, T. Tsurui, A. R. Yavari, and A. L. Greer, "Unusual room-temperature compressive plasticity in nanocrystal-toughened bulk copper-zirconium glass," *Philosophical Magazine Letters*, vol. 85, no. 5, pp. 221–229, 2005.
- [14] K. Hajlaoui, A. R. Yavari, B. Doisneau et al., "Shear delocalization and crack blunting of a metallic glass containing nanoparticles: in situ deformation in TEM analysis," *Scripta Materialia*, vol. 54, no. 11, pp. 1829–1834, 2006.
- [15] K. Hajlaoui, B. Doisneau, A. R. Yavari et al., "Unusual room temperature ductility of glassy copper-zirconium caused by nanoparticle dispersions that grow during shear," *Materials Science and Engineering A*, vol. 448–451, pp. 105–110, 2007.
- [16] K. Hajlaoui, A. R. Yavari, A. LeMoulec et al., "Plasticity induced by nanoparticle dispersions in bulk metallic glasses," *Journal of Non-Crystalline Solids*, vol. 353, no. 3, pp. 327–331, 2007.
- [17] K. F. Yao, F. Ruan, Y. Q. Yang, and N. Chen, "Superductile bulk metallic glass," *Applied Physics Letters*, vol. 88, no. 12, Article ID 122106, 2006.
- [18] J. C. Ye, J. Lu, Y. Yang, and P. K. Liaw, "Study of the intrinsic ductile to brittle transition mechanism of metallic glasses," *Acta Materialia*, vol. 57, no. 20, pp. 6037–6046, 2009.
- [19] F. H. Dalla Torre, A. Dubach, J. Schällibaum, and J. F. Löffler, "Shear striations and deformation kinetics in highly deformed Zr-based bulk metallic glasses," *Acta Materialia*, vol. 56, no. 17, pp. 4635–4646, 2008.
- [20] A. Dubach, F. H. Dalla Torre, and J. F. Löffler, "Constitutive model for inhomogeneous flow in bulk metallic glasses," *Acta Materialia*, vol. 57, no. 3, pp. 881–892, 2009.
- [21] C. Q. Chen, Y. T. Pei, and J. T. M. De Hosson, "Effects of size on the mechanical response of metallic glasses investigated through in situ TEM bending and compression experiments," *Acta Materialia*, vol. 58, no. 1, pp. 189–200, 2010.
- [22] J. B. Qiang, W. Zhang, G. Q. Xie, and A. Inoue, "Unusual room temperature ductility of a Zr-based bulk metallic glass containing nanoparticles," *Applied Physics Letters*, vol. 90, no. 23, Article ID 231907, 2007.
- [23] K. Mondal, T. Ohkubo, T. Toyama, Y. Nagai, M. Hasegawa, and K. Hono, "The effect of nanocrystallization and free volume on the room temperature plasticity of Zr-based bulk metallic glasses," *Acta Materialia*, vol. 56, no. 18, pp. 5329–5339, 2008.
- [24] S.-W. Lee, M.-Y. Huh, S.-W. Chae, and J.-C. Lee, "Mechanism of the deformation-induced nanocrystallization in a Cu-based bulk amorphous alloy under uniaxial compression," *Scripta Materialia*, vol. 54, no. 8, pp. 1439–1444, 2006.
- [25] A. S. Argon, "Plastic deformation in metallic glasses," *Acta Metallurgica*, vol. 27, no. 1, pp. 47–58, 1979.
- [26] M. L. Falk, "Molecular-dynamics study of ductile and brittle fracture in model noncrystalline solids," *Physical Review B*, vol. 60, no. 10, pp. 7062–7070, 1999.
- [27] A. C. Lund and C. A. Schuh, "Yield surface of a simulated metallic glass," *Acta Materialia*, vol. 51, no. 18, pp. 5399–5411, 2003.
- [28] J. S. Langer, "Dynamics of shear-transformation zones in amorphous plasticity: formulation in terms of an effective disorder temperature," *Physical Review E*, vol. 70, no. 4, Article ID 041502, 2004.
- [29] D. Turnbull and M. H. Cohen, "Free-volume model of the amorphous phase: glass transition," *The Journal of Chemical Physics*, vol. 34, no. 1, pp. 120–125, 1961.
- [30] D. Turnbull and M. H. Cohen, "On the free-volume model of the liquid-glass transition," *The Journal of Chemical Physics*, vol. 52, no. 6, pp. 3038–3041, 1970.
- [31] M. H. Cohen and D. Turnbull, "Molecular transport in liquids and glasses," *The Journal of Chemical Physics*, vol. 31, no. 5, pp. 1164–1169, 1959.
- [32] F. Spaepen, "A microscopic mechanism for steady state inhomogeneous flow in metallic glasses," *Acta Metallurgica*, vol. 25, no. 4, pp. 407–415, 1977.
- [33] K. C. Chan, L. Liu, and J. F. Wang, "Superplastic deformation of  $Zr_{55}Cu_{30}Al_{10}Ni_5$  bulk metallic glass in the supercooled liquid region," *Journal of Non-Crystalline Solids*, vol. 353, no. 32–40, pp. 3758–3763, 2007.
- [34] G. Wang, J. Shen, J. F. Sun, Z. P. Lu, Z. H. Stachurski, and B. D. Zhou, "Tensile fracture characteristics and deformation behavior of a Zr-based bulk metallic glass at high temperatures," *Intermetallics*, vol. 13, no. 6, pp. 642–648, 2005.
- [35] R. Huang, Z. Suo, J. H. Prevost, and W. D. Nix, "Inhomogeneous deformation in metallic glasses," *Journal of the Mechanics and Physics of Solids*, vol. 50, no. 5, pp. 1011–1027, 2002.
- [36] M. Bletry, P. Guyot, Y. Bréchet, J. J. Blandin, and J. L. Soubeyroux, "Transient regimes during high-temperature deformation of a bulk metallic glass: a free volume approach," *Acta Materialia*, vol. 55, no. 18, pp. 6331–6337, 2007.
- [37] C. A. Schuh, T. C. Hufnagel, and U. Ramamurty, "Mechanical behavior of amorphous alloys," *Acta Materialia*, vol. 55, no. 12, pp. 4067–4109, 2007.
- [38] C. A. Schuh and A. C. Lund, "Atomistic basis for the plastic yield criterion of metallic glass," *Nature Materials*, vol. 2, no. 7, pp. 449–452, 2003.
- [39] K. Hajlaoui, M. A. Yousfi, Z. Tourki, G. Vaughan, and A. R. Yavari, "On the free volume kinetics during isochronal structural relaxation of Pd-based metallic glass: effect of

- temperature and deformation,” *Journal of Materials Science*, vol. 45, no. 12, pp. 3344–3349, 2010.
- [40] P. A. Duine, J. Sietsma, and A. van den Beukel, “Defect production and annihilation near equilibrium in amorphous  $\text{Pd}_{40}\text{Ni}_{40}\text{P}_{20}$  investigated from viscosity data,” *Acta Metallurgica Et Materialia*, vol. 40, no. 4, pp. 743–751, 1992.
- [41] A. van den Beukel and J. Sietsma, “The glass transition as a free volume related kinetic phenomenon,” *Acta Metallurgica Et Materialia*, vol. 38, no. 3, pp. 383–389, 1990.
- [42] J. Li, F. Spaepen, and T. C. Hufnagel, “Nanometre-scale defects in shear bands in a metallic glass,” *Philosophical Magazine A*, vol. 82, no. 13, pp. 2623–2630, 2002.
- [43] B. P. Kanungo, S. C. Glade, P. Asoka-Kumar, and K. M. Flores, “Characterization of free volume changes associated with shear band formation in Zr- and Cu-based bulk metallic glasses,” *Intermetallics*, vol. 12, no. 10-11, pp. 1073–1080, 2004.
- [44] K. Hajlaoui, T. Benameur, G. Vaughan, and A. R. Yavari, “Thermal expansion and indentation-induced free volume in Zr-based metallic glasses measured by real-time diffraction using synchrotron radiation,” *Scripta Materialia*, vol. 51, no. 9, pp. 843–848, 2004.
- [45] A. R. Yavari, A. L. Moulec, A. Inoue et al., “Excess free volume in metallic glasses measured by X-ray diffraction,” *Acta Materialia*, vol. 53, no. 6, pp. 1611–1619, 2005.
- [46] K. Georgarakis, A. R. Yavari, D. V. Louzguine-Luzgin et al., “Atomic structure of Zr-Cu glassy alloys and detection of deviations from ideal solution behavior with Al addition by x-ray diffraction using synchrotron light in transmission,” *Applied Physics Letters*, vol. 94, no. 19, Article ID 191912, 2009.
- [47] X. D. Wang, J. Bednarcik, K. Saksl, H. Franz, Q. P. Cao, and J. Z. Jiang, “Tensile behavior of bulk metallic glasses by in situ x-ray diffraction,” *Applied Physics Letters*, vol. 91, no. 8, Article ID 081913, 2007.
- [48] J. J. Lewandowski and A. L. Greer, “Temperature rise at shear bands in metallic glasses,” *Nature Materials*, vol. 5, no. 1, pp. 15–18, 2006.
- [49] K. Georgarakis, M. Aljerf, Y. Li et al., “Shear band melting and serrated flow in metallic glasses,” *Applied Physics Letters*, vol. 93, no. 3, Article ID 031907, 2008.
- [50] W. J. Wright, R. B. Schwarz, and W. D. Nix, “Localized heating during serrated plastic flow in bulk metallic glasses,” *Materials Science and Engineering A*, vol. 319–321, pp. 229–232, 2001.
- [51] A. Van Den Beukel and S. Radelaar, “On the kinetics of structural relaxation in metallic glasses,” *Acta Metallurgica*, vol. 31, no. 3, pp. 419–427, 1983.
- [52] P. de Hey, J. Sietsma, and A. Van Den Beukel, “Structural disordering in amorphous  $\text{Pd}_{40}\text{Ni}_{40}\text{P}_{20}$  induced by high temperature deformation,” *Acta Materialia*, vol. 46, no. 16, pp. 5873–5882, 1998.
- [53] H. M. Chen, J. C. Huang, S. X. Song, T. G. Nieh, and J. S. C. Jang, “Flow serration and shear-band propagation in bulk metallic glasses,” *Applied Physics Letters*, vol. 94, no. 14, Article ID 141914, 2009.
- [54] I. M. Krieger and T. J. Dougherty, “A mechanism for non-Newtonian flow in suspensions of rigid spheres,” *Transactions of the Society of Rheology*, vol. 3, pp. 137–152, 1959.
- [55] N. K. Halder, B. K. Chatterjee, and S. C. Roy, “The change of viscosity with concentration of suspended particles and a new concept of gelation,” *Journal of Physics Condensed Matter*, vol. 9, no. 42, pp. 8873–8878, 1997.
- [56] S. Wright, L. Zhang, S. Sun, and S. Jahanshahi, “Viscosity of a  $\text{CaO-MgO-Al}_2\text{O}_3\text{-SiO}_2$  melt containing spinel particles at 1646 K,” *Metallurgical and Materials Transactions B*, vol. 31, no. 1, pp. 97–104, 2000.
- [57] H. J. Chang, D. H. Kim, Y. M. Kim, Y. J. Kim, and K. Chattopadhyay, “On the origin of nanocrystals in the shear band in a quasicrystal forming bulk metallic glass  $\text{Ti}_{40}\text{Zr}_{29}\text{Cu}_9\text{Ni}_8\text{Be}_{14}$ ,” *Scripta Materialia*, vol. 55, no. 6, pp. 509–512, 2006.
- [58] M. Avrami, “Kinetics of phase change. II Transformation-time relations for random distribution of nuclei,” *The Journal of Chemical Physics*, vol. 8, no. 2, pp. 212–224, 1940.
- [59] S. Yoon, G. Bae, Y. Xiong et al., “Strain-enhanced nanocrystallization of a CuNiTiZr bulk metallic glass coating by a kinetic spraying process,” *Acta Materialia*, vol. 57, no. 20, pp. 6191–6199, 2009.
- [60] Y. F. Deng, L. L. He, Q. S. Zhang, H. F. Zhang, and H. Q. Ye, “HRTEM analysis of nanocrystallization during uniaxial compression of a bulk metallic glass at room temperature,” *Ultramicroscopy*, vol. 98, no. 2–4, pp. 201–208, 2004.
- [61] D. T. A. Matthews, V. Ocelík, P. M. Bronsveld, and J. Th. M. De Hosson, “An electron microscopy appraisal of tensile fracture in metallic glasses,” *Acta Materialia*, vol. 56, no. 8, pp. 1762–1773, 2008.
- [62] H. E. Kissinger, “Reaction kinetics in differential thermal analysis,” *Analytical Chemistry*, vol. 29, no. 11, pp. 1702–1706, 1957.
- [63] T. Ozawa, “Kinetic analysis of derivative curves in thermal analysis,” *Journal of Thermal Analysis*, vol. 2, no. 3, pp. 301–324, 1970.
- [64] S. X. Song, H. Bei, J. Wadsworth, and T. G. Nieh, “Flow serration in a Zr-based bulk metallic glass in compression at low strain rates,” *Intermetallics*, vol. 16, no. 6, pp. 813–818, 2008.

## Research Article

# Fluoride Nanoscintillators

**Luiz G. Jacobsohn,<sup>1</sup> Kevin B. Sprinkle,<sup>1</sup> Steven A. Roberts,<sup>1</sup> Courtney J. Kucera,<sup>1</sup>  
Tiffany L. James,<sup>1</sup> Eduardo G. Yukihara,<sup>2</sup> Timothy A. DeVol,<sup>3</sup> and John Ballato<sup>1</sup>**

<sup>1</sup> Center for Optical Materials Science and Engineering Technologies (COMSET), School of Materials Science and Engineering, Clemson University, Clemson, SC 29634, USA

<sup>2</sup> Physics Department, Oklahoma State University, Stillwater, OK 74078, USA

<sup>3</sup> Department of Environmental Engineering and Earth Sciences, Clemson University, Clemson, SC 29625-6510, USA

Correspondence should be addressed to Luiz G. Jacobsohn, luiz@clemson.edu

Received 10 May 2010; Revised 23 July 2010; Accepted 28 September 2010

Academic Editor: Quanqin Dai

Copyright © 2011 Luiz G. Jacobsohn et al. This is an open access article distributed under the Creative Commons Attribution License, which permits unrestricted use, distribution, and reproduction in any medium, provided the original work is properly cited.

A preliminary investigation of the scintillation response of rare earth-doped fluoride nanoparticles is reported. Nanoparticles of  $\text{CaF}_2 : \text{Eu}$ ,  $\text{BaF}_2 : \text{Ce}$ , and  $\text{LaF}_3 : \text{Eu}$  were produced by precipitation methods using ammonium di-*n*-octadecylthiophosphate (ADDP) as a ligand that controls growth and lessens agglomeration. The structure and morphology were characterized by means of X-ray diffraction and transmission electron microscopy, while the scintillation properties of the nanoparticles were determined by means of X-ray and  $^{241}\text{Am}$  irradiation. The unique aspect of scintillation of nanoparticles is related to the migration of carriers in the nanoscintillator. Our results showed that even nanoparticles as small as  $\sim 4$  nm in size effectively scintillate, despite the diffusion length of *e-h* pairs being considerably larger than the nanoparticles themselves, and suggest that nanoparticles can be used for radiation detection.

## 1. Introduction

Scintillators are luminescent materials that are used in the detection of ionizing radiation. Accordingly, they find use in a wide range of security, medical, industrial, and research applications. Since the discovery of scintillator  $\text{NaI} : \text{Tl}$  in 1948, there has been continuous interest and investment in new materials, and, as a result, hundreds of scintillators are known today [1–7]. Some of the most used scintillators are alkali, alkali-earth, and rare earth (RE) halides, including  $\text{NaI} : \text{Tl}$ ,  $\text{LiF} : \text{Eu}$ ,  $\text{BaF}_2 : (\text{Ce})$ ,  $\text{CaF}_2 : \text{Eu}$ ,  $\text{CeF}_3$ , and  $\text{LaBr}_3 : \text{Ce}$ . Unfortunately, many of these materials are hygroscopic, which impose severe limitations on their synthesis and use.

Over the past 10 years, there has been significant interest in the investigation and evaluation of the performance of nanoscale materials, with virtually all classes of materials having been prepared as nanoparticles, particularly luminescent ones [8–14]. Nanoparticles are generally defined as having sizes that range from 1 to 100 nm and consequently have high surface-to-volume ratios. The relative dominance of surface atoms in nanoparticles often allows for property manipulation. For example, Stouwdam and van Veggel [15]

and Kömpe et al., [16] reported a substantially increased quantum yield from RE-doped nanoparticles following surface modifications, while Cooke et al. observed significant changes in the luminescence lifetime of  $\text{Y}_2\text{SiO}_5 : \text{Ce}$  nanoparticles dispersed in different liquids [17, 18]. To date, the investigation of luminescent nanoparticles has focused mostly on quantum dots for lighting and display applications, while their application as scintillators is essentially unexplored [19–25]. Nanoparticles correspond to a new realm of opportunity for scintillation technologies, and this work provides a preliminary investigation of the scintillation response of RE-doped fluoride nanoparticles.

Scintillation corresponds to the emission of light upon excitation due to ionizing radiation, and scintillation performance is mainly characterized by luminosity, speed (lifetime), and emission wavelength, with ruggedness, radiation resistance, and thermal and chemical stability being important characteristics of the scintillator material as well. Scintillation efficiency,  $\eta$ , can be described by the combination of three processes: conversion,  $\beta$ , transfer,  $Q$ , and luminescence,  $S$ , summarized in the relation,  $\eta = \beta SQ$  [26] and discussed in detail below.

The first process corresponds to how efficiently the energy of the incoming radiation is used to produce electron-hole ( $e-h$ ) pairs. For gamma-rays,  $\beta$  is commonly estimated by dividing the energy of the gamma-ray by 2 to 2.5 times the value of the bandgap energy. Once created, free electrons and holes migrate through the lattice of the scintillator material. While still energetic, they can ionize other atoms and the new free electrons can further ionize other atoms, generating a cascade. Through numerous inelastic interactions with bound electrons, they lose energy and eventually become incapable of creating further ionization. The duration of this process is estimated to be  $10^{-15}$  to  $10^{-13}$  s and generates conduction band electrons, valence band holes, excitons, and plasmons. Once below the ionization threshold, these free electrons and holes lose enough energy to strongly interact with the vibrations of the lattice (electron-phonon interactions) and thermalize within  $10^{-12}$  to  $10^{-11}$  s, moving to the bottom of the conduction band and to the top of the valence band, respectively. Typically,  $e-h$  pairs have diffusion length of about 100 nm in ionic crystals [27].

During this migration through the lattice, a fraction of the  $e-h$  pairs is lost, either trapped or recombined nonradiatively at quenching centers, resulting in a decrease in the number of pairs available to produce luminescence. Only those pairs that reach the luminescent centers contribute to scintillation, and the efficiency of this process is given by  $S$ . The remaining  $e-h$  pairs that recombine at the luminescence centers generate scintillation, and the intrinsic efficiency of the radiative recombination at the luminescent center is quantified by  $Q$ . Table 1 illustrates these quantities for some bulk fluoride crystals, together with their luminosity [26].

Moreover, a few RE-doped single crystal lanthanum fluoride scintillators have been previously investigated.  $\text{LaF}_3:\text{Ce}$  is a fast scintillator, with a reported luminosity of 2200 photons/MeV at 10%  $\text{CeF}_3$  doping [28], and  $\text{LaF}_3:\text{Nd}$  shows weak scintillation of 270 photons/MeV at 173 nm [29]. While the choice of host and dopant determines the efficiency of the conversion and luminescence processes, the unique aspect of scintillation in nanoparticles is related to the migration of the carriers through the nanoscintillator.

## 2. Experimental Procedures

**2.1. Synthesis of Nanoparticles.** Solution precipitation takes advantage of the solubility of certain compounds to promote chemical reactions and the formation of precipitates, which, in our case, are the nanoparticles. The solubility of a substance corresponds to its ability to dissolve into a homogeneous solution in presence of a solvent. When dissolution occurs, molecules of the solvent arrange and bond themselves around the molecules of the solute, generating heat, increasing entropy, and making the solution more thermodynamically stable than the solute alone. Several different species can be formed in the solution, with the solubility and the composition of its soluble components depending on the pH. The chemical properties of the solvent and solute, such as hydrogen bonding, dipole moment, and polarizability play major roles in this process. Most

nitrate, sulfate, acetate, chloride, bromide, iodide, alkali metals, and  $\text{NH}_4$  compounds are soluble in water and can be used as precursors, while carbonates, sulfites, sulfides, phosphates, hydroxides, and oxides are insoluble. Synthesis of RE-doped fluoride nanoparticles was carried out by means of a modified solution precipitation method, where soluble metal nitrates ( $\text{Ca}(\text{NO}_3)_2 \cdot 4\text{H}_2\text{O}$  (Fisher, 99.9%),  $\text{Eu}(\text{NO}_3)_3 \cdot 6\text{H}_2\text{O}$  (Alfa Aesar, 99.9%),  $\text{Ba}(\text{NO}_3)_2$  (Fisher, reagent grade),  $\text{Ce}(\text{NO}_3)_3 \cdot 6\text{H}_2\text{O}$  (Acros Organic, 99.5%), and  $\text{La}(\text{NO}_3)_3 \cdot 6\text{H}_2\text{O}$  (Aldrich, 99.99%)), and ammonium fluoride (Acros Organic, >98%) were used as the precursors. The solubility of a substance is further affected by the temperature and the nature of the solvent, and also on the presence of other substances dissolved in the solvent, particularly complex-forming anions (ligands). Two precursor solutions were used. One of them, contained  $\text{NH}_4\text{F}$ , the source of fluorine, and the ligand ammonium di-*n*-octadecyldithiophosphate (ADDP) in 1:1 ethanol:water at 75°C. The other solution contained the nitrates dissolved in water and was the source of the host and dopant metals.

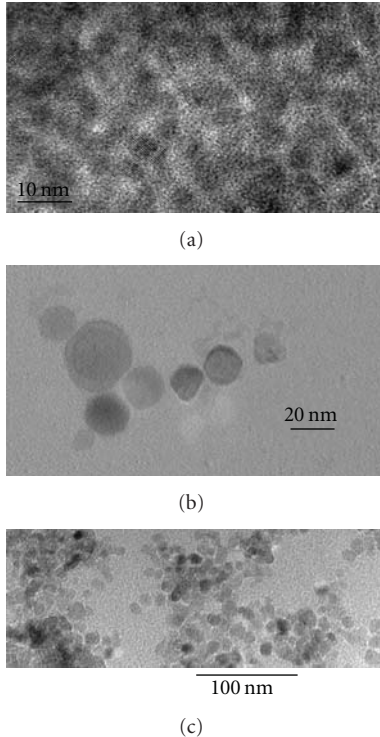
Solvents can affect the solubility, stability, and reaction rates, allowing for thermodynamic and kinetic control over a chemical reaction. The polarity, dipole moment, polarizability, and hydrogen bonding of a solvent determine the types of compounds it is able to dissolve and the solvents and other liquid compounds it is miscible in. Generally, polar solvents dissolve polar compounds, and nonpolar solvents dissolve nonpolar compounds. Further, the choice of the solvent should take into account the reaction mechanism. Protic solvents like water solvate anions via hydrogen bonding, favoring the dissociative reaction mechanism, while aprotic solvents such as acetone or dichloromethane solvate cations via dipole interaction, favoring the interchange mechanism.

Of particular interest is the use of ligands during the synthesis of nanoparticles to control growth, avoid particle agglomeration, and provide dispersability in organic solvents. A ligand is an ion or molecule that bonds itself to a metal atom forming covalent or ionic bonds; chelation occurs when more than one chemical bond is formed with the central metal ion. Ligands also can be used as a “capping” agent to inactivate the metal so that it cannot react with other elements or ions to produce precipitates. In this work, the ligand ADDP is used in order to control growth and to avoid agglomeration of nanoparticles, as already has been demonstrated for the synthesis of other nanomaterials [15, 30–36]. ADDP was synthesized as follows [30].  $\text{P}_2\text{S}_5$  (0.02 mol) and octadecanol (0.07 mol) were heated at 75°C for 3 hours, and the resulting suspension cooled to room temperature at which point dichloromethane was added to solution, followed by filtration. The solvent was evaporated, the residue added into hexane, and ammonia was bubbled through the solution. The resulting precipitate was separated by filtration, washed with hexane, and dried. Water was purified using a Nanopure Diamond purification system from Barnstead International.

The synthesis of  $\text{CaF}_2:\text{Eu}$ ,  $\text{BaF}_2:\text{Ce}$ , and  $\text{LaF}_3:\text{Eu}$  nanoparticles consisted of dropwise addition of the nitrate solution into the fluorinated solution while stirring to form the nanoparticles in suspension. Rare earth doping levels

TABLE 1: Parameters relevant to the scintillation performance of selected fluoride scintillators.

Scintillator	Bandgap (eV)	$\beta$	Q	S	$\eta$	Luminosity (photons/MeV)
CeF <sub>3</sub>	10.4	0.61	1.0	0.13	0.08	3200
Ce <sub>0.5</sub> La <sub>0.5</sub> F <sub>3</sub>	10.4	0.61	1.0	0.16	0.1	4000
CaF <sub>2</sub> : Eu	12.2	0.63	1.0	~1	0.6	24000
BaF <sub>2</sub> (@310 nm)	10.6	<0.72	~1	>0.33	0.24	9950

FIGURE 1: Selected TEM images of fluoride nanoscintillators: (a) LaF<sub>3</sub> : Eu, (b) BaF<sub>2</sub> : Ce, and (c) CaF<sub>2</sub> : Eu.

were 3 mol% for hosts CaF<sub>2</sub> and BaF<sub>2</sub> and 1 mol% for LaF<sub>3</sub>. The final solution is stirred for 10 minutes and then cooled down to room temperature. Further, the precipitates were cleaned by washing in ethanol and water, followed by dispersion in dichloromethane (Acros, anhydrous, AcroSeal, 99.9%) and precipitation with the addition of 20 mL of ethanol. The resultant powder was dried for 2 days over P<sub>2</sub>O<sub>5</sub> in a desiccator. The nanoparticles could be dispersed in tetrahydrofuran (Acros, anhydrous, AcroSeal, 99.9%) for characterization and testing [31].

**2.2. Characterization.** Samples in powder form were characterized for their morphology, structure, and scintillating properties. Morphological and particle size analysis was carried out using Hitachi H7600T transmission electron microscope with 120 kV acceleration voltage. Structural characterization was carried out through X-ray diffraction (XRD) measurements using a Scintag XDS 4000 diffractometer equipped with a Cu K $\alpha$  source aiming at phase identification.

Scintillation response to two sources of ionizing radiation, namely, X-rays from Ag and the natural decay of <sup>241</sup>Am, was carried out using radioluminescence (RL) and differential pulse height distribution measurements, respectively. RL measurements used a 40 kV Bullet X-ray tube combined with a Ocean Optics USB-2000 miniature fiber optic spectrometer. The distance from the X-ray target to the sample was ~3 cm, and the X-ray tube was operated at 100  $\mu$ A. For each measurement, a crucible with 57 mm<sup>2</sup> area was filled with nanopowder such that each sample had the same area exposed to the X-rays. Three measurements were carried for each sample yielding a reproducibility of about 10%–15%. No correction for differential light scattering, possibly arising from the different grain size distribution and powder packing in the crucibles, was attempted. Differential pulse height distribution measurements used a Hidex Triathler scintillation counter with a Hamamatsu R850-photomultiplier tube and a 1  $\mu$ Ci <sup>241</sup>Am ( $E_{\alpha}$  = 5.5 MeV,  $E_{\gamma}$  = 60 keV) source. The Triathler was configured with logarithmic amplification to accentuate the difference in the differential pulse height spectra. In our measurements, the relative positions of the sample, detector and source were kept fixed, with the plated <sup>241</sup>Am source being suspended ~1 cm above power contained in a 3.7 mL borosilicate glass vial. The electronic noise background was determined by measuring an empty flask in identical conditions as the nanopowder sample.

### 3. Results and Discussion

The morphology of the nanoparticles, characterized by transmission electron microscopy (TEM), is shown in Figure 1. All the nanoparticles were found to have spheroidal shapes, and analysis of numerous images yielded average size and size distributions of each nanoscintillator. LaF<sub>3</sub> : Eu, CaF<sub>2</sub> : Eu, and BaF<sub>2</sub> : Ce nanoparticles were  $4.4 \pm 0.8$  nm (size  $\pm$  standard deviation),  $10 \pm 2$  nm, and  $18 \pm 3$  nm in size, respectively.

The structure of the nanoparticles was determined by XRD to be face-centered cubic for the alkali earth fluorides with space group Fm $\bar{3}$ m, in agreement with the International Centre for Diffraction Data powder diffraction files 35-0816 for CaF<sub>2</sub>, and 04-0452 for BaF<sub>2</sub>. The structure of LaF<sub>3</sub> : Eu nanoparticles was determined to be hexagonal with centrosymmetric space group P $\bar{3}$ c1, in agreement with powder diffraction file 32-0483 [36].

The photoluminescence of LaF<sub>3</sub> : Eu nanoparticles and the cathodoluminescence of submicrometric particles have been reported before [15, 30, 35, 37, 38], while to the best

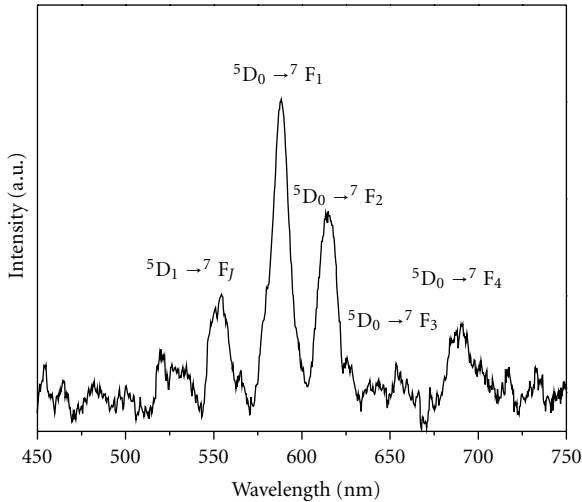


FIGURE 2: RL spectrum of  $\text{LaF}_3:\text{Eu}$  nanoscintillator.

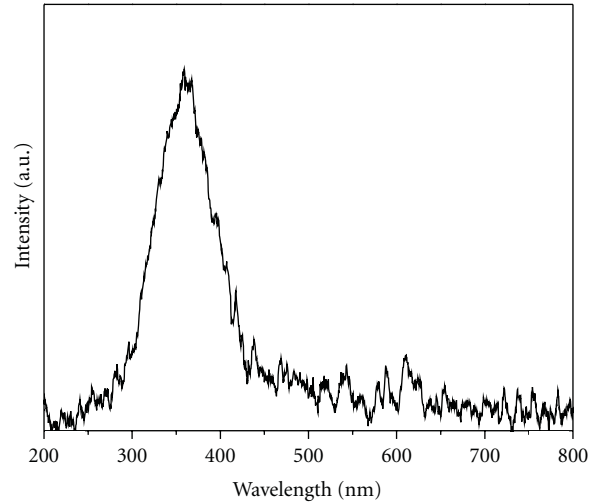


FIGURE 3: RL spectrum of  $\text{BaF}_2:\text{Ce}$  nanoscintillator.

of our knowledge, the scintillation response of  $\text{LaF}_3:\text{Eu}$  has not been investigated to date. Radioluminescence of these nanoscintillators under X-ray irradiation is presented in Figure 2, where a series of lines corresponding to the  ${}^5\text{D}_{0,1} \rightarrow {}^7\text{F}_j$  transitions can be seen. Emission at 588 nm dominates the spectrum, while the relatively high intensity of the hypersensitive transition  ${}^5\text{D}_0 \rightarrow {}^7\text{F}_2$  at 614 nm shows the existence of structural disorder that distort the inversion symmetry around the  $\text{Eu}^{3+}$  ions. Such a result is not surprising due to reduced dimensions of these nanoparticles and the consequent high fraction of atoms on the surface. It is well known that the loss of the three-dimensional crystalline periodicity of the atomic potential that exists inside a solid, and the lack of atoms to counter-balance and fully compensate chemical bonds and charge requirements result in structural modifications of the surface layer. The observation of intense emission due to electric dipole transitions of  $\text{Eu}^{3+}$  ions is ascribed to these modifications, similarly to the observations reported in [35].

Undoped  $\text{BaF}_2$  is known to luminesce due to cross luminescence and self-trapped exciton recombination, while the presence of Ce is known to eliminate these recombination mechanisms [see [39] and references therein]. Vissert et al. carried out a detailed investigation of the effects of Ce doping on the luminescence of this scintillator, and identified three distinct luminescent centers related to the Ce dopant, named centers *Ce1*, *Ce2*, and *Ce3*, with the dominance of a given center depending on the Ce concentration. For concentrations around 1 mol% and higher, photoluminescence emission was observed in the approximate range of 330–370 nm and ascribed to center *Ce2*. Those authors also determined the photon output under X-ray excitation of  $\text{BaF}_2:\text{Ce}$  for a wide range of Ce concentrations and based on their results the RL emission of a 3 mol% doped crystal is due to the *Ce2* center [39]. Figure 3 presents the RL spectrum of  $\text{BaF}_2:\text{Ce}$  nanoparticles investigated in this work under X-ray irradiation. The nanoparticles scintillate at 350 nm, and no sign of the self-trapped exciton radiative recombination at

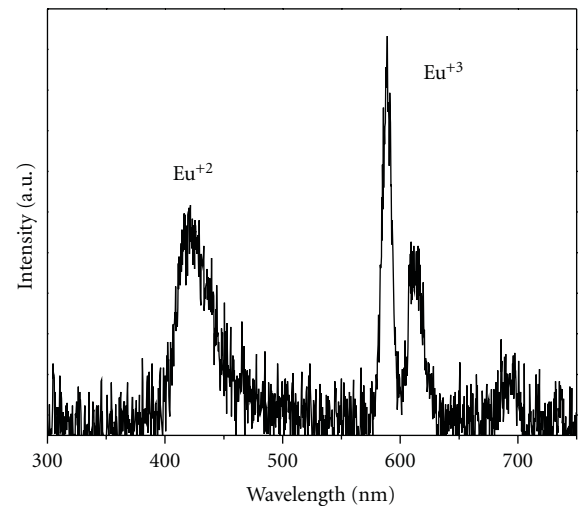


FIGURE 4: RL spectrum of  $\text{CaF}_2:\text{Eu}$  nanoscintillator.

around 300 nm was observed. Similar results were observed in 1 mol% Ce doped  $\text{BaF}_2$  ceramics and crystals [40, 41].

The photoluminescence response of  $\text{CaF}_2:\text{Eu}$  nanoparticles showed that emission is composed of electronic transitions from  $\text{Eu}^{2+}$  and  $\text{Eu}^{3+}$  ions. Similarly to the  $\text{LaF}_3:\text{Eu}$  nanoparticles, structural disorder manifested in terms of deviations from inversion symmetry around the  $\text{Eu}^{3+}$  ion made the hypersensitive transition  ${}^5\text{D}_0 \rightarrow {}^7\text{F}_2$  particularly intense [36]. Radioluminescence results are shown in Figure 4, where a broad band centered at 420 nm due to the emission of  $\text{Eu}^{2+}$ , and the emission lines in the 550–750 nm range due to the  ${}^5\text{D}_1 \rightarrow {}^7\text{F}_j$  transitions of  $\text{Eu}^{3+}$  can be observed. Similarly to  $\text{LaF}_3:\text{Eu}$ , the relatively intense emission of the  ${}^5\text{D}_1 \rightarrow {}^7\text{F}_2$  transition at 611 nm shows the existence of structural disorder that distort the inversion symmetry around the  $\text{Eu}^{3+}$  ions.

The scintillation response of  $\text{CaF}_2:\text{Eu}$  nanoparticles under  ${}^{241}\text{Am}$  irradiation determined by means of differential pulse height distribution measurements is presented in

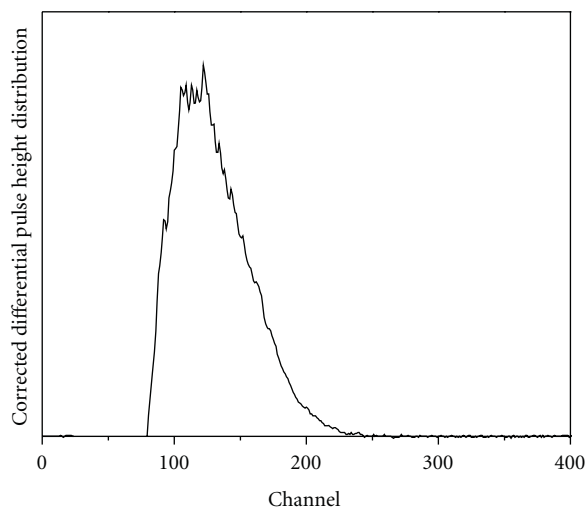


FIGURE 5: Corrected differential pulse height distribution measurement of  $\text{CaF}_2:\text{Eu}$  nanoscintillator.

Figure 5 after the subtraction of the electronic noise, where a photopeak centered around channel 120 can be observed. This signal is due the irradiation of 5.5 MeV alpha particles from the  $^{241}\text{Am}$  source, since shielding of the alpha particles resulted in no detectable net signal under the experimental conditions employed here. Under irradiation of X-rays and alpha particles, a great number of  $e-h$  pairs are formed. As discussed in the introduction, the migration of the  $e-h$  pairs through the scintillator is inherent to the scintillation mechanism and scintillation occurs when they recombine at the RE ions. The net scintillation intensity is determined by the competition between radiative recombination at the luminescence sites versus nonradiative recombination at quenching centers, particularly on the surface of the nanoparticles, and trapping of the carriers. Given the fact that the diffusion length of  $e-h$  pairs in the alkali halides is around 100 nm [42], and tens of nm in oxides and oxy-sulfides [43, 44], it is interesting to observe efficient scintillation when the dimensions of the nanoparticles are considerably smaller than the diffusion length, concomitant to a relatively high probability of nonradiative recombination on the surface of the nanoparticles. This result has relevant implications on the use of nanoparticles for radiation detection.

#### 4. Summary and Conclusions

The use of luminescent nanoparticles as scintillators is a new field, and in this work, a preliminary survey of the scintillation response of fluoride nanoscintillators  $\text{CaF}_2:\text{Eu}$ ,  $\text{BaF}_2:\text{Ce}$ , and  $\text{LaF}_3:\text{Eu}$  was carried out using both X-rays and  $^{241}\text{Am}$  sources. The unique aspect of scintillation in nanoparticles is related to the migration of the carriers through the nanoscintillator, and our results showed that even nanoparticles as small as  $\sim 4$  nm in size effectively scintillate under irradiation. This is an interesting result given that the diffusion length of  $e-h$  pairs in many scintillators

is determined to be in the range of tens to a 100 nm, and significant nonradiative recombination at the surface of the nanoparticles should be expected. These results also show that RE-doped fluoride nanoparticles can be used for radiation detection of a wide range of ionizing radiations, and that this topic is worth further consideration and deeper investigation.

#### Acknowledgments

The authors acknowledge the partial support of DTRA through Grant no. HDTRA1-08-1-0015 and DARPA through Grant no. N66001-04-1-8933.

#### References

- [1] S. E. Derenzo, W. W. Moses, J. L. Cahoon, R. C. C. Perera, and J. E. Litton, "Prospects for new inorganic scintillators," *IEEE Transactions on Nuclear Science*, vol. 37, no. 1, pp. 203–208, 1990.
- [2] G. Blasse, "Search for new inorganic scintillators," *IEEE Transactions on Nuclear Science*, vol. 38, no. 1, pp. 30–31, 1991.
- [3] M. Ishii and M. Kobayashi, "Single crystals for radiation detectors," *Progress in Crystal Growth and Characterization of Materials*, vol. 23, pp. 245–311, 1992.
- [4] G. Blasse, "Scintillator materials," *Chemistry of Materials*, vol. 6, no. 9, pp. 1465–1475, 1994.
- [5] G. Blasse, "Luminescent materials: is there still news?" *Journal of Alloys and Compounds*, vol. 225, no. 1-2, pp. 529–533, 1995.
- [6] S. E. Derenzo, M. J. Weber, E. Bourret-Courchesne, and M. K. Klintonberg, "The quest for the ideal inorganic scintillator," *Nuclear Instruments and Methods in Physics Research A*, vol. 505, no. 1-2, pp. 111–117, 2003.
- [7] B. D. Millbrath, A. J. Peurrung, M. Bliss, and W. J. Weber, "Radiation detector materials: an overview," *Journal of Materials Research*, vol. 23, no. 10, pp. 2561–2581, 2008.
- [8] H. Chander, "Development of nanophosphors—a review," *Materials Science and Engineering R: Reports*, vol. 49, no. 5, pp. 113–155, 2005.
- [9] C. Li and J. Lin, "Rare earth fluoride nano-/microcrystals: synthesis, surface modification and application," *Journal of Materials Chemistry*, vol. 20, no. 33, pp. 6831–6847, 2010.
- [10] C. Zhang, C. Li, C. Peng et al., "Facile and controllable synthesis of monodisperse  $\text{CaF}_2$  and  $\text{CaF}_2:\text{Ce}^{3+}/\text{Tb}^{3+}$  hollow spheres as efficient luminescent materials and smart drug carriers," *Chemistry*, vol. 16, no. 19, pp. 5672–5680, 2010.
- [11] C. Li, J. Yang, P. Yang, H. Lian, and J. Lin, "Hydrothermal synthesis of lanthanide fluorides  $\text{LnF}_3$  ( $\text{Ln} = \text{La to Lu}$ ) nano-/microcrystals with multiform structures and morphologies," *Chemistry of Materials*, vol. 20, no. 13, pp. 4317–4326, 2008.
- [12] Z. Quan, D. Yang, P. Yang et al., "Uniform colloidal alkaline earth metal fluoride nanocrystals: nonhydrolytic synthesis and luminescence properties," *Inorganic Chemistry*, vol. 47, no. 20, pp. 9509–9517, 2008.
- [13] C. Li, Z. Quan, J. Yang, P. Yang, and J. Lin, "Highly uniform and monodisperse  $\beta\text{-NaYF}_4:\text{Ln}^{3+}$  ( $\text{Ln} = \text{Eu, Tb, Yb/Er, and Yb/Tm}$ ) hexagonal microprism crystals: hydrothermal synthesis and luminescent properties," *Inorganic Chemistry*, vol. 46, no. 16, pp. 6329–6337, 2007.

- [14] Z. L. Wang, Z. W. Quan, P. Y. Jia et al., "A facile synthesis and photoluminescent properties of redispersible  $\text{CeF}_3$ ,  $\text{CeF}_3:\text{Tb}^{3+}$ , and  $\text{CeF}_3:\text{Tb}^{3+}/\text{LaF}_3$  (core/shell) nanoparticles," *Chemistry of Materials*, vol. 18, no. 8, pp. 2030–2037, 2006.
- [15] J. W. Stouwdam and F. C. J. M. van Veggel, "Improvement in the luminescence properties and processability of  $\text{LaF}_3/\text{Ln}$  and  $\text{LaPO}_4/\text{Ln}$  nanoparticles by surface modification," *Langmuir*, vol. 20, no. 26, pp. 11763–11771, 2004.
- [16] K. Kömpe, O. Lehmann, and M. Haase, "Spectroscopic distinction of surface and volume ions in cerium(III)- and terbium(III)-containing core and core/shell nanoparticles," *Chemistry of Materials*, vol. 18, no. 18, pp. 4442–4446, 2006.
- [17] D. W. Cooke, J.-K. Lee, B. L. Bennett et al., "Luminescent properties and reduced dimensional behavior of hydrothermally prepared  $\text{Y}_2\text{SiO}_5:\text{Ce}$  nanophosphors," *Applied Physics Letters*, vol. 88, no. 10, Article ID 103108, 3 pages, 2006.
- [18] R. E. Muenchausen, L. G. Jacobsohn, B. L. Bennett, E. A. McKigney, J. F. Smith, and D. W. Cooke, "A novel method for extracting oscillator strength of select rare-earth ion optical transitions in nanostructured dielectric materials," *Solid State Communications*, vol. 139, no. 10, pp. 497–500, 2006.
- [19] W. Chen, G. Huang, H. Lu, D. E. McCready, A. G. Joly, and J.-O. Bovin, "Utilizing nanofabrication to construct strong, luminescent materials," *Nanotechnology*, vol. 17, no. 10, pp. 2595–2601, 2006.
- [20] I. H. Campbell and B. K. Crone, "Quantum-dot/organic semiconductor composites for radiation detection," *Advanced Materials*, vol. 18, no. 1, pp. 77–79, 2006.
- [21] S. E. Létant and T.-F. Wang, "Semiconductor quantum dot scintillation under  $\gamma$ -ray irradiation," *Nano Letters*, vol. 6, no. 12, pp. 2877–2880, 2006.
- [22] E. A. McKigney, R. E. Del Sesto, L. G. Jacobsohn et al., "Nanocomposite scintillators for radiation detection and nuclear spectroscopy," *Nuclear Instruments and Methods in Physics Research A*, vol. 579, no. 1, pp. 15–18, 2007.
- [23] J. A. Johnson, S. Schweizer, B. Henke et al., "Eu-activated fluorochlorozirconate glass-ceramic scintillators," *Journal of Applied Physics*, vol. 100, no. 3, Article ID 034701, 5 pages, 2006.
- [24] Y. S. Zhao, Z. Yu, A. Douraghy, A. F. Chatziioannou, Y. Mo, and Q. Pei, "A facile route to bulk high-Z polymer composites for gamma ray scintillation," *Chemical Communications*, no. 45, pp. 6008–6010, 2008.
- [25] E. A. McKigney, R. E. Muenchausen, D. W. Cooke et al., "LaFM<sub>3</sub>:Ce nanocomposite scintillator for gamma-ray detection," in *Hard X-Ray and Gamma-Ray Detector Physics IX*, vol. 6706 of *Proceedings of SPIE*, San Diego, Calif, USA, August 2007.
- [26] A. Lempicki, A. J. Wojtowicz, and E. Berman, "Fundamental limits of scintillator performance," *Nuclear Instruments and Methods in Physics Research A*, vol. 333, no. 2-3, pp. 304–311, 1993.
- [27] P. A. Rodnyi, *Physical Processes in Inorganic Scintillators*, CRC Press, Boca Raton, Fla, USA, 1997.
- [28] W. W. Moses and S. E. Derenzo, "The scintillation properties of cerium-doped lanthanum fluoride," *Nuclear Instruments and Methods in Physics Research A*, vol. 299, no. 1–3, pp. 51–56, 1990.
- [29] P. Dorenbos, J. T. M. de Haas, and C. W. E. van Eijk, "The intensity of the 173 nm emission of  $\text{LaF}_3:\text{Nd}^{3+}$  scintillation crystals," *Journal of Luminescence*, vol. 69, no. 4, pp. 229–233, 1996.
- [30] J. W. Stouwdam, G. A. Hebbink, J. Huskens, and F. C. J. M. van Veggel, "Lanthanide-doped nanoparticles with excellent luminescent properties in organic media," *Chemistry of Materials*, vol. 15, no. 24, pp. 4604–4616, 2003.
- [31] J. R. DiMaio, B. Kokuoz, T. L. James, and J. Ballato, "Structural determination of light-emitting inorganic nanoparticles with complex core/shell architectures," *Advanced Materials*, vol. 19, no. 20, pp. 3266–3270, 2007.
- [32] J. R. DiMaio, C. Sabatier, B. Kokuoz, and J. Ballato, "Controlling energy transfer between multiple dopants within a single nanoparticle," *Proceedings of the National Academy of Sciences of the United States of America*, vol. 105, no. 6, pp. 1809–1813, 2008.
- [33] J. R. DiMaio, B. Kokuoz, and J. Ballato, "White light emissions through down-conversion of rare-earth doped  $\text{LaF}_3$  nanoparticles," *Optics Express*, vol. 14, no. 23, pp. 11412–11417, 2006.
- [34] J. DiMaio, B. Kokuoz, T. L. James, T. Harkey, D. Monofsky, and J. Ballato, "Photoluminescent characterization of atomic diffusion in core-shell nanoparticles," *Optics Express*, vol. 16, no. 16, pp. 11769–11775, 2008.
- [35] V. Sudarsan, F. C. J. M. van Veggel, R. A. Herring, and M. Raudsepp, "Surface  $\text{Eu}^{3+}$  ions are different than "bulk"  $\text{Eu}^{3+}$  ions in crystalline doped  $\text{LaF}_3$  nanoparticles," *Journal of Materials Chemistry*, vol. 15, no. 13, pp. 1332–1342, 2005.
- [36] L. G. Jacobsohn, C. J. Kucera, T. L. James et al., "Preparation and characterization of rare earth doped fluoride nanoparticles," *Materials*, vol. 3, pp. 2053–2068, 2010.
- [37] D. Pi, F. Wang, X. Fan, M. Wang, and Y. Zhang, "Luminescence behavior of  $\text{Eu}^{3+}$  doped  $\text{LaF}_3$  nanoparticles," *Spectrochimica Acta A*, vol. 61, no. 11-12, pp. 2455–2459, 2005.
- [38] Z.-L. Wang, H. L. W. Chan, H.-L. Li, and J. H. Hao, "Highly efficient low-voltage cathodoluminescence of  $\text{LaF}_3:\text{Ln}^{3+}$  ( $\text{Ln}=\text{Eu}^{3+}, \text{Ce}^{3+}, \text{Tb}^{3+}$ ) spherical particles," *Applied Physics Letters*, vol. 93, no. 14, Article ID 141106, 3 pages, 2008.
- [39] R. Visser, P. Dorenbos, C. W. E. van Eijk, A. Meijerink, G. Blasse, and H. W. den Hartog, "Energy transfer processes involving different luminescence centres in  $\text{BaF}_2:\text{Ce}$ ," *Journal of Physics: Condensed Matter*, vol. 5, no. 11, pp. 1659–1680, 1993.
- [40] S. Kh. Batygov, L. S. Bolyasnikova, V. A. Demidenko et al., " $\text{BaF}_2:\text{Ce}^{3+}$  scintillation ceramics," *Doklady Physics*, vol. 53, no. 9, pp. 485–488, 2008.
- [41] R. Visser, P. Dorenbos, C. W. E. van Eijk, R. W. Hollander, and P. Schotanus, "Scintillation properties of  $\text{Ce}^{3+}$  doped  $\text{BaF}_2$  crystals," *IEEE Transactions on Nuclear Science*, vol. 38, no. 2, pp. 178–183, 1991.
- [42] K. Schwartz, *Atomic Physics Methods in Modern Research*, Springer, Berlin, Germany, 1997.
- [43] E. L. Benitez, D. E. Husk, S. E. Schnatterly, and C. Tarrío, "A surface recombination model applied to large features in inorganic phosphor efficiency measurements in the soft X-ray region," *Journal of Applied Physics*, vol. 70, no. 6, pp. 3256–3260, 1991.
- [44] V. B. Mikhailik, H. Kraus, G. Miller, M. S. Mykhaylyk, and D. Wahl, "Luminescence of  $\text{CaWO}_4$ ,  $\text{CaMoO}_4$ , and  $\text{ZnWO}_4$  scintillating crystals under different excitations," *Journal of Applied Physics*, vol. 97, no. 8, Article ID 083523, 8 pages, 2005.

## Research Article

# Electrodeposition of Nanometer-Sized Ferric Oxide Materials in Colloidal Templates for Conversion of Light to Chemical Energy

James M. Gardner, Su Kim, Peter C. Searson, and Gerald J. Meyer

Departments of Chemistry and Materials Science and Engineering, Johns Hopkins University,  
3400 North Charles Street, Baltimore, MD 21218, USA

Correspondence should be addressed to Gerald J. Meyer, meyer@jhu.edu

Received 2 June 2010; Accepted 23 July 2010

Academic Editor: William W. Yu

Copyright © 2011 James M. Gardner et al. This is an open access article distributed under the Creative Commons Attribution License, which permits unrestricted use, distribution, and reproduction in any medium, provided the original work is properly cited.

Colloidal crystal templates were prepared by gravitational sedimentation of 0.5 micron polystyrene particles onto fluorine-doped tin oxide (FTO) electrodes. Scanning electron microscopy (SEM) shows that the particles were close packed and examination of successive layers indicated a predominantly face-centered-cubic (fcc) crystal structure where the direction normal to the substrate surface corresponds to the (111) direction. Oxidation of aqueous ferrous solutions resulted in the electrodeposition of ferric oxide into the templates. Removal of the colloidal templates yielded ordered macroporous electrodes (OMEs) that were the inverse structure of the colloidal templates. Current integration during electrodeposition and cross-sectional SEM images revealed that the OMEs were about 2  $\mu\text{m}$  thick. Comparative X-ray diffraction and infrared studies of the OMEs did not match a known phase of ferric oxide but suggested a mixture of goethite and hematite. The spectroscopic properties of the OMEs were insensitive to heat treatments at 300°C. The OMEs were utilized for photoassisted electrochemical oxidation. A sustained photocurrent was observed from visible light in aqueous photoelectrochemical cells. Analysis of photocurrent action spectra revealed an indirect band gap of 1.85 eV. Addition of formate to the aqueous electrolytes resulted in an approximate doubling of the photocurrent.

## 1. Introduction

There is an urgent need to find inexpensive and sustainable inorganic materials for converting solar photons into chemical energy. Splitting water with metal oxides and sunlight is a very appealing idea that has caught the attention of scientists for decades [1]. One approach has been to utilize a metal oxide photoelectrode that can photo-oxidize water and provide electrons to a platinum electrode for proton reduction [2]. Shown in Figure 1 is a simplified version of such a cell. To aid in hydrogen gas collection and to prevent  $\text{O}_2$  reduction at the platinum electrode the two electrodes can be separated by a salt bridge or porous membrane.

Fujishima and Honda first reported sustained water splitting through this approach with  $\text{TiO}_2$  [2]. Unfortunately, the unfavorable band gap of rutile  $\text{TiO}_2$  (3.1 eV) resulted in a very low solar conversion efficiency (<1%). Later, other wide band gap metal oxides were shown to work in a

similar fashion [3–5]. Hematite,  $\alpha\text{-Fe}_2\text{O}_3$ , has a much more favorable 2.2 eV band gap for solar harvesting and therefore absorbs about 40% of the air mass 1.5 solar spectrum [6–8]. Previous researchers found that the energetic position of the valence band edge in hematite is appropriate for water oxidation [9–21]. In fact, iron oxides are amongst the smallest band gap semiconductors that are stable toward oxygen evolution and are certainly the least expensive of them. However, overall charge collection efficiencies from hematite in photoelectrochemical cells has been disappointingly low [6].

Much of the early work on hematite photoelectrochemistry was done in the 1970–1980s; however, recently there have been a few promising reports [22–34]. Poor solar charge collection efficiency was attributed to low minority (hole) diffusion lengths [30]. In other words, photogenerated valence band holes do not efficiently reach the hematite-water interface and primarily recombine in the bulk. In

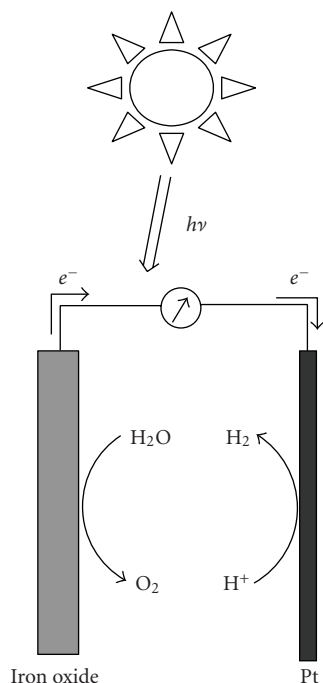


FIGURE 1: Photoelectrosynthetic cell for splitting water into  $\text{H}_2$  and  $\text{O}_2$ . The two electrodes can be separated by a physical barrier to aid in gas collection.

principle, this problem can be circumvented with iron oxide electrodes that have architectures tailored towards high surface area and minimal internal volume such that all photogenerated holes reach the solution interface.

New processing techniques that have been developed in the last twenty years may enable the production of semiconductor materials with architectures ideal for charge capture at a solution interface. Colloidal templates offer interesting possibilities in this regard as they could allow ferric oxide structures to be controlled with considerable precision [35, 36]. The average distance photogenerated holes would need to travel to reach the interface can be systematically tuned by varying the size of the colloidal particles used in the template. High surface area, porous materials that can be fine tuned to optimize hole capture at the aqueous interface are expected to be ideal for light harvesting and oxygen evolution in photoelectrosynthetic cells. Furthermore, hole transfer and/or oxidation catalysts, such as  $\text{RuO}_2$  and  $\text{IrO}_2$  could be included at desired locations within the structure to decrease oxidation overpotentials and improve kinetics [1]. Recently we have initiated experiments to establish whether colloidal templates could be used to fabricate ferric oxide in ordered macroporous thin films. Here we report that this can indeed be accomplished and report the synthesis of ordered ferric oxide electrodes. Photoelectrochemical studies with the templated ferric oxide materials reveal small sustained photocurrents that may be consistent with water oxidation, but the present architecture is not suitable for practical application in photoassisted water oxidation.

## 2. Experimental

**2.1. Materials.**  $\text{FeCl}_2 \cdot 4\text{H}_2\text{O}$  (Aldrich, 99%), L-ascorbic acid (Aldrich, >99%), NaCl (Mallinckrodt Chemicals, >99.0%), 1-methylimidazole (Aldrich, 99%), polystyrene (PS) microbeads (Polysciences,  $0.5 \mu\text{m}$  diameter), ethanol (Aaper Alcohol, anhydrous 200 Proof), NaOH (Fisher, 97.5%), NaCHOO (Aldrich, 99+%), and  $\text{Na}_2\text{SO}_4$  (EMD, 99.0+%) were used without further purification. Electrolytes for electrodepositions used HPLC grade water; all other solutions used deionized water. Conductive fluorine doped tin oxide glass, FTO (Hartford Glass,  $\text{SnO}_2:\text{F}$ ) and Au evaporated Si wafers were cleaned with water and ethanol prior to electrodeposition.

**2.2. Templating.** The assembly of the colloidal crystalline template followed literature preparations, described briefly as follows [37, 38]. Sheets of FTO or wafers of gold evaporated on silicon were cut to  $4.0 \text{ cm} \times 2.5 \text{ cm}$  dimensions and uses as substrates. They were first sonicated in glass vials with absolute ethanol, rinsed with deionized water, and dried under compressed air. Viton and Teflon o-rings were also rinsed with deionized water and dried under compressed air. The Viton o-ring was placed on the conductive side of the substrate. The Teflon o-ring was placed on top of the Viton o-ring. Both rings were clamped onto the substrate using binder clips. The PS particles were diluted by 1:8 v:v in deionized water and stored at  $4^\circ\text{C}$ . Prior to assembly the suspension was sonicated for two minutes. A  $170 \mu\text{L}$  aliquot of the diluted PS particle suspension was carefully pipetted onto the substrate and was placed in a humidity chamber at room temperature and 85% humidity. After six days the clamps and o-rings were removed leaving an ordered colloidal crystal template. The substrate was cut to the width of the template yielding a templated electrode  $1.0 \text{ cm} \times 4.0 \text{ cm}$ , which was stored in a humidity chamber until use.

**2.3. Electrodeposition.** Ferric oxide was electrodeposited into the colloidal crystalline templates. Electrodeposition was carried out in an Ar purged, septa sealed, three electrode cell with the colloidal crystal template as the working electrode, FTO as the counter electrode, and Ag/AgCl (KCl saturated) as a reference electrode. All potentials are reported with respect to the Ag/AgCl reference ( $U_{\text{eq}} = +0.110 \text{ V SHE}$ ). The electrodeposition solution contained  $50 \mu\text{L}$  of 1 M  $\text{FeCl}_2$  solution,  $150 \mu\text{g}$  of L-ascorbic acid, and 5 mL of a 0.4 M NaCl and 0.1 M 1-methylimidazole electrolytic solution [39]. Ferric oxide was deposited at  $-0.30 \text{ V}$  under a slow purge of nitrogen in the head space until  $-0.30 \text{ C/cm}^2$  were passed. The film was then immersed in toluene for ten minutes. The electrodeposited ferric oxide adhered to the FTO as an ordered macroporous electrode (OME). The OME were removed from the toluene and stored in sealed glass vials until use. Preparation of the template and electrodeposition onto Au evaporated Si wafers followed the same methods used for OMEs on FTO.

**2.4. Characterization.** Environmental scanning electron microscope (ESEM) images were taken on an FEI Quanta 200 Environmental SEM at a water vapor pressure of 1.8 kPa. Cross sectional SEM images of colloidal crystalline templates and ferric oxide OME deposited on Au that had been evaporated onto Si wafers were acquired with a JEOL 6700 F Scanning Electron Microscope. The UV/Visible electronic spectra were acquired on a Cary 500. Fourier transform infrared (FTIR) spectra were acquired on a Thermo Nicolet Nexus 670 FTIR with a Smart Golden Gate ATR attachment. X-ray diffractograms (XRD) were acquired on a Philips X'Pert Pro X-ray Diffraction System using Cu-K $\alpha$  radiation. For XRD measurements, the ferric oxide OME was removed from the FTO substrate with a razor blade. All other characterization techniques were acquired on intact ferric oxide OME.

**2.5. Photoelectrochemistry.** Photocurrent action spectra were recorded with a Keithley 5000 electrometer under short circuit conditions in a custom-built liquid junction Teflon cell with a Pt mesh counter electrode. The electrolyte was 0.1 M NaCl at pH 9.5 adjusted with NaOH. The light source was a 100 W Xe arc lamp (Spectra Physics) attached to a monochromator (Oriel Instruments Corner Stone 1/4 m). Incident irradiances were measured with a UDT high sensitivity silicon diode optometer.

Photocurrents were also measured in a three-electrode arrangement with a BAS CV50-W potentiostat. The working electrode was a ferric oxide OME with a Pt mesh counter electrode and a Ag/AgCl reference electrode. The aqueous electrolytes used were either 0.5 M Na<sub>2</sub>SO<sub>4</sub> or 0.1 M NaCHOO/0.5 M Na<sub>2</sub>SO<sub>4</sub>. In a typical experiment, the applied bias was ramped from 0.0 V to +1.3 V at a scan rate of 2 mV/s. This was then repeated with the ferric oxide OME illuminated with  $20 \pm 1$  mW/cm<sup>2</sup> of 413.1 nm light from a Continuum Kr ion laser. The photocurrents are reported as the total current measured under illumination minus the dark current.

### 3. Results

The colloidal crystal templates were prepared by gravitational sedimentation of polystyrene (PS) particles onto fluorine-doped tin oxide (FTO) electrodes. The quality of the crystal was dependent on the particle concentration, temperature, and relative humidity. The conditions used ensured controlled evaporation of the solvent and sufficiently slow sedimentation to result in well-ordered crystals. Faster evaporation rates typically resulted in defects such as cracks or voids that led to large volumes of solid in the replica after deposition. Figure 2 shows SEM images of a typical 4  $\mu$ m thick colloidal crystal template formed by this technique. The image shows that the particles were close packed, and examination of successive layers confirmed a predominantly face-centered-cubic (fcc) crystal structure where the direction normal to the substrate surface corresponds to the (111) direction.

Ordered macroporous electrodes (OMEs) of ferric oxide were formed by electrodeposition into the templates at

−0.30 V (Ag/AgCl). The deposition charge of 0.30 C/cm<sup>2</sup> corresponded to an OME thickness of 2  $\mu$ m, in reasonably good agreement with values obtained from cross-sectional SEM images ( $2.8 \pm 0.1$   $\mu$ m). The PS particles were removed by immersion in toluene that left an orange-red OME on the FTO substrate.

A representative plan view SEM image of a ferric oxide OME is shown in Figure 3(a). The top surface revealed a close packed mesostructure that was a replica of the colloidal crystal template. The domain size was 15–50  $\mu$ m and the OMEs were free from cracks or voids. The surface roughness factor, or rugosity, of a 2.8  $\mu$ m thick OME was about 25 corresponding to about 6.5 layers of template as seen in the cross-sectional SEM, Figure 3(b).

Attenuated total reflection Fourier transform infrared, ATR-FTIR, spectroscopic characterization of the OMEs were performed, Figure 4. The broad O-H stretch at 3200 cm<sup>−1</sup> and overtone at 1600 cm<sup>−1</sup> are diagnostic of adsorbed water [41]. The intensity of these bands decreased after heating the OME at 300°C for 30 minutes. The heat treatment did not significantly change the FTIR spectra of other regions of the spectra.

X-ray diffraction (XRD) analysis of the electrodeposited ferric oxide showed weak intensity and broad angular distribution of the diffraction peaks, Figure 5. Superimposed on this data are the literature values for the diffraction peaks of goethite and hematite [40, 42].

Shown in Figure 6(a) is the transmittance spectrum of a ferric oxide OME. The transmittance is near zero in the ultraviolet region and increased to near unity in the near-IR region. At longer wavelengths some of the transmission loss can be attributed to light scattering by the film.

The photocurrent efficiency of the ferric oxide OMEs was evaluated in two- and three-electrode arrangements in aqueous electrolytes at pH 9.5. The incident photon-to-current efficiencies (IPCEs) were calculated with

$$\text{IPCE} = \frac{[1240 \text{ eV nm}][\text{photocurrent density } (\mu\text{A cm}^{-2})]}{[\text{wavelength (nm)}][\text{irradiance (mW cm}^{-2})]} \quad (1)$$

Here the photocurrents were measured on OMEs of known area with a potentiostat or an electrometer. The irradiance was quantified with a calibrated silicon photodiode in the same arrangement.

Shown in Figure 6(a) is the IPCE recorded as a function of the excitation wavelength, a photocurrent action spectrum, measured under short circuit conditions. The maximum observed IPCE was  $0.7 \pm 0.1\%$  at 370 nm. This value is likely an underestimation of the true photocurrent yield, because no corrections were made for light absorption and scattering by the FTO substrate. The IPCE tailed into the visible region with no measurable photocurrent response at wavelengths longer than 600 nm.

The gradual increase in the photocurrent magnitude with increasing photon energy is typical of indirect semiconductors. For an indirect band gap semiconductor:

$$\text{IPCE} \cdot h\nu = A(h\nu - E_g)^2, \quad (2)$$

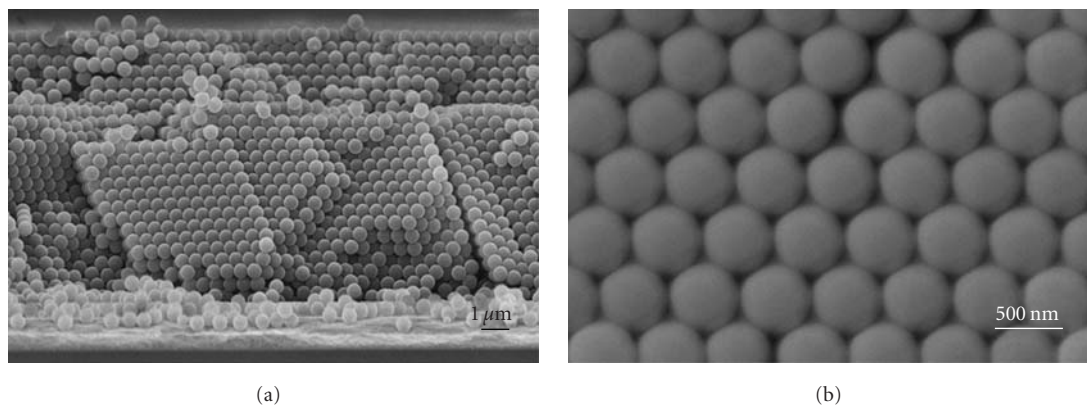


FIGURE 2: (a) Cross section and (b) plan view SEM image of a colloidal crystal template formed from 500 nm polystyrene (PS) particles.

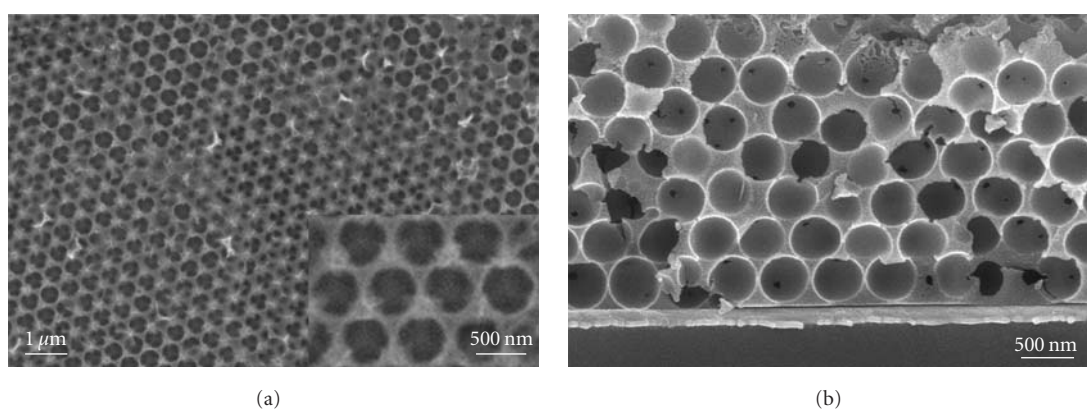


FIGURE 3: (a) A plan view ESEM image of an electrodeposited ferric oxide OME surface fabricated by deposition into a colloidal crystal assembled from 0.5  $\mu\text{m}$  diameter polystyrene particles. Inset: OME at higher magnification. (b) An SEM image of a cross section of a ferric oxide OME.

where  $h\nu$  is the excitation energy,  $A$  is a constant, and  $E_g$  is the band gap [3, 43]. Figure 6(b) shows a plot of  $[\text{IPCE} \cdot h\nu]^{1/2}$  versus  $h\nu$  illustrating linear behavior over a wide range of photon energies. The band gap was obtained from extrapolation of the linear region. For a large number of samples the band gap was determined to be  $E_g = 1.85 \pm 0.05$  eV.

Shown in Figure 7 are current-voltage curves for the OMEs in the dark and under illumination. Data are shown in the presence and absence of formate ion. The difference between the current collected in the dark and under illumination was the photocurrent. The photocurrents in the presence and absence of formate were converted to IPCEs to correct for differences in electrode area and light intensity. The observed IPCE was nearly twice as large in the presence of formate as in its absence for all potentials where measurable photocurrents were observed.

#### 4. Discussion

The electrodeposition of ferric oxides into colloidal crystal templates has been successfully achieved for the first time.

Removal of the colloidal templates resulted in ordered macroporous electrodes (OMEs) that were utilized for photoassisted electrochemical oxidation. Our results suggest a possible new direction toward the realization of efficient charge capture from excitation of iron oxides with solar photons.

Environmental scanning electron microscopy revealed ferric oxide OME materials with architectures that would be expected based on the inverse structure of the colloidal templates. Infrared studies and X-ray diffraction data did not clearly match a known phase of ferric oxide [39, 40, 42]. The diffraction pattern showed peaks that were consistent with the major diffraction lines for a mixture of goethite and hematite, which represent the two most common polymorphs of ferric oxide [40, 44]. Very minor spectroscopic changes were observed after heat treatments at 300°C, conditions where crystalline ferric oxides, such as  $\alpha\text{-FeO(OH)}$ ,  $\beta\text{-FeO(OH)}$ , and  $\gamma\text{-FeO(OH)}$ , and ferrihydrite, are known to be converted to the more thermodynamically stable hematite [40]. The stability of the ferric oxide OMEs to elevated temperature is surprising and could be exploited for additional processing steps such as the deposition of oxygen evolution catalysts.

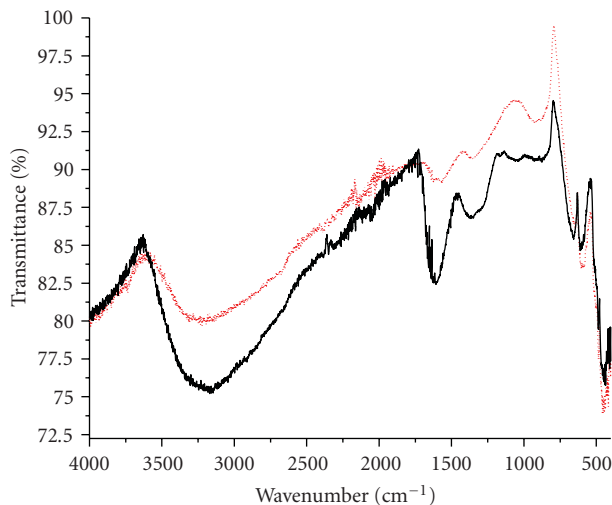


FIGURE 4: ATR-FTIR spectra of an electrodeposited ferric oxide OME like that in Figure 2 before (solid) and after (dotted) annealing at 300°C.

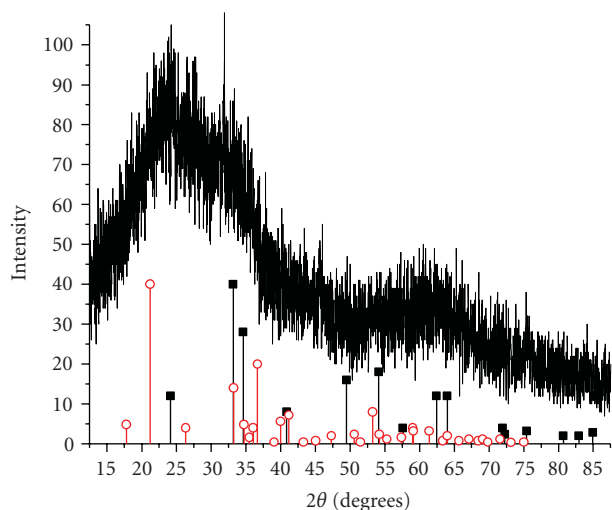


FIGURE 5: X-ray diffraction pattern of an electrodeposited ferric oxide OME. Also shown for comparison are the peaks for goethite (open circles) and hematite (closed squares) crystals using Cu-K $\alpha$  radiation [40].

When utilized in alkaline aqueous photoelectrochemical cells the ferric oxide OMEs yielded a small sustained photocurrent. The direction of the current was consistent with an oxidation reaction at the illuminated OME and n-type behavior [8]. Under short-circuit conditions the maximum incident photon-to-current (IPCE) efficiency was  $0.7 \pm 0.1\%$ . Due to low photocurrent densities, no attempts were made to quantify if the photocurrent was from the formation of oxygen. Photocurrent action spectra revealed a maximum at about 370 nm that tailed into the visible region. A photocurrent was measured with green light and wavelengths  $>500$  nm. Analysis of the photocurrent action spectra revealed an indirect band gap of 1.85 eV. This is significantly smaller than that measured for other

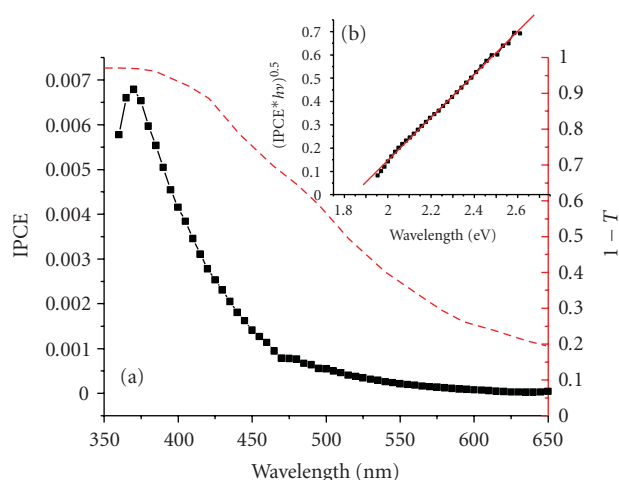


FIGURE 6: (a) A comparison of the short circuit incident photon-to-current efficiency (IPCE, squares) of a ferric oxide OME in 0.1 M NaCl at pH 9.5. Also shown is the transmittance spectrum (1-T, dashes) of the same material in air. (b) Band gap analysis of the IPCE.

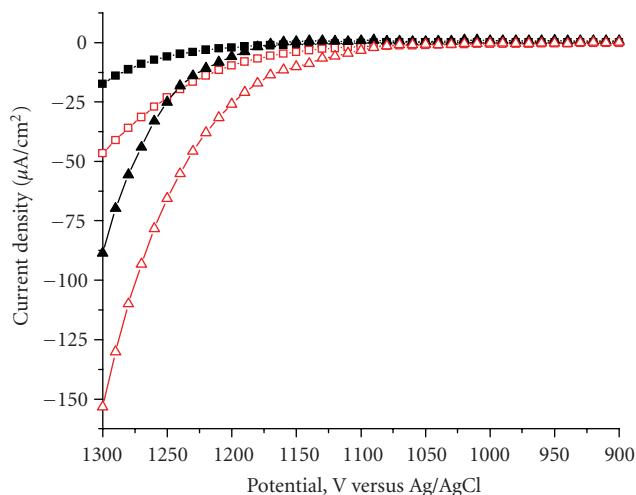


FIGURE 7: Current-voltage curves of electrodeposited ferric oxide OMEs in 0.5 M Na<sub>2</sub>SO<sub>4</sub> (squares) and 0.5 M Na<sub>2</sub>SO<sub>4</sub> with 0.1 M NaCHOO (triangles). The data were measured in the dark (closed) and under illumination (open) with 20 mW/cm<sup>2</sup> of 413 nm light excitation.

ferric oxides, Table 1, and is nearly ideal for water splitting applications [40, 44]. The comparatively small band gap allows for more efficient solar photon harvesting by the OME than by other ferric oxide phases.

In a 3-electrode photoelectrochemical cell, a gradual increase in the photocurrent was observed as the applied potential was increased. The addition of formate to the electrolyte resulted in an approximate doubling of the magnitude of the photocurrent. It is known that the one electron oxidation of formate produces a highly energetic radical that can inject electrons into the conduction band of some semiconductors, effectively doubling the current [45, 46]. Kennedy and Frese have previously suggested that

TABLE 1: Band Gaps of Common Ferric Oxides.

Ferric Oxide	$E_g$ (eV)	References
Hematite	2.20	[40, 44]
Goethite	2.10	[40, 44]
Akaganeite	2.12	[40, 44]
Lepidocrocite	2.06	[40, 44]
Ferric Oxide OME	1.85	here

current doubling occurs at illuminated hematite electrodes [15] and these results indicate that it also present with ferric oxide OMEs. At potentials greater than +1.2 V versus Ag/AgCl a dark oxidation current increased dramatically so that such positive excursions were avoided.

Small photocurrents observed at hematite single crystal and thin film electrodes have previously been attributed to short minority carrier (hole) diffusion lengths [6]. In previous work, ordered arrays of hematite nanorods were employed to minimize the distance holes that travel to reach the aqueous interface. Indeed, an increased photocurrent efficiency was observed [30, 47]. In principle, a benefit of ordered nanorod arrays over the OMEs studies here is the direct path for electron transport to the current collector that minimizes transit time by reducing lateral electron transport. On the other hand, high aspect ratio nanorod or nanowire arrays tend to be fragile with no lateral connectivity to provide the structural support present in the interconnected porous architecture of OMEs.

The largest solid features in the ferric oxide OME reported here come from the tetrahedral and octahedral sites in the colloidal crystal template [38]. The tetrahedral sites are formed from four spheres where the centers of the spheres form a tetrahedron. Equivalently, the tetrahedral site results from a sphere that occupies a threefold hollow site on a close packed plane. The octahedral sites are formed from six spheres and correspond to the unoccupied threefold hollow sites in the close-packed planes. For the OMEs fabricated here with 500 nm particles as templates, the diameters of the large solid regions, corresponding to the largest spheres that can fit into the tetrahedral and octahedral sites. These are 113 nm and 207 nm, respectively [38]. Thus the longest distances for carrier diffusion in these structures are 57 nm and 104 nm. Kennedy and Frese reported hole diffusion lengths of 2–4 nm [15], while Dare-Edwards et al. found them to be somewhat larger, 20 nm [9]. This photoelectrochemical data is consistent, at least qualitatively, with the short lifetimes of electron-hole pairs photogenerated in colloidal hematite solutions [48].

If the hole diffusion lengths reported for hematite are relevant to the ferric oxide OMEs, a significant fraction of holes would not reach the aqueous interface to form oxygen-oxygen bonds. This likely explains the low photocurrent efficiency observed. In future work could be rigorously tested with the methodology developed here but with smaller beads as templates. We note that 20 nm beads are commercially available and are predicted to yield ferric oxide OMEs with solid features only 2–4 nm in radius. This is very close to the

hole diffusion length estimated for hematite and would be expected to increase the solar conversion efficiency for water splitting.

## 5. Conclusion

The electrodeposition of ferric oxides into colloidal crystal templates was successfully achieved. The resultant ordered macroporous electrodes were about 2 microns thick with the inverse structure of the colloidal templates. Spectroscopic characterization did not match a known phase of ferric oxide but suggested a mixture of goethite and hematite. The photocurrent action spectra in the visible region revealed a more favorable band gap (1.85 eV) than known polymorphs of ferric oxide. However, the photocurrents were disappointingly small, even with a substantial positive applied potential. Holes that were photogenerated in the centers of octahedral and tetrahedral sites within these ordered macroscopic electrodes must traverse hundreds of nanometers to reach the aqueous interface. Charge recombination likely limits the hole diffusion length and therefore represents a significant loss mechanism in the solar energy conversion efficiency. While the efficiency toward practical water splitting was disappointing for these specific ferric oxide mesoporous electrodes, the ability to synthesize finely tuned architectures on the nanometer length scale provides exciting new opportunities for future energy applications.

## Acknowledgments

This work was supported by the National Science Foundation and the Johns Hopkins MRSEC.

## References

- [1] A. J. Bard and M. A. Fox, "Artificial photosynthesis: solar splitting of water to hydrogen and oxygen," *Accounts of Chemical Research*, vol. 28, no. 3, pp. 141–145, 1995.
- [2] A. Fujishima and K. Honda, "Electrochemical photolysis of water at a semiconductor electrode," *Nature*, vol. 238, no. 5358, pp. 37–38, 1972.
- [3] M. A. Butler, "Photoelectrolysis and physical properties of the semiconducting electrode  $\text{WO}_2$ ," *Journal of Applied Physics*, vol. 48, no. 5, pp. 1914–1920, 1977.
- [4] G. Hodes, D. Cahen, and J. Manassen, "Tungsten trioxide as a photoanode for a photoelectrochemical cell (PEC)," *Nature*, vol. 260, no. 5549, pp. 312–313, 1976.
- [5] M. S. Wrighton, A. B. Ellis, P. T. Wolczanski, D. L. Morse, H. B. Abrahamson, and D. S. Ginley, "Strontium titanate photoelectrodes. Efficient photoassisted electrolysis of water at zero applied potential," *Journal of the American Chemical Society*, vol. 98, no. 10, pp. 2774–2779, 1976.
- [6] M. Anderman and J. H. Kennedy, "Semiconductor electrodes: IRON OXIDE ( $\text{Fe}_2\text{O}_3$ )," in *Studies in Physical and Theoretical Chemistry*, H. O. Finklea, Ed., vol. 55, Elsevier, Amsterdam, The Netherlands, 1988.
- [7] NREL Reference Solar Spectral Irradiance: Air Mass 1.5, <http://rredc.nrel.gov/solar/spectra/am1.5/>.
- [8] Y. V. Pleskov and Y. Y. Gurevich, *Semiconductor Photoelectrochemistry*, Consultants Bureau, New York, NY, USA, 1986.

- [9] M. P. Dare-Edwards, J. B. Goodenough, A. Hamnett, and P. R. Trevellick, "Electrochemistry and photoelectrochemistry of iron(III) oxide," *Journal of the Chemical Society, Faraday Transactions 1*, vol. 79, no. 9, pp. 2027–2041, 1983.
- [10] K. L. Hardee and A. J. Bard, "Semiconductor electrodes. V. The application of chemically vapor deposited iron oxide films to photosensitized electrolysis," *Journal of the Electrochemical Society*, vol. 123, no. 7, pp. 1024–1026, 1976.
- [11] K. L. Hardee and A. J. Bard, "Semiconductor electrodes. X. Photoelectrochemical behavior Of several polycrystalline metal oxide electrodes in aqueous solutions," *Journal of the Electrochemical Society*, vol. 124, no. 2, pp. 215–224, 1977.
- [12] K. Itoh and J. O. Bockris, "Thin film photoelectrochemistry: iron oxide," *Journal of the Electrochemical Society*, vol. 131, no. 6, pp. 1266–1271, 1984.
- [13] K. Itoh and J. O. Bockris, "Stacked thin-film photoelectrode using iron oxide," *Journal of Applied Physics*, vol. 56, no. 3, pp. 874–876, 1984.
- [14] J. H. Kennedy and M. Anderman, "Photoelectrolysis of water at  $\alpha$ -Fe<sub>2</sub>O<sub>3</sub> electrodes in acidic solution," *Journal of the Electrochemical Society*, vol. 130, no. 4, pp. 848–852, 1983.
- [15] J. H. Kennedy and K. W. Frese Jr., "Photooxidation of water at  $\alpha$ -Fe<sub>2</sub>O<sub>3</sub> electrodes," *Journal of the Electrochemical Society*, vol. 125, no. 5, pp. 709–714, 1978.
- [16] J. H. Kennedy and K. W. Frese Jr., "Flatband potentials and donor densities of polycrystalline  $\alpha$ -Fe<sub>2</sub>O<sub>3</sub> determined from mott-schottky plots," *Journal of the Electrochemical Society*, vol. 125, no. 5, pp. 723–726, 1978.
- [17] J. H. Kennedy, R. Shinar, and J. Ziegler, "Alpha-Fe<sub>2</sub>O<sub>3</sub> photoanodes doped with silicon," *Journal of The Electrochemical Society*, vol. 127, no. 10, pp. 2307–2309, 1980.
- [18] M. M. Khader, G. H. Vurens, I.-K. Kim, M. Salmeron, and G. A. Somorjai, "Photoassisted catalytic dissociation of H<sub>2</sub>O to produce hydrogen on partially reduced  $\alpha$ -Fe<sub>2</sub>O<sub>3</sub>," *Journal of the American Chemical Society*, vol. 109, no. 12, pp. 3581–3585, 1987.
- [19] A. F. Sammells and P. G. P. Ang, "Enhanced photoeffects at n-type iron oxide electrodes by electrocatalysis and peroxide effects," *Journal of the Electrochemical Society*, vol. 126, no. 10, pp. 1831–1832, 1979.
- [20] J. E. Turner, M. Hendewerk, J. Parmeter, D. Neiman, and G. A. Somorjai, "Characterization of doped iron oxide electrodes for the photodissociation of water," *Journal of the Electrochemical Society*, vol. 131, no. 8, pp. 1777–1783, 1984.
- [21] S. M. Wilhelm, K. S. Yun, L. W. Ballenger, and N. Hackerman, "Semiconductor properties of iron oxide electrodes," *Journal of the Electrochemical Society*, vol. 126, no. 3, pp. 419–423, 1979.
- [22] U. Björkstén, J. Moser, and M. Grätzel, "Photoelectrochemical studies onnanocrystalline hematite films," *Chemistry of Materials*, vol. 6, no. 6, pp. 858–863, 1994.
- [23] I. Cesar, A. Kay, J. A.G. Martinez, and M. Grätzel, "Translucent thin film Fe<sub>2</sub>O<sub>3</sub> photoanodes for efficient water splitting by sunlight: nanostructure-directing effect of Si-doping," *Journal of the American Chemical Society*, vol. 128, no. 14, pp. 4582–4583, 2006.
- [24] K. Ehrensberger, A. Frei, P. Kuhn, H. R. Oswald, and P. Hug, "Comparative experimental investigations of the water-splitting reaction with iron oxide Fe<sub>1-y</sub>O and iron manganese oxides (Fe<sub>1-x</sub>Mn<sub>x</sub>)<sub>1-y</sub>O," *Solid State Ionics*, vol. 78, no. 1-2, pp. 151–160, 1995.
- [25] M. A. Gondal, A. Hameed, Z. H. Yamani, and A. Suwaiyan, "Laser induced photo-catalytic oxidation/splitting of water over  $\alpha$ -Fe<sub>2</sub>O<sub>3</sub>, WO<sub>3</sub>, TiO<sub>2</sub> and NiO catalysts: activity comparison," *Chemical Physics Letters*, vol. 385, no. 1-2, pp. 111–115, 2004.
- [26] S. U. M. Khan and J. Akikusa, "Photoelectrochemical splitting ofwater at nanocrystalline n-Fe<sub>2</sub>O<sub>3</sub> thin-film electrodes," *Journal of Physical Chemistry B*, vol. 103, no. 34, pp. 7184–7189, 1999.
- [27] W. B. Ingler Jr., J. P. Baltrus, and S. U. M. Khan, "Photoresponse of p-Type zinc-doped iron(III) oxide thin films," *Journal of the American Chemical Society*, vol. 126, no. 33, pp. 10238–10239, 2004.
- [28] D. K. Zhong, J. Sun, H. Inumaru, and D. R. Gamelin, "Solar water oxidation by composite catalyst/ $\alpha$ -Fe<sub>2</sub>O<sub>3</sub> photoanodes," *Journal of the American Chemical Society*, vol. 131, no. 17, pp. 6086–6087, 2009.
- [29] J. S. Jang, J. Lee, H. Ye, F.-R. F. Fan, and A. J. Bard, "Rapid screening of effective dopants for Fe<sub>2</sub>O<sub>3</sub> photocatalysts with Scanning electrochemical microscopy and investigation of their photoelectrochemical properties," *Journal of Physical Chemistry C*, vol. 113, no. 16, pp. 6719–6724, 2009.
- [30] T. Lindgren, H. Wang, N. Beermann, L. Vayssieres, A. Hagfeldt, and S.-E. Lindquist, "Aqueous photoelectrochemistry of hematite nanorod array," *Solar Energy Materials and Solar Cells*, vol. 71, no. 2, pp. 231–243, 2002.
- [31] S. A. Majumder and S. U. M. Khan, "Photoelectrolysis of water at bare and electrocatalyst covered thin film iron oxide electrode," *International Journal of Hydrogen Energy*, vol. 19, no. 11, pp. 881–887, 1994.
- [32] C. J. Sartoretti, B. D. Alexander, R. Solarska, I. A. Rutkowska, J. Augustynski, and R. Cerny, "Photoelectrochemical oxidation of water at transparent ferric oxide film electrodes," *Journal of Physical Chemistry B*, vol. 109, no. 28, pp. 13685–13692, 2005.
- [33] C. J. Sartoretti, M. Ulmann, B. D. Alexander, J. Augustynski, and A. Weidenkaff, "Photoelectrochemical oxidation of water at transparent ferric oxide film electrodes," *Chemical Physics Letters*, vol. 376, no. 1-2, pp. 194–200, 2003.
- [34] Z. Zhou, L. Jiang, and J. Zhang, "Photoelectric characterization of a thin film of iron oxide  $\alpha$ -Fe<sub>2</sub>O<sub>3</sub>," *Gazzetta Chimica Italiana*, vol. 123, no. 8, pp. 471–473, 1993.
- [35] K. E. Davis, W. B. Russel, and W. J. Glantschnig, "Disorder-to-order transition in settling suspensions of colloidal silica: X-ray measurements," *Science*, vol. 245, no. 4917, pp. 507–510, 1989.
- [36] O. D. Velev, T. A. Jede, R. F. Lobo, and A. M. Lenhoff, "Porous silica via colloidal crystallization," *Nature*, vol. 389, no. 6650, pp. 447–448, 1997.
- [37] Y. Hao, F. Q. Zhu, C. L. Chien, and P. C. Searson, "Fabrication and magnetic properties of ordered macroporous nickel structures," *Journal of the Electrochemical Society*, vol. 154, no. 2, pp. D65–D69, 2007.
- [38] D. Hung, Z. Liu, N. Shah, Y. Hao, and P. C. Searson, "Finite size effects in ordered macroporous electrodes fabricated by electrodeposition into colloidal crystal templates," *Journal of Physical Chemistry C*, vol. 111, no. 8, pp. 3308–3313, 2007.
- [39] S. Peulon, H. Antony, L. Legrand, and A. Chausse, "Thin layers of iron corrosion products electrochemically deposited on inert substrates: synthesis and behaviour," *Electrochimica Acta*, vol. 49, no. 17-18, pp. 2891–2899, 2004.
- [40] R. M. Cornell and U. Schwertmann, *The Iron Oxides: Structure, Properties, Reactions, Occurrences, and Uses*, John Wiley & Sons, Weinheim, Germany, 2nd edition, 2003.
- [41] R. M. Silverstein, G. C. Bassler, and T. C. Morrill, *Spectrometric Identification of Organic Compounds*, John Wiley & Sons, New York, NY, USA, 4th edition, 1981.

- [42] U. Schwertmann and R. M. Cornell, *Iron Oxides in the Laboratory: Preparation and Characterization*, John Wiley & Sons, Weinheim, Germany, 1991.
- [43] E. J. Johnson, "Absorption near the fundamental edge," in *Semiconductors and Semimetals*, R. K. Willardson and A. C. Beer, Eds., vol. 3, Academic Press, New York, NY, USA, 1967.
- [44] J. K. Leland and A. J. Bard, "Photochemistry of colloidal semiconducting iron oxide polymorphs," *Journal of Physical Chemistry*, vol. 91, no. 19, pp. 5076–5083, 1987.
- [45] S. R. Morrison and T. Freund, "Chemical role of holes and electrons in ZnO photocatalysis," *The Journal of Chemical Physics*, vol. 47, no. 4, pp. 1543–1551, 1967.
- [46] S. R. Morrison and T. Freund, "Chemical reactions of electrons and holes at the ZnO/electrolyte-solution interface," *Electrochimica Acta*, vol. 13, no. 6, pp. 1343–1349, 1968.
- [47] T. Lindgren, L. Vayssieres, H. Wang, and S.-E. Lindquist, "Photo-oxidation of water at hematite electrodes," in *Chemical Physics of Nanostructured Semiconductors*, A. I. Kokorin and D. W. Bahnemann, Eds., VSP, Utrecht, The Netherlands, 2003.
- [48] N. J. Cherepy, D. B. Liston, J. A. Lovejoy, H. Deng, and J. Z. Zhang, "Ultrafast studies of photoexcited electron dynamics in  $\gamma$ - and  $\alpha$ -Fe<sub>2</sub>O<sub>3</sub> semiconductor nanoparticles," *Journal of Physical Chemistry B*, vol. 102, no. 5, pp. 770–776, 1998.

## Research Article

# CdSe Quantum Dots Sensitized Mesoporous TiO<sub>2</sub> Solar Cells with CuSCN as Solid-State Electrolyte

Guanbi Chen, Lei Wang, Yu Zou, Xia Sheng, Hongjuan Liu, Xiaodong Pi, and Deren Yang

State Key Laboratory of Silicon Materials and Department of Materials Science Engineering, Zhejiang University, Hangzhou 310027, China

Correspondence should be addressed to Deren Yang, mseyang@zju.edu.cn

Received 1 May 2010; Revised 29 June 2010; Accepted 16 August 2010

Academic Editor: Bo Zou

Copyright © 2011 Guanbi Chen et al. This is an open access article distributed under the Creative Commons Attribution License, which permits unrestricted use, distribution, and reproduction in any medium, provided the original work is properly cited.

Mesoporous TiO<sub>2</sub> is functionalized by 3-mercaptopropyl trimethoxysilane (MPTMS) to anchor CdSe quantum dots (QDs). The resulting TiO<sub>2</sub>/CdSe is combined with solid-state electrolyte (CuSCN) to form solar cells. It is found that the efficiency of electron injection from QDs to TiO<sub>2</sub> can be improved owing to the substitution of the long chains of organic capping agents at the surface of QDs with MPTMS. The hydrolyzate of MPTMS forms an insulating barrier layer to reduce the recombination at the TiO<sub>2</sub>/CdSe interface, leading to the increase of open-circuit voltage ( $V_{oc}$ ).

## 1. Introduction

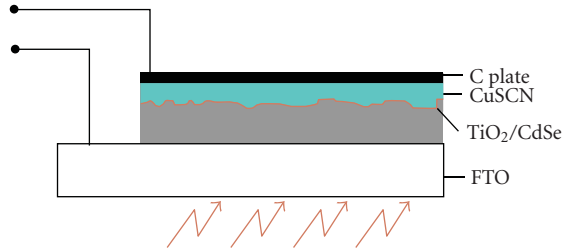
As the supplies of fossil fuel are expected to decrease, energy conservation and alternative energy sources are actively investigated to achieve sustainable development [1]. Low-cost and high-efficiency dye-sensitized solar cells are regarded as an excellent candidate for exploiting solar energy, which is one of the most important alternative energies [2]. Semiconductor Quantum Dots (QDs) can also serve a sensitizer for light harvesting assemblies in solar cells [3]. The size quantization of QDs leads to the capability of tuning visible-spectrum response and varying band offsets to modulate the vectorial charge transfer across QDs with different sizes [4]. By anchoring different-sized QDs on mesoporous electrodes, researchers hope to prepare rainbow solar cells which took advantages of both the faster electron injection of small QDs and the greater absorption range of large QDs [5]. Among other benefits of the use of QDs in solar cells, hot electrons can generate carrier multiplication in QDs [6, 7]. Solar photon conversion with efficiency up to about 66% has been estimated [3].

Solar cells based on mesoporous TiO<sub>2</sub> sensitized by PbS [8], InP [9], CdS [10], and CdSe QDs [11] have been reported. However, it has been said that the surface capping of QDs is an integral part of its electronic system and can alter the energy levels position [12]. It has been shown in

the work on CdSe QDs-sensitized TiO<sub>2</sub> that bifunctional surface modifiers with shorter chains can assemble QDs on TiO<sub>2</sub> [4, 5]. Mainly, the effects of the modifiers are limited to reduce the spaces between QDs and TiO<sub>2</sub>, increasing the electron injection efficiency. What is more, in most of QDs-sensitized solar cells liquid electrolytes are used as hole transfer media. Although solid-state electrolytes have been employed in solar cells with extremely thin absorbers (ETA) such as CdSe [13], CuInS<sub>2</sub> [14], CdS [15], In<sub>2</sub>S<sub>3</sub> [16], Cu<sub>2-x</sub>S [17], and Sb<sub>2</sub>S<sub>3</sub> [18], they have been rarely used in QDs-sensitized solar cells. In this paper, we use 3-mercaptopropyl trimethoxysilane (MPTMS) as the surface modifier to link preprepared CdSe QDs and mesoporous TiO<sub>2</sub>. Hydrolyzate of MPTMS (SiO<sub>2</sub>) forms an insulating barrier layer to reduce the recombination at the TiO<sub>2</sub>/CdSe interface [19]. In our QDs-sensitized solar cells, p-type CuSCN is the solid-state electrolyte, and all the processes are nonvacuum including electrode preparation.

## 2. Experimental Details

Mesoporous TiO<sub>2</sub> electrodes were prepared by use of a classical method [20]. In brief, commercial TiO<sub>2</sub> nanoparticles (P25, Degussa AG, Germany) were mixed with water, acetylacetone and detergent (OP10). The mixture was then ground for about 1 h to obtain TiO<sub>2</sub> paste which was painted



SCHEME 1: Structural sketch of our CdSe QDs sensitized mesoporous TiO<sub>2</sub> solar cell with CuSCN as solid-state electrolyte.

on a conduction FTO glass substrate as TiO<sub>2</sub> electrodes. On the substrate, two parallel adhesive tapes were covered to control the film thickness and shape of TiO<sub>2</sub>. After drying in air, the TiO<sub>2</sub> electrodes were annealed at 550 °C for 1 h. After cooled in furnace to about 100 °C, the TiO<sub>2</sub> electrodes were taken out and placed into a 1% MPTMS ethanol solution. It took at least 24 h to finish the immersion, which aimed to functionalize the surface of TiO<sub>2</sub> with bifunctional surface modifiers. The TiO<sub>2</sub> electrodes were subsequently washed with ethanol several times. They were finally blow-dried with N<sub>2</sub>.

CdSe QDs were prepared using a similar method to that used in [21]. Selenium powder and cadmium myristate were placed into a three-neck flask with adequate amount of octadecene (ODE). After 10-minute degassing, the mixture was heated to 240 °C at a rate of 25 °C/s while being stirred. The temperature was held at 240 °C for 1 h. After washing with ethanol and n-hexane for several times, CdSe QDs with a mean size of about 5 nm were produced. These CdSe QDs might be well dispersed in hexane.

Surface-modified TiO<sub>2</sub> electrodes were immersed in CdSe/hexane solution for approximately 15 h. After drying in air, TiO<sub>2</sub>/QDs electrodes were preheated to 80 °C. Dilute CuSCN/(CH<sub>3</sub>CH<sub>2</sub>CH<sub>2</sub>)<sub>2</sub>S solution was dropped on TiO<sub>2</sub>/QDs electrodes to reach certain thickness at 80 °C [22]. Conducting carbon paste was then coated on CuSCN films with a simple doctor-blade method. The solar cells were defined by a mask in the drop-cast deposition of carbon paste. The uncovered films by carbon electrodes were scraped away to delimitate the working areas. The complete structure of solar cells was illustrated in Scheme 1 and labeled as SC-modified (C/CuSCN/CdSe(modified)/TiO<sub>2</sub>/FTO). To find out the effect of surface modifier on the performance of solar cells, solar cells with the same preparation procedure as described before except that TiO<sub>2</sub> electrodes were not treated with MPTMS were also prepared and labeled as SC-unmodified (C/CuSCN/CdSe(unmodified)/TiO<sub>2</sub>/FTO). What should be noted was that since the wettability between oil-chelating QDs and TiO<sub>2</sub> particles was poor, QDs solutions were dropped directly onto TiO<sub>2</sub> films instead of absorption. For comparison, solar cells made by use of TiO<sub>2</sub> electrodes without MPTMS treatment and CdSe QDs sensitization were also prepared and labeled as SC-refer (C/CuSCN/TiO<sub>2</sub>/FTO).

The morphology of TiO<sub>2</sub> electrodes was investigated by use of an atomic force microscopy (AFM) AFM, nanoscope

III). Absorption spectra were recorded using a UV-Vis spectrophotometer (Hitachi Model U-4 100). A homemade platform based on Keithley 4200S was employed to study the current-voltage (*I-V*) characteristics of solar cells under the illumination of a tungsten halogen lamp (intensity of 50 mW/cm<sup>2</sup> by photometer).

### 3. Results and Discussion

Figure 1 shows the differences in surface morphology between an as-grown TiO<sub>2</sub> and CdSe QDs-sensitized TiO<sub>2</sub> characterized by AFM. It can be seen that the as-grown TiO<sub>2</sub> is porous with a mean particle size of about 20 nm, the same as previously reported in [2]. It should be noted that the porosity and grain size are crucial to electron transport in nanocrystalline TiO<sub>2</sub> electrodes [23]. After sensitized by CdSe QDs, the TiO<sub>2</sub> becomes rougher. The root-mean-square (RMS) roughness increases by about 5 nm, from 12 nm to 17 nm. It may be a coincidence that the roughness increment is close to the diameter of CdSe QDs applied (mentioned in the following). However, we assume monolayer absorption of CdSe QDs at the surface of TiO<sub>2</sub>, as reported in [5]. The monolayer absorption facilitates the penetration of CdSe QDs to the porous network of TiO<sub>2</sub>, whereas some pores may be too cabin for the QDs to transport. The additional roughness enhancement could be due to the absorption of QDs or not in different areas.

The absorption spectra for a TiO<sub>2</sub> electrode and CdSe QDs-sensitized TiO<sub>2</sub> electrodes (modified and unmodified) are shown in Figure 2. Due to the large bandgap of TiO<sub>2</sub> (3.2 eV), we ascribe this apparent absorption in visible wavelength range mainly to scattering effect. It is seen that the CdSe QDs sensitized TiO<sub>2</sub> films absorb photons more efficiently in the wavelength range of 400–650 nm, due to the limitation of CdSe QDs absorption edge. The absorption peak at about 600 nm corresponds to the 1S transition of CdSe QDs. By comparing the 1S transition peak position to that reported by Yu et al. [24], we estimate that the CdSe QDs are about 5 nm. The absorbance of modified TiO<sub>2</sub> films shows little increase as the exposure time in QDs solution increases, indicating monolayer absorption of CdSe QDs at the surface of TiO<sub>2</sub>. In this mode of absorption, it is assumed that QDs can be anchored onto both exterior and interior surfaces of mesoscopic TiO<sub>2</sub> films through molecule linkers [4]. We find higher absorbance in unmodified TiO<sub>2</sub> films which are prepared directly by drop-casting QDs than that of modified TiO<sub>2</sub> films. This indicates that more CdSe QDs are deposited on the films, however packed in a multilayer form possibly.

Figure 3 shows the *I-V* curves for the SC-refer in the dark and light. It is evident that the TiO<sub>2</sub>/CuSCN interface gives rise to a rectification effect since SnO<sub>2</sub>/TiO<sub>2</sub> and CuSCN/graphite junctions are both considered to be ohmic contact [25]. It can also be concluded from the curve that a weak built-in electric field points from CuSCN to TiO<sub>2</sub> since applying positive bias to CuSCN layer leads to a positive current, which indicates that our CuSCN layer is p type and can serve as a hole transport layer. Though we obtain a rectification ratio of about 30, the numerical fitted

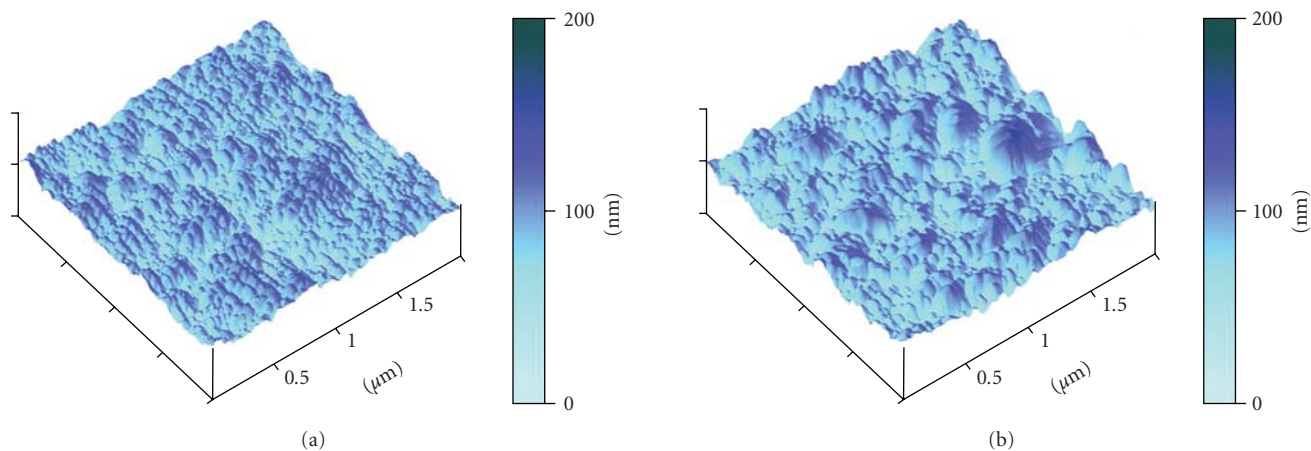


FIGURE 1: AFM images of (a) an as-grown  $\text{TiO}_2$  electrode and (b) a CdSe QDs sensitized  $\text{TiO}_2$  electrode.

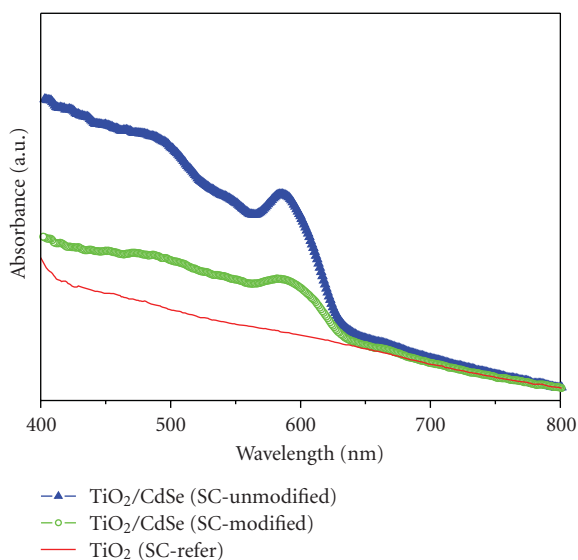


FIGURE 2: Absorption spectra of a  $\text{TiO}_2$  electrode and CdSe QDs sensitized  $\text{TiO}_2$  electrode.

reverse saturation current is about  $0.0065 \text{ mA/cm}^2$ , which is much higher than the data reported in the literature [20]. We ascribe the poor performance of the diode to the weak filling of CuSCN into porous  $\text{TiO}_2$  films, resulting in a reduced working area. Under illumination, photovoltaic effect can be observed although the open voltage ( $V_{oc}$ ) is rather low. This is not hard to understand since only ultraviolet light can be absorbed by the high bandgap materials of  $\text{TiO}_2$  and CuSCN.

Figure 4 illustrates the  $I$ - $V$  characteristics of the SC-unmodified. Compared with the SC-refer, it unexpectedly shows that the photocurrent is even smaller. Although CdSe QDs between CuSCN and  $\text{TiO}_2$  electrodes improve light absorption and consequently lead to more light-induced carriers and higher current, it has been recently reported that the organic capping agent of QDs remains on the surface [26]. Therefore, we assume that organic residuals could form a high series resistance of the device and lower

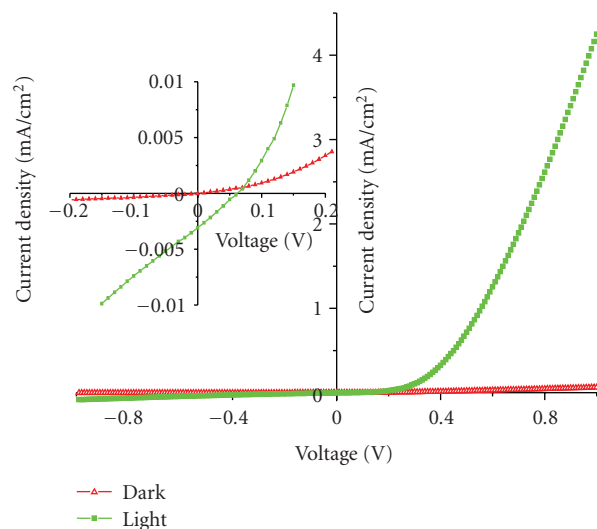


FIGURE 3:  $I$ - $V$  curves of an SC-refer (C/CuSCN/ $\text{TiO}_2$ /FTO) under dark and light (inset is the enlarged image).

the photocurrent. In addition, the multilayer pileup of QDs and much weaker filling of CuSCN into porous  $\text{TiO}_2$  films because of this layer can make this even worse. On the other side, the long organic chain between  $\text{TiO}_2$  and QDs could serve as barrier layer, increasing the shunt resistance and the  $V_{oc}$  afterwards.

In contrast to the drop casting method, both the  $V_{oc}$  and  $J_{sc}$  of SC-modified increase when CdSe QDs are modified as demonstrated in Figure 5. As a short chain surface modifier, MPTMS reduces the space between QDs and  $\text{TiO}_2$ . As mentioned above, there exist organic capping agents with long chains at the surface of QDs. By substituting these long chains with short ones, the carrier injection efficiency can be improved [4]. In addition, hydrolyzate of MPTMS is  $\text{SiO}_2$ , forming an insulating barrier between QDs and  $\text{TiO}_2$ . The insulating layer is a “tunnel barrier”, reducing the pseudo-first-order recombination rate, as indicated in [27].

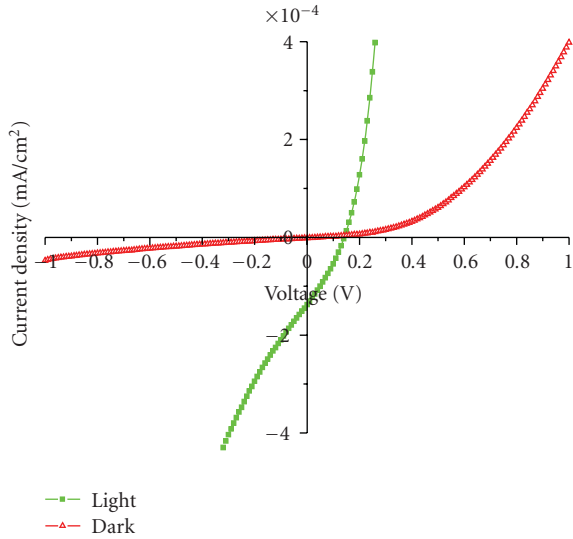


FIGURE 4:  $I$ - $V$  curves of a SC-unmodified (C/CuSCN/ CdSe(unmodified)/TiO<sub>2</sub>/FTO) under dark and light.

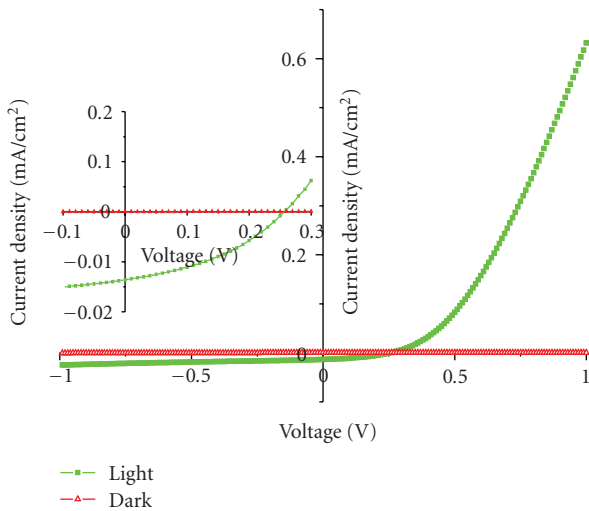


FIGURE 5:  $I$ - $V$  curves of a SC-modified (C/CuSCN/ CdSe(modified)/TiO<sub>2</sub>/FTO) under dark and light (inset is the enlarged image).

Generally speaking, the insulating layers increase the shunt resistance of devices and suppress shunt current. This leads to the increase in  $V_{oc}$  compared with SC-unmodified. What is more, the monolayer absorption mode of QDs lowers the series resistance and increase the  $J_{sc}$  consequently. Since the electron transfers from excited QDs to electrodes by tunneling through the insulating layer, the thickness of it should not be too large [19, 26].

Although the performances of our devices are relatively not as good as that reported in the earlier works [4, 5], we successfully employ solid-state electrolyte of CuSCN in QDs-sensitized solar cells and indicate the beneficial effects of MPTMS. In addition, considering the all nonvacuum process during the preparation of our solar cells (including

electrodes preparation) and the low energy density of our light, there can be great promoting potentials for our devices. Probable technology routes are the growth of  $p$ -type layers or TiO<sub>2</sub> electrodes to enhance the junction area, surface engineering to reduce the recombination in the QDs/TiO<sub>2</sub> interface, and QDs control to improve light absorption and electron injection.

## 4. Conclusions

CdSe QDs sensitized mesoporous TiO<sub>2</sub> solar cells with CuSCN as solid-state electrolyte have been prepared. The effect of MPTMS as a surface modifier on the  $I$ - $V$  characteristics of solar cells is investigated. The surface modifier substitutes the long chains of organic capping agents at the surface of QDs, shortening the space between QDs and TiO<sub>2</sub> and improving the electron injection efficiency from QDs to TiO<sub>2</sub>. In addition, the hydrolyzate of MPTMS forms an insulating barrier layer, leading to the increase of shunt resistance and open-circuit voltage of the devices.

## Acknowledgments

The authors thank Weiming Qiu for his kind help in AFM characterization and Jipeng Cheng for his deep discussion in experiments. The authors appreciate the financial supports from Program for Changjiang Scholar and Innovative Team in University, Program 973 (no. 2007CB613403) and the foundation of 2008KR0001 of MOST.

## References

- [1] M. S. Dresselhaus and I. L. Thomas, "Alternative energy technologies," *Nature*, vol. 414, no. 6861, pp. 332–337, 2001.
- [2] B. O'Regan and M. Grätzel, "A low-cost, high-efficiency solar cell based on dye-sensitized colloidal TiO<sub>2</sub> films," *Nature*, vol. 353, no. 6346, pp. 737–740, 1991.
- [3] A. J. Nozik, "Quantum dot solar cells," *Physica E*, vol. 14, no. 1-2, pp. 115–120, 2002.
- [4] I. Robel, V. Subramanian, M. Kuno, and P. V. Kamat, "Quantum dot solar cells. Harvesting light energy with CdSe nanocrystals molecularly linked to mesoscopic TiO<sub>2</sub> films," *Journal of the American Chemical Society*, vol. 128, no. 7, pp. 2385–2393, 2006.
- [5] A. Kongkanand, K. Tvrđy, K. Takechi, M. Kuno, and P. V. Kamat, "Quantum dot solar cells. Tuning photoresponse through size and shape control of CdSe-TiO<sub>2</sub> architecture," *Journal of the American Chemical Society*, vol. 130, no. 12, pp. 4007–4015, 2008.
- [6] R. D. Schaller and V. I. Klimov, "High efficiency carrier multiplication in PbSe nanocrystals: implications for solar energy conversion," *Physical Review Letters*, vol. 92, no. 18, Article ID 186601, 1 pages, 2004.
- [7] A. Franceschetti, J. M. An, and A. Zunger, "Impact ionization can explain carrier multiplication in PbSe quantum dots," *Nano Letters*, vol. 6, no. 10, pp. 2191–2195, 2006.
- [8] P. Hoyer and R. Könenkamp, "Photoconduction in porous TiO<sub>2</sub> sensitized by PbS quantum dots," *Applied Physics Letters*, vol. 66, p. 349, 1995.
- [9] A. Zaban, O. I. Mičić, B. A. Gregg, and A. J. Nozik, "Photosensitization of nanoporous TiO<sub>2</sub> electrodes with InP

- quantum dots,” *Langmuir*, vol. 14, no. 12, pp. 3153–3156, 1998.
- [10] K. G. U. Wijayantha, L. M. Peter, and L. C. Otley, “Fabrication of CdS quantum dot sensitized solar cells via a pressing route,” *Solar Energy Materials and Solar Cells*, vol. 83, no. 4, pp. 363–369, 2004.
- [11] Q. Shen, D. Arae, and T. Toyoda, “Photosensitization of nanostructured TiO<sub>2</sub> with CdSe quantum dots: effects of microstructure and electron transport in TiO<sub>2</sub> substrates,” *Journal of Photochemistry and Photobiology A*, vol. 164, no. 1–3, pp. 75–80, 2004.
- [12] M. Soreni-Harari, N. Yaacobi-Gross, D. Steiner et al., “Tuning energetic levels in nanocrystal quantum dots through surface manipulations,” *Nano Letters*, vol. 8, no. 2, pp. 678–684, 2008.
- [13] C. Lévy-Clément, R. Tena-Zaera, M. A. Ryan, A. Katty, and G. Hodes, “CdSe-sensitized p-CuSCN/nanowire n-ZnO heterojunctions,” *Advanced Materials*, vol. 17, no. 12, pp. 1512–1515, 2005.
- [14] I. Kaiser, K. Ernst, Ch.-H. Fischer et al., “Eta-solar cell with CuInS<sub>2</sub> : a photovoltaic cell concept using an extremely thin absorber (eta),” *Solar Energy Materials and Solar Cells*, vol. 67, no. 1–4, pp. 89–96, 2001.
- [15] G. Larramona, C. Choné, A. Jacob et al., “Nanostructured photovoltaic cell of the type titanium dioxide, cadmium sulfide thin coating, and copper thiocyanate showing high quantum efficiency,” *Chemistry of Materials*, vol. 18, no. 6, pp. 1688–1696, 2006.
- [16] D. Kieven, T. Dittrich, A. Belaidi et al., “Effect of internal surface area on the performance of ZnO/In<sub>2</sub>S<sub>3</sub> /CuSCN solar cells with extremely thin absorber,” *Applied Physics Letters*, vol. 92, no. 15, Article ID 153107, 3 pages, 2008.
- [17] M. Page, O. Niitsoo, Y. Itzhaik, D. Cahen, and G. Hodes, “Copper sulfide as a light absorber in wet-chemical synthesized extremely thin absorber (ETA) solar cells,” *Energy and Environmental Science*, vol. 2, no. 2, pp. 220–223, 2009.
- [18] Y. Itzhaik, O. Niitsoo, M. Page, and G. Hodes, “Sb<sub>2</sub>S<sub>3</sub> -sensitized nanoporous TiO<sub>2</sub> solar cells,” *Journal of Physical Chemistry C*, vol. 113, no. 11, pp. 4254–4256, 2009.
- [19] A. Kay and M. Grätzel, “Dye-sensitized core-shell nanocrystals: improved efficiency of mesoporous tin oxide electrodes coated with a thin layer of an insulating oxide,” *Chemistry of Materials*, vol. 14, no. 7, pp. 2930–2935, 2002.
- [20] M. K. Nazeeruddin, A. Kay, I. Rodicio et al., “Conversion of light to electricity by cis-X<sub>2</sub> bis(2,2′-bipyridyl-4,4′-dicarboxylate)ruthenium(II) charge-transfer sensitizers (X = Cl<sup>-</sup>, Br<sup>-</sup>, I<sup>-</sup>, CN<sup>-</sup>, and SCN<sup>-</sup>) on nanocrystalline TiO<sub>2</sub> electrodes,” *Journal of the American Chemical Society*, vol. 115, no. 14, pp. 6382–6390, 1993.
- [21] Y. A. Yang, H. Wu, K. R. Williams, and Y. C. Cao, “Synthesis of CdSe and CdTe nanocrystals without precursor injection,” *Angewandte Chemie - International Edition*, vol. 44, no. 41, pp. 6712–6715, 2005.
- [22] P. Wang, S. M. Zakeeruddin, J. E. Moser, M. K. Nazeeruddin, T. Sekiguchi, and M. Grätzel, “A stable quasi-solid-state dye-sensitized solar cell with an amphiphilic ruthenium sensitizer and polymer gel electrolyte,” *Nature Materials*, vol. 2, no. 6, pp. 402–407, 2003.
- [23] Q. Shen and T. Toyoda, “Studies of optical absorption and electron transport in nanocrystalline TiO<sub>2</sub> electrodes,” *Thin Solid Films*, vol. 438–439, pp. 167–170, 2003.
- [24] W. W. Yu, L. Qu, W. Guo, and X. Peng, “Experimental determination of the extinction coefficient of CdTe, CdSe, and CdS nanocrystals,” *Chemistry of Materials*, vol. 15, no. 14, pp. 2854–2860, 2003.
- [25] C. Rost, I. Sieber, S. Siebentritt, M. C. Lux-Steiner, and R. Könenkamp, “Spatially distributed p-n heterojunction based on nanoporous TiO<sub>2</sub> and CuSCN,” *Applied Physics Letters*, vol. 75, no. 5, pp. 692–694, 1999.
- [26] B. D. Yuhas and P. Yang, “Nanowire-based all-oxide solar cells,” *Journal of the American Chemical Society*, vol. 131, no. 10, pp. 3756–3761, 2009.
- [27] B. C. O’Regan, S. Scully, A. C. Mayer, E. Palomares, and J. Durrant, “The effect of Al<sub>2</sub>O<sub>3</sub> barrier layers in TiO<sub>2</sub>/Dye/CuSCN photovoltaic cells explored by recombination and DOS characterization using transient photovoltage measurements,” *Journal of Physical Chemistry B*, vol. 109, no. 10, pp. 4616–4623, 2005.

## Research Article

# Preparation of Nanoporous TiO<sub>2</sub> Electrodes for Dye-Sensitized Solar Cells

Hsiue-Hsyan Wang,<sup>1,2</sup> Chaochin Su,<sup>1</sup> Huei-Siou Chen,<sup>1</sup> Yi-Cheng Liu,<sup>1</sup> Yi-Wen Hsu,<sup>1</sup> Nai-Mu Hsu,<sup>3</sup> and Wen-Ren Li<sup>3</sup>

<sup>1</sup>Institute of Organic and Polymeric Materials, National Taipei University of Technology, Taipei 10608, Taiwan

<sup>2</sup>Department of Chemical and Materials Engineering, National Ilan University, 1, Sec.1, Shen-Lung Road, I-Lan 260, Taiwan

<sup>3</sup>Department of Chemistry, National Central University, Chung-Li 32001, Taiwan

Correspondence should be addressed to Chaochin Su, f10913@ntut.edu.tw and Wen-Ren Li, ch01@ncu.edu.tw

Received 20 May 2010; Revised 19 August 2010; Accepted 24 August 2010

Academic Editor: William W. Yu

Copyright © 2011 Hsiue-Hsyan Wang et al. This is an open access article distributed under the Creative Commons Attribution License, which permits unrestricted use, distribution, and reproduction in any medium, provided the original work is properly cited.

Nano-porous TiO<sub>2</sub> thin films have been widely used as the working electrodes in dye-sensitized solar cells (DSSCs). In this work, the phase-pure anatase TiO<sub>2</sub> (a-TiO<sub>2</sub>) and rutile TiO<sub>2</sub> (r-TiO<sub>2</sub>) have been prepared using hydrothermal processes. The investigation of photo-to-electron conversion efficiency of DSSCs fabricated from mixed-TiO<sub>2</sub> with a-TiO<sub>2</sub> and r-TiO<sub>2</sub> ratio of 80:20 (A8R2) was performed and compared to that from commercial TiO<sub>2</sub> (DP-25). The results showed higher efficiency of DSSC for A8R2 cells with same dependence of cell efficiency on the film thickness for both A8R2 and DP-25 cells. The best efficiency obtained in this work is 5.2% from A8R2 cell with TiO<sub>2</sub> film thickness of 12.0 μm. The correlation between the TiO<sub>2</sub> films thickness and photoelectron chemical properties of DSSCs fabricated from A8R2 and DP-25 was compared and discussed.

## 1. Introduction

Worldwide scientific community has invested much attention in dye sensitized solar cells (DSSCs) with possibilities of high energy conversion efficiency and low fabrication cost [1]. In DSSC, titanium dioxide (TiO<sub>2</sub>) is one of the most promising materials used for nano-porous thin film due to its appropriate energy levels, dye adsorption ability, low cost, and easy preparation [2]. Extensive research on the photochemistry and photophysics of TiO<sub>2</sub>-based DSSCs has shown that the light harvesting efficiency of TiO<sub>2</sub> is influenced by its crystalline phase, particle size, surface area, dye affinity, and film porosity. TiO<sub>2</sub> exists in two major phases: anatase and rutile. The anatase phase (a-TiO<sub>2</sub>) gained much attention due to its more active surface chemistry and smaller particles for more dye adsorption. Anatase is metastable and can be transformed irreversibly to thermodynamically more stable and condense rutile phase at higher temperature. The rutile phase TiO<sub>2</sub> (r-TiO<sub>2</sub>), due to the high refractive index, has excellent light-scattering characteristics, which is a profitable property of

the perspective of effective light harvesting. Combination of anatase and rutile TiO<sub>2</sub> can be more effective than the pure phase owing to the electron-holes separation at the interface between phases and the formation of inter-band gap trap which may influence interparticle carrier transportation. The commercial Degussa P-25 TiO<sub>2</sub> (DP-25) composed of a-TiO<sub>2</sub> and r-TiO<sub>2</sub> at a ratio of 80:20 is known to be one of the most active photocatalysts due to the synergic effect [3]. In this paper, the phase pure a-TiO<sub>2</sub> and r-TiO<sub>2</sub> nanoparticles were first synthesized [4, 5]. The photoanodes from mixed-TiO<sub>2</sub> with a-TiO<sub>2</sub>-to-r-TiO<sub>2</sub> ratio of 80:20 (A8R2) which resemble the phase ratio in DP-25 were then fabricated. Finally, the film characteristics and the DSSC performance of the A8R2 photoanodes were investigated and compared to those made of commercial DP-25.

## 2. Experimental Details

*2.1. Preparation and Characterization of a-TiO<sub>2</sub>, r-TiO<sub>2</sub>, and Spin-Coated TiO<sub>2</sub> Electrodes.* The preparation of TiO<sub>2</sub>

nanoparticles involves controlled hydrolysis of Ti precursor followed by peptization. Detailed descriptions of the temperature dependent TiO<sub>2</sub> nanoparticles formation can be found in our previous works [6, 7]. Briefly, titanium (IV) n-butoxide (TNB) was mixed with 2 M acetic acid (for a-TiO<sub>2</sub>) or 3 M hydrogen chloride (for r-TiO<sub>2</sub>) at room temperature and carefully stirred until a translucent TiO<sub>2</sub> sol was obtained. The TiO<sub>2</sub> sol was then transferred to a Teflon-lined autoclave to perform the hydrothermal treatment at 200°C for 5 h (for a-TiO<sub>2</sub>) or 220°C for 8 h (for r-TiO<sub>2</sub>) followed by drying at 150°C for 8 h. These procedures resulted in the formation of oval-shaped a-TiO<sub>2</sub> and bar-shaped r-TiO<sub>2</sub> (see below). The TiO<sub>2</sub> samples were characterized by transmission electron microscopy (TEM, Hitachi) for particle shape and size, X-ray diffraction (XRD, Japan MAC Science) for crystal phase and domain size, and Brunauer, Emmett and Teller method (BET, Micromeritics Gemini V) for surface area analysis.

The TiO<sub>2</sub> films were made by spreading TiO<sub>2</sub> pastes on the fluorine-doped SnO<sub>2</sub> conducting glass (FTO, Solaronix, sheet resistance 8 Ω/□) by spin coating technique. Two kinds of TiO<sub>2</sub> pastes containing A8R2 and DP-25 were prepared by mixing-grinding the TiO<sub>2</sub> sample with distilled water, acetylacetone, and Triton X-100. Extensive stirring and sonication was proceeded to ensure complete dispersion of TiO<sub>2</sub> nanoparticles and to facilitate the spreading of the colloid on FTO. Droplets of each paste were placed onto the FTO substrate mounted on the turning table of a spin coater (IVY Semiconductor). Adhesive tapes were placed on the edges of FTO to form a guide for spreading the pastes with spin rate of 1000 rpm. After drying in air the TiO<sub>2</sub> electrodes were heated at 100°C for 15 min followed by annealing at 450°C for 30 min. The resulted electrodes were cooled to 80°C and immediately soaked in a 0.3 mM of solution of N719 dye in ethanol for overnight. Thickness of the TiO<sub>2</sub> film was controlled by multiple coating processes in which the coated substrates were subjected repeatedly to spin-coating and drying steps. The thickness of TiO<sub>2</sub> films were measured by an Alpha-step profiler (Perthometer S2). The surface morphology and crystal phase of TiO<sub>2</sub> films were characterized by SEM (Hitachi S-2400) and XRD (PANalytical X'Pert PRO MPD), respectively.

**2.2. Dye-Sensitized Solar Cell Assembly and Performance Measurement.** To assemble the DSSCs, the electrolyte of LiI (0.1 M), I<sub>2</sub> (0.05 M), 1,2-dimethyl-3-propyl imidazolium iodide (0.5 M), and 4-tert-butylpyridine (0.5 M) in acetonitrile was applied to the Pt counter electrodes (20 nm on FTO) which were placed over the N719-adsorbed TiO<sub>2</sub> electrodes. The edges of the cell were sealed with a 50 μm polyimide tape spacer. The active cell area studied in this work is 0.25 cm<sup>2</sup>. The photocurrent-voltage characteristics were performed using a Keithley model 2400 source measuring unit. A solar simulator with 300 W Xenon lamp (Oriel) served as a light source, and its light intensity was adjusted by using an NREL-calibrated monocrystalline Silica solar cell for AM1.5 radiation. The electron transport properties were investigated using electrochemical impedance spectroscopy (EIS) with 10 mV alternative signal in the frequency range

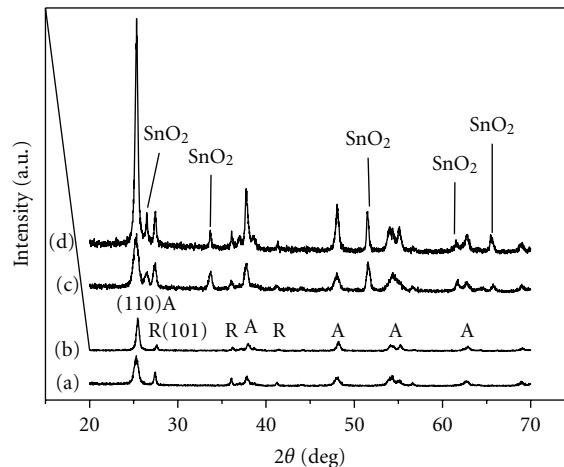


FIGURE 1: A series of XRD patterns for A8R2 powder (a), DP-25 powder (b), A8R2 film (c), and DP-25 film (d).

of  $10^{-2}$ – $10^5$  Hz. The amount of adsorbed dye was determined by desorbing the dye from TiO<sub>2</sub> into a solution of 0.1 M NaOH and analyzed by UV-visible spectrophotometer (JASCO V-630).

### 3. Results and Discussion

**3.1. Preparation and Characterization of a-TiO<sub>2</sub>, r-TiO<sub>2</sub>, and Mixed-Phase TiO<sub>2</sub> Photoelectrode.** The parameter-controlled sol-hydrothermal reactions employed in the present work led to the formation of a-TiO<sub>2</sub> and r-TiO<sub>2</sub> nanocrystallites. Various kinds of techniques were used for characterization of the products which was demonstrated in our previous works [6, 8]. After mixing a-TiO<sub>2</sub> with r-TiO<sub>2</sub> and spin-coating on FTO substrate, a porous TiO<sub>2</sub> film was obtained. Figure 1 shows the XRD patterns of the A8R2 powder (Figure 1(a)) and A8R2 film (Figure 1(c)). The diffraction patterns of DP-25 powder (Figure 1(b)) and DP-25 film (Figure 1(d)) are also shown for comparison. The XRD pattern of A8R2 film exhibited peaks corresponding to anatase and rutile phase indicating the presence of stable mixed-phase TiO<sub>2</sub> film after 30 min calcination at 450°C. Several peaks appear at  $2(\theta) = 26.6, 33.9,$  and  $51.8$  of Figures 1(c) and 1(d) which are due-to-SnO<sub>2</sub> from FTO substrate. The phase ratio of a-TiO<sub>2</sub> and r-TiO<sub>2</sub> is calculated from the equation of  $F_r = 1.26I_r/(I_a + 1.26I_r)$ , where  $I_r$  and  $I_a$  are the strongest intensities of rutile (110) and anatase (101) peaks, respectively. The calculated a-TiO<sub>2</sub> : r-TiO<sub>2</sub> ratio on A8R2 film is 63 : 37 which is deviated from the original ratio for mixed powder samples prior to calcination. The lower anatase content in calcined A8R2 film designates the possibility of phase transformation from anatase to rutile (A → R) upon calcination [9]. Similar transformation also occurs on the spin-coated DP-25 film in which the final anatase to rutile ratio is 73.4:26.5. Note that the A8R2 sample holds the higher extent of A → R compared to DP-25 due to the more compact arrangement of a-TiO<sub>2</sub> in A8R2 allowing the facile phase transformation (see below).

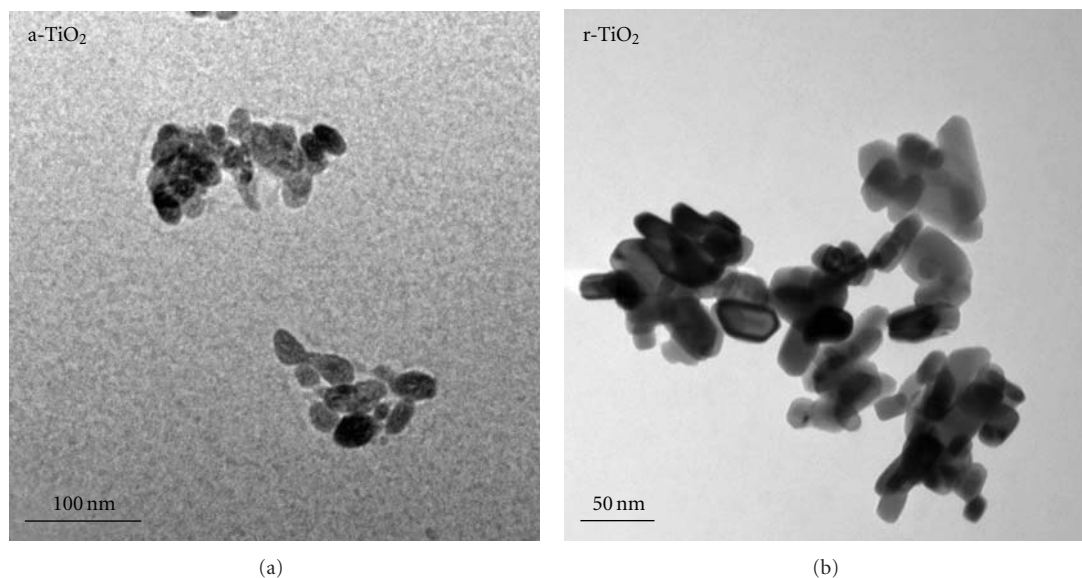


FIGURE 2: TEM micrographs of TiO<sub>2</sub> samples: anatase TiO<sub>2</sub> (a-TiO<sub>2</sub> (a)) and rutile TiO<sub>2</sub> (r-TiO<sub>2</sub> (b)).

The phase ratio and crystallite sizes of a-TiO<sub>2</sub> and r-TiO<sub>2</sub> in A8R2 and DP-25 calculated by Scherrer equation are summarized in Table 1.

Figure 2 shows the TEM micrograph of pure a-TiO<sub>2</sub> (b) with distinct irregular oval structure and r-TiO<sub>2</sub> (a) with characteristic nanobar structure. The average of particle size is ~16 nm for a-TiO<sub>2</sub> and 40 × 20 nm in width × length for r-TiO<sub>2</sub>. The DP-25 TiO<sub>2</sub> nanoparticles are polygonal in shape with average size of 30 nm (not shown). The particle size of nanocrystals can also be estimated from BET surface area measurement. The a-TiO<sub>2</sub>, r-TiO<sub>2</sub>, and DP-25 nanoparticles possess specific surface area of 116, 27, and 50 m<sup>2</sup>/g, respectively. Based on an assumption of all anatase phase spherical particles and use of TiO<sub>2</sub> solid density of 3.84 g/cm<sup>3</sup> to convert the BET specific surface areas to particle diameters, the corresponding particle dimension for a-TiO<sub>2</sub>, r-TiO<sub>2</sub>, and DP-25 is 13, 56, and 29 nm, respectively, which is consistent with the TEM size measurement. The smaller particle size of a-TiO<sub>2</sub> in A8R2 is on account of the more dense and compact structure of A8R2 film compared to the DP-25 film (see below SEM images). The results of TiO<sub>2</sub> particle size derived from TEM and BET are also summarized in Table 1 and compared with the crystalline size obtained from XRD. The results show good agreement in TiO<sub>2</sub> particle size within the experimental error.

The spin-coated A8R2 films appeared to be smooth under visual inspection although the film showed some inhomogeneity at the edges. The SEM micrograph of TiO<sub>2</sub> film made of A8R2 sample (Figure 3(a)) shows a rough surface layer containing large TiO<sub>2</sub> chunks in which the individual TiO<sub>2</sub> particles are hardly visible. The chunk structure is likely formed through the aggregation of bar-shape r-TiO<sub>2</sub> arranged in a side-by-side configuration. Another possible reason for the appearance of irregular chunks on the A8R2 layer is the stress-induced surface rumpling caused by the fast cooling after 450°C calcination. The chunk-free and almost

smooth area exhibits more compact structure than the DP-25 based film as shown in Figure 3(b). Presumably, this is due to the small a-TiO<sub>2</sub> particles forming the high density A8R2 film. It is also noted from Figure 3(b) that the film made from DP-25, even with high porosity, showed appearance of breaks which may influence the electron transport and result in lower cell efficiency than that of A8R2 (see below). The A8R2 nanoparticles, on the other hand, can restrict the constriction resulting in the continuous less-crack and porous films upon calcination. Nevertheless, for both TiO<sub>2</sub> films, the crack produced voids in the preceding layer can be filled by the A8R2 and DP-25 paste during the next spin-coating process.

**3.2. Application of Mixed-Phase TiO<sub>2</sub> Photoelectrodes to DSSCs and the Photoelectrochemical Performance Measurement.** The above prepared A8R2 and DP-25 photoelectrodes were used to fabricate the solar cells for photoelectrochemical performance study [10, 11]. Figure 4 showed the typical current-voltage characteristics of N719-sensitized DSSCs for various film thickness of A8R2 films (a) and DP-25 films (b). Table 2 lists the photoelectric data of the DSSCs in Figure 4 including the amount of dye adsorbed on TiO<sub>2</sub> ( $A_{\text{dye}}$ ), the short-circuit photocurrent density ( $J_{\text{sc}}$ ), the open circuit voltage ( $V_{\text{OC}}$ ), the fill factor (FF), and the conversion efficiency ( $\eta$ ). It is apparent that the DSSC performance largely depends on the TiO<sub>2</sub> film thickness because changing the film thickness changes  $A_{\text{dye}}$ ,  $J_{\text{sc}}$ , and,  $\eta$  owing to the change of total TiO<sub>2</sub> surface area. To clarify relationship between the thickness, surface properties of the TiO<sub>2</sub> films, and the photoelectrochemical characteristics of the cells, comparison of  $\eta$  of DSSCs and the corresponded  $J_{\text{sc}}$  using A8R2 TiO<sub>2</sub> and DP-25 as a function of film thickness is plotted and shown in Figure 5(a). It is found that there is a parallel increase of efficiency for A8R2 cells (solid squares) and DP-25 cells (open squares) for TiO<sub>2</sub> film thickness

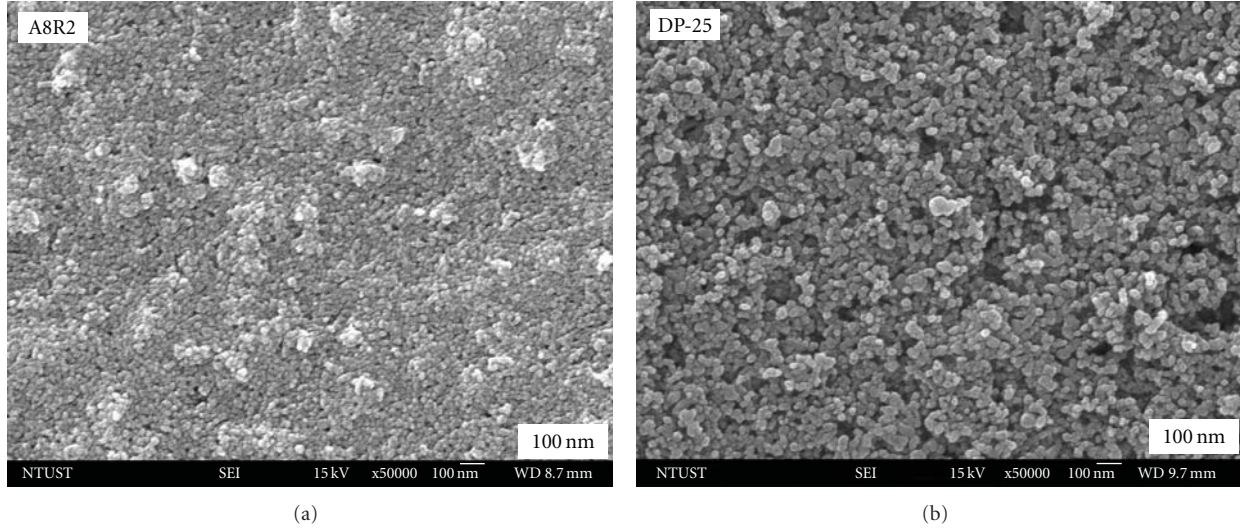


FIGURE 3: Top-view SEM micrographs of A8R2 (a) and DP-25 (b) spin coated on FTO substrates.

TABLE 1: Phase ratio from XRD of TiO<sub>2</sub> samples (A8R2 and DP-25) before (powder) and after (film) calcination, comparison of TiO<sub>2</sub> crystallite size (A8R2 and DP-25) of anatase (A) and rutile (R) from XRD, and particle size (A8R2 and DP-25, powder only) obtained from TEM and BET.

TiO <sub>2</sub> Sample	Phase ratio (%)		Crystallite size (nm)		TEM (nm)	BET (nm)
A8R2 powder	80.4 (A <sup>a</sup> )	20.0 (R <sup>b</sup> )	14.8 (A)	26.0 (R)	16.0 (A)	13.0 (A)
A8R2 film	63.0 (A)	37.0 (R)	13.1 (A)	26.3 (R)	30 × 60 (R)	56 (R)
DP-25 powder	80.7 (A)	19.3 (R)	22.5 (A)	25.6 (R)	30	29
DP-25 film	73.4 (A)	26.5 (R)	22.6 (A)	27.3 (R)		

<sup>a</sup>A: anatase phase. <sup>b</sup>R: rutile phase.

up to  $\sim 9 \mu\text{m}$ . Further increase in the thickness stabilizes the efficiency at an almost constant value upon increasing the thickness of TiO<sub>2</sub> thin films. The maximum efficiency acquired in DSSC using the A8R2 TiO<sub>2</sub> with film thickness of  $12 \mu\text{m}$  was 5.20% with  $J_{\text{sc}}$  of  $10.67 \text{ mA/cm}^2$ ,  $V_{\text{OC}}$  of 0.73 V, and FF of 0.69; while  $\eta$  of the cell using DP-25 with film thickness of  $16 \mu\text{m}$  reached 3.76% with  $J_{\text{sc}}$  of  $8.63 \text{ mA/cm}^2$ ,  $V_{\text{OC}}$  of 0.74 V, and FF of 0.59. The FF of DSSC is manipulated by device assembling technique which would affect the efficiency. Table 2 shows reasonable FF values compared with the other cases reported in the literatures [12, 13] and guarantee us a basic device fabrication technology.

It is generally believed that thicker TiO<sub>2</sub> film would uptake more N719 molecules leading to the enhancement in the photocurrent of the DSSC. As shown also in Figure 5(a), the influence of film thickness on  $J_{\text{sc}}$  of DSSCs constructed with A8R2 (solid triangles) and DP-25 (open triangles) demonstrates the consistent dependence of the film thickness on  $\eta$ . However, the variation of  $A_{\text{dye}}$  shows a continuous increase upon increasing of film thickness as shown in Figure 5(b) for both A8R2 (solid triangles) and DP-25 (solid squares). This result indicates the limited electron transport for thick films due to the increase of recombination centers and requisite path length of the injected electron to be collected by FTO. Moreover, when the TiO<sub>2</sub> films are thicker,

the films become less transparent which is detrimental to the light harvesting as well as DSSC performance.

Based on Figure 5, the A8R2 cells in general have superior performance than DP-25 cells. The efficiency and current density from average of seven A8R2 cells present in Table 2 are  $\sim 27.7\%$  ( $\eta$ ) and 29% ( $J_{\text{sc}}$ ) higher than those from average of six DP-25 cells. Higher efficiency and current density might be attributed to, first, the higher amount of adsorbed N719 for the A8R2 cell, owing to larger surface area of A8R2 powder ( $71$  and  $50 \text{ m}^2/\text{g}$  for A8R2 and DP-25, resp.) and more compact structure of A8R2 film (Figure 3). Higher UV absorption intensity of the N719 adsorbed on A8R2 film than DP-25 film (not shown) also supports this conclusion. Secondly, it could be due to the less cracks of A8R2 films (see above) which improved the short-circuit photocurrent [14]. Finally, with similar phase ratio of anatase to rutile TiO<sub>2</sub>, the electron transport of A8R2 film containing the one dimension (1D) bar-shape r-TiO<sub>2</sub> is expected to be faster than the DP-25 film containing polygonal TiO<sub>2</sub>. The electron transport properties of the DSSCs with TiO<sub>2</sub> electrodes made of A8R2 and DP-25 films were investigated by electrochemical impedance spectroscopy (EIS). According to the EIS spectra shown in Figure 6, the charge-transfer resistance at DP-25 electrode interface is larger than that at A8R2 interface. After the impedance data analysis by Zahner

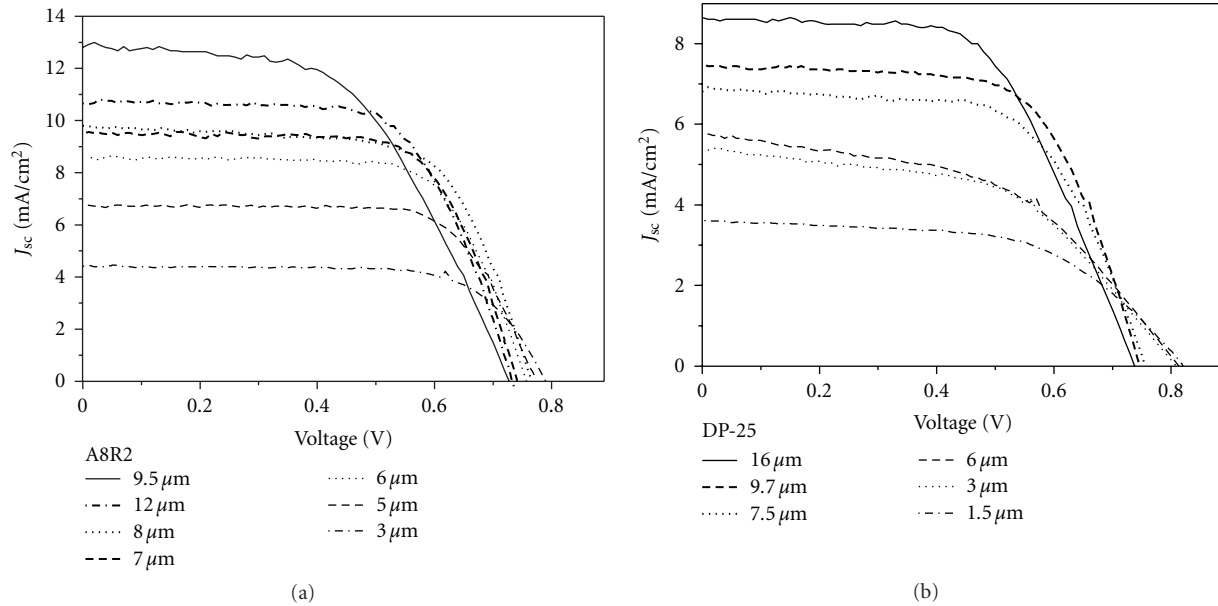


FIGURE 4: Photocurrent-voltage characteristics of DSSCs with different thicknesses of A8R2 films (a) and DP-25 films (b).

TABLE 2:  $I$ - $V$  characteristic data for all DSSCs fabricated by A8R2 and DP-25 electrodes with various film thickness.

TiO <sub>2</sub> Sample	Thickness ( $\mu\text{m}$ )	$A_{\text{dye}}^{\text{a}}$ ( $\mu\text{mole}/\text{cm}^2$ )	$J_{\text{sc}}^{\text{b}}$ ( $\text{mA}/\text{cm}^2$ )	$V_{\text{OC}}^{\text{c}}$ (V)	FF <sup>d</sup>	$\eta^{\text{e}}$ (%)
A8R2-1	3.0	0.014	4.41	0.79	0.75	2.61
A8R2-2	5.0	0.043	6.71	0.77	0.72	3.71
A8R2-3	6.0	0.101	8.57	0.76	0.70	4.54
A8R2-4	7.0	0.110	9.53	0.74	0.69	4.89
A8R2-5	8.0	0.118	9.80	0.77	0.66	4.97
A8R2-6	9.5	0.159	10.50	0.74	0.67	4.92
A8R2-7	12.0	0.201	10.67	0.73	0.69	5.20
P25-1	1.5	0.022	3.43	0.82	0.56	1.69
P25-2	3.0	0.036	5.40	0.80	0.57	2.34
P25-3	6.0	0.059	5.93	0.80	0.54	2.38
P25-4	7.5	0.060	6.78	0.76	0.63	3.25
P25-5	9.7	0.064	7.49	0.75	0.64	3.61
P25-6	16.0	0.107	8.63	0.74	0.59	3.76

<sup>a</sup> $A_{\text{dye}}$ : amount of dye adsorbed on TiO<sub>2</sub>. <sup>b</sup> $J_{\text{sc}}$ : short-circuit photocurrent density. <sup>c</sup> $V_{\text{OC}}$ : open circuit voltage. <sup>d</sup>FF: fill factor. <sup>e</sup> $\eta$ : cell efficiency.

software through fitting the data with appropriate equivalent circuit [15], the estimate electron transport resistance for DSSCs with DP-25 and A8R2 is 0.239  $\Omega$  and 0.105  $\Omega$ , respectively. This result is consistent with the superior efficiency of A8R2 cell than the DP-25 cell.

To confirm that the A8R2 cell has the optimized a-TiO<sub>2</sub>-to-r-TiO<sub>2</sub> ratio for cell performance, we have fabricated DSSCs based on the mixed a-TiO<sub>2</sub> and r-TiO<sub>2</sub> composite films with weight ratio (wt%) of 9:1 (A9R1), 8:2 (A8R2) and 7:3 (A7R3). It was found that for the similar thickness of TiO<sub>2</sub> films, the A8R2 cell showed higher efficiency ( $\eta$ ) by about 6.0% and 3.4% respectively, compared to A9R1 and A7R3 cells. With the increase of the r-TiO<sub>2</sub> content from A9R1 to A8R2,  $\eta$  was enhanced due to the faster electron transport rate as envisaged above. Upon further

increase of r-TiO<sub>2</sub> content to A7R3, the cell efficiency decreased, presumably because less dye molecules had been adsorbed. This result could be attributed to the decrease of total surface area for sensitizers due to the smaller specific surface area of r-TiO<sub>2</sub> (27 m<sup>2</sup>/g) compared to that of a-TiO<sub>2</sub> (116 m<sup>2</sup>/g). A more precise fine-tuning of the a-TiO<sub>2</sub>-to-r-TiO<sub>2</sub> ratio to optimize DSSC performance would require further experimental investigation.

#### 4. Conclusion

Irregular oval-shape a-TiO<sub>2</sub> and bar-shape r-TiO<sub>2</sub> nanoparticles were prepared by hydrolysis and peptization of TNB followed by hydrothermal treatment. The cell efficiency of DSSCs made from mixed-phase A8R2 and DP-25 showed

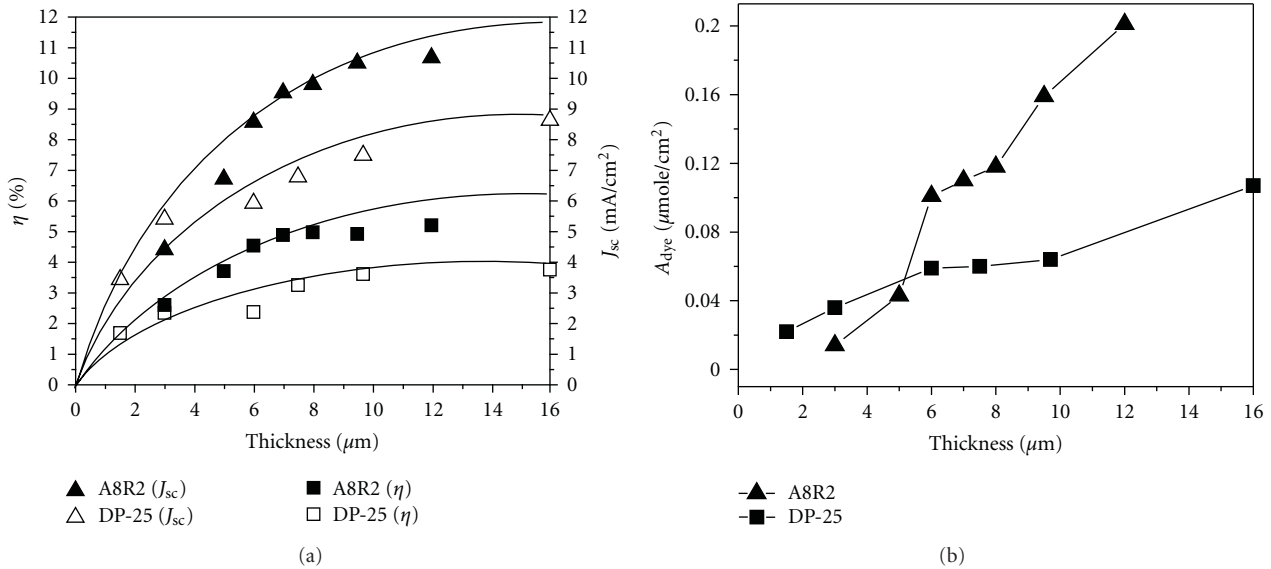


FIGURE 5: Influence of film thickness on conversion efficiency ( $\eta$  (a)), current density ( $J_{sc}$  (a)), and amount of adsorbed dye ( $A_{dye}$  (b)) on  $\text{TiO}_2$  films.

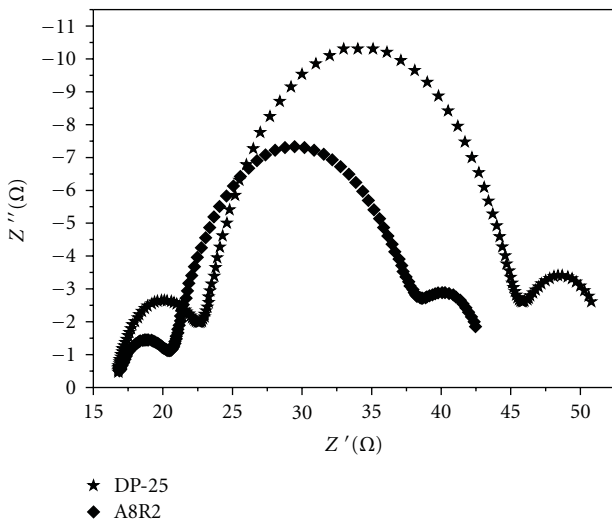


FIGURE 6: EIS spectra of the DSSCs made of DP-25 and A8R2 films.

the similar thickness dependence. The efficiency increases with film thickness and reaches a maximum plateau at thickness above  $\sim 9 \mu\text{m}$ . The A8R2 film shows more compact structure with consistent and superior DSSC performance than DP-25 cells. This could be due to the higher amount of adsorbed N719 on A8R2 film, less cracks of A8R2 film, and faster electron transport of A8R2 film containing the 1D bar-shape  $r\text{-TiO}_2$ .

### Acknowledgment

The authors gratefully acknowledge the financial support of the National Science Council of Taiwan, Taiwan (Contract no. NSC96-2113-M-027-005-MY2 and NSC 96-2113-M-008-002-MY3).

### References

- [1] B. O'Regan and M. Grätzel, "A low-cost, high-efficiency solar cell based on dye-sensitized colloidal  $\text{TiO}_2$  films," *Nature*, vol. 353, no. 6346, pp. 737–740, 1991.
- [2] U. Diebold, "The surface science of titanium dioxide," *Surface Science Reports*, vol. 48, no. 5-8, pp. 53–229, 2003.
- [3] N.-G. Park, J. Van de Lagemaat, and A. J. Frank, "Comparison of dye-sensitized rutile- and anatase-based  $\text{TiO}_2$  solar cells," *Journal of Physical Chemistry B*, vol. 104, no. 38, pp. 8989–8994, 2000.
- [4] C.-C. Wang and J. Y. Ying, "Sol-gel synthesis and hydrothermal processing of anatase and rutile titania nanocrystals," *Chemistry of Materials*, vol. 11, no. 11, pp. 3113–3120, 1999.
- [5] H. Cheng, J. Ma, Z. Zhao, and L. Qi, "Hydrothermal preparation of uniform nanosize rutile and anatase particles," *Chemistry of Materials*, vol. 7, no. 4, pp. 663–671, 1995.
- [6] H.-S. Chen, C. Su, J.-L. Chen, T.-Y. Yang, N.-M. Hsu, and W.-R. Li, "Preparation and characterization of pure rutile  $\text{TiO}_2$  nanoparticles for photocatalytic study and thin films for dye-sensitized solar cells," *Journal of Nanomaterials*. In press.
- [7] C. Su, C.-M. Tseng, L.-F. Chen, B.-H. You, B.-C. Hsu, and S.-S. Chen, "Sol-hydrothermal preparation and photocatalysis of titanium dioxide," *Thin Solid Films*, vol. 498, no. 1-2, pp. 259–265, 2006.
- [8] H.-S. Chen, C. Su, C.-K. Lin, Y.-F. Hsieh, C.-K. Yang, and W.-R. Li, "Hydrothermal preparation of anatase  $\text{TiO}_2$  nanoparticles for dye-sensitized solar cells," *Journal of Chemical Engineering of Japan*, vol. 42, supplement 1, pp. 36–42, 2009.
- [9] Y. Hu, H.-L. Tsai, and C.-L. Huang, "Phase transformation of precipitated  $\text{TiO}_2$  nanoparticles," *Materials Science and Engineering A*, vol. 344, no. 1-2, pp. 209–214, 2003.
- [10] A. Fujishima and K. Honda, "Electrochemical photolysis of water at a semiconductor electrode," *Nature*, vol. 238, no. 5358, pp. 37–38, 1972.
- [11] M. Grätzel, "Photoelectrochemical cells," *Nature*, vol. 414, no. 6861, pp. 338–344, 2001.

- [12] Y. Guo, N.-H. Lee, H.-J. Oh et al., "Preparation of titanate nanotube thin film using hydrothermal method," *Thin Solid Films*, vol. 516, no. 23, pp. 8363–8371, 2008.
- [13] M. C. Kao, H. Z. Chen, S. L. Young, C. Y. Kung, and C. C. Lin, "The effects of the thickness of TiO<sub>2</sub> films on the performance of dye-sensitized solar cells," *Thin Solid Films*, vol. 517, no. 17, pp. 5096–5099, 2009.
- [14] L. Han, N. Koide, Y. Chiba, and T. Mitate, "Modeling of an equivalent circuit for dye-sensitized solar cells," *Applied Physics Letters*, vol. 84, no. 13, pp. 2433–2435, 2004.
- [15] J.-J. Wu, G.-R. Chen, H.-H. Yang, C.-H. Ku, and J.-Y. Lai, "Effects of dye adsorption on the electron transport properties in ZnO-nanowire dye-sensitized solar cells," *Applied Physics Letters*, vol. 90, no. 21, Article ID 213109, 2007.

## Research Article

# Preparation and Characterization of Pure Rutile TiO<sub>2</sub> Nanoparticles for Photocatalytic Study and Thin Films for Dye-Sensitized Solar Cells

Huei-Siou Chen,<sup>1</sup> Chaochin Su,<sup>1</sup> Ji-Lian Chen,<sup>1</sup> Tsai-Yin Yang,<sup>1</sup> Nai-Mu Hsu,<sup>2</sup> and Wen-Ren Li<sup>2</sup>

<sup>1</sup>Institute of Organic and Polymeric Materials, National Taipei University of Technology, Taipei 106, Taiwan

<sup>2</sup>Department of Chemistry, National Central University, Chung-Li 320, Taiwan

Correspondence should be addressed to Chaochin Su, f10913@ntut.edu.tw and Wen-Ren Li, ch01@ncu.edu.tw

Received 31 May 2010; Accepted 8 September 2010

Academic Editor: William W. Yu

Copyright © 2011 Huei-Siou Chen et al. This is an open access article distributed under the Creative Commons Attribution License, which permits unrestricted use, distribution, and reproduction in any medium, provided the original work is properly cited.

Pure rutile-phase TiO<sub>2</sub> (r-TiO<sub>2</sub>) was synthesized by a simple one pot experiment under hydrothermal condition using titanium (IV) n-butoxide as a Ti-precursor and HCl as a peptizer. The TiO<sub>2</sub> products were characterized by XRD, TEM, ESCA, and BET surface area measurement. The r-TiO<sub>2</sub> were rodlike in shape with average size of ~61 × 32 nm at hydrothermal temperature of 220°C for 10 h. Hydrothermal treatment at longer reaction time increased the tendency of crystal growth and also decreased the BET surface area. The degradation of methylene blue was selected as a test reaction to confer the photocatalytic activity of as-obtained r-TiO<sub>2</sub>. The results showed a strong correlation between the structure evolution, particle size, and photocatalytic performance of r-TiO<sub>2</sub>. Furthermore, the r-TiO<sub>2</sub>-based solar cell was prepared for the photovoltaic characteristics study, and the best efficiency of ~3.16% was obtained.

## 1. Introduction

Titanium dioxide (TiO<sub>2</sub>), is one of the most popular and promising materials in the field of photocatalytic applications due to its strong oxidizing power, high photostability, and redox selectivity [1]. When TiO<sub>2</sub> is irradiated by photons with an energy higher than or equal to its band gap (~3.2 eV), through photon absorption, the electrons can be promoted to the conduction band, generating holes in the valence band. The photogenerated electrons and holes migrate to the TiO<sub>2</sub> surfaces where they can induce reduction and/or oxidation of adsorbed molecules. TiO<sub>2</sub> is also a commonly used semiconductor for photon-electron transfer processes. In the dye-sensitized solar cells (DSSCs) invented by Grätzel et al., nanosized TiO<sub>2</sub> particles were used for preparing working electrodes, and the cell performance was found to be improved significantly when compared to the flat layered photoelectrodes [2]. The TiO<sub>2</sub> crystal exists in two major forms: rutile and anatase

[3, 4]. Anatase is thermodynamically metastable and can be transformed irreversibly to rutile phase at high temperatures [3, 5]. Most of the chemistry researchers have paid greater attention to anatase TiO<sub>2</sub> than rutile TiO<sub>2</sub> (r-TiO<sub>2</sub>) in both photocatalytic reactions and photoelectrochemical cell because anatase phase of TiO<sub>2</sub> had been considered to be more active than rutile. Several excellent properties of r-TiO<sub>2</sub>, such as chemical inertness, superior light scattering characteristics, and lower cost [3, 6], however, make it a potentially important phase in photocatalytic and photovoltaic applications. Wang et al. reported the high photocatalytic activity of r-TiO<sub>2</sub> for decomposition of rhodamine-B in water under artificial solar light irradiation [7]. Bacsá and Kiwi found that the presence of r-TiO<sub>2</sub> showed enhanced catalytic activity compared to pure anatase TiO<sub>2</sub> during the degradation of *p*-coumaric acid [8]. Rutile phase has also been shown to be more active than anatase in photodecomposition of H<sub>2</sub>S [9], and photooxidation of H<sub>2</sub>O with Fe<sup>3+</sup> [10]. Park et al. showed that the photovoltaic

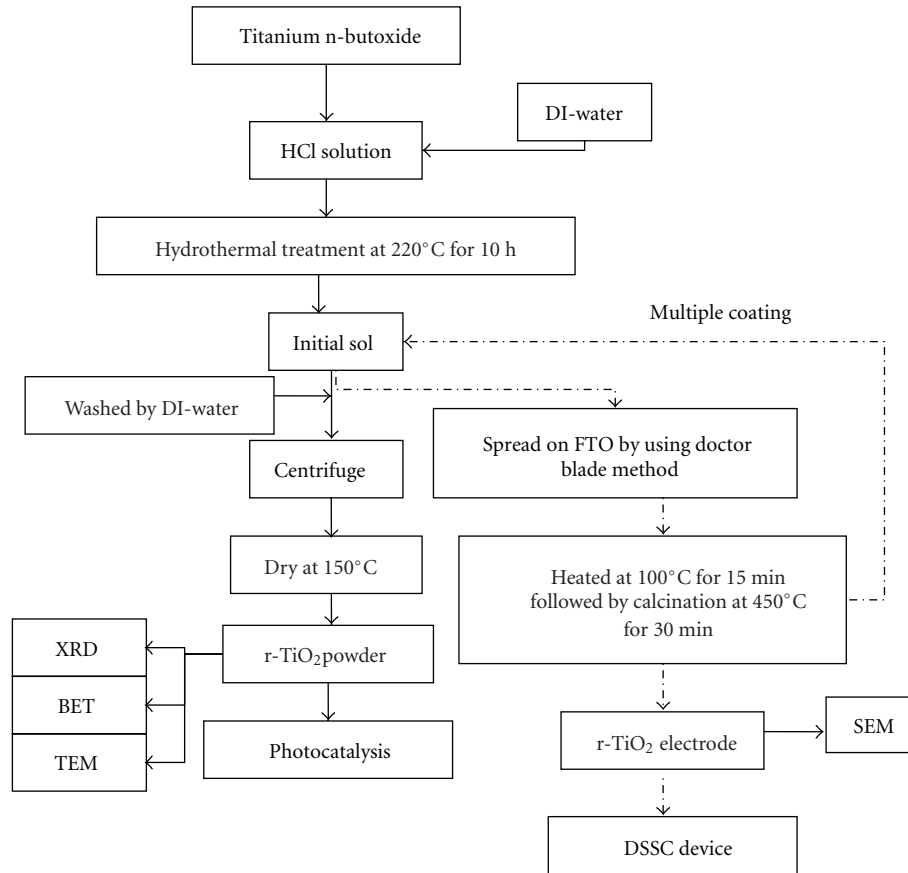


FIGURE 1: Flow chart of the method for preparing r-TiO<sub>2</sub> by sol-hydrothermal synthesis.

characteristics of rutile TiO<sub>2</sub>-based DSSCs are comparable to those of anatase TiO<sub>2</sub>-based solar cells [11, 12]. However, due to the insufficient TiO<sub>2</sub> film thickness which is less than 5 μm, the electron injection current and the photon to electron conversion efficiency are limited. It has been proposed that porous film electrodes composed of one-dimensional (1D) nanomaterials provide direct electron conducting channels to the electrodes, thus the solar cell efficiency can be enhanced [13]. Previously, we had successfully prepared the 1D rod-shaped r-TiO<sub>2</sub> nanoparticles by sol-hydrothermal procedure [14]. In continuation of the previous work, we are presenting here with more detailed investigation of the influence of hydrothermal conditions, including the acid concentration and hydrothermal duration on the crystal structure, particle size, particle morphology, and photocatalytic activity of r-TiO<sub>2</sub> nanoparticles. The photocatalytic activity of the derived r-TiO<sub>2</sub> photocatalysts was tested by methylene blue degradation reactions under UV illumination. We also prepared nanocrystalline r-TiO<sub>2</sub> films up to 21 μm in thickness for DSSC study. The effect of r-TiO<sub>2</sub> film thickness and morphology on the photoelectrochemical properties was examined. The overall efficiency of r-TiO<sub>2</sub>-based DSSC device is rationalized in terms of r-TiO<sub>2</sub> film thickness and amount of dye adsorbed into the electrodes to find a meaningful property-efficiency correlation.

## 2. Experimental

**2.1. Hydrothermal Synthesis of Rutile TiO<sub>2</sub> Nanorods.** Figure 1 shows the schematic diagram for preparing r-TiO<sub>2</sub> nanorods. This procedure is based on the previous sol-hydrothermal process for synthesis of TiO<sub>2</sub> nanoparticles [15] with some modification. Titanium (IV) n-butoxide (Ti(O-Bu)<sub>4</sub>, ACROS), as a Ti precursor, was added slowly to hydrogen chloride solution (HCl) under magnetic stirring until a clear sol was formed. Then, distilled water was added dropwise into the sol and continuously stirred for three days. The white mixture formed was then transferred to a Teflon-lined autoclave, 40% filled, and heated at 220°C for various durations. After cooling to room temperature, the products presented in the bottom layer were washed with distilled water several times and finally dried at 150°C to obtain crystallized products. The such-obtained TiO<sub>2</sub> samples were characterized by the transmission electron microscope (TEM, Hitachi, H-7100) for microstructural properties and X-ray diffraction (XRD, Japan MAC Science, MXP 18) for crystalline phase. All peaks measured by XRD analysis were assigned by comparing with those of JCPDS data. The crystal size of the TiO<sub>2</sub> during different states of heat treatment was obtained by the XRD line profile analysis. The Brunauer, Emmett, and Teller (BET) surface area was obtained from nitrogen adsorption-desorption data

(Micromeritics, ASAP-2010). The chemical composition was verified using the electron spectroscopy for chemical analysis (ESCA, VG Scientific ESCALAB 250).

**2.2. Photocatalysis by Rutile TiO<sub>2</sub> Nanorods.** The photocatalytic reaction was carried out in a custom-made photoreactor (FanChun Technology Inc., PR-2000) [16]. The system is open to air atmosphere with sixteen UV-lamps in total (wavelength  $253.7 \pm 0.8$  nm, Sankyo Denki Co., LTD.) circulating a quartz reaction cell. The power at the position of the reactor center, measured in the air by a power meter (Moletron, PM 150x), was about  $(1.2 \pm 0.2)$  mWcm<sup>-2</sup>. UV-Vis spectrometry (JASCO V-630) was used to monitor the absorption spectra of methylene blue (MB) as a function of illumination time. Before the photoreaction experiment, the aqueous solution of MB with initial concentration ( $[C_0]$ ) of  $5 \times 10^{-5}$  mol/l (M) was stirred utterly in the presence of r-TiO<sub>2</sub> sample in the dark to ensure the complete equilibrium of adsorption process. During illumination, a 4 mL aliquot was sampled at various time intervals and centrifuged to separate MB solution for analysis. The photocatalytic efficiencies of the r-TiO<sub>2</sub> samples prepared by hydrothermal treatment for various duration (1, 5, 10, 15, 20, and 24 h) were compared.

**2.3. Preparation of Rutile TiO<sub>2</sub> Photoanodes and DSSC Performance Measurement.** A doctor-blading technique was used to prepare the r-TiO<sub>2</sub> films on an FTO- (F-doped tin oxide-) coated conductive glass ( $2 \times 3.3 \times 0.3$  cm<sup>3</sup>, Solaronix, sheet resistance  $8 \Omega\text{cm}^{-2}$ ) as DSSC photoanodes. Two edges of the FTO substrate were covered with Scotch tapes. The r-TiO<sub>2</sub> sol obtained after hydrothermal treatment for 10 h was directly applied to one of the bare edges and flattened with a home-made doctor blade by shearing across the tape-covered edges. The resulted r-TiO<sub>2</sub> electrodes were dried at 100°C for 15 min followed by subsequent calcination at 450°C for 30 min in order to remove the organic residues from the final products and to complete the crystallization. Thickness of the film was controlled by multiple coating process in which the coated substrates were subjected repeatedly to doctor-blade coating, drying, and calcination steps (Figure 1). The thickness of the r-TiO<sub>2</sub> films was measured by a Mahr Alpha-step profiler (Perthometer S2) and confirmed by the scanning electron microscopy (SEM, Hitachi S-2400) images of cross sections. The surface morphology and crystal phase of r-TiO<sub>2</sub> films were investigated by SEM and XRD, respectively.

For photosensitization studies, the r-TiO<sub>2</sub> electrodes with working area of 0.25 cm<sup>2</sup> were immersed in ethyl alcohol containing  $3 \times 10^{-4}$  M N3 dye (Ru[L2(NCS)2], L = 2,2'-bipyridine-4,4'-dicarboxylic acid, Solaronix) for 24 h at room temperature. The Pt counter electrodes with mirror finish were prepared by sputtering deposition (Hitachi E-1045 ion sputter) of a 20 nm layer of Pt on top of FTO substrates. To assemble the DSSC, the electrolyte of 0.5 M LiI (Acros, 99%), 0.05 M I<sub>2</sub> (Showa, 99.8%), 0.5 M 4-*tert*-butylpyridine-TBP (Aldrich, 99%), and 0.5 M 1,2-dimethyl-3-propylimidazolium iodide-DMPII (IonLic-Tech. >98%) in acetonitrile was applied to the Pt electrode, which was

then placed over the dye-coated r-TiO<sub>2</sub> electrode to form a sandwich-type clamped cell for photovoltaic study.

The photocurrent versus voltage (I-V) curves were measured using a computerized digital multimeter (Keithley, 2400) under the AM1.5 irradiation (1 sun), provided by a class A Thermo Oriel Xenon lamp light source (300 W). The incident power density was 100 mW cm<sup>-2</sup> using NREL-calibrated monocrystalline Si-Solar cell (PVM134 reference cell, PV Measurement Inc.) for calibration. The efficiencies were calculated by Forter software.

### 3. Results and Discussion

**3.1. Characterization of Rutile TiO<sub>2</sub> Nanorods.** The sol-hydrothermal reaction employed in the present work led to the formation of nanocrystalline TiO<sub>2</sub>. The crystal properties depend on the peptization and hydrothermal treatment, such as acid concentration and time period. The previous study showed that using different acids in a hydrothermal reaction resulted in the formation of different TiO<sub>2</sub> phase [17]. The product was pure rutile from an HCl medium, however, if the concentration of HCl was reduced to 1.5 M, besides rutile, anatase phase was generated as a side product. This implied that the formation of anatase by using HCl as a peptizer was more difficult than that of rutile phase. Based on this result, we selected an HCl concentration of 3 M for the preparation of r-TiO<sub>2</sub> in the study presented here. Figure 2 shows a series of XRD patterns for r-TiO<sub>2</sub> after hydrothermal treatment at 220°C for various duration. For convenience, the r-TiO<sub>2</sub> samples are hereinafter abbreviated as Ht-A-B, where A and B represent the hydrothermal temperature (°C) and heating duration (h), respectively. It can be seen that pure rutile TiO<sub>2</sub> could be successfully obtained with 3 M HCl for the studied hydrothermal period from 1 to 24 hrs. This result infers that the complete formation of rutile phase could be accomplished in the solution at relatively low temperatures under appropriate conditions. In a general sol-gel process for preparing TiO<sub>2</sub>, the primary formed structure phase observed at low temperature is anatase which transforms to thermodynamically most stable and more condense rutile phase only upon calcinating at temperature above 500°C [1]. Note that the rutile XRD peaks became sharper as hydrothermal treatment prolonged indicating the formation of larger r-TiO<sub>2</sub>. The crystal sizes of r-TiO<sub>2</sub> obtained by analyzing the half maximum (FWHM) of (110) peak at  $2\theta = 27.45$  degree using the Scherrer equation with wavelength of the radiation of 1.5405 Å are summarized in Table 1.

The above XRD results indicate formation of r-TiO<sub>2</sub> crystals that can be confirmed by the ESCA measurement. Figure 3 shows the typical ESCA survey spectra of r-TiO<sub>2</sub> samples. The peaks appearing on the left side showed the Ti2p doublet with bonding energies of 459.4 eV for Ti2p<sub>3/2</sub> and 464.9 eV for Ti2p<sub>1/2</sub>. The right side spectrum showed the O1s peak with binding energy of 530.4 eV. Those binding energies of Ti2p and O1s from r-TiO<sub>2</sub> samples are all in good agreement with those in standard spectrum of TiO<sub>2</sub>. Compared to the individual photoelectron peaks for O1s and Ti2p from nonbonded Ti and O elements, different binding energies due to the chemical shifts were found. The binding

TABLE 1: The XRD crystal domain, TEM particle size, BET surface area of r-TiO<sub>2</sub> samples, and their photocatalytic activities for photodecomposition of methylene blue in aqueous solution.

r-TiO <sub>2</sub> sample	Domain size (nm)	Particle size in length $\times$ width (nm)	BET (m <sup>2</sup> /g)	Reaction rate $k_a$ (min <sup>-1</sup> )
Ht-220-1	9.92	26.3 $\times$ 10.8	161.72	$7.56 \times 10^{-3}$
Ht-220-5	20.58	50.5 $\times$ 18.5	46.73	$8.61 \times 10^{-3}$
Ht-220-10	25.73	60.9 $\times$ 31.7	35.45	$9.29 \times 10^{-3}$
Ht-220-15	28.39	71.1 $\times$ 31.0	28.71	$1.52 \times 10^{-2}$
Ht-220-20	29.41	62.8 $\times$ 31.9	28.44	$1.10 \times 10^{-2}$
Ht-220-24	31.60	76.9 $\times$ 36.5	18.93	$1.04 \times 10^{-2}$

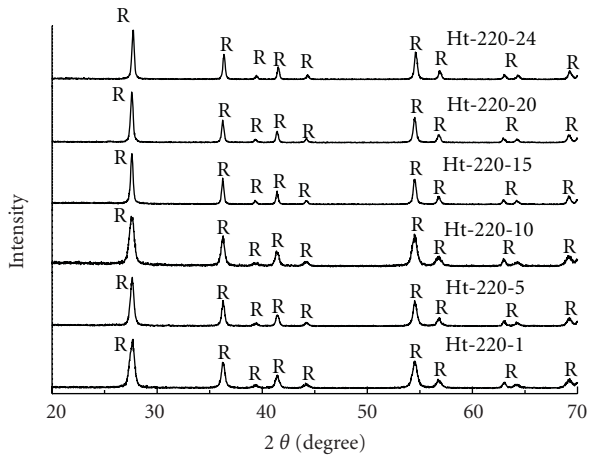


FIGURE 2: A series of XRD peaks for the prepared r-TiO<sub>2</sub> powders after hydrothermal treatment for various duration.

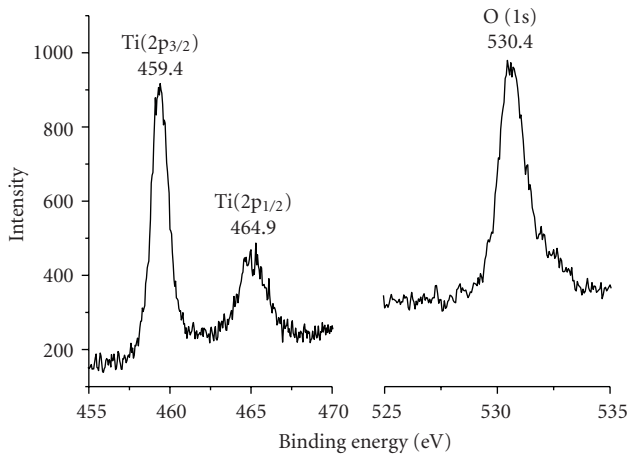


FIGURE 3: The ESCA spectra of r-TiO<sub>2</sub> sample for Ti 2p (left side) and O 1s (right side).

energy of the core level electron depends critically on the species to which it is bonded. Charge transfer from Ti to O leaves Ti (and O) with partial positive (and negative) charges, leading to a shift in core level to higher (Ti2p<sub>3/2</sub>, 453.7 to 459.4 eV; Ti2p<sub>1/2</sub>, 461.2 to 464.9 eV) and lower (O1s, 531 to 530.4 eV) binding energies associated with increased (and

decreased) Coulombic attraction between core electron and the nucleus of Ti (and O) [14].

The crystal growth in different stage of hydrothermal process was traced by TEM. Figure 4 shows the TEM micrographs of r-TiO<sub>2</sub> samples hydrothermally treated at 220°C for (a) 1, (b) 5, (c) 10, (d) 15, (e) 20, and (f) 24 h. As shown in Figure 4, in the initial stage of newly formed TiO<sub>2</sub> sol, the shape of the TiO<sub>2</sub> was observed as elliptical (Figure 4(a)) with average size of 26.3  $\times$  10.8 nm. Upon increasing the autoclaving time, the r-TiO<sub>2</sub> crystallites build up rod-like morphology progressively. Prolonging the hydrothermal treatment also increases the average particle dimension based on the weighted-average analysis. In other words, increasing autoclaving time promotes the tendency of crystal growth under the present experimental conditions as expected from XRD analysis. In addition, a broad particle size distribution (not shown) was observed in terms of width and length, indicating that the nucleation of r-TiO<sub>2</sub> is much slower than its growth. The range of particle size is from 26.3  $\times$  10.8 to 76.9  $\times$  36.5 nm in length  $\times$  width as listed in Table 1. Nevertheless, the crystals of small size from XRD indicate the incomplete crystallization for hydrothermal treatment up to 24 h.

The size variation of r-TiO<sub>2</sub> can also be seen from BET surface area measurement. The results listed in Table 1 show the dependence of the surface area of r-TiO<sub>2</sub> on the hydrothermal reaction time. It can be seen that the specific surface area shifts towards smaller values for longer heat treatment. The TiO<sub>2</sub> sample with one hour of hydrothermal treatment at 220°C possesses high specific surface area (162 m<sup>2</sup>/g) which then decreased appreciably with a limited value around 19 m<sup>2</sup>/g after 24 h of hydrothermal treatment. This result confirms the observation from TEM and indicates an increase in the particle size of r-TiO<sub>2</sub> in increasing the reaction time. Obviously, this is due to the progressive aggregation of small crystallites into larger particles. It is known that the TiO<sub>2</sub> crystals grow from TiO<sub>6</sub> octahedra that are terminated by the surface Ti-OH groups. During the hydrothermal treatment under acidic condition, the surface hydroxyl groups can be protonated to form Ti-OH<sub>2</sub><sup>+</sup> which then combines readily with another Ti-OH to form Ti-O-Ti oxygen bridge by eliminating a water molecule (dehydration) through which the crystals grow to a larger size [4]. It is noted that the growth of rutile TiO<sub>2</sub> proceeded via oriented coalescence of the first formed TiO<sub>2</sub> nanorods as demonstrated by many side-by-side aggregated r-TiO<sub>2</sub>

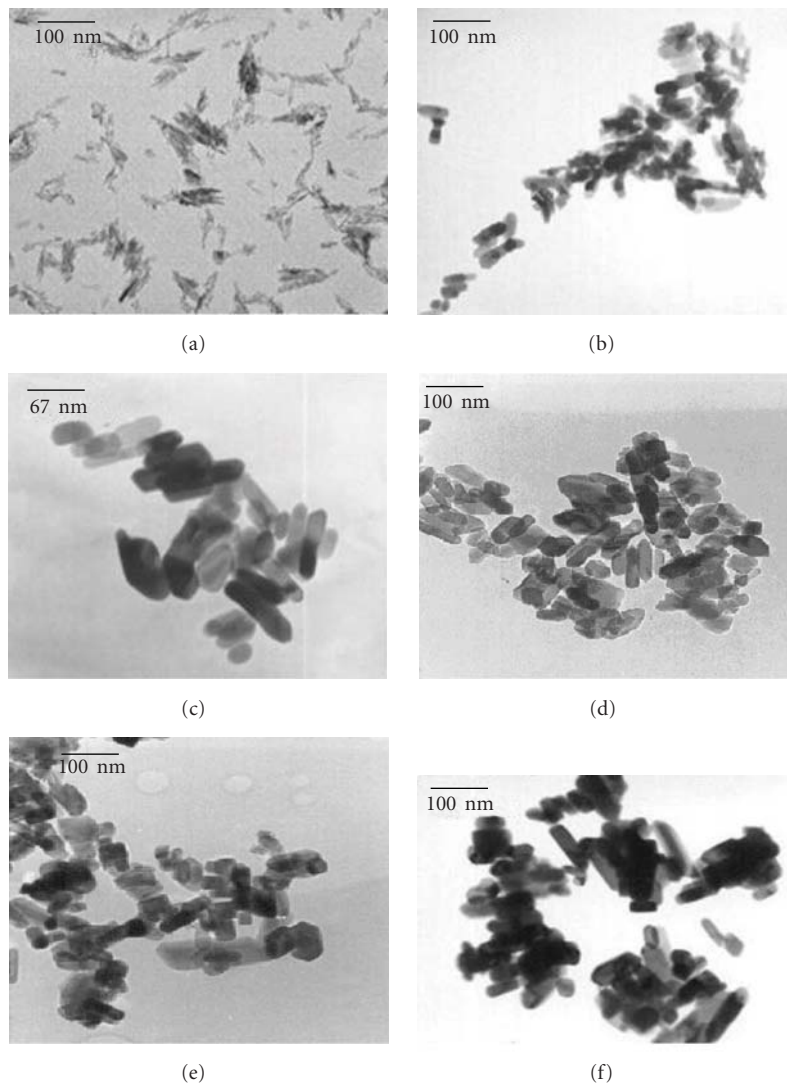


FIGURE 4: The TEM micrographs of r-TiO<sub>2</sub> samples hydrothermally treated at 220°C for (a) 1, (b) 5, (c) 10, (d) 15, (e) 20, and (f) 24 hrs.

(Figures 4(c)–4(f)) and the simultaneous increase of width and length of r-TiO<sub>2</sub> from TEM analysis.

**3.2. Photocatalytic Activity of Rutile TiO<sub>2</sub>.** In order to study the photocatalytic activity of the above-prepared r-TiO<sub>2</sub>, the photodecomposition of methylene blue (MB) was investigated in aqueous heterogeneous suspensions under the acidic condition. We chose pH 3.85 to study the photodegradation of MB because it decomposed scarcely in the absence of TiO<sub>2</sub> upon irradiation up to 7 h [16]. The maximal absorption of MB solutions is at 614 and 664 nm under our experimental conditions. The photodegradation was studied by monitoring the variation of intensity at 664 nm. Figure 5 plots the relative concentration  $[C]/[C_0]$  of MB against irradiation time of r-TiO<sub>2</sub> samples prepared by hydrothermal treatment at 220°C for different time period. With r-TiO<sub>2</sub>, the MB showed significant decrease in the absorbance upon irradiation. It is noted that varying the hydrothermal-treated period changes the photocatalytic efficiency of r-TiO<sub>2</sub>. The

photocatalytic activity of r-TiO<sub>2</sub> increases with an increase in hydrothermal time from 1 to 15 h, but it decreases for r-TiO<sub>2</sub> with further hydrothermal treatment (20 and 24 h). There are two major variables that can vary during the hydrothermal process: crystallinity and surface area. Increasing the hydrothermal time increases the crystalline domain of r-TiO<sub>2</sub> based on XRD analysis but decreases the specific surface area based on BET measurement (Table 1). Increase in crystallinity is a positive change in photocatalytic activity since amorphous titania is known to have very low photocatalytic efficiency [1, 18]. Decrease in surface area, on the other hand, is a negative change in photocatalytic activity due to the reduction of surface hydroxyl groups (–OH). The photocatalysis is basically a surface phenomenon that is being very sensitive to the amount of surface OH groups which may act as the principal reactive oxidant in the photoreactions of TiO<sub>2</sub> [19]. To derive the kinetic information, the decay of absorption due to the photodecomposition of MB was tentatively assumed to follow the first-order kinetics:

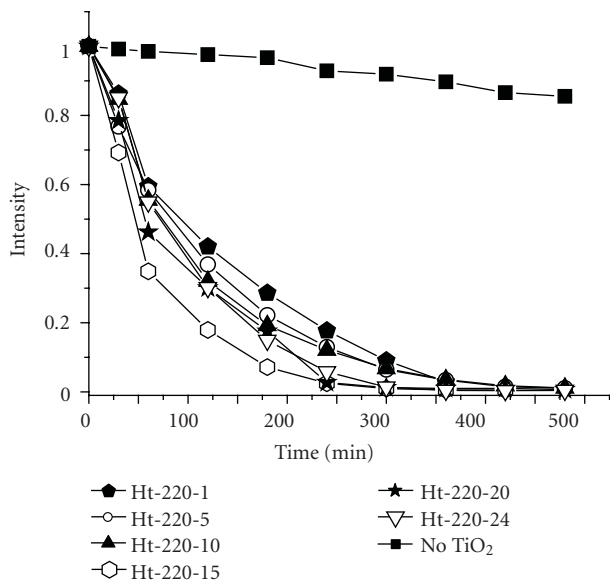


FIGURE 5: The variation of MB intensity at the  $\lambda_{\max} = 664$  nm as a function of UV irradiation time in the absence (black solid square) and presence of r-TiO<sub>2</sub> samples prepared for various hydrothermal time.

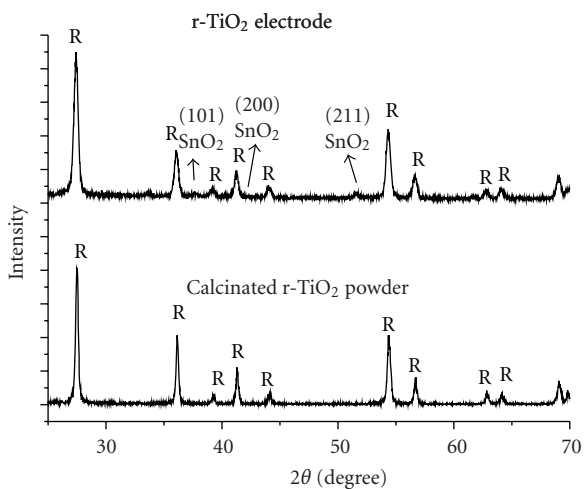


FIGURE 6: The XRD spectra for r-TiO<sub>2</sub> electrode and r-TiO<sub>2</sub> powder after calcination at 450°C.

rate =  $-d[C]/dt = k_a[C]$ , where  $k_a$  is the apparent rate constant for MB decomposition and  $[C]$  is the concentration of MB. To determine the reaction rate constant, curves of the variation of MB concentration as a function of illumination time were fit into this model. The rate constants for photodecomposition of MB using various r-TiO<sub>2</sub> samples are also listed in Table 1. At longer hydrothermal-treated period (up to 15 h), the MB decomposition rate increases which is associated with the improvement of r-TiO<sub>2</sub> crystallinity. Further hydrothermal treatment for more than 20 h, the photocatalysis efficiency of r-TiO<sub>2</sub> is deteriorated, which is believed to be due to the decrease in surface area.

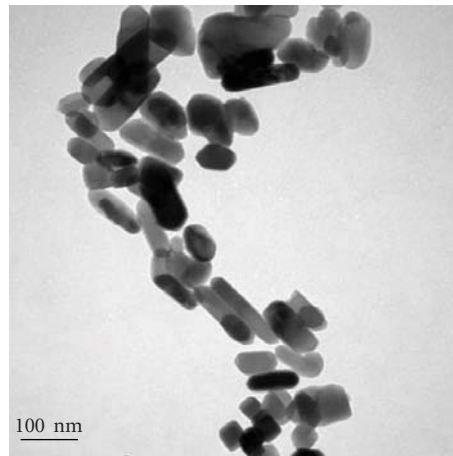


FIGURE 7: TEM picture of 450°C calcined r-TiO<sub>2</sub> powder.

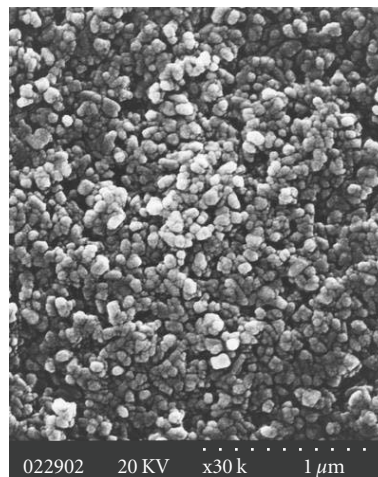


FIGURE 8: A top-view SEM image of r-TiO<sub>2</sub> electrodes.

**3.3. Application of Rutile TiO<sub>2</sub> to DSSCs.** DSSC is a quite complicated system, and there are many factors influencing the cell efficiency [20]. One of the most important parameters is the TiO<sub>2</sub> electrode. The crystal phase, particle shape, diameter, and surface composition of TiO<sub>2</sub> samples used will affect the dye adsorption, electron transport, and electrolyte diffusion in the cell as well as the light-to-electricity conversion efficiency. In this work, we chose r-TiO<sub>2</sub> samples obtained after 10 h hydrothermal treatment to prepare the photoanodes for DSSC study because of higher surface area with good crystallinity. As shown in Table 1, the specific surface area shifts towards smaller values for further heat treatment. The film preparation procedure and condition also play significant effect in the resultant electrode property, in particular, the film morphology and porosity. The r-TiO<sub>2</sub> electrodes were prepared according to the procedures described in Section 2.3. The XRD pattern as shown in Figure 6 exhibited peaks corresponding to rutile phase TiO<sub>2</sub> indicating the presence of stable rutile phase after 30 min 450°C calcination. Several small peaks appear at  $2\theta = 38.0, 42.6,$  and  $51.8$  are assigned to SnO<sub>2</sub> from

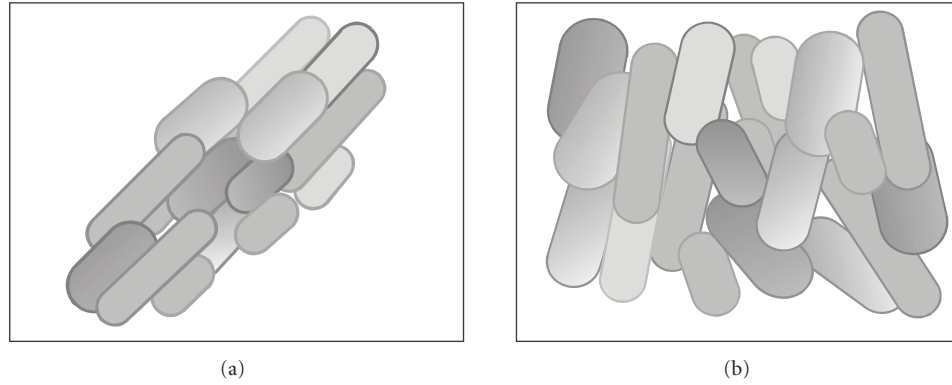


FIGURE 9: Model of the crystal enlargement of r-TiO<sub>2</sub> upon calcination on substrate-free (a) and substrate-limited (b) conditions.

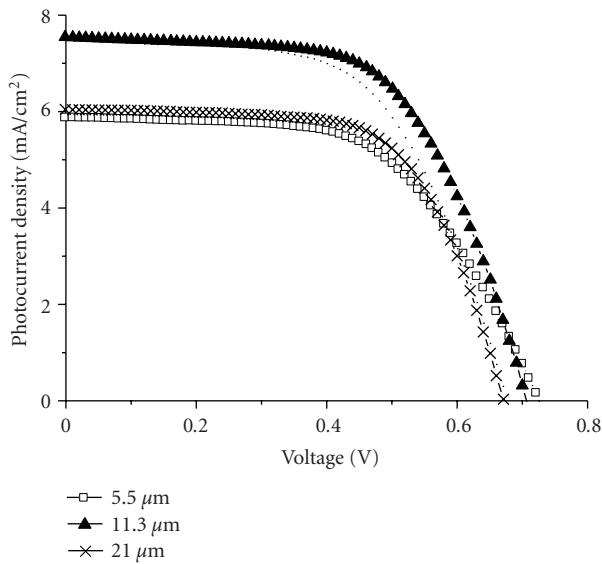


FIGURE 10: Photocurrent-voltage characteristics of the dye-sensitized solar cells with different thickness of r-TiO<sub>2</sub> films.

FTO substrate. In order to see the heat treatment effect on r-TiO<sub>2</sub> morphology, the TEM image was acquired from calcinated r-TiO<sub>2</sub> paste. As shown in Figure 7, the r-TiO<sub>2</sub> powders kept the rod shape morphology even with 450°C calcination process. Contrarily, the rod-like microstructure is somehow diminished on calcinated r-TiO<sub>2</sub> electrodes prepared from the same pastes as shown in Figure 8 from SEM. Only irregular and shorter-rod particles with larger particle size (100 nm) were observed. Although it is not clear why the rod shape can not be kept on r-TiO<sub>2</sub> film, there could be one possible reason as depicted in Figure 9. The surface energy effect is beneficial to the side-by-side (length) arrangement between rod-shaped r-TiO<sub>2</sub> particles. As mentioned earlier, the growth of rutile TiO<sub>2</sub> proceeded via oriented coalescence of the first formed TiO<sub>2</sub> nanorods. In 3 dimensions, the r-TiO<sub>2</sub> nanorods are freely moved and chances are the simultaneous growth of r-TiO<sub>2</sub> in both length and width directions. On r-TiO<sub>2</sub> film, however, one of the dimensions for r-TiO<sub>2</sub> nanorods to move is limited

TABLE 2: Performance characteristics of DSSCs based on the r-TiO<sub>2</sub> electrode with different thickness.

Thickness (μm)	J <sub>sc</sub> (mA/cm <sup>2</sup> )	V <sub>oc</sub> (V)	FF	η (%)	Dye <sub>ads</sub> (μmole/cm <sup>2</sup> )
5.5	5.99	0.73	0.58	2.51	0.22
11.3	7.55	0.70	0.60	3.16	0.28
21.0	6.03	0.67	0.66	2.68	0.40

and only nearby r-TiO<sub>2</sub> nanorods aggregate to form larger but shorter r-TiO<sub>2</sub> particles.

Figure 10 showed the typical current-voltage (J-V) characteristics of N3-sensitized r-TiO<sub>2</sub> solar cells measured at 1 sun light intensity for various r-TiO<sub>2</sub> film thickness. Table 2 lists the photoelectric data, including photocurrent density (J<sub>sc</sub>), open-circuit voltage (V<sub>oc</sub>), fill factor (FF), apparent cell efficiency (η), and the dye adsorption density (Dye<sub>ads</sub>) of the DSSCs in Figure 10. It is generally expected that the DSSC performance largely depends on the TiO<sub>2</sub> film thickness because changing the film thickness changes the amount of dye adsorbed on TiO<sub>2</sub> owing to the change of total TiO<sub>2</sub> surface area. For the homogeneously harvested light by the adsorbed dye molecules, one would also expect the approximately linearly dependence of photocurrent density with the film thickness [21]. It can be seen from Table 2 that when the film thickness increased by 2-fold, from 5.5 to 11.3 μm, the J<sub>sc</sub> only improved by 26%, from 5.99 to 7.55 mA/cm<sup>2</sup>. The increase of J<sub>sc</sub>, however, is consistent with that of Dye<sub>ads</sub> which increases ~27%, from 0.22 to 0.28 μmole/cm<sup>2</sup> and that of cell efficiency by ~26% from 2.51 to 3.16. These results indicate that the photocurrent as well as cell efficiency are limited by the number of adsorbed dye molecules for film thickness up to 11.3 μm. A small decrease (5%) of V<sub>oc</sub> with film thickness may be due to the offsetting effect associated with the J<sub>sc</sub> and the number of recombination centers on surface area of the film [12]. Further increase of r-TiO<sub>2</sub> film thickness from 11.3 to 21.0 μm, although the amount of dye adsorption increases by 43%, from 0.28 to 0.40 μmole/cm<sup>2</sup>, the J<sub>sc</sub> decreases by 20% from 7.55 to 6.03 mA/cm<sup>2</sup> as well as cell efficiency by ~15% from 3.16 to 2.68. This is due to the increase in the

numbers of recombination centers and the longer mean path of the injected electron to travel inside the cell. Moreover, when the TiO<sub>2</sub> films are thicker, the films become more opaque. Due to the various light absorption mechanism, the irradiation intensity decays significantly upon travelling through the thick films which is therefore detrimental to the DSSC performance [21].

#### 4. Conclusions

Pure rutile phase TiO<sub>2</sub> nanorods have successfully been synthesized under the hydrothermal conditions. Hydrothermal-treated duration shows significant effects on the crystal domain, particle dimension, and photocatalytic activity of r-TiO<sub>2</sub>. Hydrothermal treatment at longer reaction time increases the tendency of crystal growth based on TEM/XRD and the BET surface area decreased as well. The photocatalytic activity of r-TiO<sub>2</sub> increases with an increase of hydrothermal time from 1 to 15 h due to the increase of crystal domain, but it decreases for r-TiO<sub>2</sub> with further hydrothermal treatment (20 and 24 h) due to the decrease in surface area. Dye-sensitized solar cells with working area of 0.25 cm<sup>2</sup> were fabricated from various thicknesses of electrode layers made of r-TiO<sub>2</sub> nanorods. The best-performing DSSC evaluated under 1 sun condition gave current density ~7.55 mA/cm<sup>2</sup>, open circuit voltage ~0.70 V, fill factor ~60%, and energy conversion efficiency ~3.16%.

#### Acknowledgments

The authors gratefully acknowledge the financial support from the National Science Council of Taiwan, Republic of China (Contract no. NSC96-2113-M-027-005-MY2). The authors also acknowledge the kind help from Professor H.-W. Fang for film thickness measurement.

#### References

- [1] C. Su, B.-Y. Hong, and C.-M. Tseng, "Sol-gel preparation and photocatalysis of titanium dioxide," *Catalysis Today*, vol. 96, no. 3, pp. 119–126, 2004.
- [2] B. O'Regan and M. Grätzel, "A low-cost, high-efficiency solar cell based on dye-sensitized colloidal TiO<sub>2</sub> films," *Nature*, vol. 353, no. 6346, pp. 737–740, 1991.
- [3] W. W. So, S. B. Park, K. J. Kim, and S. J. Moon, "Phase transformation behavior at low temperature in hydrothermal treatment of stable and unstable titania sol," *Journal of Colloid and Interface Science*, vol. 191, no. 2, pp. 398–406, 1997.
- [4] H. Yin, Y. Wada, T. Kitamura et al., "Hydrothermal synthesis of nanosized anatase and ruffle TiO<sub>2</sub> using amorphous phase TiO<sub>2</sub>," *Journal of Materials Chemistry*, vol. 11, no. 6, pp. 1694–1703, 2001.
- [5] H. Kominami, J.-I. Kato, S.-Y. Murakami et al., "Synthesis of titanium(IV) oxide of ultra-high photocatalytic activity: high-temperature hydrolysis of titanium alkoxides with water liberated homogeneously from solvent alcohols," *Journal of Molecular Catalysis A: Chemical*, vol. 144, no. 1, pp. 165–171, 1999.
- [6] H.-Y. Byun, R. Vittal, D. Y. Kim, and K.-J. Kim, "Beneficial role of cetyltrimethylammonium bromide in the enhancement of photovoltaic properties of dye-sensitized rutile TiO<sub>2</sub> solar cells," *Langmuir*, vol. 20, no. 16, pp. 6853–6857, 2004.
- [7] Y. Wang, L. Zhang, K. Deng, X. Chen, and Z. Zou, "Low temperature synthesis and photocatalytic activity of rutile TiO<sub>2</sub> nanorod superstructures," *Journal of Physical Chemistry C*, vol. 111, no. 6, pp. 2709–2714, 2007.
- [8] R. R. Bacsa and J. Kiwi, "Effect of rutile phase on the photocatalytic properties of nanocrystalline titania during the degradation of p-coumaric acid," *Applied Catalysis B: Environmental*, vol. 16, no. 1, pp. 19–29, 1998.
- [9] D. D. Beck and R. W. Siegel, "Dissociative adsorption of hydrogen sulfide over nanophase titanium dioxide," *Journal of Materials Research*, vol. 7, no. 10, pp. 2840–2845, 1992.
- [10] T. Ohno, D. Haga, K. Fujihara, K. Kaizaki, and M. Matsumura, "Unique effects of iron(III) ions on photocatalytic and photoelectrochemical properties of titanium dioxide," *Journal of Physical Chemistry B*, vol. 101, no. 33, pp. 6415–6419, 1997.
- [11] N.-G. Park, G. Schlichthörl, J. van de Lagemaat, H. M. Cheong, A. Mascarenhas, and A. J. Frank, "Dye-sensitized TiO<sub>2</sub> solar cells: structural and photoelectrochemical characterization of nanocrystalline electrodes formed from the hydrolysis of TiCl<sub>4</sub>," *Journal of Physical Chemistry B*, vol. 103, no. 17, pp. 3308–3314, 1999.
- [12] N.-G. Park, J. van de Lagemaat, and A. J. Frank, "Comparison of dye-sensitized rutile- and anatase-based TiO<sub>2</sub> solar cells," *Journal of Physical Chemistry B*, vol. 104, no. 38, pp. 8989–8994, 2000.
- [13] Y. Suzuki, S. Ngamsinlapasathian, R. Yoshida, and S. Yoshikawa, "Partially nanowire-structured TiO<sub>2</sub> electrode for dye-sensitized solar cells," *Central European Journal of Chemistry*, vol. 4, no. 3, pp. 476–488, 2006.
- [14] C. Su, C.-M. Tseng, L.-F. Chen, B.-H. You, B.-C. Hsu, and S.-S. Chen, "Sol-hydrothermal preparation and photocatalysis of titanium dioxide," *Thin Solid Films*, vol. 498, no. 1–2, pp. 259–265, 2006.
- [15] M. Wu, G. Lin, D. Chen et al., "Sol-hydrothermal synthesis and hydrothermally structural evolution of nanocrystal titanium dioxide," *Chemistry of Materials*, vol. 14, no. 5, pp. 1974–1980, 2002.
- [16] C. Su, K.-F. Lin, Y.-H. Lin, and B.-H. You, "Preparation and characterization of high-surface-area titanium dioxide by sol-gel process," *Journal of Porous Materials*, vol. 13, no. 3, pp. 251–258, 2006.
- [17] Y.-F. Xie, *Preparation and characterization of TiO<sub>2</sub> by sol-gel from hydrothermal to calcination from nano-powder to nano-film*, M.S. thesis, National Taipei University of Technology, 2006.
- [18] B. Ohtani, Y. Ogawa, and S.-I. Nishimoto, "Photocatalytic activity of amorphous-anatase mixture of titanium(IV) oxide particles suspended in aqueous solutions," *Journal of Physical Chemistry B*, vol. 101, no. 19, pp. 3746–3752, 1997.
- [19] M. R. Hoffmann, S. T. Martin, W. Choi, and D. W. Bahnemann, "Environmental applications of semiconductor photocatalysis," *Chemical Reviews*, vol. 95, no. 1, pp. 69–96, 1995.
- [20] J. Jiu, S. Isoda, F. Wang, and M. Adachi, "Dye-sensitized solar cells based on a single-crystalline TiO<sub>2</sub> nanorod film," *Journal of Physical Chemistry B*, vol. 110, no. 5, pp. 2087–2092, 2006.
- [21] K. Hou, B. Tian, F. Li, Z. Bian, D. Zhao, and C. Huang, "Highly crystallized mesoporous TiO<sub>2</sub> films and their applications in dye sensitized solar cells," *Journal of Materials Chemistry*, vol. 15, no. 24, pp. 2414–2420, 2005.

## Research Article

# Comparative Solid Phase Photocatalytic Degradation of Polythene Films with Doped and Undoped TiO<sub>2</sub> Nanoparticles

Wasim Asghar,<sup>1</sup> Ishtiaq A. Qazi,<sup>1</sup> Hassan Ilyas,<sup>1</sup> Aftab Ahmad Khan,<sup>2</sup> M. Ali Awan,<sup>1</sup> and M. Rizwan Aslam<sup>1</sup>

<sup>1</sup>Institute of Environmental Science and Engineering, School of Civil and Environmental Engineering, National University of Sciences and Technology (NUST), Sector H-12, Islamabad 44000, Pakistan

<sup>2</sup>Advanced Engineering Research Organization (AERO), Hassan Abdal 43730, Pakistan

Correspondence should be addressed to Wasim Asghar, wasim@iese.edu.pk

Received 19 February 2010; Accepted 14 April 2010

Academic Editor: Bo Zou

Copyright © 2011 Wasim Asghar et al. This is an open access article distributed under the Creative Commons Attribution License, which permits unrestricted use, distribution, and reproduction in any medium, provided the original work is properly cited.

Comparative photocatalytic degradation of polythene films was investigated with undoped and metal (Fe, Ag, and Fe/Ag mix) doped TiO<sub>2</sub> nanoparticles under three different conditions such as UV radiation, artificial light, and darkness. Prepared photocatalysts were characterized by XRD, SEM, and EDS techniques. Photocatalytic degradation of the polythene films was determined by monitoring their weight reduction, SEM analysis, and FTIR spectroscopy. Weight of PE films steadily decreased and led to maximum of 14.34% reduction under UV irradiation with Fe/Ag mix doped TiO<sub>2</sub> nanoparticles and maximum of 14.28% reduction under artificial light with Ag doped TiO<sub>2</sub> nanoparticles in 300 hrs. No weight reduction was observed under darkness. Results reveal that polythene-TiO<sub>2</sub> compositing with metal doping has the potential to degrade the polythene waste under irradiation without any pollution.

## 1. Introduction

Titanium dioxide (TiO<sub>2</sub>) is one of the most well-known efficient photocatalysts. The capability of TiO<sub>2</sub>-based photocatalyst to degrade gaseous and aqueous contamination makes it a good candidate for use in air clean up and water purification. However, most applications so far are limited to UV light irradiation because the light absorption edge of pure TiO<sub>2</sub> is lower than 380 nm. Therefore, the development of modified titania with high activity under visible light ( $\lambda > 380$  nm) should take full advantage of the main part of the solar spectrum (mostly 400–600 nm) [1].

The most promising approach of activation of TiO<sub>2</sub>, in the visible light region, is modification of its chemical structure to shift the absorption spectrum to the visible light region [2–4]. This type of modification involves introduction of doping with metal and nonmetal species. To prepare an effective visible light, active photocatalyst doping should produce states in the band gap of TiO<sub>2</sub> that absorbs visible light [5].

The process of recycling polymers is expensive and time consuming; only a small percentage of the plastic waste is currently being recycled [6]. Biodegradable plastics have shown considerable promise in this context [7, 8]. However, the biodegradable plastics till now cannot completely solve the problem due to their chemical stability and nonaffordable cost [9]. More recently, photo degradation of plastics has also started receiving attention. The composition of plastic and TiO<sub>2</sub> nanoparticles (NPs) has been proven to be a new and useful way to decompose solid polymer in open air. Investigations on the photo degradation of polyvinyl chloride (PVC), polystyrene (PS), and polythene (PE) have been carried out [10–12]. More specifically, a few recent reports describe the use of TiO<sub>2</sub> and goethite and so forth as the photocatalyst for oxidative degradation of PE with very encouraging results [13, 14].

The present study was focused on solid phase photocatalytic degradation of polyethylene plastic with TiO<sub>2</sub> as photocatalyst and Fe, Ag metals as dopants. PE-TiO<sub>2</sub> composite films were prepared and their photocatalytic

degradation under ultraviolet irradiation, artificial light and darkness was studied.

## 2. Materials and Methods

**2.1. Chemical Reagents.** GPR TiO<sub>2</sub> (BDH Chemicals Ltd., England) and chemical reagents like iron (III) nitrate nonahydrate, silver nitrate, and cyclohexane (Merck, Germany) were used in this study. All chemicals were of analytical grade and used without further purification. PE originating from QAPCO Petrochemical Corp., Qatar was purchased from the local market.

**2.2. Preparation of Doped TiO<sub>2</sub> Nanoparticles.** Fe doped, Ag doped, and Fe/Ag mix doped TiO<sub>2</sub> NPs were prepared by the liquid impregnation (LI) method by the following steps. 3 g of GPR TiO<sub>2</sub> was added to 100 mL distilled water and then the required amount of iron (III) nitrate nonahydrate, for doping, was added to TiO<sub>2</sub> suspension, where the Fe concentration was of 1% (mole ratio) versus TiO<sub>2</sub>. The slurry was stirred well and allowed to rest for 24 hours and then dried in an air oven at 100°C for 12 hours [15]. The dried solids were ground in an agate mortar and calcinated at 500°C for 3 hours in a furnace. Same steps were repeated with silver nitrate as precursor for Ag doped TiO<sub>2</sub> NPs where the Ag concentration was of 1% (mole ratio) versus TiO<sub>2</sub>. For Fe/Ag mix doped TiO<sub>2</sub>, iron (III) nitrate nonahydrate and silver nitrate were used as the precursors for Fe and Ag, respectively. The mole ratio, with respect to TiO<sub>2</sub>, for both Fe and Ag was 0.5% each. GPR TiO<sub>2</sub> was calcinated at 500°C for 3 hours when used as undoped TiO<sub>2</sub> NPs source.

**2.3. Preparation of PE-TiO<sub>2</sub> Composite Films.** Polymer stock solution was prepared by dissolving 1 g of PE in 100 mL cyclohexane at 70°C under vigorous stirring for 60 minutes. Following this, TiO<sub>2</sub> NPs were suspended uniformly in the above solution to give 1.0% (weight) contents with respect to the total mass of PE. An aliquot of 20 mL of PE-TiO<sub>2</sub> prepared solution was spread as a disc ( $r = 4$  cm) on a glass plate and first dried for 20 minutes at 70°C, then dried for 48 hours at room temperature [16]. Weight of the resulting PE-TiO<sub>2</sub> composite films was 0.2 gm approximately. Same procedure was followed to prepare the composite films of PE with Fe, Ag, and Fe/Ag mix doped TiO<sub>2</sub> NPs.

## 3. Characterization

### 3.1. Characterization of TiO<sub>2</sub> Nanoparticles

**3.1.1. X-Ray Diffraction Analysis.** Crystal size of the prepared photocatalyst was studied by powder XRD technique. X-ray diffraction patterns were obtained on JEOL JDX-II X-ray diffractometer using Cu-K<sub>α</sub> radiation at an angle of  $2\theta$  from 10° to 80°. The crystallite size was determined from the X-ray diffraction patterns, based on the Scherer equation [14]

$$L = \frac{k\lambda}{\beta \cos \theta} \quad (1)$$

TABLE 1: Crystal sizes of doped and undoped TiO<sub>2</sub> nanoparticles.

Sr. no.	Sample name	Crystal size (nm)	
		Maximum	Minimum
1	Undoped TiO <sub>2</sub>	42.52	26.72
2	Fe doped TiO <sub>2</sub>	42.52	26.72
3	Ag doped TiO <sub>2</sub>	42.52	11.27
4	Fe/Ag mix doped TiO <sub>2</sub>	42.52	20.09

where  $k$  is a shape factor = 0.9,  $\lambda$  is the radiation wavelength = 1.54051° A,  $\theta$  is the Bragg angle,  $\beta$  = full width of a diffraction line at one half of maximum intensity in radian.

**3.1.2. SEM Study.** SEM study of doped and undoped TiO<sub>2</sub> NPs was conducted with JEOL JSM-6460 scanning electron microscope to see the distribution of metal on the surface of TiO<sub>2</sub> in doped species.

**3.1.3. EDS Analysis.** Energy dispersive spectroscopic (EDS) analysis was conducted with Oxford INCA X-sight 200 to perform the quantitative analysis of the TiO<sub>2</sub> both in doped and undoped conditions.

### 3.2. Characterization of Polythene Films

**3.2.1. Weight Reduction Analysis.** Photo degradation study of the PE films was conducted based on weight reduction. Weighing balance, with 0.0001 gm sensitivity (Denver Instrument Company XE Series, model 100A) was used for weight measurements.

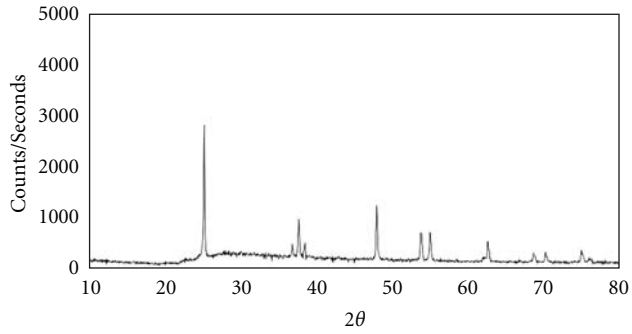
**3.2.2. Surface Morphology and Thickness Analysis.** Surface morphology & thickness analysis of PE films was conducted with JEOL JSM-6460 scanning electron microscope before and after the 300 hours of UV exposure.

**3.2.3. FTIR Analysis.** To get the qualitative analysis of the PE films, FTIR analysis was conducted with Perkin Elmer Spectrum BX-II FTIR spectrometer before and after irradiation.

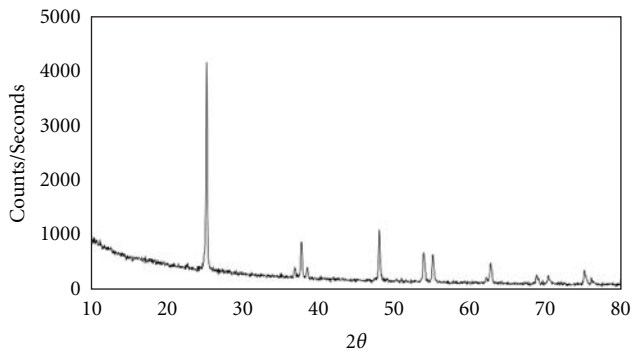
## 4. Results and Discussions

### 4.1. Characterization of TiO<sub>2</sub> Nanoparticles

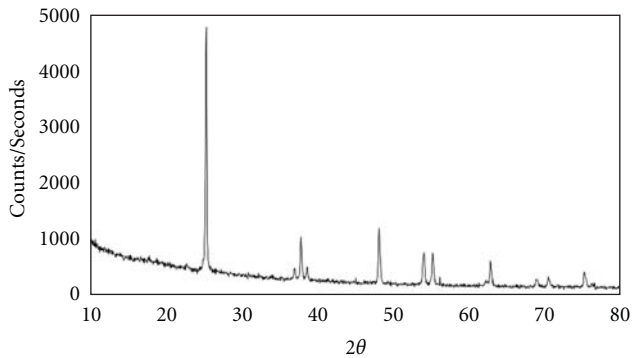
**4.1.1. X-Ray Diffraction Analysis.** Table 1 shows the results of X-ray diffraction analysis, which demonstrate a variation in nanoparticles size as compared to a previous study [15]. This study reported that the average size of prepared Ag doped TiO<sub>2</sub> NPs was 14 nm while Ag doped TiO<sub>2</sub> NPs prepared in current study were in the 11.27 to 42.52 nm range. This difference may be due to the TiO<sub>2</sub> source, as GPR TiO<sub>2</sub> was used as TiO<sub>2</sub> source in the current study while P-25 Degussa was used in the previous one. Figure 1 shows the respective XRD patterns of doped and undoped TiO<sub>2</sub> NPs.



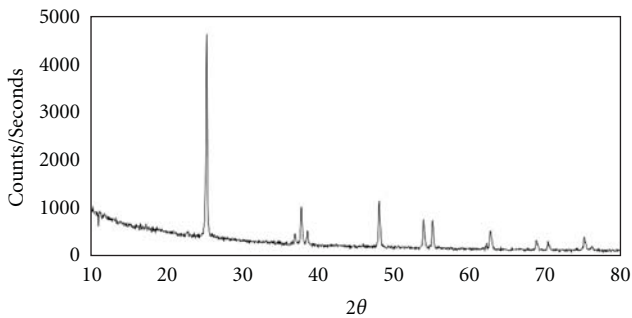
(a)



(b)



(c)



(d)

FIGURE 1: XRD patterns: (a) undoped  $\text{TiO}_2$ , (b) Fe doped  $\text{TiO}_2$ , (c) Ag doped  $\text{TiO}_2$ , and (d) Fe/Ag mix doped  $\text{TiO}_2$ .

TABLE 2: EDS analysis of doped and undoped  $\text{TiO}_2$  nanoparticles.

Sr. no.	Sample name	Elements in percent ratio		
		Ti	Fe	Ag
1	Undoped $\text{TiO}_2$	100.00	—	—
2	Fe doped $\text{TiO}_2$	99.08	0.92	—
3	Ag doped $\text{TiO}_2$	99.09	—	0.91
4	Fe/Ag mix doped $\text{TiO}_2$	98.99	0.48	0.53

TABLE 3: Photo catalyzed weight reduction (maximum) of pure PE films and PE- $\text{TiO}_2$  composite films.

Sr. no.	Sample name	Maximum weight reduction (%)		
		UV	Artificial light	Dark
1	Pure PE	3.32	0.65	No reduction
2	PE + $\text{TiO}_2$	10.6	6.51	= do =
3	PE + Fe doped $\text{TiO}_2$	13.49	11.9	= do =
4	PE + Ag doped $\text{TiO}_2$	13.75	14.28	= do =
5	PE + Fe/Ag mix doped $\text{TiO}_2$	14.34	13.18	= do =

**4.1.2. SEM Analysis.** Figure 2 shows the images of doped and undoped  $\text{TiO}_2$  NPs obtained with scanning electron microscope. These images show that the distribution of the dopant metals on the surface of  $\text{TiO}_2$  is not uniform and doped species contain irregular shaped particles which are aggregations of tiny crystals. SEM analysis verifies the results of previous reported work [15].

**4.1.3. EDS Analysis.** Figure 3 shows the EDS spectra of doped and undoped  $\text{TiO}_2$  NPs. EDS analysis shows that the percent composition is not consistent in the doped  $\text{TiO}_2$  NPs. It varies from point to point showing that composition of the prepared NPs is not homogeneous. It confirms the SEM results. Average composition of doped and undoped NPs is given as in Table 2.

## 4.2. Characterization of Polythene Films

**4.2.1. Weight Reduction Analysis.** Pure PE and PE- $\text{TiO}_2$  composite films were exposed with UV and artificial light constantly for 300 hours under ambient conditions. Parallel studies were conducted with no irradiation under darkness.  $\text{TiO}_2$  photocatalyst absorbs only UV light ( $\lambda < 380$  nm), thus only UV light plays a role in solar degradation of PE- $\text{TiO}_2$  composite plastic. In order to reveal the photocatalytic degradation behavior the photo degradation reaction was conducted under ambient air in a lamp-housing box (50 cm  $\times$  40 cm  $\times$  30 cm) as shown in Figure 4. Pure PE and PE- $\text{TiO}_2$  doped & undoped composite films were irradiated by two 6W UVL-56 UV lamps. The primary wavelength of the lamps was 365 nm and the light intensity measured with ABM Model 150 digital intensity meter was 1.4 mW/cm<sup>2</sup> at 3 cm away from the lamps. For artificial light source a common household energy saver bulb of TORNADO 24 watt was used. Table 3 shows the summary of the photo catalyzed

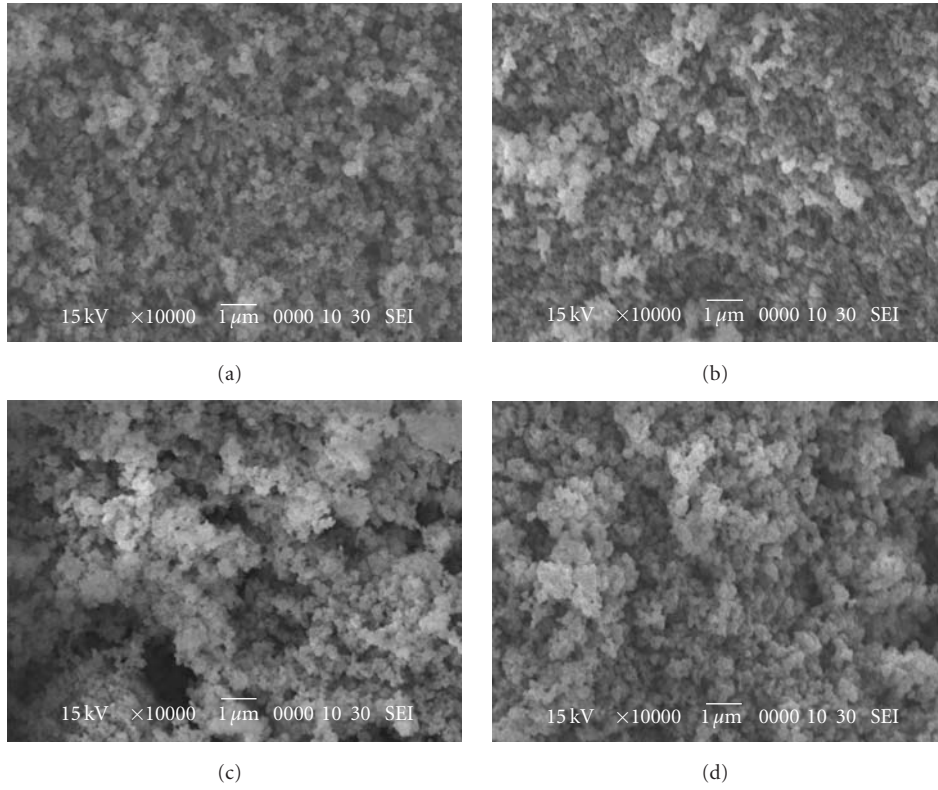


FIGURE 2: SEM images of  $\text{TiO}_2$  NPs: (a) undoped  $\text{TiO}_2$ , (b) Fe doped  $\text{TiO}_2$ , (c) Ag doped  $\text{TiO}_2$ , and (d) Fe/Ag mix doped  $\text{TiO}_2$ .

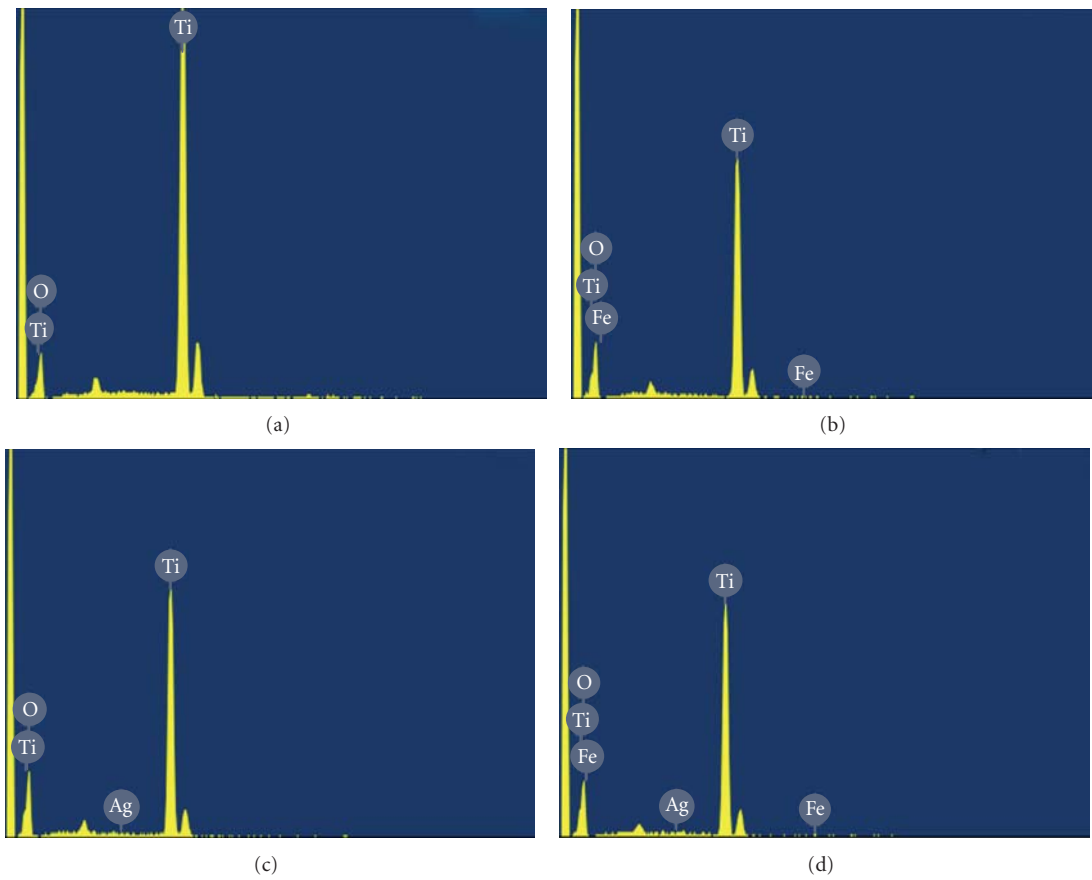


FIGURE 3: EDS spectra of  $\text{TiO}_2$  NPs: (a) undoped  $\text{TiO}_2$ , (b) Fe doped  $\text{TiO}_2$ , (c) Ag doped  $\text{TiO}_2$ , and (d) Fe/Ag mix doped  $\text{TiO}_2$ .

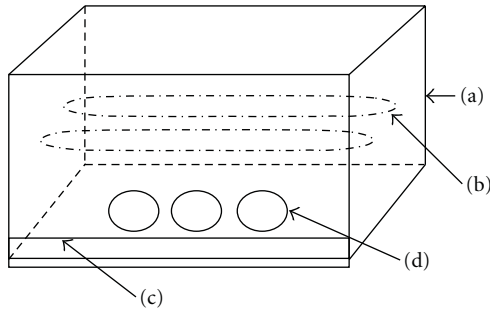


FIGURE 4: Schematic diagram of photocatalytic reactor: (a) lamp housing box, (b) two ultraviolet lamps, (c) air and water inlet, and (d) sample dishes.

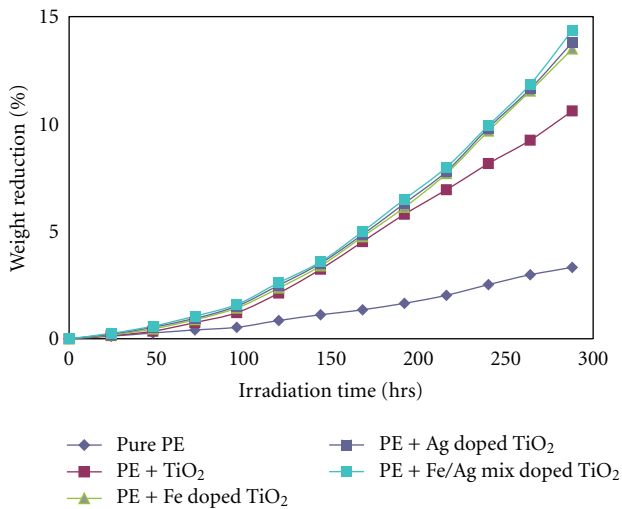


FIGURE 5: Effect of UV irradiation on the photocatalytic degradation of PE films.

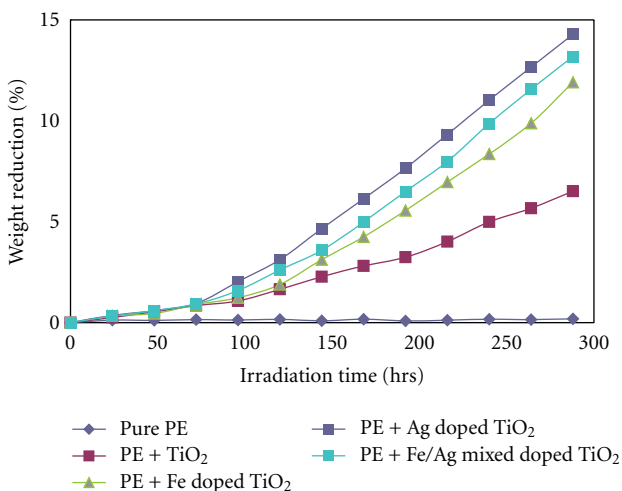


FIGURE 6: Effect of artificial light on the photocatalytic degradation of PE films.

weight loss of pure PE film and PE-TiO<sub>2</sub> composite films with Fe, Ag, and Fe/Ag mix doping under UV irradiation, artificial light and darkness. Figure 5 shows the details of percent weight reduction under UV light and Figure 6 shows the details of percent weight reduction under artificial light. Negligible change was detected in all PE films with or without TiO<sub>2</sub> under darkness.

**4.2.2. Polythene Film Thickness.** Almost twofold increase in the thickness of polythene films was observed after UV irradiation for 300 hours from 22–28  $\mu\text{m}$  range to 58–61  $\mu\text{m}$  range as shown in Figure 7. This increase in thickness after degradation may possibly be due to the released species like CO<sub>2</sub> causing swelling, affecting the overall thickness of the PE films.

**4.2.3. Surface Morphology of Polythene Films.** Scanning electron microscope analysis was carried out to observe the surface changes of the films following photo degradation. Figures 8(a) and 8(b) show that the surface of the PE film was smooth before UV irradiation but after UV exposure, due to photo degradation, cavities appeared randomly on the surface of the film. Figures 8(c), 8(d), 8(e), and 8(f) show the texture of PE films with undoped TiO<sub>2</sub>, Fe doped TiO<sub>2</sub>, Ag doped TiO<sub>2</sub> and Fe/Ag mix doped TiO<sub>2</sub> under UV irradiation, respectively. After irradiation, there were some cavities in the PE film which had also been observed by other workers [14]. The formation of these cavities might be due to the escape of volatile products from PE matrix. More cavities were found on the surface of PE-TiO<sub>2</sub> composite film. Figures 8(c), 8(d), 8(e), and 8(f) show that the degradation is greater than that of PE-TiO<sub>2</sub> composite film. These results were in accordance with the weight loss data shown in Figures 7 and 8. SEM images suggested that the degradation of PE matrix started from PE-TiO<sub>2</sub> interface and led to the formation of cavities around TiO<sub>2</sub> particles. It implied that the active oxygen species generated on TiO<sub>2</sub> surface diffused and degraded the polymer matrix. This is further strengthened by the thickness analysis of the PE films.

**4.2.4. Spectroscopic Analysis.** Figure 9 shows the FTIR spectra of pure PE films before and after irradiation and PE-TiO<sub>2</sub> (doped and undoped) composite films after UV irradiation. Spectrum of the PE film before irradiation show the characteristic absorption peaks of long alkyl chain in the region of 2919  $\text{cm}^{-1}$ , 2857  $\text{cm}^{-1}$ , 1475  $\text{cm}^{-1}$ , and 715  $\text{cm}^{-1}$ . Figures 9(b), 9(c), 9(d), 9(e), and 9(f) show the FTIR spectra of the PE, PE-TiO<sub>2</sub>, PE-Fe doped TiO<sub>2</sub>, PE-Ag doped TiO<sub>2</sub>, and PE-Fe/Ag mix doped TiO<sub>2</sub> after irradiation, respectively. There were new absorption peaks for composite films in the region of 1716  $\text{cm}^{-1}$ , 1629  $\text{cm}^{-1}$ , and 1175  $\text{cm}^{-1}$ , which could be assigned to C=O, C=C and C–O stretching vibrations, respectively [10]. The Peak at 3507  $\text{cm}^{-1}$  can be assigned to –OH stretching that may be formed by the hydrolysis reaction.

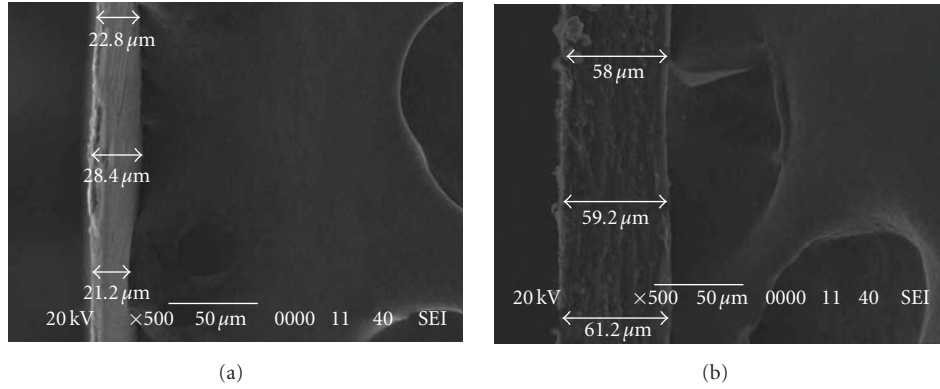


FIGURE 7: Thickness of PE films: (a) before and (b) after irradiation.

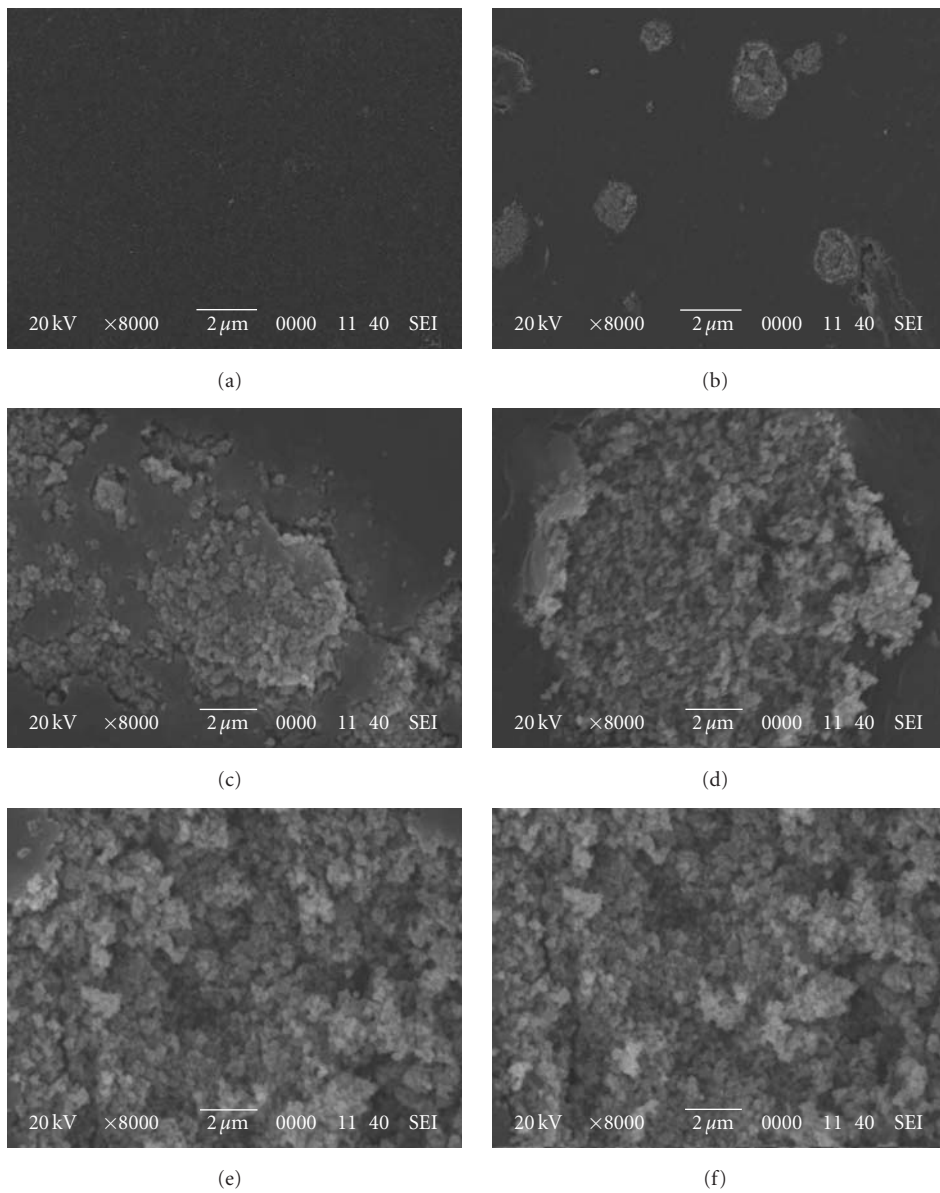


FIGURE 8: SEM images of PE films before and after irradiation: (a) PE film before irradiation, (b) PE film after irradiation, (c) PE-TiO<sub>2</sub> film after irradiation, (d) PE-Fe doped TiO<sub>2</sub> film after irradiation, (e) PE-Ag doped TiO<sub>2</sub> film after irradiation, and (f) PE-Fe/Ag mix doped TiO<sub>2</sub> film after irradiation.

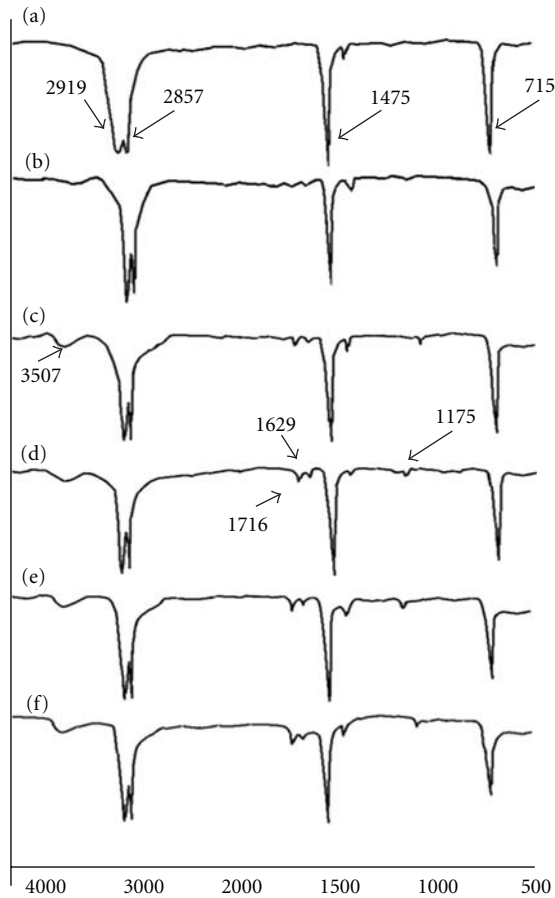
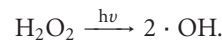
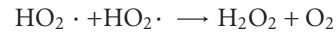
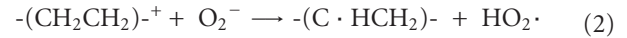
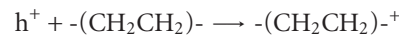
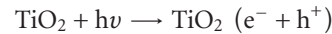


FIGURE 9: FTIR spectra of PE films before and after irradiation: (a) PE film before irradiation, (b) PE film after irradiation, (c) PE-TiO<sub>2</sub> film after irradiation, (d) PE-Fe doped TiO<sub>2</sub> film after irradiation, (e) PE-Ag doped TiO<sub>2</sub> film after irradiation, and (f) PE-Fe/Ag mix doped TiO<sub>2</sub> film after irradiation.

**4.2.5. Degradation Mechanism of Polythene Films.** Photo degradation of pure PE has been extensively studied [17]. The reaction of pure PE film under UV irradiation occurs via direct absorption of photons by the PE macromolecule to create excited states and then undergo chain scission, branching, cross-linking and oxidation reactions [18]. For composite films, photocatalytic degradation is the main reaction, which is quite different from the photolytic degradation of pure PE film. For PE-TiO<sub>2</sub>, the photo degradation of PE mainly happens on the film surface where electrons or holes combine with adsorbed oxygen molecules or hydroxyl ion to produce O<sub>2</sub><sup>-</sup> or ·OH, two very important reactive oxygen species for the degradation of PE. In the photocatalytic degradation of PE-TiO<sub>2</sub>/Fe/Ag, not only O<sub>2</sub><sup>-</sup> and ·OH but also the holes that are generated in the ground state of Fe/Ag play an important role. Efficient holes production occurs in the ground state of Fe/Ag under irradiation. Although holes in the ground state of Fe/Ag have lower oxidative ability than those in the valence band of TiO<sub>2</sub>, it is energetically favorable for these to participate in the oxidation of PE polymer. Further dopants like Fe and Ag can act as both h<sup>+</sup>/e<sup>-</sup> traps

to reduce the recombination rate of h<sup>+</sup>/e<sup>-</sup> pairs and enhance the photocatalytic activity [19]



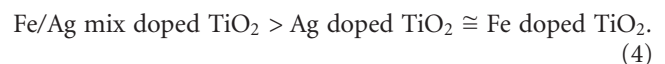
Embedded TiO<sub>2</sub> NPs can generate enough ·OH to photo degrade inner PE. The active oxygen species described above, initiate the degradation reaction by attacking neighboring polymer chains [7]. The degradation process spatially extends into the polymer matrix through the diffusion of the reactive oxygen species. Once the carbon-centered radicals are introduced in the polymer chain, their successive reactions lead to the chain cleavage with the oxygen incorporation and species containing carbonyl & carboxyl groups are produced. These intermediates can be further photo catalytically oxidized to CO<sub>2</sub> and H<sub>2</sub>O by the aid of reactive oxygen species [20].

## 5. Conclusions

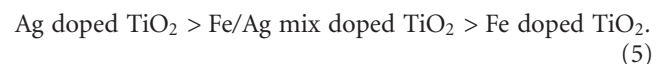
Doping of TiO<sub>2</sub> NPs by Liquid Impregnation method alters its characteristics such as particle size and surface morphology. The effect of mix doping is midway between that of the doping effect by a single metal alone. This indicates that metal ratios can be adjusted to get a desired impact for a particular requirement. This idea was implied and verified in the photo degradation of PE under UV and artificial light irradiation. Photo degradation of PE-TiO<sub>2</sub> films occurred at faster rate and was more complete than the simple photo degradation of pure PE films under UV and artificial light irradiation. Among the PE-TiO<sub>2</sub> films, the degradation of doped TiO<sub>2</sub> composite film was greater than the undoped TiO<sub>2</sub> composite film both under UV and artificial light irradiation. Overall degradation trend can be represented as



Catalytic trend among the doped TiO<sub>2</sub> NPs under UV irradiation can be represented as



Catalytic trend among the doped TiO<sub>2</sub> NPs under artificial light can be represented as



It is our observation that development of this kind of composite polymer can lead to an environmental friendly polythene product.

## References

- [1] C.-C. Pan and J. C. S. Wu, "Visible-light response Cr-doped  $\text{TiO}_{2-x}\text{N}_x$  photocatalysts," *Materials Chemistry and Physics*, vol. 100, no. 1, pp. 102–107, 2006.
- [2] D. Nabi, I. Aslam, and I. A. Qazi, "Evaluation of the adsorption potential of titanium dioxide nanoparticles for arsenic removal," *Journal of Environmental Sciences*, vol. 21, no. 3, pp. 402–408, 2009.
- [3] C. He, Y. Yu, X. Hu, and A. Larbot, "Influence of silver doping on the photocatalytic activity of titania films," *Applied Surface Science*, vol. 200, no. 1–4, pp. 239–247, 2002.
- [4] M. S. Hegde, K. Nagaveni, and S. Roy, "Synthesis, structure and photocatalytic activity of nano  $\text{TiO}_2$  and nano  $\text{Ti}_{1-x}\text{M}_x\text{O}_{2-\delta}$  ( $\text{M} = \text{Cu}, \text{Fe}, \text{Pt}, \text{Pd}, \text{V}, \text{W}, \text{Ce}, \text{Zr}$ )," *Journal of Physics*, vol. 65, no. 4, pp. 641–645, 2005.
- [5] W. Ren, Z. Ai, F. Jia, L. Zhang, X. Fan, and Z. Zou, "Low temperature preparation and visible light photocatalytic activity of mesoporous carbon-doped crystalline  $\text{TiO}_2$ ," *Applied Catalysis B: Environmental*, vol. 69, no. 3–4, pp. 138–144, 2007.
- [6] C. Yan, X. Mei, W. He, and S. Zheng, "Present situation of residue pollution of mulching plastic film and controlling measures," *Transactions of the Chinese Society of Agricultural Engineering*, vol. 22, no. 11, pp. 269–272, 2006.
- [7] P. Mormile, L. Petti, M. Rippa, B. Immirzi, M. Malinconico, and G. Santagata, "Monitoring of the degradation dynamics of agricultural films by IR thermography," *Polymer Degradation and Stability*, vol. 92, no. 5, pp. 777–784, 2007.
- [8] A. Sharma and A. Sharma, "Degradation assessment of low density polythene (LDP) and polythene (PP) by an indigenous isolate of *Pseudomonas stutzeri*," *Journal of Scientific and Industrial Research*, vol. 63, no. 3, pp. 293–296, 2004.
- [9] S.-Y. Lee, J.-H. Yoon, J.-R. Kim, and D.-W. Park, "Degradation of polystyrene using clinoptilolite catalysts," *Journal of Analytical and Applied Pyrolysis*, vol. 64, no. 1, pp. 71–83, 2002.
- [10] S. H. Kim, S.-Y. Kwak, and T. Suzuki, "Photocatalytic degradation of flexible PVC/ $\text{TiO}_2$  nanohybrid as an eco-friendly alternative to the current waste landfill and dioxin-emitting incineration of post-use PVC," *Polymer*, vol. 47, no. 9, pp. 3005–3016, 2006.
- [11] S. Chakrabarti, B. Chaudhuri, S. Bhattacharjee, P. Das, and B. K. Dutta, "Degradation mechanism and kinetic model for photocatalytic oxidation of PVC-ZnO composite film in presence of a sensitizing dye and UV radiation," *Journal of Hazardous Materials*, vol. 154, no. 1–3, pp. 230–236, 2008.
- [12] J. Shang, M. Chai, and Y. Zhu, "Solid-phase photocatalytic degradation of polystyrene plastic with  $\text{TiO}_2$  as photocatalyst," *Journal of Solid State Chemistry*, vol. 174, no. 1, pp. 104–110, 2003.
- [13] X. U. Zhao, Z. Li, Y. Chen, L. Shi, and Y. Zhu, "Solid-phase photocatalytic degradation of polyethylene plastic under UV and solar light irradiation," *Journal of Molecular Catalysis A*, vol. 268, no. 1–2, pp. 101–106, 2007.
- [14] G. L. Liu, D. W. Zhu, S. J. Liao, L. Y. Ren, J. Z. Cui, and W. B. Zhou, "Solid-phase photocatalytic degradation of polyethylene-goethite composite film under UV-light irradiation," *Journal of Hazardous Materials*, vol. 172, no. 2–3, pp. 1424–1429, 2009.
- [15] M. A. Behnajady, N. Modirshahla, and M. Shokri, "Enhancement of photocatalytic activity of  $\text{TiO}_2$  nanoparticles by silver doping: photo deposition versus liquid impregnation methods," *Global NEST Journal*, vol. 10, pp. 1–7, 2008.
- [16] M. H. Habibi, M. N. Esfahani, and T. A. Egerton, "Photochemical characterization and photocatalytic properties of a nanostructure composite  $\text{TiO}_2$  film," *International Journal of Photoenergy*, vol. 2007, Article ID 13653, 8 pages, 2007.
- [17] F. Fallania, G. Ruggeria, and S. Broncoci, "Modification of surface and mechanical properties of polyethylene by photo-initiated reactions," *Polymer Degradation and Stability*, vol. 82, pp. 257–261, 2003.
- [18] M. Scoconi, S. Cimmino, and M. Kaci, "Photo-stabilisation mechanism under natural weathering and accelerated photo-oxidative conditions of LDPE films for agricultural applications," *Polymer*, vol. 41, no. 22, pp. 7969–7980, 2000.
- [19] W.-C. Hung, Y.-C. Chen, H. Chu, and T.-K. Tseng, "Synthesis and characterization of  $\text{TiO}_2$  and  $\text{Fe/TiO}_2$  nanoparticles and their performance for photocatalytic degradation of 1,2-dichloroethane," *Applied Surface Science*, vol. 255, no. 5, pp. 2205–2213, 2008.
- [20] X. Zhao, Z. Li, Y. Chen, L. Shi, and Y. Zhu, "Enhancement of photocatalytic degradation of polyethylene plastic with CuPc modified  $\text{TiO}_2$  photocatalyst under solar light irradiation," *Applied Surface Science*, vol. 254, no. 6, pp. 1825–1829, 2008.

## Research Article

# Photocatalytic Degradation of Nitro and Chlorophenols Using Doped and Undoped Titanium Dioxide Nanoparticles

Hassan Ilyas, Ishtiaq A. Qazi, Wasim Asgar, M. Ali Awan, and Zahir-ud-din Khan

School of Civil and Environmental Engineering, National University of Sciences and Technology, H-12, Islamabad, Pakistan

Correspondence should be addressed to Hassan Ilyas, hassan@iese.edu.pk

Received 19 February 2010; Revised 13 April 2010; Accepted 1 June 2010

Academic Editor: William W. Yu

Copyright © 2011 Hassan Ilyas et al. This is an open access article distributed under the Creative Commons Attribution License, which permits unrestricted use, distribution, and reproduction in any medium, provided the original work is properly cited.

Pure and Ag-TiO<sub>2</sub> nanoparticles were synthesized, with the metallic doping being done using the Liquid Impregnation (LI) method. The resulting nanoparticles were characterized by analytical methods such as scanning electron micrographs (SEMs), Energy Dispersive Spectroscopy (EDS), and X-ray diffraction (XRD). XRD analysis indicated that the crystallite size of TiO<sub>2</sub> was 27 nm to 42 nm while the crystallite size of Ag-TiO<sub>2</sub> was 11.27 nm to 42.52 nm. The photocatalytic activity of pure TiO<sub>2</sub> and silver doped TiO<sub>2</sub> was tested by photocatalytic degradation of *p*-nitrophenol as a model compound. Ag-TiO<sub>2</sub> nanoparticles exhibited better results (98% degradation) as compared to pure TiO<sub>2</sub> nanoparticles (83% degradation) in 1 hour for the degradation of *p*-nitrophenol. Ag-TiO<sub>2</sub> was further used for the photocatalytic degradation of 2,4-dichlorophenol (99% degradation), 2,5-dichlorophenol (98% degradation), and 2,4,6-trichlorophenol (96% degradation) in 1 hour. The degree of mineralization was tested by TOC experiment indicating that 2,4-DCP was completely mineralized, while 2,5-DCP was mineralized upto 95 percent and 2,4,6-TCP upto 86 percent within a period of 2 hours.

## 1. Introduction

Advanced oxidation processes (AOPs) are techniques used for the degradation of harmful organic pollutants resistant to conventional treatment methods. AOPs depend on in situ generation of highly reactive radical specie such as OH<sup>•</sup> that breakdown a number of organic compounds without being selective [1–3] using chemical or light energy. The process employing a semiconductor activated by UV or visible light to degrade aquatic or atmospheric pollutants is called photocatalysis which results in partial or complete mineralization of the organic compounds [4, 5].

Titanium dioxide (TiO<sub>2</sub>), a metal oxide semiconductor has been found to be one of the most effective photocatalysts due to its high efficiency and stability. TiO<sub>2</sub> has a band gap of 3.2 eV that allows UV light to excite the valance electrons and inject these into the conduction band leaving holes in the valance band [6]. The high rate of electron-hole recombination in TiO<sub>2</sub>, however, limits the efficiency of the photocatalyst which can be arrested, to some extent, by doping with metallic elements such as silver [7]. On the other

hand, the antibacterial action of silver, particularly in the colloidal form, is also well known [8].

Metal-doped titanium dioxide has been used for the degradation of many organic pollutants in general [2, 3] and for phenols in particular [9–11]. Chlorophenols have low taste and odour thresholds and exhibit high toxicity and carcinogenic character [9]. They are very toxic and poorly biodegradable compounds, that are not effectively degraded by direct biological methods [10]. Consequently, their elimination in wastewaters and drinking water is of great interest.

In the present work, TiO<sub>2</sub> nanoparticles were synthesized by calcination while metallic doping with silver was achieved using Liquid Impregnation [12]. These nanosized catalysts were characterized by the techniques such as X-ray diffraction (XRD), Scanning Electron Microscopy (SEM), and Energy Dispersive Spectroscopy (EDS). Photocatalytic degradation using the nanosized particles was then studied with *p*-nitrophenol as a model compound followed by of 2,4-dichlorophenol, 2,5-dichlorophenol, and 2,4,6-trichlorophenol.

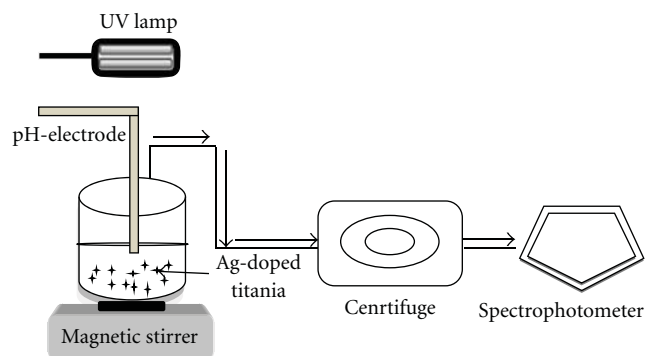


FIGURE 1: Schematic Diagram of Experimental Setup of Photocatalysis.

## 2. Experimental

**2.1. Materials.**  $\text{TiO}_2$  (GPR, BDH Chemicals Ltd. Poole England),  $\text{AgNO}_3$ , *p*-nitrophenol (purity 99%), 2,4-dichlorophenol, 2,5-dichlorophenol, and 2,4,6-trichlorophenol (GR, Merck, Germany).

**2.2. Photocatalyst Preparation.** In case of pure  $\text{TiO}_2$  nanoparticles,  $\text{TiO}_2$  was calcined at  $500^\circ\text{C}$  for 3 hours, to obtain the nanosized crystal structure. Silver-doped  $\text{TiO}_2$  nanoparticles were prepared by following the method of reference [12] described below.

1 g  $\text{TiO}_2$  was added to 100 ml deionized water in a 500 ml Pyrex beaker. For silver doping 1% (molar ratio) of  $\text{AgNO}_3$  was also added to the suspension. The resulting slurry was thoroughly mixed by vigorous stirring and allowed to settle, at room temperature, over night. The liquid so obtained was dried in an oven at  $100^\circ\text{C}$  for 12 hours to get rid of any remaining moisture. The solid material resulting from this step was calcined, at  $500^\circ\text{C}$  for 3 hours in a furnace. This resulted in fine particles of silver-doped  $\text{TiO}_2$ , herein after referred to as Ag- $\text{TiO}_2$ .

**2.3. Characterization of  $\text{TiO}_2$  and Ag- $\text{TiO}_2$  Nanoparticles.** The phases of the synthesized particles were analyzed by JEOL JDX-II X-ray Diffractometer. Crystallite size of the prepared particles was determined from the broadening of the anatase main peak by the Scherrer equation. The external morphology of the particles was examined using an electron microscope JEOL JSM 6460. EDS analysis was carried out using the Oxford INCA X-sight 200 System.

**2.4. The Photocatalysis Process.** The schematic diagram of the experimental setup of photocatalysis experiment is shown in Figure 1. 0.004 g of high purity *p*-nitrophenol was dissolved in 200 ml deionized water in a 250 ml beaker and transferring it to a 1 L analytical flask. The beaker was thoroughly rinsed, twice, and the washings were added to the solution in the 1 L flask. The volume was made up, with deionised water, to 1 L to obtain a stock solution of 4 ppm *p*-nitrophenol.

An aliquot of the solution was taken and its pH (monitored with the HACH Sension 1 pH meter) was adjusted to 7

with drop-wise addition of dilute NaOH (1N) solution. The resulting solution had a slight yellow tinge whose absorbance was measured at 400 nm in a 4 cm path length glass cell in a UV visible spectrophotometer (HACH DR 2400). Deionized water in a glass cell of the same dimensions served as a blank. The absorbance so obtained served as the reference value for determining the proportionate reduction in the concentration ( $C_e$ ) of the phenol, after exposing the solution to UV light under the conditions of (a) no  $\text{TiO}_2$ , (b) with  $\text{TiO}_2$ , and (c) with Ag- $\text{TiO}_2$  as described below.

To investigate the photocatalytic degradation, *p*-nitrophenol solution of 4 ppm was taken in a container. Ag- $\text{TiO}_2$  nanoparticles with a dose of 0.05 g/50 ml was added. It was placed under 20 W Blak-Ray UV lamp (with a wavelength peak at 365 nm and intensity of  $1.4\text{ mW/cm}^2$ ) and with continuous stirring. After every experiment the solution was centrifuged on (Sigma 204 instrument) at 4000 rpm for 10 minutes. The degradation of centrifuged solution was measured at 400 nm on UV visible spectrophotometer (HACH DR 2400) and the degree of mineralization was carried out using Analytik jena TOC multi N/C 3100 analyzer.

Similar experiments were performed with 2,4-dichlorophenol, 2,5-dichlorophenol, and 2,4,6-trichlorophenol. Stock solutions of these compounds were prepared by dissolving 0.004 gm of the above three compounds in deionized water and diluting to 1 liter. The chlorophenols were also exposed to UV light under conditions similar to those for *p*-nitrophenol. Here the baseline for the individual compounds was established by using the standard 4-aminopyrene method [13].

## 3. Results

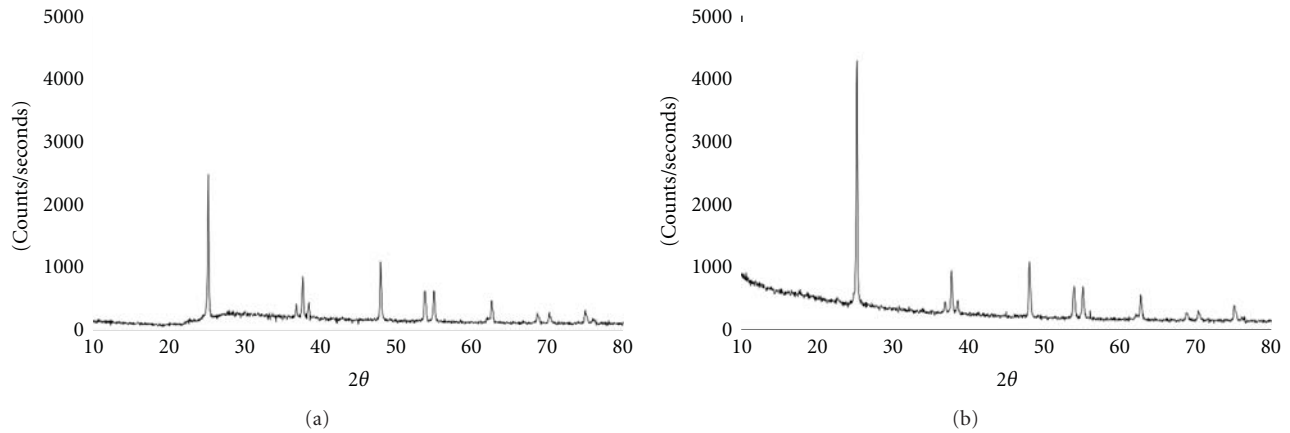
### 3.1. $\text{TiO}_2$ Nanoparticle Characterization

**3.1.1. X-Ray Diffraction.** The crystal phase of laboratory prepared nanoparticles was identified using JEOL JDX-II X-ray diffractometer. XRD patterns are shown in Figure 2. The data indicates that the major phase of all the prepared nanoparticles is anatase. The crystallite size of prepared nanoparticles determined from the broadening of the anatase main peak by Scherrer equation [12] is shown in Table 1.  $\text{TiO}_2$  is in a range of 27 nm to 42 nm while the crystallite size of Ag- $\text{TiO}_2$  is 11.27 nm to 42.52 nm. Our results are in consonance with those reported earlier [7] where Ag- $\text{TiO}_2$  nanoparticles dimensions were reported to be between 15 nm and 37 nm,

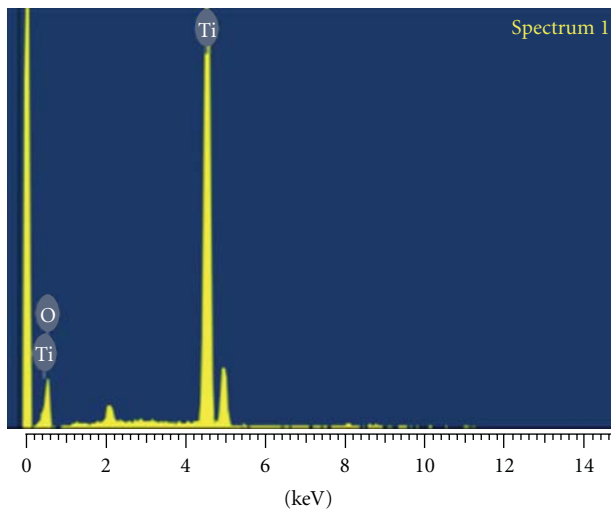
$$D_p = \frac{0.94\lambda}{\beta_{1/2} \cos \theta} \quad (1)$$

(see [12]).

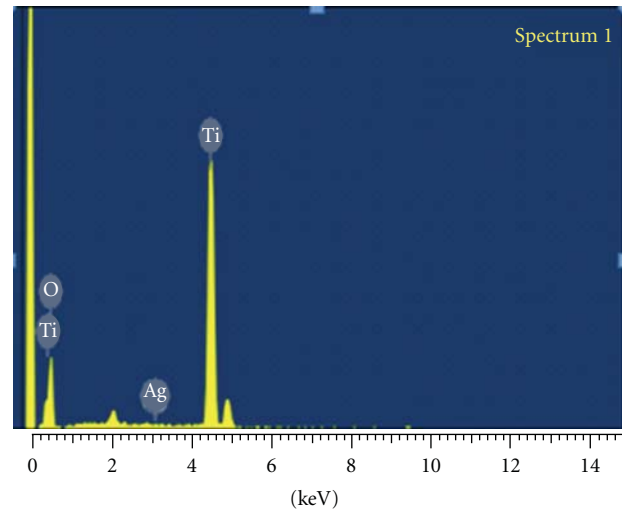
**3.1.2. EDS.** The EDS-spectra of  $\text{TiO}_2$  (Figure 3) and Ag- $\text{TiO}_2$  (Figure 4) was obtained using the Oxford INCA X-sight 200 equipment. In similarity to an earlier work using EDS [7], the presence of three distinct X-ray lines associated with O  $K\alpha$ , Ag  $K\alpha$ , and Ti  $K\alpha$ , is clearly evident. The results

FIGURE 2: X-ray diffraction pattern (a) TiO<sub>2</sub> (b) Ag-TiO<sub>2</sub>.TABLE 1: Crystallite properties of undoped and Ag-doped TiO<sub>2</sub>.

Sr. No.	Particles	Particles Size (nm)		Surface Area (m <sup>2</sup> /g)	Pore Diameter (° A)
		Maximum	Minimum		
1	Undoped TiO <sub>2</sub>	42.52	26.72	74.30	131.06
2	Ag-TiO <sub>2</sub>	42.52	11.27	77.74	129.65



Full scale 929 cts cursor. -0.201 keV(0 cts)

FIGURE 3: EDS pattern of TiO<sub>2</sub> Nanoparticles prepared by Calcination.

Full scale 929 cts cursor. -0.201 keV(0 cts)

FIGURE 4: EDS pattern of Ag-TiO<sub>2</sub> Nanoparticles prepared by Liquid Impregnation Method.

indicate that Ti, O, and Ag are the constitutive elements of the nanoparticles prepared by the Liquid Impregnation method and no extraneous elements are present.

**3.1.3. SEM.** The SEM images of pure titania and Ag-doped titania obtained using (JEOL JSM 6460 Scanning Electron Microscope) are shown in Figures 5 and 6 whereby the porous and sponge-like network of irregularly shaped particles is amply demonstrated. Surface roughness and

shaped complexity of the particles is high in case of Ag-TiO<sub>2</sub> which results in a high surface area. SEM images were taken from different sites of sample and then compared. The resulting image shows that silver is not uniformly deposited on the surface of titania nanoparticles, as found by other authors [12].

**3.1.4. Surface Area and Pore Size Analysis.** Figures 7 and 8 show the nitrogen adsorption isotherms and BJH pore

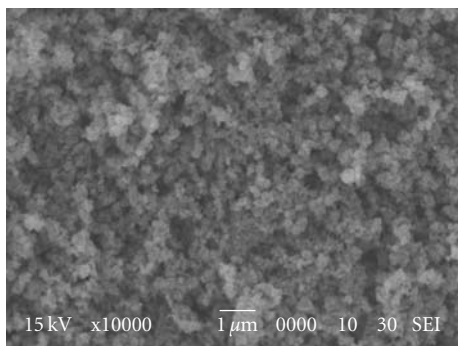


FIGURE 5: SEM micrograph of TiO<sub>2</sub> nanoparticles.

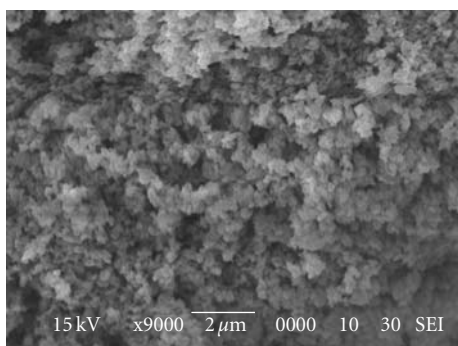


FIGURE 6: SEM micrograph of Ag-TiO<sub>2</sub> nanoparticles.

size distribution curves of doped TiO<sub>2</sub> and undoped TiO<sub>2</sub> samples, respectively, obtained by Surface and Pore Size Analyzer NOVA WIN 2200e. The Brunauer-Emmett-Teller (BET) specific surface areas and pore volumes of doped TiO<sub>2</sub> and undoped TiO<sub>2</sub> are summarized in Table 1. Results reveal that doping results in positive impact on surface area and pore diameter of the TiO<sub>2</sub> nanoparticles.

### 3.2. Optimization Studies.

**3.2.1. Photodegradation of *p*-Nitrophenol.** For the optimization of the photocatalytic process, photocatalytic degradation of *p*-nitrophenol with pure TiO<sub>2</sub> was studied by varying the parameters of light intensity, pH, and irradiation time. The concentration was determined by preparing the calibration curve of *p*-nitrophenol on spectrophotometer.

**3.2.2. Effect of UV Lamp Distance.** The effect of UV light intensity on the degradation of *p*-nitrophenol was studied by varying the distance of UV lamp from the target. Figure 9 shows the relationship of UV light intensity in terms of lamp distance from the sample and percent photocatalytic degradation. As expected, the higher light intensity excited the TiO<sub>2</sub> particles to generate more electron hole pairs. The holes decompose the *p*-nitrophenol molecules adsorbed on the surface of TiO<sub>2</sub> particles and oxidize them to water resulting in their efficient degradation [14].

TABLE 2: Percent degradation of phenolic compounds in one hour.

Nanoparticles	Compounds	Percentage Degradation in 1hr
Pure TiO <sub>2</sub>	<i>p</i> -nitrophenol	83
Ag- TiO <sub>2</sub>	<i>p</i> -nitrophenol	98.3
Ag- TiO <sub>2</sub>	2,4-dichlorophenol	98.9
Ag- TiO <sub>2</sub>	2,5-dichlorophenol	98.55
Ag- TiO <sub>2</sub>	2,4,6-trichlorophenol	96.41

**3.2.3. Effect of pH.** The degree of photocatalytic degradation of *p*-nitrophenol was found to be affected by a change in pH. Figure 10 shows that the photocatalytic degradation of *p*-nitrophenol was high between pH 2 and pH 4, while the degradation efficiency was lower in the alkaline environment above 7 pH. Titania surface will remain positively charged in acidic medium (pH < 7) and negatively charged in alkaline medium (pH > 7). Titanium dioxide is reported to have higher oxidizing activity at lower pH but excess H<sup>+</sup> at very low pH can decrease reaction rate. This observation confirms the finding of other researchers [15].

**3.2.4. Degradation versus Irradiation Time.** One of the very important parameters that was studied for the photocatalytic degradation of *p*-nitrophenol was time of degradation. The degradation rate was observed to increase with increase in irradiation time as shown in Figure 11.

In view of these results, subsequent experiments were carried out at a pH of 4 with UV lamp distance of 5 cm from the target surface of the solution in the china dish.

**3.2.5. Comparative Degradation of *p*-Nitrophenol by Pure TiO<sub>2</sub> and Ag-TiO<sub>2</sub>.** Comparative photocatalytic degradation of *p*-nitrophenol was also investigated in the presence of UV light. Ag-TiO<sub>2</sub> nanoparticles show better results (98% degradation) as compared to pure TiO<sub>2</sub> nano particles (83% degradation) in 1 hour as shown in Figure 12. This is due to the positive effect of silver on the photoactivity of TiO<sub>2</sub> at degradation of *p*-nitrophenol that may be explained by its ability to trap electrons, thus, reducing the recombination of light-generated electron-hole pairs at TiO<sub>2</sub> surface. These results encouraged the use of Ag-doped TiO<sub>2</sub> for the degradation of chlorophenols.

**3.3. Photocatalytic Degradation of Chlorophenols.** When chlorination is done, phenols present in water react with chlorine to form chlorophenols. These chlorophenols are carcinogenic and impart an odour to the water making it unfit for secondary use. Three commonly known chlorophenols were selected which are 2,4-dichlorophenol, 2,5-dichlorophenol, and 2,4,6-trichlorophenol for the photocatalytic degradation using Ag-TiO<sub>2</sub> nanoparticles. The concentration was determined by preparing the calibration curves of chlorophenols using the 4-aminoantipyrene method [13].

As depicted in Figure 13, starting with the same initial concentration, the transformation rate of chlorophenols

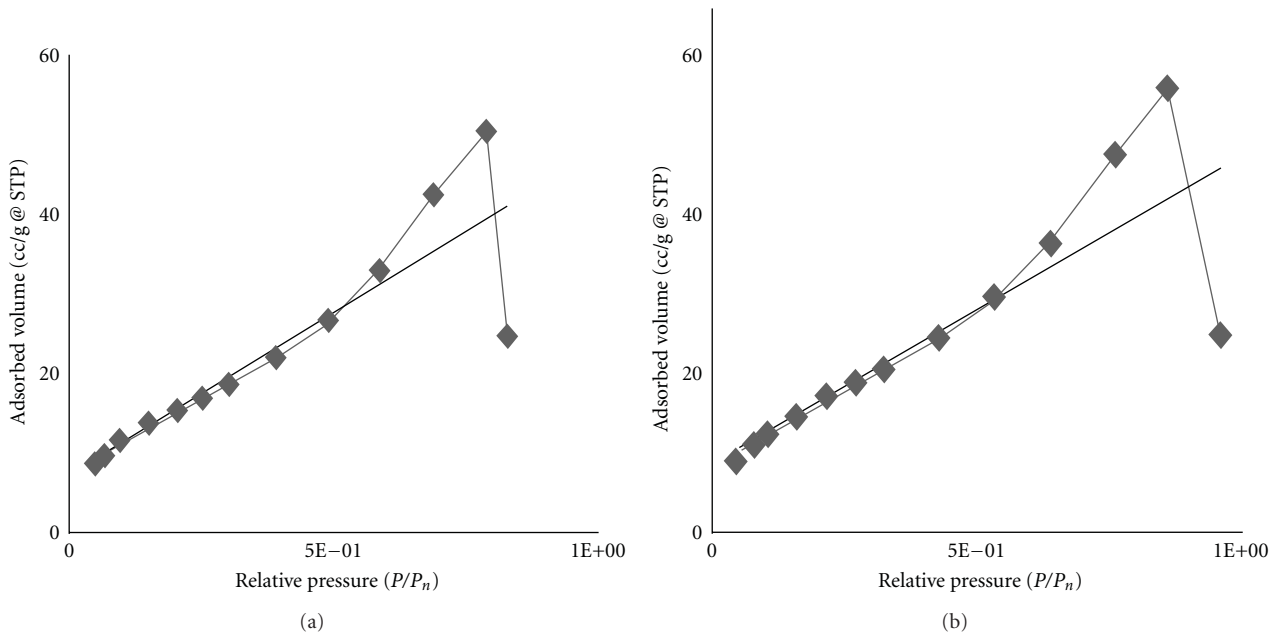


FIGURE 7: Nitrogen adsorption curve for doped and undoped  $\text{TiO}_2$  (a) Undoped  $\text{TiO}_2$  (b) Ag-doped  $\text{TiO}_2$ .

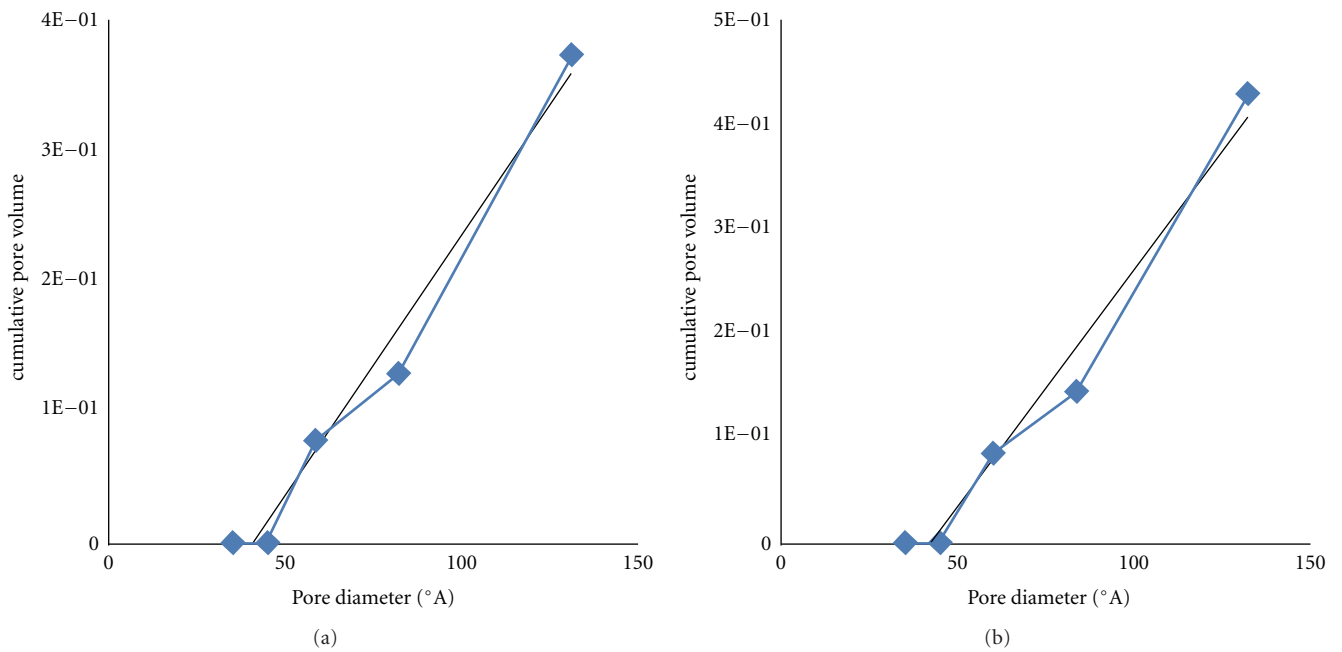


FIGURE 8: Pore size distribution curve for doped and undoped  $\text{TiO}_2$  (a) Undoped  $\text{TiO}_2$  (b) Ag-doped  $\text{TiO}_2$ .

decreases as the number of chlorines on the phenolic ring increases. The addition of chlorine atom has previously been found to reduce the degradation rate of chlorophenols, [16]. In this study, it seems that the increase in the number of chlorine atoms on the phenolic ring makes the chlorophenols less responsive to UV degradation as the photo transformation rate of 2,4-DCP and 2,5-DCP was higher than that of 2,4,6-TCP, as shown in Table 2.

**3.4. Total Organic Carbon (TOC) Analysis.** In the experimental work, photocatalytic degradation of the above discussed phenolic compounds was primarily monitored using absorption spectroscopy. This, however, does not indicate the degree of mineralization of the organic compounds. Following an earlier study [17], the oxidative mineralization was therefore examined by measuring the Total Organic Carbon (TOC) in the solution. The TOC measurements were

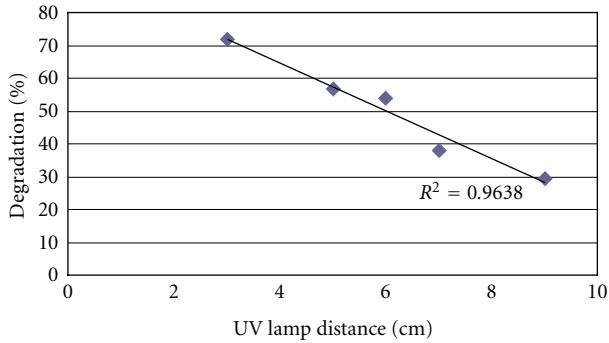


FIGURE 9: Effect of UV lamp distance on photodegradation of *p*-nitrophenol due to change in distance of UV lamp.

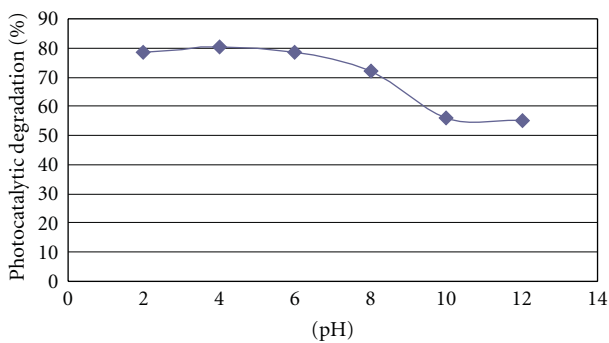


FIGURE 10: Represent the effect of change in pH on photocatalytic degradation of *p*-Nitrophenol.

TABLE 3: Reaction Constants of photocatalytic process with TiO<sub>2</sub> and Ag-TiO<sub>2</sub> for phenolic compounds.

Nanoparticles	Compounds	$K'(\text{min}^{-1}) \times 10^{-2}$ <sup>a</sup>
Pure TiO <sub>2</sub>	<i>p</i> -nitrophenol	2.4
Ag-TiO <sub>2</sub>	<i>p</i> -nitrophenol	6.6
Ag-TiO <sub>2</sub>	2,4-dichlorophenol	7.7
Ag-TiO <sub>2</sub>	2,5-dichlorophenol	6.2
Ag-TiO <sub>2</sub>	2,4,6-trichlorophenol	3.6

<sup>a</sup>Apparent first-order reaction Constants ( $k'$ ).

made using Analytik jena TOC multi N/C 3100 analyzer by direct injection of the aqueous solution after centrifugation.

As discussed above in photocatalytic degradation, the chlorophenols are converted into inorganic products like CO<sub>2</sub>, H<sub>2</sub>O and Cl<sup>-</sup> [18]. Figure 14 gives the results of the TOC experiment indicating that 2,4-DCP was completely mineralized, while 2,5-DCP was mineralized up to 95 percent and 2,4,6-TCP upto 86 percent within the period of 120 minutes. The mineralization efficiency of the above said compounds was calculated by the following formula:

Mineralization efficiency

$$= \frac{\text{TOC}(\text{stock}) - \text{TOC}(\text{after Photocatalysis}) \times 100}{\text{TOC}(\text{stock})}$$

(2)

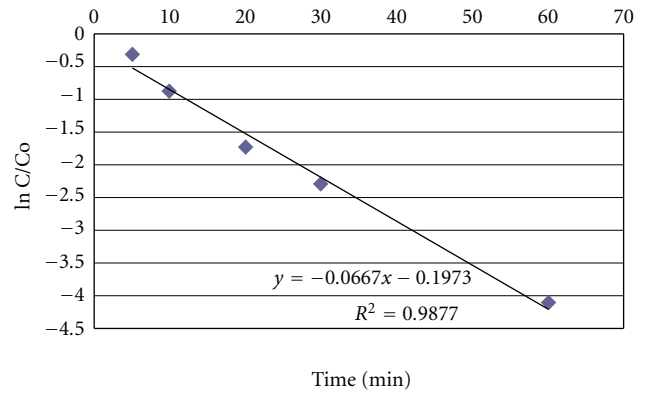
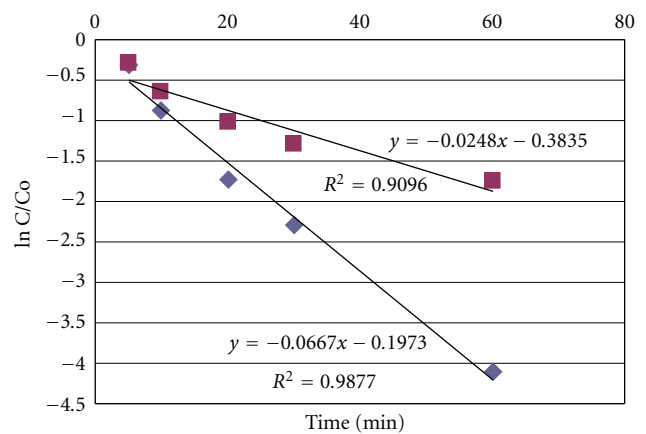
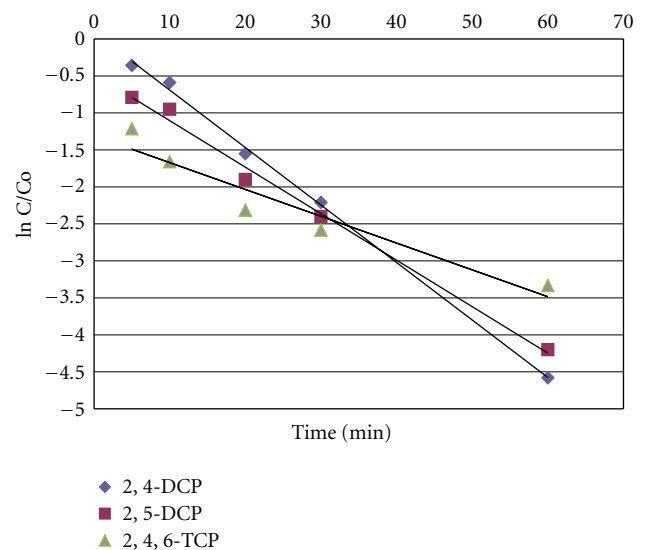


FIGURE 11: Photocatalytic degradation of *p*-Nitrophenol w.r.t irradiation time.



◆ Ag-TiO<sub>2</sub>  
 ■ TiO<sub>2</sub>

FIGURE 12: Comparative photocatalytic degradation of *p*-nitrophenol with pure and Ag-doped Titania Nanoparticles.



◆ 2, 4-DCP  
 ■ 2, 5-DCP  
 ▲ 2, 4, 6-TCP

FIGURE 13: Photocatalytic degradation of phenolic compounds using Ag-TiO<sub>2</sub> nanoparticle on spectrophotometer.

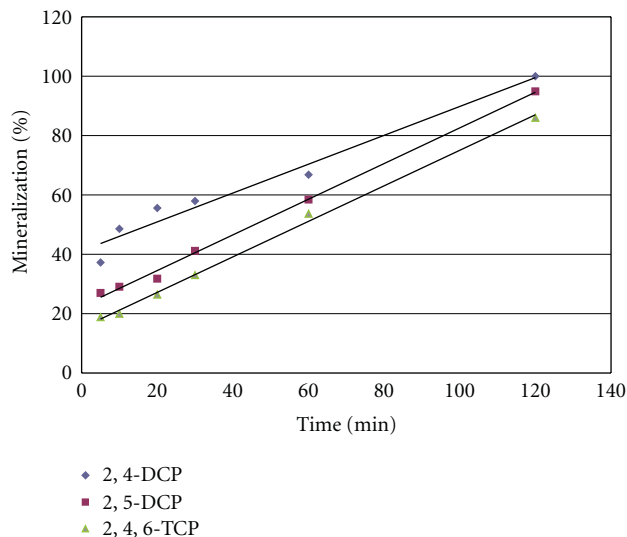


FIGURE 14: Percent mineralization of phenolic compound based on TOC analysis.

3.5. *The Reaction Kinetics.* The photocatalytic degradation of organic pollutants generally follows the Langmuir-Hinshelwood mechanism [16],

$$r = -\frac{dC}{dt} = k\theta = k\frac{KC}{1+KC}, \quad (3)$$

where  $k$  is the true rate constant which depends upon mass of catalyst, the flux of efficient photons, and the coverage in oxygen.  $K$  is the adsorption constant,  $t$  is the time, and  $C$  is the concentration of the organic pollutant. For the low initial concentrations of pollutants, the term  $KC$ , in the denominator, can be neglected and the photocatalytic oxidation rate approaches first order kinetics described by

$$r = -\frac{dC}{dt} = kKC = k'C, \quad (4)$$

where  $k'$ , the apparent rate constant, is also known as the pseudo-first order rate constant. The integral form of the rate equation is

$$\ln \frac{C}{C_0} = -k't, \quad (5)$$

where  $C_0$  is the initial concentration.

Values of  $k'$  for experiments described in this study are given in Table 3.  $k'$  values in Table 3, compare well with the values reported in a previous study [7], which used pure and 1 to 2 mmol Ag-TiO<sub>2</sub> for degradation of *p*-nitrophenol as compared to 1% molar ratio in our case.

## 4. Conclusion

Pure TiO<sub>2</sub> (42.52–26.72 nm), and silver-doped TiO<sub>2</sub> (42.52–11.27 nm) nanoparticles were synthesized through calcination and Liquid Impregnation method. Ag-TiO<sub>2</sub> exhibited good potential for the photocatalytic degradation of phenolic

compounds in acidic environment (pH 4). More than 95% photocatalytic degradation of phenolic compounds could be achieved in 1 hour using Ag-TiO<sub>2</sub> was achieved during 1 hour. Photocatalytic mineralization of 2,4-DCP (100%), 2,5-DCP (95%), and 2,4,6-TCP (86%) was achieved using Ag-TiO<sub>2</sub>, after a period of 2 hours.

Langmuir-Hinshelwood kinetic model provided a good fit to the photocatalytic degradation of phenolic compounds, used in this study.

## References

- [1] T. Kudo, Y. Nakamura, and A. Ruike, "The design of highly active rectangular column-structured titanium oxide photocatalysts and their application in purification systems," *Journal of Catalysis Today*, vol. 122, pp. 14–19, 2003.
- [2] G. Zayani, L. Bousselemi, F. Mhenni, and A. Ghrabi, "Solar photocatalytic degradation of commercial textile azo dyes: performance of pilot plant scale thin film fixed-bed reactor," *Journal of Desalination*, vol. 246, no. 1–3, pp. 344–352, 2009.
- [3] U. I. Gaya and A. H. Abdullah, "Heterogeneous photocatalytic degradation of organic contaminants over titanium dioxide," *Journal of Photochemistry and Photobiology C*, vol. 9, no. 1, pp. 1–12, 2008.
- [4] C. Guillard, J. Disdier, J.-M. Herrmann et al., "Comparison of various titania samples of industrial origin in the solar photocatalytic detoxification of water containing 4-chlorophenol," *Journal of Catalysis Today*, vol. 54, no. 2-3, pp. 217–228, 1999.
- [5] W. A. Zeltner and D. T. Tompkin, *Ashrae Transactions vol. III*, vol. 2, American Society of Heating and Air-Conditioning Engineers, Atlanta, Ga, USA, 2005.
- [6] C. Kormann, D. W. Bahnemann, and M. R. Hoffmann, "Preparation and characterization of quantum-size titanium dioxide," *Journal of Physical Chemistry*, vol. 92, no. 18, pp. 5196–5201, 1988.
- [7] M. S. Lee, S.-S. Hong, and M. Mohseni, "Synthesis of photocatalytic nanosized TiO<sub>2</sub>-Ag particles with sol-gel method using reduction agent," *Journal of Molecular Catalysis A*, vol. 242, no. 1-2, pp. 135–140, 2005.
- [8] D. Guin, S. V. Manorama, J. N. L. Latha, and S. Singh, "Photoreduction of silver on bare and colloidal TiO<sub>2</sub> nanoparticles/nanotubes: synthesis, characterization, and tested for antibacterial outcome," *Journal of Physical Chemistry C*, vol. 111, no. 36, pp. 13393–13397, 2007.
- [9] C. C. Wang, C. M. Lee, and C. H. Kuan, "Removal of 2,4-dichlorophenol by suspended and immobilized *Bacillus insolitus*," *Journal of Chemosphere*, vol. 41, no. 3, pp. 447–452, 2000.
- [10] X.-H. Xu, W.-R. Zhao, Y.-Q. Huang, and D.-H. Wang, "2-chlorophenol oxidation kinetic by photo-assisted Fenton process," *Journal of Environmental Sciences*, vol. 15, no. 4, pp. 475–481, 2003.
- [11] M. P. Ormad, J. L. Ovelleiro, and J. Kiwi, "Photocatalytic degradation of concentrated solutions of 2,4-dichlorophenol using low energy light. Identification of intermediates," *Applied Catalysis B: Environmental*, vol. 32, no. 3, pp. 157–166, 2001.
- [12] M. A. Behnajady, N. Modirshahla, M. Shokri, and B. Rad, "Enhancement of photocatalytic activity of TiO<sub>2</sub> nanoparticles by silver doping: photodeposition versus liquid impregnation methods," *Global NEST Journal*, vol. 10, no. 1, pp. 1–7, 2008.

- [13] A. D. Eaton, L. S. Clesceri, E. W. Rice, and A. E. Greenberg, *Standard Methods for Examination of Water and Wastewater*, 21st edition, 2005.
- [14] I. T. Horváth, "Heterogeneous photocatalytic degradation of organic contaminants over titanium dioxide: a review of fundamentals, progress and problems," *Journal of Encyclopedia Catalysis*, vol. 5, p. 577, 2003.
- [15] Z. Guo, R. Ma, and G. Li, "Photocatalytic property of colloidal TiO<sub>2</sub> nanoparticles prepared by sparking process," *Journal of Chemical Engineering*, vol. 119, p. 55, 2006.
- [16] J.-M. Herrmann, "Heterogeneous photocatalysis: state of the art and present applications," *Journal of Catalysis*, vol. 34, no. 1–4, pp. 49–65, 2005.
- [17] D. Behar, C. Gonzalez, and P. Neta, "Reaction kinetics in ionic liquids: pulse radiolysis studies of 1-butyl-3-methylimidazolium salts," *Journal of Physical Chemistry A*, vol. 105, no. 32, pp. 7607–7614, 2001.
- [18] B. Neppolian, H. C. Choi, S. Sakthivel, B. Arabindoo, and V. Murugesan, "Solar light induced and TiO<sub>2</sub> assisted degradation of textile dye reactive blue 4," *Journal of Chemosphere*, vol. 46, no. 8, pp. 1173–1181, 2002.

## Research Article

# Influence of Lithium on Nanosized Films of Fe<sub>2</sub>O<sub>3</sub>

A. Turković,<sup>1</sup> M. Ivanda,<sup>1</sup> M. Bitenc,<sup>2</sup> and Z. Crnjak Orel<sup>2</sup>

<sup>1</sup>Institute "Ruđer Bošković", P.O.Box 180, 10002 Zagreb, Croatia

<sup>2</sup>National Institute of Chemistry, Hajdrihova 19, 1000 Ljubljana, Slovenia

Correspondence should be addressed to A. Turković, turkovic@irb.hr

Received 20 April 2010; Revised 17 August 2010; Accepted 22 September 2010

Academic Editor: William W. Yu

Copyright © 2011 A. Turković et al. This is an open access article distributed under the Creative Commons Attribution License, which permits unrestricted use, distribution, and reproduction in any medium, provided the original work is properly cited.

We have investigated nanosized thin films of  $\alpha$ -Fe<sub>2</sub>O<sub>3</sub> (hematite) and  $\alpha$ -Fe<sub>2</sub>O<sub>3</sub> with addition of Li, by the impedance spectroscopy (IS), the Raman spectroscopy, scanning electron microscopy (SEM), and X-ray diffraction (XRD). Combining all of these methods, and earlier obtained thermally stimulated currents (TSC) on the same samples, the dependence of structural and electrical properties upon percentage of Li added into the matrix of these metal-oxide films was found. The comparison of IS, Raman, SEM, XRD, and TSC results reveals the increase of the size of nanoparticles upon inducing 1% of Li in Fe<sub>2</sub>O<sub>3</sub> matrix followed by the decrease of the size of nanoparticles in the case of samples with 10% Li, as well as the decrease (increase) of conductivity, respectively. These changes are explained by the structural and morphological changes caused by the impact of Li<sup>+</sup> ions in the charge transfers. This material is suitable for application in the galvanic cell of second generation that could be used as solar-cells backup.

## 1. Introduction

Thin-films containing nanosized grains of Fe<sub>2</sub>O<sub>3</sub> are widely used in research into mainly magnetic and electronic devices [1–5]. Their capacity for incorporating lithium ions is important in the construction of galvanic cells of second generation [6–17].

The one of newest and attractive application of Fe based batteries as high capacity LiFePO<sub>4</sub> and LiFeYPO<sub>4</sub> cells would be in electric vehicles [18]. Our intention is to construct charge-discharge Fe<sub>2</sub>O<sub>3</sub>-electrode battery with polymer electrolyte [19, 20]. Further plan is to attach it to solar-cells [21–24] in order to preserve accumulated charge to use it in cloudy weather.

Films of iron oxide derived by the chemical deposition method route were investigated by the impedance spectroscopy (IS), Raman spectroscopy, SEM, and XRD in order to determine their electrical, structural, and morphological properties. Our goal was to establish the relation between electrical and the structural properties in nanostructured Fe<sub>2</sub>O<sub>3</sub> and Fe<sub>2</sub>O<sub>3</sub>: Li films on glass substrate.

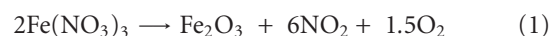
IS was applied to measure the resistance of nanostructured Fe<sub>2</sub>O<sub>3</sub> films with different contents of lithium. In our previous work [25], TSC spectra, often used in characterization of high resistive or semi-insulating (SI)

materials [26, 27], were measured on the same samples, in order to investigate possible defects with deep levels in the forbidden energy gap and to see relation of it to the different percentages of Li.

By Raman and XRD measurements, we have determined, besides the hematite nature of our samples, that they are composed of the nanosized crystalline grains in the size range from 10 nm to 200 nm, which was also proved by SEM investigation. It was also found that the variation of Li<sup>+</sup>-ion content is related to the changes of the nanoparticles ( $d < 5$  nm) related to the acoustic phonons determined by the low frequency Raman measurements. We have also found samples' steadiness during the eight-month period.

## 2. Experimental

The samples were nanostructured Fe<sub>2</sub>O<sub>3</sub> films deposited on the glass substrates and were prepared using chemical vapor deposition procedure shown on Figure 1. One percent water solution of Fe(NO<sub>3</sub>)<sub>3</sub> with LiNO<sub>3</sub> in 1 and 10 of at. % regarding Fe and small quantity of HNO<sub>3</sub> was sprayed onto substrate heated at 593 K. The reaction is:



The home made apparatus for the preparation procedure was described previously [28].

The impedance measurements were performed using a homemade device consisting of an Impedance analyzer I-100 and sample holder with built-in thermocouple copper-constantan with cold junction compensator OMEGA-CJ. Measurements were performed in vacuum of  $10^{-2}$  mbar. PC using software developed in our laboratory recorded the impedance response. Impedance spectra were measured in the frequency range from 100 KHz to 1 MHz. The samples (cubic-formed platelets consisting of  $\text{Fe}_2\text{O}_3$  film on the glass substrate, with surface area of  $100 \text{ mm}^2$  and 2.5 mm thickness) mounted between two zinc electrodes were placed in a spring-contacted apparatus compressing the cell between zinc/teflon cylinders. The idea was to measure glass substrate without  $\text{Fe}_2\text{O}_3$ , and then with  $\text{Fe}_2\text{O}_3$  films with different contents of Li. Measurements were consistent with model circuits [29], representing the sample/electrode systems as parallel sample resistance and capacitance in series with two impedances representing the electrode and sample characteristics.

TSC measurements were performed in the DL-4960 liquid nitrogen cryostat (Bio-Rad), using Keithley K-617 electrometer, under +10 V applied bias voltage, where contacts show ohmic behavior. Samples were heated in the dark until 360 K (in order to empty all deep traps/levels) and then cooled in dark to 85 K. After that, samples were illuminated with the white light during 600 seconds. Another fifty seconds samples were kept in the dark at 85 K and then temperature ramp with  $\beta = 0.4 \text{ K/s}$  was activated. During that, regular TSC spectra were recorded.

Raman spectra were recorded using Dilor Z24 Raman triple monochromator in a  $45^\circ$  scattering configuration using 2 W of cylindrically focused 514.5 nm argon ion laser excitation. Micro-Raman spectra were recorded using Jobin Yvon T64000 in a backscattering configuration with objective LWD 50X of cylindrically focused 514.5 nm argon ion laser excitation.

The grain size, the crystallinity, and the morphology were observed using scanning field emission electron microscopy (SEM, Zeiss, Supra 35 VP).

The identification and classification of prepared samples were made by the X-ray diffraction using a D4 Endeavor, Bruker AXS.

### 3. Results and Discussion

The primary goal of impedance spectroscopy measurements was to determine the electrical conductivity of the  $\text{Fe}_2\text{O}_3$  films and then  $\text{Fe}_2\text{O}_3$  films with different contents of Li. Conductivity results were collected using Zn electrodes with continuous heating in a noninterrupted range between the room temperature of 295 K and 305 K. The conductivity values  $\sigma$  were calculated using the following equation:

$$\sigma = \frac{l}{SR} (\Omega\text{cm}^{-1}), \quad (2)$$

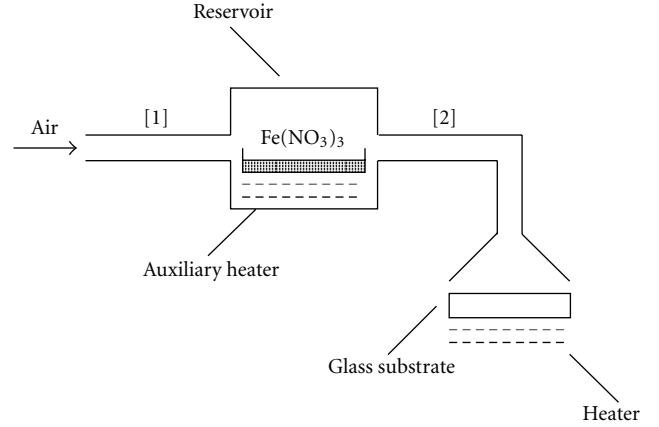


FIGURE 1: The Layout of the home made apparatus for CVD preparation of  $\text{Fe}_2\text{O}_3$  thin films on glass substrate.

TABLE 1: Obtained parameters for different  $\text{Fe}_2\text{O}_3$  samples: measurement temperature in degrees of K, resistivity  $R$  in  $\text{k}\Omega\text{cm}$  obtained by IS, low-frequency Raman modes  $n$  in  $\text{cm}^{-1}$ , and their respective nanosizes  $d$  in nm of  $\text{Fe}_2\text{O}_3$  films on the glass substrate.

sample	$T/\text{K}$	$R/\text{k}\Omega\text{cm}$	$n/\text{cm}^{-1}$	$d/\text{nm}$
$\text{Fe}_2\text{O}_3$	298	40	95	2.0
$\text{Fe}_2\text{O}_3$ with 1% Li	298	250	50	3.9
$\text{Fe}_2\text{O}_3$ with 10% Li	298	54	60	3.2

where  $l$  and  $S$  are the thickness and the area of samples, respectively.  $R$  is the sample resistance estimated from the ac admittance data, after fitting to the experimental curves.

Measurements with Zn electrodes were performed in impedance and admittance modes. Both measurements were performed because the bulk resistivity of the thin film of  $\text{Fe}_2\text{O}_3$ ,  $R_b$ , was more accurately determined from admittance, while charge transfer resistance,  $R_{ct}$ , was determined from impedance measurements.

Figure 2 is showing an example of ac admittance data for the sample of  $\text{Fe}_2\text{O}_3$  obtained at room temperature and equivalent circuits.

At low temperatures, the geometrical capacity was neglected. Its typical values are rather low ( $\sim\text{pF}$ ) deriving from a very high capacitive resistance in the  $C_g$  branch compared with the parallel  $R_b$ . So, the influence of  $C_g$  on the impedance on this parallel circuit can be neglected (Figure 2(b)).

We observed another arc at lower frequencies, which is attributed to a capacity between grain boundaries. By grains we assume crystallites divided by double layers between them. As  $R_{gb}$  was much bigger than  $R_b$ , its influence to the impedance circuit could be neglected so that only  $C_{gb}$  was left.

Figure 3 shows the conductivity plot in the range from 295 to 305 K for  $\text{Fe}_2\text{O}_3$  and  $\text{Fe}_2\text{O}_3$ : Li samples. Resistivities ( $R$ ) obtained from admittance measurements at room temperature are shown in the second column of Table 1.

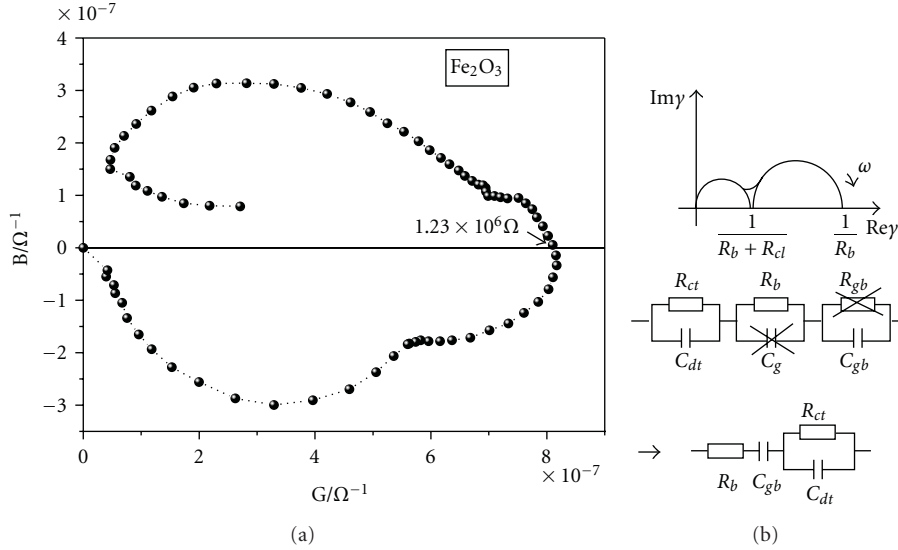


FIGURE 2: (a) Admittance spectra  $\text{Fe}_2\text{O}_3$  thin film measured at room temperature and (b) equivalent circuits and schematic admittance plot for Zn electrodes.

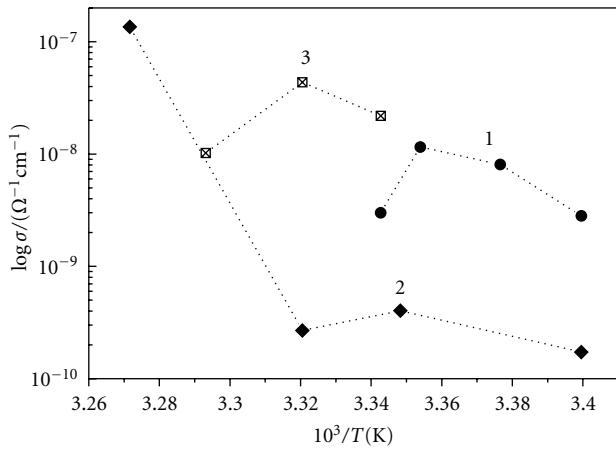


FIGURE 3:  $\log \sigma$  versus  $1000/T$  for  $\text{Fe}_2\text{O}_3$  (1),  $\text{Fe}_2\text{O}_3$  with 1% (2) and  $\text{Fe}_2\text{O}_3$  with 10% of Li (3) measured with Zn electrodes.

Figure 4. shows TSC spectra of three  $\text{Fe}_2\text{O}_3$  samples with different Li content, e.a. pure  $\text{Fe}_2\text{O}_3$  (0% Li), with 1% and finally with 10% of Li, respectively. This figure, showing (a) low- and (b) high-temperature regions, illustrates changes in the defect concentrations related to the different Li contents. Low-temperature TSC spectra are characterized by the negative peak around 155 K, related to the deep trap  $T_2$  (with activation energy,  $E_a = 0.28$  eV) and calculated by equation [25]:

$$E_a = k T_m \ln \left( \frac{T_m^4}{\beta} \right), \quad (3)$$

where  $k$  is the Boltzman's constant,  $T_m$  is temperature of TSC peak maximum (in K), and  $\beta$  is heating rate in K/s. It was observed in  $\text{Fe}_2\text{O}_3$  Li-free samples and in TSC of  $\text{Fe}_2\text{O}_3$  with 1% Li. According to the literature [30, 31], we assign our

TABLE 2: Main parameters of deep traps found in  $\text{Fe}_2\text{O}_3$  samples.

Trap	$T_1$	$T_2$	$T_3$	$T_4$	$T_5$
$E_a$ (eV)	0.18	0.28	0.36	0.64	0.68
$T_m$ (K)	107	155	188	308	327

peak  $T_2$  to the hole trap. Two neighboring peaks,  $T_1$  (with  $T_m = 107$  K and  $E_a = 0.18$  eV) as well as  $T_3$  (at 188 K, 0.36 eV) should correspond to electron traps. TSC spectrum of the sample with 10% Li shows the increase of  $T_1$  and  $T_3$  concentrations, which "screened" negative peak  $T_2$ . It can be explained by abundant release of oppositely charged carriers—electrons from  $T_1$  and  $T_3$  traps and/or by the decrease of the holes traps concentration caused by the structural changes after Li entered into the structure. It should be noticed that doping with 1% of Li causes increase in  $T_2$  hole trap concentration, while further doping (10%) increases  $T_1$  and  $T_3$  peaks. The same observation can be applied for TSC peaks in high-T region. Namely, peaks  $T_4$  (at 308 K, 0.64 eV) and  $T_5$  (327 K, 0.68 eV) decrease in samples with 1% Li and enormously increase in samples with 10% Li content. Main deep trap parameters are presented in Table 2.

In this work, we have determined nanosized values for the acoustic phonons in  $\text{Fe}_2\text{O}_3$  by using the method of low-frequency Raman scattering that had been tested on different powder systems in our previous work [32]. Generally, this method is based on the work of Duval et al. [33], who showed that the maximum of the low-frequency mode of a free particles,  $n$ , corresponds to the angular momentum  $l = 0$  and it is given by

$$n = 0.7(v_l/(d \cdot c)), \quad (4)$$

where  $c$  is the velocity of light in vacuum,  $v_l$  is the longitudinal velocity of sound, and  $d$  is particle diameter. In calculations, we have used  $v_l = 8300$  m/s of a- $\text{Fe}_2\text{O}_3$  [34].

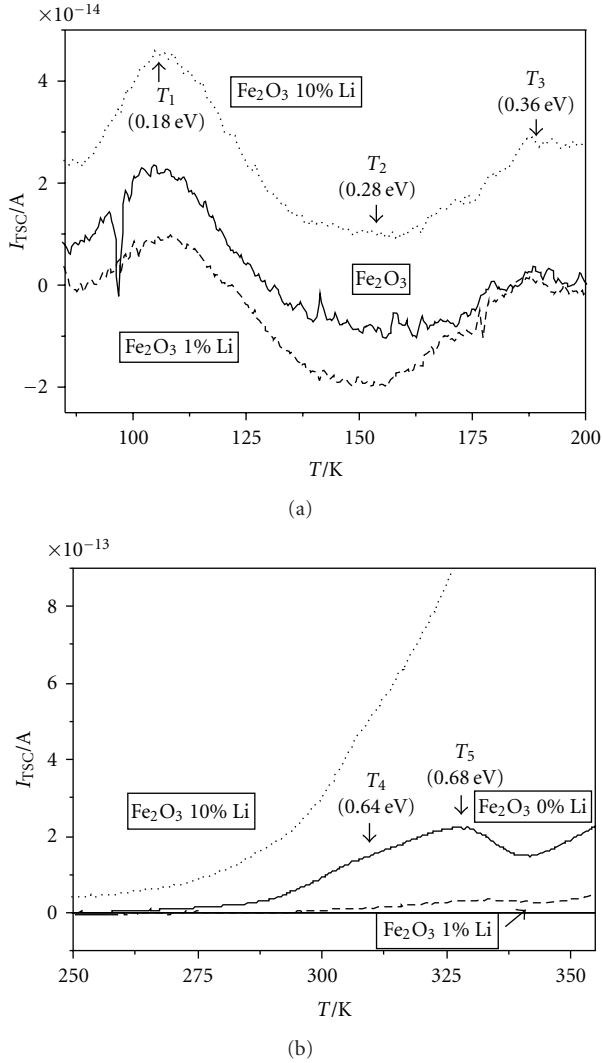


FIGURE 4: TSC spectra of (a) low- and (b) high-temperature region of three samples with different Li content, e.a. Fe<sub>2</sub>O<sub>3</sub> (Li free), Fe<sub>2</sub>O<sub>3</sub> with 1% and Fe<sub>2</sub>O<sub>3</sub> with 10% of Li.

The results of calculations are presented in Table 1. Raman spectra, measured at room temperature and used in Fe<sub>2</sub>O<sub>3</sub> nanosizes determination, are shown at Figure 5. Average nanosizes in sample with 1% of Li increased regarding to the original Li free sample from 2.0 nm to 3.9 nm. After addition of 10% of Li, nanosizes were reduced to 3.2 nm.

We have performed assignation of Raman lines according to the literature [35–38] as hematite and it is shown in Table 3. Hematite,  $\alpha$ -Fe<sub>2</sub>O<sub>3</sub> with corundum structure belongs to the  $D_{3d}^6$  crystal space group, which gives seven characteristic phonon lines  $2A_{1g} + 5E_g$  that are Raman-active fundamentals. Additional Raman experiments were performed after period of 8 months showing stability of hematite phase. Shift of the Raman lines towards higher frequencies upon insertion of Li<sup>+</sup>-ions into the structure is also showing nanostructured [39, 40] nature of the films.

In further discussion, we will try to correlate the results of three types of measurements (IS, TSC [25], and Raman) in

order to gain insight in microscopic resistivity increase upon addition of Li.

Charge transport in simple 3d oxide crystals such as  $\alpha$ -Fe<sub>2</sub>O<sub>3</sub> can be described in terms of hopping and narrow-band conduction by polarons [41]. The electron transition in  $\alpha$ -Fe<sub>2</sub>O<sub>3</sub> usually occurs between the partially filled 3d orbital and the nearly empty sp orbital of O. In a narrow band semiconductors like  $\alpha$ -Fe<sub>2</sub>O<sub>3</sub>, disorder may produce localized states in the whole band. The disorder potential between adjacent states is [41]

$$W_D \geq 6(2Jz), \quad (5)$$

where  $J$  is the overlap integral between 3d orbitals and  $z$  the number of nearest neighbours. In this case, conduction takes place by phonon-assisted hopping of electrons.

The polaron theory that is in detail presented in [41] is one of the possible approaches to interpret our data. Here we introduce view of nanosized acoustic phonons in Raman spectra as quasiparticles, when coupled to the electron, that is, nanoparticle. Low-frequency Raman showed that adding of 1% Li induced significant changes in the nanoparticle size (2 nm  $\rightarrow$  3.9 nm), which is the increase of 95%, and accordingly in the conduction mechanism. Li<sup>+</sup> ions affected holes traps as determined by TSC [25] by increasing their concentration, while electron traps concentration decreased. Activation energies of electrons' and holes' traps  $T_1 - T_5$  remained almost the same (0.18, 0.28, 0.36, 0.64, and 0.68 eV), respectively [25]. One possible explanation is that Li<sup>+</sup> ions combined with related defects in the unit cell causing decrease of overlap integrals and accordingly decrease in the disorder potential  $W_D$ . This induced tensions in the structure that resulted by the nanoparticle enlargement and accordingly its mobility decreases. Increase in resistivity for more than six times was observed (Table 1). The situation is quite different in samples with 10% Li: nanoparticle size decreased from 3.9 nm to 3.2 nm and resistivity simultaneously decreased almost to the value of the referent Li free sample. The increase of the conductivity is due to structural disorder created by Li<sup>+</sup> ions, which are having ten times greater concentration than in the sample with 1% Li. In such disordered structure, disorder potential can vanish and nanoparticle can easily move through the sample. The mechanism of hopping electrons can also occur and add to the conductivity increase. The same observation can be applied for TSC peaks in high- $T$  region, namely, peaks  $T_4$  (at 308 K, 0.64 eV) and  $T_5$  (327 K, 0.68 eV) decrease in samples with 1% Li and enormously increase in samples with 10% Li [25]. These two peaks represent deep traps and as they decrease upon addition of 1% of Li, the conductivity also decreases, which is in agreement with IS measurements (Table 1). Further increase of Li content to 10% increases concentrations of these traps and conductivity increases, due to enlarged release of electrons from traps, which is also in accordance with IS results. The increase in deep traps concentrations indicates that samples with 10% Li are amorphous.

Scanning field emission electron microscopy and XRD measurements were performed in order to check the grain size, the crystallinity, and the morphology, revealed by other methods.

TABLE 3: Raman wave numbers and assignments of the hematite films prior and after addition of  $\text{Li}^+$  ions.

Assignment	Raman shift/ $\text{cm}^{-1}$					
	$\text{Fe}_2\text{O}_3$	1		2		
	$\text{Fe}_2\text{O}_3$	$\text{Fe}_2\text{O}_3 + 1\% \text{ Li}$	$\text{Fe}_2\text{O}_3 + 10\% \text{ Li}$	$\text{Fe}_2\text{O}_3$	$\text{Fe}_2\text{O}_3 + 1\% \text{ Li}$	$\text{Fe}_2\text{O}_3 + 10\% \text{ Li}$
	78 w	56 sh	69 vw			
	99 sh					
A1g(1)	213 vs	221 w	221 m	223 s	223 sh	219 vw
Eg(1)				241 sh	245 w	241 vw
					267 sh	
Eg(1)	282 vs	286 vs	284 m	290 vs	297 m	296 m
Eg(1)	395 w	402 vs	393 s	404 s	407 vs	407 s
A1g(2)		488 w	490 w	490 vw		
Eg(1)	586 w	608 w	600 w	608 w	609 w	608 w

1: First measurement, 2: Second measurement after 8 months: vs: very strong, s: strong, m: medium, sh: shoulder, w: weak, vw: very weak.

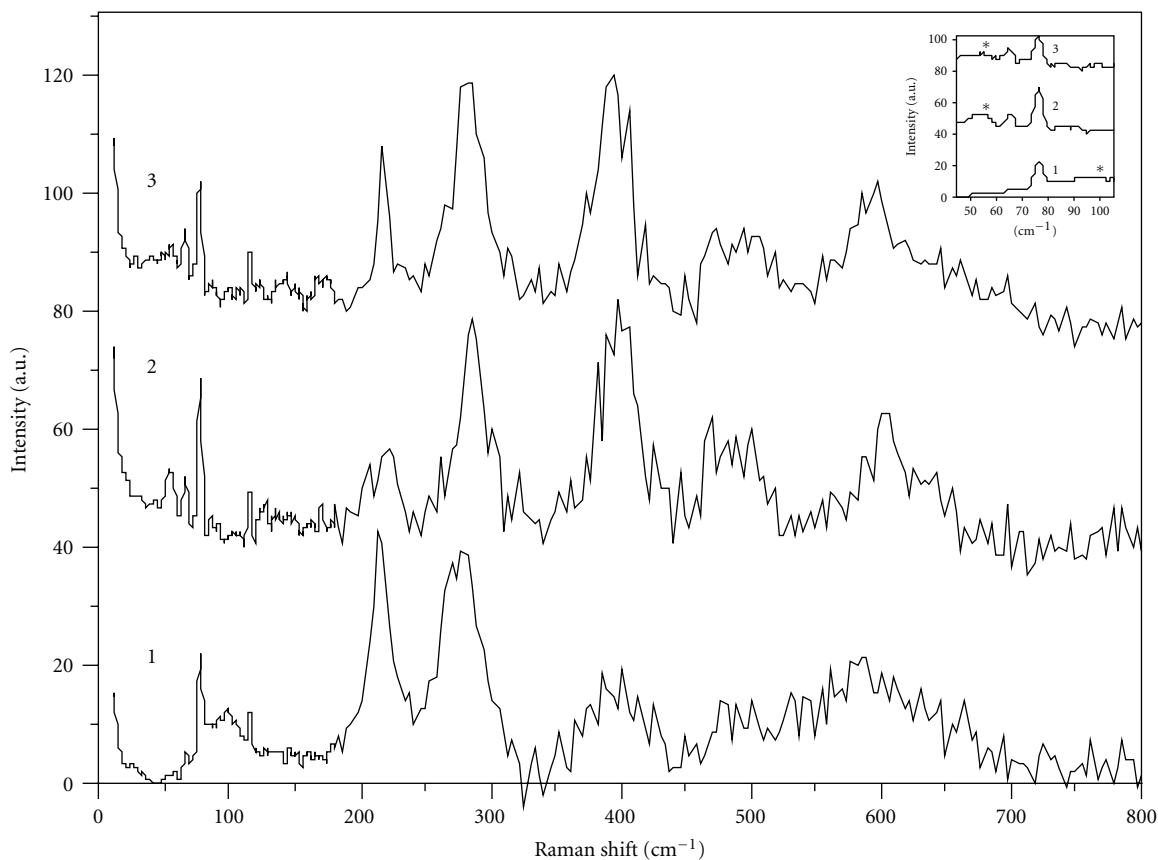


FIGURE 5: Raman spectra of Li free  $\text{Fe}_2\text{O}_3$  (1),  $\text{Fe}_2\text{O}_3$  with 1% (2), and  $\text{Fe}_2\text{O}_3$  with 10% of Li (3). Inset shows low-frequency region of the same spectra pointing out low frequency modes revealing nanosizes.

SEM photographs of  $\alpha\text{-Fe}_2\text{O}_3$  and of the same material with added Li ions are shown on Figure 6. It is clearly visible on lower magnification that sample (a) shows much more homogeneous surface than the samples (c) and (e). The crystallinity is changed and films (c) and (e) became partly and completely amorphous, respectively. The surface of sample (e) shows good homogeneity and on higher

magnification some nanoagglomerated grains are visible. Figures 6(b), 6(d), and 6(f) present SEM photographs of the same films after 8 months, demonstrating no significant difference upon earlier results.

On higher magnification in Figure 7, it is shown that film  $\text{Fe}_2\text{O}_3$  is formed from nanograins in the radius,  $R$ , range from 75 nm to 240 nm. The maximum for grain size distribution

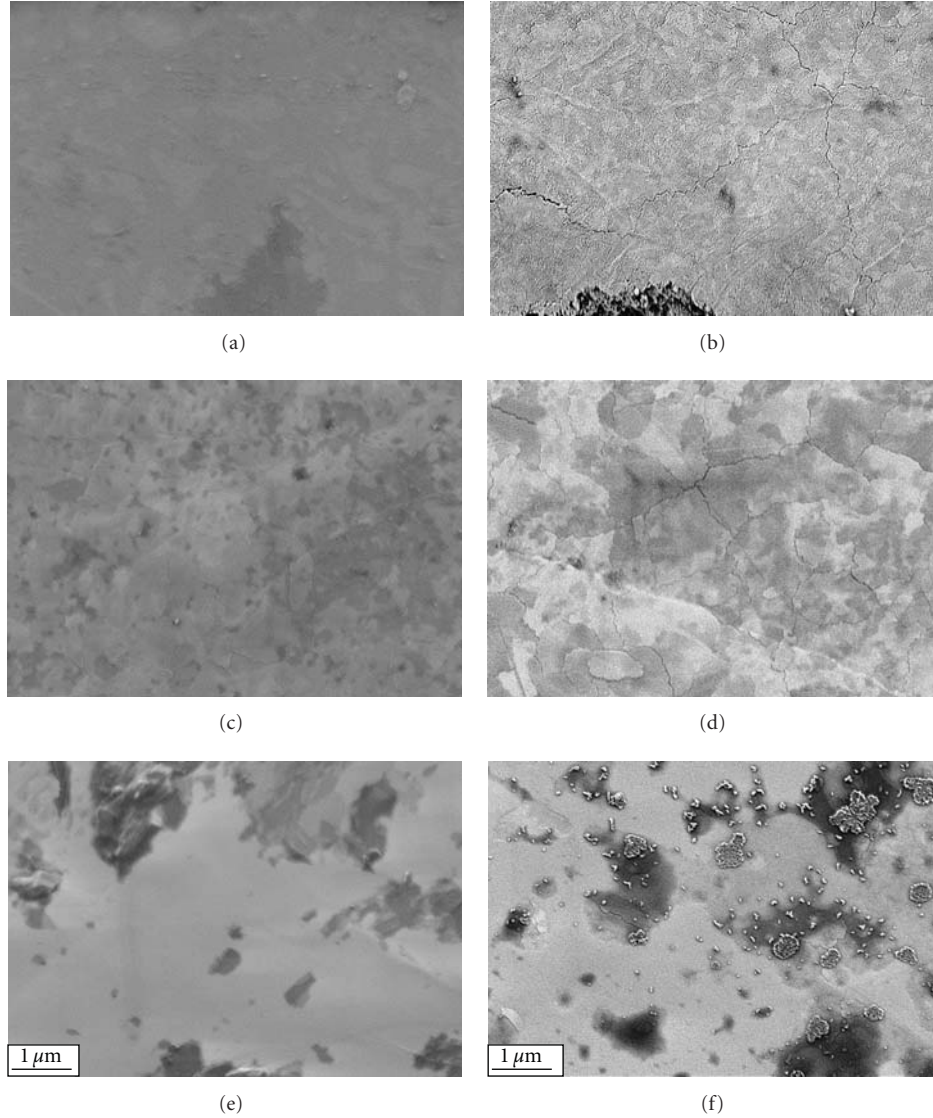


FIGURE 6: SEM photographs Li free  $\text{Fe}_2\text{O}_3$  (a),  $\text{Fe}_2\text{O}_3$  with 1% (c) and  $\text{Fe}_2\text{O}_3$  with 10% of Li (e), and the same films after 8 months (b), (d), and (f), respectively.

is at  $R = 120$  nm as fitted to Lorentian shape. It is confirmed that the grains are crystalline as shown on XRD spectra shown on Figure 8. The tensions in the crystalline structure are seen as cracks in Figure 7.

The results of the XRD measurements of the samples prepared as films on the glass substrate are presented on Figure 8. The prepared film on Figure 8(a) showed the characteristic diffractogram of hematite structure (reference code 01-079-1741, mineral name: Hematite, synthetic, ICSD name: Iron Oxide).

We have calculated grain sizes in  $\text{Fe}_2\text{O}_3$  by using Debye-Scherrer formula:

$$D = \frac{0.9 \cdot \lambda}{\beta \cos \theta}, \quad (6)$$

where  $D$  is diameter of grain,  $\lambda$  is the wavelength of the X-ray beam,  $\beta$  is the width at the half height of the particular

line in radians, and  $\cos \theta$  is the position of the peak in  $2\theta$  scale.  $D$  values were obtained in the range from 20 nm to 110 nm, which is in agreement with the nanometre range of grain sizes observed on SEM photograph shown in Figure 7.

At Figure 8(b), only one small intensity peak at  $39.295^\circ$  with  $D = 27$  nm is shown. The recordings were with the same intensity (see  $y$ -axes) as in Figure 8(a). Figure 8(c) is not showing any crystalline lines. Figure 8 clearly shows amorphization of the sample upon addition of  $\text{Li}^+$  ions, from pure crystalline hematite (a), through amorphous phase with 1% Li (b) and to completely amorphous phase with 10% Li (c).

#### 4. Conclusion

As a conclusion, the present study showed that IS, Raman spectroscopy, SEM, and XRD could be applied for grain

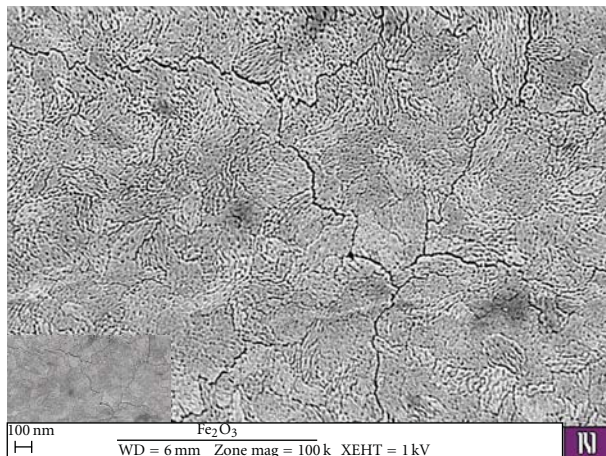


FIGURE 7: SEM photograph Li free  $\text{Fe}_2\text{O}_3$  (a), with higher magnification of 100.00 K.

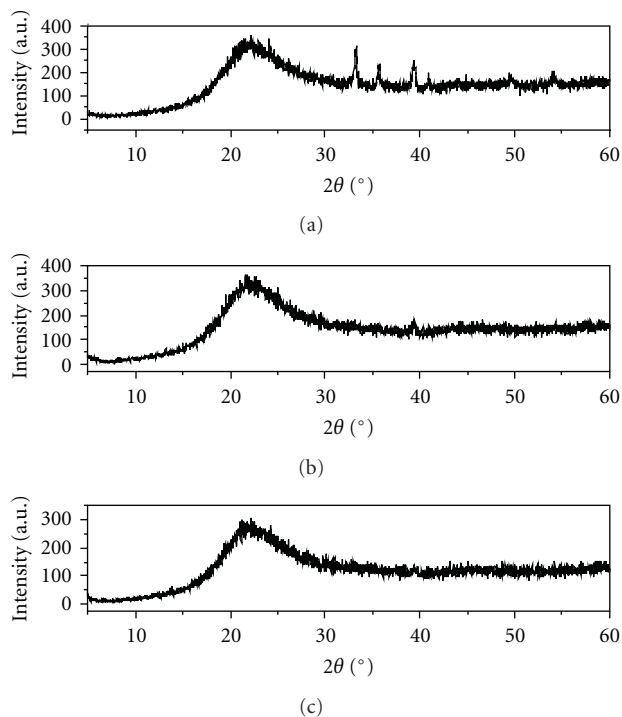


FIGURE 8: XRD spectra of  $\text{Fe}_2\text{O}_3$  (a),  $\text{Fe}_2\text{O}_3$  with 1% (b), and  $\text{Fe}_2\text{O}_3$  with 10% of Li (c).

size and conductivity determination in nanosized films of  $\text{Fe}_2\text{O}_3$  and  $\text{Fe}_2\text{O}_3$ : Li on glass substrate. The results obtained with IS, Raman spectroscopy and previously, with TSC analysis [25], together with XRD and SEM give complementary data to build a model of the charge transport in these nanostructured films. IS revealed trends in conductivity changes, while TSC gave insight in deep traps concentration changes related to the increase of Li percentage in  $\text{Fe}_2\text{O}_3$ . By the low-frequency Raman spectroscopy, it was possible to follow changes of the nanoparticles (which are acoustic phonons

coupled to electrons with the nanosize diameter range  $d < 5$  nm), during the structural changes induced by the introduction of Li into the  $\text{Fe}_2\text{O}_3$ . It was observed that nanoparticles sizes are increasing with addition of Li to the films, and a little bit decreasing with further increase of Li content. Also, Raman spectroscopy showed that we were dealing with nanostructured  $\alpha$ - $\text{Fe}_2\text{O}_3$  (hematite) films. Samples also showed steadiness, during rest period of eight months. XRD measurements additionally proved that samples are  $\alpha$ - $\text{Fe}_2\text{O}_3$ , hematite phase of iron oxide. SEM patterns, as well as Raman and XRD, showed that the addition of  $\text{Li}^+$  ions have changed nanostructure of the samples from the crystalline grains in the diameter range  $D > 20$  nm to the amorphous phase.

Here we point out the distinction between the two terms, nanoparticles and nanograins, used in this paper, as they are describing noncrystalline and crystalline forms, respectively. Nanoparticles could be possibly seen as seeds for the amorphization process during the increase of Li percentage in our samples.

This particular morphology is suitable for application in an advanced electrochemical cell concept, which could be used as charge storage for solar cells.

## Acknowledgments

The authors thank the Croatian and the Slovenian Ministries of Science and Technology for financially supporting this work.

## References

- [1] J. Zhu and K. J. Tseng, "Reducing dielectric losses in MnZn ferrites by adding  $\text{TiO}_2$  and  $\text{MoO}_3$ ," *IEEE Transactions on Magnetics*, vol. 40, no. 5, pp. 3339–3345, 2004.
- [2] C. N. R. Rao, G. U. Kulkarni, P. J. Thomas, V. V. Agrawal, U. K. Gautam, and M. Ghosh, "Nanocrystals of metals, semiconductors and oxides: novel synthesis and applications," *Current Science*, vol. 85, no. 7, pp. 1041–1045, 2003.
- [3] L. L. Casas, A. Roig, E. Rodríguez, E. Molins, J. Tejada, and J. Sort, "Silica aerogel-iron oxide nanocomposites: structural and magnetic properties," *Journal of Non-Crystalline Solids*, vol. 285, no. 1–3, pp. 37–43, 2001.
- [4] T. Mizushima, A. Makino, F. Kaneko, and S. Kobayashi, "Soft magnetic properties of single crystalline Mn-Zn ferrites containing  $\text{Er}_2\text{O}_3$ ," *Materials Transactions, JIM*, vol. 32, no. 12, pp. 1177–1179, 1991.
- [5] Z. Y. Ling, M. R. Xiong, and Q. Q. Zhang, "Effects of iron deficiency on magnetic properties of  $(\text{Ni}_{0.76}\text{Zn}_{0.24})\text{O}(\text{Fe}_2\text{O}_3)_{0.575}$  ferrite," *Journal of Magnetism and Magnetic Materials*, vol. 219, no. 1, pp. 9–14, 2000.
- [6] Y. Zhang, X.-P. Gao, H. Hu et al., "Electrochemical performance of carbon nanotubes filled with  $\text{Fe}_2\text{O}_3$  as anode materials for Li-ion batteries," *Chinese Journal of Inorganic Chemistry*, vol. 20, no. 9, pp. 1013–1017, 2004.
- [7] T. Grygar, P. Bezdička, D. Hradil, and L. Pikna, "Electrochemical analysis of metal oxides," *Solid State Phenomena*, vol. 90–91, pp. 45–50, 2003.
- [8] T. Matsumura, N. Sonoyama, R. Kanno, and M. Takano, "Lithiation mechanism of new electrode material for lithium ion cells—the  $\alpha$ - $\text{Fe}_2\text{O}_3$ - $\text{SnO}_2$  binary system," *Solid State Ionics*, vol. 158, no. 3–4, pp. 253–260, 2003.

- [9] S. Komaba, K. Suzuki, and N. Kumagai, "Synthesis of nanocrystalline  $\text{Fe}_2\text{O}_3$  for lithium secondary battery cathode," *Electrochemistry*, vol. 70, no. 7, pp. 506–510, 2002.
- [10] C.-W. Kwon, A. Poquet, S. Mornet, G. Campet, J. Portier, and J.-H. Choy, "A new polypyrrole/maghemite hybrid as a lithium insertion electrode," *Electrochemistry Communications*, vol. 4, no. 2, pp. 197–200, 2002.
- [11] W. Wong-Ng, R. S. Roth, T. A. Vanderah, and H. F. McMurdie, "Phase equilibria and crystallography of ceramic oxides," *Journal of Research of the National Institute of Standards and Technology*, vol. 106, no. 6, pp. 1097–1134, 2001.
- [12] N. Cui and J. L. Luo, "Effects of oxide additions on electrochemical hydriding and dehydriding behavior of  $\text{Mg}_2\text{Ni}$ -type hydrogen storage alloy electrode in 6 M KOH solution," *Electrochimica Acta*, vol. 44, no. 5, pp. 711–720, 1998.
- [13] S. Ito, K. Ui, N. Koura, and K. Akashi, "Lithium secondary battery using potassium- $\beta$ -ferrite as a new cathode active material," *Solid State Ionics*, vol. 113–115, pp. 17–21, 1998.
- [14] J. Sarradin, M. Ribes, A. Guessous, and K. Elkacemi, "Study of  $\text{Fe}_2\text{O}_3$ -based thin film electrodes for lithium-ion batteries," *Solid State Ionics*, vol. 112, no. 1-2, pp. 35–40, 1998.
- [15] A. M. Mastral, M. J. Perez-Surrio, and J. M. Palacios, "Thermal and chemical modifications on a low rank coal by iron addition in swept fixed bed hydrolysis," *Fuel*, vol. 77, no. 6, pp. 585–590, 1998.
- [16] S. Ito, K. Ui, N. Hoshi, H. Kurosawa, N. Koura, and K. Akashi, "K<sup>+</sup>- $\beta$ -ferrite as a new cathode active material for lithium secondary battery," vol. 7, no. C1, pp. C1-161–C1-162.
- [17] A. Guerrero, A. Romero, R. D. Morales, and F. Chavez, "Thermodynamic analysis of the soda ash smelting of lead acid battery residue in a rotary furnace," *Canadian Metallurgical Quarterly*, vol. 36, no. 2, pp. 121–130, 1997.
- [18] GWL group, Europe; <http://www.yttrium-power.com/>.
- [19] A. Turković, A. Drašner, D. Šokčević, M. Ritala, T. Asikainen, and M. Leskelä, "Comparison between CVD and ALE produced  $\text{TiO}_2$  cathodes in  $\text{Zn}/(\text{PEO})_4\text{ZnCl}_2/\text{TiO}_2, \text{SnO}_2$  or ITO galvanic cells," *Journal de Physique IV*, vol. 5, no. C5, pp. 1133–1139, 1995.
- [20] A. Turković and Z. Crnjak Orel, "Electrical and optical properties of  $\text{zn}/(\text{PEO})_4\text{ZnCl}_2/[\text{CeO}_2 \text{ or } \text{CeO}_2\text{-SnO}_2(17\%)]$ ; ITO thin film galvanic cells," *Solid State Ionics*, vol. 89, no. 3-4, pp. 255–261, 1996.
- [21] A. Turkovic, H. Zorc, D. Kontrec, and V. Vranesa, "Comparative study of organo-metallic dyes and fullerenes in dye-sensitized  $\text{TiO}_2$  solar cells," *Strojarstvo*, vol. 38, no. 6, p. 257, 1996.
- [22] A. Turković and Z. C. Orel, "Dye-sensitized solar cell with  $\text{CeO}_2$  and mixed  $\text{CeO}_2/\text{SnO}_2$  photoanodes," *Solar Energy Materials and Solar Cells*, vol. 45, no. 3, pp. 275–281, 1997.
- [23] Y. Wang, T. Yu, X. Chen et al., "Enhancement of photoelectric conversion properties of  $\text{SrTiO}_3/\alpha\text{-Fe}_2\text{O}_3$  heterojunction photoanode," *Journal of Physics D*, vol. 40, no. 13, pp. 3925–3930, 2007.
- [24] M. B. Sahana, C. Sudakar, G. Setzler et al., "Bandgap engineering by tuning particle size and crystallinity of  $\text{SnO}_2\text{-Fe}_2\text{O}_3$  nanocrystalline composite thin films," *Applied Physics Letters*, vol. 93, no. 23, Article ID 231909, 2008.
- [25] A. Turković, M. Pavlović, M. Ivanda, M. Gaberšček, and Z. C. Orel, "Influence of intercalated lithium on structural and electrical properties of  $\text{V}_2\text{O}_5$ , mixed V/Ce oxide, and  $\text{Fe}_2\text{O}_3$ ," *Journal of the Electrochemical Society*, vol. 153, no. 1, pp. A122–A126, 2006.
- [26] Z. Fang, L. Shan, T. E. Schlesinger, and A. G. Milnes, "Study of defects in LEC-grown undoped SI-GaAs by thermally stimulated current spectroscopy," *Materials Science and Engineering B*, vol. 5, no. 3, pp. 397–408, 1990.
- [27] M. Pavlović, U. V. Desnica, and J. Gladić, "Complete set of deep traps in semi-insulating GaAs," *Journal of Applied Physics*, vol. 88, no. 8, pp. 4563–4570, 2000.
- [28] A. Turković, D. Šokčević, T. Valla, M. Milun, and J. Rukavina, "Thermal stability of CV deposited  $\text{TiO}_2$  Thin Films. XPS and AES characterisation," *Fizika A*, vol. 2, pp. 23–34, 1993.
- [29] A. Turković and Z. Crnjak Orel, "Electrical and optical properties of  $\text{zn}/(\text{PEO})_4\text{ZnCl}_2/[\text{CeO}_2 \text{ or } \text{CeO}_2\text{-SnO}_2(17\%)]$ ; ITO thin film galvanic cells," *Solid State Ionics*, vol. 89, no. 3-4, pp. 255–261, 1996.
- [30] S. Singh, "TSC curves in (ZnO-MgO): Fe, O photoconductor: existence of negative and oscillatory characters," *Journal of Materials Science*, vol. 8, no. 6, pp. 848–850, 1973.
- [31] C.-H. Lee, G.-N. Jeon, S.-C. Yu, and S.-Y. Ko, "Simultaneous measurement of thermally stimulated luminescence and thermally stimulated current of ZnSe single crystal," *Journal of Physics D*, vol. 28, no. 7, pp. 1951–1957, 1995.
- [32] M. Ivanda, A. M. Tonejc, I. Djerdj et al., "Determination of nanosized particles distribution by low frequency Raman scattering: comparison to electron microscopy," in *Lecture Notes in Physics: Nanoscale Spectroscopy and Its Applications to Semiconductor Research*, Y. Watanabe, S. Heun, G. Salviati, and N. Yamamoto, Eds., pp. 16–27, Springer, New York, NY, USA, 2002.
- [33] E. Duval, A. Boukenter, and B. Champagnon, "Vibration eigenmodes and size of microcrystallites in glass: observation by very-low-frequency Raman scattering," *Physical Review Letters*, vol. 56, no. 19, pp. 2052–2055, 1986.
- [34] Y. Shapira, "Ultrasonic behavior near the spin-flop transitions of hematite," *Physical Review*, vol. 184, no. 2, pp. 589–600, 1969.
- [35] I. R. Beattie and T. R. Gilson, "The single-crystal Raman spectra of nearly opaque materials. Iron(III) oxide and chromium(III) oxide," *Journal of the Chemical Society A*, pp. 980–986, 1970.
- [36] D. L. A. de Faria, S. Venâncio Silva, and M. T. De Oliveira, "Raman microspectroscopy of some iron oxides and oxyhydroxides," *Journal of Raman Spectroscopy*, vol. 28, no. 11, pp. 873–878, 1997.
- [37] D. Bersani, P. P. Lottici, and A. Montenero, "Micro-Raman investigation of iron oxide films and powders produced by sol-gel syntheses," *Journal of Raman Spectroscopy*, vol. 30, no. 5, pp. 355–360, 1999.
- [38] O. N. Shebanova and P. Lazor, "Raman study of magnetite ( $\text{Fe}_3\text{O}_4$ ): laser-induced thermal effects and oxidation," *Journal of Raman Spectroscopy*, vol. 34, no. 11, pp. 845–852, 2003.
- [39] A. Turković, M. Ivanda, V. Vraneša, and A. Drašner, "Raman spectroscopy of thermally annealed  $\text{TiO}_2$  thin films obtained by chemical vapour deposition and the spray method," *Vacuum*, vol. 43, no. 5–7, pp. 471–473, 1992.
- [40] S. Musić, M. Gotić, M. Ivanda et al., "Chemical and microstructural properties of  $\text{TiO}_2$  synthesized by sol-gel procedure," *Materials Science and Engineering B*, vol. 47, no. 1, pp. 33–40, 1997.
- [41] I. G. Austin, "Polaron conduction in disordered 3d oxides," *Journal of Non-Crystalline Solids*, vol. 2, pp. 474–483, 1970.

## Research Article

# Atomic-Level Investigation of $\text{CH}_x$ and $\text{C}_2\text{H}_x$ Adsorption on $\beta$ -SiC (111) Surface for CVD Diamond Growth from DFT Calculations

Naichao Chen and Fanghong Sun

School of Mechanical Engineering, Shanghai Jiao Tong University, Shanghai 200240, China

Correspondence should be addressed to Fanghong Sun, sunfanghong@sjtu.edu.cn

Received 30 April 2010; Accepted 28 June 2010

Academic Editor: Bo Zou

Copyright © 2011 N. Chen and F. Sun. This is an open access article distributed under the Creative Commons Attribution License, which permits unrestricted use, distribution, and reproduction in any medium, provided the original work is properly cited.

The focus of this paper is on the adsorption of unsaturated hydrocarbon molecules on  $\beta$ -SiC (111) surfaces during diamond film growth. The  $\text{CH}_x$  and  $\text{C}_2\text{H}_x$  molecules have been investigated to obtain a specific insight into absorbing diamond processes on the atomic scale. Structural and electronic properties of  $\text{CH}_x$  and  $\text{C}_2\text{H}_x$  adsorption on the Si- and C-terminated surfaces have been studied by first-principles calculations based on density functional theory (DFT). From the calculated energetics and geometries, we find that  $\text{C}_2\text{H}_x$  adsorption on the Si-terminated surfaces has six possible surface reconstructions. For the C-terminated surface, there exist eight possible surface reconstructions. Five surface reconstructions, including  $\text{CH}_2$  adsorption on the Si- and C-terminated surface,  $\text{CH}-\text{CH}_2$  and  $\text{CH}=\text{CH}_2$  adsorption on the C-terminated surface, and  $\text{C}_2\text{H}_5$  adsorption on the Si-terminated surface, have the largest hydrogen adsorption energies and more stability of surface reconstructions. Calculations demonstrate that the Si-terminated surface is energetically more favorable for fabricating CVD diamond coatings than the C-terminated surface.

## 1. Introduction

A variety of chemical vapor deposition (CVD) techniques are able to deposit diamond films [1–3]. The intrinsic reactivity of a hetero-substrate under CVD plasma strongly determines the mechanisms competing with diamond nucleation. These mechanisms have often detrimental consequences on the quality of the interface with diamond [4, 5]. The chemical kinetic model of CVD has been developed to study the detailed descriptions of both gas-phase and surface processes occurring in gas-activated deposition of diamond film [2, 3, 6]. Several reaction pathways describing deposition of diamond initiated by different gaseous species, including the  $\text{CH}_3$ ,  $\text{C}_2\text{H}_2$ , C [3], and several  $\text{C}_2\text{H}_x$  [6] species, have provided a specific insight into chemical processes. These techniques are capable of identifying the activation of the growing surface. In addition, the theoretical model has been employed to investigate diamond formation by combining mass, momentum, and energy balance equations for the gas flow with detailed chemical mechanisms for the gas phase and surface chemistry [2, 7]. The gas phase composition profile and surface chemical kinetics for diamond formation have been solved. However, these types of issues do not well

and enough describe the growth mechanism of diamond film and the acquiring diamond film of high quality efficiently. The surface diffusion [1] and quantum-mechanical calculations and localized kinetic analysis [8] farther highlight an understanding of the atomic-scale dynamics that lead to the CVD of diamond formation.

Recently, the CVD diamond coatings on SiC substrates have been investigated [5, 9, 10]. The formation of carbon phase and the roughening of the 3C-SiC surface have been observed [4]. Therefore, adsorption of unsaturated hydrocarbon molecules on SiC surfaces is of great importance to investigate the initial-stage growth of diamond film on SiC substrates. At the same time, the SiC surface and its reconstructions have attracted much attention both in experiment [11] and theory [12] due to its fundamental interest and technological importance in recent years. Progresses in several theoretical applications, such as *ab initio* [13, 14] and empirical molecular dynamic [15, 16], have provided more specific insight into absorbing processes on the atomic scale. The surface relaxation and reconstructing behaviors have been derived from these calculations. The chemisorption of  $\text{C}_2\text{H}_2$  and  $\text{CH}_3$  molecules onto the silicon carbide terminated ( $2\times 1$ ) surface suggests that optimal  $\text{C}_2\text{H}_2$

chemisorption has been found to occur with the adsorbate molecule situated above the cave site, while optimal  $\text{CH}_3$  chemisorption has been observed to present with the  $\text{CH}_3$  radicals bonding directly to the surface dangling bonds [17]. Structural and electronic properties of acetylene and ethylene adsorbed on  $\beta$ -SiC (001) surface with dimer site have been investigated based on density functional theory [18, 19]. However, the mechanism underlying diamond deposition [1, 6] has suggested that the carbon-carbon bond oriented in a direction parallel to the dimer site has not always occurred in the progress of the CVD diamond film growth. Up to now, the mechanisms of the CVD diamond formation on  $\beta$ -SiC surfaces have been seldom studied.

This state of the art has motivated the present study. The purpose of present work is to concentrate on the adsorption of hydrocarbons on the  $\beta$ -SiC (111) surface. Obviously, the growth species cannot be limited to only acetylene and ethylene in the process of CVD diamond film growth. In this paper, the  $\text{CH}_x$  and  $\text{C}_2\text{H}_x$  adsorption on the  $\beta$ -SiC (111) surface has been studied by first-principles pseudopotential plane-wave method within the density functional theory (DFT). The geometry optimization has provided the surface relaxation and configuration. In addition, all the total energies of the surface reconstructions have been calculated to obtain structural properties. Thus, our computational results could promote the proper understanding on the growth mechanism of CVD diamond film on the  $\beta$ -SiC (111) surface.

## 2. Theoretical Model

Various complex prototypes occurred on the  $\beta$ -SiC (111) substrate surface are very hard to ascertain [20]. Therefore, the substrate surface in this work is assumed as the ideal  $\beta$ -SiC (111) structure in order to reduce the complexity. Although this study focused on these simple cases, the atomic-level investigation might be useful for understanding the real processors in the growth mechanism of CVD diamond film on the  $\beta$ -SiC (111) surface.

In order to account for per molecular adsorption on the  $\beta$ -SiC (111) substrate surface, the study is first made of determining the covalently bonds to  $\text{CH}_x$  and  $\text{C}_2\text{H}_x$  gaseous species. The chemical reaction mechanism described by the chemical kinetics of diamond deposition [6] showed the conversion of  $\text{CH}_x$  and  $\text{C}_2\text{H}_x$  gaseous species into the surface species. The models have been designed to be as many as possible. In this paper, all the structural and electronic properties of  $\text{CH}_x$  and  $\text{C}_2\text{H}_x$  gaseous species adsorbed on the  $\beta$ -SiC (111) substrate surface have been studied. Namely, the  $\text{CH}_x$  gaseous species includes the C, CH,  $\text{CH}_2$ , and  $\text{CH}_3$  molecules; the  $\text{C}_2\text{H}_x$  gaseous species includes the  $\text{C}_2$ ,  $\text{C}_2\text{H}$ ,  $\text{C}_2\text{H}_2$ ,  $\text{C}_2\text{H}_3$ ,  $\text{C}_2\text{H}_4$ , and  $\text{C}_2\text{H}_5$  molecules. The detailed analysis of making these models is presented in following parts.

Geometry optimizations, especially the movement of unsaturated hydrocarbon atoms, have been firstly studied to contribute to a fundamental understanding of surface reconstructions by the chemistry of hydrocarbons on the  $\beta$ -SiC (111) surfaces, which is of crucial technological importance.

TABLE 1: The surface reactions on the  $\beta$ -SiC (111) surface.

No.	Si-terminated surface reactions	C-terminated surface reactions
1	$\text{Si}_{d(s)} + \text{H}_{(g)} \leftrightarrow \text{Si}_d\text{-H}(s)$	$\text{C}_{d(s)} + \text{H}_{(g)} \leftrightarrow \text{C}_d\text{-H}(s)$
2	$\text{Si}_{d(s)} + \text{C}_{(g)} \leftrightarrow \text{Si}_d\text{-C}(s)$	$\text{C}_{d(s)} + \text{C}_{(g)} \leftrightarrow \text{C}_d\text{-C}(s)$
3	$\text{Si}_{d(s)} + \text{CH}_{(g)} \leftrightarrow \text{Si}_d\text{-CH}(s)$	$\text{C}_{d(s)} + \text{CH}_{(g)} \leftrightarrow \text{C}_d\text{-CH}(s)$
4	$\text{Si}_{d(s)} + \text{CH}_2_{(g)} \leftrightarrow \text{Si}_d\text{-CH}_2(s)$	$\text{C}_{d(s)} + \text{CH}_2_{(g)} \leftrightarrow \text{C}_d\text{-CH}_2(s)$
5	$\text{Si}_{d(s)} + \text{CH}_3_{(g)} \leftrightarrow \text{Si}_d\text{-CH}_3(s)$	$\text{C}_{d(s)} + \text{CH}_3_{(g)} \leftrightarrow \text{C}_d\text{-CH}_3(s)$
6	$\text{Si}_{d(s)} + \text{C}_2_{(g)} \leftrightarrow \text{Si}_d\text{-C}_2(s)$	$\text{C}_{d(s)} + \text{C}_2_{(g)} \leftrightarrow \text{C}_d\text{-C}_2(s)$
7	$\text{Si}_{d(s)} + \text{C}_2\text{H}_{(g)} \leftrightarrow \text{Si}_d\text{-C}_2\text{H}(s)$	$\text{C}_{d(s)} + \text{C}_2\text{H}_{(g)} \leftrightarrow \text{C}_d\text{-C}_2\text{H}(s)$
8	$\text{Si}_{d(s)} + \text{C}_2\text{H}_2_{(g)} \leftrightarrow \text{Si}_d\text{-C}_2\text{H}_2(s)$	$\text{C}_{d(s)} + \text{C}_2\text{H}_2_{(g)} \leftrightarrow \text{C}_d\text{-C}_2\text{H}_2(s)$
9	$\text{Si}_{d(s)} + \text{C}_2\text{H}_3_{(g)} \leftrightarrow \text{Si}_d\text{-C}_2\text{H}_3(s)$	$\text{C}_{d(s)} + \text{C}_2\text{H}_3_{(g)} \leftrightarrow \text{C}_d\text{-C}_2\text{H}_3(s)$
10	$\text{Si}_{d(s)} + \text{C}_2\text{H}_4_{(g)} \leftrightarrow \text{Si}_d\text{-C}_2\text{H}_4(s)$	$\text{C}_{d(s)} + \text{C}_2\text{H}_4_{(g)} \leftrightarrow \text{C}_d\text{-C}_2\text{H}_4(s)$
11	$\text{Si}_{d(s)} + \text{C}_2\text{H}_5_{(g)} \leftrightarrow \text{Si}_d\text{-C}_2\text{H}_5(s)$	$\text{C}_{d(s)} + \text{C}_2\text{H}_5_{(g)} \leftrightarrow \text{C}_d\text{-C}_2\text{H}_5(s)$

TABLE 2: The nomenclature of the structures of  $\text{C}_2\text{H}_x$  adsorption.

Name used	Structure	
	Si-terminated surface	C-terminated surface
$X_d\text{-C}_2\text{H(I)}$	$\text{Si}_d\text{-C-CH}$	$\text{C}_d\text{-C-CH}$
$X_d\text{-C}_2\text{H(II)}$	$\text{Si}_d\text{-CH-C}$	$\text{C}_d\text{-CH-C}$
$X_d\text{-C}_2\text{H}_2\text{(I)}$	$\text{Si}_d\text{-C-CH}_2$	$\text{C}_d\text{-C-CH}_2$
$X_d\text{-C}_2\text{H}_2\text{(II)}$	$\text{Si}_d\text{-CH}_2\text{-C}$	$\text{C}_d\text{-CH}_2\text{-C}$
$X_d\text{-C}_2\text{H}_2\text{(III)}$	$\text{Si}_d\text{-CH-CH}$	$\text{C}_d\text{-CH-CH}$
$X_d\text{-C}_2\text{H}_2\text{(IV)}$	$\text{Si}_d\text{-C=CH}_2$	$\text{C}_d\text{-C=CH}_2$
$X_d\text{-C}_2\text{H}_2\text{(V)}$	$\text{Si}_d\text{-CH=CH}$	$\text{C}_d\text{-CH=CH}$
$X_d\text{-C}_2\text{H}_3\text{(I)}$	$\text{Si}_d\text{-C-CH}_3$	$\text{C}_d\text{-C-CH}_3$
$X_d\text{-C}_2\text{H}_3\text{(II)}$	$\text{Si}_d\text{-CH-CH}_2$	$\text{C}_d\text{-CH-CH}_2$
$X_d\text{-C}_2\text{H}_3\text{(III)}$	$\text{Si}_d\text{-CH}_2\text{-CH}$	$\text{C}_d\text{-CH}_2\text{-CH}$
$X_d\text{-C}_2\text{H}_3\text{(IV)}$	$\text{Si}_d\text{-CH=CH}_2$	$\text{C}_d\text{-CH=CH}_2$
$X_d\text{-C}_2\text{H}_4\text{(I)}$	$\text{Si}_d\text{-CH-CH}_3$	$\text{C}_d\text{-CH-CH}_3$
$X_d\text{-C}_2\text{H}_4\text{(II)}$	$\text{Si}_d\text{-CH}_2\text{-CH}_2$	$\text{C}_d\text{-CH}_2\text{-CH}_2$
$X_d\text{-C}_2\text{H}_5$	$\text{Si}_d\text{-CH}_2\text{-CH}_3$	$\text{C}_d\text{-CH}_2\text{-CH}_3$

The associated energy variation of the species adsorbed on the surface has terminally provided the structural and electronic reconstructions. It is well known that the most stable structure always has the minimum energy among the structures with atoms of the same element. In order to obtain the feasible surface reconstructions, the total energies of the  $\text{CH}_x$  and  $\text{C}_2\text{H}_x$  adsorption on the  $\beta$ -SiC (111) surface have been calculated by DFT method. The two substrate surfaces [20], Si- and C-terminated surfaces, have been developed to investigate different SiC surfaces in this work. The associated chemical reaction model is provided in Table 1.

The surface sites are defined as follows. " $X_d$ " represents a radical site; " $X_dR$ " represents an " $R$ " bonded to " $X_d$ " radical. " $X$ " denotes Si or C atom; " $R$ " denotes  $\text{CH}_n$  ( $n = 0, 1, 2, 3$ ) or  $\text{C}_2\text{H}_m$  ( $m = 0, 1, 2, 3, 4, 5$ ). The subscript  $s$  in each chemical reactor represents the surface site, and  $g$  means the vapor gas. In order to distinguish the  $\text{CH}_x$  and  $\text{C}_2\text{H}_x$  adsorption on the Si- or C-terminated surface, the symbols are employed to represent the associated surface reconstructions. The nomenclatures are given in Table 2.

TABLE 3: The difference in total energy between C adsorption and the other  $\text{CH}_x$  adsorption on Si- and C-terminated surfaces.

Species	Si-terminated surface (eV)	C-terminated surface (eV)
CH	-17.9042	-17.0661
$\text{CH}_2$	-35.4609	-34.5021
$\text{CH}_3$	-52.3329	-51.4378

The calculations have been carried out by the DFT method which implemented in the simulation tool of DMol<sup>3</sup> [21–23]. The surface has been modeled as a slab using only one  $\beta$ -SiC (111) unit cell for simplifying the structures and concentrating on the effectiveness of the  $\text{CH}_x$  and  $\text{C}_2\text{H}_x$  adsorption on the  $\beta$ -SiC (111) surface. The slab consisted of two crystal lattices with four layers, and the bottom dangling bonds layers are saturated by hydrogen atoms. The slab is separated from the neighboring slab in the (111) direction by 10 Å of vacuum thickness. The Monkhorst-Pack [24] scheme with  $8 \times 8 \times 2$   $k$ -point mesh has been employed for the Brillouin zone integration and geometry optimization.

### 3. Results and Discussions

The total energies of the surface reconstructions in this work refer to the energy of a specific arrangement of atoms based on the equations of quantum mechanics. The zero of energy is taken to be the infinite separation of all electrons and nuclei. Total energy is generally negative, corresponding to a bound state. In addition, total energy reflects the well-known fact that the most stable surface reconstruction only has the minimum total energy.

The total energies of all  $\text{CH}_x$  and  $\text{C}_2\text{H}_x$  species adsorbed on activated sites are shown in Figure 1 (where DB is dangling bond). The periodic models of Si-terminated surface behave very similarly to C-terminated surface. The results indicate that the difference between Si- and C-terminated surfaces is small in comparison. There are clearly some significant variations in the calculated reconstruction energies (and hence in the predicted minimum energy structures) that must be mentioned (Figure 1(c)). As can be seen by comparing the values for the various structural models, the maxima correspond to the  $\text{C}_2\text{H}_2$  (II) species, and the difference is less than 0.1 hartree.

The computational results reveal that the silicon or carbon atom saturated by hydrogen atoms on the top layer surface is the most effective in increasing the stabilities of  $\text{CH}_x$  and  $\text{C}_2\text{H}_x$  adsorption on the  $\beta$ -SiC (111) surface by comparing surface with dangling bond. This is in good agreement with earlier surface studies [25]. The associated values suggest that the  $\text{CH}_3$  radical molecule could form the most stable surface reconstruction among the  $\text{CH}_x$  adsorptions on the  $\beta$ -SiC (111) surface, which is consistent with the results of theoretical calculations [26]. The value of difference in Table 3 indicates that the hydrogen adsorption energy of C species adsorbed on the Si-terminated surface is a more attractive possibility than that of the C adsorption on the C-terminated surface. The difference in total energy between them has reached as high as 0.838 eV per ( $1 \times 1$ ) unit

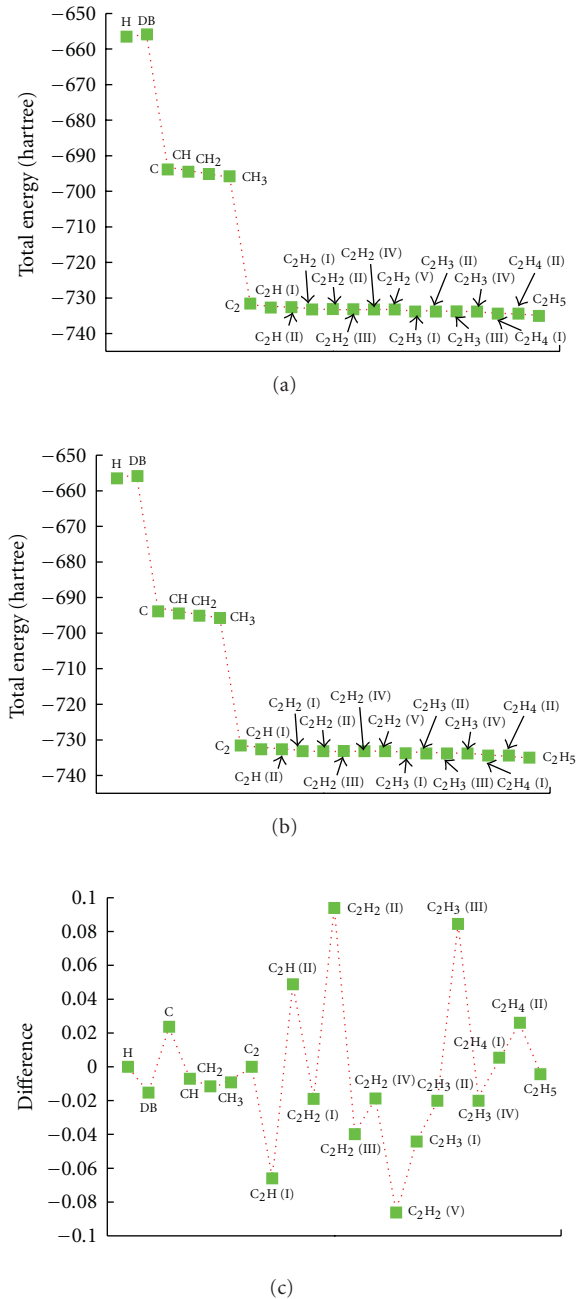


FIGURE 1: Total energies of  $\text{CH}_x$  and  $\text{C}_2\text{H}_x$  adsorption on the  $\beta$ -SiC (111) surface. (a) Total energies of  $\text{CH}_x$  and  $\text{C}_2\text{H}_x$  adsorption on the Si-terminated surface, (b) total energies of  $\text{CH}_x$  and  $\text{C}_2\text{H}_x$  adsorption on the C-terminated surface, and (c) the difference in total energies of  $\text{CH}_x$  and  $\text{C}_2\text{H}_x$  adsorption between Si- and C-terminated surfaces.

cell. At the same time, the  $\text{CH}_2$  species has greater relevant step towards the formation of adsorbing the hydrogen by comparison with the  $\text{CH}$  species. The corresponding difference is 0.500 and 0.682 eV, respectively. These results agree with the previous theoretical studies very closely [27]. The calculated values of total energies suggest that the Si-terminated surface is easier to adsorb the  $\text{CH}_x$  molecules than the C-terminated surface.

TABLE 4: The difference in total energy between  $C_2$  adsorption and the other  $C_2H_x$  adsorption on Si- and C-terminated surfaces.

Species	Si-terminated surface (eV)	C-terminated surface (eV)
$C_2H$ (I)	-29.8228	-28.0097
$C_2H$ (II)	-26.6949	-28.0061
$C_2H_2$ (I)	-44.2762	-43.7435
$C_2H_2$ (II)	-41.2048	-43.7434
$C_2H_2$ (III)	-43.3547	-42.253
$C_2H_2$ (IV)	-44.2761	-43.7485
$C_2H_2$ (V)	-44.974	-42.6138
$C_2H_3$ (I)	-60.3894	-59.1696
$C_2H_3$ (II)	-61.1584	-60.5944
$C_2H_3$ (III)	-58.3127	-60.5957
$C_2H_3$ (IV)	-61.158	-60.5945
$C_2H_4$ (I)	-76.5272	-76.6586
$C_2H_4$ (II)	-75.967	-76.6585
$C_2H_5$	-93.4121	-93.2752

However, the  $C_2H_x$  species is complex as various prototypes can exist under certain conditions, including C–C and C=C bond. In this paper, all of the  $C_2H_x$  allotropes are studied in theory by DFT method to obtain the structural properties (see Table 4). Our results reveal that the  $C_2H$  (I) adsorption on the Si-terminated surface is slightly favored with respect to the C-terminated surface. Interestingly, total energies of  $C_2H$  (I) and  $C_2H$  (II) species adsorbed on C-terminated surface remain slightly the same, which indicates that the relative position of the intramolecular hydrogen bond has small influences on the stability of the surface reconstruction. The calculated results based on the analysis of total energies suggest that these two surface reconstructions will occur at the same time during the CVD diamond formation. Figure 2(a) shows the optimized structure model for  $C_2H$  (II) adsorption, where the adsorbed molecule has a C–H bond length of 2.27 Å. As far as the energetics and the geometries are concerned, we confirm that the  $C_2H$  (II) adsorption on C-terminated surface cannot present in the process of CVD diamond film growth.

Five allotropes of  $C_2H_2$  species are investigated in this paper. As can be seen the  $C_2H_2$  (I) adsorption holds the most stability of surface reconstruction among the five allotropes. By comparison of the total energies of  $C_2H_2$  (I) and  $C_2H_2$  (II) adsorption, it is no surprise to find that these two surface reconstructions have the same probability occurring during diamond formation, while the C–H bond length of 2.10 Å indicates that the  $C_2H_2$  (II) adsorption does not occur in practical CVD diamond coating (see Figure 2(b)). Interestingly, the geometry optimization shows that the  $C_2H_2$ (II) adsorption can terminally migrate to  $C_2H_2$  (I) adsorption. Consequently,  $C_2H_2$  (I) species is energetically more favorable for fabricating CVD diamond coatings than  $C_2H_2$ (II) species. Due to the large total energy, the  $C_2H_2$ (II) adsorption is hard to form the surface reconstruction in situ.

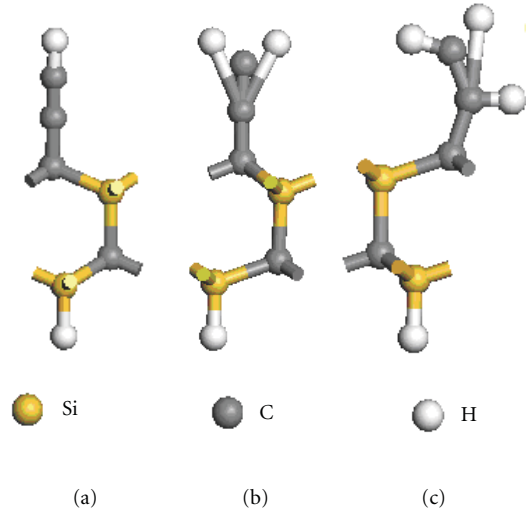


FIGURE 2: The optimizing geometry of  $C_2H_x$  adsorption on the C-terminated surface: (a) the CH–C adsorption, (b) the  $CH_2$ –C adsorption, and (c) the  $CH_2$ –CH adsorption.

For  $C_2H_2$ (IV) and  $C_2H_2$ (V) species with a C=C bond, the  $C_2H_2$ (IV) adsorption on the C-terminated surface is slightly favored with respect to  $C_2H_2$ (V) adsorption. Conversely, the  $C_2H_2$ (V) adsorption on the Si-terminated surface is found to be the most effective in the stability of surface reconstruction. In addition, from the calculated adsorption energies, the species with a C=C bond are energetically more favorable for fabricating CVD diamond coatings than those with a C–C bond. This conclusion is evident by looking at the result of kinetic Monte Carlo (KMC) simulations [1].

Similarly, the  $C_2H_3$  adsorption on the  $\beta$ -SiC (111) surface has four surface reconstructions. For the Si-terminated surface, the calculated results reveal that the  $C_2H_3$  (II) and  $C_2H_3$  (IV) adsorption has the most favorable stability of surface reconstructions. It is worth noting that more hydrogen atoms saturating the top layer species, such as C– $CH_3$  adsorption, will result in more stability of the surface reconstructions. Additionally, the simulations also find very similar values for  $Si_d$ –CH– $CH_2$  and  $Si_d$ –CH= $CH_2$  surface reconstructions. This is consistent with the adsorbing activity of  $Si_d$ –C– $CH_2$  and  $Si_d$ –C= $CH_2$  surface reconstructions, while this state differs significantly for both  $Si_d$ –CH–CH surface reconstruction and  $Si_d$ –CH=CH surface reconstruction. Obviously, the carbon-carbon single or double bonds do not play a valid role in determining the stability of surface reconstructions. For the C-terminated surface,  $C_2H_3$  (III) adsorption holds the most stability of surface reconstruction. From the calculated geometry, the length of C–H bond is 2.08 Å (see Figure 2(c)), which suggests that  $C_2H_3$  (III) adsorption does not exist during CVD diamond formation. Therefore,  $C_2H_3$  (II) species and  $C_2H_3$  (IV) species are considered as the most stability of surface reconstruction among the  $C_2H_3$  adsorption on the C-terminated surface. Thus, the  $C_2H_3$  (II) and  $C_2H_3$  (IV) adsorption can present at the same time during the diamond film growth.

For the  $C_2H_4$  adsorption, two surface reconstructions are investigated. The calculated results find that  $C_2H_4$  (I) adsorption on the Si-terminated surface has more stability than that of the  $C_2H_4$  (II), while the  $C_2H_4$  (I) adsorption on the C-terminated surface has the same probability with respect to  $C_2H_4$  (II) adsorption.  $C_2H_5$  adsorption on the  $\beta$ -SiC (111) surface has only one surface reconstruction, where both two carbon atoms are saturated by hydrogen atoms.

Therefore, from the energetics and the geometry, we find that the position of hydrogen atoms on the  $C_2H_x$  species is the most effective among the stabilities of surface reconstructions. For the C-terminated surface, the surface reconstruction with the saturated carbon atoms on the top layer species is slightly favorable stability with respect to those with dangling bond. However, for the Si-terminated surface, the saturated carbon atom on the sublayer species is useful for the stability of surface reconstructions. Meanwhile, C-CH adsorption on Si- or C-terminated surface has more stability than the C-C adsorption with fully dangling bond. In addition,  $C_2H_5$  adsorption on the C-terminated surface can be formed concurrently at different surface locations through many instances of reactions, such as adsorbing one hydrogen atoms on  $C_2H_4$  species. The calculated values indicate that the  $C_2H_4$  species has larger hydrogen adsorption energy than the others. Therefore,  $C_2H_5$  adsorption has the most favorable stability of surface reconstruction. For the Si-terminated surface, the CH-CH<sub>2</sub> and CH=CH<sub>2</sub> species hold the highest hydrogen adsorption energy, which make these two species more stable. Interestingly, the Si- and C-terminated surfaces do not present the similar properties of adsorbing the CH<sub>x</sub> and C<sub>2</sub>H<sub>x</sub> molecules. The calculated results demonstrate that the Si-terminated surface is much easier to deposit the diamond film than the C-terminated surface.

#### 4. Conclusions

In this paper, the CH<sub>x</sub> and C<sub>2</sub>H<sub>x</sub> adsorption on the  $\beta$ -SiC (111) surface has been investigated to highlight specific insight into the initial-stage growth of diamond film on SiC substrates. The geometry optimization and energies of all the surface reconstructions have been calculated by the DFT method. The calculation of the energetics and the geometry shows that C<sub>2</sub>H<sub>x</sub> adsorption on the Si-terminated surfaces has six possible surface reconstructions, including C-CH, CH=CH, CH-CH<sub>2</sub>, CH=CH<sub>2</sub>, CH-CH<sub>3</sub>, and CH<sub>2</sub>-CH<sub>3</sub> species. The CH-CH<sub>2</sub> and CH=CH<sub>2</sub> species hold the largest hydrogen adsorption energy. For the C-terminated surface, there exist eight possible surface reconstructions which include C-CH, C-CH<sub>2</sub>, C=CH<sub>2</sub>, CH-CH<sub>2</sub>, CH=CH<sub>2</sub>, CH-CH<sub>3</sub>, CH<sub>2</sub>-CH<sub>2</sub>, and CH<sub>2</sub>-CH<sub>3</sub> species. The hydrogen adsorption energies indicate that C<sub>2</sub>H<sub>5</sub> adsorption has the most stability of surface reconstruction. Meanwhile, the CH<sub>2</sub> adsorption on the Si- or C-terminated surface also has the largest hydrogen adsorption energy. Calculations also indicate that position of hydrogen atoms on the C<sub>2</sub>H<sub>x</sub> species is related to the stabilities of surface reconstructions. The calculated results demonstrate that the Si-terminated surface is energetically more favorable for fabricating CVD diamond coatings than the C-terminated surface.

#### Acknowledgments

This paper is sponsored by the National Natural Science Foundation of China (no. 50975177), the National High-tech R&D Program (863 Program) of China in the Field of Advanced Manufacturing (2009AA044304-1), the Shanghai Science and Technology Plan of Action for Technical Standards for Innovation and Special (08DZ0501700), and the Shanghai Science and Technology Plan of Action for Nano Science and Technology for Innovation and Special (0952nm01700).

#### References

- [1] A. Netto and M. Frenklach, "Kinetic Monte Carlo simulations of CVD diamond growth-Interplay among growth, etching, and migration," *Diamond and Related Materials*, vol. 14, no. 10, pp. 1630–1646, 2005.
- [2] D. E. Kassmann and T. A. Badgwell, "Analysis of process modifications for efficient diamond chemical vapor deposition," *Diamond and Related Materials*, vol. 5, no. 9, pp. 895–906, 1996.
- [3] M. E. Coltrin and D. S. Dandy, "Analysis of diamond growth in subatmospheric dc plasma-gun reactors," *Journal of Applied Physics*, vol. 74, no. 9, pp. 5803–5820, 1993.
- [4] J. C. Arnault, S. Saada, S. Delclos et al., "In situ study of the initial stages of diamond deposition on 3C-SiC (100) surfaces: towards the mechanisms of diamond nucleation," *Diamond and Related Materials*, vol. 16, no. 4–7, pp. 690–694, 2007.
- [5] S. Chowdhury, E. de Barra, and M. T. Laugier, "Study of mechanical properties of CVD diamond on SiC substrates," *Diamond and Related Materials*, vol. 13, no. 9, pp. 1625–1631, 2004.
- [6] M. Frenklach and H. Wang, "Detailed surface and gas-phase chemical kinetics of diamond deposition," *Physical Review B*, vol. 43, no. 2, pp. 1520–1545, 1991.
- [7] D. E. Kassmann and T. A. Badgwell, "Modeling diamond chemical vapor deposition in a rotating disk reactor," *Diamond and Related Materials*, vol. 5, no. 3–5, pp. 221–225, 1996.
- [8] X. An, G. Liu, F. Wang, and S. Liu, "Electronic structure study of growth species adsorption and reaction on cluster models for the diamond surface using LDA method," *Diamond and Related Materials*, vol. 12, no. 12, pp. 2169–2174, 2003.
- [9] S. Chowdhury, E. de Barra, and M. T. Laugier, "Hardness measurement of CVD diamond coatings on SiC substrates," *Surface and Coatings Technology*, vol. 193, no. 1–3, pp. 200–205, 2005.
- [10] S. Chowdhury, M. T. Laugier, and J. Henry, "XRD stress analysis of CVD diamond coatings on SiC substrates," *International Journal of Refractory Metals and Hard Materials*, vol. 25, no. 1, pp. 39–45, 2007.
- [11] B. Stankiewicz and L. Jurczyk, "Computations of STM images of SiC(0 0 1)-c(2 × 2) surface," *Surface Science*, vol. 507–510, pp. 463–467, 2002.
- [12] W. Lu, P. Krüger, and J. Pollmann, "Atomic and electronic structure of  $\beta$ -SiC(001)-(3 × 2)," *Physical Review B*, vol. 60, no. 4, pp. 2495–2504, 1999.
- [13] A. M. Mazzone, "Acetylene adsorption on Si(1 0 0): a study of the role of surface steps," *Surface Science*, vol. 601, no. 1, pp. 218–226, 2007.
- [14] W. Lu, P. Krüger, and J. Pollmann, "Ab initio studies on the  $\beta$ -SiC(001)-(5 × 2) surface," *Physical Review B*, vol. 61, no. 4, pp. 2680–2687, 2000.

- [15] C. Koitzsch, D. Conrad, K. Scheerschmidt, and U. Gösele, "Empirical molecular dynamic study of SiC(0001) surface reconstructions and bonded interfaces," *Journal of Applied Physics*, vol. 88, no. 12, pp. 7104–7109, 2000.
- [16] M. Schaible, "Empirical molecular dynamics modeling of silicon and silicon dioxide: a review," *Critical Reviews in Solid State and Materials Sciences*, vol. 24, no. 4, pp. 265–323, 1999.
- [17] A. J. Dyson and P. V. Smith, "Empirical potential study of the chemisorption of C<sub>2</sub>H<sub>2</sub> and CH<sub>3</sub> on the  $\beta$ -SiC(001) surface," *Surface Science*, vol. 396, no. 1–3, pp. 24–39, 1998.
- [18] J. Wieferink, P. Krüger, and J. Pollmann, "First-principles study of acetylene adsorption on  $\beta$ -SiC (001)-(3 × 2)," *Physical Review B*, vol. 75, no. 15, Article ID 153305, 2007.
- [19] J. Wieferink, P. Krüger, and J. Pollmann, "First-principles study of acetylene and ethylene adsorption on  $\beta$ -SiC(001)-(2 × 1)," *Physical Review B*, vol. 73, no. 11, Article ID 115309, 12 pages, 2006.
- [20] J. Pollmann, P. Krüger, and M. Sabisch, "Atomic and electronic structure of SiC surfaces from ab-initio calculations," *Physica Status Solidi B*, vol. 202, no. 1, pp. 421–445, 1997.
- [21] B. Delley, "An all-electron numerical method for solving the local density functional for polyatomic molecules," *The Journal of Chemical Physics*, vol. 92, no. 1, pp. 508–517, 1990.
- [22] B. Delley, "Fast calculation of electrostatics in crystals and large molecules," *Journal of Physical Chemistry*, vol. 100, no. 15, pp. 6107–6110, 1996.
- [23] B. Delley, "From molecules to solids with the DMol<sup>3</sup> approach," *Journal of Chemical Physics*, vol. 113, no. 18, pp. 7756–7764, 2000.
- [24] H. J. Monkhorst and J. D. Pack, "Special points for Brillouin-zone integrations," *Physical Review B*, vol. 13, no. 12, pp. 5188–5192, 1976.
- [25] S. J. Harris, "Mechanism for diamond growth from methyl radicals," *Applied Physics Letters*, vol. 56, no. 23, pp. 2298–2300, 1990.
- [26] A. J. Dyson and P. V. Smith, "A molecular dynamics study of the chemisorption of C<sub>2</sub>H<sub>2</sub> and CH<sub>3</sub> on the Si(001)-(2 × 1) surface," *Surface Science*, vol. 375, no. 1, pp. 45–54, 1997.
- [27] Y. A. Mankelevich and P. W. May, "New insights into the mechanism of CVD diamond growth: single crystal diamond in MW PECVD reactors," *Diamond and Related Materials*, vol. 17, no. 7–10, pp. 1021–1028, 2008.

## Research Article

# Size-Dependent Elastic Modulus and Vibration Frequency of Nanocrystals

Lihong Liang, Hansong Ma, and Yueguang Wei

*INM, Institute of Mechanics, Chinese Academy of Sciences, Beijing 100190, China*

Correspondence should be addressed to Lihong Liang, lianglh@lnm.imech.ac.cn

Received 27 May 2010; Revised 1 July 2010; Accepted 7 July 2010

Academic Editor: Quanqin Dai

Copyright © 2011 Lihong Liang et al. This is an open access article distributed under the Creative Commons Attribution License, which permits unrestricted use, distribution, and reproduction in any medium, provided the original work is properly cited.

The elastic properties and the vibration characterization are important for the stability of materials and devices, especially for nanomaterials with potential and broad application. Nanomaterials show different properties from the corresponding bulk materials; the valid theoretical model about the size effect of the elastic modulus and the vibration frequency is significant to guide the application of nanomaterials. In this paper, a unified analytical model about the size-dependent elastic modulus and vibration frequency of nanocrystalline metals, ceramics and semiconductors is established based on the inherent lattice strain and the binding energy change of nanocrystals compared with the bulk crystals, and the intrinsic correlation between the elasticity and the vibration properties is discussed. The theoretical predictions for Cu, Ag, Si thin films, nanoparticles, and TiO<sub>2</sub> nanoparticles agree with the experimental results, the computational simulations, and the other theoretical models.

## 1. Introduction

Nanomaterials, including nanoparticles, nanowires, nanotubes, and nanoscale thin films, have been found to show different physical, chemical, and mechanical properties from the corresponding bulk materials [1–16], such as the phonon frequency blue shift of nano-semiconductors and nanometals [2–7], the elastic modulus increase of thin films and nanoparticles [8–14], the melting temperature, and the thermal conductivity decrease of nanocrystals [15, 16]; these peculiar properties bring potential and broad application in microelectronics, optics, sensor, and so forth. While the elasticity and the vibration characterization of nanomaterials directly determines the stability and the reliability of the devices; therefore, to understand the size effect of elasticity and vibration properties and their theoretical mechanism is important. The theoretical explanations for the size effect of the elastic modulus are related with the surface effect by introducing the surface energy contribution in the continuum mechanics [11] or by the computational simulations reflecting the surface stress [8, 9] or surface relaxation influence [13, 17]. The size effect of the phonon frequency is attributed to the phonon confinement [3], the surface pressure [18], or the interfacial vibration effects [19],

and so forth. Although various theoretical interpretations were, respectively, proposed for the elastic modulus and the phonon frequency change of nanomaterials [2–6, 8–11, 13, 14, 17–19], a unified theory about the size-dependent elastic modulus and phonon frequency, with all parameters having clear physical meaning, is lacking, which is helpful to understand the physical mechanism and the inherent correlation of the elasticity and the vibration properties, and helpful to guide the application of nanomaterials.

It is known that the Young's modulus  $Y$  and the phonon vibration frequency  $\nu$  are both related with the force constant  $k$  [20, 21]

$$Y = \frac{k}{h}, \quad \nu = CK^{1/2}, \quad (1)$$

where  $h$  is the atomic distance in equilibrium or the bond length, and  $C$  is a constant. The force constant  $k = d^2u(r)/dr^2_{(r=h)}$ , where  $u(r)$  denotes the interatomic potential, which is a function of the atomic distance  $r$ ; therefore, the Young's modulus and the vibration frequency are both inherently related with the atomic interaction energy and the atomic distance. Recently, an analytic thermodynamic equation for the surface stress and the size-dependent lattice strain of nanocrystals has been established [22]. In terms

of this equation, the bond length change of nanocrystals compared with the bulk crystals can be determined. Thus, it is also possible to develop an analytic thermodynamic equation for the size-dependent elastic modulus and vibration frequency combining with the consideration of the binding energy change, which will be useful for the estimation of elasticity and the vibration properties of nanomaterials and for understanding the effect of the thermodynamic parameters on the elasticity and the vibration properties.

In this paper, a quantitative unified model without any free parameter for the size-dependent elastic modulus and vibration frequency of single crystal thin films and nanocrystals with grain boundaries is established based on the size-dependent bond length and bond energy. The predictions of the model for the enhancement of the elastic modulus and the vibration frequency of Cu, Ag, Si thin films, nanoparticles, and TiO<sub>2</sub> nanoparticles agree with the results of the molecular dynamics (MD) simulations, the continuum mechanics calculations, and the experimental measurements of different authors.

## 2. Model

According to the theory of the solid state physics, the interatomic potential of an ideal crystal can be expressed as  $u(r) = [pq/(p-q)]e[(h/r)^p/p - (h/r)^q/q]$ , where  $e$  is the atomic binding energy or the bond energy, and the coefficients  $p$  and  $q$  depend on the shapes of the potential curves (when  $p = 12$  and  $q = 6$ , the potential is the Lennard-Jones (L-J) potential) [33]. Therefore,  $k = d^2u(r)/dr^2|_{r=h} = pqe/h^2$  and combining with (1),

$$Y = \frac{C'e}{h^3}, \quad \nu = \frac{C''e^{1/2}}{h}, \quad (2)$$

where  $C' = pq$  and  $C'' = C(pq)^{1/2}$  are constants for a crystal, that is, the elastic modulus and the phonon vibration frequency are both dependent on the bond length  $h$  and the bond energy  $e$  of the crystal. Note that for metals, ceramics and semiconductors, the EAM (embedded-atom method) potential, the Morse potential, and the Tersoff potential are more appropriate, respectively, but the intrinsic relations among the force constant, the elastic modulus, the frequency, the bond energy, and the bond length are the same as those in the simple L-J potential as shown in (2). Let  $Y(D)$  and  $\nu(D)$  denote the size-dependent Young's modulus and vibration frequency of nanomaterials, where  $D$  is the thickness of single crystal thin films or the diameter of nanoparticles or the grains, assuming that (2) is still applicable to nanomaterials,  $Y(D) = C'e(D)/h(D)^3$ ,  $\nu(D) = C''e(D)^{1/2}/h(D)$ , where  $e(D)$  and  $h(D)$  are the corresponding size-dependent average bond energy and bond length of nanomaterials, respectively. Then the ratio  $Y(D)/Y$  and  $\nu(D)/\nu$  can be written as

$$\frac{Y(D)}{Y} = \left[ \frac{h}{h(D)} \right]^3 \left[ \frac{e(D)}{e} \right], \quad \frac{\nu(D)}{\nu} = \left[ \frac{h}{h(D)} \right] \left[ \frac{e(D)}{e} \right]^{1/2}. \quad (3)$$

In (3), the size-dependent bond length  $h/h(D)$  is related with the inherent lattice strain  $\varepsilon = [h(D) - h]/h$  of nanocrystals. According to the Laplace-Young equation [34], the

hydrostatic pressure acting on a small solid sphere particle immersed in the liquid  $P = 4\sigma/D$ , with the isotropic surface stress  $\sigma$  and the diameter  $D$ , will induce an elastic strain  $\varepsilon$  in the particle. Under the small strain,  $\varepsilon = \Delta D/D = \Delta A/(2A) = \Delta V/(3V)$  with the area  $A$  and the volume  $V$  of the particle. Combining with the definition of the compressibility  $\kappa = -\Delta V/(VP)$ ,  $P = -3B\varepsilon$ , where  $B = 1/\kappa$  is the bulk modulus; therefore,  $\varepsilon = -4\kappa\sigma/(3D)$ . According to the thermodynamic definition of the surface stress [22],  $\sigma = \partial G/\partial A = \partial(\gamma A)/\partial A = \gamma + A\partial\gamma/\partial A \approx \gamma + A\Delta\gamma/\Delta A$ , where  $G$  is the surface/interface excess Gibbs free energy,  $\gamma$  is the surface/interface energy,  $\Delta A/A = -8\kappa\sigma/(3D)$ ,  $\Delta\gamma = \gamma - \gamma_b$  with the bulk surface/interface energy  $\gamma_b$ , thus,  $\gamma = \gamma_b - (\sigma - \gamma)8\kappa\sigma/(3D)$ . Considering the size dependence of the surface/interface energy,  $\gamma = \gamma_b(1 - D_0/D)$ , where  $D_0$  is a minimum critical size, and  $D_0 = 2h, 3h$  for thin films and particles, respectively [22]. Therefore, the intrinsic surface stress  $\sigma = \pm[(3\gamma_b D_0)/(8\kappa)]^{1/2}$ , where the positive sign denotes the tension stress, the negative denotes the compression stress,  $\gamma_b = 2hS_v H_m/(3V_c R)$  is the bulk solid-liquid interface energy [23],  $S_v$  denotes the vibrational part of the melting entropy,  $H_m$  is the melting enthalpy,  $V_c$  is the molar volume of crystals, and  $R$  is the ideal gas constant. Thus,  $\varepsilon = \pm(2/3D)\sqrt{\kappa D_0 h S_v H_m/(V_c R)}$  for free-standing single crystal particles and thin films, similarly,  $\varepsilon = -2\kappa\sigma/(3D) = \pm(1/3D)\sqrt{\kappa D_0 h S_v H_m/(V_c R)}$  for nanocrystalline materials with grain boundaries considering the smaller strain of solid-solid interfaces [23]. Therefore,

$$\frac{h}{h(D)} = \frac{1}{1 \pm (f/3D)\sqrt{\kappa D_0 h S_v H_m/(V_c R)}}, \quad (4)$$

where  $f = 1, 2$  for nanocrystals with grain boundaries and single crystal thin films, respectively, the negative denotes the lattice contraction, and the positive denotes the lattice expansion. Note that  $\kappa$  in (4) is assumed to be size-independent as the first-order approximation, which does not lead to a big error on the  $Y(D)/Y$  value in (3) since  $\varepsilon \ll 1$  [22]. According to (4), the  $D$ -dependent average bond length of nanocrystals can be obtained by some available thermodynamic parameters such as the vibration entropy and the melting enthalpy.

The size dependence of the average bond energy is related with the size effects of the cohesive energy of crystals and the coordination number of atoms. Let the coordination number of an atom in the bulk crystals be  $Z$ , and the corresponding cohesive energy of one molar single crystal  $E = (ZN_0)e/2$  for the bulk materials, where  $N_0$  is Avogadro constant, that is,  $e = 2E/(ZN_0)$ . For thin films and nanoparticles, the size-dependent cohesive energy  $E(D) = [(Z-m)y + Z(1-y)]N_0e(D)/2$  considering the larger surface-volume-ratio and the surfacial breaking bond effect, where  $y = D_0/D$  represents the ratio of the surface atoms number to the volume atoms number, and  $m$  denotes the decrease of the surfacial atomic coordination number compared with  $Z$ , that is,  $e(D) = 2E(D)/[(Z-my)N_0]$ . Therefore,  $e(D)/e = [E(D)/E]/[1-ym/Z]$ . Approximately,  $E - E(D) = \gamma_0 A$ , where  $\gamma_0$  is the surface or solid-solid interface energy for free-standing thin films, or nanocrystals with grain boundaries,

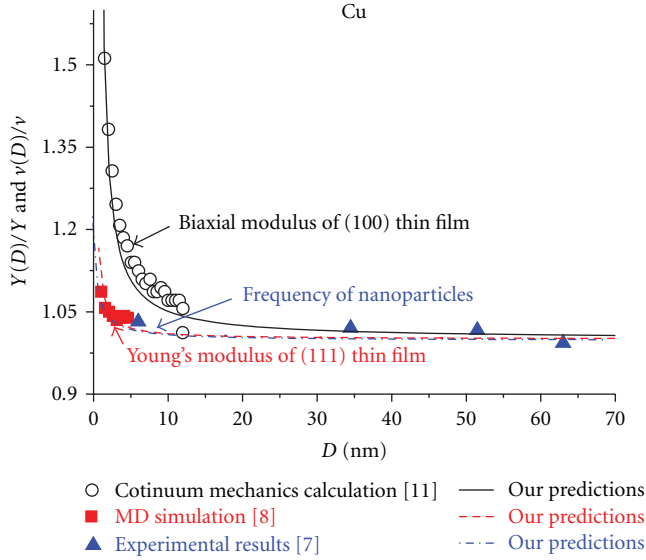


FIGURE 1: Size-dependent elastic modulus and vibration frequency of Cu thin films and nanocrystals. In (6),  $S_v \approx S_m = H_m/T_m = 9.613 \text{ Jmol}^{-1} \text{ K}^{-1}$  for metals [23],  $T_m$  is the melting temperature.  $m = 3, 4$ , respectively, for (111) and (100) faces corresponding to the computational simulation [8] and continuum mechanics calculation [11] of thin films. For nanocrystalline Cu, the solid-solid interface energy  $\gamma_0 \approx 2\gamma_b = 4hS_vH_m/(3V_cR) = 0.724 \text{ Jm}^{-2}$  [23], for Cu thin films,  $\gamma_0$  is the surface energy. Other related parameters are in Table 1.

and  $A$  is the surface/interface area,  $A = (2/D)V_c$  for thin films and  $A = (3/D)V_c$  for nanocrystals with grain boundaries. Thus, we have

$$\frac{e(D)}{e} = \frac{1 - \gamma_0 A/E}{1 - (D_0/D)(m/Z)}. \quad (5)$$

According to (5), the  $D$ -dependent average bond energy of nanocrystals can be obtained by the available thermodynamic parameters such as the cohesive energy and the surface/interface energy. Finally, substituting (4) and (5) into (3), the size-dependent elastic modulus and vibration frequency can be determined as follows:

$$\frac{Y(D)}{Y} = \left[ \frac{1}{1 \pm f/3D\sqrt{\kappa D_0 h S_v H_m / (V_c R)}} \right]^3 \frac{1 - \gamma_0 A/E}{1 - (D_0/D)(m/Z)},$$

$$\frac{v(D)}{v} = \left[ \frac{Y(D)}{Y} \right]^{1/3} \left[ \frac{1 - \gamma_0 A/E}{1 - (D_0/D)(m/Z)} \right]^{3/2}. \quad (6)$$

### 3. Results and Discussion

Figure 1 shows the thickness-dependent Young's modulus and biaxial modulus of Cu thin films and the diameter-dependent vibration frequency of Cu nanoparticles. Figure 2 shows the grain diameter-dependent bulk modulus and vibration frequency of  $\text{TiO}_2$  nanocrystals. Figure 3 shows the thickness-dependent biaxial modulus of Ag thin films and

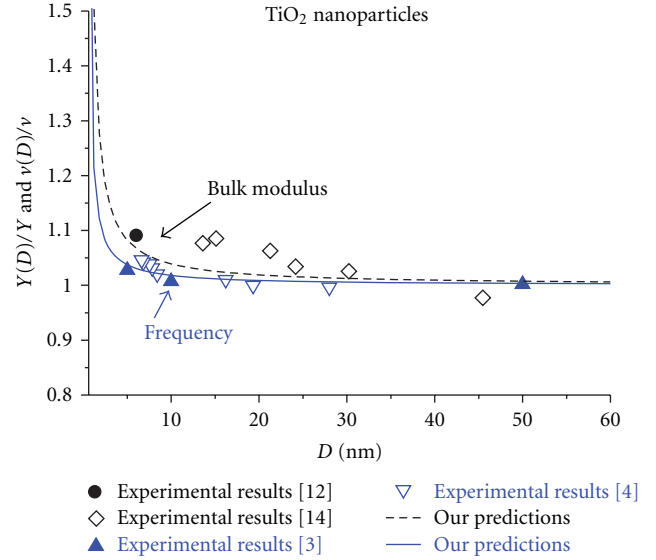


FIGURE 2: Size-dependent elastic modulus and vibration frequency of  $\text{TiO}_2$  nanocrystals. In (6),  $h = a/\sqrt{2}$  with the lattice constant  $a = 0.458 \text{ nm}$  [24].  $S_v \approx 0.4S_m = 0.4H_m/T_m = 12.576 \text{ Jmol}^{-1} \text{ K}^{-1}$  for semiconductors [25].  $V_c = M/\rho$  with the molar mass  $M = 79.88 \text{ g mol}^{-1}$  and the density  $\rho = 3.84 \text{ g cm}^{-3}$  [24],  $m = 7$ ,  $\gamma_0 \approx 2\gamma_b$ . Other parameters are in Table 1.

the diameter-dependent vibration frequency of Ag nanoparticles. Figure 4 shows the thickness-dependent Young's modulus of Si thin films and the diameter-dependent vibration frequency of Si nanocrystals. The lines are our theoretical predictions based on (6) and some available thermodynamic parameters [24–32]; the symbols are the results of the MD simulations [8, 9], the continuum mechanics and the semicontinuum model calculations [11, 13], the phonon dispersion calculation [5], and the experimental measurements [2–4, 7, 12–14]. The agreement between our model's predictions and the experimental results, and the simulations and the calculations of other groups can be found from the figures. It can be seen that the elastic modulus of nanomaterials in the size range of 1–50 nm increases about 1%–50%, and the frequency of nanomaterials in the size range of 1–70 nm increases about 1%–30%; especially the size effects of the modulus and the frequency are obvious and should be considered in the size of smaller than about 20 nm and 10 nm, respectively, due to the larger change of the bond length and the bond energy in the smaller scale. The enhancement of the frequency is smaller than that of the elastic modulus for the same nanosystems, which is reasonable since  $Y(D)/Y = [v(D)/v]^2 [h/h(D)]$  based on (3) and the background of the lattice contraction, that is,  $h/h(D) > 1$  (The negative is taken in (6)). The lattice constants of  $\text{TiO}_2$  nanoparticles [35] and some metallic nanocrystals [22] have been observed to decrease compared with the corresponding bulk crystals. The above relation is also in agreement with the general knowledge of  $Y \propto v^2$ , which implies that the elasticity change is originated from the lattice vibration change of nanocrystals.

TABLE 1: The related parameters in (4)–(6).

	$h$ (nm)	$H_m$ (K Jmol <sup>-1</sup> )	$T_m$ (K)	$B$ (GPa)	$V_c$ (cm <sup>3</sup> mol <sup>-1</sup> )	$\gamma_0$ (Jm <sup>-2</sup> )	$E$ (KJ mol <sup>-1</sup> )	$Z$
Cu	0.2556 [26]	13.05 [27]	1357.6 [27]	137.8 [28]	7.1 [27]	1.952 [29]	336 [30]	12
TiO <sub>2</sub>	0.3239	66.88 [24]	2128 [24]	220 [31]	20.802	2.1	672.4 [24]	14
Ag	0.2194 [26]	11.3 [27]	1234 [27]	103.6 [28]	10.3 [27]	1.2 [29]	284 [30]	12
Si	0.3368 [26]	50.55 [27]	1685 [27]	235.4 [28]	12.1 [27]	1.568 [32]	446 [30]	16

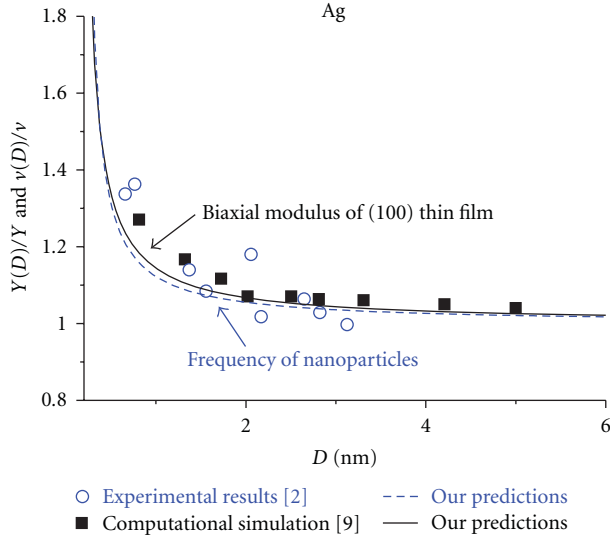


FIGURE 3: Size-dependent elastic modulus and vibration frequency of Ag thin film and nanocrystals. In (6),  $S_v \approx H_m/T_m = 9.157 \text{ Jmol}^{-1}\text{K}^{-1}$ ,  $m = 4$ . For nanocrystalline Ag,  $\gamma_0 \approx 2\gamma_b = 0.4 \text{ Jm}^{-2}$ , for Ag thin films,  $\gamma_0$  is the surface energy. Other related parameters are in Table 1.

According to (3), when the average bond length contracts and the bond energy increases with reducing size of nanocrystals, the elastic modulus and the vibration frequency enhance. The model indicates that the modulus enhancement and the phonon frequency blue shift originate from several contributions: one is the intrinsic surface tension stress and the average lattice contraction of nanocrystals determined by (4), which causes the change of the lattice vibration and the elastic properties compared with the corresponding bulk counterparts; at the same time, the average atomic binding strengthening, resulted from the intrinsic small size effect (the cohesive energy change) and the surface breaking bonds and the large surface ratio based on (5), contributes to the elastic and vibration behavior change. In fact, the physics of our model in some degree conforms to the theory of the surface bond contraction and the bond strengthening [21, 36]. On the other hand, our model implies not only the surface effect but also the internal contribution, for example, the bond length contraction and the bond energy increase of the interior atoms originated from the phonon confinement effect have both influence on the elasticity and the vibration behavior of nanocrystals, which is nonlinearly dependent on  $1/D$  different from the previous discussion [37].

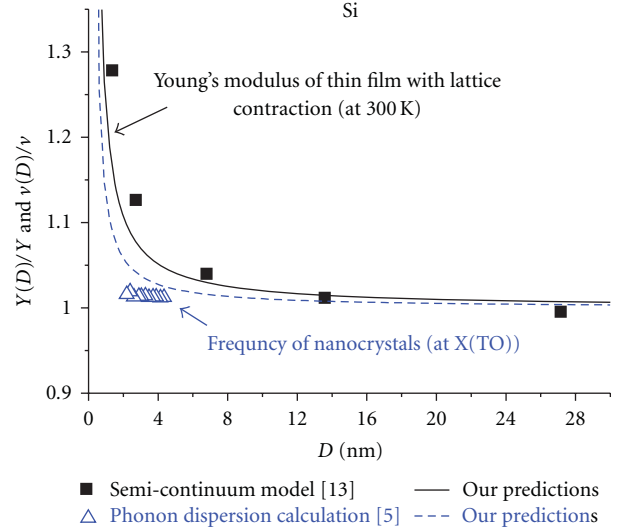


FIGURE 4: Size-dependent elastic modulus and vibration frequency of Si thin film and nanocrystals. In (6),  $S_v = 6.72 \text{ Jmol}^{-1}\text{K}^{-1}$  [25],  $m = 6$ . For nanocrystalline Si,  $\gamma_0 \approx 2\gamma_b = 1.06 \text{ Jm}^{-2}$ , for Si thin films,  $\gamma_0$  is the surface energy. Other related parameters are in Table 1.

Note that the model prediction is based on the isotropic assumption for nanoparticles. When the change trends of the bond length and the bond energy are different in different orientations, the elasticity and the vibration behavior will exhibit diversity. For example, the modulus decrease and the frequency red shift were observed for some nanosolids [18, 38], which may be because of the bond length expansion and the bond energy decrease. According to (3), even if the bond length expands, as long as the bond energy enhances enough to compensate for it, or the bond energy decreases but the bond length contracts enough, the modulus increase and the frequency blue shift may occur, vice versa. In that case, the surface stress and the lattice strain state, the surface atomic coordinate number and the surface/interface energy will be different.

## 4. Conclusion

In conclusion, the elastic modulus and the vibration frequency of metal, ceramic, and semiconductor nanocrystals are dependent on the thickness of thin films and the diameter of nanoparticles. This size effect is modeled by considering the size-dependent bond length and bond energy related with the surface effect and the interior contribution.

The model is expressed by some available thermodynamic parameters, and the predictions for Cu, Ag, Si thin films, nanoparticles, and TiO<sub>2</sub> nanoparticles are in agreement with the computational simulations, the continuum mechanics calculations, and the experimental results.

## Acknowledgment

The financial supports from the NSFC under Grants no. 10802088, 10832008, 10702070, 10932011 and The LNM initial funding for young investigators are acknowledged.

## References

- [1] H. Gleiter, "Nanostructured materials: basic concepts and microstructure," *Acta Materialia*, vol. 48, no. 1, pp. 1–29, 2000.
- [2] M. Fujii, T. Nagareda, S. Hayashi, and K. Yamamoto, "Low-frequency Raman scattering from small silver particles embedded in SiO<sub>2</sub> thin films," *Physical Review B*, vol. 44, no. 12, pp. 6243–6248, 1991.
- [3] D. Bersani, P. P. Lottici, and X.-Z. Ding, "Phonon confinement effects in the Raman scattering by TiO<sub>2</sub> nanocrystals," *Applied Physics Letters*, vol. 72, no. 1, pp. 73–75, 1998.
- [4] W. F. Zhang, Y. He, M. S. Zhang, Z. Yin, and Q. Chen, "Raman scattering study on anatase TiO<sub>2</sub> nanocrystals," *Journal of Physics D*, vol. 33, no. 8, pp. 912–916, 2000.
- [5] X. Hu and J. Zi, "Reconstruction of phonon dispersion in Si nanocrystals," *Journal of Physics: Condensed Matter*, vol. 14, no. 41, pp. L671–L677, 2002.
- [6] L.-H. Liang, C.-M. Shen, X.-P. Chen, W.-M. Liu, and H.-J. Gao, "The size-dependent phonon frequency of semiconductor nanocrystals," *Journal of Physics: Condensed Matter*, vol. 16, no. 3, pp. 267–272, 2004.
- [7] O. A. Yeshchenko, I. M. Dmitruk, A. M. Dmytruk, and A. A. Alexeenko, "Influence of annealing conditions on size and optical properties of copper nanoparticles embedded in silica matrix," *Materials Science and Engineering B*, vol. 137, no. 1–3, pp. 247–254, 2007.
- [8] F. H. Streitz, K. Sieradzki, and R. C. Cammarata, "Elastic properties of thin fcc films," *Physical Review B*, vol. 41, no. 17, pp. 12285–12287, 1990.
- [9] F. H. Streitz, R. C. Cammarata, and K. Sieradzki, "Surface-stress effects on elastic properties. I. Thin metal films," *Physical Review B*, vol. 49, no. 15, pp. 10699–10706, 1994.
- [10] L. H. Liang, J. C. Li, and Q. Jiang, "Size-dependent elastic modulus of Cu and Au thin films," *Solid State Communications*, vol. 121, no. 8, pp. 453–455, 2002.
- [11] R. Dingreville, J. M. Qu, and M. Cherkaoui, "Surface free energy and its effect on the elastic behavior of nano-sized particles, wires and films," *Journal of the Mechanics and Physics of Solids*, vol. 53, no. 8, pp. 1827–1854, 2005.
- [12] V. Pischedda, G. R. Hearne, A. M. Dawe, and J. E. Lowther, "Ultra-stability and enhanced stiffness of ~6nm TiO<sub>2</sub> nanoanatase and eventual pressure-induced disorder on the nanometer scale," *Physical Review Letters*, vol. 96, no. 3, Article ID 035509, 4 pages, 2006.
- [13] J.-H. Zhang, Q.-A. Huang, H. Yu, and J. Wang, "The influence of surface effects on size-dependent mechanical properties of silicon nanobeams at finite temperature," *Journal of Physics D*, vol. 42, no. 4, Article ID 045409, 6 pages, 2009.
- [14] B. Chen, H. Zhang, K. A. Dunphy-Guzman et al., "Size-dependent elasticity of nanocrystalline titania," *Physical Review B*, vol. 79, no. 12, Article ID 125406, 8 pages, 2009.
- [15] Q. Jiang, H. X. Shi, and M. Zhao, "Melting thermodynamics of organic nanocrystals," *Journal of Chemical Physics*, vol. 111, no. 5, pp. 2176–2180, 1999.
- [16] L. H. Liang and B. Li, "Size-dependent thermal conductivity of nanoscale semiconducting systems," *Physical Review B*, vol. 73, no. 15, Article ID 153303, 4 pages, 2006.
- [17] J.-G. Guo and Y.-P. Zhao, "The size-dependent elastic properties of nanofilms with surface effects," *Journal of Applied Physics*, vol. 98, no. 7, Article ID 074306, 11 pages, 2005.
- [18] J. Meng, G. Zou, Q. Ciu, Y. Zhao, and Z. Zhu, "Raman scattering from PbTiO<sub>3</sub> of various grain sizes at high hydrostatic pressures," *Journal of Physics: Condensed Matter*, vol. 6, no. 32, pp. 6543–6548, 1994.
- [19] X. L. Wu, G. G. Siu, S. Tong, et al., "Raman scattering of alternating nanocrystalline silicon/amorphous silicon multilayers," *Applied Physics Letters*, vol. 69, no. 4, pp. 523–525, 1996.
- [20] W. D. Nix and H. Gao, "An atomistic interpretation of interface stress," *Scripta Materialia*, vol. 39, no. 12, pp. 1653–1661, 1998.
- [21] C. Q. Sun, B. K. Tay, X. T. Zeng et al., "Bond-order-bond-length-bond-strength (bond-OLS) correlation mechanism for the shape-and-size dependence of a nanosolid," *Journal of Physics: Condensed Matter*, vol. 14, no. 34, pp. 7781–7795, 2002.
- [22] Q. Jiang, L. H. Liang, and D. S. Zhao, "Lattice contraction and surface stress of fcc nanocrystals," *Journal of Physical Chemistry B*, vol. 105, no. 27, pp. 6275–6277, 2001.
- [23] Q. Jiang, D. S. Zhao, and M. Zhao, "Size-dependent interface energy and related interface stress," *Acta Materialia*, vol. 49, no. 16, pp. 3143–3147, 2001.
- [24] R. C. Weast, *Handbook of Chemistry and Physics*, Chemical Rubber, Cleveland, Ohio, USA, 70th edition, 1989–1990.
- [25] A. R. Regel' and V. M. Glazov, "Entropy of melting of semiconductors," *Semiconductors*, vol. 29, no. 5, p. 405, 1995.
- [26] H. W. King, in *Physical Metallurgy*, R. W. Cahn, Ed., p. 60, North-Holland, Amsterdam, The Netherlands, 1970.
- [27] *Table of Periodic Properties of the Elements*, Sargent-Welch Scientific, Skokie, Ill, USA, 1980.
- [28] E. A. Brandes, Ed., *Smithells Metals Reference Book*, Butterworth, London, UK, 6th edition, 1983.
- [29] L. Vitos, A. V. Ruban, H. L. Skriver, and J. Kollár, "The surface energy of metals," *Surface Science*, vol. 411, no. 1–2, pp. 186–202, 1998.
- [30] C. Kittel, *Introduction to Solid State Physics*, John Wiley & Sons, Chichester, UK, 5th edition, 1976.
- [31] V. Swamy, E. Holbig, L. S. Dubrovinsky, V. Prakapenka, and B. C. Muddle, "Mechanical properties of bulk and nanoscale TiO<sub>2</sub> phases," *Journal of Physics and Chemistry of Solids*, vol. 69, no. 9, pp. 2332–2335, 2008.
- [32] D. M. Bird, L. J. Clarke, R. D. King-Smith, M. C. Payne, I. Stich, and A. P. Sutton, "First principles calculation of the structure and energy of Si(113)," *Physical Review Letters*, vol. 69, no. 26, pp. 3785–3788, 1992.
- [33] J.-G. Guo, L.-J. Zhou, and Y.-P. Zhao, "Size-dependent elastic modulus and fracture toughness of the nanofilm with surface effects," *Surface Review and Letters*, vol. 15, no. 5, pp. 599–603, 2008.
- [34] R. C. Cammarata and K. Sieradzki, "Surface and interface stresses," *Annual Review of Materials Science*, vol. 24, no. 1, pp. 215–234, 1994.
- [35] V. Swamy, L. S. Dubrovinsky, N. A. Dubrovinskaia et al., "Compression behavior of nanocrystalline anatase TiO<sub>2</sub>," *Solid State Communications*, vol. 125, no. 2, pp. 111–115, 2003.

- [36] M. Gu, Y. Zhou, L. Pan, Z. Sun, S. Wang, and C. Q. Sun, "Temperature dependence of the elastic and vibronic behavior of Si, Ge, and diamond crystals," *Journal of Applied Physics*, vol. 102, no. 8, Article ID 083524, 4 pages, 2007.
- [37] M. Fujii, Y. Kanzawa, S. Hayashi, and K. Yamamoto, "Raman scattering from acoustic phonons confined in Si nanocrystals," *Physical Review B*, vol. 54, no. 12, pp. R8373–R8376, 1996.
- [38] X. Y. Qin, X. R. Zhang, G. S. Cheng, and L. D. Zhang, "The elastic properties of nanostructured Ag measured by laser ultrasonic technique," *Nanostructured Materials*, vol. 10, no. 4, pp. 661–672, 1998.

## Research Article

# Initial Stage of Consolidation of Silicon-Carbide Nanocrystals under Pressure: A Tight-Binding Molecular-Dynamics Study

**Kenji Tsuruta**

*The Graduate School of Natural Science and Technology, Okayama University, 3-1-1 Tsushima-Naka, Okayama 700-8530, Japan*

Correspondence should be addressed to Kenji Tsuruta, [tsuruta@elec.okayama-u.ac.jp](mailto:tsuruta@elec.okayama-u.ac.jp)

Received 27 May 2010; Accepted 6 July 2010

Academic Editor: Bo Zou

Copyright © 2011 Kenji Tsuruta. This is an open access article distributed under the Creative Commons Attribution License, which permits unrestricted use, distribution, and reproduction in any medium, provided the original work is properly cited.

Tight-binding molecular-dynamics (TBMDs) simulations are performed to study atomic and electronic structures during high-temperature consolidation processes of nanocrystalline silicon carbide under external pressure. We employ a linear-scaling method (the Fermi-operator expansion method) with a scalable parallel algorithm for efficient calculations of the long time-scale phenomena. The results show that microscopic processes of the consolidation depend strongly on initial orientations of the nanocrystals. It is observed that an orientational rearrangement of the nanocrystals initially misaligned is induced by an instantaneous shearing force between nanocrystals, whereas the aligned system undergoes densification without shearing. Analysis on an effective-charge distribution and an average bond-order distribution reveals electronic-structure evolutions during these processes.

## 1. Introduction

Nanocrystalline ceramics have been one of the most fascinating research subjects because of their promising properties for industrial applications, such as larger fracture toughness, higher sinterability than conventional ceramics, and superplastic behavior at elevated temperatures [1, 2]. Especially, Silicon-Carbide-based micro/nanostructures have been also viewed as a building block for new optoelectronic devices and nuclear-radiation detectors [3, 4]. Polycrystalline SiC has been known to have limitation of its usefulness due to the low sinterability [5]. As in other nanocrystalline ceramics, reduction of the size of SiC powder leads to lower sintering temperature and higher degree of densification. Ohyanagi et al. have reported [6] that nanocrystalline SiC (nc-SiC) without additives has an onset temperature of sintering, which is significantly lower than that of coarse-grained powders. Such a high sinterability of pure nc-SiC and the better radiation resistance possessed by highly densified nc-SiC have also been indicated by classical molecular-dynamics simulations [7, 8]. Further understanding of consolidation processes of nc-SiC from an electronic-structure level leads to an essential improvement in designing and optimizing materials

performance especially in optoelectronic applications. The density-functional-theory (DFT-) based electronic-structure calculation is known to have an advantage in its accuracy and transferability compared with other semiempirical methods including the tight-binding approach and, thus, has been widely adopted for various types of materials simulation. However, due to rather heavy demands for computer resources in the DFT calculations, high-temperature and/or long time-scale phenomena such as consolidation processes of nanocrystals are far beyond being approached by the method. Semi-empirical tight-binding molecular dynamics method [9] with highly optimized parallel algorithms is a key to approaching alternatively to this demand.

In this paper, we report on parallel tight-binding molecular-dynamics (TBMDs) simulations of consolidation of nanocrystalline SiC with a diameter  $\sim 2.4$  nm. The Fermi-operator expansion method (FOEM) [10] has been employed to calculate efficiently the electronic part of the energy and forces in the TBMD simulations. We have also implemented a constant-pressure MD algorithm to virtually simulate the consolidation processes and it has been run on our parallel PC cluster. Using the parallel TBMD method, we investigate characteristics in the initial stage of consolidation,

that is, interparticle interactions just before and after the initial contact between SiC nanocrystallites, by comparing two different mutual orientations of the crystallites. Analysis on an effective ionic charge and a bond-order distribution is used to characterize evolutions of local electronic states during the consolidation.

## 2. Methodology

*2.1. Tight-Binding Total Energy Model of Silicon Carbide.* In the tight-binding (TB) model [9], the total energy of a system consisting of  $N$  atoms is defined as

$$E_{\text{tot}} = E_{\text{kin}} + E_{\text{bs}} + E_{\text{rep}}, \quad (1)$$

where  $E_{\text{kin}}$  stands for the kinetic energy of ions,  $E_{\text{bs}}$  is the band-structure energy of valence electrons, and  $E_{\text{rep}}$  represents the repulsive term that takes into account the core-core interactions between ions and neglected contributions in  $E_{\text{bs}}$  to the true electronic energy, such as a correction for double counting of electron-electron interactions. The repulsive energy is modeled by the sum of short-range 2-body interaction. The band-structure energy is calculated by diagonalizing the effective one-electron Hamiltonian matrix. Each off-diagonal element of the TB Hamiltonian involves interactions between valence electrons within the two-center hopping approximation. The electronic contribution to interatomic forces, that is, derivatives of  $E_{\text{bs}}$  with respect to the atomic coordinates, can be obtained through the Hellmann-Feynman (HF) theorem.

Parameterization of matrix elements in the semi-empirical TB Hamiltonian is an essential ingredient for TBMD simulations. For SiC systems, we have chosen Mercer's parameterization of the TB Hamiltonian [11], which is based on an  $sp^3$  orthogonal basis. It also includes environment-dependent contributions to the onsite energies through intra-atomic terms. These terms give important contributions to variation of the electron transfer between Si and C atoms, especially for inhomogeneous systems, although it does not include explicitly the Coulomb interaction between ions. The original parameterization by Mercer, however, leads to some discrepancies with experimental data such as the lattice constant and the interfacial energies. Minor modifications of the parameters, have therefore, been made so that magnitudes of these discrepancies are reduced [12].

*2.2. Linear Scaling Parallel Algorithm for TBMD with NPT Ensemble.* In ordinary electronic-structure calculations, the Schrödinger equation with a one-electron Hamiltonian is solved through numerical diagonalization of the Hamiltonian matrix which requires the computational cost proportional to  $N^3$ , where  $N$  is the rank for valence band in the matrix. Although the semi-empirical TB method reduces significantly the cost for constructing the Hamiltonian by the *a priori* parameterization of each matrix element as functions of atomic positions, this  $N$  dependence of the CPU time becomes overwhelming when the simulation deals over one thousand of atoms and/or for more than thousands of time

steps, which are essential for realistic simulations of nanostructured materials. Several new methods have already been proposed to resolve this problem [13]. Among them, we have adopted the Fermi-operator expansion method, proposed originally by Goedecker and Colombo [10]. This algorithm is based on a moment expansion of a pseudodensity matrix (the Fermi operator) of the TB Hamiltonian by Chebyshev polynomials. Combining an appropriate truncation at a finite order of the expansion and a truncation in the multiplication between each element of the matrix at a physical cut-off distance, the computational complexity in evaluating the band-structure energy and the HF forces is reduced to that proportional to  $N$  (linear scaling). Moreover, a second-order approximation in updating the Chebyshev polynomials is used in order to gain further efficiency. This technique accelerates the calculations about twice as fast as those with ordinary recursion algorithm for calculating the polynomials.

The truncation at the physical distance between atomic sites can make the data structures localized, hence a scalable parallelization can easily be achieved in the present algorithm. We employed a spatial domain-decomposition technique for calculating matrix-matrix multiplication. In this algorithm, data transmission between neighboring nodes is performed only for near-boundary atoms and matrix elements because of the spatially localized nature of the density matrix. Internode data transmission is performed using the standard MPI library. We have been developing and testing the fortran code based on this algorithm on various computational platforms, including massively (over 1,000 CPU) parallel architectures [13]. Also, this algorithm has been used successfully for other studies on nanostructured SiC systems [12, 14]. In the present study, we have performed the parallel TBMD simulations on our 160 cores parallel PC cluster.

In the TBMD simulations, we used a velocity-Verlet algorithm [15], with the time step of 0.2 fs (femtosecond). Temperature of the system and size/shape of the MD cell were controlled using the explicit reversible integrator algorithm [16] so as to realize the system to be an *NPT* ensemble at a thermal equilibrium. In the calculation of internal stresses for *NPT* dynamics, we employed a symmetric decomposition method of the TB Hamiltonian [17]. The criterion of convergence in the HF force calculation by the Chebyshev expansion was set with  $1.0 \times 10^{-2}$  eV/Å per atom, and the pseudoelectronic temperature was chosen to be 0.1 eV. These values gave a reasonable accuracy and numerical stability in the present simulations at a high temperature (1500 K).

## 3. Results

*3.1. Preparation of SiC Nanocrystals.* A spherical nanocrystal of 3C-SiC was initially prepared by removing atoms within a spherical region of radius about 12 Å in the perfect crystal. In addition, some atoms less bonded (i.e., having only one or two nearest neighbors within a cutoff distance 2.3 Å) on the surface of the cutout sphere were removed so that the overall stoichiometry in the nanocrystal was maintained.

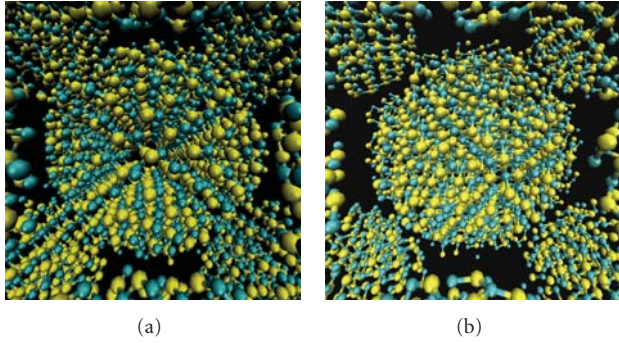


FIGURE 1: Initial configurations of the (a) aligned and (b) randomly oriented SiC nanocrystals. Large (yellow) and small (blue) spheres represent Si atom and C atom, respectively. Bonds are drawn for Si-C pairs within the distance less than 2.0 Å.

The nanocrystal, thus, prepared contains 504 Si atoms and 504 C atoms. Four copies of the nanocrystal were then placed at the positions of face-centered cubic (FCC) cell with a periodicity 42 Å for three {100} directions, respectively. The FCC configuration was chosen because we assumed that before consolidation the system had been well thermalized so that it could be modeled as an ideal close-packed mutual positions. In setting the crystallographic orientations of each nanocrystal, we prepared two sets of the system; one with four nanocrystals aligned mutually so that all the axes of the crystallites coincide with those of the cubic periodic cell, and the other with randomly oriented four nanocrystals. Figure 1 illustrates the initial configuration of the system with (a) aligned and (b) misaligned nanocrystals. Each shows one crystallite at center plus three crystallites and their images appeared due to the periodic-boundary condition in the simulation cell. The central nanocrystal is thus surrounded virtually by twelve nanocrystals. As shown in the figure, the initial cell size (42 Å) was given so that the nanocrystals do not touch each other and, hence, can be regarded initially as independent systems.

Subsequently, we ran TBMD simulations with an *NVT* ensemble in order to thermalize the systems before applying an external pressure. Starting at the room temperature, the system was gradually heated to 1500 K and was then thermalized for 5000 MD steps (1 ps). During this heating/thermalization procedure, the centers-of-mass of the four nanocrystals were kept at the original FCC positions so that the nanocrystals do not interact with each other. Also, angular momentum of each nanocrystal was kept zero during the simulation in order to eliminate artificial rotations of the crystallites.

**3.2. Consolidation Processes: Evolution of Internal Stress.** After the initial thermalization processes were completed, we switched to constant-pressure MD runs for consolidation simulation. The applied external pressure is 1 GPa and the temperature is kept at 1500 K. The external pressure 1 GPa is chosen so that fluctuation of the internal stresses is suppressed by the pressure during the densification. Also,

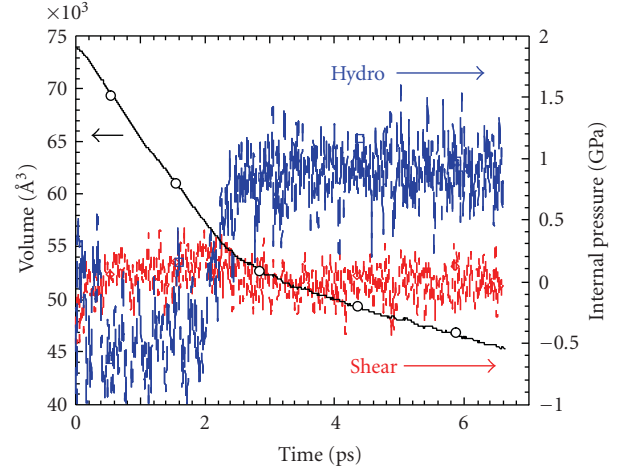


FIGURE 2: Time evolutions of system volume and internal stresses in the consolidation processes of the aligned nanocrystals.

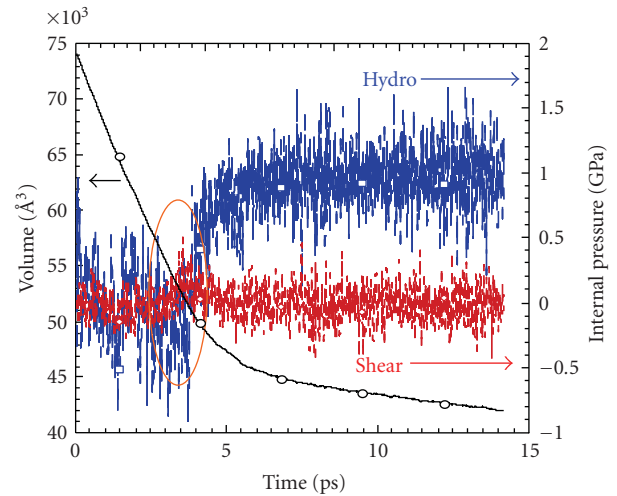


FIGURE 3: Same as in Figure 2, but for the case of the initially misaligned nanocrystals. The circle highlights an instantaneous shear induction at which nanocrystals pairs begin to touch with each other.

in the previous reports [6, 7, 14], an onset of sintering has been found around the 1500–1700 K. Thus, we focus on monitoring the time evolution at the temperature of 1500 K. Figures 2 and 3 depict evolutions of the system volume and hydrostatic and shear component of the internal stress during the MD runs for the aligned (Figure 2) and the misaligned (Figure 3) systems. Starting from the original cell size, the system volumes in both cases are decreased linearly with time. At around 0.5 ps in Figure 2, the hydrostatic component of the internal stress is shifted from zero to a negative value in average, indicating the system being under tension. Since the surface atoms begins to interact with others on neighboring crystallites at the time step, this behavior of the internal stress can be attributed to an attractive force exerted between nanocrystals in the aligned case. At around 2 ps, the aligned system is changed to be

under compression and the hydrostatic stress of the system is then increased to 1 GPa so as to balance with the external pressure.

On the other hand, figure 3 shows that the hydrostatic pressure is essentially zero upto about 3 ps in the case of misaligned nanocrystals. Since the average surface distances between neighboring crystallites are approximately the same in both cases of Figures 2 and 3 at around the same elapse time, this difference indicates that an effective intercluster interaction depends sensitively on the mutual orientations of the nanocrystals. At around 3 ps in Figure 3, the hydrostatic pressure in the system with the misaligned nanocrystals begins to increase until the stress reaches around the equilibrium value of 1 GPa. Also, the shear component of the internal stress in the misaligned case exhibits a pulse-like increase at around 3.5 ps (highlighted by a circle in the figure). At this time step, some of the nanocrystal pairs begin to touch with each other and rotate their mutual orientations as if they spontaneously optimize their grain-boundary structure. This observation is discussed again in the next section.

Sintering is, in general, driven by free-energy reduction, and the free energy one should consider in an  $NPT$  ensemble is the Gibbs free energy. It is not easy to estimate the absolute value of the free energy directly from MD simulations, here we only consider the enthalpy reduction, assuming the entropy contribution to the energy is relatively small. In the present  $NPT$ -MD simulations, the enthalpy has also been monitored. In both the aligned and the misaligned cases, it is found that the decrease of the enthalpy, which is about 10% reduction, after the first contact between nanocrystals is attributed to the decrease of both the internal energy and the pressure-volume term ( $PV$ ), but the main contribution comes from that of the internal energy. Thus, it implies that the free-energy change which drives the initial stage of consolidation of SiC nanocrystals is mainly due to the surface-energy reduction by the formation of inter-crystallite bonds. We will see in the next section that this interpretation is also consistent with the analysis on time evolutions of effective-charge distributions.

**3.3. Consolidation Processes: Effective Ionic Charge and Bond Order.** In order to characterize evolution of local electronic states during the initial stage of consolidation of SiC nanocrystals, we perform the electron-population analysis based on the Mulliken's scheme [12, 18]. An effective ionic charge for each atom is then calculated by subtracting the formal valence (4) of Si and C atom from the calculated electron population  $n_i$  at  $i$ th atomic site calculated by

$$n_i = \sum_{\alpha=s,px,py,pz} \int F_{i\alpha,i\alpha}(\epsilon) d\epsilon, \quad (2)$$

where  $\alpha$  is the orbital index, and  $F_{i\alpha,i\alpha}(\epsilon)$  represents the diagonal matrix element of the Fermi-operator as a function of the energy level  $\epsilon$ , obtained approximately by the Chebyshev polynomials explained in Chap. 2. In our TB model, these values for cations and anions in the perfect crystal are  $\pm 1.83$ , respectively.

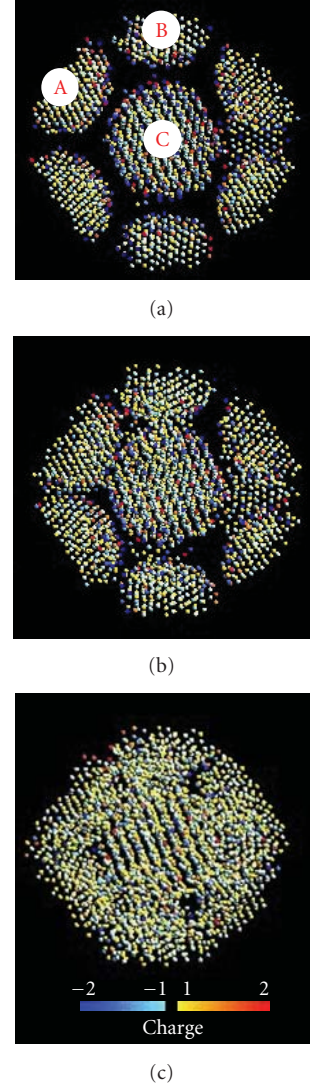


FIGURE 4: Cross-sectional views of atomic positions and an effective charge at each atomic site in the consolidation process of the initially misaligned nanocrystals; at (a) 0 ps, (b) 3.5 ps, and (c) 10 ps after starting densification.

In Figure 4, we plot a time evolution of spatial distribution of the atoms in the misaligned nanocrystals and their effective charge on a cross section at the (111) plane of the MD cell. At the initial step, depicted in Figure 4(a), the effective charge varies from  $-2$  to  $-1$  on anions and from  $1$  to  $2$  on cations, and larger variations can be found mainly on the surface of each nanocrystal due to the existence of dangling bonds on the surfaces. After starting the densification, the system is shrinking and at 3.5 ps nanocrystal pairs (A-C and B-C pair in Figure 4) touch with each other forming grain boundaries, as shown in Figure 4(b). It should be noted that the crystallographic orientations of the central (C) and the touched (A, and B) crystallites are changed slightly from the original ones. This indicates that the shearing force exerted between these nanocrystals results in a spontaneous adjustment of mutual

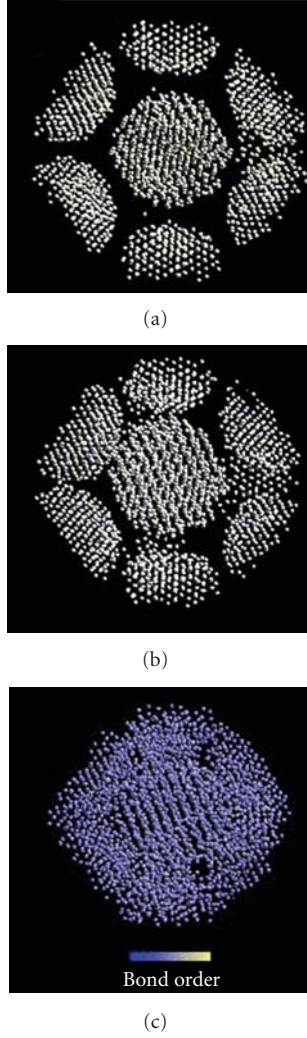


FIGURE 5: Same as in Figure 4, but for an average bond order at each atomic site. The color represents values of the bond order scaled from 0 (blue) to 1 (white).

orientations between them, as discussed in the previous section. After about 5 ps elapsed, all the nanocrystals begin to form grain boundaries, as shown in Figure 4(c). At this stage, the effective-charge distribution becomes more uniform compared to that in Figures 4(a) and 4(b) due to a significant reduction of dangling bonds on the interfaces. Thus the system evolves to the next consolidation stage, that is, the neck growth via diffusion processes on the interface [14].

We also characterize the local electronic states, which are related particularly to covalent bonding, via an average bond order [18], calculated as

$$\bar{\theta}_i = \frac{1}{4N_{\text{n.n.}}^{(i)}} \sum_{j \in \text{n.n.}} \sum_{\alpha} \int F_{i\alpha, j\alpha}(\epsilon) d\epsilon, \quad (3)$$

where “n.n.” stands for the nearest neighbor atoms within 2.3 Å around the  $i$ th atomic site with  $N_{\text{n.n.}}^{(i)}$  being the number of its n.n. atoms. This quantity is a measure of strength of

covalent bonding in the system, whereas the variation of the electron population given by (2), which is an energy integral of the local density of states, represents the electron transfer between cation and anion.

Figure 5 shows time evolution of the average bond order during the consolidation. The color indicates the value of  $\bar{\theta}_i$  scaled between 0 (blue) and 1 (white). Unlike the inhomogeneity shown in Figure 4, the bond-order distribution is rather uniform in Figure 5(a) and does not change much even when the nanocrystal pairs begin to touch with each other, as in Figure 5(b). It is, however, remarkable in Figure 5(c) that the bond order decreases rapidly once after the process is evolved to the stage where the internal stress balances with the external pressure. This phenomenon may be indicating a delocalization of electrons at the bonds as an effect of the compressive stress.

## 4. Conclusion

Using a linear-scaling parallel algorithm, we have performed large-scale/long time-scale TBMD simulations with  $NPT$  ensembles for analyses of the initial stage of consolidation of nanocrystalline SiC with a diameter of 2.4 nm. It is revealed that an effective intercluster interaction is strongly dependent on the mutual orientations of nanocrystals at high temperature. The densification under an external pressure at 1500 K proceeds without large change of crystallographic orientation between aligned nanocrystals, whereas initially misaligned nanocrystals exhibits an instantaneous shearing motion of the crystallites on the contact of their surfaces prior to the grain-boundary formation. The time evolution of local electronic structures in the consolidation process has been studied by monitoring the effective ionic charge and the average bond order on each atomic site. It is found that the inhomogeneity of the charge distribution at the surfaces of crystallites is observed to be reduced during the consolidation due to the bond formations and reconstruction at the interfaces. The evolution of the bond-order distribution indicates a tendency of electron delocalization on covalent bonds due to the high internal stress induced by the external pressure.

## Acknowledgment

This work was supported by Grant-in-Aid for Scientific Research on Priority Areas “Nanomaterials Science for Atomic Scale-Modification 474” from MEXT of Japan.

## References

- [1] R. Hull, R. M. Osgood Jr., J. Parisi, and H. Warlimont, Eds., *Nanocrystals: Synthesis, Properties and Applications*, Springer, Berlin, Germany, 2007.
- [2] T. Tokiyama, Y. Shinoda, T. Akatsu, and F. Wakai, “Enhancement of high-temperature deformation in fine-grained silicon carbide with Al doping,” *Materials Science and Engineering B*, vol. 148, no. 1–3, pp. 261–264, 2008.
- [3] J.-W. Lee and K. S. Lim, “Dramatic improvement of performance of visible hydrogenated amorphous silicon carbide

- based p-i-n thin-film light-emitting diodes by two-step hydrogenation,” *Applied Physics Letters*, vol. 69, no. 4, pp. 547–549, 1996.
- [4] Z. C. Feng, Ed., *SiC Power Materials*, Springer, Berlin, Germany, 2004.
- [5] M. G. Bothara, P. Vijay, S. V. Atre et al., “Design of experiment approach for sintering study of nanocrystalline SiC fabricated using plasma pressure compaction,” *Science of Sintering*, vol. 41, no. 2, pp. 125–133, 2009.
- [6] M. Ohyanagi, T. Yamamoto, H. Kitaura, Y. Kodera, T. Ishii, and Z. A. Munir, “Consolidation of nanostructured SiC with disorder-order transformation,” *Scripta Materialia*, vol. 50, no. 1, pp. 111–114, 2004.
- [7] A. Chatterjee, R. K. Kalia, A. Nakano et al., “Sintering, structure, and mechanical properties of nanophase SiC: a molecular-dynamics and neutron scattering study,” *Applied Physics Letters*, vol. 77, no. 8, pp. 1132–1134, 2000.
- [8] N. Swaminathan, P. J. Kamenski, D. Morgan, and I. Szlufarska, “Effects of grain size and grain boundaries on defect production in nanocrystalline 3C-SiC,” *Acta Materialia*, vol. 58, no. 8, pp. 2843–2853, 2010.
- [9] “Tight-binding approach to computational materials science,” in *Proceedings of the Materials Research Society Symposium*, D. A. Papaconstantopoulos, M. J. Mehl, Erwin S. C., and M. R. Pederson, Eds. P. E. A. Turchi, A. Gonis, and L. Colombo, Eds., vol. 491, p. 221, Warrendale, Pa, USA, 1998.
- [10] S. Goedecker and L. Colombo, “Efficient linear scaling algorithm for tight-binding molecular dynamics,” *Physical Review Letters*, vol. 73, no. 1, pp. 122–125, 1994.
- [11] J. L. Mercer, “Tight-binding models for compounds: application to SiC,” *Physical Review B*, vol. 54, no. 7, pp. 4650–4659, 1996.
- [12] K. Tsuruta, H. Totsuji, and C. Totsuji, “Neck formation processes of nanocrystalline silicon carbide: a tight-binding molecular dynamics study,” *Philosophical Magazine Letters*, vol. 81, no. 5, pp. 357–366, 2001.
- [13] F. Shimojo, T. J. Campbell, R. K. Kalia et al., “Scalable molecular-dynamics algorithm suite for materials simulations: design-space diagram on 1024 Cray T3E processors,” *Future Generation Computer Systems*, vol. 17, no. 3, pp. 279–291, 2000.
- [14] K. Tsuruta, H. Totsuji, and C. Totsuji, “Parallel tight-binding molecular dynamics for high-temperature neck formation processes of nanocrystalline silicon carbide,” *Materials Transactions*, vol. 42, no. 11, pp. 2261–2265, 2001.
- [15] M. P. Allen and D. J. Tidesly, *Computer Simulation of Liquids*, Oxford Clarendon Press, Oxford, UK, 1987.
- [16] G. J. Martyna, M. E. Tuckerman, D. J. Tobias, and M. L. Klein, “Explicit reversible integrators for extended systems dynamics,” *Molecular Physics*, vol. 87, no. 5, pp. 1117–1157, 1996.
- [17] P. Klein and H. M. Urbassek, “Pressure control in tight-binding molecular dynamics: application to a-Si formation,” *Physica Status Solidi*, vol. 207, no. 1, pp. 33–44, 1998.
- [18] R. S. Mulliken, “Electronic population analysis on LCAO-MO molecular wave functions. I,” *The Journal of Chemical Physics*, vol. 23, no. 10, pp. 1833–1840, 1955.

## Research Article

# Effect of the Dispersibility of Nano-CuO Catalyst on Heat Releasing of AP/HTPB Propellant

Yi Yang, Xinjie Yu, Jun Wang, and Yaxue Wang

School of Chemical Engineering, Nanjing University of Science and Technology, Nanjing 210094, China

Correspondence should be addressed to Yi Yang, yyi301@163.com

Received 30 May 2010; Accepted 1 August 2010

Academic Editor: Quanqin Dai

Copyright © 2011 Yi Yang et al. This is an open access article distributed under the Creative Commons Attribution License, which permits unrestricted use, distribution, and reproduction in any medium, provided the original work is properly cited.

Kneading time is adjusted to change the dispersibility of nano-CuO in AP/HTPB (Ammonia Perchlorate/Hydroxyl-Terminated Polybutadiene) composite propellants. Nano-CuO/AP is prepared to serve as the other dispersing method of nano-CuO, named predispersing procedure. Several kinds of heat releasing, thermal decomposition by DSC, combustion heat in oxygen environment, and explosion heat in nitrogen environment, are characterized to learn the effect of dispersibility of nano-CuO catalyst on heat releasing of propellants. With pre-dispersing procedures, thermal decomposition temperature of nano-CuO/AP and its propellant are about 25°C and 8.6°C lower than that of AP simple mixed with nano-CuO and its propellant, respectively. Comparing propellant with simple mixed nano-CuO kneading 3 hours, combustion heat and explosion heat of propellant with nano-CuO/AP increase about 1.4% and 1.7%, respectively. However, because of the breaking of nano-CuO/AP structure during kneading procedure, combustion heat and explosion heat of all the samples are decreased with the increase of kneading time after 3 hours.

## 1. Introduction

In recent years, there has been an explosion of interest in the synthesis, structure, properties, and applications of nanomaterials, mainly because of the fact that materials confined in one or more dimension can exhibit interesting properties, such as catalysis. Copper oxide (CuO) has been reported as a thermal decomposition catalyst of AP (Ammonia Perchlorate,  $\text{NH}_4\text{ClO}_4$ ) [1]. It naturally becomes a traditional combustion catalyst of AP/HTPB (Hydroxyl-Terminated Polybutadiene) composite propellants. As a result of the development of nanotechnology, researches on nanocatalysts, including nanometer CuO, are surged up. However, most researches tend to focus on the catalysis of the diameter or variety of nanomaterials [2, 3]. Although some of them emphasized the dispersibility improvement technologies of nanomaterials, little attention has been paid to the relationship between dispersibility and catalysis of nanomaterials.

Heat releasing or energy releasing is one of the most important properties of thermal decomposition and combustion of propellants. Catalysts always play a key role in heat releasing procedure of propellant. As one of the most

important factors of nanomaterials, dispersibility plays a key role in the effect of catalysis of nanomaterials. Because of little diameter and proportion, nanocatalyst becomes the most difficult dispersing composition of many combustion systems. However, the excellent catalysis of nanocatalyst still attracts many researchers to study [4–6]. As nanocatalysts likely perform much higher catalysis efficiency than microcatalysts, the dispersibility of nanocatalysts is much important than that of microcatalysts. On the other hand, the dispersibility of nanocatalysts also affected its catalysis crucially [7–9]. Therefore, the dispersibility of nanocatalyst is very important to the heat releasing of propellants.

In this paper, kneading time has been ranged from 1 hour to 5 hours to improve the dispersibility of nano-CuO combustion catalyst in composite propellant. Pre-dispersing procedure has been applied to the propellant by adding nano-CuO/AP composite particles instead of simple mixture of nano-CuO and AP. Several kinds of heat releasing, thermal decomposition by DSC, combustion heat in oxygen environment, and explosion heat in nitrogen environment, have been tested to check the relationship of heat releasing with the dispersibility of nano-CuO catalyst in AP/HTPB composite propellants.

TABLE 1: Thermal decomposition temperature of HTPB propellant with nano-CuO particles.

Kneading Time (h)	Area 1 (°C)	Area 2 (°C)	Area 3 (°C)	Mean Value (°C)	STD (°C)	RSD (%)
1 h	321.51	337.98	310.07	323.19	14.03	4.34
2 h	319.59	328.42	310.93	319.65	8.75	2.74
3 h	308.55	316.17	303.64	309.45	6.31	2.04
4 h	302.33	300.47	308.18	303.66	4.02	1.32
5 h	298.07	293.87	300.96	297.63	3.57	1.20

## 2. Experimental Procedures

Nanometer copper oxide (CuO), 40 nm in average diameter, was used as the combustion catalyst in AP/HTPB composite solid propellant. Kneading machine was used to disperse nanocatalyst as well as other compositions of AP/HTPB propellant. Kneading time ranged from 1 to 5 hours to change the dispersibility of nano-CuO catalyst in the propellant.

QM-ISP2-CL model planetary ball mill was used to prepare the nano-CuO/AP composite particles. The pre-dispersing method was applied to improve the dispersibility of nano-CuO before adding it into the propellant. First, nano-CuO was dispersed in ethanol by ultrasonic. Then AP was mixed with the nano-CuO with the weight ratio of 4 : 1. The mixture was milled in the planetary ball mill for 30 minutes at 70 rpm. Nano-CuO/AP composite particles were obtained by drying and grinding the milled mixture. When the catalyst added in the propellant in the form of nano-CuO/AP composite, the amount of AP was deducted from the original proportion.

To test thermal decomposition temperature of AP and AP/HTPB propellant, DSC studies were performed with the USA SDTQ-600 differential scanning calorimeter under an atmosphere of N<sub>2</sub> (at a rate of 20 mL/min) and at a heating rate of 10 k/min. XRY-1C oxidation bomb calorimeter was applied to test combustion heat (in 3 MPa O<sub>2</sub> environment) and explosion heat (in 3 MPa N<sub>2</sub> environment) of AP/HTPB propellant.

## 3. Results and Discussions

**3.1. DSC Thermal Decomposition of AP.** Ammonia Perchlorate (AP) is one of the main compositions of AP/HTPB composite propellant. The content of AP is up to 70 percent in the composite propellant. Most catalysts in the composite propellant act on the composition of AP. Therefore, many researches study the catalysis of nanocatalyst on AP/HTPB propellant by testing the thermal decomposition of AP with nanocatalyst [10, 11]. Figure 1 shows thermal decomposition curves of AP tested by DSC.

High-decomposition temperatures of AP are decreased 112.83°C and 137.62°C by adding with simple mixed nano-CuO and nano-CuO/AP composite catalysts, respectively. The nanometer catalysts show excellent catalysis on the thermal decomposition of AP. While the thermal decomposition temperature of nano-CuO/AP composite is much lower than that of AP simple mixed with nano-CuO. Better catalysis on AP of nano-CuO can be attributed to better dispersibility of nano-CuO catalyst. Simple mixing method is difficult to

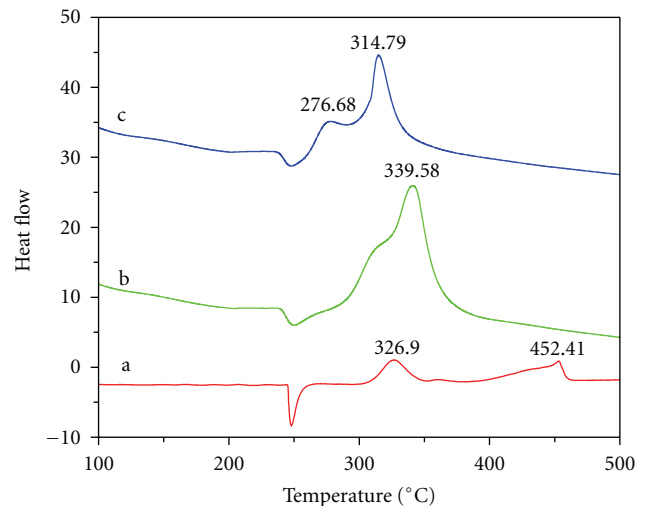


FIGURE 1: DSC thermal decomposition curves of AP. (a) pure AP; (b) nano-CuO simple mixed with AP; (c) nano-CuO/AP composite.

get enough dispersibility of nanocatalyst in AP, while the dispersibility of nano-CuO can be improved at a perfect level in the form of nano-CuO/AP composite particles.

**3.2. DSC Thermal Decomposition of Propellant.** Table 1 shows the thermal decomposition temperature data of HTPB propellant with nano-CuO catalyst. The kneading time of each sample ranged from 1 hour to 5 hours. Three representative areas of each sample were chosen to test its decomposition temperature by DSC. Standard deviation (STD) and relative standard deviation (RSD) of the test results of each sample were calculated and listed in Table 1.

Kneading procedures are always employed to improve the composition dispersity of HTPB propellants as well as nano-CuO catalyst. Because of little diameter and proportion, nanocatalyst becomes the most difficult dispersing composition of HTPB propellants. Therefore, the dispersity of nanocatalyst becomes one of the key factors of propellant properties, including its heat releasing amount and procedures. From Table 1, as the kneading time increase, the mean values of decomposition temperature of samples decrease smoothly from 323.19°C to 297.63°C. HTPB propellants with higher dispersity of nano-CuO catalyst show lower decomposition temperature. Meanwhile, the RSD values of samples decrease from 4.34% to 1.20% with the increase of kneading time. It means that the increasing of nano-CuO dispersibility in HTPB propellant not only decreases the

TABLE 2: Thermal decomposition temperature of HTPB propellant with nano-CuO/AP composite.

Kneading Time (h)	Area I ( $^{\circ}\text{C}$ )	Area II ( $^{\circ}\text{C}$ )	Area III ( $^{\circ}\text{C}$ )	Mean Value ( $^{\circ}\text{C}$ )	STD ( $^{\circ}\text{C}$ )	RSD (%)
1 h	310.11	327.39	309.17	315.56	10.26	3.25
2 h	308.66	303.32	316.84	309.61	6.81	2.20
3 h	302.81	308.53	301.17	304.17	3.86	1.27
4 h	296.72	293.43	295.03	295.06	1.65	0.56
5 h	293.81	292.29	294.78	293.63	1.26	0.43

TABLE 3: Combustion heat data of propellant with simple mixed nano-CuO.

Kneading Time (h)	Area A (J/g)	Area B (J/g)	Area C (J/g)	Mean Value (J/g)	STD (J/g)	RSD (%)
1 h	16156	15741	15562	15819	304.6	1.93
2 h	16201	15839	15690	15910	262.8	1.65
3 h	15752	16216	16037	16002	234.0	1.46
4 h	15836	16202	16011	16016	183.1	1.14
5 h	16139	16331	15949	16190	191.2	1.18

decomposition temperature, but also decreases the deviation of decomposition temperature.

The preparation of nano-CuO/AP composite is a pre-dispersing method to improve the dispersity of nano-CuO in HTPB propellant. The amount of AP in the nano-CuO/AP composite has been deducted before adding it into the propellant. Table 2 lists the decomposition temperature of HTPB propellant with nano-CuO/AP composite catalyst. With the similar tendency of Table 1, the mean value of decomposition temperature and RSD value in Table 2 decrease dramatically with the increase of kneading time of HTPB propellant, from  $315.56^{\circ}\text{C}$  to  $293.63^{\circ}\text{C}$  and from 3.25% to 0.43%, respectively.

However, when compared with Table 1 at the same kneading time, taking 3 hours for example, all the RSD values and mean values of decomposition temperature in Table 2 are much lower. It means that the pre-dispersing method, the preparation of nano-CuO/AP composite, can effectively improve the dispersity of nano-CuO catalyst in HTPB propellant and decrease the decomposition temperature of HTPB propellant.

Figure 2 shows the DSC curves of AP/HTPB propellant kneaded 4 hours. Compared with the blank sample, thermal decomposition peaks of the two other samples with nano-CuO are combined together as one peak. And the thermal decomposition temperatures are much lower than the low decomposition temperature of blank sample. With pre-dispersing procedures, the thermal decomposition temperature of propellant with nano-CuO/AP is  $8.6^{\circ}\text{C}$  lower than that of propellant with simple mixed nano-CuO.

**3.3. Combustion Heat Testing.** Combustion heat data of propellant with simple mixed nano-CuO catalyst and with nano-CuO/AP are contented in Tables 3 and 4, respectively. Three areas of each propellant sample have been chosen randomly to test combustion heat in 3 MPa  $\text{O}_2$  environment. Every combustion heat data of the three areas is a mean value of three testing data. Take the data 16,201 J/g of area A

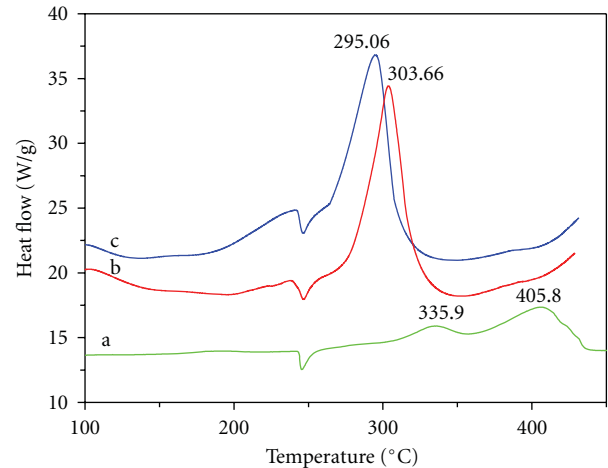


FIGURE 2: DSC curves of AP/HTPB propellant kneaded 4 hours. (a) Blank sample (b) Propellant with nano-CuO (Area 1); (c) Propellant with nano-CuO/AP (Area III).

kneading 2 hours in Table 3, for example it is the mean value of three data 15,351 J/g, 16,683 J/g, and 16,569 J/g.

From the combustion data in Tables 3 and 4, as the kneading time is increasing, the RSD of combustion heat is decreasing sharply. The mean value of combustion heat in Table 3 is increased steadily with the kneading time increase. The RSD of combustion heat in Table 4 is much lower than that of in Table 3 as a whole. However, after 3 hours kneading, the mean value of combustion heat in Table 4 decreases with the kneading increase. The strange phenomenon could be speculated that the composite structure of nano-CuO/AP in the propellant is broken gradually after 3 h kneading. The breaking of nano-CuO/AP leads to nano-CuO in the form of simple mixing in the propellant sample. Therefore, when kneading time increases to 5 hours, the combustion heat of propellant in Table 4 decreases to the value of propellant with simple mixed nano-CuO kneading 2 hours. It means that the

TABLE 4: Combustion heat data of propellant with nano-CuO/AP.

Kneading Time (h)	Area a (J/g)	Area b (J/g)	Area c (J/g)	Mean Value (J/g)	STD (J/g)	RSD (%)
1 h	15943	16230	15632	15935	299.2	1.88
2 h	16219	15788	16223	16077	250.2	1.56
3 h	16375	16259	16032	16222	174.5	1.08
4 h	16379	16003	16131	16171	191.2	1.18
5 h	16207	15722	15984	15971	242.8	1.52

TABLE 5: Explosion heat of propellant with simple mixed nano-CuO.

Kneading Time (h)	Area (1) (J/g)	Area (2) (J/g)	Area (3) (J/g)	Mean Value (J/g)	STD (J/g)	RSD (%)
1 h	5832	6089	6339	6087	253.5	4.16
2 h	6306	6402	6108	6272	149.9	2.39
3 h	6332	6517	6281	6377	123.9	1.94
4 h	6268	6049	6206	6174	110.9	1.80
5 h	6055	6121	6271	6149	110.6	1.80

TABLE 6: Explosion heat of propellant with nano-CuO/AP composite.

Kneading Time (h)	Area (I) (J/g)	Area (II) (J/g)	Area (III) (J/g)	Mean Value (J/g)	STD (J/g)	RSD (%)
1 h	5954	6336	6272	6187	211.8	3.42
2 h	6047	6371	6229	6216	162.4	2.61
3 h	6419	6491	6539	6483	60.4	0.93
4 h	6238	6281	6375	6298	70.0	1.11
5 h	6229	6245	6363	6279	73.2	1.17

kneading procedure promote the reunion of nano-CuO after the breaking of nano-CuO/AP composite structure.

**3.4. Explosion Heat Study of Propellant.** Tables 5 and 6 list the explosion heat data of propellant with simple mixed nano-CuO catalyst and with nano-CuO/AP, respectively. With the same testing procedures of combustion heat, three areas of each propellant sample have been chosen randomly to test explosion heat in 3 MPa N<sub>2</sub> environment. And each explosion heat data of the three areas is a mean value of three testing data.

In Table 5, the explosion heat of propellant with simple mixed nano-CuO is increased with the increase of kneading time, while the STD and RSD of explosion heat decreased. Meanwhile, the decrease ratios of STD and RSD of the explosion heat are very smooth when kneading time of propellant less than 3 hours. That is to say, after 3 hours kneading, the dispersibility of nano-CuO catalyst in propellant is improved to a maximum by kneading method. There is no use to improve the dispersibility of nanocatalyst by increasing kneading time for the simple mixed nano-CuO catalyst in AP/HTPB composite propellant. Other methods should be employed to improve the dispersibility of nanocatalyst in the propellant.

The tendency of the data, mean value of explosion heat, STD, and RSD, in Table 5, is very similar Table 6. The explosion heat value of these data increase with the kneading time before 3 hours, and the value decrease with the kneading

time after 3 hours. The value of STD and RSD of explosion heat decreases with the kneading time less than 3 hours then increases smoothly. As the tendency of data in Table 6, one of the reasons should be the gradual breaking of the nano-CuO/AP composite particles after 3 h kneading, which result from the too long kneading time. The breaking changes the dispersity of nano-CuO in the propellant. And it provides new probabilities for reunion of nano-CuO catalyst particles.

However, as we can see in Table 2, there is no influence of the breaking of the nano-CuO/AP composite particles on the thermal decomposition temperature of HTPB propellant. Far from the situation in Table 6, the decomposition temperatures of the propellants, in Table 2, are still decreasing with the increase of kneading time after 3 hours. One possible reason for this is that because the decomposition rate, or heat releasing rate, of thermal decomposition of HTPB propellant is much slower than that of combustion and explosion; the effect of the breaking of nano-CuO/AP composite on combustion and explosion is more obvious than that of thermal decomposition of HTPB propellant. Therefore, it seems that there is no or little influence on the thermal decomposition temperatures of HTPB propellants in Table 2.

Similar with the data of combustion heat testing, the explosion heat data of propellant with nano-CuO/AP composite in Table 6 is much higher than the data in Table 5 at all the kneading times. With pre-dispersing procedures, added with nano-CuO/AP composite, propellants exhibit good performance on explosion heat releasing. And the RSD values in Table 6 are less than those in Table 5. Less

RSD value is the stand of less change, or less instability, of the explosion heat releasing of the propellant sample. It means that the propellants in Table 6 could be show higher explosion heat and more steady explosive procedures than samples in Table 5. It is only because of the pre-dispersing procedures by adding nano-CuO/AP composite in the propellants in Table 6.

From the data of Table 1 to Table 6, taking kneading efficiency and heat releasing into account, the preference kneading time should be set to 3 hour for AP/HTPB composite propellant added with nano-CuO, instead of the traditional kneading time, 2 hours, for micrometer catalyst of AP/HTPB composite propellant.

#### 4. Conclusions

The dispersibility of nano-CuO has been adjusted by changing the kneading time of AP/HTPB composite propellant. Nano-CuO/AP composite has been prepared, as a pre-dispersing method of nano-CuO, to improve the dispersibility of nano-CuO in AP as well as AP/HTPB propellant. With the improvement of the dispersibility of nano-CuO, increasing kneading time or adding composite, DSC thermal decomposition temperature of AP and AP/HTPB propellant decreases markedly. However, the combustion heat and explosion heat of propellants with nano-CuO/AP, tested in O<sub>2</sub> and N<sub>2</sub> environment, increase then decrease on 3 hours of kneading time. This is partly because of the breaking of nano-CuO/AP composite structure and leads to the reunion of nano-CuO particles.

#### Acknowledgment

This paper was supported by the Nature Science Foundation of China (50306008 and 50876046).

#### References

- [1] A. A. Said and R. Al-Qasmi, "The role of copper cobaltite spinel,  $Cu_xCo_{3-x}O_4$  during the thermal decomposition of ammonium perchlorate," *Thermochimica Acta*, vol. 275, no. 1, pp. 83–91, 1996.
- [2] L. Liu, F. Li, L. Tan, L. Ming, and Y. Yi, "Effects of nanometer Ni, Cu, Al and NiCu powders on the thermal decomposition of ammonium perchlorate," *Propellants, Explosives, Pyrotechnics*, vol. 29, no. 1, pp. 34–38, 2004.
- [3] L.-J. Chen, G.-S. Li, P. Qi, and L.-P. Li, "Thermal decomposition of ammonium perchlorate activated via addition of NiO nanocrystals," *Journal of Thermal Analysis and Calorimetry*, vol. 92, no. 3, pp. 765–769, 2008.
- [4] Z. Yu, Y. Sun, W. Wei, L. Lu, and X. Wang, "Preparation of  $NdCrO_3$  nanoparticles and their catalytic activity in the thermal decomposition of ammonium perchlorate by DSC/TG-MS," *Journal of Thermal Analysis and Calorimetry*, vol. 97, no. 3, pp. 903–909, 2009.
- [5] K. Zhang, C. Rossi, G. A. Ardila Rodriguez, C. Tenailleau, and P. Alphonse, "Development of a nano- AlCuO based energetic material on silicon substrate," *Applied Physics Letters*, vol. 91, no. 11, Article ID 113117, 2007.
- [6] K. Zhong, P. Jin, and Q. Chen, "Ni hollow nanospheres: preparation and catalytic activity," *Journal of Nanomaterials*, vol. 2006, Article ID 37375, 7 pages, 2006.
- [7] Y.-H. Hu, J.-P. Liu, J. Xu, and D.-Z. Wang, "Dispersion mechanism of nano-magnetite coated with oleate in aqueous carrier," *Journal of Central South University of Technology*, vol. 15, no. 5, pp. 663–668, 2008.
- [8] M. Kawaraya, "Dispersibility of nano-TiO<sub>2</sub> paste with fine ceramic beads and morphology of the mesoporous film," *Journal of Chemical Engineering of Japan*, vol. 40, no. 3, pp. 255–258, 2007.
- [9] J. K. Kim, D. Z. Wo, L. M. Zhou, H. T. Huang, K. T. Lau, and M. Wang, "Dispersibility and degradation properties characterization of nano titanium dioxide photocatalysis material," *Key Engineering Materials*, vol. 334-335, pp. 565–568, 2007.
- [10] G. Duan, J. Zhu, C. Kan, X. Yang, L. Lu, and X. Wang, "Preparation of novel structural nanosized Y<sub>2</sub>O<sub>3</sub> powders and their catalytic activity on the decomposition of NH<sub>4</sub>ClO<sub>4</sub>," *Reaction Kinetics and Catalysis Letters*, vol. 92, no. 2, pp. 247–256, 2007.
- [11] V. F. Komarov, "Catalysis and inhibition of the combustion of ammonium perchlorate based solid propellants," *Combustion, Explosion and Shock Waves*, vol. 35, no. 6, pp. 670–683, 1999.

## Research Article

# In Situ Investigation of the Silicon Carbide Particles Sintering

Yu Niu,<sup>1</sup> Feng Xu,<sup>1</sup> Xiaofang Hu,<sup>1</sup> Jianhua Zhao,<sup>1</sup> Hong Miao,<sup>1</sup> Xiaoping Wu,<sup>1</sup>  
and Zhong Zhang<sup>2</sup>

<sup>1</sup>Key Laboratory of Mechanical Behavior and Design of Materials, Chinese Academy Sciences,  
University of Science and Technology of China, Hefei 230026, China

<sup>2</sup>National Center for Nanoscience and Technology of China, Beijing 100190, China

Correspondence should be addressed to Feng Xu, xufeng3@ustc.edu.cn

Received 31 May 2010; Accepted 31 July 2010

Academic Editor: Jaetae Seo

Copyright © 2011 Yu Niu et al. This is an open access article distributed under the Creative Commons Attribution License, which permits unrestricted use, distribution, and reproduction in any medium, provided the original work is properly cited.

A real-time observation of the microstructure evolution of irregularly shaped silicon carbide powders during solid state sintering is realized by using synchrotron radiation computerized topography (SR-CT) technique. The process of sintering neck growth and material migration during sintering are clearly distinguished from 2D and 3D reconstructed images. The sintering neck size of the sample is presented for quantitative analysis of the sintering kinetics during solid state sintering. The neck size-time curve is obtained. Compared with traditional sintering theories, the neck growth exponent (7.87) obtained by SR-CT experiment is larger than that of the two-sphere model. Such condition is discussed and shown in terms of sintering neck growth, in which the sintering process slows down when the particle shape is irregular rather than spherical.

## 1. Introduction

Silicon carbide ceramic was the earliest forms of artificial abrasives because of its high mechanical strength. Stable chemical properties, high thermal conductivity, thermal expansion coefficient, and other fine performance characteristics have allowed silicon carbide to become widely used in various fields such as coating materials, refractory, and metallurgy [1–3]. Solid state sintering is the key process of preparation of silicon carbide ceramics. Researching the internal microstructure evolution of the sample during the sintering process is important because the microstructure of the material plays a decisive role in macroscopic properties [4–6]. This topic has been extensively investigated since the 1950s [7–9]. Studies on the microstructure improvement of the ceramic materials are meaningful for increasing the production process and improving material properties. However, in the study of solid state sintering, the experimental study of microstructure evolution result has not yet attained a satisfactory level in comparison to theoretical work and numerical simulation. This situation may be attributed to the difficulty of observing the internal microstructure morphology of the sample during the heating process of the

solid state sintering in real time. Generally, after solid state sintering, the sample is observed postmortem by scanning electronic microscopy (SEM). Although SEM can provide high resolution photos, this experimental method has eminent shortcomings: (1) cutting and polishing of the samples are bound to damage the original structure; (2) interruption of sintering process and dropping of temperature bring unpredictable impact to the microstructure.

Using SR-CT technique, in situ observation of material under action of outside field (e.g., pressure field, temperature field, etc.) becomes possible [10, 11]. For the limitation of experimental skills, only a few scholars have conducted research on solid state sintering process by this method. Vagnon et al. did research on stress varying during solid state sintering process of steel powder compacts by SR-CT [12]. Through this technology, Olmos et al. researched the solid state sintering process of a mixture of metallic powder [13]. Grain evolution of boron carbide powders is observed and discussed in this paper during sintering using SR-CT technique [14].

In this paper, the microstructure evolution of silicon carbide powder is investigated in situ by SR-CT technique during the solid sintering process. Using filter back projection

arithmetic and digital image processing method, 2D sections and 3D reconstructions of the internal microstructure of samples at different sintering times are carried out. The features of the typical morphology evolution of solid sintering are observed. The size of the sintering neck in each cross-section image is calculated by using watershed algorithm. Neck size-time curve is obtained and compared with existing theories. The linear relationship between neck size logarithm and time logarithm during isothermal sintering is obtained and shown as the neck size-time double logarithm curve, as described in traditional sintering theories. Sintering neck growth exponent is obtained as  $n = 7.87$ , which is a little bigger than the conclusion of two-sphere model, and the reason is qualitatively analyzed.

## 2. Experiment

**2.1. Technical Principle.** SR-CT technique is a nondestructive testing method by which the specimen passed through by synchrotron radiation X-ray is placed in a rotation, and the projection images of the specimens are received by an X-ray charge-coupled device (CCD). One projection image is collected each time a specimen turns for an angle. After obtaining a set of projection data, reconstruction algorithm is used to obtain the internal microstructure of the sectional images. The 3D images of the microstructure can be obtained from a series of sectional images. Reconstruction algorithms applied in SR-CT technique are mainly filtered by back projection and iterative algorithms. Taking the limited time into account, filtered back projection algorithm is employed in this paper.

**2.2. Equipment and Experimental Procedure.** Silicon carbide powder for this experiment is chemically pure (99.9%). The average diameter is approximately  $125\ \mu\text{m}$ . The experiment was carried out on the 4W1A beam line at the Beijing Synchrotron Radiation Facility (BSRF), Beijing, China. A schematic of such SR-CT projection imaging facility is given in Figure 1. A wide collimated synchrotron radiation X-ray (up to  $14\ \text{mm} \times 10\ \text{mm}$ ) with energy range from 3 to 24 keV is available. An X-ray with 24 keV selected by silicon single-crystal monochromator was used in this test. The samples were heated in a sintering furnace specifically designed for SR-CT. This furnace has range of a room temperature to  $1600^\circ\text{C}$ , an even temperature region of  $2\ \text{cm}^3$ , and the highest heating rate of  $300^\circ\text{C}/\text{h}$ . There is a corundum cylinder connecting with a rotation device in the furnace. The MRS102 rotation device, with angle resolution of  $0.00125^\circ$  and repeatable positioning accuracy of  $0.005^\circ$ , was provided by the Beijing Optical Instrument Factory. The samples were introduced on top of the corundum cylinder. The synchrotron radiation X-ray passed through samples and reached an X-ray CCD detector, which recorded the intensity message of X-ray. The CCD including a  $1300 \times 1030$  pixels chip with a unit pixel of  $10.9 \times 10.9\ \mu\text{m}^2$  offered an 8-bit dynamic range. At different sintering times, the sample was imaged at different projection angles (in the range of  $0\text{--}180^\circ$ ). Typically, 180 shadow images of the sample

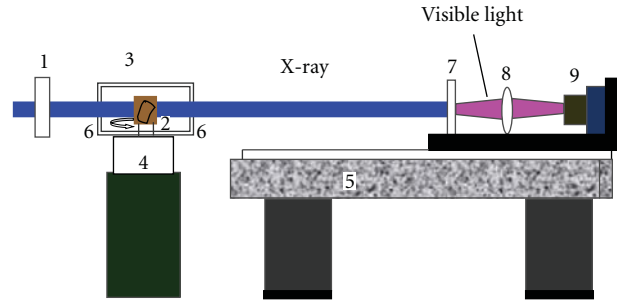


FIGURE 1: Schematic diagram of SR-CT projection imaging facility 1. X-ray source 2. Sample 3. Sintering furnace 4. Rotation device 5. Antivibration platform 6. Holes 7. Fluorescent target 8. Optical 9.CCD.

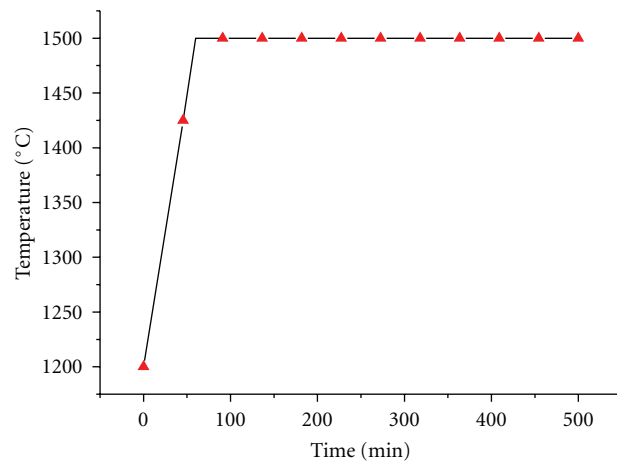


FIGURE 2: Heating process and record point.

were acquired. These images were then processed by the filtered back projection algorithm [15, 16].

Temperature is an important parameter in sintering. In order to compare with the conclusion of traditional theory and experiment, an isothermal sintering process was designed for eliminating the influence of temperature change.

In this experiment, the sintering temperature reached  $1500^\circ\text{C}$  with the highest heating rate. The temperature was held at  $1500^\circ\text{C}$ . Temperature-time curve is shown in Figure 2.

## 3. Results

A 2D cross-correlation algorithm was used to detect cross-section images at different sintering times. The reconstructed images of the same cross-section at different times are shown in Figure 3. Grayscale range is from 0 to 255; the closer to 255, the higher the relative density, which means white represents particles and black represents holes.

Vertical section and 3D reconstructed images can also be obtained by treating the cross-section images with

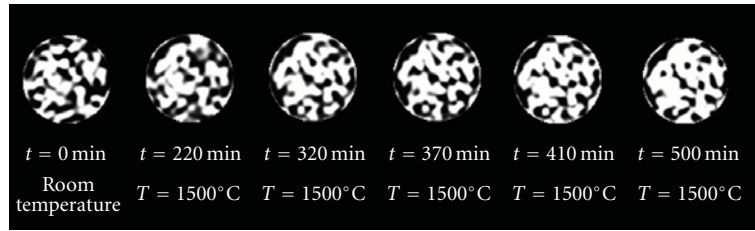


FIGURE 3: Reconstructed images of the same cross-section of the sample at different sintering periods.

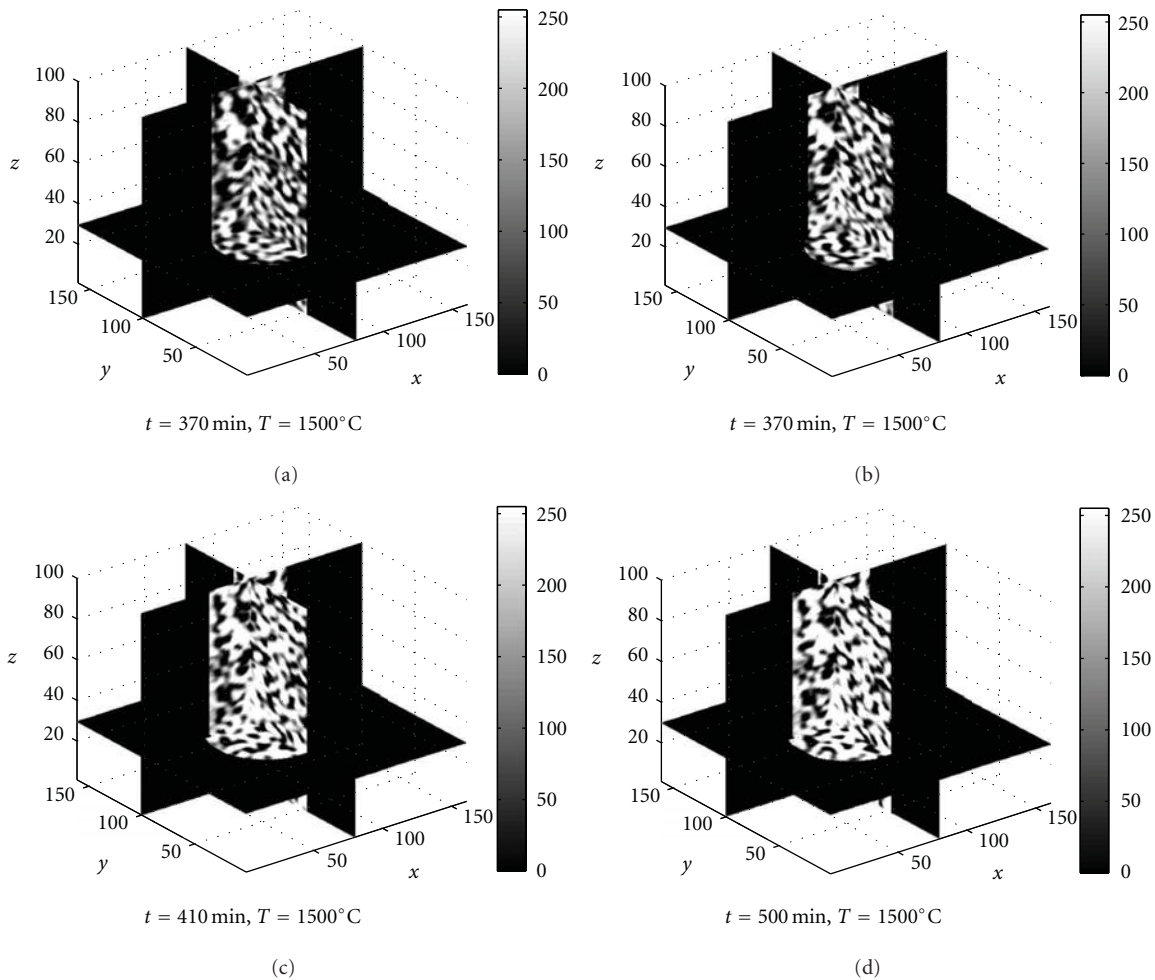


FIGURE 4: Sectional view in different directions.

digital image processing method. For quick identification, a Cartesian coordinate system is considered and shown in Figure 4. The plane  $XOY$  is defined as the initial cross-section of the reconstructed part of the sample.

By applying 3D reconstruction algorithm, a series of the cross-section images was assembled to obtain a 3D image and the sections in any position of the sample, as shown in Figure 4.

Figure 5 shows the 3D reconstructed images of the sample. The 3D morphology evolution of the sample by increasing the sintering time can be clearly observed from Figure 5.

#### 4. Discussion

Various sintering phenomena could be observed clearly from the reconstructed images (Figures 3–5), such as the growth of sintering neck, the interconnected pores becoming isolated and spherical, the sample becoming dense, and so forth.

At different sintering times, 100 consecutive cross-sections at the same ordinate (from  $z = 1$  to  $z = 100$ ) of the sample were selected. Sintering neck in each section was extracted. First, the watershed method was applied for segmentation of the section image (Figure 6(b)). Next, the connection between the different particles was considered

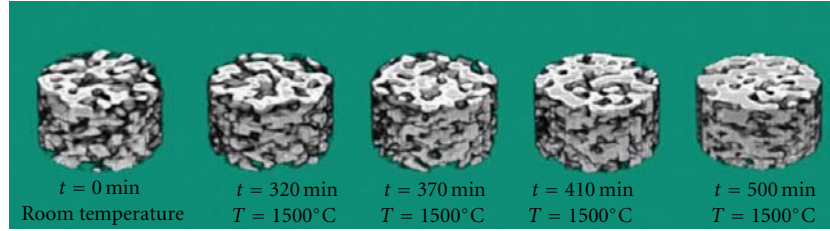


FIGURE 5: Three-dimensional reconstructed images of the sample at different sintering periods.

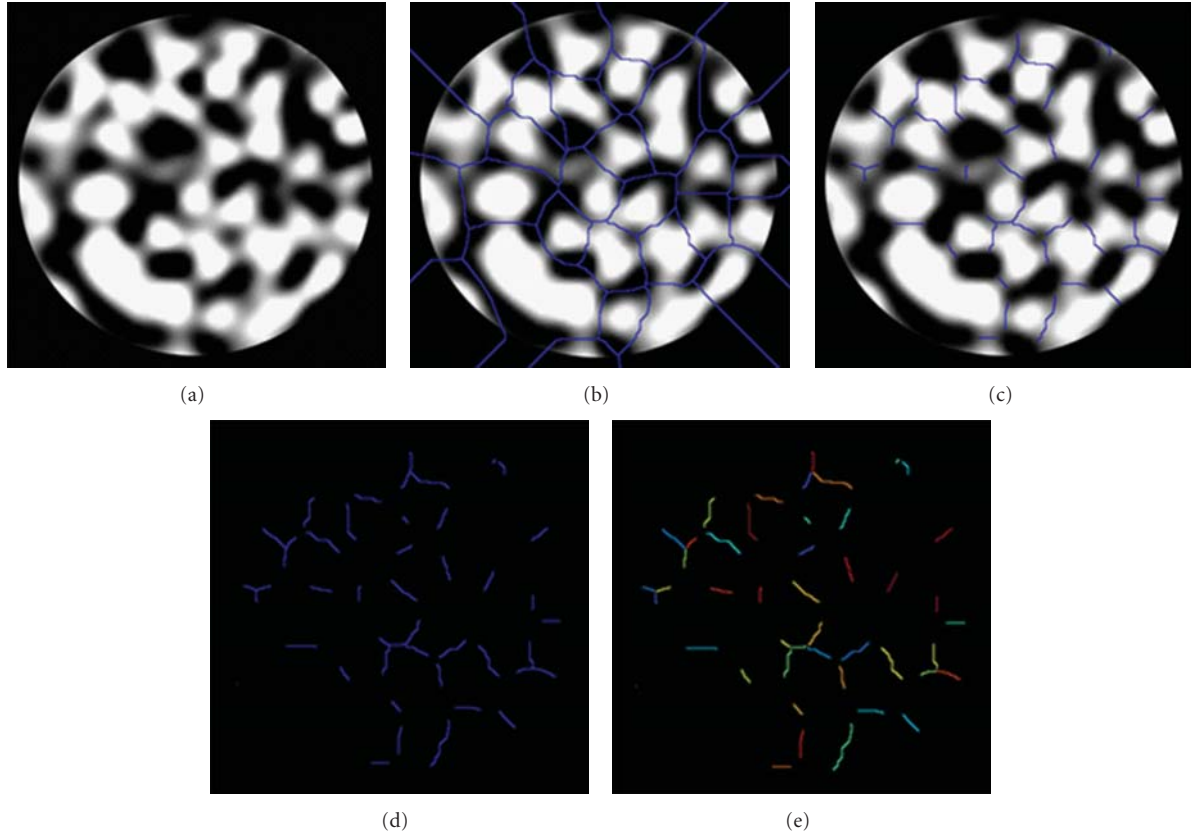


FIGURE 6: The process of extracting the sintering neck.

as a sintering neck (Figure 6(c)). Sintering necks were extracted (Figure 6(d)). Finally, different sintering necks were distinguished by employing texture segmentation and watershed [17] (Figure 6(e)).

In order to verify the uniformity of the statistical parameters in spatial location, the distribution of sintering neck size in each cross-section was summarized, as shown in Figure 7. Distribution suggests that once the time is determined, the size of sintering neck would not change with the spatial location in the direction of z-axis. Therefore, the neck growth with the average sizes at different moments during the sintering process (Figure 8) was analyzed.

Neck growth has great influence on shrinkage during solid state sintering and plays an important role in determining the main diffusion mechanism and calculating the diffusion coefficient of the material [18]. Therefore,

many scholars have researched sintering neck growth under various mechanisms in theory. Various forms of neck growth equation have been obtained [19].

The dynamics of stable neck-growth as summarized by Kucsyński is shown in the formula below:

$$\left(\frac{x}{a}\right)^n = \frac{F(T)}{a^m} t. \quad (1)$$

In our observation of the sintering process, grain growth was not obvious. We believe that when the degree of densification is low, the grain size changes only slightly. In other words, the average grain size is a constant. Moreover, Figure 9 shows that a good linear relationship of  $\ln(x) - \ln(t)$  is consistent with the conclusions of Kucsyński. The reciprocal of the slope of the straight line represents the sintering neck growth exponent  $n$ . Thus, according to our

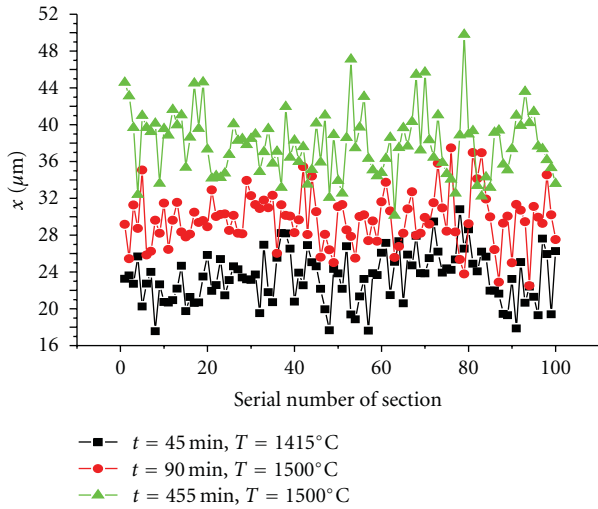


FIGURE 7: The distribution of sintering neck size in different sections.

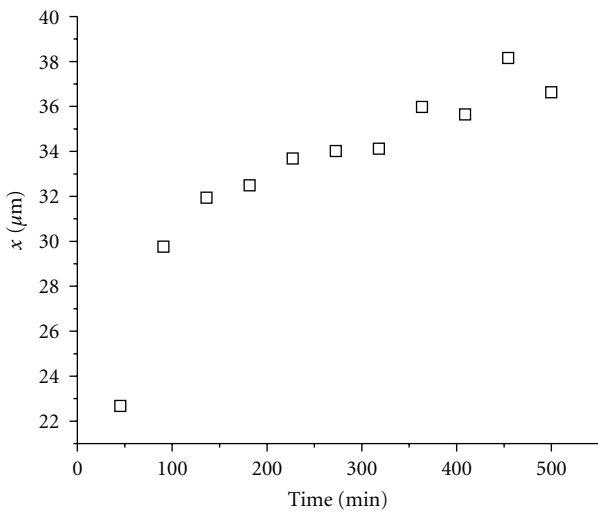


FIGURE 8: Mean neck size in different sintering times.

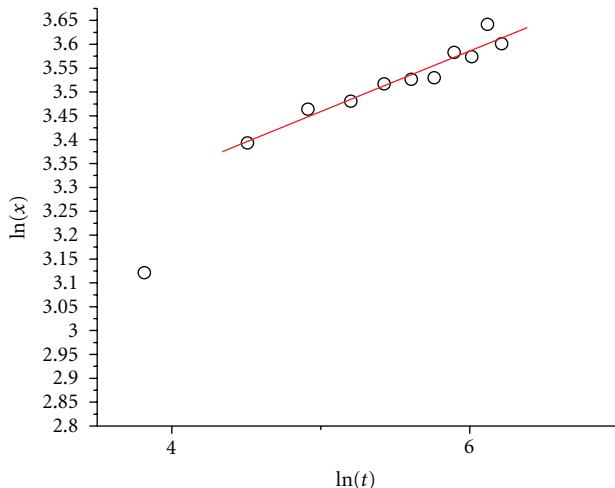


FIGURE 9: Double logarithm curve of mean neck size and time.

experimental results, if  $\ln(x) - \ln(t)$  slope of the line fitted by least squares is 0.127, then  $n = 7.87$ . This value is larger than the result deduced by the two-sphere model ( $n = 2-7$ ) [20]. In other words, the neck growth rate of irregularly shaped particles is smaller. Such condition can be attributed to that the shape of the particle has important influence on sintering neck growth rate. Takayasu and others pointed out that the sintering process of polyhedral particles is slower than that of the spherical particles [21]. The shape of particles determines the initial contact between particles and the size of dihedral angle, and all of these are important factors for sintering neck growth. In addition, compared to spherical particles, the more complex geometry of particles is, the greater the specific surface area is. Thus, the distance of surface diffusion is increased, and the effect of diffusion is reduced. During our experiments, the powders were irregularly shaped silicon carbide particles used in common industrial production. Inevitably, such shape displays disadvantages in neck growth, explaining why the sintering of spherical particles is better than the same process applied in irregularly shaped particles taking neck growth in consideration. However, from the view of phenomenology, the law of  $(x/a)^n = K \cdot t$  still exists during the sintering of irregular-shaped particles.

In addition, the value of  $n$  was close to 7. According to exponential criterion, such relationship is presented between different values of  $n$  and main mechanisms, such that  $n = 5$  indicates bulk diffusion taking the most part,  $n = 6$  indicates grain boundary diffusion, and  $n = 7$  indicates surface diffusion. In our experiment, surface diffusion played a leading role during sintering. The effect of surface diffusion on sintering nonmetallic powders (MgO,  $\text{Al}_2\text{O}_3$ ) was quantitatively estimated in 1989 [22], and it was concluded that the shrinkage between two particles is reduced 4-5 orders of magnitude for the participation of surface diffusion. Furthermore, it is pointed out that such a negative impact is more serious on ceramic powders with covalent bonds such as SiC, BN and AlN. In our experiment, the microstructure of the sample changed dramatically; however, the densification failed to reach high degrees. Integrating previous conclusions, the surface diffusion is believed to play a significant role in this phenomenon.

## 5. Conclusion

The microstructure evolution of irregular-shaped silicon carbide powder was observed in situ with the SR-CT technique during solid state sintering process.

- (1) A series of 2D and 3D reconstructed images of silicon carbide powder during sintering process was obtained. The microstructure evolution of silicon carbide powder and many sintering phenomena during three sintering stages were clearly observed.
- (2) Neck growth between irregularly shaped ceramic powders during sintering process was calculated. Neck growth exponent was identified as  $n = 7.87$ , and compared with the conclusion of the two-sphere model.

- (3) By comprehending different sintering mechanisms, a qualitative analysis of the reason why the neck growth exponent is bigger than the result of traditional theory has been conducted, explaining why the irregular-shaped particles reduce the rate of the sintering when compared with the spherical ones taking sintering neck growth into consideration. Meanwhile, the importance of the original shape of particles to neck growth has been pointed out experimentally.

## Foundation Item

Projects nos. 10902108, 10732080, and 10872190 supported by the National Nature Science Foundation of China, Project supported by the National Basic Research Program of China (973 Program, Grant no. 2007CB936800), and Project supported by BSRF Foundation.

## Acknowledgments

This paper was supported by the National Nature Science Foundation of China under Contract nos. 10902108, 10732080, and 10872190, the National Basic Research Program of China (973 Program) no. 2007CB936800, and BSRF Foundation. The authors warmly thank Zhu Peiping Huang Wanxia and Yuan Qingxi for their help in preparing the experiments, as well as Qu Hongyan, Li Yongcun for fruitful discussions and assistance in conducting the experiments.

## References

- [1] V. Luchinin and Y. Tairov, "Silicon carbide, a diamond-like material with controllable nanostructure-depending properties," *Nanoindustry*, vol. 1, no. 1, pp. 36–40, 2010.
- [2] R. Yilmaz, "Thermal diffusivity measurement of SiC fibre reinforced BMAS glass ceramic composites exposed mechanical damage," *Journal of the European Ceramic Society*, vol. 27, no. 2-3, pp. 1223–1228, 2007.
- [3] K. Y. Cheong and Z. Lockman, "Growth mechanism of cubic-silicon carbide nanowires," *Journal of Nanomaterials*, vol. 2009, Article ID 572865, 5 pages, 2009.
- [4] J. L. Shi, "Solid state sintering (I)—pore microstructural model and thermodynamic stability, densification equation," *Journal of the Chinese Ceramic Society*, vol. 25, no. 5, pp. 499–513, 1997.
- [5] J. L. Shi, "Solid state sintering (II)—relation between coarsening and densification and mass transport path," *Journal of the Chinese Ceramic Society*, vol. 25, no. 6, pp. 657–668, 1997.
- [6] J. L. Shi, "Solid state sintering (III)—experimental study on grain and pore growth, and densification of superfine zirconia powder compacts," *Journal of the Chinese Ceramic Society*, vol. 26, no. 1, pp. 1–13, 1998.
- [7] R. L. Coble, "Initial sintering of alumina and hematite," *Journal of American Ceramic Society*, vol. 41, no. 2, pp. 55–62, 1958.
- [8] R. L. Coble, "Sintering crystalline solids. I. intermediate and final state diffusion models," *Journal of Applied Physics*, vol. 32, no. 5, pp. 787–792, 1961.
- [9] R. L. Coble, "Sintering crystalline solids. II. experimental test of diffusion models in powder compacts," *Journal of Applied Physics*, vol. 32, no. 5, pp. 793–799, 1961.
- [10] M. Di Michiel, J. M. Merino, D. Fernandez-Carreiras et al., "Fast microtomography using high energy synchrotron radiation," *Review of Scientific Instruments*, vol. 76, no. 4, Article ID 043702, 7 pages, 2005.
- [11] X. Li, X. Hu, Y. Hu, and Y. Kan, "Synchrotron radiation tomography for reconstruction of layer structures and internal defects of composite materials," *Chinese Journal of Lasers B*, vol. 8, no. 6, pp. 503–508, 1999.
- [12] A. Vagnon, O. Lame, D. Bouvard, M. Di Michiel, D. Bellet, and G. Kapelski, "Deformation of steel powder compacts during sintering: correlation between macroscopic measurement and in situ microtomography analysis," *Acta Materialia*, vol. 54, no. 2, pp. 513–522, 2006.
- [13] L. Olmos, T. Takahashi, D. Bouvard et al., "Analysing the sintering of heterogeneous powder structures by in situ microtomography," *Philosophical Magazine*, vol. 89, no. 32, pp. 2949–2965, 2009.
- [14] F. Xu, X. F. Hu, Y. Niu, J. H. Zhao, and Q. X. Yuan, "In situ observation of grain evolution in ceramic sintering by SR-CT technique," *Transactions of Nonferrous Metals Society of China*, vol. 19, no. 3, pp. S684–S688, 2009.
- [15] P. Grunert, J. Mäurer, and W. Müller-Forell, "Accuracy of stereotactic coordinate transformation using a localisation frame and computed tomographic imaging—part I: influence of the mathematical and physical properties of the CT on the image of the rods of the localisation frame and the determination of their centres," *Neurosurgical Review*, vol. 22, no. 4, pp. 173–187, 1999.
- [16] T. G. Zhuang, "The theory and arithmetic of computed-tomography," in *CT Reconstruction Algorithm*, pp. 30–60, Shanghai Jiao Tong University Press, Shanghai, China, 1992.
- [17] R. C. Gonzalez, R. E. Woods, and S. L. Eddins, "Digital image processing using Matlab," in *Digital Image Processing*, M. D. Yan, Ed., pp. 315–317, Publishing House of Electronics Industry, Beijing, China, 2005.
- [18] D. L. Johnson, "New method of obtaining volume, grain-boundary, and surface diffusion coefficients from sintering data," *Journal of Applied Physics*, vol. 40, no. 1, pp. 192–200, 1969.
- [19] S. L. Kang, "Sintering-densification, grain growth, and microstructure," in *Sintering Theory*, J. Hill, Ed., pp. 51–52, Elsevier, London, UK, 2005.
- [20] J. S. Guo, "Powder sintering theory," in *Sintering Theory*, F. Xiao, Ed., pp. 41–43, Metallurgy Industry Press, Beijing, China, 1998.
- [21] T. Ikegami, "Early-stage sintering in a powder compact of polyhedral particles: I. Models," *Ceramics International*, vol. 25, no. 5, pp. 415–424, 1999.
- [22] R. Pampuch and J. Lis, "Specific aspects of sintering of micropowders," *Solid State Phenomena*, vol. 8-9, pp. 83–93, 1990.

## Research Article

# Li<sub>4</sub>Ti<sub>5</sub>O<sub>12</sub> Heattreated under Nitrogen Ambient with Outstanding Rate Capabilities

Rui Xu,<sup>1</sup> Junrong Li,<sup>2</sup> Zilong Tang,<sup>1</sup> and Zhongtai Zhang<sup>1</sup>

<sup>1</sup> State Key Laboratory of New Ceramics and Fine Processing, Department of Materials Science and Engineering of Tsinghua University, Beijing 100084, China

<sup>2</sup> China Astronaut Center, Beijing 100094, China

Correspondence should be addressed to Zilong Tang, tzl@tsinghua.edu.cn

Received 1 June 2010; Revised 12 September 2010; Accepted 28 September 2010

Academic Editor: Quanqin Dai

Copyright © 2011 Rui Xu et al. This is an open access article distributed under the Creative Commons Attribution License, which permits unrestricted use, distribution, and reproduction in any medium, provided the original work is properly cited.

The powders of spinel Li<sub>4</sub>Ti<sub>5</sub>O<sub>12</sub> were prepared by heat treating the mixture of rutile TiO<sub>2</sub> and Li acetate at 800°C for 3 h under a nitrogen atmosphere and, for comparison, under air as well. The powders heated under N<sub>2</sub> show a remarkably higher-rate capability and better cycle stability. The discharge capacity of Li<sub>4</sub>Ti<sub>5</sub>O<sub>12</sub> heated under N<sub>2</sub> at 19°C (corresponding to a 3.2-minute total discharge) reached 107 mA h g<sup>-1</sup>, 22 mA h g<sup>-1</sup> higher than that of Li<sub>4</sub>Ti<sub>5</sub>O<sub>12</sub> heated under air, which was 85 mA h g<sup>-1</sup>. The former material also shows a much better cycle stability, with no discharge capacity loss after 300 cycles at 6°C or 16.3°C. The results indicate that heat treatment under low-oxygen partial pressure atmosphere such as N<sub>2</sub> could significantly improve the high-rate performance of spinel Li<sub>4</sub>Ti<sub>5</sub>O<sub>12</sub>.

## 1. Introduction

There has been increasing interest in developing spinel lithium titanate (Li<sub>4</sub>Ti<sub>5</sub>O<sub>12</sub>) as a potential anode for application in lithium ion rechargeable batteries [1–14] due to its long cycle life, excellent lithium ion intercalation and deintercalation reversibility, and “zero-strain” intercalation characteristics. Spinel Li<sub>4</sub>Ti<sub>5</sub>O<sub>12</sub> has a main discharge plateau of about 1.55 V versus lithium, which makes it a very promising anode material for many lithium ion batteries using high-voltage materials such as LiCoO<sub>2</sub> and LiMnO<sub>2</sub> as their cathodes. However, although spinel Li<sub>4</sub>Ti<sub>5</sub>O<sub>12</sub> exhibits no structural change during charge/discharge process, its electron conductivity is low [15]. This affects its rate capability and cycle stability, for which the experimental values are not nearly as good as the theoretical ones. In order to increase Li<sub>4</sub>Ti<sub>5</sub>O<sub>12</sub> conductivity, several strategies have been taken, including incorporating a conducting second phase such as Ag [16], Cu [17], CuO<sub>x</sub> [18], or Li<sub>2</sub>CuTi<sub>3</sub>O<sub>8</sub> [19], doping with alien-valent metal ions such as Ta<sup>5+</sup> [20] or Al<sup>3+</sup> [21], and synthesizing nanosized [22, 23] Li<sub>4</sub>Ti<sub>5</sub>O<sub>12</sub>. Another effective method is heat treating Li<sub>4</sub>Ti<sub>5</sub>O<sub>12</sub> under a reduced or low-oxygen partial pressure atmosphere [24].

In this work, the electrochemical characteristics of Li<sub>4</sub>Ti<sub>5</sub>O<sub>12</sub> heat treated under N<sub>2</sub> atmosphere were studied, with emphasis on their high-rate properties. X-ray diffraction (XRD) analysis, scanning electron microscopy (SEM) observations, and galvanostatic discharge/charge tests were used to characterize the material.

## 2. Experimental

Spinel Li<sub>4</sub>Ti<sub>5</sub>O<sub>12</sub> powders were prepared by using 9 g commercially available rutile TiO<sub>2</sub> (AR) and 12 g Li acetate (AR) [25]. The starting materials were thoroughly mixed in ethanol solvent and dried at 100°C for 7 h. The dried and mixed product was then heated at 800°C for 3 h under air or N<sub>2</sub> atmosphere, followed by natural cooling in the furnace.

The morphologies of the as-prepared powders were characterized by scanning electron microscopy (SEM) performed on Hitachi S4500. Powder X-ray diffraction (XRD) was performed on a Rigaku D/max-RB diffractometer operating in transmission mode with Cu K $\alpha$  radiation ( $\lambda = 1.5418 \text{ \AA}$ ). The BET-specific surface area was measured with a Quantachrome NOVA 4000 system, using the N<sub>2</sub> absorption-desorption method at liquid nitrogen temperature.

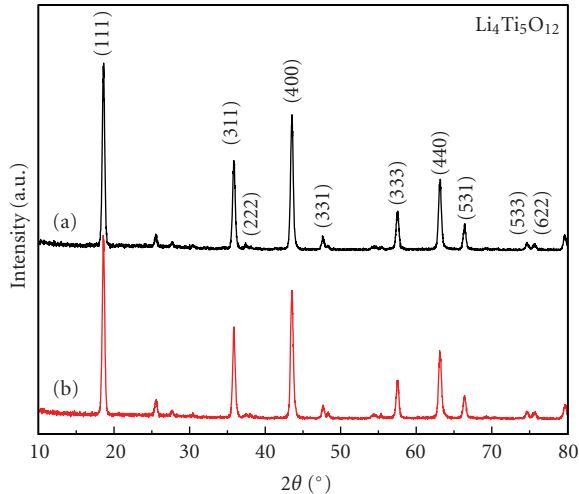


FIGURE 1: X-ray diffraction patterns of  $\text{Li}_4\text{Ti}_5\text{O}_{12}$  heat treated under (a)  $\text{N}_2$  and (b) air.

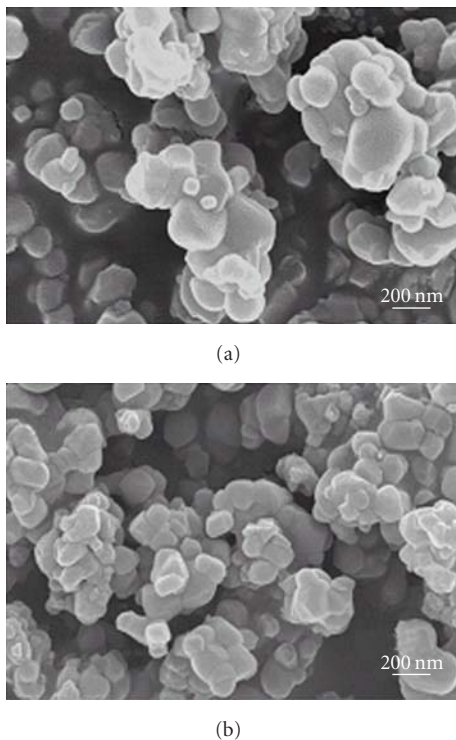


FIGURE 2: SEM images of  $\text{Li}_4\text{Ti}_5\text{O}_{12}$  heat treated under (a) air and (b)  $\text{N}_2$ .

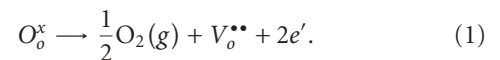
To fabricate the cathodes for the battery test cells, the as-prepared  $\text{Li}_4\text{Ti}_5\text{O}_{12}$  powders, Super P carbon black, and polyvinylidene fluoride (PVDF) binder were mixed homogeneously in a weight ratio of 80:10:10 in an N-methyl pyrrolidinone (NMP) solvent. The electrode films, which used carbon-covered aluminum foil as the current collector, were fabricated using the tape-casting method [23]. The loading of active material was  $1\text{-}2\text{ mg cm}^{-2}$ . The coin-type half cell (CR2032 size) contained the as-fabricated electrode

film, a lithium metal counter electrode, a microporous polyethylene separator, and electrolyte of a 1 M solution of  $\text{LiPF}_6$  in ethylene carbonate/dimethyl carbonate (EC/DMC) (1:1 vol %; Merck). The cell was constructed and handled in an Ar-filled vacuum glove box.

The discharge/charge tests were carried out using a LAND Celltest 2001 A (Wuhan, China) system between 2.5 and 1 V versus the Li counter electrode. First, the test cell was discharged for  $\text{Li}^+$  ions to intercalate into the cathode, and then the test cell was charged and held at 2.5 V to fully charge before discharge. The constant current charge and discharge rates are the same. Cyclic voltammogram was recorded from 1.0 to 2.5 V at a scan rate of  $10\text{ mV s}^{-1}$ , using IM6e electrochemical workstation (Germany).

### 3. Results and Discussion

Figure 1 shows the XRD patterns of as-prepared  $\text{Li}_4\text{Ti}_5\text{O}_{12}$  powders after heat treatment under air or  $\text{N}_2$  atmosphere at  $800^\circ\text{C}$  for 3 h. The diffraction peaks of both samples can be indexed as spinel lithium titanate (cubic phase, space group  $\text{Fd}\bar{3}\text{m}$  space group), except two small peaks at around  $25^\circ$  and  $55^\circ$  which probably correspond to remaining unreacted  $\text{TiO}_2$ . The only difference between the two XRD patterns is that the diffraction peaks for the sample heated under  $\text{N}_2$  are slightly shifted to the lower  $2\theta$  values compared to the one heated under air. This indicates that the lattice parameter of the former is larger than that of the latter. This is in good agreement with previous results of  $\text{Li}_4\text{Ti}_5\text{O}_{12}$  heat treated under  $\text{H}_2/\text{Ar}$  atmosphere [24]. The larger lattice parameter for  $\text{Li}_4\text{Ti}_5\text{O}_{12}$  powders heat treated under  $\text{N}_2$  atmosphere could be attributed to the reduction of some  $\text{Ti}^{4+}$  ions into  $\text{Ti}^{3+}$  when heated under low-oxygen partial pressure atmosphere, as the sizes of  $\text{Ti}^{3+}$  ions are larger than those of  $\text{Ti}^{4+}$ . The presence of  $\text{Ti}^{3+}$  ions could also explain the darker color of  $\text{Li}_4\text{Ti}_5\text{O}_{12}$  powders heat treated under  $\text{N}_2$  atmosphere, which is light yellow (while the sample heated under air is white). It is believed that the reduction of some  $\text{Ti}^{4+}$  ions into  $\text{Ti}^{3+}$  is ascribed to the increase in electron concentration, which results from nonstoichiometry of  $\text{Li}_4\text{Ti}_5\text{O}_{12}$  at low-oxygen partial pressures.



This relatively high electron concentration of  $\text{Li}_4\text{Ti}_5\text{O}_{12}$  treated under reducing or low-oxygen partial pressure atmosphere compared to that of  $\text{Li}_4\text{Ti}_5\text{O}_{12}$  treated under air has been noted in previous works [20, 24].

The SEM images of the two samples are shown in Figure 2. The diameter of the  $\text{Li}_4\text{Ti}_5\text{O}_{12}$  particle treated under air (Figure 2(a)) was almost the same as that treated under  $\text{N}_2$  atmosphere (Figure 2(b)), in agreement with BET-specific surface areas of the two samples, which are  $3.70\text{ m}^2\text{ g}^{-1}$  and  $3.78\text{ m}^2\text{ g}^{-1}$ , respectively.

The charge/discharge properties and rate capabilities of the test cells containing  $\text{Li}_4\text{Ti}_5\text{O}_{12}$  heat treated under air or  $\text{N}_2$  atmosphere as the electrode material were tested and analyzed. A comparison of the rate capabilities of the test cells is shown in Figure 3(a); the data shows that extremely

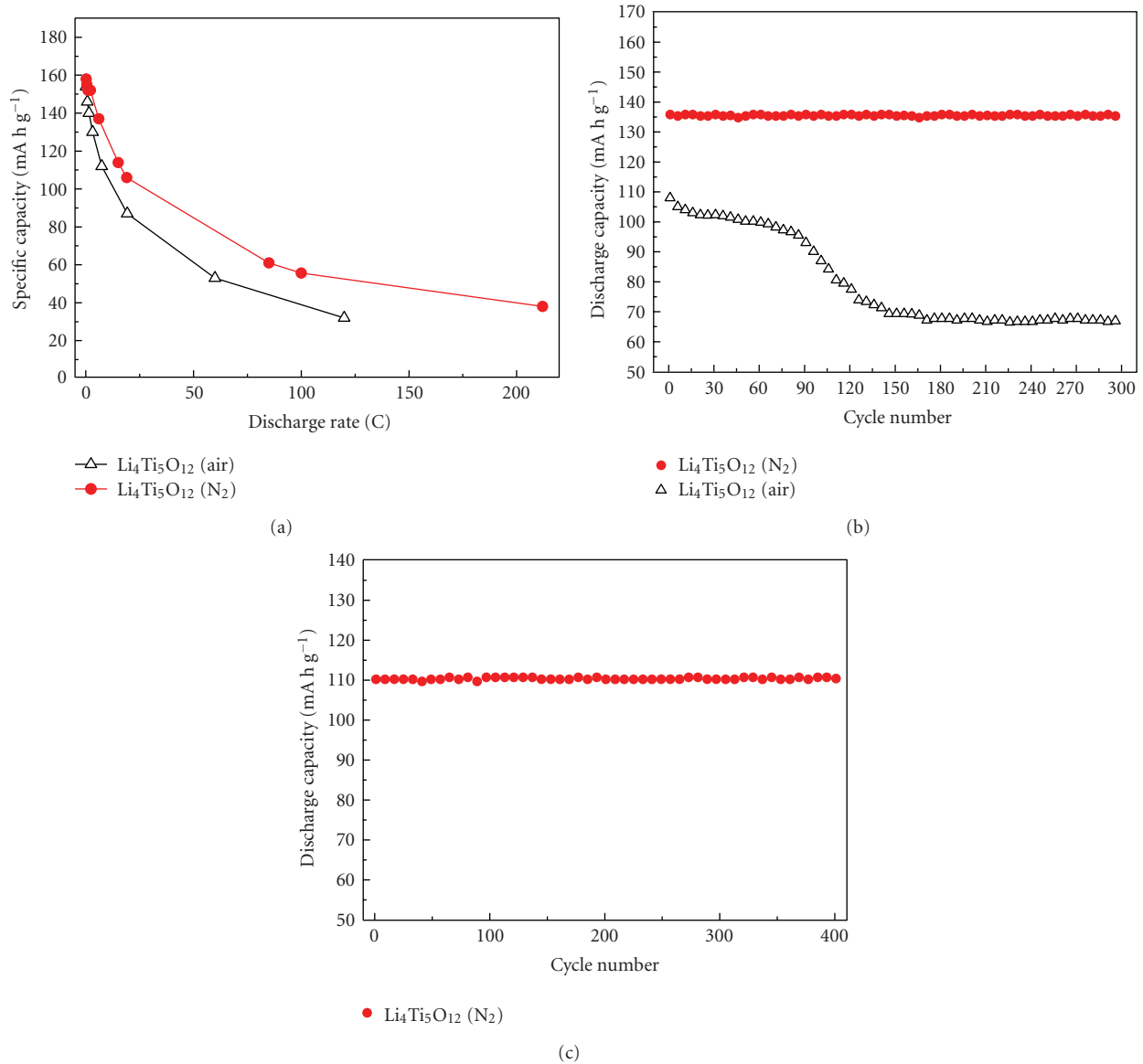


FIGURE 3: Electrochemical properties of  $\text{Li}_4\text{Ti}_5\text{O}_{12}$  heat treated under air or  $\text{N}_2$  ambient. (a) Discharge capacity of the two samples under various rates. (b) Capacity retentions of the two samples when performing full charge/discharge cycles at 6 C. (c) Capacity retentions of  $\text{Li}_4\text{Ti}_5\text{O}_{12}$  heat treated under  $\text{N}_2$  ambient when performing full charge/discharge cycles at 16.3 C.

high rates can be achieved for  $\text{Li}_4\text{Ti}_5\text{O}_{12}$  heat treated under  $\text{N}_2$  atmosphere. It can be seen that at low discharge rates (<0.5 C), the specific capacities of the two test cells are very close. As the discharge rate increases, the capacity of the  $\text{Li}_4\text{Ti}_5\text{O}_{12}$  heat treated under  $\text{N}_2$  atmosphere is remarkably higher than that heated under air. The former could reach a discharge capacity of 107 mA h g<sup>-1</sup> at 19 C (1680 mA g<sup>-1</sup> of current density), 22 mA h g<sup>-1</sup> higher than the latter, which had a discharge capacity of only 85 mA h g<sup>-1</sup>. At a 85 C rate (4920 mA g<sup>-1</sup> of current density), a capacity of more than 60 mA h g<sup>-1</sup> could still be obtained, and a capacity of nearly 40 mA h g<sup>-1</sup> was achieved at a 212 C (8240 mA g<sup>-1</sup> of current density) rate for the  $\text{Li}_4\text{Ti}_5\text{O}_{12}$  heat treated under  $\text{N}_2$  atmosphere. This result is within expectations because

the  $\text{Li}_4\text{Ti}_5\text{O}_{12}$  heat treated under  $\text{N}_2$  atmosphere has an increased electron concentration. The comparison of the rate capabilities of the test cells confirms that the heat treatment under  $\text{N}_2$  atmosphere for  $\text{Li}_4\text{Ti}_5\text{O}_{12}$  can largely improve its rate capability.

The change in discharge capacities with cycle numbers of the two samples at a 6 C rate (800 mA g<sup>-1</sup> of current density) is shown in Figure 3(b), respectively. It shows that the cycling performance of the  $\text{Li}_4\text{Ti}_5\text{O}_{12}$  heat treated under  $\text{N}_2$  atmosphere is much better than that heat treated under air. After charging/discharging at 6 C for 300 cycles, the former sample still remains 100% in discharge capacity, showing 135 mA h g<sup>-1</sup>, while the latter sample capacity slowly fades as the cycle number increases and quickly drops

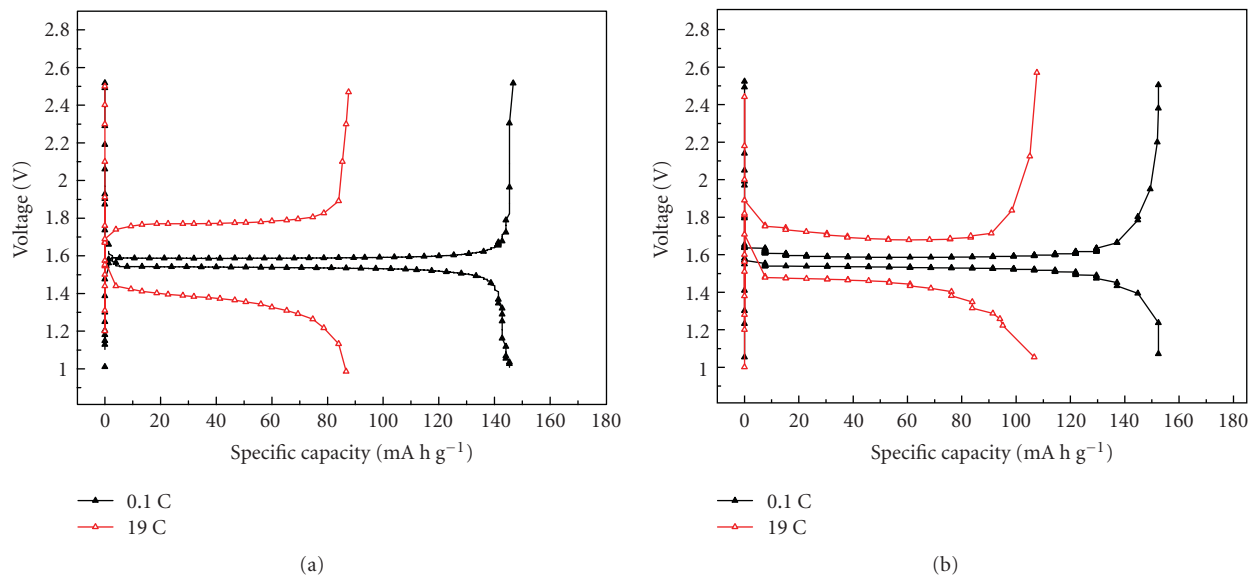


FIGURE 4: Charge discharge performance (0.1 C) of  $\text{Li}_4\text{Ti}_5\text{O}_{12}$  heat treated under (a) air and (b)  $\text{N}_2$ .

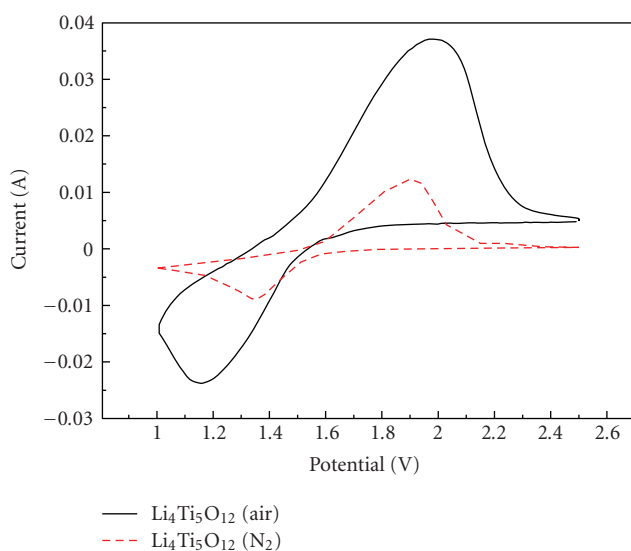


FIGURE 5: Cyclic voltammograms of test cells containing  $\text{Li}_4\text{Ti}_5\text{O}_{12}$  heat treated under air or  $\text{N}_2$  atmosphere as cathode materials at scan rate of  $10 \text{ mV s}^{-1}$ .

after 90 cycles. After about 140 cycles, the discharge capacity retention of the  $\text{Li}_4\text{Ti}_5\text{O}_{12}$  heat treated under air is only 68%, showing  $67 \text{ mA h g}^{-1}$ . The high-rate cycling stability for the  $\text{Li}_4\text{Ti}_5\text{O}_{12}$  heat treated under  $\text{N}_2$  atmosphere at 16.3 C ( $1650 \text{ mA g}^{-1}$  of current density) is also excellent. As shown in Figure 3(c), it keeps 100% in discharge capacity after 400 cycles, showing  $109 \text{ mA h g}^{-1}$ . From these results, it can be concluded that heat treatment under a reducing atmosphere such as  $\text{N}_2$  could not only improve  $\text{Li}_4\text{Ti}_5\text{O}_{12}$  high-rate capability significantly, but could also greatly enhance its cycling stability at high rates.

Figure 4 shows the charge/discharge curves for the test cells at 0.1 C ( $7 \text{ mA g}^{-1}$  of current density) and 19 C ( $1680 \text{ mA g}^{-1}$  of current density). When comparing the voltage profile of  $\text{Li}_4\text{Ti}_5\text{O}_{12}$  heat treated under  $\text{N}_2$  atmosphere with the one of that heat treated under air, it can be seen that the former sample has more sloping charge/discharge curves. This indicates that the  $\text{Li}_4\text{Ti}_5\text{O}_{12}$  heat treated under  $\text{N}_2$  has a more evident pseudocapacitive faradaic kinetics, which is due to its higher electron conductivity. From Figure 4, it can be observed that when charging and discharging at a rate of 0.1 C, the capacity and plateau voltage of the two cells were very close: around  $150 \text{ mA h g}^{-1}$  and 1.60 V, respectively. At 19 C, the capacity of the  $\text{Li}_4\text{Ti}_5\text{O}_{12}$  heat treated under air was much smaller than that of the  $\text{Li}_4\text{Ti}_5\text{O}_{12}$  heat treated under  $\text{N}_2$ . At 19 C, both test cells have more sloping voltage profiles than at 0.1 C, indicating a more evident surface-confined charge-transfer kinetics (known as the pseudocapacitive faradaic kinetics) existing along with diffusion-controlled kinetics as lithium intercalating/deintercalating in  $\text{Li}_4\text{Ti}_5\text{O}_{12}$ . Due to their higher polarization under higher rates, both cells charge plateau voltages are higher than those charging at low rates, and meanwhile the discharge plateau voltages are lower.

Cyclic voltammogram was recorded, as shown in Figure 5, from 1.0 to 2.5 V at a scan rate as high as  $10 \text{ mV s}^{-1}$ . The two samples both have broad redox peaks under a high scan rate, which is in good agreement with the sloping voltage profile during the galvanostatic discharge/charge cycles at high rates, indicating a concurrence of both pseudocapacitive lithium intercalation mechanism and diffusion-controlled kinetics during the process. The two redox peaks of the  $\text{Li}_4\text{Ti}_5\text{O}_{12}$  heat treated under  $\text{N}_2$  atmosphere appear at 1.35 V and 1.9 V (versus  $\text{Li}^+/\text{Li}$ , depending on the scan rate), while those of  $\text{Li}_4\text{Ti}_5\text{O}_{12}$  heat treated under air appear at 1.15 V and 2.0 V. The results show that under a high charge/discharge rate, the  $\text{Li}_4\text{Ti}_5\text{O}_{12}$  heat treated under  $\text{N}_2$

atmosphere has relatively low polarization compared to that heat treated under air, which results from its higher electron concentration. This lower polarization under high charge/discharge rates of the  $\text{Li}_4\text{Ti}_5\text{O}_{12}$  heat treated under  $\text{N}_2$  atmosphere leads to its better rate capability.

#### 4. Conclusions

The spinel  $\text{Li}_4\text{Ti}_5\text{O}_{12}$  powders were prepared by heat treating the mixture of rutile  $\text{TiO}_2$  and Li acetate under nitrogen atmosphere, and, for comparison, under air. The two samples have similar particle size and specific surface area, but the powders heated under  $\text{N}_2$  showed better rate capability and cycle stability in comparison with those heated under air. The discharge capacity of  $\text{Li}_4\text{Ti}_5\text{O}_{12}$  heated under air at 19 C was  $85 \text{ mA h g}^{-1}$ , while the capacity of  $\text{Li}_4\text{Ti}_5\text{O}_{12}$  heated under  $\text{N}_2$  reached  $107 \text{ mA h g}^{-1}$ . Meanwhile, the cycle stability of the  $\text{Li}_4\text{Ti}_5\text{O}_{12}$  heated under  $\text{N}_2$  was also much better than that of the sample heated under air, indicating that heat treatment under reducing or low-oxygen partial pressure atmosphere such as  $\text{N}_2$  could greatly improve the high-rate performance of spinel  $\text{Li}_4\text{Ti}_5\text{O}_{12}$ .

#### Acknowledgments

R. Xu thanks F. Y. Kang, L. Zou, and X. Fan for the help with electrochemical workstation for cyclic voltammogram measurements and AC impedance measurements. Language revision help from H. Howard is gratefully acknowledged. The Support from the Natural Science Foundation of China (no. 50602050) and the National High Technology Research and Development Program of China (863 Program, no. 2007AA03Z235) is gratefully acknowledged.

#### References

- [1] T. Ohzuku, A. Ueda, N. Yamamoto, and Y. Iwakoshi, "Factor affecting the capacity retention of lithium-ion cells," *Journal of Power Sources*, vol. 54, no. 1, pp. 99–102, 1995.
- [2] K. M. Colbow, J. R. Dahn, and R. R. Haering, "Structure and electrochemistry of the spinel oxides  $\text{LiTi}_2\text{O}_4$  and  $\text{Li}^{3/4}\text{Ti}^{5/3}\text{O}_4$ ," *Journal of Power Sources*, vol. 26, no. 3, pp. 397–402, 1989.
- [3] K. Zaghib, M. Simoneau, M. Armand, and M. Gauthier, "Electrochemical study of  $\text{Li}_4\text{Ti}_5\text{O}_{12}$  as negative electrode for Li-ion polymer rechargeable batteries," *Journal of Power Sources*, vol. 81–82, pp. 300–305, 1999.
- [4] A. Guerfi, S. Sévigny, M. Lagacé, P. Hovington, K. Kinoshita, and K. Zaghib, "Nano-particle  $\text{Li}_4\text{Ti}_5\text{O}_{12}$  spinel as electrode for electrochemical generators," *Journal of Power Sources*, vol. 119, pp. 88–94, 2003.
- [5] T. Ohzuku, A. Ueda, and N. Yamamoto, "Zero-strain insertion material of  $\text{Li}[\text{Li}_{1/3}\text{Ti}_{5/3}]\text{O}_4$  for rechargeable lithium cells," *Journal of the Electrochemical Society*, vol. 142, no. 5, pp. 1431–1435, 1995.
- [6] M. M. Thackeray, "Structural considerations of layered and spinel lithiated oxides for lithium ion batteries," *Journal of the Electrochemical Society*, vol. 142, no. 8, pp. 2558–2563, 1995.
- [7] E. Ferg, R. J. Gummow, A. de Kock, and M. M. Thackeray, "Spinel anodes for lithium-ion batteries," *Journal of the Electrochemical Society*, vol. 141, no. 11, pp. L147–L150, 1994.
- [8] T. Ohzuku, Y. Iwakoshi, and K. Sawai, "Formation of lithium-graphite intercalation compounds in nonaqueous electrolytes and their application as a negative electrode for a lithium ion (shuttlecock) cell," *Journal of the Electrochemical Society*, vol. 140, no. 9, pp. 2490–2497, 1993.
- [9] K. Zaghib, M. Armand, and M. Gauthier, "Electrochemistry of anodes in solid-state Li-ion polymer batteries," *Journal of the Electrochemical Society*, vol. 145, no. 9, pp. 3135–3140, 1998.
- [10] S. Scharner, W. Weppner, and P. Schmid-Beurmann, "Evidence of two-phase formation upon lithium insertion into the  $\text{Li}_{1.33}\text{Ti}_{1.67}\text{O}_4$  spinel," *Journal of the Electrochemical Society*, vol. 146, no. 3, pp. 857–861, 1999.
- [11] D. Peramunage and K. M. Abraham, "Preparation of micron-sized  $\text{Li}_4\text{Ti}_5\text{O}_{12}$  and its electrochemistry in polyacrylonitrile electrolyte-based lithium cells," *Journal of the Electrochemical Society*, vol. 145, no. 8, pp. 2609–2615, 1998.
- [12] S. Huang, Z. Wen, X. Zhu, and X. Yang, "Research on  $\text{Li}_4\text{Ti}_5\text{O}_{12}/\text{Cu}_x\text{O}$  composite anode materials for lithium-ion batteries," *Journal of the Electrochemical Society*, vol. 152, no. 7, pp. A1301–A1305, 2005.
- [13] V. S. Hernandez, "Stoichiometry, structures and polymorphism of spinel-like phases,  $\text{Li}_{1.33x}\text{Zn}_{2-2x}\text{Ti}_{1+0.67x}\text{O}_4$ ," *Journal of Materials Chemistry*, vol. 6, no. 9, pp. 1533–1536, 1996.
- [14] M. M. Thackeray, P. J. Johnson, L. A. de Picciotto, P. G. Bruce, and J. B. Goodenough, "Electrochemical extraction of lithium from  $\text{LiMn}_2\text{O}_4$ ," *Materials Research Bulletin*, vol. 19, no. 2, pp. 179–187, 1984.
- [15] A. Guerfi, P. Charest, K. Kinoshita, M. Perrier, and K. Zaghib, "Nano electronically conductive titanium-spinel as lithium ion storage negative electrode," *Journal of Power Sources*, vol. 126, no. 1–2, pp. 163–168, 2004.
- [16] S. Huang, Z. Wen, X. Zhu, and Z. Gu, "Preparation and electrochemical performance of Ag doped  $\text{Li}_4\text{Ti}_5\text{O}_{12}$ ," *Electrochemistry Communications*, vol. 6, no. 11, pp. 1093–1097, 2004.
- [17] S. Huang, Z. Wen, B. Lin, J. Han, and X. Xu, "The high-rate performance of the newly designed  $\text{Li}_4\text{Ti}_5\text{O}_{12}/\text{Cu}$  composite anode for lithium ion batteries," *Journal of Alloys and Compounds*, vol. 457, no. 1–2, pp. 400–403, 2008.
- [18] S. Huang, Z. Wen, X. Zhu, and X. Yang, "Research on  $\text{Li}_4\text{Ti}_5\text{O}_{12}/\text{Cu}_x\text{O}$  composite anode materials for lithium-ion batteries," *Journal of the Electrochemical Society*, vol. 152, no. 7, pp. A1301–A1305, 2005.
- [19] D. Wang, H. -Y. Xu, M. Gu, and C. -H. Chen, " $\text{Li}_2\text{CuTi}_3\text{O}_8 - \text{Li}_4\text{Ti}_5\text{O}_{12}$  double spinel anode material with improved rate performance for Li-ion batteries," *Electrochemistry Communications*, vol. 11, no. 1, pp. 50–53, 2009.
- [20] J. Wolfenstine and J. L. Allen, "Electrical conductivity and charge compensation in Ta doped  $\text{Li}_4\text{Ti}_5\text{O}_{12}$ ," *Journal of Power Sources*, vol. 180, no. 1, pp. 582–585, 2008.
- [21] H. Zhao, Y. Li, Z. Zhu, J. Lin, Z. Tian, and R. Wang, "Structural and electrochemical characteristics of  $\text{Li}_{4-x}\text{Al}_x\text{Ti}_5\text{O}_{12}$  as anode material for lithium-ion batteries," *Electrochimica Acta*, vol. 53, no. 24, pp. 7079–7083, 2008.
- [22] L. Kavana and M. Grätzel, "Facile synthesis of nanocrystalline  $\text{Li}_4\text{Ti}_5\text{O}_{12}$  (Spinel) exhibiting fast Li insertion," *Electrochemical and Solid-State Letters*, vol. 5, no. 2, pp. A39–A42, 2002.
- [23] J. Li, Z. Tang, and Z. Zhang, "Controllable formation and electrochemical properties of one-dimensional nanostructured spinel  $\text{Li}_4\text{Ti}_5\text{O}_{12}$ ," *Electrochemistry Communications*, vol. 7, no. 9, pp. 894–899, 2005.

- [24] J. Wolfenstine, U. Lee, and J. L. Allen, "Electrical conductivity and rate-capability of  $\text{Li}_4\text{Ti}_5\text{O}_{12}$  as a function of heat-treatment atmosphere," *Journal of Power Sources*, vol. 154, no. 1, pp. 287–289, 2006.
- [25] J. Kim and J. Cho, "Spinel  $\text{Li}_4\text{Ti}_5\text{O}_{12}$  nanowires for high-rate Li-ion intercalation electrode," *Electrochemical and Solid-State Letters*, vol. 10, no. 3, pp. A81–A84, 2007.